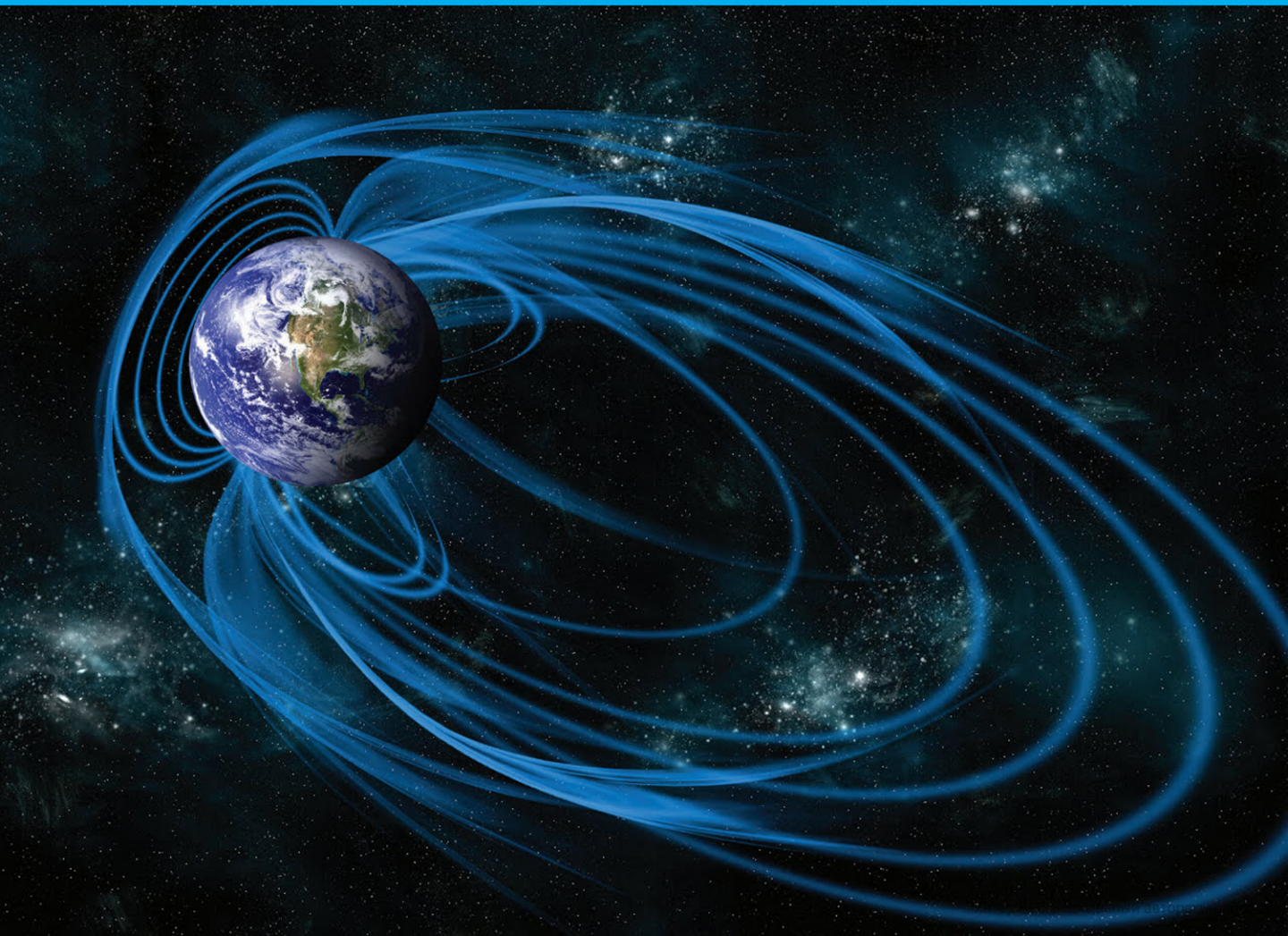Second Edition

Foundations of
Geophysical Electromagnetic
Theory and Methods

Michael S. Zhdanov

FOUNDATIONS OF GEOPHYSICAL ELECTROMAGNETIC THEORY AND METHODS

FOUNDATIONS OF GEOPHYSICAL ELECTROMAGNETIC THEORY AND METHODS

Second Edition

MICHAEL S. ZHDANOV
University of Utah,
Salt Lake City, UT, United States

Notices

Knowledge and best practice in this field are constantly changing. As new research and experience broaden our understanding, changes in research methods, professional practices, or medical treatment may become necessary.

Practitioners and researchers must always rely on their own experience and knowledge in evaluating and using any information, methods, compounds, or experiments described herein. In using such information or methods they should be mindful of their own safety and the safety of others, including parties for whom they have a professional responsibility.

To the fullest extent of the law, neither the Publisher nor the authors, contributors, or editors, assume any liability for any injury and/or damage to persons or property as a matter of products liability, negligence or otherwise, or from any use or operation of any methods, products, instructions, or ideas contained in the material herein.

For information on all Elsevier publications
visit our website at https://www.elsevier.com/books-and-journals

Working together
to grow libraries in
developing countries

www.elsevier.com • www.bookaid.org

CONTENTS

PART 1 INTRODUCTION TO FIELD THEORY

PART 2   FOUNDATIONS OF ELECTROMAGNETIC THEORY

PART 3 INVERSION AND IMAGING OF ELECTROMAGNETIC FIELD DATA

PART 4   GEOPHYSICAL ELECTROMAGNETIC METHODS

PREFACE TO THE SECOND EDITION

This book is a new edition of my original book entitled "Geophysical Electromagnetic Theory and Methods," published in 2009.

Over the last years significant progress has been made in electromagnetic geophysics. In this new edition, I have included additional material reflecting the recent developments in geophysical electromagnetic methods. A special focus is given to recent advances in marine and airborne electromagnetic methods.

Several new sections have been included. They are related to the new effective methods of electromagnetic modeling (e.g., contraction preconditioning in integral equation and finite difference numerical schemes and an edge-based finite element method) and inversion (e.g., efficient Fréchet derivative calculation of the forward modeling operator).

The section on the induced polarization (IP) method is significantly expanded. It now includes a generalized effective-medium theory of the IP effect (GEMTIP) based on a model of the multiphase heterogeneous medium filled with elliptical inclusions. A new section on nonlinear regularized inversion of IP data using a GEMTIP model has also been added in the chapter on direct current and induced polarization methods. A chapter on 3D magnetotelluric (MT) inversion has been expanded to include a new section describing the MT phase tensor and its inversion.

This new edition includes also a separate chapter dedicated to the principles and new developments in airborne electromagnetic methods. Several very successful and important techniques for mineral exploration, based on airborne electromagnetic (AEM) methods, have been introduced over the last decades, including the airborne natural field method (e.g., ZTEM). However, until recently, the interpretation of AEM data was mostly based on one-dimensional layered earth models. This limited the effectiveness of the airborne surveys in exploration for natural resources significantly, because the geological structure of typical exploration targets is three-dimensional. The recent development of rigorous three-dimensional methods of the inversion of AEM data has resulted in a paradigm change in airborne electromagnetics by allowing the geophysicist to produce undistorted images of the targets. This recent development is outlined in a new book chapter as well.

Another chapter of the new edition presents several case histories on the successful application of electromagnetic methods for tectonic studies and for mineral, oil and gas exploration. This new chapter complements the theoretical parts of the book by providing an illustration of how advanced electromagnetic theory and methods can improve out ability to see "unseeable" subsurface geological formations.

Salt Lake City, Utah   Michael S. Zhdanov
May, 2017

PREFACE

Geophysical methods are based on studying the propagation of the different physical fields within the earth's interior. One of the most widely used fields in geophysics is the electromagnetic field generated by natural or artificial (controlled) sources. Electromagnetic methods comprise one of the three principle technologies in applied geophysics (the other two being seismic methods and potential field methods). In this book the author presents both the foundations and the most recent achievements of electromagnetic geophysical methods in the framework of a unified systematic exposition.

The book is divided into four parts covering the foundations of field theory and its applications to applied electromagnetic geophysics, including new emerging methods of marine electromagnetic exploration. The first part is an introduction to field theory required for understanding the basics of geophysical electromagnetic theory. The second part contains all the principal elements of geophysical electromagnetic theory from a description of the fundamental Maxwell's equations to modern methods of modeling electromagnetic fields in complex 3-D geoelectrical formations. The following part, Part 3, deals with important aspects of the electromagnetic methods, which include principles of the regularized solution of ill-posed inverse electromagnetic problems, one-dimensional and multidimensional imaging and inversion of electromagnetic data, and general interpretation techniques. The final part, Part 4, covers specific geophysical electromagnetic methods.

While the foundations of electromagnetic theory, used in geophysical methods, were established more than a century and a half ago in the works of Ampere, Faraday, Maxwell, Gauss, and many other great scientists, the most remarkable advances in geophysical exploration technology were made at the end of the 20th century and are continuing to be made in the 21st century. In this book I emphasize the link between the great discoveries in physics and mathematics and practical advances in exploration methods. I also would like to attract the attention of the readers to the fact that our understanding of the basic laws of electromagnetism has been changing recently.

The fundamental system of electromagnetic field equations, Maxwell's equations, was developed as a generalization of the basic laws of electromagnetism established in the first half of the 19th century. In the framework of classical theory, the electromagnetic field is described by the electric and magnetic vector fields, and Maxwell's equations represent a system of differential equations with respect to these vector fields.

During the last decade, an alternative approach to the formulation of Maxwell's equations has been developed. This approach is based on the algebraic theory of differential forms, and it results in a very compact and symmetric system of differential form equations which is also presented in the book (Chapters 1 and 2, Appendices A and B). This new approach to the formulation and understanding of the basic properties of the laws of electromagnetism has a strong potential to stimulate the future development of electromagnetic geophysics. That is why I found it useful to include this advanced material in the manuscript. At the same time, in Chapter 3, I present a classical description of electromagnetic theory, using the traditional Gibbsian vector form of Maxwell's equations. The reader who is more interested in practical applications than in a new theoretical development in electromagnetism may skip the sections of Chapters 1 and 2 dedicated to differential form representation, and begin reading directly with the traditional theory of Maxwell's equations, presented in Chapter 3.

Another critical development of electromagnetic geophysics during the past several decades has been taking place in the computational methods associated both with forward modeling and with the inversion of geophysical data. We consider different aspects of forward modeling in Chapters 4, 5, and 6, starting with simple models of electromagnetic induction in the earth, examining field propagation in horizontally stratified media, and developing advanced methods of numerical computer simulation of the electromagnetic field in complex inhomogeneous geoelectrical structures. In Chapters 7, 8, and 9 we will discuss important aspects of the inversion and imaging of electromagnetic data which are common to all geophysical methods. These aspects include the formulation of the principles of regularized inversion of ill-posed geophysical inverse problems and the development of effective numerical inversion algorithms. I demonstrate that this approach provides an effective tool for comprehensive inversion of electromagnetic data. However, inversion meets significant difficulties because of the enormous amount of computations required in the case of the multitransmitter and multireceiver data acquisition systems typical for modern electromagnetic geophysical surveys. There exists, however, an alternative approach to the solution of this problem based on the principles of electromagnetic holography/migration, which extends to electromagnetic cases the methods of optical and radio holography and of seismic migration. I review the physical and mathematical principles of electromagnetic migration in Chapter 9.

Thus, the first three parts of the book comprise the theoretical foundation of applied electromagnetic geophysics. They are followed by the final part, 4, which exposes the major geophysical electromagnetic methods. Part 4 opens with Chapter 10 outlining the electromagnetic properties of rocks and minerals in both the parametric and existential senses. In Chapter 11, I consider the practical aspects of the generation and measurement of electromagnetic fields in geophysical applications. These chapters are followed by four chapters describing the most widely used geophysical methods – direct current and induced polarization methods, magnetotelluric and controlled-source methods, as well as marine, airborne, and other techniques. These chapters also contain some updated material from the book "The Geoelectrical Methods in Geophysical Exploration," by M. S. Zhdanov and G. W. Keller, published in 1994. In particular, Part 4 includes several sections formulating the foundations and principles of modern IP methods, airborne electromagnetic induction methods, and marine MT and controlled-source electromagnetic methods of hydrocarbon exploration. Note that each chapter in the book concludes with a list of references. A master bibliography is given at the end of the text, for convenience.

In summary, the goal of this book is to bring together the fundamental theory of electromagnetic fields and the practical aspects of geophysical exploration for mineral and energy resources.

In this book, I present also some of the research results created by the author with the support of the Consortium for Electromagnetic Modeling and Inversion (CEMI), a research and educational program in applied geophysics based at the Department of Geology and Geophysics, University of Utah (http://www.cemi.utah.edu/). CEMI is an industry-sponsored consortium formed by many major national and international petroleum and mining exploration companies and geophysical organizations. I am very grateful to the members of the CEMI consortium for their continuing support of this research.

The author is also indebted to a great number of his teachers, colleagues, and students at both Moscow State University and the University of Utah. Among many, I would like to single out my long-term fruitful collaboration with my teacher, Professor Mark N. Berdichevsky, who stimulated my early interest in electromagnetic geophysics.

I also wish to acknowledge my gratitude to Professor Vladimir I. Dmitriev of Moscow State University and to Professor George V. Keller of the Colorado School of Mines for their contribution to some of the material presented in this book.

I also thank Professor Frank Brown and other colleagues in the Department of Geology and Geophysics, University of Utah, for creating a supportive environment for my research. I am thankful to all my past and present graduate students and research associates, who have worked together with me on many exciting projects in electromagnetic geophysics. Thanks are expressed particularly to my former graduate student, Dr. Leif Cox, who read the manuscript with great care and made a number of useful suggestions and corrections.

In conclusion, I wish to express my deep gratitude to my wife, Olga Zhdanov, for her constant encouragement during the work on the manuscript.

Salt Lake City, Utah   Michael S. Zhdanov
October, 2008

INTRODUCTION

Many of the theories and methods of modern-day EM geophysics are based on a few fundamental laws developed in the nineteenth century, such as Ohm's law, Ampere's law, and Faraday's law.

Georg Simon Ohm (Fig. 1), born on March 16, 1787, in Erlangen, Bavaria, contributed the key concept of the theory of electricity, which is now famously known as the Ohm's law, which forms the foundation of the modern geoelectrical methods of exploration. After becoming a professor of mathematics at the age of 30 in the Jesuit's College in Koln in 1817, he spent many years studying the relationship between voltage and current. His recognition of what we now accept as being so obvious, that voltage and current are linearly related, defining a quantity we call resistance, was very coolly received by his peers. In frustration over this lack of recognition, he finally resigned his position and moved to the Polytechnique School at Nurnberg in 1833. After long years of effort, his work became acceptable, and in 1841 he was awarded the Copley Medal of the Royal Society of London. He died on July 7, 1854, in Munich at the age of 67.

We should note that, until the early 19th century, electricity and magnetism were treated by scientists as two different natural phenomena, which were not related to each other. Andre' Marie Ampere (Fig. 2) was the first who experimentally observed that there was always a magnetic field associated with current flow, and the strength of the magnetic field was proportional to the amount of current flow-

FIGURE 1

Georg Simon Ohm. (https://en.wikipedia.org/wiki/Georg_Ohm#/media/File:Georg_Simon_Ohm3.jpg)

xxiii

FIGURE 2

Andre' Marie Ampere. (https://en.wikipedia.org/wiki/Andr%C3%A9-Marie_Amp%C3%A8re#/media/File:Ampere_Andre_1825.jpg)

ing. This was a fundamental contribution to the science of electromagnetism, which became known as Ampere's law.

Ampere was French, born in Polemieux, near Lyons, in January, 1775. He took passionate delight in learning from his early infancy, and is said to have worked out lengthy sums using pebbles and biscuit crumbs even before he knew figures. He later claimed that he knew as much about mathematics at age eighteen as he ever knew.

During Ampere's eighteenth year, Lyons was occupied by the Army of the Convention, and his father, who had been opposed to the Revolution, was thrown into prison, and later, hanged. Ampere went into deep depression, and for a year was mentally incompetent. However, by 1796, he was giving private lessons in mathematics and languages, and by 1801 he had become a professor of physics and chemistry at Bourg, but after two years returned to the Lyceum in Lyons as Professor of Mathematics. He moved to the Polytechnic School at Paris in 1805, and was elected Professor of Analysis in 1809. On the 18th of September, 1820, he presented a paper before the Academy of Sciences, defining the magnetic force accompanying current flow, a phenomenon now known as Ampere's law. He died in Marseilles in June, 1836, at the age of 61.

Ampere's discovery that a magnetic field can be generated by the flow of an electric current was fascinating and, for the first time in the history of science provided a link between electricity and magnetism. However, the question remained whether or not the reverse relation hold, in other words, whether a magnetic field could be the source of an electric current. The scientist, who dedicated many years of research trying to answer this fundamental question, was Michael Faraday (Fig. 3). Faraday
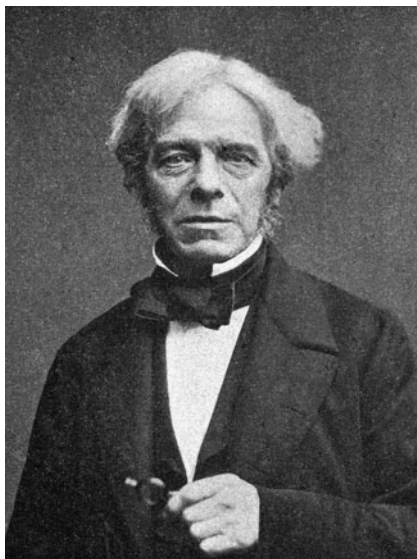
was born on September 22, 1791, at Newington, Surrey, which was then located in the countryside south of London. His father was a blacksmith.

Michael received no formal education, but was apprenticed to a bookseller and bookbinder in 1805, at the age of 14. In this shop, he developed a keen interest in reading science. In 1812, at the age of 21, he attended a series of lectures given by Sir Humphrey Davy at the Royal Institution of Great Britain. He sent his notes of the lectures to Humphrey Davy with a petition for employment, persuading Humphrey Davy to hire him as a research assistant at the Royal Institution. His first great experiment was done in 1821, in which he caused a current-carrying wire to rotate in the field of a horseshoe magnet. He continued with this effort despite the criticisms of fellow scientists who were unsuccessful in reproducing this early experiment, and finally, over a period of ten days in 1831, he carried out a convincing demonstration of the phenomenon of electromagnetic induction – Faraday's law.

In later years, he met with considerable difficulties in continuing his research, probably because of the effect of mercury poisoning resulting from working long hours in the poorly ventilated basement rooms of the Royal Institution. Faraday used a purely intuitive approach to science, eschewing any use of mathematics, but placing strong demands on the mental processes. He retired in 1858 to a royal palace, Hampton Court, made available to him at the suggestion of the Prince Consort, Albert. After he died on August 25, 1867, a collection of ninety-five diplomas of learned societies, bound with his own hand, was found in his personal effects.

These three fundamental physical laws were discovered quite independently, based on physical experiments, and reflected different aspects of electromagnetic phenomena. At the time, it was not clear if and how these laws were related. It required the genius of another Englishman of great distinction,
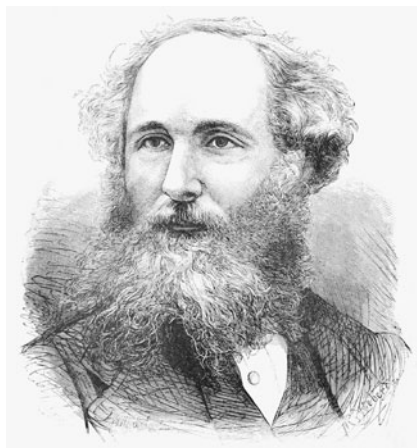
FIGURE 4

James Clerk Maxwell. (https://en.wikisource.org/wiki/Popular_Science_Monthly/Volume_17/May_1880/Sketch_of_James_Clerk_Maxwell#/media/File:PSM_V17_D008_James_Clerk_Maxwell.jpg)

James Clerk Maxwell (Fig. 4) to recognize that Ohm's law, Faraday's law, and Ampere's law were properties of a great whole, that whole now being called the *electromagnetic field*.

James Clerk Maxwell was born on June 13, 1831 in Edinburgh. His patronym was actually Clerk, with the added name Maxwell being derived from his mother's family name. He was raised on a country estate, Glenlair, in Kirkcudbright. His family provided him with the best education that his time offered. This included first the Edinburgh Academy, where his country ways were not readily accepted by his classmates; he came to be known by the nickname "Dafty." After spending three years at the University in Edinburgh, Maxwell went to Cambridge in the Autumn of 1850. But, before leaving Edinburgh at the age of 19, James had already had two papers published by the Royal Society. In 1860, he was appointed to King's College, London, where he spent the most productive years of his life. In 1855, he noted that Faraday had seen in his mind's eye lines of force traversing all over space, while the great mathematicians (Gauss, Weber, Rieman, the Neumans) had seen only centers of force acting through distance. After translating Faraday's results into mathematical form, Maxwell saw that all the earlier results coincided to form a uniform theory of electromagnetic phenomena. Maxwell noted that several of the most fertile methods of research discovered by the mathematicians could be expressed much better in terms of ideas derived from Faraday than in their original form. Maxwell's "Treatise on Electricity and Magnetism" appeared in 1873, defining the unification of optics and electrodynamics. Then, after a brief teaching engagement in Aberdeen, Maxwell became the first director of the newly founded Cavendish Laboratory at Cambridge. He died on November 5, 1879, at the age of 47.

Maxwell's equations are the quintessence of the development of electromagnetic theory; after their statement, further development, including that used in the geoelectrical methods, was only a matter of performing the appropriate mathematical manipulations.

The early study of electrical and electromagnetic (EM) phenomena in relation to the problems of finding ore and other mineral deposits was stimulated by a growing demand from the mining industry.

FIGURE 5

Conrad Schlumberger. (Courtesy of DGG from https://ro.wikipedia.org/wiki/Conrad_%C8%99i_Marcel_Schlumberger#/media/File:Schlumberger.jpg)

Robert Fox (1830) was probably the first scientist who considered a possible application of spontaneous polarization phenomena in locating ore bodies. The first experiments measuring electrical conductivity to locate copper-bearing loads were conducted by James Fisher in Michigan, U.S.A., in 1893 (Jakosky, 1940). From 1912 to 1914, the Schlumberger brothers, Marcel and Conrad, conducted the first direct current (DC) geophysical surveys in France for tectonic study. In 1916, Wenner advanced a method for measuring earth resistivity (Wenner, 1928) that was taken up for ore prospecting by Lundberg (1922), Gish and Rooney (1925), and Heiland (1926). Wenner made significant efforts in developing the principles of interpreting DC data. However, the DC method did not gain much practical ground until the concept of apparent resistivity was introduced by the Schlumberger brothers in 1922, which made data analysis and interpretation much more geologically meaningful and easier to conduct.

The intriguing saga of the Schlumberger family is told in probably the most comprehensive way in the recent book by Oristaglio and Dorozynski (2009). The exciting idea of using an electric field for "seeing" through the ground was conceived of by Conrad Schlumberger as early as 1912. However, the advent of World War I in 1914 delayed the practical implementation of the idea. Only in 1919 did Paul Schlumberger offer financial support to his sons, Conrad and Marcel (Figs. 5 and 6), to develop

Marcel Schlumberger. (http://wiki.seg.org/wiki/File:Marcel_Schlumberger_headshot.png#filelinks)

the revolutionary new technology of electrical prospecting. On 12 November 1919, the father and sons formalized their agreement, marking the beginning of a new era in exploration geophysics.

Initially, the Schlumberger brothers' field experiments to use electrical measurements to map subsurface formations did not result in significant discoveries. The first major commercial success came in the 1930s when the firm founded by the Schlumberger brothers was invited to work in the former Soviet Union. It was in the Azerbaijan oil fields and the Caucasus Mountains that resistivity well logging started its triumphant march over the planet. The pioneering work of the Schlumberger brothers stimulated the creation and development of the Russian school of EM geophysicists, which produced a significant number of distinguished geophysicists and led to major geologic discoveries in the Ural Mountains and eastern Siberia in the 1940s and 1950s.

With the practical application of electrical methods in exploration of the subsurface, the need for mathematical solutions for the behavior of electromagnetic fields interacting with reasonable models of the earth became apparent. In this respect, Sabba S. Stefanescu (Fig. 7) built the mathematical basis for electromagnetic modeling. Stefanescu was born in Bucharest on the 20th of July, 1902, to a family of distinguished intellectuals, being the third son of Professor Sabba Stefanescu, a corresponding member of the Romanian Academy. His interest in mathematics was recognized early, while he attended high school classes at the St. Sava Lycee. During World War I, while his father was assigned to a diplomatic post in France, he and his family escaped from Romania, crossing the whole of Russia from west to east during the early days of the Russian Civil War, finally reaching Paris by crossing the Arctic Ocean from easternmost Russia.

Sabba Stefanescu continued his schooling in Paris, completing his preparatory studies at Saint Louis Lycee in 1918, completing his studies for the B.Sc. degree in Science at the Sorbonne in 1919,

FIGURE 7

Sabba Stefanescu. (https://ro.wikipedia.org/wiki/Sabba_%C8%98tef%C4%83nescu#/media/File:Sabba_%C5%9Etef%C4%83nescu_480x640.jpg)

and from 1920 on, continued his studies at the Paris School of Mines. He then returned to Bucharest in 1923, where he served in the Bureau of Mines as an inspector briefly, following which, he worked as a mining engineer for the Petrosani Enterprise. This stage of his career was interrupted by ill health, and after recovery, he was appointed to the Faculty of the Drilling Department of the Polytechnical School as an assistant lecturer.

In 1927, his career turned to geophysics when he joined the Prospecting Section of the Romanian Geological Institute. The Prospecting Section became in fact a Department of Applied Geophysics. Young Sabba Stefanescu fostered the use and further development of electrical methods in his position there. During a visit to Paris and discussions with Professor Conrad Schlumberger, Stefanescu became particularly interested in the calculation of field behavior in a layered earth. Over the next several years, he formulated the solution as the Hankel integral transforms, which are fundamental to the science of electrical prospecting still. In ensuing years, he extended this analytical approach from the case of DC behavior to the case of electromagnetic induction.

Sabba Stefanescu married Elena Ionescu Dolj in 1937. His only son, Ion Sabba Stefanescu, born in 1947, has become a professor of nuclear physics. In 1946, Dr. Sabba Stefanescu was elected a corresponding member of the Romanian Academy. In 1950, he was appointed Head of the first Chair of Geophysics in Romania.

Another influential scientists of the 20th century, who contributed enormously in electromagnetic geophysics, was Tikhonov (Fig. 8).

Andrei Nikolaevich Tikhonov was born in 1906 in Gzhatsk (now Gagarin), about 120 km east of Moscow, Russia. In 1919, at thirteen years of age, he started working as a railway clerk. In 1922, still

not quite 16 years of age, he was accepted as a student in the Department of Physics and Mathematics at Moscow State University, where he has spent most of his career. After his graduation, he continued on the faculty of the Department of Physics and Geophysics, but also collaborated with the Geophysical Institute of the Academy of Sciences. While his early work dealt with essentially mathematical topics such as topology, he gradually became heavily involved with the application of mathematics to geological and geophysical problems. During the Second World War, his professional career took a crucial turn: he was charged by the Geophysical Institute of the Academy of Sciences to carry out a mathematically-based evaluation of the effectiveness of DC electrical methods for use in minerals prospecting. This led him to a consideration of the inverse problem, which up until then had been considered by mathematicians to be unsolvable. In 1943, Tikhonov's first paper on inversion, based on practical results from a DC survey for oil in the Ural's forelands, showed that such ill-posed problems could be solved and laid the basis for a new topic in applied mathematics, the regularization theory of the solution of ill-posed set problems.

Tikhonov's studies have played a major role in the development of electromagnetic methods in geophysics. His early theoretical suggestions about the design of both natural-field and controlled-source electromagnetic methods led his colleagues to a highly successful application of these methods in the search for oil and gas in the Soviet Union immediately following the Second World War. However, his interests in applied mathematics have covered many fields in the natural sciences; including atmospheric physics, ecology, and tomographic investigations of the human brain. Prof. Tikhonov also made notable contributions in nuclear physics. He guided research in the numerical modeling of thermonuclear reactions, doing his calculations on the first Soviet computer, the "Arrow".

In 1969, Academician Tikhonov founded the Department of Computational Mathematics and Cybernetics at the Moscow State University. He served as Dean of the Department for the following 20 years.

Not only Tikhonov developed the foundations of the solution of inverse geophysical problems, but he also proposed a new method for determining the electrical structure of the earth using naturally existing EM fields rather than fields generated by a controlled source. This contribution was made by Tikhonov in 1950 in the USSR, practically simultaneously and independently with Cagniard (1953) in France, and Rikitake (1950) in Japan. Knowledge of the existence of telluric currents is far from recent. As early as in 1868, Sir George Biddell Airy, English mathematician and astronomer, made the first coordinated study of earth currents and their relationship to magnetic variations (Airy, 1868). In 1862, one of the first field experiments to measure telluric currents was carried out by Lamont (1862) in the Alps. Terada (1917) appears to have been the first to measure the dependence of the magnetic field relationships on the conductivity of the ground.

The Schlumberger brothers observed telluric currents during their experiments with DC measurements on the ground as well. They were also the first to suggest that telluric currents could be used for oil and gas exploration. However, practical measurements showed significant variations and instability in telluric current behavior, which made it difficult to develop any reasonable technique for interpreting telluric current data. The main sources of this instability were associated with complex processes in the ionosphere and magnetosphere, which were unknown at that time.

The core of the discovery made independently by Tikhonov and by Cagniard was that the effect of processes in the ionosphere and magnetosphere could be canceled if the electric field components of the telluric field were normalized by the magnetic field components.

Tikhonov and Cagniard introduced a concept of magnetotelluric impedances defined as a ration of the mutually orthogonal components of electric and magnetic fields. At the time, this was a revolutionary idea because it let geophysicists transform observed field data in the predictions of the resistivity of rock formations. This opened the way for the development of a new exploration technique, the magnetotelluric (MT) method. The power of the Tikhonov and Cagniard approach is that, on the one hand, it is based on a simple geoelectrical model; on the other hand, it provides a geophysically and geologically meaningful result using a simple interpretation technique.

Mark Naumovich Berdichevsky was the first to realize the importance of accounting for the effects of horizontal geoelectrical inhomogeneities on MT data. He introduced the tensor measurements in the MT method, which soon became widely used all over the world. The transition to tensor-based data processing resulted in a major increase in the amount of information extracted from MT observations. Another major contribution of Berdichevsky in geoelectrics was the development, in collaboration with Vladimir Ivanovich Dmitriev, of a distortion theory of MT sounding curves (Berdichevsky and Dmitriev, 1976a).

Since the time when the Schlumberger brothers began their work, electrical prospecting methods have transformed dramatically, starting from a simple resistivity method and developing into a complicated technology based on complex EM surveys with natural and controlled sources. Not only have the methods and equipment changed, but our ideas about EM fields, their generation and measurement, and geoelectrical models used for interpretation have also advanced tremendously. For many years, the basic model for interpretation was a 1D model of a layered earth or a 2D model. However, during the last 20 years, geophysicists have begun using 3D models for interpretation as well. This advancement

has required developing the corresponding mathematical methods of interpretation, based on modern achievements of EM theory and computer science in numerical modeling and inversion.

It is important to emphasize that the areas of practical application of electrical and EM methods are very diversified. EM measurements are conducted on land, in the air, in the sea, and within boreholes. These methods are applied in the mining industry; in oil and gas exploration; in geotechnical, engineering, groundwater, and environmental geophysics; and in regional and crustal tectonic studies.

In this book, I will outline the foundations of electromagnetic theory as applied in geophysics. The fundamental principles of EM geophysics have been developed in the framework of classical EM theory, where the EM field is described by the electric and magnetic vector fields; and Maxwell's equations represent a system of differential equations with respect to these vector fields. However, it is more natural from the physical and geophysical points of view to describe the EM field by the corresponding flux and work or voltage of the field instead of using traditional vector representations (Zhdanov, 2009, 2010). Indeed, it is very well known that the flux of a field through a given surface and the work or voltage of the field along a given path represent the most important physical entities studied and measured in geophysical experiments. That is why a representation of an EM field in the form of corresponding flux and voltage appears to be extremely well suited for a description of EM phenomena.

One of the most challenging problems in EM methods is the development of effective interpretation schemes for 3D inhomogeneous geologic formations. In the last decade of the 20th century and in the beginning of the 21st century, methods for numerical and analytical modeling of the interaction of EM fields with earth structures developed rapidly. This development was driven by the availability of high-performance computers, including PC clusters. These modeling capabilities made possible the extraction of much more information from the field data than was possible previously when only heuristic interpretation was feasible.

Several techniques are available for EM forward modeling. They are based on numerical implementation of the differential-equation (DE) approach, finite-difference (FD) or finite-element (FE) methods, or the integral equation (IE) approach. The foundations of all these methods are presented in this book.

The methods for solving 3D EM inverse problems usually are based on optimizing the model parameters by applying different inversion techniques. The simplest are the Monte Carlo methods, which determine the wanted parameters by random or regular trial- and- error procedures. Because of the limitations of computing time, Monte Carlo methods have found limited applications in EM geophysics. The more widely used approaches are based on applying gradient-type methods of optimization.

We should note, as seen from Maxwell's equations, that EM fields are related nonlinearly to the conductivity of the earth. Therefore, EM inverse problems are characterized first of all by their nonlinearity. Another major difficulty in inversion is related to its ill-posedness, which means that the existence, uniqueness, and/or stability of solutions is in question. The inherent nonlinearity of EM problems makes the ill-posedness more severe. To overcome this difficulty and obtain a stable solution of ill-posed inverse problems, we must apply the regularization theory, which was developed in the pioneering work of Tikhonov (e.g., Tikhonov and Arsenin, 1977). Remarkably, the development of the regularization theory by Tikhonov was motivated by the needs of solving the inversion problem for electrical prospecting. The theory of regularization provides a solid basis for the solution of electromagnetic inverse problems. We will present the foundations of this theory in the book.

The book also contains a description of physical-mathematical principles of practically all major geophysical electromagnetic methods. These methods include DC methods, natural field (magnetotelluric) methods, and controlled source electromagnetic methods in the frequency and time domain.

The book is concluded with a chapter presenting case histories of application of the EM methods for regional tectonic study, mineral exploration, and oil and gas exploration.

REFERENCES AND RECOMMENDED READING TO INTRODUCTION

Airy, G. B., 1868, Comparison of magnetic disturbances recorded by the self-registering magnetometers at the Royal Observatory, Greenwich, with magnetic disturbances deduced from the corresponding terrestrial galvanic currents recorded by the self-registering galvanometers of the Royal Observatory: Philosophical Transactions of the Royal Society of London, **158**, 465–472.

Berdichevsky, M. N., and V. I. Dmitriev, 1976a, Basic principles of interpretation of magnetotelluric sounding curves, in A. Adam, ed., Geoelectric and geothermal studies: Akademiai Kaido, 165–221.

Cagniard, L., 1953, Basic theory of the magneto-telluric method of geophysical prospecting: Geophysics, **18**, 605–635.

Fox, R. W., 1820, On the electromagnetic properties of metalliferous veins in the mines of Cornwall: Philosophical Transactions of the Royal Society of London, **120**, 399–414.

Gish, O. H., and W. J. Rooney, 1925, Measurement of resistivity of large masses of undisturbed earth: Terrestrial Magnetism and Atmospheric Electricity, **30**, 161–188.

Heiland, C. A, 1926, Instruments and methods for the discovery of useful mineral deposits: Engineering and Mining Journal, **121** (9), 47–49.

Jakosky, J. J., 1940, Exploration geophysics, 2nd ed.: Times-Mirror Press.

Lamont, J. V., 1862, Der Erdstrom und der Zusammen desselben mit dem Erdmagnetismus: Leopold-Voss-Verlag.

Lundberg, H., 1922, Practical experience in electrical prospecting: Geological Survey of Sweden.

Maxwell, J. C., 1954, A treatise on electricity and magnetism: Dover Publications, New York (unabridged and unaltered republication of the third edition of 1891), 506 pp.

Oristaglio, M., and A. Dorozynski, 2009, A sixth sense: The life and science of Henry-Georges Doll, oilfield pioneer and inventor: Overlook Duckworth.

Rikitake, T., 1950, Electromagnetic induction within the earth and its relation to the electrical state of the earth's interior. 2: Bulletin of the Earthquake Research Institute, University of Tokyo, **28**, 263–283.

Terada, T., 1917, On rapid periodic variations of terrestrial magnetism: Journal of the College of Science, Imperial University of Tokyo, **37**, 56–84.

Tikhonov, A. N., 1950, On the determination of electrical characteristics of deep layers of the earth's crust in Russian: Doklady, **73**, 295–297.

Tikhonov, A. N., and V. Y. Arsenin, 1977, Solution of ill-posed problems: V. H. Winston and Sons.

Wenner, F., 1928, A method of measuring earth resistivity: U. S. Bureau of Standards Bulletin, 258.

Zhdanov, M. S., 2009, Geophysical electromagnetic theory and methods: Elsevier.

Zhdanov, M. S., 2010, Maxwell's equations and numerical electromagnetic modeling in the context of the theory of differential forms, in J. Kazahara, V. Korneev, and M. S. Zhdanov, eds., Active geophysical monitoring: Elsevier Science&Technology, 300–325.

INTRODUCTION TO FIELD THEORY

DIFFERENTIAL CALCULUS OF VECTOR FIELDS AND DIFFERENTIAL FORMS

1

CONTENTS

We begin our discussion with the basic differential and integral relationships of the field theory. In this chapter, I also introduce the important concepts of work and flux of the field. Using these concepts, the different vector formulations of the Gauss's and Stokes's theorems will be introduced and analyzed. On the basis of Gauss's theorem, we will develop a set of fundamental integral relations, which are known as Green's formulas. Another powerful mathematical approach to study the physical fields is based on the concept of differential forms. I will provide the definitions and canonical representations of differential forms in three-dimensional Euclidean space. The chapter will be concluded by establishing a close relationship between the exterior differential operation of the calculus of the forms and the gradient, curl, and divergence operations of the conventional vector calculus.
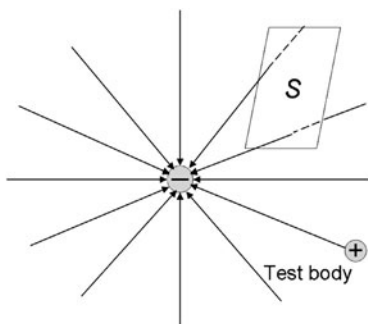
FIGURE 1.1

Force lines of the electric field of a negatively charged sphere.

1.1 THE BASIC DIFFERENTIAL RELATIONSHIPS OF FIELD THEORY
1.1.1 CONCEPT OF THE PHYSICAL FIELD

Originally, a notion of the field was used for graphical representation of the basic electromagnetic laws. We know, for example, that according to the Coulomb law, a small negatively charged sphere attracts any positively charged small test body with a force inversely proportional to the square of the distance between the sphere and the body (Fig. 1.1). This force is called an *electric force*. The vector of this force is directed along a line connecting the centers of both bodies. Thus, the straight lines in our figure show the direction of the force for different locations of the test body. The arrows show that the force is directed toward the negatively charged sphere.

We can select a rectangular piece of surface S in the space, as shown in Fig. 1.1, and calculate the number of force lines crossing this surface. The lines in our model are always perpendicular to the surface of the sphere. Therefore, we have a dense distribution of these lines close to the sphere and a sparse distribution far away from the sphere. Moreover, it is easy to show that if we increase the distance from the sphere to the surface S by two or three times, the number of these lines crossing the surface will decrease by four and nine times respectively.

Thus, the force lines show the direction of the force, and the density of these lines characterize the strength of the electric interaction between the two bodies. In other words, our graphical representation not only gives us a very clear qualitative description of the electric force distribution in the space, but also provides some quantitative characteristics of the electric force (its direction and strength).

We should note that, we have introduced the force lines to demonstrate the behavior of the test body at different distances from the sphere. However, we can assume that these lines, or the *field* represented by these lines, exist even in the absence of the test body! Thus, we arrive at a notion of the *electric field*. The corresponding lines are called *the vector lines or force lines of the electric field*. A similar discussion can be applied to the magnetic field, as well.

Note that, according to our representation of the electric or magnetic fields through the notion of the force lines, these fields are present everywhere in space, not only at the one point where the test body is located.
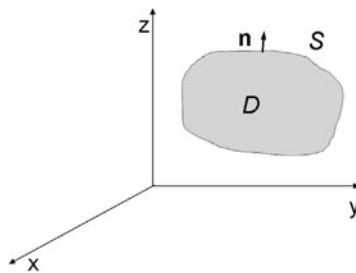
FIGURE 1.2

Domain D bounded by a closed surface S, and a Cartesian system of coordinates (x, y, z).

The concept of the physical field was introduced in physics by Michael Faraday. This concept was born from his believe that electric charges (or material bodies) could not act at a distance, which was a standard point of view of the majority of the scientists in the 19th century. Indeed, according to the action-at-a-distance approach, if we have a small negatively charged sphere in the otherwise empty space only, this sphere would not have any force associated with it. At the moment when we bring a positively charged small test body, the sphere would instantaneously attract it with the force determined by the Coulomb law. Thus, this force will be created out of nothing, which would violate, according to Faraday, the principle of conservation of force or energy. Contrary to this scenario, the field theory assumes that the electric or magnetic fields are present everywhere in space. The test bodies react to these fields at the place where we put them. This action is local, and not at a distance, and there is no creation of the force from nowhere. We can see now that Faraday envisioned that the fields were as real as the material bodies, the fields were interacting with the bodies and with each other, and the material bodies interacted with the field.

Thus, following Faraday, we can conclude that electric and magnetic fields are propagated everywhere throughout a space. Therefore, one can assign a specific value of the electric or magnetic fields at any point of observation. This is a major property of the *field*.

Based on these ideas, we can now give the following mathematical definition of a field F.

Let us introduce a Cartesian system of coordinates (x, y, z) and consider a domain D in the space (Fig. 1.2).

Definition 1. We say that we have *a field F* in some domain D of a space, if for any point $\mathbf{r} = (x, y, z)$ from D, it is assigned one specific physical value $F = F(x, y, z)$.

Thus, the *field* can be formed by any physical value which is a function of the observation point.

In general, physical fields can be characterized by different mathematical objects. For example, if some physical value is represented by a number which is independent of the selected system of coordinates, we call the corresponding field *a scalar field*. The temperature distribution in some volume gives us an example of a scalar field.

Many physical values are described by vectors at every observation point. In this case we speak about the *vector fields*. Electric and magnetic fields are typical examples of vector fields. However, the combined force field formed by the electric and magnetic components of an electromagnetic field can

be described by a differential form Fecko (2006). In this case we can speak about the *differential form fields* (see Appendix A).

Some complex physical values can be characterized by tensors. In this case we call the corresponding field *a tensor field*. For example, the deformations of an elastic medium are described by the field of the deformation tensor.

Note that, in a general case, the field may depend on the time of observation t:

$$F = F(x, y, z, t).$$

We will use the following definitions:

Definition 2. The field F is called nonstationary if it depends on time.

Definition 3. The field F is called stationary if it does not depend on time.

The electromagnetic theory operates with the vector fields representing the electric and magnetic phenomena. In order to understand the foundations of the electromagnetic theory, one should be able to use the corresponding methods of vector field analysis. We will begin our discussion with a summary of the main algebraic and differential operations on vector fields.

1.1.2 DOT (SCALAR) AND CROSS (VECTOR) PRODUCTS OF VECTORS

We introduce in a three-dimensional (3-D) space some Cartesian system of coordinates with the basis $(\mathbf{d}_x, \mathbf{d}_y, \mathbf{d}_z)$. Any vector in this space can be represented as a linear combination of the vectors of the basis:

$$\mathbf{B} = B_x \mathbf{d}_x + B_y \mathbf{d}_y + B_z \mathbf{d}_z. \tag{1.1}$$

Here the values B_x, B_y, B_z are called the *scalar components of a vector* $\mathbf{B}$.

The magnitude of the vector is equal to:

$$B = \sqrt{B_x^2 + B_y^2 + B_z^2}.$$

Definition 4. The *dot (scalar) product* of two vectors,

$$\mathbf{a} = a_x \mathbf{d}_x + a_y \mathbf{d}_y + a_z \mathbf{d}_z$$

and

$$\mathbf{b} = b_x \mathbf{d}_x + b_y \mathbf{d}_y + b_z \mathbf{d}_z,$$

is $\mathbf{a} \cdot \mathbf{b} = a_x b_x + a_y b_y + a_z b_z = \mathbf{b} \cdot \mathbf{a}$.

The dot (scalar) product can be also defined as

$$\mathbf{a} \cdot \mathbf{b} = ab \cos(\widehat{\mathbf{a}, \mathbf{b}}), \tag{1.2}$$

where a and b are the magnitudes of vectors $\mathbf{a}$ and $\mathbf{b}$ respectively, and $\widehat{(a, b)}$ is an angle between the two vectors.

As a simple application, one can prove the cosine formula of plane trigonometry:

$$c^2 = a^2 + b^2 - 2ab\cos\widehat{(\mathbf{a}, \mathbf{b})},$$

where a, b, and c are the sides of a triangle, and $\widehat{(\mathbf{a}, \mathbf{b})}$ is an angle between a and b.

Definition 5. *The cross (or vector) product* $\mathbf{a} \times \mathbf{b}$ of vectors $\mathbf{a}$ and $\mathbf{b}$ is the vector perpendicular to both of them, and its magnitude equals the area of the parallelogram formed by these vectors: $|\mathbf{a} \times \mathbf{b}| = ab\sin\widehat{(\mathbf{a}, \mathbf{b})}$.

The cross product can be calculated using matrix notations:

$$\mathbf{c} = \mathbf{a} \times \mathbf{b} = \begin{vmatrix} \mathbf{d}_x & \mathbf{d}_y & \mathbf{d}_z \\ a_x & a_y & a_z \\ b_x & b_y & b_z \end{vmatrix}. \tag{1.3}$$

From the latter it follows that:

$$\mathbf{a} \times \mathbf{b} = -\mathbf{b} \times \mathbf{a}.$$

Definition 6. The *triple scalar product* of the three vectors $\mathbf{a}$, $\mathbf{b}$, and $\mathbf{c}$ is a scalar equal to the volume of the parallelepiped formed by these vectors:

$$\mathbf{a} \cdot [\mathbf{b} \times \mathbf{c}] = (\mathbf{a}, \mathbf{b}, \mathbf{c}) = -(\mathbf{b}, \mathbf{a}, \mathbf{c}) \tag{1.4}$$

and

$$\mathbf{a} \cdot [\mathbf{b} \times \mathbf{c}] = \begin{vmatrix} a_x & a_y & a_z \\ b_x & b_y & b_z \\ c_x & c_y & c_z \end{vmatrix}.$$

Definition 7. The *triple vector product* of the vectors $\mathbf{a}$, $\mathbf{b}$, and $\mathbf{c}$ is a vector determined as the difference of the following two vectors:

$$\mathbf{a} \times [\mathbf{b} \times \mathbf{c}] = \mathbf{b}(\mathbf{a} \cdot \mathbf{c}) - \mathbf{c}(\mathbf{a} \cdot \mathbf{b}). \tag{1.5}$$

1.1.3 VECTOR DIFFERENTIAL OPERATORS

In general we assume that both scalar U and vector $\mathbf{B}$ are functions of a position of point M with a radius-vector $\mathbf{r}$ in some Cartesian system of coordinates. At every point M the scalar value is defined by its magnitude and sign, while the vector value is characterized by its magnitude and direction. Thus, we have scalar, $U(\mathbf{r})$, and vector, $\mathbf{B}(\mathbf{r})$, fields, respectively. The vector field $\mathbf{B}(\mathbf{r})$, according to Eq. (1.1), can be represented using its scalar components:

$$\mathbf{B}(\mathbf{r}) = B_x(\mathbf{r})\,\mathbf{d}_x + B_y(\mathbf{r})\,\mathbf{d}_y + B_z(\mathbf{r})\,\mathbf{d}_z.$$

We also assume that these fields are given within some domain D and that the scalar field $U(\mathbf{r})$ and all scalar components of the vector field $\mathbf{B}(\mathbf{r})$ are continuously differentiable within this domain. In this case, we can introduce the corresponding differential operators for the scalar and vector fields.

Gradient of a scalar field

Let us introduce a constant vector $\mathbf{l} = l\,\mathbf{d}_l$, oriented along the unit vector $\mathbf{d}_l$ with the magnitude l.

We can calculate a derivative of the scalar field $U(\mathbf{r})$ along a direction $\mathbf{l}$:

$$\frac{\partial U}{\partial l} = \lim \frac{\Delta U}{\Delta l}, \quad \Delta l \to 0.$$

This directional derivative can be calculated using Cartesian coordinates, as

$$\frac{\partial U}{\partial l} = \frac{\partial U}{\partial x}\frac{\partial x}{\partial l} + \frac{\partial U}{\partial y}\frac{\partial y}{\partial l} + \frac{\partial U}{\partial z}\frac{\partial z}{\partial l}, \tag{1.6}$$

where

$$\frac{\partial x}{\partial l} = \cos(\widehat{\mathbf{l},\mathbf{d}_x}), \;\; \frac{\partial y}{\partial l} = \cos(\widehat{\mathbf{l},\mathbf{d}_y}), \;\; \frac{\partial z}{\partial l} = \cos(\widehat{\mathbf{l},\mathbf{d}_z}).$$

Definition 8. A *gradient of a scalar field* is equal to a vector field with the scalar components determined by the corresponding partial derivatives of the scalar field in the x, y, and z directions, respectively:

$$gradU(\mathbf{r}) = \frac{\partial U(\mathbf{r})}{\partial x}\mathbf{d}_x + \frac{\partial U(\mathbf{r})}{\partial y}\mathbf{d}_y + \frac{\partial U(\mathbf{r})}{\partial z}\mathbf{d}_z. \tag{1.7}$$

Comparing Eq. (1.6) with the definition of the dot product (1.2), we immediately conclude that

$$\frac{\partial U}{\partial l} = gradU \cdot \mathbf{d}_l, \tag{1.8}$$

because

$$\mathbf{d}_l = \cos(\widehat{\mathbf{l},\mathbf{d}_x})\mathbf{d}_x + \cos(\widehat{\mathbf{l},\mathbf{d}_y})\mathbf{d}_y + \cos(\widehat{\mathbf{l},\mathbf{d}_z})\mathbf{d}_z.$$

From Eqs. (1.8) and (1.2) we have at once:

$$\left|\frac{\partial U}{\partial l}\right| = |gradU|\cos\varphi, \text{ and } \frac{\partial U}{\partial l} \le |gradU|, \tag{1.9}$$

where φ is an angle between the vectors $\mathbf{l}$ and $gradU$.

Fig. 1.3 represents a polar diagram of the absolute value of the directional derivative, $|\partial U/\partial l|$, versus the angle, φ. We can see from this figure and from Eq. (1.9) that the direction of the gradient is the direction of the maximum increase of the scalar field, and the magnitude of the gradient is the rate of this field increase.
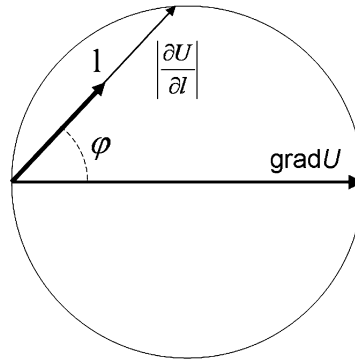
FIGURE 1.3

A polar diagram of the absolute value of the directional derivative, $|\partial U/\partial l|$, versus the angle, φ, between the vectors $\mathbf{l}$ and $grad U$.

Divergence and curl (rotation) of the vector field

Let us introduce now the operators of the differentiations of the vector field $\mathbf{B}(\mathbf{r})$. In principle, one can consider any linear combination of the partial derivatives of the different components of the vector field $\mathbf{B}(\mathbf{r})$. However, the important requirement is that, in order to be physically meaningful, the result of this differentiation should be independent of the system of coordinates (x, y, z). This requirement reduces dramatically the possible choices for the vector differentiation operators.

We will demonstrate in Chapter 2 that the following operators are independent (invariant) of the coordinate system:

$$
div\mathbf{B}(\mathbf{r}) = \frac{\partial B_x(\mathbf{r})}{\partial x} + \frac{\partial B_y(\mathbf{r})}{\partial y} + \frac{\partial B_z(\mathbf{r})}{\partial z}, \tag{1.10}
$$

$$
curl\mathbf{B}(\mathbf{r}) = \begin{vmatrix} \mathbf{d}_x & \mathbf{d}_y & \mathbf{d}_z \\ \frac{\partial}{\partial x} & \frac{\partial}{\partial y} & \frac{\partial}{\partial z} \\ B_x(\mathbf{r}) & B_y(\mathbf{r}) & B_z(\mathbf{r}) \end{vmatrix}. \tag{1.11}
$$

An operator of Eq. (1.10) is called a *divergence operator* of vector field $\mathbf{B}(\mathbf{r})$, and an operator of Eq. (1.11) is called a *curl (rotation) operator* of vector field $\mathbf{B}(\mathbf{r})$.

The del operator ∇

The collection of the partial derivative operators is commonly called *the del operator:*

$$
\nabla = \mathbf{d}_x \frac{\partial}{\partial x} + \mathbf{d}_y \frac{\partial}{\partial y} + \mathbf{d}_z \frac{\partial}{\partial z}.
$$

Using the del operator, one can express the vector differential (vector calculus) operators gradient, divergence, and curl in compact form:

$$grad U(\mathbf{r}) = (\mathbf{d}_x \frac{\partial}{\partial x} + \mathbf{d}_y \frac{\partial}{\partial y} + \mathbf{d}_z \frac{\partial}{\partial z}) U(\mathbf{r}) = \nabla U(\mathbf{r}), \tag{1.12}$$

$$div\mathbf{B}(\mathbf{r}) = \nabla \cdot \mathbf{B}(\mathbf{r}), \tag{1.13}$$

$$curl\mathbf{B}(\mathbf{r}) = \nabla \times \mathbf{B}(\mathbf{r}). \tag{1.14}$$

Second derivatives of the scalar and vector fields

We can write five main second derivatives of the vector calculus

$$div grad U = \nabla \cdot \nabla U = \nabla^2 U, \tag{1.15}$$

$$curl grad U = \nabla \times \nabla U, \tag{1.16}$$

$$div curl\mathbf{B} = \nabla \cdot [\nabla \times \mathbf{B}], \tag{1.17}$$

$$curl curl\mathbf{B} = \nabla \times [\nabla \times \mathbf{B}], \tag{1.18}$$

$$grad div\mathbf{B} = \nabla[\nabla \cdot \mathbf{B}], \tag{1.19}$$

where we use a standard notation ∇^2 for the Laplacian operator:

$$\nabla \cdot \nabla = \nabla^2.$$

Using the rules of vector algebra, it is easy to calculate the expressions for the second derivatives, assuming that all second partial derivatives of the scalar field U and of the scalar component of the vector field $\mathbf{B}$ are continuous functions. For example,

$$curl grad U = \nabla \times \nabla U = \begin{vmatrix} \mathbf{d}_x & \mathbf{d}_y & \mathbf{d}_z \\ \frac{\partial}{\partial x} & \frac{\partial}{\partial y} & \frac{\partial}{\partial z} \\ \frac{\partial}{\partial x} & \frac{\partial}{\partial y} & \frac{\partial}{\partial z} \end{vmatrix} U = 0, \tag{1.20}$$

because the determinant of the matrix with two equal rows is identically equal to zero. Thus, we conclude that the curl of any gradient is identically equal to zero.

Similarly, we can calculate the divergence of the curl using the triple scalar product:

$$div curl\mathbf{B} = \nabla \cdot [\nabla \times \mathbf{B}] = \begin{vmatrix} \frac{\partial}{\partial x} & \frac{\partial}{\partial y} & \frac{\partial}{\partial z} \\ \frac{\partial}{\partial x} & \frac{\partial}{\partial y} & \frac{\partial}{\partial z} \\ B_x & B_y & B_z \end{vmatrix} = 0. \tag{1.21}$$

Therefore the divergence of any curl is equal to zero as well.

We can use formula (1.5) for the triple vector product of the vectors ∇, ∇ and $\mathbf{B}$ to compute the curl of the curl operator:

$$curlcurl\mathbf{B} = \nabla \times [\nabla \times \mathbf{B}] = \nabla(\nabla \cdot \mathbf{B}) - (\nabla \cdot \nabla)\mathbf{B}.$$

Then:

$$\nabla \times [\nabla \times \mathbf{B}] = graddiv\mathbf{B} - (\nabla \cdot \nabla)\mathbf{B}.$$

Thus we obtain:

$$curlcurl\mathbf{B} = graddiv\mathbf{B} - (\nabla \cdot \nabla)\mathbf{B}. \tag{1.22}$$

The expression for formula (1.19) comes from Eq. (1.22):

$$graddiv\mathbf{B} = curlcurl\mathbf{B} + (\nabla \cdot \nabla)\mathbf{B}. \tag{1.23}$$

Finally, we can write the formula for the Laplacian of the vector field using the vector differential operators:

$$(\nabla \cdot \nabla)\mathbf{B} = graddiv\mathbf{B} - curlcurl\mathbf{B}. \tag{1.24}$$

1.1.4 DIFFERENTIATION OF THE PRODUCTS OF SCALAR AND VECTOR FIELDS

In this section we will discuss how the differentiation of the products of the scalar and vector fields can be carried out. This differentiation will be widely used in electromagnetic theory, which is the main subject of this text. However, in application of the del operator it is important to understand that this is a vector differential operator which satisfies the vector operation rules and the partial differentiation rules simultaneously.

We will begin with a simple case of a product of two scalar fields: $U(\mathbf{r})$ and $V(\mathbf{r})$. The rules of the differentiation of the product of two scalar fields are similar to those of the product of two functions. For example, the gradient of the product UV is calculated as:

$$grad(UV) = \nabla(UV) = \nabla(\overset{\downarrow}{U}V) + \nabla(U\overset{\downarrow}{V}),$$

where the vertical arrows show the field which is actually differentiated by the del operator. We can take the field V in the first term and the field U in the second term out of the parentheses, because they are not affected by the del operator (there are no arrows above). Thus, we find:

$$grad(UV) = V(\nabla U) + U(\nabla V) = VgradU + UgradV. \tag{1.25}$$

In a similar way, one can calculate the divergence of the product of a scalar field U and a vector field $\mathbf{B}$:

$$div(U\mathbf{B}) = \nabla \cdot (U\mathbf{B}) = \nabla \cdot (\overset{\downarrow}{U}\mathbf{B}) + \nabla \cdot (U\overset{\downarrow}{\mathbf{B}})$$
$$= (\nabla U) \cdot \mathbf{B} + U(\nabla \cdot \mathbf{B}) = gradU \cdot \mathbf{B} + Udiv\mathbf{B}. \tag{1.26}$$

The curl of the product of a scalar field U and a vector field $\mathbf{B}$ is equal to:

$$curl(U\mathbf{B}) = \nabla \times (U\mathbf{B}) = \nabla \times (\overset{\downarrow}{U}\mathbf{B}) + \nabla \cdot \times (U\overset{\downarrow}{\mathbf{B}})$$
$$= \nabla U \times \mathbf{B} + U(\nabla \times \mathbf{B}) = grad U \times \mathbf{B} + U\,curl\mathbf{B}. \tag{1.27}$$

Finally, as an example, we will find the divergence of the cross product of two vector fields, $\mathbf{A}$ and $\mathbf{B}$, using the rules of the triple scalar product:

$$div[\mathbf{A} \times \mathbf{B}] = \nabla \cdot [\mathbf{A} \times \mathbf{B}] = (\nabla, \mathbf{A}, \mathbf{B}) = (\nabla, \overset{\downarrow}{\mathbf{A}}, \mathbf{B}) + (\nabla, \mathbf{A}, \overset{\downarrow}{\mathbf{B}})$$
$$= (\mathbf{B}, \nabla, \mathbf{A}) - (\mathbf{A}, \nabla, \mathbf{B}) = \mathbf{B} \cdot curl\mathbf{A} - \mathbf{A} \cdot curl\mathbf{B}. \tag{1.28}$$

1.2 THE BASIC INTEGRAL RELATIONSHIPS OF FIELD THEORY
1.2.1 CONCEPT OF WORK AND FLUX OF A FIELD

We are given a scalar field $U(\mathbf{r})$ and a vector field $\mathbf{B}(\mathbf{r})$ in 3-D space. Let us assume that L denotes a smooth (differentiable) line and S denotes a smooth (differentiable) surface. We also introduce the vector elements of the line and surface, the vectors $d\mathbf{l}$ and $d\mathbf{s}$:

$$d\mathbf{l} = \boldsymbol{\tau}\,dl, \ d\mathbf{s} = \mathbf{n}ds, \tag{1.29}$$

where dl and ds are the increments of length and surface area, respectively; $\boldsymbol{\tau}$ is a unit (tangential) vector to the line L, and $\mathbf{n}$ is a unit (normal) vector to the surface S, indicating the positive direction along the line and the positive direction of the normal to the surface, respectively.

There are standard conventions for choosing the positive directions of vectors $\mathbf{n}$ and $\boldsymbol{\tau}$, respectively. If the surface S is a closed surface bounding some domain (volume) D, as shown in Fig. 1.2, then the outward normal to the surface is positive.

If the surface S is an open surface bounded by the closed contour L, as shown in Fig. 1.4, the positive normal depends on the choice of the positive direction along the contour L. It is usually required that traversing of the contour in the positive direction $\boldsymbol{\tau}$ can be treated as a clockwise movement for the observer looking in the direction of the positive normal $\mathbf{n}$.

We can introduce the concept of *work*, W, of a vector field $\mathbf{B}$ along the curve L, as the following line integral:

$$W = \int_L \mathbf{B}(\mathbf{r}) \cdot d\mathbf{l}. \tag{1.30}$$

Definition 9. The *circulation* of the vector field is a work along a closed path C:

$$W = \oint_C \mathbf{B}(\mathbf{r}) \cdot d\mathbf{l}. \tag{1.31}$$

Let us assume that, vector field $\mathbf{B}(\mathbf{r})$ is equal to the gradient of a scalar field $U(\mathbf{r})$:

$$\mathbf{B} = grad U. \tag{1.32}$$
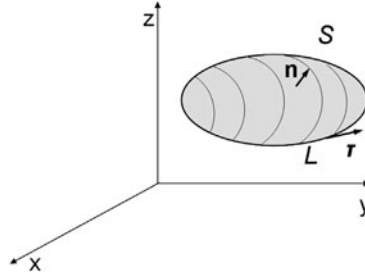
Formulation of Stokes's theorem. The direction of the positive normal to the surface S depends on the choice of the positive direction along the contour L. A standard convention is that, traversing of the contour in the positive direction τ can be treated as a clockwise movement for the observer looking in the direction of the positive normal $\mathbf{n}$.

We can formulate the following important theorem.

Theorem 1.1. *The work along the path L of the vector field* $\mathbf{B}(\mathbf{r})$ *equal to the gradient of a scalar field* $U(\mathbf{r})$ *is equal to the difference of the scalar field* $U(\mathbf{r})$ *at the end point,* $\mathbf{b}$, *and at the starting point,* $\mathbf{a}$, *of the path:*

$$W = \int_L \mathbf{B}(\mathbf{r}) \cdot d\mathbf{l} = U(\mathbf{b}) - U(\mathbf{a}). \tag{1.33}$$

Proof. Let us substitute Eq. (1.32) into (1.33). The direct calculations show that

$$W = \int_L \mathbf{B}(\mathbf{r}) \cdot d\mathbf{l} = \int_L grad U \cdot d\mathbf{l} = \int_L \frac{\partial U}{\partial l} dl$$
$$= \int_L dU = U(\mathbf{b}) - U(\mathbf{a}). \tag{1.34}$$

Thus, the work becomes independent of the path. In particular, any circulation of the vector field $\mathbf{B} = grad U$ is equal to zero. Such a vector field is called *a conservative field.*

We will now give several definitions related to the surface integrals of the scalar and vector fields.

Definition 10. *The flux of the scalar field* $U(\mathbf{r})$ *through the surface S is equal to the surface integral of the product of the scalar field and the vector element of the surface:*

$$\mathbf{F}_U^S = \iint_S U d\mathbf{s}. \tag{1.35}$$

Definition 11. *The scalar flux of the vector field* $\mathbf{B}(\mathbf{r})$ *through the surface S is equal to the surface integral of the scalar product of the vector field and the vector element of the surface:*

$$F_{\mathbf{B}}^S = \iint_S \mathbf{B} \cdot d\mathbf{s}. \tag{1.36}$$

Definition 12. *The vector flux of the vector field* $\mathbf{B}(\mathbf{r})$ *through the surface* S *is equal to the vector product of the vector field and the vector element of the surface:*

$$\mathbf{F}_{\mathbf{B}}^{S} = \iint_{S} \mathbf{B} \times d\mathbf{s}. \tag{1.37}$$

Thus, the flux of a scalar field U and the vector flux of a vector field $\mathbf{B}$ are vectors, while a scalar flux of the vector field is a scalar.

1.2.2 GAUSS'S THEOREM AND ITS VECTOR FORMULATIONS

We consider that vector field $\mathbf{B}$ and its first derivatives are continuous functions everywhere over volume D, bounded by a piece-wise smooth surface S (Fig. 1.2). Gauss's theorem describes a relationship between the volume integral of the vector derivatives of the vector field and a surface integral of the vector field itself over the boundary of the volume. There exist several equivalent forms of Gauss's theorem.

1st vector form of Gauss's theorem

The traditional form of Gauss's theorem states that *the volume integral of the divergence of the vector field* $\mathbf{B}$ *integrated over the volume* D *enclosed by the surface* S *equals scalar flux of the vector field* $\mathbf{B}$ *through this surface:*

$$\iiint_{D} div\mathbf{B}dv = \iint_{S} \mathbf{B} \cdot d\mathbf{s}, \tag{1.38}$$

where $d\mathbf{s} = \mathbf{n}ds$, and $\mathbf{n}$ is a unit outward normal vector to the surface S (see Fig. 1.2).

2nd vector form of Gauss's theorem

We can obtain an alternative form of Gauss's theorem, assuming that vector field $\mathbf{B}$ is given as a product of a scalar field U and some arbitrary constant vector $\mathbf{c}$:

$$\mathbf{B} = U\mathbf{c}. \tag{1.39}$$

Taking into account in Eq. (1.38) that

$$div\mathbf{B} = gradU \cdot \mathbf{c},$$

and

$$\mathbf{B} \cdot d\mathbf{s} = U\mathbf{c} \cdot d\mathbf{s},$$

we have

$$\iiint_{D} gradU \cdot \mathbf{c}dv = \iint_{S} U\mathbf{c} \cdot d\mathbf{s}.$$

The last formula can be written in equivalent form as

$$\mathbf{c} \cdot \left(\iiint_D gradU \, dv - \iint_S U d\mathbf{s} \right) = 0. \tag{1.40}$$

Since $\mathbf{c}$ is an arbitrary vector, we may select

$$\mathbf{c} = \left(\iiint_D gradU \, dv - \iint_S U d\mathbf{s} \right).$$

It is clear now that Eq. (1.40) holds only if the term in parenthesis is zero. Therefore, we finally obtain:

$$\iiint_D gradU \, dv = \iint_S U d\mathbf{s}. \tag{1.41}$$

The second vector form of Gauss's theorem states that *the volume integral of the gradient of a scalar field U integrated over the volume D enclosed by the surface S equals scalar flux of the field U through the surface S.*

3rd vector form of Gauss's theorem

We introduce now a vector field **B** as

$$\mathbf{B} = \mathbf{A} \times \mathbf{c}, \tag{1.42}$$

where **A** is an auxiliary vector field, and **c** is an arbitrary constant vector. In this case

$$div\mathbf{B} = \nabla \cdot [\mathbf{A} \times \mathbf{c}]$$

$$= \nabla \cdot \left[\overset{\downarrow}{\mathbf{A}} \times \mathbf{c} \right] + \nabla \cdot \left[\mathbf{A} \times \overset{\downarrow}{\mathbf{c}} \right] = (\mathbf{c}, \nabla, \mathbf{A}) = \mathbf{c} \cdot curl\mathbf{A}$$

and

$$\mathbf{B} \cdot d\mathbf{s} = [\mathbf{A} \times \mathbf{c}] \cdot d\mathbf{s} = -\mathbf{c} \cdot [\mathbf{A} \times d\mathbf{s}].$$

Applying Gauss's formula (1.38) to the vector field (1.42), we obtain:

$$\iiint_D \mathbf{c} \cdot curl\mathbf{A} \, dv = - \iint_S \mathbf{c} \cdot [\mathbf{A} \times d\mathbf{s}].$$

In a similar manner as we did above, we can eliminate arbitrary vector **c** from the last formula and obtain the third vector form of Gauss's theorem:

$$\iiint_D curl\mathbf{A} \, dv = - \iint_S [\mathbf{A} \times d\mathbf{s}]. \tag{1.43}$$

The last equation states that *the volume integral of the curl of the vector field* **A** *integrated over the volume D enclosed by the surface S equals (with the negative sign) the vector flux of the field* **A** *through the surface S*.

We will see in the next chapters that Gauss's theorem has found wide applications in electromagnetic theory.

1.2.3 STOKES'S THEOREM AND ITS VECTOR FORMULATIONS

It was shown above that Gauss's theorem relates the volume integral of the vector derivatives of the field to the surface integral of the field itself. Stokes's theorem allows us to make the next step – to reduce the surface integral to the line integral of the field.

1st vector form of Stokes's theorem

Let us consider an open surface S shown in Fig. 1.4, bounded by the closed contour L. We chose the positive directions of vectors **n** and $\boldsymbol{\tau}$, according to a standard convention, formulated above. Traversing of the contour in the positive direction $\boldsymbol{\tau}$ is clockwise for the observer looking in the direction of the positive normal **n**. We assume again that vector field **B** and its first derivatives are continuous functions everywhere over volume D, containing a piece-wise smooth surface S.

The first vector form of Stokes's theorem states that *the scalar flux of the curl of the vector field* **B** *through an open surface S is equal to the circulation of this field along the closed boundary L of the surface*:

$$\iint_S curl\mathbf{B} \cdot d\mathbf{s} = \oint_L \mathbf{B} \cdot d\mathbf{l}. \tag{1.44}$$

For example, if S is a closed surface, it has no boundary and the circulation vanishes:

$$\iint_S curl\mathbf{B} \cdot d\mathbf{s} = 0. \tag{1.45}$$

Therefore, we find immediately that the scalar flux of the curl of a vector field through a closed surface is always equal to zero.

2nd vector form of Stokes's theorem

We can produce an alternate form of the Stokes's theorem by substitution:

$$\mathbf{B} = U\mathbf{c}$$

in Eq. (1.44). In this case:

$$curl\mathbf{B} = \nabla \times (U\mathbf{c}) = \nabla \times \left(\overset{\downarrow}{U}\mathbf{c}\right) + \nabla \times \left(U\overset{\downarrow}{\mathbf{c}}\right) = \nabla U \times \mathbf{c} = gradU \times \mathbf{c},$$

and we have

$$\iint_S [gradU \times \mathbf{c}] \cdot d\mathbf{s} = -\mathbf{c} \cdot \iint_S gradU \times ds = \mathbf{c} \cdot \oint_L Ud\mathbf{l}.$$

Since the choice of vector **c** is arbitrary, we can eliminate this vector from the last formula. As a result, we arrive at the second vector form of the Stokes's theorem:

$$\iint_S gradU \times d\mathbf{s} = - \oint_L U d\mathbf{l}. \tag{1.46}$$

The last formula states that *the vector flux of the gradient of a scalar field through an open surface is equal to the line integral of this field along the closed boundary L of the surface.*

1.2.4 GREEN'S FORMULAS

On the basis of Gauss's theorem, one can develop a set of useful integral relations which are known as Green's formulas.

1st Green's formula

Let us assume that two continuously differentiable scalar fields a and b are given in some domain D. We introduce a new vector field $\mathbf{B} = a\, gradb$. The divergence of this field is equal to:

$$div\mathbf{B} = grada \cdot gradb + a\nabla^2 b.$$

Substituting the last expression in Gauss's formula (1.38), we have:

$$\iiint_D (grada \cdot gradb + a\nabla^2 b)dv = \iint_S a\frac{\partial b}{\partial n}ds, \tag{1.47}$$

where, according to Eq. (1.8),

$$\frac{\partial b}{\partial n} = gradb \cdot \mathbf{n}$$

is a derivative of the scalar field b along a direction $\mathbf{n}$.

2nd Green's formula

We can assume now that vector field $\mathbf{B}$ is equal to:

$$\mathbf{B} = b\, grada.$$

According to the first Green's formula, we have

$$\iiint_D (grada \cdot gradb + b\nabla^2 a)dv = \iint_S b\frac{\partial a}{\partial n}ds. \tag{1.48}$$

Subtracting Eq. (1.48) from Eq. (1.47), we obtain:

$$\iiint_D (a\nabla^2 b - b\nabla^2 a)dv = \iint_S \left(a\frac{\partial b}{\partial n} - b\frac{\partial a}{\partial n} \right) ds. \tag{1.49}$$

Formula (1.49) is called a Green's theorem. We will use this formula in the following chapters of the book to develop the theory of the Green's functions.

3rd Green's formula

The third Green's formula is derived from Eq. (1.49) if scalar field a is a constant equal to 1:

$$a = 1.$$

In this case we find immediately:

$$\iiint_D \nabla^2 b \, dv = \iint_S \frac{\partial b}{\partial n} ds = \iint_S grad \, b \cdot d\mathbf{s}. \tag{1.50}$$

The last formula states that *the volume integral of the Laplacian of a scalar field U integrated over volume D enclosed by the surface S equals to the scalar flux of the gradient of this field through the surface.*

1.3 DIFFERENTIAL FORMS IN FIELD THEORY
1.3.1 CONCEPT OF THE DIFFERENTIAL FORM

The differential forms were originally introduced in differential geometry to study the properties of the lines and surfaces in multidimensional mathematical spaces. However, it was realized not so long ago that these forms provide a very elegant and powerful tool to study the physical fields as well. We can treat the differential forms as another mathematical language which, similar to the standard Gibbsian vectorial language, can be used to describe the physical fields.

In order to emphasize a similarity between the differential forms and vectors, let us recall some integral formulas of vector calculus introduced in the previous section.

We have introduced the work, W, of a vector field $\mathbf{B}$ along the curve L, as the following line integral (see Eq. (1.30)):

$$W = \int_L \mathbf{B} \cdot d\mathbf{l}. \tag{1.51}$$

We have also introduced a scalar flux of the vector field $\mathbf{B}(\mathbf{r})$ through the surface S as a surface integral of the scalar product of the vector field and the vector element of the surface (see Eq. (1.36)):

$$F_{\mathbf{B}}^S = \iint_S \mathbf{B} \cdot d\mathbf{s}. \tag{1.52}$$

We have also formulated Gauss's and Stokes's theorems (Eqs. (1.38) and (1.44)):

$$\iiint_D div\mathbf{B} \, dv = \iint_S \mathbf{B} \cdot d\mathbf{s}, \tag{1.53}$$

and

$$\iint_S curl\mathbf{B} \cdot d\mathbf{s} = \oint_L \mathbf{B} \cdot d\mathbf{l}. \tag{1.54}$$

In all formulas (1.51) through (1.54) we have differential expressions – $\mathbf{B} \cdot d\mathbf{l}$, $\mathbf{B} \cdot d\mathbf{s}$, and $div\mathbf{B}dv$ – which are integrated over a curve, L, surface, S, or volume, D, respectively. These expressions are called *differential forms*.

In particular, a differential expression $\mathbf{B} \cdot d\mathbf{l}$, which is integrated over a curve, represents the elementary work, dW, of the vector field $\mathbf{B}$ along an infinitesimally small vector element of curve $d\mathbf{l}$. It is called a *differential 1-form* $\underset{(1)}{\varphi}$:

$$\underset{(1)}{\varphi} = \mathbf{B} \cdot d\mathbf{l} = dW. \tag{1.55}$$

A differential expression $\mathbf{B} \cdot d\mathbf{s}$, which is integrated over a surface, describes an elementary scalar flux, $dF_{\mathbf{B}}^{ds}$, of the vector field $\mathbf{B}$ through an infinitesimally small vector element of surface $d\mathbf{s}$. It is called a *differential 2-form* $\underset{(2)}{\psi}$:

$$\underset{(2)}{\psi} = \mathbf{B} \cdot d\mathbf{s} = dF_{\mathbf{B}}^{ds}. \tag{1.56}$$

Finally, a differential expression $div\mathbf{B}dv$, which is integrated over a volume, is equal to an elementary source, dQ, of the vector field $\mathbf{B}$ within an infinitesimally small element of volume dv. We call this expression a *differential 3-form* $\underset{(3)}{\theta}$:

$$\underset{(3)}{\theta} = qdv = dQ, \tag{1.57}$$

where

$$q = div\mathbf{B}.$$

We will find in Chapter 2 that divergence of the vector field $\mathbf{B}$ can be treated as a source of this field. Thus, all three forms represent the scalar values of the work, flux, and source of the vector field, respectively.

We immediately see from Eq. (1.55) that, for a given vector field $\mathbf{B}$, the work, dW, depends on the selected vector element of the curve, vector $d\mathbf{l}$. At the same time Eqs. (1.56) and (1.57) show that, the scalar flux, $dF_{\mathbf{B}}^{ds}$, depends on the selected vector element of surface $d\mathbf{s}$, while the source, dQ, is a function of the element of volume dv. The infinitesimally small elementary vector $d\mathbf{l}$, according to the definition, is an oriented (directed) segment of line. The infinitesimally small oriented element of surface $d\mathbf{s}$ can be described as an oriented parallelogram formed by two vectors, $d\mathbf{a}$ and $d\mathbf{b}$, as shown in Fig. 1.5. The infinitesimally small element of volume dv is usually represented as a parallelepiped formed by three vectors, $d\mathbf{a}$, $d\mathbf{b}$, and $d\mathbf{c}$, as shown in Fig. 1.6. Note that we can think of vectors, $d\mathbf{a}$, $d\mathbf{b}$, and $d\mathbf{c}$ as infinitesimal increments in the directions of vectors $\mathbf{a}$, $\mathbf{b}$, and $\mathbf{c}$, respectively.

According to the rules of vector algebra, we have:

$$d\mathbf{s} = d\mathbf{a} \times d\mathbf{b}, \text{ and } dv = (d\mathbf{a}, d\mathbf{b}, d\mathbf{c}).$$
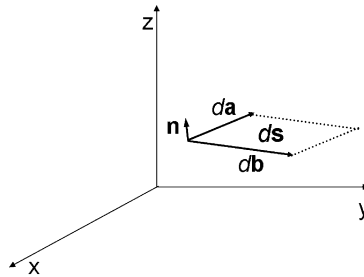
FIGURE 1.5

An infinitesimally small vector element of surface $d\mathbf{s}$ is described as an oriented parallelogram formed by two vectors, $d\mathbf{a}$ and $d\mathbf{b}$.
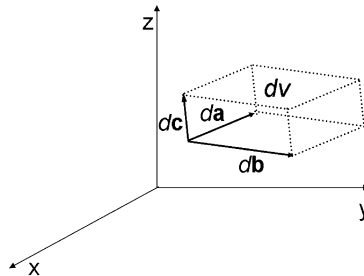
FIGURE 1.6

An infinitesimally small element of volume dv is represented as a parallelepiped formed by three vectors, $d\mathbf{a}$, $d\mathbf{b}$, and $d\mathbf{c}$.

Thus, we conclude, that a 1-form $\underset{(1)}{\varphi}$ is a function of one vector, $d\mathbf{l}$, a 2-form $\underset{(2)}{\psi}$ is a function of two vectors, $d\mathbf{a}$ and $d\mathbf{b}$, and a 3-form $\underset{(3)}{\theta}$ is a function of three vectors, $d\mathbf{a}$, $d\mathbf{b}$, and $d\mathbf{c}$, respectively:

$$\underset{(1)}{\varphi} = \underset{(1)}{\varphi}(d\mathbf{l}) = \mathbf{B} \cdot d\mathbf{l}, \quad \underset{(2)}{\psi} = \underset{(2)}{\psi}(d\mathbf{a}, d\mathbf{b}) = \mathbf{B} \cdot [d\mathbf{a} \times d\mathbf{b}],$$

$$\underset{(3)}{\theta} = \underset{(3)}{\theta}(d\mathbf{a}, d\mathbf{b}, d\mathbf{c}) = div\mathbf{B}(d\mathbf{a}, d\mathbf{b}, d\mathbf{c}). \tag{1.58}$$

Another important observation is that all three of these forms are linear functions of their arguments (vectors), because the cross and the triple scalar products of the vectors are linear algebraic operations. In other words, the differential forms introduced above are nothing else but linear functions of one (in the case of the 1-form), two (in the case of the 2-form) and three (in the case of the 3-form) vector arguments.

It follows immediately from Eqs. (1.58) that 2-form and 3-form are antisymmetric linear functions:

$$\underset{(2)}{\psi}\,(d\mathbf{a}, d\mathbf{b}) = -\underset{(2)}{\psi}\,(d\mathbf{b}, d\mathbf{a}),$$

$$\underset{(3)}{\theta}\,(d\mathbf{a}, d\mathbf{b}, d\mathbf{c}) = -\underset{(3)}{\theta}\,(d\mathbf{b}, d\mathbf{a}, d\mathbf{c}), \quad \underset{(3)}{\theta}\,(d\mathbf{a}, d\mathbf{b}, d\mathbf{c}) = -\underset{(3)}{\theta}\,(d\mathbf{a}, d\mathbf{c}, d\mathbf{b}), \quad etc. \tag{1.59}$$

For consistency, we can say that the 1-form, $\underset{(1)}{\varphi}$, is antisymmetric as well, because it depends on one vector argument only.

We also introduce a 0-form as a scalar function of the coordinates: $\underset{(0)}{\varphi} = f(\mathbf{r})$.

1.3.2 EXTERIOR (WEDGE) PRODUCT OF THE LINEAR FORMS

We have found in the previous section that the conventional differential forms of vector calculus (the expressions that are integrated over a line, surface, or volume) are described by antisymmetric linear functions of one, two, or three vector arguments. These linear functions (differential forms) represent new mathematical objects which are very useful in a description of electromagnetic field equations. We will demonstrate in the following chapters of the book that the differential forms provide the most natural and elegant mathematical tool for a description of the electromagnetic fields. In order to be able to apply these functions to electromagnetic theory, we should introduce the mathematical rules of operation on the differential forms, which define the *algebra* of the differential forms.

The simplest operation is addition. It is obvious that the addition of two antisymmetric linear forms is determined as a conventional summation of two functions. This operation satisfies the traditional commutative and associative laws, and also the distributive laws with respect to multiplication by a scalar.

The multiplication of the differential forms requires introducing a special algebraic operation, an exterior product, which we will discuss in detail below.

In the case of vectors, we can use different multiplication operations, e.g., dot and cross products of the vectors. In principle, it is easy to consider a product, f, of two forms, φ and ψ, as a product of two linear functions of vector arguments. For example, if $\varphi = \varphi(d\mathbf{l})$ and $\psi = \psi(d\mathbf{a}, d\mathbf{b})$, we have

$$f = f(d\mathbf{l}, d\mathbf{a}, d\mathbf{b}) = \varphi(d\mathbf{l})\,\psi(d\mathbf{a}, d\mathbf{b}), \tag{1.60}$$

where multiplication on the right-hand side of Eq. (1.60) is conducted in the conventional way as a product of two scalar values, φ and ψ. The only problem with this definition is that the product of the two antisymmetric linear functions, φ and ψ, is no longer an antisymmetric function! Indeed, one can see that

$$f(d\mathbf{l}, d\mathbf{a}, d\mathbf{b}) \neq -f(d\mathbf{a}, d\mathbf{l}, d\mathbf{b}).$$

In order to keep the result of multiplication within the class of antisymmetric linear functions, we should apply an antisymmetrization operation to the conventional product (1.60). As a result, we arrive

at the following multiplication operation, which is called the exterior (or wedge) product, denoted by symbol $\wedge$, and defined as:

$$\Omega = \varphi \wedge \psi = \{\varphi\,(d\mathbf{l})\,\psi\,(d\mathbf{a}, d\mathbf{b}) + \varphi\,(d\mathbf{a})\,\psi\,(d\mathbf{b}, d\mathbf{l}) + \varphi\,(d\mathbf{b})\,\psi\,(d\mathbf{l}, d\mathbf{a})$$

$$-\varphi\,(d\mathbf{l})\,\psi\,(d\mathbf{b}, d\mathbf{a}) - \varphi\,(d\mathbf{a})\,\psi\,(d\mathbf{l}, d\mathbf{b}) - \varphi\,(d\mathbf{b})\,\psi\,(d\mathbf{a}, d\mathbf{l})\}. \tag{1.61}$$

It is easy to check that the new linear function, $\Omega = \Omega\,(d\mathbf{l}, d\mathbf{a}, d\mathbf{b})$, is indeed an antisymmetric function.

In the case of the product of two 1-forms, $\varphi\,(d\mathbf{a})$ and $\chi\,(d\mathbf{b})$, the exterior product is given by the formula:

$$\Phi\,(d\mathbf{a}, d\mathbf{b}) = \varphi\,(d\mathbf{a}) \wedge \chi\,(d\mathbf{b}) = \left[\varphi\,(d\mathbf{a})\,\chi\,(d\mathbf{b}) - \varphi\,(d\mathbf{b})\,\chi\,(d\mathbf{a})\right], \tag{1.62}$$

which is again an antisymmetric function:

$$\Phi\,(d\mathbf{a}, d\mathbf{b}) = -\left[\varphi\,(d\mathbf{b})\,\chi\,(d\mathbf{a}) - \varphi\,(d\mathbf{a})\,\chi\,(d\mathbf{b})\right] = -\Phi\,(d\mathbf{b}, d\mathbf{a}). \tag{1.63}$$

In summary, we can see that addition and exterior multiplication operations of 1-forms satisfy the following laws:

1) the commutative and associative laws of addition:

$$\varphi + \chi = \chi + \varphi \text{ and } \varphi + (\chi + \eta) = (\varphi + \chi) + \eta; \tag{1.64}$$

2) the anticommutative law of exterior multiplication:

$$\varphi \wedge \chi = -\chi \wedge \varphi; \tag{1.65}$$

3) the distributive law of multiplication over addition:

$$\varphi \wedge (\chi + \eta) = \varphi \wedge \chi + \varphi \wedge \eta \text{ and } (\varphi + \chi) \wedge \eta = \varphi \wedge \eta + \chi \wedge \eta. \tag{1.66}$$

It comes immediately from the anticommutative law (1.65) that

$$\varphi \wedge \varphi = 0. \tag{1.67}$$

We can see now that the exterior product of two 1-forms generates a 2-form, while the exterior product of three 1-forms produces a 3-form.

1.3.3 CANONICAL REPRESENTATIONS OF THE DIFFERENTIAL FORMS IN THREE-DIMENSIONAL EUCLIDEAN SPACE

The important fact of the differential form theory is that any 2-form and any 3-form can be expressed as the exterior products of two 1-forms and three 1-forms respectively. These representations are called the *canonical representations* for the differential forms. The interested reader may find a derivation of these representations in Appendix A. The following table presents a summary of these canonical representations for differential forms in three-dimensional Euclidean space E_3:

$$\text{0-forms} \quad : \quad \underset{(0)}{\varphi} = f, \tag{1.68}$$

$$\text{1-forms} \quad : \quad \underset{(1)}{\varphi} = \sum_{\alpha=x,y,z} \varphi_\alpha d\alpha = \varphi_x dx + \varphi_y dy + \varphi_z dz = \boldsymbol{\varphi} \cdot d\mathbf{r}, \qquad (1.69)$$

$$\text{2-forms} \quad : \quad \underset{(2)}{\psi} = \sum_{\alpha,\beta=x,y,z} \psi_{\alpha\beta} d\alpha \wedge d\beta$$

$$= \psi_{yz} dy \wedge dz + \psi_{zx} dz \wedge dx + \psi_{xy} dx \wedge dy = \boldsymbol{\psi} \cdot d\boldsymbol{\Sigma}, \qquad (1.70)$$

$$\text{3-forms} \quad : \quad \underset{(3)}{\theta} = \theta dx \wedge dy \wedge dz = \theta dv. \qquad (1.71)$$

In the last formulas we use the following notations:

$$\boldsymbol{\varphi} = (\varphi_x, \varphi_y, \varphi_z), \ d\mathbf{r} = (dx, dy, dz),$$

$$\boldsymbol{\psi} = \psi_{yz} \mathbf{d}_x + \psi_{zx} \mathbf{d}_y + \psi_{xy} \mathbf{d}_z,$$

$$d\boldsymbol{\Sigma} = ds_x \mathbf{d}_x + ds_y \mathbf{d}_y + ds_z \mathbf{d}_z,$$

where ds_x, ds_y, and ds_z are the combinations of the exterior products of differentials,

$$ds_x = dy \wedge dz, ds_y = dz \wedge dx, ds_z = dx \wedge dy,$$

and, according to formulas (A.21), (A.24), and (A.27) from Appendix A,

$$\theta = \left(a_x b_y c_z + a_y b_z c_x + a_z b_x c_y - a_x b_z c_y - a_y b_x c_z - a_z b_y c_x\right).$$

The canonical representations (1.68)–(1.71) for the differential forms can be written in the compact form:

$$\underset{(p)}{\omega}(\mathbf{r}) = \sum_{\alpha_1,...\alpha_p=x,y,z} \omega_{\alpha_1,...\alpha_p} d\alpha_1 \wedge .... \wedge d\alpha_p, \ p = 0, 1, 2, 3, \qquad (1.72)$$

where $\omega_{\alpha_1,...\alpha_p}$ stands for φ_α, $\psi_{\alpha\beta}$, and θ, respectively, and α_p denotes one of the variables x, y, or z. For example,

$$\omega_\alpha = \varphi_\alpha, \ \ \omega_{\alpha_1,\alpha_2} = \psi_{\alpha_1\alpha_2}, \ \omega_{\alpha_1,\alpha_2,\alpha_3} = \theta.$$

1.3.4 THE EXTERIOR DERIVATIVE

Let us assume that some physical field in three-dimensional Euclidean space is described by the differential forms. For example, this field can represent a potential of the electric field (which is described by 0-form $\underset{(0)}{\varphi}$), or elementary work of the electric field (which is described by 1-form $\underset{(1)}{\varphi}$), or an elementary flux of a magnetic field (which is described by 2-form $\underset{(2)}{\psi}$), or an elementary volume charge of an electric field (which is described by 3-form $\underset{(3)}{\theta}$). We know that the physical field usually varies in space

and it is a function of the radius-vector $\mathbf{r}$ of the point of observation. Therefore, the corresponding differential forms vary in space and are the functions of the observation point as well:

$$\underset{(0)}{\varphi = f(\mathbf{r})}, \quad \underset{(1)}{\varphi = \varphi(\mathbf{r})}, \quad \underset{(2)}{\psi = \psi(\mathbf{r})}, \quad \underset{(3)}{\theta = \theta(\mathbf{r})}. \tag{1.73}$$

Thus, we have arrived at a concept of the *differential form fields* similar to the vector fields considered above. Taking into account that these new fields according to Eq. (1.73) depend on the point of observation, we can consider some method of their differentiation similar to the vector field differentiation introduced above. However, we should be careful in introducing this differential operation. The main requirement should be that the result of the form's differentiation should produce the differential form as well.

The calculus of differential forms is based on a special differential operation called the *exterior derivative* (see Appendix B). This operation can be treated as a generalization of conventional vector differential operations. We will find out in this section, however, that all three different vector differential operations, (gradient, divergence, and curl), can be represented as a single exterior differential operator.

0-forms

In the case of the simplest 0-form described by a function $f(\mathbf{r})$, the exterior differential is equivalent to the full differential of the function:

$$df = \frac{\partial f}{\partial x}dx + \frac{\partial f}{\partial y}dy + \frac{\partial f}{\partial z}dz. \tag{1.74}$$

In three-dimensional Euclidean space this differential operation is closely related to the conventional vector differential operators. Indeed, using gradient operation, we can represent Eq. (1.74) as

$$df = \frac{\partial f}{\partial x}dx + \frac{\partial f}{\partial y}dy + \frac{\partial f}{\partial z}dz = grad\, f(\mathbf{r}) \cdot d\mathbf{r}. \tag{1.75}$$

We can see that in this case the exterior differential operator d can be treated as a counterpart of the vector del operator ∇. We can introduce a symbolic differential 1-form d_{E_3} as follows:

$$d_{E_3} = dx\frac{\partial}{\partial x} + dy\frac{\partial}{\partial y} + dz\frac{\partial}{\partial z} = d\mathbf{r} \cdot \nabla. \tag{1.76}$$

Then Eq. (1.75) can be written as

$$df = d_{E_3}f = d\mathbf{r} \cdot \nabla f = \nabla f \cdot d\mathbf{r}.$$

Therefore, the exterior derivative of the 0-form is equivalent to the gradient of the corresponding scalar field.

1-forms

The exterior differential of the 1-form field $\varphi(\mathbf{r})$ is calculated as an exterior product of the differential operator 1-form d_{E_3} and a given 1-form φ:

$$
\begin{aligned}
d\varphi &= d_{E_3} \wedge \varphi = d_{E_3} \wedge (\boldsymbol{\varphi} \cdot d\mathbf{r}) \\
&= \left(\frac{\partial \varphi_y}{\partial x} - \frac{\partial \varphi_x}{\partial y} \right) dx \wedge dy + \left(\frac{\partial \varphi_z}{\partial y} - \frac{\partial \varphi_y}{\partial z} \right) dy \wedge dz + \left(\frac{\partial \varphi_x}{\partial z} - \frac{\partial \varphi_z}{\partial x} \right) dz \wedge dx \\
&= curl\boldsymbol{\varphi} \cdot d\boldsymbol{\Sigma} = \left[\boldsymbol{\nabla} \times \boldsymbol{\varphi} \right] \cdot d\boldsymbol{\Sigma},
\end{aligned} \tag{1.77}
$$

where we took into account representations (1.69) and (1.70) for the differential forms and the property (1.67) of the wedge product.

According to the canonical representation (1.69), every 1-form can be described by a vector field $\boldsymbol{\varphi}$. Therefore, the exterior derivative of the 1-form is equivalent to the curl of the corresponding vector field.

2-forms

The exterior differential of the 2-form field $\psi(\mathbf{r})$ is obtained by the wedge product of the exterior differential d_{E_3} and a given 2-form ψ. Taking into account Eq. (1.70), we can calculate this derivative using the following expression:

$$
\begin{aligned}
d\psi &= d_{E_3} \wedge \psi = d_{E_3} \wedge (\boldsymbol{\psi} \cdot d\boldsymbol{\Sigma}) \\
&= \frac{\partial \psi_{yz}}{\partial x} dx \wedge dy \wedge dz + \frac{\partial \psi_{zx}}{\partial y} dy \wedge dz \wedge dx + \frac{\partial \psi_{xy}}{\partial z} dz \wedge dx \wedge dy \\
&= \left(\frac{\partial \psi_{yz}}{\partial x} + \frac{\partial \psi_{zx}}{\partial y} + \frac{\partial \psi_{xy}}{\partial z} \right) dx \wedge dy \wedge dz = (div\boldsymbol{\psi}) \, dv = (\boldsymbol{\nabla} \cdot \boldsymbol{\psi}) \, dv.
\end{aligned} \tag{1.78}
$$

According to the canonical representation (1.70), every 2-from can be described by a vector field $\boldsymbol{\psi}$. Therefore, the exterior derivative of the 2-form is equivalent to the divergence of the corresponding vector field.

3-forms

The exterior differential of a 3-form $\underset{(3)}{\theta} = \theta dx \wedge dy \wedge dz$ can be calculated as an exterior product of the differential operator d_{E_3} and this 3-form:

$$
d_{E_3} \wedge \underset{(3)}{\theta} = d\theta \wedge dx \wedge dy \wedge dz.
$$

The last expression is equal to zero according to the anticommutative law (1.65) and Eq. (1.67):

$$
d_{E_3} \wedge \underset{(3)}{\theta} = \left(\frac{\partial \theta}{\partial x} dx + \frac{\partial \theta}{\partial y} dy + \frac{\partial \theta}{\partial z} dz \right) \wedge dx \wedge dy \wedge dz = 0. \tag{1.79}
$$

Thus we can see that, the exterior differential operation in three-dimensional space corresponds to either the gradient, curl, or divergence of conventional vector calculus:

$$0\text{-forms} \quad : \quad d_{E_3} \underset{(0)}{\varphi} \; = \; d_{E_3} f = grad\, f(\mathbf{r}) \cdot d\mathbf{r} = \nabla f(\mathbf{r}) \cdot d\mathbf{r}, \tag{1.80}$$

$$1\text{-forms} \quad : \quad d_{E_3} \underset{(1)}{\varphi} \; = \; d_{E_3} \wedge (\boldsymbol{\varphi} \cdot d\mathbf{r}) = curl\, \boldsymbol{\varphi} \cdot d\boldsymbol{\Sigma} = \left[\nabla \times \boldsymbol{\varphi} \right] \cdot d\boldsymbol{\Sigma}, \tag{1.81}$$

$$2\text{-forms} \quad : \quad d_{E_3} \underset{(2)}{\psi} \; = \; d_{E_3} \wedge (\boldsymbol{\psi} \cdot d\boldsymbol{\Sigma}) = (div\, \boldsymbol{\psi})\, dv = (\nabla \cdot \boldsymbol{\psi})\, dv, \tag{1.82}$$

$$3\text{-forms} \quad : \quad d_{E_3} \underset{(3)}{\theta} \; = \; d_{E_3} \wedge (\theta\, dv) = 0. \tag{1.83}$$

The beauty of the exterior differentiation operator is that it includes all varieties of vector differential operations. In addition, this operator allows us to extend naturally the differentiation operation for multidimensional spaces.

REFERENCES AND RECOMMENDED READING TO CHAPTER 1

Arfken, G., and H. J. Weber, 1995, Mathematical methods for physicists, 4th ed.: Academic Press, San Diego, New York, Boston, London, Tokyo, Toronto, 1029 pp.

Davis, H. F., and A. D. Snider, 1979, Introduction to vector analysis: Allyn & Bacon. Boston.

Fecko, M., 2006, Differential geometry and Lie groups for physicists: Cambridge University Press, 697 pp.

FOUNDATIONS OF FIELD THEORY

CONTENTS

In this chapter we will discuss the general principles of geophysical field theory and of field generations. We will find out that there can exist only two types of field excitation – sources and vortices. We will analyze the general physical meaning of a source or a vortex of a field. The theory of field generation will help us to develop a classification of vector fields. In the discussion of the basic principles of the classical theory of stationary scalar and vector fields, I will follow closely the lecture notes of Dmitriev et al. (2004). I should note also that one of the most comprehensive expositions of classical field theory was given by Alpin (1966). The interested reader may find additional details about the foundations of geophysical field theory in the books by Kaufman (1992, 1994a, 1994b).

The electromagnetic field, which is the main subject of this book, is, in general, a nonstationary field depending both on spatial and time coordinates. That is why we will study carefully the theory of nonstationary fields as well. I will demonstrate that this theory can be developed in the most elegant and complete way by using the technique of differential forms introduced in Chapter 1.

2.1 FIELD GENERATION

2.1.1 HARMONIC FUNCTIONS; LIOUVILLE'S THEOREM

In this section we will study the *harmonic functions*, which play a crucial role in the field theory. These functions arise in the theory of gravity, magnetic, and electromagnetic fields. We will give first the following definitions.

Definition 14. The function $U(\mathbf{r})$ determined in domain D is called *harmonic* in this domain if it is twice continuously differentiable in this domain and satisfies Laplace's equation:

$$\nabla^2 U(\mathbf{r}) = 0. \tag{2.1}$$

Definition 15. The function $a(\mathbf{r})$ determined in the entire space is called *regular at infinity* if there is a number R_0 and a sphere with the radius R_0 such that, for any $r = |\mathbf{r}| > R_0$, we have:

$$|a(\mathbf{r})| \leq \frac{c_1}{r}, \quad |grad\, a(\mathbf{r})| \leq \frac{c_2}{r^2}, \tag{2.2}$$

where c_1 and c_2 are two positive coefficients.

A simple example of the harmonic function is a product of exponential and a sine functions:

$$U_1(\mathbf{r}) = \exp(x)\cos y.$$

It is easy to verify that this function satisfies Laplace's equation:

$$\nabla^2 U_1(\mathbf{r}) = \frac{\partial^2}{\partial x^2}\left[\exp(x)\cos y\right] + \frac{\partial^2}{\partial y^2}\left[\exp(x)\cos y\right] = \exp(x)\left[\cos y - \cos y\right] = 0.$$

The beauty of the harmonic functions, which justifies their name, has been long recognized by mathematicians and physicists. These functions possess many wonderful properties, which make them so useful in mathematics and physics. In this book we will discuss just a small number of the most important properties of the harmonic functions. We will begin with the following theorem.

Theorem 16. *Liouville's theorem: If the function $U(\mathbf{r})$ is harmonic in the entire space and is a regular function in infinity, then this function is identically equal to zero: $U(\mathbf{r}) \equiv 0$.*

Proof. Let us introduce a Cartesian system of coordinates and draw a sphere S with a radius R from the origin of the coordinates. We denote by D the volume of the sphere.

We can write the first Green's formula for this sphere:

$$\iiint_D \left(grad\, a \cdot grad\, b + a\nabla^2 b\right) dv = \iint_S a\frac{\partial b}{\partial n} ds = \iint_S a\, grad\, b \cdot d\mathbf{s}.$$

Assuming that

$$a = b = U(\mathbf{r}),$$

we can write:

$$\iiint_D (gradU \cdot gradU + U\nabla^2 U)dv = \iint_S U\ gradU \cdot d\mathbf{s}.$$

Taking into account that $U(\mathbf{r})$ is harmonic function, $\nabla^2 U \equiv 0$, we have:

$$\iiint_D (gradU)^2 dv = \iint_S U\ gradU \cdot d\mathbf{s}.$$

Let us estimate the absolute value of the volume integral:

$$\iiint_D (gradU)^2 dv = \left| \oint_S U \cdot gradU \cdot d\mathbf{s} \right| \le \iint_S |u|\,|gradu|ds. \tag{2.3}$$

However, we know that the function $U(\mathbf{r})$ is regular in infinity. Therefore:

$$|u| \le \frac{c_1}{r}; \quad |gradu| \le \frac{c_2}{r^2}.$$

Substituting the last formula into Eq. (2.3), we have:

$$\iiint_D (gradU)^2 dv \le \iint_S \frac{c_1 c_2}{R^3} ds = \frac{4\pi c_1 c_2}{R} \to 0, R \to \infty.$$

It is well known that, if the integral of the nonnegative continuous function is equal to zero, the function itself is identically equal to zero. Thus, $gradU = 0$.

From the last formula we have

$$U = const.$$

However, according to the regularity at infinity, the following condition takes place:

$$U \to 0 \text{ when } r \to \infty.$$

Therefore, finally we have:

$$U = 0. \qquad \qquad \square$$

We can summarize the main statement of Liouville's theorem as follows: there does not exist any nonzero harmonic function in the entire space, which is regular at infinity. Therefore, one should consider either the harmonic function in the closed domain of a space, or this function will not attenuate at infinity. For example, function $U_1(\mathbf{r}) = \exp(x)\cos y$, introduced above, does not go to zero at infinity.

2.1.2 UNIQUENESS OF DETERMINATION OF THE SCALAR FIELD BY ITS GRADIENT AND THE VECTOR FIELD BY ITS DIVERGENCE AND CURL

In many practical applications, we deal with the problem of finding a field from its vector derivatives. In this case it is important to understand when this problem has a unique solution. We will discuss several important uniqueness theorems for the scalar and vector fields which provide an answer to this question.

Determination of the scalar field by its gradient

Let us consider a scalar field $U(\mathbf{r})$ determined in the entire three-dimensional space. We assume that this field is continuously differentiable in the space and its gradient is equal to some vector field $\mathbf{B}_g(\mathbf{r})$:

$$gradU = \mathbf{B}_g.$$

We can formulate the following theorem:

Theorem 17. *If a scalar field $U(\mathbf{r})$ is continuously differentiable in the entire space and is regular at infinity, then the problem of determining this field from its gradient, $\mathbf{B}_g$, has a unique solution.*

Proof. Suppose that this theorem is not correct. Then there exist two scalar fields, U_1 and U_2, with the same gradient:

$$gradU_1 = gradU_2 = \mathbf{B}_g. \tag{2.4}$$

Let us introduce a difference field, U', as

$$U' = U_1 - U_2.$$

According to Eq. (2.4), the gradient of the difference field is equal to zero:

$$gradU' = \mathbf{0}.$$

The field with the zero gradient is identically equal to a constant:

$$U' \equiv c = const.$$

However, according to the regularity at infinity of both solutions, U_1 and U_2, the difference field must be regular at infinity as well:

$$U \to 0 \text{ when } r \to \infty.$$

Therefore, we have no other choice for constant c but zero:

$$U' = U_1 - U_2 \equiv 0,$$

which completes the proof of the theorem. □

Determination of the vector field by its divergence and curl

We consider now a vector field $\mathbf{B}(\mathbf{r})$ determined in the entire three-dimensional space. We assume that this field is continuously differentiable in the space and its divergence and curl are equal to some scalar field, $q(\mathbf{r})$, and vector field, $\mathbf{j}(\mathbf{r})$, respectively:

$$div\mathbf{B} = q, \quad curl\mathbf{B} = \mathbf{j}. \tag{2.5}$$

The problem is to find vector field $\mathbf{B}(\mathbf{r})$ if $q(\mathbf{r})$ and $\mathbf{j}(\mathbf{r})$ are known. We can formulate the following uniqueness theorem for this problem.

Theorem 18. *If all scalar components of the vector field* **B**(**r**) *are continuously differentiable in the entire space and are regular at infinity, then the problem of determining this field from its divergence, q*(**r**), *and its curl,* **j**(**r**), *has a unique solution.*

Proof. The proof of this theorem is similar to the previous case of a scalar field. Suppose that this theorem is not correct. Then there exist two vector fields, $\mathbf{B}_1$ and $\mathbf{B}_2$, with the same divergence and with the same curl:

$$div\mathbf{B}_1 = div\mathbf{B}_2 = q; \quad curl\mathbf{B}_1 = curl\mathbf{B}_2 = \mathbf{j}. \tag{2.6}$$

Let us introduce the difference field $\mathbf{B}'$:

$$\mathbf{B}'(\mathbf{r}) = \mathbf{B}_1(\mathbf{r}) - \mathbf{B}_2(\mathbf{r}).$$

This field satisfies the equations:

$$\begin{aligned} div\mathbf{B}' &= 0, \\ curl\mathbf{B}' &= 0. \end{aligned} \tag{2.7}$$

Therefore the Laplacian of this field, according to formula (1.24), is equal to:

$$(\nabla \cdot \nabla)\mathbf{B}' = grad\,div\mathbf{B}' - curl\,curl\mathbf{B}' = 0. \tag{2.8}$$

From the last equation we see that the scalar components of the field $\mathbf{B}'(\mathbf{r})$ in some Cartesian coordinate system satisfy Liouville's theorem, because all of them are harmonic functions, and they are regular at infinity:

$$\nabla^2 B_x(\mathbf{r}) = 0, \ \nabla^2 B_y(\mathbf{r}) = 0, \ \nabla^2 B_z(\mathbf{r}) = 0.$$

Therefore, based on Liouville's theorem, we conclude that all scalar components of the difference field are identically equal to zero in the entire space, and the difference vector field $\mathbf{B}'$ is identically equal to zero as well:

$$\mathbf{B}'(\mathbf{r}) \equiv 0,$$

which contradicts our original assumption that we have two different solutions. □

2.1.3 FIELD GENERATION CONDITIONS

Theorems 17 and 18 introduced in the previous section help us to understand the conditions required for a vector field generation. Let us note first that we say that the vector field exists if it is not identically equal to zero in the entire space. According to the two theorems proved above, the necessary conditions for vector field **B**(**r**) to exist are as follows.

a) The divergence of the vector field **B**(**r**) is not equal to zero in some domain Q, while the curl of the vector field **B**(**r**) can be identically equal to zero in the entire space:

$$\begin{aligned} div\mathbf{B}(\mathbf{r}) &\neq 0, \ \mathbf{r} \in Q, \\ curl\mathbf{B}(\mathbf{r}) &\equiv 0. \end{aligned} \tag{2.9}$$

b) The curl of the vector field $\mathbf{B}(\mathbf{r})$ is not equal to zero in some domain Q, while the divergence of the vector field $\mathbf{B}(\mathbf{r})$ can be identically equal to zero in the entire space:

$$
\begin{aligned}
&div\mathbf{B}(\mathbf{r}) \equiv 0, \\
&curl\mathbf{B}(\mathbf{r}) \neq 0, \quad \mathbf{r} \in Q.
\end{aligned}
\tag{2.10}
$$

c) The divergence of the vector field $\mathbf{B}(\mathbf{r})$ is not equal to zero in some domain Q, while the curl of the vector field $\mathbf{B}(\mathbf{r})$ is not equal to zero in some domain P:

$$
\begin{aligned}
&div\mathbf{B}(\mathbf{r}) \neq 0, \ \mathbf{r} \in Q, \\
&curl\mathbf{B}(\mathbf{r}) \neq 0, \quad \mathbf{r} \in P.
\end{aligned}
\tag{2.11}
$$

Note that domains Q and P may coincide, overlap, or be two completely separated domains.

We will give now a few definitions.

Definition 19. The physical objects which generate a field are called the *field generators*.

Theorems 17 and 18 and Eqs. (2.9) through (2.11) show that there exist only two types of field generators: one with nonzero divergence and zero curl, and another one with a nonzero curl and a divergence of zero.

Definition 20. *Source* is a type of field generator that produces nonzero divergence of vector field $\mathbf{B}(\mathbf{r})$. The divergence of a vector field is called *a volume density of its sources q*:

$$
div\mathbf{B}(\mathbf{r}) = q(\mathbf{r}).
\tag{2.12}
$$

Definition 21. *Vortex* is a type of field generator that produces a nonzero curl. The curl of a vector field is called *a volume density of its vortices* $\mathbf{j}$:

$$
curl\mathbf{B}(\mathbf{r}) = \mathbf{j}(\mathbf{r}).
\tag{2.13}
$$

Thus, we come to the important conclusion that any vector field can be generated by the sources or vortices only. There are no any other types of field generators! Any vector field which has no sources and/or vortices and is regular at infinity is identically equal to zero. This result was formulated originally in the geophysical literature by Dmitriev et al. (2004). This rigorous mathematical result can be applied to any physical field. Therefore, the first question which should be addressed in studying any physical field is a question about the nature of its sources and vortices. We will examine this question in application to the electromagnetic field theory in the next chapters of the book.

2.1.4 SOURCES OF THE FIELD AND THEIR PHYSICAL MEANING

We examine now more carefully the physical meaning of the sources and vortices of vector fields. Let us begin with the sources. We assume that the vector field $\mathbf{B}(\mathbf{r})$ is given in the entire three-dimensional space and that all scalar components of the vector field $\mathbf{B}(\mathbf{r})$ are continuously differentiable functions. Consider a volume D, bounded by a piece-wise smooth surface S (Fig. 2.1). We can integrate both sides of Eq. (2.12) over this volume:

$$
\iiint_D div\mathbf{B}(\mathbf{r})dv = \iiint_D q(\mathbf{r})dv.
\tag{2.14}
$$
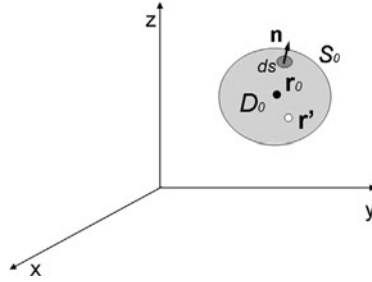
FIGURE 2.1

The volume density of the sources of the vector field **B** is calculated as a limit of the integral over volume D_0, bounded by a closed surface S_0, of the divergence of the vector field divided by the volume D_0 when the volume tends to zero: $D_0 \to 0$.

Applying a theorem of average value to both parts of the last formula, we can write:

$$\iiint_{D_0} div\mathbf{B}(\mathbf{r})dv = div\mathbf{B}(\mathbf{r}') \iiint_{D_0} dv = div\mathbf{B}(\mathbf{r}') D_0 = q(\mathbf{r}') D_0,$$

where $\mathbf{r}'$ is some internal point from $D_0 : \mathbf{r}' \in D_0$.

We can contract now the entire volume D_0 into one point $\mathbf{r}_0$ located inside the volume (see Fig. 2.1) and calculate a limit of the integral over volume D_0 of the divergence of the vector field divided by the volume D_0 when the volume tends to zero: $D_0 \to 0$:

$$\lim_{D_0 \to 0} \left[\left(\iiint_{D_0} div\mathbf{B}(\mathbf{r})dv \right) / D_0 \right] = \lim_{D_0 \to 0} \left[\left(div\mathbf{B}(\mathbf{r}') \iiint_{D_0} dv \right) / D_0 \right] = q(\mathbf{r}_0), \quad (2.15)$$

where we took into account that $\mathbf{r}' \to \mathbf{r}_0$, when $D_0 \to 0$.

We can give an equivalent representation of the source density, $q(\mathbf{r}_0)$, using Gauss's theorem (1.38):

$$q(\mathbf{r}_0) = \lim_{D_0 \to 0} \left[\left(\iint_{S_0} \mathbf{B} \cdot d\mathbf{s} \right) / D_0 \right], \quad (2.16)$$

where S_0 is a closed boundary of the volume D_0.

Based on formula (2.16), we conclude that the volume density of the source of the vector field **B** can be calculated as a limit of the scalar flux of the vector field **B** through a closed surface S_0, bounding the volume, divided by the volume D_0 when the volume tends to zero: $D_0 \to 0$.

Note that, according to Eq. (2.12), we have:

$$div\mathbf{B}(\mathbf{r}_0) = \lim_{D_0 \to 0} \left[\left(\iint_{S_0} \mathbf{B} \cdot d\mathbf{s} \right) / D_0 \right]. \quad (2.17)$$

Thus, we have arrived at a definition of the divergence of the vector field which is independent (invariant) of the selection of the system of coordinates.

Definition 22. The divergence of a vector field **B** is equal to the limit of the scalar flux of the vector field **B** through a closed surface S_0, divided by the volume D_0 bounded by S_0, when the volume tends to zero: $D_0 \to 0$.

Therefore, the divergence operator represents a *volume derivative* of the field.

In order to understand better the physical meaning of a source, we will use a hydrodynamic analogy. Let us consider some volume filled with a liquid. We will denote by $\mathbf{V}(\mathbf{r})$ the vector field of the velocity of the liquid movement at every given point $\mathbf{r}$. We assume also that the density of the liquid (its mass contained in the unit of volume) is ρ.

Let us introduce a vector field $\mathbf{B}^{hd}$ ("**h**ydro**d**ynamic" field) as

$$\mathbf{B}^{hd}(\mathbf{r}) = \rho \mathbf{V}(\mathbf{r}). \tag{2.18}$$

According to Eq. (2.16), the volume density of the sources of the field $\mathbf{B}^{hd}$ introduced by formula (2.18) can be approximately written as

$$q(\mathbf{r}_0) \approx \left(\iint_{S_0} \mathbf{B}^{hd} \cdot d\mathbf{s} \right) / D_0, \tag{2.19}$$

where D_0 is a small enough volume.

We can select an arbitrary small element ds of the surface S_0 and calculate the mass, dQ, of the liquid flowing through ds over the time interval Δt:

$$dQ = \rho (\mathbf{V} \cdot \mathbf{n}) \, ds \Delta t = \mathbf{B}^{hd} \cdot d\mathbf{s} \Delta t, \tag{2.20}$$

where $d\mathbf{s} = \mathbf{n} ds$, and $\mathbf{n}$ is a unit vector normal to the surface element ds (see Fig. 2.1). The total mass, Q, of the liquid flowing through the entire surface S_0 over the time interval Δt is equal to the integral of dQ over the surface:

$$Q = \iint_{S_0} dQ = \iint_{S_0} \rho (\mathbf{V} \cdot \mathbf{n}) \, ds \Delta t = \iint_{S_0} \mathbf{B}^{hd} \cdot d\mathbf{s} \Delta t. \tag{2.21}$$

Thus, the scalar flux of the vector field $\mathbf{B}^{hd}$ through the surface S_0 is equal to the mass of the liquid flowing through the entire surface S_0 per the unit of time:

$$\iint_{S_0} \mathbf{B}^{hd} \cdot d\mathbf{s} = Q/\Delta t. \tag{2.22}$$

Substituting the last formula into Eq. (2.19), we finally have:

$$div\mathbf{B}^{hd}(\mathbf{r}_0) = q(\mathbf{r}_0) \approx Q/(\Delta t D_0). \tag{2.23}$$

We can see from the last equation that the divergence of the "hydrodynamic" vector field determines the total mass of the liquid that has appeared (if $q(\mathbf{r}_0) > 0$), or disappeared (if $q(\mathbf{r}_0) < 0$) within the unit of volume over the unit of time. In other words, the divergence characterizes the volume density of the sources (if $q(\mathbf{r}_0) > 0$) or sinks (if $q(\mathbf{r}_0) < 0$) of the "hydrodynamic" vector field $\mathbf{B}^{hd}$.

Thus, the volume density of the sources is equal to the amount of liquid that has appeared ($Q > 0$) or disappeared ($Q < 0$) in the unit of volume during the unit of time.
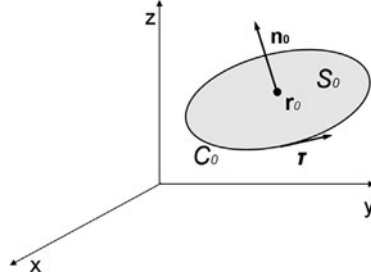
FIGURE 2.2

The volume density of the vortices of the vector field **B** is calculated as a limit of a scalar flux of the curl of the vector field over surface S_0, bounded by a closed contour C_0, divided by the area S_0 when the area tends to zero: $S_0 \to 0$.

2.1.5 VORTICES OF THE FIELD AND THEIR PHYSICAL MEANING

In this section we will study the vortices of the vector field. As above, we assume that the vector field $\mathbf{B}(\mathbf{r})$ is given in the entire three-dimensional space and that all scalar components of the vector field $\mathbf{B}(\mathbf{r})$ are continuously differentiable functions. Consider an arbitrary point $\mathbf{r}_0$, and draw a unit vector $\mathbf{n}_0$ from this point in an arbitrary direction (Fig. 2.2). We can also draw a circle C_0 in a plane perpendicular to vector $\mathbf{n}_0$ with the origin at the point $\mathbf{r}_0$. We denote by S_0 a round piece of plane bounded by the circle C_0.

We can integrate both sides of Eq. (2.13) over this surface:

$$\iint_{S_0} curl\mathbf{B}(\mathbf{r}) \cdot d\mathbf{s} = \iint_{S_0} \mathbf{j}(\mathbf{r}) \cdot d\mathbf{s}, \tag{2.24}$$

where the vector element of the surface is equal to: $d\mathbf{s} = \mathbf{n}_0 ds$.

Applying a theorem of average value to both parts of the last formula, we can write:

$$\iint_{S_0} curl\mathbf{B}(\mathbf{r}) \cdot d\mathbf{s} = \left[curl\mathbf{B}(\mathbf{r}') \cdot \mathbf{n}_0\right] \iint_{S_0} ds$$
$$= \left[curl\mathbf{B}(\mathbf{r}') \cdot \mathbf{n}_0\right] S_0 = \left[\mathbf{j}(\mathbf{r}') \cdot \mathbf{n}_0\right] S_0 = j_{n_0}(\mathbf{r}') S_0, \tag{2.25}$$

where $j_{n_0}(\mathbf{r}') = \mathbf{j}(\mathbf{r}') \cdot \mathbf{n}_0$ is the normal component of the density of vortex $\mathbf{j}$, and $\mathbf{r}'$ is some internal point from S_0: $\mathbf{r}' \in S_0$.

We contract now the entire surface S_0 into its center point $\mathbf{r}_0$ (see Fig. 2.2). Let us calculate the limit of the surface integral in expression (2.24) divided by the surface area S_0 when the area tends to zero: $S_0 \to 0$:

$$\lim_{S_0 \to 0}\left[\left[\iint_{S_0} curl\mathbf{B}(\mathbf{r}) \cdot d\mathbf{s}\right] / S_0\right] = \lim_{S_0 \to 0}\left[\left[(\mathbf{j}(\mathbf{r}') \cdot \mathbf{n}_0)\iint_{S_0} ds\right] / S_0\right] = j_{n_0}(\mathbf{r}_0), \tag{2.26}$$

where we took into account that $\mathbf{r}' \to \mathbf{r}_0$, when $S_0 \to 0$.

Using Stokes's theorem (1.44), we can write an equivalent representation of the vortex density, $j_{n_0}(\mathbf{r}_0)$:

$$j_{n_0}(\mathbf{r}_0) = \lim_{D_{S0} \to 0} \left[\left(\oint_{C_0} \mathbf{B} \cdot d\mathbf{l} \right) / S_0 \right], \tag{2.27}$$

where C_0 is a contour boundary of the surface S_0.

According to Eqs. (2.13) and (2.27), we have:

$$curl\mathbf{B}(\mathbf{r}_0) \cdot \mathbf{n}_0 = \lim_{D_{S0} \to 0} \left[\left(\oint_{C_0} \mathbf{B} \cdot d\mathbf{l} \right) / S_0 \right]. \tag{2.28}$$

Eq. (2.28) can be treated as a definition of the curl of the vector field **B**, which is independent (invariant) of the selection of the coordinate systems.

Definition 23. The curl of a vector field **B** at a point $\mathbf{r}_0$ is equal to the vector **j**, whose projection on any direction $\mathbf{n}_0$ is determined by a limit of the circulation of the vector field **B** along the circle C_0 (located within the plane perpendicular to vector $\mathbf{n}_0$ with the center at the point $\mathbf{r}_0$) divided by the area S_0 of a round piece of plane bounded by the circle C_0, when the area tends to zero: $S_0 \to 0$.

Therefore, the curl operator represents a *surface derivative* of the field.

In order to understand better the physical meaning of the curl operator and of the vortex of a field, we will use again a hydrodynamic analogy. We assume that a vector field $\mathbf{B}^{hd}$ is a "hydrodynamic" field, defined according to formula (2.18), which describes the movement of a liquid within some volume. Eqs. (2.27) and (2.28) show that the projection of the vortex **j** of the field $\mathbf{B}^{hd}$ in the direction $\mathbf{n}_0$ can be approximately expressed as a contour integral:

$$\mathbf{j}(\mathbf{r}_0) \cdot \mathbf{n}_0 \approx \left(\oint_{C_0} \mathbf{B}^{hd} \cdot d\mathbf{l} \right) / S_0, \tag{2.29}$$

for a small circle C_0.

Let us introduce a small test paddle wheel with the rim coinciding with the small circle C_0 and with the axis of the wheel coinciding with the vector $\mathbf{n}_0$ as shown in Fig. 2.3.

The moving liquid presses on the paddles of the wheel and forces it to rotate. The moment of the force, $d\mathbf{M}$, acting on the paddles located along an element of arc, dl, of the wheel is proportional to the projection of the vector field $\mathbf{B}^{hd}$ on the vector $\boldsymbol{\tau}$, tangential to the wheel, and is parallel to the wheel axis, vector $\mathbf{n}_0$:

$$d\mathbf{M} = k \left(\mathbf{B}^{hd} \cdot \boldsymbol{\tau} dl \right) \mathbf{n}_0, \tag{2.30}$$

where k is a coefficient depending on the geometry of the paddles, the viscosity of the liquid, and other hydrodynamic factors.

The total moment of the forces rotating the paddle wheel are given by the following integral:

$$\mathbf{M} = \oint_{C_0} d\mathbf{M} = k \oint_{C_0} \left(\mathbf{B}^{hd} \cdot \boldsymbol{\tau} dl \right) \mathbf{n}_0 = k \oint_{C_0} \left(\mathbf{B}^{hd} \cdot d\mathbf{l} \right) \mathbf{n}_0. \tag{2.31}$$
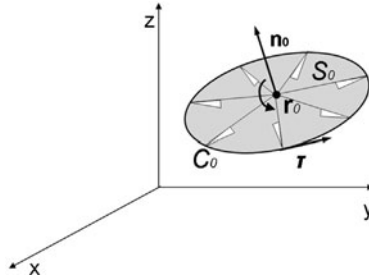
FIGURE 2.3

Illustration of the physical meaning of the curl operator and of the vortex of a field, using a hydrodynamic analogy. The volume density of the vortex is proportional to the total moment of the forces rotating the test paddle wheel, i.e. the curl operator characterizes the rotation of the vector field.

Taking into account Eq. (2.29), we have:

$$\mathbf{j}(\mathbf{r}_0) \cdot \mathbf{n}_0 \approx \left(\oint_{C_0} \mathbf{B}^{hd} \cdot d\mathbf{l} \right) / S_0$$

and

$$\mathbf{M} = k \, (\mathbf{j}(\mathbf{r}_0) \cdot \mathbf{n}_0) \, \mathbf{n}_0 / S_0 = k\mathbf{j}(\mathbf{r}_0)/S_0,$$

or

$$curl\mathbf{B}^{hd} = \mathbf{j}(\mathbf{r}_0) = \mathbf{M} \, (S_0/k) \,. \tag{2.32}$$

We can see from the last equation that the curl of the "hydrodynamic" vector field determines the moment of forces rotating the small test paddle wheel submerged in the liquid. In other words, the volume density of the vortex is proportional to the total moment of the forces rotating the test paddle wheel, i.e. the curl operator characterizes the rotation of the vector field. This is the reason why the curl operator is often called rot – the *rotational* operator.

2.1.6 SOURCE FIELD AND VORTEX FIELD

We have established in the previous sections that any vector field is generated by sources or vortices only. There are no other types of field generators. Let us consider now the fields which are generated by sources only, or by vortices only.

Definition 24. We call a vector field $\mathbf{B}_q$ a *source field* if it has no vortices in the entire space:

$$curl\mathbf{B}_q \equiv 0. \tag{2.33}$$

The source field $\mathbf{B}_q$ is generated by the sources only. The volume density of the sources, q, is determined by the divergence of the source field:

$$q = div\mathbf{B}_q. \tag{2.34}$$

A typical example of the source field is a gravity field **g**. The volume density of the sources of the gravity field according to Newton's law is proportional to the density ρ of masses:

$$div\mathbf{g} = -4\pi\gamma\rho, \tag{2.35}$$

where γ is the universal gravitational constant. We can see that masses are actually negative sources of the gravity field, which corresponds to the fact that the masses attract each other.

Another example of the source field is a static electric field **D** in the homogeneous space. This field satisfies the equation:

$$div\mathbf{D} = q, \tag{2.36}$$

where q is a volume density of electric charges. Thus, in this case the charges are the sources of the electrostatic field.

Definition 25. We call a vector field $\mathbf{B}_j$ a *vortex field* if it has no sources in the entire space:

$$div\mathbf{B}_j \equiv 0. \tag{2.37}$$

The vortex field $\mathbf{B}_j$ is generated by the vortices only. The volume density of the vortices, **j**, is determined by the curl of the vortex field:

$$\mathbf{j} = curl\mathbf{B}_j. \tag{2.38}$$

A typical example of the vortex field is magnetic field **B**. We shall demonstrate in Chapter 3 that, according to Ampere's law, the volume density of the vortices of the magnetic field **B** is equal to the volume density of the electric current **j** :

$$curl\mathbf{B} = \mathbf{j}.$$

Thus, we conclude that the electric current represents a vortex of the magnetic field.

2.2 STATIONARY FIELD EQUATIONS AND METHODS OF THEIR SOLUTIONS
2.2.1 POISSON'S EQUATIONS FOR SCALAR AND VECTOR FIELDS
Scalar field equations

We have proved in the previous section uniqueness Theorem 17, according to which a scalar field $U(\mathbf{r})$ is uniquely determined by its gradient if it is continuously differentiable in the entire space and is regular at infinity.

Thus, the following equation,

$$gradU = \mathbf{B}_g, \tag{2.39}$$

can be treated as an equation of the scalar field $U(\mathbf{r})$, if the vector field $\mathbf{B}_g(\mathbf{r})$ is known.

Let us calculate a divergence of the vector field $\mathbf{B}_g$:

$$div\mathbf{B}_g = div\,grad\,U = q,$$

or

$$\nabla^2 U = q. \tag{2.40}$$

Eq. (2.40) is called a *scalar Poisson's equation*. It is easy to show that this equation has a unique solution. Indeed, assuming that we have two different solutions that are regular at infinity, U_1 and U_2, we immediately conclude that their difference, $U' = U_1 - U_2$, satisfies to Laplace's equation:

$$\nabla^2 U' = q,$$

and U' is regular at infinity. Therefore, according to Liouville's Theorem 16, U' is identically equal to zero in the entire space and

$$U_1 \equiv U_2.$$

Thus, every scalar field satisfies Poisson's equation (2.40), with the right-hand part equal to the volume density of the gradient of a scalar field. Usually, we can assume that the sources, q, of the gradient of a scalar field U are known. The goal is to solve Eq. (2.40) with respect to the scalar field U.

Vector field equations

Consider an arbitrary vector field $\mathbf{B}$, whose scalar components are continuously differentiable in the entire space and regular at infinity. We have proved in the previous sections that this field is uniquely determined by its sources and vortices. The field is related to the volume densities of its sources, q, and vortices, $\mathbf{j}$, by a system of equations:

$$\begin{aligned} div\mathbf{B} &= q, \\ \mathbf{curl}\,\mathbf{B} &= \mathbf{j}. \end{aligned} \tag{2.41}$$

We can write a corresponding vector Poisson's equation for a vector field as well. Indeed, according to vector formula (1.24), we have:

$$(\nabla \cdot \nabla)\mathbf{B} = grad\,div\mathbf{B} - curl\,curl\mathbf{B} = \mathbf{grad}q - \mathbf{curlj}. \tag{2.42}$$

Thus, we arrive at the *vector Poisson's equation:*

$$\nabla^2 \mathbf{B} = \mathbf{p}, \quad \text{where } \mathbf{p} = grad\,q - \mathbf{curlj}. \tag{2.43}$$

We can see that the right-hand side of Eq. (2.43) is formed by a combination of the gradient of the source density and a curl of the vortex density. This combination is called *a generalized density of the vector field generators*, $\mathbf{p}$.

In many practical situations we assume that the sources, q, and vortices, $\mathbf{j}$, of the vector field $\mathbf{B}$ are known. The goal is to find this field. In other words, we have to solve the vector Poisson's equation (2.43).

We will introduce below a technique for solving the Poisson's equations.

2.2.2 POINT SOURCE; DIRAC SINGULAR FUNCTION

In modern physics we consider both continuous and discrete distributions of the sources and vortices of the vector field (e.g., electric charges and currents). We have introduced above the notions of the volume density of these sources and vortices for continuous distributions only. It is convenient to retain these notions for discrete distributions as well. In order to apply the concept of volume density to the point sources, one can use the idea of the δ-function, introduced by Dirac in 1939. In this section we will describe a mathematical concept of a singular function, which provides a useful tool for a solution of the field equations. Let us consider some electric charge Q_0 distributed along the x axis. The amount of charge distributed along the x axis from the left end to the point x is equal to $Q(x)$. We introduce the density of charge distribution as:

$$q(x) = \lim_{\Delta x \to 0} \frac{Q(x + \Delta x/2) - Q(x - \Delta x/2)}{\Delta x} = \frac{dQ}{dx}.$$

Let us consider a case when all of the charge is concentrated in one point x':

$$Q_0(x) = \begin{cases} 0, & x < x' \\ Q_0, & x \geq x' \end{cases}.$$

Then the density $q(x)$ satisfies the following conditions:

$$q(x) = 0, \ x \neq x', \tag{2.44}$$

$$q(x') = \lim_{\Delta x \to 0} \frac{Q(x' + \Delta x/2) - Q(x' - \Delta x/2)}{\Delta x} \to \infty, \tag{2.45}$$

$$\int_{-\infty}^{+\infty} Q(x)dx = Q_0. \tag{2.46}$$

We can introduce a Dirac singular delta-function, $\delta(x - x')$, under the condition that this function represents the density of a point unit charge. In this case, density $q(x)$ is equal to

$$q(x) = Q_0 \delta(x - x').$$

Let us determine the basic properties of the Dirac singular delta-function. First of all, according to formulae (2.44) and (2.45), this function is equal to zero everywhere except at the point x', and it is equal to infinity at this point:

$$\delta(x - x') = \begin{cases} 0, & x \neq x' \\ \infty, & x = x' \end{cases}. \tag{2.47}$$

Second, according to formula (2.46), the integral of this function over the entire axis x is equal to one:

$$\int_{-\infty}^{+\infty} \delta(x - x')dx = 1. \tag{2.48}$$

We consider now the following convolution-type integral of a product of any continuous function, $f(x)$, and a delta-function:

$$\int_a^b f(x)\delta(x - x')dx, \text{ when } x' \in (a, b).$$

Direct calculations show that:

$$\int_a^b f(x)\delta(x - x')dx = \int_{x'-\varepsilon}^{x'+\varepsilon} f(x)\delta(x - x')dx$$

$$= f(x' + \alpha\varepsilon) \int_{x'-\varepsilon}^{x'+\varepsilon} \delta(x - x')dx = f(x' + \alpha\varepsilon) \to f(x'), \text{ when } \varepsilon \to 0, \tag{2.49}$$

where $|\varepsilon| < 1$.

Thus we have:

$$\int_a^b f(x)\delta(x - x')dx = \begin{cases} f(x'), & x' \in (a, b) \\ 0, & x' \notin (a, b) \end{cases}. \tag{2.50}$$

Thus, we have proved that the convolution of any continuous function with the delta function results in the value of the original function at the corresponding singular point, x', of the delta function.

In a similar way, one can introduce a Dirac singular function in 3D case, $\delta(\mathbf{r} - \mathbf{r}')$. The main property of this function is that a volume convolution of $\delta(\mathbf{r} - \mathbf{r}')$ with a continuous function, $f(\mathbf{r})$, is equal to the value of this function at the corresponding singular point, $\mathbf{r}'$, of the delta function:

$$\iiint_D f(\mathbf{r})\delta(\mathbf{r} - \mathbf{r}') = \begin{cases} f(\mathbf{r}'), & \mathbf{r}' \in D \\ 0, & \mathbf{r}' \notin D \end{cases}. \tag{2.51}$$

The Dirac singular functions represent an example of the generalized functions, which are studied in the corresponding advanced mathematical courses, where the interested reader can find more details about their properties. In the framework of this text we will use only one major property of these functions, expressed by Eqs. (2.50) and (2.51). This property serves as a basis for introduction of the Green's function, which is the subject of the next section.

2.2.3 FUNDAMENTAL GREEN'S FUNCTION FOR THE LAPLACE EQUATION

The Green's function for the Laplace equation has a very simple physical meaning. It is introduced as a solution of a scalar Poisson's equation for a point source. We will give the following rigorous definition of the Green's function.

Definition 26. The function $G(\mathbf{r} - \mathbf{r}')$ is called a fundamental Green's function for Laplace's equation if it

(i) satisfies the following Poisson's equation:

$$\nabla^2 G(\mathbf{r} - \mathbf{r}') = -\delta(\mathbf{r} - \mathbf{r}'); \tag{2.52}$$

(ii) has a spherical symmetry with respect to the point $\mathbf{r}'$:

$$G(\mathbf{r} - \mathbf{r}') = G(|\mathbf{r} - \mathbf{r}'|);$$

(iii) goes to zero at infinity:

$$G(\mathbf{r} - \mathbf{r}') \to 0, |\mathbf{r} - \mathbf{r}'| \to \infty.$$

Let us find the Green's function. We write Eq. (2.52) in a spherical system of coordinates, r, φ, θ, with the origin at a singular point $\mathbf{r}'$:

$$\frac{1}{r^2}\frac{\partial}{\partial r}(r^2\frac{\partial G}{\partial r}) + \frac{1}{r^2\sin\theta}\frac{\partial}{\partial\theta}(\sin\theta\frac{\partial G}{\partial\theta}) + \frac{1}{r^2\sin^2\theta}\frac{\partial^2 G}{\partial\varphi^2} = -\delta(r). \tag{2.53}$$

Due to the spherical symmetry of the Green's function (condition (ii)), all angular derivatives in Eq. (2.52) are equal to zero, and we have:

$$\frac{1}{r^2}\frac{\partial}{\partial r}(r^2\frac{\partial G}{\partial r}) = 0. \tag{2.54}$$

The general solution of Eq. (2.54) can be written as:

$$G = -c_1/r + c_2, \tag{2.55}$$

where the constant c_2 should be equal to zero because of condition (iii) at infinity:

$$c_2 = 0$$

The unknown constant c_1 can be found from condition (i) – that the Green's function is a scalar field generated by a unit point source. Indeed, integrating Poisson's equation (2.52) over a ball D_R of a radius R with the center in the origin of coordinates, we find:

$$\iiint_{D_R} \nabla^2 G dv = -\iiint_{D_R} \delta(\mathbf{r} - \mathbf{r}')dv = -1. \tag{2.56}$$

At the same time, using Gauss's theorem and Eq. (2.55), we find:

$$\iiint_{D_R} \nabla^2 G dv = \iint_{S_R} \frac{\partial G}{\partial r}ds = 4\pi c_1. \tag{2.57}$$

From Eqs. (2.56) and (2.57), we have at once:

$$c_1 = -1/4\pi,$$

and

$$G(\mathbf{r} - \mathbf{r}') = \frac{1}{4\pi |\mathbf{r} - \mathbf{r}'|}. \tag{2.58}$$

Solution of the scalar field equations

The Green's function can be effectively used for solving the equations of the scalar and vector fields. We will begin with the scalar field equation:

$$\nabla^2 u(\mathbf{r}) = q(\mathbf{r}), \tag{2.59}$$

where function $q(\mathbf{r})$, describing the sources of the scalar field, is defined in some local domain V and is identically equal to zero everywhere outside this domain. In other words, we assume that the sources of the scalar field are concentrated within some local domain of the space. We also assume that the function $u(\mathbf{r})$ is regular at infinity. Our goal is to find an expression for the scalar field $u(\mathbf{r})$ generated by the known source $q(\mathbf{r})$. To do so, we select an arbitrary point $\mathbf{r}'$ and around it draw a sphere, C_R, with a radius great enough that the volume V falls within the ball O_R bounded by the sphere C_R; that is, $V \in O_R$. We now write the expression for the Green's theorem (1.49) within the volume O_R:

$$\iiint_{O_R} (a\nabla^2 b - b\nabla^2 a)dv = \iint_{C_R} \left(a\frac{\partial b}{\partial n} - b\frac{\partial a}{\partial n} \right) ds. \tag{2.60}$$

Let us assume in the last equation that:

$$a = u(\mathbf{r}), \text{ and } b = G(\mathbf{r} - \mathbf{r}').$$

Taking into account Eqs. (2.52) and (2.59) and the main property of the delta-function (2.51), we find:

$$u(\mathbf{r}') = -\iiint_V G(\mathbf{r} - \mathbf{r}')q(\mathbf{r})dv - \iint_{C_R} \left(u(\mathbf{r})\frac{\partial G(\mathbf{r} - \mathbf{r}')}{\partial n} - G(\mathbf{r} - \mathbf{r}')\frac{\partial u(\mathbf{r})}{\partial n} \right) ds. \tag{2.61}$$

In the derivation of the last formula we take into account that the volume integral is taken over domain V only, because the source function, $q(\mathbf{r})$, is identically equal to zero everywhere outside this domain.

According to expression (2.58) for the Green's function and the condition that $u(\mathbf{r})$ is regular at infinity, the kernel of the surface integral decreases as $1/r^3$ as $|\mathbf{r}| \to \infty$. Consequently, if the radius, R, is expanded without limit, the surface integral along C_R will tend to zero. Hence, we find

$$u(\mathbf{r}') = -\frac{1}{4\pi} \iiint_V \frac{q(r)}{|\mathbf{r} - \mathbf{r}'|} dv. \tag{2.62}$$

The last formula provides a solution of the scalar field Eq. (2.59).

Solution of the vector field equations

One can solve the vector Poisson's equation (2.43) using the same ideas as we have applied for the solution of the scalar equation. We assume that all scalar components of the vector field $\mathbf{B}(\mathbf{r})$ are described by the functions, regular at infinity, and the sources and the vortices of this field are concentrated within some local domain of the space, V. Repeating a derivation, similar to one conducted above for a scalar field, we can obtain a vector analogue of the scalar equation (2.62):

$$\mathbf{B}(\mathbf{r}') = -\frac{1}{4\pi} \iiint_V \frac{\mathbf{p}(r)}{|\mathbf{r} - \mathbf{r}'|} dv, \tag{2.63}$$

where

$$\mathbf{p} = grad\,q - \mathbf{curl\,j}. \tag{2.64}$$

Substituting Eq. (2.64) into (2.63), we finally arrive at the integral representation for the vector field in the form of the volume integral of the densities of its sources and vortices:

$$\mathbf{B}(\mathbf{r}') = -\frac{1}{4\pi} \iiint_V \frac{grad\,q(\mathbf{r})}{|\mathbf{r} - \mathbf{r}'|} dv + \frac{1}{4\pi} \iiint_V \frac{\mathbf{curl\,j}(\mathbf{r})}{|\mathbf{r} - \mathbf{r}'|} dv. \tag{2.65}$$

Thus, we conclude that any stationary vector field can be uniquely determined by its sources and/or vortices.

2.3 SCALAR AND VECTOR POTENTIALS OF THE STATIONARY FIELD
2.3.1 SCALAR POTENTIAL OF THE SOURCE FIELD

Let us consider the source field $\mathbf{B}_q$, which is generated by the sources only. This field satisfies the equations

$$div\mathbf{B}_q = q,$$
$$curl\mathbf{B}_q = 0.$$

We assume as usual that the sources are concentrated within some local domain of the space, V. Therefore, the corresponding integral representation (2.65) for the source field takes the form:

$$\mathbf{B}_q(\mathbf{r}') = -\frac{1}{4\pi} \iiint_V \frac{grad\,q(\mathbf{r})}{|\mathbf{r} - \mathbf{r}'|} dv = -\frac{1}{4\pi} \iiint_{O_R} \frac{grad\,q(\mathbf{r})}{|\mathbf{r} - \mathbf{r}'|} dv, \tag{2.66}$$

where O_R is an arbitrary large ball with the center at the point $\mathbf{r}'$, which contains the entire volume V. The integrand in expression (2.66) can be represented in equivalent form as:

$$\frac{grad\,q(\mathbf{r})}{|\mathbf{r} - \mathbf{r}'|} = grad\left(\frac{q(\mathbf{r})}{|\mathbf{r} - \mathbf{r}'|}\right) + grad'\left(\frac{q(\mathbf{r})}{|\mathbf{r} - \mathbf{r}'|}\right), \tag{2.67}$$

where "prime" at the symbol of the gradient denotes the differentiation with respect to variable $\mathbf{r}'$.

Substituting expression (2.67) into (2.66), and using the second vector form of Gauss's theorem (1.41), we find:

$$\mathbf{B}_q(\mathbf{r}') = -\frac{1}{4\pi} \iint_{C_R} \frac{q(\mathbf{r})}{|\mathbf{r} - \mathbf{r}'|} d\mathbf{s} - grad'\left\{\frac{1}{4\pi} \iiint_{O_R} \frac{q(\mathbf{r})}{|\mathbf{r} - \mathbf{r}'|} dv\right\}.$$

The surface integral over sphere C_R vanishes because $q(\mathbf{r}) = 0$ outside domain V. Thus, finally we have:

$$\mathbf{B}_q(\mathbf{r}') = -grad'\left\{\frac{1}{4\pi} \iiint_V \frac{q(\mathbf{r})}{|\mathbf{r} - \mathbf{r}'|} dv\right\}. \tag{2.68}$$

Thus, we have found that the source field $\mathbf{B}_q$ can be expressed as the gradient of some scalar field U:

$$\mathbf{B}_q(\mathbf{r}') = grad'U(\mathbf{r}'),$$

where

$$U(\mathbf{r}') = -\frac{1}{4\pi} \iiint_V \frac{q(\mathbf{r})}{|\mathbf{r} - \mathbf{r}'|} dv. \tag{2.69}$$

This scalar field $U(\mathbf{r})$ is called a scalar potential of the source field $\mathbf{B}_q(\mathbf{r})$. Thus, we have proved that any source field can be expressed using a corresponding scalar potential.

2.3.2 VECTOR POTENTIAL OF THE VORTEX FIELD

We consider now the vortex field $\mathbf{B}_j$, which is generated by the vortices only. This field satisfies the equations:

$$div\mathbf{B}_j = 0,$$
$$curl\mathbf{B}_j = \mathbf{j}.$$

We also assume that all the vortices are concentrated within the local domain V. In this case, integral representation (2.65) for the vortex field takes the form:

$$\mathbf{B}_j(\mathbf{r}') = \frac{1}{4\pi} \iiint_V \frac{curl\mathbf{j}(\mathbf{r})}{|\mathbf{r} - \mathbf{r}'|} dv = \frac{1}{4\pi} \iiint_{O_R} \frac{curl\mathbf{j}(\mathbf{r})}{|\mathbf{r} - \mathbf{r}'|} dv. \tag{2.70}$$

According to the rules of vector calculus (1.27), the following equation holds:

$$curl(g\mathbf{P}) = grad g \times \mathbf{P} + g\, curl\mathbf{P}. \tag{2.71}$$

Assuming in the last formula that

$$g = \frac{1}{|\mathbf{r} - \mathbf{r}'|} \text{ and } \mathbf{P} = \mathbf{j}(\mathbf{r}),$$

we can write the expression under the integral sign in formula (2.70) in equivalent form as:

$$\frac{curl\mathbf{j}(\mathbf{r})}{|\mathbf{r} - \mathbf{r}'|} = curl\left(\frac{\mathbf{j}(\mathbf{r})}{|\mathbf{r} - \mathbf{r}'|}\right) + curl'\left(\frac{\mathbf{j}(\mathbf{r})}{|\mathbf{r} - \mathbf{r}'|}\right). \tag{2.72}$$

In the derivation of Eq. (2.72) we take into account that

$$grad g \times \mathbf{P} = -grad'g \times \mathbf{P} = curl'(g\mathbf{P}),$$

and

$$curl'\mathbf{P} = curl'\mathbf{j}(\mathbf{r}) = 0.$$

The last equation holds because the curl operator $curl'$ differentiates with respect to the radius-vector $\mathbf{r}'$, while vector field $\mathbf{j}(\mathbf{r})$ is independent of $\mathbf{r}'$.

We substitute expression (2.72) into (2.70), and take into account the third vector form of Gauss's theorem (1.43). As a result, we find:

$$\mathbf{B}_j(\mathbf{r}') = -\frac{1}{4\pi} \iint_{C_R} \frac{\mathbf{j}(\mathbf{r}) \times d\mathbf{s}}{|\mathbf{r} - \mathbf{r}'|} + \mathbf{curl}' \left\{ \frac{1}{4\pi} \iiint_{O_R} \frac{\mathbf{j}(\mathbf{r})}{|\mathbf{r} - \mathbf{r}'|} dv \right\}.$$

The surface integral over sphere C_R vanishes because $\mathbf{j}(\mathbf{r}) = 0$ outside domain V. Thus, finally we have:

$$\mathbf{B}_j(\mathbf{r}') = \mathbf{curl}' \left\{ \frac{1}{4\pi} \iiint_{O_R} \frac{\mathbf{j}(\mathbf{r})}{|\mathbf{r} - \mathbf{r}'|} dv \right\}. \tag{2.73}$$

We have found that the vortex field $\mathbf{B}_j$ is expressed as the curl of some vector field $\mathbf{A}$:

$$\mathbf{B}_j(\mathbf{r}') = \mathbf{curl}'\mathbf{A}(\mathbf{r}'),$$

where

$$\mathbf{A}(\mathbf{r}') = \frac{1}{4\pi} \iiint_{O_R} \frac{\mathbf{j}(\mathbf{r})}{|\mathbf{r} - \mathbf{r}'|} dv. \tag{2.74}$$

The vector field $\mathbf{A}(\mathbf{r})$ is called a vector potential of the vortex field $\mathbf{B}_j(\mathbf{r})$. The fundamental result is that any vortex field can be expressed using a corresponding vector potential.

2.3.3 HELMHOLTZ THEOREM AND CLASSIFICATION OF THE VECTOR FIELDS

Based on the results developed in the previous sections, we can formulate the following theorem.

Theorem 27. *Helmholtz theorem: Any vector field in three-dimensional space can be represented using the corresponding scalar and vector potentials, U and **A**, as:*

$$\mathbf{B} = grad U + \mathbf{curl}\mathbf{A}. \tag{2.75}$$

The Helmholtz theorem also shows that any vector field can be decomposed into a sum of a source field, $\mathbf{B}_q$, and a vortex field, $\mathbf{B}_j$:

$$\mathbf{B} = \mathbf{B}_q + \mathbf{B}_j. \tag{2.76}$$

This is a very important result, which is widely used in electromagnetic theory.

In summary, we can give the following classification of the vector fields.

There exist two major types of vector fields: the source field and the vortex field.

The source field, $\mathbf{B}_q$, has no vortices in the entire 3D space; it is generated by the sources only. The volume density of the sources is equal to the divergence of the source field:

$$div\mathbf{B}_q = q.$$

The vortex field, $\mathbf{B}_j$, has no sources in the entire 3D space; it is generated by the vortices only. The volume density of the vortices is equal to the curl of the vortex field:

$$\mathbf{curl}\mathbf{B}_j = \mathbf{j}.$$

Definition 28. The field $\mathbf{B}_\Delta$, which has no sources and vortices in some domain D, is called a Laplacian field.

According to the vector identity (1.24), the Laplacian field satisfies to the Laplace equation in domain D:

$$(\nabla \cdot \nabla)\mathbf{B}_\Delta = grad\,div\mathbf{B}_\Delta - curl\,curl\mathbf{B}_\Delta = 0. \tag{2.77}$$

Based on Liouville's theorem, we can state that, if some field is Laplacian in the entire 3D space, and all its scalar components are regular at infinity, then this field is identical to zero.

Finally, the Helmholtz theorem allows us to formulate the following statement.

Theorem 29. *Principle of fields superposition: If the source, q, and vortex, $\mathbf{j}$, of a vector field $\mathbf{B}$ are the linear combinations of some "elementary" sources and vortices, q_i and $\mathbf{j}_k$:*

$$q = \sum_{i=1}^{I} q_i, \ \ \mathbf{j} = \sum_{k=1}^{K} \mathbf{j}_k, \tag{2.78}$$

then field $\mathbf{B}$ itself is a linear combination of the source fields $\mathbf{B}_{q_i}$ and vortex fields $\mathbf{B}_{j_k}$, generated by every "elementary" source and vortex separately:

$$\mathbf{B} = \sum_{i=1}^{I} \mathbf{B}_{q_i} + \sum_{k=1}^{K} \mathbf{B}_{j_k}. \tag{2.79}$$

Proof. According to Eqs. (2.65) and (2.78), we can write:

$$\mathbf{B}(\mathbf{r}') = -\frac{1}{4\pi}\iiint_V \frac{grad\left[\sum_{i=1}^{I} q_i(\mathbf{r})\right]}{|\mathbf{r} - \mathbf{r}'|}dv + \frac{1}{4\pi}\iiint_V \frac{curl\left[\sum_{k=1}^{K} \mathbf{j}_k(\mathbf{r})\right]}{|\mathbf{r} - \mathbf{r}'|}dv. \tag{2.80}$$

Taking the summation signs outside of the integrals, we have:

$$\mathbf{B}(\mathbf{r}') = \sum_{i=1}^{I}\left[\frac{-1}{4\pi}\iiint_V \frac{grad\,q_i(\mathbf{r})}{|\mathbf{r} - \mathbf{r}'|}dv\right] + \sum_{k=1}^{K}\left[\frac{1}{4\pi}\iiint_V \frac{curl\,\mathbf{j}_k(\mathbf{r})}{|\mathbf{r} - \mathbf{r}'|}dv\right]$$

$$= \sum_{i=1}^{I} \mathbf{B}_{q_i} + \sum_{k=1}^{K} \mathbf{B}_{j_k}, \tag{2.81}$$

where

$$\mathbf{B}_{q_i} = \frac{-1}{4\pi}\iiint_V \frac{grad\,q_i(\mathbf{r})}{|\mathbf{r} - \mathbf{r}'|}dv$$

and

$$\mathbf{B}_{j_k} = \frac{1}{4\pi}\iiint_V \frac{curl\,\mathbf{j}_k(\mathbf{r})}{|\mathbf{r} - \mathbf{r}'|}dv.$$

Formula (2.81) completes the proof of the superposition principle.

2.4 NONSTATIONARY FIELDS AND DIFFERENTIAL FORMS
2.4.1 NONSTATIONARY VECTOR FIELDS AND DIFFERENTIAL FORMS IN FOUR-DIMENSIONAL SPACE E_4

The most effective way of presenting the theory of nonstationary (time-dependent) fields is based on the theory of differential forms. We introduce the four-dimensional Euclidean space E_4 (see Appendix A), which has three conventional spatial coordinates, $x_1 = x$, $x_2 = y$, and $x_3 = z$, and the fourth coordinate, x_4, equal to time: $x_4 = t$.

Any scalar, U, or vector, $\mathbf{A}$, functions of the space coordinates (x_1, x_2, x_3) and time coordinate t can be treated as the functions defined in the four-dimensional space E_4. We can still apply to these functions the scalar and vector Poisson's equations (2.40) and (2.43), and the divergence and curl equations (2.41):

$$\nabla^2 U = q, \quad \nabla^2 \mathbf{A} = \mathbf{p}_A, \tag{2.82}$$

$$div\mathbf{A} = q_A, \quad curl\mathbf{B} = \mathbf{j}_A \tag{2.83}$$

where

$$\mathbf{p}_A = grad q_A - curl\mathbf{j}_A.$$

However, now all scalar and vector functions in Eqs. (2.82) and (2.83) depend on spatial radius-vector $\mathbf{r} = (x_1, x_2, x_3)$ and time coordinate t.

We can also introduce vector fields $\mathbf{H}(\mathbf{r}, t)$, $\mathbf{D}(\mathbf{r}, t)$, and $\mathbf{j}(\mathbf{r}, t)$, which all are nonstationary (time-dependent) vector functions in three-dimensional space, and a scalar function $q(\mathbf{r}, t)$. The remarkable fact is that any pair of nonstationary fields, $\mathbf{H}(\mathbf{r}, t)$ and $\mathbf{D}(\mathbf{r}, t)$, satisfies a set of differential equations which have exactly the same structure as the Maxwell's equation of electromagnetic theory! We will derive these equations using the differential form theory.

In Appendix A we have developed a general theory of the differential forms in four-dimensional Minkowskian space M_4. Using a similar technique, one can show that, using the vector and scalar fields $\mathbf{A}$, $\mathbf{H}$, $\mathbf{D}$, $\mathbf{j}$, and q, we can define differential forms of five different orders in the four-dimensional space E_4. These forms can be expressed using the three-dimensional vector notations as:

$$\text{0-forms} \quad : \quad \underset{(0)}{\Omega} = U, \tag{2.84}$$

$$\text{1-forms} \quad : \quad \underset{(1)}{\Omega} = \alpha = \mathbf{A} \cdot d\mathbf{r} - U dt, \tag{2.85}$$

$$\text{2-forms} \quad : \quad \underset{(2)}{\Omega} = \psi = \mathbf{D} \cdot d\mathbf{\Sigma} - (\mathbf{H} \cdot d\mathbf{r}) \wedge dt, \tag{2.86}$$

$$\text{3-forms} \quad : \quad \underset{(3)}{\Omega} = \gamma = q dv - (\mathbf{j} \cdot d\mathbf{\Sigma}) \wedge dt, \tag{2.87}$$

$$\text{4-forms} \quad : \quad \underset{(4)}{\Omega} = \theta = q dv \wedge dt. \tag{2.88}$$

Let us describe first the physical meaning of all of these forms. The 0-form $\underset{(0)}{\Omega} = U$ represents a scalar field, U, in the four-dimensional Euclidean space E_4. The 1-form $\alpha = \mathbf{A} \cdot d\mathbf{r} - U dt$ is called *a four-potential*. It can be treated as a sum of elementary work, dW_A, of the vector field $\mathbf{A}$ along a vector element $d\mathbf{r}$ and a time differential of a scalar field U.

The 2-form $\psi = \mathbf{D} \cdot d\mathbf{\Sigma} - (\mathbf{H} \cdot d\mathbf{r}) \wedge dt$ is nothing else but a combined scalar flux, $dF_{\mathbf{D}}^{d\mathbf{\Sigma}}$, of the vector field $\mathbf{D}$ through a vector element of surface $d\mathbf{\Sigma}$ and a time differential of work, $dW_{\mathbf{H}}$, of the vector field $\mathbf{H}$ along a vector element $d\mathbf{r}$.

The 3-form $\gamma = q\,dv - (\mathbf{j} \cdot d\mathbf{\Sigma}) \wedge dt$ is called *a four-current*. It represents a combined elementary source, q, within an element of volume dv and a time differential of a scalar flux, $dF_{\mathbf{j}}^{d\mathbf{\Sigma}}$, of the vector field $\mathbf{j}$ through a vector element of surface $d\mathbf{\Sigma}$. Finally, the 4-form $\theta = q\,dv \wedge dt$ is a time differential of an elementary source, q, within an element of volume dv.

As shown in Appendix A for Minkowskian space M_4, any p-form in four dimensional space E_4 can be split into two terms which are called its *spatial*, Ω_s, *and temporal*, Ω_τ, *components*:

$$\underset{(p)}{\Omega} = \Omega_s + \Omega_t \wedge dt.$$

Note that the time coordinate and the spatial coordinates are mutually orthogonal in E_4. Therefore, any differential form equation in the space E_4, e.g.,

$$\underset{(p)}{\Omega} = 0,$$

can be split into separate equations for the spatial and temporal components:

$$\Omega_s = 0, \text{ and } \Omega_\tau = 0.$$

2.4.2 DIFFERENTIAL FORM EQUATIONS

In this section we will summarize the basic differential equations for the differential forms in the four-dimensional space E_4.

Exterior derivative of a scalar field and a generalized source 1-form

We begin with the exterior derivative of the 0-form:

$$d\underset{(0)}{\Omega} = dU = gradU \cdot d\mathbf{r} + \frac{\partial}{\partial t}U\,dt = \underset{(1)}{g}. \tag{2.89}$$

According to Eq. (2.85), the 1-form $\underset{(1)}{g}$ can be written as:

$$\underset{(1)}{g} = g_{1s} + g_{1\tau}dt = \mathbf{g}_1 \cdot d\mathbf{r} + g_{1\tau}dt. \tag{2.90}$$

Splitting Eq. (2.89) into its spatial and temporal parts, we find:

$$g_{1s} = \mathbf{g}_1 \cdot d\mathbf{r} = gradU \cdot d\mathbf{r} \text{ and } g_{1\tau} = \frac{\partial}{\partial t}U. \tag{2.91}$$

The 1-form $\underset{(1)}{g}$ is called *a generalized source form of the 0-form field* $\underset{(0)}{\Omega}$. Its spatial component is equal to the work of the gradient of a scalar field U along a vector element $d\mathbf{r}$, while its temporal component is equal to the time derivative of the scalar field U.

Exterior derivative of a four-potential and a generalized source 2-form

It is demonstrated in Appendix B that the exterior derivative of the four-potential 1-form α is given by the following expression:

$$d \underset{(1)}{\Omega} = d \wedge \alpha = curl\mathbf{A} \cdot d\mathbf{\Sigma} - \left(grad U + \frac{\partial \mathbf{A}}{\partial t} \right) \cdot d\mathbf{r} \wedge dt = \underset{(2)}{g}, \tag{2.92}$$

where $\underset{(2)}{g}$ is a generalized source 2-form:

$$\underset{(2)}{g} = g_{2s} + g_{2\tau} dt = \mathbf{j}_A \cdot d\mathbf{\Sigma} - \left(grad U + \frac{\partial \mathbf{A}}{\partial t} \right) \cdot d\mathbf{r} \wedge dt, \tag{2.93}$$

and $\mathbf{j}_A = curl\mathbf{A}$.

Splitting Eq. (2.93) into its spatial and temporal equations, we find:

$$g_{2s} = \mathbf{j}_A \cdot d\mathbf{\Sigma} \text{ and } g_{2\tau} = -\left(grad U + \frac{\partial \mathbf{A}}{\partial t} \right) \cdot d\mathbf{r}. \tag{2.94}$$

Exterior derivative of a 2-form and a four-current

Similarly, we can find the exterior derivative of the 2-form:

$$d \underset{(2)}{\Omega} = d \wedge \psi = (div\mathbf{D}) \, dv + \left(\frac{\partial}{\partial t} \mathbf{D} - curl\mathbf{H} \right) \cdot d\mathbf{\Sigma} \wedge dt = \underset{(3)}{g}, \tag{2.95}$$

where $\underset{(3)}{g}$ is a generalized source 3-form equal to the four-current γ^{ψ}:

$$\underset{(3)}{g} = g_{3s} + g_{3\tau} dt = q^{\psi} dv - \left(\mathbf{j}^{\psi} \cdot d\mathbf{\Sigma} \right) \wedge dt = \gamma^{\psi}, \tag{2.96}$$

and

$$\mathbf{j}^{\psi} = curl\mathbf{H} - \frac{\partial}{\partial t} \mathbf{D} \text{ and } q^{\psi} = div\mathbf{D}. \tag{2.97}$$

From Eqs. (2.96) and (2.97) we find the spatial and temporal components of the generalized source 3-form (four-current γ^{ψ}):

$$g_{3s} = (div\mathbf{D}) \, dv, \ g_{3\tau} = \left(\frac{\partial}{\partial t} \mathbf{D} - curl\mathbf{H} \right) \cdot d\mathbf{\Sigma}. \tag{2.98}$$

Exterior derivatives of a 3-form and of a 4-form

Finally, the exterior derivative of a 3-form is equal to:

$$d \underset{(3)}{\Omega} = d \wedge \gamma = -\left[div\mathbf{j} + \frac{\partial}{\partial t} q \right] dv \wedge dt = \underset{(4)}{g}. \tag{2.99}$$

The generalized source 4-form $g_{(4)}$, according to Eq. (2.88), can be written as:

$$g_{(4)} = g_{3\tau} dt = q^\gamma dv \wedge dt, \tag{2.100}$$

where

$$q^\gamma = -div\mathbf{j} - \frac{\partial}{\partial t} q.$$

The exterior derivative of the 4-form θ in a four-dimensional space is always equal to zero (see Appendix B):

$$d \wedge \theta = 0.$$

We can summarize all these results as:

$$0\text{-forms} \quad : \quad dU = gradU \cdot d\mathbf{r} + \frac{\partial}{\partial t} U dt, \tag{2.101}$$

$$1\text{-forms} \quad : \quad d \wedge \alpha = curl\mathbf{A} \cdot d\mathbf{\Sigma} - \left(gradU + \frac{\partial \mathbf{A}}{\partial t} \right) \cdot d\mathbf{r} \wedge dt, \tag{2.102}$$

$$2\text{-forms} \quad : \quad d \wedge \psi = (div\mathbf{D}) \, dv + \left(\frac{\partial}{\partial t} \mathbf{D} - curl\mathbf{H} \right) \cdot d\mathbf{\Sigma} \wedge dt, \tag{2.103}$$

$$3\text{-forms} \quad : \quad d \wedge \gamma = - \left[div\mathbf{j} + \frac{\partial}{\partial \tau} q \right] dv \wedge dt, \tag{2.104}$$

$$4\text{-forms} \quad : \quad d \wedge \theta = 0. \tag{2.105}$$

2.4.3 AMPERE-TYPE DIFFERENTIAL FORMS AND A CONTINUITY EQUATION

According to Eqs. (2.95) and (2.96), we have the following differential equation for any 2-form $\psi = \mathbf{D} \cdot d\mathbf{\Sigma} - (\mathbf{H} \cdot d\mathbf{r}) \wedge d\tau$:

$$d \wedge \psi = \gamma^\psi, \tag{2.106}$$

where the corresponding four-current 3-form γ^ψ is equal to:

$$\gamma^\psi = q^\psi dv - \left(\mathbf{j}^\psi \cdot d\mathbf{\Sigma} \right) \wedge dt, \tag{2.107}$$

and

$$\mathbf{j}^\psi = curl\mathbf{H} - \frac{\partial}{\partial t} \mathbf{D} \text{ and } q^\psi = div\mathbf{D}. \tag{2.108}$$

Note that, according to the basic property of the exterior derivative operator, the double application of the external differential is identically equal to zero. Therefore, the four-current γ^ψ satisfies the equation:

$$d \wedge \gamma^\psi = d \wedge (d \wedge \psi) = 0. \tag{2.109}$$

The last equation can be written, according to formula (2.99), as:

$$div\mathbf{j}^\psi + \frac{\partial}{\partial t}q^\psi = 0. \tag{2.110}$$

We will see in the next chapters of the book that Eqs. (2.108) represents exactly the Maxwell's equations if vector fields $\mathbf{D}$ and $\mathbf{H}$ are treated as the electric and magnetic fields, respectively. Correspondingly, Eq. (2.110) represents a conservation law for the four-current and is called *the continuity equation* because it has the form of the continuity equation of the electromagnetic theory.

Eq. (2.106) is called *a fundamental differential equation for 2-forms*, because any 2-form in the four-dimensional space E_4 must satisfy to this equation. We will demonstrate in Chapter 3 that Eqs. (2.108) are nothing else but the first and fourth Maxwell's equations for electric field $\mathbf{D}$ and magnetic field $\mathbf{H}$, which describe Ampere's law of electromagnetism with the Maxwell's displacement current $\partial\mathbf{D}/\partial t$. Thus, Maxwell's equations appear naturally from the general theory of differential forms.

The 2-form ψ, which satisfies the fundamental equation (2.106), is called *an Ampere-type differential form*. We should note, however, that actually every 2-form in the four-dimensional space E_4 is an Ampere-type form. Its spatial component, ψ_s, is called an *electric displacement 2-form D*, while its temporal component, ψ_s, is called a *magnetic 1-form H*:

$$D = \psi_s = \mathbf{D} \cdot d\mathbf{\Sigma}, \quad H = \psi_\tau = \mathbf{H} \cdot d\mathbf{r}. \tag{2.111}$$

Thus, the Ampere-type differential form can be written as:

$$\psi = D - H \wedge dt. \tag{2.112}$$

2.4.4 FARADAY-TYPE DIFFERENTIAL FORMS AND THE FOUR-POTENTIAL

Let us consider now a special class of 2-forms, which satisfies Eq. (2.106) with a zero right-hand part:

$$d \wedge \phi = 0. \tag{2.113}$$

In other words, we assume now that the corresponding four-current is equal to zero, $\gamma^\phi = 0$, and a 2-form ϕ is an exact form (see Appendix B).

In this case, according to de Rham's theorem (see Appendix B) there exists an 1-form (four-potential) α,

$$\alpha = \mathbf{A} \cdot d\mathbf{r} - U dt,$$

such that

$$\phi(\mathbf{r}) = d \wedge \alpha(\mathbf{r}). \tag{2.114}$$

Eq. (2.114) can be written in an equivalent way as:

$$\phi = \mathbf{B} \cdot d\mathbf{\Sigma} + (\mathbf{E} \cdot d\mathbf{r}) \wedge dt = d \wedge \alpha(\mathbf{r})$$
$$= curl\mathbf{A} \cdot d\mathbf{\Sigma} - \left(grad U + \frac{\partial\mathbf{A}}{\partial t} \right) \cdot d\mathbf{r} \wedge dt, \tag{2.115}$$

where $\mathbf{B}$ and $\mathbf{E}$ are some conventional nonstationary (time-dependent) vector functions in three-dimensional space. These functions, according to formulas (2.113) and (2.97), satisfy the following equations:

$$curl\mathbf{E} = -\frac{\partial \mathbf{B}}{\partial t} \text{ and } div\mathbf{B} = 0. \tag{2.116}$$

We will demonstrate in Chapter 3 that Eqs. (2.116) are nothing else but the second and the third Maxwell's equations for electric field $\mathbf{E}$ and magnetic field $\mathbf{B}$, which describe the Faraday law of electromagnetic induction and the fact of absence of the magnetic charges. That is why the 2-form ϕ, which satisfies Eq. (2.113) is called *a Faraday-type differential form*. Its spatial component, ϕ_s, is called a *magnetic induction* 2-form B, while its temporal component, ϕ_τ, is called an electric 1-form E:

$$B = \phi_s = \mathbf{B} \cdot d\mathbf{\Sigma}, \quad E = \phi_\tau = \mathbf{E} \cdot d\mathbf{r}. \tag{2.117}$$

Thus, the Faraday-type differential form can be written as:

$$\psi = B + E \wedge dt. \tag{2.118}$$

Eq. (2.115) shows that every Faraday-type form can be expressed by the corresponding four-potential α. Splitting Eq. (2.115) into its spatial and temporal equations, we find that:

$$B = \mathbf{B} \cdot d\mathbf{\Sigma} = curl\mathbf{A} \cdot d\mathbf{\Sigma}, \quad E = \mathbf{E} \cdot d\mathbf{r} = -\left(grad U + \frac{\partial \mathbf{A}}{\partial t}\right) \cdot d\mathbf{r}. \tag{2.119}$$

Finally we arrive at the conventional representation for the vector fields $\mathbf{B}$ and $\mathbf{E}$ by the vector $\mathbf{A}$ and scalar U potentials:

$$\mathbf{B} = curl\mathbf{A} \text{ and } \mathbf{E} = -\left(grad U + \frac{\partial \mathbf{A}}{\partial t}\right). \tag{2.120}$$

2.4.5 NONSTATIONARY VECTOR FIELD EQUATIONS

Let us summarize the major results, we have obtained in this section. We have started our analysis with the arbitrary vector fields $\mathbf{H}(\mathbf{r}, t)$ and $\mathbf{D}(\mathbf{r}, t)$. We then introduced a corresponding Ampere-type differential form as:

$$\psi = \mathbf{D} \cdot d\mathbf{\Sigma} - (\mathbf{H} \cdot d\mathbf{r}) \wedge dt = D - H \wedge dt, \tag{2.121}$$

where $D = \mathbf{D} \cdot d\mathbf{\Sigma}$, $H = \mathbf{H} \cdot d\mathbf{r}$.

We have also established that there exist a vector field $\mathbf{j}^\psi(\mathbf{r}, t)$ and a scalar field $q^\psi(\mathbf{r}, t)$, which are determined by the original fields $\mathbf{H}(\mathbf{r}, t)$ and $\mathbf{D}(\mathbf{r}, t)$ according to formulae (2.108) and (2.106), which we will reproduce here for convenience:

$$\mathbf{j}^\psi = curl\mathbf{H} - \frac{\partial}{\partial t}\mathbf{D} \text{ and } q^\psi = div\mathbf{D}, \tag{2.122}$$

$$d \wedge \psi = (div\mathbf{D})\, dv + \left(\frac{\partial}{\partial t}\mathbf{D} - curl\mathbf{H}\right) \cdot d\mathbf{\Sigma} \wedge dt = \gamma^\psi. \tag{2.123}$$

These fields, $\mathbf{j}^{\psi}(\mathbf{r}, t)$ and $q^{\psi}(\mathbf{r}, t)$, can be combined together in the corresponding four-current 3-form γ^{ψ} equal to:

$$\gamma^{\psi} = q^{\psi} dv - \left(\mathbf{j}^{\psi} \cdot d\mathbf{\Sigma}\right) \wedge dt. \tag{2.124}$$

According to Eq. (2.95), we conclude that Ampere-type differential 2-form ψ and four-current 3-form γ^{ψ} are related to each other through a simple differential equation:

$$d \wedge \psi = \gamma^{\psi}. \tag{2.125}$$

Finally, expression (2.125) shows that 3-form γ^{ψ} is exact; therefore, its differential is equal to zero:

$$d \wedge \gamma^{\psi} = 0,$$

which results in the continuity Eq. (2.110).

Thus, we have expressed the major differential equations for the nonstationary vector fields in a very simple and elegant form (2.125). The simplicity and symmetry of this equation indicates that the differential forms provide a natural representation for the vector fields in four-dimensional space E_4. Note that these forms are introduced as a linear combination of the flux of the vector field $\mathbf{D}$ through a vector element of the surface, $D = \mathbf{D} \cdot d\mathbf{\Sigma}$, and a time differential of the work of the vector field $\mathbf{H}$ along a vector element of a line, $H = \mathbf{H} \cdot d\mathbf{r}$.

This fact indicates that the flux and the work of the vector fields should play an extremely important role in the electromagnetic field theory. We will find in the next chapter that the electric and/or magnetic flux and work indeed represent the major characteristics of the electromagnetic field.

REFERENCES AND RECOMMENDED READING TO CHAPTER 2

Alpin, L. M., 1966, Theory of the field: Nedra, Moscow, 384 pp.

Davis, H. F., and A. D. Snider, 1979, Introduction to vector analysis: Allyn & Bacon, Boston.

Dmitriev, V. I., M. N. Berdichevsky, and A. A. Bulychov, 2004, Lectures on the theory of the geophysical fields: Geophysical department of Moscow State University, Moscow.

Fecko, M., 2006, Differential geometry and Lie groups for physicists: Cambridge University Press, 697 pp.

Kaufman, A. A., 1992, Geophysical field theory and method, Part A, Gravitational, electric and magnetic fields: Academic Press, New York, 581 pp.

Kaufman, A. A., 1994a, Geophysical field theory and method, Part B, Electromagnetic fields I: Academic Press, New York, 217 pp.

Kaufman, A. A., 1994b, Geophysical field theory and method, Part C, Electromagnetic Fields II: Academic Press, New York, 335 pp.

FOUNDATIONS OF ELECTROMAGNETIC THEORY

2

ELECTROMAGNETIC FIELD EQUATIONS

3

CONTENTS

The fundamental theory for the behavior of electromagnetic fields became firmly established in the 19th century. I will not present here the details of the discovery of the basic laws of electricity and magnetism. Nor will I describe the special contributions of such great scientists as Volt, Coulomb, Oersted, Ohm, Gauss, Ampere, Faraday, Maxwell, and many others, who built the foundations of electromagnetic theory. Instead, I will refer interested readers to books on the history of physics, where many wonderful stories can be found (e.g., Whittaker, 1960a, 1960b). However, the reader can find some biographical data, related to Ohm, Ampere, Faraday, and Maxwell, in Introduction.

Based on these fundamental discoveries, we know without a doubt that current flow is accompanied by a predictable magnetic field, that when a magnetic field varies with time, a predictable electric field is generated, and that electric flux (current) and magnetic flux are conserved. In the second half of the 19th century, the principal physical laws characterizing the behavior and interaction of the electric and magnetic fields were unified in the comprehensive theory of electromagnetic fields by James Maxwell in his *Treatise on Electromagnetism*, first published in 1873. Formulation of this theory represents one of the most important events in physics since Newton's time. In fact, Maxwell was the first to

57

introduce the mathematical equations and physical laws which govern the electromagnetic field. Any effort to use electromagnetic fields to explore the earth must be firmly based on these physical laws and their mathematical consequences.

The fundamental system of electromagnetic field equations, the Maxwell's equations, was developed by generalization of the basic laws of electromagnetism established in the first half of the 19th century. In the framework of the classical theory, the EM field is described by electric and magnetic vector fields, and Maxwell's equations represent a system of differential equations with respect to these vector fields.

During the last decades, an alternative approach was developed to the formulation of Maxwell's equations. This approach is based on the algebraic theory of differential forms, formulated in the previous chapters, and results in a very compact and symmetric system of differential form equations.

The differential forms were originally introduced in differential geometry to study the properties of the lines and surfaces in multidimensional mathematical spaces. However, it was realized not so long ago that these forms provide a very elegant and powerful tool to study physical fields as well. We can treat the differential forms as another mathematical language which, similar to the vectorial language, can be used to describe physical fields. In fact, it was shown in Chapter 2 that, in a four-dimensional space-time continuum, the differential forms can be treated as linear combinations of the differentials of the flux, the work, and/or the source of vector fields. Therefore, the Maxwell's equations for the differential forms contain the differentials of the flux and work of electric and magnetic fields. This property of differential forms indicates that it is more suitable to consider the electric and/or magnetic flux and work as major characteristics of the EM field, instead of using the conventional vectorial representations. This approach seems to be quite reasonable from the geophysical point of view as well, because in geophysical experiments we, as a rule, measure the flux and the work (or voltage) of electric and magnetic fields.

In this chapter, I present a parallel development of electromagnetic theory based on the traditional Gibbsian vector formalism (using grad, div, and curl), and using the methods of differential forms. I believe that this new approach to the formulation and understanding of the basic properties of the laws of electromagnetism will stimulate the future development of electromagnetic geophysics. This approach also has tremendous advantages in computational electromagnetics, which is one of the main components of modern geophysical methods.

Moreover, a remarkable fact, demonstrated in Chapter 2, is that, based on the fundamental differential equations for the forms in a four-dimensional space, any pair of the arbitrary vector fields $\mathbf{H}(\mathbf{r}, t)$ and $\mathbf{D}(\mathbf{r}, t)$ satisfies a system of differential equations, which is similar to the classical Maxwell's equations for electromagnetic fields! In other words, we know now that if a 2-form in the four-dimensional space-time E_4 is comprised by two arbitrary vector fields, $\mathbf{H}(\mathbf{r}, t)$ and $\mathbf{D}(\mathbf{r}, t)$, then these fields must automatically satisfy a system of Maxwell's equations.

Thus, Maxwell's equations appear naturally from the basic equations of the field theory for the differential forms. There do not exist any other equations for a pair of nonstationary vector fields but equations of the Maxwell's type. The basic laws of electromagnetism are actually imprinted in the fundamental differential relationships between vector fields and differential forms.

In this chapter, I will also develop the basic aspects of electromagnetic theory which are common to the many techniques of electrical exploration that will be discussed later in the book. In so doing, we restrict our examination of electromagnetic theory to cases which are appropriate for those fields as they interact with the earth. Because of the strong attenuation experienced by electromagnetic waves as

they penetrate a conductive material, we restrict our interest to such fields only in the quasi-stationary and stationary regimes; that is, for cases in which the electromagnetic field components vary only slowly with time, or not at all. We have excluded from detailed consideration the cases in which electromagnetic fields vary relatively rapidly in time; in such cases, radiative transport of energy becomes important. If the medium through which the waves are moving is conductive, the energy is attenuated rapidly and is of little use in geophysical exploration. If the medium is an insulator, the electromagnetic waves can travel for considerable distances; the theory for electromagnetic radiation is covered thoroughly in many texts on radio waves and radar.

3.1 MAXWELL'S EQUATIONS AND BOUNDARY CONDITIONS
3.1.1 BASIC EQUATIONS IN THE THEORY OF ELECTROMAGNETIC FIELDS

The theory for electrical prospecting has been developed from the laws governing the behavior of electromagnetic fields in an inhomogeneous conducting earth. Maxwell's equations, which are a mathematical formulation of the laws describing the behavior of electromagnetic fields, are the basis of this theory. In fact, Maxwell's efforts to develop a general mathematical framework for electromagnetic phenomena were motivated by the Faraday's concept of the field. Maxwell was able to put into mathematical form the Faraday's representation of the electric and magnetic fields as the lines of forth. In the original mathematical expressions, which Maxwell had developed by 1864, he was dealing with twenty equations with twenty variables. In his great *Treatise on Electricity and Magnetism* published in 1873 he represented his equations in more mathematically concise way. However, these equations were still written without the use of the vector differential operators, which were introduced in the field theory later.

The classical form of Maxwell's equations consists of the two vector equations and two scalar equations shown below:

$$\nabla \times \mathbf{H} = \mathbf{j} + \partial \mathbf{D}/\partial t = \mathbf{c}, \tag{3.1}$$

$$\nabla \times \mathbf{E} = -\partial \mathbf{B}/\partial t, \tag{3.2}$$

$$\nabla \cdot \mathbf{B} = 0, \tag{3.3}$$

$$\nabla \cdot \mathbf{D} = q. \tag{3.4}$$

Here, $\mathbf{H}$ and $\mathbf{B}$ are the vector magnetic and induction fields, respectively (see Appendices C and D for conventions about naming the various electromagnetic field components); $\mathbf{E}$ and $\mathbf{D}$ are the vector electric and displacement fields, respectively; q is the electrical charge density; $\mathbf{j}$ is the conduction current density; and $\mathbf{c}$ is the total current density (the sum of conduction and displacement currents). The pairs of fields, $\mathbf{E}$ and $\mathbf{D}$, $\mathbf{H}$ and $\mathbf{B}$, are related by the following expressions, known as the constitutive equations:

$$\mathbf{D} = \epsilon \mathbf{E}, \tag{3.5}$$

$$\mathbf{B} = \mu \mathbf{H}, \tag{3.6}$$

where ϵ and μ are the dielectric constant (permittivity) and the magnetic permeability, respectively.

Maxwell's equations were introduced by generalization of the basic laws of electromagnetism established in the first half of the 19th century and by describing these laws in the terms of the field

theory envisioned by Faraday. It is interesting to note that in fact all these equations can be derived directly from the basic differential equations of the field theory, formulated in Chapter 2. Indeed, let us introduce two electromagnetic differential 2-forms, M and F, according to the formulae:

$$M = \mathbf{D} \cdot d\mathbf{\Sigma} - (\mathbf{H} \cdot d\mathbf{r}) \wedge dt = D - H \wedge dt, \tag{3.7}$$

$$F = \mathbf{B} \cdot d\mathbf{\Sigma} + (\mathbf{E} \cdot d\mathbf{r}) \wedge dt = B + E \wedge dt, \tag{3.8}$$

where $D = \mathbf{D} \cdot d\mathbf{\Sigma}$, $H = \mathbf{H} \cdot d\mathbf{r}$, $B = \mathbf{B} \cdot d\mathbf{\Sigma}$, and $E = \mathbf{E} \cdot d\mathbf{r}$.

Following Misner et al. (1973) and Deschamps (1981) we will call these forms Maxwell's field, M, and forth field, F, respectively. Thus, we can see that the forth field is a linear combination of the magnetic induction flux, B, and a time differential of the electric voltage (work), $E \wedge dt$, while the Maxwell's field is a linear combination of electric displacement flux, D, and a time differential of the work of the magnetic field, $H \wedge dt$. These physical entities, magnetic induction flux and electric displacement flux, electric voltage and magnetic work, represent the fundamental properties of what we call *electromagnetic field*.

Using the basic properties of differential 2-forms, discussed in Chapter 2, we can write the following differential equations for the Maxwell's field, M, and forth field, F, respectively:

$$d \wedge M = \gamma^e, \tag{3.9}$$

$$d \wedge F = \gamma^m, \tag{3.10}$$

where the corresponding electric, γ^e, and magnetic, γ^m, four-currents are equal to:

$$\gamma^e = q \, dv - (\mathbf{j} \cdot d\mathbf{\Sigma}) \wedge dt, \tag{3.11}$$

$$\gamma^m = q^m dv - \left(\mathbf{j}^m \cdot d\mathbf{\Sigma}\right) \wedge dt. \tag{3.12}$$

Here, the functions q^m and $\mathbf{j}^m$ are the magnetic charge density and the magnetic current density, respectively.

According to formulae (2.122) and (2.123), from the differential equation (3.9) for Maxwell's field M we obtain immediately Maxwell's first and the fourth Eqs. (3.1) and (3.4):

$$curl\mathbf{H} = \mathbf{j} + \frac{\partial}{\partial t}\mathbf{D} \tag{3.13}$$

and

$$div\mathbf{D} = q, \tag{3.14}$$

where Eq. (3.13) is a mathematical form of Ampere's law.

Taking into account that the exterior differential of the four-current γ^e, according to (3.9), is equal to zero,

$$d \wedge \gamma^e = d \wedge d \wedge M = 0,$$

and considering formula (2.99), we arrive at the *continuity equation* for electric current density $\mathbf{j}$ and the charge density q:

$$\nabla \cdot \mathbf{j} = -\frac{\partial q}{\partial t}. \tag{3.15}$$

In a similar way, from the differential equation (3.10) for the forth field F we obtain immediately a generalization of Maxwell's second and third Eqs. (3.2) and (3.3), which allows the existence of the magnetic charges:

$$curl\mathbf{E} = -\mathbf{j}^m - \frac{\partial}{\partial t}\mathbf{B} \tag{3.16}$$

and

$$div\mathbf{B} = q^m. \tag{3.17}$$

Note that the magnetic four-current γ^m satisfies the same differential equation as the electric four-current:

$$d \wedge \gamma^m = d \wedge d \wedge F = 0.$$

Therefore, the magnetic charges and current, in general cases, are related by the continuity equation as well:

$$\nabla \cdot \mathbf{j}^m = -\frac{\partial q^m}{\partial t}. \tag{3.18}$$

Introducing the magnetic charges makes Maxwell's equation symmetrical. However, in the real world we do not observe the magnetic charges, which results in the Faraday-type equation for the forth field:

$$d \wedge F = 0. \tag{3.19}$$

This equation, written in vectorial notations, brings us to Maxwell's original second and third Eqs. (3.2) and (3.3):

$$curl\mathbf{E} = -\frac{\partial}{\partial t}\mathbf{B} \tag{3.20}$$

and

$$div\mathbf{B} = 0. \tag{3.21}$$

In fact, we will demonstrate in the next section that Eqs. (3.19) and (3.20) represent a mathematical form of Faraday's law for electromagnetic induction. Thus, the whole system of Maxwell's equations automatically appears from the general theory of nonstationary fields. This remarkable fact demonstrates the power of mathematical theory. We can see now that the basic laws of electromagnetism are actually hidden in the fundamental differential relationships between the vector fields and differential forms.

In summary, we can represent now the full system of Maxwell's equations in a very compact and elegant form as:

$$d \wedge M = \gamma^e, \tag{3.22}$$
$$d \wedge F = 0, \tag{3.23}$$

where

$$M = \mathbf{D} \cdot d\mathbf{\Sigma} - (\mathbf{H} \cdot d\mathbf{r}) \wedge dt = D - H \wedge dt, \tag{3.24}$$

and

$$F = \mathbf{B} \cdot d\mathbf{\Sigma} + (\mathbf{E} \cdot d\mathbf{r}) \wedge dt = B + E \wedge dt. \tag{3.25}$$

It was demonstrated in Chapter 2 that any Faraday-type form can be expressed by the corresponding four potential α. Taking into account that the forth field F is a Faraday-type form, we can use Eq. (2.119), according to which:

$$B = \mathbf{B} \cdot d\mathbf{\Sigma} = curl\mathbf{A} \cdot d\mathbf{\Sigma}, \ E = \mathbf{E} \cdot d\mathbf{r} = -\left(gradU + \frac{\partial \mathbf{A}}{\partial t} \right) \cdot d\mathbf{r}. \tag{3.26}$$

From the last formula we obtain a classical representation of the magnetic and electric fields using *electromagnetic potentials*, $\mathbf{A}$ and U:

$$\mathbf{B} = curl\mathbf{A} \text{ and } \mathbf{E} = -\left(gradU + \frac{\partial \mathbf{A}}{\partial t} \right). \tag{3.27}$$

Another important feature of the differential form of Maxwell's equations (3.22) and (3.23) is that they describe the relationships between the elementary fluxes and the work of the different EM field components, while the original Maxwell's equations (3.1)–(3.4) deal with the vectors of EM fields themselves. Thus, the new mathematical form of Maxwell's equations emphasizes the importance of the fluxes and the work of the EM field. This form also emphasizes an importance of Faraday's vision of the field as a web of lines of force, filling and crossing the space.

We will see in the following sections of this chapter and in the following chapters of the book, that, indeed, the flux of the field through a given surface and the work of the field along a given path represent the most important physical entities which are studied and measured in the geophysical experiment. That is why the new form of Maxwell's equations (3.22) and (3.23) appears to be extremely well suited for description of geophysical EM phenomena. The interested reader can find more details about the applications of the differential forms to electromagnetic problems in the monograph by Lindell (2004).

3.1.2 PHYSICAL INTERPRETATION OF MAXWELL'S EQUATIONS

Let us examine the physical significance of each of the four equations listed above. The second vector equation (3.2) represents the electromagnetic induction law discovered by Faraday. Indeed, let us consider an arbitrary smooth surface, S, bounded by a curve, L, and find the flux of the vector curl $\mathbf{E}$ across this surface (Fig. 3.1):

$$\iint_S \nabla \times \mathbf{E} \cdot \mathbf{n} ds = -\iint_S \frac{\partial \mathbf{B}}{\partial t} \cdot \mathbf{n} ds = -\frac{\partial}{\partial t} \iint_S \mathbf{B} \cdot \mathbf{n} ds, \tag{3.28}$$

where $\mathbf{n}$ is a unit vector outwardly normal to the surface S.

Applying Stoke's theorem, the surface integral on the left in Eq. (3.28) can be transformed to:

$$\iint_S \nabla \times \mathbf{E} \cdot \mathbf{n} ds = \oint_L \mathbf{E} \cdot \boldsymbol{\tau} \, d\ell. \tag{3.29}$$
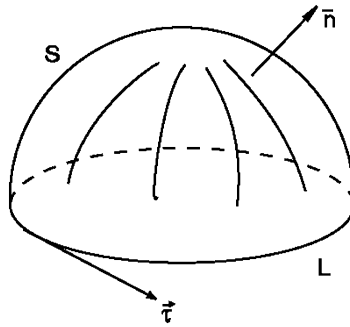
FIGURE 3.1

Calculation of the flux of the vectors curl**E** or curl**H** over the surface S.

Substituting this relationship into Eq. (3.28), we have

$$\oint_L \mathbf{E} \cdot \boldsymbol{\tau} d\ell = -\frac{\partial}{\partial t} \iint_S \mathbf{B} \cdot \mathbf{n} ds, \tag{3.30}$$

where $\boldsymbol{\tau}$ is a unit vector tangent to the line L. Note that, in the last equation the term on the left is the work of electric field **E**, and the term on the right is the flux of magnetic field **B**.

We will examine the particular case in which S is bounded by a conducting filament L (for example, L is a thin wire). The line integral of the electric field **E** along the path L is the electromotive force (EMF) observed in that circuit:

$$\oint_L \mathbf{E} \cdot \boldsymbol{\tau} d\ell = EMF. \tag{3.31}$$

Also,

$$\iint_S \mathbf{B} \cdot \mathbf{n} ds = \Phi, \tag{3.32}$$

where Φ is the magnetic flux permeating the circuit.

Substituting these last two definitions into Eq. (3.30), we find that the EMF observed in a closed circuit is equal to (with the negative sign) the time-rate of change of the magnetic flux permeating the circuit:

$$EMF = -\partial\Phi/\partial t. \tag{3.33}$$

That is, we have derived Faraday's law for electromagnetic induction. This law was experimentally established by Faraday in 1831.

Returning to Maxwell's first equation (3.1), we should note that, this equation was designed originally to reflect the link between the electric current and the magnetic field, discovered by Oersted in 1820 and later formulated in the form of Ampere's law. According to this law the curl of the magnetic field should be equal to the electric current density. However, Maxwell found that it was not enough
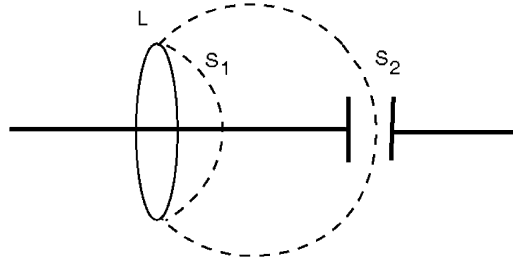
FIGURE 3.2

Illustration of the concept of displacement currents introduced by Maxwell.

to consider the conduction currents only in this term in order to satisfy the entire system of four equations. To avoid this difficulty he generalized the expression for the current density by adding to the conduction current caused by the movement of electric charge another term, proportional to the rate of the time variation of electric displacement field **D**. Indeed, let us calculate the flux of the vector curl **H** over the surface S (see Fig. 3.1):

$$\iint_S \nabla \times \mathbf{H} \cdot \mathbf{n} ds = \iint_S \mathbf{j} \cdot \mathbf{n} ds + \iint_S \frac{\partial \mathbf{D}}{\partial t} \cdot \mathbf{n} ds$$
$$= \iint_S \mathbf{c} \cdot \mathbf{n} ds. \qquad (3.34)$$

According to Stoke's theorem, the left-hand term in this equation is the circulation of the vector **H** along the circuit L. Moreover, the right-hand term is the vector flux of total current density over the surface S; that is, the total current I^{total} through the circuit L is:

$$\oint_L \mathbf{H} \cdot \boldsymbol{\tau} d\ell = I^{total}. \qquad (3.35)$$

This last equation represents a mathematical expression of Ampere's law: the circulation of the magnetic field **H** around any closed circuit is equal to the total current through this circuit.

In accord with Eq. (3.34):

$$I^{total} = \iint_S \mathbf{j} \cdot \mathbf{n} ds + \iint_S \frac{\partial \mathbf{D}}{\partial t} \cdot \mathbf{n} ds. \qquad (3.36)$$

The first term in this equation is the magnitude of the conduction current, I, through the circuit, L, while the second term is the magnitude of the displacement current, I^{dis}. The concept of displacement currents was first introduced by Maxwell. This concept permits us to consider electrical circuits that include capacitors through which alternating current can flow (Fig. 3.2). Capacitors do not comprise circuit breaks for the flow of alternating current. Let us encircle the filament L and compute the circulation of the magnetic field vector **H** along this path. From Ampere's law, this value will equal the flow of electrical current either through the surface S_1, which cuts the current-carrying conductor, or

through the surface S_2, passing through the capacitor:

$$\oint_L \mathbf{H} \cdot \boldsymbol{\tau} dl = \iint_{S_1} \mathbf{c} \cdot \mathbf{n} ds = \iint_{S_2} \mathbf{c} \cdot \mathbf{n} ds. \tag{3.37}$$

An ordinary conduction current flows through the surface S_1, which intersects the conducting fila-ment. At the same time, this current does not flow through S_2 but, in view of the fact that the circuit is continuous for the flow of alternating current (in accord with Eq. (3.37)), there is a displacement current flowing between the plates of the capacitor in order to provide continuity for the conduction current:

$$\mathbf{j}^{dis} = \partial \mathbf{D} / \partial t.$$

Thus, the total current density, $\mathbf{c}$, is the combination of conduction currents and displacement currents:

$$\mathbf{c} = \mathbf{j} + \mathbf{j}^{dis}. \tag{3.38}$$

Maxwell's first equation (3.34) indicates that both displacement currents and conduction currents contribute in the same way to the magnetic field. We note that, while conduction currents result from the flow of charges, and displacement is the rate of change of the field $\mathbf{D}$, both of these processes contribute a magnetic field.

The conception of displacement current reflects the scientific genius of Maxwell. The concept led to the discovery of radio waves and the modern development of broadcast technology. According to Eq. (3.2), a time-varying magnetic field gives rise to an associated electric field, while according to Eq. (3.1) that same electric field gives rise to a magnetic field. The two, the electric and magnetic fields, continuously interact, reinforcing each other, and, as a consequence, they can propagate to great distances in space. This is the basis for our understanding of electromagnetic waves and related phe-nomena in contemporary electrodynamics.

On the basis of the first two of Maxwell's equations (Eqs. (3.1) and (3.2)), we accept that the magnetic field $\mathbf{H}$ arises from conduction and displacement currents, while the electric field $\mathbf{E}$ arises from a time varying induction field, $\mathbf{B}$.

The fourth of the Maxwellian equations reflects the fact that electric charges are the source of the electric displacement field, $\mathbf{D}$. That is, this relationship is the mathematical expression of Coulomb's law, in accord with which the electric field, $\mathbf{E}$, created by electrical charge in a homogeneous isotropic medium with a dielectric constant ϵ, is linearly proportional to the size of the charge Q and inversely proportional to distance r^2 and $4\pi\epsilon$:

$$\mathbf{E} = (Q/4\pi\epsilon r^2)\mathbf{d}_r, \tag{3.39}$$

where $\mathbf{d}_r$ is a unit vector directed along the radius vector. This law was established by Coulomb in 1789 by measuring the attractions and repulsions of electric charges by means of a torsion balance which he invented.

Finally, the third Maxwellian equation is Gauss's law of nonexistence of magnetic charges. It is an expression of the experimentally observed fact that in the real world there is no such thing as magnetic charge. The magnetic induction field, $\mathbf{B}$, is purely a vortex field. Its source is electrical current.

Let us now examine the physical meaning of the equation for continuity of current (3.15). For this, we integrate Eq. (3.15) over some volume D, bounded by the surface S, and make use of Gauss's theorem:

$$\iint_S \mathbf{j} \cdot d\mathbf{s} = -\iiint_D \frac{\partial q}{\partial t} dv. \tag{3.40}$$

The scalar flux of the vector current density across a surface S is called the electric current:

$$I = \iint_S \mathbf{j} \cdot d\mathbf{s}. \tag{3.41}$$

Also, the right-hand part of Eq. (3.40) represents the change in electric charge Q within the volume D per unit time:

$$-\iiint_D \frac{\partial q}{\partial t} dv = -\partial Q/\partial t. \tag{3.42}$$

Substituting these two expressions in Eq. (3.40), we have

$$I = -\partial Q/\partial t. \tag{3.43}$$

This last equation is the mathematical expression of the condition of conservation of charge: charge is neither created nor destroyed. If current flows out of a closed surface, the quantity of charge within the surface decreases in an amount per unit time which exactly balances the outward flow of current. Apparent exceptions to this law of conservation might be considered, such as the photoelectric effect in which charge can be created. However, in such a case, there will be equal quantities of positive and negative charge, so that the total charge remains constant.

In addition, it has been observed experimentally that current density in an extended medium (particularly for earth materials) is linearly proportional to the electric field vector $\mathbf{E}$. This is often known as Ohm's law in differential form:

$$\mathbf{j} = \sigma \mathbf{E}, \tag{3.44}$$

where σ is the electrical conductivity of the medium. Often, we speak of the inverse of the conductivity, which is the electrical resistivity, represented by the character $\rho = 1/\sigma$.

Ohm's law as it is generally used in electrical technology is written as

$$U = IR, \tag{3.45}$$

where U is the drop in voltage (electromotive force) along a conductor of uniform cross section, I is current and R is resistance, calculated as

$$R = \rho \ell/S. \tag{3.46}$$

Here, ℓ and S are the length and cross-sectional area normal to the direction of current flow, respectively, and ρ is the electrical resistivity. This law was discovered experimentally by Ohm in 1827 and later on was stated by Faraday in 1832 based on his representation of electric field in a form of lines of force.

In the particular case in which we place a cylindrical conductor in a uniform electric field **E** directed along the axis of the conductor and integrate Eq. (3.44) over the volume of the conductor, V,

$$\iiint_V j \, dv = \iiint_V \sigma E \, dv, \tag{3.47}$$

where j and E are the magnitudes of the vectors j and **E** respectively. Considering that E, and consequently j, are constant within the conductor, Eq. (3.47) can be written as

$$j S \ell = \sigma E S \ell.$$

The product of j and S is the current in the conductor:

$$j S = I, \tag{3.48}$$

while the product of E and ℓ is the voltage drop along the conductor:

$$E \ell = U. \tag{3.49}$$

Substituting Eq. (3.49) and (3.48) into (3.47), and considering (3.46), we confirm Ohm's law (Eq. (3.45)).

It should be noted that in Eqs. (3.1) to (3.4), we have not taken the origin of the fields into account. In this respect, currents and charges arise not only by the action of electrical forces, but also as a result of mechanical forces, chemical forces, and others. Those parts of the currents and charges that arise because of other than electromagnetic forces are termed extrinsic.

In order to include extrinsic currents and charges in Maxwell's equations, we write them as:

$$\nabla \times \mathbf{H} = \mathbf{j} + \mathbf{j}^e + \partial \mathbf{D}/\partial t, \tag{3.50}$$

$$\nabla \times \mathbf{E} = -\partial \mathbf{B}/\partial t, \tag{3.51}$$

$$\nabla \cdot \mathbf{B} = 0, \tag{3.52}$$

$$\nabla \cdot \mathbf{D} = q + q^e, \tag{3.53}$$

where $\mathbf{j}^e$ and q^e are the densities of extrinsic currents and charges, respectively. These also must satisfy a condition of conservation:

$$\nabla \cdot \mathbf{j}^e = -\partial q^e / \partial t. \tag{3.54}$$

It should be noted that Eqs. (3.52) and (3.53) follow from Eqs. (3.50) and (3.51) with the continuity equations, (3.15) and (3.54).

Naturally, we must recognize that Maxwell's equations as written here in differential form are valid only in a medium in which the properties ϵ, μ, and σ vary slowly enough in space that the fields **E**, **D**, **B**, and **H** can be differentiated with respect to space coordinates. If the properties do vary discontinuously, Maxwell's equations must be augmented with appropriate boundary conditions.
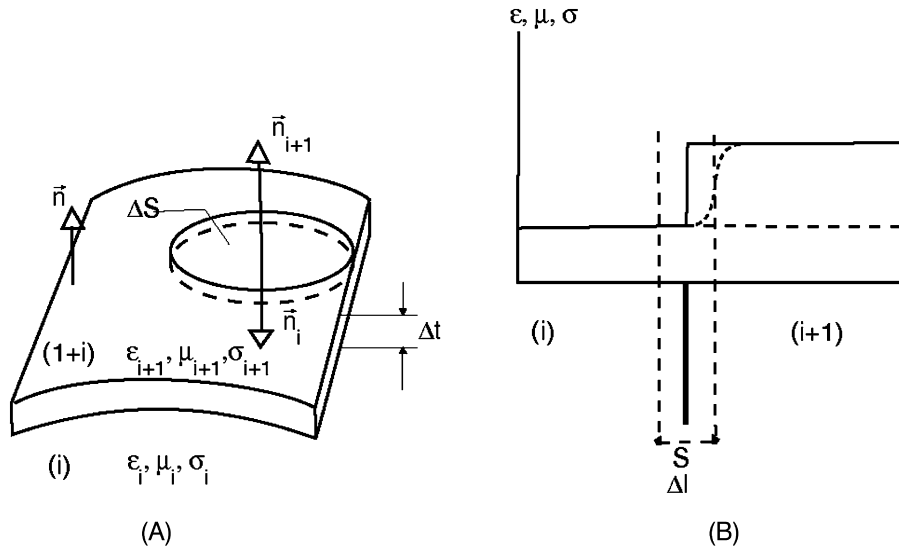
FIGURE 3.3

Formulation of the boundary conditions for electromagnetic field: the surface S separating medium (i) from medium $(i + 1)$ is replaced with a very thin transitional layer with a thickness $\Delta \ell$ in which the parameters ϵ, μ, and σ vary rapidly but continuously.

3.1.3 BOUNDARY CONDITIONS FOR THE VECTOR FIELD

At a boundary between different regions in the earth, the properties ϵ, μ, and σ probably change abruptly. Referring to Eqs. (3.5) and (3.6), we see that this results in a discontinuous change in several of the fields. Therefore, in solving problems in electromagnetic induction in the earth, it is necessary to have boundary conditions – conditions that relate the field strengths at points immediately adjacent to each other on either side of a boundary across which the properties of the medium change abruptly – in addition to Maxwell's equations.

Boundary conditions are specific to each problem to be solved. However, we can formulate boundary conditions for an important and commonly met case, in which a surface S separates two media identified by the indices (i) and $(i + 1)$. On either side of this surface, the properties of the two media are constant, or vary spatially so slowly that within some small region about any arbitrary point the properties can be considered to be constant. We designate as **n** the unit vector normal to a point on the surface S directed from medium (i) to medium $(i + 1)$, as shown in Fig. 3.3. We also assume that there are no extrinsic currents or charges on the surface. We accept the condition of conjugate vectors for the electromagnetic field on the surface S. In so doing, we replace the surface S separating medium (i) from medium $(i + 1)$ with a very thin transitional layer with a thickness $\Delta \ell$ in which the parameters ϵ, μ, and σ vary rapidly but continuously, as in Fig. 3.3B. In such a layer, Maxwell's equations are still valid.

Using Maxwell's equations, we determine the relationship between field components at the inner and outer edges of the transitional layer and then take a limit as $\Delta\ell \to 0$. So doing, we find the condition for continuity.

In the transitional layer, we form a vertical cylinder V of a small cross section ΔS (Fig. 3.3A) and examine the flux of the vector field $\mathbf{B}$ across the surface of the cylinder Σ. From Gauss's theorem, and on the strength of Eq. (3.3), this flux is:

$$\iint_\Sigma \mathbf{B} \cdot \mathbf{n}_\Sigma \, dS = \iiint_V \nabla \cdot \mathbf{B} dV = 0, \tag{3.55}$$

where V is the volume of the cylinder and $\mathbf{n}_\Sigma$ is the unit vector normal to the surface Σ.

Inasmuch as ΔS is small, we can assume that $\mathbf{B}$ is constant over the cylinder. Now, Eq. (3.55) can be written as an approximation:

$$(\mathbf{B} \cdot \mathbf{n}_i)\Delta S + (\mathbf{B} \cdot \mathbf{n}_{i+1})\Delta S + (\text{the portion on the side surface}) = 0, \tag{3.56}$$

where $\mathbf{n}_{i+1}$ and $\mathbf{n}_i$ are the outward-pointing normals to the upper and lower ends of the cylinder, respectively (Fig. 3.3A).

Let us designate the normal components of the induction field $\mathbf{B}$ at the surface S, but measured in medium (i) or medium $(i + 1)$ with the symbols $B_n^{(i)}$ and $B_n^{(i+1)}$ respectively. When we reduce the thickness of the surface layer, or as $\Delta\ell \to 0$, we see from Fig. 3.3A that $\mathbf{n}_{i+1} \to \mathbf{n}$ and $\mathbf{n}_i \to -\mathbf{n}$, so that $\mathbf{B} \cdot \mathbf{n}_{i+1} \to B_n^{(i+1)}$ and $\mathbf{B} \cdot \mathbf{n}_i \to -B_n^{(i)}$. Consequently, on taking the limit in Eq. (3.56) as $\Delta\ell \to 0$ and assuming that the effect of the side surface of the cylinder tends to zero as the height of the cylinder goes to zero, we obtain:

$$B_n^{(i+1)}\Delta S - B_n^{(i)}\Delta S = 0. \tag{3.57}$$

Dividing by ΔS, we get the final equation showing that *the normal component of the magnetic field vector is continuous across the boundaries*:

$$B_n^{(i)} = B_n^{(i+1)}. \tag{3.58}$$

Let us consider the vector for the density of the total current, $\mathbf{c}$. In accord with Eq. (3.1),

$$\nabla \cdot (\nabla \times \mathbf{H}) = \nabla \cdot \mathbf{c} = 0,$$

meaning that $\mathbf{c}$, like $\mathbf{B}$, is purely a vortex field. Following the same logic, we can show that the normal component of *the total current is continuous across the interface*:

$$\mathbf{c}_n^{(i)} = \mathbf{c}_n^{(i+1)}. \tag{3.59}$$

Let us examine the displacement field $\mathbf{D}$. We calculate the vector flux of $\mathbf{D}$ on the surface of the cylinder V in Fig. 3.3A from Maxwell's fourth equation (3.4) using Gauss's theorem:

$$\iint_\Sigma \mathbf{D} \cdot \mathbf{n}_\Sigma \, dS = \iiint_V \nabla \cdot \mathbf{D} dV = \iiint_V q \, dV = Q, \tag{3.60}$$

where Q is the total charge within the cylinder, given by $Q = q\Delta\ell\Delta S$.
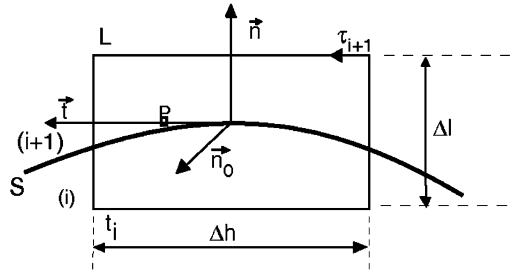
FIGURE 3.4

The behavior of the tangential components of the electromagnetic field in the transitional layer with a thickness $\Delta\ell$ in which the parameters ϵ, μ, and σ vary rapidly but continuously.

In the limit, as $\Delta\ell \rightarrow 0$, as previously, the left-hand expression in (3.60) is

$$\lim_{\Delta\ell\rightarrow0}\iint_{\Sigma} \mathbf{D} \cdot \mathbf{n}_{\Sigma} dS = D_n^{(i+1)}\Delta S - D_n^{(i)}\Delta S.$$

As the point approaches the end of the cylinder, the total charge Q appears as an infinitely large charge density, q. In this limiting case, the product $q\Delta\ell$ can be interpreted to be a surface charge density:

$$\lim_{\substack{\Delta\ell\rightarrow0 \\ q\rightarrow\infty}} q\Delta\ell = \eta.$$

The surface charge density, η, is defined as the charge per unit surface area, $\eta = Q/\Delta S$.
Thus, in going to the limit $\Delta\ell \rightarrow 0$ in Eq. (3.60), we have

$$D_n^{(i+1)}\Delta S - D_n^{(i)}\Delta S = Q\Delta S/\Delta S = \eta\Delta S.$$

Hence,

$$D_n^{(i+1)} - D_n^{(i)} = \eta. \tag{3.61}$$

The presence of a charge on the surface S creates a discontinuity in the normal component of the vector $\mathbf{D}$!

We now examine the behavior of the tangential components of the electromagnetic field. In so doing, we make use of a right-angle cylinder with a circumference lying in a plane defining the normal $\mathbf{n}$ on the surface S and normal to the direction $\boldsymbol{\tau}$ of the tangential component of the field $\mathbf{H}$, as shown in Fig. 3.4.

In accord with Maxwell's first equation,

$$\nabla \times \mathbf{H} = \mathbf{c}.$$

We designate the part of the plane within the circumference L as P, and the positive unit vector normal to P as $\mathbf{n}_o$. Let us examine the flux of the vector $\mathbf{c}$ through the plane P:

$$\iint_P \mathbf{c} \cdot \mathbf{n}_o dS = \iint_P \nabla \times \mathbf{H} \cdot \mathbf{n}_o dS.$$

From Stoke's theorem, we have:

$$\iint_P \mathbf{c} \cdot \mathbf{n}_o dS = \int_L \mathbf{H} \cdot \boldsymbol{\tau}_L d\ell. \tag{3.62}$$

If we assume that the diameter of the path L is sufficiently small, $\Delta h \ll 1$, we can assume that $\mathbf{H}$ is constant over the upper and lower faces of the domain bounded by L. Then the line integral in Eq. (3.62) is approximately:

$$\int_L \mathbf{H} \cdot \boldsymbol{\tau}_L d\ell = \mathbf{H} \cdot \boldsymbol{\tau}_i \Delta h + \mathbf{H} \cdot \boldsymbol{\tau}_{i+1} \Delta h + \text{(a fraction contributed by the side lines)}.$$

We will designate the tangential components of the field $\mathbf{H}$ on S determined in the media (i) or $(i+1)$ as $H_\tau^{(i)}$ or $H_\tau^{(i+1)}$, respectively. It is obvious (Fig. 3.4) that, as $\Delta \ell \to 0$,

$$\mathbf{H} \cdot \boldsymbol{\tau}_{i+1} \to H_\tau^{(i+1)},$$

$$\mathbf{H} \cdot \boldsymbol{\tau}_i \to -H_\tau^{(i)},$$

and that the contribution of the side lines approaches zero.
Hence,

$$\int_L \mathbf{H} \cdot \boldsymbol{\tau}_L d\ell \xrightarrow{\Delta\ell \to 0} H_\tau^{(i+1)} \Delta h - H_\tau^{(i)} \Delta h. \tag{3.63}$$

Moreover, in view of the small area within L, we can assume that $\vec{c}$ is constant along L, so that

$$\iint_P \mathbf{c} \cdot \mathbf{n}_o dS = \mathbf{c} \cdot \mathbf{n}_0 \Delta\ell \Delta h,$$

$$= \left(\sigma \mathbf{E} + \frac{\partial \mathbf{D}}{\partial t} \right) \cdot \mathbf{n}_0 \Delta\ell \Delta h. \tag{3.64}$$

Because the vectors $\mathbf{E}$ and $\partial \mathbf{D}/\partial t$ are always bounded, then for any finite value of σ, the right-hand part of Eq. (3.64) tends to zero uniformly as $\Delta\ell \to 0$. Comparing Eq. (3.62) with (3.63), we see:

$$H_\tau^{(i+1)} \Delta h - H_\tau^{(i)} \Delta h = 0.$$

Consequently

$$H_\tau^{(i+1)} = H_\tau^{(i)},$$

if σ_i and σ_{i+1} are finite.

In the same way, using Maxwell's second equation, we find that

$$E_\tau^{(i)} = E_\tau^{(i+1)}.$$

We have now developed the following boundary conditions for a vector electromagnetic field.

- For the normal components of the field:

$$B_n^{(i+1)} - B_n^{(i)} = 0, \tag{3.65}$$

$$D_n^{(i+1)} - D_n^{(i)} = \eta, \tag{3.66}$$

where η is the surface charge density on the boundary S, defined as the amount of electrical charge per unit area of the surface. The normal component of magnetic induction $\mathbf{B}$ is continuous across the boundary separating the two media, but the electric displacement vector $\mathbf{D}$ is discontinuous, with the size of the discontinuity being the electrical charge density.

- For the tangential components of the field at a boundary between media with finite conductivities

$$H_\tau^{(i+1)} - H_\tau^{(i)} = 0, \tag{3.67}$$

$$E_\tau^{(i+1)} - E_\tau^{(i)} = 0. \tag{3.68}$$

Both the tangential component of the electric field $\mathbf{E}$ and the tangential component of the magnetic field $\mathbf{H}$ are continuous across a boundary separating any two finitely conducting media.

Using these expressions, Eqs. (3.65) through (3.68), with Eqs. (3.5), (3.6), and (3.44), we have a complete representation for the boundary conditions for tangential and normal components of the vectors $\mathbf{H}$, $\mathbf{B}$, $\mathbf{D}$, and $\mathbf{E}$.

3.1.4 THE FIELD IN A HOMOGENEOUS MEDIUM

Let us examine a simplified set of Maxwell's equations valid for a medium which is both homogeneous and isotropic; that is, we require the properties ϵ, μ, and σ to be constant in time and space. Then:

$$\nabla \times \mathbf{H} = \sigma \mathbf{E} + \epsilon \partial \mathbf{E} / \partial t, \tag{3.69}$$

$$\nabla \times \mathbf{E} = -\mu \partial \mathbf{H} / \partial t, \tag{3.70}$$

$$\nabla \cdot \mathbf{H} = 0, \tag{3.71}$$

$$\nabla \cdot \mathbf{E} = 0. \tag{3.72}$$

In the last of these four equations, the electric charge density, q, is zero because, as is usually shown in an elementary course on electromagnetic field theory, no charge can collect in a homogeneous conducting medium. There are no free charges in such a medium.

For many of the useful problems in electrical prospecting, it is desirable to separate the variables in Maxwell's equations, that is, to write equations for the electric and magnetic fields separately. To

accomplish this, we first perform the curl operation on both sides of Eq. (3.70), and then by substitution in Eq. (3.69), we obtain

$$\nabla \times \nabla \times \mathbf{E} + \mu\epsilon\partial^2\mathbf{E}/\partial t^2 + \mu\sigma\partial\mathbf{E}/\partial t = 0. \tag{3.73}$$

Similarly, by performing the curl operation of Eq. (3.69) and substituting it into (3.70), we obtain

$$\nabla \times \nabla \times \mathbf{H} + \mu\epsilon\partial^2\mathbf{H}/\partial t^2 + \mu\sigma\partial\mathbf{H}/\partial t = 0. \tag{3.74}$$

Knowing the vector identity

$$\nabla \times \nabla \times \mathbf{A} = \nabla (\nabla \cdot \mathbf{A}) - \nabla^2\mathbf{A},$$

where the symbol ∇^2 indicates the vector Laplacian operator, and considering the divergence condition in Eq. (3.72), we can write the relationship in Eq. (3.73) as

$$\nabla^2\mathbf{E} - \mu\epsilon\partial^2\mathbf{E}/\partial t^2 - \mu\sigma\partial\mathbf{E}/\partial t = 0. \tag{3.75}$$

Similarly, from Eq. (3.74), we have

$$\nabla^2\mathbf{H} - \mu\epsilon\partial^2\mathbf{H}/\partial t^2 - \mu\sigma\partial\mathbf{H}/\partial t = 0. \tag{3.76}$$

Eqs. (3.75) and (3.76), which completely describe the electric and magnetic fields in a homogeneous medium, are called the *telegraphers' equations*.

3.2 TIME-HARMONIC ELECTROMAGNETIC FIELD

In the solution of many of the problems that arise in electrical prospecting, we will consider fields which vary in time as a harmonic function (cisoidal, either a cosinusoidal or sinusoidal function of time, or a combination of the two) at some specific though arbitrary angular frequency, ω. Such a field is called a *monochromatic field*.

We note that, with few exceptions, any field which is a more arbitrary function of time can be synthesized using a sum of cisoidal functions because, as is well known, any reasonably well behaved function of time can be replaced with a Fourier series or a Fourier integral of its spectral components. So, to simplify the mathematical analysis of many problems encountered in electrical exploration, we can consider behavior at one frequency at a time; that is, a monochromatic field.

Let us consider, for example, a magnetic field $\mathbf{H}$ with three components lying along the direction vectors $\mathbf{d}_x$, $\mathbf{d}_y$, and $\mathbf{d}_z$ in a Cartesian coordinate system varying cosinusoidally with time:

$$\mathbf{H}(t) = H_x \cos(\omega t - \phi_x)\mathbf{d}_x + H_y \cos(\omega t - \phi_y)\mathbf{d}_y + H_z \cos(\omega t - \phi_z)\mathbf{d}_z, \tag{3.77}$$

where ω is the frequency measured in radians per second, and H_x, H_y, H_z and ϕ_x, ϕ_y, ϕ_z are the amplitudes and phases of the corresponding magnetic field components.

We rewrite Eq. (3.77) through the use of Euler's formula,

$$e^{-i(\omega t-\phi)} = \cos(\omega t - \phi) - i \, \sin(\omega t - \phi), \tag{3.78}$$

with

$$\cos(\omega t - \phi) = \text{Re } e^{-i(\omega t - \phi)}, \tag{3.79}$$

where Re is the operator which takes the real part of a complex number. With Eq. (3.79), Eq. (3.77) can be written as

$$\mathbf{H}(t) = H_x \text{Re } e^{-i(\omega t - \phi_x)} \mathbf{d}_x + H_y \text{Re } e^{-i(\omega t - \phi_y)} \mathbf{d}_y + H_x \text{Re } e^{-i(\omega t - \phi_z)} \mathbf{d}_z$$
$$= \text{Re } \left\{ [H_x e^{i\phi_x} \mathbf{d}_x + H_y e^{i\phi_y} \mathbf{d}_y + H_z e^{i\phi_z} \mathbf{d}_z] e^{-i\omega t} \right\}. \tag{3.80}$$

We will call the quantity

$$\hat{\mathbf{H}} = H_x e^{i\phi_x} \mathbf{d}_x + H_y e^{i\phi_y} \mathbf{d}_y + H_z e^{i\phi_z} \mathbf{d}_z$$

the complex vector field, noting that the complex vector is not a vector in the usual sense because the coefficients of the unit directions vectors are complex numbers. Then, we rewrite Eq. (3.80) as

$$\mathbf{H} = Re(\hat{\mathbf{H}} e^{-i\omega t}). \tag{3.81}$$

In the same way, we define the complex vector magnetic induction field, the complex electric field, the complex displacement field, and the complex charge density, $\hat{q}$:

$$\hat{\mathbf{B}} = B_x e^{i\psi_x} \mathbf{d}_x + B_y e^{i\psi_y} \mathbf{d}_y + B_z e^{i\psi_z} \mathbf{d}_z,$$
$$\hat{\mathbf{E}} = E_x e^{i\alpha_x} \mathbf{d}_x + E_y e^{i\alpha_y} \mathbf{d}_y + E_z e^{i\alpha_z} \mathbf{d}_z,$$
$$\hat{\mathbf{D}} = D_x e^{i\beta_x} \mathbf{d}_x + D_y e^{i\beta_y} \mathbf{d}_y + D_z e^{i\beta_z} \mathbf{d}_z,$$
$$\hat{q} = q e^{i\theta},$$

where $B_{x(y,z)}$, $\psi_{x(y,z)}$, $E_{x(y,z)}$, $\alpha_{x(y,z)}$, $D_{x(y,z)}$, $\beta_{x(y,z)}$, q, and θ are the amplitudes and phases of the corresponding vectors $\mathbf{B}$, $\mathbf{E}$, and $\mathbf{D}$, and the scalar q. Also

$$\mathbf{B} = \text{Re}(\hat{\mathbf{B}} e^{-i\omega t}),$$
$$\mathbf{D} = \text{Re}(\hat{\mathbf{D}} e^{-i\omega t}),$$
$$\mathbf{E} = \text{Re}(\hat{\mathbf{E}} e^{-i\omega t}),$$
$$q = \text{Re}(\hat{q} e^{-i\omega t}). \tag{3.82}$$

Substituting Eqs. (3.81) and (3.82) into Maxwell's equations, (3.1) through (3.4), and considering the linearity of the operations curl, div, $\partial / \partial t$, and Re, we have

$$\text{Re}(\nabla \times \hat{\mathbf{H}} e^{-i\omega t}) = \text{Re}(\sigma \hat{\mathbf{E}} e^{-i\omega t}) + \text{Re}(\hat{\mathbf{D}} \frac{\partial}{\partial t} e^{-i\omega t}),$$
$$\text{Re}(\nabla \times \hat{\mathbf{E}} e^{-i\omega t}) = - \text{Re}(\hat{\mathbf{B}} \frac{\partial}{\partial t} e^{-i\omega t}),$$
$$\text{Re}(\nabla \cdot \hat{\mathbf{B}} \ e^{-i\omega t}) = 0,$$
$$\text{Re}(\nabla \cdot \hat{\mathbf{D}} \ e^{-i\omega t}) = \text{Re}(\hat{q} e^{-i\omega t}). \tag{3.83}$$

In carrying out the indicated differentiation in the system of Eqs. (3.83), we note that the only term which is a function of time is the exponential term, which differentiates as:

$$\frac{\partial}{\partial t}\left(e^{-i\omega t}\right) = -i\omega e^{-i\omega t}.$$

Carrying out the differentiation and implying the operation *Re* without writing it, we have:

$$\nabla \times \hat{\mathbf{H}}e^{-i\omega t} = \sigma\hat{\mathbf{E}}e^{-i\omega t} - i\omega\epsilon\hat{\mathbf{E}}e^{-i\omega t},$$
$$\nabla \times \hat{\mathbf{E}}e^{-i\omega t} = i\omega\mu\hat{\mathbf{H}}e^{-i\omega t},$$
$$\nabla \cdot (\mu\hat{\mathbf{H}})e^{-i\omega t} = 0,$$
$$\nabla \cdot (\epsilon\hat{\mathbf{E}})e^{-i\omega t} = \hat{q}e^{-i\omega t}. \tag{3.84}$$

The system of Eqs. (3.83) is a subset of Eq. (3.84), and so, if the complex vectors $\hat{\mathbf{H}}$, $\hat{\mathbf{E}}$, $\hat{\mathbf{B}}$, and $\hat{\mathbf{D}}$ satisfy system (3.84), then the real vectors $\mathbf{H}$, $\mathbf{B}$, $\mathbf{E}$, and $\mathbf{D}$ automatically satisfy Maxwell's equations. Dividing each of the set of Eqs. (4.203) by the factor $e^{-i\omega t}$, we finally arrive at Maxwell's equations in frequency domain:

$$\nabla \times \hat{\mathbf{H}} = \sigma\hat{\mathbf{E}} - i\omega\epsilon\hat{\mathbf{E}},$$
$$\nabla \times \hat{\mathbf{E}} = i\omega\mu\hat{\mathbf{H}},$$
$$\nabla \cdot (\mu\hat{\mathbf{H}}) = 0,$$
$$\nabla \cdot (\epsilon\hat{\mathbf{E}}) = \hat{q}. \tag{3.85}$$

From here on, we will delete the brevet sign over $\mathbf{H}$, $\mathbf{E}$, and q for simplicity in notation and refer to the complex vector field simply as a *vector field*. In so doing, we must remember that in examining fields which satisfy equations containing complex parameters, such as is the case with $i\omega\mu$ in Eq. (3.85), we have not only a real vector field but also an imaginary vector field. In order to obtain physically meaningful results, we must remember that these are complex vectors with the multiplier $e^{-i\omega t}$ and carry along the real part for the results obtained using Eqs. (3.81)–(3.82).

Finally, we must point out that the boundary conditions for complex vector fields are exactly the same as the boundary conditions for real fields.

3.3 ELECTROMAGNETIC ENERGY AND POYNTING'S THEOREM

In this section we investigate the basic theorems characterizing the distribution of the energy of the electromagnetic field. We consider an electromagnetic field generated by the sources (extraneous currents $\mathbf{j}^e$), concentrated within some domain Q and propagated in a medium with a given distribution of electromagnetic parameters ε, μ, and σ. For the sake of simplicity, domain Q is considered to be local (bounded). This means that there is a sphere, C_R, with its center at the origin of the Cartesian coordinate system and of a radius R (Fig. 3.5), big enough that domain Q belongs completely to the ball O_R bounded by the sphere $C_R : Q \subset O_R$. Let us surround the domain Q by another
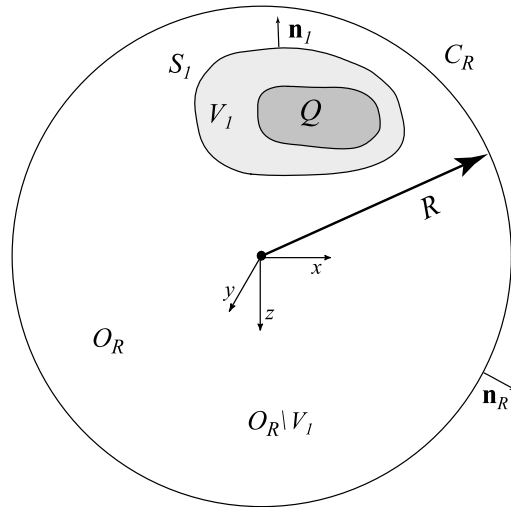
FIGURE 3.5

Derivation of Poynting's theorem, the energy inequality, and Lorentz lemma.

domain, V_1, which completely contains the domain Q (Fig. 3.5). It is evident that the change of field energy within the volume V_1 must be associated with a flow of energy through the surface S_1 of V_1 from or toward the sources. A relation between the rate of change of the energy stored in the electromagnetic field and the energy flow is given by Poynting's theorem (Stratton, 1941; Kong, 2000).

3.3.1 RADIATION CONDITIONS

Before considering Poynting's theorems, we should analyze the field behavior on the sphere C_R when its radius R tends to infinity. Based on physical intuition, one should expect that the field generated by an arbitrary source, located within the bounded domain Q of space, can be approximated accurately enough by a spherical wave at a large distance from the source and should comprise only a divergent (or so-called "outgoing") electromagnetic wave. The transverse field in this spherically divergent wave should decay like $1/r$ at large distances $r = |\mathbf{r}|$ from the origin of the coordinates, so that the product of the field $f(\mathbf{r})$ and the distance r is bounded,

$$r f(\mathbf{r}) \text{ is bounded,} \tag{3.86}$$

where f stands for any component of electromagnetic field transverse to the radius-vector $\mathbf{r}$. Another property of the divergent spherical wave is that it behaves locally like a plane wave traveling to infinity, with each field component transverse to $\mathbf{r}$ behaving as $\exp(ikr)$. The last requirement can be

mathematically expressed by the following formula (Felsen and Marcuvitz, 1994):

$$\lim_{r \to \infty} r \left[\frac{\partial}{\partial r} f(\mathbf{r}) - i \frac{\omega}{c} f(\mathbf{r}) \right] = 0. \tag{3.87}$$

These conditions, introduced by Sommerfeld (1912, 1952), are called *"Sommerfeld radiation conditions."* We will see below that radiation conditions ensure the obvious physical requirement that the energy of the electromagnetic field travels away from the source domain, i.e. the electromagnetic sources radiate energy outwards from these sources.

3.3.2 POYNTING'S THEOREM IN THE TIME DOMAIN

Poynting's theorem can be derived based on the first two Maxwell's equations (3.50) and (3.51):

$$\nabla \times \mathbf{H} = \sigma \mathbf{E} + \mathbf{j}^e + \frac{\partial \mathbf{D}}{\partial t}, \tag{3.88}$$

$$\nabla \times \mathbf{E} = -\frac{\partial \mathbf{B}}{\partial t}. \tag{3.89}$$

Note that the dot product $\mathbf{E} \cdot \mathbf{j}^e$ has the dimensions of energy per unit volume per unit time. Scalar multiplying the first Maxwell's equation (3.88) by $\mathbf{E}$, we find

$$\mathbf{E} \cdot \nabla \times \mathbf{H} = \sigma \mathbf{E} \cdot \mathbf{E} + \mathbf{E} \cdot \mathbf{j}^e + \mathbf{E} \cdot \frac{\partial \mathbf{D}}{\partial t}. \tag{3.90}$$

In a similar way we can obtain from the second Maxwell's equation (3.89) an expression containing the terms which have dimensions of energy per unit volume per unit time, by scalar multiplication of each term of this equation by $\mathbf{H}$:

$$\mathbf{H} \cdot \nabla \times \mathbf{E} = -\mathbf{H} \cdot \frac{\partial \mathbf{B}}{\partial t}. \tag{3.91}$$

Subtracting Eq. (3.90) from (3.91) and using the vector identity

$$\mathbf{H} \cdot \nabla \times \mathbf{E} - \mathbf{E} \cdot \nabla \times \mathbf{H} = \nabla \cdot (\mathbf{E} \times \mathbf{H}), \tag{3.92}$$

we obtain

$$\nabla \cdot (\mathbf{E} \times \mathbf{H}) = -\left[\mathbf{E} \cdot \mathbf{j}^e + \sigma \mathbf{E} \cdot \mathbf{E} + \mathbf{E} \cdot \frac{\partial \mathbf{D}}{\partial t} + \mathbf{H} \cdot \frac{\partial \mathbf{B}}{\partial t} \right]. \tag{3.93}$$

Expression (3.93) represents a differential form of Poynting's theorem.

The energy flow of the electromagnetic field can be calculated using the Poynting vector $\mathbf{P}$, introduced by the following formula:

$$\mathbf{P} = \mathbf{E} \times \mathbf{H}. \tag{3.94}$$

The Poynting vector $\mathbf{P}$ may be interpreted as the intensity of EM energy flow at a given point, that is the energy per second crossing a unit area whose normal is oriented in the direction of the vector

$\mathbf{E} \times \mathbf{H}$. Integrating expression (3.93) over domain V_1 and applying the Gauss formula, we obtain an integral form of Poynting's theorem:

$$F_t = \iint_{S_1} (\mathbf{E} \times \mathbf{H}) \cdot \mathbf{n}_1 ds = \iint_{S_1} \mathbf{P} \cdot \mathbf{n}_1 ds$$
$$= -\left\{ \iiint_{V_1} \mathbf{E} \cdot \mathbf{j}^e dv + \iiint_{V_1} \sigma \mathbf{E} \cdot \mathbf{E} dv + \iiint_{V_1} \left[\mathbf{E} \cdot \frac{\partial \mathbf{D}}{\partial t} + \mathbf{H} \cdot \frac{\partial \mathbf{B}}{\partial t} \right] dv \right\}, \tag{3.95}$$

where F_t is the total energy flow of the electromagnetic field through the surface S_1 of the domain V_1, and $\mathbf{n}_1$ is a unit vector of normal to the surface S_1, directed outwards from the domain V_1. The first term on the right-hand side of Eq. (3.95) represents the power introduced through the extraneous currents $\mathbf{j}^e$. The second term represents the power dissipated in Joule heat within the domain V_1. The third term represents the rate of decrease of electric and magnetic energy stored in the volume V_1.

Poynting's theorem states that the diminishing of electromagnetic energy stored within the volume V_1 (the third term on the right-hand side of Eq. (3.95)) is partly accounted for by the energy flow F_t outside domain V_1, by the energy loss accounted for by the Joule heat, and is partly compensated by the power introduced through the extraneous currents.

In linear isotropic media the last formula takes the form

$$F_t = \iint_{S_1} \mathbf{P} \cdot \mathbf{n}_1 ds$$
$$= -\left\{ \iiint_{V_1} \mathbf{E} \cdot \mathbf{j}^e dv + \iiint_{V_1} \sigma |\mathbf{E}|^2 dv + \frac{1}{2} \frac{\partial}{\partial t} \iiint_{V_1} \left[\varepsilon |\mathbf{E}|^2 + \mu |\mathbf{H}|^2 \right] dv \right\}. \tag{3.96}$$

3.3.3 ENERGY INEQUALITY IN THE TIME DOMAIN

An important property of the energy flow F_t out of domain V_1, containing sources $\mathbf{j}^e$, is that its integral over a time period, $\int_{-\infty}^t F_t dt$, is always nonnegative independently of the type of the extraneous sources. To prove this we introduce a domain $O_R \backslash V_1$ formed by the ball O_R without domain V_1 (Fig. 3.5). We can apply now Poynting's theorem (3.96) to the volume $O_R \backslash V_1$, taking into account that extraneous currents $\mathbf{j}^e = 0$ in $O_R \backslash V_1$:

$$- \iint_{S_1} \mathbf{P} \cdot \mathbf{n}_1 ds + \iint_{C_R} \mathbf{P} \cdot \mathbf{n}_R ds$$
$$= -\left\{ \iiint_{O_R \backslash V_1} \sigma |\mathbf{E}|^2 dv + \frac{1}{2} \frac{\partial}{\partial t} \iiint_{O_R \backslash V_1} \left[\varepsilon |\mathbf{E}|^2 + \mu |\mathbf{H}|^2 \right] dv \right\}, \tag{3.97}$$

where $\mathbf{n}_R$ is a unit vector of a normal to the surface C_R, directed outside domain O_R, and we have changed the sign of the integral over S_1, because now the outer normal to $O_R \backslash V_1$ is directed opposite to the vector $\mathbf{n}_1$. Setting $R \to \infty$ in (3.97) and taking into account that, according to the radiation conditions (Harrington, 1961; Kong, 2000), the surface integral over C_R tends to zero at infinity,

$$\iint_{C_R} \mathbf{P} \cdot \mathbf{n}_R ds \to 0 \text{ for } R \to \infty,$$

we arrive at the following formula:

$$-\iint_{S_1} \mathbf{P} \cdot \mathbf{n}_1 ds$$
$$= -\left\{ \iiint_{CV_1} \sigma \, |\mathbf{E}|^2 \, dv + \frac{1}{2} \frac{\partial}{\partial t} \iiint_{CV_1} \left[\varepsilon \, |\mathbf{E}|^2 + \mu \, |\mathbf{H}|^2 \right] dv \right\}, \tag{3.98}$$

where domain CV_1 is a complement of the domain V_1 to the entire space.

From the last formula we conclude that

$$F_t = \iint_{S_1} \mathbf{P} \cdot \mathbf{n}_1 ds$$
$$= \iiint_{CV_1} \sigma \, |\mathbf{E}|^2 \, dv + \frac{1}{2} \frac{\partial}{\partial t} \iiint_{CV_1} \left[\varepsilon \, |\mathbf{E}|^2 + \mu \, |\mathbf{H}|^2 \right] dv. \tag{3.99}$$

Now we integrate both sides of Eq. (3.99) over a time period:

$$\int_{-\infty}^{t} F_t \, dt = \int_{-\infty}^{t} \iint_{S_1} \mathbf{P} \cdot \mathbf{n}_1 ds \, dt$$
$$= \int_{-\infty}^{t} \iiint_{CV_1} \sigma \, |\mathbf{E}|^2 \, dv \, dt + \frac{1}{2} \iiint_{CV_1} \left[\varepsilon \, |\mathbf{E}|^2 + \mu \, |\mathbf{H}|^2 \right] dv. \tag{3.100}$$

Taking into account that all integrals on the right-hand side of expression (3.100) are nonnegative, we arrive at the important energy inequality,

$$\int_{-\infty}^{t} F_t \, dt \geq 0, \tag{3.101}$$

and

$$\int_{-\infty}^{t} F_t \, dt = 0,$$

if and only if $\mathbf{E} = 0$, and $\mathbf{H} = 0$ in CV_1, which may happen, as we will see below, only if there is no source in the entire space $\mathbf{j}^e \equiv 0$.

Formula (3.101) has a clear physical interpretation: the total energy radiated out of the domain with sources of electromagnetic field, over the time period from the initial field generation until any time t, is always nonnegative. Thus, the electromagnetic sources continuously radiate energy outside these sources!

Substituting expression (3.96) for F_t in (3.101), we finally obtain:

$$\int_{-\infty}^{t} \iiint_{V_1} \sigma \, |\mathbf{E}|^2 \, dv \, dt + \frac{1}{2} \iiint_{V_1} \left[\varepsilon \, |\mathbf{E}|^2 + \mu \, |\mathbf{H}|^2 \right] dv$$
$$\leq -\int_{-\infty}^{t} \iiint_{V_1} \mathbf{E} \cdot \mathbf{j}^e \, dv \, dt. \tag{3.102}$$

The last inequality means that the energy introduced through the extraneous currents $\mathbf{j}^e$ always exceeds the sum of the energy dissipated in Joule heat within the domain V_1 and the electric and magnetic energy stored in the volume V_1. In other words, there is always a net radiation of electromagnetic energy from any source.

If $\mathbf{j}^e \equiv 0$, then

$$\int_{-\infty}^{t} \iiint_{V_1} \sigma \, |\mathbf{E}|^2 \, dv dt + \frac{1}{2} \iiint_{V_1} \left[\varepsilon \, |\mathbf{E}|^2 + \mu \, |\mathbf{H}|^2 \right] dv = 0.$$

An obvious result follows immediately from this equation, namely that in this case the electromagnetic field is equal to zero as well:

$$\mathbf{E} \equiv 0, \ \mathbf{H} \equiv 0.$$

3.3.4 POYNTING'S THEOREM IN THE FREQUENCY DOMAIN

In the frequency domain equations (3.88) and (3.89) take the form

$$\nabla \times \mathbf{H} = \sigma \mathbf{E} + \mathbf{j}^e - i\omega\varepsilon \mathbf{E} = \widetilde{\sigma} \mathbf{E} + \mathbf{j}^e, \tag{3.103}$$

$$\nabla \times \mathbf{E} = i\omega\mu\mathbf{H}, \tag{3.104}$$

where $\widetilde{\sigma} = \sigma - i\omega\varepsilon$ is a complex electric conductivity.

The energy flow of the electromagnetic field in this case can be calculated using the complex Poynting vector $\mathbf{P}$ (Stratton, 1941), introduced by the following formula:

$$\mathbf{P} = \frac{1}{2}\mathbf{E} \times \mathbf{H}^*, \tag{3.105}$$

where asterisk "$*$", as usual, indicates a complex conjugate value.

The real part of the complex Poynting vector $\mathbf{P}$ may also be interpreted as the intensity of EM energy flow at a given point, that is the energy per second crossing a unit area whose normal is oriented in the direction of the vector $\mathbf{E} \times \mathbf{H}^*$.

For example, the total energy flow of electromagnetic field through the surface S_1 of the domain V_1, containing domain Q (Fig. 3.5), is equal to

$$F_\omega = \text{Re} \iint_{S_1} \mathbf{P} \cdot \mathbf{n}_1 ds = \frac{1}{2} \text{Re} \iint_{S_1} (\mathbf{E} \times \mathbf{H}^*) \cdot \mathbf{n}_1 ds, \tag{3.106}$$

where $\mathbf{n}_1$ is a unit vector normal to the surface S_1, directed outwards from the domain V_1.

In view of the Gauss formula, expression (3.106) can be cast in the form

$$F_\omega = \text{Re} \iiint_{V_1} \nabla \cdot \mathbf{P} dv = \frac{1}{2} \text{Re} \iiint_{V_1} \nabla \cdot (\mathbf{E} \times \mathbf{H}^*) \, dv. \tag{3.107}$$

We can obtain Poynting's theorem by taking the scalar product of the second equation for the total field (3.104) with $\mathbf{H}^*$ and the complex conjugate of the first Eq. (3.103) with $\mathbf{E}$, and subtracting one

from the other:

$$2\nabla \cdot \mathbf{P} = \nabla \cdot (\mathbf{E} \times \mathbf{H}^*) = \mathbf{H}^* \cdot \nabla \times \mathbf{E} - \mathbf{E} \cdot \nabla \times \mathbf{H}^*$$
$$= -\tilde{\sigma}^* |\mathbf{E}|^2 - \mathbf{E} \cdot \mathbf{j}^{e*} + i\omega\mu |\mathbf{H}|^2. \tag{3.108}$$

Substituting Eq. (3.108) into (3.107), we obtain

$$F_\omega = \frac{1}{2}\mathrm{Re}\iint_{S_1}(\mathbf{E} \times \mathbf{H}^*) \cdot \mathbf{n}_1 ds = -\frac{1}{2}\iiint_{V_1}\left\{\sigma |\mathbf{E}|^2 + \mathrm{Re}\left(\mathbf{E} \cdot \mathbf{j}^{e*}\right)\right\}dv. \tag{3.109}$$

This is Poynting's theorem in the frequency domain (Stratton, 1941). It says that the energy flow outside the domain V_1 is formed by the balance between the energy dissipated in heat per unit volume per second, and the energy introduced through the extraneous currents $\mathbf{j}^e$.

We can prove, also, that in the frequency domain the energy flow F_ω is always nonnegative.

Following the technique outlined above for the time domain case, we apply Poynting's theorem to the volume $O_R \backslash V_1$, taking into account that extraneous currents $\mathbf{j}^e = 0$ in $O_R \backslash V_1$:

$$-\frac{1}{2}\iiint_{O_R\backslash V_1}\left\{\sigma |\mathbf{E}|^2\right\}dv$$
$$= -\frac{1}{2}\mathrm{Re}\iint_{S_1}(\mathbf{E} \times \mathbf{H}^*) \cdot \mathbf{n}_1 ds + \frac{1}{2}\mathrm{Re}\iint_{C_R}(\mathbf{E} \times \mathbf{H}^*) \cdot \mathbf{n}_R ds. \tag{3.110}$$

Setting $R \to \infty$ in (3.110) and noting that, according to the radiation conditions, the integral over C_R goes to zero (Harrington, 1961), we find

$$\frac{1}{2}\mathrm{Re}\iint_{S_1}(\mathbf{E} \times \mathbf{H}^*) \cdot \mathbf{n}_1 ds = \frac{1}{2}\iiint_{CV_1}\sigma |\mathbf{E}|^2 dv > 0, \tag{3.111}$$

and

$$\frac{1}{2}\mathrm{Re}\iint_{S_1}(\mathbf{E} \times \mathbf{H}^*) \cdot \mathbf{n}_1 ds = \frac{1}{2}\iiint_{CV_1}\sigma |\mathbf{E}|^2 dv = 0,$$

if and only if $\sigma \equiv 0$.

In other words, we have found that the total energy flow F_ω of the electromagnetic field through the surface S_1 of the domain V_1 containing the extraneous sources of the field, is always positive, and is equal to zero if and only if the conductivity of the medium is zero (the case of a lossless medium):

$$F_\omega \geq 0, \text{ and } F_\omega = 0, \text{ if and only if } \sigma \equiv 0. \tag{3.112}$$

Substituting Eq. (3.109) into (3.111), we find

$$\iiint_{V_1}\left\{\sigma |\mathbf{E}|^2 + \mathrm{Re}\left(\mathbf{E}^* \cdot \mathbf{j}^e\right)\right\}dv \leq 0,$$

or

$$\iiint_{V_1}\sigma |\mathbf{E}|^2 dv \leq -\iiint_{V_1}\mathrm{Re}\left(\mathbf{E}^* \cdot \mathbf{j}^e\right)dv, \tag{3.113}$$

for any lossy medium ($\sigma \neq 0$). Energy inequality (3.112) means that we have steadily positive energy flow out of a domain containing a source within a lossy medium.

3.4 ELECTROMAGNETIC GREEN'S TENSORS
3.4.1 GREEN'S TENSORS IN THE FREQUENCY DOMAIN

The electromagnetic Green's tensors $\widehat{\mathbf{G}}_E$, $\widehat{\mathbf{G}}_H$ are introduced as the fields of an elementary electric source (Zhdanov, 1988; Felsen and Marcuvitz, 1994). They satisfy Maxwell's equations

$$\nabla \times \widehat{\mathbf{G}}_H = \widetilde{\sigma} \widehat{\mathbf{G}}_E + \widehat{\mathbf{I}} \delta \left(\mathbf{r} - \mathbf{r}' \right),$$
$$\nabla \times \widehat{\mathbf{G}}_E = i \omega \mu \widehat{\mathbf{G}}_H, \tag{3.114}$$

where $\widehat{\mathbf{G}}_H \left(\mathbf{r} \mid \mathbf{r}' \right)$ and $\widehat{\mathbf{G}}_E \left(\mathbf{r} \mid \mathbf{r}' \right)$ are the magnetic and electric Green's tensors, $\widehat{\mathbf{I}}$ is the identity tensor, and $\delta(\mathbf{r})$ is three-dimensional Dirac delta-function $\delta(\mathbf{r}) = \delta(x)\delta(y)\delta(z)$, satisfying the condition

$$\iiint_V f(\mathbf{r})\delta(\mathbf{r}' - \mathbf{r})dv = \begin{cases} f(\mathbf{r}'), & \mathbf{r}' \in V, \\ 0, & \mathbf{r}' \notin \overline{V}, \end{cases} \tag{3.115}$$

where $\overline{V} = V + S$ is domain V with its boundary S.

Eqs. (3.114) suggest that, in a homogeneous domain, $\widehat{\mathbf{G}}_E$ and $\widehat{\mathbf{G}}_H$ satisfy the Helmholtz equations

$$\nabla^2 \widehat{\mathbf{G}}_E + \widetilde{k}^2 \widehat{\mathbf{G}}_E = -i \omega \mu \widehat{\mathbf{I}} \delta \left(\mathbf{r} - \mathbf{r}' \right), \tag{3.116}$$
$$\nabla^2 \widehat{\mathbf{G}}_H + \widetilde{k}^2 \widehat{\mathbf{G}}_H = -\nabla \times \widehat{\mathbf{I}} \delta \left(\mathbf{r} - \mathbf{r}' \right). \tag{3.117}$$

The importance of Green's functions in electromagnetic theory is dictated by the following considerations. According to the basic property of the δ-function (3.115), any source, $\mathbf{j}^e(\mathbf{r}')$, can be represented as a sum of elementary current sources:

$$\mathbf{j}^e(\mathbf{r}') = \iiint_{V_\infty} \mathbf{j}^e(\mathbf{r}) \cdot \widehat{\mathbf{I}} \delta(\mathbf{r}' - \mathbf{r})dv, \tag{3.118}$$

where the volume integral is calculated over the entire infinite space V_∞ and $\widehat{\mathbf{I}}$ is the identity tensor. Eq. (3.118) indicates that the density of the distribution of elementary current is described by the tensor expression $\widehat{\mathbf{I}}\delta(\mathbf{r}' - \mathbf{r})$.

Taking into account the linear character of Maxwell's equations and using the superposition principle, we find that the sum of electromagnetic fields produced by elementary currents must be equal to the field generated by the original current source $\mathbf{j}^e(\mathbf{r}')$. In other words, the electromagnetic field $\{\mathbf{E}, \mathbf{H}\}$ generated by the source described as a linear combination of some other elementary sources is equal to the linear combination (with the same coefficients) of the fields $\left\{ \widehat{\mathbf{G}}_E, \widehat{\mathbf{G}}_H \right\}$ generated by the individual elementary current sources. Therefore, we can conclude that with the knowledge of electromagnetic Green's tensors $\widehat{\mathbf{G}}_E$ and $\widehat{\mathbf{G}}_H$ one can also find the solution of Maxwell's equations for an arbitrary allocation of extraneous electric currents $\mathbf{j}^e(\mathbf{r})$, as the convolution of the corresponding Green's functions with the function $\mathbf{j}^e(\mathbf{r})$, i.e.,

$$\mathbf{E}\left(\mathbf{r}_j\right) = \iiint_{V_\infty} \widehat{\mathbf{G}}_E\left(\mathbf{r}_j \mid \mathbf{r}\right) \cdot \mathbf{j}^e\left(\mathbf{r}\right) dv = \mathbf{G}_E\left(\mathbf{j}^e\right),$$

$$\mathbf{H}\left(\mathbf{r}_j\right) = \iiint_{V_\infty} \widehat{\mathbf{G}}_H\left(\mathbf{r}_j \mid \mathbf{r}\right) \cdot \mathbf{j}^e\left(\mathbf{r}\right) dv = \mathbf{G}_H\left(\mathbf{j}^e\right), \tag{3.119}$$

where $\mathbf{G}_E$ and $\mathbf{G}_H$ are the electric and magnetic Green's operators, and $\mathbf{r}_j$ is the position of the observation point.

3.4.2 GREEN'S TENSORS IN THE TIME DOMAIN

The time domain electromagnetic Green's tensors $\widehat{\mathbf{G}}_E$, $\widehat{\mathbf{G}}_H$ are introduced, as in frequency domain, as the fields of an elementary electric source (Felsen and Marcuvitz, 1994). They follow the Maxwell's equations

$$\nabla \times \widehat{\mathbf{G}}_H = \sigma\widehat{\mathbf{G}}_E + \varepsilon\partial\widehat{\mathbf{G}}_E/\partial t + \widehat{\mathbf{I}}\delta\left(\mathbf{r} - \mathbf{r}'\right)\delta\left(t - t'\right),$$

$$\nabla \times \widehat{\mathbf{G}}_E = -\mu\partial\widehat{\mathbf{G}}_H/\partial t, \tag{3.120}$$

where $\widehat{\mathbf{G}}_H = \widehat{\mathbf{G}}_H\left(\mathbf{r}, t \mid \mathbf{r}', t'\right)$ and $\widehat{\mathbf{G}}_E = \widehat{\mathbf{G}}_E\left(\mathbf{r}, t \mid \mathbf{r}', t'\right)$ are the magnetic and electric Green's tensors in the time domain.[1]

They are causal:

$$\widehat{\mathbf{G}}_E\left(\mathbf{r}, t \mid \mathbf{r}', t'\right) \equiv 0, \ \widehat{\mathbf{G}}_H\left(\mathbf{r}, t \mid \mathbf{r}', t'\right) \equiv 0, \ t \leq t'.$$

Eq. (3.120) suggests that in a homogeneous domain $\widehat{\mathbf{G}}_E$ also satisfies the equation

$$\nabla \times \nabla \times \widehat{\mathbf{G}}_E + \mu\varepsilon\frac{\partial^2\widehat{\mathbf{G}}_E}{\partial t^2} + \mu\sigma\frac{\partial\widehat{\mathbf{G}}_E}{\partial t} = -\mu\widehat{\mathbf{I}}\delta\left(\mathbf{r} - \mathbf{r}'\right)\delta'\left(t - t'\right), \tag{3.121}$$

where the prime superscript over the delta function denotes its time derivative.

The EM Green's tensors exhibit symmetry and can be shown, using the Lorentz lemma, to satisfy the following *reciprocity relations* (Felsen and Marcuvitz, 1994):

$$\widehat{\mathbf{G}}_E\left(\mathbf{r}, t \mid \mathbf{r}', t'\right) = \widetilde{\widehat{\mathbf{G}}}_E\left(\mathbf{r}', -t' \mid \mathbf{r}, -t\right),$$

$$\widehat{\mathbf{G}}_H\left(\mathbf{r}, t \mid \mathbf{r}', t'\right) = \widetilde{\widehat{\mathbf{G}}}_H\left(\mathbf{r}', -t' \mid \mathbf{r}, -t\right), \tag{3.122}$$

where a tilde denotes the operation of transposition. I will present a proof of these relationships in the next section.

The last conditions show that by replacing source and receiver (i.e. the points $\mathbf{r}'$ and $\mathbf{r}$) and by going simultaneously to the reverse time $-t$, (therefore, by retaining the causality, because the condition $t < t'$ in ordinary time implies the condition $-t > -t'$ in reverse time), we obtain the equivalent electromagnetic field, described by the Green's tensors $\widehat{\mathbf{G}}_E\left(\mathbf{r}', t' \mid \mathbf{r}, t\right)$ and $\widehat{\mathbf{G}}_H\left(\mathbf{r}', t' \mid \mathbf{r}, t\right)$.

---

[1] Note that we use the same symbols for Green's tensors in the time and frequency domains to simplify the notations. One can easily recognize the corresponding tensor by checking for arguments t or ω in the corresponding equations.

Following Morse and Feshbach (1953) and Felsen and Marcuvitz (1994), we can also introduce the adjoint Green's tensors:

$$\widehat{\mathbf{G}}_E^+\left(\mathbf{r},t\mid\mathbf{r}',t'\right)=\widetilde{\widehat{\mathbf{G}}}_E\left(\mathbf{r}',t'\mid\mathbf{r},t\right),$$
$$\widehat{\mathbf{G}}_H^+\left(\mathbf{r},t\mid\mathbf{r}',t'\right)=\widetilde{\widehat{\mathbf{G}}}_H\left(\mathbf{r}',t'\mid\mathbf{r},t\right).$$
(3.123)

They satisfy the equations, obtained from (3.120) by reversing the sign of all space-time coordinates:

$$\nabla\times\widehat{\mathbf{G}}_H^+=-\sigma\widehat{\mathbf{G}}_E^+ +\partial\widehat{\mathbf{G}}_E^+/\partial t -\widehat{\mathbf{I}}\delta\left(\mathbf{r}-\mathbf{r}'\right)\delta\left(t-t'\right),$$
$$\nabla\times\widehat{\mathbf{G}}_E^+ =-\mu\partial\widehat{\mathbf{G}}_H^+/\partial t,$$
(3.124)

and Eq. (3.121) takes the form

$$\nabla\times\nabla\times\widehat{\mathbf{G}}_E^+ +\mu\varepsilon\frac{\partial^2\widehat{\mathbf{G}}_E^+}{\partial t^2}-\mu\sigma\frac{\partial\widehat{\mathbf{G}}_E^+}{\partial t}=\mu\,\widehat{\mathbf{I}}\delta\left(\mathbf{r}-\mathbf{r}'\right)\delta'\left(t-t'\right).$$
(3.125)

The adjoint Green's tensors are anticausal:

$$\widehat{\mathbf{G}}_E^+\left(\mathbf{r},t\mid\mathbf{r}',t'\right)\equiv 0,\ \widehat{\mathbf{G}}_H^+\left(\mathbf{r},t\mid\mathbf{r}',t'\right)\equiv 0,\ t\geq t'.$$

Electromagnetic Green's tensors represent an important tool in the solution of the forward and inverse electromagnetic problems and in migration imaging.

3.5 RECIPROCITY RELATIONS

Green's electromagnetic tensors for an isotropic medium satisfy the *reciprocity relations* which reflect the symmetry of the electromagnetic field in an inhomogeneous medium. The traditional way of deriving these relations is based on the *Lorentz lemma* (Zhdanov, 1988; Felsen and Marcuvitz, 1994), which is formulated for the case of electromagnetic fields excited by electric ($\mathbf{j}^e$) and magnetic ($\mathbf{j}^m$) sources in an inhomogeneous isotropic medium.

3.5.1 LORENTZ LEMMA

We assume that two sets of sources, $\left\{\mathbf{j}_a^e,\mathbf{j}_a^m\right\}$ and $\left\{\mathbf{j}_b^e,\mathbf{j}_b^m\right\}$, are located within a domain Q and that both generate electromagnetic fields of the same frequency ω. We denote by $\{\mathbf{E}^a,\mathbf{H}^a\}$ and $\left\{\mathbf{E}^b,\mathbf{H}^b\right\}$ the fields produced by a-type and b-type sources, respectively. These fields satisfy the corresponding Maxwell's equations:

$$\nabla \times \mathbf{H}^a = \tilde{\sigma}\mathbf{E}^a + \mathbf{j}_a^e, \tag{3.126}$$

$$\nabla \times \mathbf{E}^a = i\omega\mu\mathbf{H}^a - \mathbf{j}_a^m, \tag{3.127}$$

$$\nabla \times \mathbf{H}^b = \tilde{\sigma}\mathbf{E}^b + \mathbf{j}_b^e, \tag{3.128}$$

$$\nabla \times \mathbf{E}^b = i\omega\mu\mathbf{H}^b - \mathbf{j}_b^m. \tag{3.129}$$

Calculating the dot products of Eq. (3.126) with $\mathbf{E}^b$, Eq. (3.129) with $\mathbf{H}^a$, Eq. (3.127) with $\mathbf{H}^b$, and Eq. (3.128) with $\mathbf{E}^a$, we obtain the expression

$$\nabla \cdot \left\{ \left[\mathbf{E}^b \times \mathbf{H}^a \right] - \left[\mathbf{E}^a \times \mathbf{H}^b \right] \right\} = \mathbf{E}^a \cdot \mathbf{j}_b^e + \mathbf{H}^b \cdot \mathbf{j}_a^m - \mathbf{E}^b \cdot \mathbf{j}_a^e - \mathbf{H}^a \cdot \mathbf{j}_b^m. \tag{3.130}$$

Integrating (3.130) over a ball O_R, containing domain Q (see Fig. 3.5) and applying the Gauss theorem, we find

$$\iint_{C_R} \left\{ \left[\mathbf{E}^b \times \mathbf{H}^a \right] - \left[\mathbf{E}^a \times \mathbf{H}^b \right] \right\} \cdot \mathbf{n}_R ds$$
$$= \iiint_{O_R} \left[\mathbf{E}^a \cdot \mathbf{j}_b^e + \mathbf{H}^b \cdot \mathbf{j}_a^m - \mathbf{E}^b \cdot \mathbf{j}_a^e - \mathbf{H}^a \cdot \mathbf{j}_b^m \right] dv.$$

Now let the radius R of the ball O_R tend to infinity. The surface integral over a sphere C_R vanishes due to radiation conditions (3.86) and (3.87), and we arrive at a mathematical formulation of the Lorentz lemma:

$$\iiint_{V_\infty} \left[\mathbf{E}^a \cdot \mathbf{j}_b^e + \mathbf{H}^b \cdot \mathbf{j}_a^m - \mathbf{E}^b \cdot \mathbf{j}_a^e - \mathbf{H}^a \cdot \mathbf{j}_b^m \right] dv = 0, \tag{3.131}$$

where V_∞, as usual, denotes the entire infinite space.

We can derive another formulations of Lorentz lemma by considering the complex conjugate electromagnetic field $\{\mathbf{E}^{b*}, \mathbf{H}^{b*}\}$ produced by b-type source. In this case expression (3.130) for the divergence of the difference of the corresponding cross products of the electric and magnetic fields takes the form:

$$\nabla \cdot \left\{ \left[\mathbf{E}^{b*} \times \mathbf{H}^a \right] - \left[\mathbf{E}^a \times \mathbf{H}^{b*} \right] \right\} = \mathbf{E}^a \cdot \mathbf{j}_b^{e*} + \mathbf{H}^{b*} \cdot \mathbf{j}_a^m - \mathbf{E}^{b*} \cdot \mathbf{j}_a^e - \mathbf{H}^a \cdot \mathbf{j}_b^{m*}$$
$$+ \left(\tilde{\sigma}^* - \tilde{\sigma} \right) \mathbf{E}^{b*} \cdot \mathbf{E}^a - 2i\omega\mu\mathbf{H}^a \cdot \mathbf{H}^{b*}. \tag{3.132}$$

Integrating Eq. (3.132) over a ball O_R, containing domain Q (see Fig. 3.5) and applying the Gauss theorem, we find for $R \to \infty$:

$$\iiint_{V_\infty} \left[\mathbf{E}^a \cdot \mathbf{j}_b^{e*} + \mathbf{H}^{b*} \cdot \mathbf{j}_a^m - \mathbf{E}^{b*} \cdot \mathbf{j}_a^e - \mathbf{H}^a \cdot \mathbf{j}_b^{m*} \right] dv$$
$$= -\iiint_{V_\infty} \left[\left(\tilde{\sigma}^* - \tilde{\sigma} \right) \mathbf{E}^{b*} \cdot \mathbf{E}^a - 2i\omega\mu\mathbf{H}^a \cdot \mathbf{H}^b \right] dv. \tag{3.133}$$

In a similar way, based on the Maxwell's equations (3.126) through (3.129), we can derive an expression for the divergence of the sum of the corresponding cross products of the electric and magnetic

fields:

$$\nabla \cdot \left\{ \left[\mathbf{E}^{b*} \times \mathbf{H}^a \right] + \left[\mathbf{E}^a \times \mathbf{H}^{b*} \right] \right\}$$
$$= -\mathbf{E}^a \cdot \mathbf{j}_b^{e*} - \mathbf{H}^{b*} \cdot \mathbf{j}_a^m - \mathbf{E}^{b*} \cdot \mathbf{j}_a^e - \mathbf{H}^a \cdot \mathbf{j}_b^{m*} - \left(\widetilde{\sigma}^* + \widetilde{\sigma} \right) \mathbf{E}^{b*} \cdot \mathbf{E}^a. \tag{3.134}$$

Integrating Eq. (3.134) over a ball O_R, containing domain Q and applying the Gauss theorem, we obtain for $R \to \infty$:

$$\iiint_{V_\infty} \left[\mathbf{E}^a \cdot \mathbf{j}_b^{e*} + \mathbf{H}^{b*} \cdot \mathbf{j}_a^m + \mathbf{E}^{b*} \cdot \mathbf{j}_a^e + \mathbf{H}^a \cdot \mathbf{j}_b^{m*} \right] dv$$
$$= -\iiint_{V_\infty} \left[\left(\widetilde{\sigma}^* + \widetilde{\sigma} \right) \mathbf{E}^{b*} \cdot \mathbf{E}^a \right] dv. \tag{3.135}$$

Eqs. (3.133) and (3.135) represent the modified formulations of Lorentz lemma. The Lorentz lemma and its different formulations provide a basis for a reciprocity theorem, which relates two independent sets of electromagnetic fields and sources in one and the same medium.

3.5.2 RECIPROCITY RELATIONS FOR THE GREEN'S TENSORS AND ELECTROMAGNETIC FIELDS

We now can use the Lorentz lemma to derive the reciprocity relations for the Green's electromagnetic tensor. Let us assume that the electric dipoles with moments $\mathbf{a}$ and $\mathbf{b}$ are located at points with the radius-vectors $\mathbf{r}'$ and $\mathbf{r}''$,

$$\mathbf{j}_a^e = \mathbf{a}\delta \left(\mathbf{r} - \mathbf{r}' \right), \ \ \mathbf{j}_b^e = \mathbf{b}\delta \left(\mathbf{r} - \mathbf{r}'' \right), \tag{3.136}$$

and that there are no magnetic-type sources,

$$\mathbf{j}_a^m = 0, \ \ \mathbf{j}_b^m = 0. \tag{3.137}$$

According to formulae (3.119), we can write

$$\mathbf{E}^a \left(\mathbf{r} \right) = \widehat{\mathbf{G}}_E \left(\mathbf{r} \mid \mathbf{r}' \right) \cdot \mathbf{a}, \ \ \mathbf{E}^b \left(\mathbf{r} \right) = \widehat{\mathbf{G}}_E \left(\mathbf{r} \mid \mathbf{r}'' \right) \cdot \mathbf{b},$$
$$\mathbf{H}^a \left(\mathbf{r} \right) = \widehat{\mathbf{G}}_H \left(\mathbf{r} \mid \mathbf{r}' \right) \cdot \mathbf{a}, \ \text{and} \ \mathbf{H}^b \left(\mathbf{r} \right) = \widehat{\mathbf{G}}_H \left(\mathbf{r} \mid \mathbf{r}'' \right) \cdot \mathbf{b}. \tag{3.138}$$

Substituting expressions (3.136) through (3.138) into the Lorentz lemma (3.131), we find

$$\iiint_{V_\infty} \left\{ \left[\widehat{\mathbf{G}}_E \left(\mathbf{r} \mid \mathbf{r}' \right) \cdot \mathbf{a} \right] \cdot \mathbf{b}\delta \left(\mathbf{r} - \mathbf{r}'' \right) - \left[\widehat{\mathbf{G}}_E \left(\mathbf{r} \mid \mathbf{r}'' \right) \cdot \mathbf{b} \right] \cdot \mathbf{a}\delta \left(\mathbf{r} - \mathbf{r}' \right) \right\} dv = 0.$$

Taking into account the basic property of the delta-function, we obtain from this formula

$$\mathbf{b} \cdot \left[\widehat{\mathbf{G}}_E \left(\mathbf{r}'' \mid \mathbf{r}' \right) \cdot \mathbf{a} \right] = \mathbf{a} \cdot \left[\widehat{\mathbf{G}}_E \left(\mathbf{r}' \mid \mathbf{r}'' \right) \cdot \mathbf{b} \right].$$

The last formula directly implies that

$$\widehat{\mathbf{G}}_E \left(\mathbf{r}'' \mid \mathbf{r}' \right) = \widetilde{\widehat{\mathbf{G}}}_E \left(\mathbf{r}' \mid \mathbf{r}'' \right), \tag{3.139}$$

where the large tilde denotes the operation of transposition.

Reciprocity relation (3.139) shows that the electric field component excited at $\mathbf{r}''$ in the direction of $\mathbf{b}$ by an electric current element $\mathbf{a}$ at $\mathbf{r}'$ is identical with the electric field component excited at $\mathbf{r}'$ in the direction of $\mathbf{a}$ by an electric current element $\mathbf{b}$ at $\mathbf{r}''$.

In conclusion, we consider the reciprocity relations between the magnetic and electric fields generated by the electric and magnetic currents, respectively. We now assume that the electric dipole with moment $\mathbf{a}$ is located at a point with the radius-vectors $\mathbf{r}'$, and the magnetic dipole with moment $\mathbf{b}$ is located at a point with the radius-vector $\mathbf{r}''$ respectively,

$$\mathbf{j}_a^e = \mathbf{a}\delta\left(\mathbf{r} - \mathbf{r}'\right), \ \ \mathbf{j}_b^m = \mathbf{b}\delta\left(\mathbf{r} - \mathbf{r}''\right), \tag{3.140}$$

while the sources $\mathbf{j}_a^m$ and $\mathbf{j}_b^e$ are equal to zero:

$$\mathbf{j}_a^m = 0, \ \ \mathbf{j}_b^e = 0. \tag{3.141}$$

Substituting expressions (3.140) and (3.141) into the Lorentz lemma (3.131), we find

$$\iiint_{V_\infty} \left[-\mathbf{E}^b \cdot \mathbf{j}_a^e - \mathbf{H}^a \cdot \mathbf{j}_b^m\right] dv$$
$$= -\iiint_{V_\infty} \left[\mathbf{E}^b\left(\mathbf{r}\right) \cdot \mathbf{a}\delta\left(\mathbf{r} - \mathbf{r}'\right) + \mathbf{H}^a\left(\mathbf{r}\right) \cdot \mathbf{b}\delta\left(\mathbf{r} - \mathbf{r}''\right)\right] dv = 0.$$

Taking into account the basic property of the delta-function, we obtain from this formula

$$\mathbf{H}^a\left(\mathbf{r}''\right) \cdot \mathbf{b} = -\mathbf{E}^b\left(\mathbf{r}'\right) \cdot \mathbf{a}. \tag{3.142}$$

Reciprocity relation (3.142) shows that the magnetic field component excited at $\mathbf{r}''$ in the direction of $\mathbf{b}$ by an electric current element $\mathbf{a}$ at $\mathbf{r}'$ is equal to the electric field component (multiplied by the minus sign) excited at $\mathbf{r}'$ in the direction of $\mathbf{a}$ by a magnetic current element $\mathbf{b}$ at $\mathbf{r}''$.

3.5.3 ELECTROMAGNETIC GREEN'S TENSOR REPRESENTATION THEOREMS

The electromagnetic Green's tensor representation theorems provide the fundamental integral equations for Green's tensors in the arbitrary inhomogeneous media. They can be used for modeling, analytical continuation, and migration of electromagnetic fields. A general form of the Green's function representation theorems for arbitrary wavefields can be found in Wapenaar (2007). We present here a derivation of these theorems based on Lorentz lemma.

We consider arbitrary domain V_1, bounded by a closed surface S_1, containing domain Q (see Fig. 3.5). We assume also that the sources of electromagnetic field, $\{\mathbf{j}_a^e, \mathbf{j}_a^m\}$ and $\{\mathbf{j}_b^e, \mathbf{j}_b^m\}$, are concentrated within domain Q only. Integrating Eq. (3.132) over domain V_1, containing domain Q, and applying the Gauss theorem, we find:

$$\iint_{S_1} \left\{\left[\mathbf{E}^{b*} \times \mathbf{H}^a\right] - \left[\mathbf{E}^a \times \mathbf{H}^{b*}\right]\right\} \cdot d\mathbf{s}$$
$$= \iiint_Q \left[\mathbf{E}^a \cdot \mathbf{j}_b^{e*} + \mathbf{H}^{b*} \cdot \mathbf{j}_a^m - \mathbf{E}^{b*} \cdot \mathbf{j}_a^e - \mathbf{H}^a \cdot \mathbf{j}_b^{m*}\right] dv$$

$$+ \iiint_{V_1} \left[(\tilde{\sigma}^* - \tilde{\sigma}) \mathbf{E}^{b*} \cdot \mathbf{E}^a - 2i\omega\mu \mathbf{H}^a \cdot \mathbf{H}^{b*} \right] dv. \tag{3.143}$$

In a similar way, integrating Eq. (3.134) over a domain V_1, containing domain Q, we can write:

$$\iint_{S_1} \left\{ \left[\mathbf{E}^{b*} \times \mathbf{H}^a \right] + \left[\mathbf{E}^a \times \mathbf{H}^{b*} \right] \right\} \cdot d\mathbf{s}$$

$$= - \iiint_Q \left[\mathbf{E}^a \cdot \mathbf{j}_b^{e*} + \mathbf{H}^{b*} \cdot \mathbf{j}_a^m + \mathbf{E}^{b*} \cdot \mathbf{j}_a^e + \mathbf{H}^a \cdot \mathbf{j}_b^{m*} \right] dv$$

$$- \iiint_{V_1} \left[(\tilde{\sigma}^* + \tilde{\sigma}) \mathbf{E}^{b*} \cdot \mathbf{E}^a \right] dv. \tag{3.144}$$

We assume again that electromagnetic fields $\{\mathbf{E}^a, \mathbf{H}^a\}$ and $\left\{\mathbf{E}^b, \mathbf{H}^b\right\}$ are generated by the electric dipoles with moments $\mathbf{a}$ and $\mathbf{b}$ located at points with the radius-vectors $\mathbf{r}'$ and $\mathbf{r}''$, and that there are no magnetic-type sources (see Eqs. (3.136) and (3.137)). We also assume that $\mathbf{a}$ and $\mathbf{b}$ are real vectors ($\mathrm{Im}\,\mathbf{a} = 0$ and $\mathrm{Im}\,\mathbf{b} = 0$).

Substituting expressions (3.136) through (3.138) into the volume integral over domain Q in Eq. (3.143) and taking into account the basic property of the delta-function, we find:

$$\iiint_Q \left[\mathbf{E}^a \cdot \mathbf{j}_b^{e*} + \mathbf{H}^{b*} \cdot \mathbf{j}_a^m - \mathbf{E}^{b*} \cdot \mathbf{j}_a^e - \mathbf{H}^a \cdot \mathbf{j}_b^{m*} \right] dv$$

$$= \iiint_Q \left[\mathbf{E}^a \cdot \mathbf{j}_b^{e*} - \mathbf{E}^{b*} \cdot \mathbf{j}_a^e \right] dv$$

$$= \mathbf{b} \cdot \left[\widehat{\mathbf{G}}_E \left(\mathbf{r}'' \mid \mathbf{r}' \right) \cdot \mathbf{a} \right] - \mathbf{a} \cdot \left[\widehat{\mathbf{G}}_E^* \left(\mathbf{r}' \mid \mathbf{r}'' \right) \cdot \mathbf{b} \right]. \tag{3.145}$$

According to the reciprocity theorem for the Green's tensors, we have

$$\mathbf{b} \cdot \left[\widehat{\mathbf{G}}_E \left(\mathbf{r}'' \mid \mathbf{r}' \right) \cdot \mathbf{a} \right] = \mathbf{a} \cdot \left[\widehat{\mathbf{G}}_E \left(\mathbf{r}' \mid \mathbf{r}'' \right) \cdot \mathbf{b} \right]. \tag{3.146}$$

Therefore, Eq. (3.145) can be written as:

$$\iiint_Q \left[\mathbf{E}^a \cdot \mathbf{j}_b^{e*} - \mathbf{E}^{b*} \cdot \mathbf{j}_a^e \right] dv$$

$$= \mathbf{b} \cdot \left[\widehat{\mathbf{G}}_E \left(\mathbf{r}'' \mid \mathbf{r}' \right) \cdot \mathbf{a} \right] - \mathbf{b} \cdot \left[\widehat{\mathbf{G}}_E^* \left(\mathbf{r}'' \mid \mathbf{r}' \right) \cdot \mathbf{a} \right]$$

$$= 2i\mathbf{b} \cdot \left[\mathrm{Im}\,\widehat{\mathbf{G}}_E \left(\mathbf{r}'' \mid \mathbf{r}' \right) \cdot \mathbf{a} \right]. \tag{3.147}$$

We can derive a similar expression for the volume integral over domain Q in Eq. (3.144):

$$\iiint_Q \left[\mathbf{E}^a \cdot \mathbf{j}_b^{e*} + \mathbf{H}^{b*} \cdot \mathbf{j}_a^m + \mathbf{E}^{b*} \cdot \mathbf{j}_a^e + \mathbf{H}^a \cdot \mathbf{j}_b^{m*} \right] dv$$

$$= \iiint_Q \left[\mathbf{E}^a \cdot \mathbf{j}_b^{e*} + \mathbf{E}^{b*} \cdot \mathbf{j}_a^e \right] dv$$

$$= \mathbf{b} \cdot \left[\widehat{\mathbf{G}}_E \left(\mathbf{r}'' \mid \mathbf{r}' \right) \cdot \mathbf{a} \right] + \mathbf{a} \cdot \left[\widehat{\mathbf{G}}_E^* \left(\mathbf{r}' \mid \mathbf{r}'' \right) \cdot \mathbf{b} \right]$$

$$= 2\mathbf{b} \cdot \left[\mathrm{Re}\,\widehat{\mathbf{G}}_E \left(\mathbf{r}'' \mid \mathbf{r}' \right) \cdot \mathbf{a} \right]. \tag{3.148}$$

Substituting formulas (3.147) and (3.148) into Eqs. (3.143) and (3.144), respectively, we obtain the following integral representations for the imaginary and real parts of the Green's tensor $\widehat{\mathbf{G}}_E$:

$$\mathbf{b} \cdot \left[\operatorname{Im} \widehat{\mathbf{G}}_E \left(\mathbf{r}'' \mid \mathbf{r}' \right) \cdot \mathbf{a} \right]$$
$$= -\frac{1}{2} i \iint_{S_1} \left\{ \left[\mathbf{E}^{b*} \times \mathbf{H}^a \right] - \left[\mathbf{E}^a \times \mathbf{H}^{b*} \right] \right\} \cdot d\mathbf{s}$$
$$+ \frac{1}{2} i \iiint_{V_1} \left[\left(\widetilde{\sigma}^* - \widetilde{\sigma} \right) \mathbf{E}^{b*} \cdot \mathbf{E}^a - 2i\omega\mu \mathbf{H}^a \cdot \mathbf{H}^{b*} \right] dv, \qquad (3.149)$$

$$\mathbf{b} \cdot \left[\operatorname{Re} \widehat{\mathbf{G}}_E \left(\mathbf{r}'' \mid \mathbf{r}' \right) \cdot \mathbf{a} \right]$$
$$= -\frac{1}{2} \iint_{S_1} \left\{ \left[\mathbf{E}^{b*} \times \mathbf{H}^a \right] + \left[\mathbf{E}^a \times \mathbf{H}^{b*} \right] \right\} \cdot d\mathbf{s}$$
$$- \frac{1}{2} \iiint_{V_1} \left[\left(\widetilde{\sigma}^* + \widetilde{\sigma} \right) \mathbf{E}^{b*} \cdot \mathbf{E}^a \right] dv. \qquad (3.150)$$

In order to obtain the integral representation for the Green's tensor $\widehat{\mathbf{G}}_E$, we multiply Eq. (3.149) by imaginary unit, i, and sum the left-hand and the right-hand parts of this equation with the corresponding parts of Eq. (3.150):

$$\mathbf{b} \cdot \left[\widehat{\mathbf{G}}_E \left(\mathbf{r}'' \mid \mathbf{r}' \right) \cdot \mathbf{a} \right]$$
$$= -\iint_{S_1} \left[\mathbf{E}^a \times \mathbf{H}^{b*} \right] \cdot d\mathbf{s} - \iiint_{V_1} \left[\widetilde{\sigma}^* \mathbf{E}^{b*} \cdot \mathbf{E}^a - i\omega\mu \mathbf{H}^a \cdot \mathbf{H}^{b*} \right] dv. \qquad (3.151)$$

Note that the last formula can be obtained directly from the Poynting's theorem.

Eqs. (3.149), (3.150), and (3.151) provide mathematical formulations of electromagnetic Green's tensor representation theorems. Note that, according to Eqs. (3.138), the fields $\{\mathbf{E}^a, \mathbf{H}^a\}$ and $\{\mathbf{E}^b, \mathbf{H}^b\}$ represent the Green's tensors themselves. Therefore, formulas (3.149), (3.150), and (3.151) describe the integral relationships between the different Green's tensors.

REFERENCES AND RECOMMENDED READING TO CHAPTER 3

Alpin, L. M., 1966, Theory of the field: Nedra, Moscow, 384 pp.

Deschamps, G. A., 1981, Electromagnetics and differential forms: Proceedings IEEE, **69** (6), 676-696.

Felsen, L., and N. Marcuvitz, 1994, Radiation and scattering of waves, IEEE Press, New York, 888 pp.

Harrington, R. F., 1961, Time harmonic electromagnetic fields: McGraw-Hill Book Co., New York, 480 pp.

Kaufman, A. A., 1992, Geophysical field theory and method, Part A, Gravitational, electric and magnetic fields: Academic Press, New York, 581 pp.

Kaufman, A. A., and G. V. Keller, 1985, Inductive mining prospecting, Part I: Theory: Elsevier, Amsterdam, 620 pp.

Kong, J. A., 1975, Theory of electromagnetic waves: John Wiley & Sons, New York, 348 pp.

Kong, J. A., 2000, Electromagnetic wave theory: EMW Publishing, Cambridge, Massachusetts, USA, 1007 pp.

Lindell, I. V., 2004, Differential forms in electromagnetics: IEEE Press, John Wiley & Sons, 253 pp.

Maxwell, J. C., 1954, A treatise on electricity and magnetism: Dover Publ., New York, (unabridged and unaltered republication of the third edition of 1891), 506 pp.

Misner, C. W., K. S., Thorne, and J. A., Wheeler, 1973, Gravitation: Freeman, San Francisco, 1279 pp.

Morse, P. M., and H. Feshbach, 1953, Methods of theoretical physics, McGraw Hill Book Co., New York, 1978 pp.

Novozhilov, U. V., and U. A. Yappa, 1981, Electrodynamics: Mir Publishers, Moscow, 352 pp.

Schey, H. M., 1973, Div, grad, curl, and all that: An informal text on vector calculus: W. W. Norton & Co., New York, 163 pp.

Sommerfeld, A., 1912, Die Greensche Function der Schwingungsgleichung. Jahresher: D. D. Math. Vereinigung, **21**, 309 pp.

Sommerfeld, A., 1952, Electrodynamics, lectures on theoretical physics, Vol. III: Academic Press, New York, 371 pp.

Slater, J. C., and N. H. Frank, 1947, Electromagnetism: McGraw-Hill, New York, 240 pp.

Stratton, J., 1941, Electromagnetic theory: McGraw-Hill, New York, 615 pp.

Tamm, I. E., 1979, Fundamentals of the theory of electricity: Mir Publishers, Moscow, 684 pp.

Tralli, N., 1963, Classical electromagnetic theory: McGraw-Hill, New York, 308 pp.

Wapenaar, K., 2007, General representations for wavefield modeling and inversion in geophysics: Geophysics, **72** (5), SM5-SM17.

Whittaker, E., 1960a, A history of the theories of aether and electricity: Vol. I: The classical theories, Harper and Brothers, New York, 434 pp.

Whittaker, E., 1960b, A history of the theories of aether and electricity: Vol. II: The modern theories, Harper and Brothers, New York, 319 pp.

Zhdanov, M. S., 1988, Integral transforms in geophysics: Springer-Verlag, Berlin, Heidelberg, New York, London, Paris, Tokyo, 367 pp.

Zhdanov, M. S., and G. Keller, 1994, The geoelectrical methods in geophysical exploration: Elsevier, Amsterdam, London, New York, Tokyo, 873 pp.

Zhdanov, M. S., 2002, Geophysical inverse theory and regularization problems: Elsevier, Amsterdam, New York, Tokyo, 628 pp.

MODELS OF ELECTROMAGNETIC INDUCTION IN THE EARTH

CONTENTS

In constructing the theory for electromagnetic methods in geophysical exploration, simplified models of electromagnetic field behavior are widely used. Principal among these are the wave, quasi-stationary and static models. Let us now examine the features of each of these models of fields. Note that in this and following sections of the book we will use the traditional notations, *grad*, *div*, *curl*, for vector differential operators to emphasize the physical meaning of the corresponding equations.

4.1 MODELS OF ELECTROMAGNETIC FIELDS

The *wave equation model* is useful in studying the propagation of fields in insulating media. When $\sigma = 0$, the telegraphers' equations (3.75) and (3.76) can be written as follows:

$$\nabla^2 \mathbf{E} - \mu \epsilon \, \partial^2 \mathbf{E}/\partial t^2 = 0, \tag{4.1}$$

$$\nabla^2 \mathbf{H} - \mu \epsilon \, \partial^2 \mathbf{H}/\partial t^2 = 0. \tag{4.2}$$

These equations are called *wave equations*. They describe the nature of electromagnetic wave propagation in nonconducting media.

In many of the applications of electrical prospecting we use electromagnetic fields which vary relatively slowly in time. In such cases, we can neglect the terms involving the second derivatives with respect to time in comparison with those involving the first derivative when we use the telegraphers' equations (3.75) and (3.76):

$$\nabla^2 \mathbf{E} - \mu\sigma \, \partial\mathbf{E}/\partial t = 0, \tag{4.3}$$

$$\nabla^2 \mathbf{H} - \mu\sigma \, \partial\mathbf{H}/\partial t = 0. \tag{4.4}$$

These two equations are often referred to as *diffusion equations* because they have the same form as Fick's equation, which describes the diffusion of chemical species. Thus, we describe the propagation of electromagnetic fields into conductive media as *electromagnetic diffusion*, or *quasi-stationary* (*quasi-static*) behavior.

We obtain the equation of the quasi-stationary model of the field that we use in practice by neglecting the effect of displacement currents in Maxwell's equations (that is, we drop the term $\partial\mathbf{D}/\partial t$), but we retain the term representing electromagnetic induction (the term $\partial\mathbf{B}/\partial t$ in Maxwell's second equation):

$$curl \; \mathbf{H} = \sigma\mathbf{E}, \tag{4.5}$$

$$curl \; \mathbf{E} = -\partial\mathbf{B}/\partial t, \tag{4.6}$$

$$div \; \mathbf{B} = 0, \tag{4.7}$$

$$div \; \mathbf{E} = -\frac{1}{\sigma}\mathbf{E} \cdot grad \; \sigma. \tag{4.8}$$

We should note that Eq. (4.8) follows from the validity of Eq. (4.5).

A *static* field is one which is essentially independent of time. For such a field, we set all derivatives with respect to time to zero:

$$curl \; \mathbf{H} = \mathbf{j}, \;\; curl \; \mathbf{E} = 0,$$
$$div \; \mathbf{B} = 0, \;\; div \; \mathbf{D} = q. \tag{4.9}$$

Equations corresponding to (3.75) and (3.76) for a homogeneous medium can be written as:

$$\nabla^2\mathbf{E} = 0, \;\; \nabla^2\mathbf{B} = 0. \tag{4.10}$$

So, static electric and magnetic fields in homogeneous media and in the absence of external currents will satisfy Laplace's equation. The models for electromagnetic field behavior enumerated above are the fundamental theoretical basis for electromagnetic prospecting. In the sections which follow, we will examine in more detail the two models for electromagnetic field behavior which are most suitable for use in electromagnetic exploration. These are the static and quasi-stationary models.

4.2 STATIC ELECTROMAGNETIC FIELDS

In this text, we recognize three main groups of electromagnetic exploration methods; natural-field electromagnetic methods, controlled-source electromagnetic methods, and direct-current (DC) methods. The DC methods include vertical electric sounding (VES), resistivity profiling, resistivity mapping, and usually, the induced polarization (IP) method. The theory for the DC methods is developed under the assumption that constant currents are used, though in fact, we need only assume that the rate of variation of the currents is slow enough that our measurements will be the same as those obtained with true direct current in the limit. Rewriting the equations for static electromagnetic fields (Eq. (4.9)) and considering Eqs. (3.5), (3.6) and (3.44), we have

$$curl\ \mathbf{H} = \mathbf{j},\ curl\ \mathbf{E} = 0,\ div\ \mathbf{B} = 0,\ div\ \mathbf{D} = q,$$
$$\mathbf{D} = \epsilon\mathbf{E},\ \mathbf{j} = \sigma\mathbf{E},\ \mathbf{B} = \mu\mathbf{H}. \tag{4.11}$$

In comparing these equations with the complete system of Maxwell's equations (Eqs. (3.1) through (3.4)), we note that the mutual relationships between the electric and magnetic fields that is so striking in the full form is less obvious in these more restrictive equations for static behavior. The electric field creates conduction currents (sometimes also called *galvanic* currents) which are accompanied by a magnetic field, but the magnetic field now has no appreciable effect on the electric field. If there are no conduction currents (as when the medium is nonconducting), system (4.11) separates into two simultaneous but independent sets of equations, one representing the equations for *electrostatic fields* and the other, for *magnetostatic fields*.

4.2.1 ELECTROSTATIC FIELDS AND ELECTROSTATIC POTENTIALS

In electrostatics, we study the fields accompanying an immobile charge distribution. If the charge does not move, there is no current and no magnetic field. In such a situation, we need use only the following equations from the set (4.11):

$$curl\ \mathbf{E} = 0, \tag{4.12}$$
$$div\ \mathbf{D} = q, \tag{4.13}$$
$$\mathbf{D} = \epsilon\mathbf{E}. \tag{4.14}$$

Eq. (4.12) permits us to define a scalar potential function as:

$$\mathbf{E} = -grad\ U^e, \tag{4.15}$$

where U^e is the *electrostatic potential*.

We note that the choice of a negative sign in Eq. (4.15) is completely arbitrary, but is done to satisfy the convention that the electric field vector $\mathbf{E}$ should point in the direction of decreasing potential.

We define now the electrostatic potential from the field itself. Consider two points in space, A and B, connected by some smooth curve L_{AB} described by a unit positive tangent vector, $\boldsymbol{\tau}$. The voltage drop along this curve is computed from the electric field $\mathbf{E}$ by integration along the curve:

$$U_{AB} = \int_{L_{AB}} \mathbf{E} \cdot d\ell, \tag{4.16}$$

where

$$\int_{L_{AB}} \mathbf{E} \cdot d\ell = -\int_{L_{AB}} \mathrm{grad}\, U^e \cdot \boldsymbol{\tau} d\ell$$

$$= -\int_{L_{AB}} \frac{\partial U^e}{\partial \tau} d\ell = -\int_{L_{AB}} dU^e = U^e(A) - U^e(B). \tag{4.17}$$

The voltage drop between two points in an electrostatic field is independent of the path along which the electric field is integrated but depends only on the locations of the end points. In particular, the integrated electric field along any closed path is zero:

$$\oint_L \mathbf{E}_{AB} \cdot d\ell = 0.$$

We note that the voltage drop in a field $\mathbf{E}$ along a path AB is numerically equal (with a negative sign) to the work done against an external force, W, in carrying a unit positive electric charge from point A to point B:

$$W_{AB} = -\int_{L_{AB}} \mathbf{E} \cdot d\ell = U^e(B) - U^e(A). \tag{4.18}$$

Eqs. (4.15) and (4.18) allow us to move back and forth between the use of the electric field vector, $\mathbf{E}$, and the electrostatic potential, U^e, in describing the electrostatic field. Inasmuch as both descriptions are equivalent, we usually choose to deal with the scalar potential, which provides a simpler description than does the electric field vector.

We must note that the electrostatic potential, U^e, in Eq. (4.17) is not unique, inasmuch as the addition of any constant, U_o, to the potential, U^e, has no effect on these equations:

$$\mathrm{grad}(U^e + U_o) = \mathrm{grad}U^e + \mathrm{grad}U_o = \mathrm{grad}U^e.$$

The obvious solution to this ambiguity is to establish the requirement that the potential infinitely far from any charge be zero. This condition is quite acceptable from a physical point of view because we expect field effects of a charge to be confined to a finite region around the charge and to tend to zero as distance from the charge tends to become infinite.

In Eq. (4.18), let the point A tend to move to infinity and apply the condition $U^e(\infty) \to 0$:

$$W_{\infty B} = -\int_{L_{\infty B}} \mathbf{E} \cdot d\ell = U^e(B). \tag{4.19}$$

This provides a physical concept of electric potential. The potential at any point B is numerically the work done in carrying a unit charge from infinity to the designated point, working against the force of the electric field.

A surface over which the potential, U^e, has a constant value is called an *equipotential surface*. At every place on this surface, the field vector, $\mathbf{E}$, is directed normal to the surface. The equation for an equipotential surface is

$$U^e(x, y, z) = const. \tag{4.20}$$

Differentiating Eq. (4.20), we get

$$dU^e = (\partial U^e/\partial x)dx + (\partial U^e/\partial y)dy + (\partial U^e/\partial z)dz = 0. \tag{4.21}$$

The differentials dx, dy, dz are the components of the radius vector, $d\mathbf{r}$, defining the path along which we wish to determine the change in the function U^e, but because $dU^e = 0$, this vector lies on the equipotential surface. Moreover, the derivatives $\partial U^e/\partial x$, $\partial U^e/\partial y$, and $\partial U^e/\partial z$ are components of the gradient vector:

$$grad\ U^e = -\mathbf{E},$$

and it follows from Eq. (4.21) that

$$dU^e = -(\mathbf{E} \cdot d\mathbf{r}) = 0.$$

Thus, the vectors $\mathbf{E}$ and $d\mathbf{r}$ are orthogonal.

The group of curves which pass orthogonally through a series of equipotential surfaces describe the *flux* of the electric field, $\mathbf{E}$.

Substituting Eq. (4.15) in Eq. (4.14), we find an expression for the displacement field $\mathbf{D}$ in terms of the electrostatic potential:

$$\mathbf{D} = -\epsilon\ grad\ U^e. \tag{4.22}$$

Hence, in view of Eq. (4.13), it follows that U^e satisfies the equation

$$div(\epsilon\ grad\ U^e) = \epsilon\nabla^2 U^e + grad\ \epsilon \cdot grad\ U^e = -q. \tag{4.23}$$

If the medium is homogeneous, that is, if $\epsilon = constant$, the electrostatic potential is the solution of Poisson's equation:

$$\nabla^2 U^e = -q/\epsilon. \tag{4.24}$$

In portions of the medium free of charge, this equation becomes Laplace's equation:

$$\nabla^2 U^e = 0. \tag{4.25}$$

The fundamental problem in electrostatics consists of determining the scalar potential, U^e, which satisfies Poisson's equation throughout space, which tends to zero at infinity, and which obeys necessary boundary conditions at any boundaries which may exist. These boundary conditions will be established in the next section.

4.2.2 BOUNDARY CONDITIONS FOR ELECTROSTATIC POTENTIAL

The general form of the boundary conditions for vector electromagnetic fields has already been established. These conditions remain valid for electrostatic fields.

Let a surface S be the boundary separating medium (i) from medium $(i + 1)$, and $\mathbf{n}$ be a unit normal vector to S, directed from medium (i) to medium $(i + 1)$. In accord with Eqs. (3.68) and (3.66), we have:

$$\mathbf{E}_\tau^{(i+1)} = \mathbf{E}_\tau^{(i)}, \quad \mathbf{D}_n^{(i+1)} - \mathbf{D}_n^{(i)} = \eta, \tag{4.26}$$

where η is the surface density of charge on S, the indices τ and n indicate tangential and normal components of the vector field on the surface, S.

We designate the derivatives of the potential in the normal and tangential directions as $\partial U^e / \partial n$ and $\partial U^e / \partial \tau$, respectively. Then, on the basis of Eq. (4.15), the boundary conditions (4.26) can be written for electrostatic potential as follows:

$$\left(\frac{\partial U^e}{\partial \tau}\right)^{(i+1)} = \left(\frac{\partial U^e}{\partial \tau}\right)^{(i)},$$

$$\epsilon_{(i+1)} \left(\frac{\partial U^e}{\partial n}\right)^{(i+1)} - \epsilon_i \left(\frac{\partial U^e}{\partial n}\right)^{(i)} = -\eta. \tag{4.27}$$

The potential must be continuous across the boundary S so that the work done in carrying a unit positive charge across the discontinuity will be zero. Therefore

$$U^{(i+1)} = U^{(i)}. \tag{4.28}$$

The first equation in (4.27) follows from (4.28), and so, to have two independent boundary conditions, we make the following choices:

$$U^{e,(i+1)} = U^{e,(i)},$$

and

$$\epsilon_{(i+1)}(\partial U^e / \partial n)^{(i+1)} - \epsilon_i (\partial U^e / \partial n)^{(i)} = -\eta. \tag{4.29}$$

Regions filled with conductive materials play an important role in electrostatic problems. Within such regions, charges move freely, giving rise to conduction currents with a density $\mathbf{j} = \sigma \mathbf{E}$, in accord with Eq. (3.44). It is clear that electric charge within the conductive region will give rise to an electrostatic voltage, or, there will be no current flow only if the electrostatic field within the conductor is zero and if the tangential component of the electric field is zero at every point on the surface of the conductive region. It is further required that the electrostatic potential U^e inside the conductor be constant, and that the surface of the conductive region be an equipotential surface. Therefore, the boundary conditions (4.26) at the surface of a conductive region can be written as:

$$E_\tau^{(i+1)} = 0, \quad D_n^{(i+1)} = \eta, \tag{4.30}$$

and for the electrostatic potential as:

$$U^{e,(i+1)} = constant,$$

$$\epsilon_{(i+1)}(\partial U^e / \partial n)^{(i+1)} = -\eta, \tag{4.31}$$

where the conductive region is indicated by the index (i).

4.2.3 CALCULATION OF THE ELECTROSTATIC FIELD OF A SPECIFIED CHARGE DISTRIBUTION

We now examine the solution of Poisson's equation (Eq. (4.24)) for a simple case in which the charge is distributed in some volume V of a homogeneous and isotropic medium characterized by a constant dielectric permeability, ϵ.

For simplicity, we will assume that a point charge, Q, is located at the origin. In accord with Eq. (3.39), the radial component of the electric field, E_r, at a radial distance, r, from the charge will be

$$E_r(\mathbf{r}) = Q/4\pi\epsilon r^2. \tag{4.32}$$

We will calculate the potential at a point B defined by the radius vector $\mathbf{r}'$ using Eq. (4.17):

$$U^e(B) = U^e(\mathbf{r}\prime) = -\int_\infty^{r'} \frac{Q}{4\pi\epsilon r^2} dr$$
$$= \frac{Q}{4\pi\epsilon} \int_\infty^{r'} d\left(\frac{1}{r}\right) = \frac{Q}{4\pi\epsilon r'}. \tag{4.33}$$

We see that the equipotential surfaces for the field about a point charge are a set of concentric spheres. The vector flux lines for the field $\mathbf{E}$ are a family of straight lines radiating from the origin.

It can easily be shown that, if the point charge Q were located at some point defined by the radius vector $\mathbf{r}$ rather than at the origin, the electrostatic potential at the point $\mathbf{r}'$ would be

$$U^e(\mathbf{r}') = Q/(4\pi\epsilon|\mathbf{r} - \mathbf{r}'|). \tag{4.34}$$

Now consider a charge uniformly distributed through some volume V. We subdivide the volume into elementary subvolumes dv and designate the amount of charge in each as dQ. The ratio

$$dQ/dv = q(\mathbf{r}) \tag{4.35}$$

is the definition of the *volumetric electric charge density* distributed through V.

The contribution to the total potential at some observation point defined by $\mathbf{r}'$ from a single elementary volume dv will be designated as $dU^e(\mathbf{r})$. If the elementary volumes are reasonably small, we can use Eq. (4.34), treating the charge distributed over the elementary volume as though it were a point charge located at the center of the volume element:

$$dU^e(\mathbf{r}') = dQ/(4\pi\epsilon|\mathbf{r} - \mathbf{r}'|). \tag{4.36}$$

Integrating Eq. (4.36) over the entire volume V and taking Eq. (4.35) into account, we obtain an expression for the electrostatic potential due to the charge distributed uniformly through the volume:

$$U^e(\mathbf{r}') = \frac{1}{4\pi\epsilon} \iiint_V \frac{q(\mathbf{r})}{|\mathbf{r} - \mathbf{r}'|} dv. \tag{4.37}$$

This equation is the solution to Poisson's equation, (4.24).

4.2.4 ANALOGY BETWEEN CONSTANT CURRENT FIELDS AND ELECTROSTATIC FIELDS

We now show that in regions containing neither free charges nor extrinsic currents, an analogy exists between direct current fields and electrostatic fields – *the electrostatic analogy*.

We can write equations specifically for constant current using Eq. (4.12), expressing the continuity condition (3.15) for the condition $\partial q/\partial t = 0$:

$$curl\ \mathbf{E} = 0,\ div\ \mathbf{j} = 0,\ \mathbf{j} = \sigma\mathbf{E}. \tag{4.38}$$

Recall that in the case of electrostatic fields, the equivalent equations for $q = 0$ are:

$$curl\ \mathbf{E} = 0,\ div\ \mathbf{D} = 0,\ \mathbf{D} = \epsilon\mathbf{E}. \tag{4.39}$$

It is most important to realize that the two sets of equations are the same; only the symbology differs. These two sets of equations represent an analogy between the two situations, the flow of constant current in one case, and the flow of electric flux in the other case, when we consider that $\mathbf{j}$ trades roles with $\mathbf{D}$ as σ trades roles with ϵ:

$$\mathbf{j} \Longleftrightarrow \mathbf{D},\ \text{and } \sigma \Longleftrightarrow \epsilon. \tag{4.40}$$

This analogy permits us to use the solution of a problem in electrostatics for the solution of a corresponding problem in direct current flow. As an example, we can readily determine the electric field from the DC potential:

$$\mathbf{E} = -grad\ U, \tag{4.41}$$

where U is an electric potential, which, in analogy to the electrostatic potential U^e, satisfies the Laplace equation as in (4.25):

$$\nabla^2 U = 0. \tag{4.42}$$

In analogy with Eq. (4.19), the DC electric potential is obtained from the electric field $\mathbf{E}$ as

$$U(B) = -\int_{L_{\infty,B}} \mathbf{E} \cdot d\ell. \tag{4.43}$$

At a boundary separating two conductive regions with different conductivities, σ_i and σ_{i+1}, the following boundary conditions for the DC electric potential hold:

$$U^{(i+1)} = U^{(i)},$$

and

$$\sigma_{i+1}\left(\frac{\partial U}{\partial n}\right)^{(i+1)} = \sigma_i\left(\frac{\partial U}{\partial n}\right)^{(i)}. \tag{4.44}$$
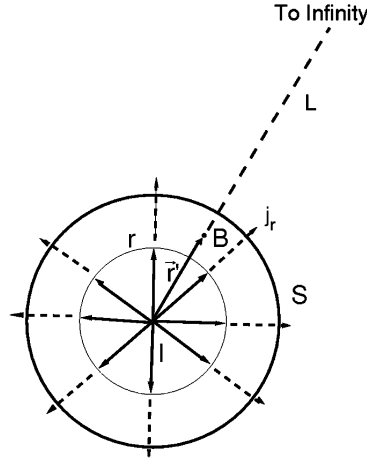
FIGURE 4.1

A scheme of the current distribution of a point source in an isotropic and homogeneous medium with constant conductivity, σ.

These boundary conditions have been obtained from Eq. (4.29) by substituting σ for ϵ (remembering that the analogy is valid only for the case in which there is no electric charge; that is, $\eta = 0$).

As a simple example, let us consider the problem of current distribution in an isotropic and homogeneous medium with constant conductivity, σ. We place the origin at the point source of current and draw a spherical surface, S_r, with a radius r, as shown in Fig. 4.1. The current flux, **j**, must flow through this surface uniformly, so:

$$\iint_{S_r} \mathbf{j} \cdot d\mathbf{s} = \iint_{S_r} j_r ds = I. \tag{4.45}$$

We expect the current flow from the point source to be completely symmetric in view of the uniformity of the medium (Fig. 4.1); we also expect j_r to be constant over this surface. Therefore, j_r can be factored from beneath the integral signs:

$$j_r \iint_{S_r} ds = j_r 4\pi r^2 = I,$$

or

$$j_r = I/4\pi r^2. \tag{4.46}$$

From Ohm's law in differential form (Eq. (3.44)), we have

$$E_r = I/4\pi \sigma r^2. \tag{4.47}$$

This equation permits us to find the DC electric potential at some point B located at the tip of a radius vector $\mathbf{r}'$ due to a point source of current. To do so, we substitute Eq. (4.47) in Eq. (4.43) and integrate along a radial $L_{\infty B}$:

$$U_B = U(\mathbf{r}') = -\int_{\infty}^{r'} E_r dr = -\int_{\infty}^{r'} \frac{I}{4\pi\sigma r^2} dr = I/4\pi\sigma r'. \tag{4.48}$$

Let us examine a problem in which current is supplied to a medium with conductivity σ using a metal electrode of arbitrary shape, the electrode having a conductivity σ_0 which is far greater than that of the conductive medium with which it is in contact ($\sigma_0 \gg \sigma$). This is a problem of importance in a wide variety of electrical field techniques which require electrode contacts to drive current into the earth. In the absence of surface charges, and in accord with Eqs. (3.66) and (3.68), the boundary conditions for the vector $\mathbf{D}$ are:

$$D_n^{(1)} = D_n^{(0)},$$
$$D_\tau^{(1)}/D_\tau^{(0)} = \epsilon^{(1)}/\epsilon^{(0)}, \tag{4.49}$$

where the index (1) refers to the medium in which the electrode is embedded and the index (0) indicates the material of the electrode. On the basis of the boundary conditions which have already been established for the tangential and normal components of current density at the surface of the electrode in Eq. (4.40), we can use the following conditions:

$$j_n^{(1)} = j_n^{(0)},$$

and

$$j_\tau^{(1)}/j_\tau^{(0)} \ll 1 \text{ or } j_\tau^{(1)} \approx 0. \tag{4.50}$$

The current flow out of the electrode is equal to the current flow into the medium; there is no tangential current flow along the surface of the electrode. This set of boundary conditions (Eq. (4.50)) is analogous to the boundary conditions for the electrostatic case at the boundary between a conductor and a dielectric material if we swap the surface charge density on the conductor, η, for the current density, $j_n^{(1)}$, flowing from the electrode. Also, the total charge on the conductor $Q = \iint_S \eta \, ds$ in the electrostatic case swaps for the total current emitted by the electrode in the DC case:

$$I = \iint_S j_n^{(0)} ds.$$

To summarize, for electrodes of general shape (in the DC case) or conductive bodies (in the electrostatic case), we have established the following analogy:

Current flow in conductive media		Electric flux in insulating media
$\mathbf{j}$, current density	$\rightleftharpoons$	$\mathbf{D}$, electric field
σ, electrical conductivity	$\rightleftharpoons$	ϵ, dielectric permittivity
I, total current from electrode	$\rightleftharpoons$	Q, total charge

This analogy is of immense value in that many electrostatic problems have already been solved, and the results can be transferred to the DC case with no real effort.

4.2.5 DIRECT CURRENT FLOW, ASSOCIATED MAGNETIC FIELD, AND THE BIOT-SAVART LAW

The relationship of magnetic field strength to the flux of direct current is specified by the following equations from set (4.11):

$$curl\ \mathbf{H} = \mathbf{j}, \tag{4.51}$$

$$div\ \mathbf{B} = 0, \tag{4.52}$$

$$\mathbf{B} = \mu\mathbf{H}. \tag{4.53}$$

In addition, it is necessary to require conservation of the current:

$$div\ \mathbf{j} = 0. \tag{4.54}$$

Eq. (4.52) ensures that the magnetic field accompanying current flow is also conserved, so that we can write

$$\mathbf{B} = curl\mathbf{A}^{\mu}, \tag{4.55}$$

which is a definition of $\mathbf{A}^{\mu}$, the *magnetic vector potential*.

If the medium is both uniform and isotropic in magnetic properties (that is, if the magnetic permeability, μ, is both scalar and constant), by substituting Eq. (4.55) into Eq. (4.51), we have

$$curl\ curl\ \mathbf{A}^{\mu} = \mu\mathbf{j}. \tag{4.56}$$

It was demonstrated in Chapter 2 that for unique determination of a vector field, it is necessary to know either its curl or its divergence (that is, either its vorticity or its sources). In Eq. (4.55), we have specified the vorticity of the field $\mathbf{A}^{\mu}$, but we have said nothing about its sources. The vector potential $\mathbf{A}^{\mu}$ can be specified more completely by considering its divergence. We can impose additional conditions on $\mathbf{A}^{\mu}$ without reducing the generality of the potential, a process known as adopting *a gauge for vector potential*. In dealing with the theory for static magnetic fields, we most commonly use the *Coulomb Gauge*:

$$div\ \mathbf{A}^{\mu} = 0.$$

Using the vector identity

$$curl\ curl\ \mathbf{F} = grad\ div\ \mathbf{F} - \nabla^2\mathbf{F}, \tag{4.57}$$

which is valid for any vector, including the vector $\mathbf{F} = \mathbf{A}^{\mu}$, Eq. (4.56) can be written as

$$\nabla^2\mathbf{A}^{\mu} = -\mu\mathbf{j}. \tag{4.58}$$

This last equation carries the name *Poisson's vector equation*. In regions with no current flow, such as insulators, the magnetic vector potential satisfies *Laplace's vector equation*,

$$\nabla^2\mathbf{A}^{\mu} = 0. \tag{4.59}$$

The fundamental problem met in analysis of static magnetic fields is that of determining the magnetic field from a specified distribution of electric currents. It is attacked by solving Poisson's vector equation, (Eq. (4.58)), for the magnetic potential and by substituting the vector potential $\mathbf{A}^\mu$ in Eq. (4.55). In solving this problem, we make use of Cartesian orthonormal basis vectors $\{\mathbf{d}_x, \mathbf{d}_y, \mathbf{d}_z\}$ as before and expand the vectors $\mathbf{A}^\mu$ and $\mathbf{j}$ on these basis vectors:

$$\mathbf{A}^\mu = A_x^\mu \mathbf{d}_x + A_y^\mu \mathbf{d}_y + A_z^\mu \mathbf{d}_z,$$
$$\mathbf{j} = j_x \mathbf{d}_x + j_y \mathbf{d}_y + j_z \mathbf{d}_z. \tag{4.60}$$

Substituting Eq. (4.60) into Eq. (4.58), we obtain the following system of scalar Poisson's equations:

$$\nabla^2 A_\alpha^\mu = -\mu j_\alpha, \tag{4.61}$$

where the subscript α indicates one of the indices x, y, z.

But we have already solved Poisson's scalar equation. We have previously derived Eq. (4.37) in this chapter, giving the solution to Poisson's equation (4.24) for the scalar electrostatic potential. Comparing Eq. (4.24) with Eq. (4.61), we see that the latter differs from the former only in that $U^e \Longleftrightarrow A_\alpha^\mu$, $q \Longleftrightarrow j_\alpha$, and $\epsilon \Longleftrightarrow 1/\mu$. Making these interchanges in Eq. (4.37), we find

$$A_\alpha^\mu(\mathbf{r}') = \frac{\mu}{4\pi} \iiint_V \frac{j_\alpha(\mathbf{r})}{|\mathbf{r} - \mathbf{r}'|} dv, \alpha = x, y, z; \tag{4.62}$$

where V is the volume within which electric currents are flowing. Substituting Eq. (4.62) into Eq. (4.60), we obtain the final result:

$$\mathbf{A}^\mu(\mathbf{r}') = \frac{\mu}{4\pi} \iiint_V \frac{\mathbf{j}(\mathbf{r})}{|\mathbf{r} - \mathbf{r}'|} dv. \tag{4.63}$$

This equation also provides a solution for Poisson's equation, Eq. (4.58). Now, we use Eq. (4.55) to find the magnetic fields of the currents,

$$\mathbf{B}(\mathbf{r}) = \frac{\mu}{4\pi} curl' \iiint_V \frac{\mathbf{j}(\mathbf{r})}{|\mathbf{r} - \mathbf{r}'|} dv, \tag{4.64}$$

where the prime ($'$) on the curl operator indicates that the differentiation is carried out with respect to the variable $\mathbf{r}'$. Moreover, the integration indicated in Eq. (4.64) is to be carried out over the variable $\mathbf{r}$, and so, the operator $curl'$ can be factored into the integral signs:

$$\mathbf{B}(\mathbf{r}) = \frac{\mu}{4\pi} \iiint_V curl' \left[\frac{\mathbf{j}(\mathbf{r})}{|\mathbf{r} - \mathbf{r}'|} \right] dv. \tag{4.65}$$

Using the following vector identity:

$$curl\, U\mathbf{F} = grad\, U \times \mathbf{F} + U\, curl\, \mathbf{F}, \tag{4.66}$$

and defining variables as $U = 1/|\mathbf{r} - \mathbf{r}'|$ and $\mathbf{F} = \mathbf{j}(\mathbf{r})$, we find:

$$curl' \left[\frac{\mathbf{j}(\mathbf{r})}{|\mathbf{r} - \mathbf{r}'|} \right] = grad' \left[\frac{1}{|\mathbf{r} - \mathbf{r}'|} \right] \times \mathbf{j}(\mathbf{r}) + \frac{curl'\mathbf{j}(\mathbf{r})}{|\mathbf{r} - \mathbf{r}'|}. \tag{4.67}$$

But the current density $\mathbf{j}(\mathbf{r})$ is a function of the variable $\mathbf{r}$, while the differentiation is carried out with respect to the variable $\mathbf{r}'$, and so, $curl'\mathbf{j}(\mathbf{r}) = 0$, and

$$curl' \left[\frac{\mathbf{j}(\mathbf{r})}{|\mathbf{r} - \mathbf{r}'|} \right] = \frac{(\mathbf{r} - \mathbf{r}') \times \mathbf{j}(\mathbf{r})}{|\mathbf{r} - \mathbf{r}'|^3},$$

and so,

$$\mathbf{B}(\mathbf{r}) = \frac{\mu}{4\pi} \iiint_V \frac{(\mathbf{r} - \mathbf{r}') \times \mathbf{j}(\mathbf{r})}{|\mathbf{r} - \mathbf{r}'|^3} dV. \tag{4.68}$$

Eq. (4.68) is the general form of the *Biot-Savart law*. Suppose we wish to use Eq. (4.68) to compute the magnetic field $\mathbf{H}(\mathbf{r})$ for a linear current flowing with constant density $\mathbf{j}_o = j_o \boldsymbol{\tau}$ along a thin cylindrical structure (a wire) lying on the line L (here $\boldsymbol{\tau}$ is a unit tangent vector to L). Then:

$$\begin{aligned} \mathbf{H}(\mathbf{r}') &= \frac{1}{\mu} \mathbf{B}(\mathbf{r}') = \frac{1}{4\pi} \int_{\Delta s} j_o ds \int_L \frac{(\mathbf{r} - \mathbf{r}') \times \mathbf{r}}{|\mathbf{r} - \mathbf{r}'|^3} d\ell \\ &= \frac{I_0}{4\pi} \int_L \frac{(\mathbf{r} - \mathbf{r}') \times d\mathbf{l}}{|\mathbf{r} - \mathbf{r}'|^3}, \end{aligned} \tag{4.69}$$

where I_0 is the current flowing in the cylindrical conductor with a cross section S, $I_0 = \iint_S j_o ds$, and $d\mathbf{l} = \boldsymbol{\tau} d\ell$ is an oriented flow element. The physical law expressed by Eq. (4.69) states that any element of linear current flow, $I_0 d\mathbf{l}$ contributes an element of magnetic field strength $d\mathbf{H}(\mathbf{r}')$, given by

$$d\mathbf{H}(\mathbf{r}') = \frac{1}{4\pi} \frac{(\mathbf{r} - \mathbf{r}') \times I_0 d\mathbf{l}}{|\mathbf{r} - \mathbf{r}'|^3}. \tag{4.70}$$

This is precisely the result obtained experimentally in 1820 by Biot and Savart!

4.2.6 POINT AND DIPOLE SOURCES ON A UNIFORM EARTH

The very first step in understanding the use of DC electrical methods is that of determining the electric field around a single pole source of current on the surface of a completely uniform earth characterized by a resistivity ρ (see Fig. 4.2).

Let us name the current electrode A (conventional nomenclature uses the letter A to designate a current injection electrode, while the current return electrode is designated B). The current driven into the electrode A flows entirely in the lower half-space, inasmuch as the conductivity in the upper half-space (the atmosphere) is zero. The total current into electrode A spreads uniformly into the uniform earth. As a consequence, the current density vector, $\mathbf{j}$, at each point in the lower half-space describes a set of current flow lines which spread radially along straight paths into the earth.
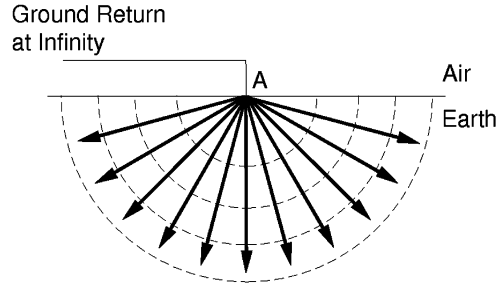
FIGURE 4.2

Geometric behavior of current flow from a point source on the surface of a uniform earth. The current flows with radial symmetry as shown by the solid arrows. Surfaces of equal voltage are hemispheres as shown by the dotted lines.

Next, let us consider a hemispherical surface, S, with radius, r, centered on the electrode A. It is clear that the total current, I, emitted from the electrode A passes through this surface, and that, for the uniform earth, the current density is uniform over this surface. Consequently, the current density at any point M on the hemispherical surface will be:

$$j = I/2\pi r^2. \tag{4.71}$$

Using Ohm's law, the amplitude of the electric field, E, at the observation point M can be expressed as:

$$E = \rho j = I\rho/2\pi r^2.$$

The vector $\mathbf{E}$ is directed along a radius vector connecting the points A and M. Designating the vector from A to M as $\mathbf{r}$, the electric field can be written as:

$$\mathbf{E} = (I\rho/2\pi r^2)\mathbf{r}/r, \tag{4.72}$$

where $\mathbf{r}/r$ is a radially directed unit vector.

Let us use a Cartesian coordinate system initially, with the coordinates x, y, z centered at the point A, and with the z axis taken as positive downwards (a convention particularly appropriate when we wish to look downwards into the earth), and with the x, y axes lying in the plane of the earth's surface. The observation point, M, is designated by the coordinates $M(x, y, z)$. The scalar length of the vector $\mathbf{r}$ will be:

$$r = (x^2 + y^2 + z^2)^{1/2}.$$

The components of the vector $\mathbf{E}$ projected onto the Cartesian coordinate directions are:

$$E_x = \frac{I\rho}{2\pi r^2}\frac{x}{r},$$

$$E_y = \frac{I\rho}{2\pi r^2}\frac{y}{r},$$

$$E_z = \frac{I\rho}{2\pi r^2}\frac{z}{r}. \tag{4.73}$$

We should note that in these expressions the vertical component of the electric field at the earth's surface is always zero. Physically, this means that no current will cross the earth's surface to flow in the upper half-space, the air. In looking at these equations, it can readily be determined that the electric field is the derivative (with a minus sign) of the function:

$$U = I\rho/2\pi r. \tag{4.74}$$

This formula states a fact which we will use extensively in the future, that the potential is inversely proportional to the distance from the source if the earth is uniform.

It is worthwhile to compare this last formula for electric potential with one developed earlier for a full space occupied by material with a uniform and isotropic resistivity, ρ (Eq. (4.48)). The two formulas differ only by the factor 2. If, in Eq. (4.74), we use a current $I/2$ rather than the current I, the two expressions are the same.

The physical explanation is straightforward. In the full space, the current I has twice the volume to spread through in comparison with the half-space; and so the current density will be only half as great.

The mathematical concept of a *point* electrode, or source of current, as used above is an idealization. In reality, the electric field is generated by current flowing between two electrode contacts, A and B, fed by batteries or some form of mechanical current generator. The electrodes driven into the earth often have the form of a metal stake, rod, or pin. The fact that current is provided to the earth by other than a point source is almost always ignored in developing the theory for DC electrical methods. This assumption is rationalized by pointing out that if the separation between electrodes A and B is very large compared to the dimensions of the electrodes themselves, the inaccuracy introduced by considering the electrodes to behave as point sources is quite negligible. Only in very small-scale electrical surveys, such as might be used in exploring archaeological sites at depths of a fraction of a meter, will this assumption come into question.

It should be clearly understood that a single-pole current source is a mathematical abstraction, and cannot be achieved in practice. Provision must be made for all current that flows into the ground to be returned in some way to the energy source. This is done most simply by providing a current return electrode, B, in contact with the earth. At least two electrode contacts are thus needed to carry out a DC electrical survey, though more than two can be used so long as all the current supplied to the ground is accounted for by return paths through other electrodes.

The use of two electrodes, A and B, to supply and recover current to the ground, at first appears to complicate the pattern of current flow in the ground. In place of the simple radial pattern of current flow lines as shown in Fig. 4.2, the flow pattern becomes curvilinear, beginning on one point electrode, A, and ending on the other current electrode, B (Fig. 4.3). The flow lines appear to be circular (for the uniform half-space under consideration), but in fact, each current flow filament is a segment of a hypercircle.

What is the distribution of electric potential or electric field in a uniform isotropic half-space when two current electrodes are used? Consider two current electrodes separated by a distance ℓ on the surface of that half-space, with a current I flowing into electrode A and a current $-I$ flowing out of
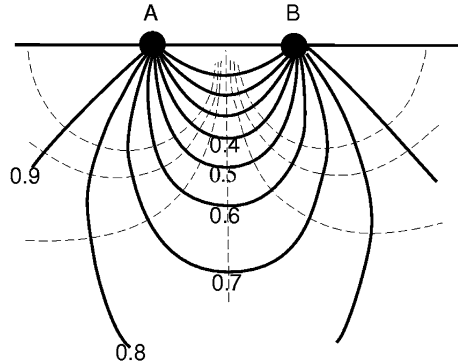
FIGURE 4.3

Flow of current between two source electrodes implanted in the surface of a uniform half-space. Each of the solid lines separates regions within which one-tenth of the total current flows. The dashed lines are lines of equal voltage.

electrode B. Let us place the origin of a Cartesian coordinate system at the point A. Again, the positive z direction is downwards, and the x, y axes lie in the plane of the earth's surface. However, in this case, we can further specify that the x direction is along the line connecting electrodes A and B. Let us consider an observation point $M(x, y, z)$ located within the earth. Point M lies at a distance r_1 from the point A and at a distance r_2 from point B. If we assume the earth to be a linear medium (which our knowledge of physical properties suggests is true), electric currents will satisfy the principle of superposition: the potential for two independent current sources will be the exact sum of the individual potentials created by the two sources acting separately. In accord with this assumption of linearity of the medium, the electric potential at the point P is

$$U(M) = U_A(M) + U_B(M), \qquad (4.75)$$

where $U_A(M)$ is the electric potential created at the point M by current from the source A, and $U_B(M)$ is the electric potential created at the point M by the current from source B.

$$U_A(M) = I\rho/2\pi r_1,$$
$$U_B(M) = -I\rho/2\pi r_2. \qquad (4.76)$$

The total potential at point M is the simple sum of these two contributions:

$$U(M) = \frac{I\rho}{2\pi}\left(\frac{1}{r_1} - \frac{1}{r_2}\right). \qquad (4.77)$$

Often, electric potentials are described with plots of equipotential lines or surfaces. An equipotential line or surface is defined as the locus of all points at which the potential is a constant:

$$\frac{I\rho}{2\pi}\left(\frac{1}{r_1} - \frac{1}{r_2}\right) = constant.$$

One important equipotential surface is that at which the electric potential is zero, which for a uniform earth and two source electrodes that provide equal currents of opposite sign to the medium, occurs when r_1 equals r_2. The zero equipotential surface is a vertical plane perpendicular to the x axis and situated halfway between the points A and B.

In an isotropic medium, the electric current vector is normal to any equipotential surface. On the zero equipotential plane, the electric current is parallel to the x axis. Therefore, at points on this plane, current density vectors are collinear with the x axis, and have but a single nonzero component $j_x : \mathbf{j} = (j_x, 0, 0)$ and, from Ohm's law,

$$j_x = E_x/\rho,$$

which is a simple scalar equation.

In accord with an equation developed earlier (Eq. (4.41)), we can write

$$E_x = -\partial U/\partial x$$

and

$$j_x = -\frac{1}{\rho}\frac{\partial U}{\partial x}. \tag{4.78}$$

Substituting the equation for electric potential (Eq. (4.77)) into this last expression, we have

$$j_x = -\frac{I}{2\pi}\frac{\partial}{\partial x}\left(\frac{1}{r_1} - \frac{1}{r_2}\right). \tag{4.79}$$

The two distances, r_1 and r_2, are

$$r_1 = (x^2 + y^2 + z^2)^{1/2}; \quad r_2 = [(x - L)^2 + y^2 + z^2]^{1/2},$$

where L is a distance between two source electrodes, A and B.

Substituting these distances in Eq. (4.79) and differentiating with respect to x, we have:

$$j_x = \frac{I}{2\pi}\left\{\frac{x}{(x^2 + y^2 + x^2)^{3/2}} + \frac{(x - L)}{[(x - L)^2 + y^2 + z^2]^{3/2}}\right\}. \tag{4.80}$$

In particular, at points on the equipotential plane P (with $x = L/2$), the current density is:

$$j_x = \frac{IL}{2\pi(L^2/4 + y^2 + z^2)^{3/2}}. \tag{4.81}$$

We can analyze the current density along a vertical profile at the midpoint between electrodes A and B by setting $y = 0$ in this last expression

$$j_x(z) = \frac{IL}{2\pi(L^2/4 + z^2)^{3/2}}. \tag{4.82}$$
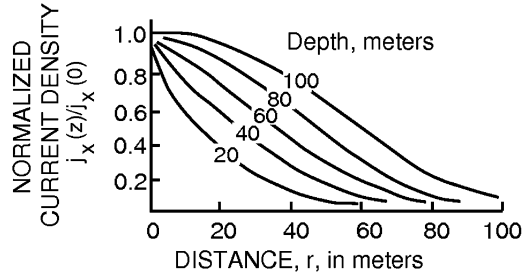
FIGURE 4.4

Plots of the normalized current density, $j_x(z)/j_x(0)$, versus depth for various separations, L.

The ratio of the current density at some depth, z, to that at the surface, $z = 0$, is:

$$\frac{j_x(z)}{j_x(0)} = \frac{1}{[1 + (2z/L)^2]^{3/2}}. \tag{4.83}$$

The results of such an analysis are shown graphically in Fig. 4.4 with profiles of the normalized current density $j_x(z)/j_x(0)$ for various separations, L. An important feature of these curves to be noted is that for larger values of L, the amount of current density at a given depth increases. In particular, these calculations have shown that in the case of a uniform half-space, half of the total current flows above the depth $z = L/2 = AB/2$, and half flows below this depth. Because of this, the quantity $AB/2$ has become widely accepted as a measure of the distance of penetration of the current. We will use this measure extensively in further considerations of the DC methods.

We will next examine cases in which the depth of the observation point M is large compared to the separation L between the current electrodes A and B. In electrical exploration, such a closely spaced pair of current sources is termed a *current dipole*. In discussing current dipole sources, we make use of the vector from point A to point B, represented by the notation $d\mathbf{l}$, and define the distance from the dipole pair to the measurement point M in terms of a single radius vector, $\vec{r}$, from the electrode A. In this new notation, the quantities r_1 and r_2 used previously become:

$$r_1 = |\mathbf{r}| = r, \quad r_2 = |\mathbf{r} + d\mathbf{l}|. \tag{4.84}$$

Substituting Eq. (4.84) into Eq. (4.77), we obtain an expression for the electric potential generated by a current dipole source:

$$\begin{aligned}
U_D(M) = U_D(\mathbf{r}) &= \frac{I\rho}{2\pi} \left(\frac{1}{|\mathbf{r}|} - \frac{1}{|\mathbf{r} + d\mathbf{l}|} \right) \\
&= \frac{I\rho}{2\pi} \left[\left(\frac{1}{|\mathbf{r}|} - \frac{1}{|\mathbf{r} + d\mathbf{l}|} \right) /d\ell \right] d\ell.
\end{aligned} \tag{4.85}$$

If the length $d\ell$ is sufficiently small in comparison with the distance r, the term in parentheses can be taken to be approximately the derivative of $1/r$ with respect to $d\ell$:

$$\left[\left(\frac{1}{|\mathbf{r}|} - \frac{1}{|\mathbf{r}+d\mathbf{l}|}\right)/d\ell\right] \approx -\frac{\partial(1/r)}{\partial\ell}. \qquad (4.86)$$

Replacing the term in brackets in Eq. (4.85) by the derivative, we have:

$$U_D(r) = -\frac{\partial(I\rho/2\pi r)}{\partial\ell}d\ell = -\frac{\partial U(\mathbf{r})}{\partial\ell}d\ell = -grad\ U(\mathbf{r})\cdot d\mathbf{l}, \qquad (4.87)$$

where $U(\vec{r})$ is the expression for the electric potential due to a single pole source of current. Thus, the potential for a dipole source is merely the derivative of the potential for a single-pole source taken in the direction of the dipole axis.

Consider the gradient of the single-pole potential:

$$grad\ U(\mathbf{r}) = -\frac{I\rho}{2\pi}\frac{\mathbf{r}}{r^3}.$$

The dipole potential can be written as:

$$U_D(\mathbf{r}) = \frac{I\rho}{2\pi r^2}[(\mathbf{r}/r)\cdot d\mathbf{l}] = \frac{\rho}{2\pi r^2}[(\mathbf{r}/r)\cdot\mathbf{p}], \qquad (4.88)$$

where the product $Id\mathbf{l}$ is the measure of the strength of the dipole source, and which is called the *current dipole moment*, measured in units of ampere-meters:

$$\mathbf{p} = Id\mathbf{l}. \qquad (4.89)$$

Finally, we find the expression for the electric field due to a current dipole source at the surface of a homogeneous isotropic medium by substituting Eq. (4.88) into Eq. (4.41):

$$E_D(\mathbf{r}) = -grad\ U_D(\mathbf{r}) = -grad\left(\frac{\rho}{2\pi r^3}\right)(\mathbf{r}\cdot\mathbf{p}) - \frac{\rho}{2\pi r^3}grad\ (\mathbf{r}\cdot\mathbf{p})$$

$$= \frac{3\rho}{2\pi r^3}\frac{\mathbf{r}}{r}\left[\frac{\mathbf{r}}{r}\cdot\mathbf{p}\right] - \frac{\rho}{2\pi r^3}\mathbf{p}. \qquad (4.90)$$

4.2.7 DC POTENTIAL IN AN ANISOTROPIC EARTH

In Chapter 10, we shall see that an earth which is stratified on a fine scale can be considered to be anisotropic. If we analyze the behavior of DC potential in a uniform anisotropic earth, we find that the anisotropy has an important effect which must be recognized when the electrical geophysical method is used. Consider that a current I is driven into a homogeneous but anisotropic earth through a point electrode, A, at the origin of a Cartesian coordinate system. The earth is characterized by two values of resistivity, ρ_ℓ, for horizontal current flow and ρ_{tr} for vertical current flow. At any point in the medium, the current density vector has the components:

$$j_x = \frac{E_x}{\rho_\ell} = -\frac{1}{\rho_\ell}\frac{\partial U}{\partial x},$$

$$j_y = \frac{E_y}{\rho_\ell} = -\frac{1}{\rho_\ell}\frac{\partial U}{\partial y},$$

$$j_z = \frac{E_z}{\rho_{tr}} = -\frac{1}{\rho_{tr}}\frac{\partial U}{\partial z}. \tag{4.91}$$

The usual requirement that the divergence of the current density vector is zero except at the electrode A, must be met:

$$div\,\mathbf{j} = \frac{\partial j_x}{\partial x} + \frac{\partial j_y}{\partial y} + \frac{\partial j_z}{\partial z} = \frac{1}{\rho_\ell}\left(\frac{\partial^2 U}{\partial x^2} + \frac{\partial^2 U}{\partial y^2}\right) + \frac{1}{\rho_{tr}}\frac{\partial^2 U}{\partial z^2} = 0. \tag{4.92}$$

This equation can be converted into the form of Laplace's equation by a transformation of variables which corresponds physically to stretching the anisotropic space into an isotropic space:

$$\xi = \sqrt{\rho_\ell}x,$$

$$\eta = \sqrt{\rho_\ell}y,$$

$$\zeta = \sqrt{\rho_{tr}}z. \tag{4.93}$$

Once we have substituted the transformed coordinates for x, y, z, Eq. (4.92) takes the form of Laplace's equation when it is expressed in terms of spherical coordinates with $R^2 = \xi^2 + \eta^2 + \zeta^2$. Inasmuch as the problem is symmetrical with respect to the two angular coordinates, the full form of Laplace's equation simplifies to

$$\frac{\partial}{\partial R}\left(R^2\frac{\partial U}{\partial R}\right) = 0. \tag{4.94}$$

Integrating once with respect to R, we have:

$$R^2\frac{\partial U}{\partial R} = C, \tag{4.95}$$

where C is a constant of integration. Dividing both sides of this equation by R^2, we have a form which can be integrated again, yielding an expression for the potential, U:

$$U = -\frac{C}{R} + D.$$

The constant, D, can be evaluated by requiring that the potential at a great distance from the source be zero; therefore, D must also be zero. The constant, C, is evaluated by considering the total current flowing from the source electrode, A. The components of the current density vector are:

$$j_x = -\frac{1}{\rho_\ell}\frac{\partial U}{\partial x} = \frac{-Cx}{\rho_\ell^{3/2}(x^2 + y^2 + \lambda^2 z^2)^{3/2}},$$

$$j_y = -\frac{1}{\rho_\ell}\frac{\partial U}{\partial y} = \frac{-Cy}{\rho_\ell^{3/2}(x^2 + y^2 + \lambda^2 z^2)^{3/2}},$$

$$j_z = -\frac{1}{\rho_{tr}}\frac{\partial U}{\partial z} = \frac{-Cz}{\rho_\ell^{3/2}(x^2 + y^2 + \lambda^2 z^2)^{3/2}}, \tag{4.96}$$

where $\lambda^2 = \rho_{tr}/\rho_\ell$. This is the definition of the coefficient of anisotropy used in Chapter 10. We now see that the definition of this coefficient as the square root of the ratio of resistivities in the principal directions in the medium is theoretically convenient. The magnitude of the current density vector is:

$$|\mathbf{j}| = (j_x^2 + j_y^2 + j_z^2)^{1/2} = \frac{|C|(x^2 + y^2 + z^2)^{1/2}}{\rho_\ell^{3/2}(x^2 + y^2 + \lambda^2 z^2)^{3/2}}. \tag{4.97}$$

The spherical and Cartesian coordinates are related as follows:

$$x^2 + y^2 = R^2 \sin^2\theta, \ \ z^2 = R^2 \cos^2\theta.$$

The magnitude of the current density vector in spherical coordinates is

$$|\mathbf{j}| = \frac{|C|}{\rho_\ell^{3/2} R^2 [1 + (\lambda^2 - 1)\cos^2\theta]^{3/2}}. \tag{4.98}$$

Consider a hemisphere of radius R_1 drawn around the current electrode, A. The current is everywhere normal to the surface of this hemisphere, so the total current can be found by integrating the magnitude of the current density vector over the surface of the hemisphere:

$$\begin{aligned} I = \iint_S |\mathbf{j}|\,dS &= \int_0^{2\pi}\int_0^{\pi/2} |\mathbf{j}|\,R^2\sin\theta\,d\theta\,d\psi \\ &= \int_0^{2\pi}\int_0^{\pi/2} \frac{|C|\sin\theta}{\rho_\ell^{3/2}[1 + (\lambda^2 - 1)\cos^2\theta]^{3/2}}d\theta\,d\psi. \end{aligned} \tag{4.99}$$

The integration with respect to ψ is straightforward:

$$I = 2\pi \int_0^{\pi/2} \frac{|C|\sin\theta}{\rho_\ell^{3/2}[1 + (\lambda^2 - 1)\cos^2\theta]^{3/2}}d\theta. \tag{4.100}$$

This integral is a tabulated form for $\alpha = \cos\theta$:

$$I = 2\pi \int_0^1 \frac{|C|}{\rho_\ell^{3/2}}[1 + (\lambda^2 - 1)\alpha^2]^{-3/2}d\alpha = \frac{2\pi |C|}{\rho_\ell^{3/2}\lambda}. \tag{4.101}$$

Solving this last expression for C and considering that, according to Eq. (4.97) $C < 0$, we can now write the expression for potential as

$$U = \frac{I\lambda\rho_\ell^{3/2}}{2\pi\rho_\ell^{1/2}(x^2 + y^2 + \lambda^2 z^2)^{1/2}}. \tag{4.102}$$

In an anisotropic medium, the potential, U, is inversely proportional to the distance from the current source, but the constant of proportionality is a function of the angle θ. The equation for an equipotential surface is:

$$x^2 + y^2 + \lambda^2 z^2 = \left(\frac{2\pi U}{I\lambda\rho_\ell}\right)^{-2} = constant. \tag{4.103}$$

The equipotential surfaces described by this equation are ellipsoids of revolution.

If the potential were to be measured on the surface of the half-space at a distance, a, from the current source, it will be found that

$$U = \frac{I\lambda\rho_\ell}{2\pi a}. \tag{4.104}$$

Let us now normalize this potential observed over an anisotropic earth by dividing it by the potential that would have been measured over a homogeneous isotropic half-space with the resistivity ρ_ℓ:

$$U/U_n = 2\pi a\frac{U}{I\rho_\ell} = \lambda. \tag{4.105}$$

The potential over a uniform anisotropic half-space is larger than the potential over a uniform isotropic half-space by the factor, λ!

Consider that we drill a hole and measure the potential at a depth a from the source electrode on the z axis. The measured potential will be:

$$U = \frac{I\rho_\ell}{2\pi a}, \tag{4.106}$$

and the normalized potential is

$$U/U_n = 2\pi a\frac{U}{I\rho_\ell} = 1. \tag{4.107}$$

The potential is proportional to the longitudinal resistivity of an anisotropic medium when the electrode pair is placed transversely to the bedding, but is proportional to the quantity, λ when the electrode pair is oriented longitudinally with respect to the axes of anisotropy. This phenomenon is known as the *paradox of anisotropy*. It is of great importance in the interpretation of DC electrical sounding surveys.

4.3 ELECTROMAGNETIC FIELD DIFFUSION IN CONDUCTIVE MEDIA

We obtain the form of the quasi-stationary equation that we use in practice by neglecting the effect of displacement currents in Maxwell's equations (that is, we drop the term $\partial\mathbf{D}/\partial t$), but we retain the term representing electromagnetic induction (the term $\partial\mathbf{B}/\partial t$ in Maxwell's second equation):

$$curl\ \mathbf{H} = \sigma\mathbf{E}, \tag{4.108}$$

$$curl\ \mathbf{E} = -\partial \mathbf{B}/\partial t, \tag{4.109}$$

$$div\ \mathbf{B} = 0, \tag{4.110}$$

$$div\ \mathbf{E} = -\frac{1}{\sigma}\mathbf{E} \cdot grad\ \sigma. \tag{4.111}$$

In many of the applications of electrical prospecting we use electromagnetic fields which vary relatively slowly in time. In such cases, we can neglect the terms involving the second derivatives with respect to time in comparison with those involving the first derivative when we use the telegraphers' equations (3.75) and (3.76). As a result, we arrive at diffusion equations:

$$\nabla^2 \mathbf{E} - \mu\sigma\,\partial \mathbf{E}/\partial t = 0, \tag{4.112}$$

$$\nabla^2 \mathbf{H} - \mu\sigma\,\partial \mathbf{H}/\partial t = 0. \tag{4.113}$$

Thus, we describe the propagation of electromagnetic fields into conductive media as *electromagnetic diffusion*, or *quasi-stationary* behavior.

The *quasi-stationary* model of electromagnetic field behavior is characteristic of the majority of techniques used in geoelectric exploration; it occurs under conditions in which the components of the electromagnetic fields vary slowly enough that the second derivatives with respect to time in the field equations (Eqs. (3.1)–(3.15)) can be ignored in comparison with the first derivatives. When this is done, the equations for the electromagnetic field take the form

$$curl\ \mathbf{H} = \sigma \mathbf{E}, \tag{4.114}$$

$$curl\ \mathbf{E} = -\partial \mathbf{B}/\partial t. \tag{4.115}$$

We should note here that the divergence conditions expressed in Eqs. (4.7) and (4.8) follow from Eqs. (4.5) and (4.6) in the more general case, and so we do not need to include them here. We also note that, with the exclusion of the terms with second derivatives in time, we no longer have a term including the displacement vector **D** or the dielectric permeability ϵ, and so, we conclude that in the quasi-stationary regime, electromagnetic fields are independent of the dielectric properties of the medium.

4.3.1 MONOCHROMATIC QUASI-STATIC EM FIELDS

Let us assume that the time dependence of an electromagnetic field is expressed by an exponential multiplier, $e^{-i\omega t}$. We then arrive at the following equations for the complex vector fields:

$$curl\ \mathbf{H} = \sigma \mathbf{E}, \tag{4.116}$$

$$curl\ \mathbf{E} = i\omega\mu_0\mathbf{H}. \tag{4.117}$$

In this system of equations, each equation depends on both **E** and **H**; it will be much more convenient to deal mathematically with equations in which these two fields have been separated. This separation is possible in a region D characterized by a constant electrical conductivity, σ, and a constant magnetic permeability, μ. To separate the variables, we first perform the curl operation on both sides of equations ((4.116) and (4.117)):

$$curl\ curl\ \mathbf{H} = \sigma\ curl\ \mathbf{E},$$

$$curl\ curl\ \mathbf{E} = i\omega\mu_0\ curl\ \mathbf{H}. \tag{4.118}$$

Substituting Eq. (4.116) into (4.118), we write:

$$curl\ curl\ \mathbf{H} = i\omega\mu_0\sigma\mathbf{H},$$
$$curl\ curl\ \mathbf{E} = i\omega\mu_0\sigma\mathbf{E}. \tag{4.119}$$

Making use of a vector identity (Eq. (4.57)) and the divergence conditions

$$div\ \mathbf{H} = 0,$$
$$div\ \mathbf{E} = 0, \tag{4.120}$$

following from Eq. (4.117), we have

$$\nabla^2\mathbf{H} + i\omega\mu_0\sigma\mathbf{H} = 0,$$
$$\nabla^2\mathbf{E} + i\omega\mu_0\sigma\mathbf{E} = 0. \tag{4.121}$$

We will now introduce an important notation in order to simplify the writing of further equations:

$$k^2 = i\omega\mu_0\sigma, \tag{4.122}$$

where k is called a *wave number* for reasons to be explained in the next paragraph. Using this notation, Eq. (4.121) can be written in the form we will most generally use:

$$(\nabla^2 + k^2)\mathbf{H} = 0,$$
$$(\nabla^2 + k^2)\mathbf{E} = 0. \tag{4.123}$$

These are the *Helmholtz equations* describing quasi-stationary electromagnetic field behavior. They represent the separation of the variables $\mathbf{E}$ and $\mathbf{H}$ in Maxwell's equations.

The wave number k defined above appears simple, but is a parameter of great importance in dealing with the geophysical use of electromagnetic fields. It is a complex number:

$$k = (i\omega\mu_0\sigma)^{1/2} = (i)^{1/2}(i\omega\mu_0\sigma)^{1/2}. \tag{4.124}$$

Using Euler's formula, the square root of the imaginary number, $i = (-1)^{1/2}$ can be shown to be:

$$\sqrt{i} = (e^{(\pi/2)/i})^{1/2} = \pm e^{(\pi/4)i} = \pm(1+i)/\sqrt{2}.$$

By convention, we will accept the roots for which

$$Re(k) > 0, \quad Im(k) > 0. \tag{4.125}$$

That is,

$$k = e^{(\pi/4)i}(\omega\mu_0\sigma)^{1/2} = (1+i)(\omega\mu_0\sigma/2)^{1/2}. \tag{4.126}$$

We will introduce another definition, λ:

$$(\omega\mu_0\sigma/2)^{1/2} = 2\pi/\lambda, \tag{4.127}$$

so that

$$k = (1+i)2\pi/\lambda. \tag{4.128}$$

Let us determine the physical dimensions of λ and k, recognizing that $\omega = 2\pi f = 2\pi/T$, where f is the temporal frequency in hertz (Hz), and T is the period of oscillation in seconds; that $\sigma = 1/\rho$, where σ is measured in siemens per meter, and taking μ to be the magnetic permeability of free space, $\mu_0 = 4\pi \times 10^{-7}$ ohm-seconds per meter:

$$\lambda = (10^7 \rho T)^{1/2}. \tag{4.129}$$

Thus, λ is measured in units of length (meters), while k is measured in inverse meters. We will expand on the physical meaning of λ below.

4.3.2 PLANE ELECTROMAGNETIC WAVES IN A HOMOGENEOUS MEDIUM

Using the basic theory for quasi-stationary electromagnetic fields as developed above, we can now examine one of the simplest yet most useful problems in electrical prospecting – the propagation of planar electromagnetic waves in a homogeneous medium.

We are given a homogeneous and isotropic medium characterized by the properties σ and μ. We will introduce a Cartesian coordinate system, x, y, z, with the z axis directed vertically downward. Let there be a field $\mathbf{H}, \mathbf{E}$ propagating in the medium with the field being harmonic in time, acting in the quasi-stationary regime, and having the following properties.

- The vectors $\mathbf{H}$ and $\mathbf{E}$ are constant over any given horizontal plane:

$$\mathbf{E} \equiv const, \mathbf{H} \equiv const, \ \text{for } z = const. \tag{4.130}$$

- The field attenuates with travel in the $+z$ direction:

$$\mathbf{E}, \mathbf{H} \to 0 \text{ as } z \to \infty. \tag{4.131}$$

Let us investigate the properties of this field. In view of condition (4.130),

$$\frac{\partial \mathbf{E}}{\partial x} \equiv \frac{\partial \mathbf{E}}{\partial y} \equiv \frac{\partial \mathbf{H}}{\partial x} \equiv \frac{\partial \mathbf{H}}{\partial y} \equiv 0. \tag{4.132}$$

Eq. (4.132) defines a plane wave propagating in the $\pm z$ direction. For such a plane wave, the Laplace operator gives:

$$\nabla^2\mathbf{H} = \partial^2\mathbf{H}/\partial z^2, \ \nabla^2\mathbf{E} = \partial^2\mathbf{E}/\partial z^2. \tag{4.133}$$

That is, for the Helmholtz equations we have:

$$\partial^2 \mathbf{H}/\partial z^2 + k^2 \mathbf{H} = 0, \tag{4.134}$$

$$\partial^2 \mathbf{E}/\partial z^2 + k^2 \mathbf{E} = 0. \tag{4.135}$$

These are called the *one-dimensional Helmholtz equations*. Their solution is straightforward:

$$\mathbf{H} = \mathbf{H}^+ e^{ikz} + \mathbf{H}^- e^{-ikz}, \tag{4.136}$$

$$\mathbf{E} = \mathbf{E}^+ e^{ikz} + \mathbf{E}^- e^{-ikz}, \tag{4.137}$$

where $\mathbf{H}^+$, $\mathbf{H}^-$, $\mathbf{E}^+$, $\mathbf{E}^-$ are arbitrary constant vectors, in general complex, which must still be determined. Let us examine the exponential terms e^{ikz} and e^{-ikz} more carefully:

$$e^{ikz} = e^{-gz} e^{igz}, \tag{4.138}$$

$$e^{-ikz} = e^{gz} e^{-igz}, \tag{4.139}$$

where $g = 2\pi/\lambda = (\omega\mu_0\sigma/2)^{1/2}$.

The imaginary exponential term in Eqs. (4.138) and (4.139) can be rewritten using Euler's theorem:

$$e^{\pm igz} = \cos (gz) \pm i \sin (gz). \tag{4.140}$$

The imaginary exponential terms are band-limited in amplitude to the range ± 1, while the real exponential terms either approach 0, if the negative exponential is concerned, or ∞, if the positive exponential is considered. The physical reality of our problems requires that any terms which become large without limit at great depth in the earth ($z \to +\infty$) must be accompanied by a zero multiplier, and so, we can set two of the arbitrary vector constants to zero for this reason:

$$\mathbf{H}^- = 0, \ \ \mathbf{E}^- = 0.$$

Our final result is:

$$\mathbf{H} = \mathbf{H}^+ e^{ikz}, \ \ \mathbf{E} = \mathbf{E}^+ e^{ikz}. \tag{4.141}$$

It is probably necessary to take note of the fact that the procedure for setting the two arbitrary vector constants, $\mathbf{H}^-$ and $\mathbf{E}^-$, equal to zero is not general, but limited to the case of a totally uniform medium. Physically, we expect an electromagnetic wave to attenuate in the direction in which it is propagating. If there are boundaries in the medium which reflect a part of the incident field, in the more general case, all four arbitrary vector constants, $\mathbf{H}^\pm$ and $\mathbf{E}^\pm$, *can* be nonzero for given problems.

We can now express the components of the vectors $\mathbf{H}$ and $\mathbf{E}$ in Cartesian coordinates with basis vectors $\mathbf{d}_x$, $\mathbf{d}_y$, $\mathbf{d}_z$. By so doing, we can rewrite the vector equation (4.141) as a set of scalar equations. For example, for the magnetic field we have:

$$H_x = H_x^+ e^{ikz}, \ H_y = H_y^+ e^{ikz}, \ H_z = H_z e^{ikz};$$

or, in more compact notation:

$$H_{x(y,z)} = H^+_{x(y,z)} e^{ikz}. \tag{4.142}$$

Similarly, we have for the electric field components

$$E_{x(y,z)} = E^+_{x(y,z)} e^{ikz}. \tag{4.143}$$

Differentiating Eqs. (4.142) and (4.143) with respect to z, we have

$$\partial H_{x(y,z)}/\partial z = ik H_{x(y,x)},$$
$$\partial E_{x(y,z)}/\partial z = ik E_{x(y,z)}. \tag{4.144}$$

From Eqs. (4.142) and (4.143) and from Maxwell's equation (4.120), it follows that, for plane waves traveling vertically downward in the medium, the vertical components of the field, H_z and E_z, are zero. Furthermore, in view of Eq. (4.120) and Eq. (4.132), we have

$$\partial H_z/\partial z = 0, \ \ \partial E_z/\partial z = 0. \tag{4.145}$$

Substituting Eqs. (4.142) and (4.143) into (4.145) and considering that $k \neq 0$, we find that, for our vertically traveling plane wave,

$$H_z \equiv E_z \equiv 0.$$

Therefore, the field vectors in a vertically traveling plane wave lie in horizontal planes (see Fig. 4.5).

We will now examine Eqs. (4.142) and (4.143), which were developed above. First of all, let us examine the physical nature of the fields $Re(\mathbf{H}e^{-i\omega t})$, $Re(\mathbf{E}e^{-i\omega t})$. Let us look at one component of the magnetic field:

$$Re(H_x e^{-i\omega t}) = Re(H^+_x e^{ikz} e^{-i\omega t}). \tag{4.146}$$

We note that the vector constant, H^+_x, is itself complex:

$$H^+_x = H_{x0} e^{i\phi_x}, \tag{4.147}$$

where $H_{x0} = |H^+_x|$ and $\phi_z = \arg H^+_x$. Substituting (4.147) and (4.138) into (4.146), we find:

$$Re[H_x e^{-i\omega t}] = Re \left\{ H_{x0} e^{igz} e^{i\phi_x} e^{-gz} e^{-i\omega t} \right\}$$
$$= Re \left\{ H_{x0} e^{-gz} e^{i(\phi x + gz - \omega t)} \right\} = H_{x0} e^{-gz} \cos(\phi_x + gz - \omega t), \tag{4.148}$$

where $g = 2\pi/\lambda$.

Let us designate

$$H_{x0} e^{-gz} = a(z) \tag{4.149}$$
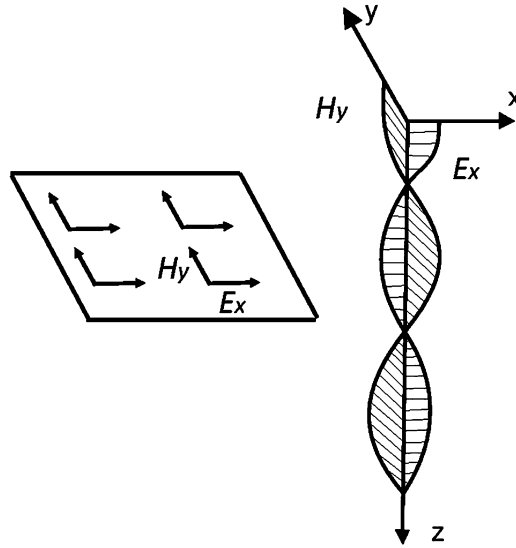
FIGURE 4.5

In a downward-traveling plane electromagnetic wave, the magnetic and electric vectors lie in horizontal planes.

as the amplitude of the field, and

$$\phi_x + gz - \omega t = \Phi(z) \tag{4.150}$$

as the phase of the field.

We see that at any instant in time, the amplitude of the field, $Re(H_x e^{-i\omega t})$ varies with z cosinusoidally, but damped with an exponential attenuating factor. The amplitude of the field is also characterized by a *wave length* given by $\lambda = 2\pi/g$ (the precise definition of wave length will be given below). The greater the wave length, the less rapidly the amplitude of the field component decays with depth; conversely, the shorter the wave length, the more rapidly attenuation with depth takes place. Thus, we can speak of the flow of the field and of a plane electromagnetic wave. However, it must be remembered that in the quasi-stationary approximation, the electromagnetic field is described neither by the telegraphers' equations nor by the wave equations, but by the diffusion equation (Eqs. (4.112) and (4.113)). The propagation of the field into the medium follows the diffusion law, and so the term *electromagnetic wave* is somewhat misleading in this case.

We now specify some definitions.

Definition 30. The *phase front of an electromagnetic wave* is the surface formed by all points having the same oscillatory phase.

In the case we have been examining, the equation for the phase front is given by:

$$\Phi(z) = \phi_x + gz - \omega t = const.$$

Hence

$$z = (\omega t - \phi_x + const)/g \qquad (4.151)$$

is the phase front of a plane wave propagating vertically in the earth. At any instant in time, t, the phase front is a horizontal plane. This is another basis for calling the wave we have been examining a plane wave, in addition to the property that **H** and **E** are constant over the phase front.

Definition 31. The *phase velocity of propagation of an electromagnetic wave* is the rate of movement of the phase front.

The rate of movement of an electromagnetic wave is obtained by differentiating Eq. (4.151) with respect to time, t:

$$v = \partial z/\partial t = (\omega/2\pi)\lambda = \lambda/T, \qquad (4.152)$$

with $\omega = 2\pi/T$, and with T being the period of an oscillation. Let us recall that, in accord with Eq. (4.129),

$$\lambda = (10^7 \rho T)^{1/2}$$

and so

$$v = (10^7 \rho/T)^{1/2}. \qquad (4.153)$$

In this expression, ρ is measured in ohm-meters, T in seconds, and v in meters per second.

And so the velocity v is larger for higher values of resistivity and for shorter periods of wave oscillation. This specification of velocity indicates that the velocity can increase without limit as the resistivity of a rock increases. In fact, however, we know that the speed of propagation of an electromagnetic field cannot exceed the velocity of light, which is about 300,000 kilometers per second (3×10^8 meters per second). This contradiction has arisen because we have considered a quasi-static model for electromagnetic waves in which displacement currents have been ignored. However, for geophysical applications in which measurements are carried out over comparatively small areas on the surface of the earth for which the linear dimensions are insignificantly small with the wave length of an electromagnetic field, the error caused by this simplification of the field behavior can be ignored.

Fig. 4.6 shows graphically the phase velocities for electromagnetic waves as a function of frequency of oscillation and resistivity of the medium. For values of resistivities normally encountered in rocks, and for the frequencies most often used in geophysical practice, the phase velocities are far lower than the speed of light.

Definition 32. The *wave length of an electromagnetic wave* is the distance between wave fronts which are separated in time by one period of oscillation.

The usual definition of wave length applies here; it is the product of phase velocity and oscillatory period:

$$\lambda = vT = (10^7 \rho T)^{1/2}. \qquad (4.154)$$
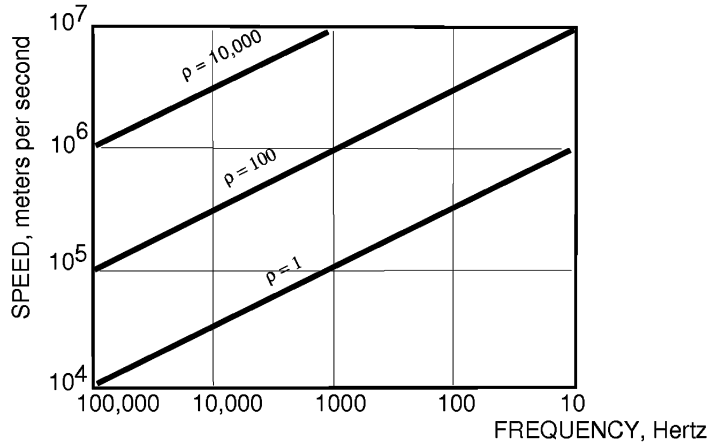
Phase velocities of electromagnetic waves traveling through a medium with uniform resistivity.

This confirms our earlier speculation that the parameter λ is in fact a wave length.

A concept of extreme importance in the theory of electrical exploration with electromagnetic fields is that of the depth of penetration of the electromagnetic field into the earth. By convention, this has been taken to be a *skin depth*.

Definition 33. The *skin depth* for an electromagnetic field propagating in a conductive earth is the distance over which the amplitude of the wave, $a(z)$ has been reduced by the factor $1/e = 0.3678794411$.

The skin depth will be characterized by the symbol δ_e. Its algebraic definition is:

$$a(z)/a(z + \delta_e) = e^1. \tag{4.155}$$

By substituting Eq. (4.149) in Eq. (4.155), we can write:

$$e^{2\pi \delta_e/\lambda} = e.$$

Converting this equation to the domain of logarithms (a *Napierian transform*), we can write:

$$\delta_e = \lambda/2\pi \approx 0.159\lambda. \tag{4.156}$$

Or, in terms of Eq. (4.154),

$$\delta_e = (10^7 \rho T/4\pi^2)^{1/2} \approx 0.159(10^7 \rho T)^{1/2}. \tag{4.157}$$

The dimension of skin depth is length.

Let us now examine Eq. (4.157) more closely. We see that the depth of penetration of an electromagnetic field is greater for larger values of resistivity, ρ. In an insulating material δ_e tends to become

infinite; that is, the field propagates to great distances with practically no attenuation. On the other hand, in highly conductive rock, δ_e tends to zero. This factor, in particular, leads to the phenomenon of *screening* of electromagnetic fields (as, for example, radio waves) by metallic conductors.

These physical phenomena can be explained heuristically as follows. As an electromagnetic field penetrates a conductor, its energy is expended on the "vibration" of free electrical charge carriers present in the conductor. The vibrations excited by the electromagnetic field represent conversion of the energy of the electromagnetic field to heat. Obviously, the conversion of electromagnetic energy to vibrational energy is greater when the number of free charge carriers in the medium is greater. As a result, the field in a conductor loses energy rapidly as it travels, and is attenuated. When an electromagnetic field travels into an extensive conductor, its energy is almost entirely lost in a zone near the entry surface; this zone is like a skin protecting the interior of the conductor from penetration by the electromagnetic field, and hence, the name skin effect.

In an insulator, there are no free charge carriers to vibrate and extract energy from the electromagnetic field, and so in such materials, the field can propagate to great distances.

An important consequence of formula (4.157) lies in the fact that the depth of penetration of a field depends on the period of oscillation, T, (or, if you wish, on frequency, ω). The longer the period of the oscillation, or the lower the frequency, the further will the field penetrate into a conductive earth. This particular behavior of an electromagnetic field is used to control the depth of penetration when a sounding of the earth is to be made. Progressively greater penetration can be obtained if measurements are made with a series of progressively lower frequencies. This procedure is the basis for the *frequency sounding* methods used widely in electromagnetic geophysics.

4.3.3 ELECTROMAGNETIC POTENTIALS

We have demonstrated in the first section of Chapter 3 that every forth field, F, which is a linear combination of the magnetic flux and electric voltage,

$$F = \mathbf{B} \cdot d\mathbf{\Sigma} + (\mathbf{E} \cdot d\mathbf{r}) \wedge dt,$$

can be expressed using the *electromagnetic potential*s (see Eqs. (3.26) and (3.27)).

A similar result could be obtained directly from Eqs. (4.116) and (4.117) of a monochromatic quasi-static EM field in a homogeneous isotropic medium. In view of Eq. (4.120), the magnetic field **H** is *solenoidal* (the magnetic flux lines flow along closed paths) and can be written as

$$\mathbf{H} = curl\, \mathbf{A}, \tag{4.158}$$

where the auxiliary field quantity **A** bears the name *electromagnetic vector potential*.[1]

Substituting Eq. (4.158) into Eq. (4.117), we have:

$$curl\, \mathbf{E} = i\omega\mu_0 curl\, \mathbf{A},$$

---

[1]In this section, for simplicity, we use the same notation, **A**, for the vector potential, as in Chapters 2 and 3. However, note, that in the previous chapters the electromagnetic vector potential was introduced for magnetic induction field **B**, while in this section we consider a vector potential for vector magnetic field **H**.

$$curl\,(\mathbf{E} - i\omega\mu_0\mathbf{A}) = 0.$$

Because the term in parentheses above has a curl of zero, it can be written as the gradient of some scalar function, U, which is named the *scalar electromagnetic potential*:

$$\mathbf{E} - i\omega\mu_0\mathbf{A} = -grad\,U,$$

and so

$$\mathbf{E} = i\omega\mu_0\mathbf{A} - grad\,U. \tag{4.159}$$

Next, we rewrite the first of Maxwell's equations (Eq. (4.116)) in terms of these electromagnetic potentials:

$$curl\,curl\mathbf{A} = i\omega\mu_0\sigma\mathbf{A} - \sigma\,grad\,U,$$

or, using the vector identity given earlier in Eq. (4.57) and the definition of Eq. (4.122):

$$\nabla^2\mathbf{A} + k^2\mathbf{A} = grad\,(div\,\mathbf{A} + \sigma U). \tag{4.160}$$

In Chapter 2 we have proved a uniqueness Theorem 18 of determining the vector field by its curl and divergence. We should note, however, that, while we have determined the curl of the vector potential in Eq. (4.158), the divergence of this potential remains undetermined. We can arbitrarily specify that:

$$div\,\mathbf{A} = -\sigma U. \tag{4.161}$$

Other convenient specifications for the divergence can be conceived; the gauge defined by Eq. (4.161) is known as the *Lorentz gauge*. With use of this gauge condition, Eq. (4.160) can be rewritten in the form of a Helmholtz equation:

$$\nabla^2\mathbf{A} + k^2\mathbf{A} = 0. \tag{4.162}$$

Substituting Eq. (4.159) into Eq. (4.120) and considering Eq. (4.161), we can write an analogous equation for the scalar potential:

$$\nabla^2 U + k^2 U = 0. \tag{4.163}$$

In summary, we have transformed a problem requiring the solution for six unknown variables (the six scalar components of the vectors $\mathbf{E}$ and $\mathbf{H}$) to a problem requiring the solution for four unknown variables (the three scalar components of the vector potential $\mathbf{A}$ and the single variable, the scalar potential U). This reduction in the number of variables allows us in many cases, as we will see below, to markedly simplify the solution of problems in electrodynamics.

4.3.4 QUASI-STATIONARY FIELD OF A DIPOLE SOURCE IN A HOMOGENEOUS MEDIUM

The utility of electromagnetic potentials can be demonstrated using as an example determination of the field from a dipole source energized with an oscillatory electric current illuminating an isotropic
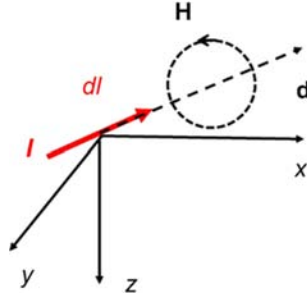
FIGURE 4.7

Current dipole in a homogeneous medium. The length, dl, is physically short. The dipole is energized with a current I, providing a dipole moment, Idl. The magnetic field, **H**, is concentric with the direction of the wire.

homogeneous medium. We suppose that a dipole of length $d\ell$ is located at the origin of a Cartesian coordinate system, and directed along an arbitrarily directed unit vector **d** (see Fig. 4.7). The dipole is driven with a current that varies harmonically in time, $I = I_0 e^{-i\omega t}$, with $I_0 = const$ being the amplitude of the current to the dipole. The properties of the medium σ and μ_0 are constant and known. We are required to determine the electromagnetic field **E** and **H** at every point in the medium surrounding the dipole source.

Initially, we will treat the simple case in which the frequency of the current driving the dipole is zero. According to the Biot-Savart law (Eq. (4.70)), the magnetic field of a dipole driven by constant current and observed at a point defined by the radius vector **r** is:

$$\mathbf{H}^0(\mathbf{r}) = (\mathbf{p} \times \mathbf{r})/4\pi r^3, \tag{4.164}$$

where **p** is the current moment of the dipole, defined as

$$\mathbf{p} = p\mathbf{d} = I_0 d\ell \mathbf{d}. \tag{4.165}$$

It is not difficult to decide that the vector potential $\mathbf{A}^0$ for a constant magnetic field $\mathbf{H}^0$ is:

$$\mathbf{A}^0 = \mathbf{p}/4\pi r. \tag{4.166}$$

To verify that this is correct, we can apply the curl operation to $\mathbf{A}^0$, using the rule for differentiating the product of a scalar, $f(\mathbf{r})$, and a vector, $\mathbf{F}(\mathbf{r})$, functions:

$$curl\ [f(\mathbf{r})\mathbf{F}(\mathbf{r})] = [grad\ f(\mathbf{r}) \times \mathbf{F}(\mathbf{r})] + f(\mathbf{r})\ curl\ \mathbf{F}(\mathbf{r}). \tag{4.167}$$

Applying this,

$$curl\ \mathbf{A}^0(\mathbf{r}) = \frac{1}{4\pi} curl\ (\mathbf{p}/r) = \frac{1}{4\pi} grad\frac{1}{r} \times \mathbf{p}$$
$$= [\mathbf{p} \times \mathbf{r}]/4\pi r^3 = \mathbf{H}^0(\mathbf{r}).$$

Let us turn now to the more general case in which $\omega \neq 0$. Using the results from Eqs. (4.158), (4.159), and (4.161) for an electromagnetic field about a dipole excited with a time-varying current, we can write the expressions for magnetic and electric fields using the vector potential $\mathbf{A}$:

$$\mathbf{H} = curl\ \mathbf{A},$$
$$\mathbf{E} = i\omega\mu_0\mathbf{A} + (1/\sigma)grad\ div\ \mathbf{A}, \tag{4.168}$$

where $\mathbf{A}$ satisfies the Helmholtz equation.

We write Eq. (4.162) in a spherical set of coordinates (r, ϕ, θ) with its origin coincident with the origin of the Cartesian system used earlier:

$$\frac{1}{r^2}\frac{\partial}{\partial r}\left(r^2\frac{\partial \mathbf{A}}{\partial r}\right) + \frac{1}{r^2 sin\ \theta}\frac{\partial}{\partial \theta}\left(sin\ \theta\frac{\partial \mathbf{A}}{\partial \theta}\right) + \frac{1}{r^2 sin^2\theta}\frac{\partial^2 \mathbf{A}}{\partial \phi^2} + k^2\mathbf{A} = 0. \tag{4.169}$$

As always, we must find a solution to this equation which tends to zero at infinity and which matches $\mathbf{A}^0$ at $\omega = o$. We note that in accord with Eq. (4.166), the potential for a constant dipole $\mathbf{A}^0$ is characterized by spherical symmetry, and so we expect the solution of Eq. (4.169) to fall in the class of spherically symmetric functions. With such symmetry, the derivatives with respect to the coordinates θ and ϕ in Eq. (4.169) disappear, and we have only

$$\frac{1}{r^2}\frac{\partial}{\partial r}\left(r^2\frac{\partial \mathbf{A}}{\partial r}\right) + k^2\mathbf{A} = 0. \tag{4.170}$$

The left-hand part of this equation can be transformed to be an exact differential:

$$\frac{1}{r}\left[\frac{1}{r}\frac{\partial}{\partial r}\left(r^2\frac{\partial \mathbf{A}}{\partial r}\right)\right] = \frac{1}{r}\left[2\frac{\partial \mathbf{A}}{\partial r} + r\frac{\partial^2 \mathbf{A}}{\partial r^2}\right] = \frac{1}{r}\frac{\partial^2}{\partial r^2}(r\mathbf{A}).$$

Consequently, Eq. (4.170) can be written as:

$$\frac{\partial^2}{\partial r^2}(r\mathbf{A}) + k^2 r\mathbf{A} = 0. \tag{4.171}$$

The general solution to Eq. (4.171) is:

$$r\mathbf{A} = \mathbf{c}_1 e^{ikr} + \mathbf{c}_2 e^{-ikr}, \tag{4.172}$$

where $\mathbf{c}_1$ and $\mathbf{c}_2$ are undetermined vector constants.

Remembering that we have accepted the convention that $Im(k) > 0$, the exponential term e^{ikr} tends to zero as $r \to \infty$, while the exponential term e^{-ikr} becomes large without limit as r increases. Consequently, physical reality requires that $\mathbf{c}_2$ be zero. So

$$\mathbf{A}(\mathbf{r}) = \mathbf{c}_1 e^{ikr}/r. \tag{4.173}$$

We evaluate the other unknown vector constant by using the limit condition as $\omega \to 0$. In accord with Eq. (4.166),

$$\lim_{\omega \to 0}\mathbf{A}(\mathbf{r}) = \mathbf{c}_1\frac{1}{r} = \mathbf{A}^0(\mathbf{r}) = \frac{\mathbf{p}}{4\pi r}, \tag{4.174}$$

so that

$$\mathbf{c}_1 = \mathbf{p}/4\pi. \tag{4.175}$$

Substituting (4.175) into (4.173), we obtain the result:

$$\mathbf{A}(\mathbf{r}) = \frac{e^{ikr}}{4\pi r}\mathbf{p}. \tag{4.176}$$

This equation specifies the vector potential for an electromagnetic field excited by a time-varying current dipole in an infinite homogeneous isotropic medium. By substituting this vector potential in Eq. (4.168), we find the vector fields $\mathbf{E}$ and $\mathbf{H}$:

$$\mathbf{H}(\mathbf{r}) = \frac{1}{4\pi} curl \left(\frac{e^{ikr}}{r}\mathbf{p} \right), \tag{4.177}$$

$$\mathbf{E}(\mathbf{r}) = \frac{i\omega\mu_0}{4\pi} \frac{e^{ikr}}{r}\mathbf{p} + \frac{1}{4\pi\sigma} grad\, div \left(\frac{e^{ikr}}{r}\mathbf{p} \right). \tag{4.178}$$

In carrying out the curl operation in Eq. (4.177), we make use of Eq. (4.167):

$$curl \left(\frac{e^{ikr}}{r}\mathbf{p} \right) = grad\frac{e^{ikr}}{r} \times \mathbf{p}, \tag{4.179}$$

while in carrying out the divergence operation on Eq. (4.178), we make use of the vector identity for divergence of the product of a scalar and vector function,

$$div[f(\mathbf{r}) \cdot \mathbf{F}(\mathbf{r})] = grad\, f(\mathbf{r}) \cdot \mathbf{F}(\mathbf{r}) + f(\mathbf{r})\, div\, \mathbf{F}(\mathbf{r}), \tag{4.180}$$

and so

$$div \left(\frac{e^{ikr}}{r}\mathbf{p} \right) = grad \left(\frac{e^{ikr}}{r} \right) \cdot \mathbf{p}. \tag{4.181}$$

In turn, the gradient term in this last equation is:

$$grad \left(\frac{e^{ikr}}{r} \right) = \frac{\partial}{\partial r} \left(\frac{e^{ikr}}{r} \right) grad\,\, \mathbf{r} = -e^{ikr}\frac{(1 - ikr)\mathbf{r}}{r^3}. \tag{4.182}$$

Substituting this result in Eqs. (4.179) and (4.181), and taking Eq. (4.177) into account, we can write:

$$\mathbf{H}(\mathbf{r}) = \frac{e^{ikr}}{4\pi r^3}(1 - ikr)[\mathbf{p} \times \mathbf{r}], \tag{4.183}$$

$$\mathbf{E}(\mathbf{r}) = \frac{i\omega\mu_0}{4\pi} \frac{e^{ikr}}{r}\mathbf{p} - \frac{1}{4\pi\sigma} grad \left(e^{ikr}\frac{(1 - ikr)}{r^3}\mathbf{p} \cdot \mathbf{r} \right). \tag{4.184}$$

We can expand these expressions algebraically as follows:

$$grad\ \left(\frac{e^{ikr}(1-ikr)}{r^3}\mathbf{p}\cdot\mathbf{r}\right) = grad\ \left(\frac{e^{ikr}(1-ikr)}{r^3}\right)(\mathbf{p}\cdot\mathbf{r}) + \frac{e^{ikr}(1-ikr)}{r^3}\ grad\ (\mathbf{p}\cdot\mathbf{r})$$

$$= -\frac{e^{ikr}(3-3ikr-k^2r^2)}{r^3}\left(\mathbf{p}\cdot\frac{\mathbf{r}}{r}\right)\frac{\mathbf{r}}{r} + \frac{e^{ikr}(1-ikr)}{r^3}\mathbf{p}. \qquad (4.185)$$

Substituting Eq. (4.185) in Eq. (4.184), and taking Eq. (4.122) into consideration, our result is:

$$\mathbf{E(r)} = -\frac{e^{ikr}}{4\pi\sigma r^3}(1-ikr-k^2r^2)\mathbf{p} + \frac{e^{ikr}}{4\pi\sigma r^3}(3-3ikr-k^2r^2)\left(\frac{\mathbf{p}\cdot\mathbf{r}}{r}\right)\frac{\mathbf{r}}{r}. \qquad (4.186)$$

In summary, Eqs. (4.183) and (4.186) are the solutions to the stated problem, that of determining the electromagnetic field vectors about a current dipole source.

4.3.5 SPHERICAL ELECTROMAGNETIC WAVES

Let us examine the solution which was determined in the last section a bit more closely. First of all, we note that the vector potential **A** described in Eq. (4.176) has spherical symmetry; that is, the value of the potential depends only on the distance, r, from the dipole source, even though the dipole has a direction specified by the dipole moment **p**. Moreover, the magnetic field **H** is orthogonal to the vectors **p** and **r** at every point in the medium. This last property arises simply because the scalar product of the vector $[\mathbf{p}\times\mathbf{r}]$ with either the vector **p** or the vector **r** is zero. Geometrically this means that if we draw a sphere with radius r around the origin and construct a plane T tangent to the sphere at some point M, the vector field **H** lies in the plane T (Fig. 4.8). More exactly, the vector **H** is directed along the line of intersection of the plane T and a plane N passing through the point M and orthogonal to the moment vector **p** of the current dipole.

Next, let us examine the orientation of the vector **E** for the electric field. To do this, we will resolve the current moment of the source, **p** into two components, one radial, $\mathbf{p}_r$, and the other tangential, $\mathbf{p}_\tau$, parallel to the plane T:

$$\mathbf{p} = \mathbf{p}_r + \mathbf{p}_\tau, \qquad (4.187)$$

where

$$\mathbf{p}_r = \left(\frac{\mathbf{p}\cdot\mathbf{r}}{r}\right)\frac{\mathbf{r}}{r}, \qquad (4.188)$$

$$\mathbf{p}_\tau = \mathbf{p} - \left(\frac{\mathbf{p}\cdot\mathbf{r}}{r}\right)\frac{\mathbf{r}}{r}. \qquad (4.189)$$

Substituting these two definitions in Eq. (4.186), we have:

$$\mathbf{E(r)} = -\frac{e^{ikr}}{4\pi\sigma r^3}(1-ikr-k^2r^2)\mathbf{p}_\tau + \frac{e^{ikr}}{2\pi\sigma r^3}(1-ikr)\mathbf{p}_r$$

$$= \mathbf{E}_\tau(\mathbf{r}) + \mathbf{E}_r(\mathbf{r}), \qquad (4.190)$$
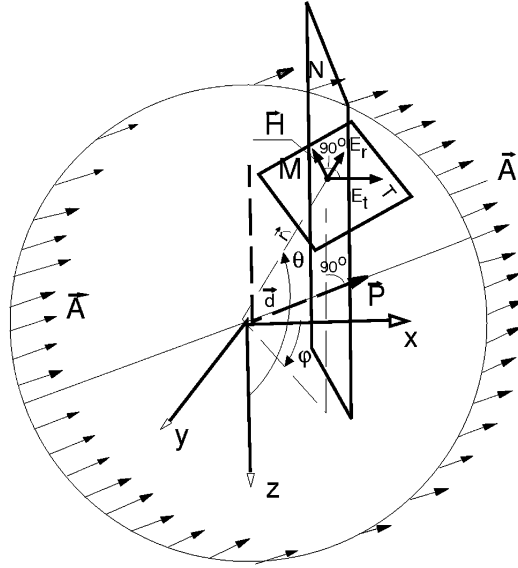
FIGURE 4.8

Geometrical representation of a spherical electromagnetic wave.

where $\mathbf{E}_\tau(\mathbf{r})$ is the tangential component of the electric field, which lies in the plane T:

$$\mathbf{E}_\tau(\mathbf{r}) = -\frac{e^{ikr}}{4\pi\sigma r^3}(1 - ikr - k^2r^2)\mathbf{p}_\tau, \tag{4.191}$$

and $\mathbf{E}_r(\mathbf{r})$ is the radial component of the electric field lying along the radius vector:

$$\mathbf{E}_r(\mathbf{r}) = \frac{e^{ikr}}{2\pi\sigma r^3}(1 - ikr)\mathbf{p}_r. \tag{4.192}$$

It is important to note that, in an isotropic material, the component $\mathbf{E}_\tau$ is always orthogonal to the magnetic field $\mathbf{H}$. In this respect, in view of (4.189), we have:

$$[\mathbf{p} \times \mathbf{r}] \cdot \mathbf{p}_\tau = [\mathbf{p} \times \mathbf{r}] \cdot \{\mathbf{p} - (\mathbf{p} \cdot \mathbf{r}/r)\mathbf{r}/r\}$$
$$= [\mathbf{p} \times \mathbf{r}] \cdot \mathbf{p} - [\mathbf{p} \times \mathbf{r}] \cdot \mathbf{r}/r(\mathbf{p} \cdot \mathbf{r}/r) = 0.$$

Hence, we find

$$\mathbf{H}(\mathbf{r}) \cdot \mathbf{E}_\tau(\mathbf{r}) = 0. \tag{4.193}$$

In summary, the vectors $\mathbf{H}$ and $\mathbf{E}_\tau$ lie in a reference plane T and are mutually orthogonal, as indicated in Fig. 4.8. This is the general structure of the electromagnetic field of a dipole source.

However, it must be stressed that all the ideas that have been developed apply to the real parts of a field, $Re(\mathbf{H}e^{-i\omega t})$ and $Re(\mathbf{E}e^{-i\omega t})$, and not to the complex vectors characterizing the field. Only the real part has any physical significance.

Next, let us examine the real part of the vector potential:

$$
\begin{aligned}
Re(\mathbf{A}e^{-i\omega t}) &= \frac{\mathbf{p}}{4\pi r} Re(e^{(ikr-i\omega t)}) \\
&= \frac{\mathbf{p}}{4\pi r} e^{-gr} \cdot Re[e^{i(gr-\omega t)}] \\
&= \frac{\mathbf{p}}{4\pi r} e^{-gr} \cos(gr - \omega t).
\end{aligned}
\tag{4.194}
$$

Here $a(r) = \frac{p}{4\pi r} e^{-gr}$ is the amplitude of the vector potential, and $\Phi(r) = 2\pi r/\lambda - \omega t$ is its phase.

We will find the phase fronts for the field from a current dipole, as was done earlier for a plane wave. The phase front is a surface formed from all points at which the phase has the same value:

$$
\Phi(r) = 2\pi r/\lambda - \omega t = const,
$$

and so

$$
r = (\omega t + const)\lambda/2\pi.
\tag{4.195}
$$

We see that, at any instant t, the phase fronts for a dipole field are spherical surfaces centered on the origin. An electromagnetic field of this form is called a spherical electromagnetic wave.

We can also use the travel time for such phase fronts to determine the speed of propagation of a spherical wave:

$$
v = dr/dt = \lambda/T = (10^7 \rho/T)^{1/2}.
\tag{4.196}
$$

The velocity of a spherical electromagnetic wave is the same as that of a plane wave! Consequently, the wave length of a spherical wave is also the same as that of a plane wave.

We should have noticed by now that the product kr has appeared repeatedly in these developments. We shall designate the modulus of this product, after division by the constant $2\sqrt{2}\pi$, the electrical distance, r_λ:

$$
r_\lambda = \frac{|kr|}{2\sqrt{2}\pi} = \frac{|1+i|}{\sqrt{2}} r/\lambda = r/\lambda.
$$

The electrical distance is dimensionless. Depending on the size of the electrical distance, r_λ, we recognize three intervals of particular interest:

- The near zone, defined as

$$
|kr| \ll 1 \text{ or } r \ll \lambda.
$$

- The intermediate zone, in which $|kr|$ has values of the order of unity,

$$|kr| \sim 1 \text{ or } r \sim \lambda.$$

- The far zone, in which

$$|kr| \gg 1 \text{ or } r \gg \lambda.$$

First of all, we note that in the intermediate zone, the electromagnetic field of a dipole is described by the full expressions, Eqs. (4.183), (4.191), and (4.192). In contrast, in the near zone, we can make an approximation as $|kr| \to 0$ in each of these equations:

$$\mathbf{H}(\mathbf{r}) = \mathbf{H}_\tau(\mathbf{r}) = \frac{1}{4\pi r^3}[\mathbf{p} \times \mathbf{r}], \tag{4.197}$$

$$\mathbf{E}_\tau(\mathbf{r}) = -\frac{1}{4\pi \sigma r^3}\mathbf{p}_\tau, \tag{4.198}$$

$$\mathbf{E}_r(\mathbf{r}) = \frac{1}{2\pi \sigma r^3}\mathbf{p}_r. \tag{4.199}$$

In the near zone, the electromagnetic field created by a dipole driven with a time-varying current is formally the same as the field of a constant current dipole.

In the far zone, where $|kr|$ is large, within each of the brackets in Eqs. (4.183), (4.191), and (4.192), we need retain only the terms with the highest powers of kr:

$$\mathbf{H}(\mathbf{r}) = \mathbf{H}_\tau(\mathbf{r}) = -ik\frac{e^{ikr}}{4\pi r^2}[\mathbf{p} \times \mathbf{r}], \tag{4.200}$$

$$\mathbf{E}_\tau(\mathbf{r}) = k^2\frac{e^{ikr}}{4\pi \sigma r}\mathbf{p}_\tau = \frac{i\omega\mu_0}{4\pi}\frac{e^{ikr}}{r}\mathbf{p}_\tau, \tag{4.201}$$

$$\mathbf{E}(\mathbf{r}) = -ik\frac{e^{ikr}}{2\pi \sigma r^2}\mathbf{p}_r. \tag{4.202}$$

We see from these equations that in the far zone, the radial component of the electric field decreases more rapidly with distance than does the tangential component, and so, at large distances, the radial component can be ignored. As a consequence, we can say that a spherical electromagnetic field at great distances from the source has but two components, one magnetic and one electric, which are orthogonal to one another and to the radius vector from the source. This behavior corresponds to the behavior of a plane wave. Distances at which this behavior is exhibited are often said to lie in the wave zone.

4.4 ELECTROMAGNETIC WAVES

The main power of Maxwell's equations is manifested by the fact that these equations allow us to evaluate the field behavior at some distant area in a later time if we know the field in the given moment in some vicinity of the point of observations. Let us consider, for example, a simple idealized experiment with a small, electrically charged sphere, located in the free space. We assume that this sphere

oscillates harmonically under the influence of some external force. The oscillations of the charges distributed over the sphere produce a variable electric field. This field generates a variable magnetic field, which in its turn, generates a variable electric field propagating away from the sphere, etc. We have established in the previous chapter that the propagation of the electromagnetic field is accompanied by the energy flow. In our experiment, the oscillating charge radiates some energy which propagates in the space with some velocity. This process is typical for the wave phenomenon.

Let us study the propagation of fields in insulating media using Maxwell's equations. When $\sigma = 0$, the telegraphers' equations (3.75) and (3.76) can be written as follows:

$$\nabla^2 \mathbf{E} - \mu \epsilon \partial^2 \mathbf{E}/\partial t^2 = 0, \tag{4.203}$$

$$\nabla^2 \mathbf{H} - \mu \epsilon \partial^2 \mathbf{H}/\partial t^2 = 0. \tag{4.204}$$

These equations are called *wave equations*. They describe the nature of electromagnetic wave propagation in nonconducting media. Any variation of the electric field generates the magnetic field; any variation of this magnetic field generates the electric field; etc. This field carries the energy and propagates in the space with the specific speed v determined, according to Eqs. (4.203) and (4.204), by the formula:

$$v = \frac{1}{\sqrt{\mu \epsilon}}. \tag{4.205}$$

It can be demonstrated based on Maxwell's equations that the vectors of electric and magnetic fields always lay in the plane perpendicular to the direction of the field propagation. Therefore, the corresponding electromagnetic wave is a transverse or shear wave. Moreover, if we substitute the expression for the magnetic permeability ($\mu_0 = 4\pi \times 10^{-7}$ henries per meter) and the dielectric constant ($\epsilon_0 = 8.854 \times 10^{-12}$ farads per meter) for a free space in formula (4.205), we will find immediately that the speed of electromagnetic wave propagation is equal to the speed of light, c:

$$v_0 = c = 300{,}000 \text{ km/s}.$$

This fact illustrates another genuine idea of Maxwell that the light is just an electromagnetic field propagation!

In the conclusion of this chapter we should note that there is a significant difference between the physics of the EM field propagation in the cases of the wave and diffusion equations. We can easily explain the nature of this difference for the model with a point δ-pulse source located in the homogeneous full space.

In the first case, the wave equation, there exists a sharp impulsive wavefront, traveling with some velocity c in the medium from the EM source location and passing across the point M located at a distance r from the source at the moment $t = r/c$. The magnitude of the EM wavefield is equal to zero at the point M prior to arrival of the wavefront and thereafter.

In the second case, the diffusion equation, the magnitude of the EM field excited by the impulsive δ-pulse source in every observational point M is about zero at early time, $t \to 0$, and then increases monotonically everywhere in the space, goes through the maximum in the different time moments for the different observation points, and decreases, being completely attenuated only as $t \to \infty$. In

other words, the diffusive EM field does not have a wavefront, it propagates instantly within the entire space. However, the time when the field reaches the maximum, depends on the distance to the source. The time it takes for the maximum to develop at a given distance can be used to define an apparent speed of the diffusive EM field propagation. We address this question in more details in Chapter 9 on electromagnetic migration.

REFERENCES AND RECOMMENDED READING TO CHAPTER 4

Alpin, L. M., 1966, Theory of the field: Nedra, Moscow, 384 pp.

Kaufman, A. A., 1992, Geophysical field theory and method, Part A, gravitational, electric and magnetic fields: Academic Press, New York, 581 pp.

Kaufman, A. A., and G. V. Keller, 1985, Inductive mining prospecting, Part I: Theory: Elsevier, Amsterdam, 620 pp.

Kong, J. A., 1975, Theory of electromagnetic waves: John Wiley & Sons, New York, 348 pp.

Maxwell, J. C., 1954, A treatise on electricity and magnetism: Dover Publ., New York, (unabridged and unaltered republication of the third edition of 1891), 506 pp.

Novozhilov, U. V., and U. A. Yappa, 1981, Electrodynamics: Mir Publishers, Moscow, 352 pp.

Schey, H. M., 1973, Div, grad, curl, and all that: An informal text on vector calculus: W. W. Norton & Co., New York, 163 pp.

Sommerfeld, A., 1952, Electrodynamics, Lectures on theoretical physics, Vol. III: Academic Press, New York, 371 pp.

Slater, J. C., and N. H. Frank, 1947, Electromagnetism: McGraw-Hill, New York, 240 pp.

Stratton, J. A., 1941, Electromagnetic theory: McGraw-Hill Book Company, New York and London, 615 pp.

Tamm, I. E., 1979, Fundamentals of the theory of electricity: Mir Publishers, Moscow, 684 pp.

Tralli, N., 1963, Classical electromagnetic theory: McGraw-Hill, New York, 308 pp.

Zhdanov, M. S., and G. Keller, 1994, The geoelectrical methods in geophysical exploration: Elsevier, Amsterdam, London, New York, Tokyo, 873 pp.

ELECTROMAGNETIC FIELDS IN HORIZONTALLY STRATIFIED MEDIA

5

CONTENTS

Perhaps the most widely used earth model when electromagnetic (EM) methods are considered is that of a set of horizontal layers. This model represents well some typical geological formations like sedimental deposits. It can also be used to describe a regional geological cross section formed by the
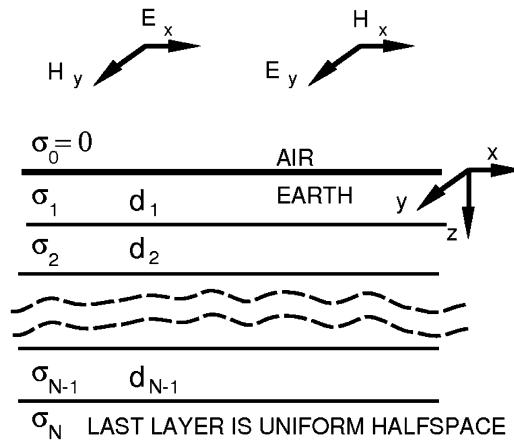
FIGURE 5.1

A model of a plane electromagnetic wave in a horizontally stratified medium. The electromagnetic field is excited in the earth by a downward-traveling plane electromagnetic wave.

horizontal layers of the earth's crust and upper mantle. This model is important in studying horizontally inhomogeneous geoelectrical structures as well. Indeed, a horizontally layered model can serve as a convenient background model for domains with anomalous conductivity distribution. In this chapter we will present the methods of the EM field calculation in horizontally layered models and conduct an analysis of the basic properties of this field. We will begin our analysis with the simplest case of a plane EM wave propagation in a layered formation.

5.1 PLANE WAVE PROPAGATION IN A LAYERED EARTH

A plane electromagnetic wave represents one of the fundamental models of an electromagnetic field used in geophysics. The advantage of this model is two-fold. On the one hand, the plane wave is the simplest possible model of electromagnetic field propagation. It is easy to obtain analytical solutions describing the propagation of a plane wave in layered media. On the other hand, this model represents a very good approximation of a natural electromagnetic field observed in magnetotelluric methods. In this section we will investigate the main properties of plane electromagnetic field propagation within horizontally layered formations.

5.1.1 PLANE ELECTROMAGNETIC WAVE IN A HORIZONTALLY STRATIFIED MEDIUM

Let us now consider the laws governing the travel of a plane electromagnetic wave into a flat earth built from a set of horizontal layers. In our examination of the problem as set up, we make use of a coordinate system with $z = 0$ at the boundary between the atmosphere and the solid earth (Fig. 5.1). The earth consists of N layers, each with a uniform conductivity, σ_i, and of a thickness, d_i. A monochromatic (single-frequency) quasi-stationary electromagnetic field is vertically incident on the earth, which we

will see, is a very good approximation in magnetotelluric problem. We will assume that the magnetic permeability is that of free space everywhere.

Referring to the results obtained earlier in Chapter 4, within each of the uniform layers, the vector electric and magnetic fields comprising a plane electromagnetic wave do satisfy the one-dimensional Helmholtz equations

$$\partial^2 \mathbf{H}/\partial z^2 + k_j^2 \mathbf{H} = 0,$$
$$\partial^2 \mathbf{E}/\partial z^2 + k_j^2 \mathbf{E} = 0, \tag{5.1}$$

for $z_{j-1} + 0 \leq z \leq z_j - 0$, and where, as usual, $k_j^2 = i\omega\mu_0\sigma_j$ is the wave number for the layer with index j, and $z_j = \sum_1^j d_i$ is the depth to the top of the layer with index j.

Solutions to these equations can be written as:

$$\mathbf{H}(z) = \mathbf{H}_j^+ e^{ik_j z} + \mathbf{H}_j^- e^{-ik_j z},$$
$$\mathbf{E}(z) = \mathbf{E}_j^+ e^{ik_j z} + \mathbf{E}_j^- e^{-ik_j z}, \tag{5.2}$$

where $\mathbf{H}_j^+, \mathbf{H}_j^-, \mathbf{E}_j^+, \mathbf{E}_j^-$, $j = 1, 2, ..., N$ are arbitrary vector constants.

Recall from Chapter 4 that electromagnetic field vectors in a plane wave will always lie in horizontal planes. Because of this, the vectors $\mathbf{E}$ and $\mathbf{H}$ will have null components in the z direction:

$$\mathbf{E} = (E_x, E_y, 0), \ \ \mathbf{H} = (H_x, H_y, 0).$$

As an example, the horizontal components of the electric field in layer j are written as:

$$E_x(z) = E_{x_j}^+ e^{ik_j z} + E_{x_j}^- e^{-ik_j z},$$
$$E_y(z) = E_{y_j}^+ e^{ik_j z} + E_{y_j}^- e^{-ik_j z}, \tag{5.3}$$

where $z_{j-1} + 0 \leq z \leq z_j - 0$ for all values of z within the layer j or on its bounding surfaces.

We now write the second of Maxwell's equations for plane electromagnetic waves, using the matrix representation of the term curl $\mathbf{E}$:

$$\begin{bmatrix} \mathbf{d}_x & \mathbf{d}_y & \mathbf{d}_z \\ \partial/\partial x & \partial/\partial y & \partial/\partial z \\ E_x & E_y & 0 \end{bmatrix} = i\omega\mu_0(H_x\mathbf{d}_x + H_y\mathbf{d}_y), \tag{5.4}$$

where $\mathbf{d}_x, \mathbf{d}_y, \mathbf{d}_z$ are unit vectors along the directions of a set of Cartesian coordinates.

Another property of plane waves is that the field components lying in the plane are instantaneously equal over the entire xy plane; therefore, the spatial derivatives with respect to these coordinates are zero:

$$\begin{bmatrix} \mathbf{d}_x & \mathbf{d}_y & \mathbf{d}_z \\ 0 & 0 & \partial/\partial z \\ E_x & E_y & 0 \end{bmatrix} = i\omega\mu_0(H_x\mathbf{d}_x + H_y\mathbf{d}_y), \tag{5.5}$$

where the differentiations are complete instead of partial, there being only one independent variable, z.

Expanding the matrix equation to obtain simpler algebraic equations, we arrive at the set:

$$H_x = -\frac{1}{i\omega\mu_0}\frac{dE_y}{dz}, \tag{5.6}$$

$$H_y = \frac{1}{i\omega\mu_0}\frac{dE_x}{dz}. \tag{5.7}$$

With appropriate substitution from the set (5.3) into the set (5.6) and (5.7), we have

$$H_x(z) = -\frac{k_j}{\omega\mu_0}(E_{y_j}^+ e^{ik_jz} - E_{y_j}^- e^{-ik_jz}), \tag{5.8}$$

$$H_y(z) = \frac{k_j}{\omega\mu_0}(E_{x_j}^+ e^{ik_jz} - E_{x_j}^- e^{-ik_jz}), \tag{5.9}$$

remembering, that these equations are valid only within the limits of the layer with the index j. Note that the magnetic field in each layer contains the same arbitrary constants as do the expressions for the electric field components.

Let us introduce the *wave impedance*, defined as:

$$Z_{xy} = E_x(z)/H_y(z), \tag{5.10}$$

$$Z_{yx} = -E_y(z)/H_x(z), \tag{5.11}$$

where Z is the ratio of an electric to a magnetic field, which has the dimensions of volts per ampere, or ohms.

The next step is to relate the tensor wave impedance to the character of the geoelectric structure of the earth. This is done by substituting the equations of set (5.3) and (5.9) into Eq. (5.10):

$$Z_{xy}(z) = \frac{\omega\mu_0}{k_j}\frac{E_{x_j}^+ e^{ik_jz} + E_{x_j}^- e^{-ik_jz}}{E_{x_j}^+ e^{ik_jz} - E_{x_j}^- e^{-ik_jz}}. \tag{5.12}$$

Remember, the impedance expression is valid only within each layer having the subscript j. This expression can be made more tractable if the numerator and denominator are divided by the factor $(E_{x_j}^+ E_{x_j}^-)^{1/2}$:

$$Z_{xy} = \frac{\omega\mu_0}{k_j}\frac{(E_{x_j}^+/E_{x_j}^-)^{1/2}e^{ik_jz} + (E_{x_j}^-/E_{x_j}^+)^{1/2}e^{-ik_jz}}{(E_{x_j}^+/E_{x_j}^-)^{1/2}e^{ik_jz} - (E_{x_j}^-/E_{x_j}^+)^{1/2}e^{-ik_jz}}. \tag{5.13}$$

If we introduce the notation,

$$q_j = -\ln(E_{xj}^+/E_{xj}^-)^{1/2},$$

the wave impedance equation becomes:

$$Z_{xy}(z) = \frac{\omega\mu_0}{k_j}\frac{e^{(ik_jz-q_j)} + e^{-(ik_jz-q_j)}}{e^{(ik_jz-q_j)} - e^{-(ik_jz-q_j)}}$$

$$= \frac{\omega\mu_0}{k_j}coth\,(ik_jz - q_j), \tag{5.14}$$

for $z_{j-1} + 0 \le z \le z_j - 0$.

By this trickery, we have reduced the two arbitrary constants for each layer, to a single arbitrary constant, q, for each layer. This set of constants is evaluated using boundary conditions at the boundaries between each layer. The horizontal components of the electric and magnetic fields are continuous across the boundaries between layers, as was pointed out in Chapter 3. Therefore, the wave impedance is also continuous across the surfaces between layers:

$$Z_{xy}(z_j - 0) = Z_{xy}(z_j + 0). \tag{5.15}$$

Substituting the left-hand term from this equation into Eq. (5.14):

$$\frac{\omega\mu_0}{k_j} coth \ (ik_j z_j - q_j) = Z_{xy}(z_j + 0),$$

and hence

$$q_j = ik_j z_j - coth^{-1} \left[\frac{k_j}{\omega\mu_0} Z_{xy}(z_j + 0) \right]. \tag{5.16}$$

Substituting this newly found value for q_j in Eq. (5.14) and substituting the z coordinate $z = z_{j-1} + 0$, we obtain:

$$Z_{xy}(z_{j-1} + 0) = -\frac{\omega\mu_0}{k_j} coth \left\{ ik_j d_j - coth^{-1} \left[\frac{k_j}{\omega\mu_0} Z_{xy}(z_j + 0) \right] \right\}. \tag{5.17}$$

This equation comprises a recursive relationship tying the wave impedance from layer $j + 1$ to the wave impedance in layer j. This recursive procedure can be used to expand the expression for wave impedance at the earth's surface (where we can measure it physically) through any number of layers, removing the arbitrary constants, q_j, one by one:

for $j = 1$,

$$Z_{xy}(+0) = -\frac{\omega\mu_0}{k_1} coth \left\{ ik_1 d_1 - coth^{-1} \left(\frac{k_1}{\omega\mu_0} Z_{xy}(z_1 + 0) \right) \right\},$$

for $j = 2$,

$$Z_{xy}(z_1 + 0) = -\frac{\omega\mu_0}{k_2} coth \left\{ ik_2 d_2 - coth^{-1} \left(\frac{k_2}{\omega\mu_0} Z_{xy}(z_2 + 0) \right) \right\},$$

.
.
.

for $j = N - 2$,

$$Z_{xy}(z_{N-3}) = -\frac{\omega\mu_0}{k_{N-2}} coth \left\{ ik_{N-2} d_{N-2} - coth^{-1} \left(\frac{k_{N-2}}{\omega\mu_0} Z_{xy}(z_{N-2} + 0) \right) \right\},$$

for $j = N - 1$,

$$Z_{xy}(z_{N-2}) = -\frac{\omega\mu_0}{k_{N-1}} coth \left\{ ik_{N-1} d_{N-1} - coth^{-1} \left(\frac{k_{N-1}}{\omega\mu_0} Z_{xy}(z_{N-1} + 0) \right) \right\}. \tag{5.18}$$

It is only reasonable to expect that, as the electromagnetic energy penetrates deeper and deeper into the earth, the energy contained in it attenuates through conversion to heat, and ultimately, at very great distances, the field strengths will reduce to very low values, disappearing at infinite depth. Therefore, in the bottom layer, there can be no terms with positive exponentials. Therefore, in the layer with conductivity σ_N, we need only retain the exponential terms with decaying exponents:

$$E_x(z) = E_{x_N}^+ e^{ik_N z},$$
$$E_y(z) = E_{y_N}^+ e^{ik_N z}, \text{ for } z_{n-1} + 0 \le z \le +\infty, \tag{5.19}$$

because, in accord with Eq. (4.125), $Im(k_n) > 0$. Hence, from (5.6) and (5.7),

$$H_x(z) = -\frac{k_N}{\omega\mu_0} E_{yN}^+ e^{ik_N z},$$
$$H_y(z) = \frac{k_N}{\omega\mu_0} E_{xN}^+ e^{ik_N z}. \tag{5.20}$$

Consequently, the impedances Z_{xy} and Z_{yx} in the layer with index N are:

$$Z_{xy}(z) = E_x(z)/H_y(z) = \frac{\omega\mu_0}{k_N},$$
$$Z_{yx}(z) = -E_y(z)/H_x(z) = \frac{\omega\mu_0}{k_N}, \tag{5.21}$$

for $z_{N-1} + 0 \le z \le \infty$.

In particular, immediately below the top of the last layer, $(z = z_{N-1} + 0)$ and:

$$Z_{xy}(z_{N-1} + 0) = \frac{\omega\mu_0}{k_N}. \tag{5.22}$$

Substituting Eq. (5.22) into Eq. (5.18), we finally arrive at an expression for the impedance at the surface of the earth:

$$Z_{xy}(+0) = \frac{\omega\mu_0}{k_1} R_N, \tag{5.23}$$

where R_N is the *layered-earth correction factor* for the plane wave impedance for the layered medium as a whole:

$$R_N = coth \left\{ -ik_1 d_1 + coth^{-1} \left[\frac{k_1}{k_2} coth \left(-ik_2 d_2 + coth^{-1} (\frac{k_2}{k_3} coth (-ik_3 d_3 + \ldots \right. \right. \right.$$
$$\left. \left. \left. + coth^{-1} \frac{k_{N-1}}{k_N} \ldots \right) \right) \right] \right\}. \tag{5.24}$$

By using the identity

$$coth (x + coth^{-1} y) \equiv tanh(x + tanh^{-1} y),$$

we can write an alternative formula for the impedance:

$$R_N = \tanh\left\{-ik_1d_1 + \tanh^{-1}\left[\frac{k_1}{k_2}\tanh\left(-ik_2d_2 + \tanh^{-1}(\frac{k_2}{k_3}\tanh\left(-ik_3d_3 + ...\right.\right.\right.\right.$$
$$\left.\left.\left.\left. + \tanh^{-1}\left[\frac{k_{N-1}}{k_N}......\right]\right)\right)\right]\right\}.$$

(5.25)

We should note that, conversion of the exponential functions to hyperbolic functions has resulted in a compact notation for impedance, but in practice it is awkard to use these formulas in calculating impedances. A much easier algorithm to program for digital computations is obtained if the layered-earth correction function is expressed in terms of the exponential functions (Keller and Frischknecht, 1966; Zhdanov and Keller, 1994). Replacing the hyperbolic functions in this last equation with their definitions as sums and differences of exponentials, we arrive at a single algorithm for the layered earth correction factor for plane wave impedance:

for $j = 1$,

$$R_N(+0) = \frac{1}{k_1}\frac{1 - K_a e^{-2k_1 d_1}}{1 + K_a e^{-2k_1 d_1}},$$

$$K_a = \frac{\frac{\rho_2 k_1}{\rho_1}R(z_1 + 0) - 1}{\frac{\rho_2 k_1}{\rho_1}R(z_1 + 0) + 1};$$

for $j = 2$,

$$R_N(z_2 + 0) = \frac{1}{k_2}\frac{1 - K_a e^{-2k_2 d_2}}{1 + K_a e^{-2k_2 d_2}},$$

$$K_a = \frac{\frac{\rho_3 k_2}{\rho_2}R(z_2 + 0) - 1}{\frac{\rho_3 k_2}{\rho_2}R(z_2 + 0) + 1};$$

.
.
.

for $j = N - 2$,

$$R_N(z_{N-2} + 0) = \frac{1}{k_{N-2}}\frac{1 - K_a e^{-2k_{N-2} d_{N-2}}}{1 + K_a e^{-2k_{N-2} d_{N-2}}},$$

$$K_a = \frac{\frac{\rho_{N-1} k_{N-2}}{\rho_{N-2}}R(z_{N-2} + 0) - 1}{\frac{\rho_{N-1} k_{N-2}}{\rho_{N-2}}R(z_{N-2} + 0) + 1};$$

for $j = N - 1$,

$$R(z_{N-1} + 0) = \frac{1}{k_{N-1}}\frac{1 - K_a e^{-2k_{N-1} d_{N-1}}}{1 + K_a e^{-2k_{N-1} d_{N-1}}},$$

$$K_a = \frac{1 - \frac{\rho_N k_{N-1}}{\rho_{N-1}} R(z_{N-1} + 0)}{1 + \frac{\rho_N k_{N-1}}{\rho_{N-1}} R(z_{N-1} + 0)};$$

and, for the lower half-space,

$$R(z_{N-1} + 0) = 1. \tag{5.26}$$

The derivation executed above was based on the determination of Z_{yx}. The same result is obtained by following the same steps with Z_{xy}, and hence, we can conclude that both parts of the wave impedance at the surface of the earth are the same:

$$Z_{xy} = Z_{yx} = Z. \tag{5.27}$$

This impedance for a horizontally uniform earth is sometimes called the Tikhonov-Cagniard (T-C) impedance, because it was introduced originally in the pioneer papers by Tikhonov (1950) and Cagniard (1953) on the foundations of the magnetotelluric (MT) method. We will discuss the principles of the MT method in Chapter 13 of the book.

The wave (T-C) impedance can be determined at the surface of the earth by determining the simultaneous magnitudes and directions of the horizontal electric and magnetic field vectors. Then, resolving these two vector measurements into orthogonal components with respect to some arbitrary Cartesian coordinate system, we have:

$$Z = E_x(+0)/H_y(+0) = -E_y(+0)/H_x(+0). \tag{5.28}$$

An extremely powerful result has been obtained: the observed impedance is dependent only on frequency and the electrical conductivity profile in the earth. It is not dependent on the strengths of the components of the electromagnetic field individually:

$$Z = \frac{\omega \mu_0}{k_1} R_N. \tag{5.29}$$

The essence of magnetotelluric sounding (MTS) method, which will be discussed in details in Chapter 13, is to observe the impedance over a spectrum of frequencies to determine conductivity as a function of depth, based on the recognition that the depths reached by a field depend on attenuation. Attenuation takes place more rapidly at high frequencies; hence, the capability of the electromagnetic field to yield information about conductivity at depth increases as the period of the oscillation increases (as the frequency decreases).

5.1.2 LOW-FREQUENCY BEHAVIOR OF WAVE IMPEDANCE

Generalizations can be made about the behavior of the wave impedance as a function of the geoelectric structure by considering asymptotic approximations (Berdichevsky and Dmitriev, 2002). For example, very useful results can be obtained by considering the asymptotic behavior at low frequencies for earth models in which the last layer is either an insulator or an ideal conductor.

Asymptotic behavior of the impedance for a model with a highly resistant basement

We begin our asymptotic analysis by considering an earth in which a single layer with conductivity σ_1 rests on a lower half-space that is insulating ($\sigma_2 = 0$). In accord with Eqs. (5.29) and (5.24), the impedance can be written as:

$$Z = \frac{\omega\mu_0}{k_1} R_2 = \frac{\omega\mu_0}{k_1} coth\left[-ik_1d_1 + coth^{-1}\left(\frac{k_1}{k_2}\right)\right]. \tag{5.30}$$

Rewriting this last expression for a special case in which $\sigma_2 \to 0$, so that $coth^{-1}(k_1/k_2) \to 0$, we have:

$$Z = \frac{\omega\mu_0}{k_1} coth\left(-ik_1d_1\right). \tag{5.31}$$

Letting frequency tend to zero (and so, the wave number k_1 also tends to zero), the asymptotic behavior for a highly resistant basement is

$$Z(\omega \to 0) = \frac{\omega\mu_0}{-ik_1^2d_1} = \frac{\omega\mu_0}{\omega\mu_0\sigma_1d_1} = \frac{1}{S_1}, \tag{5.32}$$

where $S_1 = \sigma_1d_1$, the longitudinal conductance of the overburden.

As might be expected, this highly useful result can be extended to the case in which the overburden consists of several layers, each characterized by its own conductivity. For a two-layer overburden on an insulating half-space, based on Eqs. (5.29) and (5.24), we have by the same reasoning:

$$Z = \frac{\omega\mu_0}{k_1} R_3 = \frac{\omega\mu_0}{k_1} coth\left\{-ik_1d_1 + coth^{-1}\left[\frac{k_1}{k_2}coth(-ik_2d_2)\right]\right\}, \tag{5.33}$$

where it has been recognized that $coth^{-1}(k_2/k_3) \to 0$ as $k_3 \to 0$.

As frequency tends to zero (and along with it, k_1 and k_2), the asymptotic formula is:

$$Z(\omega \to 0) \to \frac{\omega\mu_0}{k_1} coth\left(-ik_1d_1 - \frac{ik_2^2}{k_1}d_2\right) \to \frac{\omega\mu_0}{k_1} \frac{k_1}{(-ik_1^2d_1 - ik_2^2d_2)}$$

$$= \frac{\omega\mu_0}{\omega\mu_0(\sigma_1d_1 + \sigma_2d_2)} = 1/S, \tag{5.34}$$

where now $S = \sigma_1d_1 + \sigma_2d_2 = S_1 + S_2$, the cumulative conductance of the two conductive layers. This result can be extended to any number of layers covering an insulating half-space:

$$Z(\omega \to 0) = 1/S, \tag{5.35}$$

where

$$S = \sigma_1d_1 + \sigma_2d_2 + ... + \sigma_{N-1}d_{N-1} = S_1 + S_2 + ... + S_{N-1},$$

represents the cumulative conductance of all the layers comprising the overburden.

Asymptotic behavior of the impedance for a model with a highly conductive basement

Let us next consider a case in which the lower half-space is perfectly conducting, rather than an insulator. In this case, the impedance is:

$$Z = \frac{\omega\mu_0}{k_1}R_2 = \frac{\omega\mu_0}{k_1}tanh\left[-ik_1d_1 + tanh^{-1}\left(\frac{k_1}{k_2}\right)\right]. \tag{5.36}$$

It is readily seen that, as conductivity increases without limit,

$$tanh^{-1}\left(\frac{k_1}{k_2}\right) = tanh^{-1}(\sigma_1/\sigma_2)^{1/2}$$

$$= 1/2\ \ln\frac{1 + (\sigma_1/\sigma_2)^{1/2}}{1 - (\sigma_1/\sigma_2)^{1/2}} \to 0 \text{ as } \sigma_2 \to \infty.$$

As a consequence, Eq. (5.36) takes the form

$$Z = \frac{\omega\mu_0}{k_1}tanh\left(-ik_1d_1\right).$$

Taking the limit at low frequency, we have

$$Z(\omega \to 0) = -ik_1d_1\frac{\omega\mu_0}{k_1} = -i\omega\mu_0d_1. \tag{5.37}$$

A striking result – *the impedance does not depend on the resistivity in the overburden, but is a function only of the depth to the conductive lower half-space!*

If the overburden consists of two layers resting on a highly conducting lower half-space, the impedance is:

$$Z = \frac{\omega\mu_0}{k_1}tanh\left\{-ik_1d_1 + tanh^{-1}\left[\frac{k_1}{k_2}tanh(-ik_2d_2)\right]\right\}. \tag{5.38}$$

The low-frequency asymptote for this equation is:

$$Z(\omega \to 0) \to \frac{\omega\mu_0}{k_1}tanh[-ik_1d_1 + tanh^{-1}(-ik_1d_2)]$$

$$\to \frac{\omega\mu_0}{k_1}tanh[-ik_1d_1 - ik_1d_2)]$$

$$= -\frac{\omega\mu_0}{k_1}\frac{\tanh(ik_1d_1) + \tanh(ik_1d_2)}{1 + \tanh(ik_1d_1)\tanh(ik_1d_2)}, \tag{5.39}$$

and hence

$$Z(\omega \to 0) = -\frac{\omega\mu_0}{k_1}[ik_1(d_1 + d_2)] = -i\omega\mu_0D, \tag{5.40}$$

where $D = d_1 + d_2$, the depth to the top of the ideally conducting half-space.

This result can be extended to the case in which the overburden is divided into any number of layers with different resistivities:

$$Z(\omega \to 0) = -i\omega\mu_0D, \tag{5.41}$$

with D being the total thickness of the layers covering the ideal conductor. This is a very useful result; if a highly conductive layer is present in the earth, the impedance at low frequencies depends only on the depth to that conductor, and not on the conductivities within the overburden.

5.1.3 DEFINITION OF FREQUENCY WINDOWS

We can extend this asymptotic approach to cases in which a conductive or resistive layer is present in the sequence, rather than comprising the lowermost half-space. In this case, asymptotic behavior persists only over a limited range of low frequencies, not for all frequencies down to zero. A band-limited frequency interval, or frequency window, can then be identified over which the impedance depends only on the thickness or the conductance of the intermediate layer (Berdichevsky and Dmitriev, 2002). We can best examine this behavior by using a model with three layers, the middle layer being either highly resistive or highly conductive relative to the rest of the section.

Consider the three-layer model as shown in Fig. 5.2. The surface layer might be a sedimentary sequence of moderate conductivity. This is underlain by the basement complex which has a very high resistivity, with a thickness considerably greater than that of the overlying conductive layer, $d_2 \gg d_1$. The lowermost region, probably deep in the mantle, is filled with rocks of very high conductivity, essentially infinite.

To analyze the asymptotic behavior of the impedance for this model, we make use of a less demanding limit process than was used in the last section. The equation for the relaxed limit is:

$$Z(\omega \to 0) \sim -i\omega\mu_0 \frac{D_2}{1 - i\omega\mu_0 S_1 d_2}, \tag{5.42}$$

or, if $d_2 \gg d_1$

$$Z(\omega \to 0) \sim -i\omega\mu_0 \frac{D_2}{1 - i\omega\mu_0 S_1 D_2}, \tag{5.43}$$
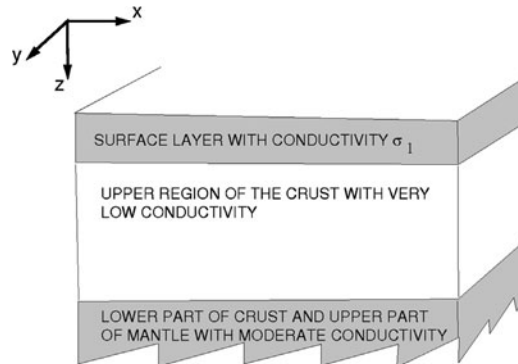
FIGURE 5.2

A horizontally layered model of the Earth's crust and upper mantle consisting of three zones with characteristic conductivity values.

where $D_1 = d_1 + d_2$ and $S_1 = \sigma_1 d_1$. Note that this asymptotic approximation is valid for the condition $|k_1 d_1| \leq 1$, which corresponds to:

$$\omega\mu_0 S_1 d_2 \leq d_2/d_1.$$

It is possible to identify two low frequency windows based on the dimensionless parameter:

$$\omega\mu_0 S_1 d_2.$$

S window: The limits for the *S* window are defined as:

$$d_2/d_1 \geq \omega\mu_0 S_1 d_2 \gg 1. \tag{5.44}$$

Within this window, in accord with Eq. (5.43), the impedance depends only on the cumulative conductance of the upper layer:

$$Z = 1/S_1. \tag{5.45}$$

D-window: At lower frequencies we identify the *D* window, with limits given by

$$\omega\mu_0 S_1 d_2 \ll 1. \tag{5.46}$$

In accord with Eq. (5.43), over this window

$$Z = -i\omega\mu_0 D_2. \tag{5.47}$$

The impedance in the *D* window depends only on the total depth to the surface of the lower conductive zone.

Summarizing,

$$Z = \begin{cases} 1/S_1 & \text{(in the } S \text{ window)} \\ -i\omega\mu_0 D_2 & \text{(in the } D \text{ window)} \end{cases}, \tag{5.48}$$

and

$$E_x = \begin{cases} H_y/S_1 \\ -i\omega\mu_0 D_2 H_y \end{cases} \; ; E_y = \begin{cases} -H_x/S_1 & \text{(in the } S \text{ window)} \\ i\omega\mu_0 D_2 H_x & \text{(in the } D \text{ window)} \end{cases}, \tag{5.49}$$

where $E_{x,y}$, $H_{x,y}$ are components of the electromagnetic field observed at the earth's surface.

The concept of *S*- and *D*-windows is widely used in applications of the magnetotelluric method.

We can summarize the results of this section as follows.

1) One can resolve the thickness of a resistive zone from the MT impedance data, but not the resistivity.

2) One can resolve the conductance (thickness-conductivity product) of a conducting zone from the MT impedance data. However, in general, the thickness and the conductivity cannot be resolved separately.

3) The position of the top of a conductor is well located by the MT impedance data, but the bottom is not.

4) To image a conductor at depth, its conductance must be greater than the total conductance of the layers above.

The reader should understand that these statements provide just a qualitative evaluation of the resolution of the MT sounding method. A qualitative resolution study requires a more rigorous analysis, which we will discuss in the chapters below.

5.2 SPECTRAL METHOD OF COMPUTING EM FIELDS IN HORIZONTALLY STRATIFIED MEDIA

We turn our attention now to the more complicated problem of computing an EM field generated by a 3-D source in the horizontally layered geoelectrical model. A number of analytical methods have been used in solving for this problem. In our approach to the subject, in view of the importance we will attach to spectral representations of electromagnetic fields, we will use the spectral method for solution of the EM problem, introduced in Zhdanov (1986) and Zhdanov and Keller (1994). We will illustrate this general method by calculating the electric potentials of a point and dipole sources on the surface of a horizontally stratified medium, and by deriving the general expressions for the EM fields generated by the electric and magnetic dipole transmitters in the frequency and time domains.

5.2.1 FOURIER TRANSFORM IN THE SPATIAL DOMAIN

Before attacking the problems stated above, we will first review some of the basic concepts and methods based on the use of Fourier transformations.

We will take $F(x, y, z)$ to be some arbitrary function defined over all of space and absolutely integrable over any horizontal plane, P_d for $z = d$, where $d_1 < d < d_2$ with d_1 and d_2 being constants. It follows from these conditions that the integral of the modulus of $F(x, y, z)$,

$$\iint_{-\infty}^{\infty} |F(x, y, z)| dx dy < \infty, \tag{5.50}$$

exists for all values of z over the interval $(d_1 d_2)$.

It should be noted that, as a consequence of condition (5.50), the function $F(x, y, z)$ tends to zero as x, y become infinitely large (for $d_1 < z < d_2$).

The spatial spectrum of the function $F(x, y, z)$ is defined as the two-dimensional Fourier transform on the plane P_z, calculated using the expression

$$S_F(k_x, k_y, z) = \iint_{-\infty}^{\infty} F(x, y, z) e^{+i(k_x x + k_y y)} dx dy, \tag{5.51}$$

where k_x and k_y are spatial frequencies.

In view of the condition of Eq. (5.50), the integral (5.51) has meaning, that is, the spatial spectrum exists, for all z within the interval (d_1, d_2).

The corresponding inverse formula for determining the function $F(x, y, z)$ in the belt $d_1 < z < d_2$ from its spatial spectrum is:

$$F(x, y, z) = \frac{1}{4\pi^2} \iint_{-\infty}^{\infty} S_F(k_x, k_y, z) e^{-i(k_x x + k_y y)} dk_x dk_y. \tag{5.52}$$

Formulas (5.51) and (5.52) comprise a Fourier transform pair, defining a reciprocal single-valued relationship between the functions $F(x, y, z)$ and $S_F(k_x, k_y, z)$.

$$F(x, y, z) \Longleftrightarrow S_F(k_x, k_y, z). \tag{5.53}$$

This relationship provides an approach to the solution of a number of electrical prospecting problems by transforming electromagnetic fields to their corresponding spatial spectrums. As we will see below, such an approach markedly simplifies the solution of many problems. Solutions are obtained as spatial spectrums, and then, using the inverse Fourier transform, the desired fields are obtained. The effectiveness of this process is based on the fact that the differentiation process which must be used in the space domain reduces to algebraic operations in the spatial frequency domain, leading to a marked reduction in the difficulties involved in obtaining solutions of the electromagnetic field equations.

Let us review some of the properties of spatial spectrums. First, let us find the spectrum for the horizontal derivative of the function F:

$$
\begin{aligned}
S_{\partial F/\partial x}(k_x, k_y, z) &= \iint_{-\infty}^{\infty} \frac{\partial F(x, y, z)}{\partial x} e^{i(k_x x + k_y y)} dx dy \\
&= \int_{-\infty}^{\infty} e^{ik_y y} \left\{ \int_{-\infty}^{\infty} \frac{\partial F(x, y, z)}{\partial x} e^{ik_x x} dx \right\} dy.
\end{aligned}
\tag{5.54}
$$

We can integrate the integral within the braces by parts:

$$
\begin{aligned}
\int_{-\infty}^{\infty} \frac{\partial F(x, y, z)}{\partial x} e^{ik_x x} dx &= \int_{-\infty}^{\infty} e^{ik_x x} dF(x, y, z) \\
&= e^{ik_x x} F(x, y, z) \Big|_{x=-\infty}^{x=\infty} - ik_x \int_{-\infty}^{\infty} F(x, y, z) e^{ik_x x} dx .
\end{aligned}
$$

In view of the fact that $F(x, y, z)$ must tend to zero as $x \to \pm\infty$, the first term on the right-hand side of this last equation must be zero, and so

$$\int_{-\infty}^{\infty} \frac{\partial F(x, y, z)}{\partial x} e^{ik_x x} dx = -ik_x \int_{-\infty}^{\infty} F(x, y, z) e^{ik_x x} dx. \tag{5.55}$$

Combining Eqs. (5.54) and (5.55) and considering Eq. (5.51), we have

$$S_{\partial F/\partial x}(k_x, k_y, z) = -ik_x S_F(k_x, k_y, z). \tag{5.56}$$

An analogous relationship for $S_{\partial F/\partial y}(k_x, k_y, z)$ is

$$S_{\partial F/\partial y}(k_x, k_y, z) = -ik_y S_F(k_x, k_y, z). \tag{5.57}$$

The spatial spectrums of the horizontal derivatives of the function F are equal to the original function multiplied by the corresponding spatial frequency, and by the quantity, $-i$.

Let us next consider the spectrum for the vertical derivative of the function $F(x, y, z)$:

$$S_{\partial F/\partial z}(k_x, k_y, z) = \iint_{-\infty}^{\infty} \frac{\partial F(x, y, z)}{\partial z} e^{i(k_x x + k_y y)} dx dy$$

$$= \frac{\partial}{\partial z} \iint_{-\infty}^{\infty} F(x, y, z) e^{i(k_x x + k_y y)} dx dy$$

$$= \frac{\partial}{\partial z} S_F(k_x, k_y, z). \tag{5.58}$$

The spectrum for the vertical derivative of the function F is the same as the vertical derivative of the function itself.

Spatial spectra have many interesting properties, which are described in standard texts on the subject (see, for example, Kharkevich, 1960, or Papoulis, 1962), but here, we need only be concerned with the application of Eqs. (5.56), (5.57) and (5.58), which, we shall see as we continue, are quite adequate for the solution of a number of problems that arise in the theory of electrical prospecting.

As a first example, let us find the spatial spectrum of the field about a point source of electric current, located in a homogeneous, isotropic, unbounded medium characterized by a resistivity, ρ. From Eq. (4.48), the potential due to the point source is:

$$U(\mathbf{r}) = I\rho/4\pi r, \tag{5.59}$$

and the scalar components of the electric field $\mathbf{E}$ are:

$$E_x = -\partial U/\partial x, \; E_y = -\partial U/\partial y, \; E_z = -\partial U/\partial z. \tag{5.60}$$

We will transform these expressions for the electric field to spatial spectrums, using the properties of these spectrums as given by Eqs. (5.56), (5.57) and (5.58):

$$e_x = ik_x u, \; e_y = ik_y u, \; e_z = -\partial u/\partial z = -u', \tag{5.61}$$

where we make use of the designations,

$$\mathbf{e} = S_{\mathbf{E}}(k_x, k_y, z), \; u = S_U(k_x, k_y, z), \tag{5.62}$$

and the prime indicates differentiation with respect to z.

So, we see, in order to compute the spectrum of the electric field, it is necessary only to find the spectrum u of the scalar potential. In accord with Eqs. (5.59) and (5.50):

$$u = \frac{I\rho}{4\pi} \iint_{-\infty}^{\infty} \frac{1}{r} e^{i(k_x x + k_y y)} dx dy. \tag{5.63}$$

This integral is tabulated:

$$\iint_{-\infty}^{\infty} \frac{1}{r} e^{i(k_x x + k_y y)} dx dy = \iint_{-\infty}^{\infty} \frac{1}{(x^2 + y^2 + z^2)^{1/2}} e^{i(k_x x + k_y y)} dx dy$$

$$= 2\pi e^{-n_0|z|}/n_0, \tag{5.64}$$

where $n_0 = (k_x^2 + k_y^2)^{1/2}$.

Note that, on the strength of the inverse Fourier transform, we can write the identity:

$$\frac{1}{2\pi} \iint_{-\infty}^{\infty} \frac{e^{-n_0|z|}}{n_0} e^{-i(k_x x + k_y y)} dx \, dy = \frac{1}{r}. \tag{5.65}$$

Substituting Eqs. (5.64) into (5.63), we write

$$u = 1/2 \; I\rho e^{-n_0|z|}/n_0. \tag{5.66}$$

Finally, substituting Eqs. (5.66) into (5.61), we can write the spectrum for the electric field:

$$\begin{aligned}
e_x &= 1/2 \; i I \rho k_x e^{-n_0|z|}/n_0, \\
e_y &= 1/2 \; i I \rho k_y e^{-n_0|z|}/n_0, \\
e_z &= 1/2 \; I\rho e^{-n_0|z|} \, \partial|z|/\partial z.
\end{aligned} \tag{5.67}$$

The derivative in this last expression is:

$$\partial|z|/\partial z = \text{signum } z = \begin{cases} 1, & z > 0 \\ 0, & z = 0 \\ -1, & z < 0 \end{cases}.$$

Therefore,

$$e_z = 1/2 \; I\rho e^{-n_0|z|} \text{signum } z = \begin{cases} \frac{1}{2} I\rho e^{-n_0 z}, & z > 0 \\ -\frac{1}{2} I\rho e^{n_0 z}, & z < 0 \end{cases}. \tag{5.68}$$

We see from this equation that, in passing through the plane $z = 0$ on which the source is located, there is a discontinuity in the spectrum of the z component of the electric field:

$$e_z|_{z=+0} - e_z|_{z=-0} = 1/2 \; I\rho - (-1/2 \; I\rho) = I\rho. \tag{5.69}$$

Here, the index $z = +0$ indicates the limit of e_z as $z \to 0$ along the positive z axis, while the index $z = -0$ indicates the limit of e_z as $z \to 0$ along the negative z axis. The spectrums for the horizontal components of the electric field as given in Eq. (5.67) are continuous across the plane $z = 0$, which contains the source.

In conclusion, we point out that Eq. (5.69) can be written in terms of the spectrum for the potential as

$$u'|_{z=+0} - u'|_{z=-0} = -I\rho. \tag{5.70}$$

These expressions for the spectrum of a point source have the required form for solution of the problem of determining fields in a horizontally stratified medium.

5.2.2 POINT SOURCE OF THE DC FIELD IN HORIZONTALLY STRATIFIED MEDIUM

We apply the spectral method first in solving for the electric potential of a point source of the DC field on the surface of a horizontally stratified medium. Let us consider a one-dimensional model of

the earth which consists of a finite number, N, of horizontally homogeneous layers characterized by resistivities, ρ_j $(j = 1, 2, ..., N)$, and thicknesses, d_j $(j = 1, 2, ..., N - 1, d_N = \infty)$.

We will assume that a point source, A, of electrical current, I, is located on the surface of the earth at $z = 0$. We are required to find the electric potential, U, and the electric field, $\mathbf{E}$, caused by this source along the surface of the earth, again at $z = 0$.

The first step is to write the mathematical representation of the problem based on the general theory for the flow of direct current in the medium as discussed in Chapter 4.

- 1. The source condition: The scalar potential in the first layer will consist of two parts, one being the normal potential, U_0, that would be observed in a half-space with the resistivity of the first layer, ρ_1, and the other, U_a, being a *disturbing potential* caused by the presence of the deeper layers:

$$U(\mathbf{r}) = I\rho_1/2\pi r + U_a(\mathbf{r}) \text{ at } +0 \leq z \leq d_1 - 0. \tag{5.71}$$

- 2. The equation for potential: Within the conducting medium, the normal potential $U_0(\mathbf{r})$ and the disturbing potential $U_a(\mathbf{r})$ have continuous second derivatives and satisfy the Laplace equation:

$$\nabla^2 U_a(\mathbf{r}) = 0 \text{ for the region } -0 \leq z \leq d_1 - 0, \tag{5.72}$$
$$\nabla^2 U(\mathbf{r}) = 0 \text{ for the region } z_j + 0 \leq z \leq z_{j+1} - 0, \, j = 1, 2, ..., N - 2, \tag{5.73}$$

where $z_j = d_1 + d_2 + ... + d_j$ (for $j = 1, 2, ..., N - 1$) is the total depth to the top of layer j.

In Eqs. (5.71) and (5.73), the symbols $+0, d_1 - 0, z_j + 0, z_j - 0$ designate the lower and upper surfaces, respectively, of the corresponding boundaries of each layer.

- 3. Boundary conditions: At the surface between the conducting earth and the insulating atmosphere, $z = 0$, there can be no vertical current flow. Therefore

$$\frac{\partial U}{\partial z}\bigg|_{z=+0} = \frac{I\rho_1}{2\pi} \cdot \frac{z}{r^3}\bigg|_{z=+0} + \frac{\partial U_a}{\partial z}\big|_{z=+0} = 0$$

and so

$$\frac{\partial U_a}{\partial z}\big|_{z=+0} = 0 . \tag{5.74}$$

At every other interface between layers, the boundary conditions on the potential and the vertical component of the current flow which must be satisfied are

$$U|_{z=z_j-0} = U|_{z=z_j+0},$$
$$\frac{1}{\rho_j}\frac{\partial U}{\partial z}\bigg|_{z=z_j-0} = \frac{1}{\rho_{j+1}}\frac{\partial U}{\partial z}\bigg|_{z=z_j+0}. \tag{5.75}$$

- 4. Condition at infinity: The potential at all points infinitely far removed from the source must be zero.

The theorem of uniqueness for the solution of a differential equation with these boundary conditions assures us of a unique solution for the scalar potential about a point source.

We now go on to the determination of the spatial spectrum for the potential $U(\mathbf{r})$:

$$u(k_x, k_y, 0) = \iint_{-\infty}^{\infty} U(\mathbf{r})e^{i(k_x x + k_y y)}dxdy,$$

and transform the conditions *1–4* into the frequency domain.

- 1a. The source condition: In accord with Eqs. (5.71) and (5.64), the spectrum of the potential in the first layer is

$$u(k_x, k_y, z) = I\rho_1 e^{-n_0 z}/n_0 + u_a(k_x, k_y, z) \text{ for the region } +0 \leq z \leq d_1 - 0, \qquad (5.76)$$

where $u_a(k_x, k_y, z)$ is the disturbing potential in the frequency domain.

- 2a. Equation for the potential spectrum: In the frequency domain, Laplace's equations (5.72) and (5.73) are written as

$$(-ik_x)^2 u_a + (-ik_y)^2 u_a + u_a'' = 0,$$
$$(-ik_x)^2 u + (-ik_y)^2 u + u'' = 0,$$

and after some straightforward algebraic operations,

$$u_a = n_0^2 u_a \text{ for the region } +0 \leq z \leq d_1 - 0, \qquad (5.77)$$

$$u'' = n^2 u \text{ for the regions } z_{j-1} \leq z \leq z_j - 0, \, j = 2, ..., N. \qquad (5.78)$$

- 3a. Boundary conditions: The boundary condition in Eq. (5.74) for the vertical derivative of the function U_a transforms into a corresponding condition for the vertical derivative of its spectrum:

$$u_a'|_{z=0} = 0. \qquad (5.79)$$

The boundary conditions of Eq. (5.75) at each interface between two layers transform to

$$u|_{z=z_j-0} = u|_{z=z_j+0},$$
$$\frac{u'}{\rho_j}\bigg|_{z=z_j-0} = \frac{u'}{\rho_{j+1}}\bigg|_{z=z_j+0}. \qquad (5.80)$$

- 4a. The condition at infinity: In the last layer, the following condition must be satisfied:

$$u(k_x, k_y, z) \to 0 \text{ as } z \to \infty. \qquad (5.81)$$

We must find spectrums u_a and u that meet these conditions. We do know that the general forms of the solutions to the differential equations (5.85) and (5.86) are

$$u_a(k_x, k_y, z) = u_a^+ e^{n_0 z} + u_a^- e^{-n_0 z} \text{ in the region } 0 \leq z \leq d_1 - 0,$$

$$u(k_x, k_y, z) = u_j^+ e^{n_0 z} + u_j^- e^{-n_0 z} \text{ in the regions } z_{j-1} + 0 \leq z \leq z_j - 0, \, j = 2, 3, ..., N, \quad (5.82)$$

where $u_a^{\pm}$, $u_j^{\pm}$ $(j = 2, 3, ..., N)$ are coefficients still to be determined, but which depend only on the spatial frequencies k_x and k_y, and not on z. The problem of evaluating the spectrum of the potential now depends on our being able to evaluate these coefficients. This, fortunately, can readily be accomplished by applying the boundary conditions and the condition at infinity.

As a first step, we will obtain a single expression for the spectrum of the potential in all of the layers, including the first. To do this, we substitute Eq. (5.82) into (5.76):

$$u(k_x, k_y, z) = u_1^+ e^{n_0 z} + u_1^- e^{-n_0 z} \text{ for } +0 \leq z \leq d_1 - 0, \quad (5.83)$$

where

$$u_1^+ = u_a^+, \; u_1^- = u_a^- + \frac{I \rho_1}{n_0}. \quad (5.84)$$

Let us take special note of the spectrum of the potential in layer N:

$$u(k_x, k_y, z) = u_N^+ e^{n_0 z} + u_N^- e^{-n_0 z}.$$

In this expression, the coefficient u_N^+ must be identically zero in order that the condition at infinity, Eq. (5.81) be satisfied. Hence

$$u(k_x, k_y, z) = u_N^- e^{-n_0 z} \text{ for } z_{N-1} + 0 \leq z. \quad (5.85)$$

We see from Eqs. (5.83), (5.82), and (5.85) that in each layer except the last, the spectrum for the potential in that layer will be the sum of two terms, one of positive exponential form and the other of negative exponential form. In the bottom layer, only a term of negative exponential form is present in the solution.

This last result has an obvious physical explanation. The exponential decay of the field of a point source with depth describes the spreading of the current as it penetrates downward, while the exponential increase with depth is associated with the return of current as though by reflection at the boundaries in the medium. In the last layer, no more return of current from lower boundaries can take place, and so, there is no increasing exponential term for the lowermost region.

Note that this behavior of the spectral potential is similar to the plane wave propagation described in the first section of this chapter (see formula (5.2)). In other words, we can treat the spectral method as a representation of the scalar potential as a superposition of the multiple plane waves in the spatial frequency domain. Therefore, for solving a scalar potential problem we can use a technique similar to one introduced in the beginning of this chapter for studying the plane wave propagation in a layered medium.

Let us consider a derived function of the potential field which plays a similar role and bears the same name as *layered-earth correction factor* in the theory of plane EM waves:

$$F(z) = u(k_x, k_y, z)/u'(k_x, k_y, z), \tag{5.86}$$

which is defined only for $z \geq +0$.

The spectrum for the electric potential at the surface of the earth, at $z = +0$, which we are seeking to find can be described formally from Eqs. (5.86), (5.76), and (5.78) as:

$$\begin{aligned} u(k_x, k_y, +0) &= F(+0)u'(k_x, k_y, +0) \\ &= F(+0)[-I\rho_1 + u'_a(k_x, k_y, +0)] = -I\rho_1 F(+0). \end{aligned} \tag{5.87}$$

We have the solution to the problem of determining the field of a point source in a layered medium if we can determine the layered-earth correction factor $F(z)$!

We note first that in the lowermost layer, for $z_{n-1} + 0 \leq z$, in accord with Eq. (5.85),

$$F(z) = \frac{u_N^- e^{-n_0 z}}{-n_0 u_N^- e^{-n_0 z}} = -\frac{1}{n_0}. \tag{5.88}$$

In other words, in the lowermost layer – the basement – the layered-earth correction factor is constant.

Next, we determine $F(z)$ for an arbitrary layer with the index j. By substitution of Eqs. (5.84) and (5.85) in (5.87), we get

$$F(z) = \frac{1}{n_0} \frac{u_j^+ e^{n_0 z} + u_j^- e^{-n_0 z_0}}{u_j^+ e^{n_0 z} - u_j^- e^{-nz}} \quad \text{where } z_{j-1} + 0 \leq z \leq z_j - 0.$$

We now divide both numerator and denominator by $a = (u_j^+ u_j^-)^{1/2}$:

$$F(z) = \frac{1}{n_0} \frac{a e^{n_0 z} + a^{-1} e^{-n_0 z}}{a e^{n_0 z} - a^{-1} e^{-n_0 z}}.$$

If we let $q_j = \ln a^{-1}$, we can rewrite this last expression as

$$\begin{aligned} F(z) &= \frac{1}{n_0} \frac{e^{(n_0 z - q_j)} + e^{-(n_0 z - q_j)}}{e^{(n_0 z - q_j)} - e^{-(n_0 z - q_j)}} \\ &= \frac{1}{n_0} coth \ (n_0 z - q_j) \text{ for } z_{j-1} + 0 \leq z \leq z_j - 0. \end{aligned} \tag{5.89}$$

This procedure has apparently reduced the number of undetermined constants by a factor of 2, since now we have $N - 1$ values of q_j to evaluate, rather than $N - 1$ pairs of values for u_j^+ and u_j^-. Applying the boundary condition (5.80),

$$\rho_j F(z_j - 0) = \rho_{j+1} F(z_j + 0) \tag{5.90}$$

which leads naturally to

$$q_j = n_0 z_j - coth^{-1}\left[\frac{\rho_{j+1} n_0}{\rho_j} F(z_j + 0)\right].$$ (5.91)

We next substitute this value for q_j into Eq. (5.89), letting $z = z_{j-1} + 0$ in that expression:

$$F(z_{j-1} + 0) = \frac{1}{n_0} coth\left\{n_0(z_{j-1} - z_j) + coth^{-1}\left[\frac{\rho_{j+1} n_0}{\rho_j} F(z_j + 0)\right]\right\}$$

$$= -\frac{1}{n_0} coth\left\{n_0 d_j - coth^{-1}\left[\frac{\rho_{j+1} n_0}{\rho_j} F(z_j + 0)\right]\right\}.$$ (5.92)

In this way, we have developed a recursive relationship relating the value of the layered-earth correction factor $F(z)$ at the top of the layer with index $(j + 1)$ to the value at the top of the layer with the index j.

Substituting this result into Eq. (5.92) for $j = 1$, $j = 2$, ..., $j = N - 2$, and $j = N - 1$, we obtain:

for $j = 1$,

$$F(+0) = -\frac{1}{n_0} coth\left\{n_0 d_1 - coth^{-1}\left[\frac{\rho_2 n_0}{\rho_1} F(z_1 + 0)\right]\right\};$$ (5.93)

for $j = 2$,

$$F(z_1 - 0) = -\frac{1}{n_0} coth\left\{n_0 d_2 - coth^{-1}\left[\frac{\rho_3 n_0}{\rho_2} F(z_2 + 0)\right]\right\};$$ (5.94)

.
.
.

for $j = N - 2$,

$$F(z_{N-3} + 0) = -\frac{1}{n_0} coth\left\{n_0 d_{N-2} - coth^{-1}\left[\frac{\rho_{N-1} n_0}{\rho_{N-2}} F(z_{N-2} + 0)\right]\right\};$$ (5.95)

for $j = N - 1$,

$$F(z_{N-2} + 0) = -\frac{1}{n_0} coth\left\{n_0 d_{N-1} - coth^{-1}\left[\frac{\rho_N n_0}{\rho_{N-1}} F(z_{N-1} + 0)\right]\right\}.$$ (5.96)

But, in accord with Eq. (5.88),

$$F(z_{N-1} + 0) = -\frac{1}{n_0}.$$ (5.97)

Substituting Eq. (5.97) into (5.96), and then, substituting Eq. (5.96) into (5.95), and repeating the process until Eq. (5.93) is reached, we obtain the following general formula for calculating the layered-earth correction factor at the surface of the earth:

$$F(+0) = -(1/n_0) R_N^0(n_0),$$ (5.98)
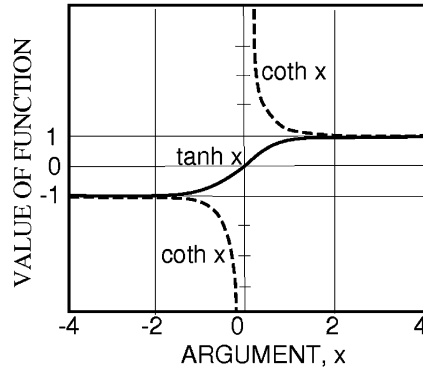
FIGURE 5.3

Values for the hyperbolic tangent and cotangent. Note that the values for tangent lie between -1 and 1, while the values for the cotangent lie only outside this range.

where the function $R_N^0(n_0)$ represents the contribution of the properties of every layer in an N-layered sequence to the behavior of a DC field in the spatial frequency domain:

$$R_N^0(n_0) = R_N^0(n_0; \rho_1, d_1, \rho_2, d_2, ..., \rho_{N-1}, d_{N-1}, \rho_N) =$$
$$= coth \left\{ n_0 d_1 + coth^{-1} \left[\frac{\rho_2}{\rho_1} coth \left(n_0 d_2 + coth^{-1} \left(\frac{\rho_3}{\rho_2} coth \left(n_0 d_3 + ... \right. \right. \right. \right. \right.$$
$$\left. \left. \left. \left. ... + coth^{-1} \left(n_0 d_{N-1} + coth^{-1} \frac{\rho_N}{\rho_{N-1}} \right) ... \right) \right) \right] \right\}, \tag{5.99}$$

where $n_0 = (k_x^2 + k_y^2)^{1/2}$.

The function $R_N^0(n_0)$ is one of several special functions which arise in sounding of a layered earth. Each is called a *layered-earth correction factor*. This one is used with direct current sounding methods. Others, which we have developed and examined in the first and in subsequent sections of this chapter, play the same role for different electromagnetic sounding methods.

The procedure of calculating a layered-earth correction factor involves one technical difficulty which we mentioned in the plane wave propagation case above. The hyperbolic tangent, which is the function we have used for expressing the layered-earth correction factor, is defined for all values of possible arguments, the inverse hyperbolic tangent is not. If the argument of the inverse lies between -1 and $+1$, the inverse does not exist (see Fig. 5.3). Because of this problem, it is necessary in some cases to use an alternative solution for q_j based on the identity

$$coth(x + coth^{-1} y) = tanh(x + tanh^{-1} y).$$

If at any time the argument for the hyperbolic cotangent in Eq. (5.98) happens to lie between -1 and 1 so that its inverse does not exist, with this identity, the line containing that function can be

rewritten as

$$R_N^0(n_0) = \tanh\left\{n_0 d_1 + \tanh^{-1}\left[\frac{\rho_2}{\rho_1}\tanh\left(n_0 d_2 + \cdots + \tanh^{-1}\left(n_0 d_{N-1} + \tanh\frac{\rho_N}{\rho_{N-1}}\right)\cdots\right)\right]\right\}.$$
(5.100)

The argument for the inverse hyperbolic function must be tested for each value of the layered-earth correction factor which is computed to determine which form of the algorithm to use. An alternate form of the same expressions can be obtained which is much more appropriate for programming for digital computations. To obtain this, we use an identity to express the inverse hyperbolic functions in terms of Napierian logarithms. The layered-earth correction factor at the surface of an N-layered earth then can be written as:

$$R_N^0(n_0) = \begin{cases} \coth\left(n_0 d_1 + \frac{1}{2}\ln\frac{(\rho_2/\rho_1)R_{N-1}^0+1}{(\rho_2/\rho_1)R_{N-1}^0-1}\right) & \text{if } (\rho_2/\rho_1)R_{N-1}^0 > 1 \\ \tanh\left(n_0 d_1 + \frac{1}{2}\ln\frac{1+(\rho_2/\rho_1)R_{N-1}^0}{1-(\rho_2/\rho_1)R_{N-1}^0}\right) & \text{if } (\rho_2/\rho_1)R_{N-1}^0 < 1 \end{cases},$$
(5.101)

where R_{N-1} is the layered-earth correction factor for an N-layered earth from which the surface layer has been removed (it is in effect the layered-earth correction factor at the top of the second layer).

For convenience, we will designate the argument of the natural logarithm as K_a or K_b as follows

$$K_a = \frac{(\rho_2/\rho_1)R_{N-1}^0 - 1}{(\rho_2/\rho_1)R_{N-1}^0 + 1} \quad \text{when } (\rho_2/\rho_1)R_{N-1}^0 > 1,$$

$$K_b = \frac{1 - (\rho_2/\rho_1)R_{N-1}^0}{1 + (\rho_2/\rho_1)R_{N-1}^0} \quad \text{when } (\rho_2/\rho_1)R_{N-1}^0 < 1.$$
(5.102)

Next, we expand the hyperbolic tangents or cotangents in exponential form:

$$R_N^0(n_0) = \frac{e^{(n_0 d_1 - 1/2\ln K_a)} + e^{-(n_0 d_1 - 1/2\ln K_a)}}{e^{(n_0 d_1 - 1/2\ln K_a)} - e^{-(n_0 d_1 - 1/2\ln K_a)}},$$
(5.103)

$$R_N^0(n_0) = \frac{e^{(n_0 d_1 - 1/2\ln K_b)} - e^{-(n_0 d_1 - 1/2\ln K_b)}}{e^{(n_0 d_1 - 1/2\ln K_b)} + e^{-(n_0 d_1 - 1/2\ln K_b)}},$$

where K_a is used when the argument lies between -1 and $+1$, and K_b is used when the argument lies outside this range. These equations can also be written as

$$R_N^0(n_0) = \frac{\frac{1}{\sqrt{K_a}}e^{n_0 d_1} + \sqrt{K_a}e^{-n_0 d_1}}{\frac{1}{\sqrt{K_a}}e^{n_0 d_1} - \sqrt{K_a}e^{-n_0 d_1}},$$
(5.104)

and

$$R_N^0(n_0) = \frac{\frac{1}{\sqrt{K_b}}e^{n_0 d_1} - \sqrt{K_b}e^{-n_0 d_1}}{\frac{1}{\sqrt{K_b}}e^{-n_0 d_1} + \sqrt{K_b}e^{-n_0 d_1}}.$$

We now divide the numerator and denominator in each of these equations by the first term in each:

$$R_N^0(n_0) = \frac{1 + K_a e^{-2n_0 d_1}}{1 - K_a e^{-2n_0 d_1}} \text{ for } |(\rho_2/\rho_1) R_{N-1}| > 1, \tag{5.105}$$

and

$$R_N^0(n_0) = \frac{1 - K_b e^{-2n_0 d_1}}{1 + K_b e^{-2n_0 d_1}} \text{ for } |(\rho_2/\rho_1) R_{N-1}| < 1.$$

However, $K_a = -K_b \equiv -K$. Therefore, we can write a single recursive expression for the DC layered-earth correction factor:

$$R_N^0(n_0) = \frac{1 - K e^{-2n_0 d_1}}{1 + K e^{-2n_0 d_1}}. \tag{5.106}$$

This same procedure can be extended progressively through the layers comprising an N-layered sequence. At the top of layer 1, the layered-earth correction factor for N layers is:

$$R_N^0(n_0) = \frac{1 - K e^{-2n_0 d_1}}{1 + K e^{-2n_0 d_1}}, \tag{5.107}$$

$$K = \frac{1 - (\rho_2/\rho_1) R_{N-1}^0(n_0)}{1 + (\rho_2/\rho_1) R_{N-1}^0(n_0)}.$$

The quantity $R_{N-1}^0(n_0)$ is the layered-earth correction factor for the same N-layered sequence with the top layer removed, yielding a sequence of $N-1$ layers:

$$R_{N-1}^0(n_0) = \frac{1 - K e^{-2n_0 d_2}}{1 + K e^{-2n_0 d_2}},$$

$$K = \frac{1 - (\rho_3/\rho_2) R_{N-2}^0(n_0)}{1 + (\rho_3/\rho_2) R_{N-2}^0(n_0)},$$

and so on until we reach a 2-layer sequence including only the lower half-space and the layer immediately above it:

$$R_2^0(n_0) = \frac{1 - K e^{-2n_0 d_{N-2}}}{1 + K e^{-2n_0 d_{N-2}}},$$

$$K = \frac{1 - (\rho_N/\rho_{N-1}) R_1^0(n_0)}{1 + (\rho_N/\rho_{N-1}) R_1^0(n_0)},$$

and finally, at the surface of the lower half-space, we recognize that the layered-earth correction factor for a uniform half-space is unity:

$$R_1^0(n_0) = 1.$$

The DC layered-earth correction factor is one of the most important mathematical expressions in the electrical prospecting methods. One reason for the importance is that the layered-earth model is the
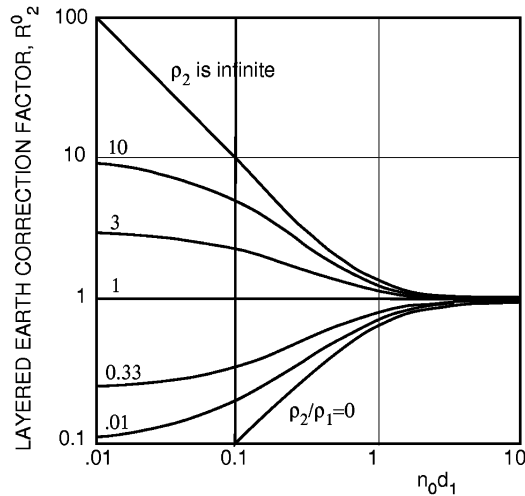
FIGURE 5.4

Layered-earth correction factor at DC for a sequence of two layers (an overburden and a lower half-space) as a function of the contrast in resistivity between two layers.

model most commonly used in interpretation. We find in this chapter that a very similar layered-earth correction factor is the basis for sounding with any version of geoelectric methods – DC sounding, MT sounding, *F*requency-*D*omain *E*lectro*M*agnetic (FDEM) sounding and *T*ime-*D*omain *E*lectro*M*agnetic (TDEM) sounding. The expression we have developed here for DC sounding is a limiting version of a more general electromagnetic layered-earth correction factor.

An extremely important property of the layered-earth correction factor is that every parameter that enters into it is dimensionless. On examination, we see that all layer thicknesses, d_i, are multiplied by the term n_0, which has the inverse units of distance, and resistivities enter only as ratios of resistivity between two successive layers, ρ_i/ρ_{i-1}. The layered-earth correction functions are totally scalable – the actual resistivity and depth scales for a geoelectric structure need not be assigned until after computations have been made.

Let us now examine the nature of layered-earth correction functions. Fig. 5.4 shows a set of DC layered-earth correction functions for the simple case of a layer with one resistivity covering a substratum of infinite thickness with another resistivity. The resistivity contrast is characterized by a scaling factor, $\eta = \rho_2/\rho_1$.

The curves in Fig. 5.4 have been plotted to bilogarithmic coordinates. This procedure is equivalent to a *Napierian transform*. Specifically, the transform is defined by the equations for changes in variables:

$$x = 2.303 \times \ln(F), \quad y = 2.303 \times \ln(n_0 d_1),$$

where x and y represent the ordinate and abscissa of the plot in Fig. 5.4.

On examining Fig. 5.4, we note that for large values of $n_0 d_1$, the layered-earth correction factor is very nearly unity; there is no correction to uniform earth resistivity. With values of $n_0 d_1$ less than unity, the value for the layered-earth correction factor departs from unity, and for very small values of $n_0 d_1$, the layered-earth correction factor approaches the value, η, which is the contrast in resistivity between the layer and the substratum. This is actually a mathematical reflection of a simple fact that, with narrow spacings relative to depth, all one sees is the top layer, and at larger separations, all ones sees is the basement.

Substitution of Eq. (5.98) into (5.87) leads to an expression for the spatial spectrum of the electric potential on the surface of the earth

$$u(k_x, k_y, +0) = (I\rho_1/n_0)R_N^0(n_0), \tag{5.108}$$

where, on the basis of the continuity of the potential and its spectrum, at $z = 0$, we take into account:

$$u(k_x, k_y, 0) = u(k_x, k_y, -0) = u(k_x, k_y, +0).$$

In accord with Eq. (5.61), the spectrums for the horizontal components of the electric field at the surface of the earth will be

$$e_x(k_x, k_y, 0) = (ik_x/n_0)I\rho_1 R_N^0(n_0),$$
$$e_y(k_x, k_y, 0) = (ik_y/n_0)I\rho_1 R_N^0(n_0). \tag{5.109}$$

This is the *wave number domain* representation of the solution to the problem.

5.2.3 ELECTRIC FIELD OF THE POINT SOURCE IN A LAYERED EARTH

We now express these two solutions, Eqs. (5.108) and (5.109), in the spatial domain by applying the inverse Fourier transformation:

$$U(x, y, 0) = \frac{I\rho_1}{4\pi^2} \iint_{-\infty}^{\infty} \frac{1}{n_0} R_N^0(n_0)e^{-i(k_x x + k_y y)} dk_x dk_y, \tag{5.110}$$

$$E_x(x, y, 0) = \frac{I\rho_1}{4\pi^2} \iint_{-\infty}^{\infty} \frac{ik_x}{n_0} R_N^0(n_0)e^{-i(k_x x + k_y y)} dk_x dk_y, \tag{5.111}$$

$$E_y(x, y, 0) = \frac{I\rho_1}{4\pi^2} \iint_{-\infty}^{\infty} \frac{ik_y}{n_0} R_N^0(n_0)e^{-i(k_x x + k_y y)} dk_x dk_y, \tag{5.112}$$

$$E_z(x, y, 0) = 0, \tag{5.113}$$

where $R_N^0(n_0)$ is determined from Eq. (5.106).

Eqs. (5.111), (5.112), and (5.113) can be combined into a single vector equation:

$$\mathbf{E}(x, y, 0) = \frac{I\rho_1}{4\pi^2} \iint_{-\infty}^{\infty} i\frac{\mathbf{n}_0}{n_0} R_N^0(n_0)e^{-i(k_x x + k_y y)} dk_x dk_y, \tag{5.114}$$

where $\mathbf{n}_0$ is the *wave vector:*

$$\mathbf{n}_0 = k_x \mathbf{d}_x + k_y \mathbf{d}_y. \tag{5.115}$$

Eqs. (5.111)–(5.113) express the solution of the diffusion equation for the field around a point source on the surface of a layered earth. In general, the equations must be evaluated numerically. However, we can consider two simple examples, those for $N = 1$ and $N = 2$.

- Let $N = 1$. This is the case of a point source on the surface of a completely uniform half-space. In this case, the expressions for the various components of the field can be obtained by taking a limit in Eq. (5.99) of $R_N^0(n_0)$ as $d_1 \to \infty$:

$$R_1^0 = \lim_{d_1 \to \infty} R_N^0(n_0) = 1. \tag{5.116}$$

In so doing, we have made use of the following expression for the hyperbolic function:

$$\coth x = \frac{e^x + e^{-x}}{e^x - e^{-x}} = \frac{1 + e^{-2x}}{1 - e^{-2x}} \to 1 \text{ as } x \to \infty. \tag{5.117}$$

Substituting Eq. (5.116) into Eq. (5.110), we write

$$\begin{aligned}
U(x, y, 0) &= \frac{I\rho_1}{4\pi^2} \iint_{-\infty}^{\infty} \frac{1}{n_0} e^{-i(k_x x + k_y y)} dk_x dk_y \\
&= \frac{I\rho_1}{2\pi} \frac{1}{(x^2 + y^2)^{1/2}}.
\end{aligned} \tag{5.118}$$

This is the same as Eq. (4.74) for the potential about a point source on the surface of a homogeneous half-space.

- Let $N = 2$. The appropriate layered-earth correction factor is:

$$R_2^0(n_0) = \coth\{n_0 d_1 + \coth^{-1}(\rho_2/\rho_1)\}. \tag{5.119}$$

But,

$$\coth^{-1}\frac{\rho_2}{\rho_1} = \frac{1}{2}\ln\frac{\rho_2 + \rho_1}{\rho_2 - \rho_1} = -\frac{1}{2}\ln K_{12} = -\ln(K_{12})^{1/2}, \tag{5.120}$$

where K_{12} will be shown to have the sense of a *reflection coefficient* for current at an interface,

$$K_{12} = (\rho_2 - \rho_1)/(\rho_2 + \rho_1). \tag{5.121}$$

Hence,

$$\begin{aligned}
R_2^0(n_0) &= \coth\left\{n_0 d_1 - \ln\sqrt{K_{12}}\right\} \\
&= \frac{1 + K_{12}e^{-2n_0 d_1}}{1 - K_{12}e^{-2n_0 d_1}} = 1 + \frac{2K_{12}e^{-2n_0 d_1}}{1 - K_{12}e^{-2n_0 d_1}}.
\end{aligned} \tag{5.122}$$

The fraction in Eq. (5.122) can be expanded as a series:

$$\frac{K_{12}e^{-2n_0d_1}}{1 - K_{12}e^{-2n_0d_1}} = \sum_{\ell=1}^{\infty} K_{12}^{\ell}e^{-2n_0d_1\ell}. \tag{5.123}$$

Substituting this expression into Eq. (5.122), we have:

$$R_2^0(n_0) = 1 + 2\sum_{\ell=1}^{\infty} K_{12}^{\ell}e^{-2n_0\ell d_1}. \tag{5.124}$$

Eq. (5.110) for the electric potential on the surface of a two-layer sequence now can be written as:

$$\begin{aligned}
U(x, y, z) &= \frac{I\rho_1}{4\pi^2} \iint_{-\infty}^{\infty} \frac{1}{n_0} R_2^0(n_0)e^{-i(k_xx+k_yy)}dk_xdk_y \\
&= \frac{I\rho_1}{4\pi^2} \left[\iint_{-\infty}^{\infty} \frac{1}{n_0}e^{-i(k_xx+k_yy)}dk_xdk_y \right. \\
&\quad \left. + 2\sum_{\ell=1}^{\infty} K_{12}^{\ell} \iint_{-\infty}^{\infty} \frac{e^{-2n_0d_1\ell}}{n_0}e^{-i(k_xx+k_yy)}dk_xdk_y \right].
\end{aligned} \tag{5.125}$$

Both integrals in Eq. (5.125) are tabulated forms:

$$\iint_{-\infty}^{\infty} \frac{1}{n_0}e^{-i(k_xx+k_yy)}dk_xdk_y = \frac{2\pi}{[x^2 + y^2]^{1/2}}, \tag{5.126}$$

$$\iint_{-\infty}^{\infty} \frac{e^{-2n_0d_1\ell}}{n_0}e^{-i(k_xx+k_yy)}dk_xdk_y = \frac{2\pi}{[x^2 + y^2 + (2\ell d_1)^2]^{1/2}}. \tag{5.127}$$

Substituting these two integral identities into Eq. (5.125), we obtain algebraically simple expressions for the potential:

$$U(x, y, 0) = \frac{I\rho_1}{2\pi} \left\{ \frac{1}{(x^2 + y^2)^{1/2}} + 2\sum_{\ell=1}^{\infty} K_{12}^{\ell}\frac{1}{[x^2 + y^2 + (2\ell d_1)^2]^{1/2}} \right\}, \tag{5.128}$$

and for the electric field:

$$E_x(x, y, 0) = \frac{I\rho_1}{2\pi} \left\{ \frac{x}{(x^2 + y^2)^{3/2}} + 2\sum_{\ell=1}^{\infty} K_{12}^{\ell}\frac{x}{[x^2 + y^2 + (2\ell d_1)^2]^{3/2}} \right\}, \tag{5.129}$$

$$E_y(x, y, 0) = \frac{I\rho_1}{2\pi} \left\{ \frac{y}{(x^2 + y^2)^{3/2}} + 2\sum_{\ell=1}^{\infty} K_{12}^{\ell}\frac{y}{[x^2 + y^2 + (2\ell d_1)^2]^{3/2}} \right\}. \tag{5.130}$$

It is of particular interest at this point to note that if the radicals in these three expressions were to be thought of as being distances (in the case of Eq. (5.128)) or distances cubed (in the case of Eqs. (5.129)
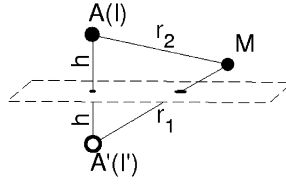
FIGURE 5.5

Geometric definition of a Kelvin image.

and (5.130)), each term would be the locus of a point in the rz plane, as indicated in Fig. 5.5. These points lie on a vertical line passing through the origin.

Consider a totally different physical problem, one in optics as shown in Fig. 5.5. A plane mirror (dashed rectangle) is assumed to lie in the plane. We insert a point source of light at point A a distance h above the mirror and observe the light at another point, M, lying on the same side of the mirror at a distance $r_2 = (x^2 + y^2 + z^2)^{1/2}$. But, we also see an image of that point source seemingly located at A' at a distance h below the plane of the mirror. The strength of the image is determined by the reflection coefficient of the mirror. If we use two parallel mirrors in this same optical experiment, with the mirrors partially transmitting and partially reflecting the light, multiple reflection will occur for light trapped between the two mirrors. At the observation point, we believe we see an infinite series of ever weakening images lying on a line passing through the points A and A'.

Consider the extension of this analysis to the analysis of direct current flow in a many-layered sequence. To use the optical analogy, one would consider a series of horizontal mirrors, each characterized by a Kelvin reflection factor. Images would have to be enumerated for every multiple path for reflections between every mirror. Such an enumeration is tedious, though the method has been used to compute a set of six layer resistivity sounding curves (Mooney and Wetzel, 1956). If the thickness of each layer is an integer multiple of some base distance so that the ratios of thicknesses are integer numbers, the problem is somewhat simplified.

5.2.4 ELECTRICAL DIPOLE SOURCE OF THE DC FIELD IN A HORIZONTALLY LAYERED MEDIUM

Commonly, a current dipole on the surface of the earth is used as a source in electrical exploration. Remember, the current moment of a dipole will be designated as $\mathbf{p} = Id\mathbf{l}$ located at the origin of a system of Cartesian coordinates on the surface of the earth. In accord with Eqs. (4.87), (4.89), and (5.110), the potential about a horizontal current dipole will be

$$U_D = -grad\ U \cdot d\mathbf{l} = -\frac{1}{I}gradU \cdot \mathbf{p} = -\frac{1}{I}\frac{\partial U}{\partial x}p_x - \frac{1}{I}\frac{\partial U}{\partial y}p_y$$

$$= i\frac{\rho_1}{4\pi^2}\iint_{-\infty}^{\infty}\left(\frac{\mathbf{n}_0}{n_0}\cdot\mathbf{p}\right)R_N^0(n_0)e^{-i(k_x x + k_y y)}dk_xdk_y, \tag{5.131}$$

where $\mathbf{n}_0 = k_x\mathbf{d}_x + k_y\mathbf{d}_y$ is a wave vector.

And for this, we find an expression for the electric field of an arbitrarily oriented horizontal current dipole on the surface of the earth

$$\mathbf{E}(x, y, 0) = -grad\, U_D$$

$$= -\frac{\rho_1}{4\pi^2} \iint_{-\infty}^{\infty} \mathbf{n}_0 \left(\frac{\mathbf{n}_0}{n_0} \cdot \mathbf{p}\right) R_N^0(n_0) e^{-i(k_x x + k_y y)} dk_x dk_y. \tag{5.132}$$

Consequently, the x and y components of the electric field take the forms

$$E_x(x, y, 0) = -\frac{\rho_1}{4\pi^2} \iint_{-\infty}^{\infty} k_x \left(\frac{\mathbf{n}_0}{n_0} \cdot \mathbf{p}\right) R_N^0(n_0) e^{-i(k_x x + k_y y)} dk_x dk_y,$$

$$E_y(x, y, 0) = -\frac{\rho_1}{4\pi^2} \iint_{-\infty}^{\infty} k_y \left(\frac{\mathbf{n}_0}{n_0} \cdot \mathbf{p}\right) R_N^0(n_0) e^{-i(k_x x + k_y y)} dk_x dk_y. \tag{5.133}$$

If we introduce a cylindrical system of coordinates, (r, ϕ) with the origin at the center of the current dipole on the surface of the earth and with the radial direction along the axis of the dipole source, then, using Eq. (5.133), it is a simple matter to specify the azimuthal, E_ϕ, and radial, E_r, components of the electric field:

$$E_r = \mathbf{E} \cdot \mathbf{d}_r,$$

$$E_\phi = \mathbf{E} \cdot \mathbf{d}_\phi,$$

where $\vec{d}_r$ is a unit vector in the radial direction,

$$\mathbf{d}_r = \frac{x}{r}\mathbf{d}_x + \frac{y}{r}\mathbf{d}_y$$

and $\vec{d}_\phi$ is a unit vector in the tangential direction

$$\mathbf{d}_\phi = -\frac{y}{r}\mathbf{d}_x + \frac{x}{r}\mathbf{d}_y, \tag{5.134}$$

and on the earth's surface, $r = (x^2 + y^2)^{1/2}$.

In a case in which the source dipole is oriented along the x axis, such that $\mathbf{p} = p\mathbf{d}_x$, by substituting Eq. (5.133) into (5.134), we get

$$E_r(r, \phi, 0) = -\frac{p}{r}\frac{\rho_1}{4\pi^2} \iint_{-\infty}^{\infty} \frac{k_x}{n_0}(k_x x + k_y y) R_N^0(n_0) e^{-i(k_x x + k_y y)} dk_x dk_y, \tag{5.135}$$

$$E_\phi(r, \phi, 0) = -\frac{p}{r}\frac{\rho_1}{4\pi^2} \iint_{-\infty}^{\infty} \frac{k_x}{n_0}(k_y x - k_x y) R_N^0(n_0) e^{-i(k_x x + k_y y)} dk_x dk_y. \tag{5.136}$$

Eqs. (5.133) and (5.136) will play a fundamental role in the theory for dipole electromagnetic soundings.

5.2.5 EXPRESSIONS FOR ELECTRIC FIELDS IN A HORIZONTALLY LAYERED MEDIUM USING THE HANKEL TRANSFORM

It should be obvious by now that the field about a point source on the surface of a horizontally stratified medium exhibits cylindrical symmetry with respect to the vertical axis (the z axis) through the source. Because of this, for many problems in electrical exploration, it is preferable to write the electric potential and the electric field in a cylindrical coordinate system, r, ϕ, z. Such expressions can be obtained, for example, by making use of the integral identity

$$\frac{1}{4\pi^2} \iint_{-\infty}^{\infty} f(n_0) e^{-i(k_x x + k_y y)} dk_x dk_y = \frac{1}{2\pi} \int_0^{\infty} f(n_0) n_0 J_0(n_0 r) dn_0, \tag{5.137}$$

where the function $f(n_0)$ must be absolutely integrable over the real axis in the range $0 \le n_0 < \infty$, $r = (x^2 + y^2)^{1/2}$, and J_0 is the Bessel's function of order zero.

Substituting

$$(I\rho_1/n_0) R_N^0(n_0) = f(n_0)$$

in Eq. (5.110) and then substituting the result in Eq. (5.137), we have:

$$U(r) = \frac{I\rho_1}{2\pi} \int_0^{\infty} R_N^0(n_0) J_0(n_0 r) dn_0. \tag{5.138}$$

The expression on the right-hand side of the equality sign in Eq. (5.138) belongs to a class of integrals known as *Hankel transforms*. Let us review how such transforms are developed.

Let $f(n_0)$ be an arbitrary absolutely integrable function on the real axis over the range $0 \le n_0 < \infty$. Then, the following pair of reciprocal single-valued integral transformations, known as the *Hankel* or *Fourier-Bessel* transforms, must exist:

$$\chi_f(r) = \int_0^{\infty} f(n_0) J_m(n_0 r) n_0 dn_0, \tag{5.139}$$

$$f(n_0) = \int_0^{\infty} \chi_f(r) J_m(n_0 r) r dr, \tag{5.140}$$

where $m = 1, 2, 3, \dots.$, and J_m is a Bessel's function of order m.

Eq. (5.138) states that the electric potential can be obtained as the zero-order Hankel transform of the layered-earth correction factor, $R_N^0(n_0)$, multiplied by the factor $I\rho_1/2\pi n_0$. The inverse also holds, considering Eq. (5.140):

$$R_N^0(n_0) = \frac{2\pi n_0}{\rho_1} \int_0^{\infty} \frac{U(r)}{I} J_0(n_0 r) r dr. \tag{5.141}$$

This illustrates a result which is quite important in the theory of electrical prospecting: the layered-earth correction factor, which is a function only of the profile of conductivity through a horizontally stratified sequence of rocks, can be determined by measuring the electric potential as a function of distance from the source, if the current I is known or held constant.

We can also express the radial component of the electric field for a point source of current through the use of Eq. (5.138):

$$E_r(r) = -\frac{\partial U(r)}{\partial r} = \frac{I\rho_1}{2\pi} \int_0^\infty R_N^0(n_0) J_1(n_0 r) n_0 dn_0, \tag{5.142}$$

where we have made use of an identity for Bessel's functions:

$$\partial J_0(n_0 r)/\partial r = -n_0 J_1(n_0 r).$$

We see that the radial component of the electric field is the Hankel transform of the layered-earth correction factor multiplied by $I\rho_1/2\pi$. The inverse transform is

$$R_N^0(n_0) = \frac{2\pi}{\rho_1} \int_0^\infty \frac{E_r(r)}{I} J_1(n_0 r) r dr. \tag{5.143}$$

Thus, measurement of the electric field as a function of distance also can be used to determine the layered-earth correction factor.

We will now turn to the determination of the components of the electric field from a current dipole source, using the Hankel transform approach. In so doing, we write the expression $\mathbf{E} = -grad\, U_D$ in polar coordinates:

$$E_r(r, \phi) = -\partial U_D/\partial r,$$

$$E_\phi(r, \phi) = -\frac{1}{r} \frac{\partial U_D}{\partial \phi}. \tag{5.144}$$

Let us suppose now that a current dipole with the moment $\mathbf{p}$ is oriented along the x axis:

$$\mathbf{p} = p\mathbf{d}_x = Id\ell\mathbf{d}_x \tag{5.145}$$

and so, the electric potential from the dipole is

$$U_D(r, \phi) = -\frac{1}{I} grad\, U \cdot \mathbf{p} = -d\ell \left(\frac{\partial U}{\partial r}\mathbf{d}_r + \frac{1}{r}\frac{\partial U}{\partial \phi}\mathbf{d}_\phi \right) \cdot \mathbf{d}_x. \tag{5.146}$$

In accord with Eq. (5.135), the unit vector $\mathbf{d}_x$ can be expressed in polar coordinates using the unit vectors $\mathbf{d}_r$ and $\mathbf{d}_\phi$:

$$\mathbf{d}_x = \frac{x}{r}\mathbf{d}_r - \frac{y}{r}\mathbf{d}_\phi = (\cos\,\phi)\mathbf{d}_r - (\sin\,\phi)\mathbf{d}_\phi. \tag{5.147}$$

Substituting Eq. (5.147) into (5.146), we can write:

$$U_D(r, \phi) = -d\ell\,(\cos\,\phi)\frac{\partial U}{\partial r} + d\ell\frac{\sin\,\phi}{r}\frac{\partial U}{\partial \phi}. \tag{5.148}$$

In the case of a laterally uniform sequence of layers, we already know that the potential function, U, exhibits cylindrical symmetry, so that derivatives with respect to ϕ will be zero. So, we actually

have:

$$U_D(r, \phi) = -d\ell \ (\cos \ \phi) \frac{\partial U(r)}{\partial r}. \tag{5.149}$$

Substituting Eq. (5.149) into (5.144), we can write:

$$E_r(r, \phi) = d\ell \ (\cos \ \phi) \frac{\partial^2 U(r)}{\partial r^2}, \tag{5.150}$$

$$E_\phi(r, \phi) = -d\ell \ (\sin \ \phi) \frac{1}{r} \frac{\partial U(r)}{\partial r}. \tag{5.151}$$

Using Eq. (5.138), we can write these last two equations as

$$E_r(r, \phi) = \frac{I\rho_1 d\ell}{2\pi} \ (\cos \ \phi) \frac{\partial^2}{\partial r^2} \int_0^\infty R_N^0(n_0) J_0(n_0 r) dn_0, \tag{5.152}$$

$$E_\phi(r, \phi) = -\frac{I\rho_1 d\ell}{2\pi} \ (\sin \ \phi) \frac{1}{r} \frac{\partial}{\partial r} \int_0^\infty R_N^0(n_0) J_0(n_0 r) dn_0. \tag{5.153}$$

Making use of tabulated identities for the Bessel's functions, we can write

$$\frac{\partial^2}{\partial r^2} J_0(n_0 r) = -n_0 \frac{\partial}{\partial r} J_1(n_0 r) = \frac{n_0}{r} J_1(n_0 r) - n_0^2 J_0(n_0 r). \tag{5.154}$$

Finally, substituting Eqs. (5.142) and (5.154) into (5.152) and (5.153), we find the following expressions for the radial and tangential components of the electric field about a current dipole source on the surface of a horizontally stratified medium:

$$E_r(r, \phi) = \frac{I\rho_1 d\ell}{2\pi r} \ (\cos \ \phi) \int_0^\infty R_N^0(n_0)[J_1(n_0 r) - n_0 r J_0(n_0 r)] n_0 dn_0, \tag{5.155}$$

$$E_\phi(r, \phi) = \frac{I\rho_1 d\ell}{2\pi r} \ (\sin \ \phi) \int_0^\infty R_N^0(n_0) J_1(n_0 r) n_0 dn_0. \tag{5.156}$$

5.3 ELECTROMAGNETIC FIELD OF AN ARBITRARY SYSTEM OF MAGNETOSPHERIC CURRENTS IN A HORIZONTALLY HOMOGENEOUS MEDIUM

In magnetotelluric method, which we will discuss in details in Chapter 13, the primary field is usually taken to be a plane wave vertically incident on the earth's surface. This model, as we have already noted, permits the easy calculation of a field in a horizontally homogeneous geoelectric medium. However, it is also important to solve the problem of excitation by an arbitrary system of magnetospheric currents. This problem is of fundamental importance to electromagnetic sounding with controlled sources also.
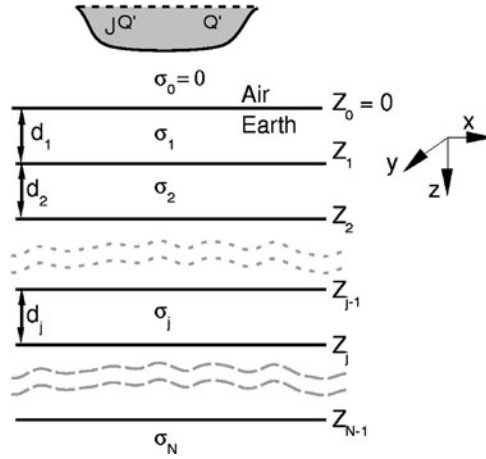
FIGURE 5.6

Model used in the problem of layered-earth excitation by an arbitrary system of magnetospheric currents.

5.3.1 SPATIAL FREQUENCY-DOMAIN (SFD) REPRESENTATION OF THE ELECTROMAGNETIC FIELD IN A HORIZONTALLY LAYERED MEDIUM

We begin with a Cartesian coordinate system with its origin on the surface of the earth and with the z axis directed downwards. At a given point, we will assume the earth consists of N homogeneous layers, each with a conductivity σ_j and a thickness d_j ($j = 1, 2, 3, ..., N$). The model is bounded by a nonconducting upper half-space at $z = 0$. The magnetic permeability, μ, is assumed to have the value for free space, μ_0. The source of the field is taken to be a current system circulating at high altitude with the density $\mathbf{j}^Q$ (Fig. 5.6). The field varies in time by the factor $e^{-i\omega t}$. However, the field varies so slowly that we can neglect displacement currents; that is, we are examining only a quasi-stationary model of the field.

In accord with Eq. (4.123), outside the region in which source currents are flowing, in the atmosphere and within the j-th layer of the earth, the magnetic and electric fields satisfy the equations:

$$\nabla^2 \mathbf{H} + k_j^2 \mathbf{H} = 0,$$
$$\nabla^2 \mathbf{E} + k_j^2 \mathbf{E} = 0, \tag{5.157}$$

where $j = 0, 1, 2, ..., N$ and $k_j^2 = i\omega\mu_0\sigma_j$.

Boundary conditions at each boundary between two layers include continuity of all components of the magnetic field $\mathbf{H}$ and of the tangential components of the electric field $\mathbf{E}$:

$$H_{x,y,z}|_{z=z_j-0} = H_{x,y,z}|_{z=z_j+0}, \tag{5.158}$$

$$E_{x,y}|_{z=z_j-0} = E_{x,y}|_{z=z_j+0}, \tag{5.159}$$

where $j = 1, 2, ..., N - 1$ and

$$z_j = \sum_{\ell=1}^{j} d_\ell, \; z_0 = 0.$$

The vertical component of the electric field exhibits a discontinuity at each boundary specified as:

$$\sigma_j E_z|_{z=z_j-0} = \sigma_{j+1} E_z |_{z=z_j+0} . \tag{5.160}$$

In addition, on the strength of Eq. (4.120)

$$div\mathbf{H} = 0,$$
$$div\mathbf{E} = 0,$$

we can claim the continuity of the vertical derivatives of the vertical components of the electric and magnetic fields at each boundary:

$$\frac{\partial H_z}{\partial z}, \frac{\partial E_z}{\partial z}\bigg|_{z=z_j-0} = \frac{\partial H_z}{\partial z}, \frac{\partial E_z}{\partial z}\bigg|_{z=z_j+0}. \tag{5.161}$$

At great depths, the fields $\mathbf{E}$ and $\mathbf{H}$ tend to zero. In studying the electromagnetic field in this horizontally layered model, it is most convenient to work in the spatial wave number domain.

We can express the magnetic and electric fields as Fourier integrals:

$$\mathbf{H} = \frac{1}{4\pi^2} \iint_{-\infty}^{\infty} \mathbf{h}e^{-i(k_x x + k_y y)} dk_x dk_y,$$
$$\mathbf{E} = \frac{1}{4\pi^2} \iint_{-\infty}^{\infty} \mathbf{e}e^{-i(k_x x + k_y y)} dk_x dk_y, \tag{5.162}$$

where k_x, k_y are spatial frequencies along the x and y axes: $\mathbf{h} = \mathbf{h}(k_x, k_y, z)$, $\mathbf{e} = \mathbf{e}(k_x, k_y, z)$ are the spatial spectrums of the magnetic and electric fields, respectively, and related to $\mathbf{H}$ and $\mathbf{E}$ through the inverse Fourier transforms:

$$\mathbf{h} = \iint_{-\infty}^{\infty} \mathbf{H} e^{i(k_x x + k_y y)} dk_x dk_y,$$
$$\mathbf{e} = \iint_{-\infty}^{\infty} \mathbf{E} e^{i(k_x x + k_y y)} dk_x dk_y. \tag{5.163}$$

On the basis of Eq. (5.157) and the properties of the spatial spectrums (5.56) and (5.57), the Helmholtz equation is satisfied in each layer and in the atmosphere:

$$\mathbf{h}'' = n_j^2 \mathbf{h},$$
$$\mathbf{e}'' = n_j^2 \mathbf{e}, \tag{5.164}$$

where the primes designate differentiation with respect to z, $n_j = (k_x^2 + k_y^2 - k_j^2)^{1/2}$, and we choose that expression for the root for which

$$Re(n_j) > 0. \tag{5.165}$$

In accord with Eq. (5.158) through Eq. (5.162):

$$h_{x,y,z} \mid_{z=z_j-0} = h_{x,y,z} \mid_{z=z_j+0}, \tag{5.166}$$

$$e_{x,y} \mid_{z=z_j-0} = e_{x,y} \mid_{z=z_j+0}, \tag{5.167}$$

$$\sigma_j e_z \mid_{z=z_j-0} = \sigma_{j+1} e_z \mid_{z=z_j+0}, \tag{5.168}$$

$$h'_z \mid_{z=z_j-0} = h'_z \mid_{z=z_j+0}, \tag{5.169}$$

$$e'_z \mid_{z=z_j-0} = e'_z \mid_{z=z_j+0}. \tag{5.170}$$

The spatial spectrums **h** and **e** approach zero as z becomes infinite.

5.3.2 LIPSKAYA-VANYAN FORMULAS CONCERNING IMPEDANCE RATIOS

For the general case of the properties of the functions which satisfy conditions (5.164)–(5.170), we can write a formalism due to Lipskaya (1953) and Vanyan (1959).

Let a function $f(z)$ satisfy the equation:

$$f''(z) = n_j^2 f(z), \tag{5.171}$$

for $z_{j-1} + 0 \le z \le z_j - 0$, $j = 1, 2, ..., N$; $z = \infty$ along with the boundary conditions

$$p_j f(z_j - 0) = p_{j+1} f(z_j + 0), \tag{5.172}$$
$$f'(z_j - 0) = f'(z_j + 0), \ i = 1, 2, ..., N - 1,$$

where p_1, p_2, ..., p_N are arbitrary constants and the function $f(z)$ tends to zero as z approaches infinity. Then, the following formula holds:

$$\frac{f(z)}{f'(z)} \bigg|_{z=+0} = -\frac{1}{n_1} R_N^*(p_1, p_2, ..., p_N), \tag{5.173}$$

where

$$R_N^*(p_1, p_2, ..., p_N) = \coth \left\{ n_1 d_1 + \coth^{-1} \left[\frac{n_1 p_2}{n_2 p_1} \coth(n_2 p_2 + ... + \coth^{-1} \frac{n_{N-1} p_N}{n_N p_{N-1}} \right] \right\}. \tag{5.174}$$

As before, this hyperbolic expression can be expanded to form a continued fraction which is easier to evaluate. Applying Lipskaya-Vanyan's theorem to all the terms in the expansion for computing the spatial field spectrums for a point source in a layered medium, we realize the problem at hand is a special case of Lipskaya-Vanyan's theorem. To prove this theorem, we write the general solution to Eq. (5.171):

$$f(z) = a_j e^{n_j z} + b_j e^{-n_j z} \tag{5.175}$$

for $z_{j-1} + 0 \leq z \leq z_j - 0$; $i = 1, 2, ..., N - 1$ and

$$f(z) = b \, e^{-n_N z} \tag{5.176}$$

for $z_{N-1} + 0 \leq z \leq \infty$.

The solution to (5.176) is written under the constraint $\mathrm{Re}(n_N) > 0$.

We examine by analogy the use of the function

$$F(z) = f(z)/f'(z)$$

in the case of the DC field in a horizontally layered medium. This function will also be called an *impedance ratio*. In accord with Eqs. (5.175) and (5.176),

$$F(z) = (1/n_j) \coth \, (n_j z - q_j), \ z_{j-1} + 0 \leq z \leq z_j - 0, \tag{5.177}$$

where $q_j = \ln(b_j/a_j)^{1/2}$; $j = 1, 2, ..., N - 1$, and

$$F(z) = -1/n_N; \ z_{N-1} + 0 \leq z \leq \infty. \tag{5.178}$$

Thus, the problem of evaluating the function F reduces to evaluation of the dimensionless quantity, q_j.

Obviously, on the strength of Eq. (5.172):

$$p_j F(z_j - 0) = p_{j+1} F(z_j + 0). \tag{5.179}$$

Substituting (5.177) into (5.179), we find

$$(p_j/n_j) \coth(n_j z_j - q_j) = p_{j+1} F(z_j + 0), \tag{5.180}$$

and so

$$q_j = n_j z_j - \coth^{-1} \left(\frac{p_{j+1} n_j}{p_j} F(z_j + 0) \right). \tag{5.181}$$

Consequently, Eq. (5.177) can be written as follows at $z = z_{j-1} + 0$:

$$F(z_{j-1} + 0) = \frac{1}{n_j} \coth \left\{ n_j z_{j-1} - n_j z_j + \coth^{-1} \left[\frac{p_{j+1} n_j}{p_j} F(z_j + 0) \right] \right\}$$

$$= -\frac{1}{n_j} \coth \left\{ n_j d_j - \coth^{-1} \left[\frac{p_{j+1} n_j}{p_j} F(z_j + 0) \right] \right\}. \tag{5.182}$$

In accord with (5.178),

$$F(z_{N-1} + 0) = -1/n_N,$$

this recurrence relationship, which has been obtained, can be expanded into the following form:

$$F(+0) = -\frac{1}{n_1}coth\left\{n_1d_1 + coth^{-1}\left[\frac{n_1p_2}{n_2p_1} \; coth\left(n_2d_2 + coth^{-1}\left(\frac{n_2p_3}{n_3p_2} \; coth\left(n_3d_3 + ..\right.\right.\right.\right.\right.$$

$$\left.\left.\left.\left.... \quad + coth^{-1}\frac{n_{N-1}p_N}{n_N p_{N-1}}\right)...\right)\right)\right]\right\}. \tag{5.183}$$

Eq. (5.183) is equivalent to relationship (5.173). Thus, we have proved Lipskaya-Vanyan's formulas.

5.3.3 HORIZONTAL POLARIZATION OF THE ELECTRIC FIELD IN A HORIZONTALLY HOMOGENEOUS EARTH, AND THE REDUCED SPATIAL WAVE NUMBER SPECTRUM

Let us now examine several important consequences flowing from Lipskaya-Vanyan's theorem. Above all, it is clear from formulas (5.166) through (5.170) that the spatial spectrums for the vertical components of the magnetic and electric fields satisfy the conditions of the theorem, and moreover, for h_z, $p_1 = p_2 = ... = p_N = 1$, and for e_z, $p_j = \sigma_j$ $(j = 1, 2, ..N)$. As a result we have:

$$\left.\frac{h_z}{h_z'}\right|_{z=+0} = -\frac{1}{n_1}R^*(1, 1, ..., 1), \tag{5.184}$$

$$\left.\frac{e_z}{e_z'}\right|_{z=+0} = -\frac{1}{n_1}R^*(\sigma_1, \sigma_2, ..., \sigma_N). \tag{5.185}$$

Let us examine the formula for the vertical component of the electric field. It can be rewritten as:

$$e_z'|_{z=+0} = -\frac{n_1}{R^*(\sigma_1, \sigma_2, ..., \sigma_N)} \; e_z|_{z=+0}. \tag{5.186}$$

We return now to Eq. (5.168) and rewrite it at the surface of the earth $(j = 0)$:

$$\sigma_0 e_z\,|_{z=-0} = \sigma_1 e_z|_{z=+0}. \tag{5.187}$$

In the problem we are examining, the conductivity of air is effectively zero, and so:

$$e_z\,|_{z=+0} = 0, \tag{5.188}$$

and hence, in view of Eq. (5.186)

$$e_z'\,|_{z=+0} = 0. \tag{5.189}$$

It follows from these conditions that immediately beneath the surface of the earth

$$e_z \equiv 0 \text{ for } z \geq +0. \tag{5.190}$$

Indeed, the general solution of Eq. (5.164) for the electric field has the form

$$e_z = e_{z_j}^+ e^{n_j z} + e_{z_j}^- e^{-n_j z}. \tag{5.191}$$

In particular, in the first layer

$$e_z = e_{z_1}^+ e^{n_1 z} + e_{z_1}^- e^{-n_1 z}. \tag{5.192}$$

Differentiating this equation with respect to z, we find

$$e_z' = n_1 (e_{z_1}^+ e^{n_1 z} - e_{z_1}^- e^{-n_1 z}). \tag{5.193}$$

Setting $z = +0$ in Eq. (5.192) and (5.193)

$$e_z |_{z=+0} = e_{z_1}^+ + e_{z_1}^-,$$
$$e_z' |_{z=+0} = n_1 (e_{z_1}^+ - e_{z_1}^-). \tag{5.194}$$

Substituting Eq. (5.194) into Eqs. (5.188) and (5.189), we obtain

$$e_{z_1}^+ + e_{z_1}^- = 0,$$
$$e_{z_1}^+ - e_{z_1}^- = 0,$$

and so

$$e_{z_1}^+ = e_{z_1}^- = 0. \tag{5.195}$$

Consequently, in view of Eqs. (5.192), (5.193), and (5.195), within the first layer

$$e_z \equiv 0, \ e_z' \equiv 0 \text{ for } +0 \leq z \leq z_1 \leq z_1 - 0. \tag{5.196}$$

We can now write the boundary conditions at the bottom surface of the first layer:

$$\sigma_1 e_z |_{z=z_1-0} = \sigma_2 e_z |_{z=z_1+0},$$
$$e_z' |_{z=z_1-0} = e_x' |_{z=z_1+0}. \tag{5.197}$$

Considering Eq. (5.196), we note that these conditions take the form:

$$e_z |_{z=z_1+0} = 0,$$
$$e_z' |_{z=z_1+0} = 0. \tag{5.198}$$

Repeating the same process as above for the first layer, we obtain the following for the second layer:

$$e_z \equiv 0, \ e_z' \equiv 0, \ \text{for } z_1 + 0 \leq z \leq z_2 - 0,$$

and so on for as many layers as are required.

Returning to formula (5.190), we transform the spatial spectrum to its image field E_z using the inverse Fourier transform:

$$E_z \equiv 0 \text{ for } z \geq +0. \tag{5.199}$$

We arrive at the following conclusion: *There is no distribution of electric currents in the magneto-sphere and ionosphere that will cause a vertical component of the electric field, and hence, a vertical*

component of current flow in a horizontally layered earth! Consequently, the electric field induced in a horizontally homogeneous earth is always horizontally polarized.

We must recognize that this an extremely important contribution to the theory of magnetotelluric and magnetovariational sounding, since it permits a marked simplification to the equations for fields in horizontally homogeneous media. In that respect, we return to Maxwell's second equation (4.117), and, considering the implications of Eq. (5.187), we write

$$
\begin{bmatrix}
\mathbf{d}_x & \mathbf{d}_y & \mathbf{d}_z \\
\partial/\partial x & \partial/\partial z & \partial/\partial z \\
E_x & E_y & 0
\end{bmatrix}
= i\omega\mu_0 (H_x \mathbf{d}_x + H_y \mathbf{d}_y + H_z \mathbf{d}_z).
$$

Hence, for the horizontal components of the field

$$
\begin{aligned}
-\partial E_y/\partial z &= i\omega\mu_0 H_x, \\
\partial E_x/\partial z &= i\omega\mu_0 H_y.
\end{aligned}
\tag{5.200}
$$

Transforming these last two formulas for the field to their spatial wave number spectrums, we obtain:

$$
-e'_y = i\omega\mu_0 h_x, \quad e'_x = i\omega\mu_0 h_y.
\tag{5.201}
$$

In accord with Eq. (5.166), the right-hand part of Eq. (5.201) is continuous at the boundaries between layers, and consequently, the left-hand parts are also continuous:

$$
e'_{x,y}\Big|_{z=z_j-0} = e'_{x,y}\Big|_{z=z_j+0}.
\tag{5.202}
$$

Combining Eqs. (5.202), (5.167), and (5.164), we see that the spatial spectrums for the horizontal components of the electric field meet the conditions for Lipskaya-Vanyan's theorem with $p_1 = p_2 = \dots = p_N = 1$. Consequently:

$$
\frac{e_x}{e'_x}\Big|_{z=+0} = \frac{e_y}{e'_y}\Big|_{z=+0} = -\frac{1}{n_1} R_N^*(1, 1, \dots, 1).
\tag{5.203}
$$

From here on, we will refer to the function $R_N^*(1, 1, \dots, 1)$ simply as R_N^*, and call it the *reduced spectral impedance*:

$$
R_N^* = \coth\left\{ n_1 d_1 + \coth^{-1}\left[\frac{n_1}{n_2} \ \coth\left(n_2 d_2 + \dots + \coth^{-1}\frac{n_{N-1}}{n_N} \right) \dots \right] \right\}.
\tag{5.204}
$$

It is evident from Eq. (5.204) that the reduced spectral impedance, R_N^*, at the given spatial wave numbers k_x and k_y is a function only of the parameters defining the geoelectric section and of the temporal frequency of the field, and does not depend on the distribution of currents in the ionosphere. Consequently, we conclude that in interpreting the results of a magnetotelluric survey, we need only determine the impedance ratios in the form of Eq. (5.184) or (5.185). The field results, in accord with Eqs. (5.184) and (5.203) depend only on the geoelectric parameters of the horizontally layered earth and not on the distribution of the ionospheric currents, j^Q. Unfortunately, we must note and stress that this simplification does not extend to the case of a horizontally inhomogeneous earth.

5.4 ELECTROMAGNETIC FIELDS GENERATED IN LAYERED EARTH BY ELECTRIC AND MAGNETIC DIPOLE TRANSMITTERS

In this section we will present a solution of the problem of an EM field in a layered earth generated by electric and magnetic dipole transmitters operating in the frequency or time domains.

5.4.1 SPECTRAL REPRESENTATION OF THE FIELD OF A HORIZONTAL CURRENT DIPOLE ON THE SURFACE OF A HORIZONTALLY LAYERED MEDIUM

Let us begin our analysis with a simple case, one in which a current dipole, energized with a time-harmonic current, is located in a homogeneous conducting medium with the properties σ and μ_0. The current moment of the source is $\mathbf{p}$, oriented along the x axis of a Cartesian coordinate system with the origin at the center of the dipole. From Eq. (4.177), the magnetic field arising from this dipole excitation is:

$$\mathbf{H}(\mathbf{r}) = \frac{1}{4\pi} curl \left(\frac{e^{ikr}}{r} p\mathbf{d}_x \right) = \frac{p}{4\pi} \begin{bmatrix} \mathbf{d}_x & \mathbf{d}_y & \mathbf{d}_z \\ \partial/\partial x & \partial/\partial y & \partial/\partial z \\ e^{ikr}/r & 0 & 0 \end{bmatrix}$$

$$= \frac{\partial}{\partial z} \left(\frac{e^{ikr}}{r} \right) \mathbf{d}_y - \frac{\partial}{\partial y} \left(\frac{e^{ikr}}{r} \right) \mathbf{d}_z. \tag{5.205}$$

Using Eqs. (5.51), (5.56), (5.57), and (5.58), we calculate the spatial spectrums of the x, y, and z components of the magnetic field:

$$h_x = 0,$$
$$h_y = \frac{p}{4\pi} \frac{\partial g}{\partial z},$$
$$h_z = ik_y \frac{p}{4\pi} g, \tag{5.206}$$

where g is the spatial spectrum of e^{ik_y}/r, computed using tabulated integrals:

$$g = \iint_{-\infty}^{\infty} \frac{e^{ikr}}{r} e^{i(k_x x + k_y y)} dx dy = \frac{2\pi e^{-n|z|}}{n}. \tag{5.207}$$

The quantity n, defined as $n = (k_x^2 + k_y^2 - k^2)^{1/2} = (k_x^2 + k_y^2 - i\omega\mu_0\sigma)^{1/2}$ is a *modified wave number*.

At this point, the inverse Fourier transform of this last equation will prove to be useful in the developments which follow:

$$\frac{e^{ikr}}{r} = \frac{1}{2\pi} \iint_{-\infty}^{\infty} \frac{e^{-n|z|}}{n} e^{-i(k_x x + k_y y)} dk_x dk_y. \tag{5.208}$$

Substituting Eq. (5.207) into (5.206), we find

$$h_x = 0,$$

$$h_y = -(p/2)e^{-n|z|} \text{ signum } (z),$$

$$h_z = ik_y \frac{p}{2n} e^{-n|z|}. \tag{5.209}$$

We now need to find the spatial spectrum of the electric field **E**. We will use the first equation of Maxwell in so doing:

$$\mathbf{E}(\mathbf{r}) = \frac{1}{\sigma} curl \ \mathbf{H}(\mathbf{r})$$

$$= \frac{1}{\sigma} \begin{bmatrix} \mathbf{d}_x & \mathbf{d}_y & \mathbf{d}_z \\ \partial/\partial x & \partial/\partial y & \partial/\partial z \\ 0 & H_y & H_z \end{bmatrix}$$

$$= \frac{1}{\sigma} \left[\left(\frac{\partial H_z}{\partial y} - \frac{\partial H_y}{\partial z} \right) \mathbf{d}_x - \frac{\partial H_z}{\partial x} \mathbf{d}_y + \frac{\partial H_y}{\partial x} \mathbf{d}_z \right] \text{ for } \mathbf{r} \neq 0. \tag{5.210}$$

Transforming this expression for **E** to a spatial spectrum, we have:

$$e_x = \frac{1}{\sigma}(-ik_y h_z - h'_y),$$

$$e_y = (ik_x/\sigma)h_z,$$

$$e_z = -(ik_x/\sigma)h_y. \tag{5.211}$$

Substituting Eq. (5.209) into Eq. (5.211), we can write

$$e_x = \frac{pe^{-n|z|}}{2n} \left(i\omega\mu_0 - \frac{k_x^2}{\sigma} \right),$$

$$e_y = -\frac{k_x k_y}{\sigma} \frac{p}{2n} e^{-n|z|},$$

$$e_z = \frac{ik_x}{\sigma} \frac{p}{2} e^{-(n|z|)} \text{signum } (z), \text{ for } z \neq 0. \tag{5.212}$$

The spatial spectrums given in Eq. (5.209) and Eq. (5.212) for the magnetic and electric fields caused by a current dipole source for the x and z components of the magnetic field and the x and y components of the electric field are continuous as one passes through the plane $z = 0$. The spectrums h_y and e_z exhibit discontinuities, the sizes of which are determined by the source dipole moment:

$$h_x|_{z=+0} - h_x|_{z=-0} = 0, \tag{5.213}$$

$$h_y|_{z=+0} - h_y|_{z=-0} = -p, \tag{5.214}$$

$$h_z|_{z=+0} - h_z|_{z=-0} = ik_y p/2n - ik_y p/2n = 0, \tag{5.215}$$

$$e_x|_{z=+0} - e_x|_{z=-0} = \frac{p}{2n} \left(i\omega\mu_0 - \frac{k_x^2}{\sigma} \right) - \frac{p}{2n} \left(i\omega\mu_0 - \frac{k_x^2}{\sigma} \right) = 0, \tag{5.216}$$
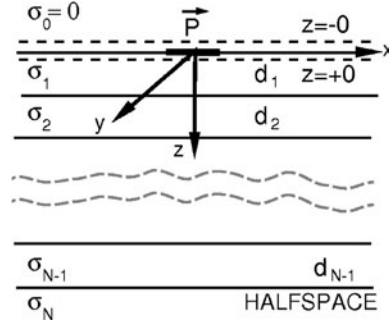
FIGURE 5.7

Current dipole source on the surface of a layered medium. The dipole is formed by a current passing along a short filament of wire. The moment, **p**, is the product of length and current strength.

$$e_y|_{z=+0} - e_y|_{z=-0} = -\frac{k_x k_y}{\sigma}\frac{p}{2n} - \left(-\frac{k_x k_y}{\sigma}\frac{p}{2n}\right) = 0, \tag{5.217}$$

$$e_z|_{z=+0} - e_z|_{z=-0} = ik_x p/2\sigma - (-ik_x p/2\sigma) = ik_x p/\sigma. \tag{5.218}$$

Later, we will use these properties of the spatial spectrums in the solution of the problem of determining the fields of a dipole source in a layered medium.

Let us suppose that a current dipole with a moment $\mathbf{p} = p\mathbf{d}_x$ is situated on the surface of a layered half-space as shown in Fig. 5.7. In order to simplify the notation a bit, we will designate a vanishingly thin region just above the earth's surface as $z = -0$, and a similar region just beneath the earth's surface as $z = +0$. We will consider that the source dipole **p** lies "between" these two regions (to be more precise, we should talk about the surfaces $z = +\epsilon$ and $z = -\epsilon$, where ϵ may be made arbitrarily small).

In the air-filled upper half-space, where $z \leq -0$, on the strength of Maxwell's first equation, curl $\mathbf{H} = 0$, and making use of the scalar potential of the magnetic field, U, we can write

$$\mathbf{H} = -grad\ U. \tag{5.219}$$

In the space wave number domain, this equation can be expressed as

$$h_x = ik_x u, \ h_y = ik_y u, \ h_z = -u',$$

where in the spectrum for u, in accord with the convention we chose earlier, we retain only the exponential term which decreases as $z \to -\infty$,

$$u(z) = u^+ e^{n_0 z}.$$

Consequently:

$$h_x|_{z=-0} = ik_x u^+, \ h_y|_{z=-0} = ik_y u^+, \ h_z|_{z=-0} = -n_0 u^+. \tag{5.220}$$

At the surface $z = +0$, in accord with Lipskaya-Vanyan's theorem, we will make use of the impedance ratios using the spectrum for the vertical component of the magnetic field h_z and its vertical derivative, $\partial h_z / \partial z$:

$$\frac{h_z}{\partial h_z / \partial z}\bigg|_{z=+0} = -\frac{1}{n_1} R_N^* = \frac{1}{i\omega\mu_0} Z^*, \tag{5.221}$$

where Z^* is called the *spectral impedance of a horizontally layered earth*:

$$Z^* = -(i\omega\mu_0 / n_1) R_N^*. \tag{5.222}$$

At this point we can review some simple property of the spectral impedance Z^*. For a homogeneous half-space, the spectral impedance is

$$Z^* = -i\omega\mu_0 / n_1 \tag{5.223}$$

inasmuch as

$$R_1^* = \lim_{d_1 \to \infty} \coth(n_1 d_1) = 1 \tag{5.224}$$

in this case. Note that, we will study the spectral impedance in more details in Chapter 13.

Hence, in view of the following equation,

$$h_z' = i k_x h_x + i k_y h_y,$$

we have:

$$h_z|_{z=+0} = \frac{1}{i\omega\mu_0} Z^* h_z'|_{z=+0} = \frac{Z^*}{i\omega\mu_0}[i k_x h_x|_{z=+0} + i k_y h_y|_{z=+0}].$$

We use Eq. (5.215) to pass through the lower surface of the plane $z = 0$ which contains the dipole source:

$$h_z|_{z=-0} = \frac{Z^*}{i\omega\mu_0}[i k_x h_x|_{z=-0} + i k_y (h_y|_{z=-0} - p)]. \tag{5.225}$$

Substituting Eq. (5.220) for the spectrum of the magnetic field in the upper half-space into Eq. (5.225), we find:

$$-n_0 u^+ = \frac{Z^*}{i\omega\mu_0}[-k_x^2 u^+ - k_y^2 u^+ - i k_y p]$$

$$= -\frac{n_0^2}{i\omega\mu_0} Z^* u^+ - \frac{i k_y p}{i\omega\mu_0} Z^*,$$

and so

$$u^+ = \frac{i k_y p Z^*}{n_0(i\omega\mu_0 - n_0 Z^*)}. \tag{5.226}$$

Substituting Eq. (5.226) in (5.220), we obtain the final result:

$$h_x|_{z=-0} = -\frac{k_x k_y p Z^*}{n_0(i\omega\mu_0 - n_0 Z^*)},$$

$$h_y|_{z=-0} = -\frac{k_y^2 p Z^*}{n_0(i\omega\mu_0 - n_0 Z^*)},$$

$$h_z|_{z=-0} = -\frac{i k_y p Z^*}{i\omega\mu_0 - n_0 Z^*}. \tag{5.227}$$

In order to determine the spectrums for the electric field, we use the impedance ratios. In accord with Lipskaya-Vanyan's theorem, at the surface $z = +0$, the following condition is met:

$$\frac{e_z}{e_z'}\bigg|_{z=+0} = -\frac{1}{n_1} R^*(\sigma_1, \sigma_2, ..., \sigma_n) = -\frac{1}{n_1} R^*(\sigma_n), \tag{5.228}$$

where $R^*(\sigma_1, \sigma_2, ..., \sigma_N) = R^*(\sigma_n)$ is given by Eq. (5.185). In view of the divergence condition, div $\mathbf{E} = 0$, within a homogeneous layer, the spectrum will be

$$e_z' = i k_x e_x + i k_y e_y. \tag{5.229}$$

Considering Eq. (5.229), we can rewrite Eq. (5.228) as

$$e_z|_{z=+0} = -\frac{1}{n_1} R^*(\sigma_n) \, e_z'\,|_{z=+0}$$

$$= -\frac{1}{n_1} R^*(\sigma_n)[i k_x e_x|_{z=+0} + i k_y e_y|_{z=+0}]. \tag{5.230}$$

Passing from the lower surface of the plane $z = 0$ to the upper by using condition (5.218), we write

$$e_z|_{z=-0} + \frac{i k_x p}{\sigma_1} = -\frac{R^*(\sigma_n)}{n_1}[i k_x e_x|_{z=-0} + i k_y e_y|_{z=-0}]. \tag{5.231}$$

Also, at the surface $z = -0$ (the boundary which separates the lower conducting half-space from the upper insulating half-space), the vertical component of the electric field and its spectrum must be equal to zero: $e_z|_{z=-0} = 0$. Consequently, Eq. (5.231) can be rewritten as

$$i k_x e_x|_{z=-0} + i k_y e_y|_{z=-0} = -\frac{i n_1 k_x p}{\sigma_1 R^*(\sigma_n)}. \tag{5.232}$$

Now, in view of Maxwell's second equation,

$$\partial E_y/\partial x - \partial E_x/\partial y = i\omega\mu_0 H_z.$$

Expressed in the wave number domain at the plane $z = -0$, we have

$$-i k_x e_y|_{z=-0} + i k_y e_x|_{z=-0} = i\omega\mu_0 h_z\,|_{z=-0}, \tag{5.233}$$

or, if we consider Eq. (5.227),

$$-ik_x e_y|_{z=-0} + ik_y e_x|_{z=-0} = \frac{\omega\mu_0 k_y p Z^*}{i\omega\mu_0 - n_0 Z^*}. \tag{5.234}$$

Eqs. (5.232) and (5.234) form a system of two linear algebraic equations relating the two unknown quantities $e_x|_{z=-0}$ and $e_y|_{z=-0}$. Solving this system of equations, we find:

$$e_x|_{z=-0} = -\frac{p}{n_0^2}\left[\frac{n_1 k_x^2}{\sigma_1 R^*(\sigma_n)} + \frac{i\omega\mu_0 k_y^2 Z^*}{i\omega\mu_0 - n_0 Z^*}\right],$$

$$e_y|_{z=-0} = -\frac{k_x k_y p}{n_0^2}\left[\frac{n_1}{\sigma_1 R^*(\sigma_n)} - \frac{i\omega\mu_0 Z^*}{i\omega\mu_0 - n_0 Z^*}\right]. \tag{5.235}$$

Carrying out an inverse Fourier transform, we obtain the spectrums of the electromagnetic field of a dipole source at the surface of a horizontally-layered medium:

$$\mathbf{H}(x, y, 0) = \frac{1}{4\pi^2}\iint_{-\infty}^{\infty} \mathbf{h}|_{z=-0}e^{-i(k_x x + k_y y)}dk_x dk_y,$$

$$\mathbf{E}(x, y, 0) = \frac{1}{4\pi^2}\iint_{-\infty}^{\infty} \mathbf{e}|_{z=-0}e^{-i(k_x x + k_y y)}dk_x dk_y. \tag{5.236}$$

5.4.2 ELECTROMAGNETIC FIELD OF A HORIZONTAL CURRENT DIPOLE AT THE SURFACE OF A HOMOGENEOUS HALF-SPACE

The expressions which have been developed for the spectrums of an electromagnetic field become much simpler in the case of a uniform half-space with a constant electrical conductivity, $\sigma_1 = constant$. In this case, in accord with results obtained earlier (Eqs. (5.223) and (5.224)), we have:

$$R^*(\sigma_1) = 1,$$
$$Z^* = -i\omega\mu_0/n_1. \tag{5.237}$$

Substituting Eq. (5.237) in Eq. (5.227), we have

$$h_x|_{z=-0} = \frac{k_x k_y p}{n_0(n_1 + n_0)} = \frac{k_x k_y p(n_1 - n_0)}{n_0(n_1^2 - n_0^2)} = -\frac{k_x k_y p}{i\omega\mu_0\sigma_1 n_0}(n_1 - n_0), \tag{5.238}$$

$$h_y|_{z=-0} = \frac{k_y^2 p}{n_0(n_1 + n_0)} = \frac{k_y^2 p(n_1 - n_0)}{n_0(n_1^2 - n_0^2)} = -\frac{k_y^2 p}{i\omega\mu_0\sigma_1 n_0}(n_1 - n_0), \tag{5.239}$$

$$h_z|_{z=-0} = \frac{ik_y p}{n_1 + n_0} = \frac{ik_y p(n_1 - n_0)}{n_1^2 - n_0^2} = -\frac{k_y p}{\omega\mu_0\sigma_1}(n_1 - n_0), \tag{5.240}$$

where, more precisely,

$$n_1^2 - n_0^2 = (k_x^2 + k_y^2 - i\omega\mu_0\sigma_1) - (k_x^2 + k_y^2) = -i\omega\mu_0\sigma_1.$$

A similar substitution of Eq. (5.237) in Eq. (5.235) yields:

$$e_x|_{z=-0} = -\frac{p}{n_0^2}\left[\frac{n_1 k_x^2}{\sigma_1} - \frac{i\omega\mu_0 k_y^2}{n_1+n_0}\right]$$

$$= -\frac{p}{n_0^2}\left[\frac{n_1 k_x^2}{\sigma_1} + \frac{k_y^2}{\sigma_1}(n_1-n_0)\right] = -\frac{p}{\sigma_1}\left(n_1 - \frac{k_y^2}{n_0}\right), \tag{5.241}$$

$$e_y|_{z=-0} = -\frac{k_x k_y p}{n_0^2}\left[\frac{n_1}{\sigma_1} + \frac{i\omega\mu_0}{n_1+n_0}\right]$$

$$= -\frac{k_x k_y p}{n_0^2}\left[\frac{n_1}{\sigma_1} - \frac{n_1-n_0}{\sigma_1}\right] = -\frac{k_x k_y p}{\sigma_1 n_0}. \tag{5.242}$$

To specify the amplitudes of the magnetic and electric fields represented Eqs. (5.238), (5.239), (5.240), (5.241), and (5.242), we evaluate the appropriate Fourier integral of the pair in Eq. (5.236). To conserve effort at this time, we will limit our considerations to the vertical component of the magnetic field and the horizontal components of the electric field. To begin, we will carry out the calculation of H_z:

$$H_z(x, y, 0) = \frac{-ip}{4\pi^2\omega\mu_0\sigma_1}\iint_{-\infty}^{\infty}(-ik_y)(n_1-n_0)e^{-i(k_x x+k_y y)}dk_x dk_y$$

$$= \frac{-ip}{4\pi^2\omega\mu_0\sigma_1}\frac{\partial}{\partial y}\{I_1 - I_2\}, \tag{5.243}$$

where

$$I_1 = \iint_{-\infty}^{\infty} n_1 e^{-i(k_x x+k_y y)}dk_x dk_y, \tag{5.244}$$

$$I_2 = \iint_{-\infty}^{\infty} n_0 e^{-i(k_x x+k_y y)}dk_x dk_y. \tag{5.245}$$

We will use Eqs. (5.208) and (5.65) in evaluating the integrals I_1 and I_2. It can readily be seen that:

$$I_1 = \left(\frac{\partial^2}{\partial z^2}\iint_{-\infty}^{\infty}\frac{e^{-n_1|z|}}{n_1}e^{-i(k_x x+k_y y)}dk_x dk_y\right)$$

$$= 2\pi\left(\frac{\partial^2}{\partial z^2}\frac{e^{ik_1\tilde{r}}}{\tilde{r}}\right)_{z=0} = -2\pi\frac{1-ik_1 r}{r^3}e^{ik_1 r}, \tag{5.246}$$

$$I_2 = \left(\frac{\partial^2}{\partial z^2}\iint_{-\infty}^{\infty}\frac{e^{-n_0|z|}}{n_0}e^{-i(k_x x+k_y y)}dk_x dk_y\right)$$

$$= 2\pi\left(\frac{\partial^2}{\partial z^2}\frac{1}{\tilde{r}}\right)_{z=0} = \frac{-2\pi}{r^3}, \tag{5.247}$$

where $\tilde{r} = (x^2 + y^2 + z^2)^{1/2}$ and $r = \tilde{r}|_{z=0} = (x^2 + y^2)^{1/2}$.

Substituting Eqs. (5.246) and (5.247) in (5.243), we can write:

$$H_z(x, y, 0) = \frac{ip}{2\pi\omega\mu_0\sigma_1} \frac{\partial}{\partial y} \left(\frac{1 - ik_1 r}{r^3} e^{ik_1 r} - \frac{1}{r^3} \right)$$

$$= \frac{ip}{2\pi\omega\mu_0\sigma_1} \frac{1}{r^4} \frac{y}{r} \left\{ 3 - e^{ik_1 r} (3 - 3ik_1 r - k_1^2 r^2) \right\}. \tag{5.248}$$

Next, we find the amplitude of E_x. Substituting from Eq. (5.241) into (5.236):

$$E_x(x, y, 0) = -\frac{p}{4\pi^2\sigma_1} \iint_{-\infty}^{\infty} n_1 e^{-i(k_x x + k_y y)} dk_x dk_y - \frac{p}{4\pi^2\sigma_1} \iint_{-\infty}^{\infty} \frac{(-ik_y)^2}{n_0} e^{-i(k_x x + k_y y)} dk_x dk_y$$

$$= -\frac{p}{4\pi^2\sigma_1} \left(I_1 + \frac{\partial^2}{\partial y^2} I_3 \right), \tag{5.249}$$

where

$$I_3 = \iint_{-\infty}^{\infty} \frac{1}{n_0} e^{-i(k_x x + k_y y)} dk_x dk_y.$$

In accord with Eq. (5.65), we have

$$I_3 = \frac{2\pi}{\tilde{r}} \bigg|_{z=0} = \frac{2\pi}{r} \tag{5.250}$$

Taking Eq. (5.250) into account in (5.249), we can write:

$$E_x(x, y, 0) = \frac{p}{2\pi\sigma_1} \left(\frac{1 - ik_1 r}{r^3} e^{ik_1 r} - \frac{\partial^2}{\partial y^2} \left(\frac{1}{r} \right) \right)$$

$$= \frac{p}{2\pi\sigma_1} \left(\frac{1 - ik_1 r}{r^3} e^{ik_1 r} + \frac{1}{r^3} - \frac{3y^2}{r^5} \right)$$

$$= \frac{p}{2\pi\sigma_1 r^3} \left(1 - 3\frac{y^2}{r^2} + (1 - ik_1 r)e^{ik_1 r} \right). \tag{5.251}$$

Using the same approach, we can calculate the y component of the electric field. From Eq. (5.242) we obtain:

$$E_y(x, y, 0) = \frac{p}{4\pi^2\sigma_1} \iint_{-\infty}^{\infty} (-ik_x)(-ik_y) \frac{1}{n_0} e^{-i(k_x x + k_y y)} dk_x dk_y$$

$$= \frac{p}{4\pi^2\sigma_1} \frac{\partial^2}{\partial x \partial y} I_3 = \frac{p}{2\pi\sigma_1} \frac{\partial^2}{\partial x \partial y} \frac{1}{r}$$

$$= \frac{p}{2\pi\sigma_1} \frac{3}{r^3} \frac{x}{r} \frac{y}{r}. \tag{5.252}$$

The problem of determining the components of the electromagnetic field of a current dipole source propagating along the surface of a homogeneous conducting half-space has been solved!
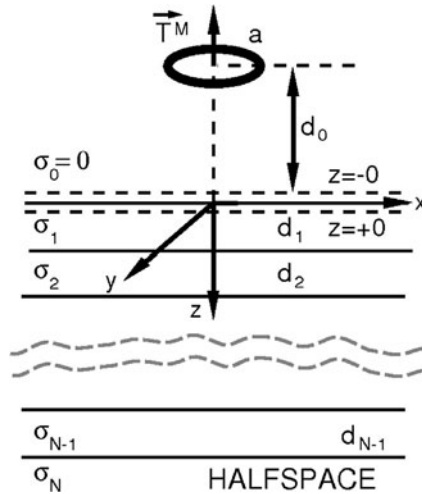
FIGURE 5.8

Vertical-axis magnetic dipole raised to a height d_0 above a stratified earth. The magnetic dipole is formed by a current-carrying loop of wire with an effective area, a, and a magnetic moment $\mathbf{I}^M$.

5.4.3 FREQUENCY DOMAIN REPRESENTATION OF THE FIELD OF A VERTICAL MAGNETIC DIPOLE ABOVE A HORIZONTALLY STRATIFIED MEDIUM

A fundamental question in the theory of electromagnetic sounding is related to the question of the fields excited in a horizontally stratified medium by a current-carrying loop of wire. In theory, if the loop is small in size, these fields are fully analogous to the fields about a magnetic dipole characterized by a magnetic moment of

$$\mathbf{I}^M = I^M \mathbf{d}_z = \pi a^2 I \mathbf{d}_z, \tag{5.253}$$

where a is the radius of the loop of wire, assuming it to be circular, and I is the strength of the current flowing in it.

We will assume that a loop lying in the horizontal plane (a *vertical-axis magnetic dipole*) is situated at a height d_0 above the conducting half-space, which is a laterally uniform geoelectric sequence of layers, $\sigma_n(z)$, as shown in Fig. 5.8. The current flowing in the loop is assumed to have a harmonic waveform, $I = I_0 e^{-i\omega t}$; displacement currents will be ignored, as usual. We are required to find the field on the surface of the earth (at $z = 0$) for such a source.

We observe first of all that in such a model, there is no galvanic connection between the source and the conductive material comprising the lower half-space; that is, currents which flow in the earth arise entirely as a consequence of electromagnetic induction. We can make use of the general theory for electromagnetic induction in the earth which will be developed in details for natural-field methods in Chapter 13. According to this theory, in the air (the upper half-space), the magnetic field and its scalar

potential can be represented as being the sum of external and internal parts:

$$\mathbf{H} = \mathbf{H}^e + \mathbf{H}^i,$$
$$\mathbf{H} = -grad\ U,$$
$$U = U^e + U^i, \tag{5.254}$$

where $\vec{H}^e$ and U^e are, respectively, the external magnetic field and its potential, which are the same, as we have stated, as the field and potential for a current-carrying loop of wire or a vertical-axis magnetic dipole located on the surface of a nonconducting half-space with conductivity σ_0.

The potential about a vertical-axis magnetic dipole with a moment $\mathbf{I}^M$ located in a nonconducting medium is well known to be

$$U^e(\mathbf{r}) = -\frac{1}{4\pi}\mathbf{I}^M \cdot grad\ \frac{1}{|\mathbf{r} - \mathbf{r}_0|}, \tag{5.255}$$

where $\mathbf{r}_0 = (0, 0, -d_0)$ is the radius vector to the center of the source dipole; and $\mathbf{r}$ is the radius vector to the point at which the field is being observed.

Considering that $\mathbf{I}^M = I^M \mathbf{d}_z$, we can write

$$U^e(\mathbf{r}) = -\frac{1}{4\pi}I^M \frac{\partial}{\partial z}\frac{1}{[x^2 + y^2 + (z + d_0)^2]^{1/2}}.$$

Expressing the function $1/[x^2 + y^2 + (z + d_0)^2]^{1/2}$ as a Fourier transform using Eq. (5.65), we have

$$U^e(x, y, z) = -\frac{I^M}{4\pi}\frac{1}{4\pi^2}\frac{\partial}{\partial z}\iint_{-\infty}^{\infty}\frac{2\pi e^{-n_0(z+d_0)}}{n_0}e^{-i(k_x x + k_y y)}dk_x dk_y, \tag{5.256}$$

where $z > -d_0$.

Consequently, the spectrum for the external part of the potential for the magnetic field at the surface of the earth (at $z = 0$) is:

$$u^e|_{z=0} = u^- = \frac{1}{2}I^M e^{-n_0 d_0}. \tag{5.257}$$

We also know from the theory for separating magnetic fields into internal and external parts (see Chapter 13) that the ratio of the two spectrums, $u^e|_{z=0} = u^-$ and $u^i|_{z=0} = u^+$, uniquely determines the impedance spectrum Z^*, which in turn depends only on the parameters describing the horizontally stratified medium. Moreover, knowing the spectrum for the external part of the potential, u^-, and the impedance, Z^*, it is completely possible to determine the internal part of the potential, u^+. Combining the internal and external parts of the potential, we can determine the complete potential of the field. To do this is a simple process in analysis.

In accord with Eq. (5.235),

$$Z^* = \frac{i\omega\mu_0}{n_0}\frac{u^+ - u^-}{u^+ + u^-} = \frac{i\omega\mu_0}{n_0}\left[1 - \frac{2u^-}{u^+ + u^-}\right].$$

Hence

$$u|_{z=0} = u^+ + u^- = \frac{2i\omega\mu_0 u^-}{i\omega\mu_0 - n_0 Z^*}. \tag{5.258}$$

After substituting Eq. (5.257) in (5.258), we obtain

$$u|_{z=0} = I^M \frac{i\omega\mu_0 e^{-n_0 d_0}}{i\omega\mu_0 - n_0 Z^*}. \tag{5.259}$$

Knowing the spectrum for the potential, it is not difficult to find the spectrums for the various components of the magnetic field on the surface of the earth:

$$h_x|_{z=0} = ik_x u|_{z=0} = ik_x I^M \frac{i\omega\mu_0 e^{-n_0 d_0}}{i\omega\mu_0 - n_0 Z^*}, \tag{5.260}$$

$$h_y|_{z=0} = ik_y u|_{z=0} = ik_y I^M \frac{i\omega\mu_0 e^{-n_0 d_0}}{i\omega\mu_0 - n_0 Z^*}. \tag{5.261}$$

In the model of a horizontally stratified medium under consideration, excitation is purely inductive, and so the electric field spectrum can be found in the same way as was done in developing the theory for the magnetotelluric method using impedance spectrums. Thus:

$$e_x|_{z=0} = Z^* h_y|_{z=0} = ik_y I^M \frac{i\omega\mu_0 e^{-n_0 d_0} Z^*}{i\omega\mu_0 - n_0 Z^*}, \tag{5.262}$$

$$e_y|_{z=0} = -Z^* h_x|_{z=0} = -ik_y I^M \frac{i\omega\mu_0 e^{-n_0 d_0} Z^*}{i\omega\mu_0 - n_0 Z^*}. \tag{5.263}$$

The spectrum for the vertical component of the magnetic field $h_z|_{z=0}$ can be determined from e_x and e_y using Eq. (5.233):

$$h_z|_{z=0} = \frac{1}{i\omega\mu_0}[-ik_x e_y|_{z=0} + ik_y e_x|_{z=0}]$$

$$= -I^M n_0^2 \frac{e^{-n_0 d_0} Z^*}{i\omega\mu_0 - n_0 Z^*}. \tag{5.264}$$

The inverse Fourier transform (Eq. (5.236)) allows us to obtain the components of the electric field from the spatial spectrums. And so, the problem posed of determining the fields of a vertical magnetic dipole situated above a horizontally stratified medium has been solved.

5.4.4 THE MAGNETIC FIELD OF A VERTICAL MAGNETIC DIPOLE ON THE SURFACE OF A UNIFORM HALF-SPACE

As was the case with a current dipole source, Eqs. (5.260), (5.261) and (5.264) are markedly simplified when the dipole is located on the surface of a uniform medium. For brevity, we will limit our considerations to the calculation of the vertical component of the magnetic field, H_z, only. The impedance for a uniform half-space is calculated from Eq. (5.237). We will also assume that the current-carrying

loop of wire lies directly on the surface of the earth with $d_0 \to 0$. Then, substituting Eq. (5.237) into (5.264), we obtain:

$$h_z|_{z=0} = \frac{I^M n_0^2}{n_1 + n_0} = \frac{I^M n_0^2}{-i\omega\mu_0\sigma_1}(n_1 - n_0).$$ (5.265)

Consequently, the expression for the vertical component of the magnetic field takes the form:

$$H_z(x, y, 0) = \frac{I^M}{4\pi^2 i\omega\mu_0\sigma_1}\tilde{\nabla}^2 \iint_{-\infty}^{\infty} (n_1 - n_0)e^{-i(k_x x + k_y y)}dk_x dk_y$$

$$= \frac{I^M}{4\pi^2 i\omega\mu_0\sigma_1}\tilde{\nabla}^2(I_1 - I_2),$$ (5.266)

where the integrals I_1 and I_2 are evaluated using Eqs. (5.246) and (5.247), and $\tilde{\nabla}^2$ is the two-dimensional Laplacian operator, defined as before as $\tilde{\nabla}^2 = \partial^2/\partial x^2 + \partial^2/\partial y^2$.

Substituting Eqs. (5.246) and (5.247) in (5.266), we can write

$$H_z(x, y, 0) = \frac{-I^M}{2\pi i\omega\mu_0\sigma_1}\tilde{\nabla}^2\left[\frac{(1 - ik_1 r)e^{ik_1 r} - 1}{r^3}\right].$$ (5.267)

It is more convenient in this last equation to express the two-dimensional Laplacian operator in a cylindrical coordinate system, r, ϕ, remembering that the expression within the square brackets is independent of the angle, ϕ:

$$H_z(r, \phi, 0) = \frac{-I^M}{2\pi i\omega\mu_0\sigma_1}\frac{1}{r}\frac{\partial}{\partial r}\left(r\frac{\partial}{\partial r}\left[\frac{(1 - ik_1 r)e^{ik_1 r} - 1}{r^3}\right]\right).$$ (5.268)

Carrying out the differentiations with respect to r indicated in Eq. (5.268), we finally arrive at the result

$$H_z(r, \phi, 0) = \frac{I^M}{2\pi i\omega\mu_0\sigma_1}\frac{1}{r^5}\left[9 - e^{ik_1 r}(9 - 9ik_1 r - 4k_1^2 r^2 + ik_1^3 r^3)\right].$$ (5.269)

Using the same kind of uncomplicated, though fundamental, considerations, it is possible to obtain the expressions for the other components of the electromagnetic field in a uniform earth.

5.4.5 NEAR AND FAR FIELDS

In the theory for electromagnetic sounding, the behavior of the various field components near the source and far from the source take on particular importance. The concepts of near- and far-field behavior have already been introduced; let us now extend them in an examination of the fields about a dipole source at the interface between the air and a uniform half-space. We should remember that the near and far parts of the field are defined in terms of the value for the *electrical distance*, r_λ, which is the magnitude of the product of the distance, r and the wave number in the medium,

$$r_\lambda = \frac{1}{2\sqrt{2}\pi}|rk_1| = r/\lambda_1,$$ (5.270)

where λ_1 is the wave length of the electromagnetic field in a homogeneous medium. Separation of the field into its several parts is done using the conditions

- a. near-field zone, when $|k_1 r| \ll 1$,
- b. intermediate field zone, when $|k_1 r| \approx 1$, and
- c. far-field zone, when $|k_1 r| \gg 1$.

We should note that in the intermediate zone, we must make use of the exact expressions for the various components, Eqs. (5.248), (5.251), and (5.252), which take the forms

$$H_z = \frac{ip \sin \theta}{2\pi \omega \mu_0 \sigma_1} \frac{1}{r^4} \{3 - e^{ik_1 r}(3 - 3ik_1 r - k_1^2 r^2)\}, \tag{5.271}$$

$$E_x = \frac{p}{2\pi \sigma_1} \frac{1}{r^3} \{3 \cos^2 \theta - 2 + e^{ik_1 r}(1 - ik_1 r)\}, \tag{5.272}$$

$$E_y = \frac{3p}{2\pi \sigma_1} \frac{1}{r^3} \cos \theta \sin \theta, \tag{5.273}$$

where $\cos \theta = x/r$ and $\sin \theta = y/r$.

In the near-field region, the exponential term, $e^{ik_1 r}$, can be expressed as:

$$e^{ik_1 r} = 1 + ik_1 r - \frac{1}{2}(k_1 r)^2 + o(k_1^2 r^2),$$

where $o(k_1^2 r^2)$ represents the contribution from terms of order higher than $(k_1 r)^2$.

Eqs. (5.271), (5.272), and (5.273) can be simplified as follows by deleting small terms. For a horizontal current dipole source, in the near field ($|k_1 r| \ll 1$) the field components are approximately determined by the following expressions:

$$H_z = \frac{ip \sin \theta}{2\pi \omega \mu_0 \sigma_1} \frac{1}{r^4} \left(3 - \left[1 + ik_1 r - \frac{(k_1 r)^2}{2} + o(k_1^2 r^2) \right] (3 - 3ik_1 - k_1^2 r^2) \right)$$

$$= \frac{ip \sin \theta}{2\pi \omega \mu_0 \sigma_1} \frac{1}{r^4} \left[-\frac{1}{2} k_1^2 r^2 + o(k_1^2 r^2) \right] \approx \frac{p \sin \theta}{4\pi r^2}, \tag{5.274}$$

$$E_x \approx \frac{p}{2\pi \sigma_1} \frac{1}{r^3} (3 \cos^2 \theta - 2 + 1) = \frac{p}{2\pi \sigma_1} \frac{1}{r^3} (3 \cos^2 \theta - 1), \tag{5.275}$$

$$E_y = \frac{3p}{2\pi \sigma_1} \frac{1}{r^3} \cos \theta \sin \theta. \tag{5.276}$$

For a vertical-axis magnetic dipole source, the vertical component of the magnetic field in the near-field region is

$$H_z = \frac{I^M}{2\pi i \omega \mu_0 \sigma_1} \frac{1}{r^5} \left(9 - \left[1 + ik_1 r - \frac{(k_1 r)^2}{2} + o(k_1^2 r^2) \right] (9 - 9ik_1 r - 4k_1^2 r^2 + ik_1^3 r^3) \right)$$

$$\approx -I^M / 4\pi r^3 \tag{5.277}$$

In examining Eqs. (5.274) and (5.277), we find that in the near field of either a current or magnetic dipole source, the vertical component of the magnetic field, H_z, is independent of the electrical conductivity of the medium, being a function only of the moment, p or I^M, of the source.

Let us now consider the behavior of the field in the far-field region. In this region, $e^{ik_1r} \approx 0$, so that Eqs. (5.271), (5.272), and (5.273) take the following forms.

For the field of a horizontal current dipole source, in the far-field region ($|k_1r| \gg 1$),

$$H_z = \frac{3ip \ \sin \ \theta}{2\pi\omega\mu_0\sigma_1} \frac{1}{r^4},$$
(5.278)

$$E_x = \frac{p}{2\pi\sigma_1} \frac{1}{r^3}(3 \ \cos^2\theta - 2),$$
(5.279)

$$E_y = \frac{3p}{2\pi\sigma_1} \frac{1}{r^3} \cos \ \theta \ \sin \ \theta.$$
(5.280)

The field of a vertical-axis magnetic dipole source in the far zone is

$$H_z = \frac{9I^M}{2\pi i\omega\mu_0\sigma_1} \frac{1}{r^5}.$$
(5.281)

Let us examine the structure of the electromagnetic field in the far zone. First of all, we recognize that the decrease in strength of the electric and magnetic field components in the far zone as a function of distance, r, is not accompanied by phase shift. The electric field in the far zone is cophasal with the current feeding the source inasmuch as the right-hand parts of Eqs. (5.279) and (5.280) are purely real terms. The oscillations of the magnetic field are shifted in phase with respect to the source current by $\pi/2$ inasmuch as the right-hand terms in Eqs. (5.278) and (5.281) contain a multiplier, $i = e^{(\pi/2)i}$. This behavior has a simple physical explanation. We can think of the electromagnetic field of either a current or magnetic dipole source as consisting of two parts; the first part propagates in the upper half-space (in the insulating atmosphere) with virtually no attenuation, and then permeates vertically into the earth, passing through the earth, and the second part propagates directly from the source to the receiver, being attenuated in the conductive earth. It should be apparent that, in areas removed from the source by distances greater than a wave length, only the first part of the field survives, and the second part is almost completely attenuated. The field, being effectively only that which propagates in the upper half-space (or, more precisely, the phase fronts of the field), travels with infinitely great speed through the air. Consequently, it travels along the earth's surface and arrives at every point in the far zone simultaneously, then penetrating to all points within the earth practically simultaneously. In the far zone, the field of a dipole source behaves in much the same way as a plane wave, because the phase fronts in the earth are horizontal planes. However, the amplitude of the field even within a planar phase front varies, attenuating with greater distance from the source. In other words, in the far zone, the propagation of the field can be described as being a *nonhomogeneous plane wave*.

We know from Eqs. (4.142) and (4.143) that a plane wave attenuates exponentially in the earth:

$$H_{x(y)}/H^+_{x(y)} = e^{ik_1z},$$
$$E_{x(y)}/E^+_{x(y)} = e^{ik_1z}.$$
(5.282)

Therefore, the skin depth of a permeating electric field in the far zone is specified by Eqs. (4.150), (4.181), and (4.182):

$$\delta_e = \frac{\lambda_1}{2\pi} = [2/(\omega\mu_0\sigma_1)]^{1/2} = (10^7\rho_1 T)^{1/2}/2\pi. \tag{5.283}$$

We have a very important consequence of this behavior; by changing the frequency, ω, or the period, T, of the current driving the source, we can change the depth to which the electromagnetic field penetrates into the earth. In other words, we can perform a vertical sounding of the conductivity profile in the earth. This is the principle on which the *frequency sounding method* is based. We will examine this topic in detail in the following chapters.

It should be noted at this point that in carrying out a sounding with a controlled source, commonly a broad range of frequencies is used, so that we deal not only with the far zone, but also with the intermediate and near zones.

5.4.6 FREQUENCY DOMAIN METHOD FOR COMPUTING TRANSIENT FIELDS

While sources driven with harmonically oscillating current are frequently used in frequency sounding, an even more widely used variant of the method employs a source which is impulsively energized. Such methods achieve efficiency by transmitting a broad band of frequencies simultaneously as an impulse, as opposed to the sequential transmission of frequencies, one at a time, in the frequency-domain method. Methods based on impulsive excitation of the source are often called *time domain electromagnetic* (*TDEM*) or *transient electromagnetic* (*TEM*) sounding methods. In calculating the behavior of impulse-excited electromagnetic fields, most commonly the field behavior is calculated in the frequency domain, and the results are Fourier transformed to obtain the description of the field in the time domain. We will now consider such a method by examining the transient field associated with an impulse-driven current dipole on the surface of a horizontally stratified medium.

Let us suppose that the current in a source dipole varies with time in an arbitrary manner, $I(t)$, so that the moment of the dipole, p, is also a function of time, $p = p(t) = I(t)d\ell$. Such a function can be represented in time using the Fourier integral transform:

$$p(t) = \frac{1}{2\pi} \int_{-\infty}^{\infty} p_\omega e^{-i\omega t} d\omega, \tag{5.284}$$

where p_ω is the frequency domain representation of the current moment of the source dipole, and $p(t)$ is the time-domain representation,

$$p_\omega = \int_{-\infty}^{\infty} p(t)e^{i\omega t} dt = \int_{-\infty}^{\infty} I(t)e^{i\omega t} dt d\ell. \tag{5.285}$$

All of the corresponding components of the time domain electromagnetic field of a dipole source can also be represented by Fourier integral transforms:

$$\mathbf{E}(t) = \frac{1}{2\pi} \int_{-\infty}^{\infty} \mathbf{E}_\omega e^{-i\omega t} d\omega,$$

$$\mathbf{H}(t) = \frac{1}{2\pi} \int_{-\infty}^{\infty} \mathbf{H}_\omega e^{-i\omega t} d\omega, \tag{5.286}$$

where $\mathbf{E}_\omega$ and $\mathbf{H}_\omega$ are complex harmonic fields; that is, complex vectors representing the components of the field of a dipole source driven by a harmonically varying electrical current. We will call such a source a *harmonic dipole* for brevity. These vectors are specified for a temporal frequency, ω, using Eqs. (5.227), (5.235), and (5.236) with $p = p_\omega$. For example, the time-domain representation of the vertical component of the magnetic field is:

$$H_z(t) = \frac{1}{2\pi} \int_{-\infty}^{\infty} \left(\frac{1}{4\pi^2} \iint_{-\infty}^{\infty} h_z|_{z=-0} e^{-i(k_x x + k_y y)} \right) p_\omega e^{-i\omega t} d\omega$$

$$= \frac{1}{2\pi} \int_{-\infty}^{\infty} H_{z\omega}^{(1)} p_\omega e^{-i\omega t} d\omega, \tag{5.287}$$

where $H_{z\omega}^{(1)}$ is the magnetic field of a harmonic dipole source with unit moment, $p = 1$:

$$H_{z\omega}^{(1)} = \frac{1}{4\pi^2} \iint_{-\infty}^{\infty} \frac{-i k_y Z^*}{i\omega\mu_0 - n_0 Z^*} e^{-i(k_x x + k_y y)} dk_x dk_y, \tag{5.288}$$

and p_ω is the frequency domain representation of the moment, $p(t)$ of a current dipole operating in the time domain. Similarly, it is possible to show that any component of the field can be expressed in the time domain using the formula

$$F(t) = \frac{1}{2\pi} \int_{-\infty}^{\infty} F_\omega^{(1)} e^{-i\omega t} d\omega, \tag{5.289}$$

where $F_\omega^{(1)}$ is the corresponding component for a harmonic dipole with unit moment, and p_ω is given by Eq. (5.285).

In summary, for the computation of time-domain electromagnetic fields, it is not necessary to solve the corresponding problem in electrodynamics anew, but instead, we can use the solutions for the field for a harmonic time function which we have already obtained. In fact, we can consider the fields of sources with a driving current of completely arbitrary wave form.

In the practice of electrical prospecting, there are two relatively standard wave forms used in time-domain excitation of dipole sources:

- 1) True impulsive currents, which approximate the form of a *Dirac delta function*, $\delta(t)$:

$$I_0 \delta(t) = \begin{cases} 0, & t \neq 0 \\ \infty & t = 0 \end{cases} \tag{5.290}$$

with

$$\int_{-\infty}^{\infty} I_0 \delta(t) dt = I_0.$$

- 2) A step wave, or instantaneous change in current from one level to another, termed a *Heaviside function*
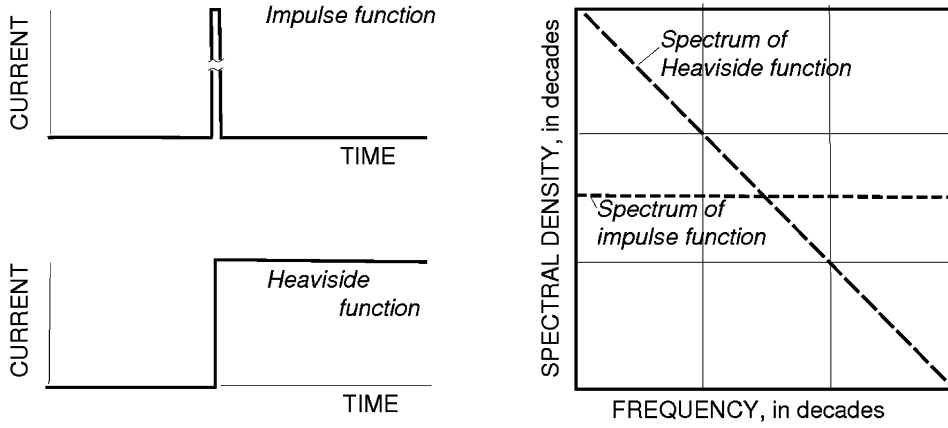
FIGURE 5.9

Two wave forms commonly used for time-domain electromagnetic soundings. The impulse wave form is of short duration but great amplitude. Ideally, for zero width and infinite amplitude, the spectrum of an impulse is constant at all frequencies. The Heaviside function is the time integral of an impulse. The spectrum of a Heaviside function declines in amplitude linearly as frequency increases.

$$I_0 H(t) = \begin{cases} 0, & t < 0 \\ I_0 & t > 0 \end{cases}. \tag{5.291}$$

For true impulsive wave forms (type 1), the frequency domain representation of the source moment is

$$p_\omega^\delta = \int_{-\infty}^{\infty} I_0 \delta(t) d\ell e^{i\omega t} dt$$

$$= I_0 d\ell \int_{-\infty}^{\infty} [\delta(t)] e^{i\omega t} dt = I_0 d\ell = p. \tag{5.292}$$

For excitation of the Heaviside form (type 2),

$$p_\omega^H = \int_{-\infty}^{\infty} [I_0 H(t) d\ell] e^{i\omega t} dt = I_0 d\ell \int_{-\infty}^{\infty} [H(t)] e^{i\omega t} dt$$

$$= p \left\{ \pi \delta(\omega) - \frac{1}{i\omega} \right\}, \tag{5.293}$$

where $p = I_0 d\ell$. These two wave forms and their spectrums are shown in Fig. 5.9.

In the case of impulsive excitation, Eq. (5.289) takes the form

$$F^\delta(t) = \frac{p}{2\pi} \int_{-\infty}^{\infty} F_\omega^{(1)} e^{-i\omega t} d\omega \tag{5.294}$$

and for Heaviside excitation, Eq. (5.289) takes the form

$$F^H(t) = \frac{p}{2\pi} \int_{-\infty}^{\infty} F_\omega^{(1)} [\pi\delta(\omega) - \frac{1}{i\omega}] e^{-i\omega t} d\omega, \tag{5.295}$$

where $p = I_0 d\ell = const$, and I_0 is a number characterizing the strength of the current to the source.

Of the two forms of excitation, the Heaviside wave form is the most widely used in time-domain electromagnetic sounding. The step wave form is easy to generate, requiring only the closing of a switch between the power supply and the transmitter cable. Well after the initiation of the Heaviside step, the field will behave as though the source were energized with direct current. For early times, there will exist a transient variation of signal with time which carries in its wave form much information about the geoelectric structure of the subsurface. The extraction of this information from a recorded transient signal comprises the fundamental process of time-domain electromagnetic sounding.

5.4.7 TRANSIENT FIELDS OF A DIPOLE SOURCE OBSERVED IN A HOMOGENEOUS MEDIUM AND ON THE SURFACE OF A HOMOGENEOUS CONDUCTING HALF-SPACE; FIELDS IN THE NEAR AND FAR ZONES

For an example of the use of time-domain sounding methods, we will consider the problem of the field about a horizontally-directed current dipole located in a homogeneous unbounded medium with the properties σ, μ_0, and which is energized with a current impulse that has the form of a delta function.

In accord with Eq. (4.177), the vertical component of the magnetic field of a harmonic dipole source with the moment $p = 1\mathbf{d}_x$ is

$$H_{z\omega}^{(1)} = -\frac{1}{4\pi} \frac{\partial}{\partial y} \left(\frac{e^{ikr}}{r} \right). \tag{5.296}$$

Substituting this expression in Eq. (5.294), we find

$$H_z^\delta(t) = -\frac{p}{4\pi} \frac{\partial}{\partial y} \left(\frac{1}{r} \left(\frac{1}{2\pi} \int_{-\infty}^{\infty} e^{ikr} e^{-i\omega t} d\omega \right) \right). \tag{5.297}$$

We can evaluate the integral within the inner brackets as follows:

$$I_1(t) = \frac{1}{2\pi} \int_{-\infty}^{\infty} e^{ikr} e^{-i\omega t} d\omega. \tag{5.298}$$

This integral is closely related to a tabulated form

$$I_1(t) = \partial I_2(t)/\partial t, \tag{5.299}$$

where

$$I_2(t) = \frac{1}{2\pi} \int_{-\infty}^{\infty} e^{ikr} [\pi\delta(\omega) - \frac{1}{i\omega}] e^{-i\omega t} d\omega$$
$$= H(t)[1 - \Phi(u)]$$

$$= \begin{array}{ll} 0, & t < 0 \\ 1 - \Phi(u(t)), & t > 0 \end{array}. \tag{5.300}$$

Here, $\Phi[u(t)]$ is a tabulated transcendental function, the *probability integral function*, defined as

$$\Phi[u(t)] = \left(\frac{2}{\pi}\right)^{1/2} \int_0^{u(t)} e^{-x^2/2} dx, \tag{5.301}$$

$$u(t) = r(\mu_0 \sigma / 2t)^{1/2}. \tag{5.302}$$

Substituting Eq. (5.300) in (5.299), for $t > 0$, we have

$$I_1(t) = -\frac{\partial}{\partial t}\Phi[u(t)] = -\left(\frac{2}{\pi}\right)^{1/2} e^{(-u^2(t)/2)}\frac{\partial u(t)}{\partial t}$$

$$= -\left(\frac{2}{\pi}\right)^{1/2} e^{(-r^2\mu_0\sigma/4t)} r \left(\frac{\mu_0\sigma}{2}\right)^{1/2}\left(-\frac{1}{2}\right)t^{-3/2}. \tag{5.303}$$

We will now define the *time-domain parameter*, τ, which is a combination of various constants that group together naturally:

$$\tau = 2\pi/(\mu_0\sigma/2t)^{1/2}. \tag{5.304}$$

This parameter has the dimensions of length, and taking the magnetic permeability to be that of free space, it is usually calculated to be

$$\tau = (2\pi\rho t \times 10^7)^{1/2}. \tag{5.305}$$

The physical significance of the time-domain parameter is as follows. Substituting Eq. (5.304) in (5.303) and doing some algebra, we obtain

$$I_1(t) = \frac{8\pi^2 r (2\pi)^{1/2}}{\mu_0\tau^3\sigma}e^{-2(\pi r/\tau)^2}. \tag{5.306}$$

Substituting Eq. (5.306) and (5.298), Eq. (5.297) can be rewritten as

$$H_z^\delta(t) = -\frac{p}{4\pi}\frac{\partial}{\partial y}\left(\frac{1}{r}\frac{8\pi^2 r(2\pi)^{1/2}}{\mu_0\tau^3\sigma}e^{-2(\pi r/\tau)^2}\right)$$

$$= -\frac{(2\pi)^{3/2}p}{\mu_0\tau^3\sigma}\frac{\partial}{\partial y}e^{-2(\pi r/\tau)^2}$$

$$= \frac{8p\pi^3(2\pi)^{1/2}}{\mu_0\sigma}\frac{y}{\tau^5}e^{-2(\pi r/\tau)^2}. \tag{5.307}$$

Let us analyze this expression. First of all, we see that the characteristic decline of the field from an impulsive source as a function of distance from the source is determined by the exponential multiplier, $e^{-2(\pi r/\tau)^2}$, in which r appears as a ratio to the length of the time-domain parameter, τ. This ratio, as also with a harmonically driven source, bears the name of *electrical distance*:

$$r_\tau = r/\tau. \tag{5.308}$$

As was the case in the frequency domain, we recognize three zones of behavior for the fields:

- 1) the near zone, for which

$$r \ll \tau,$$

- 2) the intermediate zone, in which

$$r \approx \tau,$$

and
- 3) the far zone, for which

$$r \gg \tau. \tag{5.309}$$

Comparing Eq. (5.308) and (5.270), we see that the time domain parameter τ plays the same role as does the wave length, λ, in the frequency domain. We will make use of these electrical distances to a considerable extent in our further discussion of the data obtained in electromagnetic sounding surveys. It should be noted that in the definition of the time-domain parameter, τ, there is a trade-off between time and distance in the definition of the various zones; that is, the far zone can be associated with the early part of the transient response, while the near zone can be associated with the late part of the transient waveform. Because of this reciprocity in the roles played by time and distance, sometimes the far zone is called the *early time zone* and the near zone is called the *late time zone*.

Note that, the near field corresponds to late times, because the late times have a lower frequency content, which extends the near field farther from the transmitter. At very early times, most everything is in the far field, because this corresponds to high frequencies and very short electrical distances.

The same approach can be used in computing the electric and magnetic field components about a dipole source situated on the surface of a homogeneous conducting half-space. But, the development of the expressions is considerably more complicated than in the case of a completely uniform medium. We will carry out the development for the case in which the dipole is driven with a Heaviside wave (Eq. (5.291)).

To develop the expression for the transient decay curve for the electric field in the earth, we substitute Eqs. (5.251) and (5.252) in Eq. (5.295):

$$E_x^H(t) = \frac{1}{2\pi} \int_{-\infty}^{\infty} \frac{p}{2\pi\sigma_1 r^3} \left\{ 1 - 3\left(\frac{y}{r}\right)^2 + (1 - ik_1 r)e^{ik_1 r} \right\} \left(\pi\delta(\omega) - \frac{1}{i\omega} \right) e^{-i\omega t} d\omega$$
$$= \frac{p}{2\pi\sigma_1 r^3} \left\{ \left[1 - 3\left(\frac{y}{r}\right)^2 \right] H(t) + I_2(t) - I_3(t) \right\}, \tag{5.310}$$

$$E_y^H(t) = \frac{p}{2\pi\sigma_1} \frac{3xy}{r^5} \frac{1}{2\pi} \int_{-\infty}^{\infty} \left[\pi\delta(\omega) - \frac{1}{i\omega} \right] e^{-i\omega t} d\omega$$
$$= \frac{p}{2\pi\sigma_1} \frac{3xy}{r^5} H(t), \tag{5.311}$$

where $H(t)$ is the Heaviside function, $I_2(t)$ is given by Eq. (5.300) and

$$I_3(t) = \frac{1}{2\pi} \int_{-\infty}^{\infty} ik_1 r e^{ik_1 r} [\pi \delta(\omega) - \frac{1}{i\omega}] e^{-i\omega t} d\omega$$

$$= r \frac{\partial}{\partial r}[I_2(t)] = -\left(\frac{2}{\pi}\right)^{1/2} e^{-u^2/2} u H(t), \tag{5.312}$$

where, in accord with Eqs. (5.302) and (5.304),

$$u = 2\pi r/\tau. \tag{5.313}$$

Substituting Eqs. (5.300) and (5.312) in (5.310), we can write

$$E_x^H(t) = \frac{pH(t)}{2\pi \sigma_1 r^3} \left(2 - 3\left(\frac{y}{r}\right)^{1/2} - \Phi(u) + \left(\frac{2}{\pi}\right)^{1/2} e^{-u^2/2} u\right). \tag{5.314}$$

Next, we derive the expression for the vertical component of the magnetic field caused by a current dipole located on the surface of a homogeneous conducting half-space. In so doing, it will prove to be convenient to derive the formula for the time-rate of change of the magnetic field, H_z, because this result will be closely related to the formula we have already obtained for the electric field. The time-rate of change of the magnetic field is also what is usually measured in geophysical experiments (see Chapter 11). We substitute Eq. (5.248) in (5.295), and differentiate with respect to time:

$$\frac{\partial H_z^H}{\partial t} = \frac{\partial}{\partial t}\left(\frac{1}{2\pi} \int_{-\infty}^{\infty} \frac{ip}{2\pi \omega \mu_0 \sigma_1} \frac{y}{r^5}\left[3 - e^{ik_1 r}(3 - ik_1 r - k_1^2 r^2)\right]\left[\pi \delta(\omega) - \frac{1}{i\omega}\right] e^{-i\omega t} d\omega\right)$$

$$= \frac{p}{2\pi \mu_0 \sigma_1} \frac{y}{r^5}\{3H(t) - 3I_2(t) + 3I_3(t) + I_4(t)\}, \tag{5.315}$$

where

$$I_4(t) = \frac{1}{2\pi} \int_{-\infty}^{\infty} k_1^2 r^2 e^{ik_1 r} [\pi \delta(\omega) - \frac{1}{i\omega}] d\omega = -\frac{\mu_0 \sigma_1 r^2}{2\pi} \int_{-\infty}^{\infty} e^{ik_1 r} e^{-i\omega t} d\omega$$

$$= -\mu_0 \sigma_1 r^2 I_1(t) = -\left(\frac{2}{\pi}\right)^{1/2} e^{-u^2/2} u^3 H(t). \tag{5.316}$$

Substituting Eqs. (5.300), (5.312), and (5.316) into Eq. (5.315), we obtain

$$\frac{\partial H_z^H(t)}{\partial t} = \frac{3pH(t)}{2\pi \mu_0 \sigma_1} \frac{y}{r^5}\left[\Phi(u) - \left(\frac{2}{\pi}\right)^{1/2} e^{-u^2/2} u(1 + \frac{u^2}{3})\right]. \tag{5.317}$$

In the same way, we can write the expression for the time-rate of change of the vertical component of the magnetic field caused by a magnetic dipole source driven by a Heaviside step for comparison with the result obtained above for a current dipole source. To do this, we substitute Eq. (5.269) into

Eq. (5.295):

$$
\begin{aligned}
\frac{\partial H_z^{H(M)}(t)}{\partial t} &= \\
&= \frac{\partial}{\partial t}\left(\frac{1}{2\pi}\int_{-\infty}^{\infty}\frac{I^M}{2\pi i\omega\mu_0\sigma_1}\frac{1}{r^5}[9 - e^{ik_1r}(9 - 9ik_1r - 4k_1^2r^2 + ik_1^3r^3)][\pi\delta(\omega) - \frac{1}{i\omega}]e^{-i\omega t}d\omega\right) \\
&= -\frac{I^M}{2\pi\mu_0\sigma_1}\frac{1}{r^5}\{9H(t) - 9I_2(t) + 9I_3(t) + 4I_4(t) - I_5(t)\},
\end{aligned}
\tag{5.318}
$$

where

$$
\begin{aligned}
I_5(t) &= \frac{1}{2\pi}\int_{-\infty}^{\infty}ik_1^3r^3e^{ik_1r}(\pi\delta(\omega) - \frac{1}{i\omega})e^{-i\omega t}d\omega = r\frac{\partial I_4(t)}{\partial r} \\
&= -\left(\frac{2}{\pi}\right)^{1/2}e^{-u^2/2}u^3(3 - u^2)H(t).
\end{aligned}
\tag{5.319}
$$

Substituting the expressions for the integrals (5.300), (5.312), (5.316), and (5.319) into Eq. (5.318), finally we can write

$$
\frac{\partial H_z^{H(M)}(t)}{\partial t} = -\frac{9I^M H(t)}{2\pi\mu_0\sigma_1}\frac{1}{r^5}\left[\Phi(u) - \left(\frac{2}{\pi}\right)^{1/2}e^{-u^2/2}u(1 + \frac{u^2}{3} + \frac{u^4}{9})\right].
\tag{5.320}
$$

Let us now examine the formulas in Eqs. (5.311), (5.314), (5.317) and (5.320) which describe transient fields for a homogeneous earth. As we can see from Eq. (5.311), the wave form for the y component of the electric field is exactly a Heaviside function. Prior to the initiation of the Heaviside step, $E_y^H(t) = 0$. At the instant the current in the source rises, the field becomes

$$
E_y^{H(M)}(t)|_{t\to 0} = \frac{3pxy}{2\pi\sigma_1r^5} = \frac{3p}{2\pi\sigma_1}\frac{1}{r^3}\cos\theta\,\sin\theta,
\tag{5.321}
$$

where the various quantities are defined as they were earlier for Eq. (5.271).

The behavior of the x component of the electric field, E_x^H, is more complicated. In accord with Eq. (5.314), for $t < 0$, $E_x^H = 0$, and at the moment of initiation of the Heaviside step, the field rises discontinuously to the value

$$
E_x^H(t)|_{t\to 0} = \frac{p}{2\pi\sigma_1r^3}\left[1 - 3\left(\frac{y}{r}\right)^2\right].
\tag{5.322}
$$

This last expression follows directly from Eq. (5.314) because as $t \to 0$, the function $u \to \infty$ and the probability integral function tend to unity:

$$
\Phi|_{\substack{t\to 0 \\ u\to\infty}} = 1.
\tag{5.323}
$$

Then, after some variations, the field $E_x^H(t)$ decreases monotonically with time to a limiting constant value:

$$E_x^H(t)|_{t\to\infty} = \frac{p}{2\pi\sigma_1 r^3}\left[2 - 3\left(\frac{y}{r}\right)^2\right] = \frac{p}{2\pi\sigma_1}\frac{1}{r^3}[3\cos^2\theta - 2], \tag{5.324}$$

because as $t \to \infty$, the function $u \to 0$, and

$$\Phi|_{\substack{t\to\infty \\ u\to 0}} = 0. \tag{5.325}$$

The time rate of change of the magnetic field also changes abruptly, discontinuously from zero at the time of initiation of the Heaviside step to some initial signal level. When the source is a current dipole, in accord with Eqs. (5.317) and (5.318), the initial signal level is

$$\frac{\partial H_z^H(t)}{\partial t}\bigg|_{t\to 0} = \frac{3p}{2\pi\mu_0\sigma_1}\frac{y}{r^5} = \frac{3p}{2\pi\mu_0\sigma_1}\frac{1}{r^4}\sin\theta\,, \tag{5.326}$$

and if the source is a vertical-axis magnetic dipole, in accord with Eqs. (5.320) and (5.323), the initial signal level is

$$\frac{\partial H_z^{H(M)}(t)}{\partial t}\bigg|_{t\to 0} = -\frac{9I^M}{2\pi\mu_0\sigma_1}\frac{1}{r^5}\,. \tag{5.327}$$

As time progresses, these values will vary in a complicated manner in accord with Eqs. (5.317) and (5.320), and at late times (as $t \to \infty$), they will tend to zero. In practice, it is an easy matter to measure the time rate of change of the magnetic field components by observing the EMF generated in a horizontal loop of wire; Faraday's law states that the EMF generated in such a loop will be proportional to the magnetic flux cutting the loop.

Let us turn now to the characteristic features of the transient fields observed in the near and far zones. We will consider the near zone, $r \ll \tau$, first.

We can most easily discuss the characteristics of the transient field in the near zone by considering the case of a magnetic dipole source driven by current pulses, and situated on a homogeneous half-space. In Eq. (5.307), taking a limit $r/\tau \to 0$, we have:

$$H_z^\delta(t) \approx \frac{8\pi^3 p(2\pi)^{1/2}}{\mu_0}\frac{\rho y}{\tau^5}. \tag{5.328}$$

For comparison, let us write the same expression for the magnetic field in the near zone caused by a harmonic source:

$$H_z(\omega) \approx \frac{p}{4\pi}\frac{y}{r^3}e^{-i\omega t}. \tag{5.329}$$

Compare these two formulas. First, we see that while $H_z(\omega)$ is independent of the resistivity of the medium, the time-domain signal, $H_z^\delta(t)$ is linearly proportional to ρ! Moreover, if we plot the two functions, $H_z^\delta(t)$ and $|H_z(\omega)|$ as a function of depth, z, for fixed values of x_0, y_0, t_0, and ω_0 (Fig. 5.10), we see that in the near zone the field of a harmonic dipole decreases with depth (Fig. 5.10A) while the transient field is uniform with depth (Fig. 5.10B). Consequently, within the shell of the expanding
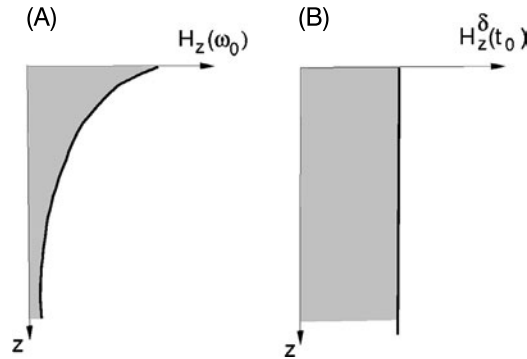
FIGURE 5.10

Comparison of curves for current density as a function of depth in the earth for frequency domain electromagnetic coupling at a single frequency (A) and for time domain electromagnetic coupling at a specific instant of time that falls within the near-zone range (B).

electromagnetic impulse, there exists a region in which the field is uniformly distributed between the source and the observation point. *In this region, the magnetic field $H_z^\delta(t)$ does not decrease with distance from the source, and, it even increases with distance along the y axis while decaying uniformly in time.* This provides the possibility, in theory at least, of investigating the geoelectric section to great depths with observations made close to the source. In practice, it is only required that a sufficiently strong pulse be applied to the source to explore to very great depths.

This particular feature of transient electromagnetic fields has been shown by Obukhov (1968) to be a general property of solutions to the diffusion equation

$$\nabla^2 \mathbf{F} = a\, \partial \mathbf{F}/\partial t$$

which is valid for all components of the electromagnetic field in the quasi-stationary approximation.

Furthermore, after injection of the impulsive signal into the earth, the field diffuses into the surrounding half-space, and for sufficiently late times, as is shown by the solution of the diffusion equation, is uniformly distributed through the medium surrounding the source.

We next carry out an asymptotic analysis of the transient field in the near zone of a magnetic dipole source on the surface of a homogeneous conducting half-space.

In the near zone, $r \ll \tau$, we expand the terms $\Phi(u)$ and $e^{-u^2/2}$ in a power series of the parameter $u = 2\pi r/\tau$, considering that u is less than unity:

$$\Phi(u) = (2/\pi)^{1/2}[u - u^3/6 - u^5/40 + o(u^5)], \tag{5.330}$$

$$e^{-u^2/2} = 1 - u^2/2 + u^4/8 + o(u^5), \tag{5.331}$$

where $o(u^5)$ is the remainder consisting of all terms with powers greater than fifth.

Substituting Eqs. (5.330) and (5.331) into Eq. (5.320), after some simplification, we obtain

$$
\begin{aligned}
\frac{\partial H_z^{H(M)}}{\partial t} &= -\frac{9I^M}{2\pi\mu_0\sigma_1}\frac{1}{r^5}\left(\frac{2}{\pi}\right)^{1/2} \times \\
&\quad \times \left(u - \frac{u^3}{6} + \frac{u^5}{40} + o(u^5) - \left[1 - \frac{u^2}{2} + \frac{u^4}{8} + o(u^5)\right]\left(u + \frac{u^3}{3} + \frac{u^5}{9}\right)\right) \\
&= -\frac{9I^M}{2\pi\mu_0\sigma_1}\frac{1}{r^5}\left(\frac{2}{\pi}\right)^{1/2}\left\{u^5\left(\frac{1}{40} - \frac{1}{9} + \frac{1}{6} - \frac{1}{8}\right) + o(u^5)\right\} \\
&\approx \frac{I^M}{5\pi\mu_0\sigma_1}\frac{1}{r^5}\left(\frac{2}{\pi}\right)^{1/2}u^5.
\end{aligned}
\tag{5.332}
$$

After substituting Eq. (5.302) into Eq. (5.332), we can write finally

$$
\frac{\partial H_z^{H(M)}}{\partial t} = \frac{I^M}{5\pi\mu_0\sigma_1}\frac{1}{r^5}\left(\frac{2}{\pi}\right)^{1/2}r^5\frac{(\mu_0\sigma_1)^{5/2}}{2^{5/2}t^{5/2}} = \frac{I^M(\mu_0\sigma_1)^{3/2}}{20\pi^{3/2}t^{5/2}}.
\tag{5.333}
$$

Thus, we see, *the time-rate of change of the vertical component of the magnetic field in the near zone of a vertical-axis magnetic dipole source is independent of the distance from the source*, *and depends only on the conductivity of the earth!* Having made this profound discovery, we must stress once again that Eq. (5.333) is valid only for late times, t, and short distances from the source, r. It is necessary to use the more exact formula, Eq. (5.320), for earlier times and greater distances.

Let us now turn to the behavior of the field in the far zone, $r \gg \tau$. As we have noted several times, the far zone corresponds to the earlier part of the transient signal, that is, for times as $t \to 0$. In the far zone, the behavior of the electric field and the time-rate of change of the magnetic field are specified by Eqs. (5.321), (5.322), (5.326) and (5.327). These formulas permit the same physical interpretation of their meaning as was appropriate for the frequency domain cases; that is, the signal which arrives at an observation point in the far zone can be divided into two parts, one traveling over the surface of the earth, and one penetrating through the earth. The first part of the signal propagates through the air with virtually no attenuation, then refracts almost vertically into the earth near the receiver. The second part travels through the earth from the source to the receiver, being attenuated and being characterized by a relatively low speed of travel. At an early stage in this process, the two parts of the signal separate in time. The first part of the field arrives at the receiver practically instantaneously, while the second part travels more slowly, with energy transferring into the late stage of the signal.

To reiterate, in the far zone, essentially only the first part of the signal is present. At any point in the far zone, we can consider that the field penetrates vertically into the earth as a plane wave, as follows from Eqs. (5.321), (5.322), (5.326), and (5.327), in which the right-hand parts are independent of time, t. This raises the question, then, as to what controls the depth of penetration of the plane wave into the earth. The answer to this question is found from Eq. (5.282) for the frequency-domain representation of the electric field by carrying out the Fourier integral transform defined in Eq. (5.295):
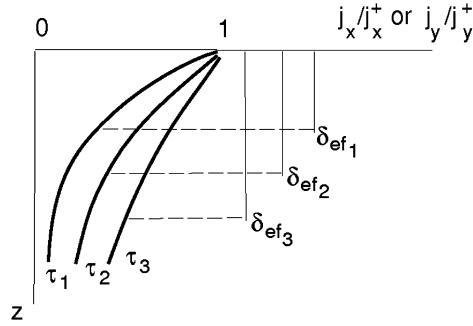
FIGURE 5.11

Change in current density as a function of depth for several instants in time.

$$\frac{E_{x(y)}^{H}(t, z)}{E_{x(y)}^{+}} = \frac{1}{2\pi} \int_{-\infty}^{\infty} \frac{E_{x(y)}(z)}{E_{x(y)}^{+}} [\pi \delta(\omega) - \frac{1}{i\omega}] e^{-i\omega t} d\omega$$

$$= \frac{1}{2\pi} \int_{-\infty}^{\infty} e^{ik_1 z} [\pi \delta(\omega) - \frac{1}{i\omega}] e^{-i\omega t} d\omega$$

$$= H(t)[1 - \Phi(2\pi z/\tau)] \tag{5.334}$$

where, as before, $\Phi(2\pi z/\tau)$ is the probability integral function of the indicated argument, and τ is the time-domain parameter, defined by Eqs. (5.304) and (5.305).

Using Ohm's law to determine current density from the electric field, we can write

$$j_{x(y)}^{H}(t, z) = j_{x(y)}^{+}[1 - \Phi(2\pi z/\tau)], \; t > 0. \tag{5.335}$$

The function $\Phi(2\pi z/\tau)$ is zero at $z = 0$, and increases rapidly, approaching unity with increasing z. Consequently, the current density, $j_{x(y)}(t, z)$, decays rapidly with depth at any given instant in time, t (see Fig. 5.11).

The curve characterizing the decay of current density with depth has an inflection point at $z = \tau/2\pi$, where the third derivative,

$$\partial^3 (2\pi z/\tau)/\partial z^3 = 0.$$

This depth has been named *the depth of penetration of a transient electromagnetic field into the earth*, and is designated with the symbol δ_{ef}:

$$\delta_{ef} = \tau/2\pi. \tag{5.336}$$

This definition of depth of penetration in the time domain is consistent with the frequency domain definition of skin depth, $\delta_e = \lambda/2\pi$, by equating wave length in the frequency domain, λ, with the time-domain parameter, τ. Substituting Eq. (5.305) in Eq. (5.336), we can write

$$\delta_{ef} = (10^7 \cdot \rho t/2\pi)^{1/2}. \tag{5.337}$$

We now see that the depth of penetration of a transient electromagnetic field into the earth is determined by the time, t, after the initiation of the transient signal. Greater times correspond to greater penetration, lesser times to lesser penetration. This provides the theoretical basis for obtaining a sounding curve, one in which the curve progressively samples the profile of conductivity or resistivity at greater depths in the earth.

In summary, we note that, while we have solved the problem of describing the field about a dipole source operating on the surface of a horizontally stratified medium in the time domain, we have not, as was also the case in the frequency domain, been able to obtain these field descriptions in the form of algebraic operations on elementary, or even transcendental functions. The components of the field for a horizontally stratified medium are described only as Fourier integral transforms of the corresponding expressions which were developed in the frequency domain.

REFERENCES AND RECOMMENDED READING TO CHAPTER 5

Berdichevsky, M. N., and V. I. Dmitriev, 2002, Magnetotellurics in the context of theory of ill-posed problems: Society of Exploration Geophysicists, 215 pp.

Cagniard, L., 1953, Basic theory of the magnetotelluric method of geophysical prospecting: Geophysics, **18**, 605–635.

Jakosky, J. J., 1940, Exploration geophysics: Times-Mirror Press, Los Angeles.

Kaufman, A. A., and G. M. Morozova, 1970, Theoretical basis for the transient sounding method in the near-zone: Nauka, Novosibirsk, 122 pp.

Keller, G. V., 1966, Dipole method for deep resistivity studies: Geophysics, **31** (6), 1088–1104.

Keller, G. V., and F. C. Frischknecht, 1966, Electrical methods in geophysical prospecting: Pergamon Press, Oxford, 517 pp.

Kharkevich, A. A., 1960, Spectra and analysis: Consultants Bureau, New York, 222 pp.

Koefoed, O., 1968, The application of the kernel function in interpreting geoelectrical resistivity measurements: Gebruder Borntraeger, Berlin, 111 pp.

Lipskaya, N. V., 1953, Some relationships between harmonics of variations of the earth electromagnetic field: Izvestia AN SSSR, Seria Geofizika, (1), 17–29.

Mooney, H. M., and W. W. Wetzel, 1956, The potentials about a point electrode and apparent resistivity curves for a two-, three-, and four-layer earth: The University of Minnesota Press, Minneapolis, 146 pp.

Obukhov, G. G., 1968, About some properties of the nonstationary electromagnetic fields in the earth and their applications in electrical prospecting: Izvestia AN SSSR, Physics of the Earth, (9), 62–71.

Papoulis, A., 1962, The Fourier integral and its applications: New York, McGraw-Hill Book Company Inc., 318 pp.

Tikhonov, A. N., 1950, On the determination of electrical characteristics of deep layers of the Earth's crust (*in Russian*): Dokladi Akademii Nauk SSSR, **73**, 295–297.

Vanyan, L. L., 1959, Some questions of theory of frequency soundings: Prikladnaya Geofizika, Nedra, **23**, 3–45.

Vanyan, L.L., 1997, Electromagnetic soundings (*in Russian*): Moscow, Scientific World, 219 pp.

Zhdanov, M. S., 1986, Electrical prospecting (*in Russian*): Moscow, Nedra, 316 pp.

Zhdanov, M. S., and G. W. Keller, 1994, The geoelectrical methods in geophysical exploration: Elsevier, Amsterdam, London, New York, Tokyo, 873 pp.

ELECTROMAGNETIC FIELDS IN INHOMOGENEOUS MEDIA

CONTENTS

In the final decade of the twentieth century and in the beginning of the twenty-first century, methods for numerical and analytical modeling of the interaction of electromagnetic fields with earth structures developed rapidly. This development was driven by the availability of high performance computers, including PC clusters, with which such models could be constructed. This modeling capability has made possible the extraction of much more information from field data than had been possible previously when only heuristic interpretation was feasible. The modern capability of geoelectrical methods is based on two technological developments: the ability to acquire great volumes of data with high accuracy, and the possibility of extracting sophisticated models of geoelectrical structures from these data using advanced numerical modeling and inversion methods. In this chapter, we will discuss numerical and analytical modeling for use both in the interpretation and in the planning of field surveys.

Numerical modeling is a term used to represent an approach in which a true earth structure is replaced by one for which a numerical approximation to Maxwell's equations can be made and evaluated. There are several techniques available for electromagnetic (EM) forward modeling. They are based on numerical implementation of the differential equation (DE) approach (finite difference, FD, or finite element, FE, methods) or the integral equation (IE) approach.

The integral equation (IE) method is a powerful tool in three-dimensional (3-D) electromagnetic (EM) modeling for geophysical applications. It was introduced originally in a pioneering paper by Dmitriev (1969), which was published in Russian and long remained unknown to western geophysicists (as well as the work of Tabarovsky, 1975). More than 40 years ago, practically simultaneously, Raiche (1974), Weidelt (1975a) and Hohmann (1975) published their famous papers on the IE method. Many more researchers have contributed to the improvement and development of this method in recent years (e.g., Wannamaker, 1991; Dmitriev and Nesmeyanova, 1992; Xiong, 1992; Xiong and Kirsch, 1992; Singer and Fainberg, 1997; Avdeev et al., 2002; Hursán and Zhdanov, 2002; Zhdanov, 2002; Singer et al., 2003; Abubakar and van der Berg, 2004; Avdeev, 2005). The main advantage of the IE method in comparison with the FD and FE methods is the fast and accurate simulation of the EM response in models with compact 2-D or 3-D bodies in a layered background. At the same time, the main area of application of FD and FE methods is the modeling of EM fields in complex structures with large-scale EM parameter variations. In principle, the IE method can handle these models; however, the demand on computer resources is tremendous, which places practical limits on its use. This happens because of the large, dense matrix arising in the IE formulation. In this direction, several approximate methods have been developed recently. These are the extended Born (localized nonlinear) approximation (Habashy et al., 1993), the quasi-linear approximation (Zhdanov and Fang, 1996a, 1996b), quasi-linear series (Zhdanov and Fang, 1997), quasi-analytic approximation and quasi-analytic series (Zhdanov et al., 2000a, 2000b), etc. In this chapter we discuss the basic principles of the IE method and introduce a family of linear and nonlinear approximations for electromagnetic modeling in conductive inhomogeneous media. The final sections of this chapter summarize the principles of the differential equation methods of electromagnetic modeling.

6.1 INTEGRAL EQUATION METHOD

6.1.1 BACKGROUND (NORMAL) AND ANOMALOUS PARTS OF THE ELECTROMAGNETIC FIELD

Consider a 3-D geoelectrical model with a normal (background) complex conductivity $\widetilde{\sigma}_b$ and local inhomogeneity D with an arbitrarily varying complex conductivity $\widetilde{\sigma} = \widetilde{\sigma}_b + \Delta\widetilde{\sigma}$. The inhomogeneity is considered to be local, so there exists some radius R_0 such that for $\sqrt{x^2 + y^2 + z^2} > R_0$ the medium has the background conductivity $\widetilde{\sigma}_b$. Within this chapter we will confine ourselves to consideration of nonmagnetic media and, hence, assume that $\mu = \mu_0 = 4\pi \times 10^{-7} H/m$, where μ_0 is the free-space magnetic permeability. The model is excited by an electromagnetic field generated by an arbitrary source with an extraneous current distribution $\mathbf{j}^e$ concentrated within some local domain Q. This field is time harmonic as $e^{-i\omega t}$. Complex conductivity includes the effect of displacement currents: $\widetilde{\sigma} = \sigma - i\omega\varepsilon$, where σ and ε are electrical conductivity and dielectric permittivity. Note that, in a case of the quasi-stationary EM field, which is a typical case for geophysical applications, the conductivity is always real; however, in this section, for completeness, we will consider a general case of Maxwell's equations with the displacement currents, which is reflected in the presence of dielectric permittivity in the expression for the complex conductivity. Our goal is to derive the integral equations for the electromagnetic field for this model. The solution of this problem is based on introducing normal (background) and anomalous electromagnetic fields.

The electromagnetic field in the model described above can be presented as a sum of the background (normal) and anomalous fields:

$$\mathbf{E} = \mathbf{E}^b + \mathbf{E}^a, \ \mathbf{H} = \mathbf{H}^b + \mathbf{H}^a, \tag{6.1}$$

where the background field is a field generated by the given sources in the model with the background (normal) distribution of conductivity $\widetilde{\sigma}_b$, and the anomalous field is produced by the anomalous conductivity distribution $\Delta\widetilde{\sigma}$.

The total electromagnetic field in this model satisfies Maxwell's equations:

$$\nabla \times \mathbf{H} = \widetilde{\sigma}\mathbf{E} + \mathbf{j}^e,$$
$$\nabla \times \mathbf{E} = i\omega\mu_0\mathbf{H}, \tag{6.2}$$

which can be written separately for the background field $\mathbf{E}^b$, $\mathbf{H}^b$,

$$\nabla \times \mathbf{H}^b = \widetilde{\sigma}_b\mathbf{E}^b + \mathbf{j}^e,$$
$$\nabla \times \mathbf{E}^b = i\omega\mu_0\mathbf{H}^b,$$

and for the anomalous field $\mathbf{E}^a$, $\mathbf{H}^a$,

$$\nabla \times \mathbf{H}^a = \widetilde{\sigma}_b\mathbf{E}^a + \mathbf{j}^a,$$
$$\nabla \times \mathbf{E}^a = i\omega\mu_0\mathbf{H}^a, \tag{6.3}$$

where $\mathbf{j}^e$ is the density of extraneous electric currents, and

$$\mathbf{j}^a(\mathbf{r}) = \Delta\widetilde{\sigma}(\mathbf{r})\mathbf{E}(\mathbf{r}) = \Delta\widetilde{\sigma}(\mathbf{r})\left[\mathbf{E}^b(\mathbf{r}) + \mathbf{E}^a(\mathbf{r})\right] \tag{6.4}$$

FIGURE 6.1

Derivation of Poynting's theorem and energy inequality for an anomalous field.

is the density of excess (anomalous) electric currents within the inhomogeneity D. Eqs. (6.3) follow from the previous equations by subtraction.

6.1.2 POYNTING'S THEOREM AND ENERGY INEQUALITY FOR AN ANOMALOUS FIELD

We now apply Poynting's theorem to the anomalous field only. We can introduce a domain V_2 with the boundary S_2 containing the inhomogeneity D (Fig. 6.1).

Applying Poynting's theorem (3.109) to the anomalous field $\mathbf{E}^a$, $\mathbf{H}^a$ distributed within the domain V_2, and taking into account Maxwell's equations (6.3) for the anomalous field, we obtain

$$F_\omega^a = -\frac{1}{2} \iiint_{V_2} \left\{ \sigma_b \left| \mathbf{E}^a \right|^2 + \mathrm{Re} \left(\mathbf{E}^a \cdot \mathbf{j}^{a*} \right) \right\} dv = \frac{1}{2} \mathrm{Re} \iint_{S_2} \left(\mathbf{E}^a \times \mathbf{H}^{a*} \right) \cdot \mathbf{n}_2 ds. \qquad (6.5)$$

The energy flow F_ω^a of the anomalous field outside the domain V_2 with the anomalous domain D, is also always nonnegative,

$$F_\omega^a \geq 0, \qquad (6.6)$$

and it is equal to zero only for a lossless background medium:

$$F_\omega^a = 0, \text{ if and only if } \sigma_b \equiv 0. \qquad (6.7)$$

The proof of this formula is similar to the proof of formula (3.112). Based on formulae (6.6) and (6.7), we can obtain, after some algebraic transformations, the following important energy inequality,

derived originally by Singer (1995) and Pankratov et al. (1995):

$$\iiint_{V_2} \left\{ \sigma_b \left| \mathbf{E}^a \right|^2 + \mathrm{Re} \left(\mathbf{E}^a \cdot \mathbf{j}^{a*} \right) \right\} dv$$

$$= \iiint_{V_2} \left\{ \sigma_b \left| \mathbf{E}^a + \frac{\mathbf{j}^a}{2\sigma_b} \right|^2 - \frac{|\mathbf{j}^a|^2}{4\sigma_b} \right\} dv < 0. \tag{6.8}$$

From the last formula we have

$$\iiint_{V_2} \sigma_b \left| \mathbf{E}^a + \frac{\mathbf{j}^a}{2\sigma_b} \right|^2 dv < \iiint_{V_2} \frac{|\mathbf{j}^a|^2}{4\sigma_b} dv. \tag{6.9}$$

Energy inequality (6.9) holds for any lossy medium.

This inequality is used in constructing the efficient integral equation methods for EM modeling based on the contraction integral equation (CIE) method (Singer, 1995; Pankratov et al., 1995; Hursán and Zhdanov, 2002; Zhdanov, 2002).

6.1.3 INTEGRAL EQUATION METHOD IN TWO DIMENSIONS

Let us consider a two-dimensional model in which there exists a localized inhomogeneity in the region Γ with complex conductivity $\widetilde{\sigma}(x, z) = \widetilde{\sigma}_b + \Delta\widetilde{\sigma}(x, z)$ embedded in a background (normal) horizontally stratified section characterized by a conductivity sequence, $\widetilde{\sigma}_b(\widetilde{\sigma}_1, \widetilde{\sigma}_2, ..., \widetilde{\sigma}_n)$ (Fig. 6.2). The structure is illuminated with an E-polarized field, which originates from linear currents distributed with a density $\mathbf{j}^e = j^e \mathbf{d}_y$ (where $\mathbf{d}_y$ is a unit vector directed along the y axis) flowing in a region Q in the upper half-space. This model is typical for geoelectrical methods. The upper half-space is usually associated with nonconductive air, while the lower half-space represents the structure of the conductive earth.

For such geoelectrical models, the electric field has but a single component, E_y, which can be represented as the sum of a background (normal) part and an anomalous part:

$$E_y = E_y^b + E_y^a, \tag{6.10}$$

where the background field is generated by the currents j^e in the horizontally stratified model without inhomogeneity, while the anomalous field is caused by the conductivity inhomogeneity.

It should be clear that the total field, E_y, satisfies the equation

$$\widetilde{\nabla}^2 E_y(\mathbf{r}) + i\omega\mu_0[\widetilde{\sigma}_b + \Delta\widetilde{\sigma}(\mathbf{r})]E_y(\mathbf{r}) = -i\omega\mu_0 j_y^e, \tag{6.11}$$

where $\widetilde{\nabla}^2$ is a two-dimensional Laplace operator, $\partial^2/\partial x^2 + \partial^2/\partial z^2$.

The background (normal) field is described by the equation

$$\widetilde{\nabla}^2 E_y^b(\mathbf{r}) + i\omega\mu_0 \widetilde{\sigma}_b E_y^b(\mathbf{r}) = -i\omega\mu_0 j_y^e. \tag{6.12}$$
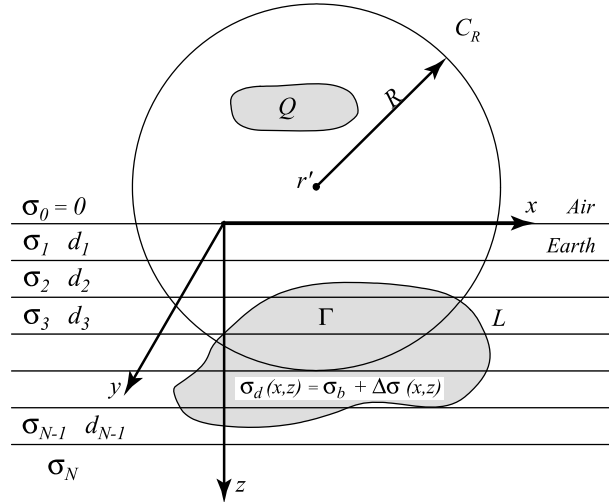
FIGURE 6.2

The two-dimensional model of a localized cylindrical inhomogeneity Γ with the conductivity $\tilde{\sigma}(x, z) = \tilde{\sigma}_b + \Delta\tilde{\sigma}(x, z)$ embedded in a background (normal) horizontally stratified section characterized by a conductivity sequence, $\tilde{\sigma}_b(\tilde{\sigma}_1, \tilde{\sigma}_2, ..., \tilde{\sigma}_n)$. The structure is illuminated with an E-polarized field, which originates from linear currents distributed with the density $\mathbf{j}^e = j^e \mathbf{d}_y$ flowing in a region Q in the upper half-space.

Subtracting the last equation from the one before it, we find an equation for the anomalous field:

$$\tilde{\nabla}^2 E_y^a(\mathbf{r}) + i\omega\mu_0\tilde{\sigma}_b E_y^a(\mathbf{r}) = -i\omega\mu_0 j_y^\Gamma(\mathbf{r}), \tag{6.13}$$

where j_y^Γ is viewed as the excess current flowing in the inhomogeneous region, Γ:

$$j_y^\Gamma(\mathbf{r}) = \Delta\tilde{\sigma}(\mathbf{r})E_y(\mathbf{r}). \tag{6.14}$$

An important role is played in the integral equation method by the Green's function for the background (normal) model of the earth. The Green's function, $G_b(\mathbf{r}'|\mathbf{r})$, depends on the positions of two points, $M(\mathbf{r})$ and $M'(\mathbf{r}')$, and is determined by a solution of the equation:

$$\tilde{\nabla}^2 G_b(\mathbf{r}'|\mathbf{r}) + i\omega\mu_0\tilde{\sigma}_b G_b(\mathbf{r}'|\mathbf{r}) = -i\omega\mu_0\delta(\mathbf{r}' - \mathbf{r}), \tag{6.15}$$

which tends to zero at infinity.

In this last equation, δ is the two-dimensional Dirac delta-function which is defined as follows:

$$\iint_D f(\mathbf{r})\delta(\mathbf{r}' - \mathbf{r})dS = \begin{cases} f(\mathbf{r}'); & \mathbf{r}' \in D, \\ 0 & \mathbf{r}' \notin \bar{D}, \end{cases} \tag{6.16}$$

where $f(\mathbf{r})$ is an arbitrarily continuous function in some domain D, and $\bar{D} = D + S$ is domain D with its boundary S.

Using the Green's function G_b, we find an expression for the background component of the electric field, E_y^b. To do so, we select an arbitrary point $\mathbf{r}'$ and around it draw a circle, C_R, with a radius great enough that the region Q falls within the region O_R bounded by the circle C_R; that is, $Q \in O_R$ (Fig. 6.2).

We now write the expression for Green's theorem within the region O_R:

$$\iint_{O_R} [E_y^b \tilde{\nabla}^2 G_b - G_b \tilde{\nabla}^2 E_y^b] ds = \oint_{C_R} [E_y^b \frac{\partial G_b}{\partial n} - G_b \frac{\partial E_y^b}{\partial n}] dl, \qquad (6.17)$$

where $E_y^b = E_y^b(\mathbf{r})$, $G_b = G_b(\mathbf{r}'|\mathbf{r})$, and $\partial/\partial n$ denotes a directional derivative in the direction of the external unit vector $\mathbf{n}$ normal to the contour C_R.

Substituting $\tilde{\nabla}^2 E_y^b$ and $\tilde{\nabla}^2 G_b$ from Eqs. (6.12) and (6.15) into this last equation, and taking into account (6.16), we find

$$i\omega\mu_0 \iint_Q G_b j_y^e ds - \oint_{C_R} [E_y^b \frac{\partial G_b}{\partial n} - G_b \frac{\partial E_y^b}{\partial n}] dl = i\omega\mu_0 E_y^b(\mathbf{r}') \text{ if } \mathbf{r}' \in O_R. \qquad (6.18)$$

According to radiation conditions (Stratton, 1941), the functions E_y^b and G_b decrease as $1/\sqrt{r}$ as $|\mathbf{r}| \to \infty$. Consequently, if the radius, R, is expanded without limit, the line integral along C_R will tend to zero. Hence, we find

$$E_y^b(\mathbf{r}') = \iint_Q G_b(\mathbf{r}'|\mathbf{r}) j_y^e(\mathbf{r}) ds. \qquad (6.19)$$

This result has a clear physical meaning: the background electric field is merely the superposition of elementary electric field contributions excited in the background geoelectrical sequence, $\tilde{\sigma}_b$, by the current filaments within the region Q. Using a similar approach, and starting with Eq. (6.13), it can be shown that the anomalous field is the superposition of elementary field contributions excited in the normal geoelectrical sequence by the excess currents, j_y^Γ, flowing within the inhomogeneous region, Γ:

$$E_y^a(\mathbf{r}') = \iint_\Gamma G_b(\mathbf{r}'|\mathbf{r}) j_y^\Gamma(\mathbf{r}) ds. \qquad (6.20)$$

Substituting the expression in Eq. (6.14) into this last equation, and considering Eq. (6.10), we find

$$E_y^b(\mathbf{r}') + \iint_\Gamma G_b(\mathbf{r}'|\mathbf{r}) \Delta\tilde{\sigma}(\mathbf{r}) E_y(\mathbf{r}) dS = E_y(\mathbf{r}'). \qquad (6.21)$$

For $\mathbf{r}' \in \Gamma$, this relationship leads to a Fredholm integral equation of the second type for the field E_y within the region Γ. The Green's function for the background sequence, G_b, which is present in Eq. (6.21), can be calculated from a simple recursive formula. Details about this procedure can be found in a monograph by Berdichevsky and Zhdanov (1984).

The derivative of the Green's function, which is needed in computing the magnetic field components, is determined similarly. In accord with Eq. (6.21) and Maxwell's second equation, we can write

$$H_x(\mathbf{r}') = H_x^b(\mathbf{r}') - \frac{1}{i\omega\mu_0} \iint_\Gamma \frac{\partial G_b}{\partial z'} \Delta\widetilde{\sigma} E_y ds,$$

$$H_z(\mathbf{r}') = H_z^b(\mathbf{r}') + \frac{1}{i\omega\mu_0} \iint_\Gamma \frac{\partial G_b}{\partial x'} \Delta\widetilde{\sigma} E_y ds. \tag{6.22}$$

6.1.4 CALCULATION OF THE FIRST VARIATION (FRÉCHET DERIVATIVE) OF THE ELECTROMAGNETIC FIELD FOR 2-D MODELS

The problem of the Fréchet derivative, or sensitivity matrix calculation for the electromagnetic field, is very important for electromagnetic inversion. It was examined in many publications (Weidelt, 1975b; Rodi, 1976; Madden and Mackie, 1989; Oldenburg, 1990; McGillivray and Oldenburg, 1990; Zhdanov and Keller, 1994; de Lugao and Wannamaker, 1996; de Lugao et al., 1997; and Zhdanov, 2002). We will consider, first, the technique for calculating the first variation of electromagnetic field for 2-D models.

Let us perturb the conductivity distribution, $\widetilde{\sigma}(x, z)$, within the region Γ. The equation for the corresponding perturbed electric field, δE_y, can be obtained by perturbing Eq. (6.11):

$$\widetilde{\nabla}^2 \delta E_y + i\omega\mu_0\widetilde{\sigma}\delta E_y = \begin{cases} -i\omega\mu_0\delta\widetilde{\sigma} E_y, & \mathbf{r} \in \Gamma \\ 0, & \mathbf{r} \notin \Gamma \end{cases}. \tag{6.23}$$

We now introduce the Green's function G_σ of the geoelectrical model with conductivity $\widetilde{\sigma} = \widetilde{\sigma}(x, z)$. The Green's function depends on the position of the points (x, z) and (x', z') and is determined by an equation similar to (6.15):

$$\widetilde{\nabla}^2 G_\sigma(\mathbf{r}'|\mathbf{r}) + i\omega\mu_0\widetilde{\sigma} G_\sigma(\mathbf{r}'|\mathbf{r}) = -i\omega\mu_0\delta(\mathbf{r}' - \mathbf{r}). \tag{6.24}$$

We now can apply Green's formula (6.17) to the perturbed electric field, δE_y, and Green's function G_σ. Repeating the derivations conducted in the previous subsection, we arrive at the formula analogous to (6.20):

$$\delta E_y(\mathbf{r}') = \iint_\Gamma G_\sigma(\mathbf{r}'|\mathbf{r})\delta\widetilde{\sigma}(\mathbf{r}) E_y(\mathbf{r}) ds. \tag{6.25}$$

The first variation of the magnetic field δH_x can be calculated from δE_y using Maxwell's equations:

$$\delta H_x(\mathbf{r}') = -\frac{1}{i\omega\mu_0} \frac{\partial \delta E_y(\mathbf{r}')}{\partial z'} = -\frac{1}{i\omega\mu_0} \iint_\Gamma \frac{\partial G_\sigma(\mathbf{r}'|\mathbf{r})}{\partial z'} \delta\widetilde{\sigma}(\mathbf{r}) E_y(\mathbf{r}) ds. \tag{6.26}$$

Formulae (6.25) and (6.26) for the first variations of the electromagnetic field provide an important tool for computing the Fréchet derivative of the forward electromagnetic operator. Actually, according to the definition (Zhdanov, 2002), the Fréchet differential $F_x(\delta\widetilde{\sigma})$ of the electromagnetic forward

modeling operator $A_{E,H}^{em}(\widetilde{\sigma})$ is given by:

$$F_{E,H}(\delta\widetilde{\sigma}) = \delta A_{E,H}^{em}(\widetilde{\sigma},\delta\widetilde{\sigma}) = \begin{cases} \delta E_y, & \text{for the electric field,} \\ \delta H_x, & \text{for the magnetic field.} \end{cases} \tag{6.27}$$

Substituting formulae (6.25) and (6.26) into (6.27), we find the expressions for the corresponding Fréchet differentials:

$$F_E(\delta\widetilde{\sigma}) = \delta E_y\left(\mathbf{r}'\right) = \iint_\Gamma G_\sigma\left(\mathbf{r}'|\mathbf{r}\right)\delta\widetilde{\sigma}\left(\mathbf{r}\right) E_y\left(\mathbf{r}\right) ds, \tag{6.28}$$

$$F_H(\delta\widetilde{\sigma}) = \delta H_x\left(\mathbf{r}'\right) = -\frac{1}{i\omega\mu_0} \iint_\Gamma \frac{\partial G_\sigma\left(\mathbf{r}'|\mathbf{r}\right)}{\partial z'}\delta\widetilde{\sigma}\left(\mathbf{r}\right) E_y\left(\mathbf{r}\right) ds. \tag{6.29}$$

Formulae (6.28) and (6.29) can be used to estimate the sensitivity of electromagnetic data to geo-electrical model parameters. For example, substituting $\delta\widetilde{\sigma}\left(\mathbf{r}\right) = \delta\left(\mathbf{r}''-\mathbf{r}\right)\delta\widetilde{\sigma}_s\left(\mathbf{r}''\right)$ into Eq. (6.28), we find a perturbation of the electric field, $\delta E_y\left(\mathbf{r}'\right)$, corresponding to the local perturbation of the complex conductivity $\delta\widetilde{\sigma}_s\left(\mathbf{r}''\right)$ at a point $\mathbf{r}''$:

$$\delta E_y\left(\mathbf{r}'\right) = G_\sigma\left(\mathbf{r}'|\mathbf{r}''\right) E_y\left(\mathbf{r}''\right)\delta\widetilde{\sigma}_s\left(\mathbf{r}''\right). \tag{6.30}$$

The differential sensitivity $s\left(\mathbf{r}'|\mathbf{r}''\right)$ of the electric field in the point $\mathbf{r}'$ to the electrical parameter at the point $\mathbf{r}''$ is calculated by the formula

$$s_E\left(\mathbf{r}'|\mathbf{r}''\right) = \frac{\delta E_y\left(\mathbf{r}'\right)}{\delta\widetilde{\sigma}_s\left(\mathbf{r}''\right)}. \tag{6.31}$$

Substituting (6.30) into (6.31), we have

$$s_E\left(\mathbf{r}'|\mathbf{r}''\right) = G_\sigma\left(\mathbf{r}'|\mathbf{r}''\right) E_y\left(\mathbf{r}''\right). \tag{6.32}$$

The integrated sensitivity, $S\left(\mathbf{r}''\right)$, of the data, collected over some observation line b over a frequency interval Ω, in accordance with the definition (8.16), is equal to

$$S_E\left(\mathbf{r}''\right) = \frac{\left\|\delta E_y\right\|_{\Omega,b}}{\delta\widetilde{\sigma}_s\left(\mathbf{r}''\right)}, \tag{6.33}$$

where the L_2 norm $\|...\|_{\Omega,b}$ is determined by the formula

$$\left\|\delta E_y\right\|_{\Omega,b} = \sqrt{\int_\Omega\int_b\left|\delta E_y\left(\mathbf{r}',\omega\right)\right|^2 dl'd\omega},$$

where "prime" over dl denotes that the integration is conducted over the variable $\mathbf{r}'$.

Therefore, the integrated sensitivity of the electric field to the local perturbation of the conductivity in point $\mathbf{r}''$ is equal to

$$S_E\left(\mathbf{r}''\right) = \sqrt{\int_\Omega\left|E_y\left(\mathbf{r}'',\omega\right)\right|^2\int_b\left|G_\sigma\left(\mathbf{r}'|\mathbf{r}''\right)\right|^2 dl'd\omega}. \tag{6.34}$$

In a similar way, we can find the differential and integrated sensitivities for magnetic field:

$$s_H\left(\mathbf{r}'|\mathbf{r}''\right) = -\frac{1}{i\omega\mu_0}\frac{\partial G_\sigma\left(\mathbf{r}'|\mathbf{r}''\right)}{\partial z'}E_y\left(\mathbf{r}''\right), \tag{6.35}$$

and

$$S_H\left(\mathbf{r}''\right) = \frac{1}{\mu_0}\sqrt{\int_\Omega\frac{\left|E_y\left(\mathbf{r}'',\omega\right)\right|^2}{\omega^2}\int_b\left|\frac{\partial G_\sigma\left(\mathbf{r}'|\mathbf{r}''\right)}{\partial z'}\right|^2 dl'd\omega}. \tag{6.36}$$

We shall use these formulae (6.34) and (6.36) in electromagnetic inversion.

6.1.5 INTEGRAL EQUATION METHOD IN THREE DIMENSIONS

We can apply an approach, similar to the one used in the 2-D case, to derive the electromagnetic integral equations in three dimensions. Electromagnetic Green's tensors, introduced in the Chapter 3, make it possible to determine the electromagnetic field of an arbitrary current distribution $\mathbf{j}\left(\mathbf{r}\right)$ within a medium with background conductivity $\widetilde{\sigma}_b$:

$$\begin{aligned}
\mathbf{E}\left(\mathbf{r}_j\right) &= \iiint_D \widehat{\mathbf{G}}_E\left(\mathbf{r}_j\mid\mathbf{r}\right)\cdot\mathbf{j}\left(\mathbf{r}\right)dv = \mathbf{G}_E\left(\mathbf{j}\right), \\
\mathbf{H}\left(\mathbf{r}_j\right) &= \iiint_D \widehat{\mathbf{G}}_H\left(\mathbf{r}_j\mid\mathbf{r}\right)\cdot\mathbf{j}\left(\mathbf{r}\right)dv = \mathbf{G}_H\left(\mathbf{j}\right),
\end{aligned} \tag{6.37}$$

where $\mathbf{G}_E$ and $\mathbf{G}_H$ are the electric and magnetic Green's operators. The proof of these formulae is similar to the proof of formula (6.19) and is based on an application of Green's theorem to the electric or magnetic field and the corresponding Green's tensors (Zhdanov, 1988, 2002).

Maxwell's equations (6.2) can be rewritten for the background medium with excess current $\mathbf{j^a} = \Delta\widetilde{\sigma}\mathbf{E}$:
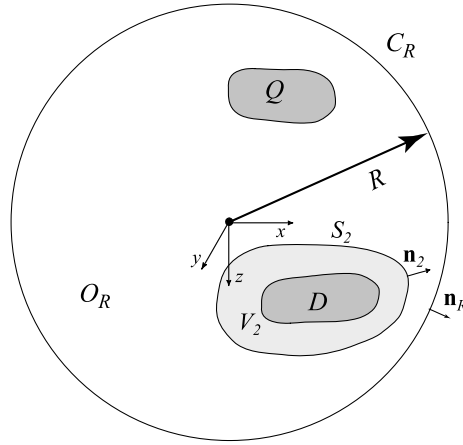
$$\begin{aligned}
\nabla\times\mathbf{H} &= \widetilde{\sigma}_b\mathbf{E} + \mathbf{j^a} + \mathbf{j}^e, \\
\nabla\times\mathbf{E} &= i\omega\mu_0\mathbf{H}.
\end{aligned} \tag{6.38}$$

We can apply the integral representations (6.37) to these equations:

$$\begin{aligned}
\mathbf{E}\left(\mathbf{r}_j\right) &= \mathbf{G}_E\left(\mathbf{j}^a\right) + \mathbf{G}_E\left(\mathbf{j}^e\right), \\
\mathbf{H}\left(\mathbf{r}_j\right) &= \mathbf{G}_H\left(\mathbf{j}^a\right) + \mathbf{G}_H\left(\mathbf{j}^e\right),
\end{aligned} \tag{6.39}$$

where the first terms describe the anomalous fields generated by the excess currents

$$\mathbf{E}^a\left(\mathbf{r}_j\right) = \mathbf{G}_E\left(\mathbf{j}^a\right) = \mathbf{G}_E\left(\Delta\widetilde{\sigma}\mathbf{E}\right), \tag{6.40}$$

$$\mathbf{H}^a\left(\mathbf{r}_j\right) = \mathbf{G}_H\left(\mathbf{j}^a\right) = \mathbf{G}_H\left(\Delta\widetilde{\sigma}\mathbf{E}\right), \tag{6.41}$$

and the second terms correspond to the background fields of the extraneous currents in the background media,

$$\mathbf{E}^b\left(\mathbf{r}_j\right) = \mathbf{G}_E\left(\mathbf{j}^e\right), \tag{6.42}$$

$$\mathbf{H}^b\left(\mathbf{r}_j\right) = \mathbf{G}_H\left(\mathbf{j}^e\right). \tag{6.43}$$

Substituting the expression for the excess current (6.4) into (6.39), we finally obtain the well known representation for the electromagnetic field as an integral over the excess currents in the inhomogeneous domain D (Raiche, 1974; Hohmann, 1975; Weidelt, 1975a):

$$\mathbf{E}\left(\mathbf{r}_j\right) = \mathbf{G}_E\left(\Delta\widetilde{\sigma}\mathbf{E}\right) + \mathbf{E}^b\left(\mathbf{r}_j\right), \tag{6.44}$$

$$\mathbf{H}\left(\mathbf{r}_j\right) = \mathbf{G}_H\left(\Delta\widetilde{\sigma}\mathbf{E}\right) + \mathbf{H}^b\left(\mathbf{r}_j\right). \tag{6.45}$$

Using integral formulae (6.44) and (6.45), one can calculate the electromagnetic field at any point $\mathbf{r}_j$, if the electric field is known within the inhomogeneity. Expression (6.44) becomes the integral equation for the electric field $\mathbf{E}(\mathbf{r})$, if $\mathbf{r}_j \in D$. Eqs. (6.44) and (6.45) form the basis for EM forward modeling.

6.1.6 CONTRACTION INTEGRAL EQUATION METHOD

In a general case the L_2 norm of the Green's operators can be arbitrarily big. Following Pankratov et al. (1995) and Zhdanov and Fang (1997), we apply some linear transformations to the Green's operator to obtain a new modified Green's operator $\mathbf{G}_E^m$ with norm less than 1. Note that, operator $\mathbf{C}$ is called a contraction operator if its norm is less then one, $\|\mathbf{C}\| < 1$. The specific form of this linear transformation is motivated by the energy inequality (6.9) for an anomalous field. Actually, we construct a new linear operator $\mathbf{G}_E^m$, which transforms the integrand from the right part of the energy inequality (6.9) into its left part:

$$\sqrt{\sigma_b}\left(\mathbf{E}^a + \mathbf{j}^a/2\sigma_b\right) = \sqrt{\sigma_b}\mathbf{G}_E\left[2\sqrt{\sigma_b}\left(\mathbf{j}^a/2\sqrt{\sigma_b}\right)\right]$$

$$+ \mathbf{j}^a/2\sqrt{\sigma_b} = \mathbf{G}_E^m\left(\mathbf{j}^a/2\sqrt{\sigma_b}\right). \tag{6.46}$$

Operator $\mathbf{G}_E^m$ can be applied to any vector function:

$$\mathbf{G}_E^m\left(\mathbf{x}\right) = \sqrt{\sigma_b}\mathbf{G}_E\left(2\sqrt{\sigma_b}\mathbf{x}\right) + \mathbf{x}, \tag{6.47}$$

$\mathbf{x} \in L_2(D)$, where $L_2(D)$ is the Hilbert space of the vector functions determined in domain D and integrable in D with the norm:

$$\|\mathbf{x}\| = \sqrt{\iiint_D |\mathbf{x}(\mathbf{r})|^2 \, dv}.$$

The remarkable property of this operator is that according to inequality (6.9),

$$\left\|\mathbf{G}_E^m\left(\mathbf{x}\right)\right\| \leq \|\mathbf{x}\|$$

for any $\mathbf{x} \in L_2(D)$. In other words the L_2 norm of the modified Green's operator is always less than or equal to one:

$$\left\|\mathbf{G}_E^m\right\| \leq 1. \tag{6.48}$$

By virtue of (6.4), Eq. (6.46) can be simplified:

$$a\mathbf{E}^a + b\mathbf{E}^b = \mathbf{G}_E^m \left[b \left(\mathbf{E}^a + \mathbf{E}^b \right) \right], \tag{6.49}$$

where

$$a = \frac{2\sigma_b + \Delta\tilde{\sigma}}{2\sqrt{\sigma_b}}, \quad b = \frac{\Delta\tilde{\sigma}}{2\sqrt{\sigma_b}}. \tag{6.50}$$

Eq. (6.49) can be rewritten with respect to the product of a and the total electric field $\mathbf{E}$, using simple algebraic transformations:

$$\tilde{\mathbf{E}} + (b - a)\mathbf{E}^b = \tilde{\mathbf{E}} - \sqrt{\sigma_b}\mathbf{E}^b = \mathbf{G}_E^m \left[ba^{-1}\tilde{\mathbf{E}} \right] = \mathbf{G}_E^m \left[ba^{-1}\tilde{\mathbf{E}} \right], \tag{6.51}$$

where $\tilde{\mathbf{E}}$ is the scaled electric field

$$\tilde{\mathbf{E}} = a\mathbf{E}. \tag{6.52}$$

Finally, we can present Eq. (6.49) in the form

$$\tilde{\mathbf{E}} = \mathbf{C}^m \left(\tilde{\mathbf{E}} \right) = \mathbf{G}_E^m \left[ba^{-1}\tilde{\mathbf{E}} \right] + \sqrt{\sigma_b}\mathbf{E}^b. \tag{6.53}$$

In this equation operator $\mathbf{C}^m \left(\tilde{\mathbf{E}} \right)$ is a contraction operator. To prove this result, consider the following inequality:

$$\left\| \mathbf{C}^m \left[a\mathbf{E}^{a(1)} - a\mathbf{E}^{a(2)} \right] \right\| = \left\| \mathbf{G}_E^m \left[\beta \left(a\mathbf{E}^{a(1)} - a\mathbf{E}^{a(2)} \right) \right] \right\|$$
$$\leq \|\beta\|_\infty \left\| \mathbf{G}_E^m \right\| \left\| a\mathbf{E}^{a(1)} - a\mathbf{E}^{a(2)} \right\|,$$

where

$$\|\beta\|_\infty = \max_{\mathbf{r} \in D} \left| \frac{b(\mathbf{r})}{a(\mathbf{r})} \right| = \max_{\mathbf{r} \in D} \frac{|\Delta\tilde{\sigma}|}{|2\sigma_b + \Delta\tilde{\sigma}|}.$$

Taking into account (6.48), we can conclude that $\mathbf{C}^m$ is a contraction operator if:

$$\|\beta\|_\infty = \left\| \frac{b}{a} \right\|_\infty < 1. \tag{6.54}$$

Simple calculations show that

$$\beta^2 = \frac{|\Delta\tilde{\sigma}|^2}{|2\sigma_b + \Delta\tilde{\sigma}|^2} = 1 - \frac{4\sigma\sigma_b}{|\tilde{\sigma} - \tilde{\sigma}_b|^2 + 4\sigma\sigma_b} < 1$$

under the natural condition that

$$0 < \sigma_{\min} \leq \sigma \leq \sigma_{\max} < \infty,$$
$$0 < \sigma_{b\,\min} \leq \sigma_b \leq \sigma_{b\,\max} < \infty.$$

Thus, we have proved that $\mathbf{C}^m$ is a contraction operator for any lossy background media (where $\sigma_{b\,\min} > 0$):

$$\left\| \mathbf{C}^m \left(\widetilde{\mathbf{E}}^{(1)} - \widetilde{\mathbf{E}}^{(2)} \right) \right\| \leq k \left\| \widetilde{\mathbf{E}}^{(1)} - \widetilde{\mathbf{E}}^{(2)} \right\|, \tag{6.55}$$

where $\|...\|$ is L_2 norm, $k < 1$, and $\widetilde{\mathbf{E}}^{(1)}$ and $\widetilde{\mathbf{E}}^{(2)}$ are any two different solutions.

For this reason integral equation (6.49) is called *a contraction integral equation (CIE)*, and we call $\mathbf{C}^m$ *a contraction Green's operator*.

Using the original Green's operator given by expression (6.37) and taking into account formula (6.47), one can rewrite Eq. (6.49) as follows:

$$\widetilde{\mathbf{E}} = \sqrt{\sigma_b}\mathbf{G}_E \left(2\sqrt{\sigma_b}ba^{-1}\widetilde{\mathbf{E}} \right) + ba^{-1}\widetilde{\mathbf{E}} + \sqrt{\sigma_b}\mathbf{E}^b,$$

or, after some transformation

$$\left(1 - ba^{-1} \right)\widetilde{\mathbf{E}} - \sqrt{\sigma_b}\mathbf{G}_E \left(\Delta\widetilde{\sigma}a^{-1}\widetilde{\mathbf{E}} \right) = \sqrt{\sigma_b}\mathbf{E}^b.$$

Note that according to (6.50),

$$1 - ba^{-1} = (a - b)\,a^{-1} = \sqrt{\sigma_b}a^{-1}.$$

Therefore, we finally obtain the following form of the contraction integral equation (CIE) with respect to the scaled electric field $\widetilde{\mathbf{E}}$:

$$\sqrt{\sigma_b}a^{-1}\widetilde{\mathbf{E}} - \sqrt{\sigma_b}\mathbf{G}_E \left(\Delta\widetilde{\sigma}a^{-1}\widetilde{\mathbf{E}} \right) = \sqrt{\sigma_b}\mathbf{E}^b. \tag{6.56}$$

This is the basic equation of the CIE method of electromagnetic modeling.

6.1.7 CALCULATION OF THE FIRST VARIATION (FRÉCHET DERIVATIVE) OF THE ELECTROMAGNETIC FIELD FOR 3-D MODELS

Following Zhdanov (2002), we can find the equations for the Fréchet derivative in the 3-D case by differentiating the corresponding Maxwell's equations. Let us write the general field equations (3.103) and (3.89) in the frequency domain, allowing for magnetic currents (for a definition of magnetic currents see section 3.1):

$$\nabla \times \mathbf{H} = \widetilde{\sigma}\mathbf{E} + \mathbf{j}^e, \tag{6.57}$$
$$\nabla \times \mathbf{E} = i\omega\mu_0\mathbf{H} - \mathbf{j}^m, \tag{6.58}$$

where $\mathbf{j}^e$ and $\mathbf{j}^m$ are the densities of extraneous electric and magnetic currents.

Let us perturb the conductivity distribution $\widetilde{\sigma}(\mathbf{r})$. Applying the perturbation operator to both sides of Eqs. (6.57) and (6.58), we obtain the equations for the corresponding variations of the electromagnetic field:

$$\nabla \times \delta\mathbf{H} = \widetilde{\sigma}\delta\mathbf{E} + \delta\widetilde{\sigma}\mathbf{E},$$
$$\nabla \times \delta\mathbf{E} = i\omega\mu_0\delta\mathbf{H}, \tag{6.59}$$

where $\delta\widetilde{\sigma}$ is the conductivity variation, and $\delta\mathbf{H}$, $\delta\mathbf{E}$ are the corresponding variations of the magnetic and electric fields.

Applying the integral equation method (formulae (6.40) and (6.41)) to the solution of Eqs. (6.59), we find that the variations of the electromagnetic field are associated with the variation of the conductivity structure by the following integral operators:

$$\delta\mathbf{E}\left(\mathbf{r}_j\right) = \mathbf{G}_E\left(\delta\widetilde{\sigma}\mathbf{E}\right), \tag{6.60}$$

$$\delta\mathbf{H}\left(\mathbf{r}_j\right) = \mathbf{G}_H\left(\delta\widetilde{\sigma}\mathbf{E}\right). \tag{6.61}$$

The last two equations provide a straightforward way to calculate the Fréchet differential (for definition see Zhdanov, 2002) of the electromagnetic operator for forward modeling of complex three-dimensional electrical structures:

$$\mathbf{F}_E(\widetilde{\sigma},\delta\widetilde{\sigma}) = \delta\mathbf{A}_E^{em}(\widetilde{\sigma},\delta\widetilde{\sigma}) = \delta\mathbf{E} = \iiint_D \widehat{\mathbf{G}}_E\left(\mathbf{r}' \mid \mathbf{r}\right) \cdot \delta\widetilde{\sigma}\left(\mathbf{r}\right)\mathbf{E}\left(\mathbf{r}\right)dv, \tag{6.62}$$

and

$$\mathbf{F}_H(\widetilde{\sigma},\delta\widetilde{\sigma}) = \delta\mathbf{A}_H^{em}(\widetilde{\sigma},\delta\widetilde{\sigma}) = \delta\mathbf{H} = \iiint_D \widehat{\mathbf{G}}_H\left(\mathbf{r}' \mid \mathbf{r}\right) \cdot \delta\widetilde{\sigma}\left(\mathbf{r}\right)\mathbf{E}\left(\mathbf{r}\right)dv. \tag{6.63}$$

Note that the arguments in the expressions for the Fréchet differentials, $\mathbf{F}_{E,H}(\widetilde{\sigma},\delta\widetilde{\sigma})$, consist of two parts. The first part, $\widetilde{\sigma}$, is a conductivity distribution, at which we calculate the forward modeling operator variation, $\delta\mathbf{A}_H^{em}$; the Green's tensors are calculated for this conductivity. The second part, $\delta\widetilde{\sigma}$, is the corresponding variation of the conductivity $\widetilde{\sigma}$. Vector $\mathbf{E}$ in expressions (6.62) and (6.63) represents the electric field for the given conductivity $\widetilde{\sigma}$.

We can estimate the sensitivity of electromagnetic data to geoelectrical model parameters by means of formulae (6.62) and (6.63).

Substituting $\delta\widetilde{\sigma}\left(\mathbf{r}\right) = \delta\left(\mathbf{r}''-\mathbf{r}\right)\delta\widetilde{\sigma}_v\left(\mathbf{r}''\right)$ in Eqs. (6.62) and (6.63), we find the perturbations of the electric and magnetic fields, $\delta\mathbf{E}\left(\mathbf{r}'\right)$, $\delta\mathbf{H}\left(\mathbf{r}'\right)$, corresponding to the local perturbation of the complex integrated conductivity $\delta\widetilde{\sigma}_v\left(\mathbf{r}''\right)$ at a point $\mathbf{r}''$:

$$\delta\mathbf{E}\left(\mathbf{r}'\right) = \widehat{\mathbf{G}}_E\left(\mathbf{r}' \mid \mathbf{r}''\right) \cdot \delta\widetilde{\sigma}_v\left(\mathbf{r}''\right)\mathbf{E}\left(\mathbf{r}''\right), \; \delta\mathbf{H}\left(\mathbf{r}'\right) = \widehat{\mathbf{G}}_H\left(\mathbf{r}' \mid \mathbf{r}''\right) \cdot \delta\widetilde{\sigma}_v\left(\mathbf{r}''\right)\mathbf{E}\left(\mathbf{r}''\right). \tag{6.64}$$

The differential sensitivities $\mathbf{s}_E\left(\mathbf{r}'|\mathbf{r}''\right)$ and $\mathbf{s}_H\left(\mathbf{r}'|\mathbf{r}''\right)$ of the electric and magnetic fields at the point $\mathbf{r}'$ to the integrated conductivity perturbation at the infinitesimally small neighborhood of the point $\mathbf{r}''$ are calculated by the formulae

$$\mathbf{s}_E\left(\mathbf{r}'|\mathbf{r}''\right) = \frac{\delta\mathbf{E}\left(\mathbf{r}'\right)}{\delta\widetilde{\sigma}_v\left(\mathbf{r}''\right)}, \; \mathbf{s}_H\left(\mathbf{r}'|\mathbf{r}''\right) = \frac{\delta\mathbf{H}\left(\mathbf{r}'\right)}{\delta\widetilde{\sigma}_v\left(\mathbf{r}''\right)}. \tag{6.65}$$

Substituting expressions (6.64) into (6.65), we finally obtain:

$$\mathbf{s}_E\left(\mathbf{r}'|\mathbf{r}''\right) = \widehat{\mathbf{G}}_E\left(\mathbf{r}' \mid \mathbf{r}''\right) \cdot \mathbf{E}\left(\mathbf{r}''\right), \; \mathbf{s}_H\left(\mathbf{r}'|\mathbf{r}''\right) = \widehat{\mathbf{G}}_H\left(\mathbf{r}' \mid \mathbf{r}''\right) \cdot \mathbf{E}\left(\mathbf{r}''\right). \tag{6.66}$$

Note that the differential sensitivities are vector functions, because they characterize the sensitivity of the vector electric and magnetic fields to the conductivity variation. From the last formulae we see

that Green's electromagnetic tensors provide the sensitivity estimation of the electromagnetic field to the model conductivity.

We can give a simple, but important physical interpretation of the expressions for sensitivities, (6.66), based on the reciprocity principle. Note that, according to definition (see Chapter 3), the Green's tensors $\widehat{\mathbf{G}}_E \left(\mathbf{r}' \mid \mathbf{r}'' \right)$ and $\widehat{\mathbf{G}}_H \left(\mathbf{r}' \mid \mathbf{r}'' \right)$, are the electric and magnetic fields at the receiver point, $\mathbf{r}'$, due to a unit electric dipole source at the point $\mathbf{r}''$ of the conductivity perturbation. Let us introduce a Cartesian system of coordinates $\{x, y, z\}$ and rewrite these tensors in matrix form:

$$\widehat{\mathbf{G}}_E \left(\mathbf{r}' \mid \mathbf{r}'' \right) = \left[\mathbf{G}_{\alpha\beta}^E \left(\mathbf{r}' \mid \mathbf{r}'' \right) \right], \ \widehat{\mathbf{G}}_H \left(\mathbf{r}' \mid \mathbf{r}'' \right) = \left[\mathbf{G}_{\alpha\beta}^H \left(\mathbf{r}' \mid \mathbf{r}'' \right) \right], \ \alpha, \beta = x, y, z.$$

The tensor component $\mathbf{G}_{\alpha\beta}^E$ is essentially an α-directed electric field at the receiver point, $\mathbf{r}'$, due to a β-directed unit electric dipole source at the point $\mathbf{r}''$. The tensor component $\mathbf{G}_{\alpha\beta}^H$ is an α-directed magnetic field at the receiver point, $\mathbf{r}'$, due to a β-directed unit electric dipole source at the point $\mathbf{r}''$. According to the reciprocity principle, these tensors can be treated also as an electric field at $\mathbf{r}''$ due to electric or magnetic current dipole sources at $\mathbf{r}'$. To be more specific, the tensor component $\mathbf{G}_{\alpha\beta}^E$ can be treated as a β-directed electric field at the point $\mathbf{r}''$, due to an α-directed unit electric current dipole source at the receiver point, $\mathbf{r}'$. Correspondingly, the tensor component $\mathbf{G}_{\alpha\beta}^H$ is a β-directed electric field (with a negative sign according to formula (3.142)) at the point $\mathbf{r}''$, due to an α-directed unit magnetic current dipole source at the receiver point, $\mathbf{r}'$. We introduce the following notations:

$$\mathbf{G}_{\alpha\beta}^E \left(\mathbf{r}' \mid \mathbf{r}'' \right) = \mathbf{E}_\alpha^e \left(\mathbf{r}'' \right) \cdot \mathbf{d}_\beta, \ \mathbf{G}_{\alpha\beta}^H \left(\mathbf{r}' \mid \mathbf{r}'' \right) = -\mathbf{E}_\alpha^m \left(\mathbf{r}'' \right) \cdot \mathbf{d}_\beta, \tag{6.67}$$

where $\mathbf{E}_\alpha^e \left(\mathbf{r}'' \right)$ and $\mathbf{E}_\alpha^m \left(\mathbf{r}'' \right)$ are the respective electric fields due to the α-directed unit electric or magnetic current dipole sources at the receiver point, $\mathbf{r}'$; $\mathbf{d}_\beta, \ \beta = x, y, z$, are the orthonormal vectors of the Cartesian basis.

The expressions for α-directed components of the sensitivities (6.66) can be rewritten in the form

$$s_{E\alpha} \left(\mathbf{r}' \mid \mathbf{r}'' \right) = \frac{\delta E_\alpha \left(\mathbf{r}' \right)}{\delta \widetilde{\sigma}_v \left(\mathbf{r}'' \right)} = \sum_{\beta = x,y,z} \mathbf{G}_{\alpha\beta}^E \left(\mathbf{r}' \mid \mathbf{r}'' \right) E_\beta \left(\mathbf{r}'' \right) = \sum_{\beta = x,y,z} \left(\mathbf{E}_\alpha^e \left(\mathbf{r}'' \right) \cdot \mathbf{d}_\beta \right) E_\beta \left(\mathbf{r}'' \right)$$

$$= \mathbf{E}_\alpha^e \left(\mathbf{r}'' \right) \cdot \sum_{\beta = x,y,z} \left(\mathbf{d}_\beta E_\beta \left(\mathbf{r}'' \right) \right) = \mathbf{E}_\alpha^e \left(\mathbf{r}'' \right) \cdot \mathbf{E} \left(\mathbf{r}'' \right), \tag{6.68}$$

and, in a similar way,

$$s_{H\alpha} \left(\mathbf{r}' \mid \mathbf{r}'' \right) = \frac{\delta H_\alpha \left(\mathbf{r}' \right)}{\delta \widetilde{\sigma}_v \left(\mathbf{r}'' \right)} = -\mathbf{E}_\alpha^m \left(\mathbf{r}'' \right) \cdot \mathbf{E} \left(\mathbf{r}'' \right), \tag{6.69}$$

where $\alpha = x, y, z$.

The final result is that the sensitivities can be obtained from the scalar product of the original electric field and the auxiliary electric fields, generated by elementary electric or magnetic dipole current sources, located at the receiver position, $\mathbf{r}'$. This result was originally demonstrated by Pellerin et al. (1993), and then a derivation based on Lorentz lemma was given by McGillivray et al. (1994).

In accordance with definition given in Chapter 8, Eq. (8.16), the integrated sensitivity $S_E\left(\mathbf{r}''\right)$ of the data, collected over some surface Σ of observations over a frequency interval Ω, is equal to

$$S_E\left(\mathbf{r}''\right) = \frac{\|\delta\mathbf{E}\|_{\Omega,\Sigma}}{\delta\widetilde{\sigma}_v},$$

where the L_2 norm $\|...\|_{\Omega,\Sigma}$ is determined by the formula

$$\|\delta\mathbf{E}\|_{\Omega,b} = \sqrt{\int_{\Omega}\iint_{\Sigma}|\delta\mathbf{E}\left(\mathbf{r}',\omega\right)|^2\,ds'd\omega}.$$

Therefore, the integrated sensitivity of the electric field to the local perturbation of the conductivity at the point $\mathbf{r}''$ is

$$S_E\left(\mathbf{r}''\right) = \sqrt{\int_{\Omega}\iint_{\Sigma}\left|\widehat{\mathbf{G}}_E\left(\mathbf{r}'\mid\mathbf{r}''\right)\cdot\mathbf{E}\left(\mathbf{r}''\right)\right|^2\,ds'd\omega}. \tag{6.70}$$

In a similar way we can find the integrated sensitivities of the magnetic field:

$$S_H\left(\mathbf{r}''\right) = \sqrt{\int_{\Omega}\iint_{\Sigma}\left|\widehat{\mathbf{G}}_H\left(\mathbf{r}'\mid\mathbf{r}''\right)\cdot\mathbf{E}\left(\mathbf{r}''\right)\right|^2\,ds'd\omega}. \tag{6.71}$$

Formulae (6.70) and (6.71) play an important role in electromagnetic inversion.

6.1.8 INTEGRAL EQUATION METHOD IN ANISOTROPIC MEDIUM

In many practical situations one has to model the electromagnetic field in anisotropic medium. Consider a 3D geoelectrical anisotropic model with the background conductivity tensor $\widehat{\sigma}_b$ and local inhomogeneity D with an arbitrarily varying anisotropic conductivity $\widehat{\sigma} = \widehat{\sigma}_b + \Delta\widehat{\sigma}$. The inhomogeneity is considered to be local, so there exists some radius R_0 such that for $\sqrt{x^2 + y^2 + z^2} > R_0$ the medium has the background conductivity $\widehat{\sigma}_b$. We assume that $\mu = \mu_0 = 4\pi \times 10^{-7} H/m$, where μ_0 is the free-space magnetic permeability. The model is excited by a known background electromagnetic field, $\mathbf{E}^b$, $\mathbf{H}^b$, generated by an arbitrary electric current distribution $\mathbf{j}\left(\mathbf{r}\right)$ within a medium with background conductivity $\widehat{\sigma}_b$. This field is time harmonic as $e^{-i\omega t}$.

The electromagnetic field in the model described above can be presented as a sum of the background and anomalous fields:

$$\mathbf{E} = \mathbf{E}^b + \mathbf{E}^a, \ \mathbf{H} = \mathbf{H}^b + \mathbf{H}^a, \tag{6.72}$$

where the background field is a field generated by the given sources in the model with the background distribution of conductivity $\widehat{\sigma}_b$, and the anomalous field is produced by the anomalous conductivity distribution $\Delta\widehat{\sigma}$.

The anomalous electric field is related to the electric current induced in the inhomogeneity,

$$\mathbf{j^a} = \Delta\widehat{\sigma}\cdot\mathbf{E}, \tag{6.73}$$

according to the following integral formulas:

$$\mathbf{E}^a\left(\mathbf{r}_j\right) = \mathbf{G}_E\left(\Delta\widehat{\boldsymbol{\sigma}}\cdot\mathbf{E}\right) = \iiint_D \widehat{\mathbf{G}}_E\left(\mathbf{r}_j\mid\mathbf{r}\right)\cdot\mathbf{j}^{\mathbf{a}}\left(\mathbf{r}\right)dv, \tag{6.74}$$

$$\mathbf{H}^a\left(\mathbf{r}_j\right) = \mathbf{G}_H\left(\Delta\widehat{\boldsymbol{\sigma}}\cdot\mathbf{E}\right) = \iiint_D \widehat{\mathbf{G}}_H\left(\mathbf{r}_j\mid\mathbf{r}\right)\cdot\mathbf{j}^{a}\left(\mathbf{r}\right)dv, \tag{6.75}$$

where $\mathbf{r}_j$ is an observation point; $\widehat{\mathbf{G}}_E$ and $\widehat{\mathbf{G}}_H$ are electromagnetic Green's tensors defined for an unbounded conductive medium with the background conductivity $\widehat{\boldsymbol{\sigma}}_b$; and $\mathbf{G}_E$ and $\mathbf{G}_H$ are the electric and magnetic Green's operators, defined above.

Substituting the expressions for anomalous electric field, (6.74), and for the excess current (6.73) into (6.72), we finally obtain a representation for electromagnetic field as an integral over the excess currents in the anisotropic inhomogeneous domain D:

$$\mathbf{E}\left(\mathbf{r}_j\right) = \mathbf{G}_E\left(\Delta\widehat{\boldsymbol{\sigma}}\cdot\mathbf{E}\right) + \mathbf{E}^b\left(\mathbf{r}_j\right), \tag{6.76}$$

$$\mathbf{H}\left(\mathbf{r}_j\right) = \mathbf{G}_H\left(\Delta\widehat{\boldsymbol{\sigma}}\cdot\mathbf{E}\right) + \mathbf{H}^b\left(\mathbf{r}_j\right). \tag{6.77}$$

Using integral formulas (6.76) and (6.77) (the field equations), one can calculate the electromagnetic field in any point $\mathbf{r}_j$, if the electric field is known within the inhomogeneity. Expression (6.76) becomes the domain integral equation for the electric field $\mathbf{E}\left(\mathbf{r}\right)$, if $\mathbf{r}_j \in D$. Eqs. (6.76) and (6.77) form the basis for EM forward modeling in anisotropic medium.

Note that, in a general case, conductivity tensors, $\widehat{\boldsymbol{\sigma}}$, may have arbitrary structure. We assume for simplicity that the axis of the Cartesian coordinate system coincide with the principle axis of the anomalous conductivity tensor. In this case, the matrix of the conductivity tensor becomes diagonal with the conductivities in the directions x, y, and z located along the main diagonal:

$$\Delta\widehat{\boldsymbol{\sigma}}\left(\mathbf{r}\right) = \begin{bmatrix} \sigma_x\left(\mathbf{r}\right) & 0 & 0 \\ 0 & \sigma_y\left(\mathbf{r}\right) & 0 \\ 0 & 0 & \sigma_z\left(\mathbf{r}\right) \end{bmatrix}.$$

The most common situation for geophysical applications, however, is the case of transverse isotropic conductivity. In this case, the matrix of the conductivity tensor becomes diagonal with the equal horizontal conductivities, $\sigma_h\left(\mathbf{r}\right) = \sigma_x\left(\mathbf{r}\right) = \sigma_y\left(\mathbf{r}\right)$, in the horizontal directions x, y, and the vertical conductivity $\sigma_v\left(\mathbf{r}\right) = \sigma_z\left(\mathbf{r}\right)$, located along the main diagonal:

$$\widehat{\boldsymbol{\sigma}}\left(\mathbf{r}\right) = \begin{bmatrix} \sigma_h\left(\mathbf{r}\right) & 0 & 0 \\ 0 & \sigma_h\left(\mathbf{r}\right) & 0 \\ 0 & 0 & \sigma_v\left(\mathbf{r}\right) \end{bmatrix}. \tag{6.78}$$

A coordinate system with axes parallel to the principal axes of the conductivity tensor is convenient, because in transversely isotropic media the conductivity tensor has two equal "horizontal" components, and one vertical component. However, in practice, the orientation of the axes of the anisotropy of the medium can be "tilted" with respect to a selected Cartesian coordinate system. In this case, the components of the conductivity tensor in the Cartesian coordinates can be obtained from the components,

given in the principal axes, by applying the appropriated rotation transformation, using the rotation matrix (Moran and Gianzero, 1979; Zhdanov et al., 2001).

The anisotropy coefficient λ is defined according to the following formula:

$$\lambda = \sqrt{\sigma_h/\sigma_v}. \tag{6.79}$$

6.1.9 DISCRETE FORM OF THE ANISOTROPIC IE FORWARD MODELING METHOD

In order to present the anisotropic IE method in numerical form, we divide the domain D with anomalous conductivity into elementary cells, D_n, formed by some rectangular grid: $D = \overset{N}{\underset{n=1}{\cup}} D_n$. We assume that $\Delta\widehat{\sigma}(\mathbf{r})$ has the constant values within each cell. Therefore, a discrete form of the domain integral equation for the electric field, (6.76), can be described by the following matrix equation (Zhdanov, 2002, 2015):

$$\widehat{\mathbf{A}}\mathbf{e}_D = \mathbf{e}_D^b, \tag{6.80}$$

where

$$\widehat{\mathbf{A}} = \widehat{\mathbf{I}} - \widehat{\mathbf{G}}_D\widehat{\sigma}, \tag{6.81}$$

and $\widehat{\sigma}$ is a $(3N \times 3N)$ diagonal matrix of anomalous conductivities:

$$\widehat{\sigma} = \begin{bmatrix} \Delta\widetilde{\sigma}_{x1} & \cdots & 0 & 0 & \cdots & 0 & 0 & \cdots & 0 \\ & & & \vdots & & & & & \\ 0 & \cdots & \Delta\widetilde{\sigma}_{xN} & 0 & \cdots & 0 & 0 & \cdots & 0 \\ 0 & \cdots & 0 & \Delta\widetilde{\sigma}_{y1} & \cdots & 0 & 0 & \cdots & 0 \\ & & & \vdots & & & & & \\ 0 & \cdots & 0 & 0 & \cdots & \Delta\widetilde{\sigma}_{yN} & 0 & \cdots & 0 \\ 0 & \cdots & 0 & 0 & \cdots & 0 & \Delta\widetilde{\sigma}_{z1} & \cdots & 0 \\ & & & \vdots & & & & & \\ 0 & \cdots & 0 & 0 & \cdots & 0 & 0 & \cdots & \Delta\widetilde{\sigma}_{zN} \end{bmatrix}. \tag{6.82}$$

Vectors-rows, $\mathbf{e}_D$ and $\mathbf{e}_D^b$, are the vectors of the total and background electric fields formed by the x, y and z components of these fields at the centers of the cells D_n of the anomalous domain D:

$$\mathbf{e}_D = [E_x^1, E_x^2, ...E_x^N, E_y^1, E_y^2, ...E_y^N, E_z^1, E_z^2, ...E_z^N]^T,$$

$$\mathbf{e}_D^b = [E_x^{b,1}, E_x^{b,2}, ...E_x^{b,N}, E_y^{b,1}, E_y^{b,2}, ...E_y^{b,N}, E_z^{b,1}, E_z^{b,2}, ...E_z^{b,N}]^T.$$

These vectors have order $3N$. The $3N \times 3N$ matrix $\widehat{\mathbf{G}}_D$ is formed by the volume integrals over the elementary cells D_n of the components of the corresponding electric Green's tensor $\widehat{\mathbf{G}}_E$, acting inside the domain D.

We introduce also the vectors, $\mathbf{e}$, $\mathbf{h}$, and $\mathbf{e}^b$, $\mathbf{h}^b$, representing the discrete total and background electric and magnetic fields at the observation points. Then integral formulae (6.76) and (6.77) can be

cast in the following discrete forms:

$$\mathbf{e} = \widehat{\mathbf{G}}_E \widehat{\boldsymbol{\sigma}} \mathbf{e}_D + \mathbf{e}^b, \tag{6.83}$$

$$\mathbf{h} = \widehat{\mathbf{G}}_H \widehat{\boldsymbol{\sigma}} \mathbf{e}_D + \mathbf{h}^b, \tag{6.84}$$

where matrices $\widehat{\mathbf{G}}_E$ and $\widehat{\mathbf{G}}_H$ are discrete analogs of the corresponding Green's tensors (Zhdanov, 2002, 2015). These matrices consist of the volume integrals over elementary cell D_n of the components of the corresponding electric or magnetic Green's tensor acting from the anomalous domain to the receivers. After finding $\mathbf{e}_D$ from Eq. (6.81), we can substitute it in Eqs. (6.83) and (6.84) to calculate the electromagnetic field in the receiver positions.

Thus, forward electromagnetic modeling based on the IE method is reduced to the solution of the matrix equation (6.83) in the unknown vector $\mathbf{e}_D$ of electric field components inside domain D. The equation is a $3N \times 3N$ linear system,

$$\widehat{\mathbf{A}} \mathbf{e}_D = \mathbf{e}_D^b, \tag{6.85}$$

where

$$\widehat{\mathbf{A}} = \widehat{\mathbf{I}} - \widehat{\mathbf{G}}_D \widehat{\boldsymbol{\sigma}}. \tag{6.86}$$

Matrix $\widehat{\mathbf{A}}$ is a $3N \times 3N$ dense matrix. For a small number of unknowns, direct solvers are practical, especially in the case of multiple sources. For a large-scale problem, one can use different types of iterative methods, for example, the Complex Generalized Minimal Residual (CGMRM) method, as a solver of the system of linear equations arising in the IE method (Zhdanov, 2002, 2015).

The computed electric and magnetic fields are then used in Eqs. (6.83) and (6.84) to determine the EM field in the receivers.

6.1.10 CONTRACTION INTEGRAL EQUATION AS THE PRECONDITIONED CONVENTIONAL INTEGRAL EQUATION

Following Hursán and Zhdanov (2002) and Zhdanov (2002, 2015), one can use the contraction integral equation (CIE) method, which is based on preconditioning Eq. (6.86) with contraction operators to improve the conditioning of the matrix system. The contraction integral equation (6.56) can be treated as the preconditioned conventional integral equation (6.44). This fact becomes especially important in numerical implementation of the CIE method.

In discrete form, Eq. (6.56) can be written as

$$\widehat{\mathbf{M}}_1 \left(\widehat{\mathbf{I}} - \widehat{\mathbf{G}}_D \widehat{\boldsymbol{\sigma}} \right) \widehat{\mathbf{M}}_2 \widetilde{\mathbf{e}}_D = \widehat{\mathbf{M}}_1 \mathbf{e}_D^b, \tag{6.87}$$

where, as above, $3N \times 3N$ matrix $\widehat{\mathbf{G}}_D$ is formed by the volume integrals over the elementary cells D_n of the components of the corresponding electric Green's tensor $\widehat{\mathbf{G}}_E$, acting inside the domain D; $\widehat{\boldsymbol{\sigma}}$ and $\widehat{\mathbf{M}}_1$ are the $3N \times 3N$ diagonal matrices of the anomalous conductivities and the square root of the background conductivities respectively, similar to matrix (6.82):

$$\widehat{\boldsymbol{\sigma}} = \mathbf{diag} \left(\Delta \widetilde{\sigma}_1, \Delta \widetilde{\sigma}_2, ..., \Delta \widetilde{\sigma}_N, \Delta \widetilde{\sigma}_1, \Delta \widetilde{\sigma}_2, ..., \Delta \widetilde{\sigma}_N, \Delta \widetilde{\sigma}_1, \Delta \widetilde{\sigma}_2, ..., \Delta \widetilde{\sigma}_N \right),$$

$$\widehat{\mathbf{M}}_1 = \mathbf{diag}\left(\sqrt{\sigma_1^b}, \sqrt{\sigma_2^b}, ..., \sqrt{\sigma_N^b}, \sqrt{\sigma_1^b}, \sqrt{\sigma_2^b}..., \sqrt{\sigma_N^b}, \sqrt{\sigma_1^b}, \sqrt{\sigma_2^b}..., \sqrt{\sigma_N^b}\right),$$

and where

$$\widetilde{\mathbf{e}}_D = \widehat{\mathbf{M}}_2^{-1}\mathbf{e}_D, \tag{6.88}$$

with $\widehat{\mathbf{M}}_2$ defined as the diagonal matrix

$$\widehat{\mathbf{M}}_2 = \mathbf{diag}\left(a_1^{-1}, a_2^{-1}, ..., a_N^{-1}, a_1^{-1}, a_2^{-1}, ..., a_N^{-1}, a_1^{-1}, a_2^{-1}, ..., a_N^{-1}\right), \tag{6.89}$$

where, according to (6.50),

$$a_i = \frac{2\sigma_{bi} + \Delta\widetilde{\sigma}_i}{2\sqrt{\sigma_{bi}}}, \ i = 1, 2, ..., N.$$

Considering (6.85) and (6.86), we can easily see that Eq. (6.87) is just the preconditioned variant of (6.85),

$$\widetilde{\mathbf{A}}\widetilde{\mathbf{e}}_D = \widetilde{\mathbf{e}}_D^b, \tag{6.90}$$

where

$$\widetilde{\mathbf{A}} = \widehat{\mathbf{M}}_1\widehat{\mathbf{A}}\widehat{\mathbf{M}}_2, \ \widetilde{\mathbf{e}}_D^b = \widehat{\mathbf{M}}_1\mathbf{e}_D^b, \tag{6.91}$$

and

$$\mathbf{e}_D = \widehat{\mathbf{M}}_2\widetilde{\mathbf{e}}_D. \tag{6.92}$$

Thus, we have transformed the original matrix equation (6.85) into the preconditioned equation

$$\widehat{\mathbf{M}}_1\widehat{\mathbf{A}}\widehat{\mathbf{M}}_2\left(\widehat{\mathbf{M}}_2^{-1}\mathbf{e}_D\right) = \widehat{\mathbf{M}}_1\mathbf{e}^b, \tag{6.93}$$

where $\widehat{\mathbf{M}}_1$ is the left preconditioner, and $\widehat{\mathbf{M}}_2$ is the right preconditioner.

Note that there are different mathematical methods for introducing preconditioners for a general matrix equation (Golub and Van Loan, 1996). The main goal is to construct a matrix $\widehat{\mathbf{M}}_1\widehat{\mathbf{A}}\widehat{\mathbf{M}}_2$, which produces a significantly higher convergence rate of iteration than the original matrix $\widehat{\mathbf{A}}$. Note that the act of finding a good preconditioner is that of making $\widetilde{\mathbf{A}} = \widehat{\mathbf{M}}_1\widehat{\mathbf{A}}\widehat{\mathbf{M}}_2$ as close as possible to the identity matrix. In the case of the CIE method we reach this goal by using the contraction Green's operator with the norm always less than or equal to one. In other words, we take into account the physical nature of our system of equations and find the preconditioners based on the fundamental physical law that the energy flow of the anomalous electromagnetic field outside the domain containing the conductivity inhomogeneity is always positive.

6.2 INTEGRAL EQUATION METHOD IN MODELS WITH INHOMOGENEOUS BACKGROUND CONDUCTIVITY

In the framework of the IE method, the conductivity distribution is divided into two parts: 1) the background conductivity, σ_b, which is used for Green's functions calculation, and 2) the anomalous conductivity, $\Delta\sigma_a$, within the domain of integration, D. It was emphasized in the original paper by Dmitriev (1969) that the main limitation of the IE method is that the background conductivity model must have a simple structure to allow for an efficient Green's function calculation. The most widely used background models in EM exploration are those formed by horizontally homogeneous layers. The theory of Green's functions for layered one-dimensional (1-D) models is very well developed and lays the foundation for efficient numerical algorithms. Any deviation from this 1-D background model must be treated as an anomalous conductivity.

In some practical applications, however, it is difficult to describe a model using horizontally layered background conductivity. As a result, the domain of integration may become too large, which increases significantly the size of the modeling domain and of the required computer memory and computational time for IE modeling. We could overcome these computational difficulties if the IE method would allow us to use variable 3-D background conductivity. This would also be helpful in modeling EM data for multiple geological models with some common geoelectrical features, like a known topographic or bathymetric inhomogeneities (in the case of marine EM), or salt-dome structures. The conventional approach would require running the full 3-D IE method for all domains with anomalous conductivity every time we change the parameters within one domain only. This situation occurs, for example, when we have known information about the existence of specific geological structures which should be considered in modeling and/or inversion.

In the present section of the book, following the paper by Zhdanov et al. (2006a), we extend the formulation of the IE method to a more general case of models with an inhomogeneous background conductivity (IBC). Our method is based on the separation of the effects due to excess electric current, $\mathbf{j}^{\Delta\sigma_b}$, induced in the inhomogeneous background domain from those due to the anomalous electric current, $\mathbf{j}^{\Delta\sigma_a}$, in the location of the anomalous conductivity, respectively. As a result, we arrive at a system of integral equations which uses the same simple Green's functions for the layered model as in the original IE formulation. However, the new equations take into account the effect of the variable background conductivity distribution. We also consider an approach to the accuracy control of the IBC IE method. This approach provides us with the ability to improve the accuracy of computations by applying the IBC technique iteratively.

6.2.1 MODEL WITH INHOMOGENEOUS BACKGROUND CONDUCTIVITY

We consider a 3-D geoelectrical model with horizontally layered (normal) conductivity, σ_n, inhomogeneous background conductivity, $\sigma_b = \sigma_n + \Delta\sigma_b$, within a domain D_b, and anomalous conductivity, $\Delta\sigma_a$, within a domain D_a (Fig. 6.3). The model is excited by an EM field generated from an arbitrary source which is time harmonic as $e^{-i\omega t}$. The EM field in this model satisfies the Maxwell's equations:

$$\nabla \times \mathbf{H} = \sigma_n \mathbf{E} + \mathbf{j} = \sigma_n \mathbf{E} + \mathbf{j}^{\Delta\sigma_b} + \mathbf{j}^{\Delta\sigma_a} + \mathbf{j}^e,$$
$$\nabla \times \mathbf{E} = i\omega\mu_0 \mathbf{H},$$

(6.94)
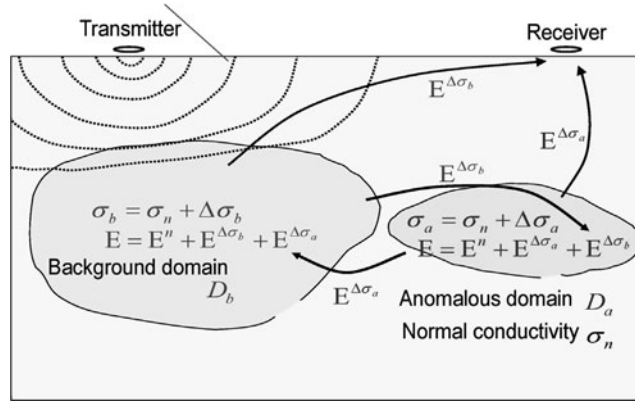
FIGURE 6.3

A sketch of 3D geoelectrical model with horizontally layered (normal) conductivity, σ_n, inhomogeneous background conductivity, $\sigma_b = \sigma_n + \Delta\sigma_b$, within a domain D_b, and anomalous conductivity, $\Delta\sigma_a$, within a domain D_a. The EM field in this model is a sum of the normal fields, $\mathbf{E}^n$, $\mathbf{H}^n$, generated by the given source(s) in the model with normal distribution of conductivity, σ_n, a variable background effect, $\mathbf{E}^{\Delta\sigma_b}$, $\mathbf{H}^{\Delta\sigma_b}$, produced by the inhomogeneous background conductivity, $\Delta\sigma_b$, and the anomalous fields, $\mathbf{E}^{\Delta\sigma_a}$, $\mathbf{H}^{\Delta\sigma_a}$, due to the anomalous conductivity distribution, $\Delta\sigma_a$.

where:

$$\mathbf{j}^{\Delta\sigma_a} = \begin{cases} \Delta\sigma_a\mathbf{E}, & \mathbf{r} \in D_a, \\ 0, & \mathbf{r} \notin D_a \end{cases} \tag{6.95}$$

is the anomalous current within the local inhomogeneity, D_a, and:

$$\mathbf{j}^{\Delta\sigma_b} = \begin{cases} \Delta\sigma_b\mathbf{E}, & \mathbf{r} \in D_b, \\ 0, & \mathbf{r} \notin D_b \end{cases} \tag{6.96}$$

is the excess current within the inhomogeneous background domain, D_b.

Eqs. (6.94)–(6.96) show that one can represent the EM field in this model as a sum of the normal fields, $\mathbf{E}^n$, $\mathbf{H}^n$, generated by the given source(s) in the model with normal distribution of conductivity, σ_n, a variable background effect, $\mathbf{E}^{\Delta\sigma_b}$, $\mathbf{H}^{\Delta\sigma_b}$, produced by the inhomogeneous background conductivity, $\Delta\sigma_b$, and the anomalous fields, $\mathbf{E}^{\Delta\sigma_a}$, $\mathbf{H}^{\Delta\sigma_a}$, due to the anomalous conductivity distribution, $\Delta\sigma_a$, as

$$\mathbf{E} = \mathbf{E}^n + \mathbf{E}^{\Delta\sigma_b} + \mathbf{E}^{\Delta\sigma_a}, \; \mathbf{H} = \mathbf{H}^n + \mathbf{H}^{\Delta\sigma_b} + \mathbf{H}^{\Delta\sigma_a}. \tag{6.97}$$

The total EM field in this model can be written as:

$$\mathbf{E} = \mathbf{E}^b + \mathbf{E}^{\Delta\sigma_a}, \; \mathbf{H} = \mathbf{H}^b + \mathbf{H}^{\Delta\sigma_a}, \tag{6.98}$$

where the background EM field, $\mathbf{E}^b$, $\mathbf{H}^b$, is a sum of the normal fields and those caused by the inhomogeneous background conductivity:

$$\mathbf{E}^b = \mathbf{E}^n + \mathbf{E}^{\Delta\sigma_b}, \; \mathbf{H}^b = \mathbf{H}^n + \mathbf{H}^{\Delta\sigma_b}. \tag{6.99}$$

Following the standard logic of the IE method (Zhdanov, 2002), we write the integral representations for the EM fields of the given current distribution,

$$\mathbf{j}^{\Delta\sigma}(\mathbf{r}) = \mathbf{j}^{\Delta\sigma_b}(\mathbf{r}) + \mathbf{j}^{\Delta\sigma_a}(\mathbf{r}) = \Delta\sigma_b \mathbf{E}(\mathbf{r}) + \Delta\sigma_a \mathbf{E}(\mathbf{r}),$$

within a medium of normal conductivity, σ_n:

$$\begin{aligned} \mathbf{E}(\mathbf{r}_j) &= \mathbf{E}^n + \iiint_{D_b} \widehat{\mathbf{G}}_E(\mathbf{r}_j \mid \mathbf{r}) \cdot \Delta\sigma_b \mathbf{E}(\mathbf{r}) \, dv + \iiint_{D_a} \widehat{\mathbf{G}}_E(\mathbf{r}_j \mid \mathbf{r}) \cdot \Delta\sigma_a \mathbf{E}(\mathbf{r}) \, dv, \\ \mathbf{H}(\mathbf{r}_j) &= \mathbf{H}^n + \iiint_{D_b} \widehat{\mathbf{G}}_H(\mathbf{r}_j \mid \mathbf{r}) \cdot \Delta\sigma_b \mathbf{E}(\mathbf{r}) \, dv + \iiint_{D_a} \widehat{\mathbf{G}}_H(\mathbf{r}_j \mid \mathbf{r}) \cdot \Delta\sigma_a \mathbf{E}(\mathbf{r}) \, dv, \end{aligned} \tag{6.100}$$

where the first integral terms describe the excess part of the background fields generated by the excess currents in the inhomogeneous background domain, D_b:

$$\mathbf{E}^{\Delta\sigma_b}(\mathbf{r}_j) = \iiint_{D_b} \widehat{\mathbf{G}}_E(\mathbf{r}_j \mid \mathbf{r}) \cdot \Delta\sigma_b \mathbf{E}(\mathbf{r}) \, dv = \mathbf{G}_E^{D_b}(\Delta\sigma_b \mathbf{E}), \tag{6.101}$$

$$\mathbf{H}^{\Delta\sigma_b}(\mathbf{r}_j) = \iiint_{D_b} \widehat{\mathbf{G}}_H(\mathbf{r}_j \mid \mathbf{r}) \cdot \Delta\sigma_b \mathbf{E}(\mathbf{r}) \, dv = \mathbf{G}_H^{D_b}(\Delta\sigma_b \mathbf{E}), \tag{6.102}$$

and the second terms describe the anomalous fields generated by the anomalous domain, D_a:

$$\begin{aligned} \mathbf{E}^{\Delta\sigma_a}(\mathbf{r}_j) &= \mathbf{E}(\mathbf{r}_j) - \mathbf{E}^n(\mathbf{r}_j) - \mathbf{E}^{\Delta\sigma_b}(\mathbf{r}_j) \\ &= \iiint_{D_a} \widehat{\mathbf{G}}_E(\mathbf{r}_j \mid \mathbf{r}) \cdot \Delta\sigma_a \mathbf{E}(\mathbf{r}) \, dv = \mathbf{G}_E^{D_a}(\Delta\sigma_a \mathbf{E}), \end{aligned} \tag{6.103}$$

$$\begin{aligned} \mathbf{H}^{\Delta\sigma_a}(\mathbf{r}_j) &= \mathbf{H}(\mathbf{r}_j) - \mathbf{H}^n(\mathbf{r}_j) - \mathbf{H}^{\Delta\sigma_b}(\mathbf{r}_j) = \\ &= \iiint_{D_a} \widehat{\mathbf{G}}_H(\mathbf{r}_j \mid \mathbf{r}) \cdot \Delta\sigma_a \mathbf{E}(\mathbf{r}) \, dv = \mathbf{G}_H^{D_a}(\Delta\sigma_a \mathbf{E}). \end{aligned} \tag{6.104}$$

In these last equations, the symbols $\mathbf{G}_E^{D_a, D_b}$ and $\mathbf{G}_H^{D_a, D_b}$ denote the electric and magnetic Green's operators with a volume integration of D_a or D_b, respectively. Note that according to notation (6.99), Eqs. (6.103) and (6.104) can be rewritten in the form:

$$\mathbf{E}^{\Delta\sigma_a}(\mathbf{r}_j) = \mathbf{E}(\mathbf{r}_j) - \mathbf{E}^n(\mathbf{r}_j) - \mathbf{E}^{\Delta\sigma_b}(\mathbf{r}_j) = \mathbf{G}_E^{D_a}\left(\Delta\sigma_a\left(\mathbf{E}^b + \mathbf{E}^{\Delta\sigma_a}\right)\right), \tag{6.105}$$

$$\mathbf{H}^{\Delta\sigma_a}(\mathbf{r}_j) = \mathbf{H}(\mathbf{r}_j) - \mathbf{H}^n(\mathbf{r}_j) - \mathbf{H}^{\Delta\sigma_b}(\mathbf{r}_j) = \mathbf{G}_H^{D_a}\left(\Delta\sigma_a\left(\mathbf{E}^b + \mathbf{E}^{\Delta\sigma_a}\right)\right). \tag{6.106}$$

Using integral equations (6.105)–(6.106), one can calculate the EM field at any point $\mathbf{r}_j$ if the electric field is known within the inhomogeneity. Eq. (6.105) becomes the integral equation for the electric field $\mathbf{E}(\mathbf{r})$ if $\mathbf{r}_j \in D_a$.

The basic idea of a new IE formulation is that we can take into account the EM field induced in the anomalous domain by the excess currents in the background inhomogeneity, $\mathbf{j}^{\Delta\sigma_b}$, but would ignore the return induction effects by the anomalous currents $\mathbf{j}^{\Delta\sigma_a}$. In other words, we assume that the anomalous electric fields, $\mathbf{E}^{\Delta\sigma_a}$, are much smaller than the background fields, $\mathbf{E}^b$, inside the domain of integration, D_b, in Eqs. (6.101) and (6.102):

$$\mathbf{E}^{\Delta\sigma_b}(\mathbf{r}_j) \approx \mathbf{G}_E^{D_b}\left(\Delta\sigma_b\mathbf{E}^b\right) = \mathbf{G}_E^{D_b}\left(\Delta\sigma_b\left(\mathbf{E}^n + \mathbf{E}^{\Delta\sigma_b}\right)\right),\tag{6.107}$$

$$\mathbf{H}^{\Delta\sigma_b}(\mathbf{r}_j) \approx \mathbf{G}_H^{D_b}\left(\Delta\sigma_b\mathbf{E}^b\right) = \mathbf{G}_H^{D_b}\left(\Delta\sigma_b\left(\mathbf{E}^n + \mathbf{E}^{\Delta\sigma_b}\right)\right).\tag{6.108}$$

Eqs. (6.107) and (6.108) show that finding the excess part of the background fields requires a solution of the conventional IE for the electric fields in media with inhomogeneous background conductivity distribution (without the anomalous domain D_a). Therefore, we can calculate the background fields using Eqs. (6.99) and substitute them into Eqs. (6.105)–(6.106). The last system of equations can be solved using the standard IE approach as well.

We should note that the technique outlined above is very different from the conventional Born approximation (see the next section), because we solve the corresponding integral equations (6.107) and (6.108) with respect to the anomalous field. With the Born approximation, one does not solve any integral equation. Instead, the background field is just integrated over the domain with anomalous conductivity (anomalous domain D_a in our case). In our approach, we ignore the secondary field in the inhomogeneous background domain, D_b, due to the return induction effects of the anomalous currents $\mathbf{j}^{\Delta\sigma_a}$ induced in the anomalous domain D_a only, when we solve the first integral equation for the background field. The effect of this secondary field is assumed to be very small compared with the normal field and the secondary field induced in the inhomogeneous background itself. We will discuss in the next section a technique for the accuracy control of this condition.

Another important question is how the inhomogeneous background conductivity (IBC) should be selected. We recommend that the regional geoelectrical structures should be included in the inhomogeneous background, while the local geological target (e.g., a petroleum reservoir or a mining target) should be associated with the domain with the anomalous conductivity. At the same time, it is reasonable to include in the IBC model some known geological structures, like known topographic or bathymetric inhomogeneities (in the case of marine EM), or salt dome, in order to reduce the modeling domain to the area of investigation only.

6.2.2 ACCURACY CONTROL OF THE IBC IE METHOD

We have demonstrated above that the IBC IE method is based on an idea that we can ignore a secondary field induced by the currents in the anomalous domain D_a when we solve the integral equation (6.107) for the background field $\mathbf{E}^b$ in the domain D_b. The assumption is that this returned induction field is very small compared with the normal field and an anomalous part of the background field induced in the background conductivity. The obvious condition where this approximation can be employed is that the effect of the induced field $\mathbf{G}_E^{D_b}\left(\Delta\sigma_b\left(\mathbf{E}^{\Delta\sigma_a}\right)\right)$ in an inhomogeneous background from the

anomalous body is much smaller than the effect of the background field itself inside the domain of integration, D_b:

$$\left\| \mathbf{E}^b - \mathbf{G}_E^{D_b} \left(\Delta\sigma_b \left(\mathbf{E}^b + \mathbf{E}^{\Delta\sigma_a} \right) \right) - \mathbf{E}^n \right\|_{D_b} / \left\| \mathbf{E}^b \right\|_{D_b} = \varepsilon_1^b \ll 1, \tag{6.109}$$

where $\|...\|_{D_b}$ denotes the L_2 norm calculated over domain D_b:

$$\left\| \mathbf{E}^b \right\|_{D_b}^2 = \iiint_{D_b} \left| \mathbf{E}^b (\mathbf{r}) \right|^2 dv.$$

We can also evaluate the possible errors of ignoring the return response of the currents induced in the inhomogeneous background on the field in the anomalous domain D_a:

$$\left\| \mathbf{E}^a - \mathbf{G}_E^{D_a} \left(\Delta\sigma_a \left(\mathbf{E}^a + \mathbf{E}^{\Delta\sigma_b(1)} \right) \right) - \mathbf{E}^n \right\|_{D_a} / \left\| \mathbf{E}^a \right\|_{D_a} = \varepsilon_1^a, \tag{6.110}$$

where:

$$\mathbf{E}^{\Delta\sigma_b(1)} \left(\mathbf{r}_j \right) = \mathbf{G}_E^{D_b} \left(\Delta\sigma_b \left(\mathbf{E}^b + \mathbf{E}^{\Delta\sigma_a} \right) \right), \quad \mathbf{r}_j \in D_a,$$

and:

$$\mathbf{E}^a = \mathbf{E}^n + \mathbf{E}^{\Delta\sigma_a}.$$

A simple observation based on formulas (6.109) and (6.110) is that, the accuracy of the IBC IE method should depend on the electrical distance between a domain with inhomogeneous background conductivity and an anomalous domain: $r_\lambda = r/\lambda$, where r is a geometric distance, and λ is a corresponding wave length in the layered background. The larger this distance, the smaller the return effect of the currents induced in the anomalous domain on the IBC domain, and vice versa. However, even in the case of the anomalous domain attached to the IBC domain, we still have a reasonable accuracy of the IBC IE method. In addition, we should note that the accuracy of the IBC IE method should also depend on the shape and relative aspect of the domains D_a and D_b.

Condition (6.109) makes it possible to evaluate the accuracy of the IBC IE method in a general case in comparison with the conventional IE method. Indeed, one can apply the IE method for the computations of the background field $\mathbf{E}^b$ and the anomalous field $\mathbf{E}^{\Delta\sigma_a}$ using two separate integral equations, (6.105) and (6.107). After that we can evaluate the possible error in the background field computations, ε_1^b, and in the anomalous field calculations, ε_1^a, using the proposed technique.

The remarkable fact is that the above condition not only provides us with the ability to control the accuracy of our computations, but it also shows how to improve the accuracy by applying the IBC technique iteratively. Indeed, if we find the error ε_1^b is too large, we can solve the rigorous integral equation (6.101) for the background electric field, taking into account the anomalous field $\mathbf{E}^{\Delta\sigma_a}$ computed in the previous step:

$$\mathbf{E}^b \left(\mathbf{r}_j \right) = \mathbf{G}_E^{D_b} \left(\Delta\sigma_b \left(\mathbf{E}^b + \mathbf{E}^{\Delta\sigma_a} \right) \right) + \mathbf{E}^n \left(\mathbf{r}_j \right), \quad \mathbf{r}_j \in D_b. \tag{6.111}$$

We denote by $\mathbf{E}^{b(2)}$ a solution of Eq. (6.111). Now we can use this updated background field $\mathbf{E}^{b(2)}$ in integral equation (6.105) for the anomalous field:

$$\mathbf{E}^{\Delta\sigma_a}\left(\mathbf{r}_j\right) = \mathbf{G}_E^{D_a}\left(\Delta\sigma_a\left(\mathbf{E}^{b(2)} + \mathbf{E}^{\Delta\sigma_a}\right)\right),\ \mathbf{r}_j \in D_a. \tag{6.112}$$

A solution of the last equation gives us a second iteration of the anomalous electric field, $\mathbf{E}^{\Delta\sigma_a(2)}$.

We can check the accuracy of the second round of the IBC IE method for domains D_a and D_b using the following estimates, respectively:

$$\left\|\mathbf{E}^{a(2)} - \mathbf{G}_E^{D_a}\left(\Delta\sigma_a\left(\mathbf{E}^{a(2)} + \mathbf{E}^{\Delta\sigma_b(2)}\right) - \mathbf{E}^n\right)\right\|_{D_a} / \left\|\mathbf{E}^{a(2)}\right\|_{D_a} = \varepsilon_2^a,$$

$$\left\|\mathbf{E}^{b(2)} - \mathbf{G}_E^{D_b}\left(\Delta\sigma_b\left(\mathbf{E}^{b(2)} + \mathbf{E}^{\Delta\sigma_a(2)}\right) - \mathbf{E}^n\right)\right\|_{D_b} / \left\|\mathbf{E}^{b(2)}\right\|_{D_b} = \varepsilon_2^b, \tag{6.113}$$

where

$$\mathbf{E}^{a(2)} = \mathbf{E}^n + \mathbf{E}^{\Delta\sigma_a(2)},\ \text{and}$$

$$\mathbf{E}^{\Delta\sigma_b(2)}\left(\mathbf{r}_j\right) = \mathbf{G}_E^{D_b}\left(\Delta\sigma_b\left(\mathbf{E}^{b(2)} + \mathbf{E}^{\Delta\sigma_a(2)}\right)\right),\ \mathbf{r}_j \in D_a.$$

The iterative process described above is continued until we reach the required accuracy of the background field calculations in both domains, D_a and D_b. We should note in conclusion that this iterative process always converges if we use the contraction integral equation (CIE) method (Hursán and Zhdanov, 2002) as a main algorithm for the solution of the corresponding EM field integral equations (6.107) and (6.105).

6.3 FAMILY OF LINEAR AND NONLINEAR INTEGRAL APPROXIMATIONS OF THE ELECTROMAGNETIC FIELD

The main difference between the integral representations in potential and electromagnetic field theory is that in the first case the solution of the forward modeling problem is given in a form of direct quadrature, while in the second case we have to solve a system of integral equations. There is, however, an important approach to the fast solution of EM integral equations, based on neglecting the anomalous (scattered) EM fields under the Green's integral operators. This approach is usually called *the Born approximation*.

The Born approximation was developed originally to describe quantum mechanical scattering (Born, 1933; Born and Wolf, 1980). Since the basic idea behind this method has broad applications, it is possible to apply the Born approximation to different geophysical problems as well. For example, it has been used quite extensively and successfully in seismic geophysics (Bleistein, 1984; Bleistein and Gray, 1985; Tarantola, 1987).

Let us formulate a general forward EM problem so that the anomalous conductivity can be treated as a perturbation from a known background (or "normal") conductivity distribution. The solution of the EM problem in this case contains two parts: 1) the linear part, which can be interpreted as a direct

scattering of the source field by the inhomogeneity without taking into account coupling between scattering (excess) currents, and 2) the nonlinear part, which is composed of the combined effects of the anomalous conductivity and the unknown scattered field in the inhomogeneous structure. The Born approximation is based on the assumption that this last part, which represents the actual nonlinearity of the physical problem, is negligible when compared to the first linear part. As a result, a linear expression is obtained for the solution of the EM induction problem in a form of simple quadrature over the inhomogeneous domain, similar to the forward modeling solution for potential fields. This makes the method especially attractive for geophysical applications.

The Born approximation has been widely used in inverse schemes, because it provides a linearized approach to the solution of inverse problems (Oristaglio, 1989; Habashy et al., 1993). However, the Born approximation works reasonably well only for small conductivity contrasts, relatively small inhomogeneities, and low frequencies, ω (Born and Wolf, 1980; Habashy et al., 1993). It has limited application for solving general 3-D electromagnetic problems, because the Born approximation breaks down when the "anomalous induction number" of the anomalous region, that is $\omega\mu\Delta\sigma L^2$ (where L is the upper bound of the distance between any two points belonging to the region D with anomalous conductivity $\Delta\sigma$, and μ is the magnetic permeability) gets too large. It also has problems for high contrast bodies even in the case of a stationary field or direct current (DC) approximation.

Habashy et al. (1993) and Torres-Verdin and Habashy (1994) introduced an extended Born approximation for the EM field, based on the assumption that the internal electrical field has a small spatial gradient, which can be neglected inside an inhomogeneous structure. This new approximation for the internal field is given by the projection of the background or normal electric field (i.e. the electric field excited in the absence of the conductivity inhomogeneity) onto a scattering tensor. It is shown that the scattering tensor does not depend on the illuminating sources and is a nonlinear functional of the anomalous conductivity distribution. In addition, they demonstrated the efficiency of the new approximation which remains accurate within a wide frequency band for large anomalous structures and large conductivity contrasts.

In a series of publications, Zhdanov and Fang (1996a, 1996b, 1997) and Zhdanov et al. (2000a) presented an approach to the extension of the Born method, based on so-called quasi-linear and quasi-analytical approximations. In the following sections I will present an overview of a family of linear and nonlinear integral approximations of the electromagnetic field in inhomogeneous media, which can be used both for forward modeling and inversion.

6.3.1 BORN AND EXTENDED BORN APPROXIMATIONS

We consider again the basic integral equation of 3-D EM forward modeling (6.44), written for the anomalous electric field:

$$\mathbf{E}^a\left(\mathbf{r}_j\right) = \iiint_D \widehat{\mathbf{G}}_E\left(\mathbf{r}_j \mid \mathbf{r}\right) \cdot \left\{\Delta\widetilde{\sigma}\left(\mathbf{r}\right)\left[\mathbf{E}^b\left(\mathbf{r}\right) + \mathbf{E}^a\left(\mathbf{r}\right)\right]\right\} dv. \tag{6.114}$$

The conventional Born approximation $\mathbf{E}^B\left(\mathbf{r}_j\right)$ for the anomalous field can be obtained from (6.114) if the anomalous field is negligibly small inside D in comparison with the background field:

$$\mathbf{E}^B\left(\mathbf{r}_j\right) = \iiint_D \widehat{\mathbf{G}}_E\left(\mathbf{r}_j \mid \mathbf{r}\right) \cdot \left[\Delta\widetilde{\sigma}\left(\mathbf{r}\right)\mathbf{E}^b\left(\mathbf{r}\right)\right] dv. \tag{6.115}$$

The approximation (6.115) works reasonably well only for small conductivity contrasts between background media, a relatively small inhomogeneity and low frequencies (Berdichevsky and Zhdanov, 1984).

Habashy et al. (1993) and Torres-Verdin and Habashy (1994) developed the extended Born approximation, which replaces the total field in the integral (6.114) not with the background field, as in the Born approximation, but with its projection onto a scattering tensor $\widehat{\Gamma}(\mathbf{r})$:

$$\mathbf{E}(\mathbf{r}) = \mathbf{E}^b(\mathbf{r}) + \mathbf{E}^a(\mathbf{r}) = \widehat{\Gamma}(\mathbf{r}) \cdot \mathbf{E}^b(\mathbf{r}). \tag{6.116}$$

The expression for the scattering tensor is obtained from Eq. (6.114) by approximating $\mathbf{E}(\mathbf{r})$ in the integral by its value at the peak point $\mathbf{r} = \mathbf{r}_j$ of the Green's tensor:

$$\begin{aligned}
\mathbf{E}^a(\mathbf{r}_j) &= \mathbf{E}(\mathbf{r}_j) - \mathbf{E}^b(\mathbf{r}_j) \\
&\approx \left[\iiint_D \widehat{\mathbf{G}}_E(\mathbf{r}_j \mid \mathbf{r}) \, \Delta\widetilde{\sigma}(\mathbf{r}) \, dv \right] \cdot \mathbf{E}(\mathbf{r}_j),
\end{aligned}$$

or

$$\mathbf{E}(\mathbf{r}_j) \approx \left[\widehat{\mathbf{I}} - \iiint_D \widehat{\mathbf{G}}_E(\mathbf{r}_j \mid \mathbf{r}) \, \Delta\widetilde{\sigma}(\mathbf{r}) \, dv \right]^{-1} \cdot \mathbf{E}^b(\mathbf{r}_j), \tag{6.117}$$

where $\widehat{\mathbf{I}}$ is the identity tensor. Therefore, we have an analytical expression for the scattering tensor,

$$\widehat{\Gamma}(\mathbf{r}_j) = \left[\widehat{\mathbf{I}} - \iiint_D \widehat{\mathbf{G}}_E(\mathbf{r}_j \mid \mathbf{r}) \, \Delta\widetilde{\sigma}(\mathbf{r}) \, dv \right]^{-1}, \tag{6.118}$$

which is independent of the illuminating sources.

Note that approximation (6.117) is often referred to as *a localized nonlinear (LN) approximation*.

6.3.2 QUASI-LINEAR APPROXIMATION AND TENSOR QUASI-LINEAR EQUATION

The quasi-linear (QL) approximation is based on the assumption that the anomalous field $\mathbf{E}^a$ inside the inhomogeneous domain is linearly proportional to the background field $\mathbf{E}^b$ through some tensor $\widehat{\lambda}$ (Zhdanov and Fang, 1996a):

$$\mathbf{E}^a(\mathbf{r}) \approx \widehat{\lambda}(\mathbf{r}) \cdot \mathbf{E}^b(\mathbf{r}). \tag{6.119}$$

Substituting formula (6.119) into (6.114), we obtain the QL approximation $\mathbf{E}^a_{QL}(\mathbf{r})$ for the anomalous field:

$$\mathbf{E}^a_{QL}(\mathbf{r}_j) = \mathbf{G}_E\left[\Delta\widetilde{\sigma}\left(\widehat{\mathbf{I}} + \widehat{\lambda}(\mathbf{r}) \right) \cdot \mathbf{E}^b \right]. \tag{6.120}$$

The last formula gives us *the tensor quasi-linear (TQL) equation* with respect to the electrical reflectivity tensor $\widehat{\lambda}$:

$$\widehat{\lambda}(\mathbf{r}_j) \cdot \mathbf{E}^b(\mathbf{r}_j) = \mathbf{G}_E\left[\Delta\widetilde{\sigma}\widehat{\lambda}(\mathbf{r}) \cdot \mathbf{E}^b \right] + \mathbf{E}^B(\mathbf{r}_j), \tag{6.121}$$

where $\mathbf{E}^B\left(\mathbf{r}_j\right)$ is the Born approximation (6.115), and $\mathbf{G}_E\left[\Delta\widetilde{\sigma}\widehat{\boldsymbol{\lambda}}\left(\mathbf{r}\right)\cdot\mathbf{E}^b\right]$ is a linear operator of $\widehat{\boldsymbol{\lambda}}\left(\mathbf{r}\right)$:

$$\mathbf{G}_E\left[\Delta\widetilde{\sigma}\widehat{\boldsymbol{\lambda}}\left(\mathbf{r}\right)\cdot\mathbf{E}^b\right]=\iiint_D\widehat{\mathbf{G}}_E\left(\mathbf{r}_j\mid\mathbf{r}\right)\cdot\left[\Delta\sigma\left(\mathbf{r}\right)\widehat{\boldsymbol{\lambda}}\left(\mathbf{r}\right)\cdot\mathbf{E}^b\left(\mathbf{r}\right)\right]dv. \tag{6.122}$$

The original QL approximation, introduced by Zhdanov and Fang (1996a), is based on the numerical solution of a minimization problem arising from the TQL equation (6.121):

$$\left\|\widehat{\boldsymbol{\lambda}}\left(\mathbf{r}_j\right)\cdot\mathbf{E}^b\left(\mathbf{r}_j\right)-\mathbf{G}_E\left[\Delta\widetilde{\sigma}\widehat{\boldsymbol{\lambda}}\left(\mathbf{r}\right)\cdot\mathbf{E}^b\right]-\mathbf{E}^B\left(\mathbf{r}_j\right)\right\|=\min. \tag{6.123}$$

The advantage of this approach is that we can determine the electrical reflectivity tensor $\widehat{\boldsymbol{\lambda}}$ by solving a minimization problem (6.123) on a coarse grid. The accuracy of the QL approximation depends only on the accuracy of this discretization of $\widehat{\boldsymbol{\lambda}}$, and, in principle, can be made arbitrarily good. The disadvantage, however, is that, similar to the full integral equation (IE) method, the QL approach still requires solution of the corresponding system of linear equations arising from the minimization problem (6.123).

6.3.3 QL APPROXIMATION USING A MULTIGRID APPROACH

A simple modification of the QL equation (6.119) was introduced by Guozhong et al. (2004) for 3-D EM modeling in anisotropic formations for well-logging applications. They assumed that the anomalous field is linear proportional to the absolute value of the background field:

$$\mathbf{E}^a\left(\mathbf{r}\right)\approx\boldsymbol{\lambda}\left(\mathbf{r}\right)\left|\mathbf{E}^b\left(\mathbf{r}\right)\right|, \tag{6.124}$$

where $\boldsymbol{\lambda}\left(\mathbf{r}\right)=(\lambda_x,\lambda_y,\lambda_z)$ is an electrical reflectivity vector.

Note that exact representation (6.124) always exists because the corresponding electrical reflectivity vector can always be found for any given anomalous and background electric fields. Formula (6.124) becomes an approximation if we use some approximate method for evaluation of the electrical reflectivity vector.

The original QL approximation, introduced by Zhdanov and Fang (1996a, 1996b), is based on the numerical solution of a minimization problem arising from the TQL equation (6.121). The advantage of this approach is that we can determine the electrical reflectivity tensor $\widehat{\boldsymbol{\lambda}}$ by solving a minimization problem (6.123) on a coarse grid. We have noticed above that, the accuracy of the QL approximation depends only on the accuracy of this discretization of $\widehat{\boldsymbol{\lambda}}$. In essence, this means that we can apply the multigrid approach in the framework of the QL approximation (Ueda and Zhdanov, 2006). We discretize the conductivity distribution in the model and the electric fields using two grids, $\sum_c$ and $\sum_f$, where $\sum_c$ is a coarse discretization grid and $\sum_f$ is a fine discretization grid, where each block of the original grid $\sum_c$ is divided into additional smaller cells. First, we solve integral equation (6.114) on a coarse grid to determine the total electric field $\mathbf{E}$. After that we can find the anomalous field $\mathbf{E}^a$ on the coarse grid $\sum_c$,

$$\mathbf{E}^a\left(\mathbf{r}_c\right)=\mathbf{E}\left(\mathbf{r}_c\right)-\mathbf{E}^b\left(\mathbf{r}_c\right), \tag{6.125}$$

where $\mathbf{r}_c$ denotes the centers of the cells of the grid $\sum_c$ with coarse discretization.

In the framework of the multigrid approach, the components of the electrical reflectivity vector on a coarse grid are found by direct calculations as:

$$\lambda_x (\mathbf{r}_c) = E_x^a (\mathbf{r}_c) / \left| \mathbf{E}^b (\mathbf{r}_c) \right|, \tag{6.126}$$

$$\lambda_y (\mathbf{r}_c) = E_y^a (\mathbf{r}_c) / \left| \mathbf{E}^b (\mathbf{r}_c) \right|, \tag{6.127}$$

$$\lambda_z (\mathbf{r}_c) = E_z^a (\mathbf{r}_c) / \left| \mathbf{E}^b (\mathbf{r}_c) \right|, \tag{6.128}$$

assuming that $\left| \mathbf{E}^b (\mathbf{r}_c) \right| \neq 0$.

After we have found $\boldsymbol{\lambda} (\mathbf{r}_c)$, we use a fine discretization grid $\sum_f$ describing the conductivity distribution in the same model. We determine the $\boldsymbol{\lambda} (\mathbf{r}_f)$ values on this new grid by linear interpolation (where $\mathbf{r}_f$ denotes the centers of the cells of the grid $\sum_f$ with fine discretization). We compute the anomalous electric field $\mathbf{E}^a (\mathbf{r}_f)$ in the centers of the cells of the new grid $\sum_f$ with fine discretization using expression (6.124):

$$\mathbf{E}^a (\mathbf{r}_f) \approx \boldsymbol{\lambda} (\mathbf{r}_f) \left| \mathbf{E}^b (\mathbf{r}_f) \right|.$$

We can find now the total electric field $\mathbf{E} (\mathbf{r}_f)$ on a new grid, as:

$$\mathbf{E} (\mathbf{r}_f) = \mathbf{E}^a (\mathbf{r}_f) + \mathbf{E}^b (\mathbf{r}_f). \tag{6.129}$$

Finally, we compute the observed fields in the receivers using the discrete analog of the integral equation (IE) form of Maxwell's equations for the grid with fine discretization.

6.3.4 QUASI-ANALYTICAL SOLUTIONS FOR A 3-D ELECTROMAGNETIC FIELD

In this section we analyze different approximate solutions of the tensor quasi-linear (TQL) equation (6.121) following the paper by Zhdanov et al. (2000a).

Solution for a scalar reflectivity coefficient

In the framework of the quasi-linear approach, the electrical reflectivity tensor can be selected to be a scalar (Zhdanov and Fang, 1996a): $\widehat{\boldsymbol{\lambda}} = \lambda$. In this case, integral equation (6.121) can be cast in the form

$$\lambda (\mathbf{r}_j) \mathbf{E}^b (\mathbf{r}_j) = \mathbf{G}_E \left[\Delta \widetilde{\sigma} \lambda \mathbf{E}^b \right] + \mathbf{E}^B (\mathbf{r}_j). \tag{6.130}$$

Following ideas of the extended Born approximation outlined above, we use the fact that the Green's tensor $\widehat{\mathbf{G}}_E (\mathbf{r}_j \mid \mathbf{r})$ exhibits either singularity or a peak at the point where $\mathbf{r}_j = \mathbf{r}$. Therefore, one can expect that the dominant contribution to the integral $\mathbf{G}_E \left[\Delta \widetilde{\sigma} \lambda \mathbf{E}^b \right]$ in Eq. (6.130) is from some vicinity of the point $\mathbf{r}_j = \mathbf{r}$. Assuming also that $\lambda (\mathbf{r})$ is slowly varying within domain D, one can write

$$\lambda (\mathbf{r}_j) \mathbf{E}^b (\mathbf{r}_j) \approx \lambda (\mathbf{r}_j) \mathbf{G}_E \left[\Delta \widetilde{\sigma} \mathbf{E}^b \right] + \mathbf{E}^B (\mathbf{r}_j)$$
$$= \lambda (\mathbf{r}_j) \mathbf{E}^B (\mathbf{r}_j) + \mathbf{E}^B (\mathbf{r}_j). \tag{6.131}$$

Taking into account that we are looking for a scalar reflectivity tensor, it is useful to introduce a scalar equation based on the vector equation (6.131). We can obtain a scalar equation by taking the scalar product of both sides of Eq. (6.131) with the complex conjugate background electric field:

$$\lambda\left(\mathbf{r}_j\right)\mathbf{E}^b\left(\mathbf{r}_j\right)\cdot\mathbf{E}^{b*}\left(\mathbf{r}_j\right)$$
$$=\lambda\left(\mathbf{r}_j\right)\mathbf{E}^B\left(\mathbf{r}_j\right)\cdot\mathbf{E}^{b*}\left(\mathbf{r}_j\right)+\mathbf{E}^B\left(\mathbf{r}_j\right)\cdot\mathbf{E}^{b*}\left(\mathbf{r}_j\right). \tag{6.132}$$

Dividing Eq. (6.132) by the square of the background field and assuming that

$$\mathbf{E}^b\left(\mathbf{r}_j\right)\cdot\mathbf{E}^{b*}\left(\mathbf{r}_j\right)\neq0, \tag{6.133}$$

we obtain

$$\lambda\left(\mathbf{r}_j\right)=\frac{g\left(\mathbf{r}_j\right)}{1-g\left(\mathbf{r}_j\right)}, \tag{6.134}$$

where

$$g\left(\mathbf{r}_j\right)=\frac{\mathbf{E}^B\left(\mathbf{r}_j\right)\cdot\mathbf{E}^{b*}\left(\mathbf{r}_j\right)}{\mathbf{E}^b\left(\mathbf{r}_j\right)\cdot\mathbf{E}^{b*}\left(\mathbf{r}_j\right)}. \tag{6.135}$$

Note that in the points where the background field vanishes we can select λ equal to (-1):

$$\lambda\left(\mathbf{r}_j\right)=-1,\ \text{if}\ \mathbf{E}^b\left(\mathbf{r}_j\right)\cdot\mathbf{E}^{b*}\left(\mathbf{r}_j\right)=0.$$

Substituting (6.134) into (6.1), we find

$$\mathbf{E}\left(\mathbf{r}\right)=\mathbf{E}^a\left(\mathbf{r}\right)+\mathbf{E}^b\left(\mathbf{r}\right)\approx[\lambda\left(\mathbf{r}\right)+1]\,\mathbf{E}^b\left(\mathbf{r}\right)=\frac{1}{1-g\left(\mathbf{r}\right)}\mathbf{E}^b\left(\mathbf{r}\right). \tag{6.136}$$

Therefore from (6.44) and (6.45) we finally determine

$$\mathbf{E}^a_{QA}\left(\mathbf{r}_j\right)=\mathbf{E}\left(\mathbf{r}_j\right)-\mathbf{E}^b\left(\mathbf{r}_j\right)=\iiint_D\widehat{\mathbf{G}}_E\left(\mathbf{r}_j\mid\mathbf{r}\right)\cdot\left[\frac{\Delta\widetilde{\sigma}\left(\mathbf{r}\right)}{1-g\left(\mathbf{r}\right)}\mathbf{E}^b\left(\mathbf{r}\right)\right]dv, \tag{6.137}$$

and

$$\mathbf{H}^a_{QA}\left(\mathbf{r}_j\right)=\mathbf{H}\left(\mathbf{r}_j\right)-\mathbf{H}^b\left(\mathbf{r}_j\right)=\iiint_D\widehat{\mathbf{G}}_H\left(\mathbf{r}_j\mid\mathbf{r}\right)\cdot\left[\frac{\Delta\widetilde{\sigma}\left(\mathbf{r}\right)}{1-g\left(\mathbf{r}\right)}\mathbf{E}^b\left(\mathbf{r}\right)\right]dv. \tag{6.138}$$

Formulae (6.137) and (6.138) give quasi-analytical (QA) solutions for 3-D electromagnetic fields. Note that the only difference between the QA approximation and the Born approximation (6.115) is in the presence of the scalar function $\left[1-g\left(\mathbf{r}\right)\right]^{-1}$. That is why the computational expense of generating the QA approximation and the Born approximation is practically the same. On the other hand, it was demonstrated by Zhdanov et al. (2000a), that the accuracy of the QA approximation is much higher than the accuracy of the Born approximation.

Solution for a reflectivity tensor

The QA solutions developed in the previous section were based on the assumption that the electrical reflectivity tensor was a scalar. This assumption reduces the areas of practical applications of the QA approximations because in this case the anomalous (scattered) field is polarized in a direction parallel to the background field within the inhomogeneity. However, in general cases, the anomalous field may be polarized in a direction different from that of the background field, which could generate additional errors in the scalar QA approximation. To overcome this difficulty, we introduce in this section a tensor quasi-analytical (TQA) approximation. The TQA approximation uses a tensor $\widehat{\boldsymbol{\lambda}}$, which permits different polarizations for the background and anomalous (scattered) fields.

In the general case of a tensor $\widehat{\boldsymbol{\lambda}}(\mathbf{r}_j)$, we can assume that the product $\widehat{\boldsymbol{\lambda}}(\mathbf{r}) \cdot \mathbf{E}^b(\mathbf{r})$ is a smoothly varying function of the coordinates, and it can be taken outside the integral over the anomalous domain D. As a result, we obtain from the TQL equation (6.121)

$$\widehat{\boldsymbol{\lambda}}(\mathbf{r}_j) \cdot \mathbf{E}^b(\mathbf{r}_j) \approx \mathbf{G}_E \left[\Delta \widetilde{\sigma} \widehat{\mathbf{I}}\right] \cdot \left[\widehat{\boldsymbol{\lambda}}(\mathbf{r}_j) \cdot \mathbf{E}^b(\mathbf{r}_j)\right] + \mathbf{E}^B(\mathbf{r}_j)$$
$$= \widehat{\mathbf{g}}(\mathbf{r}_j) \cdot \left[\widehat{\boldsymbol{\lambda}}(\mathbf{r}_j) \cdot \mathbf{E}^b(\mathbf{r}_j)\right] + \mathbf{E}^B(\mathbf{r}_j),$$

or

$$\left[\widehat{\mathbf{I}} - \widehat{\mathbf{g}}(\mathbf{r}_j)\right] \cdot \left[\widehat{\boldsymbol{\lambda}}(\mathbf{r}_j) \cdot \mathbf{E}^b(\mathbf{r}_j)\right] = \mathbf{E}^B(\mathbf{r}_j), \qquad (6.139)$$

where

$$\widehat{\mathbf{g}}(\mathbf{r}_j) = \mathbf{G}_E \left[\Delta \widetilde{\sigma}(\mathbf{r}) \widehat{\mathbf{I}}\right]. \qquad (6.140)$$

Note that in the original definition of the Green's operators (3.119), the argument of $\mathbf{G}_E$ was a vector. In expression (6.140) we extend this definition to include a tensor argument $\widehat{\mathbf{T}}$:

$$\mathbf{G}_E\left(\widehat{\mathbf{T}}\right) = \iiint_{V_\infty} \widehat{\mathbf{G}}_E\left(\mathbf{r}_j \mid \mathbf{r}\right) \cdot \widehat{\mathbf{T}}(\mathbf{r}) \, dv, \qquad (6.141)$$

where $\mathbf{G}_E\left(\widehat{\mathbf{T}}\right)$ now becomes a tensor of the second rank. This means that the Green's operator applied to a vector generates a vector field, while the Green's operator applied to a tensor, generates a tensor field. We shall use this extended definition throughout the book.

Solving Eq. (6.139) gives

$$\widehat{\boldsymbol{\lambda}}(\mathbf{r}_j) \cdot \mathbf{E}^b(\mathbf{r}_j) = \left[\widehat{\mathbf{I}} - \widehat{\mathbf{g}}(\mathbf{r}_j)\right]^{-1} \cdot \mathbf{E}^B(\mathbf{r}_j). \qquad (6.142)$$

Substituting (6.142) into (6.119) and using (6.1), we obtain

$$\mathbf{E}(\mathbf{r}) = \mathbf{E}^a(\mathbf{r}) + \mathbf{E}^b(\mathbf{r}) \approx \left[\widehat{\boldsymbol{\lambda}}(\mathbf{r}) + \widehat{\mathbf{I}}\right] \cdot \mathbf{E}^b(\mathbf{r})$$
$$= \left[\widehat{\mathbf{I}} - \widehat{\mathbf{g}}(\mathbf{r})\right]^{-1} \cdot \mathbf{E}^B(\mathbf{r}) + \mathbf{E}^b(\mathbf{r}). \qquad (6.143)$$

Therefore, from (6.44) and (6.45) we find

$$\mathbf{E}^a_{TQA}\left(\mathbf{r}_j\right) = \mathbf{E}\left(\mathbf{r}_j\right) - \mathbf{E}^b\left(\mathbf{r}_j\right)$$
$$= \iiint_D \widehat{\mathbf{G}}_E\left(\mathbf{r}_j \mid \mathbf{r}\right) \cdot \Delta\widetilde{\sigma}\left(\mathbf{r}\right) \left\{\left[\widehat{\mathbf{I}} - \widehat{\mathbf{g}}\left(\mathbf{r}\right)\right]^{-1} \cdot \mathbf{E}^B\left(\mathbf{r}\right) + \mathbf{E}^b\left(\mathbf{r}\right)\right\} dv, \tag{6.144}$$

and

$$\mathbf{H}^a_{TQA}\left(\mathbf{r}_j\right) = \mathbf{H}\left(\mathbf{r}_j\right) - \mathbf{H}^b\left(\mathbf{r}_j\right)$$
$$= \iiint_D \widehat{\mathbf{G}}_H\left(\mathbf{r}_j \mid \mathbf{r}\right) \cdot \Delta\widetilde{\sigma}\left(\mathbf{r}\right) \left\{\left[\widehat{\mathbf{I}} - \widehat{\mathbf{g}}\left(\mathbf{r}\right)\right]^{-1} \cdot \mathbf{E}^B\left(\mathbf{r}\right) + \mathbf{E}^b\left(\mathbf{r}\right)\right\} dv, \tag{6.145}$$

where, according to (6.140) and (6.141),

$$\widehat{\mathbf{g}}\left(\mathbf{r}_j\right) = \mathbf{G}_E\left[\Delta\widetilde{\sigma}\left(\mathbf{r}\right)\widehat{\mathbf{I}}\right] = \iiint_D \widehat{\mathbf{G}}_E\left(\mathbf{r}_j \mid \mathbf{r}\right) \Delta\widetilde{\sigma}\left(\mathbf{r}\right) dv. \tag{6.146}$$

We call expressions (6.144) and (6.145) tensor quasi-analytical (TQA) approximations for an electromagnetic field. These approximations provide a more accurate solution for a forward problem than a scalar QA approximation (Zhdanov et al., 2000a). However, it involves computing the tensor multiplier $\left[\widehat{\mathbf{I}} - \widehat{\mathbf{g}}\left(\mathbf{r}\right)\right]^{-1}$, which is more time consuming than calculation of the scalar coefficient $\left[1 - g\left(\mathbf{r}\right)\right]^{-1}$ in the case of the scalar QA approximation.

6.3.5 QUASI-ANALYTICAL AND QUASI-BORN APPROXIMATIONS FOR A MODEL WITH VARIABLE BACKGROUND

In this section we introduce a formulation of the QA approximation for models with variable backgrounds, which results in more accurate integral representation for the Fréchet derivative as well.

We assume now that the conductivity within a 3-D geoelectrical model can be represented by the normal (horizontally layered) conductivity σ_{norm}, background conductivity, $\sigma_b = \sigma_{norm} + \Delta\sigma_b$, and an arbitrarily varying conductivity, $\sigma = \sigma_b + \Delta\sigma_a$, within a domain D.

In this model, the electromagnetic field can be presented as a sum of the background field, $\mathbf{E}^b$, $\mathbf{H}^b$, and the anomalous field, $\mathbf{E}^{\Delta\sigma_a}$, $\mathbf{H}^{\Delta\sigma_a}$:

$$\mathbf{E} = \mathbf{E}^b + \mathbf{E}^{\Delta\sigma_a}, \ \mathbf{H} = \mathbf{H}^b + \mathbf{H}^{\Delta\sigma_a}, \tag{6.147}$$

where the background field is a field generated by the given sources in the model with a background distribution of conductivity σ_b, and the anomalous field is produced by the anomalous conductivity distribution $\Delta\sigma_a$:

$$\mathbf{E}^{\Delta\sigma_a}\left(\mathbf{r}_j\right) = \mathbf{E}\left(\mathbf{r}_j\right) - \mathbf{E}^n\left(\mathbf{r}_j\right) - \mathbf{E}^{\Delta\sigma_b}\left(\mathbf{r}_j\right) = \mathbf{G}_E\left(\Delta\sigma_a\mathbf{E}\right), \tag{6.148}$$
$$\mathbf{H}^{\Delta\sigma_a}\left(\mathbf{r}_j\right) = \mathbf{H}\left(\mathbf{r}_j\right) - \mathbf{H}^n\left(\mathbf{r}_j\right) - \mathbf{H}^{\Delta\sigma_{ab}}\left(\mathbf{r}_j\right) = \mathbf{G}_H\left(\Delta\sigma_a\mathbf{E}\right). \tag{6.149}$$

Note that formulae (6.148) and (6.149) can be rewritten in the form:

$$\mathbf{E}^{\Delta\sigma_a}\left(\mathbf{r}_j\right) = \mathbf{G}_E\left(\Delta\sigma_a\left(\mathbf{E}^b + \mathbf{E}^{\Delta\sigma_a}\right)\right), \tag{6.150}$$

$$\mathbf{H}^{\Delta\sigma_a}\left(\mathbf{r}_j\right) = \mathbf{G}_H\left(\Delta\sigma_a\left(\mathbf{E}^b + \mathbf{E}^{\Delta\sigma_a}\right)\right). \tag{A-5}$$

Following the main ideas of the QL approximation, we assume that, inside the local inhomogeneity D, the anomalous field $\mathbf{E}^{\Delta\sigma_a}$ is linearly proportional to the background electric field $\mathbf{E}^b$:

$$\mathbf{E}^a = \mathbf{E}^{\Delta\sigma_a} = \widehat{\boldsymbol{\lambda}}_a \cdot \mathbf{E}^b. \tag{6.151}$$

Substituting (6.151) into (6.150) and (A-5), we arrive at the QL approximation of the anomalous electromagnetic field for a model with a variable background conductivity (QLVB approximation):

$$\mathbf{E}^{\Delta\sigma_a} \approx \mathbf{E}^{QLVB} = \mathbf{G}_E\left[\Delta\sigma_a\left(\widehat{\mathbf{I}}+\widehat{\boldsymbol{\lambda}}_a\right)\cdot\mathbf{E}^b\right], \tag{6.152}$$

$$\mathbf{H}^{\Delta\sigma_a} \approx \mathbf{H}^{QLVB} = \mathbf{G}_H\left[\Delta\sigma_a\left(\widehat{\mathbf{I}}+\widehat{\boldsymbol{\lambda}}_a\right)\cdot\mathbf{E}^b\right]. \tag{6.153}$$

Therefore, we have the following equation for $\widehat{\boldsymbol{\lambda}}_a$:

$$\widehat{\boldsymbol{\lambda}}_a \cdot \mathbf{E}^b = \mathbf{G}_E\left[\Delta\sigma_a\left(\widehat{\mathbf{I}}+\widehat{\boldsymbol{\lambda}}_a\right)\cdot\mathbf{E}^b\right]. \tag{6.154}$$

In the framework of the quasi-linear approach, the electrical reflectivity tensor can be selected to be a scalar: $\widehat{\boldsymbol{\lambda}}_a = \lambda_a$. In this case, integral formula (6.154) can be cast in the form:

$$\lambda_a\left(\mathbf{r}_j\right)\mathbf{E}^b\left(\mathbf{r}_j\right) = \mathbf{G}_E\left[\Delta\sigma_a\lambda_a\mathbf{E}^b\right] + \mathbf{E}^{QB}\left(\mathbf{r}_j\right), \tag{6.155}$$

where $\mathbf{E}^{QB}$ is the quasi-Born approximation of the anomalous electric field (we call this term a "quasi-Born" approximation, because in the case of the conventional Born approximation one should use the normal electric field inside the Green's operator):

$$\mathbf{E}^{QB} = \mathbf{G}_E\left[\Delta\sigma_a\mathbf{E}^b\right]. \tag{6.156}$$

Note that, the quasi-Born approximation of the anomalous magnetic field has the following form:

$$\mathbf{H}^{QB} = \mathbf{G}_H\left[\Delta\sigma_a\mathbf{E}^b\right]. \tag{6.157}$$

Following the ideas of the original QA approximation, we use the fact that the Green's tensor $\widehat{\mathbf{G}}_E\left(\mathbf{r}_j \mid \mathbf{r}\right)$ exhibits either singularity or a peak at the point where $\mathbf{r}_j = \mathbf{r}$. Therefore, one can expect that the dominant contribution to the integral $\mathbf{G}_E\left[\Delta\sigma_a\lambda\mathbf{E}^b\right]$ in Eq. (6.155) is from some vicinity of the point $\mathbf{r}_j = \mathbf{r}$. Assuming also that $\lambda_a\left(\mathbf{r}\right)$ is slowly varying within domain D, one can write:

$$\lambda_a\left(\mathbf{r}_j\right)\mathbf{E}^b\left(\mathbf{r}_j\right) \approx \lambda_a\left(\mathbf{r}_j\right)\mathbf{G}_E\left[\Delta\sigma_a\mathbf{E}^b\right] + \mathbf{E}^{QB}\left(\mathbf{r}_j\right)$$
$$= \lambda_a\left(\mathbf{r}_j\right)\mathbf{E}^Q\left(\mathbf{r}_j\right) + \mathbf{E}^Q\left(\mathbf{r}_j\right). \tag{6.158}$$

Note that, expression (6.158) represents a vector equation, while we have just one scalar unknown function, $\lambda_a\left(\mathbf{r}_j\right)$. Taking into account that we are looking for a scalar reflectivity tensor, it is useful to

introduce a scalar equation based on the vector equation (6.158). We can obtain a scalar equation by taking the scalar product of both sides of Eq. (6.158) with the complex conjugate background electric field:

$$
\begin{aligned}
\lambda_a\left(\mathbf{r}_j\right) \mathbf{E}^b\left(\mathbf{r}_j\right) \cdot \mathbf{E}^{b*}\left(\mathbf{r}_j\right) \\
= \lambda_a\left(\mathbf{r}_j\right) \mathbf{E}^{QB}\left(\mathbf{r}_j\right) \cdot \mathbf{E}^{b*}\left(\mathbf{r}_j\right) + \mathbf{E}^{QB}\left(\mathbf{r}_j\right) \cdot \mathbf{E}^{b*}\left(\mathbf{r}_j\right).
\end{aligned}
\tag{6.159}
$$

Dividing Eq. (6.159) by the square of the normal field and assuming that

$$
\mathbf{E}^b\left(\mathbf{r}_j\right) \cdot \mathbf{E}^{b*}\left(\mathbf{r}_j\right) \neq 0,
\tag{6.160}
$$

we obtain:

$$
\lambda_a\left(\mathbf{r}_j\right) = \lambda_a\left(\mathbf{r}_j\right) g^Q\left(\mathbf{r}_j\right) + g^Q\left(\mathbf{r}_j\right),
\tag{6.161}
$$

where:

$$
g^Q\left(\mathbf{r}_j\right) = \frac{\mathbf{E}^{QB}\left(\mathbf{r}_j\right) \cdot \mathbf{E}^{b*}\left(\mathbf{r}_j\right)}{\mathbf{E}^b\left(\mathbf{r}_j\right) \cdot \mathbf{E}^{b*}\left(\mathbf{r}_j\right)}.
$$

Solving Eq. (6.161), we find:

$$
\lambda_a\left(\mathbf{r}_j\right) = \frac{g^Q\left(\mathbf{r}_j\right)}{1 - g^Q\left(\mathbf{r}_j\right)}.
\tag{6.162}
$$

Note that, at the points, where the background field vanishes, we can select λ_a equal to (-1):

$$
\lambda_a\left(\mathbf{r}_j\right) = -1, \text{ if } \mathbf{E}^b\left(\mathbf{r}_j\right) \cdot \mathbf{E}^{b*}\left(\mathbf{r}_j\right) = 0.
$$

Substituting (6.162) into (6.147), we find:

$$
\mathbf{E}\left(\mathbf{r}\right) \approx \left[\lambda_a\left(\mathbf{r}\right) + 1\right] \mathbf{E}^b\left(\mathbf{r}\right) = \frac{1}{1 - g^Q\left(\mathbf{r}\right)} \mathbf{E}^b\left(\mathbf{r}\right).
\tag{6.163}
$$

Therefore, from Eqs. (6.148) and (6.149), we finally determine:

$$
\mathbf{E}_{QAVB}^{\Delta\sigma_a}\left(\mathbf{r}_j\right) = \iiint_D \widehat{\mathbf{G}}_E\left(\mathbf{r}_j \mid \mathbf{r}\right) \cdot \left[\frac{\Delta\sigma_a\left(\mathbf{r}\right)}{1 - g^Q\left(\mathbf{r}\right)} \mathbf{E}^b\left(\mathbf{r}\right)\right] dv,
\tag{6.164}
$$

and

$$
\mathbf{H}_{QAVB}^{\Delta\sigma_a}\left(\mathbf{r}_j\right) = \iiint_D \widehat{\mathbf{G}}_H\left(\mathbf{r}_j \mid \mathbf{r}\right) \cdot \left[\frac{\Delta\sigma_a\left(\mathbf{r}\right)}{1 - g^Q\left(\mathbf{r}\right)} \mathbf{E}^b\left(\mathbf{r}\right)\right] dv.
\tag{6.165}
$$

Eqs. (6.164) and (6.165) give quasi-analytical solutions with the variable background (QAVB) for 3-D electromagnetic fields. We should note that formulae (6.164) and (6.165) provide more accurate approximation of the anomalous field than the original QA approximations developed by Zhdanov et al. (2000a), because they are based on the linear relationship between the anomalous and the background fields, while the original approximations used a similar relationship between the anomalous and the normal fields. In the case of the high conductivity contrast between the inhomogeneity and

the horizontally-layered background, the accuracy of the original QL and QA approximations may decrease, while using the appropriate variable background model can make this approximation as close to the true field as required.

6.3.6 QUASI-ANALYTICAL SOLUTIONS FOR 2-D ELECTROMAGNETIC FIELDS

Assume now that both the electromagnetic field and the complex conductivity $\widetilde{\sigma}$ in a geoelectrical model are two-dimensional, i.e., they vary only along the directions x and z in some Cartesian system of coordinates, and they are constant in the y direction. In this case, repeating the derivations described above for the 3-D case, we can obtain the following quasi-analytical expressions for a 2-D electromagnetic field:

$$E_{QAy}^{a}(\mathbf{r}_j) \approx \iint_D G_b(\mathbf{r}_j \mid \mathbf{r}) \frac{\Delta\widetilde{\sigma}(\mathbf{r})}{1 - g(\mathbf{r})} E_y^b(\mathbf{r})ds, \tag{6.166}$$

and similarly for magnetic field components

$$H_{QAx}^{a}(\mathbf{r}_j) \approx -\frac{1}{i\omega\mu_0} \iint_D \frac{\partial G_b(\mathbf{r}_j \mid \mathbf{r})}{\partial z} \frac{\Delta\widetilde{\sigma}(\mathbf{r})}{1 - g(\mathbf{r})} E_y^b(\mathbf{r})ds, \tag{6.167}$$

$$H_{QAz}^{a}(\mathbf{r}_j) \approx \frac{1}{i\omega\mu_0} \iint_D \frac{\partial G_b(\mathbf{r}_j \mid \mathbf{r})}{\partial x} \frac{\Delta\widetilde{\sigma}(\mathbf{r})}{1 - g(\mathbf{r})} E_y^b(\mathbf{r})ds, \tag{6.168}$$

where

$$g(\mathbf{r}) = \frac{E_y^B(\mathbf{r})}{E_y^b(\mathbf{r})}, \ \text{if } E_y^b(\mathbf{r}) \neq 0. \tag{6.169}$$

These formulae can serve as a new effective quasi-analytical tool in the solution of both direct and inverse 2-D electromagnetic problems. Numerical tests demonstrate that these approximations produce a very accurate result for 2-D models (Dmitriev et al., 1999).

6.3.7 LOCALIZED NONLINEAR APPROXIMATION

We will demonstrate now that the TQA approximation can be treated as a modification of the extended Born (localized nonlinear – LN) approximation, introduced above. Let us rewrite Eq. (6.143) in the form

$$\mathbf{E}(\mathbf{r}) = \left[\widehat{\mathbf{I}} - \widehat{\mathbf{g}}(\mathbf{r})\right]^{-1} \cdot \mathbf{E}^B(\mathbf{r}) + \left[\widehat{\mathbf{I}} - \widehat{\mathbf{g}}(\mathbf{r})\right]^{-1} \cdot \left\{\left[\widehat{\mathbf{I}} - \widehat{\mathbf{g}}(\mathbf{r})\right] \cdot \mathbf{E}^b(\mathbf{r})\right\}$$

$$= \left[\widehat{\mathbf{I}} - \widehat{\mathbf{g}}(\mathbf{r})\right]^{-1} \cdot \left[\mathbf{E}^B(\mathbf{r}) - \widehat{\mathbf{g}}(\mathbf{r}) \cdot \mathbf{E}^b(\mathbf{r})\right] + \left[\widehat{\mathbf{I}} - \widehat{\mathbf{g}}(\mathbf{r})\right]^{-1} \cdot \mathbf{E}^b(\mathbf{r}). \tag{6.170}$$

Taking into account once again the fact that the Green's tensor $\widehat{\mathbf{G}}_E(\mathbf{r}_j \mid \mathbf{r})$ exhibits either a singularity or a peak at the point where $\mathbf{r}_j = \mathbf{r}$, one can calculate the Born approximation $\mathbf{G}_E\left[\Delta\widetilde{\sigma}(\mathbf{r})\mathbf{E}^b(\mathbf{r})\right]$ using the formula

$$\mathbf{E}^B(\mathbf{r}_j) = \mathbf{G}_E\left[\Delta\widetilde{\sigma}(\mathbf{r})\mathbf{E}^b(\mathbf{r})\right] \approx \widehat{\mathbf{g}}(\mathbf{r}_j) \cdot \mathbf{E}^b(\mathbf{r}_j).$$

In the framework of this approach

$$\mathbf{E}^B(\mathbf{r}) - \widehat{\mathbf{g}}(\mathbf{r}) \cdot \mathbf{E}^b(\mathbf{r}) \approx 0. \tag{6.171}$$

This approximation is particularly appropriate if the background field is a smoothly varying function of the coordinates; it forms the basis of localized nonlinear approximations (Habashy et al., 1993).

Under this assumption

$$\mathbf{E}(\mathbf{r}) = \mathbf{E}^a(\mathbf{r}) + \mathbf{E}^b(\mathbf{r}) \approx \left[\widehat{\mathbf{I}} - \widehat{\mathbf{g}}(\mathbf{r})\right]^{-1} \cdot \mathbf{E}^b(\mathbf{r}). \tag{6.172}$$

Therefore, from (6.44) and (6.45) we find

$$\begin{aligned}
\mathbf{E}_{LN}^a(\mathbf{r}_j) &= \mathbf{E}(\mathbf{r}_j) - \mathbf{E}^b(\mathbf{r}_j) \\
&= \iiint_D \widehat{\mathbf{G}}_E(\mathbf{r}_j \mid \mathbf{r}) \cdot \left\{ \Delta\widetilde{\sigma}(\mathbf{r}) \left[\widehat{\mathbf{I}} - \widehat{\mathbf{g}}(\mathbf{r})\right]^{-1} \cdot \mathbf{E}^b(\mathbf{r}) \right\} dv,
\end{aligned} \tag{6.173}$$

and

$$\begin{aligned}
\mathbf{H}_{LN}^a(\mathbf{r}_j) &= \mathbf{H}(\mathbf{r}_j) - \mathbf{H}^b(\mathbf{r}_j) \\
&= \iiint_D \widehat{\mathbf{G}}_H(\mathbf{r}_j \mid \mathbf{r}) \cdot \left\{ \Delta\widetilde{\sigma}(\mathbf{r}) \left[\widehat{\mathbf{I}} - \widehat{\mathbf{g}}(\mathbf{r})\right]^{-1} \cdot \mathbf{E}^b(\mathbf{r}) \right\} dv.
\end{aligned} \tag{6.174}$$

Formulae (6.173) and (6.174) give the localized nonlinear (LN) approximation introduced by Habashy et al. (1993), and the tensor

$$\left[\widehat{\mathbf{I}} - \widehat{\mathbf{g}}(\mathbf{r})\right]^{-1} = \widehat{\mathbf{\Gamma}}(\mathbf{r})$$

is the scattering tensor introduced above.

Thus, we can see that the difference between the tensor quasi-analytical approximation and the localized nonlinear approximation is determined by a term:

$$\begin{aligned}
\mathbf{E}_{TQA}^a(\mathbf{r}_j) &- \mathbf{E}_{LN}^a(\mathbf{r}_j) \\
&= \iiint_D \widehat{\mathbf{G}}_E(\mathbf{r}_j \mid \mathbf{r}) \cdot \left\{ \Delta\widetilde{\sigma}(\mathbf{r}) \widehat{\mathbf{\Gamma}}(\mathbf{r}) \cdot \left[\mathbf{E}^B(\mathbf{r}) - \widehat{\mathbf{g}}(\mathbf{r}) \cdot \mathbf{E}^b(\mathbf{r})\right] \right\} dv.
\end{aligned} \tag{6.175}$$

Note that both TQA and LN approximations use the same scattering tensor $\widehat{\mathbf{\Gamma}}(\mathbf{r})$, which is based on the principle that the effect of the electric field in the Green's integral operator is localized. The only difference is that in the case of LN approximation, we use this principle twice for computing both the scattering tensor and the expression for the Born approximation $\mathbf{E}^B(\mathbf{r}_j)$ on the right-hand side of the tensor quasi-linear equation (6.121), while in the case of TQA approximation we use the exact formula for $\mathbf{E}^B(\mathbf{r}_j)$. That is why we can consider TQA as a partially localized approximation. At the same time, this difference results in different behaviors of these two approximations for different electrical models (Zhdanov et al., 2000a).

6.3.8 LOCALIZED QUASI-LINEAR APPROXIMATION

Let us analyze again the equations of the QL approximation

$$\mathbf{E}^a\left(\mathbf{r}_j\right) \approx \widehat{\boldsymbol{\lambda}}\left(\mathbf{r}_j\right) \cdot \mathbf{E}^b\left(\mathbf{r}_j\right), \tag{6.176}$$

and

$$\mathbf{E}^a_{QL}\left(\mathbf{r}_j\right) = \mathbf{G}_E\left(\Delta\widetilde{\sigma}\left(\widehat{\mathbf{I}}+\widehat{\boldsymbol{\lambda}}\left(\mathbf{r}\right)\right)\cdot\mathbf{E}^b\left(\mathbf{r}\right)\right). \tag{6.177}$$

Following the same principle that was used in deriving the localized nonlinear approximation, we assume that the dominant contribution to the integral $\mathbf{G}_E\left[\Delta\widetilde{\sigma}\widehat{\boldsymbol{\lambda}}\cdot\mathbf{E}^b\right]$ in Eq. (6.177) is from some vicinity of the point $\mathbf{r}_j = \mathbf{r}$. Assuming also that $\mathbf{E}^b\left(\mathbf{r}_j\right)$ is slowly varying within the domain D, one can rewrite Eq. (6.177) as

$$\mathbf{E}^a_{QL}\left(\mathbf{r}_j\right) \approx \mathbf{G}_E\left(\Delta\widetilde{\sigma}\left(\widehat{\mathbf{I}}+\widehat{\boldsymbol{\lambda}}\left(\mathbf{r}\right)\right)\right)\cdot\mathbf{E}^b\left(\mathbf{r}_j\right), \tag{6.178}$$

where the tensor Green's operator is given by the formula

$$\mathbf{G}_E\left(\Delta\widetilde{\sigma}\left(\widehat{\mathbf{I}}+\widehat{\boldsymbol{\lambda}}\left(\mathbf{r}\right)\right)\right) = \iiint_D \widehat{\mathbf{G}}_E\left(\mathbf{r}_j\mid\mathbf{r}\right)\cdot\left\{\Delta\widetilde{\sigma}\left(\mathbf{r}\right)\left[\widehat{\mathbf{I}}+\widehat{\boldsymbol{\lambda}}\left(\mathbf{r}\right)\right]\right\}dv. \tag{6.179}$$

Comparing (6.176) and (6.179), we find that

$$\widehat{\boldsymbol{\lambda}}\left(\mathbf{r}_j\right)\cdot\mathbf{E}^b\left(\mathbf{r}_j\right) \approx \mathbf{G}_E\left(\Delta\widetilde{\sigma}\left(\widehat{\mathbf{I}}+\widehat{\boldsymbol{\lambda}}\left(\mathbf{r}\right)\right)\right)\cdot\mathbf{E}^b\left(\mathbf{r}_j\right),$$

where the electrical reflectivity tensor can be determined, similar to the original QL approximation, from the solution of the minimization problem:

$$\left\|\widehat{\boldsymbol{\lambda}}\left(\mathbf{r}_j\right)\cdot\mathbf{E}^b\left(\mathbf{r}_j\right) - \mathbf{G}_E\left(\Delta\widetilde{\sigma}\left(\widehat{\mathbf{I}}+\widehat{\boldsymbol{\lambda}}\left(\mathbf{r}\right)\right)\right)\cdot\mathbf{E}^b\left(\mathbf{r}_j\right)\right\|_{L_2(D)} = \min. \tag{6.180}$$

Noting that

$$\left\|\widehat{\boldsymbol{\lambda}}\left(\mathbf{r}_j\right)\cdot\mathbf{E}^b\left(\mathbf{r}_j\right) - \mathbf{G}_E\left(\Delta\widetilde{\sigma}\left(\widehat{\mathbf{I}}+\widehat{\boldsymbol{\lambda}}\left(\mathbf{r}\right)\right)\right)\cdot\mathbf{E}^b\left(\mathbf{r}_j\right)\right\|_{L_2(D)} \leq$$
$$\left\|\widehat{\boldsymbol{\lambda}}\left(\mathbf{r}_j\right) - \mathbf{G}_E\left(\Delta\widetilde{\sigma}\left(\widehat{\mathbf{I}}+\widehat{\boldsymbol{\lambda}}\left(\mathbf{r}\right)\right)\right)\right\|_{L_2(D)}\left\|\mathbf{E}^b\left(\mathbf{r}_j\right)\right\|_{L_2(D)},$$

we can substitute

$$\left\|\widehat{\boldsymbol{\lambda}}\left(\mathbf{r}_j\right) - \mathbf{G}_E\left(\Delta\widetilde{\sigma}\left(\widehat{\mathbf{I}}+\widehat{\boldsymbol{\lambda}}\left(\mathbf{r}\right)\right)\right)\right\|_{L_2(D)} = \min, \tag{6.181}$$

for the minimization problem (6.180).

The solution of Eq. (6.181) gives us *a localized electrical reflectivity tensor* $\widehat{\boldsymbol{\lambda}}_L\left(\mathbf{r}\right)$, which is obviously source independent. Expression (6.177) with $\widehat{\boldsymbol{\lambda}}_L\left(\mathbf{r}\right)$ determined according to (6.181), is called *a localized quasi-linear (LQL) approximation* (Zhdanov and Tartaras, 2002):

$$\mathbf{E}^a_{LQL}\left(\mathbf{r}_j\right) \approx \mathbf{G}_E\left(\Delta\widetilde{\sigma}\left(\widehat{\mathbf{I}}+\widehat{\boldsymbol{\lambda}}_L\left(\mathbf{r}\right)\right)\cdot\mathbf{E}^b\left(\mathbf{r}\right)\right). \tag{6.182}$$

In a similar way we can find a localized quasi-linear approximation for the magnetic field:

$$\mathbf{H}^a_{LQL}\left(\mathbf{r}_j\right) \approx \mathbf{G}_H\left(\Delta\tilde{\sigma}\left(\widehat{\mathbf{I}}+\widehat{\boldsymbol{\lambda}}_L\left(\mathbf{r}\right)\right)\cdot\mathbf{E}^b\left(\mathbf{r}\right)\right). \tag{6.183}$$

The LQL approximation has a similar background to the localized nonlinear (LN) approximation, but there are some important differences. The LN approximation also replaces the total field inside inhomogeneity with a product of the background field and a scattering tensor $\widehat{\boldsymbol{\Gamma}}\left(\mathbf{r}\right)$,

$$\mathbf{E}^a_{LN}\left(\mathbf{r}\right) \approx \widehat{\boldsymbol{\Gamma}}\left(\mathbf{r}\right)\cdot\mathbf{E}^b\left(\mathbf{r}\right). \tag{6.184}$$

However, the scattering tensor is defined explicitly through an integral of the anomalous conductivity. In contrast, the reflectivity tensor in the LQL approximation is determined as the solution of the minimization problem (6.181). Note also that the reflectivity tensor is assumed to be slowly varying, and therefore the minimization problem (6.181) can be computed on a much coarser grid than the field itself.

Another important difference between the LQL approximation and LN approximation is that for the former one can choose different types of reflectivity tensors. For example, one can introduce a scalar or diagonal reflectivity tensor.

In the case of a scalar reflectivity tensor $\widehat{\boldsymbol{\lambda}}_L = \lambda_L\widehat{\mathbf{I}}$, and

$$\mathbf{E}^a\left(\mathbf{r}\right) \approx \lambda_L\left(\mathbf{r}\right)\mathbf{E}^b\left(\mathbf{r}\right). \tag{6.185}$$

Substituting formula (6.185) into (6.182), we obtain the scalar LQL approximation $\mathbf{E}^a_{LQL}\left(\mathbf{r}\right)$ for the anomalous field:

$$\mathbf{E}^a_{LQL}\left(\mathbf{r}\right) = \mathbf{G}_E\left(\Delta\tilde{\sigma}\left(1+\lambda_L\left(\mathbf{r}\right)\right)\mathbf{E}^b\right), \tag{6.186}$$

where the scalar reflectivity coefficient $\lambda_L\left(\mathbf{r}\right)$ is determined by the solution of an optimization problem:

$$\left\|\lambda_L\left(\mathbf{r}\right)\widehat{\mathbf{I}} - \mathbf{G}_E\left(\Delta\tilde{\sigma}\left(1+\lambda_L\left(\mathbf{r}\right)\right)\widehat{\mathbf{I}}\right)\right\|_{L_2(D)} = \min. \tag{6.187}$$

In the special case of the diagonal reflectivity tensor $\widehat{\boldsymbol{\lambda}}_L = \mathbf{diag}\boldsymbol{\lambda}_L$,

$$\widehat{\boldsymbol{\lambda}}_L = \mathbf{diag}\boldsymbol{\lambda}_L = \begin{bmatrix} \lambda_x & 0 & 0 \\ 0 & \lambda_y & 0 \\ 0 & 0 & \lambda_z \end{bmatrix},$$

where $\boldsymbol{\lambda}_L$ is a reflectivity vector

$$\boldsymbol{\lambda}_L = \begin{bmatrix} \lambda_x \\ \lambda_y \\ \lambda_z \end{bmatrix},$$

we have

$$\mathbf{E}^a\left(\mathbf{r}\right) \approx \mathbf{diag}\boldsymbol{\lambda}_L\left(\mathbf{r}\right)\cdot\mathbf{E}^b\left(\mathbf{r}\right). \tag{6.188}$$

Substituting formula (6.188) into (6.182) we obtain a LQL approximation $\mathbf{E}_{LQL}^a (\mathbf{r})$ for the anomalous field:

$$\mathbf{E}_{LQL}^a (\mathbf{r}) = \mathbf{G}_E \left(\Delta \widetilde{\sigma} \left(\widehat{\mathbf{I}} + \mathbf{diag} \boldsymbol{\lambda}_L (\mathbf{r}) \right) \cdot \mathbf{E}^b \right), \tag{6.189}$$

where the reflectivity vector $\boldsymbol{\lambda}_L (\mathbf{r})$ is determined as the solution of an optimization problem:

$$\left\| \mathbf{diag} \boldsymbol{\lambda}_L (\mathbf{r}) - \mathbf{G}_E \left(\Delta \widetilde{\sigma} \left(\widehat{\mathbf{I}} + \mathbf{diag} \boldsymbol{\lambda}_L (\mathbf{r}) \right) \right) \right\|_{L_2(D)} = \min. \tag{6.190}$$

6.4 DIFFERENTIAL EQUATION METHODS

In the previous sections we developed numerical methods of electromagnetic modeling based on discretization of the corresponding integral representations for the electromagnetic field. However, we can arrive at numerical solutions directly based on the differential form of Maxwell's equations. This approach has its own advantages and disadvantages over the integral equation method. The advantage is that one can apply a very flexible grid for discretization of the model parameters using differential methods. The disadvantage is that we now have to discretize the entire modeling domain, while in the integral equation method one should discretize only the domain with the anomalous conductivity distribution. Differential methods have found wide applications in geophysics because of the ease with which they handle a very complicated model of geological structures. I will discuss in this section the basic ideas of using differential methods in electromagnetic forward modeling.

6.4.1 FIELD EQUATIONS AND BOUNDARY CONDITIONS

Let us assume that the region of modeling, V, is bounded by a surface ∂V. For numerical modeling we can use the original coupled first-order Maxwell's equations (3.103)–(3.104), or the corresponding second order partial differential equations for electric or magnetic fields. In the first case we should formulate and solve the corresponding boundary-value problem for electric and magnetic fields simultaneously. In the second case, one can solve separately the corresponding equations for the electric or magnetic fields, which we reproduce here for convenience:

$$\mu \nabla \times \left(\frac{1}{\mu} \nabla \times \mathbf{E} \right) - \widetilde{k}^2 \mathbf{E} = i \omega \mu \mathbf{j^e},$$

$$\widetilde{\sigma} \nabla \times \left(\frac{1}{\widetilde{\sigma}} \nabla \times \mathbf{H} \right) - \widetilde{k}^2 \mathbf{H} = \widetilde{\sigma} \nabla \times \left(\frac{1}{\widetilde{\sigma}} \mathbf{j}^e \right), \tag{6.191}$$

where $\mathbf{j}^e$ is the density of extraneous electric current; $\widetilde{k}^2$ is the corresponding wave number:

$$\widetilde{k}^2 = i \omega \mu \widetilde{\sigma} = i \omega \mu \sigma + \omega^2 \mu \varepsilon. \tag{6.192}$$

In the case of the quasi-stationary field, which is the common case in geophysical exploration, we usually ignore the displacement currents (see Chapter 4), which results in a simplification of system

(6.191):

$$\mu \mathbf{\nabla} \times \left(\frac{1}{\mu} \mathbf{\nabla} \times \mathbf{E} \right) - k^2 \mathbf{E} = i\omega\mu\mathbf{j^e},$$

$$\sigma \mathbf{\nabla} \times \left(\frac{1}{\sigma} \mathbf{\nabla} \times \mathbf{H} \right) - k^2 \mathbf{H} = \sigma \mathbf{\nabla} \times \left(\frac{1}{\sigma} \mathbf{j}^e \right), \tag{6.193}$$

where the wave number k^2 is given by

$$k^2 = i\omega\mu\sigma.$$

Solving the corresponding equation for the electric field, we can determine the magnetic field from the second Maxwell's equation:

$$\mathbf{H} = \frac{1}{i\omega\mu} \mathbf{\nabla} \times \mathbf{E}. \tag{6.194}$$

In a similar way, solving the corresponding equation for the magnetic field, we can determine the electric field from the first Maxwell's equation,

$$\mathbf{E} = \frac{1}{\widetilde{\sigma}} \mathbf{\nabla} \times \mathbf{H} - \frac{1}{\widetilde{\sigma}} \mathbf{j}^e, \tag{6.195}$$

which is simplified for the quasi-stationary field outside the source:

$$\mathbf{E} = \frac{1}{\sigma} \mathbf{\nabla} \times \mathbf{H}. \tag{6.196}$$

Maxwell's equations (3.103)–(3.104), or the second order differential equations (6.191) and (6.193), are supplemented with a boundary-value condition, i.e., with the additional equations for the electric or magnetic fields on the boundary ∂V of the volume V,

$$L_b\mathbf{E} = \mathbf{R}_E, \text{ or } L_b\mathbf{H} = \mathbf{R}_H, \tag{6.197}$$

where L_b is the corresponding boundary differential operator, and $\mathbf{R}_E$ and $\mathbf{R}_H$ are the boundary values for the electric or magnetic fields. Note that the traditional statements of the boundary-value problems are based on application of *Dirichlet boundary-value conditions* of the first, second, or the third order, formed by means of linear combinations of the field itself and its derivative normal to the boundary. Dirichlet boundary conditions of the first order fix the values of the field at the boundary. Dirichlet boundary conditions of the second order, or *Neumann boundary conditions*, fix the value of the gradient of the field normal to the boundary; and Dirichlet boundary conditions of the third order, or *Cauchy boundary conditions*, fix both the value and the normal gradient of the field at the boundary (Morse and Feshbach, 1953).

Usually, the boundary of the modeling volume is set so far from the conductivity anomaly that it is possible to neglect the anomalous field there. In this case, the simplest Dirichlet boundary conditions of the first order can be implemented by choosing the background (normal) field values as the boundary values. The background field is usually selected as one-dimensional, but it can be two-dimensional, if the background distribution of the electromagnetic parameters is two-dimensional. Another approach

is based on the simplest Neumann boundary conditions, which requires that the normal gradient of the field is zero on the boundary.

Note, however, that application of the aforementioned simple conditions requires the size of the modeling region to exceed the size of the inhomogeneous region V_a many times over, in order to be able to neglect the effect of the anomalous field at the boundary. To overcome this limitation one can use asymptotic boundary conditions, developed for 2-D models by Weaver and Brewitt-Taylor (1978), and extended to 3-D models by Zhdanov et al. (1982) and Berdichevsky and Zhdanov (1984). These conditions are based on the analysis of the asymptotic behavior of the electromagnetic field far away from the geoelectrical anomalies. For example, in the three-dimensional case the asymptotic boundary condition for a magnetic field in free space is written in the form

$$L_b \mathbf{H} = (1 + \mathbf{r} \cdot \nabla) \left[\mathbf{H}(\mathbf{r}) - \mathbf{H}^b(\mathbf{r}) \right] = 0. \tag{6.198}$$

The accuracy of condition (6.198) is estimated as $O\left(1/|\mathbf{r}|^2\right)$. One can find expressions for asymptotic boundary conditions of higher order of accuracy with respect to distance, $|\mathbf{r}|$, in Berdichevsky and Zhdanov (1984).

In high frequency modeling the absorbing boundary conditions (ABC), based on the Perfect Matched Layer (PML) can be used as well (Berenger, 1993; Chew and Weedon, 1994). In the framework of this approach we introduce an artificial layer at the boundary, filled with PML material, which absorbs the outgoing electromagnetic waves, so that almost no reflections occur at the boundary. The absorbing boundary conditions dramatically reduce the required modeling region in microwave frequency applications.

The system of equations defined by (3.103)–(3.104) and (6.191) or (6.193), and by the corresponding Dirichlet (6.197), asymptotic (6.198), or absorbing boundary conditions, forms a boundary-value problem for the electromagnetic field.

In geophysical applications, it is important to incorporate different types of sources in electromagnetic modeling. The most convenient way to do this is based on the separation of the field into the background (normal) and anomalous parts:

$$\mathbf{E} = \mathbf{E}^b + \mathbf{E}^a, \ \mathbf{H} = \mathbf{H}^b + \mathbf{H}^a, \tag{6.199}$$

where the background field is a field generated by the given sources $\mathbf{j}^e$ in the model with the background (normal) distribution of conductivity $\widetilde{\sigma}_b$, and the anomalous field is produced by the anomalous conductivity distribution $\Delta\widetilde{\sigma}$. The advantage of this approach is that we can use known analytical solutions for the background field and solve numerically the boundary-value problem for the anomalous field only.

According to Eqs. (6.3), the corresponding Maxwell's equations for the anomalous field have the form

$$\begin{aligned} \nabla \times \mathbf{H}^a &= \widetilde{\sigma}_b \mathbf{E}^a + \mathbf{j}^a \\ \nabla \times \mathbf{E}^a &= i\omega\mu\mathbf{H}^a, \end{aligned} \tag{6.200}$$

where

$$\mathbf{j}^a(\mathbf{r}) = \Delta\widetilde{\sigma}(\mathbf{r})\mathbf{E}(\mathbf{r}) = \Delta\widetilde{\sigma}(\mathbf{r}) \left[\mathbf{E}^b(\mathbf{r}) + \mathbf{E}^a(\mathbf{r}) \right] \tag{6.201}$$

is the density of excess electric currents within the inhomogeneity D.

Substituting the excess electric current $\mathbf{j}^a$ for the extraneous electric current $\mathbf{j}^e$, and the background conductivity $\widetilde{\sigma}_b$ for the total conductivity $\widetilde{\sigma}$ in Eq. (6.191), we obtain the separate equations for the electric and magnetic anomalous fields:

$$\mu\mathbf{\nabla}\times\left(\frac{1}{\mu}\mathbf{\nabla}\times\mathbf{E}^a\right)-\widetilde{k}_b^2\mathbf{E}^a=i\omega\mu\mathbf{j^a},$$

$$\widetilde{\sigma}_b\mathbf{\nabla}\times\left(\frac{1}{\widetilde{\sigma}_b}\mathbf{\nabla}\times\mathbf{H}^a\right)-\widetilde{k}_b^2\mathbf{H}^a=\widetilde{\sigma}_b\mathbf{\nabla}\times\left(\frac{1}{\widetilde{\sigma}_b}\mathbf{j}^a\right),\tag{6.202}$$

where $\widetilde{k}_b^2=i\omega\mu\widetilde{\sigma}_b=i\omega\mu\sigma_b+\omega^2\mu\varepsilon$.

Taking into account (6.201), we finally find after some algebra,

$$\mu\mathbf{\nabla}\times\left(\frac{1}{\mu}\mathbf{\nabla}\times\mathbf{E}^a\right)-\widetilde{k}^2\mathbf{E}^a=i\omega\mu\Delta\widetilde{\sigma}\mathbf{E}^b,$$

$$\mathbf{\nabla}\times\left(\frac{1}{\widetilde{\sigma}_b}\mathbf{\nabla}\times\mathbf{H}^a\right)-i\omega\mu\mathbf{H}^a-\mathbf{\nabla}\times\left(\frac{\Delta\widetilde{\sigma}}{\widetilde{\sigma}_b}\mathbf{E}^a\right)=\mathbf{\nabla}\times\left(\frac{\Delta\widetilde{\sigma}}{\widetilde{\sigma}_b}\mathbf{E}^b\right).\tag{6.203}$$

Calculating the anomalous electric field from the second Maxwell's equation, and substituting it back into (6.203), we can cast the magnetic field equation in the form

$$\mathbf{\nabla}\times\left(\frac{1}{\widetilde{\sigma}}\mathbf{\nabla}\times\mathbf{H}^a\right)-i\omega\mu\mathbf{H}^a=\mathbf{\nabla}\times\left(\frac{\Delta\widetilde{\sigma}}{\widetilde{\sigma}}\mathbf{E}^b\right).\tag{6.204}$$

In the case of the quasi-stationary field, Eqs. (6.203) and (6.204) can be written as follows:

$$\mu\mathbf{\nabla}\times\left(\frac{1}{\mu}\mathbf{\nabla}\times\mathbf{E}^a\right)-k^2\mathbf{E}^a=i\omega\mu\Delta\sigma\mathbf{E}^b,$$

$$\sigma\mathbf{\nabla}\times\left(\frac{1}{\sigma}\mathbf{\nabla}\times\mathbf{H}^a\right)-k^2\mathbf{H}^a=\sigma\mathbf{\nabla}\times\left(\frac{\Delta\sigma}{\sigma}\mathbf{E}^b\right).\tag{6.205}$$

We can use the Dirichlet boundary-value conditions (6.197), asymptotic boundary conditions (6.198), or absorbing boundary conditions in the formulation of the boundary-value problem for an anomalous electromagnetic field.

6.4.2 ELECTROMAGNETIC POTENTIAL EQUATIONS AND BOUNDARY CONDITIONS

Another approach to the formulation of electromagnetic boundary-value problem is to use the electromagnetic potentials introduced in Chapter 4. This approach has been used in a number of publications on numerical electromagnetic methods (Biro and Preis, 1990; Everett and Schultz, 1996; Everett, 1999; Haber et al., 2000).

In the framework of this approach we solve the corresponding second order partial differential equations for the electromagnetic potentials, $\mathbf{A}$ and U:

$$\nabla^2\mathbf{A}+\mu_0\widetilde{\sigma}\left(i\omega\mathbf{A}-\mathbf{\nabla}U\right)=-\mu_0\mathbf{j}^e,$$

$$\mathbf{\nabla}\cdot\left[\widetilde{\sigma}\left(i\omega\mathbf{A}-\mathbf{\nabla}U\right)\right]=-\mathbf{\nabla}\cdot\mathbf{j}^e.\tag{6.206}$$

The electromagnetic field is expressed in terms of these potentials by:

$$\mathbf{E} = i\omega\mathbf{A} - \nabla U, \tag{6.207}$$

$$\mathbf{H} = \frac{1}{\mu_0}\nabla \times \mathbf{A}, \tag{6.208}$$

where the vector potential $\mathbf{A}$ satisfies the Coulomb gauge condition

$$\nabla \cdot \mathbf{A} = 0. \tag{6.209}$$

The advantage of this approach is in the simplicity of both the potential equations and the boundary-value conditions. Biro and Preis (1990) demonstrated that the Coulomb gauge can be enforced by the following boundary-value condition on the surface ∂V of the modeling region:

$$\mathbf{A} \cdot \mathbf{n}|_{\partial V} = 0. \tag{6.210}$$

This condition is motivated by the integral identity

$$\iiint_V \nabla \cdot \mathbf{A} dv = \iint_{\partial V} \mathbf{A} \cdot \mathbf{n} ds. \tag{6.211}$$

Due to the Coulomb gauge, the volume integral on the left-hand side of (6.211) is equal to zero. The boundary condition (6.210) provides the same result as well.

Similar to the field separation into the background and anomalous parts, one can represent the electromagnetic potentials as the sums of the corresponding potentials for the background and anomalous fields:

$$\mathbf{A} = \mathbf{A}^b + \mathbf{A}^a, \ U = U^b + U^a, \tag{6.212}$$

where

$$\mathbf{E}^b = i\omega\mathbf{A}^b - \nabla U^b, \ \mathbf{E}^a = i\omega\mathbf{A}^a - \nabla U^a. \tag{6.213}$$

The anomalous field potentials satisfy the equations obtained from Eqs. (6.206) by substituting the excess electric current $\mathbf{j}^a$, Eq. (6.201), for the extraneous electric current $\mathbf{j}^e$, and the background conductivity $\widetilde{\sigma}_b$ for the total conductivity $\widetilde{\sigma}$:

$$\nabla^2\mathbf{A}^a + \mu_0\widetilde{\sigma}_b\left(i\omega\mathbf{A}^a - \nabla U^a\right) = -\mu_0\mathbf{j}^a,$$
$$\nabla \cdot \left[\widetilde{\sigma}_b\left(i\omega\mathbf{A}^a - \nabla U^a\right)\right] = -\nabla \cdot \mathbf{j}^a. \tag{6.214}$$

Taking into account expressions (6.201) and (6.213), we obtain

$$\nabla^2\mathbf{A}^a + \mu_0\widetilde{\sigma}\left(i\omega\mathbf{A}^a - \nabla U^a\right) = -\mu_0\Delta\widetilde{\sigma}\mathbf{E}^b,$$
$$\nabla \cdot \left[\widetilde{\sigma}\left(i\omega\mathbf{A}^a - \nabla U^a\right)\right] = -\nabla \cdot \Delta\widetilde{\sigma}\mathbf{E}^b. \tag{6.215}$$

The formulation of the boundary-value problem for potentials is completed by adding the corresponding boundary conditions:

$$\mathbf{A} \cdot \mathbf{n}|_{\partial V} = 0, \ \text{and} \ \left.\frac{\partial U}{\partial n}\right|_{\partial V} = 0. \tag{6.216}$$
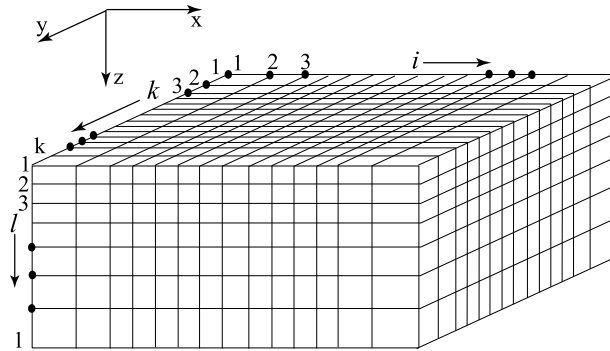
FIGURE 6.4

The model region is discretized into a number of prisms. The indices i, k, and l are used to number the grid point in the x, y, and z directions, respectively. Electromagnetic parameters, σ, μ, and ε, are assumed to be constant within each elementary prism.

Thus, in this case we have to solve the boundary-value problem for two electromagnetic potentials, vector and scalar, simultaneously.

6.4.3 FINITE DIFFERENCE APPROXIMATION OF BOUNDARY-VALUE PROBLEM

The finite difference method provides a simple but effective tool for numerically solving the electromagnetic boundary-value problem (Weaver and Brewitt-Taylor, 1978; Zhdanov et al., 1982; Zhdanov and Spichak, 1992; Weaver, 1994; Mackie et al., 1993, 1994; Smith, 1996; Zhdanov et al., 1997). It is based on a replacement of the differential operators in Eqs. (6.191), (6.193), (6.203), (6.205), (6.206), and (6.215) by the finite difference operators, acting on the discrete values of the electromagnetic field. There are several ways to obtain the discrete analogs of Maxwell's equations. In the vast majority of finite difference algorithms, the model region is discretized into a number of prisms as shown in Fig. 6.4.

A Cartesian coordinate system is defined with the z axis directed downward, and the x axis directed to the right. The indices i, k, and l are used to number the grid point in x, y, and z directions, respectively. The electromagnetic parameters, σ, μ, and ε, are assumed to be constant within each elementary prism. We denote this grid by $\sum$:

$$\sum = \left\{ (x_i, y_k, z_l) \begin{array}{lll} x_1 = x', & x_{N_I} = x'', & x_{i+1} = x_i + \Delta x_i, \\ & & i = 1, 2, ..., N_I \\ y_1 = y', & y_{N_K} = y'', & y_{k+1} = y_k + \Delta y_k, \\ & & k = 1, 2, ..., N_K \\ \\ z_1 = z', & z_{N_L} = z'', & z_{l+1} = z_l + \Delta z_l, \\ & & l = 1, 2, ..., N_L \end{array} \right\}.$$
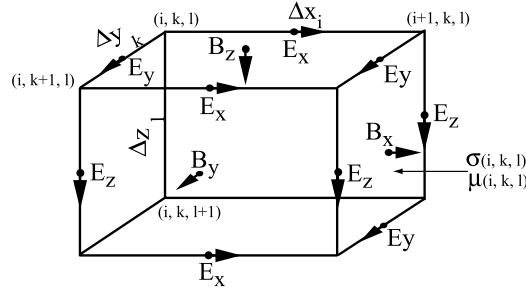
FIGURE 6.5

Discretization of the electromagnetic field on a staggered grid, according to Yee (1966) and Wang and Hohmann (1993). The electric field components, parallel to the corresponding edges, are sampled at the centers of the prism edges, while the magnetic field components, orthogonal to corresponding faces, are sampled at the centers of the prism faces.

6.4.4 DISCRETIZATION OF MAXWELL'S EQUATIONS USING A STAGGERED GRID

One common technique of field discretization is based on a staggered-grid scheme (Yee, 1966; Wang and Hohmann, 1993), which is effective in solving the coupled first order Maxwell's equations. On a staggered grid, the electric field components, parallel to the corresponding edges, are sampled at the centers of the prism edges, while the magnetic field components, orthogonal to corresponding faces, are sampled at the centers of the prism faces, as shown in Fig. 6.5. The advantage of the staggered grid is that the corresponding components of the electric field $\mathbf{E}$ and magnetic field $\mathbf{B} = \mu\mathbf{H}$, selected above, are continuous on the edges and faces of the homogeneous prisms. Thus, the staggered grid is composed of two elementary loops (Wang and Hohmann, 1993): the electric loop is formed by four $\mathbf{E}$ components parallel to the edges of one face of a prism, and the magnetic loop is composed of four adjacent $\mathbf{B}$ components, as shown in Fig. 6.6. The concept of electric and magnetic loops in a staggered grid is useful in discretizing the Maxwell's equations. For example, from the second Maxwell's equation (6.194) we have

$$\mathbf{B} = \frac{1}{i\omega} \nabla \times \mathbf{E}. \tag{6.217}$$

Integrating this equation over a face S of the prism, bounded by a rectangular contour L, and using Stokes's theorem, we find

$$\iint_S \mathbf{B} \cdot \mathbf{n} ds = \frac{1}{i\omega} \iint_S (\nabla \times \mathbf{E}) \cdot \mathbf{n} ds = \frac{1}{i\omega} \int_L \mathbf{E} \cdot \boldsymbol{\tau} dl, \tag{6.218}$$

where $\mathbf{n}$ is a unit vector, normal to the prism face, S, and $\boldsymbol{\tau}$ is the corresponding unit vector tangential to the prism edges, L; the directions of $\mathbf{n}$ and $\boldsymbol{\tau}$ are consistent with the corkscrew rule, i.e., with a corkscrew rotating in the direction $\boldsymbol{\tau}$, the point moves in the direction $\mathbf{n}$. We can evaluate the integrals in Eq. (6.218) approximately in terms of the discretized functions of the electric and magnetic fields. For node (i, k, l), the x, y, and z components of electric field $\mathbf{E}$ are sampled at $(i + \frac{1}{2}, k, l)$, $(i, k + \frac{1}{2}, l)$,
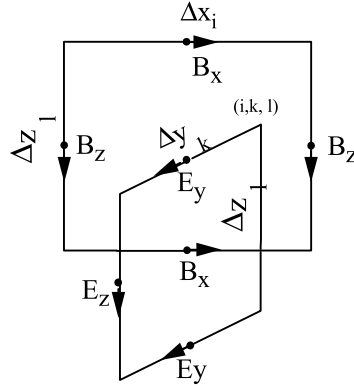
FIGURE 6.6

The concept of electric and magnetic loops in a staggered grid in discretizing Maxwell's equations (according to Wang and Hohmann, 1993). The electric loop is formed by four **E** components parallel to the edges of one face of a prism, and the magnetic loop is composed of four adjacent **B** components.

and $(i, k, l + \frac{1}{2})$, respectively, and the x, y, and z components of magnetic field **B** are sampled at $(i, k + \frac{1}{2}, l + \frac{1}{2})$, $(i + \frac{1}{2}, k, l + \frac{1}{2})$, and $(i + \frac{1}{2}, k + \frac{1}{2}, l)$, respectively. For example, at a prism face parallel to the vertical plane xz (see Fig. 6.6) the discrete version of the integral equation (6.218) is as follows:

$$i\omega B_x \left(i, k + \frac{1}{2}, l + \frac{1}{2} \right) \Delta y_k \Delta z_l = \left[E_y \left(i, k + \frac{1}{2}, l \right) - E_y \left(i, k + \frac{1}{2}, l + 1 \right) \right] \Delta y_k$$
$$+ \left[E_z \left(i, k + 1, l + \frac{1}{2} \right) - E_z \left(i, k, l + \frac{1}{2} \right) \right] \Delta z_l. \tag{6.219}$$

Similar algebraic expressions can be obtained for other faces of an elementary prism. We derive analogous formulae by numerically integrating the first Maxwell's equation. Combining all these algebraic equations together, we arrive at a full system of linear equations for the discretized values of the electromagnetic field on a staggered grid.

Note that in practical implementation it is useful to transform an unequally gridded model into one that is equally gridded by making appropriate transformations of the size of the cells, the conductivity and permeability, and the field values (Madden and Mackie, 1989). Following Mackie et al. (1993), we denote the transformed parameters by a prime superscript, and introduce the scaling factors for the transformation as

$$p_x = \frac{\Delta x}{\Delta x'}, \quad p_y = \frac{\Delta y}{\Delta y'}, \quad p_z = \frac{\Delta z}{\Delta z'}. \tag{6.220}$$

We can introduce now the transformed conductivity and magnetic permeability tensors as

$$\widehat{\boldsymbol{\sigma}}' = \begin{bmatrix} \sigma p_y p_z / p_x & 0 & 0 \\ 0 & \sigma p_x p_z / p_y & 0 \\ 0 & 0 & \sigma p_x p_y / p_z \end{bmatrix}, \tag{6.221}$$

$$\widehat{\boldsymbol{\mu}}' = \begin{bmatrix} \mu p_y p_z / p_x & 0 & 0 \\ 0 & \mu p_x p_z / p_y & 0 \\ 0 & 0 & \mu p_x p_y / p_z \end{bmatrix}. \tag{6.222}$$

In the majority of geophysical applications we assume that the medium is isotropic. However, in some important practical cases, for example in well-logging, anisotropic properties of the rock formations can play a significant role. In this case we can easily generalize the staggered grid technique for anisotropic models by taking into account the tensor character of the conductivity and permeability and applying formulae similar to (6.221)–(6.222):

$$\widehat{\boldsymbol{\sigma}}' = \begin{bmatrix} \sigma_{xx} p_y p_z / p_x & 0 & 0 \\ 0 & \sigma_{yy} p_x p_z / p_y & 0 \\ 0 & 0 & \sigma_{zz} p_x p_y / p_z \end{bmatrix}, \tag{6.223}$$

$$\widehat{\boldsymbol{\mu}}' = \begin{bmatrix} \mu_{xx} p_y p_z / p_x & 0 & 0 \\ 0 & \mu_{yy} p_x p_z / p_y & 0 \\ 0 & 0 & \mu_{zz} p_x p_y / p_z \end{bmatrix}. \tag{6.224}$$

In the last formulae we assume that $\sigma_{xx}, \sigma_{yy}, \sigma_{zz}$ and $\mu_{xx}, \mu_{yy}, \mu_{zz}$ are the principal values of the conductivity and permeability tensors, and the axes of the grid are oriented along the principal axes of these tensors.

As a result of scaling we obtain a system of linear equations for discretized values of the electromagnetic field on a staggered grid,

$$(\mathbf{D}_s + i\omega\boldsymbol{\mu}\boldsymbol{\sigma})\,\mathbf{e} = i\omega\boldsymbol{\mu}\mathbf{c}, \tag{6.225}$$

where $\mathbf{e}$ is the $3N$ vector (N is the number of the mesh nodes) of unknown values of the electric field; $\boldsymbol{\sigma}$ and $\boldsymbol{\mu}$ are the diagonal matrices of the conductivities and permeabilities in the cells of the grid; $\mathbf{D}_s$ is the complex-symmetric $3N \times 3N$ matrix of coefficients for the system, which is independent of frequency, ω and sparse with 13 nonzero entries per row; and $\mathbf{c}$ is the vector of free terms, determined by the source and the boundary-value conditions.

The choice of an efficient method of solving the linear system of FD equations is crucial in order to minimize the execution time of forward modeling algorithms. Fast solutions of large algebraic systems arising in 3D frequency domain electromagnetic modeling are known to be of major importance in geophysical applications. This is especially important for EM inversion requiring sequential solution of multiple forward problems. Recently, significant advances have been made in developing the direct solvers for forward EM problems (e.g., Streich, 2009; da Silva et al., 2012; Grayver et al., 2013; Jaysaval et al., 2014). However, the direct solvers still impose challenging memory requirements for large-scale 3D problems, which makes the iterative solvers more attractive in geophysical applications (Saad, 2003).

The system of Eqs. (6.225) is sparse, complex, and generally quite large. Beyond that, the system is very ill conditioned due to the large ratio of the size of the computational domain to the smallest grid step (Druskin and Knizhnerman, 1994), and to the presence of a highly resistive air layer.

An important consideration in numerical modeling is control of the accuracy. Errors in modeling, in general, are caused by errors of three types:

- 1) those due to the approximation involved in replacing a continuous function by a discretized function,
- 2) those that arise in the solution of the finite difference equations, and
- 3) those involved in numerical differentiation of the numerical results to obtain the field components that are not discretized (the magnetic field in the solution of the electric field equation, and the electric field in the solution of the magnetic field equation).

The most effective check on computational errors of all three types is a criterion based on the integral relationships between the fields within the region of anomalous conductivity V_a and at the surface of the earth. For example, the electric field at the observation points, $\mathbf{r}_j$, must satisfy the condition

$$\mathbf{E}\left(\mathbf{r}_j\right) = \iiint_{V_a} \widehat{\mathbf{G}}_E\left(\mathbf{r}_j \mid \mathbf{r}\right) \cdot \Delta\sigma\left(\mathbf{r}\right)\mathbf{E}\left(\mathbf{r}\right)dv + \mathbf{E}^b\left(\mathbf{r}_j\right),\qquad (6.226)$$

where $\widehat{\mathbf{G}}_E$ is the electric Green's tensor for the background (normal) conductivity model.

Substituting the values for the electric field obtained from a finite difference computation scheme into the right hand part of Eq. (6.226) and then integrating numerically, we can compare the result obtained, $\mathbf{E}^{int}$, with the finite difference solution, $\mathbf{E}^{f-d}$, at the observation points, and establish a criterion for the accuracy of the modeling:

$$\parallel \mathbf{E}^{int} - \mathbf{E}^{f-d} \parallel / \parallel \mathbf{E}^{f-d} \parallel \leq \epsilon.\qquad (6.227)$$

In essence, the use of this criterion establishes agreement between a solution obtained by finite difference modeling and a solution obtained by the integral equation method.

6.4.5 CONTRACTION PRECONDITIONER FOR A SYSTEM OF FD EQUATIONS

It is also convenient to consider the finite difference solution for the anomalous fields only, because this approach provides a relatively simple way of incorporating different types of sources in the EM modeling. We have demonstrated above in Eq. (6.205), that the anomalous electric field, $\mathbf{E}^a(x, y, z)$ satisfies the following partial differential equation (if $\mu = \mu_0$):

$$\nabla \times \nabla \times \mathbf{E}^a - i\omega\mu_0\sigma\,\mathbf{E}^a = i\omega\mu_0\sigma_a\,\mathbf{E}^b,\qquad (6.228)$$

where ω is the source angular frequency, μ_0 is the magnetic permeability of the free space, $\sigma(x, y, z)$ and $\sigma_a(x, y, z)$ are the total and anomalous conductivities respectively, and $\mathbf{E}^b(x, y, z)$ is the background electric field due to a 1D background conductivity model $\sigma_b(z)$. The equation has to be solved for $\mathbf{E}^a(x, y, z)$ numerically in some bounded domain and completed with zero Dirichlet boundary con-

ditions. We also assume that the following double inequality holds,

$$\alpha\sigma_b(z) \leq \sigma(x, y, z) \leq \beta\sigma_b(z), 0 < \alpha \leq 1 \leq \beta, \tag{6.229}$$

which controls the contrast of anomalous conductivity with respect to the background.

Given a computational grid with $N_x \times N_y \times N_z$ cells, we apply a conventional FD discretization on a staggered grid, as was done above (Yee, 1966; Yavich and Zhdanov, 2016). Introducing the diagonal matrices of discrete conductivities for the total, background, and anomalous models, $\widehat{\sigma} = \widehat{\sigma}_b + \widehat{\sigma}_a$,

$$\widehat{\sigma} = \mathbf{diag}\,(\sigma_1, \sigma_2, ..., \sigma_N, \sigma_1, \sigma_2, ..., \sigma_N, \sigma_1, \sigma_2, ..., \sigma_N)\,,$$

$$\widehat{\sigma}_a = \mathbf{diag}\,(\sigma_{a1}, \sigma_{a2}, ..., \sigma_{aN}, \sigma_{a1}, \sigma_{a2}, ..., \sigma_{aN}, \sigma_{a1}, \sigma_{a2}, ..., \sigma_{aN})\,,$$

$$\widehat{\sigma}_b = \mathbf{diag}\,(\sigma_{b1}, \sigma_{b2}, ..., \sigma_{bN}, \sigma_{b1}, \sigma_{b2}, ..., \sigma_{bN}, \sigma_{b1}, \sigma_{b2}, ..., \sigma_{bN})\,,$$

and as well as the respective discrete electric fields, $\mathbf{e} = \mathbf{e}^a + \mathbf{e}^b$, one can write a discrete form of Eq. (6.228) for anomalous electric field as follows:

$$\widehat{\mathbf{A}}\mathbf{e}^a = i\omega\mu_0\widehat{\sigma}_a\mathbf{e}^b, \tag{6.230}$$

where $\widehat{\mathbf{A}}$ is a square system matrix corresponding to the total conductivity. For layered background models, $\mathbf{e}^b$ can be computed by averaging its analytical counterpart. We denote the size of this system as $n \approx 3N_x \times N_y \times N_z$.

As discussed in section 6.4.4, the most effective way of solving the matrix equation (6.230) for large-scale problems is based on iterative methods and the use of the corresponding preconditioners. For example, Zaslavsky et al. (2011) suggested using a volume integral equation approach to arrive at an effective preconditioning operator for the FD solver for the magnetic field.

Let $\widehat{\mathbf{A}}_b$ be the FD system matrix, corresponding to the background conductivity model. Importantly, this matrix can be implicitly factorized, and the action of the inverse matrix can be efficiently computed (Zaslavsky et al., 2011; Yavich and Zhdanov, 2016). As a result, the inverse matrix, $\widehat{\mathbf{A}}_b^{-1}$, can be used as a preconditioner to matrix equation (6.230):

$$\widehat{\mathbf{A}}_b^{-1}\widehat{\mathbf{A}}\mathbf{e}^a = i\omega\mu_0\widehat{\mathbf{A}}_b^{-1}\widehat{\sigma}_a\mathbf{e}^b. \tag{6.231}$$

We will refer to the inverse matrix, $\widehat{\mathbf{A}}_b^{-1}$ as the Green's function (GF) preconditioner, because it is linear proportional to a matrix of the discrete Green's operator for the background media, $\widehat{\mathbf{G}}_b$, (Yavich and Zhdanov, 2016):

$$\widehat{\mathbf{G}}_b = i\omega\mu_0\widehat{\mathbf{A}}_b^{-1}. \tag{6.232}$$

The complexity of applying the GF preconditioner is $O(n^{4/3})$, and auxiliary memory required is near $3n$ only. Applying the analysis presented in Yavich and Zhdanov (2016), the spectral condition number of the GF preconditioned system can be estimated as follows:

$$cond(\widehat{\mathbf{A}}_b^{-1}\widehat{\mathbf{A}}) \leq \beta/\alpha. \tag{6.233}$$

This result implies that convergence of an iterative solver applied to (6.231) has minor or no dependence on the grid size and the aspect ratio of the cells, as well as the frequency, while it degrades on models with high-contrast bodies.

To minimize the impact of high conductivity contrasts, another preconditioner could be constructed. We can follow the paper by Yavich and Zhdanov (2016) and apply FD contraction operator similar to one introduced in Hursán and Zhdanov (2002) and Zhdanov (2002) for the IE method.

Let us define a matrix of the modified FD Green's operator, $\widehat{\mathbf{G}}_b^M$, and diagonal matrices, $\widehat{\mathbf{K}}_1$ and $\widehat{\mathbf{K}}_2$, according to the following formulae:

$$\widehat{\mathbf{G}}_b^M = 2i\omega\mu\widehat{\boldsymbol{\sigma}}_b^{1/2}\widehat{\mathbf{A}}_b^{-1}\widehat{\boldsymbol{\sigma}}_b^{1/2} + \widehat{\mathbf{I}},$$

$$\widehat{\mathbf{K}}_1 = \frac{1}{2}(\widehat{\boldsymbol{\sigma}} + \widehat{\boldsymbol{\sigma}}_b)\widehat{\boldsymbol{\sigma}}_b^{-1/2}, \quad \widehat{\mathbf{K}}_2 = \frac{1}{2}(\widehat{\boldsymbol{\sigma}} - \widehat{\boldsymbol{\sigma}}_b)\widehat{\boldsymbol{\sigma}}_b^{-1/2}. \tag{6.234}$$

Using these notations, Eq. (6.231) can be written in an equivalent form as follows:

$$\widehat{\mathbf{e}}^a = \widehat{\mathbf{G}}_b^M\widehat{\mathbf{K}}_2\widehat{\mathbf{K}}_1^{-1}\widehat{\mathbf{e}}^a + i\omega\mu_0\widehat{\boldsymbol{\sigma}}_b^{1/2}\widehat{\mathbf{A}}_b^{-1}\widehat{\boldsymbol{\sigma}}_a\mathbf{e}^b, \tag{6.235}$$

where

$$\widehat{\mathbf{e}}^a = \widehat{\mathbf{K}}_1\mathbf{e}^a. \tag{6.236}$$

By introducing a new operator,

$$\mathbf{C} = \mathbf{G}_b^M\mathbf{K}_2\mathbf{K}_1^{-1}, \tag{6.237}$$

we rewrite system (6.235) as follows:

$$(\mathbf{I} - \mathbf{C})\widehat{\mathbf{e}}^a = i\omega\mu_0\widehat{\boldsymbol{\sigma}}_b^{1/2}\widehat{\mathbf{A}}_b^{-1}\widehat{\boldsymbol{\sigma}}_a\mathbf{e}^b. \tag{6.238}$$

We will refer to this system as a contraction operator (CO) preconditioned system, since it was shown in Yavich and Zhdanov (2016) that $\mathbf{C}$ is a contraction operator for media of any contrast, $\|\mathbf{C}\| < 1$. Moreover, it can be proved that this preconditioned system has a smaller or equal spectral condition number than that of the GF preconditioner, implying faster or equal convergence of the corresponding iterative solvers,

$$cond(\mathbf{I} - \mathbf{C}) \leq max\{1/\alpha, \beta\}. \tag{6.239}$$

The complexity of applying the CO preconditioner is $O(n^{4/3})$ as well.

This preconditioner represents an FD analog of the preconditioner of the system of the EM integral equations based on the contraction operator, discussed in section 6.1.6. The FD contraction preconditioner can be easily constructed using the known conductivity distribution in the model. This preconditioner makes it possible to speed up the convergence of the iterative solvers of the FD equations significantly

6.4.6 DISCRETIZATION OF THE ELECTROMAGNETIC POTENTIAL DIFFERENTIAL EQUATIONS

We can use a staggered grid approach for discretizing the equations for electromagnetic potentials. We begin with the analysis of Eqs. (6.215). Following the basic principles of the balance method, we
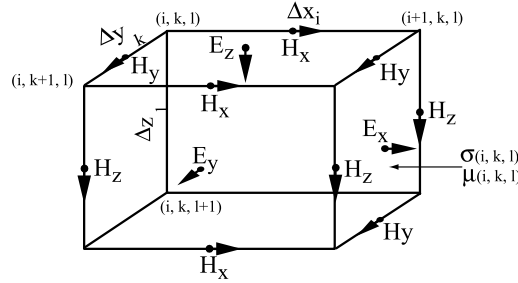
FIGURE 6.7

The staggered grid for electromagnetic field discretization in the electromagnetic potential method. The normal components of electric field **E** are defined at the centers of the cell faces, while the tangential components of magnetic field **H** are defined on the cell edges.

integrate these equations over an elementary cell V_{ikl} of the mesh $\sum$, and apply Gauss's theorem to the volume integral containing Laplacian and divergence operators:

$$\iint_{S_{ikl}} (\mathbf{n} \cdot \nabla) \mathbf{A}^a ds + \mu_0 \iiint_{V_{ikl}} \tilde{\sigma} \left(i\omega\mathbf{A}^a - \nabla U^a \right) dv = -\mu_0 \iiint_{V_{ikl}} \Delta\tilde{\sigma}\mathbf{E}^b dv,$$

$$\iint_{S_{ikl}} \tilde{\sigma} \left(i\omega\mathbf{A}^a - \nabla U^a \right) \cdot \mathbf{n} ds = - \iint_{S_{ikl}} \Delta\tilde{\sigma}\mathbf{E}^b \cdot \mathbf{n} ds, \qquad (6.240)$$

where S_{ikl} is the rectangular boundary of the cell V_{ikl}, and $\mathbf{n}$ is the unit vector normal to it, directed outward.

For the field and potential discretization, we will use the same staggered technique on the grid $\sum$ introduced above. However, now we assume that the normal components of electric field $\mathbf{E}^a$ are defined at the centers of the cell faces, while the tangential components of magnetic field $\mathbf{H}^a$ are defined on the cell edges, as it shown in Fig. 6.7. In other words, we introduce the discrete electric field functions

$$E^x_{i,k+\frac{1}{2},l+\frac{1}{2}} = E^a_x(x_i, y_{k+\frac{1}{2}}, z_{l+\frac{1}{2}}),$$
$$E^y_{i+\frac{1}{2},k,l+\frac{1}{2}} = E^a_y(x_{i+\frac{1}{2}}, y_k, z_{l+\frac{1}{2}}),$$
$$E^z_{i+\frac{1}{2},k+\frac{1}{2},l} = E^a_x(x_{i+\frac{1}{2}}, y_{k+\frac{1}{2}}, z_l),$$

and discrete vector potential and gradient of the scalar potential functions,

$$A^x_{i,k+\frac{1}{2},l+\frac{1}{2}} = A^a_x(x_i, y_{k+\frac{1}{2}}, z_{l+\frac{1}{2}}),$$
$$A^y_{i+\frac{1}{2},k,l+\frac{1}{2}} = A^a_y(x_{i+\frac{1}{2}}, y_k, z_{l+\frac{1}{2}}),$$
$$A^z_{i+\frac{1}{2},k+\frac{1}{2},l} = A^a_x(x_{i+\frac{1}{2}}, y_{k+\frac{1}{2}}, z_l),$$

and

$$U^x_{i,k+\frac{1}{2},l+\frac{1}{2}} = \nabla_x U^a(x_i, y_{k+\frac{1}{2}}, z_{l+\frac{1}{2}}) = \frac{U^a(x_{i+1}, y_{k+\frac{1}{2}}, z_{l+\frac{1}{2}}) - U^a(x_i, y_{k+\frac{1}{2}}, z_{l+\frac{1}{2}})}{\Delta x_i},$$

$$U^y_{i+\frac{1}{2},k,l+\frac{1}{2}} = \nabla_y U^a(x_{i+\frac{1}{2}}, y_k, z_{l+\frac{1}{2}}) = \frac{U^a(x_{i+\frac{1}{2}}, y_{k+1}, z_{l+\frac{1}{2}}) - U^a(x_{i+\frac{1}{2}}, y_k, z_{l+\frac{1}{2}})}{\Delta y_k}$$

$$U^z_{i+\frac{1}{2},k+\frac{1}{2},l} = \nabla_z U^a(x_{i+\frac{1}{2}}, y_{k+\frac{1}{2}}, z_l) = \frac{U^a(x_{i+\frac{1}{2}}, y_{k+\frac{1}{2}}, z_{l+1}) - U^a(x_{i+\frac{1}{2}}, y_{k+\frac{1}{2}}, z_l)}{\Delta z_l},$$

at the centers of the cell faces. The discrete conductivity functions $\widetilde{\sigma}_{i+\frac{1}{2},k+\frac{1}{2},l+\frac{1}{2}} = \widetilde{\sigma}(x_{i+\frac{1}{2}}, y_{k+\frac{1}{2}}, z_{l+\frac{1}{2}})$ and $\Delta\widetilde{\sigma}_{i+\frac{1}{2},k+\frac{1}{2},l+\frac{1}{2}} = \Delta\widetilde{\sigma}(x_{i+\frac{1}{2}}, y_{k+\frac{1}{2}}, z_{l+\frac{1}{2}})$ are defined on the dual rectangular, uneven three-dimensional mesh $\widetilde{\sum}$, introduced above.

We can evaluate now the volume and surface integrals in Eq. (6.240) approximately in terms of the discretized functions. This can be achieved by using the following relationships:

$$\mu_0 \iiint_{V_{ikl}} \widetilde{\sigma}\left(i\omega\mathbf{A}^a - \nabla U^a\right) dv \approx \frac{1}{2}\mu_0\widetilde{\sigma}_{i+\frac{1}{2},k+\frac{1}{2},l+\frac{1}{2}} \times$$

$$\times \left(i\omega \begin{pmatrix} A^x_{i,k+\frac{1}{2},l+\frac{1}{2}} + A^x_{i+1,k+\frac{1}{2},l+\frac{1}{2}} \\ A^y_{i+\frac{1}{2},k,l+\frac{1}{2}} + A^y_{i+\frac{1}{2},k+1,l+\frac{1}{2}} \\ A^z_{i+\frac{1}{2},k+\frac{1}{2},l} + A^z_{i+\frac{1}{2},k+\frac{1}{2},l+1} \end{pmatrix} - \begin{pmatrix} U^x_{i,k+\frac{1}{2},l+\frac{1}{2}} + U^x_{i+1,k+\frac{1}{2},l+\frac{1}{2}} \\ U^y_{i+\frac{1}{2},k,l+\frac{1}{2}} + U^y_{i+\frac{1}{2},k+1,l+\frac{1}{2}} \\ U^z_{i+\frac{1}{2},k+\frac{1}{2},l} + U^z_{i+\frac{1}{2},k+\frac{1}{2},l+1} \end{pmatrix} \right) V_{ikl}. \quad (6.241)$$

The surface integrals are computed using a simple difference form. For example:

$$\iint_{S_{ikl}} (\mathbf{n} \cdot \nabla)\mathbf{A}^a ds = \iint_{S_{ikl}} \frac{\partial \mathbf{A}^a}{\partial n} ds, \quad (6.242)$$

where the derivative $\partial\mathbf{A}^a/\partial n$ can be computed using a simple finite difference form.

Finally,

$$\iint_{S_{ikl}} \widetilde{\sigma}\left(i\omega\mathbf{A}^a - \nabla U^a\right) \cdot \mathbf{n} ds \approx$$

$$\left[\widetilde{\sigma}_{i+1,kl}\left(i\omega A^x_{i+1,k+\frac{1}{2},l+\frac{1}{2}} - U^x_{i+1,k+\frac{1}{2},l+\frac{1}{2}}\right) - \widetilde{\sigma}_{ikl}\left(i\omega A^x_{i,k+\frac{1}{2},l+\frac{1}{2}} - U^x_{i,k+\frac{1}{2},l+\frac{1}{2}}\right)\right] S^x_{ikl}$$

$$+ \left[\widetilde{\sigma}_{i,k+1,l}\left(i\omega A^y_{i+\frac{1}{2},k+1,l+\frac{1}{2}} - U^y_{i+\frac{1}{2},k+1,l+\frac{1}{2}}\right) - \widetilde{\sigma}_{ikl}\left(i\omega A^y_{i+\frac{1}{2},k,l+\frac{1}{2}} - U^y_{i+\frac{1}{2},k,l+\frac{1}{2}}\right)\right] S^y_{ikl}$$

$$+ \left[\widetilde{\sigma}_{ik,l+1}\left(i\omega A^z_{i+\frac{1}{2},k+\frac{1}{2},l+1} - U^z_{i+\frac{1}{2},k+\frac{1}{2},l+1}\right) - \widetilde{\sigma}_{ikl}\left(i\omega A^z_{i+\frac{1}{2},k+\frac{1}{2},l} - U^z_{i+\frac{1}{2},k+\frac{1}{2},l}\right)\right] S^z_{ikl},$$

where S^x_{ikl}, S^y_{ikl}, S^z_{ikl} are the areas of the x, y, and z faces of the elementary prismatic cell of the grid $\sum$.

The resulting system of linear algebraic equations and the accompanying boundary conditions for vector and scalar potentials can be expressed using matrix notations as

$$
\begin{bmatrix} \mathbf{D}_{1A} + i\omega\mathbf{D}_{2A} & \mathbf{D}_{1U} \\ i\omega\mathbf{D}_{3A} & \mathbf{D}_{2U} \end{bmatrix} \begin{bmatrix} \mathbf{a} \\ \mathbf{u} \end{bmatrix} = \begin{bmatrix} \mathbf{c}_A \\ \mathbf{c}_U \end{bmatrix},
\tag{6.243}
$$

where $\mathbf{a}$ is the vector of unknown values of the vector potential

$$
\left(A^x_{i,k+\frac{1}{2},l+\frac{1}{2}}, A^y_{i+\frac{1}{2},k,l+\frac{1}{2}}, A^z_{i+\frac{1}{2},k+\frac{1}{2},l} \right),
$$

$\mathbf{u}$ is the vector of unknown values of the scalar potential

$$
\left(U^a_{i,k+\frac{1}{2},l+\frac{1}{2}}, U^a_{i+\frac{1}{2},k,l+\frac{1}{2}}, U^a_{i+\frac{1}{2},k+\frac{1}{2},l} \right);
$$

$\mathbf{D}_{1A}, \mathbf{D}_{2A}, \mathbf{D}_{3A}, \mathbf{D}_{1U}$, and $\mathbf{D}_{2U}$ are the corresponding matrices of coefficients for the system, which are independent of frequency, ω; and $\mathbf{c}_A$, $\mathbf{c}_U$ are the vectors of free terms, determined by the background field and the anomalous conductivity. The system (6.243) is solved using one of the methods of linear algebra. The electric field components are determined from the simple formula:

$$
\begin{aligned}
E^x_{i,k+\frac{1}{2},l+\frac{1}{2}} &= i\omega A^x_{i,k+\frac{1}{2},l+\frac{1}{2}} - U^x_{i,k+\frac{1}{2},l+\frac{1}{2}}, \\
E^y_{i+\frac{1}{2},k,l+\frac{1}{2}} &= i\omega A^y_{i+\frac{1}{2},k,l+\frac{1}{2}} - U^y_{i+\frac{1}{2},k,l+\frac{1}{2}}, \\
E^z_{i+\frac{1}{2},k+\frac{1}{2},l} &= i\omega A^z_{i+\frac{1}{2},k+\frac{1}{2},l} - U^z_{i+\frac{1}{2},k+\frac{1}{2},l}.
\end{aligned}
$$

The magnetic field on the staggered grid is computed using formulae similar to (6.219). The calculation for the magnetic field completes the numerical algorithm of electromagnetic modeling based on electromagnetic potentials.

6.4.7 FINITE ELEMENT SOLUTION OF BOUNDARY-VALUE PROBLEMS

The method of finite elements is one of the most powerful techniques for numerical solution of boundary-value problems. The mathematical literature on the finite element method contains hundreds of publications. The foundations of this technique can be found in Tong and Rossettos (1977), Zienkiewicz and Taylor (1989), and Beltzer (1990). The method is based on a division of the modeling region into a number of comparatively small subregions (finite elements) and an approximation of the unknown function within each element as a combination of some basis functions. There are many different versions of the finite element method, depending on the type of the basis functions and the techniques for determining the coefficients of the basis function expansions. I will present here a technique based on the Galerkin method.

We introduce a complex Hilbert space $L_2(V)$ of the vector functions determined in the modeling region V and integrable in V with an inner product:

$$
(\mathbf{x}, \mathbf{y})_{L_2(V)} = \iiint_V \mathbf{x}(\mathbf{r}) \cdot \mathbf{y}^*(\mathbf{r}) \, dv.
$$

In accord with standard practice, the region V in which calculations are to be made is divided into elements. In a two-dimensional case, the common practice is to divide the region into triangular elements, involving three points in the plane at a time. For three-dimensional problems, the equivalent element would be a tetrahedral element, D_e, involving four points in space.

We introduce also a system of basis functions $\{\mathbf{v}_1(\mathbf{r}), \mathbf{v}_2(\mathbf{r}), ...\mathbf{v}_N(\mathbf{r})\}$ in the Hilbert space $L_2(V)$. In the simplest case, we can use as basis functions the linear functions of coordinates, x, y, and z, which are determined at any point within one of the elements, D_e, but are zero outside. We introduce a finite dimensional Hilbert subspace, $L_2^{(N)}$, of the space $L_2(D): L_2^{(N)} \subset L_2(D)$ spanned by the basis functions $\{\mathbf{v}_1(\mathbf{r}), \mathbf{v}_2(\mathbf{r}), ...\mathbf{v}_N(\mathbf{r})\}$. We will be looking for an approximate solution of the electromagnetic field equations in the form

$$\mathbf{E}(\mathbf{r}) \approx \sum_{n=1}^{N} a_n \mathbf{v}_n(\mathbf{r}), \tag{6.244}$$

$$\mathbf{H}(\mathbf{r}) \approx \sum_{n=1}^{N} b_n \mathbf{v}_n(\mathbf{r}), \tag{6.245}$$

where a_n, b_n $(n = 1, 2, ..., N)$ are the scalar coefficients of the expansions.

The second order electric or magnetic field equations (6.191) can be written in operator form as

$$\left(L^\mu - i\omega\mu\tilde{\sigma}\right)\mathbf{E} = i\omega\mu\mathbf{j}^{\mathbf{e}},$$
$$\left(L^\sigma - i\omega\mu\tilde{\sigma}\right)\mathbf{H} = \tilde{\sigma}\nabla \times \left(\frac{1}{\tilde{\sigma}}\mathbf{j}^e\right), \tag{6.246}$$

where L^μ and L^σ are the second order differential operators:

$$L^\mu = \mu\nabla \times \left(\frac{1}{\mu}\nabla\times\right),$$
$$L^\sigma = \tilde{\sigma}\nabla \times \left(\frac{1}{\tilde{\sigma}}\nabla\times\right). \tag{6.247}$$

We substitute expansion (6.244) into the first equation (6.246)

$$\sum_{n=1}^{N} a_n \left(L^\mu - i\omega\mu\tilde{\sigma}\right)\mathbf{v}_n = i\omega\mu\mathbf{j}^{\mathbf{e}}, \tag{6.248}$$

and, following the conventional technique of the Galerkin method, take the inner product of both sides of Eq. (6.248) with the basis function $\mathbf{v}_p$:

$$\sum_{n=1}^{N} a_n \left(L^\mu\mathbf{v}_n, \mathbf{v}_p\right)_{L_2(D)} - i\omega \sum_{n=1}^{N} a_n \left(\mu\tilde{\sigma}\mathbf{v}_n, \mathbf{v}_p\right)_{L_2(D)} = i\omega \left(\mu\mathbf{j}^{\mathbf{e}}, \mathbf{v}_p\right)_{L_2(D)}. \tag{6.249}$$

Introducing the notations

$$\left(L^{\mu}\mathbf{v}_n, \mathbf{v}_p\right)_{L_2(D)} = L^{\mu}_{pn},$$
$$\left(\mu\widetilde{\sigma}\mathbf{v}_n, \mathbf{v}_p\right)_{L_2(D)} = \widetilde{\sigma}_{pn},$$

and

$$\left(\mu\mathbf{j^e}, \mathbf{v}_p\right)_{L_2(D)} = j^E_p,$$

we can write Eq. (6.249) in the form

$$\sum_{n=1}^{N} L^{\mu}_{pn}a_n - i\omega \sum_{n=1}^{N} \widetilde{\sigma}_{pn}a_n = i\omega j^E_p. \tag{6.250}$$

Let us evaluate the component L^{μ}_{pn}:

$$L^{\mu}_{pn} = \left(L^{\mu}\mathbf{v}_n, \mathbf{v}_p\right)_{L_2(D)} = \iiint_V L^{\mu}\mathbf{v}_n\,(\mathbf{r}) \cdot \mathbf{v}^*_p\,(\mathbf{r})\,dv$$
$$= \iiint_V \nabla \times \left(\frac{1}{\mu\,(\mathbf{r})}\nabla \times \mathbf{v}_n\,(\mathbf{r})\right) \cdot \mu\,(\mathbf{r})\,\mathbf{v}^*_p\,(\mathbf{r})\,dv. \tag{6.251}$$

Note that the common practice is to compute the inner product of the differential operator L^{μ} and the basis function, using integration by parts, which in a 3-D case is based on the vector identity

$$\mathbf{R} \cdot \nabla \times \mathbf{P} - \mathbf{P} \cdot \nabla \times \mathbf{R} = \nabla \cdot (\mathbf{P} \times \mathbf{R})$$

and the Gauss theorem:

$$\iiint_V \mathbf{R} \cdot \nabla \times \mathbf{P}\,dv = \iiint_V \mathbf{P} \cdot \nabla \times \mathbf{R}\,dv + \iint_{\partial V} (\mathbf{P} \times \mathbf{R})\,ds. \tag{6.252}$$

Taking into account (6.252), we can modify (6.251) as

$$L^{\mu}_{pn} = \iiint_V \left(\frac{1}{\mu\,(\mathbf{r})}\nabla \times \mathbf{v}_n\,(\mathbf{r})\right) \cdot \left(\nabla \times \mu\,(\mathbf{r})\,\mathbf{v}^*_p\,(\mathbf{r})\right)\,dv$$
$$+ \iint_{\partial V} (\nabla \times \mathbf{v}_n\,(\mathbf{r})) \times \mathbf{v}^*_p\,(\mathbf{r})\,ds, \tag{6.253}$$

where the integral over ∂V is a surface integral over the boundary of the domain. The integrals in the last expression are usually calculated element by element due to the special selection of the basis functions in the finite-element method. Also, the surface integrals are mutually canceled out for the neighboring elements with the joint faces. Only the surface integrals over the element faces forming the boundary of the modeling region are left, and they are determined by the boundary condition of the boundary-value problem under consideration. As a result, we arrive at the following expression for the

internal elements of the matrix $L_{pn}^{\mu(int)}$:

$$L_{pn}^{\mu(int)} = \iiint_V \left(\frac{1}{\mu(\mathbf{r})} \nabla \times \mathbf{v}_n(\mathbf{r}) \right) \cdot \left(\nabla \times \mu(\mathbf{r}) \mathbf{v}_p^*(\mathbf{r}) \right) dv. \tag{6.254}$$

Finally, we can cast Eq. (6.250) for the basis function coefficients in the matrix form

$$\left(\mathbf{L}^\mu - i\omega\widetilde{\boldsymbol{\sigma}} \right) \mathbf{a} = i\omega \mathbf{j}^E, \tag{6.255}$$

where the matrices $\mathbf{L}^\mu$ and $\widetilde{\boldsymbol{\sigma}}$, and vectors, $\mathbf{a}$ and $\mathbf{j}^E$, are given by:

$$\mathbf{L}^\mu = \left[L_{pn}^\mu \right], \; \widetilde{\boldsymbol{\sigma}} = \left[\widetilde{\sigma}_{pn} \right], \; \mathbf{a} = [a_n], \; \mathbf{j}^E = \left[j_p^E \right].$$

Note that the structure of Eq. (6.255) is similar to the structure of the finite difference matrix equation (6.225). Thus one can use, for example, spectral Lanzcos decomposition method (Druskin et al., 1999) to solve this equation and to determine the coefficients $\mathbf{a} = [a_1, a_2, ...a_N]$.

Substituting the coefficients $\mathbf{a} = [a_1, a_2, ...a_N]$ into expansion (6.244) we determine the electric field, and then, from the second Maxwell's equation, find the magnetic field:

$$\mathbf{B} = \frac{1}{i\omega} \nabla \times \mathbf{E}. \tag{6.256}$$

In a similar way we can find the magnetic field using expansion (6.245) and the corresponding second order differential equation. The matrix equation for the coefficients of magnetic field expansion has the form

$$\left(\mathbf{L}^\sigma - i\omega\widetilde{\boldsymbol{\sigma}} \right) \mathbf{b} = i\omega \mathbf{j}^H, \tag{6.257}$$

where the matrix $\mathbf{L}^\sigma$, and vectors, $\mathbf{b}$ and $\mathbf{j}^H$, are given by,

$$\mathbf{L}^\sigma = \left[L_{pn}^\sigma \right], \;\; \mathbf{b} = [b_n], \; \mathbf{j}^H = \left[j_p^H \right],$$

and

$$L_{pn}^\sigma = \iiint_V \left(\frac{1}{\widetilde{\sigma}(\mathbf{r})} \nabla \times \mathbf{v}_n(\mathbf{r}) \right) \cdot \left(\nabla \times \widetilde{\sigma}(\mathbf{r}) \mathbf{v}_p^*(\mathbf{r}) \right) dv,$$
$$j_p^H = \left(\widetilde{\sigma} \nabla \times \left(\frac{1}{\widetilde{\sigma}} \mathbf{j}^e \right), \mathbf{v}_p \right)_{L_2(D)}.$$

The solution of Eq. (6.257) can be obtained by the spectral Lanzcos decomposition method (Zhdanov, 2002).

6.4.8 EDGE-BASED FINITE ELEMENT METHOD

The edge-based finite element method was introduced by Nedelec (1980). The advantage of the edge-based finite element method is that the divergence free conditions are satisfied automatically by an appropriate selection of the basis functions. The basis function of the Nedelec element is
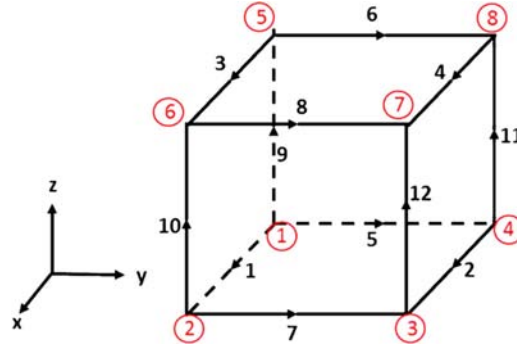
FIGURE 6.8

A rectangular element used in the edge-based finite element method. The number within a circle indicates the index of the corresponding node, and the number without a circle is the index of the corresponding edge.

a vector function defined along the element edges and at the center of each edge. The tangential continuity of electric and magnetic fields is imposed automatically on the element's interfaces while the normal components are still can be discontinuous. The edge-based finite element method was widely used in electrical engineering for over 30 years, however, it attracted the attention of the geophysical community recently only (e.g., Mukherjee and Everett, 2011; Silva et al., 2012; Cai et al., 2014).

I present the edge-based finite element method, follow the papers by Jin (2002) and Cai et al. (2014). The modeling domain can be discretized using rectangular, tetrahedron, hexahedron or other complex elements. For simplicity, we will discuss the rectangular elements first (see Fig. 6.8). Following the work by Jin (2002) and Cai et al. (2014), we denote the center of the element D_n as (x_c^n, y_c^n, z_c^n), and the edge length in the x, y, z directions as l_x^n, l_y^n, l_z^n, respectively. The tangential components of the electric field are assigned to the center of each edge. Thus, the scalar components of the anomalous electric field, $\mathbf{E}^{a(n)}$, inside the rectangular prism D_n can be expressed as follows:

$$E_x^{a(n)}(\mathbf{r}) = \sum_{i=1}^{4} e_{xi}^n N_{xi}^n(\mathbf{r}), \quad E_y^n = \sum_{i=1}^{4} e_{yi}^n N_{yi}^n(\mathbf{r}), \quad E_z^n = \sum_{i=1}^{4} e_{zi}^n N_{zi}^n(\mathbf{r}), \quad (6.258)$$

where e_{xi}^n, e_{yi}^n, e_{zi}^n $(n = 1, 2, ...N; \; i = 1, 2, 3, 4)$ are the scalar coefficients of the expansions and the scalar edge basis functions are defined by the following expressions:

$$N_{x1}^n(\mathbf{r}) = \frac{1}{l_y^n l_z^n}\left(y_c^n + \frac{l_y^n}{2} - y\right)\left(z_c^n + \frac{l_z^n}{2} - z\right), \quad (6.259)$$

$$N_{x2}^n(\mathbf{r}) = \frac{1}{l_y^n l_z^n}\left(y - y_c^n + \frac{l_y^n}{2}\right)\left(z_c^n + \frac{l_z^n}{2} - z\right), \quad (6.260)$$

$$N_{x3}^n = \frac{1}{l_y^n l_z^n}\left(y_c^n + \frac{l_y^n}{2} - y\right)\left(z - z_c^n + \frac{l_z^n}{2}\right), \quad (6.261)$$

$$N_{x4}^n (\mathbf{r}) = \frac{1}{l_y^n l_z^n} \left(y - y_c^n + \frac{l_y^n}{2} \right) \left(z - z_c^n + \frac{l_z^n}{2} \right), \tag{6.262}$$

$$N_{y1}^n (\mathbf{r}) = \frac{1}{l_z^n l_x^n} \left(z_c^n + \frac{l_z^n}{2} - z \right) \left(x_c^n + \frac{l_x^n}{2} - x \right), \tag{6.263}$$

$$N_{y2}^n (\mathbf{r}) = \frac{1}{l_z^n l_x^n} \left(z - z_c^n + \frac{l_z^n}{2} \right) \left(x_c^n + \frac{l_x^n}{2} - x \right), \tag{6.264}$$

$$N_{y3}^n (\mathbf{r}) = \frac{1}{l_z^n l_x^n} \left(z_c^n + \frac{l_z^n}{2} - z \right) \left(x - x_c^n + \frac{l_x^n}{2} \right), \tag{6.265}$$

$$N_{y4}^n (\mathbf{r}) = \frac{1}{l_z^n l_x^n} \left(z - z_c^n + \frac{l_z^n}{2} \right) \left(x - x_c^n + \frac{l_x^n}{2} \right), \tag{6.266}$$

$$N_{z1}^n (\mathbf{r}) = \frac{1}{l_x^n l_y^n} \left(x_c^n + \frac{l_x^n}{2} - x \right) \left(y_c^n + \frac{l_y^n}{2} - y \right), \tag{6.267}$$

$$N_{z2}^n (\mathbf{r}) = \frac{1}{l_x^n l_y^n} \left(x - x_c^n + \frac{l_x^n}{2} \right) \left(y_c^n + \frac{l_y^n}{2} - y \right), \tag{6.268}$$

$$N_{z3}^n (\mathbf{r}) = \frac{1}{l_x^n l_y^n} \left(x_c^n + \frac{l_x^n}{2} - x \right) \left(z - y_c^n + \frac{l_y^n}{2} \right), \tag{6.269}$$

$$N_{z4}^n (\mathbf{r}) = \frac{1}{l_x^n l_y^n} \left(x - x_c^n + \frac{l_x^n}{2} \right) \left(y - y_c^n + \frac{l_y^n}{2} \right). \tag{6.270}$$

Eq. (6.258) can be written in a more compact form as follows:

$$\mathbf{E}^{a(n)} (\mathbf{r}) = \sum_{i=1}^{12} e_i^n \mathbf{N}_i^n (\mathbf{r}), \tag{6.271}$$

where

$$\mathbf{N}_i^n (\mathbf{r}) = N_{xi}^n (\mathbf{r}) \mathbf{d}_x, \quad \mathbf{N}_{i+4}^n = N_{yi}^n (\mathbf{r}) \mathbf{d}_y, \quad \mathbf{N}_{i+8}^n = N_{zi}^n \mathbf{d}_z, \tag{6.272}$$

for $i = 1, 2, 3, 4$.

An important property of the vector edge basis functions is that they are divergence free but not curl free:

$$\nabla \cdot \mathbf{N}_i^n = 0, \quad \nabla \times \mathbf{N}_i^n \neq \mathbf{0}. \tag{6.273}$$

The vector basis functions are also continuous at the element boundaries. Therefore, the divergence-free condition of the electric field in the source free region and the continuity conditions are automatically fulfilled using the edge-based finite element formulation.

The anomalous field in the entire modeling domain, D, is given by the following expression:

$$\mathbf{E}^a (\mathbf{r}) = \sum_{n=1}^{N} \mathbf{E}^{a(n)} (\mathbf{r}) = \sum_{n=1}^{N} \sum_{i=1}^{12} e_i^n \mathbf{N}_i^n (\mathbf{r}). \tag{6.274}$$

Using the operator notations (6.246), the first equation in (6.205) can be written as follows:

$$\left(L^{\mu} - i\omega\mu\widehat{\boldsymbol{\sigma}}\right)\mathbf{E} = i\omega\mu\mathbf{j}^{b}, \tag{6.275}$$

where

$$\mathbf{j}^{b}\left(\mathbf{r}\right) = \Delta\widehat{\boldsymbol{\sigma}}\left(\mathbf{r}\right)\mathbf{E}^{b}\left(\mathbf{r}\right).$$

We substitute expansion (6.274) in Eq. (6.275),

$$\sum_{n=1}^{N}\sum_{i=1}^{12} e_{i}^{n}\left(L^{\mu} - i\omega\mu\widehat{\boldsymbol{\sigma}}\right)\mathbf{N}_{i}^{n} = i\omega\mu\mathbf{j}^{b}, \tag{6.276}$$

and, following the Galerkin method described above, take the inner product of both sides of Eq. (6.248) with the basis function $\mathbf{N}_{j}^{p}$:

$$\sum_{n=1}^{N}\sum_{i=1}^{12} e_{i}^{n}\left(L^{\mu}\mathbf{N}_{i}^{n}, \mathbf{N}_{j}^{p}\right)_{L_{2}(D)} - i\omega\sum_{n=1}^{N}\sum_{i=1}^{12} e_{i}^{n}\left(\mu\widehat{\boldsymbol{\sigma}}\mathbf{N}_{i}^{n}, \mathbf{N}_{j}^{p}\right)_{L_{2}(D)} = i\omega\left(\mu\mathbf{j}^{b}, \mathbf{N}_{j}^{p}\right)_{L_{2}(D_{n})} \tag{6.277}$$

Introducing the notations

$$\left(L^{\mu}\mathbf{N}_{i}^{n}, \mathbf{N}_{j}^{p}\right)_{L_{2}(D_{n})} = L_{ij}^{np}, \quad \left(\mu\widehat{\boldsymbol{\sigma}}\mathbf{N}_{i}^{n}, \mathbf{N}_{j}^{p}\right)_{L_{2}(D_{n})} = \sigma_{ij}^{p}, \tag{6.278}$$

and

$$\left(\mu\mathbf{j}^{b}, \mathbf{N}_{j}^{p}\right)_{L_{2}(D_{n})} = j_{j}^{p},$$

we can write Eqs. (6.277) in the following form:

$$\sum_{n=1}^{N}\sum_{i=1}^{12} e_{i}^{n}L_{ij}^{p} - i\omega\sum_{n=1}^{N}\sum_{i=1}^{12} e_{i}^{n}\sigma_{ij}^{p} = i\omega j_{j}^{p}. \tag{6.279}$$

Note that the inner products in formulas (6.278) can be calculated analytically using integration by parts, based on the vector Green's theorem (6.252) (Jin, 2002; Cai et al., 2014).

After assembling the local element matrices in Eq. (6.279) into a global system, one can obtain a sparse linear system of equations as follows:

$$\mathbf{A}\mathbf{e} = \mathbf{b}, \tag{6.280}$$

where $\mathbf{e}$ is a vector of the unknown coefficients, e_{i}^{n}.

In order to get a unique solution for this equation, proper boundary conditions need to be added. Following the work of Jin (2002) and Silva et al. (2012), we consider the homogeneous Dirichlet boundary conditions in edge element formulation:

$$\mathbf{E}^{a}|_{\partial\mathbf{D}} = \mathbf{0} \tag{6.281}$$

which holds approximately for the anomalous electric field at some distance from the domain with the anomalous conductivity. For the numerical modeling, the distance, where conditions (6.281) hold, can be determined based on the skin depth of the field.

One can use the quasi-minimum residual method with Jacobian preconditioner to solve the linear system of Eqs. (6.280). In order to capture the rapid change of electromagnetic field close to the source region and target area and to minimize the computational cost, one can use a nonuniform rectangular grid. Jacobian preconditioner works fairly well for this mesh. I should note in conclusion of this section that the FD contraction preconditioner, developed in section 6.4.5. can be applied to solve the linear system of FE equations (6.280) as well.

REFERENCES AND RECOMMENDED READING TO CHAPTER 6

Abubakar, A., and P. M. van der Berg, 2004, Iterative forward and inverse algorithms based on domain integral equations for three-dimensional electric and magnetic objects: Journal of Computational Physics, **195**, 236–262.

Avdeev, D. B., 2005, Three-dimensional electromagnetic modelling and inversion from theory to application: Surveys in Geophysics, **26**, 767–799.

Avdeev, D. B., A. V. Kuvshinov, O. V. Pankratov, and G. A. Newman, 2002, Three-dimensional induction logging problems, Part I: An integral equation solution and model comparisons: Geophysics, **67**, 413–426.

Beltzer, A. I., 1990, Variational and finite element methods, A symbolic computational approach: Springer-Verlag, Berlin, Heidelberg, New York, London, Paris, Tokyo, 254 pp.

Berdichevsky, M. N., and M. S. Zhdanov, 1981, Interpretation of Anomalous Variations of the Electromagnetic Field of the Earth: Nedra, Moscow, 327 pp.

Berdichevsky, M. N., and M. S. Zhdanov, 1984, Advanced theory of deep geomagnetic sounding: Elsevier, Amsterdam, London, New York, Tokyo, 410 pp.

Berenger, J., 1993, A perfectly matched layer for the absorption of electromagnetic waves: Journal of Computational Physics, **114**, 185–200.

Biro, O., and K. Preis, 1990, Finite element analysis of 3-D eddy currents: IEEE Transactions on Magnetics, **26** (2), 418–423.

Black, K., 1998, Spectral element approximations and infinite domains: Journal of Mathematical Systems, Estimation, and Control, **8** (2) 1–20.

Bleistein, N., 1984, Mathematical methods for wave phenomena: Academic Press Inc., (Harcourt Brace Jovanovich Publishers), New York, 341 pp.

Bleistein, N., and S. H. Gray, 1985, An extension of the Born inversion method to a depth dependent reference profile: Geophysical Prospecting, **33** (7), 999–1022.

Born, M., 1933, Optik: Springer, Berlin, 591 pp.

Born, M., and E. Wolf, 1980, Principles of optics: 2nd ed., Pergamon Press, New York, 808 pp.

Cai, H., B. Xiong, M. Han, and M. S. Zhdanov, 2014, 3D controlled-source electromagnetic modeling in anisotropic medium using edge-based finite element method: Journal of Computers and Geosciences, **73**, 164–176.

Chew, W. C., and W. H. Weedon, 1994, A 3-D perfectly matched medium from modified Maxwell's equations with stretched coordinates: Microwave and Optical Technical Letters, **7**, 599–604.

Coggon, J. Z., 1971, Electromagnetic and electrical modeling by the finite-element method: Geophysics, **36**, 132–155.

da Silva, N. V., J. V. Morgan, L. MacGregor, and M. Warner, 2012, A finite element multifrontal method for 3D CSEM modeling in the frequency domain: Geophysics, **77** (2), E101–E115.

de Lugao, P., Portniaguine, O., and M. S. Zhdanov, 1997, Fast and stable two-dimensional inversion of magnetotelluric data: Journal of Geomagnetism and Geoelectricity, **49**, 1469–1497.

de Lugao, P., and P. E. Wannamaker, 1996, Calculating the two-dimensional magnetotelluric Jacobian in finite elements using reciprocity: Geophysical Journal International, **127**, 806–810.

Dmitriev, V. I., 1969, Electromagnetic fields in inhomogeneous media: Proceeding of Computational Center, Moscow State University (*in Russian*).

Dmitriev, V. I., and N. I. Nesmeyanova, 1992, Integral equation method in three-dimensional problems of low-frequency electrodynamics: Computational Mathematics and Modeling, **3**, 313–317.

Dmitriev, V. I., E. Pozdniakova, M. S. Zhdanov, and S. Fang, 1999, Quasi-analytical solutions for EM field in inhomogeneous structures based on unified iterative quasi-linear method: 68th Annual International Meeting, SEG, Expanded Abstracts, 444–447.

Druskin, V., and L. Knizhnerman, 1994, Spectral approach to solving three-dimensional Maxwell's diffusion equations in the time and frequency domains: Radio Science, **29**, No. 937–953.

Druskin, V., L. Knizhnerman, and P. Lee, 1999, New spectral Lanczos decomposition method for induction modeling in arbitrary 3-D geometry: Geophysics, **64** (3), 701–706.

Everett, M. E., 1999, Finite element formulation of electromagnetic induction with coupled potentials: Three-dimensional electromagnetics: Published by the Society of Exploration Geophysics, Geophysical Development Series, Tulsa, OK, 444–450.

Everett, M. E., and A. Schultz, 1996, Geomagnetic induction in a heterogeneous sphere: Azimuthally symmetric test computations and the response of an undulating 660-km discontinuity: Journal of Geophysical Research, **101**, 2765–2783.

Godunov, S. K., 1959, Difference method of numerical calculating the break solutions of hydrodynamic equations (*in Russian*): Matematichesky Sbornik, **47** (3), 271–306.

Golub, G. H., and C. F. Van Loan, 1996, Matrix computations, 3rd ed., 694 pp., Johns Hopkins University Press, Baltimore.

Grayver, A. V., and M. Bürg, 2014, Robust and scalable 3-D geo-electromagnetic modelling approach using the finite element method: Geophysical Journal International, **198** (1), 110–125.

Grayver, A. V., R. Streich, and O. Ritter, 2013, Three-dimensional parallel distributed inversion of CSEM data using a direct forward solver, Geophysical Journal International, **193** (3), 1432–1446.

Guozhong, G., C. Torres-Verdin, and S. Fang, 2004, Fast 3D modeling of borehole induction measurements in dipping and anisotropic formations using a novel approximation technique: Petrophysics, **45**, 335–349.

Habashy, T. M., R. W. Groom, and B. R. Spies, 1993, Beyond the Born and Rytov approximations: a nonlinear approach to electromagnetic scattering: Journal of Geophysical Research, **98**, (B2), 1759–1775.

Haber, E., U. M. Ascher, D. A. Aruliah, and D. W. Oldenburg, 2000, Fast simulation of 3-D electromagnetic problems using potentials: Journal of Computational Physics, **163** (1), 150–171.

Hohmann, G. W., 1975, Three-dimensional induced polarization and electromagnetic modeling: Geophysics, **40** (2), 309–324.

Hursán G., and M. S. Zhdanov, 2002, Contraction integral equation method in three-dimensional electromagnetic modeling: Radio Science, **37** (6), 1089, doi: 10.1029/2001RS002513.

Jaysaval, P., D. Shantsev, and S. de la Kethulle de Ryhove, 2014, Fast multimodel finite difference controlled source electromagnetic simulations based on a Schur complement approach: Geophysics, **79** (6), E315–E327.

Jin, J. M., 2002, The finite element method: Theory and Computation of Electromagnetic Fields, 342–398.

Mackie, R. L., T. R. Madden, and P. E. Wannamaker, 1993, Three-dimensional magnetotelluric modeling using difference equations – theory and comparisons to integral equation solutions: Geophysics, **58** (2), 215–226.

Mackie, R. L., J. T. Smith, and T. R. Madden, 1994, Three-dimensional electromagnetic modeling using finite difference equations: The magnetotelluric example: Radio Science, **29**, 923–935.

Madden, T. R., and R. L. Mackie, 1989, 3-D magnetotelluric modelling and inversion: Proceedings of the IEEE, **77**, 318–332.

McGillivray, P. R., and D. W. Oldenburg, 1990, Methods for calculating Fréchet derivatives and sensitivities for the nonlinear inverse problem: A comparative study: Geophysical Prospecting, **38** (5), 499–524.

McGillivray, P. R., D. W. Oldenburg, R. G. Ellis, and T. M. Habashy, 1994, Calculation of sensitivities for the frequency-domain electromagnetic problem: Geophysical Journal International, **116**, 1–4.

Mehanee, S., and M. S. Zhdanov, 2001, 3-D finite-difference forward modeling based on the balance method: 71st Annual International Meeting, SEG, Expanded Abstracts, 1443–1446.

Moran, J. H., and S. C. Gianzero, 1979, Effects of formation anisotropy on resistivity logging measurements: Geophysics, **44**, 1266–1286.

Morse, P. M., and H. Feshbach, 1953, Methods of theoretical physics, McGraw Hill Book Co., New York, 1978 pp.

Mukherjee, S., and M. E. Everett, 2011, 3D controlled-source electromagnetic edge-based finite element modeling of conductive and permeable heterogeneities: Geophysics, **76**, F215–F226.

Nedelec, J. C., 1980, Mixed finite elements in R^3: Numerische Mathematik, **35**, 315–341.

Newman, G. A., and D. L. Alumbaugh, 1997, Three-dimensional massively parallel inversion – I. Theory: Geophysical Journal International, **128**, 345–354.

Newman, G. A., and D. L. Alumbaugh, 2000, Three-dimensional magnetotelluric inversion using non-linear conjugate gradients: Geophysical Journal International, **140**, 410–424.

Oldenburg, D. W., 1990, Inversion of electromagnetic data: an overview of new techniques: Surveys in Geophysics, **11**, 231–270.

Oristaglio, M. L., 1989, An inverse scattering formula that uses all the data: Inverse Problems, **5**, 1097–1105.

Pankratov, O. V., D. B. Avdeev, and A. V. Kuvshinov, 1995, Electromagnetic field scattering in heterogeneous earth: A solution to the forward problem: Physics of the Solid Earth (English edition), **31**, 201–209.

Pellerin, L., J. M. Johnston, and G. W. Hohmann, 1993, Three-dimensional inversion of electromagnetic data: Expanded Abstracts, 63rd Annual International Meeting, SEG, Expanded Abstracts, 360–363.

Raiche, A. P., 1974, An integral equation approach to three-dimensional modelling: Geophysical Journal of the Royal Astronomical Society, **36**, 363–376.

Rodi, W. L., 1976, A technique for improving the accuracy of finite element solutions for magnetotelluric data: Geophysical Journal of the Royal Astronomical Society, **44**, 483–506.

Saad, Y., 2003, Iterative Methods for Sparse Linear Systems: Society for Industrial and Applied Mathematics, Philadelphia, PA, USA, 2nd edn.

Samarsky, A. A., 1984, Theory of the difference schemes (*in Russian*): Nauka Publishing House, Moscow, 656 pp.

Silva, N. V., J. V. Morgan, L. MacGregor and M. Warner, 2012, A finite element multifrontal method for 3D CSEM modeling in the frequency domain: Geophysics, **77**, E101–E115.

Singer, B. Sh., 1995, Method for solution of Maxwell's equation in non-uniform media: Geophysical Journal International, **120**, 590–598.

Singer, B. Sh., and E. B. Fainberg, 1997, Fast and stable method for 3-D modeling of electromagnetic field: Exploration Geophysics **28** (2), 130–135.

Singer, B. Sh., A. Mezzatesta, and T. Wang, 2003, Integral equation approach based on contraction operators and Krylov subspace optimisation, in Macnae, J., and G. Liu, Eds., Three-dimensional electromagnetics III, Australian Society of Exploration Geophysicists.

Smith, J. T., 1996, Conservative modeling of 3-D electromagnetic fields; Part II: Bi-conjugate gradient solution and an accelerator: Geophysics, **61** (5), 1319–1324.

Stratton, J. A., 1941, Electromagnetic theory: McGraw-Hill Book Company, New York and London, 615 pp.

Streich, R., 2009. 3D finite-difference frequency-domain modeling of controlled-source electromagnetic data: Direct solution and optimization for high accuracy, Geophysics, **74** (5), F95–F105.

Tabarovsky, L. A., 1975, Application of integral equation method to geoelectrical problems: Novosibirsk, Nauka (*in Russian*).

Tarantola, A., 1987, Inverse Problem Theory: Elsevier, Amsterdam, Oxford, New York, Tokyo, 613 pp.

Tong, P., and J. N. Rossettos, 1977, Finite element method: MIT Press, Cambridge, 332 pp.

Torres-Verdin, C., and T. M. Habashy, 1994, Rapid 2.5-dimensional forward modeling and inversion via a new scattering approximation, Radio Science, **29** (4), 1051–1079.

Ueda, T., and M. S. Zhdanov, 2006, Fast numerical modeling of multitransmitter electromagnetic data using multigrid quasi-linear approximation: IEEE Transactions on Geoscience and Remote Sensing, **44** (4), 1428–1434.

Wang, T., and G. W. Hohmann, 1993, A finite difference time-domain solution for three dimensional electromagnetic modeling: Geophysics, **58** (6), 797–809.

Wannamaker, P. E., 1991, Advances in three-dimensional magnetotelluric modeling using integral equations: Geophysics, **56**, 1716–1728.

Wannamaker, P. E., J. A. Stodt, and L. Rijo, 1987, A stable finite element solution for two-dimensional magnetotelluric modeling: Geophysical Journal of the Royal Astronomical Society, **88**, 277–296.

Weaver, J. T., 1994, Mathematical methods for geoelectromagnetic induction: RSP, Willey, 330 pp.

Weaver, J. T., and C. R. Brewitt-Taylor, 1978, Improved boundary conditions for the numerical solution of E-polarization problems in geomagnetic induction: Geophysical Journal of the Royal Astronomical Society, **54**, 309–317.

Weidelt, P., 1975a, Electromagnetic induction in three-dimensional structures: Journal of Geophysics, **41** (1), 85–109.

Weidelt, P., 1975b, Inversion of two-dimensional conductivity structures: Physics of the Earth and Planetary Interiors, **10**, 282–291.

Xiong, Z., 1992, Electromagnetic modeling of 3-D structures by the method of system iteration using integral equations: Geophysics, **57**, 1556–1561.

Xiong, Z. and A. Kirsch, 1992, Three-dimensional earth conductivity inversion: Journal of Computational and Applied Mathematics, **42**, 109–121.

Yavich, N., and M. S. Zhdanov, 2016, Contraction pre-conditioner in finite-difference electromagnetic modeling: Geophysical Journal International, **206** (3): 1718–1729.

Yee, K. S., 1966, Numerical solution of initial boundary problems involving Maxwell's equations in isotropic media: IEEE Transactions on Antennas and Propagation, **14 (3)**, 302–307.

Zaslavsky, M., V. Druskin, S. Davydycheva, L. Knizhnerman, A. Abubakar, and T. Habashy, 2011, Hybrid finite-difference integral equation solver for 3D frequency domain anisotropic electromagnetic problems: Geophysics, **76** (2), F123–F137.

Zemanian, A. H., 1987, Generalized integral transforms: Dover, New York, 300 pp.

Zhdanov, M. S., 1988, Integral transforms in geophysics: Springer-Verlag, Berlin, Heidelberg, New York, London, Paris, Tokyo, 367 pp.

Zhdanov, M. S., 2002, Geophysical inverse theory and regularization problems: Elsevier, Amsterdam, London, New York, Tokyo, 628 pp.

Zhdanov, M. S., 2015, Inverse theory and applications in geophysics: Elsevier, Amsterdam, London, New York, Tokyo, 730 pp.

Zhdanov M. S., V. I. Dmitriev, S. Fang, and G. Hursán, 2000a, Quasi-analytical approximations and series in electromagnetic modeling: Geophysics, **65**, 1746–1757.

Zhdanov, M. S. and S. Fang, 1996a, Quasi-linear approximation in 3-D EM modeling: Geophysics, **61**, 646–665.

Zhdanov, M. S. and S. Fang, 1996b, 3-D quasi-linear electromagnetic inversion: Radio Science, **31** (4), 741–754.

Zhdanov, M. S. and S. Fang, 1997, Quasi linear series in 3-D EM modeling: Radio Science, **32**, (6), 2167–2188.

Zhdanov, M. S., S. Fang, and G. Hursán, 2000b, Electromagnetic inversion using quasi-linear approximation. Geophysics **65** (5), 1501–1513.

Zhdanov, M. S., N. G. Golubev, V. V. Spichak, and I. M. Varentsov, 1982, The construction of effective methods for electromagnetic modeling: Geophys. J. R. Astr. Soc., **68**, 589–607.

Zhdanov, M. S., and G. Keller, 1994, The geoelectrical methods in geophysical exploration: Elsevier, Amsterdam, London, New York, Tokyo, 873 pp.

Zhdanov, M. S., W. D. Kennedy, and E. Peksen, 2001, Foundations of tensor induction well-logging: Petrophysics, **42**, 588–610.

Zhdanov, M. S., S. K. Lee, and K. Yoshioka, 2006, Integral equation method for 3-D modeling of electromagnetic fields in complex structures with inhomogeneous background conductivity: Geophysics, **71** (6), G333–G345.

Zhdanov, M. S., and V. V. Spichak, 1989a, Mathematical modeling of three-dimensional quasi-stationary electromagnetic fields in geoelectrics (*in Russian*): DAN SSSR, **309** (1), 57–60.

Zhdanov, M. S., and V. V. Spichak, 1992, Mathematical modeling of electromagnetic fields in three-dimensional inhomogeneous media (*in Russian*): Nauka, Moscow, 188 pp.

Zhdanov, M. S., and E. Tartaras, 2002, Inversion of multi-transmitter 3-D electromagnetic data based on the localized quasi-linear approximation: Geophysical Journal International, **148**, (3), 506–519.

Zienkiewicz, O. C., and R. L. Taylor, 1989, The finite element method. 4th ed.: McGraw-Hill, New York.

Zhdanov, M. S., I. M. Varentsov, N. G. Golubev, and V. A. Krylov, 1990, Methods of modeling electromagnetic fields (*in Russian*): Nauka, Moscow, 199 pp.

Zhdanov M. S., I. M. Varentsov, J. T. Weaver, N. G. Golubev, and V. A. Krylov, 1997, Methods for modeling electromagnetic fields. Results from COMMEMI – the international project on the comparison of modeling methods for electromagnetic induction: Journal of Applied Geophysics, **37**, 1–273.

INVERSION AND IMAGING OF ELECTROMAGNETIC FIELD DATA

3

PRINCIPLES OF ILL-POSED INVERSE PROBLEM SOLUTION

CONTENTS

We have demonstrated in Chapter 6, that the problem of determining the behavior of an electromagnetic field interacting with an earth model is well defined, even if the procedures involved in that solution may be intractable at times. It has become the custom in electromagnetic geophysics to call this problem – given a geoelectrical model, to determine the electromagnetic field generated by a given source – the *forward problem*. In geophysical practice, we have to deal with quite an opposite problem of attempting to find the model causing the observed electromagnetic field behavior. This is the *inverse problem*. The process of solving the inverse problem is called *inversion*.

The inverse problem differs in important ways from the forward problem. The forward problem is almost always *well posed*. Given an earth model, we are certain that there is a single, unique solution of Maxwell's equations which describes the EM field behavior. A numerical evaluation of that solution can be accomplished with any specified accuracy of computation. In contrast, in the inverse problem, while we may be almost certain that there is a unique physical inverse solution, widely differing numerical geoelectric models may be found, which may cause almost exactly the same electromagnetic field behavior. Moreover, the accuracy with which we know the electromagnetic field behavior is contaminated to some extent by noise and measurement error. However, even in the case of very accurate observations, the inversion results may have arbitrarily large differences from one another. This lack of uniqueness on the practical level makes inverse solutions difficult if not impossible in some cases. For this reason, the inverse problem as usually encountered in geoelectrical field practice is said to be *ill posed*. The foundations of the regularization theory were developed in numerous publications of Russian mathematician Andrei N. Tikhonov (e.g., Tikhonov, 1963a, 1963b, 1999).

7.1 ILL-POSED INVERSE PROBLEMS

7.1.1 FORMULATION OF WELL-POSED AND ILL-POSED PROBLEMS

To better understand the nature of ill-posed problems and inversion as a mathematical process, let us follow the logic of Tikhonov and Arsenin (1977). Consider that a mathematical model of a phenomenon is characterized by a vector $\mathbf{m}$ which belongs to some space of models M. Let $\mathbf{d}$ be some observed indirect attributes of the phenomenon (that is, data $\mathbf{d} \in D$, where D is the space of data). An operator A relates the two:

$$\mathbf{d} = A(\mathbf{m}). \tag{7.1}$$

In general, we will expect that the $\mathbf{m}$ attributes (true data $\mathbf{d}$) are not directly observable. Instead, we have only some approximate values $\mathbf{d}_\delta$ and an estimate of their accuracy δ such that $\|\mathbf{d} - \mathbf{d}_\delta\|_D \leq \delta$, where $\|...\|_D$ is some norm ("distance" between vectors $\mathbf{d}$ and $\mathbf{d}_\delta$) in the space of data, D (for a definition and properties of the norm and normed space see Zhdanov, 2002, 2015). Solution of the inverse problem consists of the following principal steps

1) Finding out whether or not the chosen model $\mathbf{m}_\delta$ is compatible with the observational data; that is, finding a model, $\mathbf{m}_\delta \in M$, with the attributes (data) such that $\|\mathbf{d} - A(\mathbf{m}_\delta)\|_D \leq \delta$ under the condition that $\mathbf{m}_\delta \to \mathbf{m}$ as $\delta \to 0$.
2) Determining, if possible, of the errors of the approximate solutions within the adopted model; that is, the estimation of the distance between $\mathbf{m}_\delta$ and $\mathbf{m}$ using an appropriate metric.

The mathematical difficulty in solving inverse problems is that the inverse operator, A^{-1}, may not exist or may not be continuous over the domain $AM \subset D$. We can define problems as ill posed or well posed as follows. A well-posed problem must meet these requirements:

1) The solution $\overline{\mathbf{m}}$ of equation $\mathbf{d} = A(\mathbf{m})$ exists over the entire space D.
2) The solution $\overline{\mathbf{m}}$ is unique.
3) The solution is stable; that is, small perturbations of $\mathbf{d}$ cause only small perturbations of the solution.

The approximate solution of an inverse problem can be taken to be $\mathbf{m}_\delta = A^{-1}\mathbf{d}_\delta$ inasmuch as $\mathbf{m}_\delta \to \overline{\mathbf{m}}$ as $\delta \to 0$.

The problem (7.1) is ill-posed if at least one of the conditions, listed above, fails. As a consequence, the element $\mathbf{m}_\delta = A^{-1}\mathbf{d}_\delta$ (which may not even exist) is not an approximate solution inasmuch as $\mathbf{m}_\delta$ can deviate from the exact solution $\overline{\mathbf{m}}$ arbitrarily even for small δ.

Attempts to solve ill-posed problems were undertaken well before development of a coherent general approach. Simple ill-posed problems were solved intuitively. But, intuitive approaches work only when we consider relatively simple geoelectric models. Present capabilities in measuring and processing geophysical field data make it necessary to consider very complex geoelectric models. At present, through the use of the theory of regularization, we can find highly effective numerical algorithms for the solution of a wide range of inverse problems for complex geological structures. The basis of this theory is the concept of a regularizing algorithm, defined as an operator (or rule) that establishes a relationship between each pair $(\mathbf{d}_\delta, \delta)$ and an element $\mathbf{m}_\delta \in M$ such that $\mathbf{m}_\delta \to \overline{\mathbf{m}}$ as $\delta \to 0$. Regularizing algorithms have been developed for many ill-posed problems and implemented on computers. This has permitted automated processing of geophysical data.

7.1.2 CORRECTNESS SET

It can be demonstrated that the majority of electromagnetic inverse problems are ill posed, because at least one of the conditions listed above fails. The simplest way to overcome this difficulty is to narrow the class of models which are used in inversion. In this case the originally ill-posed inverse problem may become well posed. Mathematically it means that instead of considering **m** from the entire model space M, we can select **m** from some subspace of M, consisting of simpler and/or more suitable models for the given inverse problem. This idea was first proposed by Tikhonov (1963a, 1963b). He introduced a notion of the correctness set, C, of the solutions with the property that there exists an inverse operator A^{-1}, defined on $AC \subset D$, and that it is a continuous operator. The main characteristic of the correctness set is that the inverse problem becomes well posed if it is determined on the correctness set only.

Tikhonov and Arsenin (1977) introduced the mathematical principles for selecting the correctness set C. For example, if the models are described by a finite number of bounded parameters, they form a correctness set C in the Euclidean space of the model parameters. This result can be generalized for any metric space.

First, we introduce a definition.

Definition 34. The subset C of a metric space M is called *compact* if any sequence $\mathbf{m}_l \in C$ of elements in C contains a convergent subsequence $\mathbf{m}_{l_j} \in C$, which converges to an element **m** in C.

For example, it is known that any subset R of Euclidean space E_n is compact if and only if it is bounded:

$$\|x\| \leq c, \; c > 0, \; \text{for any } x \in R,$$

where $\|x\|$ denotes a length (norm) of the vector in the Euclidean space (Zhdanov, 2002).

Tikhonov and Arsenin (1977) demonstrated that any compact subset of the metric space M can be used as a correctness set for an ill-posed inverse problem (7.1).

7.1.3 QUASI-SOLUTION OF THE ILL-POSED PROBLEM

We assume now that the right-hand side of (7.1) is given with some error:

$$\mathbf{d}_\delta = \mathbf{d} + \delta\mathbf{d}, \tag{7.2}$$

where

$$\|\mathbf{d} - \mathbf{d}_\delta\|_D \leq \delta. \tag{7.3}$$

Definition 35. A quasi-solution of the problem (7.1) in the correctness set C is an element $\mathbf{m}_\delta \in C$ which minimizes the norm $\|\mathbf{d} - \mathbf{d}_\delta\|_D$, i.e.:

$$\|A\mathbf{m}_\delta - \mathbf{d}_\delta\|_D = \inf_{m \in C} \|A\mathbf{m} - \mathbf{d}_\delta\|_D, \tag{7.4}$$

where $\inf \varphi$ denotes the greatest lower bound of the variable φ.

Obviously, we can reach the minimum of the $\|A\mathbf{m} - \mathbf{d}_\delta\|_D$ in C, if the correctness set is compact. In this case the quasi-solution exists for any data $\mathbf{d}_\delta$.
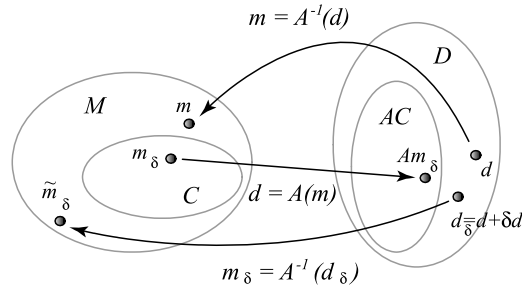
FIGURE 7.1

A quasi-solution, $\mathbf{m}_\delta$, is selected from the correctness set C under the condition that its image, $A(\mathbf{m}_\delta)$, is the closest element to the observed noisy data, $\mathbf{d}_\delta$, from the subset AC : $\|A\mathbf{m}_\delta - \mathbf{d}_\delta\|_D = \inf_{m \in C} \|A\mathbf{m} - \mathbf{d}_\delta\|_D$.

Fig. 7.1 illustrates the definition of a quasi-solution. The element $\mathbf{m} \in M$ is an exact solution of the inverse problem

$$\mathbf{d} = A(\mathbf{m}). \tag{7.5}$$

Subset AC of the data space D is an image of the correctness set C obtained as a result of the application of operator A. A quasi-solution, $\mathbf{m}_\delta$, is selected from the correctness set C under the condition that its image, $A(\mathbf{m}_\delta)$, is the closest element in the subset AC to the observed noisy data, $\mathbf{d}_\delta$.

It can be proved also that the quasi-solution is a continuous function of $\mathbf{d}_\delta$ (Tikhonov and Arsenin, 1977; Zhdanov, 2002).

The idea of the quasi-solution makes it possible to substitute the inverse problem solution by minimization of the distance $\mu_D(A\mathbf{m}, \mathbf{d}_\delta)$ in some appropriate class of suitable models. The standard method of functional minimization can be used to solve this problem and, therefore, to find the quasi-solution. In this way, we significantly simplify the inverse problem solution. However, this approach is effective only if we know *a priori* the corresponding class of the models (the correctness set) where we are searching for the solution. In many situations, it is difficult to describe this class completely, or we prefer not to restrict ourselves to some specific class. In this case we have to use a more general approach to a stable solution of the inverse problem, which will be discussed in the next sections.

7.2 FOUNDATIONS OF REGULARIZATION THEORY
7.2.1 DEFINITION OF MISFIT FUNCTIONAL

The optimality of an interpretation obtained by inversion is measured in terms of an error of fit, or, as we shall call it, a *misfit functional*. The concept is clear – error is a quantitative measure of the disagreement of the electromagnetic field computed for a hypothetical model and the electromagnetic field actually observed. However, the specific definition of error can vary, and the reasons for picking one or another definition are controlled by the physics of the inverse problem and/or by statistical considerations.
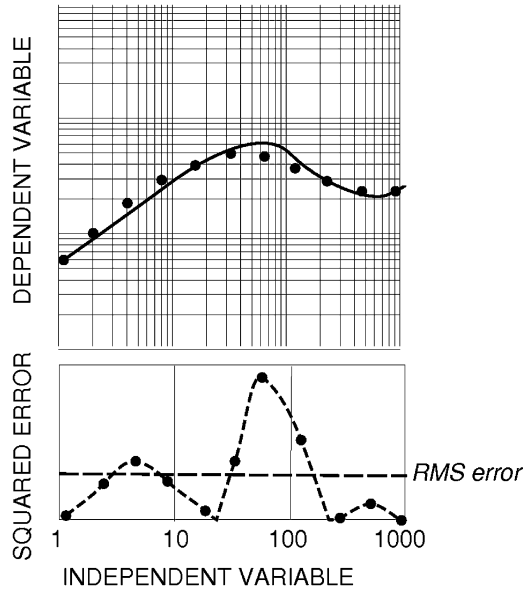
FIGURE 7.2

Definition of RMS error measure for a curve plotted in logarithmic coordinates. Errors of individual points are measured as the distance between a data point and a fitted curve when both are plotted to logarithmic coordinates.

The concept of error is demonstrated by the data set shown in Fig. 7.2. It shows a typical data set obtained by some electromagnetic method. The solid curve has been generated by some forward modeling program appropriate to the method used in acquiring the data. The N observations do not lie on the theoretical curve, nor will they ever, no matter what the optimality of modeling. One can always expect some error in measurement, but more fundamentally, one *cannot* expect the computed curve to pass exactly through the observed points even with noise-free data unless the earth behaves in exactly the way the model has been formulated. In the one-dimensional case, for example, this means the earth would have to consist exactly of a set of horizontal layers with uniform resistivities. Such will never be the case.

Fitting a set of geoelectrical data with a model is fundamentally different from synthesizing a set of data with a series approximation. For example, if one has a time series of data, it is possible to determine a finite-length Fourier series or a finite-length power series which will pass precisely through each point. Such approximations are done using series in which each term is *orthogonal* to each other; that is, the contribution of each term to the series is independent of all the other terms. The solutions to forward problems in electromagnetic geophysics are never an orthogonal set of functions, and therefore, cannot be forced to match an arbitrary set of points.

The error of fit is defined as some function of the individual differences between the fitting curve and the data at each point:

$$e_n = f(\rho_n^{pr} - \rho_n^{obs}), \quad n = 1, 2, 3, ..., N, \tag{7.6}$$

and for the misfit functional,

$$\varphi = \varphi(e_1, e_2, ..., e_n), \tag{7.7}$$

where e_n is the error of an individual data point, φ is the error measure for the set of points, ρ_n^{pr} is the predicted apparent resistivity computed for the data point n and ρ_n^{obs} is the observed resistivity for data point n.

There exist several methods for computing the misfit functional φ. The functional rule for defining the individual error, e_n, is often called the *error norm*, L. The most popular norm is the L_2, or least squares norm,

$$e_n = (\rho_n^{pr} - \rho_n^{obs})^2, \tag{7.8}$$

and

$$\varphi_{L_2} = \left\| \rho^{pr} - \rho^{obs} \right\|_{L_2}^2 = \sum_{n=1}^{N} e_n, \tag{7.9}$$

where $\|...\|_{L_2}$ denotes the L_2 norm (for a definition and properties of the L_2 norm see Zhdanov, 2002). The L_2 norm is usually considered to be appropriate for errors which follow a Gaussian distribution.

In practice, another measure of errors is frequently used, the root mean square (RMS) error, which measure the differences between data predicted by a model and data actually observed. If the observed data can be treated as uncorrelated random variables, the RMS error is the square root of the variance, known as the standard error (standard deviation) of the data:

$$\text{RMS}(\rho) = \sqrt{\frac{\sum_{n=1}^{N} (\rho_n^{pr} - \rho_n^{obs})^2}{N}}. \tag{7.10}$$

In many applications of electromagnetic method it is preferable to measure the convergence between the observed and predicted data using the logarithmic scale. In this case, the individual error, $e_n^{\ln}$, can be defined as

$$e_n^{\ln} = (\ln \rho_n^{pr} - \ln \rho_n^{obs})^2, \tag{7.11}$$

and the corresponding misfit functional of the log data will take the form:

$$\varphi_{L_2}^{\ln} = \left\| \ln \rho^{pr} - \ln \rho^{obs} \right\|_{L_2}^2 = \sum_{n=1}^{N} e_n. \tag{7.12}$$

The RMS error in the log scale can be calculated as

$$\text{RMS}(\ln \rho) = \sqrt{\frac{\sum_{n=1}^{N} (\ln \rho_n^{pr} - \ln \rho_n^{obs})^2}{N}}. \tag{7.13}$$

Fig. 7.2 presents an illustration of the RMS error measure for a curve plotted in logarithmic coordinates.

If there are extraneous outliers in the data, often called *bad points*, the importance of the bad points in defining the error measure is inappropriately large. Such points can be deleted arbitrarily, but one runs the risk of biasing the inversion process. A more rational approach is through *weighting* the error measure.

The greater the value of e_n in Eq. (7.8), the greater will be the weight an outlier is given in the error measure. Often, an L_1 or *minimax* error is used rather than the least squares error, and the corresponding misfit is calculated as

$$\varphi_{L_1} = \left\| \rho^{pr} - \rho^{obs} \right\|^2_{L_1} = \left(\sum_{n=1}^{N} \left| \rho_n^{pr} - \rho_n^{obs} \right| \right)^2, \tag{7.14}$$

where $\|...\|_{L_1}$ denotes the L_1 norm (for a definition and properties of the L_1 norm see Zhdanov, 2002).

In *robust* or *hybrid* error measures, the norm used for small errors is different from the norm used for large errors. We will discuss the principles of the robust estimation in more detail in Chapter 13, where we will use this approach for the analysis of magnetotelluric data.

7.2.2 REGULARIZING OPERATORS

The formal solution of the ill-posed inverse problem could result in unstable, unrealistic models. The regularization theory provides guidance for overcoming this difficulty. The foundations of the regularization theory were developed in numerous publications by Andrei N. Tikhonov, which were reprinted in 1999 as a special book, published by Moscow State University (Tikhonov, 1999). In this chapter, I will present a short overview of the basic principles of the Tikhonov regularization theory, following his original monograph (Tikhonov and Arsenin, 1977).

Let us consider the inverse geophysical problem described by the operator equation

$$\mathbf{d} = A(\mathbf{m}), \tag{7.15}$$

where $\mathbf{m}$ represents model parameters, and $\mathbf{d}$ is observed geophysical data. In general cases, the inverse operator A^{-1} is not continuous and, therefore, the inverse problem (7.15) is ill posed. The main idea of any regularization algorithm is to consider, instead of one ill-posed inverse problem (7.15), a family of well-posed problems,

$$\mathbf{d} = A_\alpha(\mathbf{m}), \tag{7.16}$$

which approximate the original inverse problem in some sense (Strakhov, 1968, 1969a, 1969b). The scalar parameter $\alpha > 0$ is called *a regularization parameter*. We require also that

$$\mathbf{m}_\alpha \rightarrow \mathbf{m}_t, \ \text{if} \ \alpha \rightarrow 0,$$

where $\mathbf{m}_\alpha = A_\alpha^{-1}(\mathbf{d})$ is the solution of the inverse problem (7.16), and $\mathbf{m}_t$ is the true solution of the original problem (7.15). Thus, we replace the solution of one ill-posed inverse problem with the solutions of a family of well-posed problems, assuming that these solutions, $\mathbf{m}_\alpha$, tend asymptotically to the true solution, as α tends to zero.

In other words, any regularization algorithm is based on the approximation of the noncontinuous inverse operator A^{-1} by the family of continuous inverse operators $A_\alpha^{-1}(\mathbf{d})$ that depend on the regularization parameter α. The regularization must be such that, as α vanishes, the operators in the family should approach the exact inverse operator A^{-1}.

We can see that the regularizing operators can be constructed by approximating the ill-posed equation (7.15) by the system of well-posed equations (7.16), where the corresponding inverse operators A_α^{-1} are continuous. These inverse operators can be treated as the regularizing operators:

$$A_\alpha^{-1}(\mathbf{d}) = R(\mathbf{d}, \alpha).$$

The only problem now is how to find the family of regularizing operators. Tikhonov and Arsenin (1977) suggested the following scheme for constructing regularizing operators. It is based on introducing special stabilizing and parametric functionals.

7.2.3 STABILIZING FUNCTIONALS

A stabilizing functional (or a stabilizer) is used to select from the space M of all possible models the subset M_c, which is a correctness set.

Definition 36. A nonnegative functional $s(\mathbf{m})$ in some metric space M is called *a stabilizing functional* if, for any real number $c > 0$ from the domain of functional values, the subset M_c of the elements $\mathbf{m} \in M$, for which $s(\mathbf{m}) \leq c$, is compact.

The main role of the stabilizing functional (a stabilizer) is to select the appropriate class of models for inverse problem solution. In practice, we usually select the model that is simplest in some sense, yet still fits the data. In other words, we do not want features in the model which are not needed to fit the data.

There are several common choices for a stabilizer (Zhdanov, 2002, 2015). One is based on the least squares criterion, or, in other words, on the L_2 norm for functions describing model parameters:

$$s_{L_2(\mathbf{m})} = \|\mathbf{m}\|_{L_2}^2 = (\mathbf{m}, \mathbf{m})_{L_2} = \int_V |m(\mathbf{r})|^2 \, dv = \min. \tag{7.17}$$

In the last formula we assume that the function $m(\mathbf{r})$, describing model parameters, is given within a three-dimensional domain V, and $\mathbf{r}$ is a radius-vector of an observation point. The conventional argument in support of the norm (7.17) comes from statistics and is based on an assumption that the least squares image is the best over the entire ensemble of all possible images.

We can use, also, a quadratic functional s_w:

$$s_w = \|W\mathbf{m}\|_{L_2}^2 = (W\mathbf{m}, W\mathbf{m})_{L_2} = \int_V |w(\mathbf{r}) m(\mathbf{r})|^2 \, dv = \min, \tag{7.18}$$

where $w(\mathbf{r})$ is an arbitrary weighting function, and W is a linear operator of multiplication of the function $m(\mathbf{r})$ by the weighting function $w(\mathbf{r})$.

Another stabilizer uses a minimum norm of difference between a selected model and some *a priori* model $\mathbf{m}_{apr}$:

$$s_{L_2apr(m)} = \|\mathbf{m} - \mathbf{m}_{apr}\|_{L_2}^2 = \min. \tag{7.19}$$

The minimum norm criterion (7.17), as applied to the gradient of the model parameters ∇m, brings us to a maximum smoothness stabilizing functional:

$$s_{\max sm}(\mathbf{m}) = \|\nabla\mathbf{m}\|_{L_2}^2 = (\nabla\mathbf{m}, \nabla\mathbf{m})_{L_2}$$
$$= \int_V |\nabla m(\mathbf{r})|^2 \, dv = \min. \tag{7.20}$$

In some cases, one can use the minimum norm of the Laplacian of model parameters $\nabla^2 m$,

$$s_{\max sm}(m) = \left\|\nabla^2 m\right\|^2 = \left(\nabla^2 m, \nabla^2 m\right) = \min. \tag{7.21}$$

It has been successfully used in many inversion schemes developed for geophysical data interpretation (see, for example, Constable et al., 1987; Smith and Booker, 1991; Zhdanov, 1993; Zhdanov and Fang, 1996a, 1996b). This stabilizer produces smooth models, which in many practical situations fail to describe properly the real blocky geological structures. It also can result in spurious oscillations when m is discontinuous.

One can use a total variation stabilizing functional (Rudin et al., 1992), which is essentially the L_1 norm of the gradient:

$$s_{TV}(\mathbf{m}) = \|\nabla\mathbf{m}\|_{L_1} = \int_V |\nabla m(\mathbf{r})| \, dv, \tag{7.22}$$

or a modified TV stabilizing functional:

$$s_{\beta TV}(\mathbf{m}) = \int_V \sqrt{|\nabla m(\mathbf{r})|^2 + \beta^2} \, dv, \tag{7.23}$$

where β is a small number.

The advantage of the last functional is that it does not require the function m to be continuous, only piecewise smooth (Vogel and Oman, 1998). Since the TV norm does not penalize discontinuity in the model parameters, we can remove oscillations while preserving sharp conductivity contrasts. At the same time, it imposes a limit on the total variation of m and on the combined arc length of the curves along which m is discontinuous. That is why this functional produces a much better result than maximum smoothness functionals when the blocky structures are imaged.

TV functionals $s_{TV}(\mathbf{m})$ and $s_{\beta TV}(\mathbf{m})$, however, tend to decrease the bounds of variation of the model parameters, as can be seen from (7.22) and (7.23), and in this sense they still try to "smooth" the real image. However, this "smoothness" is much weaker than in the case of traditional stabilizers (7.20) and (7.19).

One can diminish this "smoothness" effect by introducing another stabilizing functional which minimizes the area where significant variations of the model parameters and/or discontinuity occur (Portniaguine and Zhdanov, 1999a). This stabilizer is called *a minimum gradient support (MGS) functional*. For the sake of simplicity we will discuss first *a minimum support (MS) functional*, which provides a model with a minimum area of the distribution of anomalous parameters.

We introduce a support of m (denoted $\mathrm{spt}\,m$) as the combined closed subdomains of V where $m \neq 0$. We call $\mathrm{spt}\,m$ *a model parameter support*. Consider the following functional of the model parameters:

$$s_\beta(\mathbf{m}) = \int_V \frac{m^2(\mathbf{r})}{m^2(\mathbf{r}) + \beta^2} dv = \int_{\mathrm{spt}\,m} \left[1 - \frac{\beta^2}{m^2(\mathbf{r}) + \beta^2} \right] dv$$

$$= \mathrm{spt}\,m - \beta^2 \int_{\mathrm{spt}\,m} \frac{1}{m^2(\mathbf{r}) + \beta^2} dv. \tag{7.24}$$

From the last expression we can see that

$$s_\beta(\mathbf{m}) \to \mathrm{spt}\,m, \text{ if } \beta \to 0. \tag{7.25}$$

Thus, $s_\beta(\mathbf{m})$ can be treated as a functional, proportional (for a small β) to the model parameter support. We can use this functional to introduce a minimum support (MS) stabilizing functional $s_{MS}(\mathbf{m})$ as

$$s_{MS}(\mathbf{m}) = s_\beta(\mathbf{m} - \mathbf{m}_{apr}) = \int_V \frac{(m - m_{apr})^2}{(m - m_{apr})^2 + \beta^2} dv. \tag{7.26}$$

This functional has an important property: it minimizes the total area with nonzero departure of the model parameters from the given *a priori* model. Thus, a dispersed and smooth distribution of the parameters with all values different from the *a priori* model $\mathbf{m}_{apr}$ results in a big penalty function, while a well-focused distribution with a small departure from $\mathbf{m}_{apr}$ will have a small penalty function.

We can use this property of the minimum support functional to increase the resolution of blocky structures. To do so, we modify $s_{MS}(\mathbf{m})$ and introduce *a minimum gradient support (MGS) functional* as

$$s_{MGS}(\mathbf{m}) = s_\beta[\nabla \mathbf{m}] = \int_V \frac{\nabla m \cdot \nabla m}{\nabla m \cdot \nabla m + \beta^2} dv. \tag{7.27}$$

We denote by $\mathrm{spt}\,\nabla m$ the combined closed subdomains of V where $\nabla m \neq 0$. We call $\mathrm{spt}\,\nabla m$ *a gradient support*. Then, expression (7.27) can be modified:

$$s_{MGS}(\mathbf{m}) = \mathrm{spt}\,\nabla m - \beta^2 \int_{\mathrm{spt}\nabla m} \frac{1}{\nabla m \cdot \nabla m + \beta^2} dv. \tag{7.28}$$

From the last expression we can see that

$$s_{MGS}(\mathbf{m}) \to \mathrm{spt}\,\nabla m, \text{ if } \beta \to 0. \tag{7.29}$$

Thus, the functional $s_{MGS}(\mathbf{m})$ can really be treated as a functional proportional (for a small β) to the gradient support. This functional helps to generate a sharp and focused image of the inverse model. Fig. 7.3 illustrates this property of the minimum gradient support functional.

By analogy with the minimum support functional, $s_{MS}(\mathbf{m})$, we can introduce a *vertical minimum support functional* by the following formula:

$$s_{VMS}(m) = \iiint_V \left[\frac{m^2(\mathbf{r})}{\iint_S m^2(\mathbf{r})\,dxdy + \beta^2} \right] dv, \tag{7.30}$$

where S is a horizontal section of the rectangular domain V.

We introduce a vertical support of m (denote $\mathrm{vspt}(m)$) as the combined closed subdomains of S where $m \neq 0$. The functional $s_{VMS}(m)$ is equal to:

$$\begin{aligned}
s_{MS}(m) &= \int_{\mathrm{vspt}(m)} \left[\frac{\iint_S m^2(\mathbf{r})\,dxdy}{\iint_S m^2(\mathbf{r})\,dxdy + \beta^2} \right] dz \\
&= \int_{\mathrm{vspt}(m)} \left[1 - \frac{\beta^2}{\iint_S m^2(\mathbf{r})\,dxdy + \beta^2} \right] dz \\
&= \mathrm{vspt}(m) - \beta^2 \int_{\mathrm{vspt}(m)} \left[\frac{1}{\iint_S m^2(\mathbf{r})\,dxdy + \beta^2} \right] dz. \tag{7.31}
\end{aligned}$$

From the last equation we see that, the vertical minimum support functional is proportional (for a small β) to the model parameter vertical support:

$$s_{VMS}(m) \to \mathrm{vspt}(m), \ \text{if } e \to 0.$$

Thus, application of the minimum vertical support functional should result in producing the models with the anomalies having a thin dimension in the vertical direction. This kind of models are useful, for example, in geophysical exploration for relatively thin oil and gas reservoirs.

Thus, the MS or MGS stabilizers introduced above select the inverse models from a class of models with the minimum volume of the domain with the anomalous parameter distribution (MS stabilizer) or with a minimum volume of area where the gradient of the model parameters is nonzero (MGS stabilizer). These classes of models describe compact objects (minimum support) or objects with sharp boundaries (minimum gradient support), which are typical targets in geophysical exploration. We call this technique a focusing regularized inversion to distinguish it from the traditional smooth regularized inversion.

Let us analyze now more carefully how one can use a stabilizer to select an appropriate class of the models. Assume that the data $\mathbf{d}_\delta$ are observed with some noise $\mathbf{d}_\delta = \mathbf{d}_t + \delta\mathbf{d}$, where $\mathbf{d}_t$ is the true solution of the problem. In other words, we assume that the misfit (distance) between the observed data and true data is less than the given level of the errors, δ, in the observed data,

$$\|\mathbf{d}_\delta - \mathbf{d}_t\|_D \le \delta, \tag{7.32}$$

where $\delta = \|\delta\mathbf{d}\|$.

In this situation, it is natural to search for an approximate solution in the set Q_δ of the models $\mathbf{m}$ such that

$$\|A(\mathbf{m}) - \mathbf{d}_\delta\| \le \delta. \tag{7.33}$$
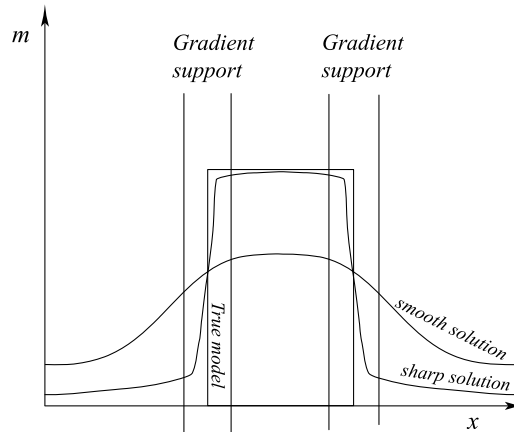
FIGURE 7.3

Illustration of the principle of the minimum gradient support inversion. A smooth inversion produces a smooth image of a true rectangular model, while the inversion with the minimum gradient support stabilizer generates a sharp image, close to the true model.

Thus, $Q_\delta \subset M$ is a set of possible solutions.

The main application of a stabilizer is to select from the set of possible solutions Q_δ the solutions that continuously depend on the data and which possesses a specific property depending on the choice of a stabilizer. Such solutions can be selected by the condition of the minimum of the stabilizing functional:

$$s(\mathbf{m}; \ \mathbf{m} \in Q_\delta) = \min. \tag{7.34}$$

We have introduced a stabilizing functional under the condition that it selects a compact subset M_C from a metric space of the model parameters. Thus, we can say that a stabilizer from a set of possible solutions, Q_δ, selects a solution, which at the same time belongs to the correctness set M_C. Fig. 7.4 helps to explain this role of the stabilizing functional.

The existence of the model, minimizing (7.34), was demonstrated by Tikhonov and Arsenin (1977). We will denote this model as $\mathbf{m}_\delta$:

$$s(\mathbf{m}_\delta; \ \mathbf{m}_\delta \in Q_\delta) = \min. \tag{7.35}$$

One can consider a model $\mathbf{m}_\delta$ as the result of an application of the operator $R(\mathbf{d}_\delta, \delta)$ to the observed data $\mathbf{d}_\delta$, depending on the parameter δ:

$$\mathbf{m}_\delta = R(\mathbf{d}_\delta, \delta) \tag{7.36}$$

The major theorem of the regularization theory states that the operator $R(\mathbf{d}_\delta, \delta)$, introduced by formula (7.36), is the regularizing operator for Eq. (7.15), and $\mathbf{m}_\delta$ can be used as an approximate solution of the inverse problem (note that in this case $\alpha = \delta$, while in general cases $\alpha = \alpha(\delta)$). The proof of this theorem can be found in Tikhonov and Arsenin (1977) and Zhdanov (2002).

$$d = A\,(m)$$

$$m_\delta = R\,(d_\delta, \delta)$$

$$d_\delta = d + \delta d$$
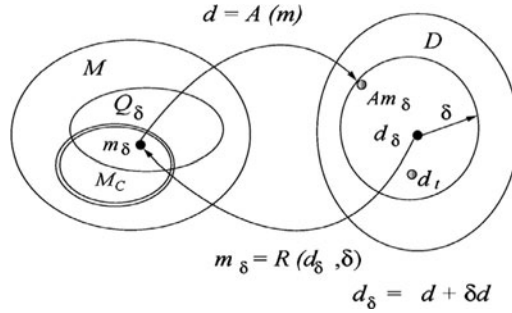
FIGURE 7.4

The stabilizing functional selects from a set of the possible solutions, Q_δ, a solution, $\mathbf{m}_\delta$, which at the same time belongs to the correctness set M_C.

7.2.4 TIKHONOV PARAMETRIC FUNCTIONAL

It has been proved by Tikhonov and Arsenin (1977) that, for a wide class of stabilizing functionals, their minimum is reached on the model $\mathbf{m}_\delta$ such that $\|A(\mathbf{m}_\delta) - \mathbf{d}_\delta\|_D = \delta$. Thus, we can solve the problem of minimization (7.34) under the condition that

$$\|A(\mathbf{m}_\delta) - \mathbf{d}_\delta\|_D = \delta. \tag{7.37}$$

In other words, one should consider the problem of minimization of the stabilizing functional (7.34), when the model $\mathbf{m}$ is subject to the constraint (7.37). A common way to solve this problem is to introduce an unconstrained *parametric functional* $P^\alpha(\mathbf{m}, \mathbf{d}_\delta)$, $\mathbf{m} \in M$, given by

$$P^\alpha(\mathbf{m}, \mathbf{d}_\delta) = \|A(\mathbf{m}_\delta) - \mathbf{d}_\delta\|_D^2 + \alpha s(\mathbf{m}), \tag{7.38}$$

and to solve the problem of minimization of this functional:

$$P^\alpha(\mathbf{m}, \mathbf{d}_\delta) = \min. \tag{7.39}$$

Functional $\|A(\mathbf{m}_\delta) - \mathbf{d}_\delta\|_D^2$ is called *a misfit functional*. Thus, the parametric functional $P^\alpha(\mathbf{m}, \mathbf{d}_\delta)$ is a linear combination of the misfit and stabilizing functionals, and the unknown real parameter α is similar to the Lagrangian multiplier. It is determined under the condition

$$\|A(\mathbf{m}_\alpha) - \mathbf{d}_\delta\|_D = \delta, \tag{7.40}$$

where $\mathbf{m}_\alpha$ is the element on which $P^\alpha(\mathbf{m}, \mathbf{d}_\delta)$ reaches its minimum. The functional $P^\alpha(\mathbf{m}, \mathbf{d}_\delta)$ is called *the Tikhonov parametric functional*.

It can be proved that, for any positive number, $\alpha > 0$, and for any data, $\mathbf{d}_\delta \in D$, we can determine an operator, $R(\mathbf{d}_\delta, \alpha)$, with the values in M, such that the model

$$\mathbf{m}_\alpha = R(\mathbf{d}_\delta, \alpha) \tag{7.41}$$

gives the minimum of the Tikhonov parametric functional $P^\alpha(\mathbf{m}, \mathbf{d}_\delta)$.

The fundamental result of the regularization theory is that *this operator*, $R(\mathbf{d}_\delta, \alpha)$, *is a regularizing operator for the problem* (7.1) (Tikhonov and Arsenin, 1977).

Thus, as an approximate solution of the inverse problem (7.1), we take the solution of another problem (7.39) (problem of minimization of the Tikhonov parametric functional $P^\alpha(\mathbf{m}, \mathbf{d}_\delta)$), close to the initial problem for the small values of the data errors δ.

7.3 REGULARIZATION PARAMETER
7.3.1 TIKHONOV METHOD OF REGULARIZATION PARAMETER SELECTION

The regularization parameter α describes the trade-off between the best fitting and most reasonable stabilization. In a case where α is selected to be too small, the minimization of the parametric functional $P^\alpha(\mathbf{m})$ is equivalent to the minimization of the misfit functional; therefore we have no regularization, which can result in an unstable incorrect solution. When α is too large, the minimization of the parametric functional $P^\alpha(\mathbf{m})$ is equivalent to the minimization of the stabilizing functional $s(\mathbf{m})$, which will force the solution to be closer to the *a priori* model. Ultimately, we would expect the final model to be exactly like the *a priori* model, while the observed data are totally ignored in the inversion. Thus, the critical question in the regularized solution of the inverse problem is the selection of the optimal regularization parameter α. The basic principles used for determining the regularization parameter α are discussed in Tikhonov and Arsenin (1977). The solution of this problem can be based on the following consideration.

Let us assume that data $\mathbf{d}_\delta$ are observed with some noise, $\mathbf{d}_\delta = \mathbf{d}_t + \delta\mathbf{d}$, where $\mathbf{d}_t$ is the true solution of the problem and the level of the errors in the observed data is equal to δ:

$$\|\mathbf{d}_\delta - \mathbf{d}_t\| \leq \delta. \tag{7.42}$$

Then the regularization parameter can be determined by the misfit condition (7.41)

$$\|A(\mathbf{m}_\alpha) - \mathbf{d}_\delta\| = \delta. \tag{7.43}$$

To justify this approach we will examine more carefully the properties of all three functionals involved in the regularization method: the Tikhonov parametric functional and the stabilizing and misfit functionals.

Let us introduce the following notations:

$$\begin{aligned}
p(\alpha) &= P^\alpha(\mathbf{m}_\alpha, \mathbf{d}_\delta), \ \text{ parametric functional,} \\
s(\alpha) &= s(\mathbf{m}_\alpha), \ \text{ stabilizing functional,} \\
i(\alpha) &= \|A(\mathbf{m}_\alpha) - \mathbf{d}_\delta\|, \ \text{ misfit functional.}
\end{aligned} \tag{7.44}$$

We examine some properties of the functions $p(\alpha), i(\alpha)$, and $s(\alpha)$.

Property 1. Functions $p(\alpha), i(\alpha)$, and $s(\alpha)$ are monotonic functions: $p(\alpha)$ and $i(\alpha)$ are not decreasing and $s(\alpha)$ is not increasing.

Proof. Let $\alpha_1 < \alpha_2$ and

$$p_k = p(\alpha_k) = P^{\alpha_k}(\mathbf{m}_{\alpha_k}, \mathbf{d}_\delta),$$
$$i_k = i(\alpha_k) = \mu_D^2(A(\mathbf{m}_{\alpha_k}), \mathbf{d}_\delta),$$
$$s_k = s(\alpha_k) = s(\mathbf{m}_{\alpha_k}).$$

The following inequality holds:

$$p_2 = i_2 + \alpha_2 s_2 \geq i_2 + \alpha_1 s_2, \tag{7.45}$$

because $\alpha_1 < \alpha_2$.

On the other hand

$$P^{\alpha_1}(\mathbf{m}_{\alpha_2}, \mathbf{d}_\delta) = i_2 + \alpha_1 s_2 \geq i_1 + \alpha_1 s_1 = p_1 = P^{\alpha_1}(\mathbf{m}_{\alpha_1}, \mathbf{d}_\delta), \tag{7.46}$$

because m_{α_1} realizes the minimum p_1 of the functional $P^{\alpha_1}(\mathbf{m}, \mathbf{d}_\delta)$.

Thus from (7.45) and (7.46) we have

$$p_2 \geq p_1 \tag{7.47}$$

for

$$\alpha_2 > \alpha_1,$$

which means that $p(\alpha)$ is a monotonic function of α.

Furthermore,

$$P^{\alpha_2}(\mathbf{m}_{\alpha_1}, \mathbf{d}_\delta) = i_1 + \alpha_2 s_1 \geq i_2 + \alpha_2 s_2 = P^{\alpha_2}(\mathbf{m}_{\alpha_2}, \mathbf{d}_\delta), \tag{7.48}$$

because $\mathbf{m}_{\alpha_2}$ realizes the minimum p_2 of the functional $P^{\alpha_2}(\mathbf{m}, \mathbf{d}_\delta)$.

Subtracting the left-hand side of inequality (7.48) from the right-hand side of inequality (7.46) and the right-hand side of inequality (7.48) from the left-hand side of inequality (7.46), we obtain

$$(\alpha_1 - \alpha_2)s_2 \geq (\alpha_1 - \alpha_2)s_1. \tag{7.49}$$

Since $\alpha_1 < \alpha_2$,

$$s_1 \geq s_2. \tag{7.50}$$

From inequalities (7.46) and (7.50) it follows that

$$i_2 - i_1 \geq \alpha_1(s_1 - s_2)$$

and hence

$$i_2 \geq i_1. \qquad \square$$

Property 2. It can be proved that the functions $p(\alpha), i(\alpha)$, and $s(\alpha)$ are continuous functions (if the element m_α is unique).

Note, also, that

$$p(\alpha) \to 0 \text{ for } \alpha \to 0,$$
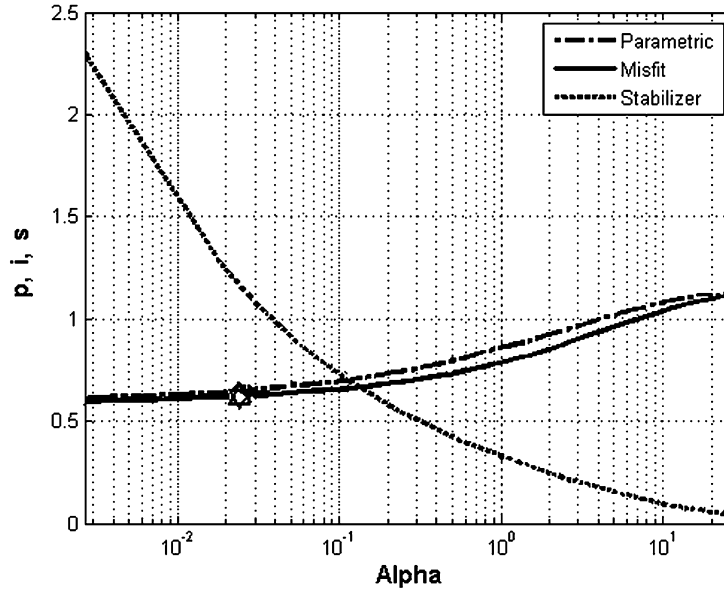
FIGURE 7.5

Illustration of the principle of optimal regularization parameter selection. The plots show the behavior of the misfit functional, parametric functional, and a stabilizer versus the logarithm of the regularization parameter, α.

and

$$p(0) = 0. \tag{7.51}$$

From the fact that

$$i(\alpha) + \alpha s(\alpha) = p(\alpha) \to 0, \text{ for } \alpha \to 0,$$

it follows that

$$i(0) = 0. \tag{7.52}$$

Thus we have proved the following theorem.

Theorem 37. *If $i(\alpha)$ is a one-to-one function, then, for any positive number $\delta < \delta_0 = \mu_D(A(\mathbf{m}_0), \mathbf{d}_\delta)$ (where $\mathbf{m}_0$ is some a priori model), there exists $\alpha(\delta)$ such that $\mu_D(A(\mathbf{m}_{\alpha(\delta)}), \mathbf{d}_\delta) = \delta$.*

Fig. 7.5 helps to explain the principle of optimal regularization parameter selection. One can see that, because of the monotonic character of the function $i(\alpha)$, there is only one point, α_0, where $i(\alpha_0) = \mu_D^2(A(\mathbf{m}_{\alpha_0}), \mathbf{d}_\delta) = \delta^2$.

Let us consider one simple numerical method for determining the parameter α. Consider, for example, a progression of numbers:

$$\alpha_k = \alpha_1 q^{k-1}, \ k = 1, 2, ..., n; \ 0 < q < 1. \tag{7.53}$$
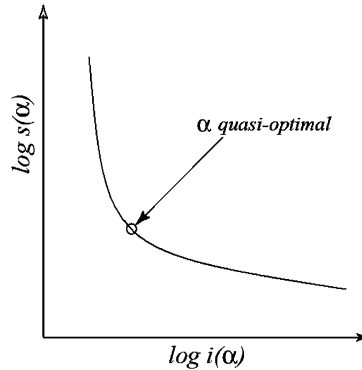
FIGURE 7.6

The L curve represents a simple curve for all possible α of the misfit functional, $i(\alpha)$, versus the stabilizing functional, $s(\alpha)$, plotted in log-log scale. The distinct corner, separating the vertical and the horizontal branches of this curve, corresponds to the quasi-optimal value of the regularization parameter α.

For any number α_k we can find the element $\mathbf{m}_{\alpha_k}$ minimizing $P^{\alpha_k}(\mathbf{m}, \mathbf{d}_\delta)$ and calculate the misfit $\mu_D(A(\mathbf{m}_{\alpha_k}), \mathbf{d}_\delta)$. The optimal value of the parameter α is the number $\alpha_0 = \alpha_{k0}$, for which, with the necessary accuracy, we have the equality

$$\mu_D(A(\mathbf{m}_{\alpha_{k0}}), \mathbf{d}_\delta) = \delta. \tag{7.54}$$

The equality (7.54) is called the *misfit condition*.

7.3.2 L-CURVE METHOD OF REGULARIZATION PARAMETER SELECTION

L-curve analysis (Hansen, 1998) represents a simple graphical tool for qualitative selection of the quasi-optimal regularization parameter.

It is based on plotting for all possible α the curve of the misfit functional, $i(\alpha)$, versus the stabilizing functional, $s(\alpha)$ (where we use notations (7.44)). The L curve illustrates the trade-off between the best fitting (minimizing a misfit) and the most reasonable stabilization (minimizing a stabilizer). In a case where α is selected to be too small, the minimization of the parametric functional $P^\alpha(\mathbf{m})$ is equivalent to the minimization of the misfit functional; therefore $i(\alpha)$ decreases, while $s(\alpha)$ increases. When α is too large, the minimization of the parametric functional $P^\alpha(\mathbf{m})$ is equivalent to the minimization of the stabilizing functional; therefore $s(\alpha)$ decreases, while $i(\alpha)$ increases. As a result, it turns out that the L-curve, when it is plotted in log-log scale, very often has the characteristic L-shape appearance (Fig. 7.6) that justifies its name (Hansen, 1998).

The distinct corner, separating the vertical from the horizontal branches of this curve, corresponds to the quasi-optimal value of the regularization parameter α. We should note that in many practical cases the plot of the misfit functional, $i(\alpha)$, versus the stabilizing functional, $s(\alpha)$, does not have a clear corner, which can be easily identified by a visual analysis. Most often this curve has a relatively smooth behavior, as shown in Fig. 7.7. In this situation the optimal value of the regularization parameter
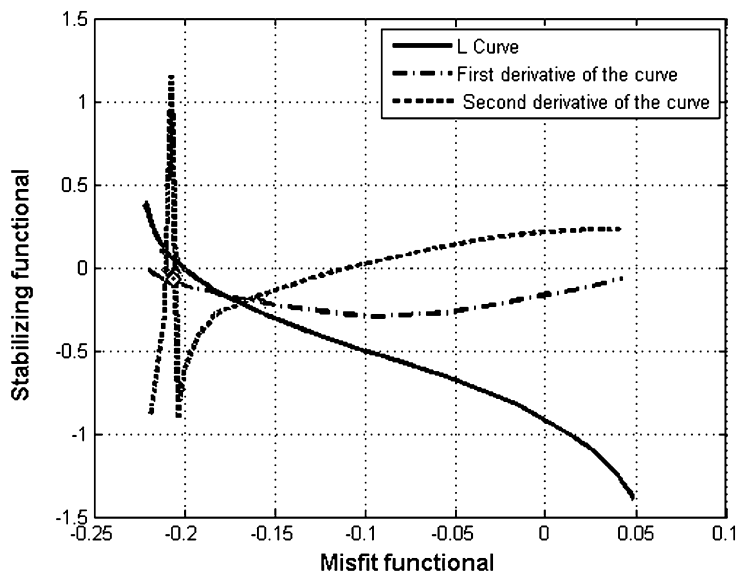
FIGURE 7.7

L-curve plot for selection of the quasi-optimal regularization parameter α. The star dot shows the point where the curvature of the curve is greatest, corresponding to the quasi-optimal value of the regularization parameter α.

can be found by plotting the curvature of the L curve. Obviously, the point with the maximum curvature corresponds to the "corner" of the L curve. Fig. 7.7 presents an example of these calculations. We show in this figure the L curve, the first derivative of the L curve, and the plot of its second derivative (the curvature). The star dot shows the point where the curvature of the curve is greatest, corresponding to the quasi-optimal value of the regularization parameter α.

REFERENCES AND RECOMMENDED READING TO CHAPTER 7

Constable, S. C., R. L. Parker, and C. G. Constable, 1987, Occam's inversion: A practical algorithm for generating smooth models from electromagnetic sounding data: Geophysics, **52** (3), 289–300.

Hansen, C., 1998, Rank-deficient and discrete ill-posed problems. Numerical aspects of linear inversion: Department of mathematical modeling, Technical University of Denmark, Lyngby, 247 pp.

Portniaguine, O., and M. S. Zhdanov, 1999, Focusing geophysical inversion images: Geophysics, **64** (3), 874–887.

Rudin, L. I., S. Osher, and E. Fatemi, 1992, Nonlinear total variation based noise removal algorithms: Physica D, **60**, 259–268.

Smith, J. T., and J. R. Booker, 1991, Rapid inversion of two- and three-dimensional magnetotelluric data: Journal of Geophysical Research, **96**, 3905–3922.

Strakhov, V. N, 1968, Numerical solution of incorrect problems representable by integral equations of convolution type (*in Russian*): DAN SSSR, **178** (2), 299.

Strakhov, V. N., 1969a, Theory of approximate solution of the linear ill-posed problems in a Hilbert space and its application in applied geophysics, Part I (*in Russian*): Izvestia AN SSSR, Fizika Zemli, (8), 30–53.

Strakhov, V. N., 1969b, Theory of approximate solution of the linear ill-posed problems in a Hilbert space and its application in applied geophysics, Part II (*in Russian*): Izvestia AN SSSR, Fizika Zemli, (9), 64–96.

Tikhonov, A. N., 1963a, Solution of ill-posed problems and the regularization method (*in Russian)*: Soviet Math Dokladi, (4), 1035–1038.

Tikhonov, A. N., 1963b, Regularization of ill-posed problems (*in Russian*): Soviet Math Dokladi, (4), 1624–1627.

Tikhonov, A. N., 1999, Mathematical geophysics (*in Russian*): Moscow State University, 476 pp.

Tikhonov, A. N. and V. Y. Arsenin, 1977, Solution of ill-posed problems: V. H. Winston and Sons, 258 pp.

Vogel, C. R., and M. E. Oman, 1998, Fast total variation based reconstruction of noisy, blurred images: IEEE Transactions on Image Processing, **7** (6), 813–824.

Zhdanov, M. S., and S. Fang, 1996a, Quasi-linear approximation in 3-D EM modeling: Geophysics, **61**, 646–665.

Zhdanov, M. S., and S. Fang, 1996b, 3-D quasi-linear electromagnetic inversion: Radio Science, **31** (4), 741–754.

Zhdanov, M. S., 1993, Tutorial: regularization in inversion theory: CWP-136, Colorado School of Mines, 47 pp.

Zhdanov, M. S., 2002, Geophysical inverse theory and regularization problems: Elsevier, Amsterdam, London, New York, Tokyo, 628 pp.

Zhdanov, M. S., 2015, Inverse theory and applications in geophysics: Elsevier, Amsterdam, London, New York, Tokyo, 730 pp.

ELECTROMAGNETIC INVERSION

Electromagnetic (EM) inverse methods are widely used in the interpretation of geophysical EM data in mineral, hydrocarbon, and groundwater exploration. During the last decade we have observed remarkable progress in the development of a multi-dimensional interpretation technique. Many papers have been published during the last 20 years on 3-D inversion of EM geophysical data (Madden and Mackie, 1989; Eaton, 1989; Zhdanov and Keller, 1994; Zhdanov and Fang, 1996b; Alumbaugh and Newman, 1997; Newman and Alumbaugh, 1997; Zhdanov and Fang, 1999; Zhdanov et al., 2000b; Zhdanov and Hursán, 2000; Sasaki, 2001; Zhdanov and Tartaras, 2002; Zhdanov and Golubev, 2003; Mackie and Watts, 2004; Siripunvaraporn et al., 2004, 2005; Gribenko and Zhdanov, 2007; Zhdanov et al., 2014a, 2014b). However, EM inversion is still one of the most difficult problems of EM geophysics.

Difficulties arise even in forward modeling because of the huge size of the numerical problem to be solved for adequate representation of the complex 3-D distribution of EM parameters in the media. As a result, computer simulation time and memory requirements could be excessive especially for realistic models. Additional difficulties are related to EM inverse problem solution. These problems are nonlinear and ill posed, because, in general cases, the solutions can be unstable and/or nonunique. In order to overcome these difficulties one should use the methods of regularization theory to obtain stable, unique solutions of the original ill-posed EM inverse problems.

In this chapter we will outline the basic principles of electromagnetic inversion and imaging based on the methods of regularization theory.

8.1 LINEAR INVERSIONS

The simplest approach to the solution of electromagnetic inverse problems is based on linearization of the forward modeling operator. This approach has found wide practical application because of the ease of its implementation, the accessibility of software for linear inversion, and the speed of numerical calculations. Linearization uses the family of linear and nonlinear approximations based on the Born method, described in Chapter 6. The simplest approach to linearization is based on the Born approximation.

8.1.1 BORN INVERSION

The simplest approach to the solution of the electromagnetic inverse problem is based on linearization of the integral equations (6.40) and (6.41) using a Born approximation:

$$\mathbf{E}^a \left(\mathbf{r}_j \right) \approx \mathbf{G}_E \left(\Delta \widetilde{\sigma} \mathbf{E}^b \right) = \iiint_D \widehat{\mathbf{G}}_E \left(\mathbf{r}_j \mid \mathbf{r} \right) \Delta \widetilde{\sigma} \left(\mathbf{r} \right) \mathbf{E}^b \left(\mathbf{r} \right) dv, \tag{8.1}$$

$$\mathbf{H}^a \left(\mathbf{r}_j \right) \approx \mathbf{G}_H \left(\Delta \widetilde{\sigma} \mathbf{E}^b \right) = \iiint_D \widehat{\mathbf{G}}_H \left(\mathbf{r}_j \mid \mathbf{r} \right) \Delta \widetilde{\sigma} \left(\mathbf{r} \right) \mathbf{E}^b \left(\mathbf{r} \right) dv. \tag{8.2}$$

Note that comparing formulae (8.1), (8.2) and (6.62), (6.63), we see that the expressions on the right-hand sides of the Born approximations can be represented as the Fréchet derivative operators calculated for the background conductivity $\widetilde{\sigma}_b$ and the anomalous conductivity $\Delta \widetilde{\sigma}$:

$$\mathbf{G}_E \left(\Delta \widetilde{\sigma} \mathbf{E}^b \right) = \mathbf{F}_E \left(\widetilde{\sigma}_b, \Delta \widetilde{\sigma} \right), \tag{8.3}$$

$$\mathbf{G}_H \left(\Delta \widetilde{\sigma} \mathbf{E}^b \right) = \mathbf{F}_H \left(\widetilde{\sigma}, \Delta \widetilde{\sigma} \right). \tag{8.4}$$

The argument in the expressions for the Fréchet differentials, $\mathbf{F}_{E,H}(\widetilde{\sigma}_b, \Delta \widetilde{\sigma})$, consists of two parts. The first part, $\widetilde{\sigma}_b$, is the background conductivity distribution, for which we calculate the forward modeling operator variation; the second part, $\Delta \widetilde{\sigma}$, is the anomalous conductivity, which plays the role of the background conductivity variation. We will use below the following simplified notations for the Fréchet differentials:

$$\mathbf{F}_{E,H}(\widetilde{\sigma}_b, \Delta \widetilde{\sigma}) = \mathbf{F}^b_{E,H}(\Delta \widetilde{\sigma}),$$

where the upper subscript "b" denotes that the differentials are calculated for the background conductivity.

Substituting the Born approximation (8.3) into formula (6.40), we arrive at the linearized form of the forward modeling operator:

$$\mathbf{E}^a = \mathbf{F}_E^b (\Delta \widetilde{\sigma}). \tag{8.5}$$

In a solution of the inverse problem we assume that the anomalous field, $\mathbf{E}^a$, and the background conductivity, $\widetilde{\sigma}_b$, are given. The goal is to find the anomalous conductivity distribution, $\Delta \widetilde{\sigma}$. In this case, formula (8.5) has to be treated as a linear equation with respect to $\Delta \widetilde{\sigma}$.

8.1.2 DISCRETE LINEAR EM INVERSE PROBLEM

We can represent the linear integral equations (8.1) and (8.2), based on the Born approximation, using more general operator notations:

$$\mathbf{d} = A(\mathbf{m}), \tag{8.6}$$

where $\mathbf{m}$ represents the conductivity model parameters, $\mathbf{d}$ are observed geophysical EM data, and A is a corresponding linear Born operator.

In practical solutions of the inverse problems encountered in electromagnetic methods, we must remember that, along with the continuous function describing the EM field, we have a finite set of these data (measurements of values for the electromagnetic field or some related numerical values at a finite number of observation points for specific times or frequencies). This set of data forms a column vector of length N_D, which we will designate as $\mathbf{d}$. As an example, consider a case in which x-component, E_x, has been measured at two points, x_1 and x_2, along a profile at two frequencies, ω_1 and ω_2. The vector $\mathbf{d}$ is:

$$\mathbf{d} = \begin{bmatrix} E_x(x_1, \omega_1) \\ E_x(x_1, \omega_2) \\ E_x(x_2, \omega_1) \\ E_x(x_2, \omega_2) \end{bmatrix}.$$

In constructing an initial model for the geoelectrical structure of the earth in one, two, or three dimensions, some organized approach to parameterization must be used in characterizing the spatial distribution of resistivity in the model. For example, in a one-dimensional model with specified locations of the boundaries between layers, the model is parameterized by a step-wise constant set of conductivity values within each layer, $\sigma_1, \sigma_2, ..., \sigma_{N_M}$. In a two-dimensional model, parameterization can be accomplished as follows. Suppose that for $x \leq x_L$, $x \geq x_R (x_L < x_R)$, and $z \geq z_b$, the geoelectrical model is described by some specified one-dimensional geoelectrical sequence:

$$\sigma(x, z) = \begin{pmatrix} \sigma_L(z) & x \leq x_L \\ \sigma_R(z) & x \geq x_R \\ \sigma_L(z) = \sigma_R(z) & z \geq z_b \end{pmatrix}. \tag{8.7}$$

The region of unknown conductivity, $\sigma(x, z)$, is located within a region of rectangular cross section $V : \{x_L \leq x \leq x_R, 0 \leq z \leq z_b\}$. The rectangle V is subdivided with some mesh (rectilinear) into

blocks or cells with constant values of conductivity, $\sigma_1, \sigma_2, ..., \sigma_{N_M}$. A column vector, $\mathbf{m}$, of length N_M of model parameters is formed from the values which uniquely describe the geoelectrical section within the designated window in the selected model. An analogous procedure is used to parameterize a three-dimensional model. In our case, for example, $m_j = \sigma_j$.

And so, after discretizing the field data, d, and distributing conductivities over the model, σ, the solution to the inverse problem stated in Eq. (8.6) can be written in matrix form:

$$\mathbf{d} = \mathbf{Am}, \tag{8.8}$$

where $\mathbf{A}$ is the $N \times L$ discrete matrix analog to the nonlinear operator A which appeared earlier in this book in the numerical solution of the Maxwell system of equations.

Expression (8.8) describes a system of N linear equations with respect to L unknown parameters, $m_1, m_2, m_3, ..., m_L$:

$$d_i = \sum_{j=1}^{L} A_{ij} m_j, \quad i = 1, 2, 3, ..., N. \tag{8.9}$$

Thus, solving the inverse problem (8.6) means solving the system of linear equations (8.9) with respect to parameters $m_1, m_2, m_3, ..., m_L$.

There exist several different methods of solving the matrix equation (8.8) (see, for example, Zhdanov, 2002). Taking into account that the electromagnetic inverse problem is ill posed, we will present below the corresponding regularization methods for its solution.

8.1.3 THE TIKHONOV REGULARIZATION METHOD OF LINEAR INVERSION

Let us consider a general approach to linear inversion based on the Tikhonov regularization technique introduced in Chapter 7. The corresponding parametric functional can be introduced in the following form:

$$P^\alpha(\mathbf{m}, \mathbf{d}) = \|\mathbf{W}_d \mathbf{Am} - \mathbf{W}_d \mathbf{d}\|^2 + \alpha \|\mathbf{W}_m \mathbf{m} - \mathbf{W}_m \mathbf{m}_{apr}\|^2,$$

where $\mathbf{W}_d$ and $\mathbf{W}_m$ are some weighting matrices of data and model (not necessarily diagonal), $\mathbf{m}_{apr}$ is some *a priori* model, and $\|...\|$ denotes the Euclidean norm in the spaces of data and models.

We will discuss some specific choices of $\mathbf{W}_d$ and $\mathbf{W}_m$ later.

We can also rewrite the functional $P^\alpha(\mathbf{m}, \mathbf{d})$ in the matrix notation:

$$\begin{aligned} P^\alpha(\mathbf{m}, \mathbf{d}) = {} & (\mathbf{W}_d \mathbf{Am} - \mathbf{W}_d \mathbf{d})^T (\mathbf{W}_d \mathbf{Am} - \mathbf{W}_d \mathbf{d}) \\ & + \alpha(\mathbf{W}_m \mathbf{m} - \mathbf{W}_m \mathbf{m}_{apr})^T (\mathbf{W}_m \mathbf{m} - \mathbf{W}_m \mathbf{m}_{apr}). \end{aligned}$$

According to the basic principles of the regularization method, we have to find a quasi-solution of the inverse problem as the model $\mathbf{m}_\alpha$ that minimizes the parametric functional

$$P^\alpha(\mathbf{m}_\alpha, \mathbf{d}) = \min.$$

The regularization parameter α is determined from the misfit condition:

$$\|\mathbf{W}_d \mathbf{Am}_\alpha - \mathbf{W}_d \mathbf{d}\| = \delta,$$

where δ is some *a priori* estimation of the level of "weighted" noise of the data:

$$\|\mathbf{W}_d \delta \mathbf{d}\| = \delta. \tag{8.10}$$

To solve this problem, following Zhdanov (2002), we calculate the first variation of $P^\alpha(\mathbf{m}, \mathbf{d})$:

$$\delta P^\alpha(\mathbf{m}, \mathbf{d}) = 2(\mathbf{W}_d \mathbf{A} \delta \mathbf{m})^T (\mathbf{W}_d \mathbf{A} \mathbf{m} - \mathbf{W}_d \mathbf{d}) + 2\alpha (\mathbf{W}_m \delta \mathbf{m})^T (\mathbf{W}_m \mathbf{m} - \mathbf{W}_m \mathbf{m}_{apr}) = 0.$$

The last equation can be rewritten as

$$\delta \mathbf{m}^T \left[(\mathbf{A}^T \mathbf{W}_d^T \mathbf{W}_d \mathbf{A} + \alpha \mathbf{W}_m^T \mathbf{W}_m) \mathbf{m} - \left(\mathbf{A}^T \mathbf{W}_d^T \mathbf{W}_d \mathbf{d} + \alpha \mathbf{W}_m^T \mathbf{W}_m \mathbf{m}_{apr} \right) \right] = 0,$$

from which we obtain at once *a regularized normal equation* for the original inverse problem (8.8),

$$(\mathbf{A}^T \mathbf{W}_d^T \mathbf{W}_d \mathbf{A} + \alpha \mathbf{W}_m^T \mathbf{W}_m) \mathbf{m}_\alpha = \mathbf{A}^T \mathbf{W}_d^T \mathbf{W}_d \mathbf{d} + \alpha \mathbf{W}_m^T \mathbf{W}_m \mathbf{m}_{apr}, \tag{8.11}$$

and its regularized solution,

$$\mathbf{m}_\alpha = (\mathbf{A}^T \mathbf{W}_d^T \mathbf{W}_d \mathbf{A} + \alpha \mathbf{W}_m^T \mathbf{W}_m)^{-1} (\mathbf{A}^T \mathbf{W}_d^T \mathbf{W}_d \mathbf{d} + \alpha \mathbf{W}_m^T \mathbf{W}_m \mathbf{m}_{apr}). \tag{8.12}$$

Usually the weighting matrices $\mathbf{W}_d$ and $\mathbf{W}_m$ are selected to be symmetric (or even diagonal), so Eq. (8.12) can be rewritten:

$$\mathbf{m}_\alpha = (\mathbf{A}^T \mathbf{W}_d^2 \mathbf{A} + \alpha \mathbf{W}_m^2)^{-1} (\mathbf{A}^T \mathbf{W}_d^2 \mathbf{d} + \alpha \mathbf{W}_m^2 \mathbf{m}_{apr}). \tag{8.13}$$

The last expression gives the regularized solution of the generalized least-squares problem.

8.1.4 DEFINITION OF THE WEIGHTING MATRICES FOR MODEL PARAMETERS AND DATA

Let us analyze the sensitivity of the data to the perturbation of one specific parameter m_k. To solve this problem, we apply the variational operator to both sides of Eq. (8.9):

$$\delta d_i = A_{ik} \delta m_k. \tag{8.14}$$

In the last formula, A_{ik} are the elements of the matrix $\mathbf{A}$ of the forward modeling operator, and there is no summation over index k. Therefore, the norm of the perturbed vector of the data can be calculated as

$$\|\delta \mathbf{d}\| = \sqrt{\sum_i (\delta d_i)^2} = \sqrt{\sum_i (A_{ik})^2} \, \delta m_k. \tag{8.15}$$

We determine the integrated sensitivity of the data to the parameter m_k as the ratio

$$S_k = \frac{\|\delta \mathbf{d}\|}{\delta m_k} = \sqrt{\sum_i (A_{ik})^2}. \tag{8.16}$$

One can see that the integrated sensitivity depends on the parameter k. In other words, the sensitivity of the data to the different parameters varies, because the contributions of the different parameters to the observation are also variable.

The diagonal matrix with the diagonal elements equal to $S_k = \|\delta \mathbf{d}\| / \delta m_k$ is called *an integrated sensitivity matrix:*

$$\mathbf{S} = \mathbf{diag}\left(\sqrt{\sum_i (A_{ik})^2}\right) = \mathbf{diag}\left(\mathbf{A}^T \mathbf{A}\right)^{1/2}. \tag{8.17}$$

In other words, it is formed by the norms of the columns of the matrix $\mathbf{A}$.

The basic idea of introducing a weighting matrix, $\mathbf{W}_m$, for the model parameters is as follows. We identify this matrix as the diagonal integrated sensitivity matrix

$$\mathbf{W}_m = [W_j] = [S_j] = \mathbf{S}. \tag{8.18}$$

Thus, the weights are selected to be equal to the sensitivities:

$$W_j = S_j. \tag{8.19}$$

We can now introduce the weighted model parameters:

$$\mathbf{m}^w = \mathbf{W}_m \mathbf{m}. \tag{8.20}$$

Using these notations, we can rewrite the inverse problem equation (8.8) as follows

$$\mathbf{d} = \mathbf{A}\mathbf{W}_m^{-1}\mathbf{W}_m\mathbf{m} = \mathbf{A}^w \mathbf{m}^w, \tag{8.21}$$

where $\mathbf{A}^w$ is a weighted forward modeling operator,

$$\mathbf{A}^w = \mathbf{A}\mathbf{W}_m^{-1}. \tag{8.22}$$

Now we perturb the data with respect to one specific weighted parameter m_k^w:

$$\delta d_i = A_{ik}^w \delta m_k^w,$$

and calculate a new integrated sensitivity S_k^w of the data to the weighted parameter m_k^w as the ratio

$$S_k^w = \frac{\|\delta \mathbf{d}\|}{\delta m_k^w} = \frac{\sqrt{\sum_i (A_{ik}^w)^2}\,\delta m_k^w}{\delta m_k^w} = \sqrt{\sum_i (A_{ik}^w)^2}$$

$$= \sqrt{\sum_i \left(A_{ik} W_k^{-1}\right)^2} = W_k^{-1}\sqrt{\sum_i (A_{ik})^2} = W_k^{-1} S_k = 1. \tag{8.23}$$

Formula (8.23) shows that the new matrix of the integrated sensitivity $\mathbf{S}^w$ is a unit matrix:

$$\mathbf{S}^w = \mathbf{I}.$$

Therefore, data are uniformly sensitive to the new weighted model parameters!

Note that the corresponding weighted stabilizing functional takes the form

$$s_w(\mathbf{m}) = (\mathbf{m} - \mathbf{m}_{apr})^T \mathbf{W}_m^2 (\mathbf{m} - \mathbf{m}_{apr}) = (\mathbf{m} - \mathbf{m}_{apr})^T \mathbf{S}^2 (\mathbf{m} - \mathbf{m}_{apr}). \tag{8.24}$$

It imposes a stronger penalty on departure from the *a priori* model for those parameters that contribute more significantly to the data.

Thus, the model weighting results in practically equal resolution of the inversion with respect to different parameters of the model.

In a similar way, we can define the diagonal data weighting matrix, formed by the norms of the rows of the matrix $\mathbf{A}$:

$$\mathbf{W}_d = \mathbf{diag}\left(\sqrt{\sum_k (A_{ik})^2}\right) = \mathbf{diag}\left(\mathbf{AA}^T\right)^{1/2}. \tag{8.25}$$

These weights make normalized data less dependent on the specific parameters of observations (for example, frequency and distance from the anomalous domain), which improves the resolution of the inverse method.

8.1.5 APPROXIMATE REGULARIZED SOLUTION OF LINEAR INVERSE PROBLEM

In practical geophysical applications the size of the linear inverse problem (8.8) can be so large, that direct matrix inversion can be extremely time consuming. This situation is typical for seismic or electromagnetic data inversion. In this case we can use a simple approach to approximate the solution of the inverse problem. The basic ideas of this technique as applied to the Born inversion in electromagnetics and acoustics were formulated by Blok and Oristaglio (1995).

We rewrite the regularized normal equation (8.11) in the form

$$(\mathbf{A}^T \mathbf{W}_d^2 \mathbf{A} + \alpha \widetilde{\mathbf{W}}_m^2)\mathbf{m}_\alpha = \mathbf{A}^T \mathbf{W}_d^2 \mathbf{d} + \alpha \widetilde{\mathbf{W}}_m^2 \mathbf{m}_{apr}, \tag{8.26}$$

where we use a tilde sign above $\mathbf{W}_m$, because we will introduce different model parameters weights in the case of an approximate solution.

Let us assume that the regularization parameter α is so big that we can neglect the term $\mathbf{A}^T \mathbf{W}_d^2 \mathbf{A}$ compared with the term $\alpha \widetilde{\mathbf{W}}_m^2$ on the left-hand side of (8.26):

$$\alpha \widetilde{\mathbf{W}}_m^2 \mathbf{m}_\alpha \approx \mathbf{A}^T \mathbf{W}_d^2 \mathbf{d} + \alpha \widetilde{\mathbf{W}}_m^2 \mathbf{m}_{apr}. \tag{8.27}$$

From the last formula we obtain at once an approximate regularized solution:

$$\mathbf{m}_\alpha \approx \alpha^{-1} \widetilde{\mathbf{W}}_m^{-2} \mathbf{A}^T \mathbf{W}_d^2 \mathbf{d} + \mathbf{m}_{apr}. \tag{8.28}$$

We can see that computing the approximate solution $\mathbf{m}_\alpha$ does not require an inversion of the matrix $\mathbf{A}$ and can be found by simple matrix multiplication. The coefficient α^{-1} can now be treated as just a scaling factor, which can be found by minimizing the misfit between the observed and predicted data:

$$\|\mathbf{Am}_\alpha - \mathbf{d}\| = \|\alpha^{-1}\mathbf{A}\widetilde{\mathbf{W}}_m^{-2}\mathbf{A}^T \mathbf{W}_d^2 \mathbf{d} + \mathbf{Am}_{apr} - \mathbf{d}\| = \min. \tag{8.29}$$

In the following chapters we will demonstrate that approximation (8.28) results in effective imaging schemes, including electromagnetic migration.

Note, however, that in the case of the approximate solution, the weighting matrix for the model parameters should be selected as the square root of the integrated sensitivity matrix:

$$\widetilde{\mathbf{W}}_m = \left[\widetilde{W}_{mj}\right] = \left[\sqrt{S_j}\right] = \sqrt{\mathbf{S}} = \mathbf{diag}\left(\sqrt[4]{\sum_k (A_{ik})^2}\right) = \mathbf{diag}\left(\mathbf{A}^T\mathbf{A}\right)^{1/4}. \tag{8.30}$$

This choice of the weighting matrix can be justified by the following consideration.

Let us denote by $\mathbf{m}_\alpha^{\widetilde{w}^2}$ the approximate regularized solution (8.28) with weights,

$$\mathbf{m}_\alpha^{\widetilde{w}^2} = \widetilde{\mathbf{W}}_m^2\mathbf{m}_\alpha. \tag{8.31}$$

According to (8.27), the weighted solution is expressed by the formula:

$$\mathbf{m}_\alpha^{\widetilde{w}^2} = \alpha^{-1}\mathbf{A}^T\mathbf{W}_d^2\mathbf{d} + \mathbf{m}_{apr}^{\widetilde{w}^2}, \tag{8.32}$$

where $\mathbf{m}_{apr}^{\widetilde{w}^2} = \widetilde{\mathbf{W}}_m^2\mathbf{m}_{apr}$.

Introducing the notation of (8.31), we rewrite the inverse problem equation (8.8) as follows:

$$\mathbf{d} = \mathbf{A}\widetilde{\mathbf{W}}_\mathbf{m}^{-2}\widetilde{\mathbf{W}}_\mathbf{m}^2\mathbf{m} = \mathbf{A}^{\widetilde{w}^2}\mathbf{m}^{\widetilde{w}^2}, \tag{8.33}$$

where $\mathbf{A}^{\widetilde{w}^2}$ is a new weighted forward modeling operator,

$$\mathbf{A}^{\widetilde{w}^2} = \mathbf{A}\widetilde{\mathbf{W}}_\mathbf{m}^{-2}. \tag{8.34}$$

Perturbing the data with respect to one specific weighted parameter $m_k^{\widetilde{w}^2}$, $\delta d_i = A_{ik}^{\widetilde{w}^2}\delta m_k^{\widetilde{w}^2}$, we calculate a new integrated sensitivity $S_k^{\widetilde{w}^2}$ of the data to one new weighted parameter $m_k^{w^2}$:

$$S_k^{\widetilde{w}^2} = \frac{\|\delta\mathbf{d}\|}{\delta m_k^{\widetilde{w}^2}} = \sqrt{\sum_i \left(A_{ik}^{\widetilde{w}^2}\right)^2} = \sqrt{\sum_i \left(A_{ik}\widetilde{W}_k^{-2}\right)^2} = \widetilde{W}_k^{-2}\sqrt{\sum_i (A_{ik})^2} = \widetilde{W}_k^{-2}S_k = 1. \tag{8.35}$$

Formula (8.35) shows that the new matrix of the integrated sensitivity $\mathbf{S}^{\widetilde{w}^2}$ is a unit matrix:

$$\mathbf{S}^{\widetilde{w}^2} = \mathbf{I}.$$

As a result, the weighted approximate regularized solution, given by formula (8.32), provides a uniform estimate of the different model parameters. However, at the final stage of inversion we should return from the weighted parameters, $\mathbf{m}_\alpha^{\widetilde{w}^2}$, to the real model parameters, $\mathbf{m}_\alpha$, using the formula

$$\mathbf{m}_\alpha = \widetilde{\mathbf{W}}_m^{-2}\mathbf{m}_\alpha^{\widetilde{w}^2} = \alpha^{-1}\widetilde{\mathbf{W}}_m^{-2}\mathbf{A}^T\mathbf{W}_d^2\mathbf{d} + \mathbf{m}_{apr}. \tag{8.36}$$

Note in conclusion that different selections of model parameter weights are dictated by the different methods of solution of the inverse problem. If we apply the direct inversion according to formula (8.12), we should use weights equal to sensitivities. If we use the approximate inversion described by formula (8.36), we select the weights as square roots of the sensitivities. In both cases the weights are selected under the condition that they provide uniform sensitivity of the solution to the observed data.

8.1.6 THE LEVENBERG-MARQUARDT METHOD

Let us consider a special case when $\mathbf{W}_d = \mathbf{I}$ and $\mathbf{W}_m = \mathbf{I}$. Then Eq. (8.13) turns out to be

$$\mathbf{m}_\alpha = (\mathbf{A}^T\mathbf{A} + \alpha\mathbf{I})^{-1}(\mathbf{A}^T\mathbf{d} + \alpha\mathbf{m}_{apr}). \tag{8.37}$$

Assume now that $\mathbf{m}_{apr} = 0$:

$$\mathbf{m}_\alpha = (\mathbf{A}^T\mathbf{A} + \alpha\mathbf{I})^{-1}\mathbf{A}^T\mathbf{d}. \tag{8.38}$$

The solution (8.38) describes the classical Levenberg-Marquardt method of damped least squares, where α plays the role of a "damping factor" (Levenberg, 1944; Marquardt, 1963).

For a better understanding of how the regularization parameter or "damping factor" α works, let us apply a singular value decomposition method to matrix $\mathbf{A}$:

$$\mathbf{A} = \mathbf{UQV}^T,$$

where $\mathbf{U}$ and $\mathbf{V}$ are orthogonal matrices and $\mathbf{Q}$ is a diagonal matrix (Zhdanov, 2002). Then we have

$$\mathbf{A}^T\mathbf{A} = \mathbf{VQ}^2\mathbf{V}^T. \tag{8.39}$$

From the last equation we obtain at once

$$(\mathbf{A}^T\mathbf{A} + \alpha\mathbf{I})^{-1} = (\mathbf{VQ}^2\mathbf{V}^T + \alpha\mathbf{VIV}^T)^{-1} = (\mathbf{V}[\mathbf{diag}(\alpha + Q_i^2)]\mathbf{V}^T)^{-1}$$
$$= \mathbf{V}[\mathbf{diag}(\frac{1}{\alpha + Q_i^2})]\mathbf{V}^T. \tag{8.40}$$

We can clearly see from Eq. (8.40) how regularization makes the nearly singular matrix well conditioned; even if $Q_i \to 0$, division by zero does not occur.

8.1.7 CONDUCTIVITY IMAGING BY THE BORN APPROXIMATION

We can now introduce a fast imaging technique based on a Born approximation. Let us recall formula (8.28) for an approximate regularized solution of the linear inverse problem. In the case of Eq. (8.5), this formula takes the form (assuming that we have no a priori model):

$$\Delta\widetilde{\sigma} \approx k\left(W_E^\star W_E\right)^{-1}\mathbf{F}_E^{b\star}\left(\mathbf{E}^a\right), \tag{8.41}$$

where $\mathbf{F}_E^{b\star}$ is an adjoint Fréchet derivative operator, W_E is a weighting operator, and the scalar coefficient k is a solution of the minimization problem:

$$\left\| k\mathbf{F}_E^b \left(\left(W_E^\star W_E \right)^{-1} \mathbf{F}_E^{b\star} \left(\mathbf{E}^a \right) \right) - \mathbf{E}^a \right\|^2 = \min. \tag{8.42}$$

Let us find, first, an explicit form of the adjoint Fréchet derivative operator $\mathbf{F}_E^{b\star}$. By definition, the adjoint operator must satisfy to the following equation (Zhdanov, 2002),

$$\left(\mathbf{F}_E^b \left(\Delta\widetilde{\sigma} \right), \mathbf{f} \right)_D = \left(\Delta\widetilde{\sigma}, \mathbf{F}_E^{b\star} \left(\mathbf{f} \right) \right)_M, \tag{8.43}$$

where $\mathbf{f} = \mathbf{f}(\mathbf{r})$ is arbitrary vector function defined in domain D.

We can rewrite formula (8.43) as (Zhdanov, 2002):

$$\begin{aligned}
\left(\mathbf{F}_E^b \left(\Delta\widetilde{\sigma} \right), \mathbf{f} \right)_D &= \iint_S \mathbf{G}_E \left(\Delta\widetilde{\sigma} \mathbf{E}^b \right) \cdot \mathbf{f}^* \left(\mathbf{r}' \right) ds' \\
&= \iint_S \left[\iiint_D \widehat{\mathbf{G}}_E \left(\mathbf{r}' \mid \mathbf{r} \right) \cdot \Delta\widetilde{\sigma} \left(\mathbf{r} \right) \mathbf{E}^b \left(\mathbf{r} \right) dv \right] \cdot \mathbf{f}^* \left(\mathbf{r}' \right) ds' \\
&= \iiint_D \Delta\widetilde{\sigma} \left(\mathbf{r} \right) \left\{ \iint_S \left[\widehat{\mathbf{G}}_E \left(\mathbf{r}' \mid \mathbf{r} \right) \cdot \mathbf{E}^b \left(\mathbf{r} \right) \right]^* \cdot \mathbf{f} \left(\mathbf{r}' \right) ds' \right\}^* dv \\
&= \left(\Delta\widetilde{\sigma}, \mathbf{F}_E^{b\star} \left(\mathbf{f} \right) \right)_M. \tag{8.44}
\end{aligned}$$

From the last formula we have

$$\left(\Delta\widetilde{\sigma}, \left[\mathbf{F}_E^{b\star} \left(\mathbf{f} \right) - \iint_S \left[\widehat{\mathbf{G}}_E \left(\mathbf{r}' \mid \mathbf{r} \right) \cdot \mathbf{E}^b \left(\mathbf{r} \right) \right]^* \cdot \mathbf{f} \left(\mathbf{r}' \right) ds' \right] \right)_M = 0. \tag{8.45}$$

Eq. (8.45) should hold for any $\Delta\widetilde{\sigma}$, for example for

$$\Delta\widetilde{\sigma}' = \mathbf{F}_E^{b\star} \left(\mathbf{f} \right) - \iint_S \left[\widehat{\mathbf{G}}_E \left(\mathbf{r}' \mid \mathbf{r} \right) \cdot \mathbf{E}^b \left(\mathbf{r} \right) \right]^* \cdot \mathbf{f} \left(\mathbf{r}' \right) ds'.$$

Therefore,

$$\left\| \mathbf{F}_E^{b\star} \left(\mathbf{f} \right) - \iint_S \left[\widehat{\mathbf{G}}_E \left(\mathbf{r}' \mid \mathbf{r} \right) \cdot \mathbf{E}^b \left(\mathbf{r} \right) \right]^* \cdot \mathbf{f} \left(\mathbf{r}' \right) ds' \right\|_M^2 = 0.$$

From the last formula we conclude that the adjoint Fréchet derivative operator $\mathbf{F}_E^{b\star}$ is given by the formula:

$$\mathbf{F}_E^{b\star} \left(\mathbf{f} \right) = \iint_S \left[\widehat{\mathbf{G}}_E \left(\mathbf{r}' \mid \mathbf{r} \right) \cdot \mathbf{E}^b \left(\mathbf{r} \right) \right]^* \cdot \mathbf{f} \left(\mathbf{r}' \right) ds' = \mathbf{E}^{b*} \left(\mathbf{r} \right) \cdot \iint_S \widetilde{\widehat{\mathbf{G}}}_E^* \left(\mathbf{r}' \mid \mathbf{r} \right) \cdot \mathbf{f} \left(\mathbf{r}' \right) ds', \tag{8.46}$$

where a tilde denotes the operation of transposition.

In a similar way we can obtain the formula for the adjoint Fréchet derivative operator $\mathbf{F}_H^{b\star}$:

$$\mathbf{F}_H^{b\star}(\mathbf{f}) = \mathbf{E}^{b*}(\mathbf{r}) \cdot \iint_S \widetilde{\widehat{\mathbf{G}}}_H^*(\mathbf{r}' \mid \mathbf{r}) \cdot \mathbf{f}(\mathbf{r}') \, ds'. \tag{8.47}$$

Substituting expression (8.46) into formula (8.41), we finally arrive at the following imaging formula:

$$\Delta\widetilde{\sigma}(\mathbf{r}) \approx k \left(W_E^* W_E \right)^{-1} \mathbf{E}^{b*}(\mathbf{r}) \cdot \iint_S \widetilde{\widehat{\mathbf{G}}}_E^*(\mathbf{r}' \mid \mathbf{r}) \cdot \mathbf{E}^a(\mathbf{r}') \, ds'. \tag{8.48}$$

In a similar way we can derive an imaging formula based on anomalous magnetic field observations:

$$\Delta\widetilde{\sigma}(\mathbf{r}) \approx k \left(W_H^\star W_H \right)^{-1} \mathbf{E}^{b*}(\mathbf{r}) \cdot \iint_S \widetilde{\widehat{\mathbf{G}}}_H^*(\mathbf{r}' \mid \mathbf{r}) \cdot \mathbf{H}^a(\mathbf{r}') \, ds'. \tag{8.49}$$

The weighting operators W_E and W_H for electric and magnetic forward operators are linear operators of the multiplication of conductivity $\Delta\widetilde{\sigma}$ by the functions $w_E(\mathbf{r})$ and $w_H(\mathbf{r})$ equal to the square root of the integrated sensitivity:

$$w_E = \sqrt{S_E}, \text{ and } w_H = \sqrt{S_H}. \tag{8.50}$$

The integrated sensitivity, S_E, in accordance with (6.70), is calculated by the formula

$$S_E(\mathbf{r}) = \sqrt{\iint_S \left| \widehat{\mathbf{G}}_E(\mathbf{r}' \mid \mathbf{r}) \cdot \mathbf{E}^b(\mathbf{r}) \right|^2 ds'} = \left\| \widehat{\mathbf{G}}_E(\mathbf{r}' \mid \mathbf{r}) \cdot \mathbf{E}^b(\mathbf{r}) \right\|_D. \tag{8.51}$$

Formula (8.51) should be treated as the integrated sensitivity of the anomalous electric field to the local conductivity anomaly located at a point with the radius vector $\mathbf{r}$. Similarly, we can find the integrated sensitivity of the anomalous magnetic field to the local conductivity anomaly, using formula (6.71):

$$S_H(\mathbf{r}) = \sqrt{\iint_S \left| \widehat{\mathbf{G}}_H(\mathbf{r}' \mid \mathbf{r}) \cdot \mathbf{E}^b(\mathbf{r}) \right|^2 ds'} = \left\| \widehat{\mathbf{G}}_H(\mathbf{r}' \mid \mathbf{r}) \cdot \mathbf{E}^b(\mathbf{r}) \right\|_D. \tag{8.52}$$

The weighting functions, according to (8.50), are equal to

$$w_E(\mathbf{r}) = \sqrt{\left\| \widehat{\mathbf{G}}_E(\mathbf{r}' \mid \mathbf{r}) \cdot \mathbf{E}^b(\mathbf{r}) \right\|_D}, \quad w_H(\mathbf{r}) = \sqrt{\left\| \widehat{\mathbf{G}}_H(\mathbf{r}' \mid \mathbf{r}) \cdot \mathbf{E}^b(\mathbf{r}) \right\|_D}. \tag{8.53}$$

Substituting formulae (8.53) into (8.48) and (8.49), we finally find:

$$\Delta\widetilde{\sigma}(\mathbf{r}) \approx k \frac{\mathbf{E}^{b*}(\mathbf{r}) \cdot \int \int_S \widetilde{\widehat{\mathbf{G}}}_E^*(\mathbf{r}' \mid \mathbf{r}) \cdot \mathbf{E}^a(\mathbf{r}') \, ds'}{\left\| \widehat{\mathbf{G}}_E(\mathbf{r}' \mid \mathbf{r}) \cdot \mathbf{E}^b(\mathbf{r}) \right\|_D}. \tag{8.54}$$

or

$$\Delta\widetilde{\sigma}(\mathbf{r}) \approx k \frac{\mathbf{E}^{b*}(\mathbf{r}) \cdot \int \int_S \widetilde{\widehat{\mathbf{G}}}_H^*(\mathbf{r}' \mid \mathbf{r}) \cdot \mathbf{H}^a(\mathbf{r}') \, ds'}{\left\| \widehat{\mathbf{G}}_H(\mathbf{r}' \mid \mathbf{r}) \cdot \mathbf{E}^b(\mathbf{r}) \right\|_D}. \tag{8.55}$$

Formulae (8.54) and (8.55) have a clear physical interpretation. Let us introduce a unit conductance $\Sigma_0 = 1$ S. According to the reciprocity theorem (see Chapter 3), the integral term in Eq. (8.54) can be treated as the complex conjugate of the electric field $\mathbf{E}^R$ (divided by the unit conductance Σ_0),

$$
\begin{aligned}
\mathbf{E}^R (\mathbf{r}) &= \iint_S \widetilde{\widehat{\mathbf{G}}}_E \left(\mathbf{r}' \mid \mathbf{r}\right) \cdot \mathbf{E}^a \left(\mathbf{r}'\right) ds' \\
&= \iint_S \widehat{\mathbf{G}}_E \left(\mathbf{r} \mid \mathbf{r}'\right) \cdot \Sigma_0 \mathbf{E}^{a*} \left(\mathbf{r}'\right) ds' / \Sigma_0 = \iint_S \widehat{\mathbf{G}}_E \left(\mathbf{r} \mid \mathbf{r}'\right) \cdot \mathbf{j}_E^S \left(\mathbf{r}'\right) ds' / \Sigma_0,
\end{aligned} \tag{8.56}
$$

generated at the point $\mathbf{r}$ by the fictitious electric current, distributed over the surface of observations S with the surface density $\mathbf{j}_E^S$, equal to the complex conjugate anomalous field multiplied by Σ_0:

$$
\mathbf{j}_E^S \left(\mathbf{r}'\right) = \Sigma_0 \mathbf{E}^{a*} \left(\mathbf{r}'\right). \tag{8.57}
$$

We have introduced the unit conductance Σ_0 in both Eqs. (8.56) and (8.57) to keep the correct dimensions of the fictitious electric current $\mathbf{j}_E^S$ and the normalized electric field $\mathbf{E}^R (\mathbf{r})$.

The approximate anomalous conductivity in formula (8.54) is obtained as a scalar product of the auxiliary field $\mathbf{E}^{R*} (\mathbf{r})$ with the complex conjugate background field at the point $\mathbf{r}$, normalized by the magnitudes of the background field and the norm of the corresponding Green's tensor at the same point:

$$
\Delta\widetilde{\sigma} (\mathbf{r}) \approx k \Delta\widetilde{\sigma}_E' (\mathbf{r}), \text{ and } \Delta\widetilde{\sigma}_E' (\mathbf{r}) = \frac{\mathbf{E}^{b*} (\mathbf{r}) \cdot \mathbf{E}^{R*} (\mathbf{r})}{\left\| \widehat{\mathbf{G}}_E \left(\mathbf{r}' \mid \mathbf{r}\right) \cdot \mathbf{E}^b (\mathbf{r}) \right\|_D}, \tag{8.58}
$$

where the scalar coefficient k is the solution of the minimization problem

$$
\left\| k \mathbf{F}_E^b \left(\Delta\widetilde{\sigma}_E' (\mathbf{r})\right) - \mathbf{E}^a \right\|^2 = \min .
$$

Formula (8.55) has a similar interpretation, only in this case we should introduce by reciprocity the magnetic field $\mathbf{H}^R$,

$$
\mathbf{H}^R (\mathbf{r}) = \iint_S \widetilde{\widehat{\mathbf{G}}}_H \left(\mathbf{r}' \mid \mathbf{r}\right) \cdot \mathbf{H}^{a*} \left(\mathbf{r}'\right) ds' = \iint_S \widehat{\mathbf{G}}_H \left(\mathbf{r} \mid \mathbf{r}'\right) \cdot \mathbf{H}^{a*} \left(\mathbf{r}'\right) ds',
$$

generated at the point $\mathbf{r}$ by the fictitious electric current, distributed over the surface of observations S with the surface density $\mathbf{j}_H^S$, determined by the expression[1]

$$
\mathbf{j}_H^S \left(\mathbf{r}'\right) = \mathbf{H}^{a*} \left(\mathbf{r}'\right).
$$

As a result, we arrive at the following formula for the anomalous conductivity:

$$
\Delta\widetilde{\sigma} (\mathbf{r}) \approx k \Delta\widetilde{\sigma}_H' (\mathbf{r}), \text{ and } \Delta\widetilde{\sigma}_H' (\mathbf{r}) = \frac{\mathbf{E}^{b*} (\mathbf{r}) \cdot \mathbf{H}^{R*} (\mathbf{r})}{\left\| \widehat{\mathbf{G}}_H \left(\mathbf{r}' \mid \mathbf{r}\right) \cdot \mathbf{E}^b (\mathbf{r}) \right\|_D}, \tag{8.59}
$$

---

[1] Note that, according to the first Maxwell's equation, the surface density of the electric current has the dimensions of magnetic field.

where the scalar coefficient k is the solution of the minimization problem

$$\left\| k\mathbf{F}_H^b \left(\Delta\widetilde{\sigma}_H' \left(\mathbf{r} \right) \right) - \mathbf{H}^a \right\|^2 = \min.$$

Note that in the definition of the auxiliary fields $\mathbf{E}^{R*} \left(\mathbf{r} \right) = \mathbf{E}^{R*} \left(\mathbf{r}, \omega \right)$ and $\mathbf{H}^{R*} \left(\mathbf{r} \right) = \mathbf{H}^{R*} \left(\mathbf{r}, \omega \right)$ we use the complex conjugate Green's tensors. It can be demonstrated that the transition to the complex conjugate function in frequency domain corresponds to changing a sign in front of time variable t in the time domain. Thus, using the convolution theorem (Arfken and Weber, 1995, p. 863–865), we can write the expressions for the auxiliary electric and magnetic fields in time domain as follows:

$$\frac{1}{2\pi} \int_{-\infty}^{+\infty} \mathbf{E}^{R*} \left(\mathbf{r}, \omega \right) e^{-i\omega t'} d\omega = \frac{1}{2\pi} \int_{-\infty}^{+\infty} \iint_S \widehat{\mathbf{G}}_E^* \left(\mathbf{r} \mid \mathbf{r}' \right) \cdot \mathbf{E}^a \left(\mathbf{r}', \omega \right) ds' e^{-i\omega t'} d\omega$$

$$= \iint_S \int_{-\infty}^{+\infty} \widehat{\mathbf{G}}_E (\mathbf{r}, -t \mid \mathbf{r}', -t') \mathbf{E}^a \left(\mathbf{r}', t \right) dt ds' = \widetilde{\mathbf{E}}^R \left(\mathbf{r}, t' \right), \quad (8.60)$$

and

$$\frac{1}{2\pi} \int_{-\infty}^{+\infty} \mathbf{H}^{R*} \left(\mathbf{r}, \omega \right) e^{-i\omega t'} d\omega = \iint_S \int_{-\infty}^{+\infty} \widehat{\mathbf{G}}_H (\mathbf{r}, -t \mid \mathbf{r}', -t') \mathbf{H}^a \left(\mathbf{r}', t \right) dt ds'$$

$$= \widetilde{\mathbf{H}}^R \left(\mathbf{r}, t' \right). \quad (8.61)$$

The minus sign in front of time variable t in the expression for the Green's tensors indicates that the electromagnetic field propagation occurs backward in time. Therefore, the fields $\widetilde{\mathbf{E}}^R \left(\mathbf{r}, t' \right)$ and $\widetilde{\mathbf{H}}^R \left(\mathbf{r}, t' \right)$ are referred to as the "back-propagated" or "back-scattering" fields. We will discuss the properties of these fields in more details in Chapter 9 on electromagnetic field migration.

8.1.8 ITERATIVE BORN INVERSIONS

Other techniques available for linearization of the original electromagnetic integral equation are based on transforming this nonlinear problem to a sequence of linear problems. Two common iterative schemes are the Born iterative and distorted-Born iterative methods (Chew, 1990).

In the Born iterative method the original integral equation for the electric field $\mathbf{E}$ is written twice: first as a domain equation (8.62) with respect to the electric field inside the anomalous domain D, and second, as a data equation (8.63) connecting the observed anomalous field (electric data $\mathbf{d}_E = \mathbf{E}^a = \mathbf{E} - \mathbf{E}^b$, or magnetic data $\mathbf{d}_H = \mathbf{H}^a = \mathbf{H} - \mathbf{H}^b$) with the electric field within the anomalous domain

$$\mathbf{E} = \mathbf{G}_E \left(\Delta\widetilde{\sigma}\mathbf{E} \right) + \mathbf{E}^b, \quad (8.62)$$

$$\mathbf{d}_E = \mathbf{G}_E \left(\Delta\widetilde{\sigma}\mathbf{E} \right), \quad \mathbf{d}_H = \mathbf{G}_H \left(\Delta\widetilde{\sigma}\mathbf{E} \right), \quad (8.63)$$

where $\mathbf{G}_E$ and $\mathbf{G}_H$ are the electric and magnetic Green's operators determined by formula (6.37).

Note that each equation, (8.62) and (8.63), is bilinear because of the product of two unknowns, $\Delta\widetilde{\sigma}$ and $\mathbf{E}$. However, if we specify one of the unknowns, the equations become linear. The iterative Born inversion is based on subsequently determining $\Delta\widetilde{\sigma}$ from Eq. (8.63) for a specified $\mathbf{E}$, and then

updating $\mathbf{E}$ from Eq. (8.62) for a predetermined $\Delta\widetilde{\sigma}$, etc. Within the framework of this method the Green's tensors $\widehat{\mathbf{G}}_E$ and $\widehat{\mathbf{G}}_H$, and the background field $\mathbf{E}^b$ stay unchanged.

In the distorted-Born iterative method, the background field and the Green's tensors are updated after each iteration according to the updated conductivity $\Delta\widetilde{\sigma}$. However, this approach is difficult to implement in practice, because it requires calculation of the Green's tensors for inhomogeneous media, which is an extremely time consuming problem in itself.

The interested reader may find more information about the iterative Born method in the monograph by Zhdanov (2002).

8.2 NONLINEAR INVERSION
8.2.1 FORMULATION OF THE NONLINEAR EM INVERSE PROBLEM

Consider a general nonlinear inverse problem for anomalous electric or magnetic fields:

$$\mathbf{d}_E = \mathbf{A}_E\left(\Delta\widetilde{\sigma}\right) = \mathbf{G}_E\left(\Delta\widetilde{\sigma}\mathbf{E}\right), \tag{8.64}$$

$$\mathbf{d}_H = \mathbf{A}_H\left(\Delta\widetilde{\sigma}\right) = \mathbf{G}_H\left(\Delta\widetilde{\sigma}\mathbf{E}\right), \tag{8.65}$$

where $\mathbf{A}_{E,H}\left(\Delta\widetilde{\sigma}\right)$ are nonlinear forward modeling operators, given by the formulae:

$$\mathbf{A}_{E,H}\left(\Delta\widetilde{\sigma}\right) = \mathbf{G}_{E,H}\left(\Delta\widetilde{\sigma}\mathbf{E}\right) = \iiint_V \widehat{\mathbf{G}}_E\left(\mathbf{r}' \mid \mathbf{r}\right) \cdot \Delta\widetilde{\sigma}\left[\mathbf{E}^b\left(\mathbf{r}\right) + \mathbf{E}^a\left(\mathbf{r}\right)\right] dv. \tag{8.66}$$

The nonlinearity of the operators $\mathbf{A}_{E,H}\left(\mathbf{r}' \mid \Delta\widetilde{\sigma}\right)$ with respect to the anomalous conductivity $\Delta\widetilde{\sigma}$ comes from the fact that the anomalous electric field $\mathbf{E}^a$ is also a function of $\Delta\widetilde{\sigma}$.

According to the conventional Tikhonov regularization method, we substitute for the solution of the inverse problems (8.64) or (8.65) a minimization of the corresponding parametric functional with, for example, a minimum norm stabilizer:

$$
\begin{aligned}
P^\alpha\left(\Delta\widetilde{\sigma}\right) = {} & \left(\mathbf{A}_{E,H}(\Delta\widetilde{\sigma}) - \mathbf{d},\ \mathbf{A}_{E,H}(\Delta\widetilde{\sigma}) - \mathbf{d}\right)_D \\
& + \alpha\left(W\left(\Delta\widetilde{\sigma} - \Delta\widetilde{\sigma}_{apr}\right),\ W\left(\Delta\widetilde{\sigma} - \Delta\widetilde{\sigma}_{apr}\right)\right)_M,
\end{aligned}
\tag{8.67}
$$

where W is the corresponding weighting operator.

The minimization problem (8.67) can be solved by the conjugate gradient methods (Press et al., 1987; Tarantola, 1987; Zhdanov, 2002).

8.2.2 REGULARIZED SOLUTION OF NONLINEAR DISCRETE EM INVERSE PROBLEM

We now return to the discrete problem, which we have discussed in section 8.1.2. The inverse EM problems (8.64) or (8.65) can be written in the form of the matrix equation:

$$\mathbf{d} = \mathbf{A}(\mathbf{m}^{true}),$$

where $\mathbf{A}$ is a nonlinear matrix operator, and $\mathbf{m}^{true}$ is a true but unknown set of conductivity model parameters. For simplicity, we assume within this section that all parameters are real numbers. However, the same technique with a little modification, can be applied to complex parameters as well.

The misfit functional $\varphi(\mathbf{m})$ can be written in the form

$$\varphi(\mathbf{m}) = (\mathbf{A}(\mathbf{m}) - \mathbf{d})^T (\mathbf{A}(\mathbf{m}) - \mathbf{d}). \qquad (8.68)$$

For a regularized solution of a nonlinear inverse problem, let us introduce a parametric functional,

$$
\begin{aligned}
P^\alpha(\mathbf{m}, \mathbf{d}) &= \|\mathbf{W}_d \mathbf{A}(\mathbf{m}) - \mathbf{W}_d \mathbf{d}\|^2 + \alpha \|\mathbf{W}_m \mathbf{m} - \mathbf{W}_m \mathbf{m}_{apr}\|^2 \\
&= (\mathbf{W}_d \mathbf{A}(\mathbf{m}) - \mathbf{W}_d \mathbf{d})^T (\mathbf{W}_d \mathbf{A}(\mathbf{m}) - \mathbf{W}_d \mathbf{d}) \\
&\quad + \alpha (\mathbf{W}_m \mathbf{m} - \mathbf{W}_m \mathbf{m}_{apr})^T (\mathbf{W}_m \mathbf{m} - \mathbf{W}_m \mathbf{m}_{apr}), \qquad (8.69)
\end{aligned}
$$

where $\mathbf{W}_d$ and $\mathbf{W}_m$ are some weighting matrices of data and model parameters, $\mathbf{m}_{apr}$ is some *a priori* model. Some possible methods of introducing $\mathbf{W}_d$ and $\mathbf{W}_m$ were discussed above. Numerical experiment demonstrates that, for iterative methods of inversion of gradient type, the recommended choice of the model parameters weighting matrix $\mathbf{W}_m$ is the square root of the integrated sensitivity matrix according to formula (8.30). This choice of matrix $\mathbf{W}_m$ is based on the simple fact that the first iteration of a gradient method, as in the approximate solution (8.36), is usually proportional to the inverse square of the matrix $\mathbf{W}_m$. Therefore, application of the weights (8.30) helps to produce a suitable first iteration close to the true model. Under these circumstances, the convergence of the entire iteration process is improved.

According to the basic principles of the regularization method, we have to find the model $\mathbf{m}_\alpha$, a quasi-solution of the inverse problem, which minimizes the parametric functional:

$$P^\alpha(\mathbf{m}, \mathbf{d}) = \min.$$

8.2.3 THE STEEPEST DESCENT METHOD FOR NONLINEAR REGULARIZED LEAST-SQUARES INVERSION

We consider an iterative algorithm for parametric functional minimization. It is reasonable to build this algorithm on the idea that, at every iteration $\mathbf{m}_n$, a parametric functional decreases. In other words we impose the *descent condition* that

$$P^\alpha(\mathbf{m}_{n+1}) < P^\alpha(\mathbf{m}_n) \text{ for all } n \geq 0. \qquad (8.70)$$

A method that imposes this condition is called a *descent method*. The question is how to find iterations $\{\mathbf{m}_n\}$ which satisfy the descent condition. To solve the problem of minimization of the parametric functional using the steepest descent method, let us calculate the first variation of $P^\alpha(\mathbf{m}, \mathbf{d})$, assuming that the operator $\mathbf{A}(\mathbf{m})$ is differentiable, so that

$$\delta \mathbf{A}(\mathbf{m}) = \mathbf{F}_m \delta \mathbf{m}, \qquad (8.71)$$

where $\mathbf{F}_m$ is the Fréchet derivative matrix of $\mathbf{A}$.

Thus, we have

$$\delta P^\alpha(\mathbf{m}, \mathbf{d}) = 2(\mathbf{W}_d \mathbf{F}_m \delta \mathbf{m})^T (\mathbf{W}_d \mathbf{A}(\mathbf{m}) - \mathbf{W}_d \mathbf{d}) + 2\alpha (\mathbf{W}_m \delta \mathbf{m})^T (\mathbf{W}_m \mathbf{m} - \mathbf{W}_m \mathbf{m}_{apr}),$$

or after some algebra

$$\delta P^{\alpha}(\mathbf{m}, \mathbf{d}) = 2(\delta\mathbf{m})^T \mathbf{F}_m^T \mathbf{W}_d^2 (\mathbf{A}(\mathbf{m}) - \mathbf{d}) + 2\alpha(\delta\mathbf{m})^T \mathbf{W}_m^2 (\mathbf{m} - \mathbf{m}_{apr}), \tag{8.72}$$

where we assume that the matrices $\mathbf{W}_d$ and $\mathbf{W}_m$ are diagonal.

In order to satisfy the descent condition (8.70), we select

$$\delta\mathbf{m} = -k^{\alpha} \mathbf{l}^{\alpha}(\mathbf{m}), \tag{8.73}$$

where k^{α} is some positive real number (length of a step) and $\mathbf{l}^{\alpha}(\mathbf{m})$ is a column matrix defining the direction of the steepest ascent of the parametric functional:

$$\mathbf{l}^{\alpha}(\mathbf{m}) = \mathbf{F}_m^T \mathbf{W}_d^2 (\mathbf{A}(\mathbf{m}) - \mathbf{d}) + \alpha \mathbf{W}_m^2 (\mathbf{m} - \mathbf{m}_{apr}). \tag{8.74}$$

Certainly, by substituting Eqs. (8.73) and (8.74) into (8.72), we have

$$\delta P^{\alpha}(\mathbf{m}, \mathbf{d}) = -2k^{\alpha} (\mathbf{l}^{\alpha}(\mathbf{m}), \mathbf{l}^{\alpha}(\mathbf{m})) < 0, \tag{8.75}$$

so $\mathbf{l}^{\alpha}(\mathbf{m})$ describes the "direction" of increasing (ascent) of the functional $\phi(\mathbf{m})$, because it is opposite to the descent direction, $\delta\mathbf{m}$. An iterative process of the method is constructed according to the formula

$$\mathbf{m}_{n+1} = \mathbf{m}_n + \delta\mathbf{m} = \mathbf{m}_n - k_n^{\alpha} \mathbf{l}^{\alpha}(\mathbf{m}_n),$$

where the coefficient k_n^{α} is defined by a line search according to the condition (Zhdanov, 2002):

$$P^{\alpha}(\mathbf{m}_{n+1}) = P^{\alpha}\left(\mathbf{m}_n - k_n^{\alpha} \mathbf{l}^{\alpha}(\mathbf{m}_n)\right) = \Phi^{\alpha}(k_n^{\alpha}) = \min. \tag{8.76}$$

8.2.4 THE NEWTON METHOD FOR NONLINEAR REGULARIZED LEAST-SQUARES INVERSION

The main idea of the Newton method is to try to solve the problem of minimization in one step:

$$\mathbf{m}_1 = \mathbf{m}_0 + \Delta\mathbf{m}. \tag{8.77}$$

Thus, instead of moving downhill along a long path formed by mutually orthogonal directions of the steepest descent, one can try to reach the minimum of the misfit functional along one direction. To determine this specific direction, $\Delta\mathbf{m}$, let us write the linearized parametric functional

$$
\begin{aligned}
P^{\alpha}(\mathbf{m}_1, \mathbf{d}) &= P^{\alpha}(\mathbf{m}_0 + \Delta\mathbf{m}, \mathbf{d}) \\
&= (\mathbf{W}_d \mathbf{A}(\mathbf{m}_0) + \mathbf{W}_d \mathbf{F}_{m_0} \Delta\mathbf{m} - \mathbf{W}_d \mathbf{d})^T (\mathbf{W}_d \mathbf{A}(\mathbf{m}_0) + \mathbf{W}_d \mathbf{F}_{m_0} \Delta\mathbf{m} - \mathbf{W}_d \mathbf{d}) \\
&\quad + \alpha(\mathbf{W}_m \mathbf{m}_0 + \mathbf{W}_m \Delta\mathbf{m} - \mathbf{W}_m \mathbf{m}_{apr})^T (\mathbf{W}_m \mathbf{m}_0 + \mathbf{W}_m \Delta\mathbf{m} - \mathbf{W}_m \mathbf{m}_{apr}). \tag{8.78}
\end{aligned}
$$

The first variation of the parametric functional is equal to

$$
\begin{aligned}
\delta_{\Delta\mathbf{m}} P^{\alpha}(\mathbf{m}_1, \mathbf{d}) &= \delta_{\Delta\mathbf{m}} P^{\alpha}(\mathbf{m}_0 + \Delta\mathbf{m}, \mathbf{d}) \\
&= (\delta\Delta\mathbf{m})^T \left[\mathbf{F}_{m_0}^T \mathbf{W}_d^2 \left(\mathbf{A}(\mathbf{m}_0) + \mathbf{F}_{m_0} \Delta\mathbf{m} - \mathbf{d} \right) + \alpha \mathbf{W}_m^2 (\mathbf{m}_0 + \Delta\mathbf{m} - \mathbf{m}_{apr}) \right].
\end{aligned}
$$

It is evident that the necessary condition for the minimum of the parametric functional,

$$\delta P^{\alpha}(\mathbf{m}_1, \mathbf{d}) = 0,$$

is satisfied only if

$$\mathbf{F}_{m_0}^T \mathbf{W}_d^2 \left(\mathbf{A}(\mathbf{m}_0) + \mathbf{F}_{m_0} \Delta \mathbf{m} - \mathbf{d} \right) + \alpha \mathbf{W}_m^2 (\mathbf{m}_0 + \Delta \mathbf{m} - \mathbf{m}_{apr}) = 0.$$

From the last equation, taking into consideration (8.74), we obtain

$$\Delta \mathbf{m} = -2 \mathbf{H}_{\alpha, m_0}^{-1} \mathbf{l}^{\alpha}(\mathbf{m}_n),$$

where

$$\mathbf{H}_{\alpha, m_0} = 2 \left(\mathbf{F}_{m_0}^T \mathbf{W}_d^2 \mathbf{F}_{m_0} + \alpha \mathbf{W}_m^2 \right)$$

is the regularized quasi-Hessian matrix.

Thus, the Newton algorithm for the nonlinear regularized least-squares inversion can be expressed by the formula

$$\mathbf{m}_{n+1} = \mathbf{m}_n - 2 \mathbf{H}_{\alpha, m_n}^{-1} \mathbf{l}^{\alpha}(\mathbf{m}_n),$$

where

$$\mathbf{H}_{\alpha, m_n} = 2 \left(\mathbf{F}_{m_n}^T \mathbf{W}_d^2 \mathbf{F}_{m_n} + \alpha \mathbf{W}_m^2 \right).$$

8.2.5 NUMERICAL SCHEMES OF THE NEWTON METHOD FOR NONLINEAR REGULARIZED LEAST-SQUARES INVERSION

The algorithm of the Newton method for a discrete inverse problem can be summarized as follows:

$$
\begin{aligned}
\mathbf{r}_n &= \mathbf{A}(\mathbf{m}_n) - \mathbf{d}, & (a) \\
\mathbf{l}_n^{\alpha_n} &= \mathbf{l}^{\alpha_n}(\mathbf{m}_n) = \mathbf{F}_{m_n}^T \mathbf{W}_d^2 \mathbf{r}_n + \alpha_n \mathbf{W}_m^2 (\mathbf{m}_n - \mathbf{m}_{apr}), & (b) \\
\mathbf{H}_{\alpha_n, m_n} &= 2 \left(\mathbf{F}_{m_n}^T \mathbf{W}_d^2 \mathbf{F}_{m_n} + \alpha_n \mathbf{W}_m^2 \right), & (c) \\
\mathbf{m}_{n+1} &= \mathbf{m}_n - 2 \mathbf{H}_{\alpha_n, m_n}^{-1} \mathbf{l}_n^{\alpha_n}(\mathbf{m}_n), & (d)
\end{aligned}
\qquad (8.79)
$$

where α_n are the subsequent values of the regularization parameter, updated on each iteration. This method is called the Newton method with adaptive regularization.

The iterative process (8.79) is terminated when the misfit reaches the given level ε_0:

$$\phi(\mathbf{m}_N) = \|\mathbf{r}_N\|^2 \leq \varepsilon_0.$$

8.2.6 NONLINEAR LEAST-SQUARES INVERSION BY THE CONJUGATE GRADIENT METHOD

The conjugate gradient method is based on the same ideas as the steepest descent, and the iteration process is very similar to the last one:

$$\mathbf{m}_{n+1} = \mathbf{m}_n + \delta \mathbf{m}_n = \mathbf{m}_n - \tilde{k}_n^\alpha \tilde{\mathbf{l}}^\alpha (\mathbf{m}_n), \tag{8.80}$$

where

$$\delta \mathbf{m}_n = -\tilde{\mathbf{k}}_\mathbf{n}^\alpha \tilde{\mathbf{l}}^\alpha (\mathbf{m}_n).$$

However, the "directions" of ascent $\tilde{\mathbf{l}}^\alpha (\mathbf{m}_n)$ are selected in a different way. At the first step we use the "direction" of the steepest ascent:

$$\tilde{\mathbf{l}}^\alpha (\mathbf{m}_0) = \mathbf{l}^\alpha (\mathbf{m}_0).$$

At the next step the "direction" of ascent is a linear combination of the steepest ascent at this step and the "direction" of ascent $\tilde{\mathbf{l}}^\alpha (\mathbf{m}_0)$ on the previous step:

$$\tilde{\mathbf{l}}^\alpha (\mathbf{m}_1) = \mathbf{l}^\alpha (\mathbf{m}_1) + \beta_1 \tilde{\mathbf{l}}^\alpha (\mathbf{m}_0).$$

At the n-th step

$$\tilde{\mathbf{l}}^\alpha (\mathbf{m}_{n+1}) = \mathbf{l}^\alpha (\mathbf{m}_{n+1}) + \beta_{n+1}^\alpha \tilde{\mathbf{l}}^\alpha (\mathbf{m}_n). \tag{8.81}$$

The regularized steepest descent directions are determined according to the formula for the least-squares method:

$$\mathbf{l}^\alpha (\mathbf{m}_n) = \mathbf{F}_{m_n}^T \mathbf{W}_d^2 (\mathbf{A}(\mathbf{m}_n) - \mathbf{d}) + \alpha \mathbf{W}_{m_n}^2 (\mathbf{m}_n - \mathbf{m}_{apr}). \tag{8.82}$$

Determination of the length of iteration step, a coefficient $\tilde{k}_n^\alpha$, can be based on the linear or parabolic line search:

$$P^\alpha (\mathbf{m}_{n+1}) = P^\alpha (\mathbf{m}_n - \tilde{k}_n^\alpha \tilde{\mathbf{l}}^\alpha (\mathbf{m}_n)) = f(\tilde{k}_n^\alpha) = \min.$$

Solution of this minimization problem gives the following best estimation for the length of the step using a linear line search:

$$\begin{aligned} \tilde{k}_n^\alpha &= \frac{\tilde{\mathbf{l}}^{\alpha T} (\mathbf{m}_n) \mathbf{l}^\alpha (\mathbf{m}_n)}{\tilde{\mathbf{l}}^{\alpha T} (\mathbf{m}_n) \left[\left(\mathbf{F}_{m_n}^T \mathbf{W}_d^2 \mathbf{F}_{m_n} + \alpha \mathbf{W}_m^2 \right) \tilde{\mathbf{l}}^\alpha (\mathbf{m}_n) \right]} \\ &= \frac{\tilde{\mathbf{l}}^{\alpha T} (\mathbf{m}_n) \mathbf{l}^\alpha (\mathbf{m}_n)}{\left\| \mathbf{W}_d \mathbf{F}_{m_n} \tilde{\mathbf{l}}^\alpha (\mathbf{m}_n) \right\|^2 + \alpha \left\| \mathbf{W}_m \tilde{\mathbf{l}}^\alpha (\mathbf{m}_n) \right\|^2}. \end{aligned} \tag{8.83}$$

One can use a parabolic line search also (Fletcher, 1995) to improve the convergence rate of the RCG method.

The CG method requires that the vectors $\tilde{\mathbf{l}}^\alpha(\mathbf{m}_n)$ introduced above will be mutually conjugate. This requirement is fulfilled if the coefficients β_n are determined by the formula (Tarantola, 1987)

$$\beta_{n+1}^\alpha = \frac{\|\mathbf{l}^\alpha(\mathbf{m}_{n+1})\|^2}{\|\mathbf{l}^\alpha(\mathbf{m}_n)\|^2}. \tag{8.84}$$

Using Eqs. (8.80), (8.81), (8.83), and (8.84), we can obtain $\mathbf{m}$ iteratively.

8.2.7 THE NUMERICAL SCHEME OF THE REGULARIZED CONJUGATE GRADIENT METHOD FOR NONLINEAR LEAST-SQUARES INVERSION

In this section we first consider a method of selecting the parameter α. The regularization parameter α describes a trade-off between the best fitting and most reasonable stabilization. In a case when α is selected to be too small, the minimization of the parametric functional $P^\alpha(\mathbf{m})$ is equivalent to the minimization of the misfit functional $\phi(\mathbf{m})$, and therefore we have no regularization, which can result in an unstable incorrect solution. When α is too large, the minimization of the parametric functional $P^\alpha(\mathbf{m})$ is equivalent to the minimization of the stabilizing functional $s(\mathbf{m})$, which will force the solution to be closer to the *a priori* model. Ultimately, we would expect the final model to be exactly like the *a priori* model, while the observed data are totally ignored in the inversion. Thus, the critical question in the regularized solution of an inverse problem is the selection of the optimal regularization parameter α.

The basic principles used for determining the regularization parameter α were discussed in the previous sections of the book. We introduced in Chapter 7 a simple numerical method to determine the parameter α. Consider for example the progression of numbers

$$\alpha_k = \alpha_1 q^{k-1}; \quad k = 1, 2, 3, \dots \ q > 0. \tag{8.85}$$

The first iteration of the steepest descent or any other gradient method is run usually with $\alpha_0 = 0$. The initial value of the regularization parameter, α_1, is determined after the first iteration, $\mathbf{m}_1$, as a ratio:

$$\alpha_1 = \frac{\|\mathbf{W}_d \mathbf{A}(\mathbf{m}_1) - \mathbf{W}_d \mathbf{d}\|^2}{\|\mathbf{W}_m \mathbf{m}_1 - \mathbf{W}_m \mathbf{m}_{apr}\|^2}.$$

In this way we have an approximate balance between the misfit and stabilizing functional. For any number α_k we can find an element $\mathbf{m}_{\alpha_k}$, minimizing $P^{\alpha_k}(\mathbf{m})$, and calculate the misfit $\| \mathbf{A}(\mathbf{m}_{\alpha_k}) - \mathbf{d} \|^2$. The optimal value of the parameter α is the number α_{k0}, for which we have

$$\| \mathbf{A}(\mathbf{m}_{\alpha_{k0}}) - \mathbf{d} \|^2 = \delta, \tag{8.86}$$

where δ is the level of noise in the observed data. The equality (8.86) is called *the misfit condition*. This algorithm, as well as the L-curve method (see Chapter 2), has clear practical limitations, because it requires a complete numerical solution of the inverse problem for each value of the regularization parameter α_k.

An alternative approach is based on the simple idea, which we have already discussed above, that the regularization parameter α can be updated in the process of the iterative inversion. For example, one can use the following algorithm for the RCG method:

$$\tilde{\mathbf{l}}^{\alpha_{n+1}}(\mathbf{m}_{n+1}) = \mathbf{l}^{\alpha_{n+1}}(\mathbf{m}_{n+1}) + \beta_{n+1}\tilde{\mathbf{l}}^{\alpha_n}(\mathbf{m}_n),$$

where α_n are the subsequent values of the regularization parameter. This method is called the *adaptive regularization method*. In order to avoid divergence, we begin an iteration from a value of α_1, which can be obtained as a ratio of the misfit functional and the stabilizer for an initial model, then reduce α_n according to formula (8.85) on each subsequent iteration and continuously iterate until the misfit condition (8.86) is reached.

The algorithm of the regularized conjugate gradient method can be summarized as follows:

$$\mathbf{r}_n = A(\mathbf{m}_n) - \mathbf{d}, \qquad (a)$$

$$\mathbf{l}_n^{\alpha_n} = \mathbf{l}^{\alpha_n}(\mathbf{m}_n) = \mathbf{F}_{m_n}^T \mathbf{W}_d^2 \mathbf{r}_n + \alpha_n \mathbf{W}_m^2(\mathbf{m}_n - \mathbf{m}_{apr}), \qquad (b)$$

$$\beta_n^{\alpha_n} = \left\| \mathbf{l}_n^{\alpha_n} \right\|^2 / \left\| \mathbf{l}_{n-1}^{\alpha_{n-1}} \right\|^2, \qquad \widetilde{\mathbf{l}}_n^{\alpha_n} = \mathbf{l}_n^{\alpha_n} + \beta_n^{\alpha_n} \widetilde{\mathbf{l}}_{n-1}^{\alpha_{n-1}}, \ \widetilde{\mathbf{l}}_0^{\alpha_0} = \mathbf{l}_0^{\alpha_0}, \quad (c) \qquad (8.87)$$

$$\widetilde{k}_n^{\alpha_n} = \left(\widetilde{\mathbf{l}}_n^{\alpha_n T} \mathbf{l}_n^{\alpha_n} \right) / \left\{ \left\| \mathbf{W}_d \mathbf{F}_{m_n} \widetilde{\mathbf{l}}_n^{\alpha_n} \right\|^2 + \alpha \left\| \mathbf{W}_m \widetilde{\mathbf{l}}_n^{\alpha_n} \right\|^2 \right\}, \qquad (d)$$

$$\mathbf{m}_{n+1} = \mathbf{m}_n - \widetilde{k}_n^{\alpha_n} \widetilde{\mathbf{l}}_n^{\alpha_n}, \qquad (e)$$

where α_n are the subsequent values of the regularization parameter. The iterative process (8.87) is terminated when the misfit reaches the given level ε_0:

$$\phi(\mathbf{m}_N) = \|\mathbf{r}_N\|^2 \le \varepsilon_0.$$

This method is called the conjugate gradient method with adaptive regularization.

8.2.8 FRÉCHET DERIVATIVE CALCULATION

In Chapter 6 we developed the expressions for the Fréchet differentials of the forward modeling electromagnetic operator (6.62) and (6.63), which we reproduce here for convenience:

$$\mathbf{F}_E(\widetilde{\sigma}, \delta\widetilde{\sigma}) = \mathbf{F}_E^{\widetilde{\sigma}} \left(\mathbf{r}' \mid \delta\widetilde{\sigma} \right) = \iiint_D \widehat{\mathbf{G}}_E^{\widetilde{\sigma}} \left(\mathbf{r}' \mid \mathbf{r} \right) \cdot \delta\widetilde{\sigma}(\mathbf{r}) \mathbf{E}(\mathbf{r}) \, dv, \qquad (8.88)$$

and

$$\mathbf{F}_H(\widetilde{\sigma}, \delta\widetilde{\sigma}) = \mathbf{F}_H^{\widetilde{\sigma}} \left(\mathbf{r}' \mid \delta\widetilde{\sigma} \right) = \iiint_D \widehat{\mathbf{G}}_H^{\widetilde{\sigma}} \left(\mathbf{r}' \mid \mathbf{r} \right) \cdot \delta\widetilde{\sigma}(\mathbf{r}) \mathbf{E}(\mathbf{r}) \, dv. \qquad (8.89)$$

In the last formulae, $\widetilde{\sigma} = \widetilde{\sigma}_b + \Delta\widetilde{\sigma}$ is a conductivity distribution, for which we calculate the forward modeling operator variation; $\delta\widetilde{\sigma}$ is the corresponding variation of the conductivity $\widetilde{\sigma}$, which is obviously equal to the variation of the anomalous conductivity, $\delta\widetilde{\sigma} = \delta\Delta\widetilde{\sigma}$. Tensors $\widehat{\mathbf{G}}_{E,H}^{\widetilde{\sigma}}$ are electric and magnetic Green's tensors calculated for the given conductivity $\widetilde{\sigma}$. Vector $\mathbf{E}$ in expressions (8.88) and (8.89) represents the total electric field, $\mathbf{E} = \mathbf{E}^b + \mathbf{E}^a$ for the given conductivity $\widetilde{\sigma}$.

Note that in the RCG algorithm (8.87) the expression $F_{E,Hn}^\star \mathbf{R}_{E,Hn}$ denotes the result of an application of the adjoint Fréchet derivative operator to the corresponding electric or magnetic residual field $\mathbf{R}_{E,Hn} = A_{E,H}(\Delta\widetilde{\sigma}_n) - \mathbf{d}_{E,H}$ on the n-th iteration.

The expressions for the adjoint Fréchet derivative operators are given by formulae (8.46) and (8.47). Based on these formulae, we can write:

$$F_{E,Hn}^{\star} \mathbf{R_n} = \mathbf{F}_{E,H}^{\widetilde{\sigma}_n \star} (\mathbf{r} \mid \mathbf{R_n}) = \iint_S \left[\widehat{\mathbf{G}}_{E,H} (\mathbf{r}' \mid \mathbf{r}) \cdot \mathbf{E}_n (\mathbf{r}) \right]^* \cdot \mathbf{R}_{E,Hn} (\mathbf{r}') \, ds'$$

$$= \mathbf{E}_n^* (\mathbf{r}) \cdot \iint_S \widetilde{\widehat{\mathbf{G}}}_{E,Hn}^* (\mathbf{r}' \mid \mathbf{r}) \cdot \mathbf{R}_{E,Hn} (\mathbf{r}') \, ds', \tag{8.90}$$

where $\mathbf{E}_n (\mathbf{r}) = \mathbf{E}^b (\mathbf{r}) + \mathbf{E}_n^a (\mathbf{r})$ is the electric field, and $\widehat{\mathbf{G}}_{E,Hn}$ are the electric or magnetic Green's tensors, computed on n-th iteration for the conductivity distribution, $\widetilde{\sigma}_n (\mathbf{r}) = \widetilde{\sigma}_b (\mathbf{r}) + \Delta\widetilde{\sigma}_n (\mathbf{r})$; a tilde denotes the operation of transposition.

According to the reciprocity theorem (see Chapter 3), the integral term in the last formula can be treated as the complex conjugate of the electric field, $\mathbf{E}_n^R (\mathbf{r})$ (in the case of the electric Green's tensor $\widehat{\mathbf{G}}_E$ and the electric residual field $\mathbf{R}_{En}$), or the complex conjugate of the magnetic field $\mathbf{H}_n^R (\mathbf{r})$ (in the case of the magnetic Green's tensor $\widehat{\mathbf{G}}_H$ and the magnetic residual field $\mathbf{R}_{Hn}$),

$$\mathbf{E}_n^{R*} (\mathbf{r}) = \iint_S \widehat{\mathbf{G}}_{En}^* (\mathbf{r} \mid \mathbf{r}') \cdot \mathbf{R}_{En} (\mathbf{r}') \, ds' = \left[\iint_S \widehat{\mathbf{G}}_{En} (\mathbf{r} \mid \mathbf{r}') \cdot \mathbf{R}_{En}^* (\mathbf{r}') \, ds' \right]^*,$$

$$\mathbf{H}_n^{R*} (\mathbf{r}) = \iint_S \widehat{\mathbf{G}}_{Hn}^* (\mathbf{r} \mid \mathbf{r}') \cdot \mathbf{R}_{Hn} (\mathbf{r}') \, ds' = \left[\iint_S \widehat{\mathbf{G}}_{Hn} (\mathbf{r} \mid \mathbf{r}') \cdot \mathbf{R}_{Hn}^* (\mathbf{r}') \, ds' \right]^*. \tag{8.91}$$

Here, the fields $\mathbf{E}_n^R (\mathbf{r})$ and $\mathbf{H}_n^R (\mathbf{r})$,

$$\mathbf{E}_n^R (\mathbf{r}) = \iint_S \widehat{\mathbf{G}}_{En} (\mathbf{r} \mid \mathbf{r}') \cdot \mathbf{R}_{En}^* (\mathbf{r}') \, ds',$$

$$\mathbf{H}_n^R (\mathbf{r}) = \iint_S \widehat{\mathbf{G}}_{Hn} (\mathbf{r} \mid \mathbf{r}') \cdot \mathbf{R}_{Hn}^* (\mathbf{r}') \, ds', \tag{8.92}$$

are generated at the point $\mathbf{r}$ inside the volume V by the fictitious electric currents distributed along the surface of observation S with the surface density $\mathbf{j}_{En}^S (\mathbf{r}')$ or $\mathbf{j}_{Hn}^S (\mathbf{r}')$, determined by the complex conjugate residual fields:

$$\mathbf{R}_{En}^* (\mathbf{r}') = \mathbf{j}_{En}^S (\mathbf{r}'); \ \ \mathbf{R}_{Hn}^* (\mathbf{r}') = \mathbf{j}_{Hn}^S (\mathbf{r}'). \tag{8.93}$$

Therefore, from (8.90) and (8.91) we find that the result of applying the adjoint Fréchet operator to the residual field is just equal to the scalar product of the complex conjugate of the electric field $\mathbf{E}_n$, computed at the n-th iteration, with the corresponding auxiliary electric $\mathbf{E}_n^{R*}$ or magnetic $\mathbf{H}_n^{R*}$ fields due to the reciprocal sources on the observation surface:

$$\mathbf{F}_E^{\widetilde{\sigma}_n \star} (\mathbf{r} \mid \mathbf{R}_{En}) = \mathbf{E}_n^* (\mathbf{r}) \cdot \mathbf{E}_n^{R*} (\mathbf{r}),$$

$$\mathbf{F}_H^{\widetilde{\sigma}_n \star} (\mathbf{r} \mid \mathbf{R}_{Hn}) = \mathbf{E}_n^* (\mathbf{r}) \cdot \mathbf{H}_n^{R*} (\mathbf{r}). \tag{8.94}$$

Thus, we can conclude, that the calculation of the terms $F_{E,Hn}^{\star} \mathbf{R}_{E,Hn}$ requires just one additional forward modeling solution on each iteration for the auxiliary electric field $\mathbf{E}_n^R$ or magnetic field $\mathbf{H}_n^R$ due to the reciprocal sources.

In the practical application of the solution of the nonlinear inverse problem described above significant difficulties are experienced, however. The most critical problem can be described as follows. The numerical calculation of the reciprocal fields $\mathbf{E}_n^R$ and $\mathbf{H}_n^R$ on the n-th iteration requires, according to formula (8.92), the knowledge of the corresponding Green's tensors $\widehat{\mathbf{G}}_{E,Hn}$ for the conductivity $\widetilde{\sigma}_n$, obtained on the previous iteration. In general cases, the function $\widetilde{\sigma}_n(\mathbf{r})$ cannot be represented by simple horizontally or cylindrically layered models, for which it is relatively easy to compute the Green's tensors. The computation of the Green's tensors for an arbitrary conductivity distribution becomes a difficult numerical problem itself, similar to the distorted-Born iterative method.

8.2.9 FRÉCHET DERIVATIVE CALCULATION USING QUASI-BORN APPROXIMATION

It was demonstrated in Chapter 6 that, in a case of the models with variable backgrounds a 3D geoelectrical model can be represented by the normal (horizontally layered) conductivity σ_{norm}, background conductivity, $\sigma_b = \sigma_{norm} + \Delta\sigma_b$, and an arbitrarily varying conductivity, $\sigma = \sigma_b + \Delta\sigma_a$, within a domain D. In this model, the EM field can be presented as a sum of the normal fields, $\mathbf{E}^n$, $\mathbf{H}^n$, generated by the given source(s) in the model with normal distribution of conductivity, σ_{norm}, a variable background effect, $\mathbf{E}^{\Delta\sigma_b}$, $\mathbf{H}^{\Delta\sigma_b}$, produced by the inhomogeneous background conductivity, $\Delta\sigma_b$, and the anomalous fields, $\mathbf{E}^{\Delta\sigma_a}$, $\mathbf{H}^{\Delta\sigma_a}$, due to the anomalous conductivity distribution, $\Delta\sigma_a$, as follows:

$$\mathbf{E} = \mathbf{E}^n + \mathbf{E}^{\Delta\sigma_b} + \mathbf{E}^{\Delta\sigma_a}, \ \mathbf{H} = \mathbf{H}^n + \mathbf{H}^{\Delta\sigma_b} + \mathbf{H}^{\Delta\sigma_a}. \tag{8.95}$$

It was shown in section 6.3.5 that the anomalous fields can be expressed using the quasi-Born approximations as follows:

$$\mathbf{E}^{\Delta\sigma_a} \approx \mathbf{E}^{QB} = \mathbf{G}_E\left[\Delta\widetilde{\sigma}\mathbf{E}^b\right] = \iiint_D \widehat{\mathbf{G}}_E(\mathbf{r}_j \mid \mathbf{r}) \cdot \left[\Delta\widetilde{\sigma}\mathbf{E}^b(\mathbf{r})\right] dv, \tag{8.96}$$

$$\mathbf{H}^{\Delta\sigma_a} \approx \mathbf{H}^{QB} = \mathbf{G}_H\left[\Delta\widetilde{\sigma}\mathbf{E}^b\right] = \iiint_D \widehat{\mathbf{G}}_H(\mathbf{r}_j \mid \mathbf{r}) \cdot \left[\Delta\widetilde{\sigma}\mathbf{E}^b(\mathbf{r})\right] dv, \tag{8.97}$$

where the Green's tensors, $\widehat{\mathbf{G}}_E$ and $\widehat{\mathbf{G}}_H$, are defined for the *normal (horizontally layered) conductivity* σ_{norm}, and the background EM field, $\mathbf{E}^b$, $\mathbf{H}^b$, is a sum of the normal fields and those caused by the inhomogeneous background conductivity:

$$\mathbf{E}^b = \mathbf{E}^n + \mathbf{E}^{\Delta\sigma_b}, \ \mathbf{H}^b = \mathbf{H}^n + \mathbf{H}^{\Delta\sigma_b}. \tag{8.98}$$

Thus, expressions (8.95) for the total EM field take the following form:

$$\mathbf{E} \approx \mathbf{E}^b + \mathbf{E}^{QB}, \ \mathbf{H} \approx \mathbf{H}^b + \mathbf{H}^{QB}. \tag{8.99}$$

By perturbing the anomalous conductivity $\delta\Delta\widetilde{\sigma}(\mathbf{r})$ we can calculate the corresponding perturbation of the electric, $\delta\mathbf{E}(\mathbf{r}_j)$, and magnetic, $\delta\mathbf{H}(\mathbf{r}_j)$ fields as follows:

$$\delta\mathbf{E}(\mathbf{r}_j) = \delta\mathbf{E}^{QB} = \iiint_D \widehat{\mathbf{G}}_E(\mathbf{r}_j \mid \mathbf{r}) \cdot \left[\delta\Delta\widetilde{\sigma}\mathbf{E}^b(\mathbf{r})\right] dv, \tag{8.100}$$

$$\delta\mathbf{H}(\mathbf{r}_j) = \delta\mathbf{H}^{QB} = \iiint_D \widehat{\mathbf{G}}_H(\mathbf{r}_j \mid \mathbf{r}) \cdot \left[\delta\Delta\widetilde{\sigma}\mathbf{E}^b(\mathbf{r})\right] dv. \tag{8.101}$$

From the last formulas, we derive the following expressions for the Fréchet derivatives based on quasi-Born approximations:

$$\frac{\partial \mathbf{E}\left(\mathbf{r}_j\right)}{\partial \Delta \widetilde{\sigma}\left(\mathbf{r}\right)} \approx \mathbf{F}_E^{QB}\left(\mathbf{r}_j \mid \mathbf{r}\right) = \widehat{\mathbf{G}}_E\left(\mathbf{r}_j \mid \mathbf{r}\right) \cdot \mathbf{E}^b\left(\mathbf{r}\right), \tag{8.102}$$

$$\frac{\partial \mathbf{H}\left(\mathbf{r}_j\right)}{\partial \Delta \widetilde{\sigma}\left(\mathbf{r}\right)} \approx \mathbf{F}_H^{QB}\left(\mathbf{r}_j \mid \mathbf{r}\right) = \widehat{\mathbf{G}}_H\left(\mathbf{r}_j \mid \mathbf{r}\right) \cdot \mathbf{E}^b\left(\mathbf{r}\right), \tag{8.103}$$

where we assume having an infinitely small domain of the conductivity perturbations.

Formulas (8.102) and (8.103) provide an effective numerical estimate of the Fréchet derivatives, which can be used in the solution of the EM inverse problems. We should emphasize once again that in these formulas the Green's tensors, $\widehat{\mathbf{G}}_E$ and $\widehat{\mathbf{G}}_H$, are defined for the normal (horizontally layered) conductivity σ_{norm}, while the background electric field, $\mathbf{E}^b$, corresponds to inhomogeneous background conductivity, $\sigma_b = \sigma_{norm} + \Delta \sigma_b$.

8.3 QUASI-LINEAR INVERSION
8.3.1 PRINCIPLES OF QUASI-LINEAR INVERSION

One approach, which can be used in 3-D inversion, is based on principles of quasi-linear (QL) approximation. According to QL approximation, the anomalous electric field $\mathbf{E}^a$ inside the inhomogeneous domain D is linearly proportional to the background field $\mathbf{E}^b$ through some electrical reflectivity tensor $\widehat{\lambda}$:

$$\mathbf{E}^a = \widehat{\lambda} \cdot \mathbf{E}^b. \tag{8.104}$$

Substituting (8.104) into (8.63), we obtain

$$\mathbf{d}_{E,H} = \mathbf{G}_{E,H}\left(\Delta \widetilde{\sigma}\left(\widehat{\mathbf{I}} + \widehat{\lambda}\right) \cdot \mathbf{E}^b\right) = \mathbf{G}_{E,H}\left(\widehat{\mathbf{m}} \cdot \mathbf{E}^\mathbf{b}\right), \tag{8.105}$$

where $\widehat{\mathbf{m}}$ is a material property tensor:

$$\widehat{\mathbf{m}} = \Delta \widetilde{\sigma}\left(\widehat{\mathbf{I}} + \widehat{\lambda}\right). \tag{8.106}$$

Note that Eq. (8.105) is linear with respect to $\widehat{\mathbf{m}}$. The reflectivity tensor $\widehat{\lambda}$ can be determined from the following linear equation inside the inhomogeneous domain D, as long as we know $\widehat{\mathbf{m}}$:

$$\widehat{\lambda} \cdot \mathbf{E}^b = \mathbf{G}_E\left(\widehat{\mathbf{m}} \cdot \mathbf{E}^\mathbf{b}\right). \tag{8.107}$$

After determining $\widehat{\mathbf{m}}$ and $\widehat{\lambda}$, it is possible to evaluate the anomalous conductivity distribution $\Delta \widetilde{\sigma}$ from Eq. (8.106). This inversion scheme reduces the original nonlinear inverse problem to three linear inverse problems: the first one (the quasi-Born inversion) for the tensor $\widehat{\mathbf{m}}$, the second one for the tensor $\widehat{\lambda}$, and the third one (correction of the result of the quasi-Born inversion) for the conductivity $\Delta \widetilde{\sigma}$. This method is called *a quasi-linear (QL) inversion* (Zhdanov and Fang, 1996b, 1999; Zhdanov et al., 2000b).

8.3.2 LOCALIZED QUASI-LINEAR INVERSION

The quasi-linear inversion, introduced above, cannot be used for interpretation of multitransmitter data, because both the reflectivity tensor $\widehat{\boldsymbol{\lambda}}$ and the material property tensor $\widehat{\mathbf{m}}$ depend on the illuminating background electromagnetic field. However, in many geophysical applications, for example, in airborne EM and in well-logging, the data are collected with moving transmitters. In this case one can build an effective inversion scheme based on the localized quasi-linear approximation, introduced in Chapter 6, which is source independent.

Following Zhdanov and Tartaras (2002), we introduce a new tensor function:

$$\widehat{\mathbf{m}}_L\left(\mathbf{r}\right) = \Delta\widetilde{\sigma}\left(\mathbf{r}\right)\left(\widehat{\mathbf{I}} + \widehat{\boldsymbol{\lambda}}_L\left(\mathbf{r}\right)\right), \tag{8.108}$$

which we call a localized material property tensor. Note that this tensor function is independent of the transmitter position, because $\widehat{\boldsymbol{\lambda}}_L$ does not depend on the background field. This is the main difference between the localized QL inversion and the original QL inversion (Zhdanov and Fang, 1999).

In the case of a scalar reflectivity tensor, we introduce a scalar parameter $m_L\left(\mathbf{r}\right)$:

$$m_L\left(\mathbf{r}\right) = \Delta\widetilde{\sigma}\left(\mathbf{r}\right)\left(1 + \lambda_L\left(\mathbf{r}\right)\right). \tag{8.109}$$

We assume now that the anomalous parts of the electric, $\mathbf{E}^a\left(\mathbf{r}_j\right)$, and/or magnetic, $\mathbf{H}^a\left(\mathbf{r}_j\right)$, fields (generated by a transmitter with one or different positions) are measured at a number of observation points, $\mathbf{r}_j$. Using LQL approximation for the observed fields, $\mathbf{d}$, we arrive at the following equation, similar to (8.105):

$$\mathbf{d} = \mathbf{G}_d\left(m_L\left(\mathbf{r}\right)\mathbf{E}^b\left(\mathbf{r}\right)\right), \tag{8.110}$$

which is linear with respect to the localized material property function $m_L\left(\mathbf{r}\right)$. In the last equation $\mathbf{d}$ stands for the electric or magnetic field, $\mathbf{E}$ or $\mathbf{H}$, and $\mathbf{G}_d$ denotes the corresponding operator $\mathbf{G}_E$ or $\mathbf{G}_H$. The main difference between Eqs. (8.110) and (8.105) is that in the framework of the LQL approximation the material property function $m_L\left(\mathbf{r}\right)$ does not depend on the illuminating source.

8.4 QUASI-ANALYTICAL INVERSION

Quasi-analytical approximations (6.137) and (6.138) provide another tool for fast and accurate electromagnetic inversion. This approach leads to a construction of the quasi-analytical (QA) expressions for the Fréchet derivative operator of a forward problem, which simplifies dramatically the forward EM modeling and inversion for inhomogeneous geoelectrical structures (Zhdanov and Hursán, 2000).

8.4.1 FRÉCHET DERIVATIVE CALCULATION

By introducing a perturbation of the anomalous conductivity $\delta\Delta\widetilde{\sigma}\left(\mathbf{r}\right)$ we can calculate the corresponding perturbation of the electric field $\delta\mathbf{E}\left(\mathbf{r}_j\right)$ on the basis of Eq. (6.137):

$$\delta\mathbf{E}\left(\mathbf{r}_j\right) = \iiint_D \widehat{\mathbf{G}}_E\left(\mathbf{r}_j \mid \mathbf{r}\right) \cdot \left[\frac{\delta\Delta\widetilde{\sigma}\left(\mathbf{r}\right)}{1 - g\left(\mathbf{r}\right)}\mathbf{E}^b\left(\mathbf{r}\right)\right] dv$$

$$+ \iiint_D \widehat{\mathbf{G}}_E \left(\mathbf{r}_j \mid \mathbf{r} \right) \cdot \left[\frac{\Delta \widetilde{\sigma} \left(\mathbf{r} \right) \delta g \left(\mathbf{r} \right)}{\left(1 - g \left(\mathbf{r} \right) \right)^2} \mathbf{E}^b \left(\mathbf{r} \right) \right] dv, \tag{8.111}$$

where

$$\delta g \left(\mathbf{r} \right) = \frac{\delta \mathbf{E}^B \left(\mathbf{r} \right) \cdot \mathbf{E}^{b*} \left(\mathbf{r} \right)}{\mathbf{E}^b \left(\mathbf{r} \right) \cdot \mathbf{E}^{b*} \left(\mathbf{r} \right)}$$

$$= \iiint_D \left[\widehat{\mathbf{G}}_E \left(\mathbf{r} \mid \mathbf{r}' \right) \cdot \delta \Delta \widetilde{\sigma} \left(\mathbf{r}' \right) \mathbf{E}^b \left(\mathbf{r}' \right) \right] \cdot \frac{\mathbf{E}^{b*} \left(\mathbf{r} \right)}{\mathbf{E}^b \left(\mathbf{r} \right) \cdot \mathbf{E}^{b*} \left(\mathbf{r} \right)} dv'. \tag{8.112}$$

Substituting Eq. (8.112) into the second integral in (8.111) and changing the notation for the integration variables, $\mathbf{r} \rightarrow \mathbf{r}'$ and $\mathbf{r}' \rightarrow \mathbf{r}$, we obtain

$$\iiint_D \widehat{\mathbf{G}}_E \left(\mathbf{r}_j \mid \mathbf{r} \right) \cdot \left[\frac{\Delta \widetilde{\sigma} \left(\mathbf{r} \right) \delta g \left(\mathbf{r} \right)}{\left(1 - g \left(\mathbf{r} \right) \right)^2} \mathbf{E}^b \left(\mathbf{r} \right) \right] dv = \iiint_D \delta \Delta \widetilde{\sigma} \left(\mathbf{r} \right) \widehat{\mathbf{K}} \left(\mathbf{r}_j \mid \mathbf{r} \right) \cdot \mathbf{E}^b \left(\mathbf{r} \right) dv, \tag{8.113}$$

where

$$\widehat{\mathbf{K}} \left(\mathbf{r}_j \mid \mathbf{r} \right) = \iiint_D \frac{\Delta \widetilde{\sigma} \left(\mathbf{r}' \right)}{\left(1 - g \left(\mathbf{r}' \right) \right)^2} \widehat{\mathbf{G}}_E \left(\mathbf{r}_j \mid \mathbf{r}' \right) \left\{ \left[\widehat{\mathbf{G}}_E \left(\mathbf{r}' \mid \mathbf{r} \right) \cdot \mathbf{E}^b \left(\mathbf{r}' \right) \right] \cdot \frac{\mathbf{E}^{b*} \left(\mathbf{r}' \right)}{\mathbf{E}^b \left(\mathbf{r}' \right) \cdot \mathbf{E}^{b*} \left(\mathbf{r}' \right)} \right\} dv'. \tag{8.114}$$

Therefore

$$\delta \mathbf{E} \left(\mathbf{r}_j \right) = \iiint_D \delta \Delta \widetilde{\sigma} \left(\mathbf{r} \right) \mathbf{F}_E \left(\mathbf{r}_j \mid \mathbf{r} \right) dv, \tag{8.115}$$

where the vector function $\mathbf{F}_E \left(\mathbf{r}_j \mid \mathbf{r} \right)$ is the kernel of the integral Fréchet derivative operator:

$$\mathbf{F}_E \left(\mathbf{r}_j \mid \mathbf{r} \right) = \left[\frac{1}{1 - g \left(\mathbf{r} \right)} \widehat{\mathbf{G}}_E \left(\mathbf{r}_j \mid \mathbf{r} \right) + \widehat{\mathbf{K}} \left(\mathbf{r}_j \mid \mathbf{r} \right) \right] \cdot \mathbf{E}^b \left(\mathbf{r} \right). \tag{8.116}$$

In a similar way, by perturbing both sides of Eq. (6.138), we can write

$$\delta \mathbf{H} \left(\mathbf{r}_j \right) = \iiint_D \delta \Delta \widetilde{\sigma} \left(\mathbf{r} \right) \mathbf{F}_H \left(\mathbf{r}_j \mid \mathbf{r} \right) dv, \tag{8.117}$$

where

$$\mathbf{F}_H \left(\mathbf{r}_j \mid \mathbf{r} \right) = \left[\frac{1}{1 - g \left(\mathbf{r} \right)} \widehat{\mathbf{G}}_H \left(\mathbf{r}_j \mid \mathbf{r} \right) + \widehat{\mathbf{K}} \left(\mathbf{r}_j \mid \mathbf{r} \right) \right] \cdot \mathbf{E}^b \left(\mathbf{r} \right). \tag{8.118}$$

In particular, considering the infinitely small domain of the conductivity perturbation, we arrive at the following formula for the Fréchet derivative of the electric and magnetic fields:

$$\frac{\partial \mathbf{E} \left(\mathbf{r}_j \right)}{\partial \Delta \widetilde{\sigma} \left(\mathbf{r} \right)} = \mathbf{F}_E \left(\mathbf{r}_j \mid \mathbf{r} \right), \quad \left. \frac{\partial \mathbf{H} \left(\mathbf{r}_j \right)}{\partial \Delta \widetilde{\sigma} \left(\mathbf{r} \right)} \right|_{\Delta \sigma_a} = \mathbf{F}_H \left(\mathbf{r}_j \mid \mathbf{r} \right). \tag{8.119}$$

The last formulas provide analytical expressions for computing the Fréchet derivative for the forward modeling operator. Note that, in this case, the amount of calculation for the forward modeling solution and for the Fréchet derivative is equivalent to computing the Born approximation.

8.4.2 INVERSION BASED ON THE QUASI-ANALYTICAL METHOD

The inversion based on the QA approximation is implemented by minimization of the corresponding Tikhonov parametric functional:

$$P^\alpha(\boldsymbol{\sigma}) = \varphi(\boldsymbol{\sigma}) + \alpha s(\boldsymbol{\sigma}),\qquad(8.120)$$

where $\varphi(\boldsymbol{\sigma})$ is a misfit functional between the theoretical values computed using the QA approximation, $\mathbf{A}_{QA}(\boldsymbol{\sigma})$, and the observed data $\mathbf{d}$; $s(\boldsymbol{\sigma})$ is a stabilizing functional, and α is a regularization parameter. The optimal value of α is determined from the misfit condition

$$\varphi(\boldsymbol{\sigma}) = \delta_d,\qquad(8.121)$$

where δ_d is the noise level of the data.

The minimization problem (8.120) can be solved using any gradient type technique, say, by the regularized conjugate gradient (RCG) method, discussed above (see formulas (8.87)). The critical point of an inversion algorithm is the calculation of the Fréchet derivative (sensitivity) operator $\mathbf{F}$ at every iteration of the CG method. The quasi-analytical solutions described above provide a very effective and elegant way of computing the Fréchet derivative (sensitivity matrix) directly, using formulas (8.116) and (8.119). As we can see, in the inversion algorithm, the background field required by the QAVB approximation is equal to the predicted electric field found on the previous iteration. Therefore, no extra computation is required to find the background field for the Fréchet derivative calculation. The corresponding numerical method of the Fréchet derivative computations is based on the discrete form of the explicit integral expressions (13.293) and (13.294), which simplifies all calculations dramatically. However, it is not necessary to keep the entire Fréchet derivative matrix in the computer memory. We can save the results of the application of the adjoint Fréchet matrix to the weighted residual field, $\mathbf{F}_n^\star \mathbf{W}_d^\star \mathbf{W}_d \mathbf{r_n}$, only. The major difference between the approach based on the adjoint operator (section 8.2.8) and QLVB method is that in the first case one has to solve the full 3D EM forward problem on every iteration of the inversion in order to find the term $\mathbf{F}_n^\star \mathbf{W}_d^\star \mathbf{W}_d \mathbf{r_n}$. In the case of QLVB approximation we do not need to solve any forward problem to find the Fréchet derivative, because we compute them by direct algebraic expressions arising from the integral representations of the Fréchet derivatives (8.119). The same algebraic expressions are used to find the optimal length of the iteration step according to RCG method (8.87). As a result, the inversion technique, based on the IE method, requires just one forward modeling on every iteration step without any extra memory usage, while the conventional inversion schemes, based on the adjoint operator require, as a rule, at least three forward modeling solutions per inversion iteration (one to compute the predicted data, another one to compute the gradient direction, and the last one for optimal calculation of the iteration step).

REFERENCES AND RECOMMENDED READING TO CHAPTER 8

Alumbaugh, D. L., and G. A. Newman, 1997, Three-dimensional massively parallel inversion - II. Analysis of a cross-well electromagnetic experiment: Geophysical Journal International, **128**, 355–363.

Arfken, G., and H. J. Weber, 1995, Mathematical methods for physicists, 4th ed.: Academic Press, San Diego, New York, Boston, London, Tokyo, Toronto, 1029 pp.

Blok, H., and M. Oristaglio, 1995, Wavefield imaging and inversion in electromagnetics and acoustics: Delft University of Technology, Report number: Et/EM 1995-21, 132 pp.

Chew, W. C., 1990, Waves and fields in inhomogeneous media: Van Nostrand Reinhold, New York, 608 pp.

Eaton, P. A., 1989, 3-D electromagnetic inversion using integral equations: Geophysical Prospecting, **37** (4), 407–426.

Fletcher, R., 1995, Practical methods of optimization: John Willey & Sons, Chichester - New-York, 436 pp.

Gribenko, A., and M. S. Zhdanov, 2007, Rigorous 3-D inversion of marine CSEM data based on the integral equation method: Geophysics, **72** (2), WA73–WA84.

Levenberg, K., 1944, A method for the solution of certain nonlinear problems in least squares: Quart. Appl. Math, **2**, 164–168.

Madden, T. R., and R. L. Mackie, 1989, 3-D magnetotelluric modelling and inversion: Proceedings of the IEEE, **77**, 318–332.

Mackie, R. L., and M. D. Watts, 2004, The use of 3D magnetotelluric inversion for exploration in complex geologic environments; potential pitfalls and real world examples: Eos, Transactions, American Geophysical Union, **85**, GP14A-01.

Marquardt, D. W., 1963, An algorithm for least squares estimation of nonlinear parameters: SIAM Journal, **11**, 431–441.

Newman, G. A., and D. L. Alumbaugh, 1997, Three-dimensional massively parallel inversion - I. Theory: Geophysical Journal International, **128**, 345–354.

Press, W. H., B. P. Flannery, S. A. Teukolsky, and W. T. Vettering, 1987, Numerical recipes, The art of scientific computing: Cambridge University Press, Cambridge, vol. I and II, 1447 pp.

Sasaki, Y., 2001, Full 3D inversion of electromagnetic data on PC: Journal of Applied Geophysics, **46**, 45–54.

Siripunvaraporn, W., G. Egbert, Y. Lenbury, and M. Uyeshima, 2005, Three-dimensional magnetotelluric inversion; data-space method: Physics of the Earth and Planetary Interiors, **150**, 3–14.

Siripunvaraporn, W., M. Uyeshima, and G. Egbert, 2004, Three-dimensional inversion for network-magnetotelluric data, Earth, Planets and Space, **56**, 893–902.

Tarantola, A., 1987, Inverse Problem Theory: Elsevier, Amsterdam, Oxford, New York, Tokyo, 613 pp.

Zhdanov, M. S., and G. Keller, 1994, The geoelectrical methods in geophysical exploration: Elsevier, Amsterdam, London, New York, Tokyo, 873 pp.

Zhdanov, M. S. and S. Fang, 1996a, Quasi-linear approximation in 3-D EM modeling: Geophysics, **61**, 646–665.

Zhdanov, M. S., and S. Fang, 1996b, 3-D quasi-linear electromagnetic inversion: Radio Science, **31** (4), 741–754.

Zhdanov, M. S., and S. Fang, 1999, 3-D quasi-linear electromagnetic modeling and inversion: Three Dimensional Electromagnetics, SEG Monograph, Tulsa, OK, 233–255.

Zhdanov, M. S., S. Fang, and G. Hursán, 2000b, Electromagnetic inversion using quasi-linear approximation: Geophysics, **65**, (5), 1501–1513.

Zhdanov, M. S., and G. Hursán, 2000, 3-D electromagnetic inversion based on quasi-analytical approximation: Inverse Problems, **16**, 1297–1322.

Zhdanov, M. S., and E. Tartaras, 2002, Inversion of multi-transmitter 3-D electromagnetic data based on the localized quasi-linear approximation: Geophysical Journal International, **148**, (3), 506–519.

Zhdanov, M. S., 2002, Geophysical inverse theory and regularization problems: Elsevier, Amsterdam, London, New York, Tokyo, 628 pp.

Zhdanov, M. S., and N. G. Golubev, 2003, Three-dimensional inversion of magnetotelluric data in complex geological structures: in J. Macnae, and G. Liu, Eds., Three-dimensional electromagnetics III, Austr. Soc. Expl. Geophys, 39 pp.

Zhdanov, M. S., M. Endo, L. H. Cox, M. Cuma, J. Linfoot, C. Anderson, N. Black, and A. V. Gribenko, 2014a, Three-dimensional inversion of towed streamer electromagnetic data: Geophysical Prospecting, **62** (3), 552–572.

Zhdanov, M. S., M. Endo, D. Yoon, M. Čuma, J. Mattsson, and J. Midgley, 2014b, Anisotropic 3D inversion of towed-streamer electromagnetic data: Case study from the Troll West Oil Province. Interpretation, **2** (3), SH97–SH113.

ELECTROMAGNETIC MIGRATION

9

CONTENTS

Inversion of three-dimensional (3-D) electromagnetic (EM) data in complex geoelectrical structures is a very challenging problem of geophysics. The conventional approach based on standard 3-D forward modeling and inversion meets significant difficulties because of the enormous amount of computations required in the case of the multitransmitter and multireceiver data acquisition systems typical for modern EM geophysical surveys. There exists, however, an alternative approach to the solution of this problem based on the principles of EM holography, which extends to EM cases the methods of optical and radio holography.

    Optical holography permits reconstruction of a volume image of the object by using a hologram displaying not only the amplitude but also the phase structure of the wavefront of light. To make it possible to record by photographic emulsion not only amplitude but phase, the reference wave of light is added. This additional wave is coherent with the object's light and interferes with it, producing diffraction patterns which form an optical hologram on the photographic emulsion. To generate a volume image it is sufficient to illuminate a hologram with a reference light wave. The wave scattered by pho-

tographic diffraction patterns is identical to the original wavefront of light scattered by an object and reproduces the volume image of the object. The ideas of optical holography have been applied to the radio-frequency domain and utilized for detection (Hendrix, 1975).

It was demonstrated by Zhdanov (1981, 2001) that a similar approach can be applied in principle to a broad band electromagnetic (EM) field for imaging an object in nontransparent media, which optical or radio-frequency signals cannot penetrate. The simplest way to do this is to place the EM transmitting/receiving system on the surface of the examined media. The transmitters generate harmonic (frequency domain) or pulse (time domain) primary EM field which propagates through the medium, containing the object, and is recorded by the receivers. Just as in the case of an optical or radio-frequency holography, it is necessary to provide a reference signal in order to measure relative phases in the frequency domain. The recorded amplitudes and phases of an electromagnetic field scattered by the object form a broad band EM hologram. As in optical and radiowave holography, we can reconstruct the volume image of the object by "illuminating" the broad band EM hologram by the reference signal. While in the optical or radio-frequency case this can be performed optically, yielding a visible image, in the case of a broad band EM field the reconstruction is done numerically using computer transformation.

In this chapter we will review the physical and mathematical principles of electromagnetic migration.

9.1 ELECTROMAGNETIC MIGRATION IN THE TIME DOMAIN

Electromagnetic migration is a type of transformation of the electromagnetic field observed at the earth's surface downward into the lower half-space. Using such a transformation, we can view the geoelectric structure from a more advantageous perspective, and in some cases actually construct an image of the earth's interior. The principles of electromagnetic migration have been developed in several publications (Zhdanov and Frenkel, 1983a, 1983b; Zhdanov, 1988; Zhdanov et al., 1988; Zhdanov and Keller, 1994; Zhdanov et al., 1996, and Zhdanov, 1999). Electromagnetic migration, similar to geopotential field migration, is based on a special form of downward continuation of the observed field or one of its components. This downward continuation is obtained as the solution of the boundary value problem in the lower half-space for the adjoint Maxwell's equations, in which the boundary values of the migration field on the earth's surface are determined by the observed electromagnetic field. However, it is important to stress that electromagnetic migration is not the same as analytic continuation, because it does not reconstruct the true electromagnetic field within the earth, but merely transforms the field.

Electromagnetic migration is similar in important features to seismic migration (Schneider, 1978; Claerbout, 1985; Zhdanov et al., 1988), but differs in that for geoelectric problems, electromagnetic migration is done on the basis of a diffusion equation rather than a wave equation.

9.1.1 PHYSICAL PRINCIPLES OF ELECTROMAGNETIC MIGRATION

For convenience, we will review some of the general concepts of seismic migration (seismic holography). Suppose that there is a local source for seismic waves at some point on the earth's surface and a system of receivers. We record the normal (vertical) motion of the earth's surface at each of the

receivers as a function of (ordinary) time, t. We introduce the concept of *reverse time*:

$$\tau = T - t, \tag{9.1}$$

where T is the time period over which the geophone response is recorded. The theorem of reciprocity permits us to interchange the roles of source and receivers without change in the field behavior, whether it be a seismic field or an electromagnetic field. Applying the theorem of reciprocity, we can imagine sources at each receiver location, each being driven by a force which emulates the signal originally recorded. In the theory of seismic migration, it is considered that the wave field is back propagating; that is, the wave field travels from the receiver array to the original source point along the same paths as the actual wave field traveled from the source to the receivers (Claerbout, 1985). When the backward traveling wave field is computed for negative times corresponding to the arrivals of the forward-traveling wave field at points in the medium, the amplitude distribution of the migrated field will indicate the locations of reflecting surfaces and diffraction points. Use of reciprocity and backward transmission of the wave field will create an image in reverse time.

In principle at least, a similar approach can be applied in interpretation of electromagnetic field behavior. Let us consider the case in which we have observed an electromagnetic field produced either by ionospheric currents or a controlled source over an array of receivers. The array of receivers will be considered to be situated on the surface of the earth for this discussion. Having recorded time-varying electromagnetic field components over the array of receivers, we then conceptually replace the receivers with an array of sources, each driven with a moment which replicates the actually recorded time-varying field components. The conceptual sources are driven in reverse time to produce a field that we will call the *migrated electromagnetic field*. Like in the seismic case, this field can "highlight" the internal structure of the earth and give us a "geoelectric image" of the earth's interior.

9.1.2 MIGRATION IN A MODEL WITH HOMOGENEOUS BACKGROUND CONDUCTIVITY

It is easy to explain the main properties of the migration field for a model with the homogeneous background conductivity. Consider a model in which the horizontal plane, $z = 0$, separates the conductive earth ($z > 0$) from the insulating atmosphere ($z < 0$). The conductivity in the earth, $\sigma(\mathbf{r})$, is an arbitrary function of the coordinates. This conductivity function can be represented as the superposition of a constant background conductivity, σ_b, and an anomalous conductivity function, $\Delta\sigma(\mathbf{r})$:

$$\sigma(\mathbf{r}) = \sigma_b + \Delta\sigma(\mathbf{r}). \tag{9.2}$$

At this point, we do not need to specify the nature of the electromagnetic field incident on the earth's surface – it can originate naturally in the ionosphere, or be produced by a controlled source on the earth's surface. Everywhere outside the anomalous region, the electromagnetic field will satisfy a diffusion equation:

$$\Delta\mathbf{H} - \mu_0\sigma_b\frac{\partial\mathbf{H}}{\partial t} = 0,$$
$$\Delta\mathbf{E} - \mu_0\sigma_b\frac{\partial\mathbf{E}}{\partial t} = 0. \tag{9.3}$$

For this simple model, we can discuss the problem of migration of any scalar component, $P(\mathbf{r}, t)$ of an observed electromagnetic field. Note first of all that everywhere outside the zones with anomalous conductivity this component would satisfy the equation:

$$\Delta P(\mathbf{r}, t) - \mu_0 \sigma_b \frac{\partial P(\mathbf{r}, t)}{\partial t} = 0. \tag{9.4}$$

Let $P^0(\mathbf{r}, t)$ represent any of the components H_x^0, H_y^0, H_z^0, E_x^0 or E_y^0 that can be observed at the earth's surface. We will define the *migration field*, P^m, obtained from a specific scalar component, P^0, of the electromagnetic field, as being the field that satisfies the following conditions:

$$P^m(\mathbf{r}, \tau)\,|_{z=0} = \begin{cases} P^0(\mathbf{r}, T - \tau)_{z=0} & \text{for } 0 \leq \tau \leq T, \\ 0 & \text{for } \tau < 0, \ \tau > T \end{cases}, \tag{9.5}$$

$$\Delta P^m(\mathbf{r}, \tau) - \mu_0 \sigma_b \frac{\partial P^m(\mathbf{r}, \tau)}{\partial \tau} = 0 \text{ for } z > 0, \tag{9.6}$$

$$P^m(\mathbf{r}, \tau) \to 0, \text{ for } |\mathbf{r}| \to \infty, \ z > 0. \tag{9.7}$$

Note that if we exchange reverse time, τ, for ordinary time, t, in Eq. (9.6), we have an equation which is the conjugate to the diffusion equation:

$$\Delta P^m(\mathbf{r}, t) + \mu_0 \sigma \frac{\partial P^m(\mathbf{r}, t)}{\partial t} = 0. \tag{9.8}$$

If the ordinary diffusion equation describes field propagation from the sources to receivers, then Eq. (9.8) describes the inverse process of propagation from receivers to sources.

The problem of establishing the migrated field reduces to continuation of the field P^0 from the earth's surface into the lower half-space in reverse time, τ. This procedure is called electromagnetic field migration.

It can be seen from these considerations that, the calculation of a migrated field is reduced to a boundary value problem described by Eqs. (9.5) through (9.7). We can now develop several techniques for the solution of these problems based on integral transformations, spectral representations in the (k, ω) domain, finite difference approximations, and so on.

We will describe these approaches in the following paragraphs.

9.1.3 MIGRATION USING INTEGRAL TRANSFORMATION

For solution of the migration problem, we will specify an arbitrary point $\mathbf{r}'$ in the lower half-space and draw a sphere about this point with radius R. The part of the sphere located in the lower half-space will be denoted as O_R and the part of the plane $z = 0$ located inside O_R will be denoted as S_R. The domain D is bounded by O_R and S_R. Let us consider a Green's function for the diffusion equation, G^d, which satisfies the equation:

$$\Delta G^d + \mu_0 \sigma_b \frac{\partial G^d}{\partial t} = \delta(\mathbf{r} - \mathbf{r}')\delta(t - t'), \tag{9.9}$$

where G^d has the form (Morse and Feshbach, 1953),

$$G^d(\mathbf{r}', t \mid \mathbf{r}, t) = -\frac{(\mu_0 \sigma_b)^{1/2}}{8\pi^{3/2}(t'-t)^{3/2}} e^{-\mu_0\sigma_b|\mathbf{r}'-\mathbf{r}|^2/4(t'-t)} H(t'-t), \tag{9.10}$$

written for a Heaviside excitation function, $H(t'-t)$:

$$H(t-t') = \begin{cases} 0; & t'-t < 0 \\ 1; & t'-t > 0 \end{cases}.$$

Let us now multiply the left- and right-hand parts of Eq. (9.6) by G^d and integrate the products over the time range $-\infty < t < \infty$ and over the space domain D. We then can transform the volume integral D to a surface integral over $S_R + O_R$ using Green's formula and taking Eq. (9.9) into consideration:

$$P^m(\mathbf{r}', t') = \int_{-\infty}^{\infty} \int_{S_R+O_R} \left(P^m \frac{\partial G^d}{\partial n} - G^d \frac{\partial P^m}{\partial n} \right) ds dt, \tag{9.11}$$

where $\mathbf{r}' \in D$. Note that this equation remains valid if we replace G^d with the sum $(G^d + g)$ where g is any arbitrary solution to the diffusion equation in D:

$$P^m(\mathbf{r}', t') = \int_{-\infty}^{\infty} \int_{S_R+O_R} \left[P^m \frac{\partial(G^d+g)}{\partial n} - (G^d+g) \frac{\partial P^m}{\partial n} \right] ds dt. \tag{9.12}$$

Assume that the auxiliary field g goes to zero as $R \to \infty$. Taking into consideration that $P^m \equiv 0$ for $\tau < 0$ and for $t > T$, we have

$$P^m(\mathbf{r}', \tau') = -\int_0^T \iint_{-\infty}^{\infty} \left[P^m \frac{\partial(G^d+g)}{\partial z} - (G^d+g) \frac{\partial P^m}{\partial z} \right] ds d\tau. \tag{9.13}$$

We know P^m at the earth's surface, but not $\partial P^m/\partial z$. But, if we take the function g as

$$g(\mathbf{r}', \tau' \mid \mathbf{r}, \tau) = -G^d(\mathbf{r}'', \tau' \mid \mathbf{r}, \tau), \tag{9.14}$$

where the point $\mathbf{r}''$ is symmetrically located to $\mathbf{r}'$ with respect to the plane $z = 0$ (that is, imaged through the earth's surface), then

$$(G^d + g)\mid_{z=0} \equiv 0.$$

Substituting from Eq. (9.14) into Eq. (9.13), after some simple algebraic operations, we have:

$$P^m(\mathbf{r}', T - \tau') = -2 \int_{t'}^T \iint_{-\infty}^{\infty} P^0(\mathbf{r}, t) \frac{\partial \tilde{G}(\mathbf{r}', t' \mid \mathbf{r}, \tau)}{\partial z} dx dy dt, \tag{9.15}$$

where $\tilde{G}$ is the conjugate to the Green's function G for the diffusion equation (Morse and Feshbach, 1953; Zhdanov, 1988).

It is noteworthy that Eq. (9.15) is the electromagnetic counterpart to the Rayleigh integral (Berkhout, 1980). Just as in the seismic application, Eq. (9.15) defines in space and normal time a

field propagating towards the surface of observation (that is, upgoing waves), as can be seen from the fact that Eq. (9.15) contains the function $\tilde{G}$, conjugated to the Green's function G of the diffusion equation. Hence, just as in the seismic case, a migration transformation of electromagnetic field components yields upgoing fields.

Also, as in the seismic case, migration of upgoing electromagnetic waves can easily be understood in the wave number-spatial frequency (k, ω) domain. The spectral algorithm for performing migration is treated in the next section.

9.2 ANALYTIC CONTINUATION AND MIGRATION IN THE (k, ω) DOMAIN
9.2.1 ANALYTIC CONTINUATION OF THE EM FIELD

The concept of *analytic continuation* is widely used in the potential field theory. It is based on an idea of extrapolation of the geophysical field from the line or surface of observation into the target area. This approach can be applied to electromagnetic fields as well (Berdichevsky and Zhdanov, 1984; Zhdanov, 1984, 1988).

An analytic continuation can be described most simply in terms of the same model we analyzed in section 9.1.1. However, in this section we will analyze the field in the (k, ω) domain. A uniformly conducting earth with electrical conductivity σ_b contains an inhomogeneity in a region D characterized by an arbitrary distribution of conductivity $\sigma_d(\mathbf{r}) = \sigma_b + \Delta\sigma(\mathbf{r})$. The distribution of the electromagnetic field, $\mathbf{E}$, $\mathbf{H}$, is known over the surface of the earth (at $z = 0$). We are required to recompute this fields at some depth, $0 < z < d$, in the earth, with d being the distance from the earth's surface to the region D with anomalous conductivity.

We will present below a solution of the analytical continuation problem based on the Fourier spectrum transform. A specified component of the EM field P can be presented in the form of the Fourier integral with respect to spatial and time frequencies, k_x, k_y, ω, as

$$P(\mathbf{r}, t) = \frac{1}{8\pi^3} \iiint\limits_{-\infty}^{\infty} p(k_x, k_y, z, \omega) e^{-i(k_x x + k_y y + \omega t)} dk_x dk_y d\omega, \tag{9.16}$$

where $p(k_x, k_y, z, \omega)$ is the 3-D Fourier transform of the field component P:

$$p(k_x, k_y, z, \omega) = \iiint\limits_{-\infty}^{\infty} P(\mathbf{r}, t) e^{i(k_x x + k_y y + \omega t)} dx\, dy\, dt. \tag{9.17}$$

Applying the Fourier transform (9.16) to Eq. (9.4), we obtain the corresponding equation in the (k, ω) domain for the spatial Fourier spectrum $p(k_x, k_y, z, \omega)$:

$$\frac{\partial^2}{\partial z^2} p = v_b^2 p, \ z \geq 0, \tag{9.18}$$

where $v_b = \left(k_x^2 + k_y^2 - i\omega\mu\sigma_b\right)^{1/2}$, $\mathrm{Re}\, v_b \geq 0$, is a wavenumber in the (k, ω) domain, and $0 < z < d$.

The general solution of Eq. (9.18) has the form:

$$p\left(k_x, k_y, z, \omega\right) = p^u\left(k_x, k_y, 0, \omega\right) e^{v_b z} + p^d\left(k_x, k_y, 0, \omega\right) e^{-v_b z}, \ z \geq 0, \tag{9.19}$$

where $p^u\left(k_x, k_y, 0, \omega\right)$ and $p^d\left(k_x, k_y, 0, \omega\right)$ are the spectrums of the upgoing and downgoing components of the field on the surface of the earth, $z = 0$.

Eq. (9.19) solves the problem of EM field downward continuation in the homogeneous layer $0 < z < d$, if we know the upgoing and downgoing parts of the field. We can use the approach developed by Berdichevsky and Zhdanov (1984) for the field separation into upgoing and downgoing parts. As an illustration, we discuss in Chapter 15 the application of this technique to the marine controlled-source EM data.

Thus, the analytic continuation of the downgoing and upgoing parts of the field is described by the formulas:

$$p^{cd}\left(k_x, k_y, z, \omega\right) = p^d\left(k_x, k_y, 0, \omega\right) e^{-v_b z}, \tag{9.20}$$

and

$$p^{cu}\left(k_x, k_y, z, \omega\right) = p^u\left(k_x, k_y, 0, \omega\right) e^{v_b z}, \tag{9.21}$$

where p^{cd} and p^{cu} are results of analytic continuation.

In order to reconstruct the analytically continued fields, P^{cd} and P^{cu}, from their spectrums, we apply the corresponding inverse Fourier transforms:

$$P^{cd}(x, y, z, t) = \frac{1}{8\pi^3} \iiint\limits_{-\infty}^{\infty} p^{cd}\left(k_x, k_y, z, \omega\right) e^{-v_b z - i\left(k_x x + k_y y + \omega t\right)} dk_x dk_y d\omega, \tag{9.22}$$

and

$$P^{cu}(x, y, z, t) = \frac{1}{8\pi^3} \iiint\limits_{-\infty}^{\infty} p^{cu}\left(k_x, k_y, z, \omega\right) e^{v_b z - i\left(k_x x + k_y y + \omega t\right)} dk_x dk_y d\omega. \tag{9.23}$$

The field proximal to a domain with anomalous conductivity at depth is representative of the location and parameters of the anomalous conductivity. Therefore, analytical continuation can be used for imaging of the geoelectrical anomalies (Zhdanov, 1988). However, because the exponential in the equation, $\exp\left(v_b z\right)$, is growing with depth, the downward continuation of the upgoing field is an unstable, ill-posed transformation, while the downward continuation of the downgoing field is stable. Electromagnetic migration provides an alternative stable solution for downward continuation. We discuss this property of the migration field in the next section.

9.2.2 MIGRATION AS A SPECTRAL TRANSFORMATION

Electromagnetic migration can best be analyzed in the frequency domain. As an example, we will consider the problem of the electric field migration. A similar result can be obtained for magnetic field migration as well.

According to the definition introduced above, the Fourier transform of the migration upgoing field within the homogeneous background ($\sigma_b = const$) satisfies the equations:

$$\frac{\partial^2}{\partial z^2}\mathbf{e}^m = v_b^2 \mathbf{e}^m, \ z \geq 0. \tag{9.24}$$

The general solution of the last equation has the form:

$$p^m\left(k_x, k_y, z, \omega\right) = a\left(k_x, k_y, 0, \omega\right)e^{v_b z} + b\left(k_x, k_y, 0, \omega\right)e^{-v_b z}, \ z \geq 0, \tag{9.25}$$

where $a\left(k_x, k_y, 0, \omega\right)$ and $b\left(k_x, k_y, 0, \omega\right)$ are the vector coefficients to be determined.

The migration field, according to a definition, should attenuate with the depth and should satisfy the boundary condition (9.5), according to which the migration field is equal to the observed field recorded in the reverse time. This boundary condition in the wave number-spatial frequency (k, ω) domain takes the form:

$$p^m\left(k_x, k_y, 0, \omega\right) = p^{u*}\left(k_x, k_y, 0, \omega\right), \tag{9.26}$$

where $p^{u*}\left(k_x, k_y, 0, \omega\right)$ is the complex conjugate spectrum of the upgoing component of the field on the surface of the earth, $z = 0$. The transition to the complex conjugate spectrum is related to the use of reverse time, τ, in the definition of the migration field.

Therefore, we have:

$$p^m\left(k_x, k_y, z, \omega\right) = p^{u*}\left(k_x, k_y, 0, \omega\right)e^{-v_b z}, \ z \geq 0. \tag{9.27}$$

Thus, comparing formulas (9.21) and (9.27), we can see that, in the case of the downward continuation, we should multiply the spectrum of the upgoing field by the function $S_c\left(k_x, k_y, \omega\right)$, exponentially increasing with the spatial and time frequencies,

$$S_c\left(k_x, k_y, \omega\right) = \exp\left(v_b z\right), \tag{9.28}$$

while in the case of migration we multiply the complex conjugate of the same spectrum, p^{u*}, by function $S_m\left(k_x, k_y, \omega\right)$ exponentially decreasing with the frequencies,

$$S_m\left(k_x, k_y, \omega\right) = \exp\left(-v_b z\right). \tag{9.29}$$

Obviously, the function $S_m\left(k_x, k_y, \omega\right)$ represents a low-pass space-time filter suppressing the high frequency components in the data, while the function $S_c\left(k_x, k_y, \omega\right)$ amplifies the high frequency components, which usually represent just data noise. Therefore, the migration transformation of the EM field is a stable procedure.

Note that a migration formula similar to (9.27) can be derived, if the observed field is given at any level $z = z_b$ within the homogeneous background medium:

$$p^m\left(k_x, k_y, z, \omega\right) = p^{u*}\left(k_x, k_y, z_b, \omega\right)e^{-v_b(z-z_b)}, \ z \geq z_b, \tag{9.30}$$

where:

$$p^{u*}\left(k_x, k_y, z_b, \omega\right) = \iiint\limits_{-\infty}^{\infty} P\left(x, y, z_b, t\right)e^{i\left(k_x x + k_y y + \omega t\right)}dxdy. \tag{9.31}$$

This situation takes place, for example, in the case of a marine EM survey, when the data are collected at some depth within the seawater layer, or at the sea bottom.

Taking the inverse Fourier transform of expression (9.30), we find:

$$P^m (x, y, z, t) = \frac{1}{8\pi^3} \iiint\limits_{-\infty}^{\infty} p^{u*} (k_x, k_y, z_b, \omega) e^{-v_b(z-z_b)-i(k_x x + k_y y + \omega t)} dk_x dk_y d\omega. \tag{9.32}$$

Eq. (9.32) represents a (k, ω)-domain algorithm of EM migration, which can be treated as an EM analog of the Gazdag (1978) seismic migration method. We can see that the migration transformation is equivalent to the filtration of the observed data using a low-pass filter characterized by the function, $S_m (k_x, k_y, k_b, z)$, which is a spectral characteristic of the EM migration transformation:

$$S_m (k_x, k_y, k_b, z) = \exp[-v_b (z - z_b)]. \tag{9.33}$$

Thus, we have obtained a spectral algorithm for the migration of the electromagnetic field which can be considered to be analogous to the seismic migration schemes of Gazdag (1978) and Stolt (1978).

9.2.3 CONVOLUTION FORM OF MIGRATION OPERATOR

Using the convolution theorem (Arfken and Weber, 1995, pp. 863–865), we can write Eq. (9.32) in the form:

$$P^m (x', y', z', \omega) = \iint\limits_{-\infty}^{\infty} K (x' - x, \; y' - y, \; z', \omega) \, P^{u*} (x, y, z_b, \omega) \, dx dy, \tag{9.34}$$

where $K (x', \; y', \; z', \omega)$ is a convolution kernel function for a migration operator given by the formula:

$$K (x', \; y', \; z', \omega) = \frac{1}{4\pi^2} \iint\limits_{-\infty}^{\infty} e^{-v_b(z'-z_b)} e^{-i(k_x x' + k_y y')} dk_x dk_y. \tag{9.35}$$

Note that expressions $P^m (x', y', z', \omega)$ and $P^{u*} (x, y, z_b, \omega)$ in formula (9.34) represent the corresponding fields in the frequency domain, ω:

$$P (x, y, z, \omega) = \frac{1}{4\pi^2} \iint\limits_{-\infty}^{\infty} p (k_x, k_y, z, \omega) e^{-i(k_x x + k_y y)} dk_x dk_y, \tag{9.36}$$

and $p (k_x, k_y, z, \omega)$ is related to $P (x, y, z, \omega)$ by a spatial frequency Fourier transform:

$$p (k_x, k_y, z, \omega) = \iint\limits_{-\infty}^{\infty} P (x, y, z, \omega) e^{i(k_x x + k_y y)} dx dy. \tag{9.37}$$

The field components in the time domain can be found using the conventional inverse Fourier transform:

$$P(x, y, z, t) = \frac{1}{2\pi} \int\limits_{-\infty}^{\infty} P(x, y, z, \omega) e^{-i\omega t} d\omega. \qquad (9.38)$$

Let us analyze Eq. (9.35) for the convolution kernel function $K(x', y', z', \omega)$. The integral in Eq. (9.35) can be expressed using a tabulated integral, $J_1(x', y', z', \omega)$ (Zhdanov and Keller, 1994, p. 348):

$$J_1(x', y', z', \omega) = \frac{1}{2\pi} \iint\limits_{-\infty}^{\infty} \frac{e^{-v_b(z'-z_b)}}{v_b} e^{-i(k_x x' + k_y y')} dk_x dk_y$$

$$= \frac{\exp(i k_b r)}{r}, \quad z \ge z_b, \qquad (9.39)$$

where $r = \sqrt{x'^2 + y'^2 + (z' - z_b)^2}$.

Indeed, comparing Eqs. (9.35) and (9.39), we can see that:

$$K(x', y', z', \omega) = -\frac{1}{2\pi} \frac{\partial}{\partial z'} J_1(x', y', z', \omega) = \frac{(z' - z_b)}{2\pi r^3} e^{i k_b r} (1 - i k_b r). \qquad (9.40)$$

Note that the wavenumber k_b is equal to:

$$k_b = (1 + i) 2\pi / \lambda_b, \qquad (9.41)$$

where λ_b is a wave length in the homogeneous background model. Substituting Eq. (9.41) into (9.40), we have:

$$K(x', y', z', \omega) = K(x'_\lambda, y'_\lambda, z'_\lambda) = \frac{(\Delta z_\lambda)}{2\pi} \frac{e^{(i-1)2\pi r_\lambda}}{r_\lambda^3 \lambda_b^2} [1 + 2\pi r_\lambda - i 2\pi r_\lambda], \qquad (9.42)$$

where dimensionless parameters x_λ, y_λ, z_λ, Δz_λ, and r_λ are equal to:

$$x_\lambda = x/\lambda_b, \; y_\lambda = y/\lambda_b, \; z_\lambda = z/\lambda_b, \; \Delta z_\lambda = (z' - z_b)/\lambda_b, \; r_\lambda = r/\lambda_b.$$

Thus, the convolution form of the migration operator, Eq. (9.34), has the form:

$$P^m(x'_\lambda, y'_\lambda, z'_\lambda) = \frac{(\Delta z_\lambda)}{2\pi} \iint\limits_{-\infty}^{\infty} \frac{e^{(i-1)2\pi R_\lambda}}{R_\lambda^3} [1 + 2\pi R_\lambda - i 2\pi R_\lambda] P^{u*}(x_\lambda, y_\lambda, z_{\lambda b}) dx_\lambda dy_\lambda, \qquad (9.43)$$

where:

$$R_\lambda = \sqrt{(x'_\lambda - x_\lambda)^2 + (y'_\lambda - y_\lambda)^2 + (\Delta z_\lambda)^2}. \qquad (9.44)$$

The migration of an electromagnetic field, as defined in Eq. (9.43), consists merely of the application of a linear filter operator in the spatial frequency domain.

9.2.4 CONSTRUCTING A DIGITAL FILTER FOR EM MIGRATION

For the purpose of this section, we call any linear system operating on a discrete data set a *digital filter*. We will demonstrate below that a digital filter for EM migration admits a realization where the output is a linear combination of a finite number of input samples. This filter has a finite number of non-null samples, which justifies the term *Finite Impulse Response (FIR) filter*. Thus, an FIR filter is nothing more than a linear combination of a finite number of samples of the input signal.

Let us demonstrate that EM migration can be approximately described by some FIR filter (Puahengsup et al., 2008). Assuming that $x' = 0$ and $y' = 0$, and sampling x_λ and y_λ with the steps Δx_λ and Δy_λ, we obtain from formula (9.43):

$$P^m\left(0, 0, z'_\lambda\right) = \sum_{n=-\infty}^{\infty} \sum_{l=-\infty}^{\infty} C_{nl} P^{u*}\left(n\Delta x_\lambda, l\Delta y_\lambda, z_{\lambda b}\right), \tag{9.45}$$

where:

$$C_{nl} = \Delta x_\lambda \Delta y_\lambda \lambda_b^2 K\left(-n\Delta x_\lambda, \; -l\Delta y_\lambda, \; z'_\lambda\right). \tag{9.46}$$

Taking into account Eq. (9.42), we finally have the following expression for the coefficients of the digital filter:

$$C_{nl} = \Delta x_\lambda \Delta y_\lambda \frac{(\Delta z_\lambda)}{2\pi} \frac{e^{(i-1)2\pi r_{nl}}}{r_{nl}^3} \left[1 + 2\pi r_{nl} - i2\pi r_{nl}\right], \tag{9.47}$$

where:

$$r_{nl} = \sqrt{(n\Delta x_\lambda)^2 + (l\Delta y_\lambda)^2 + (\Delta z_\lambda)^2}. \tag{9.48}$$

Let us write a Fourier transform for a convolution kernel function:

$$\exp\left[-\nu_b\left(z' - z_b\right)\right] = \iint\limits_{-\infty}^{\infty} K\left(x, \; y, \; z', \omega\right) e^{-i\left(k_x x + k_y y\right)} dx dy. \tag{9.49}$$

At zero spatial frequencies $k_x = k_y = 0$, we have:

$$\nu_b = (-i\omega\mu\sigma_b)^{1/2} = -ik_b = (1 - i)\, 2\pi/\lambda_b$$

and:

$$\iint\limits_{-\infty}^{\infty} K\left(x, \; y, \; z', \omega\right) dx dy = e^{-\nu_b(z' - z_b)} = e^{2\pi(i-1)\Delta z_\lambda}. \tag{9.50}$$

Therefore, the coefficients of the digital filter satisfy the conditions:

$$\sum_{n=-\infty}^{\infty} \sum_{l=-\infty}^{\infty} C_{nl} = e^{2\pi(i-1)\Delta z_\lambda}. \tag{9.51}$$

In practice, we confine ourselves to a finite number of samples, $(2N + 1)$ and $(2L + 1)$ in the x and y directions, respectively. Then formula (9.45) takes the form:

$$P^m \left(0, 0, z_\lambda'\right) = \sum_{n=-N}^{N} \sum_{l=-L}^{L} C_{nl} P^{u*} \left(n\Delta x_\lambda, l\Delta y_\lambda, z_{\lambda b}\right). \tag{9.52}$$

Errors in this approximation can be reduced by introducing the modified filter coefficients, $\widetilde{C}_{nl}$, which should satisfy the conditions:

$$\sum_{n=-N}^{N} \sum_{l=-L}^{L} \widetilde{C}_{nl} = e^{2\pi(i-1)\Delta z_\lambda}. \tag{9.53}$$

For example, if we denote by c_0 a sum of the original coefficients:

$$\sum_{n=-N}^{N} \sum_{l=-L}^{L} C_{nl} = c_0,$$

then we assume that:

$$\widetilde{C}_{nl} = aC_{nl}, \text{ where } a = c_0^{-1} e^{2\pi(i-1)\Delta z_\lambda}. \tag{9.54}$$

Indeed, in this case:

$$\sum_{n=-N}^{N} \sum_{l=-L}^{L} \widetilde{C}_{nl} = a \sum_{n=-N}^{N} \sum_{l=-L}^{L} C_{nl} = ac_0 = e^{2\pi(i-1)\Delta z_\lambda}. \tag{9.55}$$

Thus, we have constructed the following FIR filter for the migration of the electric field:

$$P^m \left(0, 0, z_\lambda'\right) = \sum_{n=-N}^{N} \sum_{l=-L}^{L} \widetilde{C}_{nl} P^{u*} \left(n\Delta x_\lambda, l\Delta y_\lambda, z_{\lambda b}\right). \tag{9.56}$$

We call the numbers, $2N$ and $2L$, the window sizes, w_x and w_y, of the digital filter in the directions x and y, respectively:

$$w_x = 2N \cdot \Delta x, \ w_y = 2L \cdot \Delta y.$$

The filter window size determines the number of horizontal samples in the input for the digital filter.

9.2.5 SPECTRAL CHARACTERISTIC OF THE DIGITAL FILTER

The spectral characteristic of the digital filter may serve as a useful indication of the accuracy of the filter. We will compare the spectral characteristic of our digital filter with the analytical characteristic.

Note that Eq. (9.45) can be written for any point $\left(x_\lambda', y_\lambda', z_\lambda'\right)$ as:

$$P^m \left(x_\lambda', y_\lambda', z_\lambda'\right) = \sum_{n=-\infty}^{\infty} \sum_{l=-\infty}^{\infty} C_{nl} P^{u*} \left(x_\lambda' - n\Delta x_\lambda, y_\lambda' - l\Delta y_\lambda, z_{\lambda b}\right). \tag{9.57}$$

Let us apply Fourier transform (9.37) to both sides of Eq. (9.57):

$$
p^m \left(k_{\lambda x}, k_{\lambda y}, z_\lambda \right) = \iint\limits_{-\infty}^{\infty} P^m \left(x_\lambda, y_\lambda, z_\lambda \right) e^{i \left(k_{\lambda x} x_\lambda' + k_{\lambda y} y_\lambda' \right)} dx_\lambda' dy_\lambda'
$$

$$
= \sum_{n=-\infty}^{\infty} \sum_{l=-\infty}^{\infty} C_{nl} \iint\limits_{-\infty}^{\infty} P^{u*} \left(x_\lambda' - n\Delta x_\lambda, y_\lambda' - l\Delta y_\lambda, z_{\lambda b} \right) e^{i \left(k_{\lambda x} x_\lambda' + k_{\lambda y} y_\lambda' \right)} dx_\lambda' dy_\lambda',
$$

(9.58)

where

$$
k_{\lambda x} = \lambda k_x, \quad k_{\lambda y} = \lambda k_y.
$$

The given upgoing field at the point, $\left(x_\lambda' - n\Delta x_\lambda, y_\lambda' - l\Delta y_\lambda, z_{\lambda b} \right)$ can be treated as a convolution between this field, $P^{u*}(x_\lambda, y_\lambda, z_{\lambda b})$, and a delta-function,

$$
\delta \left[x_\lambda - \left(x_\lambda' - n\Delta x_\lambda \right), \ y_\lambda - \left(y_\lambda' - l\Delta y_\lambda \right) \right],
$$

along the horizontal plane $z_\lambda = z_{\lambda b}$:

$$
P^{u*} \left(x_\lambda' - n\Delta x_\lambda, y_\lambda' - l\Delta y_\lambda, z_{\lambda b} \right)
$$

$$
= \iint\limits_{-\infty}^{\infty} P^{u*} \left(x_\lambda, y_\lambda, z_{\lambda b} \right) \delta \left[x_\lambda - \left(x_\lambda' - n\Delta x_\lambda \right), \ y_\lambda - \left(y_\lambda' - l\Delta y_\lambda \right) \right] dx_\lambda dy_\lambda.
$$

(9.59)

According to the convolution theorem, the Fourier transform of Eq. (9.59) can be represented as a product of the spectrum $p^{u*} \left(k_{\lambda x}, k_{\lambda y}, z_{\lambda b} \right)$ of the field $P^{u*} \left(x_\lambda, y_\lambda, z_{\lambda b} \right)$ and of the delta-function:

$$
\iint\limits_{-\infty}^{\infty} P^{u*} \left(x_\lambda' - n\Delta x_\lambda, y_\lambda' - l\Delta y_\lambda, z_{\lambda b} \right) e^{i \left(k_{\lambda x} x_\lambda' + k_{\lambda y} y_\lambda' \right)} dx_\lambda' dy_\lambda'
$$

$$
= p^{u*} \left(k_{\lambda x}, k_{\lambda y}, z_{\lambda b} \right) S_\delta \left(k_{\lambda x}, k_{\lambda y} \right),
$$

(9.60)

where

$$
S_\delta \left(k_{\lambda x}, k_{\lambda y} \right) = e^{-i \left(k_{\lambda x} n\Delta x_\lambda + k_{\lambda y} l\Delta y_\lambda \right)}.
$$

(9.61)

Substituting Eq. (9.60) into (9.58), and taking into account (9.61), we find:

$$
p^m \left(k_{\lambda x}, k_{\lambda y}, z_{\lambda b} \right) = \sum_{n=-\infty}^{\infty} \sum_{l=-\infty}^{\infty} C_{nl} e^{-i \left(k_{\lambda x} n\Delta x_\lambda + k_{\lambda y} l\Delta y_\lambda \right)} p^{u*} \left(k_{\lambda x}, k_{\lambda y}, z_{\lambda b} \right).
$$

(9.62)

Eq. (9.62) describes a (k, ω)-domain algorithm of EM migration, which represents a filtration of the observed data using a low-pass digital filter characterized by the function $\widetilde{S}_m \left(k_{\lambda x}, k_{\lambda y}, z_\lambda \right)$:

$$
p^m \left(k_{\lambda x}, k_{\lambda y}, z_\lambda \right) = \widetilde{S}_m \left(k_{\lambda x}, k_{\lambda y}, z_\lambda \right) p^{u*} \left(k_{\lambda x}, k_{\lambda y}, z_{\lambda b} \right),
$$

(9.63)

where $\widetilde{S}_m$ is a spectral characteristic of the digital filter:

$$\widetilde{S}_m\left(k_{\lambda x}, k_{\lambda y}, z_\lambda\right) = \sum_{n=-\infty}^{\infty} \sum_{l=-\infty}^{\infty} C_{nl} e^{-i\left(k_{\lambda x} n \Delta x_\lambda + k_{\lambda y} l \Delta y_\lambda\right)}. \tag{9.64}$$

It is useful to produce the plots of the spectral characteristic of the digital filter, $\widetilde{S}_m$, as the functions of the spatial frequencies, $\left(k_x, k_y\right)$, and the analytical spectral characteristic, S_m, of the migration transformation:

$$S_m\left(k_x, k_y, k_b, z\right) = e^{-\nu_b(z-z_b)}, \tag{9.65}$$

where $\nu_b = \left(k_x^2 + k_y^2 - i\omega\mu\sigma_b\right)^{1/2}$, $\mathrm{Re}\,\nu_b \geq 0$. The background conductivity, σ_b, and the depth of migration, $(z - z_b)$, should be treated as the parameters of these curves.

For example, if $k_b^2 = i\omega\mu\sigma_b$, then:

$$\nu_b = \left(k_x^2 + k_y^2 - k_b^2\right)^{1/2} = \frac{1}{\lambda}\left(k_{\lambda x}^2 + k_{\lambda y}^2 - i8\pi^2\right)^{1/2}.$$

Therefore, we have:

$$S_m\left(k_{\lambda x}, k_{\lambda y}, z_\lambda\right) = \exp\left[-\left(k_{\lambda x}^2 + k_{\lambda y}^2 - i8\pi^2\right)^{1/2}(z_\lambda - z_{\lambda b})\right]. \tag{9.66}$$

Analytical expression (9.66) should be close to the spectral characteristic of the digital filter (9.64).

The spectral characteristic of the digital filter can be used to check the accuracy of the technique by comparing it with the analytical spectral characteristic of the migration transformation. In other words, the plots of the analytical expression (9.66) should be close to the plots of the spectral characteristic of the digital filter (9.64). Fig. 9.1 presents an example of this comparison between the spectral characteristics of the analytical and digital filters. Clearly, the spectral characteristics can be considered to be the low-pass spatial filters. Consequently, migration of a field using the algorithm expressed in Eq. (9.54) is an inherently stable procedure.

9.3 FINITE DIFFERENCE MIGRATION
9.3.1 2-D FINITE DIFFERENCE MIGRATION

An especially important problem in the theory of migration is that of constructing an algorithm for migration in inhomogeneous conducting two-dimensional media, or even three-dimensional geoelectric structures. Such an algorithm can be constructed using the finite difference approximation for the desired equations describing the field.

An early effort to make use of a finite-difference algorithm for the analytic continuation of an electromagnetic field in a two-dimensionally inhomogeneous medium was described by Lee et al. (1987). They described a novel approach to constructing the subsurface geoelectric structure using the algorithm they developed. Here, we develop an analogous algorithm for electromagnetic migration,
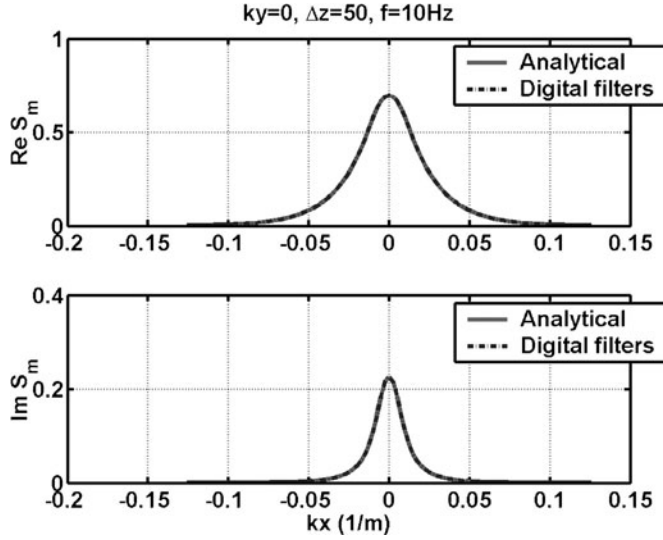
FIGURE 9.1

Comparison of the spectral characteristic of a digital filter with the analytical spectral characteristic of a migration transformation: $f = 10$ Hz; $\Delta x = \Delta y = 25$ m; $\Delta z = 50$ m; $N = L = 50$.

rather than continuation. The development we will show here for transformation of a three-dimensional geoelectric medium can be found in a book by Zhdanov et al. (1988).

We will begin our development by considering a simple problem of migration in a one-dimensional medium. Let us examine an N-layer laterally uniform geoelectric model with a conductivity-depth profile, $\sigma_b(z)$, excited by a vertically incident planar monochromatic field for frequency, ω. The conductivity profile will be step-wise constant; that is, each layer will be characterized by a conductivity, σ_ℓ, and a thickness, d_ℓ.

Let us rewrite the spectral migration algorithm (9.27) for an arbitrary scalar component of migration field P^m:

$$p^m(k_x, k_y, z', \omega) = p^{u*}(k_x, k_y, 0, \omega)e^{-v_b z'}, \qquad (9.67)$$

where $p^{u*}(k_x, k_y, 0, \omega)$ is the complex conjugate spectrum of the upgoing component of the field on the surface of the earth, $z = 0$, and $v_b = (k_x^2 + k_y^2 + i\omega\mu_0\sigma_b)^{1/2}$ for the choice of the real branch $\mathrm{Re}\, v_b > 0$.

Taking the complex conjugate values of both sides of this equation, we obtain:

$$p^{m*}(k_x, k_y, z, \omega) = p^0(k_x, k_y, 0, \omega)e^{-\widetilde{v}_b z}, \quad z \geq 0, \qquad (9.68)$$

where $\widetilde{v}_b = \left(k_x^2 + k_y^2 + i\omega\mu\sigma_b\right)^{1/2}$, $\mathrm{Re}\, \widetilde{v}_b \geq 0$, and the asterisk * denotes complex conjugate values. Note that on the right-hand side of Eq. (9.68) we have denoted by p^0 the spectrum of the upgoing

component of the field on the surface of the earth, $z = 0$:

$$p^0 \left(k_x, k_y, 0, \omega\right) = p^u \left(k_x, k_y, 0, \omega\right).$$

Thus, formula (9.68) provides the algorithm of direct transformation of the observed data into the complex conjugate migration field. In this and in subsequent sections we will analyze mainly the complex conjugate migration field and its spectrum, because this corresponds well to the reverse time, τ, representation in the time domain.

For this particular plane wave model, we can set $k_x = k_y = 0$ in Eq. (9.68) and write:

$$P^{m*}(z, \omega) = P^0(0, \omega)e^{-[i\omega\mu_o\sigma_b(z)]^{1/2}z} = P^0(0, \omega)e^{-k_b(z)z}, \tag{9.69}$$

where $k_b(z)$ is the wave number in the medium, with $\mathrm{Re}\, k_n(z) > 0$.

In particular, in the L-th layer,

$$P^{m*}(z, \omega) = P^0(0, \omega) \exp\left(-\sum_{\ell=1}^{L} k_\ell d_\ell\right), \quad z = \sum_{\ell=1}^{L} d_\ell. \tag{9.70}$$

In summary, Eq. (9.70) is a simple algorithm for one-dimensional migration in a model in which electrical conductivity varies only with depth.

We go next to a two-dimensional geoelectric model. We suppose that the region into which we wish to migrate an electromagnetic field consists of a finite number of roughly horizontal layers, each of which is vertically uniform, but characterized by a relatively slow lateral variation in wave number, $k_b(x, z)$, with the condition that

$$|grad_x k_b(x, z)| \ll 1. \tag{9.71}$$

This condition states that $k_b(x, z)$ can be considered to be constant locally in the lateral direction.

For this model, which is analogous to those described by Claerbout (1985) and by Lee et al. (1987), the complex conjugate migration field can be represented satisfactorily using Eq. (9.69):

$$P^{m*}(x, z, \omega) = Q(x, z, \omega)e^{-k_b(x,z)}, \tag{9.72}$$

where it is assumed that the multiplier Q depends only weakly on z, and $k_b(x, z) = [i\omega\mu_0\sigma_b(x, z)]^{1/2}$ is the wave number for the region of the medium meeting the condition of Eq. (9.71). This representation underlines the exponential character of the relationship of the field to depth; that is, by using instrumental recordings, either for an electromagnetic field or for a seismic wave field, it is possible to reconstruct the behavior of the field at depth in analogy to the method proposed by Claerbout (1985).

With the migrated field so determined, the frequency spectrum of that field within each homogeneous layer will obey the complementary Helmholtz equation:

$$\left(\frac{\partial^2}{\partial x^2} + \frac{\partial^2}{\partial z^2}\right) P^{m*}(x, z, \omega) - k_b^2(x, z)P^{m*}(x, z, \omega) = 0. \tag{9.73}$$

Substituting Eq. (9.72) into (9.73), ignoring all products involving $k_b(x, z)$ in view of the conditions in Eq. (9.71), and deleting the multiplying term $e^{-k_b z}$, we will have:

$$\partial^2 Q/\partial x^2 + \partial^2 Q/\partial z^2 - 2k_b \partial Q/\partial z = 0. \tag{9.74}$$

We now differentiate this last expression with respect to z and divide by $2k_b$:

$$\frac{1}{2k_b}\frac{\partial^3 Q}{\partial x^2 \partial z} + \frac{1}{2k_b}\frac{\partial^3 Q}{\partial z^3} - \frac{\partial^2 Q}{\partial z^2} = 0. \tag{9.75}$$

Combining Eqs. (9.74) and (9.75) and ignoring the term $\partial Q^3/\partial z^3$ (in view of the assumed weak relationship between Q and z), we obtain the final result:

$$\frac{1}{2k_b}\frac{\partial^3 Q}{\partial x^2 \partial z} + \frac{\partial^2 Q}{\partial x^2} - 2k_b\frac{\partial Q}{\partial z} = 0. \tag{9.76}$$

This equation contains only the first derivative with respect to z. Therefore, using it, we can compute the migrated field at some depth, $z + \Delta z$ from the known field at a shallower depth, z. To do so, following the method proposed by Lee et al. (1987), we will find a finite difference approximation to Eq. (9.76).

Let us construct a square grid, Σ, in the lower half-space (for $z \geq 0$):

$$\Sigma = (x_i, z_j) \left| \begin{array}{ll} x_{i+1} = x_i + \Delta x, & i = 1, 2, ..., N_I \\ z_{j+1} = z_j + \Delta z, & j = 1, 2, ..., N_J \end{array} \right. .$$

We will also define an auxiliary grid, $\tilde{\Sigma}$, consisting of nodal points lying on the same vertical lines as the nodal points of the grid Σ, but midway between them:

$$\tilde{\Sigma} = \{(x_i, z_{j+1/2}); z_{j+1/2} = z_j + 1/2\Delta z\}.$$

Let us now consider the discretized function $Q(i, j) = Q(x_i, z_j, \omega)$ on the grid Σ and a discretized function $k_{ij} = k_b(x_i, z_{j+1/2})$ on the grid $\tilde{\Sigma}$, where $z_{j+1/2} = z_j + \frac{1}{2}\Delta z_j$. We then rewrite Eq. (9.76) as an approximation using the discretized function $Q(i, j)$ and k_{ij}. The result is a finite difference operator which approximates the differential operators on the left-hand side of Eq. (9.76), referenced to the auxiliary grid, $\tilde{\Sigma}$. We obtain as a result:

$$a_{ij}\frac{\partial^2 Q}{\partial x^2}(i, j+1) - b_{ij}\frac{\partial^2 Q}{\partial x^2}(i, j) - \frac{2k_{ij}}{\Delta z}Q(i, j+1) + \frac{2k_{ij}}{\Delta z}Q(i, j) = 0, \tag{9.77}$$

where

$$a_{ij} = 1/2[1/(\Delta z k_{ij}) + 1]$$
$$b_{ij} = 1/2[1/(\Delta z k_{ij}) - 1]. \tag{9.78}$$

Using the finite difference approximation operator for $\partial^2 Q/\partial x^2$, Eq. (9.77) can be written as follows:

$$a_{ij}Q(i+1, j+1) + A_{ij}Q(i, j+1) + a_{ij}Q(i-1, j+1) = D_{ij}, \tag{9.79}$$

where

$$D_{ij} = b_{ij}Q(i+1, j) + B_{ij}Q(i, j) + b_{ij}Q(i-1, j), \tag{9.80}$$

$$A_{ij} = -2a_{ij} - 2k_{ij}(\Delta x)^2/\Delta z, \tag{9.81}$$

$$B_{ij} = -2b_{ij} - 2k_{ij}(\Delta x)^2/\Delta z. \tag{9.82}$$

Consider that the discretized function $Q(i, j)$ is known at the level j. In accord with Eq. (9.80), all the coefficients D_{ij} are known, and consequently, Eq. (9.79) forms a system of linear algebraic equations with a symmetrical trigonal matrix of coefficients for the unknown values for the function $Q(i, j+1)$ at the next lower level, $j+1$. In Eq. (9.79), the index i can take values running from 2 to $N_I - 1$, and so, Eq. (9.79) forms a system of $N_I - 2$ equations for N_I unknown values of $Q(i, j+1)$, $i = 1, 2, ..., H_I$. This system of equations must also be supplemented with two edge conditions – values for the function $Q(i, j)$ at the left and right edges of the grid Σ:

$$Q(1, j+1) = Q_{1, j+1},$$

$$Q(N_I, j+1) = Q_{N_I, j+1}. \tag{9.83}$$

Once the edge conditions (9.83) have been established, the system of equations can be solved readily using a variety of numerical methods, such as, for example, the rank annihilation method (Samarsky, 1984).

We must now consider the choice of edge conditions for the function $Q(i, j)$. An easy procedure for establishing these edge conditions is based on one-dimensional migration of the observed field at the left and right sides of the observed data set (that is, at nodes x_1 and x_{N_I}). In so doing, the assumption is made that outside the geoelectric structure being considered, for $x \leq x_1$ and $x \geq x_{N_I}$, the earth consists of a simple horizontally layered structure characterized by a uniform resistivity-depth profile, either $\sigma_b^L(z)$ or $\sigma_b^R(z)$, for the left and right edges, respectively. Migration is achieved using Eq. (9.83) in which for the left edge of the network we have

$$k_b(z) = k_b^L(z) = [i\omega\mu_0\sigma_b^L(z)]^{1/2} \tag{9.84}$$

and for the right edge,

$$k_b(z) = k_b^R(z) = [i\omega\mu_0\sigma_b^R(z)]^{1/2}. \tag{9.85}$$

The values for the nodal points (x_1, z_j) and (x_{N_L}, z_J) obtained in migration are found using Eq. (9.72), and then the desired edge values for the function Q are found, $Q(1, j)$ and $Q(N_I, j)$.

9.3.2 FINITE DIFFERENCE MIGRATION OF A 3-D EM FIELD

We should note that the two-dimensional algorithm for finite difference migration can readily be extended to three-dimensional cases. Indeed, in a 3-D case, formula (9.72) takes the form:

$$P^{m*}(x, y, z, \omega) = Q(x, y, z, \omega)e^{-k_b(x,y,z)}, \tag{9.86}$$

where it is assumed that the multiplier Q depends only weakly on z and $k_b(x, y, z) = [i\omega\mu_0\sigma_b(x, y, z)]^{1/2}$. According to Eq. (9.86), one can find the migration field if the function $Q(x, y, z, \omega)$ is known. This function can be calculated at different levels inside the sea bottom using a 3-D finite-difference technique similar to one developed above for 2-D fields. It can be demonstrated

that the corresponding scalar function Q satisfies the equation:

$$\frac{1}{2k_b}\left(\frac{\partial^2}{\partial x^2} + \frac{\partial^2}{\partial y^2}\right)\frac{\partial Q}{\partial z} + \left(\frac{\partial^2}{\partial x^2} + \frac{\partial^2}{\partial y^2}\right)Q - 2k_b\frac{\partial Q}{\partial z} = 0. \tag{9.87}$$

Let us introduce a discrete function $Q(i, l, j) = Q(x_i, y_l, z_j, \omega)$ on the rectangular grid $\Sigma(x_i, y_l, z_j)$, $i = 1, 2, ...N_x$, $l = 1, 2, ...N_y$, $j = 1, 2, ...N_z$, and a discrete function $k_{ilj} = k_n(x_i, y_l, z_{j+1/2})$, on the auxiliary grid $\widetilde{\Sigma}(x_i, y_l, z_{j+1/2})$ where $z_{j+1/2} = z_j + \Delta z_j/2$. We then rewrite Eq. (9.87) as an approximate finite-difference equation on the auxiliary grid $\widetilde{\Sigma}$. First, we represent the vertical derivative of Q^m approximately in the node $(x_i, y_l, z_{j+1/2})$:

$$\frac{\partial Q}{\partial z}(x_i, y_l, z_{j+1/2}) \approx \frac{Q(x_i, y_l, z_{j+1}) - Q(x_i, y_l, z_j)}{\Delta z_j}. \tag{9.88}$$

We have the following approximation for the horizontal Laplacian of Q^m as well:

$$\left(\frac{\partial^2}{\partial x^2} + \frac{\partial^2}{\partial y^2}\right)Q \approx \left(\frac{\partial^2}{\partial x^2} + \frac{\partial^2}{\partial y^2}\right)\frac{Q(x_i, y_l, z_{j+1}) + Q(x_i, y_l, z_j)}{2}. \tag{9.89}$$

Substituting (9.88) and (9.89) into (9.87), we find:

$$a_{ilj}\left(\frac{\partial^2}{\partial x^2} + \frac{\partial^2}{\partial y^2}\right)Q(x_i, y_l, z_{j+1}) - b_{ilj}\left(\frac{\partial^2}{\partial x^2} + \frac{\partial^2}{\partial y^2}\right)Q(x_i, y_l, z_j)$$
$$- \frac{2k_{ilj}}{\Delta z_j}Q(x_i, y_l, z_{j+1}) + \frac{2k_{ilj}}{\Delta z_j}Q(x_i, y_l, z_j) = 0, \tag{9.90}$$

where:

$$a_{ilj} = \frac{1}{2}\left[\frac{1}{\Delta z_j k_{ilj}} + 1\right], \quad b_{ilj} = \frac{1}{2}\left[\frac{1}{\Delta z_j k_{ilj}} - 1\right].$$

One can use the following finite-difference approximation operator for the horizontal Laplacian, representing the derivatives of Q approximately in terms of the discrete function $Q(i, l, j)$:

$$\left(\frac{\partial^2}{\partial x^2} + \frac{\partial^2}{\partial y^2}\right)Q(x_i, y_l, z_j)$$
$$= \frac{1}{(\Delta x_i)^2}\left[Q(i+1, l, j) - \left(1 + \frac{\Delta x_i}{\Delta x_{i-1}}\right)Q(i, l, j) + \frac{\Delta x_i}{\Delta x_{i-1}}Q(i-1, l, j)\right]$$
$$+ \frac{1}{(\Delta y_l)^2}\left[Q(i, l+1, j) - \left(1 + \frac{\Delta y_l}{\Delta y_{l-1}}\right)Q(i, l, j) + \frac{\Delta y_l}{\Delta y_{l-1}}Q(i, l-1, j)\right].$$

Representing the derivatives of Q approximately in terms of the discrete functions $Q(i, l, j)$ and k_{ilj}, we obtain the following finite-difference equation for $Q(i, l, j)$:

$$a_{ilj}Q(i+1, l, j+1) + a_{ilj}\left(\frac{\Delta x_i}{\Delta y_l}\right)^2 Q(i, l+1, j+1)$$

$$+ A_{ilj} Q(i, l, j+1) + a_{ilj} \frac{\Delta x_i}{\Delta x_{i-1}} Q(i-1, l, j+1)$$

$$+ a_{ilj} \left(\frac{\Delta x_i}{\Delta y_l} \right)^2 \frac{\Delta y_l}{\Delta y_{l-1}} Q(i, l-1, j+1) = D_{ilj}, \tag{9.91}$$

where $i = 2, 3, ... N_x - 1, \; l = 2, 3, ... N_y - 1, \; j = 1, 2, ... N_z - 1,$

$$D_{ilj} = b_{ilj} Q(i+1, l, j) + b_{ilj} \left(\frac{\Delta x_i}{\Delta y_l} \right)^2 Q(i, l+1, j)$$

$$+ B_{ilj} Q(i, l, j) + b_{ilj} \frac{\Delta x_i}{\Delta x_{i-1}} Q(i-1, l, j) + b_{ilj} \left(\frac{\Delta x_i}{\Delta y_l} \right)^2 \frac{\Delta y_l}{\Delta y_{l-1}} Q(i, l-1, j) \tag{9.92}$$

and coefficients $A_{ilj}, \; B_{ilj}$ are equal to:

$$A_{ilj} = -a_{ilj} \left(1 + \frac{(\Delta x_i)^2}{\Delta x_i \Delta x_{i-1}} + \frac{(\Delta x_i)^2}{(\Delta y_l)^2} + \frac{(\Delta x_i)^2}{\Delta y_l \Delta y_{l-1}} \right) - \frac{2 k_{ilj} (\Delta x_i)^2}{\Delta z_j}$$

$$B_{ilj} = -b_{ilj} \left(1 + \frac{(\Delta x_i)^2}{\Delta x_i \Delta x_{i-1}} + \frac{(\Delta x_i)^2}{(\Delta y_l)^2} + \frac{(\Delta x_i)^2}{\Delta y_l \Delta y_{l-1}} \right) - \frac{2 k_{ilj} (\Delta x_i)^2}{\Delta z_j}.$$

Note that, if the discrete function $Q(i, l, j)$ is known at a level j, one can find the coefficients D_{ilj} from Eq. (9.92). Therefore, Eq. (9.91) becomes a system of linear equations with respect to the values $Q(i, l, j+1)$ of the discrete function at the next level, $j + 1$. We also have the boundary condition at the observation surface:

$$Q^m(i, l, 1) = P^0(x_i, y_l, 0), \; i = 1, 2, ..N_x,$$

and boundary conditions for the values of the function $Q(i, l, j)$ at the left and right and back and front boundaries of the area of migration. The boundary values on the left, right, back and front sides of the migration domain can be obtained by a simple 1-D migration of the electric field downward at the sides of the observation area using simple formulas:

$$P^{m*}(x, y_B, z) = P^0(x, y_B, 0) e^{-k_b z}, \; P^{m*}(x, y_F, z) = P^0(x, y_F, 0) e^{-k_b z},$$

$$P^{m*}(x_L, y, z) = P^0(x_L, y, 0) e^{-k_b z},$$

$$P^{m*}(x_R, y, z) = P^0(x_R, y, 0) e^{-k_b z}, \; 0 < z < +\infty. \tag{9.93}$$

After all the values $Q(i, l, j)$ are found, we compute the migration field P^{m*} in the nodes of grid $\Sigma(x_i, y_l, z_j)$, using Eq. (9.86):

$$P^{m*}(x_i, y_l, z_j) = Q^m(i, l, j) e^{-k_b z_j}, \; i = 1, 2, ... N_x, \; l = 1, 2, ... N_y, \; j = 1, 2, ... N_z. \tag{9.94}$$

The solution of the finite-difference equations for the discrete function $Q(i, l, j)$ can be obtained using the same algorithm we have described above for 2-D finite difference migration.

9.4 VISUALIZATION OF GEOELECTRIC STRUCTURES BY USE OF MIGRATION IN THE FREQUENCY AND TIME DOMAINS

Visualization is a term which has come into use to describe data processing in which an image of the subsurface structure is created, rather than sets of contour maps of the observed fields. Zhdanov (1984, 1988) and Zhdanov et al. (1996) have developed techniques for visualization of deep geoelectric structures using electromagnetic migration. We will at this point give a brief description of the basic concepts on which the visualization of geoelectric structures is based. First, we examine the problem in the frequency domain.

9.4.1 MIGRATION IMAGING CONDITION IN THE FREQUENCY DOMAIN

We have to use the imaging condition in order to enhance the migration image and to produce the volume conductivity distribution from the migrated field. There are several different imaging conditions discussed in the literature (e.g., Zhdanov et al., 1996; Mittet et al., 2005; Tompkins, 2004; Hokstad and Røsten, 2007). In this section we discuss the simple imaging conditions introduced in Zhdanov et al. (1996).

The amplitude of the migration field decays downward, which results in suppression of the noise in the observed data. At the same time, the phase of the migration field is retarded with the depth essentially in the same way as for the original upgoing field. Therefore, the summation of the migration field for different frequencies results in constructive reinforcement of the amplitude at the scattering objects associated with geoelectrical inhomogeneities, and in weakening of the signal in the homogeneous areas of the sea bottom. These useful features of the migration field can be successfully used for imaging the geoelectrical structures.

We represent the observed electromagnetic field $\mathbf{E}$, $\mathbf{H}$ as being the sum of a downgoing $\mathbf{E}^d$, $\mathbf{H}^d$ field and an upgoing field, $\mathbf{E}^u$, $\mathbf{H}^u$:

$$
\begin{aligned}
\mathbf{E} &= \mathbf{E}^d + \mathbf{E}^u, \\
\mathbf{H} &= \mathbf{H}^d + \mathbf{H}^u.
\end{aligned}
\tag{9.95}
$$

A detailed technique of the EM field separation into the upgoing and downgoing parts will be discussed in Chapter 17.

Let us suppose, for example, that we have a three-dimensional model with a localized zone of anomalous electrical conductivity. It can be shown that the phases of the downgoing and upgoing fields, $\phi_d(\mathbf{r}, \omega)$ and $\phi_u(\mathbf{r}, \omega)$, differ one from the other in the background (normal part) of the three-dimensional cross section, and are functions of frequency, but near the anomalous zone, D, the differences are only weakly related to frequency (Zhdanov et al., 1996). From the physical point of view, we have the effect analogous to the seismic case, when the primary (downgoing) and the scattered (upgoing) components of the fields have the same phase at the position of the reflector. This property of the migration field is usually used as an imaging condition in a seismic phase migration algorithm (Claerbout, 1985). We use this imaging condition for an electromagnetic field as well, in which a geoelectric boundary plays the role of a reflector.

We can introduce apparent reflectivity functions, $\beta_{Ex,y}(\mathbf{r}, \omega)$ and $\beta_{Hx,y}(\mathbf{r}, \omega)$, defined as the ratio of upgoing and downgoing electric or magnetic fields,

$$\beta_{Ex,y}(\mathbf{r}, \omega) = \frac{E_{x,y}^u(\mathbf{r}, \omega)}{E_{x,y}^d(\mathbf{r}, \omega)} = \left| \frac{E_{x,y}^u(\mathbf{r}, \omega)}{E_{x,y}^d(\mathbf{r}, \omega)} \right| e_a^{i(\phi_E^u - \phi_E^d)}, \tag{9.96}$$

$$\beta_{Hx,y}(\mathbf{r}, \omega) = -\frac{H_{x,y}^u(\mathbf{r}, \omega)}{H_{x,y}^d(\mathbf{r}, \omega)} = \left| \frac{H_{x,y}^u(\mathbf{r}, \omega)}{H_{x,y}^d(\mathbf{r}, \omega)} \right| e_a^{i(\phi_H^u - \phi_H^d \pm \pi)}. \tag{9.97}$$

We noted above that, if the observation point $\mathbf{r}$ is in the vicinity of the anomalous region, D, then:

$$\phi_u(\mathbf{r}, \omega) - \phi_d(\mathbf{r}, \omega) \to \Delta\phi(\mathbf{r}), \tag{9.98}$$

where $\Delta\phi(\mathbf{r})$ depends only weakly on frequency. Therefore, we can "stack" the values of apparent reflectivity functions, $\beta_{Ex,y}$ and/or $\beta_{Hx,y}$ over a range of frequencies:

$$\overline{\beta}_{Ex,y}(\mathbf{r}) = \frac{1}{L} \sum_{l=1}^L \beta_{Ex,y}(\mathbf{r}, \omega_l), \ \ \overline{\beta}_{Hx,y}(\mathbf{r}) = \frac{1}{L} \sum_{l=1}^L \beta_{Hx,y}(\mathbf{r}, \omega_l), \tag{9.99}$$

where we use the different frequencies ($\omega_1 < \omega_2 < \omega_3 < \cdots < \omega_L$).

Then, throughout the area outside the anomalous region we will stack unlike reflectivity functions, leading to a decreased $\overline{\beta}_{Ex,y}$ and $\overline{\beta}_{Hx,y}$, but close to the anomalous zone we will have cophasal stacking, which increases $\overline{\beta}_{Ex,y}$ and $\overline{\beta}_{Hx,y}$, and so, "traces" or outlines the inhomogeneity.

It must be stressed that, with this method of visualization, it is necessary only that we be able to determine the phase of the upgoing field within the earth. If we compare the phase frequency characteristics of the analytical continuation of the upgoing field and of its complex conjugate migration, we see that they are equal!

Indeed, according to Eq. (9.68), the spectrum of the complex conjugate migration field can be calculated as follows:

$$p^{m*}(k_x, k_y, z, \omega) = p^u(k_y, k_s, 0, \omega) \exp(-\widetilde{v}_b z). \tag{9.100}$$

It was demonstrated above in Eq. (9.21) that the spectrum, p^c, characterizing the downward analytic continuation of a scalar component of the upgoing field, is equal to

$$p^c(k_x, k_y, z, \omega) = p^u(k_x, k_y, 0, \omega) \exp(v_b z), \tag{9.101}$$

where p^u is the spectrum of the upgoing field at the surface of the earth.

Considering that $\text{Re}\, v_b = \text{Re}\, \widetilde{v}_b$ and $\text{Im}\, v_b = -\text{Im}\, \widetilde{v}_b$, we see that the phase spectrum for the migrated and analytically continued fields are identically the same:

$$\phi(k_x, k_y, z, \omega) = \text{Im}\, v_b,$$

while the amplitude spectrums, $a^{m*} = e^{-\text{Re}\, v_b z'}$ and $a^{c,m} = e^{\text{Re}\, v_b z}$ differ in a significant way. This means that the migration field components, $\mathbf{E}^{m*}$ and $\mathbf{H}^{m*}$ are characterized by the same phase as the

unmigrated upgoing field. As a consequence of this, we can use the migration reflectivity functions $\beta_{Ex,y}^m(x, y, z, \omega_l)$ and $\beta_{Hx,y}^m(x, y, z, \omega_l)$ defined according to the formulas:

$$\beta_{Ex,y}^m(\mathbf{r}, \omega) = \frac{E_{x,y}^{m*}(\mathbf{r}, \omega)}{E_{x,y}^d(\mathbf{r}, \omega)}, \quad \beta_{Hx,y}^m(\mathbf{r}, \omega) = -\frac{H_{x,y}^{m*}(\mathbf{r}, \omega)}{H_{x,y}^d(\mathbf{r}, \omega)}. \tag{9.102}$$

The phase of the migration reflectivity function β^m is significantly frequency-dependent except near the inhomogeneity. Thus, stacking β^m for a spectrum of frequencies ($\omega_1 < \omega_2 < \omega_3 < \cdots < \omega_L$) results in positive reinforcement at the scatterers and destructive interference elsewhere:

$$\overline{\beta}_{Ex,y}^m(\mathbf{r}) = \frac{1}{L} \sum_{l=1}^{L} \beta_{Ex,y}^m(\mathbf{r}, \omega_l), \quad \overline{\beta}_{Hx,y}^m(\mathbf{r}) = \frac{1}{L} \sum_{l=1}^{L} \beta_{Hx,y}^m(\mathbf{r}, \omega_l). \tag{9.103}$$

The inphase summation of the migration reflectivity functions indicates the position of the boundaries between the layers with different conductivities.

9.4.2 MIGRATION IMAGING CONDITION IN THE TIME DOMAIN

Next, we can consider approaches for visualizing electromagnetic fields in the time domain. For simplicity, we will assume that the time-varying field is excited in the earth by a local surface-based impulsive source or by an impulsive plane wave.

For an example, we will compute the characteristics of the propagation of a plane impulsive wave, $d^\delta(z, t)$, excited by a δ-function impulse located at point $z = 0$ at the instant of time, $t = 0$, in a homogeneous medium with electrical conductivity, σ_b. It should be clear that the analytical expression for this wave is obtained by an appropriate Fourier transformation of the downgoing field (with unit amplitude at the earth's surface):

$$d(z, \omega) = e^{ik_b z}, \tag{9.104}$$

where $k_b = (i\omega\mu_0\sigma_b)^{1/2}$ is the wave number for the medium.

We can now write

$$\begin{aligned} d^{\delta(z,t)} &= \frac{1}{2\pi} \int_{-\infty}^{+} e^{ik_b x} e^{-i\omega t} d\omega \\ &= bz t^{-3/2} e^{-\mu_0\sigma_b z^2/4t}, \end{aligned} \tag{9.105}$$

where $b = (\mu_0\sigma_b/4\pi)^{1/2}$.

Thus, the shape of the wave excited with a δ-function wave form will change as the wave propagates to depth.

Let us analyze the changes which take place in the function $d^\delta(z, t)$ at some fixed depth, $z = const$, as time progresses. As may be seen from Eq. (9.105), at early time, with $t \rightarrow 0$, the function $d^\delta(z, t)$ is about zero, and then increases monotonically, reaching a maximum value at

$$t_0(z) = \mu_0\sigma_b z^2/6. \tag{9.106}$$

After passing through this maximum, the function decreases, being completely attenuated only as $t \to \infty$. The time it takes for the maximum to develop at a given depth can be used to define an apparent speed for the electromagnetic impulse. The speed of travel for the maximum pulse amplitude, V, is:

$$V = dz/dt_o = 3/(\mu_0 \sigma_b z). \tag{9.107}$$

We see that close to the source, the wave speed is infinitely large, but with increasing distance from the source, the impulsive wave slows its pace, and essentially comes to a halt at infinity. In more resistive media, the speed of the wave is greater, and in more conductive media, the speed of the wave is less, which resembles the behavior of the speed of movement of the phase front of a monochromatic field spreading into a conductive medium.

This behavior of the propagation of an impulsive wave can be used for visualization of geoelectric boundaries.

As we noted earlier, the difference between the phases of a migration upgoing field and a downgoing field in the vicinity of a local anomalous zone or geoelectric boundary depends only weakly on frequency. This indicates that these two fields will have the same form near a localized geoelectric anomaly or at a geoelectric boundary. Determination of those points at which the arrival times for the local extremals of the downgoing and migration fields are the same permits us to identify the position of the geoelectric inhomogeneity or geoelectric boundary.

In more general cases, the principle of visualization of a geoelectric structure in the time domain can be formulated as follows. Using a formula such as Eq. (9.106) for computing the time t_0 at which a local maximum normal field, E^d, is reached at a given point, r_0, we can calculate the migration field, E^m, at the same point and for the same instant in time. If the point r_0 falls in the anomalous region or at a geoelectrical boundary, we will have a local extremal of the migrated field as well.

9.5 MIGRATION VERSUS INVERSION

It has been demonstrated in several publications that electromagnetic migration can be treated as an approximate solution of the corresponding electromagnetic inverse problem (Zhdanov and Traynin, 1997; Zhdanov and Portniaguine, 1997; Zhdanov, 2002; Ueda and Zhdanov, 2008).

We can introduce the residual electromagnetic field as the difference between the simulated electromagnetic field for some given (background) geoelectrical model and the actual electromagnetic field. Electromagnetic migration imaging is considered as the initial step in the general electromagnetic inversion procedure, based on the minimization of the misfit functional between the observed and predicted data. By applying migration iteratively, we arrive at iterative electromagnetic migration which provides a rigorous solution of electromagnetic inverse problems. This iteration process is similar to the conventional iterative inversion discussed in Chapter 8. For example, one can use the regularized conjugate gradient (RCG) method as a basis for iterative migration.

9.5.1 FORMULATION OF THE INVERSE PROBLEM

Consider a 3-D geoelectrical model consisting of a homogeneous atmosphere and an inhomogeneous earth with conductivity $\sigma(\mathbf{r}) = \sigma_b(\mathbf{r}) + \Delta\sigma(\mathbf{r})$, where $\sigma_b(\mathbf{r})$ is some background (normal) distribution

of the conductivity, and $\Delta\sigma(\mathbf{r})$ is the anomalous conductivity, which is nonvanishing only within some domain D. We will denote the surface of the earth by Σ. We will confine ourselves to consideration of nonmagnetic media and, hence, assume that $\mu = \mu_0 = 4\pi \times 10^{-7}$ H/m, where μ_0 is the free-space magnetic permeability. The electromagnetic field in this model is generated by a source, located with the current density $\mathbf{j}^e$ in the upper half-space. Receivers are located on the surface of the earth. We assume also, that the electromagnetic field is varying in time relatively slowly, so that in the equations for this field the second derivative with respect to time, $\partial^2/\partial t^2$, can be discarded. In other words, we consider the so-called quasi-stationary model of the electromagnetic field (without displacement currents).

We can represent the total electromagnetic field, observed in this model, as the sum of the background (normal) field $\{\mathbf{E}^b, \mathbf{H}^b\}$, generated by the given source in the model with the background conductivity distribution, and the anomalous field $\{\mathbf{E}^a, \mathbf{H}^a\}$, due to an inhomogeneity $\Delta\sigma(\mathbf{r})$:

$$\mathbf{E} = \mathbf{E}^b + \mathbf{E}^a, \ \mathbf{H} = \mathbf{H}^b + \mathbf{H}^a. \tag{9.108}$$

The total electromagnetic field satisfies Maxwell's equations

$$\nabla \times \mathbf{H} = (\sigma_b + \Delta\sigma)\mathbf{E} + \mathbf{j}^e,$$
$$\nabla \times \mathbf{E} = -\mu\partial\mathbf{H}/\partial t, \tag{9.109}$$

while the anomalous field satisfies the equations

$$\nabla \times \mathbf{H}^a = \sigma_b\mathbf{E}^a + \Delta\sigma\left(\mathbf{E}^b + \mathbf{E}^a\right),$$
$$\nabla \times \mathbf{E}^a = -\mu\partial\mathbf{H}^a/\partial t. \tag{9.110}$$

The general electromagnetic inverse problem can be formulated as follows. We are given the observed total electromagnetic field on the surface of the earth and the background (normal) distribution of the conductivity $\sigma_b(\mathbf{r})$. The problem is to determine the conductivity $\sigma(\mathbf{r}) = \sigma_b(\mathbf{r}) + \Delta\sigma(\mathbf{r})$ within the anomalous domain D.

9.5.2 GENERAL CONCEPT OF THE MIGRATION ANOMALOUS FIELD

In this section we introduce first the general concept of the migration anomalous electromagnetic field and show how it can be used for fast imaging of the earth's interior. In the following sections we will demonstrate the connections between the electromagnetic migration and the solution of the electromagnetic inverse problem.

The general definition of the electromagnetic migration field in time domain was introduced in the monograph by Zhdanov (1988). According to this definition, the migration field is the solution of the adjoint Maxwell's equations. In other words, we can introduce the migration anomalous field $\mathbf{E}^{am}(\mathbf{r}, \tau), \mathbf{H}^{am}(\mathbf{r}, \tau)$ as the field, determined in reverse time $\tau = -t$, and satisfying the Maxwell's equations in the reverse time within the earth with a background conductivity σ_b:

$$\nabla \times \mathbf{H}^{am} = \sigma_b\mathbf{E}^{am} + \mathbf{j}^S_E,$$
$$\nabla \times \mathbf{E}^{am} = -\mu\partial\mathbf{H}^{am}/\partial\tau - \mathbf{j}^S_H. \tag{9.111}$$

We have included in the right-hand sides of the last equations the fictitious electric and magnetic currents, distributed over the surface of observations S with the surface densities $\mathbf{j}_E^S(\mathbf{r}, \tau)$ and $\mathbf{j}_H^S(\mathbf{r}, \tau)$ proportional to the anomalous fields in the reverse time:

$$\mathbf{j}_E^S(\mathbf{r}', \tau) = \Sigma_0 \mathbf{E}^a(\mathbf{r}', -\tau) = \Sigma_0 \left[\mathbf{E}(\mathbf{r}', -\tau) - \mathbf{E}^b(\mathbf{r}', -\tau) \right], \tag{9.112}$$

$$\mathbf{j}_H^S(\mathbf{r}', \tau) = \mathbf{H}^a(\mathbf{r}', -\tau) = \mathbf{H}(\mathbf{r}', -\tau) - \mathbf{H}^b(\mathbf{r}', -\tau). \tag{9.113}$$

We have introduced the unit conductance Σ_0 in Eq. (9.112) to keep the correct dimensions of the fictitious electric current $\mathbf{j}_E^S$.

Applying the curl operator to both sides of Eq. (9.111), we obtain a separate equation for the anomalous migration electric field:

$$\nabla \times \nabla \times \mathbf{E}^{am} = -\mu\sigma_b \frac{\partial \mathbf{E}^{am}}{\partial \tau} - \mu \frac{\partial \mathbf{j}_E^S}{\partial \tau} - \nabla \times \mathbf{j}_H^S. \tag{9.114}$$

Therefore, in reverse time τ the electric migration field satisfies the ordinary vector diffusion equation. However, in direct time, $t = -\tau$, the migration anomalous electric field satisfies the equation adjoint to (9.114):

$$\nabla \times \nabla \times \mathbf{E}^{am} = \mu\sigma_b \frac{\partial \mathbf{E}^{am}}{\partial t} + \mu \frac{\partial \mathbf{j}_E^S}{\partial t} - \nabla \times \mathbf{j}_H^S. \tag{9.115}$$

In a similar way, we can write the equation for the migration anomalous magnetic field:

$$\nabla \times \nabla \times \mathbf{H}^{am} = \mu\sigma_b \frac{\partial \mathbf{H}^{am}}{\partial t} - \sigma_b \mathbf{j}_H^S + \nabla \times \mathbf{j}_E^S. \tag{9.116}$$

In the lower half-space, free from the fictitious electric and magnetic currents, $\mathbf{j}_E^S$ and $\mathbf{j}_H^S$, we have the homogeneous equations for the migration fields:

$$\nabla \times \nabla \times \mathbf{E}^{am} = \mu\sigma_b \frac{\partial \mathbf{E}^{am}}{\partial t}, \tag{9.117}$$

$$\nabla \times \nabla \times \mathbf{H}^{am} = \mu\sigma_b \frac{\partial \mathbf{H}^{am}}{\partial t}. \tag{9.118}$$

While the ordinary diffusion equation describes the development of the process of electromagnetic field propagation in increasing time from the source to the receiver, Eqs. (9.117) and (9.118) reflects the same process in a reverse order, i.e. from the final distribution of the field at the receivers to its initial distribution at the sources. That is why, following Wang et al. (1994), Eqs. (9.117) and (9.118) can be called *the vector concentration equations*. As a result, the electromagnetic migration field can be treated as the field converging into the sources of the anomalous field, which actually coincide with the geoelectrical inhomogeneities.

9.5.3 GENERAL MIGRATION IMAGING CONDITIONS

We have introduced the migration transformation in order to generate an approximate solution of the EM inverse problem. It can be demonstrated, however, that migration imaging represents the first iteration of some rigorous inversion scheme.

According to Chapter 8, we can describe the general inverse problem as a solution of the operator equations:

$$\mathbf{d}_{E.H} = \mathbf{A}_{E,H}\left(\Delta\sigma\right) = \mathbf{G}_{E,H}\left(\Delta\sigma\mathbf{E}\right), \tag{9.119}$$

where $\mathbf{A}_{E,H}\left(\Delta\sigma\right)$ are nonlinear forward modeling operators, given by the formulae:

$$\mathbf{A}_{E,H}\left(\Delta\sigma\right) = \mathbf{G}_{E,H}\left(\Delta\sigma\mathbf{E}\right).$$

In Eq. (9.119), $\Delta\sigma$ is a model parameter vector formed by the anomalous conductivity distribution in a model with the given background conductivity σ_b, and $\mathbf{d}_{E.H}$ is a data vector formed by the anomalous electric or magnetic fields observed in the receivers:

$$\mathbf{d}_{E.H} = \left\{\mathbf{E}^a, \mathbf{H}^a\right\} = \left\{\mathbf{E}^a\left(\mathbf{r}_i\right), \mathbf{H}^a\left(\mathbf{r}_i\right), \ i = 1, 2, ...I\right\}. \tag{9.120}$$

We have derived in Chapter 8 the approximate imaging formulas (8.48) and (8.49), based on the Born approximation. These formulas can be rewritten in the form:

$$\Delta\sigma\left(\mathbf{r}\right) \approx k\left(W_E^* W_E\right)^{-1} \mathrm{Re} \int_\Omega \mathbf{E}^{b*}\left(\mathbf{r}, \omega\right) \cdot \iint_S \widetilde{\widetilde{\mathbf{G}}}_E^*\left(\mathbf{r}' \mid \mathbf{r}\right) \cdot \mathbf{E}^a\left(\mathbf{r}', \omega\right) ds' d\omega, \tag{9.121}$$

and

$$\Delta\sigma\left(\mathbf{r}\right) \approx k\left(W_H^\star W_H\right)^{-1} \mathrm{Re} \int_\Omega \mathbf{E}^{b*}\left(\mathbf{r}, \omega\right) \cdot \iint_S \widetilde{\widetilde{\mathbf{G}}}_H^*\left(\mathbf{r}' \mid \mathbf{r}\right) \cdot \mathbf{H}^a\left(\mathbf{r}', \omega\right) ds' d\omega, \tag{9.122}$$

where Ω is the frequency interval of the observed data. Note that we take the real parts of the corresponding integrals because in this chapter we consider the real conductivity only.

W_E and W_H are the linear weighting operators of the multiplication of conductivity $\Delta\sigma$ by the functions $w_E\left(\mathbf{r}\right)$ and $w_H\left(\mathbf{r}\right)$ equal to the square root of the integrated sensitivity (see formulas (8.19) and (8.53) in Chapter 8):

$$w_E = \sqrt{S_E}, \ \text{and} \ w_H = \sqrt{S_H}. \tag{9.123}$$

Eqs. (9.121) and (9.122) can serve as a basis for geophysical migration imaging. Indeed, on the right-hand side of these formulas we have the dot product of the complex conjugate background electric field, $\mathbf{E}^{b*}$, and the complex conjugate of the corresponding auxiliary fields, $\mathbf{E}^{R*}$ and $\mathbf{H}^{R*}$, defined by the equations:

$$\mathbf{E}^{R*}\left(\mathbf{r}, \omega\right) = \iint_S \widetilde{\widetilde{\mathbf{G}}}_E^*\left(\mathbf{r}' \mid \mathbf{r}\right) \cdot \mathbf{E}^a\left(\mathbf{r}', \omega\right) ds', \tag{9.124}$$

$$\mathbf{H}^{R*}\left(\mathbf{r}, \omega\right) = \iint_S \widetilde{\widetilde{\mathbf{G}}}_H^*\left(\mathbf{r}' \mid \mathbf{r}\right) \cdot \mathbf{H}^a\left(\mathbf{r}', \omega\right) ds'. \tag{9.125}$$

Note that, in the definition of the auxiliary fields, $\mathbf{E}^{R*}(\mathbf{r}, \omega)$ and $\mathbf{H}^{R*}(\mathbf{r}, \omega)$, we use the complex conjugate Green's tensors. It was demonstrated above that the transition to the complex conjugate function in the frequency domain corresponds to changing a sign in front of time variable t in the time domain. Thus, using the convolution theorem, we can write the expressions for the auxiliary electric and magnetic fields in the time domain as follows:

$$
\begin{aligned}
\widetilde{\mathbf{E}}^R(\mathbf{r}, t') &= \frac{1}{2\pi} \int_{-\infty}^{+\infty} \mathbf{E}^{R*}(\mathbf{r}, \omega) e^{-i\omega t'} d\omega \\
&= \frac{1}{2\pi} \int_{-\infty}^{+\infty} \iint_S \widehat{\mathbf{G}}_E^*(\mathbf{r} \mid \mathbf{r}') \cdot \mathbf{E}^a(\mathbf{r}', \omega) ds' e^{-i\omega t'} d\omega \\
&= \iint_S \int_{-\infty}^{+\infty} \widehat{\mathbf{G}}_E(\mathbf{r}, -t \mid \mathbf{r}', -t') \mathbf{E}^a(\mathbf{r}', t) dt ds',
\end{aligned}
\tag{9.126}
$$

and

$$
\begin{aligned}
\widetilde{\mathbf{H}}^R(\mathbf{r}, t') &= \frac{1}{2\pi} \int_{-\infty}^{+\infty} \mathbf{H}^{R*}(\mathbf{r}, \omega) e^{-i\omega t'} d\omega \\
&= \iint_S \int_{-\infty}^{+\infty} \widehat{\mathbf{G}}_H(\mathbf{r}, -t \mid \mathbf{r}', -t') \mathbf{H}^a(\mathbf{r}', t) dt ds'.
\end{aligned}
\tag{9.127}
$$

Note, that we use the same symbols for the fields in time and frequency domains to simplify the notations. The reader can easy distinguish the corresponding field by checking the arguments t or ω in the corresponding equations.

The minus sign in front of time variable t in the expression for the Green's tensors indicates that the electromagnetic field propagation occurs backward in time. Therefore, the fields $\widetilde{\mathbf{E}}^R(\mathbf{r}, t')$ and $\widetilde{\mathbf{H}}^R(\mathbf{r}, t')$ are referred to as the "back-propagated" or "back-scattering" fields. These fields satisfy to the differential equations, which can be derived directly from integral representations (9.126) and (9.127), using the properties of the Green's tensors (see section 3.4):

$$
\nabla \times \nabla \times \widetilde{\mathbf{E}}^R = \mu\sigma_b \frac{\partial \widetilde{\mathbf{E}}^R}{\partial t} + \mu \frac{\partial \mathbf{j}_E^S}{\partial t} - \nabla \times \mathbf{j}_H^S,
\tag{9.128}
$$

$$
\nabla \times \nabla \times \widetilde{\mathbf{H}}^R = \mu\sigma_b \frac{\partial \widetilde{\mathbf{H}}^R}{\partial t} - \sigma_b \mathbf{j}_H^S + \nabla \times \mathbf{j}_E^S
\tag{9.129}
$$

We can see that the last equations are similar to Eqs. (9.115) and (9.116) for the migration fields. Thus, these back-scattering fields are nothing else but the migration anomalous fields, $\mathbf{E}^{am}$, $\mathbf{H}^{am}$:

$$
\widetilde{\mathbf{E}}^R(\mathbf{r}, t') = \mathbf{E}^{am}(\mathbf{r}, t'), \quad \widetilde{\mathbf{H}}^R(\mathbf{r}, t') = \mathbf{H}^{am}(\mathbf{r}, t').
\tag{9.130}
$$

Similar equalities hold for the fields in the frequency domain as well:

$$
\widetilde{\mathbf{E}}^R(\mathbf{r}, \omega) = \mathbf{E}^{am}(\mathbf{r}, \omega), \quad \widetilde{\mathbf{H}}^R(\mathbf{r}, \omega) = \mathbf{H}^{am}(\mathbf{r}, \omega).
\tag{9.131}
$$

Substituting formulas (9.131) into Eq. (9.121), we arrive at the corresponding imaging condition:

$$\Delta\sigma\left(\mathbf{r}\right) \approx k\left(W_E^* W_E\right)^{-1}\text{Re}\int_\Omega \mathbf{E}^{b*}\left(\mathbf{r}, \omega\right)\cdot\mathbf{E}^{am*}\left(\mathbf{r}, \omega\right)d\omega. \tag{9.132}$$

In a similar way we can derive an imaging formula based on anomalous magnetic field observations:

$$\Delta\sigma\left(\mathbf{r}\right) \approx k\left(W_H^\star W_H\right)^{-1}\text{Re}\int_\Omega \mathbf{E}^{b*}\left(\mathbf{r}, \omega\right)\cdot\mathbf{H}^{am*}\left(\mathbf{r}, \omega\right)d\omega. \tag{9.133}$$

We have demonstrated above that the migration field represents a backscattering field produced by illuminating the background medium by fictitious electric and magnetic currents, distributed over the surface of observations S with the surface densities, $\mathbf{j}_E^S$ and $\mathbf{j}_H^S$, determined by the anomalous fields in the reverse time, according to formula (9.112) and (9.113). Therefore, the imaging conditions (9.132) and (9.133) are nothing else but cross-power spectrums of the background and the migration (backscattering) electric or magnetic fields.

We will call the conductivity distributions, obtained by formulas (9.132) and (9.133), the *migration apparent conductivity*.

We can present conditions (9.132) and (9.133) in the inversion theory dressing as:

$$\Delta\sigma\left(\mathbf{r}\right) \approx -k\left(W_E^* W_E\right)^{-1}\mathbf{l}_0^E\left(\mathbf{r}\right), \tag{9.134}$$

$$\Delta\sigma\left(\mathbf{r}\right) \approx -k\left(W_H^\star W_H\right)^{-1}\mathbf{l}_0^H\left(\mathbf{r}\right), \tag{9.135}$$

where $\mathbf{l}_0^E\left(\mathbf{r}\right)$ and $\mathbf{l}_0^H\left(\mathbf{r}\right)$ are the gradient directions of the forward modeling operators $\mathbf{A}_E\left(\Delta\sigma\right)$ and $\mathbf{A}_H\left(\Delta\sigma\right)$, respectively:

$$\mathbf{l}_0^E\left(\mathbf{r}\right) = -\text{Re}\int_\Omega \mathbf{E}^{b*}\left(\mathbf{r}, \omega\right)\cdot\mathbf{E}^{am*}\left(\mathbf{r}, \omega\right)d\omega, \tag{9.136}$$

$$\mathbf{l}_0^H\left(\mathbf{r}\right) = -\text{Re}\int_\Omega \mathbf{E}^{b*}\left(\mathbf{r}, \omega\right)\cdot\mathbf{H}^{am*}\left(\mathbf{r}, \omega\right)d\omega. \tag{9.137}$$

The last equations make it clear that the migration imaging indeed can be treated as the first iteration of a rigorous inversion.

9.5.4 REGULARIZED ITERATIVE MIGRATION

We have demonstrated above that migration imaging can be treated as the first iteration in the solution of electromagnetic inverse problem (9.119). Obviously, we can obtain better imaging results if we repeat the iterations. We now apply a general scheme of the regularized conjugate gradient method (see Chapter 8), to form an iterative process for electromagnetic migration. According to this scheme, a general iterative process can be described by the formulas:

$$\Delta\boldsymbol{\sigma}_{n+1} = \Delta\boldsymbol{\sigma}_n + \delta\Delta\boldsymbol{\sigma}_n = \Delta\boldsymbol{\sigma}_n - k_n^\alpha\widetilde{\mathbf{l}}^\alpha(\Delta\boldsymbol{\sigma}_n), \tag{9.138}$$

where

$$\widetilde{\mathbf{l}}^\alpha(\Delta\sigma_n) = \widetilde{\mathbf{l}}_n^\alpha = \mathbf{l}_n^\alpha + \beta_n^\alpha\widetilde{\mathbf{l}}_{(n-1)}^\alpha, \ \widetilde{\mathbf{l}}_0^\alpha = \mathbf{l}_0^\alpha, \tag{9.139}$$

$$\beta_n^\alpha = \left\| \mathbf{l}_n^\alpha \right\|_n^2 / \left\| \mathbf{l}_{(n-1)}^\alpha \right\|^2 .$$

The regularized gradient direction on the n-th iteration $\mathbf{l}_n^\alpha$ can be calculated by a formula:

$$\mathbf{l}_n^\alpha = \mathbf{l}^\alpha (\sigma_n) = \mathbf{l}_n + \alpha \mathbf{W}_m^2 (\sigma_n - \sigma_{apr}), \tag{9.140}$$

where $\mathbf{l}_n$ is a gradient direction on the nth iteration, computed using a formula similar to (9.136) or (9.137):

$$\mathbf{l}_n = \mathbf{l}_n^E = \text{Re} \int_\Omega \mathbf{E}_n^* (\mathbf{r}, \omega) \cdot \mathbf{E}_n^{m*} (\mathbf{r}, \omega) \, d\omega = \text{Re} \int_\Omega \mathbf{E}_n (\mathbf{r}, \omega) \cdot \mathbf{E}_n^m (\mathbf{r}, \omega) \, d\omega, \tag{9.141}$$

or

$$\mathbf{l}_n = \mathbf{l}_n^H = \text{Re} \int_\Omega \mathbf{E}_n^* (\mathbf{r}, \omega) \cdot \mathbf{H}_n^{m*} (\mathbf{r}, \omega) \, d\omega = \text{Re} \int_\Omega \mathbf{E}_n (\mathbf{r}, \omega) \cdot \mathbf{H}_n^m (\mathbf{r}, \omega) \, d\omega. \tag{9.142}$$

The fields $\mathbf{E}_n$, $\mathbf{E}_n^m$, and $\mathbf{H}_n^m$ are determined from the following conditions. The field $\mathbf{E}_n$ is the electric field generated in a model with the anomalous conductivity $\Delta\sigma_n$ found on the iteration number n.

The field $\mathbf{E}_n^m$ is obtained by the migration of the residual electric field found on the iteration number n:

$$\mathbf{E}_n^m (\mathbf{r}) = \mathbf{E}^m (\mathbf{r}; \mathbf{R}_{nE}),$$

where

$$\mathbf{R}_{nE} (\mathbf{r}) = \mathbf{E}_n (\mathbf{r}) - \mathbf{E} (\mathbf{r}), \ \mathbf{r} \in S$$

and $\mathbf{E} (\mathbf{r}) = \mathbf{E}^b (\mathbf{r}) + \mathbf{E}^a (\mathbf{r})$ is a total observed electric field on the surface S.

In a similar way, the field $\mathbf{H}_n^m$ is obtained by the migration of the residual magnetic field found on the iteration number n:

$$\mathbf{H}_n^m (\mathbf{r}) = \mathbf{H}^m (\mathbf{r}; \mathbf{R}_{nH}),$$

where

$$\mathbf{R}_{nH} (\mathbf{r}) = \mathbf{H}_n (\mathbf{r}) - \mathbf{H} (\mathbf{r}), \ \mathbf{r} \in S$$

and $\mathbf{H} (\mathbf{r}) = \mathbf{H}^b (\mathbf{r}) + \mathbf{H}^a (\mathbf{r})$ is a total observed electric field on the surface S.

Thus, we can describe the developed method of iterative migration as follows. On every iteration we calculate the theoretical electromagnetic response, $\mathbf{E}_n$, $\mathbf{H}_n$, for the given geoelectrical model $\Delta\sigma_n$, obtained on the previous step, calculate the residual field between this response and the observed field, $\mathbf{R}_{nE}$, $\mathbf{R}_{nH}$, and then migrate the residual field. The gradient direction is computed as an integral over the frequencies of the dot product of the migrated residual field and the theoretical response $\mathbf{E}_n$. Using this gradient direction and the corresponding value of the optimal length of the step k_n, we calculate the new geoelectrical model $\Delta\sigma_n$ on the basis of expressions (9.138) and (9.139). The iterations are terminated when the misfit between the observed and predicted data reaches the level of the noise. The optimal value of the regularization parameter α is selected using conventional principles of regularization theory, described in Chapter 8.

The migration apparent conductivity, introduced above, is used as the first iteration in this iterative process.

It is important to emphasize that, in accord with formulas (8.94) of Chapter 8, expressions (9.141) and (9.142) are nothing else but the adjoint Fréchet derivative operators applied to the electric and magnetic residual fields, $\mathbf{R}_{nE}(\mathbf{r})$ and $\mathbf{R}_{nH}(\mathbf{r})$,

$$\mathbf{F}_E^{\widetilde{\sigma}_n \star}(\mathbf{r} \mid \mathbf{R}_{En}) = \mathbf{l}_n^E = \mathrm{Re} \int_\Omega \mathbf{E}_n(\mathbf{r}, \omega) \cdot \mathbf{E}_n^m(\mathbf{r}, \omega) \, d\omega,$$

$$\mathbf{F}_H^{\widetilde{\sigma}_n \star}(\mathbf{r} \mid \mathbf{R}_{Hn}) = \mathbf{l}_n^H = \mathrm{Re} \int_\Omega \mathbf{E}_n(\mathbf{r}, \omega) \cdot \mathbf{H}_n^m(\mathbf{r}, \omega) \, d\omega. \qquad (9.143)$$

Thus, we can conclude that migration transformation provides an alternative technique to the calculations of the adjoint operator. This fact was demonstrated in the papers by Zhdanov and Traynin (1997), Zhdanov and Portniaguine (1997), and Dorn et al. (1999). Numerically, expressions (9.143) are equivalent to formulas (8.94). The only difference is that in this case we consider the multifrequency data and real conductivity, while in Chapter 8 we analyzed single frequency data and a complex conductivity. However, the approach based on the migration-type formulas (9.143) makes it possible to use the known properties of the migration field in the construction of effective numerical methods.

Finally, we can write the time domain analogs of expressions (9.141) and (9.142). Based on the convolution theorem, the formulas for gradient directions take the form:

$$\mathbf{l}_n = \mathbf{l}_n^E = \int_T \mathbf{E}_n(\mathbf{r}, t) \cdot \mathbf{E}_n^m(\mathbf{r}, -t) \, dt, \qquad (9.144)$$

or

$$\mathbf{l}_n = \mathbf{l}_n^H = \int_T \mathbf{E}_n(\mathbf{r}, t) \cdot \mathbf{H}_n^m(\mathbf{r}, -t) \, dt. \qquad (9.145)$$

Eqs. (9.144) and (9.145) show that, in the time domain, the gradient directions are computed as a convolution between the predicted and migrated fields.

Thus, we have demonstrated that the calculation of the adjoint operator, which is required in any inversion algorithm, requires back propagation of the residual field. This back propagation transformation can actually be performed by migration algorithms. Therefore, conventional migration is equivalent to the calculation of the gradient direction (adjoint Fréchet derivative) of inversion, except that it does not include convolution with the incident field.

Another important difference between inversion and migration is that the general inversion algorithms are iterative. At the same time, iterative inversion, being a solution of an ill-posed problem, requires regularization. By contrast, migration is a stable procedure because it is equivalent to one forward modeling for computing the back-propagated field. However, we have demonstrated in this chapter that any inversion algorithm can be treated as an iterative migration of the residual fields obtained on each iteration.

In this way we can see that, there is a fundamental similarity between these two approaches to the interpretation of electromagnetic data. The main difference is in the physical interpretation of the gradient directions. The approach based on the ideas of EM migration makes it possible to use different numerical algorithms of the migration, outlined above, to construct the effective numerical methods of underground imaging and inversion.

REFERENCES AND RECOMMENDED READING TO CHAPTER 9

Arfken, G., and H. J. Weber, 1995, Mathematical methods for physicists, 4th ed.: Academic Press, San Diego, New York, Boston, London, Tokyo, Toronto, 1029 pp.

Berdichevsky, M. N., and M. S. Zhdanov, 1981, Interpretation of Anomalous Variations of the Electromagnetic Field of the Earth: Nedra, Moscow, 327 pp.

Berdichevsky, M. N., and M. S. Zhdanov, 1984, Advanced theory of deep geomagnetic sounding: Elsevier, Amsterdam, London, New York, Tokyo, 410 pp.

Berkhout, A. J., 1980, Seismic migration – imaging of acoustic energy by wave field extrapolation: Elsevier, Amsterdam, Oxford, New York, 339 pp.

Claerbout, J. F, 1985, Imaging the Earth's interior: Blackwell Scientific Publications, Oxford, London, Edinburgh, 399 pp.

Dorn, O., H. Bertete-Aguire, J. G. Berryman, and G. C. Papanicolau, 1999, A nonlinear inversion for 3-D electromagnetic imaging using adjoint fields: Inverse Problems. **15**, 1523–1558.

Gazdag, J., 1978, Wave equation migration with the phase-shift method: Geophysics, **43** (7), 1342–1351.

Hendrix, C.E., 1975, Radio-frequency holography: US Patent # 3,887,923.

Hokstad, K., and T. Røsten, 2007, On the relationships between depth migration of controlled-source electromagnetic and seismic data: The Leading Edge, **26**, (3), 342–347.

Lee, S., G.A. McMechan, and S.L.V. Aiken, 1987, Phase-field imaging: The electromagnetic equivalent of seismic migration: Geophysics, **52** (5), 679–693.

Mittet, R., F. Maaø, O. M. Aakervik, and S. Ellingsrud, 2005, A two-step approach to depth migration of low-frequency electromagnetic data: 75th Annual International Meeting, SEG, Expanded Abstracts, Electronic Volume.

Morse, P. M., and H. Feshbach, 1953, Methods of theoretical physics: McGraw Hill Book Co., New York, 1978 pp.

Puahengsup, P., L. Wan, and M. S. Zhdanov, 2008, Digital filters for electromagnetic migration of marine electromagnetic data: Proceedings of Annual Meeting of Consortium for Electromagnetic Modeling and Inversion, 227–272.

Røsten, T., K. Hokstad, and B. Arntsen, 2006, 3D depth migration operators for marine controlled-source electromagnetic data: 75th Annual International Meeting, SEG, Expanded Abstracts, 770–774.

Samarsky, A. A., 1984, Theory of the difference schemes (in Russian): Nauka Publishing House, Moscow, 656 pp.

Schneider, W. A., 1978, Integral formulation for migration in two and three dimensions: Geophysics, **43** (2), 49–76.

Stolt, R. M., 1978, Migration by Fourier transform: Geophysics, **43** (1), 23–49.

Tarantola, A., 1984, Inversion of seismic reflection data in the acoustic approximation: Geophysics, **49**, 1259–1266.

Tompkins, M. J., 2004, Marine controlled-source electromagnetic imaging for hydrocarbon exploration: interpreting subsurface electrical properties: First Break, **22**, 27–33.

Ueda, T., and M. S. Zhdanov, 2008, Fast numerical methods for marine controlled-source electromagnetic (EM) survey data based on multigrid quasi-linear approximation and iterative EM migration: Exploration Geophysics **39** (1), 60–67.

Velikhov, Ye. P., M. S. Zhdanov and M. A. Frenkel, 1987, Interpretation of MHD-sounding data from the Kola Peninsula by the electromagnetic migration method: Physics of The Earth and Planetary Interiors, **45** (2), 149–160.

Wang, T., M. Oristaglio, A. Tripp, and G. W. Hohmann, 1994, Inversion of diffusive electromagnetic data by a conjugate-gradient method: Radio Science, **9** (4), 1143–1156.

Zhdanov, M. S., 1981, Continuation of non stationary electromagnetic fields in geoelectrical problems: Izvestia AN SSSR, Physics of the Earth, (12), 60–69.

Zhdanov, M. S., 1984, Analogs of Cauchy type integrals in the theory of geophysical fields (*in Russian*): Moscow, Nauka, 326 pp.

Zhdanov, M. S., 1988, Integral transforms in geophysics: Springer-Verlag, Berlin, Heidelberg, New York, London, Paris, Tokyo, 367 pp.

Zhdanov, M. S., and M. A. Frenkel, 1983a, The solution of the inverse problems on the basis of the analytical continuation of the transient electromagnetic field in reverse time: Journal of Geomagnetism and Geoelectricity, **35**, 747–765.

Zhdanov, M. S., and M. A. Frenkel, 1983b, Electromagnetic migration: in Hjelt, S. E.., Ed., The development of the deep geoelectric model of the Baltic Shield, Part 2, Univ. of Oulu, Oulu, 37–58.

Zhdanov, M. S., and G. W. Keller, 1994, The geoelectrical methods in geophysical exploration: Elsevier, Amsterdam, London, New York, Tokyo, 873 pp.

Zhdanov, M. S., V. U. Matusevich, and M. A. Frenkel, 1988, Seismic and electromagnetic migration: Nauka, Moscow, 376 pp.

Zhdanov, M. S., P. Traynin, and J. Booker, 1996, Underground imaging by frequency domain electromagnetic migration: Geophysics, **61**, 666–682.

Zhdanov, M. S., and P. Traynin, 1997, Migration versus inversion in electromagnetic imaging technique: Journal of Geomagnetism and Geoelectricity, **49**, 1415–1437.

Zhdanov, M. S., and O. Portniaguine, 1997, Time domain electromagnetic migration in the solution of the inverse problems: Geophysical Journal International, **131**, 293–309.

Zhdanov, M. S., 1999, Electromagnetic migration: in deep electromagnetic exploration, Springer-Verlag, Narosa Publishing House, New Delhi, 283–298.

Zhdanov, M. S., 2001, Method of broad band electromagnetic holographic imaging: US Patent 6,253,100 B1.

Zhdanov, M. S., 2002, Geophysical inverse theory and regularization problems: Elsevier, Amsterdam, London, New York, Tokyo, 628 pp.

GEOPHYSICAL ELECTROMAGNETIC METHODS

ELECTROMAGNETIC PROPERTIES OF ROCKS AND MINERALS

10

CONTENTS

Electromagnetic fields are of use in geophysics only because they interact with the medium through which they propagate. This interaction can, under some circumstances, be used to determine certain physical properties of rocks, these being electrical conductivity, dielectric permittivity and magnetic permeability. In this chapter, we will discuss these physical properties from three viewpoints[1]: 1) the physical phenomena which cause the properties to behave as they do, 2) the values of these physical properties for rocks as they exist in the earth, and 3) the way in which these properties respond

---

[1]This chapter was written in collaboration with G. Keller.

to environmental conditions and how they correlate with other physical and geological properties of rocks.

10.1 PROPERTIES AND UNITS

10.1.1 ELECTRICAL CONDUCTIVITY AND RESISTIVITY

Maxwell's equations are coupled to the earth through the *constitutive relationships*. These are a very general set of equations which relate force fields and the effects created in a medium by a force field. For example, Ohm (1827) described a linear relationship between voltage drop and current flow which usually exists when a material is placed in any electromagnetic field. This empirically observed relationship is now universally called *Ohm's law*, and is written as

$$\mathbf{j} = \sigma \mathbf{E}, \tag{10.1}$$

where $\mathbf{j}$ is current density, or current flow in a small cross section, and $\mathbf{E}$ is the electric field intensity, or voltage drop between two closely spaced points. The constant of proportionality which arises in Ohm's law is defined as the *electrical conductivity* of the medium.

In the metric system of units now in wide use, current density is measured in amperes per square meter, and electric field intensity is measured in volts per meter. Conductivity is the ratio of current density to electric field intensity, and so, has the units of amperes×meters/volts×square meters. The ratio of current to voltage in a circuit has been named conductance, S, with its unit value named the siemen. Therefore, logically, the proper unit for conductivity is the siemens per meter.

Because both the electric field intensity, $\mathbf{E}$, and the current density, $\mathbf{j}$, are vectors, the quantity σ, in a general case, must be a tensor of rank 3, which in Cartesian coordinates will have the nine components:

$$\widehat{\sigma} = \begin{bmatrix} \sigma_{xx} & \sigma_{xy} & \sigma_{xz} \\ \sigma_{yx} & \sigma_{yy} & \sigma_{yz} \\ \sigma_{zx} & \sigma_{zy} & \sigma_{zz} \end{bmatrix}. \tag{10.2}$$

The conductivity tensor is symmetric, in that the off-diagonal terms will have symmetrically equal values, $\sigma_{xy} = \sigma_{yx}$, and so on. If two of the coordinate directions are selected to lie in the direction of maximum and minimum conductivity (the principal directions of the conductivity tensor), the nondiagonal terms all become zero, leaving only three components along the principal diagonal:

$$\widehat{\sigma} = \begin{bmatrix} \sigma_{xx} & 0 & 0 \\ 0 & \sigma_{yy} & 0 \\ 0 & 0 & \sigma_{zz} \end{bmatrix}. \tag{10.3}$$

In isotropic materials, the three principal values of conductivity are all the same, and in effect, conductivity is a scalar quantity. In isotropic materials, the electric field vector and the current density vector are collinear; current flows along the direction of the applied electric field. In an anisotropic material, defined as one in which the three principal values of the conductivity tensor are not equal, the current density will not necessarily flow in the direction of the applied electric field. Coincidence

of directions occurs only when the electric field is directed along one of the principal directions of the tensor conductivity.

Anisotropy is a common phenomenon in rocks and minerals. If the dependence of conductivity on direction exists at the molecular level, the anisotropy is said to be intrinsic. However, an aggregate of isotropic minerals in a rock can exhibit a dependence of average conductivity on the direction of the applied electric field, and appear to be anisotropic in bulk. Such behavior is termed *structural anisotropy*.

In rocks and minerals that have structural uniformity in one plane, two of the three principal values of conductivity are equal. Almost always, these two equal values are the maximum conductivity of the material. Such materials are termed *gyrotropic*.

Often, geoelectricians choose to use the term *electrical resistivity* in place of conductivity. For an isotropic material, in which conductivity is scalar, resistivity is defined simply as its reciprocal, $\rho = \sigma^{-1}$, with units of ohm-m.

For an anisotropic material, the resistivity tensor is the inverse of the conductivity tensor.

Despite Ohm's observations, the conductivity of a material need not be a linear property; that is, the conductivity can be a function of current density or electric field intensity. For almost all earth materials, linearity of conductivity as a property is well observed. One exception which is easily recognized is the nonlinearity of current flow in air. When the electric field exceeds a threshold value, breakdown occurs, as in a lightning stroke. In exploration, the electric field intensities never approach the threshold for breakdown.

Conductivity of a mineral or rock need not be a constant. Its value can change with time, temperature, pressure, and various environmental factors.

10.1.2 DIELECTRIC PERMITTIVITY

In formulating the equations that bear his name, Maxwell realized the necessity for explaining the transfer of alternating current through discontinuous circuit elements, such as capacitors. He described the appearance of opposing charges on the two ends of a discontinuous circuit as being an *electric displacement*, measured as charge accumulation per unit area, Q/A, in coulombs per square meter. He then postulated a constitutive equation relating the amount of displacement to the applied electrical force. In differential notation, this constitutive equation has the form:

$$\mathbf{D} = \epsilon \mathbf{E}. \tag{10.4}$$

This equation defines another electrical property of the medium, ϵ, known as the dielectric permittivity. Unlike conductivity, the dielectric permittivity has a well defined value even in the absence of matter, this value being 8.854×10^{-12} farads per meter. Often, values of dielectric permittivity are tabulated as the ratio of the observed dielectric permittivity to the permittivity of free space. In such cases, the ratio is called the *relative dielectric constant*, or more casually, the dielectric constant. For some purposes, it is necessary to use the unscaled value of dielectric permittivity, while in others, only the relative dielectric constant is needed. Care must be taken to understand which value is appropriate to a given application.

In the classical theory of dielectric materials, displacement is attributed to the motion of electrons, atomic nuclei or polar molecules from neutral equilibrium positions to displaced, non-neutral positions
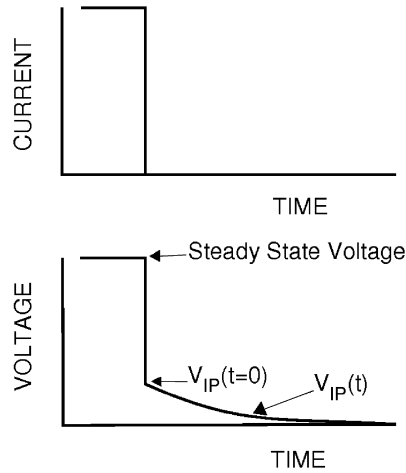
FIGURE 10.1

Characterization of geophysical induced polarization.

under the effect of an applied electric field. The electric field pulls opposite charges apart until the Coulomb force of attraction balances the applied force of the electric field.

Processes similar to displacement occur for many other reasons, including variability of the mobility with which charge can move through a material from point to point, and the occurrence of chemical reactions which store energy during current flow. These processes tend to occur at very low frequencies, and are of interest in geophysical prospecting, forming the basis for the induced polarization method of prospecting.

In geophysical applications, these low frequency polarization effects are measured using one of several pragmatic measures. In field applications, one way of measuring induced polarization is by exciting the earth with a step of current while measuring the voltage wave form with a pair of observation electrodes. The effect of low frequency polarization in the medium is to cause the observed voltage to fall slowly rather than abruptly, giving a transient decay as shown in Fig. 10.1. The induced polarization is measured in terms of the *polarizability* or the *chargeability*, defined respectively as:

Polarizability:

$$\eta_t^T = P_t^T = \Delta V_{IP}(t)/\Delta V, \tag{10.5}$$

where the superscript T indicates the duration of the current step used to excite the earth, the subscript t indicates the length of time after excitation has ceased that the transient voltage ΔV_{IP} is measured, and ΔV is the voltage between the receiving electrodes during excitation. Polarizability is measured in % or mv/v.

Chargeability:

$$M_{t_1,t_2}^T = \frac{1}{\Delta V} \int_{t_1}^{t} \Delta V_{IP} dt, \tag{10.6}$$

where t_1 and t_2 specify the time interval over which the transient voltage is integrated. Chargeability is normally expressed in milliseconds.

Another way to measure the effects of induced polarization is by determining the voltage drop between the receiving electrodes using like currents at different frequencies to excite the earth. As a consequence of induced polarization, the voltage drop observed at the higher frequency will be slightly less than the voltage observed at the lower frequency. The measure of induced polarization is the percentage difference between the two voltages for frequencies which differ by a factor of ten, a quantity named the PFED (percent frequency effect per decade).

10.1.3 MAGNETIC PERMEABILITY

The third of the main constitutive equations which play a role in the application of Maxwell's equations to the earth is that which relates magnetic field strength and magnetic induction:

$$\mathbf{B} = \mu \mathbf{H}, \tag{10.7}$$

where $\mathbf{H}$ is the magnetic field strength and $\mathbf{B}$ is the resulting magnetic induction. The unit of magnetic field strength is the tesla, also called the ampere per meter, while the unit of magnetic induction is the weber per square meter, which is the number of flux lines per square meter.

The constant of proportionality in Eq. (10.7) is the definition of the *magnetic permeability* of the medium. This property serves as the basis for magnetic methods in geophysical exploration, but also plays an essential role in the electromagnetic methods. As with conductivity and dielectric permittivity, the magnetic permeability is a tensor quantity of rank 3, and more often than not is anisotropic.

In contrast to the dielectric permittivity and conductivity properties which are usually considered to be independent of the applied field strengths at the levels used in exploration, magnetic permeability can have a complicated dependence on magnetic field strength.

If no material is present, magnetic permeability takes the value $\mu_0 = 4\pi \times 10^{-7}$ henries per meter for free space.

10.1.4 WAVE NUMBER

In Chapter 4, in solving the diffusion equation, it was established that the wave number for a medium, k, is an important parameter in determining the behavior of an electromagnetic field traveling in a conductive medium. However, the formulation for the wave number given in Eq. (4.122) is incomplete because the effect of displacement currents was ignored. While this is valid in the great majority of applications of electromagnetic theory in exploration geophysics, it will be informative in our discussion of electrical properties of rocks and minerals to establish the range of acceptability of this simplification by including the effect of displacement currents on the wave number for a material. To do this, we replace Eq. (4.116) with its more complete form, Eq. (3.69), which includes a term representing displacement currents:

$$\nabla \times \mathbf{H} = \sigma \mathbf{E} + \epsilon \partial \mathbf{E}/\partial t. \tag{10.8}$$

Using the constitutive equation, $\mathbf{D} = \epsilon \mathbf{E}$, and considering the fields in the frequency domain, Eq. (10.8) becomes:

$$\nabla \times \mathbf{H} = (\sigma - i\omega\epsilon)\mathbf{E}. \tag{10.9}$$

Equations of the set (4.121) become:

$$\nabla^2 \mathbf{H} + i\omega\mu(\sigma - i\omega\epsilon) \mathbf{H} = 0, \tag{10.10}$$

and

$$\nabla^2 \mathbf{E} + i\omega\mu(\sigma - i\omega\epsilon) \mathbf{E} = 0.$$

Thus, the definition of wave number with the inclusion of displacement currents is:

$$\widetilde{k}^2 = i\omega\mu(\sigma - i\omega\epsilon) = i\omega\mu\widetilde{\sigma}$$
$$= \omega^2\mu\epsilon + i\omega\mu\sigma, \tag{10.11}$$

where

$$\widetilde{\sigma} = \sigma - i\omega\epsilon \tag{10.12}$$

is the complex conductivity.

The second term in the definition of $\widetilde{k}^2$ reflects the existence of conduction currents, which dissipate as heat, while the first term reflects the existence of displacement currents, which allow lossless storage of energy. The modulus of the ratio of the term $i\omega\mu\sigma$ to the term $\omega^2\mu\epsilon$ is called the *loss factor*, δ (von Hippel, 1954):

$$\delta = \sigma/\omega\epsilon. \tag{10.13}$$

The loss factor is often expressed as a *loss tangent*:

$$\tan \xi = \sigma/\omega\epsilon. \tag{10.14}$$

A loss tangent of unity divides two important regimes of electromagnetic behavior. At high frequencies, the first term in the expression for the $\widetilde{k}^2$ wave number becomes dominant:

$$\widetilde{k}^2 \approx \omega^2\mu\epsilon. \tag{10.15}$$

In this regime, the wave number, k, is almost entirely real, and propagation of an electromagnetic field takes place without significant attenuation. Displacement currents are very much more important than induction or conduction currents. The electromagnetic field is said to propagate by radiation. Wave length depends on dielectric permittivity, but not on conductivity:

$$\lambda = 2\pi/\omega(\mu\epsilon)^{1/2}. \tag{10.16}$$

At very low frequencies, the second term in the definition of $\widetilde{k}^2$ is dominant:

$$\widetilde{k}^2 = k^2 = i\sigma\mu\omega. \tag{10.17}$$

The dependence on dielectric permittivity disappears (meaning that we can neglect displacement currents), and the wave number has equal real and imaginary parts:

$$k = g + ig. \tag{10.18}$$

In this range the electromagnetic field is said to propagate by diffusion in analogy with the differential equation (Fick's equation), which describes diffusion processes.

10.2 PROPERTIES IN A PARAMETRIC SENSE

The various electrical properties defined with constitutive equations in the preceding section are nominally constants in those equations. However, the electrical properties depend on many factors, some environmental, like temperature and pressure, and others which reflect the character of the rock, such as composition. The physical properties are better termed *parameters*; therefore we choose to call consideration of the relationship between the electrical properties and environmental or composition factors a study of properties in the parametric sense.

10.2.1 ELECTRIC PROPERTIES OF ROCK-FORMING MINERALS AND ROCKS
Conductivity of metals

Materials are classified generally as conductors, semiconductors, and insulators. If the conductivity of a material is greater than 10^5 S/m, it is classed as a conductor; materials with conductivities less than 10^{-8} are classed as insulators; materials in the intermediate range are semiconductors.

These boundaries are somewhat arbitrary, but the mechanisms of conduction differ significantly for materials in these ranges. Mechanisms which are important are metallic conduction, electronic semiconduction, solid electrolytic conduction, and aqueous electrolytic conduction.

Metallic conduction is one of the essential physical phenomena used in defining which materials are metals and which are not. Native metals occur in rocks infrequently, but such occurrences are of some economic importance. Two of the more important native metals are copper and gold. Other metals including platinum, iridium, osmium and iron occur in the elemental form, but are extremely rare, at least at the earth's surface. Carbon occurs commonly in the form of graphite, which exhibits the strange behavior of being a metallic conductor along one crystal plane, but a semiconductor in the third direction.

The Drude theory of metals, developed around 1900, provides a useful simplistic model for visualizing conductivity in metals. In this theory, all of the valence electrons of a metal are viewed as being detached from the nuclei of the metal atoms, forming an unstructured atmosphere, or electron gas. The electrons forming this atmosphere are in ceaseless motion, but in the absence of an applied electric field, there is no net charge transfer in this electron motion to comprise a current.

When an external electric field is applied to a metal, the electrons forming the atmosphere accelerate in the direction of the applied field, producing a current which would increase without limit if it were not for the fact that the electrons occasionally collide with the atomic nuclei in the metal. Such collisions redirect the electrons randomly, limiting the movement along electric field lines. The average time between collisions of a given electron with the atomic framework in the metal is called the relaxation time, τ, or the scattering time. This relaxation time is very short, being typically 10^{-13} seconds. Thus, one expects the conductivity of a metal to be independent of frequency over any frequency range that might be of interest in geophysics.
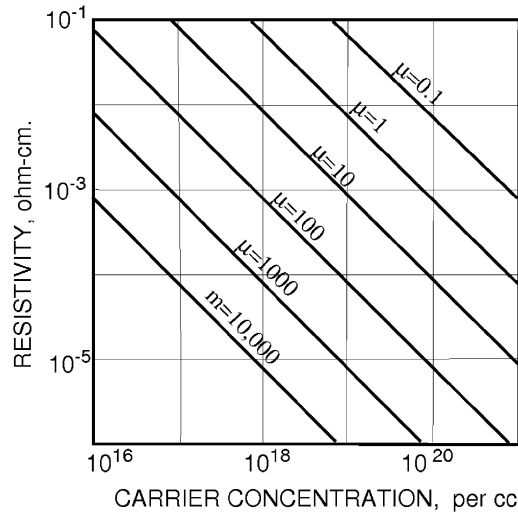
FIGURE 10.2

Conductivity as a function of free electron concentrations for various values of mobility, μ, in cgs units.

Drude's formula for metallic conductivity is:

$$\sigma = ne^2\tau/m^*, \tag{10.19}$$

where n is the number of free electrons per unit volume of the metal, e is the charge of an electron (1.6×10^{-19} coulomb), τ is the scattering time, and m^* is the mass of an electron (9.11×10^{-21} Kg).

The conductivity of a metal as a function of free electron concentration for parametric values of electron mobility is shown in Fig. 10.2. If the atoms of a metal were perfectly ordered, the probability of an electron being scattered would be very small, and the conductivity very high. In reality, imperfections in the crystal structure are always present and such imperfections interfere with the free movement of the electron atmosphere. The metals that occur in nature, such as copper, are rarely pure, but contain admixtures of various other metals. The electrical conductivity of such alloys is always less than the conductivity of the metal serving as solvent in an alloy.

Examples of this are found in Fig. 10.3, which shows graphically the conductivity of copper-based binary alloys for small amounts of dissolved other metals. For low concentrations of the impurity, the conductivity is a simple average of the conductivities of the components.

Thermal motion of metal ions about their equilibrium positions increases their cross section for the scattering of electrons. The higher the temperature, the greater the movement of the atomic nuclei about theoretical rest positions and the greater the probability that each atom will interfere with the freedom of motion of the electron atmosphere. Metals are characterized by a positive coefficient of resistivity.

The resistivities of refined metals and of several naturally occurring metallic minerals are listed in Table 10.1.
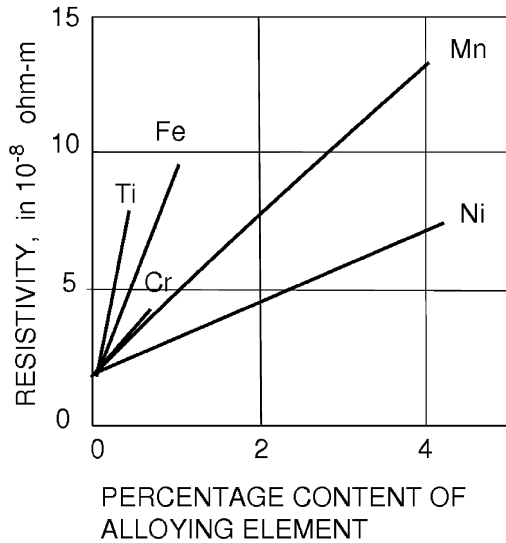
FIGURE 10.3

Resistivity of copper-based binary alloys with small amounts of metals other than copper in solution.

Conductivity of electronic semiconductors

Semiconductors are non-metallic materials in which conduction is by electron motion, but in which conduction is contributed by a significantly smaller number of conduction electrons with lower electron mobilities. Relatively few electrons are free to move through the material in a semiconductor, in comparison with the number of free electrons in a metal.

Semiconductors differ from metals in that a significant amount of energy must be added to electrons before they become dissociated from their home atoms and are free to move thorough the crystal lattice. This energy is most commonly provided as heat. As a consequence, the number of conduction electrons is found to increase with temperature according to the Stefan-Boltzmann law:

$$n_e \propto e^{-E/kT}, \tag{10.20}$$

where n_e is the number of conduction electrons, E is the energy required to raise the energy level of an electron to the point where it is free to move through the lattice, k is Boltzmann's constant ($1.380 \times 10^{-16} \, erg/deg$), and T is the absolute temperature. The activation energy, E, is a characteristic of the material. In materials containing several elements, the activation energy for electrons from different elements will differ. When several atomic species contribute conduction electrons, simple addition of terms like that in Eq. (10.20) is applicable. However, often there is such a difference between activation energies that only the species with the lowest activation energy need be considered in the conduction process.

All materials which are not true metals are electronic semiconductors to a greater or lesser extent. If activation energy is low, the material may be nearly as conductive as a metal. This is the case with many

Table 10.1 Resistivities of naturally occurring and refined metals	
Native copper	1.2 to 30 $\times$ 10^{-8} ohm-meters
Graphite, parallel to cleavage	36 to 100 $\times$ 10^{-8}
Graphite, across cleavage	28 to 9900 $\times$ 10^{-8}
Ulmanite, NiSbS	9 to 120 $\times$ 10^{-8}
Breithauptite, NiSb	3 to 50 $\times$ 10^{-8}
Lithium	8.5 $\times$ 10^{-8}
Beryllium	5.5 $\times$ 10^{-8}
Magnesium	4.0 $\times$ 10^{-8}
Aluminum	2.5 $\times$ 10^{-8}
Titanium	83.0 $\times$ 10^{-8}
Chromium	15.3 $\times$ 10^{-8}
Iron	9.0 $\times$ 10^{-8}
Nickel	6.3 $\times$ 10^{-8}
Refined copper	1.6 $\times$ 10^{-8}
Zinc	5.5 $\times$ 10^{-8}
Molybdenum	4.3 $\times$ 10^{-8}
Palladium	10.0 $\times$ 10^{-8}
Silver	1.5 $\times$ 10^{-8}
Cadmium	6.7 $\times$ 10^{-8}
Tin	10.0 $\times$ 10^{-8}
Antimony	36.0 $\times$ 10^{-8}
Tngsten	5.0 $\times$ 10^{-8}
Platinum	9.8 $\times$ 10^{-8}
Gold	2.0 $\times$ 10^{-8}
Tellurium	14.0 $\times$ 10^{-8}
Lead	19.0 $\times$ 10^{-8}
Bismuth	100. $\times$ 10^{-8}

of the sulfide ore minerals, which have conductivities in the range from a thousand to a million s/m. If the activation energy is large, a material may be nearly a perfect insulator. Most of the silicate minerals require large activation energies to provide conduction electrons, and under normal circumstances, electron conduction in silicates is negligible in comparison with ion conduction, which is discussed in the next two sections.

Inasmuch as the number of electrons available for conduction in semiconductors increases with temperature, such materials usually have a negative temperature coefficient of resistivity; that is, resistivity decreases with increasing temperature. This is not always the case, because increasing temperature also decreases mobility, as it does in metals, and this effect may more than offset the effect of an increased number of conduction electrons. In general, semiconductors may have a positive coefficient for a portion of the temperature range and a negative coefficient for other temperature ranges.
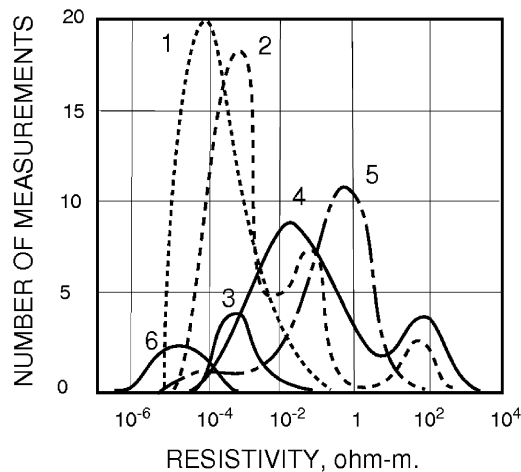
FIGURE 10.4

Histograms for the reported values of the resistivity for common minerals with high conductivity: 1) Bornite; 2) Magnetite; 3) Pyrrhotite; 4) Arsenopyrite; 5) Galena; 6) Covillite.

The important minerals that are semiconductors are the various metal/sulfur and related compounds along with some of the metal oxides. Resistivities for these minerals are listed in Table 10.2. It should be noted that wide ranges of values of resistivity are listed for some minerals, narrow ranges for others. The narrow ranges reported for some minerals probably reflect a small number of measurements rather than a more exact value for the resistivity.

Distributions (histograms) of values of resistivity for several semiconducting minerals for which many measurements have been reported are shown in Fig. 10.4. It is interesting to note that the distributions for several of the minerals show widely separated peaks, suggesting several forms or compositions of these minerals. For example, magnetite shows distribution peaks centered on 3×10^{-4}, 4×10^{-2} and 80 ohm-meters.

Despite the wide ranges of values for each mineral indicated in Table 10.2 and Fig. 10.4, the data suggest several generalizations. With few exceptions (galena, haverite, and molybdenite), the metal sulfides and arsenides are nearly as conductive as true metals. Arsenides and tellurides also have very low resistivity, but these materials may be metallic alloys, rather than semiconducting compounds. The antimony compounds and the metal oxides, except for magnetite, have relatively high resistivities.

Conduction in solid electrolytes

Most rock-forming minerals are solid electrolytes. Electrolytic conduction can take place in ionic bonded crystals. In such crystals, valence electrons are given up by anions to complete the valence shells in companion cations. The cations and ions which have taken part in this exchange of charge are then held together by the coulomb forces between oppositely charged ions. When an external electric field is applied to an ionic bonded crystal structure, the force exerted on each ion by that field is quite

Table 10.2 Resistivities of semiconducting minerals

Sulfides	
Argentite, Ag_2	1.5 to 2.0×10^{-3} ohm-m.
Bismuthinite, Bi_2S_2	3 to 570
Bornite, $Fe_2S_3.nCu_2S$	1.6 to 6000×10^{-6}
Chalcocite, Cu_2S	80 to 100×10^{-6}
Chalcopyrite, Fe_2S_3	150 to 9000×10^{-6}
Covellite	0.30 to 83×10
Galena, PbS	6.8×10^{-6} to 9.0×10^{-2}
Marcasite, FeS_2	1 to 150×10^{-3}
Metacinnabarite, 4HgS	2×10 to 1×10^{-3}
Millerite, NiS	2 to 4×10^{-7}
Molybdenite, MoS_2	0.12 to 7.5
Pyrrhotite, Fe_7S_8	2 to 160×10^{-6}
Pyrite, FeS_2	1.2 to 600×10^{-3}
Oxides	
Braunite, Mn_2O_3	0.16 to 1.0
Cassiterite, SnO_2	4.5×10^{-4} to 10,000
Ilmenite, $FeTiO_3$	0.001 to 4
Cuprite, Cu_2O	10 to 50
Magnetite, Fe_3O_4	52×10^{-6}
Pyrolusite, MnO_2	0.007 to 30
Rutile, TiO_2	29 to 910
Uraninite, UO	1.5 to 200
Tellurides	
Alteite, PbTe	20 to 200×10^{-6}
Calavarite, $AuTe_2$	6 to 12×10^{-6}
Hessite, Ag_2Te	20 to 80×10^{-6}
Sylvanite, $AgAuTe_4$	4 to 20×10^{-6}
Arsenides	
Lollingite, $FeAs_2$	2 to 270×10^{-6}
Nicollite, NiAs	0.1 to 2×10^{-6}
Skutterudite, $CoAs_3$	1 to 400×10^{-6}
Smaltite, $CoAs_2$	1 to 12×10^{-6}
Compounds of arsenic, antimony and sulfur	
Arsenopyrite, FeAsS	20 to 100×10^{-6}
Cobaltite, CoAsS	6.5 to 130×10^{-3}
Energite, Cu_3AsS_4	0.2 to 40×10^{-3}
Tetrahedrite, Cu_3SbS_3	0.30 to 30,000

small compared to the strength of the binding forces. In an ideal crystal, one would not expect any conduction by ion movement, or *solid electrolysis*, to take place.

Crystals are not ideal in nature. Electrolysis does take place when an electric field is applied. Two important types of imperfection in crystals are observed. Inherent defects in the form of atoms of the wrong valence or the wrong nuclear size in the lattice are termed Schottky defects. Breaks in the continuity of the crystal lattice not involving the presence of a strange atom are termed Frenkel defects.

All natural crystals have a greater or lesser number of imperfections in the form of impurity ions of the wrong valence substituted in the lattice, or in the form of ions missing from the lattice. At normal temperatures, all the ions in the lattice vibrate about their rest positions, with the amplitude of movement increasing with increasing temperature. Occasionally an ion will move far enough that it ends up in an interstitial position in the lattice or in a vacant lattice position. Such jumps occur continually, but in random directions so that there is normally no net movement of charge. However, when an external electric field is applied, jumps in the direction of the field are favored statistically over jumps in other directions, and a net transfer of ions takes place. There is current flow through the solid electrolyte when an external electric field is applied.

The frequency with which jumps take place follows a Stefan-Boltzmann law:

$$n_j \propto e^{-U/kT}. \tag{10.21}$$

This equation is very similar to Eq. (10.20), which describes the number of electrons raised to conduction levels in a semiconductor, but here, n is the number of ions dislocated per unit time and U is the height of the potential wall the ion must cross to move out of its lattice position. One might also note the absence of the factor 2 in the exponent in this last equation.

The conductivity of a solid electrolyte should be proportional to the number of ionic charge carriers available at any given time, with the constant of proportionality being determined by the mobility of these ions. The mobility of the ions will depend on the relative sizes of the moving ions and of the interstices in the crystal lattice. Small ions can be expected to move through a lattice more easily than large ions.

In rocks, ions consisting of several (or many) atoms bonded together with covalent bonds are common, particularly with the oxides of silicon and aluminum. In rocks, it is common to have a relatively stable lattice consisting of these super ions. The mobile ions in such a crystal are the small single-nucleus atoms, including sodium, magnesium, and iron. It was found that iron, aluminum, calcium, and sodium are deposited at the cathode after the electrolysis of silicate rock samples at high temperatures.

Conductivity in rocks exhibiting dry electrolytic conductions can usually be reasonably approximated with the equation:

$$\sigma = A_1 e^{-U_1/kT}, \tag{10.22}$$

where A_1 is a reference conductivity determined by the numbers of ions available for conduction and their mobility through the lattice, and U_1 is the activation energy required to liberate these ions. The expression for conductivity (10.22) can be linearized by plotting conductivity or resistivity on a logarithmic scale and temperature on a reciprocal Kelvin scale, as shown in Fig. 10.5. Such plots are called *Arrhenius plots*.
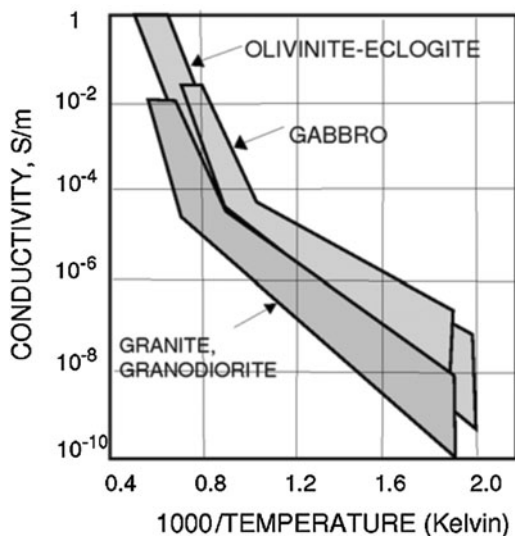
FIGURE 10.5

Generalized Arrhenius plots of conductivity as a function of inverse temperature for igneous rocks with diverse chemical makeup.

It appears that low-temperature conduction is extrinsic in origin, being due to weakly bonded impurities or defects in crystals. The high-temperature conductivity is intrinsic and is due to ions from the regular lattice which have been displaced by thermal agitation.

Extensive studies of the conductivity of rocks and minerals have shown that generally the conductivity in a dry rock at elevated temperature is primarily a function of temperature and to a lesser degree a function of composition (Fig. 10.5). At relatively low temperatures, where extrinsic conduction mechanisms are important, the more acidic rocks tend to have a higher resistivity than the more basic rocks. At high temperatures where intrinsic conduction dominates, there is little variation in conductivity that is caused by compositional differences.

Rocks probably exist in the molten state in and around volcanoes, and possibly at depth in the crust and upper mantle in areas of strong tectonic activity. Mechanisms for conduction in molten rocks are not much different from those in solid electrolytes. The ions in the molten phase may well occupy normal positions in a periodic structure. Thermal energy then dislocates a few ions at a time from their preferred positions in the melt. An external electric field will cause these dislocated ions to move through the melt as an electric current.

Conductivity in aqueous electrolytes

Water, which forms an aqueous electrolyte in the pore spaces of a rock, is the most important factor controlling the electrical conductivity of most rocks we encounter at the earth's surface. The conductivity of a water bearing rock will depend on the amount of water present in the pores, the salinity of this water, the temperature, and the way in which the water is distributed through the rock.

Table 10.3 Ion mobilities in low concentration (at 25°C, meters per second/volts per meter)

H^+	36.2×10^{-8}
OH_4^-	20.5×10^{-8}
$SO^=$	8.3×10^{-8}
Na^+	5.2×10^{-8}
CL^-	7.9×10^{-8}
K^+	7.6×10^{-8}
NO_3^-	7.4×10^{-8}
Li^+	4.0×10^{-8}
HCO_3^-	4.6×10^{-8}

When salt is dissolved in water, the constituent ions separate and move about freely in the solution. With the application of an external electric field, cations in the solution will be accelerated against the electric field, and anions will be accelerated along the electric field. This acceleration is opposed by viscous drag, which limits the maximum velocity to which the ions can be accelerated. The terminal velocity obtained with a unit electric field (1 volt/meter) being applied is defined as the mobility of an ion.

Mobility is a function of both temperature and concentration of salt in solution. Increasing the temperature decreases the viscosity of the water, permitting higher terminal velocities for the same voltage gradient. If the electrolyte contains a high concentration of ions, the motion of one ion may be inhibited by the motion of other ions close to it, reducing the terminal velocity.

Table 10.3 lists ion mobilities for some of the more common ions found in ground water, measured at a reference temperature of 25°C and in dilute solution. The salt ions all have similar mobilities; only the hydrogen and hydroxyl ions have mobilities that are markedly different. Acid and basic solutions are much more conductive for a given concentration than are solutions of salts.

Ground waters are usually close to neutrality. Therefore, it is not necessary to know the chemical makeup of the ground water in order to find its approximate conductivity, but only the concentration of salt in solution. This is further demonstrated by the curves in Fig. 10.6, which depict the conductivity of the electrolytes of common salts, acids, and bases as a function of concentration, also called salinity, at a reference temperature of 18°C.

The effect of concentration and elevated temperature on the resistivity of a solution of sodium chloride is shown in Fig. 10.7 for a temperature range from 0° to 140°C. It should be noted that at 0°, the water has not been frozen to ice because the dissolved salt has lowered the freezing point. At 100° and 140°, sufficient pressure is applied to assure that the water does not turn to steam.

Water in the pore spaces of a rock underground normally is subject to pressure from the overburden so that the vaporization point is never reached. The relationship between conductivity of an electrolyte and temperature under parametric values of pressure is shown in Fig. 10.8. Pure water passes through a critical point at a temperature of 374.15°C. Below this critical point, there is some temperature at which the water converts to steam, and this is characterized by an abrupt transition from an aqueous electrolyte to steam, with an accompanying increase in resistivity. Above the critical point, there is no phase transition, but resistivity continues to increase with temperature as the temperature is raised. The triple point for ground water is uncertain because of the effect of dissolved salts, but it is reasonable to
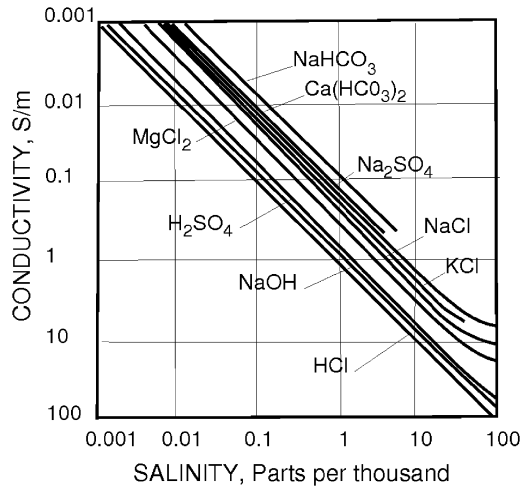
FIGURE 10.6

Dependence of the conductivity of an electrolytic solution on the amount of salt in solution at a temperature of 18°C.
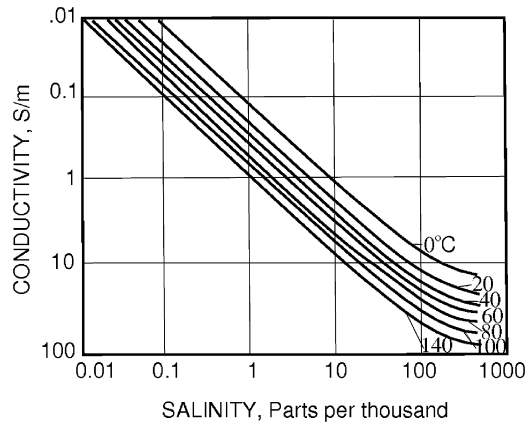
FIGURE 10.7

The effect of concentration and elevated temperature on the resistivity of a solution of sodium chloride for a temperature range from 0° to 140°C.

expect that the critical point is reached someplace within the first few tens of kilometers depth in the earth. At great depths, water should exist in a dense enough form that salts will be ionized and the rock rendered appropriately conductive. Steam and the high resistivity of a dry rock should be observed
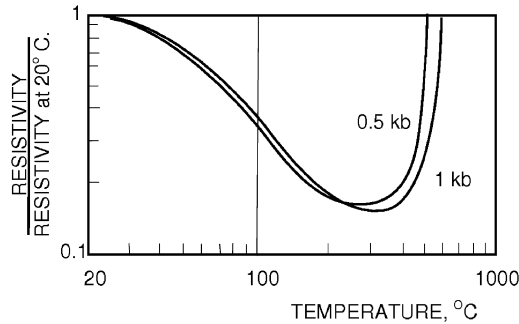
FIGURE 10.8

Relative change in the resistivity of the electrolyte with temperature, normalized to the resistivity at 20°C.

only at quite shallow depths in the earth where unusually high temperatures exist, as in the vicinity of a volcano.

The resistivity of a water bearing rock depends on the amount of water present. A great deal of research has been done in correlating resistivity of a rock and its water content. These have led to the widespread use of an empirical formula relating resistivity and porosity, known as Archie's law:

$$\sigma_t = a\sigma_w W^m, \tag{10.23}$$

where σ_t is the bulk conductivity of the rock, σ_w is the conductivity of the water contained in the pore structure, W is the water content expressed as a volume fraction of rock, and a and m are parameters whose values are assigned empirically to make the equation fit a particular group of measurements. The parameter m is also called the *cementation factor*. Often, in applying Archie's law, the quantity *formation factor* is used. This quantity is defined simply as the ratio of the resistivity of a rock to the resistivity of the water contained in it:

$$F = \sigma_w/\sigma_t. \tag{10.24}$$

In some rocks, part of the pore space may be occupied by air (above the water table) or by natural gas, carbon dioxide, or petroleum, all of which are insulators. In such a case, Archie's law is modified as follows:

$$\sigma_t = a\sigma_w S^n \Phi^m, \tag{10.25}$$

where Φ is the porosity expressed as a volume fraction of the rock, S is the fraction of the pore space filled with water, and n is an empirical parameter termed the *saturation exponent*. The saturation exponent normally has a value close to 2.

Fig. 10.9, a collection of measurements made on small samples of sandstone, shows the scatter typical of such correlation plots of resistivity and water content. The scatter is not the consequence of measurement error, but indicates variability in texture between small rock samples.
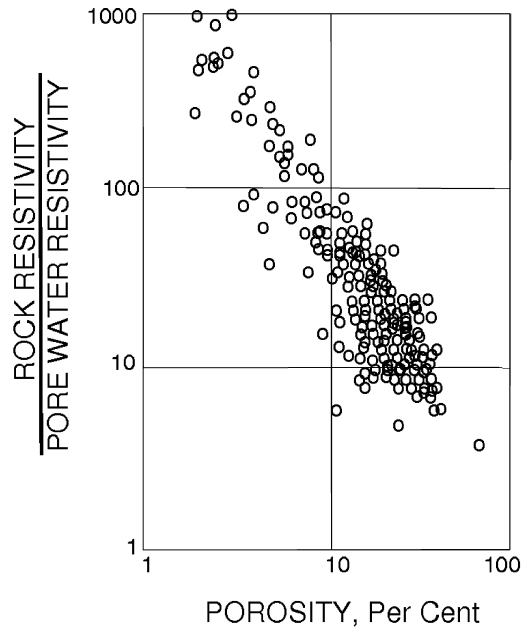
FIGURE 10.9

Scatter plot of pairs of resistivity and porosity values for water-saturated sandstones.

The value for the parameter a varies from slightly less than unity in clastic detrital rocks to values as large as 4.5 in vesicular rocks. The parameter m varies from values slightly greater than unity in dense, fractured rock to values as great as 2.3 in tightly cemented clastic rocks.

The parameters a and m appear to depend on the geometric form of the cross section of the pore along the path of current flow. Pore structures are complicated in form and difficult to describe geometrically, but at least three different styles of pore geometry can be recognized:

- intergranular space in clastic detrital rocks, which is space left over when grains are deposited to form the rock;
- vesicular porosity in rocks such as extruded lavas, where large, poorly connected pores form as expanding gas is frozen in a solidifying lava flow and similar large void spaces develop in dense limestone under the action of percolating ground water;
- fracture, joint, and microcrack pores, usually in crystalline rocks, and vugs or other large, poorly interconnected pore spaces, as in extrusive volcanic rocks.

For a given porosity and water content, fracture porosity will result in the highest rock conductivity of the three classes, while vuggy porosity will result in the lowest conductivity because of the complex geometry of the pores. Generalized resistivity-porosity correlations for rocks in which one of these
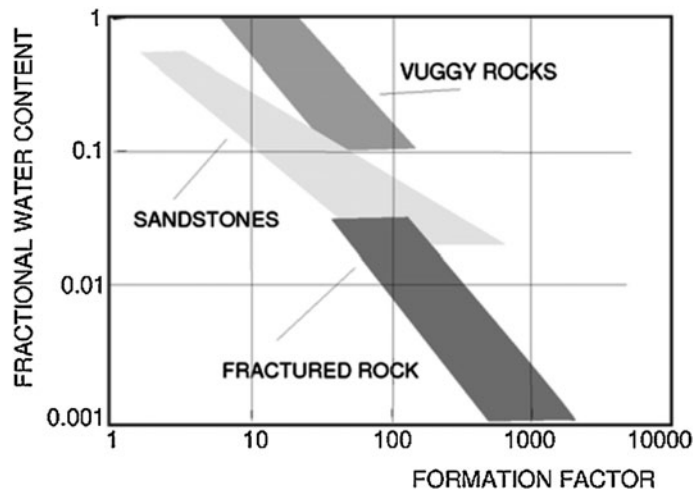
FIGURE 10.10

Generalized resistivity-water content correlations for three types of pore structure: vugs, intergranular spaces, and fractures.

Table 10.4 Forms of Archie's law for various lithologies		
Description of rock	**a**	**m**
Weakly cemented detrital rocks such as sand, sandstone and some limestones, with a porosity range from 25 to 45%, usually Tertiary in age.	0.88	1.37
Moderately well cemented sedimentary rocks, including sandstones and limestones, with a porosity range from 18 to 35%.	0.62	1.72
Well cemented sedimentary rocks with a porosity range from 5 to 25%, usually Paleozoic in age.	0.62	1.95
Highly porous volcanic rocks such as tuff, and pahoehoe, with porosity in the range of 20 to 80%.	3.5	1.44
Rocks with less than 4% porosity including dense igneous rocks and metamorphosed sedimentary rocks.	1.4	1.58

classes of porosity dominates are shown in Fig. 10.10. Values for the parameters a and m for various rock lithologies are listed in Table 10.4.

Interaction between electrolytic solutions and the rock framework

In using Eq. (10.25) to relate bulk resistivity of a rock to the porosity and the resistivity of the water in the pore space, the appropriate value for the water resistivity is not always the same as that which is measured on a sample of water extracted from the pore space. According to Eq. (10.25), the ratio of bulk resistivity to water resistivity is a constant for a given rock sample; it is independent of the resistivity of the water in the pore structure. This ratio is called the *formation factor*. In reality, it is

often found that this ratio is less when a rock is saturated with a dilute saline solution than when a rock is saturated with a highly saline solution. The cause is an increase in the conductivity of the water distributed through the pore space attributable to ionization of clay minerals.

Clay minerals, such as kaolinite, halloysite, montmorillonite, vermiculite, illite, chlorite and others, exhibit a property of absorbing substantial quantities of ions, retaining these ions in an *exchangeable state*. The common exchangeable ions absorbed by clay are Ca, Mg, H, K, Na, and NH_3, in decreasing order of abundance. The quantity of exchangeable ions attached to a clay is usually expressed in terms of the weight of ions in milliequivalents absorbed per 100 *g* of clay.

In clay-water mixtures such as may exist in pore structures, there is usually more water than needed to make the clay plastic, and the exchange ions separate from the clay mineral in a process resembling ionization. The desorbed ions form a mobile cloud around each clay particle. These ions are available to contribute to conduction when an electric field is applied.

Not all exchangeable ions will be desorbed from a clay, so that in fact, the conductivity of the pore water might be less than the value computed for a given content of a specified clay. Also, the mobility of the desorbed ions is less than the mobility of the same ions in a free solution because they remain close to the negatively charged clay particle.

Even in rocks with very low exchange capacities, pore water resistivity rarely appears to exceed 10 ohm-m. In fine-grained rocks, such as shale, apparent water resistivity will always be much lower than expected on the basis of chemical analysis of water extracted from the rock. The added salinity is relatively unimportant if the normal salinity of the pore water is high, but if the pore water is dilute, it is practically impossible to predict the resistivity of the water in the pores unless the ion exchange capacity of the rock is known.

10.2.2 INDUCED POLARIZATION

The charge displacement that occurs as a result of electron, atomic, or molecular polarization represents a balance of forces as bound charge carriers in a material are elastically displaced from their equilibrium positions in the lattice by an externally applied electric field. Other phenomena occur in materials with free charge carriers that result in displacement-like results; these lead to the creation of what geophysicists call *induced polarization*. The measurement of induced polarization has very important applications in exploration for economic mineral deposits.

Induced polarization occurs in any material which exhibits conduction by free charge carriers, and in which the mobility of those charge carriers varies from place to place in the material. A variety of processes gives rise to induced polarization, including oxidation-reduction reactions that occur when an electrolytic conductor is in contact with an electronic conductor, inertial phenomena that occur when the mobility of the free charge carriers varies from place to place, and local changes in the rate of motion of free charge carriers caused by concentrations of fixed charge in the material.

Very pronounced induced polarization occurs in rocks that contain an aqueous electrolyte in pore spaces in contact with electronically conducting minerals. At the boundary between the electrolyte and the solid mineral, as current flows, charge is transferred from ions in solution to electrons in the solid phase. Charge is transferred across the interface either by reduction if an electron from the solid phase is given up to form an anion in the solution, or by oxidation if an electron is released from an ion to the solid phase.

Even when no current is flowing, there is a potential difference between the solid phase and the electrolyte caused by the tendency for the solid to go into solution. For example, if the solid is the iron sulfide mineral pyrite, a few ferrous ions will leave the pyrite grain, and the grain will take on a negative charge. The voltage difference between the solid and a point far distant in the electrolyte is the *electrode potential*, E_e. The electrode potential depends on the specific electron-conducting solid, the nature of the solution in contact with it, and various environmental factors like pressure and temperature.

If, as is the case with most minerals, the solid is relatively insoluble in the electrolyte with which it is in contact, the tendency for ions to go into solution is quickly balanced by the tendency for similar ions already in solution to precipitate onto the solid. An equilibrium condition is established in which the number of ions going into solution equals the number of ions leaving the solution.

When current is caused to flow through such an interface, the number of ions going into solution at one face is increased, and the number coming out of solution at the other face is decreased. In most cases, the ions which take part in this process are more commonly chlorine ions and hydrogen ions, which are abundantly present in normal ground water. The reaction of these ions with the solid phase lead to the formation of hydrochloric acid on one side of the solid conducting grain. This process affects current flow in three ways:

- The reactions at the interfaces of the conductive mineral phase cause gradients in concentrations of one ion or another. This gradient in concentration gives rise to a diffusion potential in accord with the Nernst equation:

$$EMF = \frac{RT}{nF} \ln \frac{c_1}{c_2}, \tag{10.26}$$

  where R is the gas constant, T is the absolute temperature, n is valence, F is Faraday's constant, and c_1 and c_2 are the ion concentrations. When this diffusion potential is added to the normal potential gradient, these local diffusion driven voltages reduce the potential gradient at one interface.
- The oxidation process at one face and the reduction process at the other face usually will not require the same energy. One process will tend to go faster than the other. But, current must be conserved, and to assure this, the potential gradient must be increased at the face where the slower reaction takes place.
- If the mineral grain develops a resistant surface coating from the chemical processes accompanying oxidation or reduction, this too will contribute to the excess resistance to current flow.

All of these factors which require an extra potential gradient to drive a current from an electrolyte into or out of an electronic-conducting solid grain are grouped together under the name *overvoltage*. The added voltage needed to overcome the three processes described above increases as the current density is increased, as one might expect. The relation between overvoltage and current density is known as *Tafel's law*:

$$\eta = a - b \ln j, \tag{10.27}$$

where η is the overvoltage, j is the current density, and a and b are experimentally determined parameters. The parameter b usually falls between 0.09 and 0.13 at room temperatures. The value for the parameter a varies over a wide range, depending on the nature of the electronic conductor and on the properties of the electrolytic solution.

When sulfide grains are distributed in a porous rock, the size of the induced polarization which can be detected with external measurements depends on the textural characteristics of the rock. We will present a quantitative analysis of this phenomenon in a section on the generalized effective-medium theory of induced polarization (GEMTIP) in Chapter 12. In this section we will discuss qualitatively the effect various factors have on the overall resistivity and induced polarization of a mineralized rock:

- The greater the fraction of pores which are blocked by conducting grains, the greater the induced polarization.
- The amount of induced polarization will depend on the size of the sulfide grains. Two opposing factors must be considered; for a given content of conducting mineral, the amount of grain surface in contact with the electrolyte increases as grain size decreases, but the combined internal and surface resistance of a mineral grain increases as the grain size is made smaller, so that a lesser fraction of the total current will flow through pores blocked by such mineral grains. If the conducting mineral is present as a few large grains, the small amount of surface exposed will yield only a small induced polarization effect. On the other hand, if the same amount of conducting mineral is present in very small grains, the surface resistance of these grains may cause the current to flow through unblocked pores, yielding very little induced polarization. One expects that the amount of induced polarization will be greatest at some intermediate grain size.
- For the same conducting mineral content, rocks with a low total porosity will polarize to a greater extent than rocks with high porosity. In the rocks with lower porosity, a greater fraction of the total current is forced to flow through the conducting mineral grains than in high porosity rock. Hence, a small sulfide concentration in a dense igneous rock will cause more noticeable polarization than a larger sulfide concentration in a porous rock such as sandstone.
- The size of induced polarization will depend on the fraction of pore space filled with electrolyte.

Polarization which is virtually indistinguishable from oxidation-reduction effects occurs in most rocks even if they do not contain any electron-conducting minerals. The polarization appears to be caused by spatial variation in the mobility of charge characters. In geophysical exploration, it has been called *background effect*, because it tends to mask the oxidation-reduction polarization effect, which is most useful in exploration for mineral deposits.

In *oxidation-reduction* polarization, the induced polarization arises from the formation of ion accumulations at the surfaces of sulfide grains. Similar ion concentrations occur in any electrolytic conductor in which ion mobility varies from spot to spot. Ions will tend to accumulate at regions where mobility changes, just as cars will pile up behind the turnstiles on a turnpike.

One mechanism by which the mobility of an ion can be changed is by changing the viscous drag encountered as it moves through water. In most rocks, water is said to "wet" the solid minerals lining the pore structure.

The solid minerals carry a surface charge because of their crystal structure. Water molecules, which are polar, are attracted to these surfaces and wet them; that is, the water is absorbed to the solid. The net effect is that a layer of water several molecules thick is held under some pressure against the walls of the pores, with the viscosity of the bound layer of water being significantly higher than the viscosity of free water. As an ion moves through a narrow spot in a pore structure (Fig. 10.11), the contained water is more viscous, slowing the ions. There is a tendency for ions to pile up on the upstream side of such
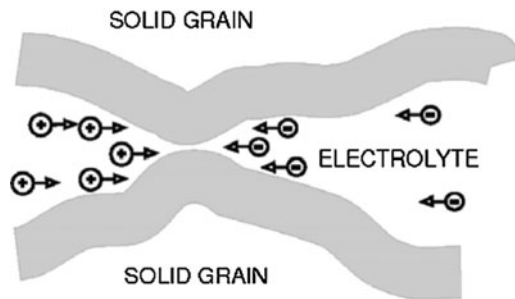
FIGURE 10.11

Illustration of the action of a bound layer of water in sieving the ions as they move through an electrolyte in the pores of a rock.

constrictions, forming cation concentrations on one side of the constriction and anion concentrations on the other. This creates the same effect as a solid conducting mineral blocking the pore.

A mechanism which changes the velocity with which ions move without actually changing their mobility occurs in rocks with fixed electrical charges distributed through the pores. Such charges occur on minerals which exhibit the phenomenon of ion exchange. When such minerals are in contact with water, they electrolyze, with ions from exchange positions in the crystal lattice going into solution. After ionization, the mineral particle left behind forms a highly charged, immobile ion which partially blocks ion movement through the pore in which it is situated. The electric field from this particle modifies the normal potential gradient causing current flow so that there are areas of abnormally low gradient on one side of the mineral particle and areas of abnormally high gradient on the other side. Ions will move slowly in areas of low gradient, causing an increase in concentration.

10.2.3 DIELECTRIC PROPERTIES OF ROCK-FORMING MINERALS

The processes contributing to dielectric displacement and polarization are classified as being electronic, atomic, molecular, and space-charge based. In electron polarization, the orbits of electrons in a material are shifted with respect to the atomic nucleus when an external electric field is applied, giving rise to polarization. Because the charge-to-mass ratio in an electron is very large, the displacement of the electron population takes place very rapidly. The electronic contribution to polarization is easy to evaluate at optical frequencies because it can be calculated from the optical index of refraction. These indices have been measured in great numbers in optical mineralogy, and extensive lists are available in handbooks on mineralogical properties. The relationship between the dielectric constant and index of refraction, n, is

$$K_e = n^2, \tag{10.28}$$

where K_e is the ratio of dielectric permittivity in a material to the dielectric permittivity of free space, ϵ/ϵ_0. A short list of values of dielectric permittivity of minerals is given in Table 10.5.

At lower frequencies, atomic polarization becomes significant. Because of the much lower charge-to-mass ratio of the atomic nucleus, atomic polarization develops more slowly than electron polariza-

Table 10.5 Dielectric permittivities of minerals

Mineral	Dielectric constant, pF/m
Galena, PbS	158
Sphalerite, ZnS	69.7
Corundum, Al_2O_3	97.2 to 117
Hematite, Fe_2O_3	207 to 212
Rutile, TiO_2	221
Water, H_2O	81.4
Halite, NaCl	50.4 to 54.8
Fluorite, CaF_2	55.4 to 60.0
Sylvite, KCl	38.8 to 54.8
Aragonite, $CaCO_3$	57.1 to 86.0
Calcite, $CaCO_3$	69.0 to 75.2
Dolomite, $CaMg(CO_3)_2$	60.1 to 70.7
Apatite, $Ca_5(F,Cl)(PO_4)_3$	65.5 to 92.8
Anglesite, $PbSO_4$	644 to 4400
Anhydrite, $CaSO_4$	50.5 to 55.7
Barite, $BaSO_4$	69.5 to 109
Celestite, $SrSO_4$	67.2
Gypsum, $CaSO_4.2H_2O$	47.7 to 106
Analcime, $NaAlSi_4H_2O$	52.0
Augite, $Ca(Mg,Fe,Al)(Al,Si)_2O_6$	61.0 to 76.0
Beryl, $Be_3Al_2Si_6O_{18}$	50.2 to 58.3
Biotite, $K(Mg,Fe)3AlSi3O10(OH)_2$	54.8 to 70.7
Epidote, $Ca(Al,Fe)_3(SiO_4)_3OH$	67.3 to 136
Leucite, $KAlSi_2O_6$	63.0
Muscovite, $KAl_3Si_3O_{10}(OH)_2$	54.8 to 70.7
Plagioclase	
var. Albite	48.2 to 49.1
var. Oligoclase	53.3 to 53.6
var. Andesine	54.8 to 57.2
var. Labradorite	57.6 to 58.5
var. Anorthite	62.3 to 64.0
Quartz, SiO_2	36.4 to 37.8
Sericite	173 to 224
Topaz, $Al_2SiO_4(F,OH)_2$	55.7 to 59.2
Zircon, $ZrSiO_4$	76.0 to 106

tion when an external electric field is applied. Even so, polarization occurs in less than a microsecond even for heavy atoms, and at frequencies near the optical range for light atoms. The force which prevents the atomic nucleus from accelerating without limit when an electric field is applied is the bonding force within the lattice. These bonding forces are not so easy to measure as is the index of refraction, so the determination of dielectric permittivity when atomic polarization is present is not as easy as in the case of electron polarization alone.
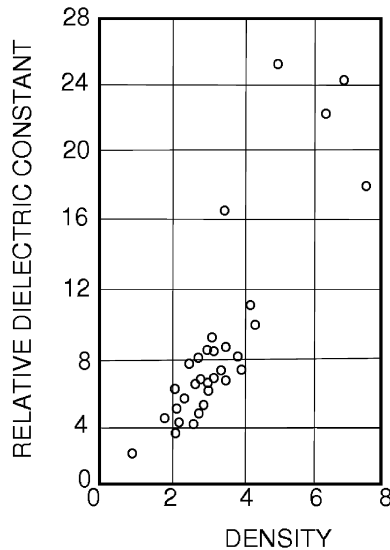
FIGURE 10.12

Correlation between the relative dielectric constant and density in minerals.

One might expect that the greater the number of atoms per unit volume in a material, the higher will be the dielectric permittivity of a material. Indeed, a correlation between the dielectric permittivity of minerals and density is observed (Fig. 10.12).

Molecular polarization can occur in materials which contain polar molecules, or molecules that have asymmetric charge structure and possess a permanent electric dipole moment (*dipole moment = charge × separation*). The polar molecule which commonly occurs in rocks is water. In water, the center of charge for the two hydrogen atoms is offset from the center of charge for the oxygen atom. When an external electric field is applied, such a molecule will rotate to align its dipole moment with the direction of the applied field. The rotation comprises a momentary electric current. During rotation, there is an effective displacement current, and on the completion of rotation, polarization will exist. The speed of rotation depends primarily on the tightness with which the water molecule is held in place.

In liquid water, the molecule rotates rapidly, and polarization occurs in a very short times. It can be seen from Fig. 10.13 that molecular polarization is fully developed in liquid water at frequencies below a few gigahertz. Liquid water exhibits the highest values of dielectric permittivity of any of the common rock-forming materials.

In ice, also a common component of rocks, molecules meet more viscous resistance to rotation when an electric field is applied than in liquid water. Molecular polarization is fully developed only at frequencies below several kilohertz at temperatures just below the freezing point (Fig. 10.14). At very cold temperatures, significant molecular polarization does not develop at frequencies above a few tens of hertz.
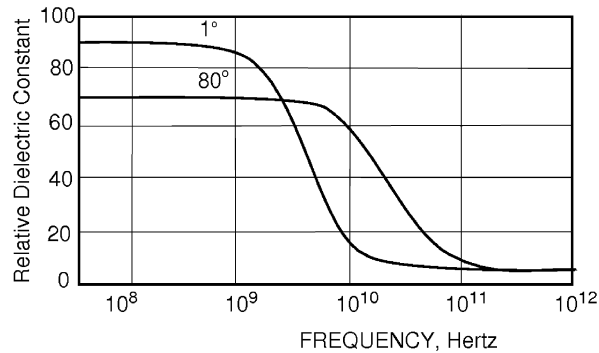
FIGURE 10.13

Molecular polarization in liquid water at a temperature of 1°C.
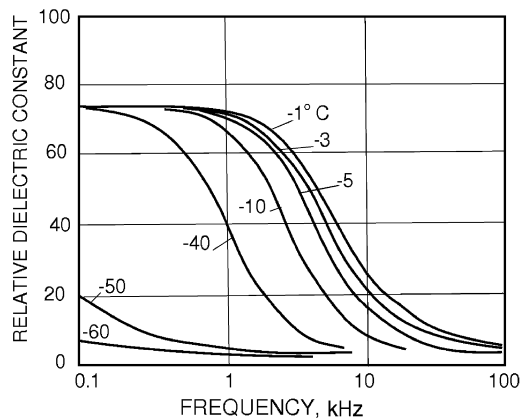
FIGURE 10.14

Relative dielectric constant of ice at various temperatures.

When displacement occurs in a material, there is a displacement current represented by the movement of charge from rest positions to displaced positions. This current persists for only a limited time, lasting from the moment at which the charge is first caused to move by the applied electric field to the moment at which the elastic restoring force brings the motion of the charge to a virtual halt. Over this time range, both the dielectric permittivity and the conductivity of the medium will vary with frequency.

One of the simpler frequency-dependent behaviors in electrical properties is caused by electron resonance, which is characterized by simple harmonic motion of an electron in its orbit when an oscil-
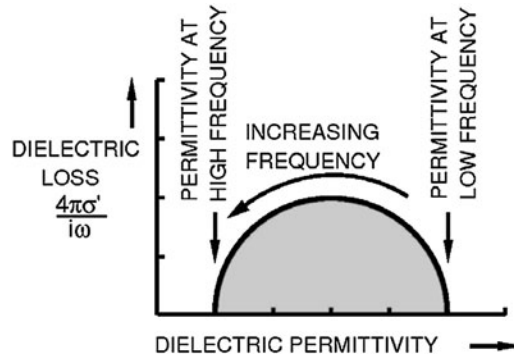
FIGURE 10.15

A Cole-Cole plot of the frequency-dependent behavior of the dielectric permittivity in a complex plane.

latory field is applied:

$$\epsilon - \epsilon_\infty = \frac{\epsilon_s - \epsilon_\infty}{1 + \omega^2 \tau}, \tag{10.29}$$

where ϵ_∞ is the high-frequency limit of relative dielectric constant, ϵ_s is the low-frequency limit, and τ is the time constant for resonance of the electron.

This behavior is often characterized graphically by a plot in the complex plane (a Cole-Cole plot), as shown in Fig. 10.15. On this plot, the imaginary response is considered to be dielectric permittivity and the real response is considered to be dielectric loss. The form of the plot is a semicircle centered on the horizontal axis. Each point along this semicircle represents a specific frequency, increasing from right to left. The intercepts of the circle on the dielectric permittivity axis occur at the values for dielectric permittivity at very high and very low frequencies, where the displacement has not yet started and where the displacement is complete.

In dealing with real materials, the physical law governing dispersion is more complicated than that for simple harmonic motion. Often, if not always, the Cole-Cole plot has the form of an arc of a circle with the origin dropped beneath the real axis, and is described by the equation:

$$\epsilon = \epsilon_\infty + (\epsilon_0 - \epsilon_\infty)/(1 + i\omega\tau)^{1-\alpha}, \tag{10.30}$$

where α is a parameter characteristic of the material.

In ideal dielectric materials, no conduction occurs except by displacement currents. In real materials, some conduction by free charge carriers takes place in addition to displacement currents. Total conduction is the sum of two components, one being by free charge carriers, and which is largely independent of frequency, and the other being by the displacement of bound charge carriers, which is strongly frequency dependent:

$$\sigma_{total} = \sigma_{AC} + \sigma_{DC}. \tag{10.31}$$
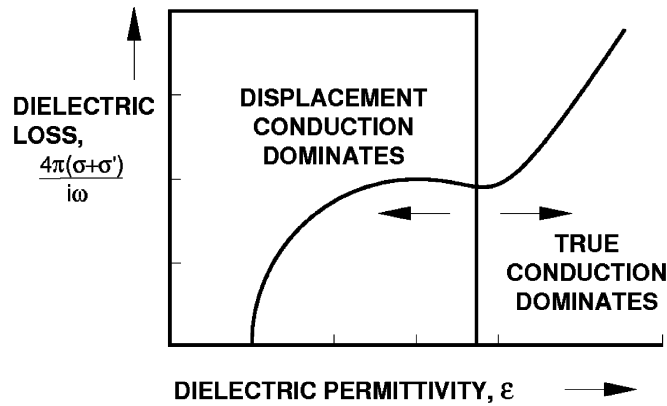
FIGURE 10.16

Cole-Cole plot for a material which exhibits both displacement current conduction and ohmic current.

On a Cole-Cole plot, the pattern is as shown in Fig. 10.16; it consists of a portion of a circular arc for high frequency behavior, with a transition to a rising straight line for low frequency behavior. The transition from the circular plot to the linear plot depends on the relative importance of displacement currents and conduction currents. With strong conduction currents, the linear portion of the plot becomes dominant.

10.2.4 MAGNETIC PROPERTIES OF MINERALS

Magnetic permeability might not be considered as an electrical property of a material, but knowledge of its value is necessary in the examination of how an electromagnetic field interacts with a material.

Most minerals behave as diamagnetic or paramagnetic materials. Rotating electrons align themselves with or against an applied magnetic field. This field may be the earth's ambient magnetic field, but in our case, we are more interested in the magnetic fields arising from current flow in the medium. Magnetic permeabilities for diamagnetic and paramagnetic minerals differ from that for free space by only a few tens or hundreds of parts per million.

A few minerals exhibit ferromagnetism, an intense magnetic polarization which can occur in some materials when large groups of atoms, termed magnetic domains, orient themselves in unison to cause a large enhancement of the magnetic field. Values for the magnetic permeability of some ferromagnetic minerals are listed in Table 10.6.

The most common ferromagnetic mineral is magnetite, and so, in most cases the magnetic permeability of a rock is determined by its magnetite content. Fig. 10.17 shows a scatter plot of values of the content of magnetite in rock and its magnetic permeability.

Ferromagnetic materials are characterized by a *Curie point* or temperature above which the material no longer exhibits ferromagnetism. Depending on the thermal gradient in the earth, rocks beyond a few tens of kilometers of depth probably will not exhibit any ferromagnetism, and the permeability can confidently be expected to be the same as that of free space.

Table 10.6 Magnetic permeabilities of minerals, H/m

Mineral	Magnetic permeability
Magnetite	2.5 to 16
Siderite	1.0035
Hematite	1.0004 to 1.001
Ankerite	1.00025
Pyrite	1.000045
Chalcopyrite	1.00035
Malachite	1.00035
Cassiterite	1.00088
Pyrolusite	1.0013
Arsenopyrite	1.0024
Chromite	1.0024
Chalcopyrite	1.06
Pyrrhotite	2.5
Ilmenite	1.36
Augite	1.0015
Hornblende	1.00015
Magnesite	1.000250 to 1.000500
Calcite	0.999988 to 0.999994
Sylvite	0.999986 to 0.999990
Anhydrite	0.999986
Graphite	0.999990
Quartz	0.999985 to 0.999988
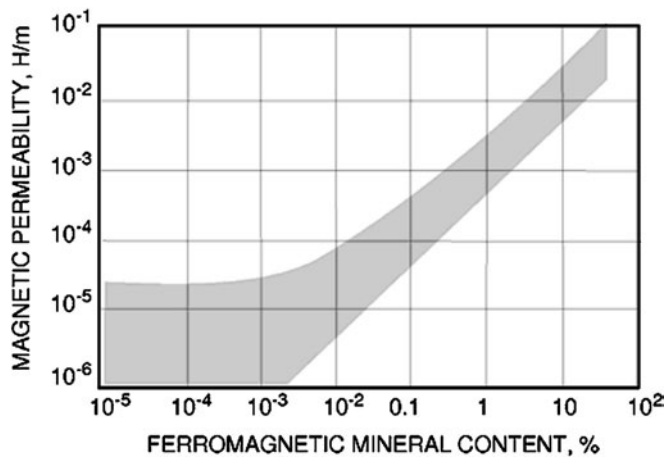
FIGURE 10.17

Correlation between magnetic permeability and the content of ferromagnetic minerals in intrusive rocks (after Dortman, 1992a, 1992b, 1992c).

10.3 EFFECTIVE CONDUCTIVITY OF HETEROGENEOUS MULTIPHASE ROCKS

10.3.1 MIXTURE OF CONDUCTIVE MINERALS IN A HOST ROCK

In most rocks at the earth's surface, the water contained in rocks accounts for rock conductivity. The presence of conductive ore minerals in rocks can be of great economic importance, but there is far less information available on the bulk resistivity of rocks containing such minerals than there is for rocks containing electrolytic solutions of ground water.

As in the case of aqueous electrolytes, the geometric description of the way in which conducting minerals are distributed through a rock is important in determining the bulk resistivity, as are the amount of conducting mineral, and its conductivity.

Habit, or the usual crystal form taken by a specific mineral, is highly variable in solid conducting minerals. Some minerals have an acicular habit, or tendency to crystallize as long, thin needles, often forming a dendritic pattern in the host rock. Perhaps the most important of such minerals is acicular hematite (Fig. 10.18), which forms conducting networks in the rock at quite low concentrations. Specular hematite has the same chemical composition, but crystallizes as discrete crystals within the host rock. It takes far less dendritic hematite than specular hematite to cause a significant reduction in rock resistivity.

Graphite is an important mineral in terms of the effect it has on rock resistivity when it is present. Graphite often tends to occur as very thin crystal sheets; these sheets coat mineral boundaries, or fracture surfaces, providing continuous paths for current conduction. A graphite content of even a few percent will render a rock highly conductive.

Graphite and hematite are not often the conducting minerals of primary interest in commercial ore deposits. For common metal sulfides and related minerals, often a relatively large concentration of ore mineral is required before the resistivity of the rock in which they occur is significantly reduced. Generally, a mineralized rock must have a conducting mineral content of several tens of percent (by weight) before the bulk resistivity becomes anomalously low (Fig. 10.19).

It is important to have a quantitative method, which would allow us to calculate the bulk conductivity of a complex rock formed by a mixture of conductive minerals and a host rock. Fortunately, there exists a very well developed effective-medium theory, which provides a solution of this problem (e.g., Stroud, 1975; Sihvola, 1999).

10.3.2 PRINCIPLES OF THE EFFECTIVE-MEDIUM THEORY

In this and the next sections, we will review the basic principles of the generalized effective-medium approach following the original paper by Zhdanov (2008a, 2008b). Our goal is to construct realistic electrical models of complex multiphase heterogeneous rocks. We begin our modeling with an example taken from a typical quartz monzonite porphyry (QMR). Fig. 10.20, left panel, presents a typical slice of a QMP rock sample. It contains grains of different minerals: quartz, feldspar, pyrite, chalcopyrite, and biotite. The right panel in the same figure is a schematic multiphase composite model of the same rock sample with the grains represented by spherical and elliptical inclusions of different sizes and orientations.

Note that, in principle, one can consider a schematic multiphase model of a reservoir rock sample as well (Fig. 10.21, left panel).
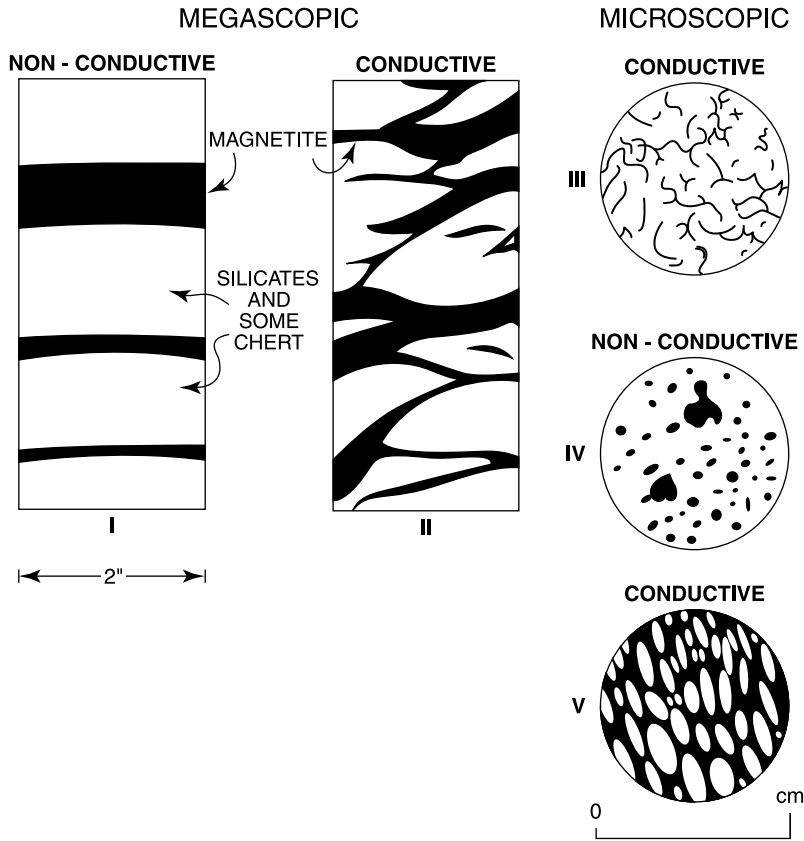
FIGURE 10.18

Polished sections of a rock showing various crystal habits of hematite.

Figs. 10.20 and 10.21 (left panel) show that we can represent a complex heterogeneous rock formation as a composite model formed by a homogeneous host medium of a volume V with a (complex) conductivity tensor $\widehat{\sigma}_0(\mathbf{r})$ (where $\mathbf{r}$ is an observation point) filled with grains of arbitrary shape and conductivity. In the present problem, the rock is composed of a set of N different types of grains, the lth grain type having a (complex) tensor conductivity $\widehat{\sigma}_l$. The grains of the lth type have a volume fraction f_l in the medium and a particular shape and orientation. Therefore, the total conductivity tensor of the model, $\widehat{\sigma}(\mathbf{r})$, has the following distribution for volume fraction f_l and volume fraction $f_0 = \left(1 - \sum_{l=1}^{N} f_l\right)$, respectively:

$$
\widehat{\sigma}(\mathbf{r}) = \begin{cases} \widehat{\sigma}_0 \text{ for volume fraction } f_0 = \left(1 - \sum_{l=1}^{N} f_l\right) \\ \widehat{\sigma}_l \text{ for volume fraction } f_l . \end{cases}
$$
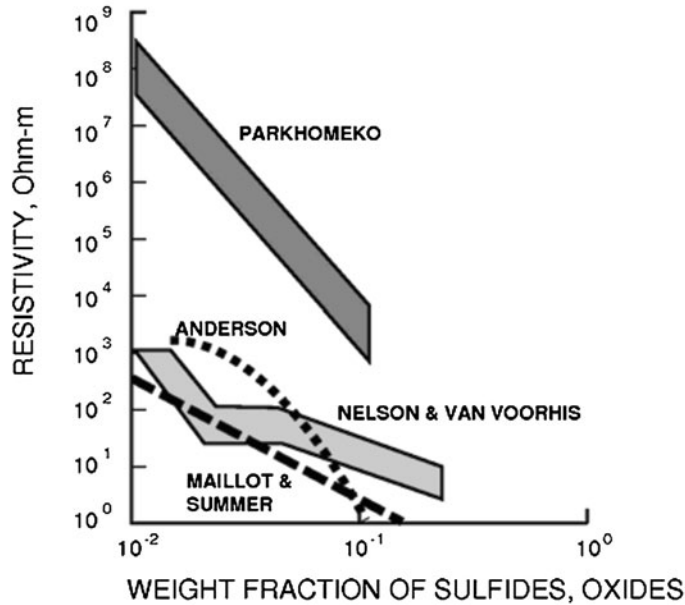
FIGURE 10.19

Correlations between rock resistivity and the content of conductive minerals as reported by various researchers.

The basic idea of the effective-medium theory (EMT) can be explained as follows (Stroud, 1975; Zhdanov, 2008a, 2008b). We substitute a homogeneous effective medium with the conductivity tensor $\widehat{\sigma}_e$ for the original heterogeneous composite model (Fig. 10.21) and subject it to a constant electric field, $\mathbf{E}^b$, equal to the average electric field in the original model:

$$\mathbf{E}^b = \langle \mathbf{E} \rangle = V^{-1} \iiint_V \mathbf{E}(\mathbf{r}) \, dv. \tag{10.32}$$

The effective conductivity is defined from the condition that the current density distribution $\mathbf{j}_e$ in an effective medium is equal to the average current density distribution in the original model:

$$\mathbf{j}_e = \widehat{\sigma}_e \cdot \mathbf{E}^b = \widehat{\sigma}_e \cdot \langle \mathbf{E} \rangle = \langle \widehat{\sigma} \cdot \mathbf{E} \rangle. \tag{10.33}$$

In order to find the effective conductivity tensor $\widehat{\sigma}_e$, we represent the given inhomogeneous composite model as a superposition of a homogeneous infinite background medium with the conductivity tensor $\widehat{\sigma}_b$ and the anomalous conductivity $\Delta \widehat{\sigma}(\mathbf{r})$:

$$\widehat{\sigma}(\mathbf{r}) = \widehat{\sigma}_b + \Delta \widehat{\sigma}(\mathbf{r}). \tag{10.34}$$

Note that this representation is not unique. There exist different methods of selecting the appropriate background conductivity $\widehat{\sigma}_b$. Some of these methods will be discussed below.
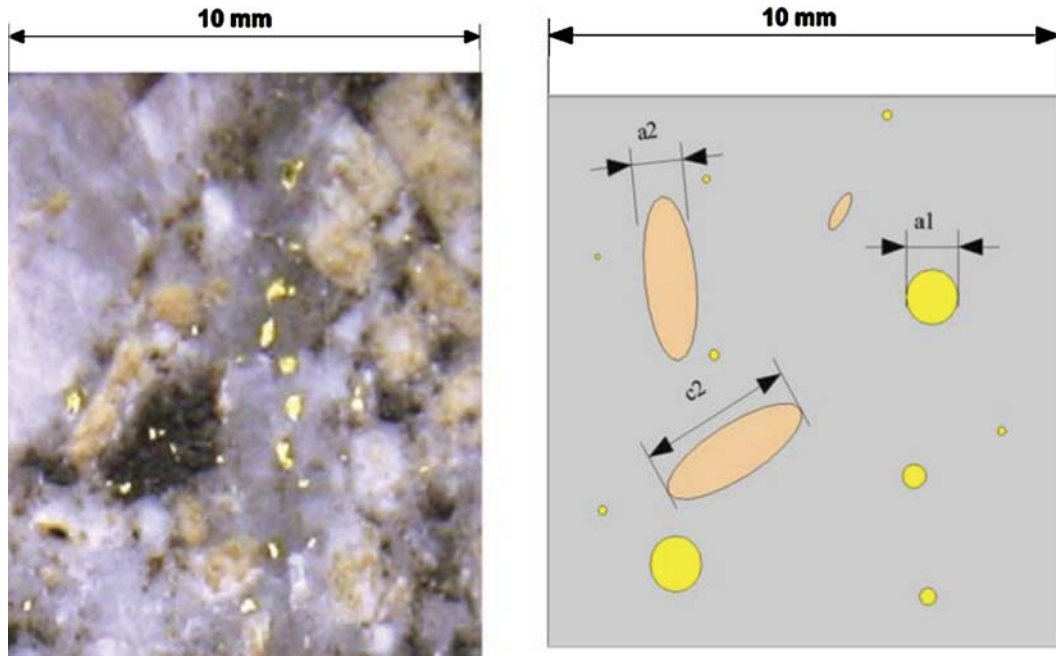
FIGURE 10.20

Multiphase composite model of general heterogeneous rocks. The left panel, presents a typical slice of a quartz monzonite porphyry (QMP) rock sample. The right panel in the same figure is a schematic multiphase composite model of the same rock sample with the grains represented by spherical and elliptical inclusions.

From Eqs. (10.34) and (10.33), we have

$$\widehat{\boldsymbol{\sigma}}_e \cdot \mathbf{E}^b = \widehat{\boldsymbol{\sigma}}_b \cdot \mathbf{E}^b + \langle \Delta\widehat{\boldsymbol{\sigma}} \cdot \mathbf{E} \rangle. \tag{10.35}$$

Thus, we can see that the effective conductivity tensor, $\widehat{\boldsymbol{\sigma}}_e$, can be found from Eq. (10.35), if one determines the average excess electric current $\langle \Delta\widehat{\boldsymbol{\sigma}} \cdot \mathbf{E} \rangle$. The last problem can be solved using the integral form of Maxwell's equations.

Following the ideas of the QL approximation (Chapter 7), we can represent the electric field as

$$\mathbf{E}\left(\mathbf{r}'\right) = \left(\widehat{\mathbf{I}} + \widehat{\boldsymbol{\lambda}}\left(\mathbf{r}'\right)\right) \cdot \mathbf{E}^b, \tag{10.36}$$

where $\widehat{\boldsymbol{\lambda}}\left(\mathbf{r}'\right)$ is an electrical reflectivity tensor, and

$$\Delta\widehat{\boldsymbol{\sigma}}\left(\mathbf{r}'\right) \cdot \mathbf{E}\left(\mathbf{r}'\right) = \widehat{\mathbf{m}}\left(\mathbf{r}'\right) \cdot \mathbf{E}^b, \tag{10.37}$$
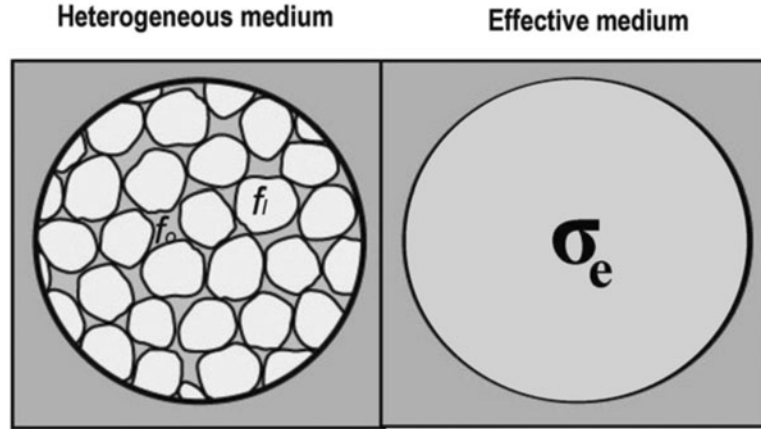
FIGURE 10.21

The left panel shows a schematic multiphase heterogeneous model of a reservoir rock sample. The right panel represents a corresponding effective-medium model.

where $\widehat{\mathbf{m}}(\mathbf{r}')$ is a material property tensor (which is similar to the susceptibility tensor in the theory of the EM field propagation in dielectrics):

$$\widehat{\mathbf{m}}(\mathbf{r}') = \Delta\widehat{\boldsymbol{\sigma}}(\mathbf{r}') \cdot \left(\widehat{\mathbf{I}} + \widehat{\boldsymbol{\lambda}}(\mathbf{r}')\right). \tag{10.38}$$

It is important to emphasize that exact representations (10.36) and (10.37) always exist because the corresponding material property tensor can always be found for any given fields $\mathbf{E}(\mathbf{r}')$ and $\mathbf{E}^b$ (Zhdanov, 2002). In the current problem we explicitly use this special case when the QL approximation is not an approximation but an exact form of the field representation.

Let us substitute (10.37) into (10.33), taking into account (10.34):

$$\mathbf{j}_e = \widehat{\boldsymbol{\sigma}}_e \cdot \mathbf{E}^b = \langle\widehat{\boldsymbol{\sigma}} \cdot \mathbf{E}\rangle = \langle(\widehat{\boldsymbol{\sigma}}_b + \Delta\widehat{\boldsymbol{\sigma}}) \cdot \mathbf{E}\rangle$$
$$= \widehat{\boldsymbol{\sigma}}_b \cdot \langle\mathbf{E}\rangle + \langle\Delta\widehat{\boldsymbol{\sigma}} \cdot \mathbf{E}\rangle = \widehat{\boldsymbol{\sigma}}_b \cdot \mathbf{E}^b + \langle\widehat{\mathbf{m}}\rangle \cdot \mathbf{E}^b.$$

From the last equation we see that

$$\widehat{\boldsymbol{\sigma}}_e = \widehat{\boldsymbol{\sigma}}_b + \langle\widehat{\mathbf{m}}\rangle. \tag{10.39}$$

Thus, in order to determine the effective conductivity of the composite medium, we have to find the average value of the material property tensor, $\langle\widehat{\mathbf{m}}\rangle$.

One can represent the electric field $\mathbf{E}(\mathbf{r})$ generated in a homogeneous anisotropic background medium by the currents induced within the anomalous conductivity $\Delta\widehat{\boldsymbol{\sigma}}(\mathbf{r})$ using the integral form of the Maxwell's equations:

$$\mathbf{E}(\mathbf{r}) = \mathbf{E}^b + \iiint_V \widehat{\mathbf{G}}_b(\mathbf{r} \mid \mathbf{r}') \cdot \left[\Delta\widehat{\boldsymbol{\sigma}}(\mathbf{r}') \cdot \mathbf{E}(\mathbf{r}')\right] dv', \tag{10.40}$$

where V is the volume occupied by all inhomogeneities, and $\widehat{\mathbf{G}}_b\left(\mathbf{r} \mid \mathbf{r}'\right)$ is a Green's tensor for the homogeneous anisotropic full space.

In order to simplify further discussion, we assume that the background model is represented by the isotropic homogeneous full space $\widehat{\boldsymbol{\sigma}}_b = \widehat{\mathbf{I}}\sigma_b$. We also restrict our discussion of the effective-medium theory to the quasi-static case, when $a_l/w_l << 1$, a_l is the characteristic size of a grain of the lth type, and w_l is a wavelength in that grain. This restriction means that we do not consider high frequencies or high contrasts of electrical resistivity in our model to simplify further derivations. In this case the Green's tensor can be represented in the form of a dyadic function:

$$\widehat{\mathbf{G}}_b\left(\mathbf{r} \mid \mathbf{r}'\right) = \nabla\nabla' g_b\left(\mathbf{r} \mid \mathbf{r}'\right), \tag{10.41}$$

where:

$$g_b\left(\mathbf{r} \mid \mathbf{r}'\right) = \frac{1}{4\pi\sigma_b\left|\mathbf{r} - \mathbf{r}'\right|}. \tag{10.42}$$

Substituting expression (10.37) into Eq. (10.40), we can write:

$$\mathbf{E}\left(\mathbf{r}\right) = \mathbf{E}^b + \iiint_V \widehat{\mathbf{G}}_b\left(\mathbf{r} \mid \mathbf{r}'\right) \cdot \left[\widehat{\mathbf{m}}\left(\mathbf{r}'\right) \cdot \mathbf{E}^b\right] dv. \tag{10.43}$$

We can represent the integrals in Eq. (10.43) as a sum of the integrals over the volumes and surfaces of all grains:

$$\mathbf{E}\left(\mathbf{r}\right) = \mathbf{E}^b + \sum_l \mathbf{E}_l\left(\mathbf{r}\right), \tag{10.44}$$

where:

$$\mathbf{E}_l\left(\mathbf{r}\right) = \iiint_{V_l} \widehat{\mathbf{G}}_b\left(\mathbf{r} \mid \mathbf{r}'\right) \cdot \left[\widehat{\mathbf{m}}\left(\mathbf{r}'\right) \cdot \mathbf{E}^b\right] dv'. \tag{10.45}$$

We have already noted that, we are restricting our discussion to the low-frequency approximation (quasi-static model of the field). In this case, we can use a QL approximation (Chapter 7) for the integrals over V_l and S_l and assume that the material property tensor is constant in V_l up to its boundary S_l:

$$\widehat{\mathbf{m}}\left(\mathbf{r}'\right) = \widehat{\mathbf{m}}_l, \quad \mathbf{r}' \in V_l. \tag{10.46}$$

Note, however, that in the case of spherical or elliptical grains the material property tensor is always constant within the spherical and/or elliptical inclusions. The rigorous proof of this simple property of the material property tensor comes from an analytical expression for the electric field of the elliptical inclusions in the homogeneous background, which can be found, for example, in Landau et al. (1984).

Consider now the integrals over one grain only:

$$\mathbf{E}_l\left(\mathbf{r}\right) = \iiint_{V_l} \widehat{\mathbf{G}}_b\left(\mathbf{r} \mid \mathbf{r}'\right) dv' \cdot \widehat{\mathbf{m}}_l \cdot \mathbf{E}^b. \tag{10.47}$$

We introduce the *volume*, $\widehat{\boldsymbol{\Gamma}}_l$, depolarization tensor as follows:

$$\widehat{\boldsymbol{\Gamma}}_l = \iiint_{V_l} \widehat{\mathbf{G}}_b\left(\mathbf{r} \mid \mathbf{r}'\right) dv'. \tag{10.48}$$

In the case of spherical or elliptical grains, one can derive the exact analytical expressions for the depolarization tensors. For example, for a spherical grain of a radius a_l, we have (Landau et al., 1984; Zhdanov, 2008a):

$$\widehat{\mathbf{\Gamma}}_l = -\frac{1}{3\sigma_b}\widehat{\mathbf{I}}. \tag{10.49}$$

Substituting (10.48) back into (10.47), we obtain:

$$\mathbf{E}_l(\mathbf{r}) = \widehat{\mathbf{\Gamma}}_l \cdot \widehat{\mathbf{m}}_l \cdot \mathbf{E}^b. \tag{10.50}$$

Then Eq. (10.50) becomes

$$\mathbf{E}_l(\mathbf{r}) = \iiint_{V_l} \widehat{\mathbf{G}}_b(\mathbf{r}\,|\,\mathbf{r}')\,dv' \cdot \widehat{\mathbf{m}}_l \cdot \mathbf{E}^b. \tag{10.51}$$

Substituting expression (10.51) back into (10.44), we find

$$\mathbf{E}(\mathbf{r}) = \mathbf{E}^b + \sum_l \iiint_{V_l} \widehat{\mathbf{G}}_b(\mathbf{r}\,|\,\mathbf{r}') \cdot \widehat{\mathbf{m}}(\mathbf{r}')\,dv' \cdot \mathbf{E}^b$$

$$= \mathbf{E}^b + \iiint_V \widehat{\mathbf{G}}_b(\mathbf{r}\,|\,\mathbf{r}') \cdot \widehat{\mathbf{m}}(\mathbf{r}')\,dv' \cdot \mathbf{E}^b. \tag{10.52}$$

10.3.3 EFFECTIVE CONDUCTIVITY OF HETEROGENEOUS MEDIUM

In this section we will derive a constructive approach for determining the effective conductivity of a heterogeneous polarizable medium. We have established above that, in order to solve this problem, we have to find the average value of the material property tensor, $\langle\widehat{\mathbf{m}}\rangle$. The last function can be found based on the integral representation (10.52).

Multiplying both sides of (10.52) by $\Delta\widehat{\boldsymbol{\sigma}}(\mathbf{r})$, we have:

$$\widehat{\mathbf{m}}(\mathbf{r}) \cdot \mathbf{E}^b = \Delta\widehat{\boldsymbol{\sigma}}(\mathbf{r}) \cdot \mathbf{E}^b + \Delta\widehat{\boldsymbol{\sigma}}(\mathbf{r}) \cdot \iiint_V \widehat{\mathbf{G}}_b(\mathbf{r}\,|\,\mathbf{r}') \cdot \widehat{\mathbf{m}}(\mathbf{r}')\,dv' \cdot \mathbf{E}^b. \tag{10.53}$$

Our goal is to find the material property tensor $\widehat{\mathbf{m}}$. Eq. (10.53) should hold for any background field, $\mathbf{E}^b$. Therefore, the following equation should hold:

$$\widehat{\mathbf{m}}(\mathbf{r}) = \Delta\widehat{\boldsymbol{\sigma}}(\mathbf{r}) + \Delta\widehat{\boldsymbol{\sigma}}(\mathbf{r}) \cdot \iiint_V \widehat{\mathbf{G}}_b(\mathbf{r}\,|\,\mathbf{r}') \cdot \widehat{\mathbf{m}}(\mathbf{r}')\,dv'. \tag{10.54}$$

The volume integral in Eq. (10.54) can be represented as a sum of two integrals: over the volume of one grain, V_l, and over the remaining volume $(V - V_l)$:

$$\iiint_V \widehat{\mathbf{G}}_b(\mathbf{r}\,|\,\mathbf{r}') \cdot \widehat{\mathbf{m}}(\mathbf{r}')\,dv'$$

$$= \iiint_{V-V_l} \widehat{\mathbf{G}}_b(\mathbf{r}\,|\,\mathbf{r}') \cdot \widehat{\mathbf{m}}(\mathbf{r}')\,dv' + \iiint_{V_l} \widehat{\mathbf{G}}_b(\mathbf{r}\,|\,\mathbf{r}') \cdot \widehat{\mathbf{m}}(\mathbf{r}')\,dv'. \tag{10.55}$$

We approximate the integral over $(V - V_l)$ by replacing $\widehat{\mathbf{m}}(\mathbf{r}')$ by its average in V, and we calculate the integral over V_l, taking into account property (10.46): $\widehat{\mathbf{m}}(\mathbf{r}') = \widehat{\mathbf{m}}_l = const$. As a result, we obtain:

$$\iiint_V \widehat{\mathbf{G}}_b (\mathbf{r} \mid \mathbf{r}') \cdot \widehat{\mathbf{m}}(\mathbf{r}') \, dv'$$
$$\approx \iiint_{V-V_l} \widehat{\mathbf{G}}_b (\mathbf{r} \mid \mathbf{r}') \, dv' \cdot \langle \widehat{\mathbf{m}} \rangle + \iiint_{V_l} \widehat{\mathbf{G}}_b (\mathbf{r} \mid \mathbf{r}') \, dv' \cdot \widehat{\mathbf{m}}_l. \tag{10.56}$$

According to the Gauss theorem, the volume depolarization tensor $\widehat{\boldsymbol{\Gamma}}_l$ is equal to:

$$\widehat{\boldsymbol{\Gamma}}_l = \nabla \iiint_{V_l} \nabla' g_b (\mathbf{r} \mid \mathbf{r}') \, dv' = \nabla \iint_{S_l} g_b (\mathbf{r} \mid \mathbf{r}') \mathbf{n}(\mathbf{r}') \, ds'. \tag{10.57}$$

We can calculate the external integral in the limit of the infinitely large volume V in a similar way, using the Gauss theorem for the external domain $(V - V_l)$:

$$\iiint_{V-V_l} \widehat{\mathbf{G}}_b (\mathbf{r} \mid \mathbf{r}') \, dv' = -\widehat{\boldsymbol{\Gamma}}_l. \tag{10.58}$$

Substituting Eqs. (10.57) and (10.58) into (10.56), we have:

$$\iiint_V \widehat{\mathbf{G}}_b (\mathbf{r} \mid \mathbf{r}') \cdot \widehat{\mathbf{m}}(\mathbf{r}') \, dv' \approx -\widehat{\boldsymbol{\Gamma}}_l \cdot \langle \widehat{\mathbf{m}} \rangle + \widehat{\boldsymbol{\Gamma}}_l \cdot \widehat{\mathbf{m}}_l. \tag{10.59}$$

The last result reduces Eq. (10.54) to:

$$\widehat{\mathbf{m}}(\mathbf{r}) = \Delta\widehat{\boldsymbol{\sigma}}(\mathbf{r}) + \Delta\widehat{\boldsymbol{\sigma}}(\mathbf{r}) \cdot \widehat{\boldsymbol{\Gamma}}_l \cdot [\widehat{\mathbf{m}}_l - \langle \widehat{\mathbf{m}} \rangle]. \tag{10.60}$$

Assuming in the last formula that $\mathbf{r} \in V_l$, we find:

$$\widehat{\mathbf{m}}_l = \Delta\widehat{\boldsymbol{\sigma}}_l + \Delta\widehat{\boldsymbol{\sigma}}_l \cdot \widehat{\boldsymbol{\Gamma}}_l \cdot [\widehat{\mathbf{m}}_l - \langle \widehat{\mathbf{m}} \rangle]. \tag{10.61}$$

Solving Eq. (10.61), we determine the material property tensor, $\widehat{\mathbf{m}}_l$, for every grain:

$$\widehat{\mathbf{m}}_l = \left[\widehat{\mathbf{I}} - \Delta\widehat{\boldsymbol{\sigma}}_l \cdot \widehat{\boldsymbol{\Gamma}}_l \right]^{-1} \cdot \Delta\widehat{\boldsymbol{\sigma}}_l \cdot \left[\widehat{\mathbf{I}} - \widehat{\boldsymbol{\Gamma}}_l \cdot \langle \widehat{\mathbf{m}} \rangle \right]. \tag{10.62}$$

Taking an average value of both sides of (10.62), and solving the resulting equation for $\langle \widehat{\mathbf{m}} \rangle$, we find:

$$\langle \widehat{\mathbf{m}} \rangle = \left\langle \left[\widehat{\mathbf{I}} - \Delta\widehat{\boldsymbol{\sigma}} \cdot \widehat{\boldsymbol{\Gamma}} \right]^{-1} \right\rangle^{-1} \left\langle \left[\widehat{\mathbf{I}} - \Delta\widehat{\boldsymbol{\sigma}} \cdot \widehat{\boldsymbol{\Gamma}} \right]^{-1} \cdot \Delta\widehat{\boldsymbol{\sigma}} \right\rangle. \tag{10.63}$$

This completes the calculation of the tensor $\widehat{\mathbf{m}}$.

Substituting (10.63) into (10.39), we finally have:

$$\widehat{\boldsymbol{\sigma}}_e = \widehat{\boldsymbol{\sigma}}_b + \langle \widehat{\mathbf{m}} \rangle$$
$$= \widehat{\boldsymbol{\sigma}}_b + \left\langle \left[\widehat{\mathbf{I}} - \Delta\widehat{\boldsymbol{\sigma}} \cdot \widehat{\boldsymbol{\Gamma}} \right]^{-1} \right\rangle^{-1} \left\langle \left[\widehat{\mathbf{I}} - \Delta\widehat{\boldsymbol{\sigma}} \cdot \widehat{\boldsymbol{\Gamma}} \right]^{-1} \cdot \Delta\widehat{\boldsymbol{\sigma}} \right\rangle. \tag{10.64}$$

Eq. (10.64) allows us to calculate the effective conductivity for any multiphase composite rock formation. We will present some examples of the practical application of this formula in Chapter 12, when we will consider a more general case of the generalized effective-medium theory of induced polarization.

10.4 PROPERTIES IN AN EXISTENTIAL SENSE
10.4.1 CONCEPTS OF A GEOELECTRIC STRUCTURE AND A GEOELECTRIC SECTION

In the preceding sections, we have seen how the electrical properties of a material are defined, and how these properties relate to a number of other factors, including those which describe the character of the electromagnetic field used to measure the properties, those which describe the environment of the material subjected to measurement, and the correlation of the electrical properties with other, perhaps more interesting properties of the material. Note, however, the question still exists as to what actually are appropriate values for the electrical properties of the earth. The purpose of this section is to describe the electrical character of the earth as it actually exists. So far, the electrical properties of single minerals and simple aggregates of minerals which form uniform rocks have been discussed. In geoelectric exploration, it is necessary to consider the way in which electrical properties characterize larger volumes of rock which may not necessarily be homogeneous. This leads to a requirement to define several concepts that are basic to the understanding of how geoelectric methods can be used in exploration of the earth. These are the concepts of a geoelectric structure and a geoelectric section. These concepts are analogs of but not the same as the concepts of geologic structures and geologic sections (Bates and Jackson, 1980).

Definition 38. Structural geology – The branch of geology that deals with the form, arrangement, and internal structure of rocks, and especially with the description, representation, and analysis of structures, chiefly on a moderate to small scale. The subject is similar to tectonics, but the latter is generally used for broader regional or historical phases.

Definition 39. The equivalent geoelectric structure consists of the geometric description of the boundaries between zones characterized by significantly different values of electrical properties in the subsurface, along with specification of those electrical properties. Geoelectric structures can be one-, two-, or three-dimensional, depending on how many dimensions are required to define them reasonably completely.

Definition 40. Stratigraphic unit – A stratum or body of adjacent strata recognized as a unit in the classification of a rock sequence with respect to any of the many characters, properties, or attributes that rocks may possess, for any purpose such as description, mapping, and correlation.

Rocks may be classified stratigraphically on the basis of lithology, fossil content, age, or properties (such as mineral content, radioactivity, seismic velocity, electric-log character, chemical composition) in categories for which formal nomenclature is lacking.

Definition 41. Geoelectric unit – An interval in a layered sequence of rocks which can be characterized by meaningful average values of electrical properties which are significantly different from similar averages in adjacent units, and which is thick enough to be recognized using some geoelectric method.

Definition 42. Geologic section – Any sequence of rock units found in a given region either at the earth's surface or below (as in a drilled well or mine shaft).

Definition 43. Geoelectric section – Characterization of the profile of electrical properties through a sequence of geoelectric units, perpendicular to the set of surfaces defining those units.

10.4.2 LONGITUDINAL CONDUCTANCE AND TRANSVERSE RESISTANCE OF THE HORIZONTALLY LAYERED GEOELECTRIC SECTION

One of the most widely used models of a geoelectric section is a horizontally layered model. However, in the case of the large number of individual layers characterizing a fine structure in terms of resistivity-depth function, we do not expect to resolve the parameters of this section with any of the surface-based electrical sounding methods. We must specify a way to define the average resistivity or average conductivity in a way which is useful in converting the true parameters of the multilayered section to the values which are meaningful in resistivity sounding. The Schlumberger brothers and others showed early in the days of electrical sounding methods that the average electrical properties for a thinly layered sequence can best be described with a set of five parameters, these parameters being defined in terms of a column of rock one meter square cut from the sequence of thin layers. This column, with a total thickness H and consisting of N horizontal beds each with its own characteristic resistivity, ρ_i, and thickness, h_i, is shown in Fig. 10.22.

We begin our definition of the Schlumbergers' parameters by considering current flow either vertically or horizontally through the column. For current flowing vertically through the length of the column, the total resistance from top to bottom is the sum of resistances met in each of the layers is

$$T = \sum_{i=1}^{N} \rho_i h_i. \tag{10.65}$$

The quantity T is termed the *transverse resistance* of the column. The units for transverse resistance are ohms.

Considering the column to be macroscopically uniform, we can define an average resistivity for current flowing transversely to the bedding:

$$\rho_{tr} = T/H = \sum \rho_i h_i / \sum h_i \tag{10.66}$$

where H is the total thickness of the assemblage of layers.

For current flowing horizontally through the column (Fig. 10.22), the resistance is calculated by considering the resistance offered in each layer to be connected in parallel with the resistances of the other layers. For resistances in parallel, it is more convenient to talk about the conductances, or inverse resistances, in each layer. The total conductance is simply the sum of the individual conductances in parallel:

$$S = \sum_{i=1}^{N} h_i / \rho_i, \tag{10.67}$$

where S is called the *longitudinal conductance*. It is measured in siemens.
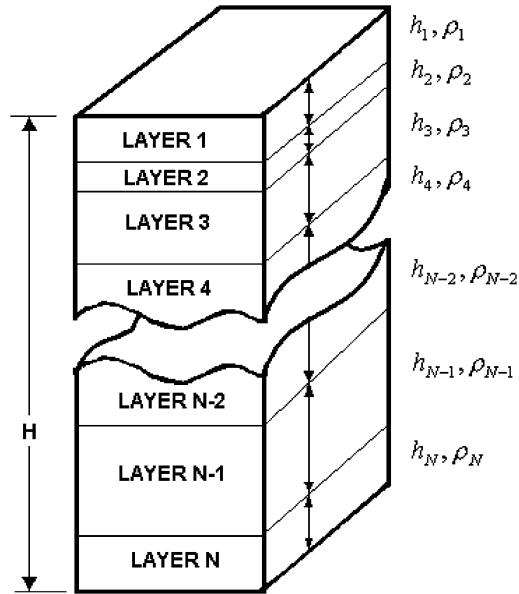
FIGURE 10.22

Column of rock one meter square hypothetically cut from a layered sequence of rocks. This column is used to define average longitudinal resistivity, average transverse resistivity, and anisotropy.

Again, by assuming that the longitudinal conductance S is distributed uniformly over the length of the column, we calculate an average longitudinal resistivity:

$$\rho_\ell = H/S = \sum h_i / \sum \frac{h_i}{\rho_i}. \tag{10.68}$$

Unless the layers all have the same resistivity values, the two average values we have defined will not be equal (try it and see). The longitudinal average resistivity will be less than the transverse average resistivity if there is any variation in resistivity in the column. This dependence of average resistivity on the direction in which current flows can be considered a form of anisotropy. By convention, the coefficient of anisotropy is defined as:

$$\lambda = \sqrt{\rho_{tr}/\rho_\ell} = \sqrt{ST/H^2}. \tag{10.69}$$

When average resistivities are calculated for a sequence of beds, anisotropy appears even though each bed is in itself isotropic. It is best to call the apparent anisotropy which arises in combining a group of beds into a single geoelectric unit *macroanistropy* to distinguish it from more basic causes for anisotropy.

Often the first step in using a resistivity or conductivity log in the compilation of electrical properties is to form an *integral conductance* curve and an *integral resistance* curve from the log trace selected.
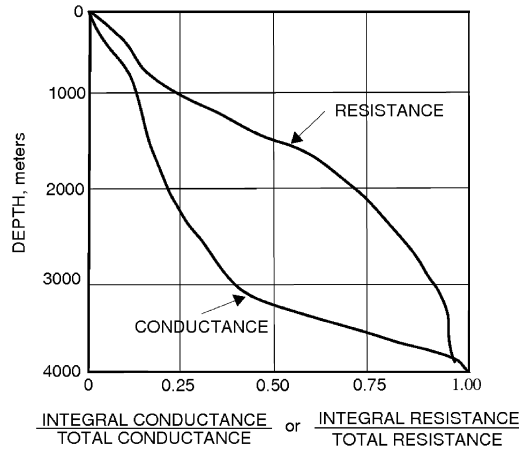
FIGURE 10.23

Integral resistance and integral conductance curves for a typical layered formation.

Integral conductance:

$$S_I = \int_0^{z_1} \sigma(z)dz. \tag{10.70}$$

Integral resistance:

$$T_I = \int_0^{z_1} \rho(z)dz. \tag{10.71}$$

In most cases, these integral curves take the form of a series of nearly straight segments (Fig. 10.23). These nearly straight segments define the geoelectric units that comprise the geoelectric section penetrated by the well.

Both the integral conductance and integral resistance curves are fitted with an arbitrary number of segments, either by eye or by a numerical fitting process that picks the intersections and slopes of the segments. The sequence of depths for the intersections of segments on both integral curves define the boundaries of each geoelectric unit. Each unit is then characterized by an interval conductance value, ΔS, and an interval resistance value, ΔT, which is the difference between the corresponding integral conductance and integral resistance at the lower and upper boundaries of each unit. It is now possible to compute two independent average resistivity values for each geoelectric unit:

$$\sigma_\ell = \Delta S/\Delta z, \tag{10.72}$$
$$\rho_{tr} = \Delta T/\Delta z, \tag{10.73}$$

where Δz is the depth interval over which the values ΔS and ΔT have been determined. These are the same as the values computed for a section made up of discrete uniform layers, as given above.
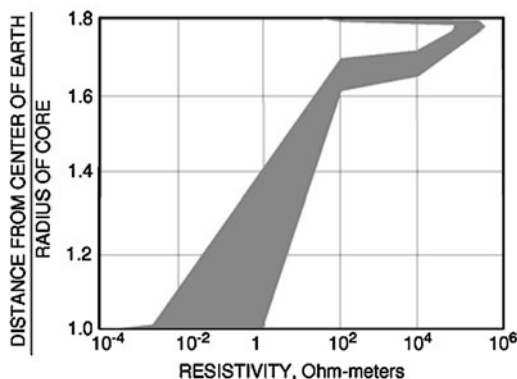
FIGURE 10.24

Summary of estimates of the resistivity-depth profile in the earth from the bottom of the mantle to the surface.

10.5 PROPERTIES OF LARGE-SCALE GEOELECTRIC STRUCTURES
10.5.1 GEOELECTRIC MESOSTRUCTURES AND MEGASTRUCTURES

Geoelectric megastructures are very large geological features that are characterized by some diagnostic electrical feature, usually a very large integrated conductance. The largest-scale megastructure on the planet Earth is the radial shell-like zonation of the electrical properties of the earth as a whole. The profile of resistivity as a function of depth in the earth has been the subject of scientific study since the middle of the 19th century. The profile of resistivity to depths of tens of kilometers has been investigated intensively in recent decades, primarily using the magnetotelluric method, about which we will learn more in subsequent chapters.

The overall resistivity-depth profile appears to divide the Earth into six roughly concentric shells, each identified by characteristic ranges of electrical conductivity Fig. 10.24.

- *Zone 1*: The surface veneer of wet rocks and the waters of the world's oceans are highly conductive, with integrated conductances ranging from a few siemens to several thousand siemens. The thickness of this zone ranges from a few hundred meters to a few tens of kilometers.
- *Zone 2*: This is a zone of highly resistive crystalline rocks that are the near-surface expression of the crust. These are relatively dry and relatively cool igneous and metamorphic rocks. The thickness of this resistant zone ranges from 10 km or less in regions of high heat flow to several hundred kilometers in cold, stable shield areas.
- *Zone 3*: A zone of gradually increasing conductivity is present beneath the resistant zone. The increasing conductivity is generally attributed to the development of thermally excited conduction mechanisms as the temperature reaches levels of a few hundred degrees (C) and higher.
- *Zone 4*: At a depth below about 300 km but above 700 km, the conductivity rapidly increases from about 0.01 S/m to a value of approximately 1 S/m. The resolution with which this change can be located is poor, so the change may occur abruptly, or it might be transitional over a depth interval of several hundred kilometers.

- *Zone 5*: Beneath zone 4, conductivity probably continues to increase gradually with depth. There is some dispute about the conductivity at the base of the mantle, with some investigators arguing that the conductivity in the bottom 500 km is no more than 100 S/m, while others insist that the conductivity is 1000 to 10,000 S/m.
- *Zone 6*: Evidence on the probable electrical conductivity of the core is indirect, based on consideration of other, better known, physical properties. Tozer (1981) argued that the conductivity of the core is probably between 100,000 and 1 million S/m.

Mesoscale geoelectric features are those which are regionally large, but not worldwide in scale. For example, over the last thirty years (1960–1990), numerous investigators have reported "anomalously conductive regions" in the lower part of the crust and the upper part of the mantle (in Zone 3). One such *crustal conductivity anomaly* is the anomaly in the vicinity of Lake Baikal, in Siberia (Berdichevsky and Dmitriev, 2002). Many hundreds of magnetotelluric soundings disclosed an elongate (up to 1000 km) anomaly in conductivity in the lower crust in this region. The anomalous zone is most shallow and most conductive along the axis of the Baikal feature, with highly conductive rocks ($\rho < 20\ ohm - m.$) beginning at depths as shallow as 16 km and extending to a depth of about 48 km. The integrated conductance of the anomalous conductor is 2000 S.

Comparable values of excess conductance in the crust have been described in a number of other locations around the earth. These anomalous crustal conductors appear to occur in regions of extensional tectonics, particularly beneath rift zones. Their explanation is not obvious. It has been suggested that they represent the shallow occurrence of molten rocks, the effect of excess water in crustal rocks of the lower crust, or the development of intensely graphitized layers of rock.

Another important electrical mesoscale structure is a sedimentary basin, particularly, a young basin filled with great thicknesses of Tertiary marine sediment. The electrical significance of such basins can be seen from the map of Fig. 10.25, a map of the conductance of Zone 1 over the area of the 48 contiguous United States. This map has been compiled on sparse data, consisting of electric logs from about 300 widely distributed wells. The electrical signature of three major sedimentary basins can be easily identified; the Imperial Valley basin in southern California exhibits conductances up to 2000 S, the Williston basin in North and South Dakota exhibits conductances of over 1000 S, and the Gulf of Mexico basin exhibits conductances of more than 5000 S offshore from Lousiana. This last value does not include conductance in the sea water covering the Gulf of Mexico basin; conductance of the world's seas and oceans is discussed in the next sections of this chapter.

10.5.2 THE OCEANS

Up to this point, we have restricted our consideration of the electrical properties of the planet Earth to the solid part. Significant parts of the planet are liquid, as in the oceans, or gaseous, as in the atmosphere. Our lack of attention to these regions follows from the fact that they are far less opaque than solid rocks, and do not often require the use of indirect exploration methods to define their character. We cannot neglect these regions altogether for several obvious reasons. Three quarters of the surface of the Earth is covered with ocean waters, and so, exploration of the solid earth in these areas requires consideration of the effect of the overlying water on the use of geoelectric methods to explore beneath them. On the other hand, the atmosphere is the source of much of the electromagnetic noise we find in carrying out electrical surveys. At least a cursory knowledge of the electrical properties of the atmo-
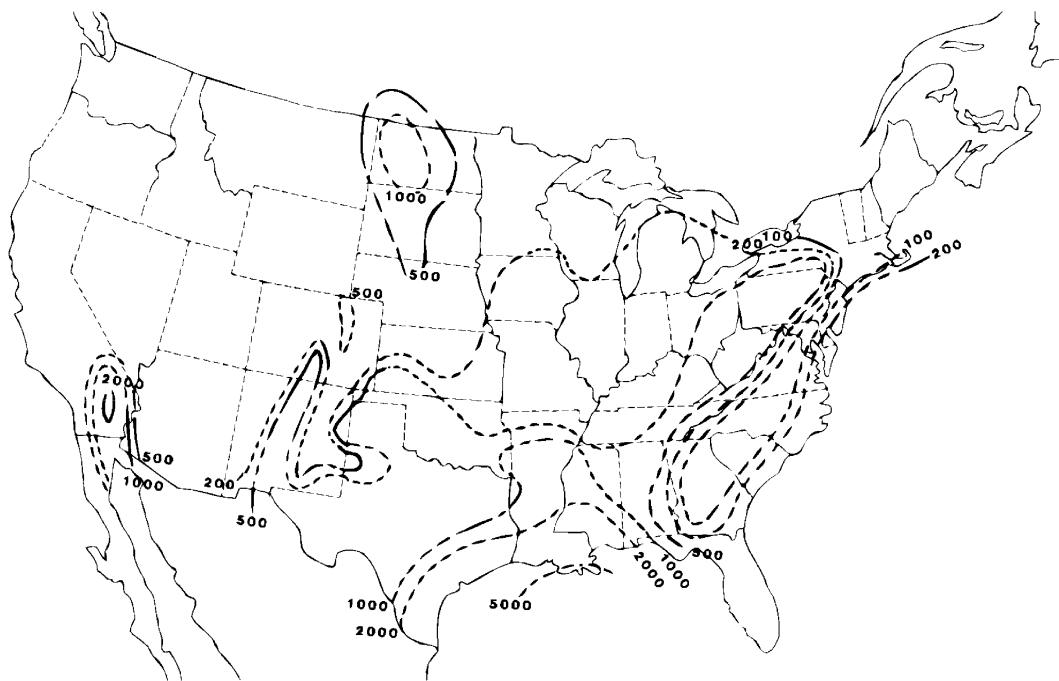
FIGURE 10.25

Total conductance in major sedimentary basins of the United States.

sphere, provided in the next section, is necessary to gain a reasonable understanding of this ambient electromagnetic field of the earth.

The world's oceans form an interconnected layer of salt water which covers 70.8 percent or 361.2 million square kilometers of the Earth's surface. The oceans have a maximum depth of slightly over 11 kilometers; the average depth is 3.79 kilometers. The mass of the oceans amounts to 1.4×10^{18} tons, but this accounts for only one-quarter of a percent of the Earth's total mass.

The distribution of ocean depths is neither uniform nor random; it is characterized by two preferred elevations for the Earth's solid surface. One preferred elevation includes the continental portions of the surface, with a peak frequency of occurrence at an elevation of less than 100 meters above sea level. This peak straddles sea level, so that about a third of its area reflects depths of the ocean of less than 500 meters. These regions covered by shallow water are considered to be part of the continental crust, and account for some 50 million square kilometers. Often these regions, called *continental shelves* if the depth of the ocean is 200 meters or less, and *continental slopes* if the depth ranges up to 1000 meters. These regions are of interest in exploration for mineral resources inasmuch as they are geologically similar to the adjacent dry parts of the continents.

A very minor part of the ocean has depths between 1 and 2 kilometers, but significantly larger parts of the oceans have depths of 2.5 to 5.5 kilometers, with the peak frequency of occurrence being
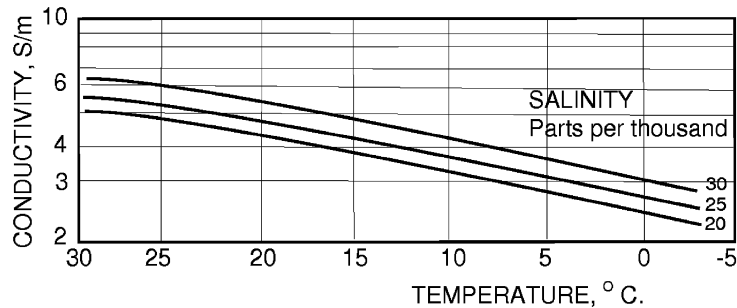
FIGURE 10.26

Conductivity of sea water as a function of total salinity and temperature.

5 kilometers. Some 150 million square kilometers of the oceans have such depths; these form the so-called *deep sea basins*.

On the whole, the oceans are quite uniform in properties, at least in comparison with the solid earth. The greatest part of the ocean volume has a salinity that lies between 34.6 and 35.0 parts per thousand of salinity, within $\pm 1/2$ percent of 34.8 parts per thousand as a best value. The Atlantic Ocean is ever so slightly more saline than the Pacific Ocean. Conductivity is very nearly proportional to salinity over these small ranges in salinity.

Temperature varies more than does the salinity, particularly in the near-surface waters. Most of the ocean waters have temperatures below 5°C, with the Atlantic Ocean being about 1° warmer than the Pacific Ocean. However, the surface waters in ice-free oceans are considerably warmer, rising to temperatures of 25°C and more.

Both temperature and salinity affect the conductivity of sea water. The variation of seawater conductivity as a function of temperature and salinity is shown by the curves in Fig. 10.26. We might note that the best value for the conductivity of the oceans as a whole is close to 3 S/m.

Sea water is more conductive than most earth materials, and occurs in large amounts. It forms a high conductance sheet covering much of the earth, as shown in Fig. 10.27. Not only must this large amount of conductance be taken into account when surveys are carried out on the surface of the sea, but also when surveys are made near the edges of the dry continents.

10.5.3 THE ATMOSPHERE

The atmosphere surrounding the earth is volumetrically the largest component of the earth's total structure. The mass of the atmosphere is only 510×10^{12} tons, but the volume is very large. At an altitude of 1000 kilometers above the earth, the density of the atmosphere has decreased by 14 orders of magnitude from that at the earth's surface.

The atmosphere consists of two significantly different parts with respect to electrical properties. Below 80 to 100 kilometers, the atmosphere is a virtual insulator. Very limited conduction takes place as a consequence of the presence of charged particles in the air, either dust particles or ions. Typical curves for the conductivity of the lower atmosphere as a function of elevation to several tens of kilometers are

FIGURE 10.27

Conductivity of the World's Ocean. Areas in black are the continents. Areas in white are oceanic areas with a conductance of less than 12 kilosiemens. Lightly shaded areas have a conductance between 12 and 18 kilosiemens. The small areas with darker shading have a conductance greater than 18 kilosiemens.
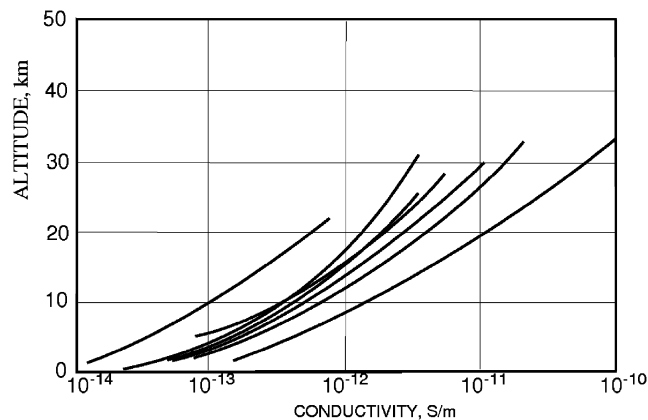
FIGURE 10.28

Conductivity profiles through the lower part of the atmosphere.

shown in Fig. 10.28. Near the surface of the earth, the conductivity is less than $10^{-12} S/m$, or some 12 to 15 orders of magnitude less than the conductivity in the underlying ocean or solid earth.

The upper part of the atmosphere is much more conductive. Above an altitude of 80 to 100 km, the atmosphere is ionized. This part is called the ionosphere. Electrical conductivity in the ionosphere is

difficult to measure. Information on the conductivity is derived largely from a theoretical analysis of conduction in an ionized gas, with some limited experimental confirmation.

Maxwell's equations alone are not adequate to explain conduction in an ionized gas. It is necessary to solve a combination of Maxwell's equations and the equation for mechanical motion (Newton's law). This leads to a problem called the magneto-hydro-dynamic (MHD) problem, in which the simultaneous flow of current and mass is considered. We suggest you read about the solution of this problem in texts such as those by Alfvén and Fälthammer (1963) and Ratcliffe (1959). The actual conductivities that exist in the ionosphere may or may not be accurately predicted by such theoretical calculations. It is difficult to determine conductivity directly, but it can be estimated indirectly from other measurements which are easier to make, such as electric field intensity and ion concentrations.

When a magnetic field is present, a *Hall* current flows in a direction normal to both the magnetic and electric field vectors, and a *Pederson* current flows in the direction of the electric field (Campbell, 2003). The values of the Hall and Pederson conductivities in the ionosphere depend on the model used in the analysis. The actual conductivities that exist in the ionosphere may or may not be accurately predicted by such theoretical calculations. It is difficult to determine conductivity directly, but it can be estimated indirectly from other measurements which are easier to make, such as electric field intensity and ion concentrations.

REFERENCES AND RECOMMENDED READING TO CHAPTER 10

Alfvén, H., and C. G. Fälthammer, 1963, Cosmical electrodynamics: The Clarendon Press, Oxford, 228 pp.

Bates, R. L., and J. L. Jackson, 1980, Glossary of geology: American Geological Institute, Falls Church, Va., 749 pp.

Berdichevsky, M. N., and V. I. Dmitriev, 2002, Magnetotellurics in the context of theory of ill-posed problems: Society of Exploration Geophysicists, Tulsa, OK, 215 pp.

Campbell, W. H., 2003, Introduction to geomagnetic fields, 2nd ed.: Cambridge University Press, 350 pp.

Carmichael, R. S., 1989, Practical handbook of physical properties of rocks and minerals: CRC Press, Boca Raton, Florida, 741 pp.

Dortman, N. B., Ed., 1992a, Handbook of petrophysics, Vol. I, Rocks and ores (*in Russian*): Nedra, Moscow, 392 pp.

Dortman, N. B., Ed., 1992b, Handbook of petrophysics, Vol. II, Techniques and methods of investigation (*in Russian*): Nedra, Moscow, 256 pp.

Dortman, N. B., Ed., 1992c, Handbook of petrophysics, Vol. III, The Earth's crust and mantle (*in Russian*): Nedra, Moscow, 286 pp.

Landau, L. D., L. P. Pitaevsky, and E. M. Lifshitz, 1984, Electrodynamics of continuous medium, 2nd ed.: Elsevier Butterworse-Heinemann.

Olhoeft, G. R., 1980, Electrical properties in rocks, *in* Y. S. Thoulaikian, W. R. Judd, and R. F. Roy, Eds., Physical properties of rocks and minerals, McGraw-Hill, New York, 257–330.

Parkhomenko, E. I., 1967, Electrical properties of rocks: Plenum Press, New York, 314 pp.

Parkhomenko, E. I., 1982, Electrical resistivity of minerals and rocks at high temperature and pressure: Review of Physics and Space Physics, **20** (2), 193–218.

Ratcliffe, J. A., 1959, The magneto-ionic theory and its applications to the ionosphere: Cambridge University Press, Cambridge, 206 pp.

Shuey, R. T., and M. Johnson, 1973, On the phenomenology of electrical relaxation in rocks: Geophysics, **38** (1), 37–48.

Shuey, R. T., 1975, Semiconducting ore minerals: Elsevier, Amsterdam, 415 pp.

Sihvola, A., 1999, Electromagnetic mixing formulas and applications: IEE Electromagnetic Waves Series, **47**, London, UK, 284 pp.

Stroud, D., 1975, Generalized effective medium approach to the conductivity of an inhomogeneous material: Physical Review B, **12**, 3368–3373.

Tozer, D. C., 1981, The mechanical and electrical properties of the earth's asthenosphere: Physics of the Earth and Planetary Interiors, **25**, 280–296.

von Hippel, A. R., 1958, Dielectrics, *in* Condon, E. U., and H. Odishaw, Eds., Handbook of Physics: McGraw-Hill, New York, 103–125.

Wait, J. R., 1959, The variable-frequency method, *in* Wait, J.R., Ed., Overvoltage research and geophysical applications: Pergamon, Oxford.

Wyllie, G., 1960, Theory of polarization and absorption in dielectrics, an introductory survey: Progress in dielectrics: John Wiley and Sons, Inc., New York, 1–28.

Zhdanov, M. S., 2002, Geophysical inverse theory and regularization problems: Elsevier, Amsterdam, London, New York, Tokyo, 628 pp.

Zhdanov, M. S., 2008a, Generalized effective-medium theory of induced polarization: Geophysics, **73** (5), F197–F211.

Zhdanov, M. S., 2008b, Geophysical technique for mineral exploration and discrimination based on electromagnetic methods and associated systems. US Patent 7,324,899 B2.

GENERATION AND MEASUREMENT OF ELECTROMAGNETIC FIELDS IN GEOPHYSICAL APPLICATIONS

CONTENTS

Electromagnetic geophysical methods are based on the study of EM field propagation in the earth and on determining the electromagnetic parameters of the earth, containing unique information about petrophysical properties, lithological characteristics, and mineral content of the rocks in the earth's interior. There are many different EM methods which can be used for different applications. The number of different modifications of EM prospecting methods is extremely large, because it is possible to transmit and to receive the different components of EM fields. The behavior of EM fields is controlled by three primary properties of the medium, these being the electrical conductivity, the dielectric permittivity, and the magnetic permeability, as well as a number of other physical phenomena. Electrical conductivity is the most useful of all the physical properties that characterize rocks and minerals in view of interest for geophysical exploration, because electrical conductivity in the earth varies by many orders of magnitude. In contrast, the other physical properties used in geophysics — acoustic wave speed, density, and magnetic susceptibility — vary over quite limited ranges.

    The effective use of electromagnetic methods in probing the earth requires not only a thorough understanding of the physics and mathematics describing the behavior of electromagnetic fields in the earth, but also, a good understanding of how one acquires the best possible measurements in the field.

We will look at this aspect of the subject in two parts: how does one generate a useful electromagnetic field (when controlled-source methods are to be used), and how does one sense the useful characteristics of the field, whether it be an electrical or magnetic field.[1]

11.1 FIELD GENERATION

In controlled-source methods, two types of sources are commonly used: a grounded wire (galvanic source) or an ungrounded loop of wire (induction source). If a grounded wire source is to be used to generate either a current field or a magnetic field, three components must be considered in its construction: a prime power supply, cabling, and a grounding structure. If an ungrounded loop is to be used to generate a magnetic field, the source consists of two subsystems, a prime power supply and a transmitter loop.

11.1.1 SOURCES OF EM FIELDS

In the design of sources, we attempt to optimize several conflicting requirements. The principal conflict is between weight and capability. Always, weight is a matter of concern. With portable equipment, the lower the weight, the greater the productivity of the field crew, providing the capability of the source is not compromised to the extent that observation of the electromagnetic field becomes tedious. Even with stationary sources of great capability, weight is an important consideration because capital investment in large sources becomes a limiting factor. Capital cost generally increases with weight according to some power law, $C \sim W^p$, where C is cost, W is weight, and p has a value probably somewhat less than unity.

Engine-driven generators usually, but not always, generate alternating current at a power-line frequency, 50 or 60 Hertz, and less commonly, at high frequencies, 400 or 1000 Hertz. For very special applications in electromagnetic surveys, these generated frequencies can be used directly to create the electromagnetic field to be measured. Usually, though, the prime generator is used to power a *waveform generator*. This can be either an electronic or mechanical device which shapes the prime power into current at a desired waveform (impulse, square wave, triangular wave, sinusoid, random step sequence, etc.) at a desired frequency. Design of a wave form generator is essentially a problem in electronics, and we will not examine it here.

The engines which drive generators are internal combustion types for power levels up to a few tens of kilowatts, diesel from a few tens of kilowatts to a few megawatts, and gas turbines at levels above a few megawatts. All of these generators are readily available on the commercial market, but if power levels greater than 25 megawatts are required, it is necessary to go to exotic generating systems. Two such exotic systems which have been used to a limited extent are magneto-hydro-dynamic (MHD) generators and ionospheric modulation (IM) systems.

MHD generators produce electrical energy in a mechanical system that does not include rotating parts, such as an engine. The essential features of an MHD system are shown in Fig. 11.1. In a combustion chamber (*plasma generator*), fuel is burned to create a stream of hot, ionized gas. This gas

---

[1]Chapter 11 was written in collaboration with G. Keller.
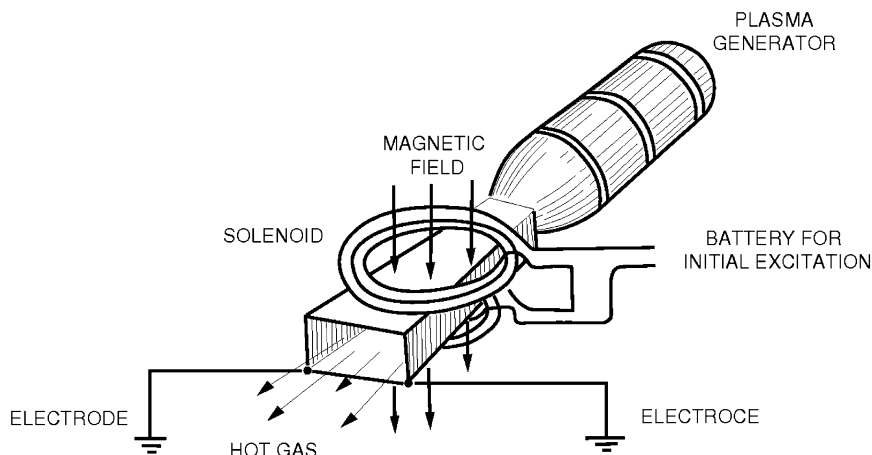
FIGURE 11.1

Elements of an uncooled magneto-hydrodynamic generator. A hot ionized gas is created in the plasma generator. This gas flows through a channel under the action of a magnetic field. The ions are directed and collected to form an output current which is then fed to the ground through electrodes.

stream is caused to flow through a *channel* wrapped with a *solenoid* with direct current supplied by a *battery for initial excitation*. The magnetic field produced by the solenoid causes the ions in the gas to deflect, so that they will flow into collectors at the end of the channel, and from there into the external circuit. Typically, the output is a few thousand volts, with power levels in stationary plants reaching many hundreds or a few thousand megawatts.

Practical limitations of MHD power systems are imposed by the need for cooling. The gas stream must be raised to a temperature of 3500 to 3700°C in order for strong ionization to take place and for reasonable efficiency of energy conversion to be obtained. Waste heat in the channel must be removed rapidly, or the channel will burn. If the channel is cooled, the weight of the cooling system makes the generator useful only in a fixed installation. For geophysical applications, uncooled or flash-cooled MHD systems are used, but the duty cycle is very short. For example, an uncooled pulse-MHD generator with 25 megawatts capability can be operated for a period of only about 10 seconds.

For very small sources, batteries are used rather than engine-driven generators. The cost of battery-supplied energy is much higher than that of mechanically-generated energy, but because the total energy used in small systems is very low, convenience is more important. Batteries store chemical energy, which is extracted when the battery is connected to an external system. A great variety of batteries is available for a great variety of applications (Mantell, 1970). Batteries were apparently first used by the Parthians (in modern Iraq) in the period 250 B.C. to 224 A.D.

Many forms of battery are available for many general and specialized uses. The most widely used, and most widely available, are dry cells. The Lechanche dry cell stores chemical energy which is released in the reaction

$$Zn + 2NH_4Cl + 2Mn_2 \rightleftharpoons Zn(NH_3)_2Cl_2 + H_2O + Mn_2O_3.$$
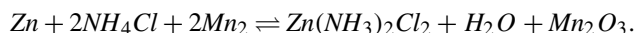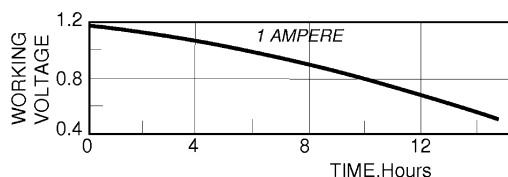
FIGURE 11.2

Voltage discharge characteristic for an alkaline-manganese primary D-cell battery discharged 24 hours per day.
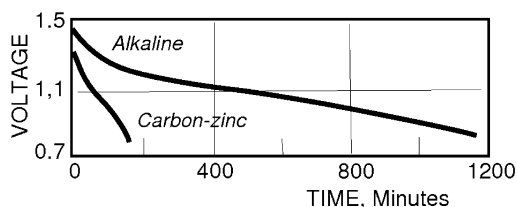
FIGURE 11.3

Comparison of discharge characteristics for alkaline-manganese and zinc-carbon D-size cells for a half-ampere continuous drain at 21°C.

Zinc of high purity is used as a container for the cell. The electrolyte is an aqueous solution of NH_4Cl and $ZnCl_2$. This paste is held in place with an absorbent material around an electrode of ground carbon and MnO_2.

The life of a dry cell battery varies with current drain, operating schedule, cutoff voltage, and age. The voltage of a battery declines continuously with use. The voltage discharge characteristic for a D-size carbon zinc battery is shown by the curves in Fig. 11.2 for various discharge currents drawn in a duty cycle of four hours per day.

Zinc-carbon batteries are designed to operate at 20°C. The higher the battery temperature during discharge, the greater the energy output. High temperature reduces storage life. Temperatures above 50°C causes rapid disintegration. Low temperatures reduce service life. At −18°C, zinc-carbon batteries are capable of providing only minimal current drains.

Alkaline dry cells consist of a zinc anode with a large surface area, a manganese dioxide cathode of high density, and a potassium hydrozide electrolyte. The alkaline cell has an advantage over conventional dry cells on a performance per unit of cost when the battery is subject to heavy or continuous current drains. The discharge characteristic of an alkaline cell for a 0.5 ampere continuous drain is compared with a similar discharge characteristic for a zinc-carbon dry cell in Fig. 11.3. Each battery is D size.

Rechargeable batteries are widely used in geophysical applications where more current delivery capability is needed. The common form of rechargeable battery is the lead cell, consisting of plates of lead oxide for the anode and sponge lead for the cathode immersed in sulfuric acid. On discharge, both the peroxide on the positive plate and the lead on the negative plate are converted to lead sulfate.
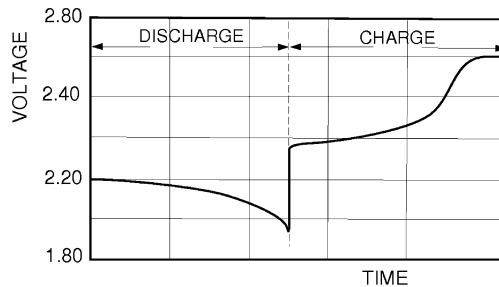
FIGURE 11.4

Charge and discharge cycles for a lead/acid storage battery.

These reactions are reversed when the battery is charged, or subjected to current input from an external source. Typical voltage and density characteristics for constant rates of discharge and recharge for such a battery are shown in Fig. 11.4.

11.1.2 CABLES

Many electrical surveying methods use a grounded cable to generate the field to be measured. In DC surveys, the field is generated by causing current to flow in the ground between two (or more) electrode contacts. In some controlled-source electromagnetic methods, a magnetic field is created by causing current to flow along a wire. The current then flows through the earth from the ends of that wire to complete the circuit. In the marine applications, the EM field is generated by causing current to flow from a submerged cable into conductive seawater. In either of these applications, we must consider the capability of the wire to carry the current output of the prime power supply.

Cables used in geophysical practice are commonly stranded copper, stranded aluminum, or stranded copper and steel. Stranded copper is the most readily available form of cable, so, we need to be aware of the physical characteristics of copper cables. Fig. 11.5 shows graphically the relationship between wire gauge and wire resistance.

Aluminum wire can provide better current carrying capacity for the same weight of cable. Aluminum is lower in density than copper, but also lower in conductivity. Considering both factors, a given weight of aluminum cable can carry 1.5 times as much current as the same weight of copper cable at the same voltage. Heavy aluminum cable is readily available, though light-weight wire is more difficult to find.

11.1.3 GROUNDING STRUCTURES

The third subsystem for a grounded-wire source is the grounding structure. One of the simplest forms of electrode is a driven rod or casing. The grounding contact resistance of such an electrode can be calculated with some degree of approximation by considering that the electrode is half of an ellipse of revolution in which the major axis is large compared with the minor. The resistance of such an
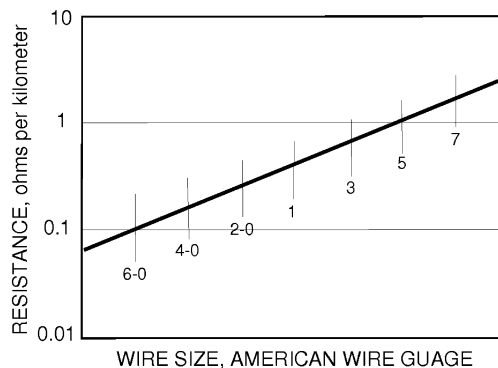
FIGURE 11.5

Resistance of stranded copper wire at 20°C.
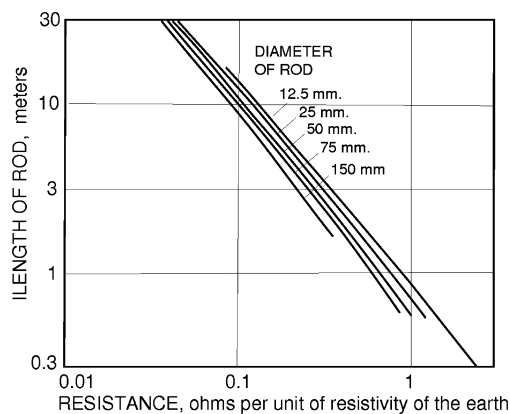
FIGURE 11.6

Resistance of a rod of elliptical shape driven into an earth with uniform resistivity. Actual resistance is obtained by multiplying the resistance indicated above by the actual resistivity of the earth.

ellipsoidal ground, normalized by the resistivity of the uniform earth, ρ, is given by the formula,

$$R_g/\rho = \frac{1}{2\pi L} \ln \frac{4L}{d},$$ (11.1)

where L is the length of the major axis (the length of the electrode) and d is the dimension of the minor axis (the diameter of the rod) for the ellipsoid. A series of curves computed from this expression is shown in Fig. 11.6.

These curves give the resistance normalized by the resistivity of the earth as a function of the length of a driven rod. It should be noted that a basic assumption in this calculation is that the entire surface
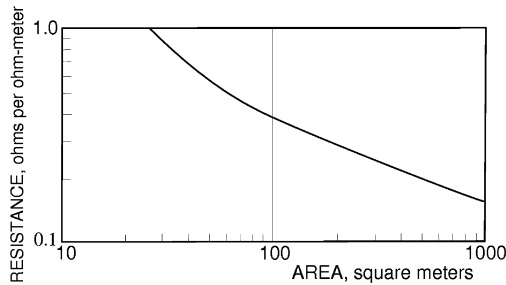
FIGURE 11.7

The minimum resistance obtainable by connecting a large number of rods in a square of given area in parallel.

of the driven rod is at the same potential. This is normally a good approximation for rods up to a hundred meters long, but for very long conductors, such as well casings several kilometers in length, the current is usually fed only at the top, and because current is lost progressively with increasing depth, the voltage at the bottom of a casing will be much less than the voltage at the top. As a consequence, at lengths greater than a few hundred meters, the resistance of a casing becomes more than would be computed using this formula. The extent of the effect depends on the relative resistivities of the casing material and the ground, and while it can be computed it is not an important factor in our considerations. Normally, the grounding resistance of a well casing is so low that whether or not it is underestimated makes little difference.

As can be seen from the curves in Fig. 11.6, the grounding resistance of a typical rod driven a meter or less into the soil is relatively high. Most soil resistivities are measured in tens of ohm-meters, and so the resistance of a short grounded rod will be measured in tens or hundreds of ohms. The resistance of a single rod is in general not sufficiently low, and in practice when driven rods are used, it is necessary to use a large number connected in parallel. The reduction in resistance obtained by such a process is not usually as great as is hoped because, unless considerable care is taken, when rods are so connected, the resistances do not necessarily comply with the usual law of independent resistances in parallel. According to Tagg (1964), the calculation of the net resistance when a large number of rods is used is difficult and can be laborious. However, exact calculations are not necessary.

Tagg has examined the expected parallel resistances for various combinations of multiple driven rods, and the results can be summarized in two illustrations. In the first (see Fig. 11.7) he has calculated the grounding resistance for a large number of rods connected in parallel and placed in a square array.

These rods are arbitrarily assumed to have a buried length of 2.6 m and a diameter of 0.025 m. Calculations indicate that the resistance is not particularly sensitive to these dimensions. The curves in Fig. 11.8 describe the relationship between grounding resistance and the number of rods when the rods are arrayed over an area as specified by the index on each curve. With an increasing number of rods within a specified area, the grounding resistance rapidly approaches asymptotically a minimum value.

Rods and well casings are one form of electrode, but often in areas where competent rock is present at shallow depths, especially in areas with dry alluvium, it is necessary to resort to wires and strips of metal buried at shallow depths. The grounding resistance for a wire of the length 2L and radius a
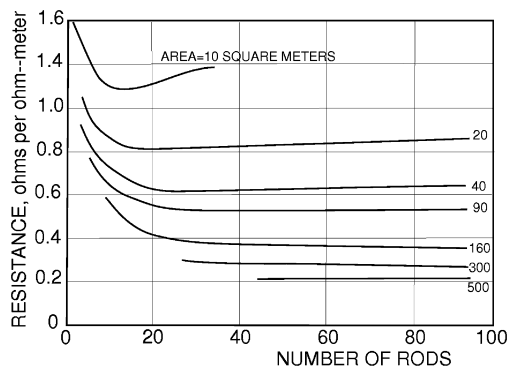
FIGURE 11.8

The minimum resistance obtainable by driving a given number of rods in a given area.
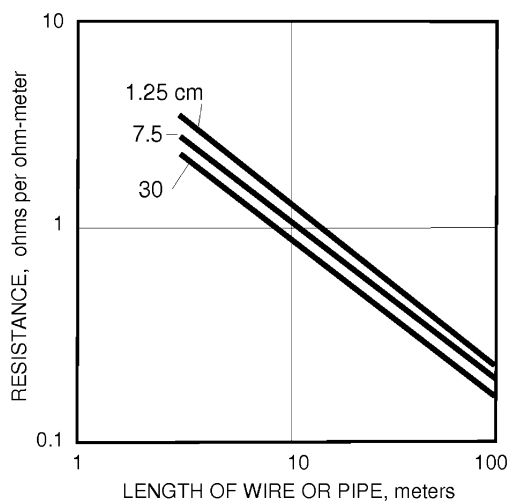
FIGURE 11.9

Grounding resistance of a length of wire or metal pipe buried at a depth of 1 meter. The label on each curve is the diameter of the conductor.

buried at a depth $S/2$ is (Tagg, 1964):

$$R_g = \frac{\rho}{4\pi L}\left[\ln\frac{4l}{a} - 1 + \ln 2L + \frac{(S^2 + 4L^2)^{1/2}}{S} + \frac{S}{2L} - \frac{(S^2 + 4L^2)^{1/2}}{2L}\right]. \qquad (11.2)$$

Resistance values calculated using this expression are plotted as curves in Fig. 11.9. These give the resistance normalized to the resistivity of the soil, ρ, which is a function of the length of a buried wire
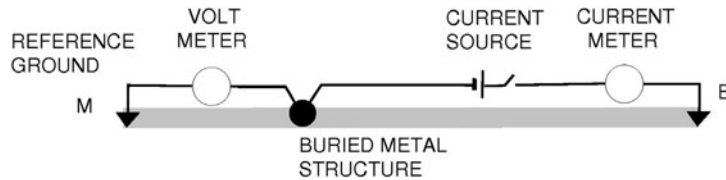
FIGURE 11.10

Three-terminal circuit to determine the approximate single-terminal resistance of a ground. Here, we wish to determine the grounding resistance of a preexisting system. A low frequency or direct current is driven through the ground to a return, B, while the voltage between the metal structure and a reference ground, M, is measured. The resistance is the ration of this voltage to the current.

or pipe with radii ranging from 0.0125 to 0.30 m, and for lengths ranging from 3 to 100 m. As in the case of a vertical pipe electrode, it has been assumed in these calculations that the entire length of the electrode is at the same potential. With a buried horizontal wire, this in fact can be accomplished by making multiple contacts with the buried wire or pipe at intervals along its length to assure that the current flows uniformly over the entire length.

Despite the fact that they are not as efficient or economical as rod or strip electrodes, considerable use is made of buried-plate electrodes. These are usually placed in pits one to four meters deep dug with a back hoe, with dimensions of 1–3 m^2. It is not easy to calculate the resistance of a plate, but an approximation can be made by considering the plate to be an isolated circle. In this case, the grounding resistance is approximately:

$$R_g = \frac{\rho}{a}\sqrt{\frac{\pi}{A}}, \tag{11.3}$$

where A is the area of the plate. Thus, a plate with 1 m^2 of area will have a resistance of 1.22 ohms/ohm-m, and a plate with an area of 4 m^2 will have a resistance of 0.45 ohms/ohm-m. In order to obtain a low resistance, it is clearly necessary to use several plates in parallel.

Grounding resistance can be estimated using the formulas given above, but it can also be measured after a grounding system has been constructed or if a pre-existing ground of unknown geometry is used. The circuit shown in Fig. 11.10 can be used to determine the single-terminal grounding resistance of a grounding structure. In this procedure, a second ground is established with a single stake or some other easy means at a distance of 50 to 100 m away. A switch is used to turn current on and off between the structure and the reference ground. The voltage drop between the metal structure and a reference electrode at a distance of 10 m or so from the structure is then measured. The approximate grounding resistance, accurate within 10 or 20%, is the ratio of voltage drop to current.

Another approach to measuring the grounding resistance of a single electrode is to establish two other grounds at moderate distances. One then measures three circuit resistances, in each of which one pair of the three electrodes is connected in parallel and the full circuit resistance to the measuring electrode is measured. One then has three equations for circuit resistances, R_1, R_2, R_3, which can be

solved for the unknown single-terminal grounding resistances, $R_{g,1}$, $R_{g,2}$, $R_{g,3}$:

$$R_1 = R_{g,1} + \frac{R_{g,2}R_{g,3}}{R_{g,3} + R_{g,2}},$$

$$R_2 = R_{g,2} + \frac{R_{g,3}R_{g,1}}{R_{g,1} + R_{g,3}},$$

$$R_3 = R_{g,3} + \frac{R_{g,1}R_{g,2}}{R_{g,2} + R_{g,1}}. \tag{11.4}$$

This method works well only when the three circuit resistances are of the same order of magnitude.

11.2 MEASUREMENT OF ELECTRIC AND MAGNETIC FIELDS
11.2.1 VOLTAGE, POTENTIAL, AND ELECTRIC FIELD

As we have seen in the many theoretical developments on which the design of a geoelectrical exploration method is based, we must measure either some features of an electric field or some features of a magnetic field, or both. It was demonstrated in Chapter 3 that the work of the electric field along a given path (the quantity called *electric voltage*) and the flux of the magnetic field through a given surface represent the most important physical characteristics of electromagnetic fields, which are studied and measured in the geophysical experiment. It was also shown in Chapter 4 that, for a low frequency electrical field, the electric voltage between two points could be expressed as that of the potential drop between two points in an electric field, where "potential" was an abstract physical concept, defined as being the negative of the work done in moving unit electric charge from infinity to the point where the potential is being measured. Thus, in reality, we do not measure the electric field **E** directly. The measurement that can be made is that of the potential drop between two points in an electric field, which actually represents the *voltage*. This is the quantity which represents the electric field in the Maxwell's equations written using the differential forms (see Chapters 2 and 3). At the same time, this is the quantity we measure when the electric field or electric potential is needed to carry out an electrical survey as designed.

The corresponding component of the electric field, e.g. E_x, can be then approximately devised as quantity:

$$E_x = -grad_x U = -\frac{\partial U}{\partial x} = \lim \frac{U(x_2) - U(x_1)}{|x_1 - x_2|}; \ |x_1 - x_2| \to 0, \tag{11.5}$$

where $U(x_1)$ and $U(x_2)$ are the electric potentials at points x_1 and x_2.

The measurement of voltage between two contacts with the earth is a reasonably straightforward procedure. However, one aspect of the measurement of voltage between two points in the earth must be carefully considered. The electrode contacts we use to make the measurement are metal, connected with metallic conductors to an electronic piece of equipment which is used to detect and record the voltage drop between two electrodes. On the other hand, almost always current conduction within the earth is electrolytic in nature. At the boundaries between the electrolytic and metallic parts of the measuring circuit, that is, at the surfaces of the metal electrode contacts, fairly complicated chemical
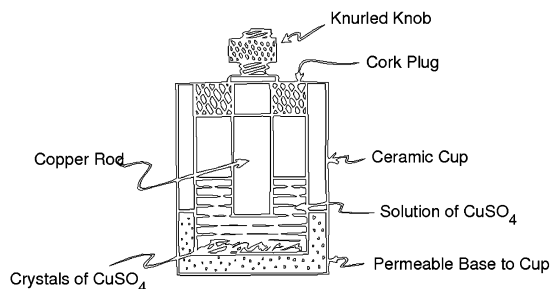
FIGURE 11.11

Construction of a porous pot salt bridge for use in detecting voltage in a material with electrolytic conduction.

reactions must occur, and these give rise to electromotive forces which are unrelated to the voltages we wish to measure as part of the geoelectrical method being used.

The chemical reactions that occur at an electrode surface in contact with an electrolyte are characterized by an *electrode potential*. Each metal has a characteristic electrode potential, which depends on the metal of the electrode and the activity of the solution with which it is in contact.

Not only does a difference in electrode material lead to the measurement of a voltage unrelated to current flow in the earth; differences in concentrations of ions in solution in the electrolyte in contact with the electrodes will also give rise to a voltage unrelated to current flow. This voltage is given by the *Nernst* equation:

$$V_e = \frac{R}{F} \frac{T}{n} \ln \frac{C_2}{C_1}, \tag{11.6}$$

where R is the gas constant, or 8.309 joule per degree C, n is the valence, F is Faraday's constant for electrolysis, or 96,494 coulombs (the ratio, $R/F = 0.861 \times 10^{-4}$ volts), T is absolute temperature, and C_1 and C_2 are the concentrations of salt in the metal in the two electrodes. Evaluation of this equation yields zero voltage if the two concentrations are the same, 58 millivolts if there is a ten-to-one ratio of concentrations, and 115 millivolts if the ratio is 100.

Clearly, good practice dictates that electrodes of like metal be used when measurements of electric field or electric potential are to be attempted. Moreover, it is desirable that these metals be immersed in a solution of one of the salts of that metal, that salt being maintained at some specified concentration. Such electrodes, called *nonpolarizing electrodes*, are routinely used in field applications.

The typical nonpolarizing electrode, also often called a *porous pot* by the field crew, consists of a semipermeable ceramic cup, usually of a design like that shown in Fig. 11.11. The active electrode is a rod of exceptionally pure metal, usually electrolytic copper, inserted in the cup, and held in place with a Bakelite or other inert stopper sealing the top of the cup. The cup is filled with a specified solution of the salt of that metal, which, in the case of a copper electrode, is copper sulfate. The strength of the solution can be 1 normal, or the solution can be forced to be saturated by adding excess crystals of copper sulfate. This solution then saturates the permeable ceramic, providing a conducting bridge between the metal electrolyte and the soil moisture with which the porous pot is in contact.

It is often stated that a disadvantage of the porous pot is that it provides an undesirably high resistance in contact with the ground. This is patently untrue for the following reasons: a 1 normal or saturated copper sulfate solution has a resistivity of the order of 0.2 ohm-meters. Even when this solution is dispersed in the semipermeable shell around it, the resistivity of the shell will be not greater than 1 ohm-meter. These values of resistivity are lower than the resistivities of most of the earth materials on which the electrodes will be placed. The contact resistance is reduced from the value which would be observed by driving the metallic rods directly into the ground.

Filaments of ground water coating the grains in the soil establish electrical continuity with the copper sulfate in the semipermeable ceramic cup. A voltage develops at this contact point, given by the Nernst equation as shown above, except expressed in terms of the ion activities in the two solutions, the pore water and the copper sulfate:

$$U_d = \frac{v - u}{v + u} \frac{R\,T}{F\,n} \ln \frac{C_2}{C_1}, \tag{11.7}$$

where u and v are the mobilities of the cations and anions, respectively.

The copper sulfate at each electrode used in measuring a voltage will be the same, but the salinity of the water in the soil or rock on which the porous pot is place can differ. Usually this difference is not great, so one expects a pair of porous pots connected to a voltage sensing device to be not more than a few millivolts.

It is sometimes common practice to improve the contact of a porous pot with the ground by "wetting it down." Some water is poured onto the plant of the porous pot. This process destroys the utility of the porous pot, which is to provide a small but stable non-current-related voltage between the electrodes used in detecting current-caused voltage drops in the earth. Wetting down a porous pot invariably leads to long-term rapid variations in the voltage observed between two pots, amounting to tens of millivolts, and caused by such things as filtration potentials. The worst possible procedure is to wet down only one of the porous pots comprising the ground circuit with salt water. This results in a permanent offset of the voltage between the two electrodes amounting to tens of microvolts.

The only electric field-related measurement that is possible in practice is that of the voltage between two points on (or in) the earth. Estimates of the electric field can be made from such voltage measurements. In one case, the ratio of the voltage between two measuring electrodes, M_1 and M_2, and the separation between those electrodes, $\overline{M_1 M_2}$, is used as an approximation of the component of the electric field in the MN direction:

$$E_{MN} \approx V_{MN}/\overline{M_1 M_2}. \tag{11.8}$$

Note that in this equation we make no implication that a limit as $\overline{M_1 M_2} \to 0$ is to be taken. In practice, an attempt to use a short MN separation often results in a poorer estimate of the electric field component than the use of even a quite long separation.

The electric field is a vector, having two scalar components when measured on the surface of the earth. For full definition of the electric field vector on the earth's surface, a measure of the voltage drop between a second pair of electrodes, O and P, is made, and

$$E_{OP} = V_{OP}/\overline{OP}. \tag{11.9}$$
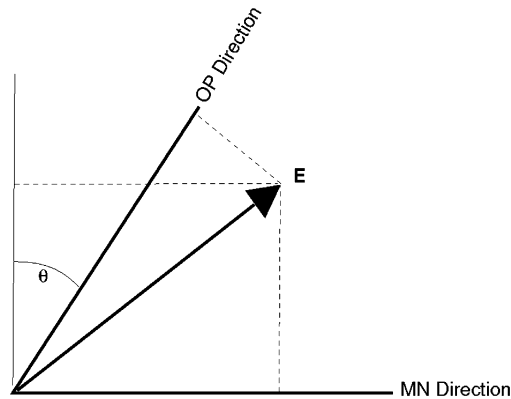
FIGURE 11.12

Often, in field operations, the electric field is measured in terms of two components which are not orthogonal. The magnitude and direction of the vector can be determined with this sketch of the various projections of the vector on the real field directions and on a set of orthogonal axes.

If the electrode pairs MN and OP lie along lines that intersect perpendicularly, the vector **E** is defined simply with the two components E_{MN} and E_{OP}. Often, in practice, it is not convenient to lay out the lines MN and OP precisely along orthogonal directions. In this case, one must determine the vector, **E**, from two nonorthogonal components. The procedure for doing this is shown graphically in Fig. 11.12. The magnitude of a vector determined from two components that are not orthogonal is given by

$$|\mathbf{E}|^2 = E_{MN}^2 + (E_{OP}\cos\theta)^2, \tag{11.10}$$

where the angle θ is the angular departure of the angle between MN and OP from $\pi/2$ (see Fig. 11.12).

Measurement of the electric field is an essential part of many electrical methods, as, for example, in the Schlumberger approach to vertical electric sounding, in bipole-dipole mapping (see Chapter 12), and in magnetotelluric methods (Chapter 13). The accuracy of the results from these important methods depends in large part on the accuracy of the approximation made in using the ratio of voltage to electrode spacing as an electric field component. We can examine the reliability of the approximation in two respects: the filtering of the spatial spectrum for the electric field which occurs when separated electrodes are used to measure it, and the impact of sampling when we attempt to measure the electric field at a number of "points" in the electromagnetic field.

The electric field is a quantity defined at each point in the field; the value at any given point can vary independently of the value at any other point, no matter how close together the points may be (in other words, the electric field can be discontinuous). The electric field can be represented in the spatial frequency domain as a Fourier transform of the function describing the point-by-point spatial behavior
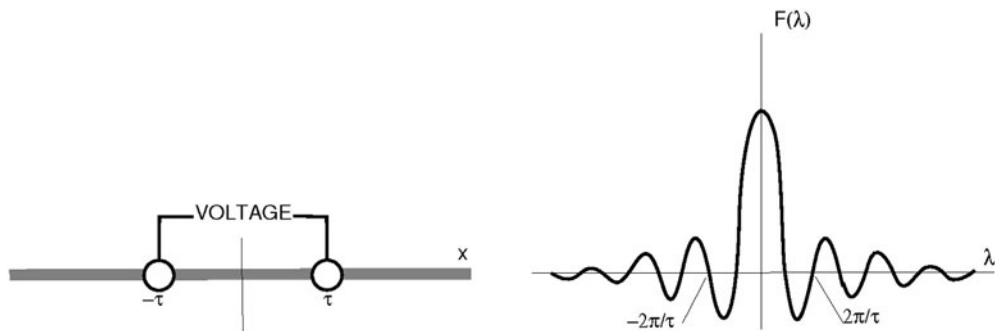
Filtering phenomenon which occurs when an electric field is measured with electrodes at a nonzero separation (on the left). The actual electric field can vary markedly between the two electrodes, with the measured voltage representing the average electric field between the electrodes. The system response of this system is shown in the space frequency domain on the right.

of the electric field:

$$\mathbf{e}\left(k_x, k_y\right) = \frac{1}{4\pi} \iint\limits_{-\infty}^{\infty} \mathbf{E} e^{-i\left(k_x x + k_y y\right)} dx dy. \tag{11.11}$$

The vector spectrum represents two separate scalar spectrums, one for each component of the electric field. When an electric field component is taken to be the ratio of voltage to separation, it is equivalent to averaging the electric field over the distance from the point M to the point N. The filter response of averaging is shown in Fig. 11.13. The greater the separation between the electrodes, the more the higher frequency spatial components of the field will be suppressed.

Suppression of the high spatial frequency components of the electric field can be a serious problem if the spatial character of the electric field is important in interpretation, as is the case when migration or continuation is used (see Chapter 9). In such applications, it is important to measure the electric field with as short an electrode separation as is possible.

Unfortunately, the use of short electrode separations in measuring electric fields can lead to significant problems, particularly when the soil layer in which the electric field is measured is not uniform in character. One such problem is the phenomenon of geologic noise when the layer at the surface of the earth has irregular patches of one or another resistivity, rather than being laterally uniform. The soil layer often will contain wet and dry patches or inclusions of boulders in a finer soil. The current flow in this soil layer will flow around patches of high resistivity and collect in patches of low resistivity, so that the electric field pattern appears to represent a highly turbulent flow of current.

Small-dimension resistivity variations at the surface of the earth can be quite arbitrary in shape, and so, a detailed, quantitative discussion of the effect they have on the electric field at the surface of the earth can be quite tedious. However, we can evaluate the distortion caused to the electric field by considering a simplified model, that of a hemispherical pod and the effect it will have on the electric field when illuminated by a planar current sheet. This problem has been analyzed in detail, with many
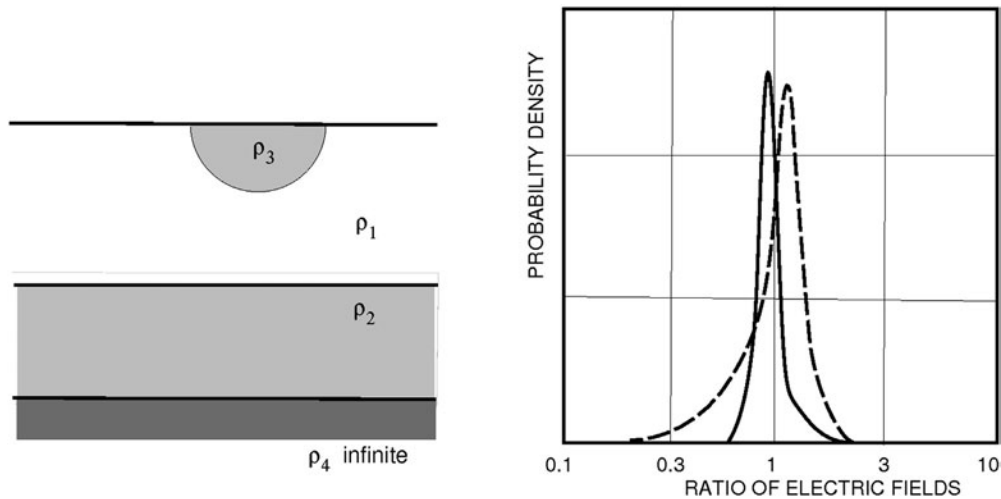
FIGURE 11.14

Probability distribution of electric field strengths measured in the vicinity of a hemispherical surface inclusion of higher or lower resistivity. The solid curve is the distribution for a resistive inclusion (9:1) and the dashed line is the distribution for a conductive inclusion (1:1/9). The electric field ratio is the normalization of the electric field with the inclusion present to that when it is absent. Note the wider distribution function and the skewing toward lower electric fields in the case of a conductive inclusion.

published results (Kunetz and Chastenet de Gery, 1956). Fig. 11.14 shows the typical electric field curves observed along a traverse crossing the center of conductive or resistive hemispherical pods. The important feature of these curves is that the electric field observed inside a hemispherical resistive pod is never more than twice the electric field that would be observed if the pod were not there, while the electric field inside a conductive pod is decreased by approximately the resistivity contrast between the pod and the surrounding medium.

These calculations pertain only to hemispherical pods, and results can be much more complicated for less symmetrical features. However, it is reasonable to generalize by saying that conductive pods at the surface of the earth will lead to greater distortion of the electric field than will resistive inclusions. This effect has been termed *geologic noise* (Keller, 1968).

Fig. 11.14 shows a pair of histograms, one for the distribution of electric field values in and around a conductive hemispherical pod and the other for those in and around a resistive hemispherical pod. We can make the following inferences:

• 1) Distortions of the electric field will be more significant when the local inhomogeneities are more conductive than the surface host rock in which they occur than when the local inhomogeneities are relatively resistive.

• 2) If the surface rock is highly resistant, geologic noise will normally be a severe problem in the measurement of the electric field.

• 3) If the surface rock is highly conductive, geologic noise is rarely a problem.

• 4) In any event, geologic noise is unlikely to cause normally distributed errors to electric field observations, so simple averaging usually is not effective in reducing geologic noise.

11.2.2 SENSING THE MAGNETIC FIELD

Measurement of the magnetic components of the electromagnetic field is in many ways more difficult than measurement of the electric components. Many varieties of sensitive magnetometers have come into use in geophysics; each has advantages and shortcomings which must be considered in designing any given electrical method which requires knowledge of the magnetic field.

Magnetic balances

The oldest form of magnetometer is the magnetic balance, no different in principle than the compasses used by early mariners. In a magnetic balance, a magnetized piece of ferromagnetic material is suspended in such a way that the torque exerted by the ambient magnetic field on the suspended magnetic material is balanced against gravity. Fig. 11.15 shows an arrangement for measuring a horizontal component of the magnetic field with a magnetic balance. A bar magnet is balanced vertically on a knife edge. The suspension of the magnet is constructed in such a way that the center of gravity is below and to the left of the suspension point. The torque exerted by the horizontal component of the magnetic field normal to the axis of the wedge on the magnetic moment of the magnet rotates the magnet until it is balanced by the force of gravity attempting to rotate the magnet about its point of suspension. In Fig. 11.15, if the strength of the horizontal component of the magnetic field increases, even slightly, the component of weight contributing to the gravitational torque, and when the magnet has rotated far enough, the two torques come into balance. In a typical sensitive magnetic balance the actual amount of rotation is small, probably less than a degree. The rotation can be detected using a light beam reflected
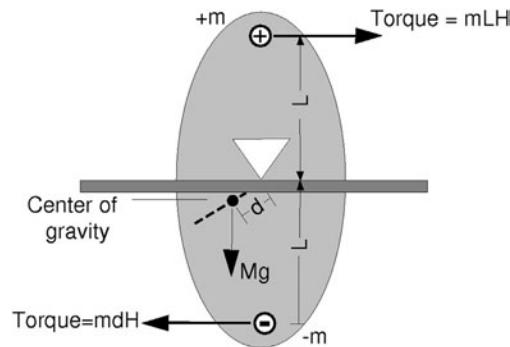
FIGURE 11.15

Principle of a magnetic balance. A magnetized rod of moment 2mL is balanced at a point slightly offset from its center of gravity. The rod rotates until the gravitational torque about the point of suspension, Mg, balances the torque imposed by the action of the horizontal component of the magnetic field on the magnet, 2mLH. The rotation needed to bring the two torques into balance is a measure of the horizontal component of magnetic field strength, H.
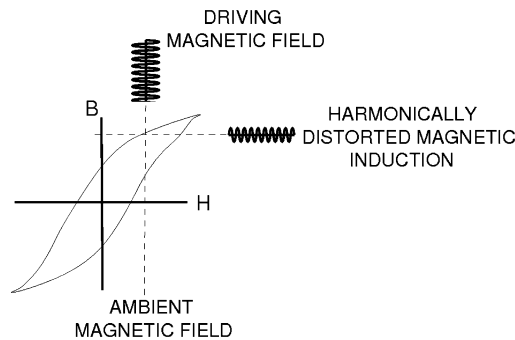
FIGURE 11.16

Principle of the flux-gate magnetometer. The sensing element is a ring or rod of ferromagnetic material with a hysteresis curve as shown. An oscillatory magnetic field (1–100 kHz) is added to the ambient magnetic field by driving a monochromatic current through a coil wound on the sensing element. Because the hysteresis curve is curved, the magnetic induction exhibits harmonic distortion. The second harmonic is separated by filtering and used to determine the strength of the ambient field.

from a mirror mounted on the magnet with the motion of the light beam being recorded on a moving strip of film.

Magnetic balances are commonly sensitive enough to provide deflections of the recorded trace of the order of a millimeter per nanotesla. The chief advantage of a magnetic balance is its simplicity and economy of cost. The principal disadvantage is the fact that it is particularly difficult to build a magnetic balance with adequate sensitivity to short-period magnetic field oscillations. Such instruments can be used only when periods to be recorded are measured in seconds and longer.

Magnetic balances have been used with considerable success in magneto-variation studies.

Flux-gate magnetometers

The magnetic flux gate has been used in geophysical surveys of the earth's geomagnetic field for many decades. The sensing element is a small rod or ring of a ferromagnetic material with very special properties. The ferromagnetic material must saturate at low coercive magnetic field strengths. Ideally, that material has a strongly nonlinear B-H curve, or relationship between applied magnetic field, H, and magnetic induction within the material, B, as shown in Fig. 11.16. Ideally, the saturation field strength at which further magnetic induction within the material becomes small is not much grater than the ambient strength of the magnetic field to be measured.

The operation of a flux gate takes place as follows. A coil of wire is wrapped around the magnetic core, whether it be a rod or a ring, and energized with an alternating voltage of very pure waveform at a single frequency, called the driving frequency, ω_0, which will drive current through the coil. Any time-varying magnetic field will add to or subtract from the instantaneous value of the total magnetic field impressed on the flux-gate core. As the changing magnetic field moves along the B-H curve, the impedance of the coil will vary, and the current flowing in the coil will vary also. The result is distortion of the waveform, which can be detected by separating the harmonic components of the net

current flowing in the coil from its fundamental. The amount of distortion is a measure of the change in ambient magnetic field from instant to instant.

In practice, the harmonic distortion is not used as a measure of the magnetic field changes. Rather, a second coil carrying time-varying direct current is used to modify the field acting on the core in such a way that harmonic distortion remains unchanged. Then, the strength of the time-varying direct current is a simple measure of the change in magnetic field strength.

The nominal sensitivity of many flux-gate magnetometers is of the order of 0.1 to 1 nanotesla. The bandwidth, or ranges of frequencies over which such a magnetometer can be used, is limited by the driving frequency. The rate at which the magnetometer can sense a change in the magnetic field depends on the time which it takes to sense a change in the second harmonic distortion of the current in the driving coil. With the necessary filtering of the distortion signal to make its measurement stable, it is possible to measure changes in the magnetic field which occur at frequencies as great as a few percent of the driving frequency. Often a driving frequency of a few kilohertz is used, so that the bandwidth of such magnetometers is a few tens of Hertz. With a particularly high driving frequency, say 50 kilohertz, the bandwidth for detecting magnetic field changes can be as great as 1 kilohertz.

SQUID magnetometers

A Superconducting Quantum Interference Device (SQUID) or Josephson Junction Magnetometer (Josephson, 1962) is based on the use of a small electrically superconducting loop, generally with an area of a few square centimeters or less, to detect a magnetic field (see Fig. 11.17).

Describing the essential characteristics of a SQUID is straightforward (Falco and Schuller, 1980; Hahlbohm and Lubbig, 1977). Consider a ring of superconducting material in which there is a narrow spot, or "weak link" (see Fig. 11.18). Josephson predicted theoretically that a super current could flow between two superconductors without a voltage drop even though they may be physically separated by a small insulating gap. The phenomenon is also observed if a superconducting ring has a narrow spot in it where the current is concentrated to such a level that the transition from superconduction to normal conduction is approached.

The superconducting SQUID combines the physical phenomena of flux quantization and Josephson tunneling. First predicted by London (1950), flux quantization was observed experimentally by Deaver and Fairbank (1961), and Doll and Nabauer (1961). They showed that the flux contained in a closed superconducting loop is quantized in units of the flux quantum $\Phi_0 = h/2e \approx 2.0678 \times 10^{-15} \ tesla \cdot m^2$. Here, $h = 2\pi \hbar$ is Plank's constant, $\hbar$ is a reduced Plank's constant, and e is the electronic charge. The great sensitivity of the SQUID devices is associated with measuring changes in the magnetic field associated with one flux quantum.

Flux quantization arises from the analysis of the macroscopic wave function:

$$\Psi = |\Psi| \, e^{i\phi(r,t)}, \tag{11.12}$$

where ϕ is the phase.

Electrons in the superconductive state groups in pairs to compensate their individual spins and form a new pseudo particle, which carries a total charge $q = 2e$ and is called a Cooper pair. In the absence of applied fields or currents, the phase $\phi(r, t)$ takes the same value throughout the superconductor for all Cooper pairs n. In the case of a loop threaded by a magnetic flux, however, the phase around the loop changes by $2\pi n$, where n is the number of enclosed flux quanta.
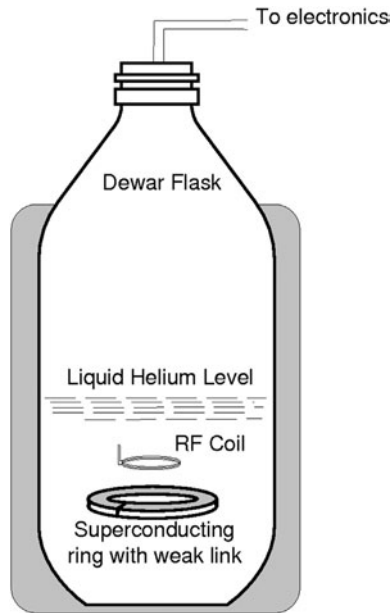
FIGURE 11.17

Main elements of a Josephson junction magnetometer. The sensing element is a ring of superconducting metal in a bath of liquid helium. The ring has a notch cut in it to form a weak link. Any change in magnetic field will cause a large current to appear in the superconducting ring. The current will increase until it exceeds the saturation current at the weak link. At that point, the resistance at the weak link interrupts the current in the ring. The process continues as long as the magnetic field varies. These changes in current in the ring are detected with a nearby coil, providing a signal which can be used to measure the changing magnetic field.

In 1962 Josephson predicted the tunneling of the Cooper pairs through a barrier separating two superconductors – the phenomenon now known as a Josephson tunneling. Josephson demonstrated that the current I_S in the superconductive state flowing through a junction is given by the expression:

$$I_s = I_c \sin \Delta\phi_w, \tag{11.13}$$

where $\Delta\phi_w = \phi_1 - \phi_2$ is the difference between the phases ϕ_1 and ϕ_2 of the condensates (in a quantum physics sense) in the two superconductive electrodes, and I_C is a constant, the critical current of the junction. The critical current is a maximum current that can be sustained before the superconductive weak links goes through transition to a normal state, which is typically 1–10 microamperes in modern SQUID magnetometers. The critical current is an important phenomenological parameter of the device that can be affected by temperature as well as by an applied magnetic field.
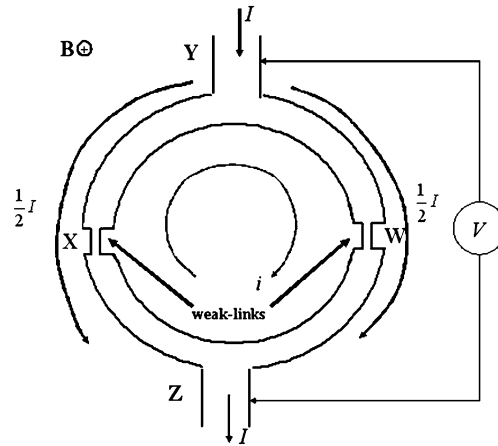
FIGURE 11.18

Superconducting quantum interference device (SQUID) as a simple magnetometer. The central element of a SQUID is a ring of superconducting material with two weak links, X and W.

Thus, Josephson predicted that a phase change occurs when current crosses a weak link in a super-conductor, with the amount of phase change being:

$$\Delta\phi_w = \sin^{-1}\left(\frac{I_s}{I_c}\right), \tag{11.14}$$

where I_s is the current passing through the weak link. This equation is also known as a *Josephson* or *weak-link current-phase* relation.

The central element of a SQUID is a ring of superconducting material with one or more weak links. An example is shown in Fig. 11.18, with weak links at points W and X whose critical current, I_C, is much less than the critical current of the main ring. This produces a very low current density making the momentum of the electron pairs small. The wavelength of the electron pairs is thus very long, leading to little difference in phase between any parts of the ring.

If a magnetic field, **B**, is applied perpendicular to the plane of the ring, a phase difference is produced in the electron-pair wave along the path XYW and WZX. A small current, i, is also induced to flow around the ring, producing a phase difference across the weak links. Normally the induced current would be of sufficient magnitude to cancel the flux in the hole of the ring, but the critical current of the weak-links prevents this.

The phase of the electron pairs can be affected not only by the current density but also quite strongly by an applied magnetic field **B**. In the presence of a magnetic field the momentum, $\mathbf{P}_q$, of a particle with charge q becomes

$$\mathbf{P}_q = m\mathbf{v} + q\mathbf{A},$$

where **A** is the magnetic vector potential, $\mathbf{B} = curl\mathbf{A}$.

For electron pairs in an applied field $\mathbf{B}$, their moment, $\mathbf{P}_e$, is now equal to

$$\mathbf{P}_e = 2m\mathbf{v} + 2e\mathbf{A}.$$

Then the difference in phases between two points with a superconductor is related to canonical momentum by

$$\Delta\phi_{XY} = 2\pi \int_X^Y \frac{\mathbf{P}_e}{h} \cdot d\mathbf{l} = \int_X^Y \{4\pi m \mathbf{v}_s / h + 4\pi e \mathbf{A} / h\} \cdot d\mathbf{l}, \tag{11.15}$$

where m and e are electron mass and charge, respectively, $\mathbf{v}_s$ is the velocity of the superconducting electrons, and $\mathbf{A}$ is the vector potential.

The change in phase in traversing an integration path which starts and ends at point X is:

$$\Delta\phi = \frac{4\pi m}{h} \oint \mathbf{v}_s \cdot d\mathbf{l} + \frac{4\pi e}{h} \oint \mathbf{A} \cdot d\mathbf{l}. \tag{11.16}$$

In an applied field $\mathbf{B}$, the phase difference is now a combination of that due to the super current across the two weak-links, $2\Delta\phi_w$, and that due to the applied field, $\Delta\phi_B$:

$$\Delta\phi = 2\Delta\phi_w + \Delta\phi_B, \tag{11.17}$$

where

$$\Delta\phi_B = \frac{4\pi e}{h} \oint \mathbf{A} \cdot d\mathbf{l}. \tag{11.18}$$

The quantum condition that the phase change around the closed path must equal $2\pi n$, can still be met by large phase differences across the weak links produced by even a small current. As shown in Eq. (11.18), the applied magnetic field produces a phase change around a ring equal to:

$$\Delta\phi_B = 2\pi \frac{\Phi_B}{\Phi_0}, \tag{11.19}$$

where Φ_B is the flux produced in the ring by the applied magnetic field (see Stokes's formula (1.44)):

$$\Phi_B = \oint \mathbf{A} \cdot d\mathbf{l} = \iint_S curl\mathbf{A} \cdot d\mathbf{s} = \iint_\mathbf{S} \mathbf{B} \cdot d\mathbf{s},$$

and $\Phi_0 = h/2e$ is the single flux quantum.

The magnetic flux, Φ_B, may not necessarily be equal to an integral number of fluxons. To ensure that the total phase change is equal to $2\pi n$, a small current should flow around the ring, having a total phase change of $2\Delta\phi_w$ across the weak links, and giving a total phase change of:

$$\Delta\phi = 2\Delta\phi_w + \Delta\phi_B = 2\pi n. \tag{11.20}$$

Taking into account Eq. (11.19), we can introduce the *flux quantization condition*:

$$2\Delta\phi_w + 2\pi \frac{\Phi_B}{\Phi_0} = 2\pi n, \tag{11.21}$$

where $\Delta\phi_w$ is the phase difference across the single Josephson junction, Φ_B is the total magnetic flux threading the loop, and $\Phi_0 = h/2e$ is the single magnetic flux quantum. Using Eq. (11.21), we can substitute the phase difference into the Josephson relations given in Eq. (11.13). This yields an expression for the super current through the superconducting loop:

$$I_s = I_c \sin \Delta\phi_w = -I_c \sin\left(\pi \frac{\Phi_B}{\Phi_0} - \pi n\right). \tag{11.22}$$

Finally, the magnitude of the circulating current is equal to:

$$|I_s| = |I_c| \left| \sin \frac{\pi \Phi_B}{\Phi_0} \right|. \tag{11.23}$$

As the flux in the ring is increased from 0 to $\Phi_0/2$, the magnitude of I_s increases to a maximum. As the flux is increased greater than $\Phi_0/2$, it is now energetically favorable for a current to flow in a clockwise direction, decreasing in magnitude to 0 as the flux reaches Φ_0. The circulating current has a periodic dependence on the magnitude of the applied field, with a period of variation of Φ_0, a very small amount of magnetic flux. Detecting this circulating current enables the use of a SQUID as a magnetometer.

The circulating current produced by a flux change in the SQUID can be detected by the use of a measuring current, I. This current divides equally between both weak-links if the ring is symmetrical. Whilst the current through the weak-links is small there will be no voltage detected across the ring. As I is increased, it reaches a critical measuring current, at which voltages begin to be detected.

In practice, the SQUID is driven at some frequency of the order of 20 MHz, superimposed on the ambient magnetic field. This distortion is detected electronically and converted to values of ambient magnetic field intensity referred to some unknown zero level. Changes in applied flux (contributed by changes in the ambient magnetic field) of less that Φ_0 can be resolved.

A SQUID magnetometer must operate at low temperatures. Composed superconductor materials have to be cooled to 4° Kelvin (liquid helium) for a low-temperature superconductive material, or to 77° Kelvin (liquid nitrogen) for a high-temperature superconductive material to operate in a superconductive state. Provision of liquid helium and nitrogen under field conditions can be a logistical problem in remote areas. The usage of liquid nitrogen for SQUID, based on high-temperature superconductive materials, is more affordable. Fig. 11.19 shows a typical SQUID magnetometer, which can be used in geophysical exploration (after http://tristantech.com/general).

Induction magnetometers

Induction magnetometers differ from most other types of magnetometer in that they detect the time rate of change of magnetic field strength, rather than the field itself. The emf induced in a coil of wire is

$$emf = -n\frac{d\varphi}{dt} = -n\mu_0 A \frac{dH}{dt} \cos\theta, \tag{11.24}$$

where n is the number of turns of wire, A is the area of the coil, φ is the magnetic flux cutting the area of the coil, and θ is the angle between the magnetic field vector, **H**, and the axis of the coil. It is also assumed in using this expression that the coil can have negligible resistance, inductance, and capacitance.

FIGURE 11.19

SQUID magnetometer.
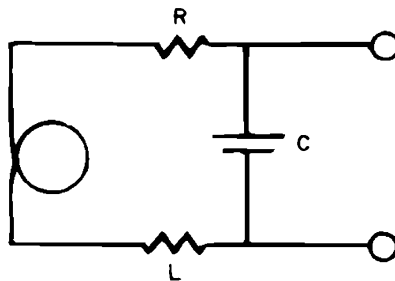
FIGURE 11.20

Representation of an induction coil as an equivalent circuit with lumped resistance, capacitance, and inductance.

If low field strengths are to be measured at low frequency, the turns-area product, nA, must be quite large. An ideal coil with 100,000 turns and a cross-sectional area of one square meter will produce an output voltage of 6.28 μV for a magnetic field change of 1 nT at a frequency of 1 Hz. Inasmuch as 250 kilometers of wire is required to construct such a coil, and because lightweight wire must be used to keep the weight of the coil down, the resistance, capacitance, and inductance of such a coil is not negligible. Under such conditions, the equivalent circuit of an induction coil is approximately that shown in Fig. 11.20.

The sensitivity of an induction coil can be increased or its resistance and capacitance decreased by winding the coil on a core of material with high magnetic permeability. The output of such a coil will be

$$emf = -nK_e\mu_0 A\frac{dH}{dt}\cos\theta, \tag{11.25}$$

where $\mu/\mu_0 = K_e$ is the effective relative magnetic permeability of the core material.
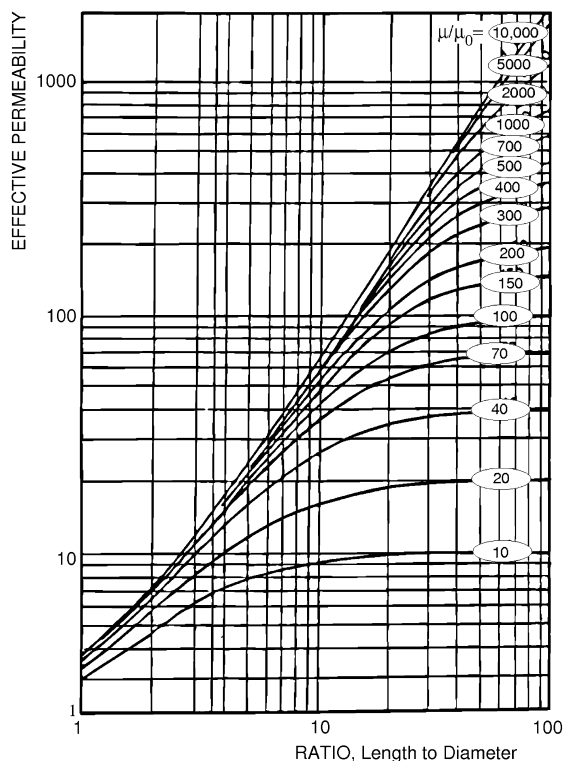
FIGURE 11.21

Effective permeability of a cylindrical rod of high-permeability material.

The true relative magnetic permeability may be as great as 10^5 for special high-permeability alloys, such as a superalloy. However, because of demagnetization, the effective permeability for a specific core will be much less than the true permeability unless the form of the core is that of a long thin rod. Fig. 11.21 shows curves relating the effective conductivity of cylindrical cores to the ratio of diameter to length for several high-permeability alloys. Consider a short rod, one in which the ratio of length to diameter is 2. The curves in Fig. 11.21 indicate that the effective permeability, and thus, the gain in sensitivity for a coil wrapped on such a core, is about 6.5 no matter which core material is used. On the other hand, if a solenoid consisting of 100,000 turns of wire were to be wound on a permalloy rod with a diameter of 7.5 mm and a length of 7.5 m, it would produce the same output voltage at low frequency as the air core coil describer above (6.28 μV) at a frequency of 1 Hz and an input signal level of 1 nT. The amount of wire required is only 250 meters, and the resistance and capacitance of the coil will be smaller by the same factor, 1000.

When the capacitance, inductance, and resistance of a coil are taken into account, there is some frequency at which a maximum output is observed; output will be lower at both higher and lower
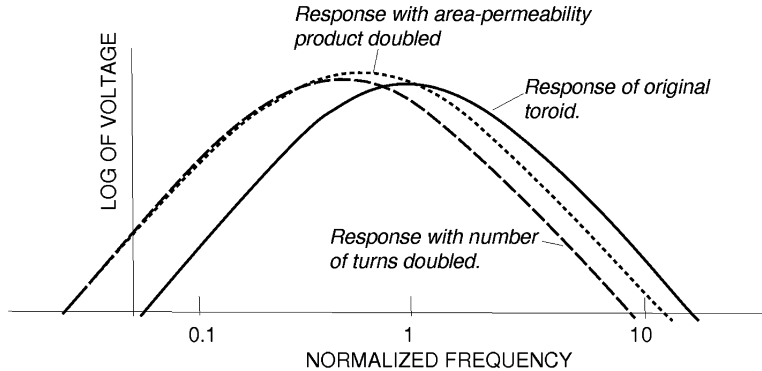
FIGURE 11.22

Changing the response of an induction coil. Increasing the number of turns will provide more output at lower frequencies but lower output at high frequencies. Increasing the area-permeability product of the coil will cause a somewhat similar change in output.

frequencies. The frequency at which the maximum output of a coil is observed is:

$$\omega_{\max} = \left(\frac{1 + R/R_m}{LC} \right), \tag{11.26}$$

where R, L, and C are the resistance, capacitance and inductance of the coil, and R_m is the input resistance of the equipment used to measure the voltage from the coil.

The characteristics of a coil can be changed be changing the number of turns, the dimensions or the permeability of the core material. As can be seen from the curves in Fig. 11.22, changing the number of turns will not change the maximum output of a coil. The output at low frequencies will increase, but the output at high frequencies will decrease. The maximum output shifts in frequency but remains approximately the same.

A comparison of the performance of commercially available SQUID magnetometers and ring-core flux-gate magnetometers is shown in Fig. 11.23. For comparison, typical ambient noise in the vertical component of the magnetic field is shown.

Optical pumping magnetometers

Still another form of sensitive magnetometer is the optical pumping magnetometer, or as it is sometimes called, a gas magnetometer (Bloom, 1960). An optical pumping magnetometer (Fig. 11.24) consists of a mono-energetic light source, an absorption cell filled with the gas of an alkali metal, a radio-frequency coil wrapped around the absorption cell, and means for measuring the radio frequency. Over the years, magnetometers have been built for geophysical field operations with rubidium, cesium, or helium gas in the absorption cell. The light source is a tube of heated gas of the same material so that the wavelength of the emitted light matches with the wavelength for absorption.

An optical pumping magnetometer takes advantage of the differences between electron energy levels in an atom of alkali metal vapor. The energy of an electron can assume one of several levels,
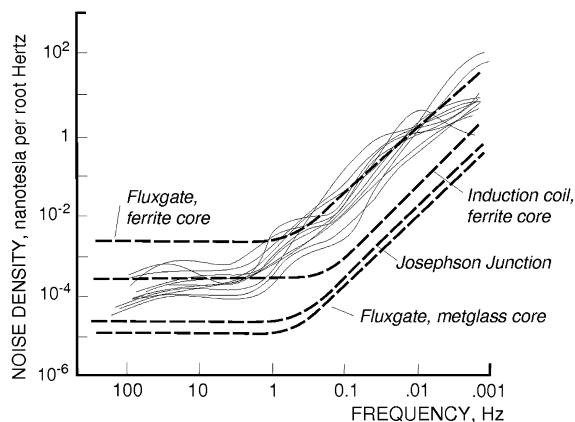
FIGURE 11.23

Typical noise characteristics of various magnetometers at low frequencies. Noise density curves for the vertical component of the Earth's magnetic field measured as part of a magnetotelluric survey during the winter months in British Columbia are shown for comparison. Amplitude density is the square root of noise power density.
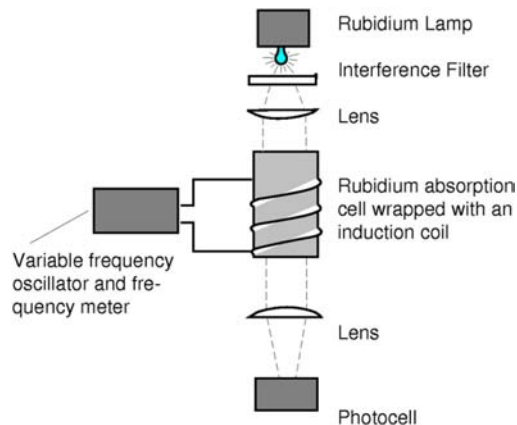
FIGURE 11.24

Principal elements of an optical pumping magnetometer. Light from a monochromatic rubidium-gas source is used to illuminate a cell containing rubidium gas. Electrons in the rubidium gas are raised to one of two energy states by absorption of energy from the light. These two states correspond to electron orbits that are oriented with or against the ambient magnetic field. These two energy states are slightly different and proportional to the ambient magnetic field. Additional energy is provided to the absorption cell by a coil wrapped around it and energized with an RF current. A servosystem adjusts the frequency so that it provides the energy to cause electrons to move from one to the other of the two excited states. When this occurs, the transmission of the cell is maximum, the photocell detects maximum absorption, and the frequency of the oscillator is a measure of the magnetic field strength.

depending on the orbit the electron follows and the orientation of the magnetic moment of the electron with respect to the ambient magnetic field (parallel or antiparallel). The stronger the ambient electromagnetic field, the greater the splitting between the energies of electrons in similar orbits, but with opposite polarizations of their moments.

The energy of all electromagnetic waves such as light is related to frequency as:

$$e = hf, \tag{11.27}$$

where e is the energy, f is frequency, and h is Planck's constant (6.626×10^{-27} erg-s). When a tube of gas is illuminated with a mono-energetic light beam at a frequency that corresponds precisely to the energy difference between a lower energy state and a higher energy state, in well designed absorption cells, the incident light will be reduced by as much as 10% to 20% on passing through the cell.

The electrons in the higher energy states will fall to a lower state spontaneously, emitting light as they do so. These electrons can drop back to state A_1 or A_2, that is, with their rotational magnetic moment aligned parallel or antiparallel to the ambient magnetic field. Those electrons which return to state A_1 are again available to be raised to state B_1 by absorbing energy from the incident light beam. Those electrons which go to state A_2 will not be excited by the incident light beam because the frequency is wrong. The process favors electrons entering the A_2 energy state, and discriminates against electrons remaining in the A_1 state. With time, the monoenergetic light beam will "pump" electrons from energy state A_2 to A_1, using state B_1 as a temporary residence.

The energy difference between levels A_1 and A_2 is small, corresponding to radio frequencies rather than optical frequencies. The energy difference is proportional to the ambient magnetic field strength. To determine the difference, a coil wrapped around the absorption cell is energized with current from a variable frequency oscillator. The frequency of this oscillator is varied so that maximum absorption is sustained. Under this condition, electrons are being converted from state A_2 to state A_1 at the same rate the mono-energetic light beam is raising them to state B_1. The oscillator frequency is then an indicator of the ambient magnetic field strength.

The difference in energy between states A_1 and A_2 corresponds to a frequency of 0.7 Hz per nT for rubidium gas or 28 Hz per nT for helium gas. The accuracy with which the magnetic field can be measured is determined by the accuracy with which the frequency of the RF oscillator can be measured.

The use of an optical pumping magnetometer in acquiring magnetotelluric data has been described by Plouff (1966).

11.3 PREPROCESSING OF THE DATA

The electromagnetic fields we use to explore the earth are usually continuous functions of time, frequency, and spatial variables. An exception, of course, is the electric field, which is discontinuous when it includes a component that is directed normal to a surface of discontinuity in conductivity in the medium, or the magnetic field, which is discontinuous when it includes a component directed normal to a surface of discontinuity in the magnetic permeability in the medium. If we were to define any of the electromagnetic field quantities precisely, we would need to know its values at an infinite number of points per unit length in space, per unity period of time in the time domain, or per unit bandwidth in the frequency domain.

11.3.1 SAMPLING IN TIME

In the equipment which is most commonly used in field practice today, the quantity which is to be measured is electronically converted to digital format. For practical reasons, when a value is converted to digital form, a binary number system is used. That is, number is expressed as:

$$N_b = \log_2(2^p N_d) = \log_2 2^p + \log_2 (N_d), \qquad (11.28)$$

where N_b is the binary conversion of a decimal number, N_d.

Binary numbers are used only as integers in computing. The binary number almost always consists of two parts: a multiplier, $\log_2 2^p$, and a mantissa, $\log_2 (N_d)$. Depending on the resolution with which we want to express the original digital value, N_d, we specify how many binary integers are to be specified in the *analog-to-digital* (*A/D*) conversion. Of course, this specification can be quite arbitrary, but certain resolutions are accepted as standards in digital computation, these being 1, 4, 8, 16, 32, and 60 binary *bits*, a bit being the analog of a digit in the base$_{10}$ or conventional number scheme. For example, in an 8-bit form the digital number 10 is written as 0001010. Note that, if one wishes to use both positive and negative numbers, the first bit is reserved for the sign.

In general, the *dynamic range* is a number defined as being the ratio of the largest number that can be expressed to the least number. In many applications, this dynamic range is expressed as:

$$Dynamic\ Range = 20\log_{10}(N_{max}/N_{min}), \qquad (11.29)$$

and measured as decibels, which is a dimensionless unit. For binary numbers, dynamic range is expressed as

$$Binary\ Dynamic\ Range = \log_2(MSB/lsb), \qquad (11.30)$$

where *MSB* indicates the value of the most significant bit and *lsb* indicates the value of the least significant bit. Obviously, the binary dynamic range is merely the number of bits used in the A/D conversion.

The binary numbers described so far are integers, To accommodate numbers that lie between the binary digits 0 and 1 (or -1 and $+1$), it is necessary to multiply the original number (in the base$_{10}$ format) by a number, 2^p, which forces the number to be converted so that it lies between the most significant bit and the least significant bit after A/D conversion. The integer, p, is carried along in binary format with the binary conversion of the scaled base$_{10}$ number.

A feature of a binary number that is of particular interest is the resolution, or ratio of the value of the least significant bit to the most significant bit. For common resolutions,

Dynamic Range, bits	Resolution
8	$3.992 \times 10^{-1}\%$
12	$2.442 \times 10^{-2}\%$
16	$1.526 \times 10^{-3}\%$
20	$0.953 \times 10^{-4}\%$

11.3.2 ANALOG-TO-DIGITAL CONVERSION

We need not dwell on the construction of equipment, but there are some features of analog-to-digital converters which we must be aware of in understanding digital processing schemes. Typically, the

signal to be converted is time varying, either because a time-varying electromagnetic field or a static signal with time-varying noise is being observed.

The first step in A/D conversion is to *sample and hold* the signal (or its combination with noise). In principle, this is accomplished by connecting the input waveform to a capacitor for a short period of time, known as the *dwell time*. At the end of the dwell time, the capacitor has been charged to a level more or less proportional to the voltage applied. This voltage persists after the input is interrupted, except that it will *droop*, as the charge discharges through whatever circuit resistance it bleeds into. The dwell time can be very short, ranging from nanoseconds to microseconds. If the signal is varying very rapidly, high frequencies with periods shorter than the dwell time will be averaged out to some extent. Normally, such high frequencies will have been rejected by analog filtering (anti-alias filtering) before the signal is presented to the sample-and-hold device.

Various approaches to convert the voltage stored on the capacitor serving as the sample-and-hold device are used. Typically, the A/D converter is an amplifier with a gain that can be programmed digitally. A simple *operational amplifier* exhibits an amplification that can be controlled with two passive components, the resistors R_i and R_j:

$$Gain = R_j / R_i. \tag{11.31}$$

For A/D conversion, the resistor R_i is constructed of a number of resistors in parallel, each having resistance

$$R_n = 2^{n-1} R, \tag{11.32}$$

where R is a reference resistor which will assign the most significant bit in the conversion, and R_n is a resistor which will assign the value, 0 or 1, to the n-th bit.

The voltage, V_R, is a reference voltage. If only switch 1 is closed, the output voltage is half the reference voltage. If only switch 2 is closed, the output voltage is one-quarter the reference voltage. If all of the switches are closed, the output is very nearly the full reference voltage.

Analog conversion is accomplished by setting the switches open or closed until the output voltage matches the input voltage from the sample-and-hold device within the resolution desired. If a switch is open, the corresponding bit is zero, and if closed, one.

A practical difficulty with this straightforward A/D conversion scheme is that each of the resistances must be exact within the same accuracy, which is listed in the table above for dynamic range as a function of the number of bits in the sample. This same principle is used in most A/D conversion schemes, but with modifications to reduce the number of resistors needed to define the bits to two.

11.3.3 FILTERING

Filtering is the process of improving the quality of a signal by removing unrelated noise components. It can consist first of the use of hardware analog devices in the field to enhance the appearance of the signal, but of most concern to us here is the use of digital filters in enhancing the data after A/D conversion. A rule well worth observing is that as little analog filtering as possible should be done in acquisition of data. Some filtering is mandatory; in particular, anti-aliasing filtering.
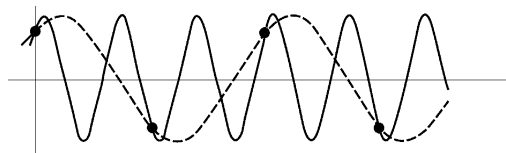
FIGURE 11.25

Nature of aliasing in sampling. If a monochromatic function is sampled at a rate of two samples per cycle or less, that function cannot be distinguished from another monochromatic function with a longer period which will also pass through the sampled points.

Aliasing

The nature of aliasing is illustrated by Fig. 11.25. The solid trace is a continuous sinusoidal function recorded with an analog system. The dotted trace is a set of samples obtained at various digitizing rates. Aliasing is the phenomenon in which the traces sampled at too low a rate appear to be taken from a signal with a frequency lower than that of the true signal. The *Nyquist criterion* states that one must obtain more than two samples per cycle of the highest frequency component in a signal in order to determine the true frequencies in that signal. That is, the Nyquist frequency cutoff is defined as

$$f_{Nyquist} = 1/(2\Delta t),\tag{11.33}$$

where Δt is the sampling interval. The Nyquist cutoff frequency and all frequencies higher must be strongly suppressed by analog filtering. After A/D conversion, there is no way that reliable information can be recovered about the signal spectrum if the signal has been undersampled. Often, the sampling rate should be specified so that the Nyquist cutoff frequency is at least 10 times as great as the highest signal frequency of interest.

We will not discuss analog filter design here, but concentrate our attention on digital filtering after A/D conversion. We will consider two types of digital processing; time-based filtering and filtering in transform domains.

Time-based filtering

Time-based filtering is developed for a signal which has been digitized at equal intervals of some independent variable, usually being taken as time, but it can equally well be position along a traverse. The most widely used digital filters are linear filters, of which there are many kinds; optimum filters, smoothing filters, coherent stacking filters, Butterworth filters, Chebyshev filters, and so on. Some nonlinear digital filtering procedures are also used in geophysical applications, particularly robusting procedures.

Consider that a signal has been recorded as a function of time, $s(t)$. Conversion of this analog signal to a digital time series can be thought of mathematically as:

$$s_i' = s(i\Delta t) = \int_0^\infty s(t) \sum_{i=0}^N \delta(t - i\Delta t)\, dt,\tag{11.34}$$

where $\sum_{i=0}^{N} \delta\,(t - i\,\Delta t)$ is the sampling function, sometimes called a *Dirac comb* (a linear combination of the Dirac pulse functions). The process described by this equation produces an ordered set of numbers, $s\,(i\,\Delta t)$, which comprise the sampled data set.

Linear filtering using some designed filter function, $f\,(\tau)$, is based on Duhamel's integral:

$$s_o\,(t) = \int_{-\infty}^{\infty} s\,(\tau)\,f\,(t - \tau)\,d\tau = s * f, \tag{11.35}$$

where $s_o(t)$ is the filtered signal. In digital form (after sampling with a Dirac comb) this equation is written as:

$$s_{oi} = \sum_{j=-M}^{M} s_j\,f_{i-j}, \tag{11.36}$$

where $2M + 1$ is the length of the digital filter, and $s_{oi} = s_o\,(i\,\Delta t)$.

Let us now turn to the design of the digital filter, $f_i = f\,(i\,\Delta t)$, $i = -M, ..., -1, 0, 1, M$.

Smoothing filters

Often, the noise to be rejected is of relatively high frequency compared to the desired signal. A simple filter consists of a running average:

$$\{f_i(\text{running average})\} = \frac{1}{2M + 1}\{1, 1, \cdots, 1\} \tag{11.37}$$

in which the $2M + 1$ filter weights all have equal weights. The amplitude response of this smoothing filter is shown in Fig. 11.26. Note that no phase response is given; because the filter is symmetrical about its midpoint, it causes no phase shift in the filtered output, s_{oi}.

The spectrum of Fig. 11.26 has an overall tendency for high frequencies to be suppressed relative to low frequencies. Other smoothing filters have been devised in which the oscillatory character has been reduced, and there is a better discrimination between low frequencies and high frequencies. Among the most widely used smoothing filters are Spencer's 15- and 21-point smoothing operators:

$$\{f_i(Spencer, 15)\} = \frac{1}{320}\{-3, -6, -5, +3, +21, +46, +67, +46, +21, +3, -5, -6, -3\} \tag{11.38}$$

$$\{f_i(Spencer, 21)\} = \frac{1}{350}\{-1, -3, -5, -5, -2, +6, +16, +33 + 47, +57, +60,$$

$$+ 57, +47, +33, +16, +6, -2, -5, -5, -3, -1\}.$$

The spectrums for these two smoothing filters are shown in Fig. 11.27.

Aliasing-to-zero filters

Often the strongest noise component in recording geoelectrical signals is at powerline frequencies. It can be necessary to suppress such noise by factors of 1000 to 1,000,000 in order to extract signals. The most effective way to reject this type of noise is by aliasing the noise to zero frequency. Such filters can
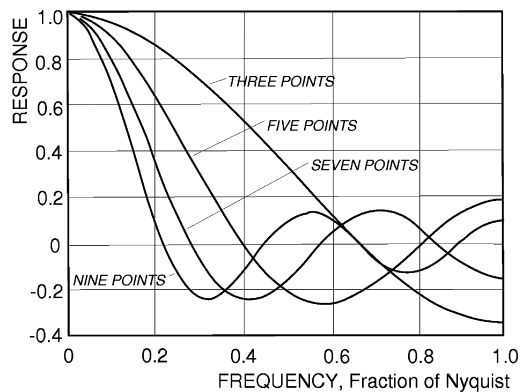
FIGURE 11.26

Frequency response of running average (boxcar) filters.
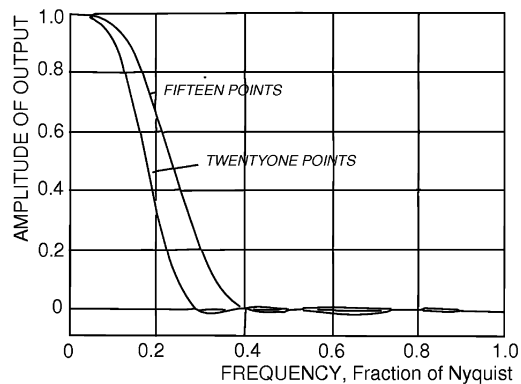
FIGURE 11.27

Frequency responses of Spencer's 15- and 21-point smoothing operators.

be used even when the signal has a strong contribution at the power line frequency without reducing the signal significantly at that frequency. An alias-to-zero filter operator consists of the weights:

$$\{f_i(alias\ to\ zero)\} = \frac{1}{2}\{1, (nzeros), -1\},$$

where n is a number selected so that the two nonzero weights of the filter operator will be positioned at the same phase of the power line noise. At a sampling rate, r, the number of zeros needed is

$$n = \frac{Ir}{2\pi f_p} - 1,$$
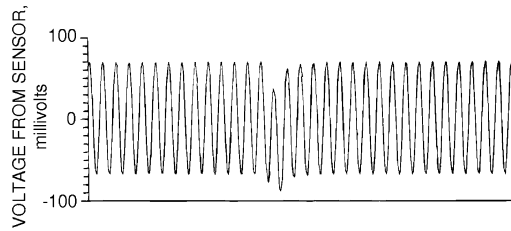
FIGURE 11.28

Example of wideband (0 to 2000 Hz) recording of the output of a vertical-axis induction loop with an area of 50,000 square meters. The principal noise component is 50 Hz industrial noise. The location is in southern Tuscany, Italy. The presence of the desired signal is indicated by the transient change in the envelope of 50 Hz noise near the center of this record.

where f_p is the power line frequency, and I is an arbitrary integer, large enough that the interval between the first and last filter weight is greater than the length of the signal. Also, the quantity I must be selected such that n is indeed an integer.

The spectrum of an aliasing-to-zero filter is not particularly interesting. It is best described in terms of its effect. Fig. 11.28 shows a typical field recording of a transient voltage buried in power-line noise (in this case, the location is in Italy and the line frequency is 50 Hz). The transient is less than 1 second long. The sampling rate is 1000 samples per second. The parameter n was set at 1999, corresponding to a time delay of two seconds between the two end members of the set of filter weights.

A short section of the same trace containing one signal is shown in Fig. 11.29 after the 50 Hz component has been almost completely suppressed, being converted to a near-zero-frequency alias with an apparent frequency of about .01 Hz. The energy of the original 50 Hz noise component has been shifted so far in frequency from the signal that it no longer masks the signal.

Alias-to-zero filtering is also the basis of *synchronous detection*. In synchronous detection, a signal is transmitted from the source to the receiver repeatedly at regular intervals, usually with alternating polarity. The parameter n of an alias-to-zero filter is set so that the filter length is the same as the number of samples taken between repeat transmissions. If the signal transmission is repeated after some integer number of cycles of power-line noise, application of the filter defined in Eq. (11.37) will suppress the line frequency and strengthen the signal in direct proportion to the number of transmissions, but the random noise will increase only in proportion to the square root of the number of transmissions.

Robust processing

Digital time series often have clearly errant values. Often, a geophysicist will merely delete such values from the time series, but good practice requires that data be deleted only on the basis of some meaningful rule. Application of such rules is termed *robusting*.

Rules can be based on statistical measures for the time series being processed. One approach is to compile a cumulative frequency of occurrence for some property of the data series, such as the deviation from zero, or the deviation from point to point. As an example, consider the signal in Fig. 11.29 after the line frequency noise component has been aliased to zero. The expected signal form is a smooth
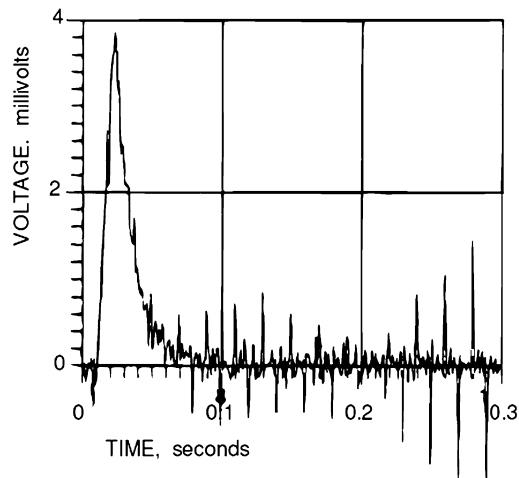
Portion of record showing single signal after the 50 Hz noise in Fig. 11.28 has been suppressed.

decaying transient, which is apparent in the data series. But, there are also repeated large deflections from this simple behavior which we know not to be possible as part of a transmitted electromagnetic field.

To develop a rule for deletion of these outliers, a frequency of occurrence curve was compiled based on the absolute value of the point-to-point differences in the time series. This curve is plotted to a linearized Gaussian scale by convention. In such a presentation, the cumulative frequency of occurrence curve for a Gaussian distribution will plot as a straight line. Often, such a plot will appear to consist of two segments with differing slope. These two segments represent different, probably independent distributions. Points identified as belonging to the segment with lower slope can be rejected from the data series on this basis. They were replaced with the geometric average of the last preceding value and next succeeding value of the time series belonging to the distribution with the higher slope. The result is shown in Fig. 11.30.

If time series are available from a number of repeat transmissions, more formal rules can be written for robusting (deleting) data. We will examine some of these rules in Chapter 13, where we will discuss the robust processing of magnetotelluric data.

11.3.4 STACKING

One remaining procedure is available for improving the quality of the signal, that being *stacking*. In this example, six signals were recorded. *Brute stacking* consists of adding together the six signals, expecting that the signal-to-noise ratio would be improved approximately as the square root of the number of signals. *Smart stacking* consists of the elimination from the stacking procedure of those signals which are obviously more noisy. One way of defining the more desirable signals to include in the stacking procedure is by calculating *similitude* between pairs of signals.
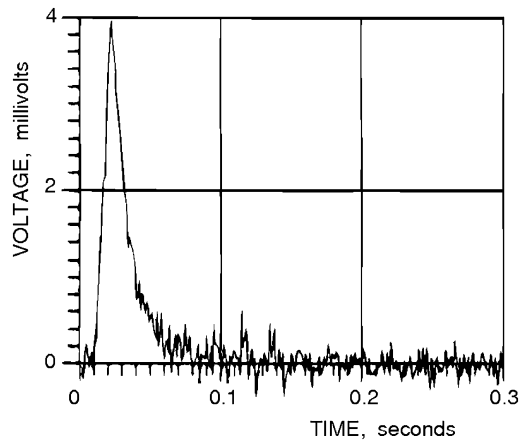
FIGURE 11.30

Single signal after statistical robusting.
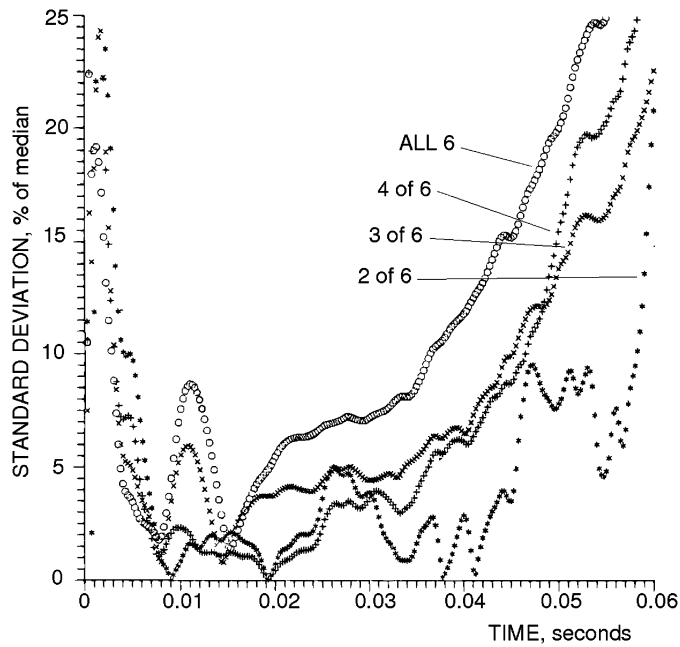
FIGURE 11.31

Standard deviation characterizing the scatter of points when several signals are stacked. These curves show the scatter on stacking 2, 3, 4, or all 6 of six signals. Selection of the signals to be stacked was based on similitude between signals.
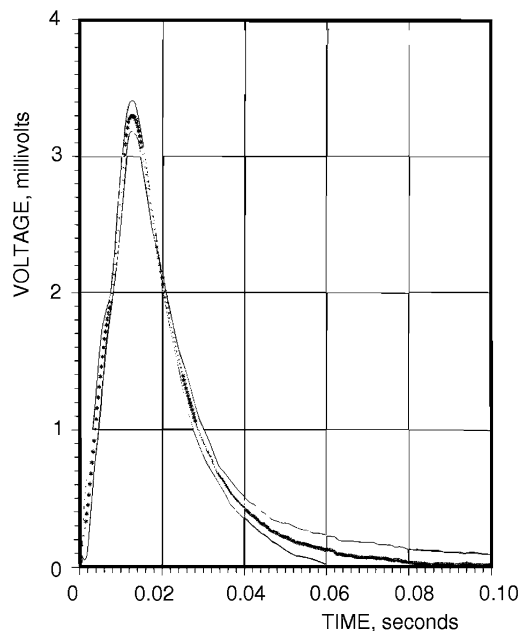
Results of stacking three signals with best similitude.

Similitude is defined as the root mean square difference between each and every pair of signals comprising a data set. For a set of n signals, the number of values of similitude which must be calculated is $(n-1)+(n-2)+\cdots+1$. For the set of six signals considered in this example, some 15 similitude values must be calculated. These similitude values can then be used to separate the signals into two groups, one with better (smaller) similitude values than the others.

Fig. 11.31 shows standard deviations point by point along stacked signals for stacking of 2, 3, 4 and all six of the signals in our example. It should be noted that the best result, defined as the lowest standard deviations, is achieved after stacking of 2 or 3 of the six signals, not for stacking all of the signals. Fig. 11.32 shows the final result of stacking 3 of the 6 signals. The dashed curves bounding the stacked curve represent the average curve with two standard deviations added and subtracted.

To develop a rule for deletion of these outliers, a frequency of occurrence curve was compiled based on the absolute value of the point-to-point differences in the time series. This curve is shown plotted to a linearized Gaussian scale. In such a presentation, the cumulative frequency of occurrence curve for a Gaussian distribution will plot as a straight line. The plot for the data of Fig. 11.31 consists of two segments with differing slope. These two segments represent different, probably independent, distributions. Points identified as belonging to the segment with lower slope can be rejected from the data series on this basis. They were replaced with the geometric average of the last preceding value and next succeeding value of the time series belonging to the distribution with the higher slope. The result is shown in Fig. 11.32.
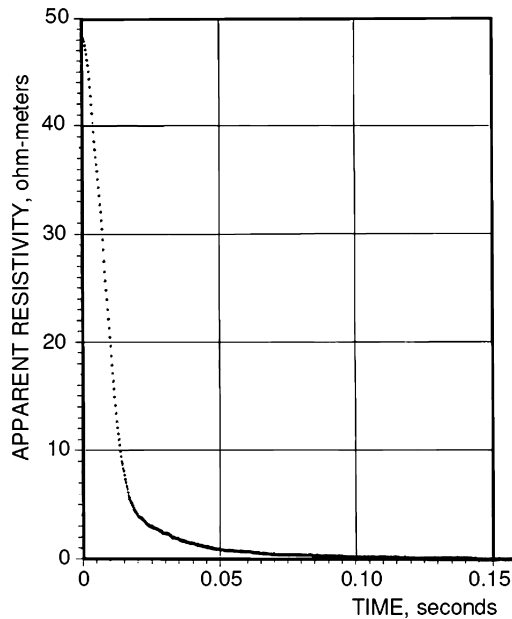
FIGURE 11.33

Stacked signal after deconvolution.

11.3.5 DECONVOLUTION

Suppression of non-signal-related noise is now complete. However, the signal is not ideal because it still includes distortion caused by the analog devices used in detecting and recording the signal. To obtain an ideal signal form, the filtered stacked signal must be deconvolved using one of the methods described in Chapter 14, section 14.1.4. Fig. 11.33 shows the signal form obtained by deconvolution of the signal form shown in Fig. 11.32.

REFERENCES AND RECOMMENDED READING TO CHAPTER 11

Blackman, R. B., 1965, Linear data smoothing and prediction in theory and practice: Addison-Wesley Publishing, Reading, Massachusetts, 182 pp.

Bloom, A. L., 1960, Optical pumping: Scientific American, **203**, 72–97.

Deaver, B. S., and W. M. Fairbank, 1961, Experimental evidence for quantized flux in superconducting cylinders: Physics Review Letters. **7**, 43–46.

Doll, R., and M. Nabauer, 1961, Experimental proof of magnetic flux quantization in a superconducting ring: Physics Review Letters. **7**, 51–52.

Falco, C. M., and I. K. Schuller, 1980, SQUIDs and their sensitivity for geophysical applications, *in* Weinstock, H., and W. C. Overton, Eds., SQUID Applications to Geophysics: Society of Exploration Geophysicists, Tulsa, pp. 13–18.

Hahlbohm, H. D., and H. Lubbig, Eds., 1977, SQUID: Superconducting quantum interference devices and their applications: Walter de Gruyter, Berlin, 606 pp.

Hamming, R. W., 1977, Digital filters: Prentice-Hall, Englewood Cliffs, New Jersey, 226 pp.

Josephson, B. D., 1962, Possible new effect in super-conductive tunneling: Phys. Letters, **1**, 251–253.

Keller, G. V., 1968, Electrical prospecting for oil: Quarterly of the Colorado School of Mines, **63** (2), 1–268.

Kharkevich, A. A., 1960, Spectra and analysis: Consultants Bureau, New York, 222 pp.

Kuc, R., 1988, Introduction to digital signal processing: McGraw-Hill, New York, 414 pp.

Kunetz, G., and J. Chastenet de Gery, 1956, La representation conforme et divers problems de potentiel dans les milieux de "permeabilite" differente: Revue de Inst. Tech. Francais Pet., October, pp. 1179–1192.

London, F., 1950, Superfluids, Vol. 1, Wiley, New York, 161 pp.

London, F., 1954, Superfluids, Vol. 2, Wiley, New York, 217 pp.

Mantell, C. L., 1970, Batteries and energy systems: McGraw-Hill, New York, 221 pp.

Meyer, S. L., 1975, Data analysis for scientists and engineers: John Wiley & Sons: 513 pp.

Parks, T. W., and C. S. Burrus, 1987, Digital filter design: John Wiley & Son, New York, 330 pp.

Plouff, D., 1966, Magnetotelluric soundings in the southwestern United States: Geophysics, **31** (6), 1145–1152.

Stearns, S. D., and R. A. David, 1988, Signal processing algorithms: Prentice-Hall, Englewood Cliffs, New Jersey, 349 pp.

Tagg, G. F., 1964, Earth Resistances: George Newnes Ltd., New York, 258 pp.

Weitkunat, R., Ed., 1990, Digital biosignal processing: Elsevier, Amsterdam.

Wiener, N., 1964, Generalized harmonic analysis and Tauberian theorems: The MIT Press, Cambridge, Massachusetts, 242 pp.

DIRECT CURRENT AND INDUCED POLARIZATION METHODS

CONTENTS

The first class of electrical geophysical methods we will examine in detail will be the DC methods. While both electromagnetic and DC methods first came into use in the early part of the 20th century, the DC methods gained early acceptance because of less demanding theoretical and instrumentation considerations. DC methods have become the most widely used geoelectric method. Techniques have been standardized, and the capabilities and limitations of the methods are widely understood and accepted.

It is important to realize that direct current is not in fact used in DC electrical surveys. The DC techniques could better be described as employing *time varying direct current*. This phrase may well be considered to be an oxymoron, but it is useful in pointing out that when we speak of a DC geoelectrical

method, we mean that theory based on DC behavior is used, not direct current. There are many sources of nearly DC voltage in the earth, and it is not easily possible to identify the DC voltage caused by current that we inject into the ground from all the other DC voltages. We make our contribution detectable by causing it to vary with time in a specified way, so that the *signature* of the signal can be recognized. The signature can be of any form, so long as the frequency is low enough that the term $\mathbf{E} = -\partial \mathbf{B}/\partial t$ in Maxwell's equations can be ignored.

A particularly important group of DC electric techniques includes those known as *vertical electric sounding* (*VES*). In traditional soundings, an assumption is made that the geoelectric structure in the area of exploration is *one dimensional*, with resistivity in the earth varying only with depth. The concept of one dimensionality is often extended to include geoelectric structures which are obviously other than one dimensional. In such cases, representation of a more complicated earth structures by a series of one dimensional resistivity-depth functions along a profile is used as a first step towards a more exact two- or three-dimensional interpretation.

Another approach to the use of DC surveys is in *horizontal profiling*. In this application, we assume that the geoelectric structure is one in which resistivity in the earth changes laterally. Surveys are then carried out by moving electrode arrays along a profile, attempting to determine the location of changes in ground resistivity along the profile.

A third approach to using DC surveys is the *electrical mapping* method. In such a survey, a single source of current flow in the ground is established; then, the electric field or the potential is mapped over the surface of the earth around the source in an area of exploration interest. Mapping the spatial behavior of the DC field is useful in that interpretations can be made fairly readily in terms of two- and three-dimensional earth structures.

A highly important time-varying electrical method is the *Induced Polarization* (*IP*) method. In this method, it is recognized that the current flow in the earth represents a very complex EM phenomenon characterized by charge polarization and accumulation in the rocks and by electrochemical reactions with some minerals, in particular the metal oxides and sulfides, causing some of the electrical energy to be stored within the rock. This energy storage is the result of (a) variations in the mobility of ions in fluids throughout the rock structure and (b) variations between ionic and electronic conductivity where metallic minerals are present. As the level of the current is changed, the rate of energy accumulation processes changes, and in particular, if the current is interrupted, these processes may partially be reversed, returning some of the accumulated energy as a current, which decays in time. The process can be considered to be roughly analogous to the charging and discharging of a capacitor. This leads to a time-varying behavior of the electric field in the earth. Mathematically, the IP phenomena can be analyzed by based on models with frequency-dependent complex conductivity distribution. One of the most popular is the Cole-Cole relaxation model and its different modifications (Cole and Cole, 1941). The parameters of the conductivity-relaxation model can be used for discrimination of different types of rock formations, which is an important goal in mineral exploration.

The generalized effective-medium theory of induced polarization (GEMTIP) was introduced recently in order to provide a link between the petrophysical properties of the rocks and their complex conductivity spectra (Zhdanov, 2008a, 2008b). GEMTIP is a rigorously formulated model, which uses effective-medium theory to describe the resistivity of the multiphase heterogeneous rocks and its relationship with the rocks' physical and electrical properties. These properties include grain size, grain shape, porosity, anisotropy, polarizability, volume fraction, and conductivity of the inclusions in the pore space (Zhdanov, 2008a).

The IP method has been found to be extraordinarily effective for use in exploration for mineral deposits since its introduction in the 1940s. I will discuss the theoretical and experimental foundations of the IP method In this Chapter, as well.

The basic premise in development of time-varying DC methods is that the term $-\partial \mathbf{B}/\partial t$ in Maxwell's equations can be considered to equal zero and therefore, no magnetic induction effects exist. However, we need not assume that all magnetic effects are absent. In fact, the equation

$$curl\,\mathbf{H} = \mathbf{j}$$

holds independently of the size of the term $-\partial \mathbf{B}/\partial t$. This equation states that we can measure a magnetic field as a means for characterizing the behavior of a time-varying direct current field. Jakosky (1940) suggested that magnetic field measurements be used in place of electric field measurements in determinations of earth resistivity, while Seigel has developed the approach of using magnetic field sensors in induced polarization surveys (Seigel and Howland-Rose, 1990). The use of magnetic field measurements in resistivity determinations has been termed the *Magnetometric resistivity method*, or MMR (Edwards, 1988a; Edwards and Howell, 1976). The use of magnetic field measurements in induced polarization surveys is called *Magnetic IP*, or MIP.

We have examined the theory for DC behavior of electromagnetic fields in Chapter 5, section 5.2. In the present chapter, we discuss the basic principles of electric soundings and induced polarization methods.

12.1 VERTICAL ELECTRIC SOUNDING AND APPARENT RESISTIVITY

Vertical electric sounding, VES, is perhaps the most commonly used strategy in the application of DC electrical methods. It is based on the concept that the electrical structure of the earth can be described with a one-dimensional resistivity function; $\rho = \rho(z)$, with the resistivity of a rock varying only with depth within the earth. In fact, we would like to believe that the lateral change in resistivity of the earth, described by $\rho = \rho(x, y)$, is so slow that at any one location, the profile $\rho(z)$ can be determined independently of the lateral variations, $\rho(x, y)$. Then, the lateral changes can be determined with a series of vertical electric soundings made along a profile or over an area and interpreted as a set of slowly changing $\rho(z)$ functions.

The theory for the spreading of direct current into a one-dimensional earth has been developed in Chapter 5. Based on this theory, we should realize that we can obtain information about resistivity at depth in the earth by knowing the electric potential, U, or the electric field, $\mathbf{E}$, on the earth's surface as a function of distance from a current source. This simple concept is the basis for various methods of electrical sounding. Let us now examine the details of how such information is gained.

12.1.1 TECHNIQUES FOR VERTICAL ELECTRIC SOUNDING

Many schemes for carrying out vertical electric soundings have been developed, starting in the early years of the 20th century. The approach has consisted of specifying some *standard electrode array* with which to study the potential or electric field as a function of distance between source electrodes and measurement electrodes. The use of a standard array makes the interpretation of the results easier,
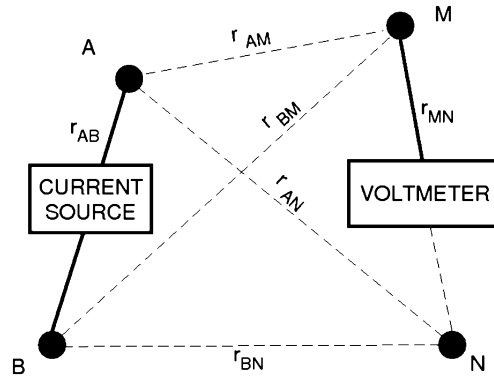
FIGURE 12.1

Plan view of a generic four-electrode array for measuring earth resistivity. The four electrodes can be arrayed quite arbitrarily, and yet an apparent resistivity value can be computed knowing only the electrode distances, the current, and the voltage.

because of consistency of the data format. Many such standard arrays have been devised over the years, each with some supposed advantages over others. Most arrays are based on the use of four electrodes as shown in Fig. 12.1. Two of the electrode contacts, A and B, are used to drive current into the ground, while the other two, M and N, are used to detect the potential drop in the earth.

In analysis of measurements made with such an array, we will assume that a current, I, is injected into the ground at point A, and, independently, a current, $-I$, is injected into the ground at point B. We measure the voltage, ΔU_{MN}, at points M and N on the surface of the earth. This voltage, according to Ohm's law, will be proportional to the strength of the current, I, and also, be dependent on the electrical properties of the earth. For example, in the simple case of a homogeneous half-space with resistivity ρ, according to Eq. (4.74) developed earlier in Chapter 4, the potential at the point M will be the sum of contributions from the currents flowing through point contacts A and B as follows:

$$U_M = \frac{I\rho}{2\pi} \left(\frac{1}{r_{AM}} - \frac{1}{r_{BM}} \right),$$

and similarly for the potential at point N

$$U_N = \frac{I\rho}{2\pi} \left(\frac{1}{r_{AN}} - \frac{1}{r_{BN}} \right),$$

where the distances $r_{AM}, r_{BM}, r_{AN}, r_{BN}$ are defined as shown in Fig. 12.1. Consequently,

$$\Delta U_{MN} = U_M - U_N = \frac{I\rho}{2\pi} \left(\frac{1}{r_{AM}} - \frac{1}{r_{BM}} + \frac{1}{r_{BN}} - \frac{1}{r_{AN}} \right). \tag{12.1}$$

In this model, ΔU_{MN} is proportional to the resistivity, ρ. The equation can be inverted to yield the resistivity of the medium in terms of measured quantities:

$$\rho = \frac{2\pi \, \Delta U_{MN}/I}{\left(\frac{1}{r_{AM}} - \frac{1}{r_{BM}} + \frac{1}{r_{BN}} - \frac{1}{r_{AN}}\right)} = K_g \frac{\Delta U_{MN}}{I}, \tag{12.2}$$

where

$$K_g = \frac{2\pi}{\frac{1}{r_{AM}} - \frac{1}{r_{BM}} + \frac{1}{r_{BN}} - \frac{1}{r_{AN}}}, \tag{12.3}$$

and K_g is the *geometric factor* for the array of electrodes being used to measure resistivity. The ratio $\Delta U_{MN}/I_{AB}$ is called the *mutual resistance*, R_m, and is measured in ohms. The mutual resistance is not a resistance in the ordinary sense inasmuch as the voltage and the current are measured in separate circuits. For the mutual resistance to be meaningful, the two circuits must be linearly coupled so that the ratio is a constant.

In the real world, the only characteristic of the field we can measure is a voltage drop between two electrode contacts. The potential and the electric fields are idealized mathematical concepts, not exactly measurable. However, if the distance r_{MN} is made small enough, the ratio $\Delta U_{MN}/r_{MN}$ comes close to the value of E_{MN}, the component of the electric field along the line connecting the electrodes M and N. We often claim to use this ratio to measure the electric field component at the point O, halfway between M and N. However, this claim is only an approximation, and in field practice, we sometimes see that the limiting process is not well observed, and the measured electric field component can be a poor estimate of the mathematical electric field. This is sometimes a significant source of error in comparing measured electric fields with computed electric fields for some model being tested in interpretation.

The measured electric field for a general four electrode array and a homogeneous earth with resistivity, ρ is

$$E_{MN} \approx \frac{\Delta U_{MN}}{r_{MN}} = \frac{I\rho}{2\pi r_{MN}} \left(\frac{1}{r_{AM}} - \frac{1}{r_{BM}} + \frac{1}{r_{BN}} - \frac{1}{r_{AN}}\right), \tag{12.4}$$

and inversion of this expression to obtain a solution for resistivity in terms of measured quantities yields

$$\rho \approx \frac{2\pi r_{MN} E_{MN}/I}{\frac{1}{r_{AM}} - \frac{1}{r_{BM}} + \frac{1}{r_{BN}} - \frac{1}{r_{AN}}} \tag{12.5}$$
$$= K_g^E Z_m,$$

where $Z_m = E_{MN}/I$ is the mutual impedance and K_g is the geometric factor for use with electric field measurements:

$$K_g^E = \frac{2\pi r_{MN}}{\frac{1}{r_{AM}} - \frac{1}{r_{BM}} + \frac{1}{r_{BN}} - \frac{1}{r_{AN}}}. \tag{12.6}$$

The most commonly used standard electrode array for sounding is the *Schlumberger array* with four collinear electrodes symmetrically located about the midpoint of the array, and with the inner two
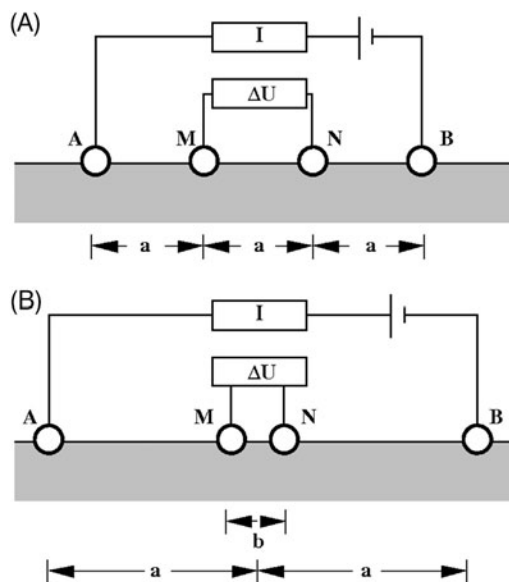
FIGURE 12.2

The Wenner (A) and Schlumberger (B) electrode arrays.

electrodes, M and N, being closely spaced so that in effect, the component of the electric field along the array axis is measured (Fig. 12.2B). The outer electrodes, A and B, are used to inject current into the earth.

Another typical electrode configuration is *Wenner array*. The Wenner array, like the Schlumberger array, makes use of four colinear electrodes, with the outer ones being designated as current electrodes and the inner pair as measurement electrodes. The single difference between the Wenner array and the Schlumberger array is that the electrodes are equally spaces in the Wenner system (Fig. 12.2A).

We will examine the theory for sounding with the Schlumberger array first, and consider other electrode arrays at a later point.

For the Schlumberger array, $r_{AN} = r_{BM}$ and $r_{AM} = r_{BN}$, and Eq. (12.6) provides the following value for the geometric factor:

$$K_g = \pi r_{AN} r_{AM} / (r_{AN} - r_{AM}). \tag{12.7}$$

By long standing convention, we speak of the *outer spacing* of the Schlumberger array as being $a = r_{AB}/2$ and the *inner spacing* as being $b = r_{MN}$. In this notation, the distances in Eq. (12.7) are

$$r_{AN} = a + b/2, \; r_{AM} = a - b/2,$$

so that

$$K_{g,\text{ Schlumberger}} = \pi(a^2 - b^2/4)/b = \pi a^2 [1 - (b/2a)^2]/b. \tag{12.8}$$

Often it can be assumed that $(b/2a)^2 \ll 1$ so that Eq. (12.8) can be simplified to

$$K'_{g,\, \text{Schlumberger}} = \pi a^2/b. \tag{12.9}$$

The first geometric factor is exact, with no approximation being made, while the second equation is based on the approximation that the inner spacing is small enough that the term $(b/a)^2$ can be ignored in comparison with unity.

It is quite reasonable that we should be able to determine the resistivity of a homogeneous half-space in this simple way. One might wonder, though, how often in practice one would encounter a homogeneous half-space. Rarely, to be sure, but the computation of geometric factors for electrode arrays has far greater significance in the practice of electrical geophysics. Presumably, we do not know if the earth is uniform before a survey is undertaken. However, the calculation of the resistivity for a homogeneous half-space can be accomplished with any set of numbers for voltage, current, and distances between electrodes. So, without assuming the earth is a homogeneous half-space, in carrying out an electrical survey, we routinely perform the numerical operation of calculating the half-space resistivity using the uniform earth geometric factor.

Why do this when we expect the number not to be correct in the majority of cases? There are two reasons. The first, and simplest, is that by normalizing the observed voltage to the current and the array dimensions, we have a single number for each set of measurements which depends only on the geoelectric structure of the earth. These numbers can then be meaningfully compared for different measurements in a single sounding, or from sounding to sounding.

The second use of this potentially incorrect resistivity value, ρ_a, and which we always call the *apparent resistivity* to protect ourselves, is that it comprises a subtle act of interpretation. By taking a set of measurements consisting of a voltage, a current, and the geometric description of four electrode contacts, and converting these to a single number with the dimensions of resistivity, the observed data have been endowed with some geological meaning. If a resistivity is said to be, say 17.2 ohm-meters, one subjectively thinks about the kinds or rocks that have similar resistivities. Thus, without performing any of the complex and tedious procedures which we will describe for interpreting electrical survey data, one can obtain an impression, though not entirely reliable, of the probable geoelectric structure merely by computing apparent resistivities.

To demonstrate this further, consider an earth consisting of two horizontal layers characterized by resistivities ρ_1 and ρ_2. We place a Schlumberger symmetrical four-electrode array, *AMNB*, on the surface of this earth. We recognize that the depth to which current permeates into the earth depends on the separation between the electrodes *A* and *B*. Let us suppose that we use an *AB* separation that is much less than the thickness of the upper layer. The current flow between electrodes *A* and *B* is almost entirely within the surface layer, with almost none penetrating deep enough to sense the presence of the second layer. A measurement made with such a short spacing would be expected to detect an apparent resistivity almost exactly equal to the resistivity of the first layer, $\rho_a \approx \rho_1$.

If now we expand the array by increasing the *AB* separation such that the outer spacing factor would be comparable in size with the thickness of the surface layer, we expect the current distribution in the earth to reflect the presence of the second layer in a recognizable way. For example, if the second layer is relatively resistive (Fig. 12.3), the current flow between electrodes *A* and *B* tends to be confined to the region above the second layer. The current density at the surface is higher than in a completely uniform earth, the electric field detected with the electrodes *M* and *N* is increased, and the apparent

NORMALIZED RESISTIVITY
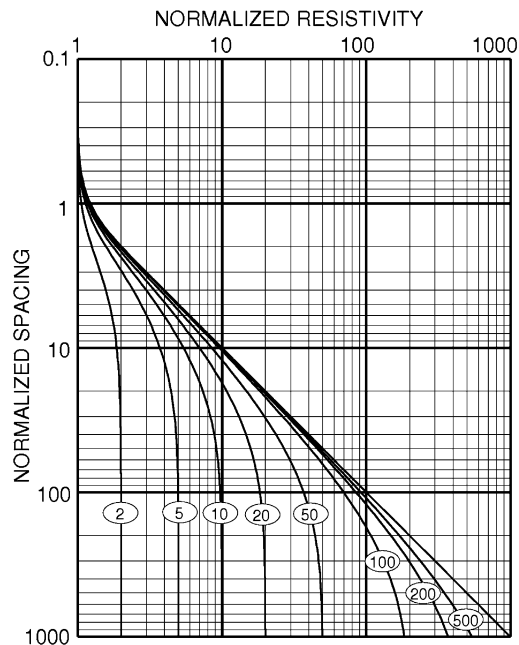
FIGURE 12.3

Apparent resistivity curves for an expanding Schlumberger array over a sequence of two layers. The upper layer has unit thickness. The contrast in resistivity between the lower and the upper layer is indicated by the label on each curve.

resistivity is increased from the value for a totally uniform half-space. Conversely, if the second layer is more conductive than the first (Fig. 12.4), current begins to drain from the upper layer into the more conductive second layer, current density in the upper layer is less than that in a totally uniform earth, the electric field detected between electrodes M and N decreases, as does the apparent resistivity computed from that electric field.

The equivalence between the spacing of an electrode array and the depth to which resistivity in the rock is sensed is further illustrated in Figs. 12.5 and 12.6. In this case, the model for which apparent resistivity sounding curves have been computed consists of three layers. The uppermost and lowermost layers have the same resistivity, while the intermediate layer has either a lower resistivity (Fig. 12.5) or a higher resistivity (Fig. 12.6). Accordingly, the apparent resistivity curves exhibit minima reflecting the presence of the conductive layer, or a maximum reflecting the presence of the resistive layer. It is important to note, however, that the relationship between electrode separation and depth of investigation is not rigorous. With the addition of layers to the section, the spacings needed to penetrate to depth become progressively greater.

Thus, by increasing the separation between the current electrodes in a Schlumberger array, we have effectively increased the depth to which we can sense the resistivity in the earth. This is the concept involved in *geometric sounding*.
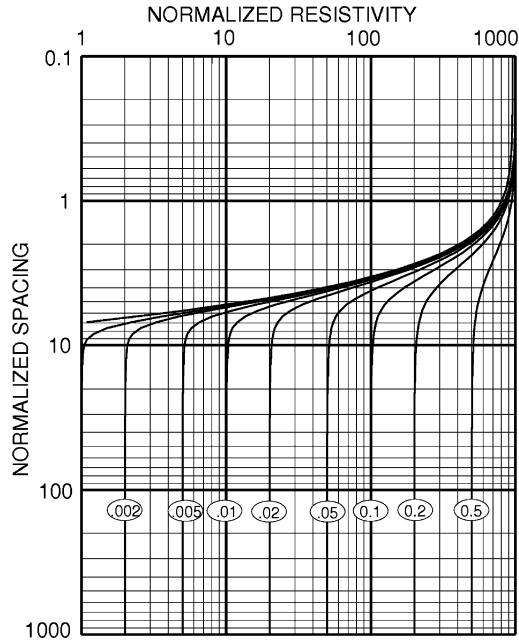
FIGURE 12.4

Apparent resistivity curves for an expanding Schlumberger array over a two-layer sequence. The upper layer has unit resistivity and unit thickness. The contrast in resistivity between the lower layer and the upper layer is indicated by the number on each curve.

To avoid creating the impression that depth of investigation is related solely to the separation between current electrodes, we call your attention to the *theorem of reciprocity,* formulated in Chapter 3. This theorem is absolutely valid; it states that if the roles of the two current electrodes, A and B, are interchanged with the roles played by the measuring electrodes, M and N, there would be no change in the measured quantities, current and voltage, no matter what the geoelectric structure of the earth is.

The depth of investigation achieved in geometric sounding is related to many things, and not merely to the geometry of the array. Suffice it to say for the present, in carrying out a sounding with the Schlumberger array, we make a series of determinations of apparent resistivity as a function of the array spacing factor.

Writing an expression for the apparent resistivity measured with an ideal Schlumberger array in which the approximation that

$$\Delta U_{MN}/b \approx E_r \tag{12.10}$$

is valid provides the result:

$$E_{MN} = \frac{I\rho_1}{\pi} \int_0^\infty R_N^0(n_0) n_0 J_1(n_0 a) dn_0, \tag{12.11}$$
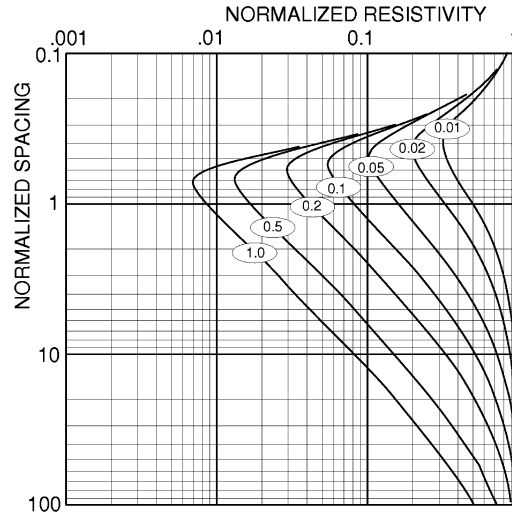
FIGURE 12.5

Apparent resistivity curves for an expanding Schlumberger array over a sequence of three layers. The upper and lower layers have unit resistivity, while the middle layer has a resistivity of 0.001 unit. The thickness of the middle layer, in units, is indicated by the label on each curve.

where $a = r_{AO}$.

This electric field is twice that given by Eq. (5.142) for a single pole source. With two source electrodes, A and B, one providing a current I and the other a current $-I$ to the ground, the current density at the measurement points is double that for a single source. Multiplying the electric field given in Eq. (12.11) by the geometric factor in Eq. (12.9), we can write for the apparent resistivity

$$\rho_a = \pi a^2 \frac{E_{MN}}{I} = \rho_1 a^2 \int_0^\infty R_N^0(n_0) n_0 J_1(n_0 a) dn_0. \tag{12.12}$$

12.1.2 THREE POINT ELECTRODE ARRAY

The Schlumberger array has generally been accepted as the "standard" electrode array for carrying out electrical resistivity soundings. However, its use is not universal. Other electrode arrays are often used for determining the resistivity profile in the earth as a function of depth. One closely related electrode array is the *three point array*, also sometimes called the *Canadian array*. It differs from the true Schlumberger array in that one of the two current electrodes is placed at a great distance from the other three. A sounding is made by moving the two closely-spaced measurement electrodes, M and N, away from the closer current electrode, A. Because the current electrode B is far removed, almost all of the voltage that is measured is contributed by the current flowing from electrode A and very little from the current flowing into electrode B.
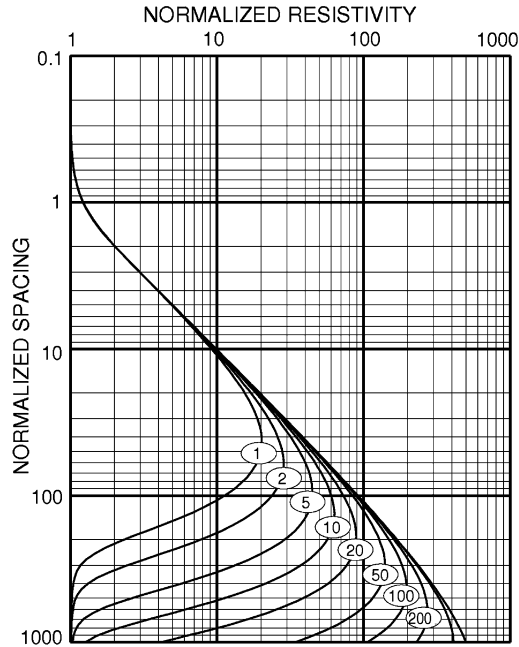
FIGURE 12.6

Apparent resistivity curves for an expanding Schlumberger array over a sequence of three layers. The upper and ower layers have unit resistivity, while the middle layer has a resistivity of 1000 units. The thickness of the middle layer, in units, is indicated by the label on each curve.

The geometric factor for the three-point array is derived from the general expression for a four electrode array by assigning the following values for the inter electrode distances:

$r_{AM} = a - b/2$

$r_{AN} = a + b/2$

$r_{MN} = b$

$r_{BM} \rightarrow \infty$

$r_{BN} \rightarrow \infty$

The corresponding geometric factor for the three point array is:

$$K_g^{Three-point} = 2\pi(a^2 - b^2/4) \approx 2\pi a^2. \tag{12.13}$$

Multiplying the electric field given in equation

$$E_{MN} = E_r(a) = \frac{I\rho_1}{2\pi} \int_0^\infty R_N^0(n_0) n_0 J_1(n_0 a) dn_0$$

by the geometric factor, we can write

$$\rho_a = 2\pi a^2 \frac{E_{MN}}{I} = \rho_1 a^2 \int_0^\infty R_N^0(n_0) n_0 J_1(n_0 a) dn_0. \tag{12.14}$$

12.1.3 DIPOLE ELECTRIC SOUNDING

Another approach to electric sounding which is widely used is the dipole electric sounding method (DES), the use of which is based largely on the work of L.M. Alpin (Alpin et al., 1966). In dipole arrays, the separations of both the current electrode pair and the measurement electrode pairs are quite small compared to the distance between the two pairs. Dipole electrode arrays have found use primarily in soundings to great depths. The advantage is that the amount of cable to be laid on the ground need not be large, even though great depths of investigation are desired. A disadvantage is that great amounts of current must be supplied to the array to achieve the desired depth of investigation.

A number of dipole electrode arrays are listed in Fig. 12.7. The separation between the centers of the source and receiving dipoles, r_{OP}, is called the *dipole array spacing*. The size of this spacing is used to characterize the depth of investigation for the dipole array, just as is the parameter $r_{AB/2}$ for the Schlumberger array.

With dipole arrays, the assumption is usually made that:

$$\Delta U_{MN} = E_{MN} r_{MN}. \tag{12.15}$$

Similarly, the current electrode pair is considered a point dipole with a moment:

$$\mathbf{p} = I \mathbf{r}_{AB}. \tag{12.16}$$

As an example, for a homogeneous half-space and referring to Eq. (4.90), the electric field from a current dipole source is:

$$\mathbf{E} = \frac{3\rho}{2\pi r^3} \frac{\mathbf{r}}{r} \left(\frac{\mathbf{r}}{r} \cdot \mathbf{p} \right) - \frac{\rho}{2\pi r^3} \mathbf{p}. \tag{12.17}$$

The dipole current moment $\mathbf{p}$ can be resolved into two orthogonal components if desired:

$$\mathbf{p} = \mathbf{p}_r + \mathbf{p}_\tau, \tag{12.18}$$

where $\mathbf{p}_r$ is the projection of $\mathbf{p}$ onto the radius vector $\mathbf{r}$ and $\mathbf{p}_\tau$ is the orthogonal (tangential) component. Alternatively, the dipole moment can be resolved into components along the x and y axes in a Cartesian coordinate system. Using the resolution into polar components, Eq. (12.17) can be rewritten as
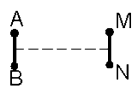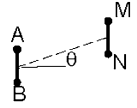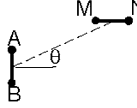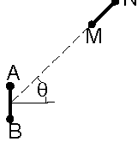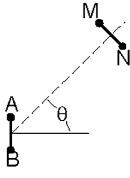
Layout	Nomenclature	Geometric Factor
	Equatorial array	$K_g = 2\pi \, r^3/bc$
	Parallel array (Broadside array)	$K_g = \dfrac{2\pi \, r^3}{bc(3\cos^2\theta - 1)}$
	Perpendicular array	$K_g = \dfrac{2\pi \, r^3}{3bc \cos\theta \, \sin\theta}$
	Radial array	$K_g = \pi r^3 / bc \cos\theta$
	Polar array (Inline array)	$K_g = \pi r^3/bc$
	Azimuthal array	$K_g = 2\pi r^3 / bc \sin\theta$

FIGURE 12.7

Geometric factors for various dipole electrode arrays. Note: **r** is the separation between dipole centers, **b** is the length of a measuring dipole, and **c** is the length of the source dipole.

$$\begin{aligned}
\mathbf{E} &= \frac{3\rho}{2\pi r^3}\mathbf{p}_r - \frac{\rho}{2\pi r^3}(\mathbf{p}_r + \mathbf{p}_\tau) \\
&= \frac{\rho}{\pi r^3}\mathbf{p}_r - \frac{\rho}{2\pi r^3}\mathbf{p}_\tau .
\end{aligned} \tag{12.19}$$

An axial dipole array is one in which all four electrodes are colinear. For this array, $\varphi = 0$, $\mathbf{p}_\tau = 0$, and $\mathbf{p} = \mathbf{p}_r$ and Eq. (12.19) becomes

$$\mathbf{E}_{axial} = (\rho/\pi r^3)\mathbf{p}, \tag{12.20}$$

and so,

$$E_{MN} = I\rho r_{AB}/\pi r^3. \tag{12.21}$$

In accord with Eq. (12.15)

$$\Delta U_{MN} = I\rho r_{AB} r_{MN}/\pi r^3. \tag{12.22}$$

If an equatorially displaced electrode array is considered instead, we have $\varphi = \pi/2$, $\mathbf{p}_r = 0$, and $\mathbf{p} = \mathbf{p}_\tau$. So:

$$\mathbf{E}_{equatorial} = -(\rho/2\pi r^3)\mathbf{p}. \tag{12.23}$$

In particular, for a parallel equatorial array,

$$E_{MN} = I\rho r_{AB}/2\pi r^3, \tag{12.24}$$

and so

$$\Delta U_{MN} = I\rho r_{AB} r_{MN}/2\pi r^3. \tag{12.25}$$

For an azimuthally displaced dipole array,

$$E_{MN} = \frac{\rho}{2\pi r^3} p_\tau = \frac{I\rho r_{AB} \sin\varphi}{2\pi r^3}, \tag{12.26}$$

and

$$\Delta U_{MN} = I\rho r_{AB} r_{MN} \sin\varphi/2\pi r^3. \tag{12.27}$$

Finally, for a radially displaced dipole array,

$$E_{MN} = \frac{\rho}{\pi r^3} p_r = \frac{I\rho r_{AB} \cos\varphi}{\pi r^3}, \tag{12.28}$$

and

$$\Delta U_{MN} = I\rho r_{AB} r_{MN} \cos\varphi/\pi r^3. \tag{12.29}$$

We can use expressions (12.26) and (12.28) for calculation of apparent resistivity
1. For an azimuthally displaced dipole array:

$$\rho_a = \frac{2\pi r^3}{r_{AB} \sin\varphi} \frac{E_{MN}}{I}. \tag{12.30}$$

For this array $E_{MN} = E_\varphi$, where in the case of the layered earth, E_φ is determined by the formula:

$$E_\phi(r, \phi) = -\frac{I\rho_1 r_{AB}}{2\pi} \sin \phi \frac{1}{r} \int_0^\infty R_N^0(n_0) J_1(n_0 r) n_0 dn_0. \tag{12.31}$$

Substituting (12.31) into (12.30), we obtain:

$$\rho_a = 2\pi r^2 \frac{E_{MN}}{I} = \rho_1 r^2 \int_0^\infty R_N^0(n_0) n_0 J_1(n_0 r) dn_0. \tag{12.32}$$

The last formula is the same as for Schlumberger array or for Three-point array.

Thus we conclude that apparent resistivity curves obtained by Schlumberger array or by three-point array or by azimuthally displaced dipole array are the same.

2. For a radially displaced dipole array,

$$\rho_a = \frac{\pi r^3}{r_{AB} \cos \varphi} \frac{E_{MN}}{I}. \tag{12.33}$$

For this array $E_{MN} = E_r$, where in the case of the layered earth, E_r is determined by the formula:

$$E_r(r, \phi) = \frac{I\rho_1 d\ell}{2\pi r} \cos \phi \int_0^\infty R_N^0(n_0)[J_1(n_0 r) - n_0 r J_0(n_0 r)] n_0 dn_0. \tag{12.34}$$

Substituting (12.34) into (12.33), we obtain:

$$\rho_a = \frac{\rho_1 r^2}{2} \int_0^\infty R_N^0(n_0)[J_1(n_0 r) - n_0 r J_0(n_0 r)] n_0 dn_0. \tag{12.35}$$

These formulas form the basis of the interpretation theory in DC Sounding methods.

Thus, we have shown that for three main type of DC arrays (Schlumberger array, three-point array and azimuthally displaced dipole array) the apparent resistivity curves in 1-D geoelectrical models can be calculated by the formula:

$$\rho_a = \rho_1 r^2 \int_0^\infty R_N^0(n_0) n_0 J_1(n_0 r) dn_0. \tag{12.36}$$

Applying inverse Hankel transform, we have:

$$R_N^0(n_0) = \int_0^\infty \frac{\rho_a(r)}{\rho_1 r} J_1(n_0 r) dr. \tag{12.37}$$

Therefore, the interpretation of the Vertical Electrical Sounding and Dipole Electrical Sounding data can be based on the analysis of the apparent resistivity curves obtained for current electrode separation (Schlumberger array) or for different separation between the centers of the source and receiving dipoles, r_{OP}.

Formulas for calculating geometric factors for apparent resistivity with dipole arrays are summarized in Fig. 12.7. These geometric factors are functions of the dipole lengths, *AB* and *MN*, and the

distance between the dipole centers, r. In a homogeneous earth, these formulas yield the correct value of resistivity for the medium. If the earth is not homogeneous, the apparent resistivity values reflect the actual resistivities in the medium in some complicated way. In field operations, one of the dipoles remains fixed in location, so that the center of the array moves as the array is expanded, or both dipoles move in opposite directions so that the center of the array remains fixed. The measured values of apparent resistivity are plotted in the Napierian domain (on a bilogarithmic graph sheet) as a function of the array spacings, r, with such a plot being termed a *DES field curve*. The resulting plot characterizes in a general way the vertical profile of resistivity in the earth.

12.2 INDUCED POLARIZATION (IP) METHODS
12.2.1 INDUCED POLARIZATION PHENOMENA

The theoretical and experimental foundations of IP methods in geophysical exploration were developed by several generations of geophysicists, starting with the pioneer research of the Schlumberger' brothers and continued by many outstanding geophysicists, including A.S. Semenov, Y.P. Bulashevich, S.M. Sheinman, V.A. Komarov, T. Madden, H. Seigel, J. Wait, S. Ward, J. Hohmann, K. Zonge, and many others (an historical review of the development of the IP method can be found in the excellent publication by Seigel et al., 2007).

The development of the IP method can be traced back to the 1950s, when both mining and petroleum companies were actively looking into the application of this method for mineral exploration. The physical-mathematical principles of the IP effect were originally formulated in pioneered works by Wait (1959) and Sheinman (1969). However, this method did not find wide application in US industry until after the work of Zonge and his associates at the Zonge Engineering and Research Organization (Zonge and Wynn, 1975) and Pelton and Ward at the University of Utah (Pelton et al., 1978). Significant contribution to the development of the IP method was made, also, by Professor Wait (1959, 1982), and by the research team at Kennecott in 1965–1977 (Nelson, 1997).

The IP method has found wide application in mining exploration. The interpretation of the IP data in mining industry was significantly approved during the last decade based on the advanced interpretation techniques developed by Oldenburg and his co-authors (e.g., Li and Oldenburg, 1991; Oldenburg and Li, 1994; Yuval and Oldenburg, 1997). There was also proposed an interesting application of the IP method in well-logging (e.g., Vinegar and Waxman, 1988). A number of successful applications of the IP method in hydrocarbon exploration were reported by Russian geophysicists (e.g., Komarov, 1980; Zonge, 1983; Kamenetsky, 1997; Davydycheva et al., 2004) as well.

The IP phenomenon is usually associated with charging and discharging effects in the ground in the process of current injecting. Fig. 12.8 schematically illustrates the typical IP effect. Suppose that we inject current into the ground and measure the electric potential difference between two electrodes. In the absence of the IP effect, if the ground is not chargeable (not polarizable), the measured potential will vary with time exactly with the same waveform as the electric current in the source, without any delay in rise-up or fall-down of the potential. However, if the ground is chargeable (polarizable), the potential will rise up and fall down with some time delay. This phenomenon is usually explained as membrane polarization which occurs when pore space narrows to within several boundary layers of thickness, or as electrode polarization, which occurs when pore space is blocked by metallic particles.
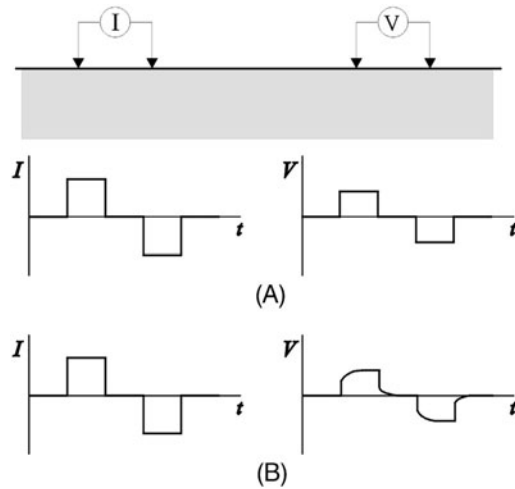
FIGURE 12.8

Sketch of the potential waveform for a current injected into nonpolarizable and polarizable ground. Panel (A) shows the case of nonpolarizable ground and (B) shows that of polarizable ground.

We will demonstrate below, however, that the same phenomenon can be mathematically explained by the propagation of a current in the complex multiphase composite geoelectrical model. The goal of the conventional IP survey is to detect these phenomena for imaging the subsurface structures by measuring the chargeability of the rock formations.

12.2.2 IP METHOD IN THE FREQUENCY AND TIME DOMAINS

In practice, two types of IP data can be acquired in exploration: time domain and frequency domain data. Figs. 12.9B and 12.9C present typical time domain potential curves obtained by IP measurement. When the current is injected (turn-on signal in the source) into the ground (Fig. 12.9A), the potential rises up immediately, but it takes some time to reach the maximum. The same behavior of the potential is observed when the current is terminated (turn-off signal in the source): the potential does not fall down to zero immediately, but it takes some time to decay to zero. The time domain chargeability is defined as the ratio of the potential at some time after turn-off, $\phi_s(t)$, to the maximum value of the potential, ϕ_η (Fig. 12.9):

$$M(t) = \phi_s(t)/\phi_\eta, \tag{12.38}$$

or as the ratio of the integral of the potential decay curve after turn-off to the maximum potential:

$$M = \frac{1}{\phi_\eta} \int_{t_1}^{t_2} \phi_s(t)\,dt. \tag{12.39}$$
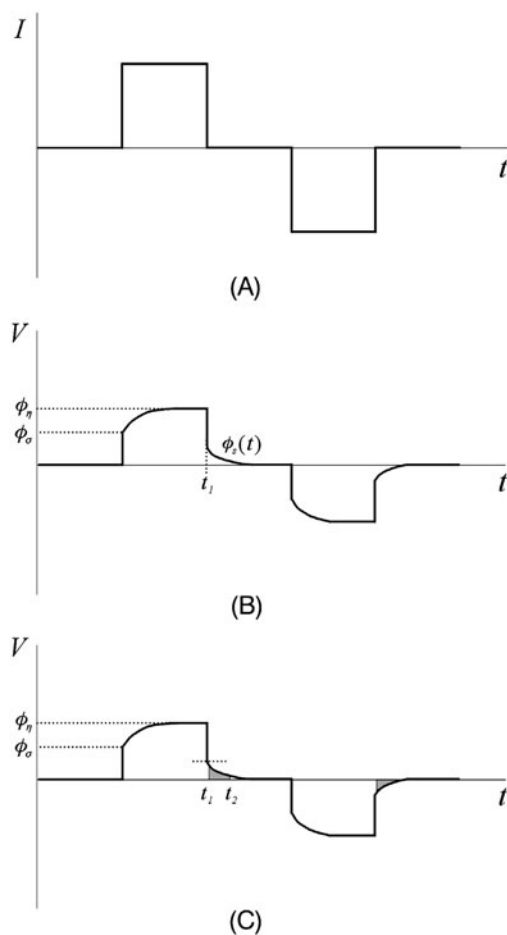
FIGURE 12.9

Representation of IP effects in the time domain. Panel (A) shows the injected current versus time. The chargeability can be represented as (B), the ratio of potential decay, or (C), the area under the decay curve, to the maximum potential.

In the frequency domain, the IP effect can be represented as a percent frequency effect (PFE), which is defined as the relative difference between the apparent resistivity with a higher frequency, $\rho_a^{f_1}$, from that with a lower frequency, $\rho_a^{f_2}$, normalized by the apparent resistivity with the high frequency, in percents (Fig. 12.10A):

$$PFE = \left(\frac{\rho_a^{f_1} - \rho_a^{f_2}}{\rho_a^{f_1}} \right) \times 100. \tag{12.40}$$

high frequency f_1 low frequency f_2

(A)

(B)
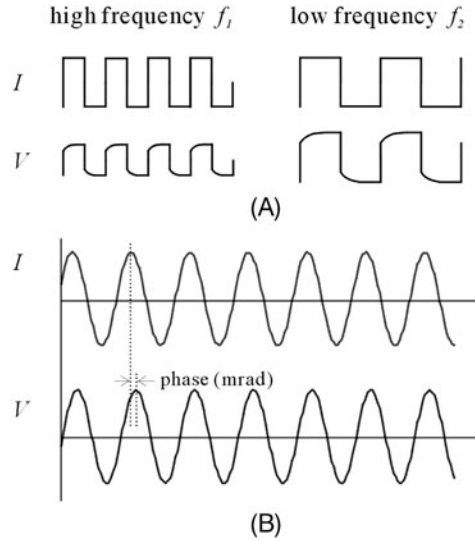
Representation of IP effects in the frequency domain. Panel (A) shows percent frequency effect, and (B) the phase difference between the current and the potential.

Another representation of IP effect in the frequency domain is the phase difference between the current in the source and the measured potential depending on frequencies of the source (Fig. 12.10B).

Note that the conventional IP method in the frequency domain is very similar to the DC resistivity method in that both methods use the electric field at a very low frequency, and IP data acquisition systems and interpretation techniques are very similar to those of the DC resistivity methods. Therefore one can define the apparent resistivity according to the standard DC resistivity formula:

$$\rho_a(\omega) = K \frac{\Delta U(\omega)}{I(\omega)}, \tag{12.41}$$

where K is a geometric factor depending on the source-receiver electrodes configuration (Luo and Zang, 1998), $\Delta U(\omega)$ is the potential measured in the receivers, and $I(\omega)$ is the strength of the injected current. For example, if we use a dipole-dipole array,

$$K = \frac{n(n+1)(n+2)(n+3)}{2}\pi l,$$

where l is the dipole length, and n is the separation index between source and receiver pair (the distance between the closest source and receiver electrodes is equal to nl).

Note that, in the presence of the IP effect the measured potential in the frequency domain is complex; therefore, the apparent resistivity is characterized by a complex number, as well:

$$\rho_a(\omega) = \operatorname{Re}\rho_a(\omega) + i\operatorname{Im}\rho_a(\omega). \tag{12.42}$$
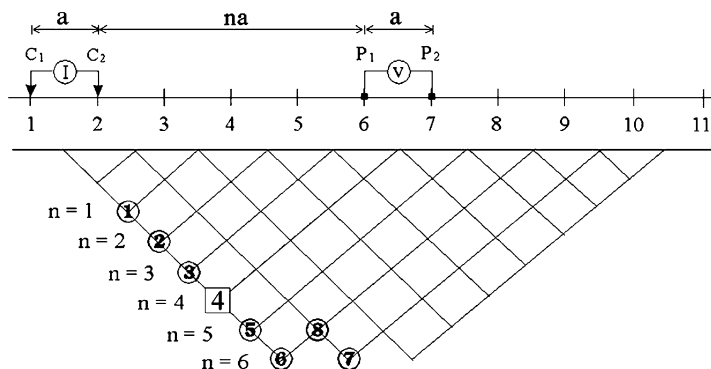
FIGURE 12.11

Pseudosection representation. The data are plotted at the midpoint of a transmitter and receiver pair versus a separation index, n.

The magnitude of the complex apparent resistivity is the same as the DC apparent resistivity:

$$\rho_a^{DC}(\omega) = |\rho_a(\omega)| = \sqrt{(\text{Re }\rho_a(\omega))^2 + (\text{Im }\rho_a(\omega))^2}, \tag{12.43}$$

and the phase is described as:

$$\phi_a(\omega) = \tan^{-1}\frac{\text{Im }\rho_a(\omega)}{\text{Re }\rho_a(\omega)}. \tag{12.44}$$

Fig. 12.11 shows the data representation in the form of a pseudosection, which is a well known data representation method in resistivity or IP surveys. The data are plotted at the midpoint of a transmitter and receiver pair versus a separation index, n. The separation index n of transmitter and receiver is defined as a distance between two adjacent stations, divided by the electric dipole length, as shown in Fig. 12.11.

The apparent resistivity magnitude and phase pseudosections provide useful images of the observed data, which can be used for qualitative interpretation. We will give some examples of these pseudosections for the typical mining targets below.

12.2.3 RESISTIVITY/IP MODEL OF A TYPICAL PORPHYRY COPPER SYSTEM IN THE SOUTHWESTERN U. S.

We consider a simplified model of a typical porphyry copper system in the southwestern U. S. Porphyry systems are important geologic targets for mineral exploration. Copper, gold, and molybdenum are among the important minerals extracted from these deposits. For modeling purposes a simplified porphyry model was constructed based on known geologic information (Titley, 1982, and Pierce and Bolm, 1995). An idealized porphyry copper system is shown in Fig. 12.12. Circulating hydrothermal fluids help concentrate economic minerals in the alteration zone surrounding the intrusion. Further
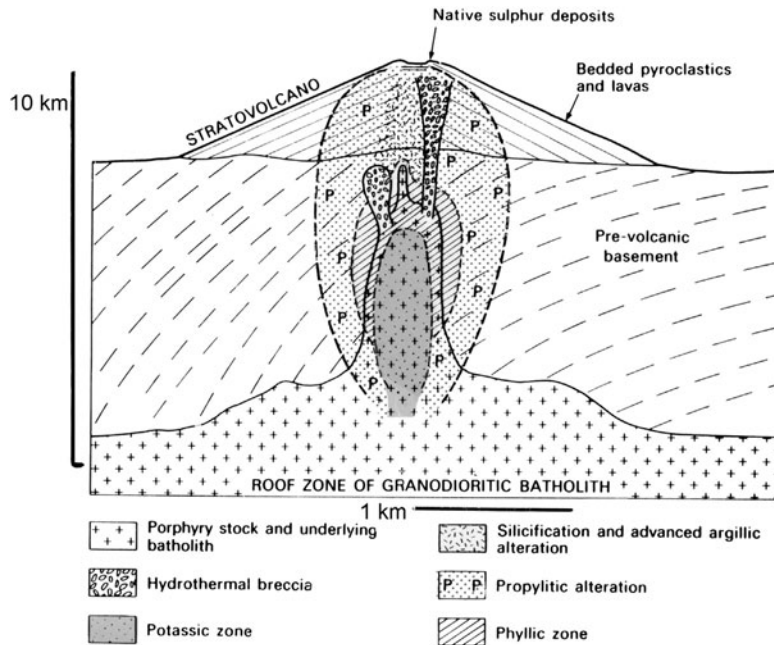
FIGURE 12.12

Porphyry genesis: a geologic overview of the creation of a porphyry deposit (after Sillitoe, 1973).

concentration of minerals can occur from weathering forming the leached cap and enriched zone. Fig. 12.13 shows a resistivity/IP model of a "typical" porphyry copper system in the southwestern U. S. (J. Inman, pers. commun.). The simplified porphyry model incorporates the classic zones seen in many porphyry deposits including supergene zones: leached cap, enriched zone and the unweathered zones: pyrite shell, chalcopyrite (ore zone), and barren core of the intrusion. A normal fault is also included near the deposit. This model is characterized by potentially strong EM coupling as well as IP effects.

We perform a modeling experiment to get an insight into the IP responses for this model. The dipole-dipole survey is simulated using integral equation modeling. To simulate the IP response as a potential difference measured by a dipole receiver, we compute the electric field along the receiver dipole location and then integrate it numerically to obtain the potential difference between two ends of the receiver bipole. The frequency of source is 1 Hz, which is a mid frequency among many frequencies generally available in modern IP instruments. Apparent resistivity and phase are calculated using Eqs. (12.43)–(12.44).

Figs. 12.14 and 12.15 show the apparent resistivity and phase pseudosections computed for a dipole length of 200 m and the maximum separation index equal to $n = 10$. Fig. 12.14 represents a pseudosection of the amplitude of apparent resistivity, and Fig. 12.15 is a phase pseudosection.

The clear apparent resistivity anomaly in Fig. 12.14 shows the conductive overburden does not hide the 150 meter deep, 80 meter thick, highly conductive enriched zone. The nearby fault produces a
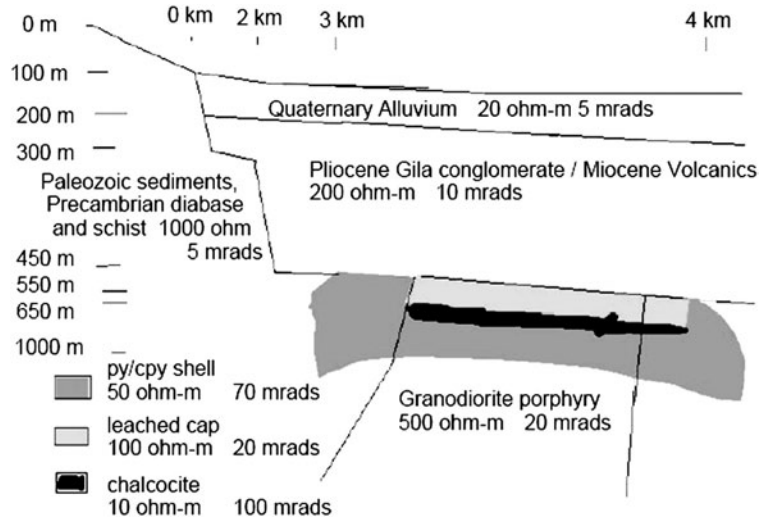
FIGURE 12.13

Southwest US copper porphyry geoelectrical model (J. Inman, pers. commun.). The figure presents basic scale information, geologic units, and geoelectrical properties. Note that there is a normal fault on the left side of the model.
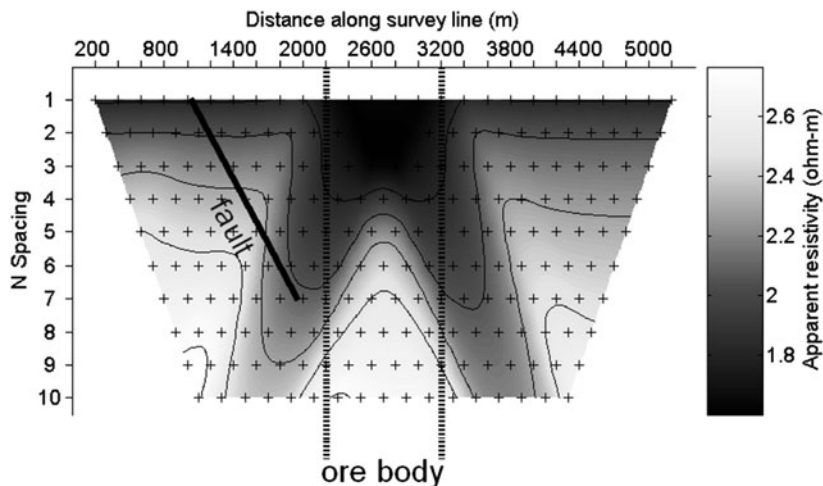
FIGURE 12.14

Apparent resistivity pseudosection for 1 Hz data. A resistivity anomaly surrounds the ore body in the center. The influence of the fault is seen in the right side of the pseudosection where the apparent resistivity is higher and creates an asymmetry in the response produced by the ore body.
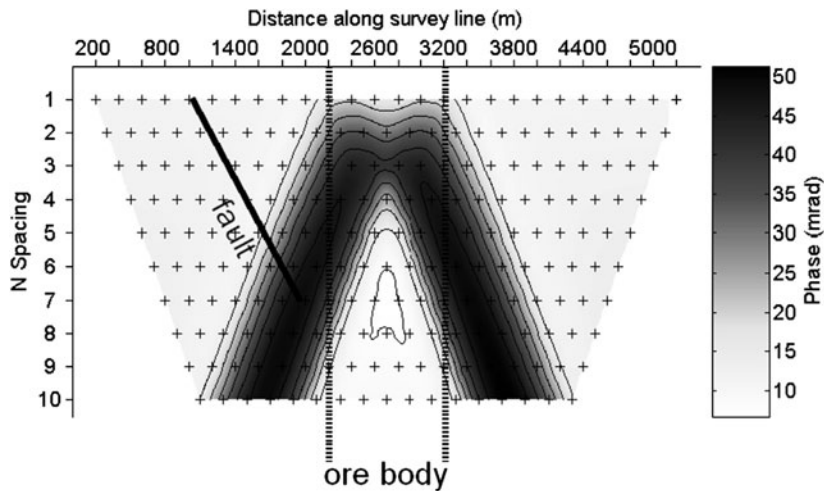
FIGURE 12.15

Apparent phase pseudosection for 1 Hz data. A phase anomaly due to the ore body is located in the center. One cannot see the influence of the fault in the phase data because it does not produce a strong enough IP response.

slight apparent resistivity anomaly in the left part of Fig. 12.14. Interestingly and fortunately it does not produce a significant phase anomaly as shown in Fig. 12.15. This has important implications for exploration where a DC resistivity anomaly may mask an ore body making the phase response important to the interpretation, indicating the importance of understanding the IP effect of the ore body and surrounding geology.

We should note that the pseudosections of the apparent resistivity and phase, shown above can be used for the qualitative interpretation of the IP data only. It is essential for the success of IP data interpretation to have a reliable method of quantitative analysis of the IP data. This analysis can be made on the basis of the appropriate conductivity model, quantitatively describing the relationships between the intrinsic characteristics of the heterogeneous rocks and their effective conductivity, which can be determined by the IP surveys. We will formulate the basic principles of the construction of this model in the next section.

12.3 PHYSICAL AND MATHEMATICAL MODELS OF THE IP PHENOMENON

Let us consider a composite geoelectrical model of rock formations based on the effective-medium approach, which generates a conductivity model with parameters directly related by analytical expressions to the physical characteristics of the microstructure of rocks and minerals (micro geometry and conductivity parameters). A composite geoelectrical model provides more realistic representation of the complex rock formations than conventional unimodal conductivity models. It allows us to model

the relationships between the physical characteristics of different types of rocks and minerals (e.g. conductivities, grain sizes, porosity, anisotropy, and polarizability) and the parameters of the relaxation model (Zhdanov, 2006, 2008a, 2008b).

Effective medium approximation for composite media has been discussed in Chapter 10. However, the form of effective-medium theory (EMT) presented in Chapter 10 does not allow including the polarizability effect in the general model of heterogeneous rocks. It has been found, however, that the effective conductivity of rocks is not necessarily a constant and real number but may vary with frequency and be complex (Shuev and Johnson, 1973). There are several explanations for these properties of effective conductivity. Most often they are explained by the physical-chemical polarization effects of mineralized particles of the rock material, and/or by the electrokinetic effects in the poroses of reservoirs (Wait, 1959; Marshall and Madden, 1959; Luo and Zang, 1998). Thus, the polarizability is caused by the complex electrochemical reactions that accompany current flow in the earth. It is manifested by accumulating electric charges on the surface of different grains forming the rock. This effect is very significant in the case of metal-electrolyte interface (Bockrig and Reddy, 1973). However, a similar effect is observed in the case of the interface between electrolyte and typical rock-forming minerals like silicate, carbonate, and others (Komarov, 1980).

It was demonstrated in Zhdanov (2008a, 2008b) that EMT formalism could be used in the theory of formation polarizability, as well. The general character of the model presented in the cited paper makes it possible to apply the developed results to study the rocks typical for mineralization zones and hydrocarbon reservoirs. This new theory allows us to develop a unified physical–mathematical model which can be used for examining the EM effects in the complex rock formations with different mineral structures and electrical properties. It takes into account the mineralization and/or fluid content of the rocks, the matrix composition, porosity, anisotropy, and polarizability of the formations. This approach will allow us to provide a link between the volume content of different minerals and/or the hydrocarbon saturation and the observed electromagnetic (EM) field data.

12.3.1 IP PHENOMENON IN THE CONTEXT OF EFFECTIVE-MEDIUM THEORY

We have discussed already the basic ideas of the effective-medium theory (EMT) in Chapter 10. Following the principles formulated in section 10.3, we represent a complex heterogeneous rock formation as a composite model formed by a homogeneous host medium of a volume V with a (complex) conductivity tensor $\widehat{\sigma}_0(\mathbf{r})$ (where $\mathbf{r}$ is an observation point) filled with grains of arbitrary shape and conductivity. The rock is composed of a set of N different types of grains, the lth grain type having (complex) tensor conductivity $\widehat{\sigma}_l$. The grains of the lth type have a volume fraction f_l in the medium and a particular shape and orientation.

The polarizability effect is usually associated with surface polarization of the coatings of the grains. This surface polarization can be related to electrochemical charge transfer between the grains and a host medium (Wong, 1979; Wong and Strangway, 1981; Klein et al., 1984). The surface polarization is manifested by accumulating electric charges on the surface of the grain. A double layer of charges is created on the grain's surface, which results in the voltage drop at this surface (Wait, 1982). It has been shown experimentally that for relatively small external electric fields used in electrical exploration, the voltage drop, Δu, is linear proportional to the normal current flow at the surface of the particle, $j_n = (\mathbf{n} \cdot \mathbf{j})$. That is, at the surface of the grain we have

$$\Delta u = k\,(\mathbf{n} \cdot \mathbf{j}),\tag{12.45}$$

where **n** is a unit vector of the outer normal to the grain's surface, and k is a surface polarizability factor, which, in general, is a complex frequency dependent function. This function is usually treated as the interface impedance which characterizes the boundary between the corresponding grain and surrounding host medium and describes the interfacial or membrane polarization. This effect is the most profound in the case of metal-electrolyte interface, and it was intensively studied in electrochemistry (Bockrig and Reddy, 1973; Marshall and Madden, 1959). However, a similar effect was found in other heterogeneous systems typical for rock formations, as well (e.g., Dukhin, 1971).

It was shown in section 10.3 that in the framework of the EMT approach, we could substitute a homogeneous effective medium with the conductivity tensor $\widehat{\sigma}_e$ for the original heterogeneous composite model and subject it to a constant electric field, $\mathbf{E}^b$, equal to the average electric field in the original model:

$$\mathbf{E}^b = \langle \mathbf{E} \rangle = V^{-1} \iiint_V \mathbf{E}\,(\mathbf{r})\,dv. \tag{12.46}$$

The effective conductivity is defined from the condition that the current density distribution $\mathbf{j}_e$ in an effective medium is equal to the average current density distribution in the original model:

$$\mathbf{j}_e = \widehat{\sigma}_e \cdot \mathbf{E}^b = \widehat{\sigma}_e \cdot \langle \mathbf{E} \rangle = \langle \widehat{\sigma} \cdot \mathbf{E} \rangle. \tag{12.47}$$

According to formula (10.39), the effective conductivity tensor, $\widehat{\sigma}_e$, is defined by the expression

$$\widehat{\sigma}_e = \widehat{\sigma}_b + \langle \widehat{\mathbf{m}} \rangle, \tag{12.48}$$

where $\widehat{\mathbf{m}}\,(\mathbf{r}')$ is material property tensor (see Eq. (10.38)).

Thus, in order to determine the effective conductivity of the composite polarized medium, we have to find the average value of the material property tensor, $\langle \widehat{\mathbf{m}} \rangle$.

It was shown in section 10.3 that one can represent the electric field $\mathbf{E}\,(\mathbf{r})$ generated in a homogeneous anisotropic background medium by the currents induced within the anomalous conductivity $\Delta \widehat{\sigma}\,(\mathbf{r})$ using integral form of the Maxwell's equations:

$$\mathbf{E}\,(\mathbf{r}) = \mathbf{E}^b + \iiint_V \widehat{\mathbf{G}}_b\,(\mathbf{r}\,|\,\mathbf{r}') \cdot \left[\Delta \widehat{\sigma}\,(\mathbf{r}') \cdot \mathbf{E}\,(\mathbf{r}') \right] dv', \tag{12.49}$$

where V is the volume occupied by all inhomogeneities, and $\widehat{\mathbf{G}}_b\,(\mathbf{r}\,|\,\mathbf{r}')$ is a Green's tensor for the homogeneous isotropic full space determined by expressions (10.41) and (10.42).

We assume, however, that in addition to electrical heterogeneity, the medium is characterized by polarizability effects which are manifested by the surface polarization of the grains. Mathematically, the surface polarization effect can be included in the general system of Maxwell's equations by adding the following boundary conditions on the surfaces S_l of the grains (Luo and Zang, 1998):

$$\left[\mathbf{n} \times \left(\mathbf{E}^+\,(\mathbf{r}') - \mathbf{E}^-\,(\mathbf{r}') \right) \right]_{S_l} = - \left[\mathbf{n} \times \nabla' \Delta u\,(\mathbf{r}') \right]_{S_l}, \tag{12.50}$$

where $\mathbf{E}^+$ designates the boundary value of electric field $\mathbf{E}\,(\mathbf{r})$ when the observation point tends to the boundary S_l of the lth grain from the inside of the grains, and $\mathbf{E}^-$ if this point tends to the boundary from the outside of the grains.

Therefore, electric field due to the surface polarization effect $\mathbf{E}^p(\mathbf{r})$ can be represented as an electric field of a specified discontinuity (12.50) (Zhdanov, 1988, p. 250):

$$\mathbf{E}^p(\mathbf{r}) = -\nabla \times \iint_S g_b(\mathbf{r} \mid \mathbf{r}') \sigma_b \left[\mathbf{n}(\mathbf{r}') \cdot (\mathbf{E}^+(\mathbf{r}') - \mathbf{E}^-(\mathbf{r}')) \right]_S ds', \tag{12.51}$$

where S stands for the superposition of all surfaces S_l of the entire ensemble of grains, $S = \bigcup\limits_{l=1}^{N} S_l$, and vector $\mathbf{n}(\mathbf{r}')$ is directed outside the grains.

The last integral can be written in an equivalent form as a field generated by the double layers co-inciding with the grains' surfaces with a dipole electric charge moment density $\mathbf{M}_S = \Delta u \mathbf{n}$ (Zhdanov, 1988, p. 144):

$$\mathbf{E}^p(\mathbf{r}) = \nabla \iint_S \nabla' g_b(\mathbf{r} \mid \mathbf{r}') \sigma_b \cdot \mathbf{n}(\mathbf{r}') \Delta u \, ds'. \tag{12.52}$$

According to (12.45), we assume that the voltage drop at the surface of the grain is proportional to the normal current:

$$\Delta u = k \left(\mathbf{n}(\mathbf{r}') \cdot \mathbf{j}(\mathbf{r}') \right) = k \left(\mathbf{n}(\mathbf{r}') \cdot \widehat{\sigma}(\mathbf{r}') \cdot \mathbf{E}(\mathbf{r}') \right), \tag{12.53}$$

where current $\mathbf{j}(\mathbf{r}')$ is taken for the internal side of the grain's surface.

Therefore, expression (12.51) becomes:

$$\begin{aligned}
\mathbf{E}^p(\mathbf{r}) &= \nabla \iint_S \nabla' g_b(\mathbf{r} \mid \mathbf{r}') \sigma_b \cdot \mathbf{n}(\mathbf{r}') \Delta u \, ds' \\
&= \iint_S \widehat{\mathbf{G}}_b(\mathbf{r} \mid \mathbf{r}') \cdot \mathbf{n}(\mathbf{r}') k \sigma_b \left(\mathbf{n}(\mathbf{r}') \cdot \widehat{\sigma}(\mathbf{r}') \cdot \mathbf{E}(\mathbf{r}') \right) ds'.
\end{aligned} \tag{12.54}$$

The total electric field caused by the effects of both the electromagnetic induction and induced polarization is equal to:

$$\begin{aligned}
\mathbf{E}(\mathbf{r}) = \mathbf{E}^b &+ \iiint_V \widehat{\mathbf{G}}_b(\mathbf{r} \mid \mathbf{r}') \cdot \left[\Delta \widehat{\sigma}(\mathbf{r}') \cdot \mathbf{E}(\mathbf{r}') \right] dv' \\
&+ \iint_S \widehat{\mathbf{G}}_b(\mathbf{r} \mid \mathbf{r}') \cdot \mathbf{n}(\mathbf{r}') k \sigma_b \left(\mathbf{n}(\mathbf{r}') \cdot \widehat{\sigma}(\mathbf{r}') \cdot \mathbf{E}(\mathbf{r}') \right) ds'.
\end{aligned} \tag{12.55}$$

Substituting expression (10.37) into formula (12.55), we can write:

$$\begin{aligned}
\mathbf{E}(\mathbf{r}) = \mathbf{E}^b &+ \iiint_V \widehat{\mathbf{G}}_b(\mathbf{r} \mid \mathbf{r}') \cdot \left[\widehat{\mathbf{m}}(\mathbf{r}') \cdot \mathbf{E}^b \right] dv' \\
&+ \iint_S \widehat{\mathbf{G}}_b(\mathbf{r} \mid \mathbf{r}') \cdot \mathbf{n}(\mathbf{r}') \left(\mathbf{n}(\mathbf{r}') \cdot \widehat{\boldsymbol{\xi}}(\mathbf{r}') \cdot \left[\widehat{\mathbf{m}}(\mathbf{r}') \cdot \mathbf{E}^b \right] \right) ds',
\end{aligned} \tag{12.56}$$

where $\widehat{\boldsymbol{\xi}}(\mathbf{r}')$ is equal to:

$$\widehat{\boldsymbol{\xi}}(\mathbf{r}') = k \sigma_b \widehat{\sigma}(\mathbf{r}') \cdot \left(\Delta \widehat{\sigma}(\mathbf{r}') \right)^{-1}. \tag{12.57}$$

We can represent the integrals in Eq. (12.56) as a sum of the integrals over the volumes and surfaces of all grains:

$$\mathbf{E}(\mathbf{r}) = \mathbf{E}^b + \sum_l \mathbf{E}_l(\mathbf{r}), \qquad (12.58)$$

where:

$$
\begin{aligned}
\mathbf{E}_l(\mathbf{r}) = &\iiint_{V_l} \widehat{\mathbf{G}}_b(\mathbf{r}\,|\,\mathbf{r}') \cdot \left[\widehat{\mathbf{m}}(\mathbf{r}') \cdot \mathbf{E}^b\right] dv' \\
&+ \iint_{S_l} \widehat{\mathbf{G}}_b(\mathbf{r}\,|\,\mathbf{r}') \cdot \mathbf{n}(\mathbf{r}') \left(\mathbf{n}(\mathbf{r}') \cdot \widehat{\boldsymbol{\xi}}(\mathbf{r}') \cdot \left[\widehat{\mathbf{m}}(\mathbf{r}') \cdot \mathbf{E}^b\right]\right) ds'.
\end{aligned}
\qquad (12.59)
$$

It was demonstrated in Chapter 10 that, we can use a QL approximation for the integrals over V_l and S_l and assume that the material property tensor is constant in V_l up to its boundary S_l:

$$\widehat{\mathbf{m}}(\mathbf{r}') = \widehat{\mathbf{m}}_l, \ \mathbf{r}' \in V_l. \qquad (12.60)$$

Consider now the integrals over one grain only:

$$
\begin{aligned}
\mathbf{E}_l(\mathbf{r}) = &\iiint_{V_l} \widehat{\mathbf{G}}_b(\mathbf{r}\,|\,\mathbf{r}')\, dv' \cdot \widehat{\mathbf{m}}_l \cdot \mathbf{E}^b \\
&+ \iint_{S_l} \widehat{\mathbf{G}}_b(\mathbf{r}\,|\,\mathbf{r}') \cdot \mathbf{n}(\mathbf{r}') \mathbf{n}(\mathbf{r}')\, ds' \cdot \widehat{\boldsymbol{\xi}}_l \cdot \widehat{\mathbf{m}}_l \cdot \mathbf{E}^b,
\end{aligned}
\qquad (12.61)
$$

where:

$$\widehat{\boldsymbol{\xi}}(\mathbf{r}') = \widehat{\boldsymbol{\xi}}_l = const, \ \mathbf{r}' \in V_l.$$

According to Eq. (10.48), the volume integral of the Green's tensor $\widehat{\mathbf{G}}_b$ is equal to the volume depolarization tensor, $\widehat{\boldsymbol{\Gamma}}_l$,

$$\widehat{\boldsymbol{\Gamma}}_l = \iiint_{V_l} \widehat{\mathbf{G}}_b(\mathbf{r}\,|\,\mathbf{r}')\, dv'. \qquad (12.62)$$

We also introduce the surface depolarization tensors, $\widehat{\boldsymbol{\Lambda}}_l$, as follows:

$$\widehat{\boldsymbol{\Lambda}}_l = \iint_{S_l} \widehat{\mathbf{G}}_b(\mathbf{r}\,|\,\mathbf{r}') \cdot \mathbf{n}(\mathbf{r}') \mathbf{n}(\mathbf{r}')\, ds'. \qquad (12.63)$$

For example, for a spherical grain of a radius a_l, we have (Zhdanov, 2008a, 2008b):

$$\widehat{\boldsymbol{\Lambda}}_l = -\frac{2}{3\sigma_b a_l} \widehat{\mathbf{I}}. \qquad (12.64)$$

Substituting (12.62) and (12.63) back into (12.61), we obtain:

$$\mathbf{E}_l(\mathbf{r}) = \widehat{\boldsymbol{\Gamma}}_l \cdot \widehat{\mathbf{m}}_l \cdot \mathbf{E}^b + \widehat{\boldsymbol{\Gamma}}_l \cdot \widehat{\mathbf{p}}_l \cdot \widehat{\mathbf{m}}_l \cdot \mathbf{E}^b = \widehat{\boldsymbol{\Gamma}}_l \cdot \widehat{\mathbf{q}}_l \cdot \mathbf{E}^b, \qquad (12.65)$$

where a surface polarizability tensor $\widehat{\mathbf{p}}$ and a volume polarizability tensor $\widehat{\mathbf{q}}$ are equal to:

$$\widehat{\mathbf{p}}\left(\mathbf{r}'\right) = \widehat{\mathbf{\Gamma}}_l^{-1} \cdot \widehat{\mathbf{\Lambda}}_l \cdot \widehat{\boldsymbol{\xi}}\left(\mathbf{r}'\right), \ \widehat{\mathbf{p}}_l = \widehat{\mathbf{p}}\left(\mathbf{r}'\right), \ \mathbf{r}' \in V_l, \tag{12.66}$$

and

$$\widehat{\mathbf{q}}\left(\mathbf{r}'\right) = \left[\widehat{\mathbf{I}} + \widehat{\mathbf{p}}\left(\mathbf{r}'\right)\right] \cdot \widehat{\mathbf{m}}\left(\mathbf{r}'\right), \ \widehat{\mathbf{q}}_l = \widehat{\mathbf{q}}\left(\mathbf{r}'\right), \ \mathbf{r}' \in V_l. \tag{12.67}$$

Then formula (12.65) becomes:

$$\mathbf{E}_l\left(\mathbf{r}\right) = \iiint_{V_l} \widehat{\mathbf{G}}_b\left(\mathbf{r} \mid \mathbf{r}'\right) dv' \cdot \widehat{\mathbf{q}}_l \cdot \mathbf{E}^b. \tag{12.68}$$

Substituting expression (12.68) back into (12.58), we find:

$$\begin{aligned}
\mathbf{E}\left(\mathbf{r}\right) &= \mathbf{E}^b + \sum_l \iiint_{V_l} \widehat{\mathbf{G}}_b\left(\mathbf{r} \mid \mathbf{r}'\right) \cdot \widehat{\mathbf{q}}\left(\mathbf{r}'\right) dv' \cdot \mathbf{E}^b \\
&= \mathbf{E}^b + \iiint_V \widehat{\mathbf{G}}_b\left(\mathbf{r} \mid \mathbf{r}'\right) \cdot \widehat{\mathbf{q}}\left(\mathbf{r}'\right) dv' \cdot \mathbf{E}^b.
\end{aligned} \tag{12.69}$$

The last formula shows that the surface polarization effect introduced by formula (12.54) can be represented by the equivalent volume polarization effect and combined with the electromagnetic induction phenomenon in one integral expression.

12.3.2 EFFECTIVE CONDUCTIVITY OF A HETEROGENEOUS POLARIZABLE MEDIUM

In this section we will derive a constructive approach for determining the effective conductivity of the heterogeneous polarizable medium. We have established above that, in order to solve this problem, we have to find the average value of the material property tensor, $\langle \widehat{\mathbf{m}} \rangle$. The last function can be found based on the integral representation (12.69).

Multiplying both sides of (12.69) by $\Delta \widehat{\boldsymbol{\sigma}}\left(\mathbf{r}\right)$, we have:

$$\widehat{\mathbf{m}}\left(\mathbf{r}\right) \cdot \mathbf{E}^b = \Delta \widehat{\boldsymbol{\sigma}}\left(\mathbf{r}\right) \cdot \mathbf{E}^b + \Delta \widehat{\boldsymbol{\sigma}}\left(\mathbf{r}\right) \cdot \iiint_V \widehat{\mathbf{G}}_b\left(\mathbf{r} \mid \mathbf{r}'\right) \cdot \widehat{\mathbf{q}}\left(\mathbf{r}'\right) dv' \cdot \mathbf{E}^b. \tag{12.70}$$

Our goal is to find the material property tensor $\widehat{\mathbf{m}}$. According to Eq. (12.67) this tensor is related to the volume polarizability tensor $\widehat{\mathbf{q}}$ by the following formula:

$$\widehat{\mathbf{m}} = \left[\widehat{\mathbf{I}} + \widehat{\mathbf{p}}\right]^{-1} \widehat{\mathbf{q}}. \tag{12.71}$$

Therefore, in order to find $\widehat{\mathbf{m}}$, we need to determine tensor $\widehat{\mathbf{q}}$ first. Multiplying both sides of (12.70) by $\left[\widehat{\mathbf{I}} + \widehat{\mathbf{p}}\right]$, we finally arrive at equation for $\widehat{\mathbf{q}}$:

$$\widehat{\mathbf{q}}\left(\mathbf{r}\right) = \Delta \widehat{\boldsymbol{\sigma}}^p\left(\mathbf{r}\right) + \Delta \widehat{\boldsymbol{\sigma}}^p\left(\mathbf{r}\right) \cdot \iiint_V \widehat{\mathbf{G}}_b\left(\mathbf{r} \mid \mathbf{r}'\right) \cdot \widehat{\mathbf{q}}\left(\mathbf{r}'\right) dv', \tag{12.72}$$

where $\Delta\widehat{\boldsymbol{\sigma}}^p(\mathbf{r})$ is a "polarized" anomalous conductivity:

$$\Delta\widehat{\boldsymbol{\sigma}}^p(\mathbf{r}) = \left[\widehat{\mathbf{I}} + \widehat{\mathbf{p}}(\mathbf{r})\right] \cdot \Delta\widehat{\boldsymbol{\sigma}}(\mathbf{r}). \tag{12.73}$$

Using similar mathematical transformations as those applied in Chapter 10 to Eq. (10.54), we can rewrite Eq. (12.72) in the form:

$$\widehat{\mathbf{q}}_l = \Delta\widehat{\boldsymbol{\sigma}}_l^p + \Delta\widehat{\boldsymbol{\sigma}}_l^p \cdot \widehat{\boldsymbol{\Gamma}}_l \cdot \left[\widehat{\mathbf{q}}_l - \langle\widehat{\mathbf{q}}\rangle\right]. \tag{12.74}$$

Note that Eq. (12.74) follows immediately from Eq. (10.61), if we substitute $\widehat{\mathbf{q}}$ for $\widehat{\mathbf{m}}$, and $\Delta\widehat{\boldsymbol{\sigma}}_l^p$ for $\Delta\widehat{\boldsymbol{\sigma}}$ in the last equation.

Solving Eq. (12.74), we determine the volume polarizability tensor, $\widehat{\mathbf{q}}_l$, for every grain:

$$\widehat{\mathbf{q}}_l = \left[\widehat{\mathbf{I}} - \Delta\widehat{\boldsymbol{\sigma}}_l^p \cdot \widehat{\boldsymbol{\Gamma}}_l\right]^{-1} \cdot \Delta\widehat{\boldsymbol{\sigma}}_l^p \cdot \left[\widehat{\mathbf{I}} - \widehat{\boldsymbol{\Gamma}}_l \cdot \langle\widehat{\mathbf{q}}\rangle\right]. \tag{12.75}$$

Taking an average value of both sides of (12.75), and solving the resulting equation for $\langle\widehat{\mathbf{q}}\rangle$, we finally find:

$$\langle\widehat{\mathbf{q}}\rangle = \left\langle\left[\widehat{\mathbf{I}} - \Delta\widehat{\boldsymbol{\sigma}}^p \cdot \widehat{\boldsymbol{\Gamma}}\right]^{-1}\right\rangle^{-1} \left\langle\left[\widehat{\mathbf{I}} - \Delta\widehat{\boldsymbol{\sigma}}^p \cdot \widehat{\boldsymbol{\Gamma}}\right]^{-1} \cdot \Delta\widehat{\boldsymbol{\sigma}}^p\right\rangle. \tag{12.76}$$

According to Eq. (12.67), the average value of the material property tensor is:

$$\langle\widehat{\mathbf{m}}\rangle = \left\langle\left[\widehat{\mathbf{I}} + \widehat{\mathbf{p}}\right]^{-1} \widehat{\mathbf{q}}\right\rangle. \tag{12.77}$$

Substituting (12.77) into (12.48), we finally have:

$$\begin{aligned}
\widehat{\boldsymbol{\sigma}}_e &= \widehat{\boldsymbol{\sigma}}_b + \left\langle\left[\widehat{\mathbf{I}} + \widehat{\mathbf{p}}\right]^{-1} \widehat{\mathbf{q}}\right\rangle \\
&= \widehat{\boldsymbol{\sigma}}_b + \left[\widehat{\mathbf{I}} + \widehat{\mathbf{p}}_0\right]^{-1} \widehat{\mathbf{q}}_0 f_0 + \sum_{l=1}^{N} \left[\widehat{\mathbf{I}} + \widehat{\mathbf{p}}_l\right]^{-1} \widehat{\mathbf{q}}_l f_l.
\end{aligned} \tag{12.78}$$

12.3.3 SELF-CONSISTENT APPROXIMATION FOR EFFECTIVE CONDUCTIVITY

Note that the simplest choice for the average value of the volume polarizability tensor $\langle\widehat{\mathbf{q}}\rangle$ is:

$$\langle\widehat{\mathbf{q}}\rangle = 0, \tag{12.79}$$

because in this case from (12.75) we have:

$$\widehat{\mathbf{q}}_l = \left[\widehat{\mathbf{I}} - \Delta\widehat{\boldsymbol{\sigma}}_l^p \cdot \widehat{\boldsymbol{\Gamma}}_l\right]^{-1} \cdot \Delta\widehat{\boldsymbol{\sigma}}_l^p, \tag{12.80}$$

and

$$\langle \widehat{\mathbf{q}} \rangle = \left\langle \left[\widehat{\mathbf{I}} - \Delta \widehat{\boldsymbol{\sigma}}^p \cdot \widehat{\boldsymbol{\Gamma}} \right]^{-1} \cdot \Delta \widehat{\boldsymbol{\sigma}}^p \right\rangle$$

$$= \left[\widehat{\mathbf{I}} - \Delta \widehat{\boldsymbol{\sigma}}_0^p \cdot \widehat{\boldsymbol{\Gamma}}_0 \right]^{-1} f_0 + \sum_{l=1}^N \left[\widehat{\mathbf{I}} - \Delta \widehat{\boldsymbol{\sigma}}_l^p \cdot \widehat{\boldsymbol{\Gamma}}_l \right]^{-1} f_l = 0. \tag{12.81}$$

Eq. (12.81) can be treated as a loose IP analog of the self-consistency condition of the conventional effective medium theory (Stroud, 1975). Detailed analysis shows that for a composite medium without IP effect, Eq. (12.81) leads to the Bruggeman method of the effective conductivity determination (Choy, 1999).

Substituting (12.80) into (12.71), we find:

$$\widehat{\mathbf{m}}_l = \left[\widehat{\mathbf{I}} + \widehat{\mathbf{p}}_l \right]^{-1} \left[\widehat{\mathbf{I}} - \Delta \widehat{\boldsymbol{\sigma}}_l^p \cdot \widehat{\boldsymbol{\Gamma}}_l \right]^{-1} \cdot \left[\widehat{\mathbf{I}} + \widehat{\mathbf{p}}_l \right] \cdot \Delta \widehat{\boldsymbol{\sigma}}_l. \tag{12.82}$$

In this case, expression (12.48) for the effective conductivity of the polarized inhomogeneous medium takes the form:

$$\widehat{\boldsymbol{\sigma}}_e = \widehat{\boldsymbol{\sigma}}_b + \left[\widehat{\mathbf{I}} + \widehat{\mathbf{p}}_0 \right]^{-1} \left[\widehat{\mathbf{I}} - \Delta \widehat{\boldsymbol{\sigma}}_0^p \cdot \widehat{\boldsymbol{\Gamma}}_0 \right]^{-1} \cdot \left[\widehat{\mathbf{I}} + \widehat{\mathbf{p}}_0 \right] \cdot \Delta \widehat{\boldsymbol{\sigma}}_0 f_0$$

$$+ \sum_{l=1}^N \left[\widehat{\mathbf{I}} + \widehat{\mathbf{p}}_l \right]^{-1} \left[\widehat{\mathbf{I}} - \Delta \widehat{\boldsymbol{\sigma}}_l^p \cdot \widehat{\boldsymbol{\Gamma}}_l \right]^{-1} \cdot \left[\widehat{\mathbf{I}} + \widehat{\mathbf{p}}_l \right] \cdot \Delta \widehat{\boldsymbol{\sigma}}_l f_l.$$

In particular, if we select the background conductivity to be equal to the host medium conductivity,

$$\widehat{\boldsymbol{\sigma}}_b = \widehat{\boldsymbol{\sigma}}_0,$$

then:

$$\widehat{\boldsymbol{\sigma}}_e = \widehat{\boldsymbol{\sigma}}_0 + \sum_{l=1}^N \left[\widehat{\mathbf{I}} + \widehat{\mathbf{p}}_l \right]^{-1} \left[\widehat{\mathbf{I}} - \Delta \widehat{\boldsymbol{\sigma}}_l^p \cdot \widehat{\boldsymbol{\Gamma}}_l \right]^{-1} \cdot \left[\widehat{\mathbf{I}} + \widehat{\mathbf{p}}_l \right] \cdot \Delta \widehat{\boldsymbol{\sigma}}_l f_l, \tag{12.83}$$

because $\Delta \widehat{\boldsymbol{\sigma}}_0 = 0$.

Note that, for heterogeneous media without polarizability, formula (12.83) corresponds to the Maxwell-Garnett theory of the composite geoelectrical medium (Choy, 1999).

The last formula provides a general solution of the effective conductivity problem for an arbitrary multiphase composite polarized medium. This formula allows us to find the effective conductivity for inclusions with arbitrary shape and electrical properties. That is why the new composite geoelectrical model of the IP effect may be used to construct the effective conductivity for realistic rock formations typical for mineralization zones and/or petroleum reservoirs.

12.3.4 ANISOTROPY EFFECT IN IP DATA

We consider first a composite model with isotropic grains of arbitrary shape. In this case all conductivities become scalar functions:

$$\widehat{\boldsymbol{\sigma}}_0 = \widehat{\mathbf{I}} \sigma_0, \ \Delta \widehat{\boldsymbol{\sigma}}_l = \widehat{\mathbf{I}} \Delta \sigma_l, \ \Delta \widehat{\boldsymbol{\sigma}}_l^p = \left(\widehat{\mathbf{I}} + \widehat{\mathbf{p}}_l \right) \Delta \sigma_l$$
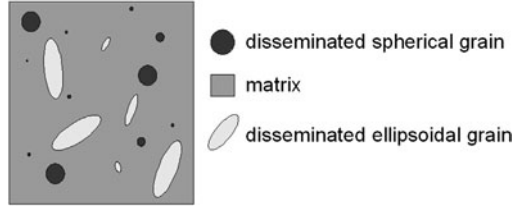
FIGURE 12.16

An example of electrically isotropic media: a multiphase model of the rock is composed of a set of the grains with nonisometric shape but random orientation.

and, according to formula (12.66):

$$\widehat{\mathbf{p}}_l = \xi_l \widehat{\mathbf{\Gamma}}_l^{-1} \cdot \widehat{\mathbf{\Lambda}}_l, \tag{12.84}$$

where ξ_l is equal to:

$$\xi_l = k_l \sigma_0 \sigma_l \left(\Delta \sigma_l \right)^{-1}.$$

Therefore, we can write:

$$\begin{aligned}
\widehat{\sigma}_e &= \widehat{\sigma}_b + \left\langle \left[\widehat{\mathbf{I}} + \widehat{\mathbf{p}} \right]^{-1} \widehat{\mathbf{q}} \right\rangle \\
&= \widehat{\mathbf{I}} \sigma_0 + \sum_{l=1}^{N} \left[\widehat{\mathbf{I}} + \widehat{\mathbf{p}}_l \right]^{-1} \left[\widehat{\mathbf{I}} - \left(\widehat{\mathbf{I}} + \widehat{\mathbf{p}}_l \right) \Delta \sigma_l \widehat{\mathbf{\Gamma}}_l \right]^{-1} \left[\widehat{\mathbf{I}} + \widehat{\mathbf{p}}_l \right] \Delta \sigma_l \, f_l.
\end{aligned} \tag{12.85}$$

It can be demonstrated that if the grains have nonisometric shape (e.g., ellipsoidal shape) but random orientation (see Fig. 12.16), averaging of the tensor terms in expression (12.85) will result in scalarization. Therefore, the effective medium conductivity will become a scalar function. However, if all the grains are oriented in one specific direction as shown in Fig. 12.17, the effective conductivity of this medium will become anisotropic. Thus, the effective conductivity may be a tensor in spite of the fact that the background medium and all the grains are electrically isotropic.

12.3.5 FUNDAMENTAL IP MODEL I: EFFECTIVE RESISTIVITY OF THE ISOTROPIC MULTIPHASE HETEROGENEOUS MEDIUM FILLED WITH SPHERICAL INCLUSIONS

It was demonstrated in the pioneer work of Pelton (1977), that the Cole-Cole relaxation model (Cole and Cole, 1941) can represent well the typical complex conductivity of polarized rock formations. In the framework of this model, the complex resistivity, $\rho(\omega)$, is described by the following well known expression:

$$\rho(\omega) = \rho \left(1 - \eta \left(1 - \frac{1}{1 + (i\omega\tau)^C} \right) \right), \tag{12.86}$$
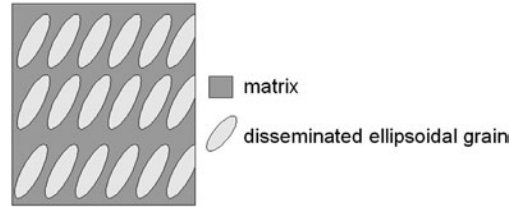
FIGURE 12.17

An example of electrically anisotropic media: a multiphase model of the rock is composed of a set of ellipsoidal grains oriented in one direction.

where ρ is the DC resistivity [Ohm-m]; ω is the angular frequency [rad/sec]; τ is the time parameter; η is the intrinsic chargeability (Seigel, 1959a); and C is the relaxation parameter. The dimensionless intrinsic chargeability, η, characterizes the intensity of the IP effect.

Fig. 12.18 presents examples of typical complex resistivity curves with the Cole-Cole model parameters defined according to Table 12.1.

One can see a significant difference between the solid and dashed curves in this plot, which correspond to the different Cole-Cole models with different parameters.

Note also that the Cole-Cole curve gives us just one possible example of the relaxation model. There are several other models discussed in the geophysical literature (see, for example, Kamenetsky, 1997). One of the important practical questions is the relationship between the Cole-Cole model parameters and the petrophysical characteristics of mineralized rocks. There were several publications specifically dedicated to the solution of this problem. However, most of the published results provide just a qualitative indication of the correlation between the Cole-Cole parameters and specific mineralization characteristics of the rocks, such as mineral grain sizes and physical properties.

One of the reasons for electrical conductivity relaxation in rocks is the heterogeneity of formations containing microscopic inclusions of different minerals. In the pioneered work by Wait (1982, p. 77), a simplified model of the composite medium as a loading of spherical conducting particles in a resistive background was introduced. The effective conductivity for this model was determined based on the equations of the static electric field. This model provided a foundation for the phenomenological theory of induced electrical polarization.

In this section we will show that Wait's model appears as a special case of a GEMTIP model, introduced in Zhdanov (2008a, 2008b). We consider, as an example, an isotropic multiphase composite model, with all model parameters described by the scalar functions. A composite model is formed by a homogeneous host medium of a volume V with a conductivity σ_0 filled with grains of spherical shape. We assume also that we have a set of N different types of grains, the lth grain type having radius a_l, conductivity σ_l, and surface polarizability k_l. In this model, both the volume and the surface depolarization tensors are constant scalar tensors equal to (Zhdanov, 2008a, 2008b):

$$\widehat{\boldsymbol{\Gamma}}_l = \Gamma_l \widehat{\mathbf{I}} = -\widehat{\mathbf{I}} \frac{1}{3\sigma_b} \widehat{\mathbf{I}}, \quad \widehat{\boldsymbol{\Lambda}}_l = \Lambda_l \widehat{\mathbf{I}} = -\frac{2}{3\sigma_b a_l} \widehat{\mathbf{I}}. \tag{12.87}$$
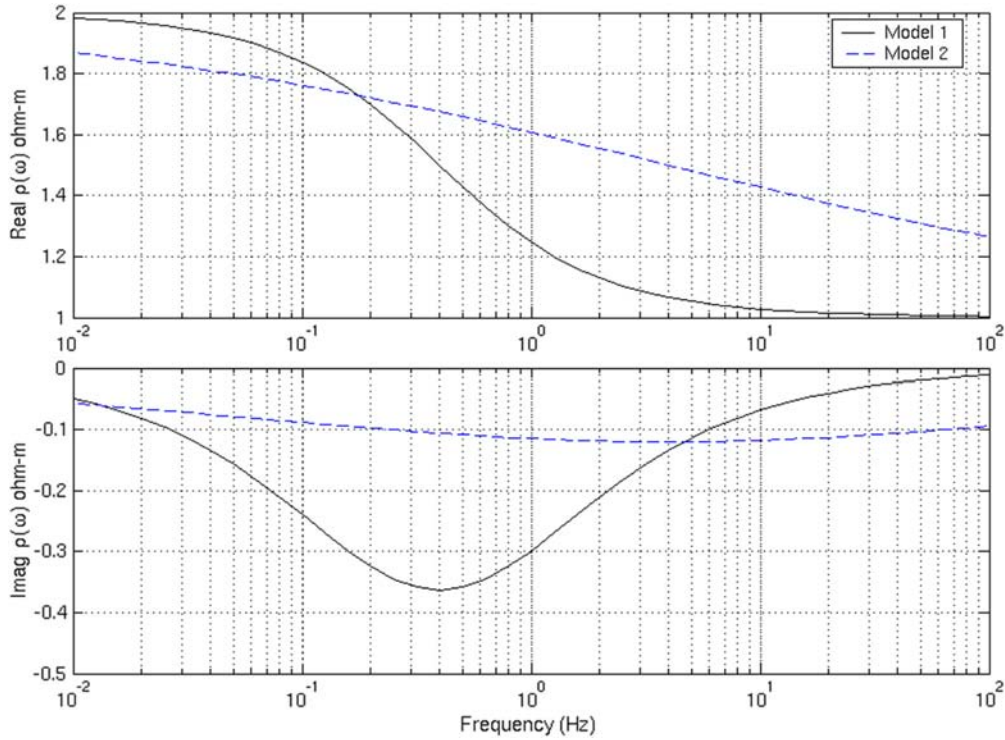
FIGURE 12.18

Examples of typical complex resistivity curves with the Cole-Cole model parameters. The upper panel shows the real part of the complex resistivity, while the bottom panel presents the imaginary part of the complex resistivity.

Table 12.1	Parameters of the Cole-Cole models
Model 1	**Model 2**
$\rho_1 = 2$ Ohm-m,	$\rho_2 = 2$ Ohm-m,
$\eta_1 = 0.5$,	$\eta_2 = 0.5$,
$\tau_1 = 0.4$,	$\tau_2 = 0.04$,
$C_1 = 0.8$,	$C_2 = 0.3$.

The corresponding tensor formulas for conductivities, tensors $\widehat{\mathbf{m}}$ and $\widehat{\mathbf{q}}$, can be substituted by the scalar equations. For example, Eq. (12.75) for $\widehat{\mathbf{q}}$ takes the form:

$$q_l = \left[1 - \Delta\sigma_l^p \Gamma_l\right]^{-1} \Delta\sigma_l^p \left[1 - \Gamma_l \langle q \rangle\right], \tag{12.88}$$

and Eq. (12.71) for $\hat{\mathbf{m}}$ becomes:

$$
\begin{aligned}
m_l &= \left[1 + p_l\right]^{-1} q_l \\
&= \left[1 - (1 + p_l) \Delta\sigma_l \Gamma_l\right]^{-1} \Delta\sigma_l \left[1 - \Gamma_l \langle q \rangle\right],
\end{aligned}
\tag{12.89}
$$

where, according to (12.66) and (12.57):

$$
p_l = 2k_l a_l^{-1} \sigma_b \sigma_l \left(\Delta\sigma_l\right)^{-1}.
\tag{12.90}
$$

Formula (12.76) for $\langle \hat{\mathbf{q}} \rangle$ is simplified, as well:

$$
\langle q \rangle = \left\langle \left[1 - (1 + p_l) \Delta\sigma_l \Gamma_l\right]^{-1} \right\rangle^{-1} \left\langle \left[1 - (1 + p_l) \Delta\sigma_l \Gamma_l\right]^{-1} (1 + p_l) \Delta\sigma_l \Gamma_l \right\rangle.
\tag{12.91}
$$

In the framework of the self-consistent theory, the effective conductivity will be given by a scalar form of expression (12.82):

$$
m_l = \left[1 - (1 + p_l) \Delta\sigma_l \Gamma_l\right]^{-1} \Delta\sigma_l.
\tag{12.92}
$$

Substituting formula (12.92) into (12.48), we obtain the following scalar formula for the effective conductivity of the polarized inhomogeneous medium:

$$
\begin{aligned}
\sigma_e &= \sigma_b + \left\langle \left[1 - (1 + p_l) \Delta\sigma_l \Gamma_l\right]^{-1} \Delta\sigma_l \right\rangle \\
&= \sigma_b + \left[1 - (1 + p_0) \Delta\sigma_0 \Gamma_0\right]^{-1} \Delta\sigma_0 f_0 + \sum_{l=1}^{N} \left[1 - (1 + p_l) \Delta\sigma_l \Gamma_l\right]^{-1} \Delta\sigma_l f_l.
\end{aligned}
\tag{12.93}
$$

In particular, assuming $\sigma_b = \sigma_0$ and, therefore, $\Delta\sigma_0 = 0$, we write:

$$
\sigma_e = \sigma_0 + \sum_{l=1}^{N} \left[1 - (1 + p_l) \Delta\sigma_l \Gamma_l\right]^{-1} \Delta\sigma_l f_l.
\tag{12.94}
$$

Substituting expression (12.87) for volume depolarization tensor and Eq. (12.92) for p_l, we finally find:

$$
\sigma_e = \sigma_0 \left\{ 1 + 3 \sum_{l=1}^{N} \left[f_l \frac{\sigma_l - \sigma_0}{2\sigma_0 + \sigma_l + 2k_l a_l^{-1} \sigma_0 \sigma_l} \right] \right\}.
$$

Multiplying the numerator and denominator by $\rho_l \rho_0$, (where $\rho_0 = 1/\sigma_0$, $\rho_l = 1/\sigma_l$), we obtain an equivalent expression for the effective resistivity of the composite polarized medium:

$$
\rho_e = \rho_0 \left\{ 1 + 3 \sum_{l=1}^{N} \left[f_l \frac{\rho_0 - \rho_l}{2\rho_l + \rho_0 + 2k_l a_l^{-1}} \right] \right\}^{-1}.
\tag{12.95}
$$

It is well-known from the experimental data that the surface polarizability factor is a complex function of frequency. Let us represent the surface polarizability of the lth grain as:

$$k_l = b_l \, (i\omega\tau_l)^{-C_l} , \tag{12.96}$$

where:

$$b_l = a_l \, (2\rho_l + \rho_0) \, /2.$$

Therefore:

$$k_l = \frac{a_l}{2} \, (2\rho_l + \rho_0) \, (i\omega\tau_l)^{-C_l} . \tag{12.97}$$

Thus, after some algebra, we have:

$$\rho_e = \rho_0 \left\{ 1 + \sum_{l=1}^{N} \left[f_l M_l \left[1 - \frac{1}{1 + (i\omega\tau_l)^{C_l}} \right] \right] \right\}^{-1} , \tag{12.98}$$

where

$$M_l = 3 \frac{\rho_0 - \rho_l}{2\rho_l + \rho_0} . \tag{12.99}$$

Note that, in the case of the metallic particles, one can assume that $\rho_l/\rho_0 \ll 1$, and we have:

$$M_l \approx 3. \tag{12.100}$$

Following Wait (1982), we adopt the model:

$$k_l = \alpha_l \, (i\omega)^{-C_l} , \tag{12.101}$$

which fits the experimental data, where α_l are some empirical surface polarizability coefficients, measured in the units $[\alpha_l] = \left(Ohm \times m^2 \right) / \sec^{C_l}$.

Therefore from (12.101) and (12.97), we obtain:

$$\tau_l = \left[\frac{a_l}{2\alpha_l} \, (2\rho_l + \rho_0) \right]^{1/C_l} . \tag{12.102}$$

Formula (12.98) provides a general analytical expression for the effective conductivity of the multiphase heterogeneous polarized medium, typical for mineralization zones.

In the case of a two-phase composite model, we have a homogeneous host medium of a volume V with a (complex) resistivity ρ_0 and spherical inclusions with the resistivity ρ_1. Formula (12.95) is simplified:

$$\rho_e = \rho_0 \left\{ 1 + f_1 M_1 \left[1 - \frac{1}{1 + (i\omega\tau_1)^{C_1}} \right] \right\}^{-1} . \tag{12.103}$$

After some algebra, we arrive at the conventional Cole-Cole formula for the effective resistivity:

$$\rho_e = \rho_0 \left\{ 1 - \eta \left[1 - \frac{1}{1 + (i\omega\tau)^C} \right] \right\}, \tag{12.104}$$

where:

$$\eta = \frac{3 f_1 (\rho_0 - \rho_1)}{2\rho_1 + \rho_0 + 3 f_1 (\rho_0 - \rho_1)}, \tag{12.105}$$

and

$$\tau = \left[\frac{a_1}{2\alpha_1} \left(2\rho_1 + \rho_0 + 3 f_1 (\rho_0 - \rho_1) \right) \right]^{1/C}. \tag{12.106}$$

Note that in formula (12.104) we use the same notations as in the original Cole-Cole formula (12.86).

12.3.6 FUNDAMENTAL IP MODEL II: EFFECTIVE RESISTIVITY OF THE MULTIPHASE HETEROGENEOUS MEDIUM FILLED WITH ELLIPTICAL INCLUSIONS

Another fundamental IP model exists for a special case of inclusions with ellipsoidal shape, where the solution of the GEMTIP formulas can be obtained in close form, similar to a model with spherical inclusions. The advantage of the model with ellipsoidal inclusions is that in this case one can use different shapes of ellipsoids, from oblate to prolate, to model different types of heterogeneous rock formations and different types of inclusions. At the same time, for ellipsoidal geometry of the grains, the surface and volume depolarization tensors, $\widehat{\Lambda}_l$ and $\widehat{\Gamma}_l$, can be calculated in close form using the volume and surface integrals. Indeed, in the following sections we will demonstrate how the expressions for the depolarization tensors can be simplified for elliptical grains.

According to formulas (12.62) and (12.63), we write the expressions for the volume, $\widehat{\Gamma}$, and surface, $\widehat{\Lambda}$, depolarization tensors as follows:

$$\widehat{\Gamma} = \iiint_V \widehat{G}_b (\mathbf{r} \mid \mathbf{r}') \, dv', \tag{12.107}$$

and

$$\widehat{\Lambda} = \iint_S \widehat{G}_b (\mathbf{r} \mid \mathbf{r}') \cdot \mathbf{n} (\mathbf{r}') \mathbf{n} (\mathbf{r}') \, ds', \tag{12.108}$$

where V is the volume occupied by the grain, S is the surface of the grain, $\mathbf{n} (\mathbf{r}')$ is a unit vector of the outer normal to the surface S, and $\mathbf{n} (\mathbf{r}') \mathbf{n} (\mathbf{r}')$ denotes a dyadic product of two normal vectors.

Tensor function $\widehat{G}_b (\mathbf{r} \mid \mathbf{r}')$ is a Green's tensor for the homogeneous anisotropic full space, which can be represented in the form of a dyadic Green's function:

$$\widehat{G}_b (\mathbf{r} \mid \mathbf{r}') = \nabla\nabla' g_b (\mathbf{r} \mid \mathbf{r}'),$$

where $\nabla\nabla'$ stands for a dyadic product of two operators, ∇ and ∇'.

In the case of a quasi-static model of the field and isotropic homogeneous full space ($\widehat{\boldsymbol{\sigma}}_b = \widehat{\mathbf{I}}\sigma_b$):

$$g_b\left(\mathbf{r} \mid \mathbf{r}'\right) = \frac{1}{4\pi\sigma_b \left|\mathbf{r} - \mathbf{r}'\right|}. \tag{12.109}$$

Note that, the volume depolarization tensor $\widehat{\boldsymbol{\Gamma}}$ can be represented in the form of a surface integral, as well. Indeed, according to the Gauss theorem, the volume depolarization tensor $\widehat{\boldsymbol{\Gamma}}$ is equal to:

$$\widehat{\boldsymbol{\Gamma}} = \iiint_V \widehat{\mathbf{G}}_b\left(\mathbf{r} \mid \mathbf{r}'\right) dv' = \iiint_V \nabla\nabla' g_b\left(\mathbf{r} \mid \mathbf{r}'\right) dv'$$
$$\nabla \iiint_V \nabla' g_b\left(\mathbf{r} \mid \mathbf{r}'\right) dv' = \nabla \iint_S g_b\left(\mathbf{r} \mid \mathbf{r}'\right) \mathbf{n}\left(\mathbf{r}'\right) ds'. \tag{12.110}$$

Calculation of the volume depolarization tensor, $\widehat{\boldsymbol{\Gamma}}$, for an ellipsoidal grain

The volume depolarization tensor $\widehat{\boldsymbol{\Gamma}}$ of an ellipsoidal grain can be determined as (Stratton, 1941; Landau et al., 1984, pp. 37–44) a diagonal tensor with the components equal to:

$$\Gamma_{\alpha\alpha} = -\frac{a_x a_y a_z}{2\sigma_b} \int_0^\infty \frac{ds}{(s + a_\alpha) R_s} =$$
$$-\frac{3V}{8\pi\sigma_b} \int_0^\infty \frac{ds}{(s + a_\alpha) R_s} = -\frac{1}{\sigma_b}\gamma_\alpha, \tag{12.111}$$

where a_x, a_y, a_z are the semi-axes of the ellipsoidal grain, $V = 4\pi a_x a_y a_z/3$ is a volume of the ellipsoid, and γ_α are depolarization factors:

$$\gamma_\alpha = \frac{3V}{8\pi} \int_0^\infty \frac{ds}{(s + a_\alpha) R_s}, \quad R_s = \sqrt{(s + a_x)(s + a_y)(s + a_z)}. \tag{12.112}$$

Note that the depolarization factors satisfy the conditions:

$$\gamma_x + \gamma_y + \gamma_z = 1. \tag{12.113}$$

In particular, for a spherical grain we obtain immediately the known result:

$$\Gamma_{xx} = \Gamma_{yy} = \Gamma_{zz} = -\frac{1}{3\sigma_b}. \tag{12.114}$$

For a cylindrical inclusion with the axis parallel to the axis z, $(a_z \to \infty)$, we have:

$$\Gamma_{zz} = 0, \ \Gamma_{xx} = \Gamma_{yy} = -\frac{1}{2\sigma_b}. \tag{12.115}$$

In the case of the inclusion represented by the flat horizontal thin sheet $(a_x, a_y \to \infty)$, one can find:

$$\Gamma_{xx} = \Gamma_{yy} = 0, \ \Gamma_{zz} = -\frac{1}{\sigma_b}. \tag{12.116}$$

Note that, for ellipsoids of revolution (spheroidal-shape particles) with the axis z aligned with the axis of revolution of the ellipsoid, the horizontal semi-axes of the ellipsoid are equal ($a_x = a_y = a$, and $a_z = b$). In this case, the elliptical integrals in (12.111) can be expressed by analytical functions (Landau et al., 1984, pp. 37–44), with:

$$\gamma_z = \gamma, \ \gamma_x = \gamma_y = \frac{1}{2}(1 - \gamma) \tag{12.117}$$

and

$$\Gamma_{zz} = \Gamma = -\frac{\gamma}{\sigma_b}, \ \Gamma_{xx} = \Gamma_{yy} = -\frac{1}{2\sigma_b}(1 + \sigma_b\Gamma). \tag{12.118}$$

The value of γ is determined by the eccentricity, e, of a spheroid.

For example, in the case of the prolate spheroid ($b > a$) with $e = \sqrt{1 - a^2/b^2}$, we have:

$$\gamma = \frac{1 - e^2}{e^3}\left(\tanh^{-1}e - e\right). \tag{12.119}$$

Note that, if $e \to 1$, the spheroid transforms into a long thin rod.

For the oblate spheroid ($b < a$), with eccentricity $e = \sqrt{a^2/b^2 - 1}$, we have:

$$\gamma = \frac{1 + e^2}{e^3}\left(e - \tan^{-1}e\right). \tag{12.120}$$

Calculation of the surface depolarization tensor, $\overset{\wedge}{\Lambda}$, for an ellipsoidal grain

Now let us calculate the surface depolarization tensor for ellipsoidal grains. To simplify the calculations, we will consider the ellipsoids of revolution only. Introducing a system of coordinates x, y, z with the axis z aligned with the axis of revolution of the ellipsoid, we represent the equation of the surface of the ellipsoid as:

$$\frac{x^2}{a^2} + \frac{y^2}{a^2} + \frac{z^2}{b^2} = 1,$$

where $a = a_x = a_y$, $b = a_z$ are equatorial and polar radii of the ellipsoid, respectively.

In particular, we can write the equation for the surface of the ellipsoid in cylindrical coordinates (ρ, φ, z) as:

$$x = \rho\cos\varphi; \ \ y = \rho\sin\varphi; \ \ \rho = (a/b)\sqrt{b^2 - z^2}; \ \ z \in [-b, b]. \tag{12.121}$$

The expression for the surface depolarization tensor (12.108) in the center of the ellipsoid ($\mathbf{r} = 0$) takes the form:

$$\overset{\wedge}{\Lambda} = -\frac{a}{4\pi\sigma_b b^2}\int\limits_0^{2\pi}d\varphi\int\limits_{-b}^{b}\overset{\wedge}{\mathbf{g}}(\mathbf{r}') \cdot \overset{\wedge}{\mathbf{N}}(\mathbf{r}')\, Q(\mathbf{r}')dz', \tag{12.122}$$

where:

$$\overset{\wedge}{\mathbf{N}} = \mathbf{n}\left(\mathbf{r}'\right)\mathbf{n}\left(\mathbf{r}'\right),$$ (12.123)

and:

$$\overset{\wedge}{\mathbf{g}}\left(\mathbf{r}'\right) = \nabla\nabla'\frac{1}{|\mathbf{r}'|}.$$ (12.124)

Note that vector $\mathbf{n}\left(\mathbf{r}'\right) = (n_x,\ n_y,\ n_z)$ is a unit vector normal to the ellipsoid:

$$n_x = \frac{b\sqrt{b^2 - z'^2}}{Q}\cos\varphi;\ n_y = \frac{b\sqrt{b^2 - z'^2}}{Q}\sin\varphi;\ n_z = \frac{az'}{Q},\ Q = \sqrt{b^4 - (b^2 - a^2)z'^2}.$$

Therefore, expression (12.123) takes the form:

$$\overset{\wedge}{\mathbf{N}} = \begin{pmatrix} n_x^2 & n_x n_y & n_x n_z \\ n_x n_y & n_y^2 & n_y n_z \\ n_x n_z & n_y n_z & n_z^2 \end{pmatrix} = \begin{pmatrix} n_{11} & n_{12} & n_{13} \\ n_{21} & n_{22} & n_{23} \\ n_{31} & n_{32} & n_{33} \end{pmatrix},$$ (12.125)

where the scalar components n_{ki} are calculated as:

$$n_{11} = \frac{b^2(b^2 - z^2)}{Q^2}\cos^2\varphi;\ n_{12} = \frac{b^2(b^2 - z^2)}{Q^2}\sin\varphi\cos\varphi;\ n_{13} = \frac{abz\sqrt{(b^2 - z^2)}}{Q^2}\cos\varphi;$$

$$n_{21} = \frac{b^2(b^2 - z^2)}{Q^2}\sin\varphi\cos\varphi;\ n_{22} = \frac{b^2(b^2 - z^2)}{Q^2}\sin^2\varphi;\ n_{23} = \frac{abz\sqrt{(b^2 - z^2)}}{Q^2}\sin\varphi;$$

$$n_{31} = \frac{abz\sqrt{(b^2 - z^2)}}{Q^2}\cos\varphi;\ n_{32} = \frac{abz\sqrt{(b^2 - z^2)}}{Q^2}\sin\varphi;\ n_{33} = \frac{a^2 z^2}{Q^2};\ Q = \sqrt{b^4 - (b^2 - a^2)z^2}.$$ (12.126)

We can write a similar matrix representation for tensor $\overset{\wedge}{\mathbf{g}}$:

$$\overset{\wedge}{\mathbf{g}} = \begin{pmatrix} g_{11} & g_{12} & g_{13} \\ g_{21} & g_{22} & g_{23} \\ g_{31} & g_{32} & g_{33} \end{pmatrix},$$ (12.127)

where the scalar components g_{ij} are calculated as:

$$g_{11} = \frac{b^3 \left[3a^2(b^2 - z^2)\cos^2\varphi - R^2\right]}{R^5};$$

$$g_{11} = \frac{b^3 \left[3a^2(b^2 - z^2)\sin^2\varphi - R^2\right]}{R^5}; \quad g_{33} = \frac{b^3[3b^2z^2 - R^2]}{R^5};$$

$$g_{12} = g_{21} = \frac{3a^2b^3(b^2 - z^2)}{R^5}\sin\varphi\cos\varphi; \quad g_{13} = g_{31} = \frac{3ab^4z\sqrt{b^2 - z^2}}{R^5}\cos\varphi;$$

$$g_{23} = g_{32} = \frac{3ab^4z\sqrt{b^2 - z^2}}{R^5}\sin\varphi; \quad R = \sqrt{a^2b^2 + (b^2 - a^2)z^2}. \tag{12.128}$$

Substituting expressions (12.123)–(12.128) into formula (12.122), after some algebra, we will find:

$$\widehat{\Lambda} = -\frac{1}{\sigma_b}\begin{bmatrix} \lambda & 0 & 0 \\ 0 & \lambda & 0 \\ 0 & 0 & \lambda_z \end{bmatrix},$$

where:

$$\lambda = \frac{ab^3}{2}\int_0^b \frac{[2a^2b^2 - (b^2 - a^2)z^2](b^2 - z^2)}{[a^2b^2 + (b^2 - a^2)z^2]^{5/2}\sqrt{b^4 - (b^2 - a^2)z^2}}dz, \tag{12.129}$$

and:

$$\lambda_z = ba^3\int_0^b \frac{[3b^4 - b^2a^2 - (b^2 - a^2)z^2]z^2}{[a^2b^2 + (b^2 - a^2)z^2]^{5/2}\sqrt{b^4 - (b^2 - a^2)z^2}}dz. \tag{12.130}$$

Note that, in the case of a spherical grain with a radius a,

$$\lambda = \lambda_z = \frac{2}{3a},$$

and the surface depolarization tensor takes the form:

$$\widehat{\Lambda} = -\frac{2}{3\sigma_b a}\widehat{\mathbf{I}}. \tag{12.131}$$

In a general case of the ellipsoidal grains one should numerically calculate the integrals (12.129) and (12.130).

The surface depolarization tensor for spheroidal-shape grains is equal to:

$$\widehat{\Lambda}_l = -\frac{1}{\sigma_0}\begin{bmatrix} \lambda_l & 0 & 0 \\ 0 & \lambda_l & 0 \\ 0 & 0 & \lambda_{lz} \end{bmatrix},$$

where $\lambda_l = \lambda_{lx} = \lambda_{ly}$, and λ_{lz} can be calculated using the integrals (12.129) and (12.130).

Effective conductivity tensor of a multiphase composite anisotropic medium filled with ellipsoidal inclusions

Substituting the corresponding expressions for the surface and volume depolarization tensors in Eq. (12.83), after some lengthy but straightforward algebra, we arrive at a general analytical solution for the principal components of the effective conductivity tensor of a multiphase composite anisotropic medium filled with ellipsoidal inclusions:

$$\sigma_{e\alpha} = \sigma_0 + \sum_{l=1}^{N} (\sigma_l - \sigma_0) \, f_l \left[1 + \frac{\sigma_l - \sigma_0}{\sigma_0} \gamma_{l\alpha} + k_l \sigma_l \lambda_{l\alpha} \right]^{-1}, \ \alpha = x, y, z, \tag{12.132}$$

where k_l is a surface polarizability factor, and $\gamma_{l\alpha}$ and $\lambda_{l\alpha}$ are scalar coefficients defined by geometrical parameters of the grains (see formulas above).

In particularly, for the case of randomly oriented elliptical inclusions, conductivity of the polarized inhomogeneous medium can be calculated by taking an average over the orientation in formula (12.132). As a result, we obtain the following formula for effective conductivity, σ_e:

$$\sigma_e = \sigma_0 \left[1 + \frac{1}{3} \sum_{l=1}^{N} f_l D_l \right], \tag{12.133}$$

where:

$$D_l = \sum_{\alpha=x,y,z} D_{l\alpha}.$$

The expression for the effective resistivity, $\rho_e = 1/\sigma_e$, of a medium filled with completely randomly oriented ellipsoidal grains can be written as follows:

$$\rho_e = \rho_0 \left[1 + \frac{1}{3} \sum_{l=1}^{N} f_l D_l \right]^{-1}, \tag{12.134}$$

where:

$$D_{l\alpha} = \frac{\rho_0 - \rho_l}{\rho_l + \gamma_{l\alpha} (\rho_0 - \rho_1) + k_l \lambda_{l\alpha}}. \tag{12.135}$$

It can be shown that, if the inclusions are conductive, $\rho_l \ll \rho_0$, then formula (12.134) is simplified as follows:

$$\rho_e = \rho_0 \left\{ 1 + \sum_{l=1}^{N} \frac{f_l}{3} \sum_{\alpha=x,y,z} \frac{1}{\gamma_{l\alpha}} \left[1 - \frac{1}{1 + s_{l\alpha} (i\omega\tau_l)^{C_l}} \right] \right\}^{-1}, \tag{12.136}$$

where ρ_0 is the DC resistivity of the host matrix, ω is the frequency, f_l is the fraction volume parameter, τ_l is the time constant, and C_l is a relaxation parameter of the lth grain, respectively.

The coefficients $\gamma_{l\alpha}$ and $s_{l\alpha}$ ($l = 1, 2, ...N$; $\alpha = x, y, z$) are the structural coefficients defined by the geometrical characteristics of the ellipsoidal inclusions used to approximate the grains, $s_{l\alpha} = r_{l\alpha}/\overline{a}_l$, and $\overline{a}_l$ is an average value of the equatorial (a_{lx} and a_{ly}) and polar (a_{lz}) radii of the ellipsoidal grains, i.e.:

$$\overline{a}_l = \frac{(a_{lx} + a_{ly} + a_{lz})}{3}, \quad r_{l\alpha} = 2\frac{\gamma_{l\alpha}}{\lambda_{l\alpha}}, \tag{12.137}$$

where $\gamma_{l\alpha}$ and $\lambda_{l\alpha}$ are the diagonal components of the volume and surface depolarization tensors described below.

The GEMTIP resistivity model for a two-phase medium ($N = 1$) with randomly oriented ellipsoidal inclusions is given by the following formula:

$$\rho_e = \rho_0 \left\{ 1 + \frac{f_1}{3} \sum_{\alpha=x,y,z} \frac{1}{\gamma_{\alpha,1}} \left[1 - \frac{1}{1 + s_{\alpha,1}(i\omega\tau_1)^{C_1}} \right] \right\}^{-1}. \tag{12.138}$$

The effective resistivity of a three-phase medium with randomly oriented ellipsoidal inclusions can be expressed as follows ($N = 2$):

$$\rho_e = \rho_0 \left\{ 1 + \sum_{l=1}^{2} \frac{f_l}{3} \sum_{\alpha=x,y,z} \frac{1}{\gamma_{\alpha,l}} \left[1 - \frac{1}{1 + s_{\alpha,l}(i\omega\tau_l)^{C_l}} \right] \right\}^{-1}. \tag{12.139}$$

Note that, for spheroidal grains the equatorial radii are equal to each other ($a_{lx} = a_{ly} = a_l$), the polar radius is denoted by b_l ($a_{lz} = b_l$), and equation for $s_{l\alpha}$ takes the following form:

$$s_{l\alpha} = [3/(2 + \varepsilon_l)] (r_{l\alpha}/a_l), \tag{12.140}$$

where ε_l is an ellipticity, $\varepsilon_l = b_l/a_l$, of the lth type of grains.

In the case of a two-phase composite model with spherical inclusions formula (12.140) is simplified, and formula (12.136) transforms into an expression similar to Cole-Cole formula of complex resistivity (12.104).

Table 12.2 presents a list of parameters used in the multiphase ellipsoidal GEMTIP model (12.136).

Thus, elliptical GEMTIP model is a generalization of the classical Cole-Cole model, which appears in a special case of inclusions with spherical shape. The elliptical GEMTIP model provides analytical expressions connecting the effective electrical parameters of the rocks with the intrinsic petrophysical and geometrical characteristics of the composite medium: the mineralization of the rocks, the matrix composition, and the polarizability of the formations.

12.4 NONLINEAR REGULARIZED INVERSION OF IP DATA BASED ON THE GEMTIP MODEL

The quantitative interpretation of IP data in a complex 3-D environment is a very challenging problem, because it is complicated by coupling with the electromagnetic induction effects. This prob-

Table 12.2 List of parameters of the multiphase ellipsoidal GEMTIP model ($l = 1, 2, ...N$)

Parameter	Name	Units	Description
ρ_e	effective resistivity	Ohm-m	resulting effective resistivity
ρ_0	matrix resistivity	Ohm-m	matrix resistivity of rock
f_l	grain volume fraction	m^3	volume fraction of the lth grain
a_l	grain equatorial radius	m	equatorial radius of the spheroid
b_l	grain polar radius	m	polar radius of the spheroid
ε_l	ellipticity	–	$\varepsilon_l = b_l/a_l$
e_l	eccentricity	–	$e_l = \sqrt{1 - a_l^2/b_l^2}$ (prolate spheroid: $b_l > a_l$)
e_l	eccentricity	–	$e_l = \sqrt{a_l^2/b_l^2 - 1}$ (oblate spheroid: $b_l < a_l$)
τ_l	time constant	sec	time constant of the lth grain
C_l	relaxation parameters	–	decay coefficient
ω	angular frequency	sec^{-1}	EM angular frequency
$\gamma_{l\alpha}$	structural parameter	–	function of ellipticity ε_l
$\lambda_{l\alpha}$	structural parameter	–	function of ellipticity ε_l
$r_{l\alpha}$	structural parameter	–	$r_{l\alpha} = 2\frac{\gamma_{l\alpha}}{\lambda_{l\alpha}}$
$s_{l\alpha}$	structural parameter	–	$s_{l\alpha} = [3/(2 + \varepsilon_l)](r_{l\alpha}/a_l)$

lem was considered in the paper by Li and Oldenburg (2000), where the authors presented an algorithm based upon a linearized equation for the IP response. This approach is based on an assumption that the chargeability is relatively small and the IP data can be expressed as a linear functional of the intrinsic chargeability (Li and Oldenburg, 2000). The corresponding linear inverse problem is then solved to obtain the chargeability model under an assumption that the data are not affected by EM coupling. The main limitation of this linearized approach is that it ignores the nonlinear effects which are significant in IP phenomena. Also, it is impossible to use a linearized approach if we need to recover not just the chargeability, but other parameters of the conductivity relaxation model. In the paper by Yoshioka and Zhdanov (2005) a technique for three-dimensional nonlinear inversion of IP data based on the Cole-Cole relaxation model was developed based on the localized quasi-linear approximation (LQL), introduced in Chapter 6. The method takes into account the nonlinear nature of both electromagnetic induction and IP phenomena and inverts the data for the Cole-Cole model parameters. It was demonstrated by Yoshioka and Zhdanov (2005) that both the electrical conductivity and the chargeability distributions, as well as the other parameters of the Cole-Cole model can be recovered from the observed IP data simultaneously.

In this chapter, we present a method of 3D inversion of the IP data based on the GEMTIP conductivity relaxation model. The developed method takes into account the nonlinear nature of both electromagnetic induction and IP phenomena and inverts the EM data in the parameters of the GEMTIP model. The goal of the inversion is to determine the electrical conductivity and the intrinsic chargeability distributions, as well as the other parameters of the relaxation model simultaneously. The recovered parameters of the relaxation model can be used for the discrimination of different rocks, and in this way may provide an ability to distinguish between uneconomic mineral deposits and zones of economic mineralization using geophysical remote sensing technology.

The solution of this problem requires development of effective numerical methods for both EM forward modeling and inversion in inhomogeneous media. These problems are extremely difficult, especially in three-dimensional cases. The difficulties arise even in the forward modeling because of the huge size of the numerical problem to be solved to adequately represent the complex 3D distribution of EM parameters of the media, required in mining exploration. As a result, the time and the memory requirements of the computer simulation could be excessive even for practically realistic models. Our approach is based on applying parallel computing for modeling and inversion. Additional difficulties are related to inversion for GEMTIP parameters. This problem is nonlinear and ill posed, because, in general case, the solution can be unstable and nonunique. In order to overcome these difficulties we use the methods of regularization theory to obtain a stable, unique solution of the original ill-posed EM inverse problem (Zhdanov, 2002, 2015). We use the integral equation (IE) method for forward modeling and the re-weighted regularized conjugate gradient (RRCG) method for the inversion, which have proved to be effective techniques in geophysical applications (Zhdanov, 2009).

We applied the developed novel method of 3D inversion of the IP data for the comprehensive interpretation of geophysical survey data collected in Mongolia for exploration of a mineral deposit.

12.4.1 REGULARIZED INTEGRAL EQUATION (IE)-BASED INVERSION FOR COMPLEX RESISTIVITY

There are several advantages to using the IE method in IP data inversion in comparison with the more traditional finite-difference (FD) approach. First, IE forward modeling requires the calculation of the Green's tensors for the background conductivity model. These tensors can be precomputed only once and saved for multiple use on every iteration of an inversion, which speeds up the computation of the predicted data (Gribenko and Zhdanov, 2007). Finally, IE forward modeling and inversion require the discretization of the domain of inversion only, while in the framework of the FD method one has to discretize the entire modeling domain, which includes not only the area of investigation but an additional domain surrounding this area (including the areas in the air as well). For this reason, the IE inversion method requires just one forward modeling on every iteration step, which speeds up the computations and results in a relatively fast but rigorous inversion method. To obtain a stable solution of a 3D inverse problem, we apply a regularization method based on a focusing stabilizing functional (Zhdanov, 2002). This stabilizer helps generate a sharp and focused image of the anomalous conductivity distribution, which is important in mineral exploration with the goal of delineating the boundaries of a prospective target.

We know that the EM field recorded at the receiver can be represented as a sum of the background EM field, $\mathbf{E}^b$, $\mathbf{H}^b$ and the anomalous EM field, $\mathbf{E}^a$, $\mathbf{H}^a$:

$$\mathbf{E} = \mathbf{E}^b + \mathbf{E}^a, \tag{12.141}$$

$$\mathbf{H} = \mathbf{H}^b + \mathbf{H}^a. \tag{12.142}$$

The anomalous electromagnetic field is related to the electric current induced in the inhomogeneity, $j = \Delta\sigma\mathbf{E}$, according to the following integral formulas (Zhdanov, 2002):

$$\mathbf{E}^a(\mathbf{r}_j) = \int\int\int_D \widehat{\mathbf{G}}_E(\mathbf{r}_j \,|\, \mathbf{r}) \cdot \Delta\sigma(\mathbf{r})\mathbf{E}(\mathbf{r})dv = \mathbf{G}_E\left[\Delta\sigma\mathbf{E}\right], \tag{12.143}$$

$$\mathbf{H}^a(\mathbf{r}_j) = \int \int \int_D \widehat{\mathbf{G}}_H(\mathbf{r}_j \,|\mathbf{r}) \cdot \Delta\sigma(\mathbf{r})\mathbf{H}(\mathbf{r})dv = \mathbf{G}_H[\Delta\sigma\mathbf{H}], \qquad (12.144)$$

where $\widehat{\mathbf{G}}_E(\mathbf{r}_j \,|\mathbf{r})$ and $\widehat{\mathbf{G}}_H(\mathbf{r}_j \,|\mathbf{r})$ are the electric and magnetic Green's tensors defined for an unbounded conductive medium with the background (horizontally-layered) conductivity σ_b; $\mathbf{G}_E$ and $\mathbf{G}_H$ are the corresponding Green's linear operators; and domain D represents a volume with an arbitrary varying conductivity, $\sigma_a = \sigma_b + \Delta\sigma_a$, within a domain D.

By using both integral equations (12.143) and (12.144) we vastly simplify both the forward and inverse problems of the IP method. Our problem can now be written in the classic form of the operator equation:

$$\mathbf{d} = A(\Delta\boldsymbol{\sigma}), \qquad (12.145)$$

where $\Delta\boldsymbol{\sigma}$ is a vector formed by the anomalous conductivities within the targeted domain. The inversion is based on minimization of the Tikhonov parametric functional, $P^\alpha(\Delta\boldsymbol{\sigma})$, with the corresponding stabilizer $S(\Delta\boldsymbol{\sigma})$:

$$P^\alpha(\Delta\boldsymbol{\sigma}) = \|\mathbf{W}_d(A(\Delta\boldsymbol{\sigma}) - \mathbf{d}\|_{L_2}^2 + \alpha S(\Delta\boldsymbol{\sigma}), \qquad (12.146)$$

where $\mathbf{W}_d$ is the data weighting matrix, and α is a regularization parameter (used to balance the misfit and stabilizer terms in Eq. (12.146)). By minimizing parametric functional $P^\alpha(\Delta\boldsymbol{\sigma})$ we can find the solution of the inverse problem. A standard technique to find a minimum of $P^\alpha(\Delta\boldsymbol{\sigma})$ is to apply a gradient type minimization method (see Chapters 7 and 8). One can use the regularized conjugate gradient method (RCGM) to find the solution of the inverse problem. The mathematical outline of the RCGM method is as follows:

$$\mathbf{r}_n = A(\mathbf{m}_n) - \mathbf{d}, \qquad (a)$$

$$\mathbf{l}_n^{\alpha_n} = \mathbf{l}^{\alpha_n}(\mathbf{m_n}) = \mathbf{F}_n^T \mathbf{W}_d^2 \mathbf{r}_n + \alpha_n \mathbf{W}_m^2(\mathbf{m_n} - \mathbf{m}_{apr}), \qquad (b)$$

$$\beta_n^{\alpha_n} = \left\|\mathbf{l}_n^{\alpha_n}\right\|^2 / \left\|\mathbf{l}_{n-1}^{\alpha_{n-1}}\right\|^2, \quad \widetilde{\mathbf{l}}_n^{\alpha_n} = \mathbf{l}_n^{\alpha_n} + \beta_n^{\alpha_n}\widetilde{\mathbf{l}}_{n-1}^{\alpha_{n-1}}, \ \widetilde{\mathbf{l}}_0^{\alpha_0} = \mathbf{l}_0^{\alpha_0}, \quad (c) \qquad (12.147)$$

$$\widetilde{k}_n^{\alpha_n} = \left(\widetilde{\mathbf{l}}_n^{\alpha_n T}\mathbf{l}_n^{\alpha_n}\right) / \left\{\left\|\mathbf{W}_d\mathbf{F}_n\widetilde{\mathbf{l}}_n^{\alpha_n}\right\|^2 + \alpha\left\|\mathbf{W}_m\widetilde{\mathbf{l}}_n^{\alpha_n}\right\|^2\right\}, \qquad (d)$$

$$\mathbf{m}_{n+1} = \mathbf{m}_n - \widetilde{k}_n^{\alpha_n}\widetilde{\mathbf{l}}_n^{\alpha_n}, \qquad (e)$$

where $\mathbf{W}_m$ is the weighting matrix of the model parameters, and $\mathbf{F}_n$ is the matrix of the Fréchet derivative of the forward modeling operator A.

The iterative process (12.147) is terminated when the misfit reaches the given level of noise in the data, ε_0:

$$\phi(\mathbf{m}_N) = \|\mathbf{r}_N\|^2 \le \varepsilon_0^2.$$

In the previous section, we introduced for simplicity, the frequency dependant complex resistivity for a two-phase model with elliptical inclusions, described by the following formula

$$\rho_e = \rho_0 \left\{ 1 + \frac{f}{3} \sum_{\alpha=x,y,z} \frac{1}{\gamma_\alpha} \left[1 - \frac{1}{1 + s_\alpha (i\omega\tau)^{C_1}} \right] \right\}^{-1}, \tag{12.148}$$

where ρ_0 is the DC resistivity (Ohm-m); ω is the angular frequency (rad/sec), τ is the time parameter; and C is the relaxation parameter. The coefficients γ_α and s_α ($\alpha = x, y, z$) are the structural coefficients defined by geometrical characteristics of the ellipsoidal inclusions used to approximate the grains:

$$s_\alpha = r_\alpha / \bar{a}, \tag{12.149}$$

and $\bar{a}$ is an average value of the equatorial (a_x and a_y) and polar (a_z) radii of the ellipsoidal grains, i.e.

$$\bar{a} = \frac{(a_x + a_y + a_z)}{3}, \tag{12.150}$$

$$r_\alpha = 2 \frac{\gamma_\alpha}{\lambda_\alpha}, \tag{12.151}$$

where γ_α and λ_α are the diagonal components of the volume and surface depolarization tensors described above.

In the case of spherical inclusions of radius a, $\gamma_\alpha = 1/3$, $\lambda_\alpha = 2/3a$, $r_\alpha = a$, and $s_\alpha = 1$, for $\alpha = x.y.z$. Therefore, formula (12.148) can be simplified a follows:

$$\rho_e = \rho_0 \left\{ 1 + 3f \left[1 - \frac{1}{1 + (i\omega\tau)^{C_1}} \right] \right\}^{-1}. \tag{12.152}$$

After some algebra, we can transform formula (12.152) in a form similar to the conventional Cole-Cole formula for the effective resistivity:

$$\rho_e = \rho_0 \left(1 - \eta \left(1 - \frac{1}{1 + (i\omega\tau)^C} \right) \right), \tag{12.153}$$

where ρ is the DC resistivity (Ohm-m); ω is the angular frequency (rad/sec), τ is the time parameter; η is the intrinsic chargeability (Seigel, 1959a, 1959b), and C is the relaxation parameter. The dimensionless intrinsic chargeability, η, characterizes the intensity of the IP effect.

However, the inversion will be run with respect to the conductivity, therefore, it is more convenient to express the conductivity using formula (12.152):

$$\sigma_e = \sigma_0 \left(1 + 3f \left(1 - \frac{1}{1 + (i\omega\tau)^C} \right) \right). \tag{12.154}$$

In this case the anomalous conductivity, $\Delta\tilde{\sigma}$, is equal to

$$\Delta\tilde{\sigma} = \sigma(\omega) - \sigma_b. \tag{12.155}$$

Thus

$$\Delta \widetilde{\sigma} = \sigma_0 f(\eta, \tau, C) - \sigma_b = \sigma_0 \left(1 + 3f \left(1 - \frac{1}{1 + (i\omega\tau)^C} \right) \right) - \sigma_b, \tag{12.156}$$

where function $f(\eta, \tau, C)$ is equal

$$f(\eta, \tau, C) = \left(1 + 3f \left(1 - \frac{1}{1 + (i\omega\tau)^C} \right) \right). \tag{12.157}$$

12.4.2 REGULARIZED INVERSION FOR THE GEMTIP MODEL PARAMETERS

We have demonstrated above that in the case of the IP effect, the conductivity becomes a complex and frequency dependent function, $\sigma = \sigma(\omega)$, which increases significantly the number of unknown parameters of the inversion. We can reduce this number by approximating the conductivity relaxation curve using, for example, a GEMTIP model (12.154).

Indeed, let us substitute expression (12.156) for the anomalous conductivity into operator Eq. (12.145):

$$\mathbf{d} = A(\sigma f(\eta, \tau, C) - \sigma_b) = A_G(\mathbf{m}), \tag{12.158}$$

where A_G is a GEMTIP forward modeling operator, and $\mathbf{m}$ is a vector of the GEMTIP model parameters $[\sigma, \eta, \tau, C]$.

We can reformulate now the inverse problem with respect to the GEMTIP model parameters $\mathbf{m}$.

The inversion, as above, is based on minimization of the Tikhonov parametric functional, $P^\alpha(\mathbf{m})$, with the corresponding stabilizer $S(m)$ (Tikhonov and Arsenin, 1977):

$$P^\alpha(\mathbf{m}) = \|\mathbf{W}_d(A_G(\mathbf{m}) - \mathbf{d}\|_{L_2}^2 + \alpha S(\mathbf{m}), \tag{12.159}$$

where $\mathbf{W}_d$ is the data-weighting matrix, and α is a regularization parameter. There are several possible choices for the stabilizer (Zhdanov, 2002, 2015). In the current project, for simplicity, we use the minimum norm stabilizer (S_{MN}), which is equal to the square L_2 norm of the difference between the current model $\mathbf{m}$ and an appropriate a priori model $\mathbf{m}_{apr}$:

$$S_{MN}(\mathbf{m}) = \|\mathbf{W}_m(\mathbf{m} - \mathbf{m}_{apr})\|_{L_2}^2,$$

where $\mathbf{W}_m$ is the weighting matrix of the model parameters.

The most common approach to minimization of the parametric functional $P(\mathbf{m})$ is based on using gradient-type methods. For example, we provided a summary of the regularized conjugate gradient (RCG) algorithm of the parametric functional minimization in expression (12.147) above.

The appropriate selection of the data and model parameters weighting matrices is very important for the success of the inversion. We determine the data weights as a diagonal matrix formed by the inverse absolute values of the background field. Computation of the model weighting matrix, $\mathbf{W}_m$, is based on sensitivity analysis. In the current paper, we select $\mathbf{W}_m$ as the square root of the sensitivity matrix for the model in each iteration:

$$\mathbf{W}_m^{(n)} = \sqrt{\text{diag}\left(\mathbf{F}_{m_n}^* \mathbf{F}_{m_n}^* \right)}.$$

As a result, we obtain a uniform sensitivity of the data to different model parameters (Zhdanov, 2015).

We apply the adaptive regularization method. The regularization parameter α is updated in the process of the iterative inversion as follows:

$$\alpha_n = \alpha_1 q^{n-1}; \ n = 1, 2, 3, \cdots; \ 0 < q < 1.$$

In order to avoid divergence, we begin an iteration from a value of α_1, which can be obtained as a ratio of the misfit functional and the stabilizer for an initial model, then reduce α_n according to the last formula on each subsequent iteration and continuously iterate until the misfit condition is reached:

$$r_{n0}^w = \left\| \mathbf{r}_{n0}^w \right\| = \| \mathbf{W}_d \left[\mathbf{A} \left(\mathbf{m}_{\alpha_{n0}} \right) - \mathbf{d} \right] \| / \| \mathbf{W}_d \mathbf{d} \| \leq \delta, \tag{12.160}$$

where r_{n0}^w is the normalized weighted residual, and δ is the relative level of noise in the weighted observed data.

Fréchet derivative calculation using the Quasi-Born approximation

We assume, as above, that the conductivity within a 3D geoelectrical model can be presented by the background (horizontally layered) conductivity σ_b, and an arbitrary varying conductivity, $\sigma_a = \sigma_b + \Delta\sigma_a$, within a domain D.

In this model, the anomalous field is produced by the anomalous conductivity distribution $\Delta\sigma_a$, and it can be calculated according to formulas (12.143) and (12.144). Using these integral representations, we can express the corresponding Fréchet derivatives, $\mathbf{F}_E$ and $\mathbf{F}_H$, as follows:

$$\mathbf{F}_E \left(\mathbf{r}_j | \mathbf{r} \right) = \left. \frac{\partial \mathbf{E} \left(\mathbf{r}_j \right)}{\partial \Delta\sigma_a \left(\mathbf{r} \right)} \right|_{\Delta\sigma_a} = \left. \frac{\partial \mathbf{E}^{\Delta\sigma_a} \left(\mathbf{r}_j \right)}{\partial \Delta\sigma_a \left(\mathbf{r} \right)} \right|_{\Delta\sigma_a} = \left. \frac{\partial \mathbf{G}_E \left(\mathbf{r}_j | \mathbf{r} \right) \left[\Delta\sigma_a \left(\mathbf{r} \right) \mathbf{E} \left(\mathbf{r} \right) \right]}{\partial \Delta\sigma_a \left(\mathbf{r} \right)} \right|_{\Delta\sigma_a},$$

$$\mathbf{F}_H \left(\mathbf{r}_j | \mathbf{r} \right) = \left. \frac{\partial \mathbf{H} \left(\mathbf{r}_j \right)}{\partial \Delta\sigma_a \left(\mathbf{r} \right)} \right|_{\Delta\sigma_a} = \left. \frac{\partial \mathbf{H}^{\Delta\sigma_a} \left(\mathbf{r}_j \right)}{\partial \Delta\sigma_a \left(\mathbf{r} \right)} \right|_{\Delta\sigma_a} = \left. \frac{\partial \mathbf{G}_H \left(\mathbf{r}_j | \mathbf{r} \right) \left[\Delta\sigma_a \left(\mathbf{r} \right) \mathbf{E} \left(\mathbf{r} \right) \right]}{\partial \Delta\sigma_a \left(\mathbf{r} \right)} \right|_{\Delta\sigma_a}.$$

We can treat the electric field $\mathbf{E}^{(n)} \left(\mathbf{r} \right)$, found on iteration number n, as the electric field in the above equations for a subsequent iteration $(n + 1)$, $\mathbf{E} \left(\mathbf{r} \right) = \mathbf{E}^{(n)} \left(\mathbf{r} \right)$. In this case, the Fréchet derivatives at iteration number n can be found by direct integration from the last two equations involving the electric field $\mathbf{E}^{(n)} \left(\mathbf{r} \right)$ computed on the current iteration:

$$\mathbf{F}_{E,H} \left(\mathbf{r}_j | \mathbf{r} \right) = \left. \frac{\partial \mathbf{G}_{E,H} \left(\mathbf{r}_j | \mathbf{r} \right) \left[\Delta\sigma_a \left(\mathbf{r} \right) \mathbf{E} \left(\mathbf{r} \right) \right]}{\partial \Delta\sigma_a \left(\mathbf{r} \right)} \right|_{\Delta\sigma_a} \approx \mathbf{G}_{E,H} \left(\mathbf{r}_j | \mathbf{r} \right) \mathbf{E}^{(n)} \left(\mathbf{r} \right).$$

Note that, the electric field $\mathbf{E}^{(n)} \left(\mathbf{r} \right)$ is calculated using the rigorous IE forward modeling method at each iteration step to compute the predicted data (EM field at the receivers). Therefore, no extra computation is required to find the electric field for the Fréchet derivative calculation.

In the case of time domain EM data, the Fréchet derivatives also need to be transformed into time domain. This can be accomplished by the same technique as that for EM fields, i.e., by the Fourier

transform using digital filtering techniques. For example, in the case of a causal step turnoff response, the Fréchet derivative in time domain can be expressed as follows:

$$\mathbf{f}_{E,H}(t) = -\frac{2}{\pi} \int_0^\infty \frac{\text{Im}\left[\mathbf{F}_{E,H}(\omega)\right]}{\omega} \cos(\omega t) \, d\omega.$$

As a result, our inversion technique, based on the IE method, requires just one forward modeling on every iteration step, while the conventional inversion scheme requires, as a rule, at least three forward modeling solutions per inversion iteration (one to compute the predicted data, another one to compute the gradient direction, and at least one for optimal calculation of the iteration step). This approach results in a very efficient inversion method.

Calculation of the Fréchet derivatives with respect to the GEMTIP model parameters

In the current section, we consider the GEMTIP model describing a two-phase composite medium. This GEMTIP model is characterized by four parameters (conductivity of the host medium, σ_0, fraction volume f, time constant, τ, and relaxation coefficient, C). Therefore, the Fréchet derivatives with respect to each GEMTIP parameter are required to invert the IP data.

The Fréchet derivative of the EM fields with respect to the conductivity of the host medium can be computed as follows:

$$\mathbf{F}_{E,H}^{\sigma_0}\left(\mathbf{r}_j|\mathbf{r}\right) = \mathbf{F}_{E,H}^{\sigma_e}\left(\mathbf{r}_j|\mathbf{r}\right) \cdot \frac{\partial \sigma_e}{\partial \sigma_0},$$

$$\frac{\partial \sigma_e}{\partial \sigma_0} = 1 + 3f \left\{ 1 - \frac{1}{1 + (i\omega\tau)^C} \right\}.$$

The Fréchet derivative of the EM fields with respect to the fraction volume can be computed as follows:

$$\mathbf{F}_{E,H}^{f}\left(\mathbf{r}_j|\mathbf{r}\right) = \mathbf{F}_{E,H}^{\sigma_e}\left(\mathbf{r}_j|\mathbf{r}\right) \cdot \frac{\partial \sigma_e}{\partial f},$$

$$\frac{\partial \sigma_e}{\partial f} = 3\sigma_0 \left\{ 1 - \frac{1}{1 + (i\omega\tau)^C} \right\}.$$

The Fréchet derivative of the EM fields with respect to the time constant can be determined as:

$$\mathbf{F}_{E,H}^{\tau}\left(\mathbf{r}_j|\mathbf{r}\right) = \mathbf{F}_{E,H}^{\sigma_e}\left(\mathbf{r}_j|\mathbf{r}\right) \cdot \frac{\partial \sigma_e}{\partial \tau},$$

$$\frac{\partial \sigma_e}{\partial \tau} = \frac{\sigma_0 i\omega C (i\omega\tau)^{C-1} \left\{ 3f - (1 + 3f)(i\omega\tau)^C \right\}}{\left\{ 1 + (i\omega\tau)^C \right\}^2}.$$

The Fréchet derivative of the EM fields with respect to the relaxation coefficient is equal to:

$$\mathbf{F}_{E,H}^{C}\left(\mathbf{r}_j|\mathbf{r}\right) = \mathbf{F}_{E,H}^{\sigma_e}\left(\mathbf{r}_j|\mathbf{r}\right) \cdot \frac{\partial \sigma_e}{\partial C},$$

$$\frac{\partial \sigma_e}{\partial C} = \frac{\sigma_0 3 f \left(i\omega\tau\right)^C \ln\left(i\omega\tau\right)}{\left\{1 + \left(i\omega\tau\right)^C\right\}^2}.$$

Note that, in all formulas above the Fréchet derivative with respect to the effective conductivity is given by the following expression:

$$\mathbf{F}_{E,H}^{\sigma_e} \left(\mathbf{r}_j | \mathbf{r}\right) = \frac{\partial \mathbf{G}_{E,H} \left(\mathbf{r}_j | \mathbf{r}\right) \left[\Delta\sigma_e \left(\mathbf{r}\right) \mathbf{E}\left(\mathbf{r}\right)\right]}{\partial \Delta\sigma_e \left(\mathbf{r}\right)}.$$

In order to compute the Fréchet derivatives in the time domain, one can use the Fourier transform, as was discussed above.

12.4.3 QUANTITATIVE INTERPRETATION OF IP DATA – THE ROAD AHEAD

We have demonstrated above that the analysis of IP phenomena has to be based on models with frequency dependent complex conductivity distribution. One of the most popular is the Cole-Cole relaxation model, which we used in the method discussed in the previous section. However, a similar approach can be extended to the case of conductivity relaxation model based on a generalized effective-medium theory of induced polarization (GEMTIP) introduced in previous sections. In this case one can determine the parameters of the GEMTIP model of the rocks forming the geological sections, using the remote EM/IP measurements on the ground. The GEMTIP model, in principle, can be used for both mineral containing rocks and reservoir rocks. The geoelectrical parameters of this model are determined by the intrinsic petrophysical and geometrical characteristics of the composite medium: the mineralization and/or fluid content of the rocks, the matrix composition, porosity, anisotropy, and polarizability of the formations. Therefore, the effective complex conductivity of this new model may serve as a basis for determining the intrinsic characteristics of the polarizable rock formation from the observed electrical data, such as the volume content of the different minerals and/or the hydrocarbon saturation.

Until recently, these parameters have been determined mostly in the physical lab by direct analysis of the rock samples. In principle, the same parameters of the rock formations can be determined in the field from the geophysical observations using a composite geoelectrical model of the rock formations, considered above. A new composite geoelectrical model provides more realistic representation of the complex rock formations than the conventional unimodal conductivity models. It may allow us to model the relationships between the physical characteristics of different types of minerals (e.g. conductivities and sulfide grain sizes) and the parameters of the relaxation model. As a result, one can determine the internal structure and physical characteristics of the different rock formations by remote geophysical techniques without drilling the wells. The solution of this problem requires development of effective numerical methods for EM forward modeling and inversion in inhomogeneous media, based on the ideas and principles formulated in Parts 2 and 3 of this text.

In summary, the goal of the EM/IP geophysical survey should be to determine the electrical conductivity and the intrinsic chargeability distributions as well as the other parameters of the relaxation model simultaneously. The recovered parameters of the relaxation model can be used for the discrimination of different rocks, and in this way will provide the ability to distinguish between uneconomic mineral deposits and zones of economic mineralization using geophysical remote sensing technology,

which is an important goal in mineral and hydrocarbon exploration. A case study of application of the IP method for mineral exploration is given in Chapter 17.

REFERENCES AND RECOMMENDED READING TO CHAPTER 12

Alfano, L., 1984, A computation method for D. C. geoelectric fields: *in* Rapolla, A., and G. V. Keller, Eds., Geophysics of Geothermal Areas: State of the Art and Future Development: Colorado School of Mines Press, Golden, Colorado, 127–152.

Alpin, L. M., M. N. Berdichevsky, G. A. Vedrintsev, and A. M. Zagarmistr, 1966, Dipole methods for measuring earth conductivity: New York, Consultants Bureau, 302 pp.

Berryman, J. G., 2006, Effective medium theories for multicomponent poroelastic composites: Journal of Engineering Mechanics, **132**, 519–531.

Bernabini, M., and E. Cardarelli, 1991, Geoelectrical surveys of dipping structures: Geophysical Prospecting, **39** (7), 953–966.

Bertin, J., and J. Loeb, 1976, Experimental and theoretical aspects of induced polarization, Vol. **1**, Presentation and application of the IP method case histories: Gebruder Borntraeger, Berlin, 250 pp.

Bockrig, J., and A. K. N. Reddy, 1973, Modern electrochemistry: Vols. **1** and **2**: Plenum Press.

Bruggeman, D. A., 1935, Effective medium model for the optical properties of composite material: Annals Physics Leipzig.

Chastenet de Gery, J., and G. Kunetz, 1956, Potential and apparent resistivity over dipping beds: Geophysics, **21** (3), 780–793.

Choy, T.C., 1999, Effective medium theory, principles and applications: Oxford Science Publications, 182 pp.

Cole, K. S., and R. H. Cole, 1941, Dispersion and absorption in dielectrics: Journal of Chemistry and Physics, **9**, 343–351.

Davydycheva, S., N. Rykhlinsky, and P. Legeido, 2004, An electrical prospecting method for oil search using induced polarization effect: 74th Annual International Meeting, SEG, Expanded Abstracts, Electronic Volume.

Dieter, K., N. R. Paterson, and F. S. Grant, 1969, I.P. and resistivity type curves for three dimensional bodies: Geophysics, **34** (4), 615–632.

Dukhin, S. S., 1971, Dielectric properties of disperse systems: *in* Surface and Colloid Science, **3**, Wiley Interscience.

Edwards, R. N., 1988a, A downhole magnetometric resistivity technique for electrical sounding beneath a conductive surface layer: Geophysics, **53** (4), 528–536.

Edwards, R. N., and E. C. Howell, 1976, A field test of the magnetometric resistivity (MMR) method: Geophysics, **41** (6), 1170–1183.

Edwards, R. N., and M. N. Nabighian, 1990, The magnetometric resistivity method: *in* Nabighian, M. N., and J. D. Corbett, Eds., Electromagnetic methods in applied geophysics, Volume 2, Applications: Society of Exploration Geophysicists, Tulsa, Oklahoma, 47–104.

Emond, A. M., 2007, Electromagnetic modeling of porphyry systems from the grain-scale to the deposit-scale using the generalized effective medium theory of induced polarization: M.S. thesis, University of Utah.

Emond, A., M. S. Zhdanov, and E. U. Petersen, 2006, Electromagnetic modeling based on the rock physics description of the true complexity of rocks: applications to porphyry copper deposits: 76th Annual International Meeting, SEG, Expanded Abstracts, Electronic Volume.

Fletcher, R., 1995, Practical methods of optimization: John Willey & Sons, Chichester–New-York, 436 pp.

Furness, P., 1992, An integral equation for the geoelectric response of thin resistive bodies: Geophysical Prospecting, **40** (7), 701–720.

Habberjam, G. M., 1979, Apparent resistivity observations and the use of square array techniques: Gebruder Borntraeger, Berlin, 152 pp.

Harrington, R. F., 1968, Field Computation by Moment Methods: MacMillan, New York.

Harthill, N., 1978, A quadripole resistivity survey of the Imperial Valley, California: Geophysics, **43** (7), 1485–1500.

Hohmann, G. W., 1988, Numerical modeling for electromagnetic methods in geophysics: *in* Nabighian, M. N., and J. D. Corbett, Eds., Electromagnetic methods in applied geophysics – Theory, Volume 1, Society of Exploration Geophysicists, Tulsa, Oklahoma, 313–364.

Hummel, J. N., 1932, Foundations of geoelectrical methods of prospecting (*in German*): Beitrage zur angewandten Geophysik, **5**, 32–132.

Jakosky, J. J., 1940, Exploration Geophysics: Times-Mirror Press, Los Angeles.

Kamenetsky, F. M., 1997, Transient geo-electromagnetics: GEOS, Moscow, 162 pp.

Kazatchenko, E., M. Markov, and A. Mousatov, 2004, Joint Inversion of Acoustic and Resistivity Data for Carbonate Microstructure Evaluation: Petrophysics, **45**, 130–140.

Keller, G. V., 1966, Dipole method for deep resistivity studies: Geophysics, **31** (6), 1088–1104.

Keller, G. V., and Frischknecht, F. C., 1966, Electrical Methods in Geophysical Prospecting: Pergamon Press, Oxford, 517 pp.

Keller, G. V., R. Furgerson, C. Y. Lee, N. Harthill, and J. J. Jacobson, 1975, The dipole mapping method: Geophysics, **40** (3), 451–472.

Klein, J. D., T. Biegler, and M. D. Horne, 1984, Mineral interfacial processes in the method of induced polarization: Geophysics, **49** (7), 1105–1114.

Komarov, V. A., 1980, Electrical prospecting by induced polarization method: Nedra, Leningrad.

Kolundzija, B. M., and A. R. Djordjevic, 2002, Electromagnetic modeling of composite metallic and dielectric structures: Artech House.

Koefoed, O., 1968, The application of the kernel function in interpreting geoelectrical resistivity measurements: Gebruder Borntraeger, Berlin, 111 pp.

Kunetz, G., 1966, Principles of direct current resistivity prospecting: Gebruder Borntraeger, Berlin, 103 pp.

Landau, L. D., L. P. Pitaevsky, and E. M. Lifshitz, 1984, Electrodynamics of continuous medium, 2nd ed.: Elsevier Butterworse-Heinemann.

Landauer, R., 1978, Electrical conductivity in inhomogeneous media: AIP Conference Proceedings, **40**, 2–45.

Li, Y., and D. W. Oldenburg, 2000, 3-D inversion of induced polarization data: Geophysics, **65** (6), 1931–1945.

Li, Y., and D. W. Oldenburg, 1991, Aspects of charge accumulation in DC resistivity experiments: Geophysical Prospecting, **39** (6), 803–826.

Luo Y., and G. Zang, 1998, Theory and application of spectral induced polarization: Society of Exploration Geophysicists, Tulsa, OK, 171 pp.

MacInnes, S. 2007, Complex resistivity modeling: Presented at the IP Symposium of 77th Annual International Meeting, SEG.

Maillet, R., 1947, The fundamental equations of electrical prospecting: Geophysics, **12** (4), 529–556.

Maillet, R., and H. G. Doll, 1932, Sur un theorem relatif aux milieux electgriquement anisotropes et ses applications a la prospection electrique en courant continu: Erganzungs-Hefte fur angewandte Geophysik: **3**, 109–124.

Marshall, D. J., and T. R. Madden, 1959, Induced polarization, a study of its causes: Geophysics, **24** (4), 790–816.

Mendelson, K. S., and M. H. Cohen, 1982, The effect of grain anisotropy on the electrical properties of sedimentary rocks: Geophysics, **47** (2), 257–263.

Molano, C. E., M. Salamanca, and R. A. van Overmeeren, 1990, Numerical modeling of standard and continuous vertical electrical soundings: Geophysical Prospecting, **38** (7), 705–718.

Nelson, P. H., 1997, Induced polarization research at Kennecott, 1965–1977: The Leading Edge, **16** (1), 29–33.

Niwas, S., and M. Israel, 1989, Matrix method for the transformation of resistivity sounding data of one electrode configuration to that of another configuration: Geophysical Prospecting, **37** (2), 209–221.

Norris, A. N., P. Sheng, and A. J. Callegari, 1985, Effective medium theories for two-phase dielectric media: Applied Physics Letters, **57**, 1990–1996.

Oldenburg, D., and Y. Li, 1994, Inversion of induced polarization data: Geophysics, **59** (9), 1327–1341.

Pekeris, C. L., 1940, Direct method of interpretation in resistivity prospecting: Geophysics, **5** (1), 31–42.

Pelton, W. H., 1977, Interpretation of induced polarization and resistivity data: Ph.D. thesis, University of Utah.

Pelton, W. H., S. H. Ward, P. G. Hallof, W. R. Sill, and P. H. Nelson, 1978, Mineral discrimination and removal of inductive coupling with multifrequency IP: Geophysics, **43** (3), 588–609.

Pierce, F. W., and J. G. Bolm, Eds., 1995, Porphyry Copper Deposits of the American Cordillera: Arizona Geological Society Digest 20.

Richtmyer, R. D., and K. W. Morton, 1967, Difference methods for initial value problems: John Wiley and Sons, New York, 401 pp.

Schlumberger, C., 1920, Etude sur la prospection electrique du sours-sol: Gauthier-Villars et Cie., Paris.

Seigel, H. O., 1959a, A theory for induced polarization effects (for step-function excitation): *in* Wait, J. R., (Ed.), Overvoltage Research and Geophysical Applications, Pergamon Press, New York, pp. 4–21.

Seigel, H. O., 1959b, Mathematical formulation and type curves for induced polarization: Geophysics, **24** (3), 547–565.

Seigel, H. O., and A. W. Howland-Rose, 1990, Magnetic induced polarization method: *in* Ward, S. H., Ed., Induced Polarization, Applications and Case Histories: Society of Exploration Geophysicists, Tulsa, Oklahoma, 23–56.

Seigel, H. O., M. Nabighian, D. Parasnis, and K. Vozoff, 2007, The early history of the induced polarization method: The Leading Edge, **26** (3), 312–321.

Sen, P., C. Scala, and M. H. Cohen, 1981, A self-similar model for sedimentary rocks with application to the dielectric constant of fused glass beads: Geophysics, **46** (5), 781–796.

Sheinman, S. M., 1969, Contemporary physical foundations of the electrical prospecting theory: Nedra, Moscow.

Sheng, P., 1991, Consistent modeling of the electrical and elastic properties of sedimentary rocks: Geophysics, **56** (8), 1236–1243.

Shuey, R. T., and M. Johnson, 1973, On the phenomenology of electrical relaxation in rocks: Geophysics, **38** (1), 37–48.

Shwartz, L. M., 1994, Effective medium theory of electrical condition in two-component anisotropic composites: Physica A, **207**, 131–136.

Sihvola, A., 1999, Electromagnetic mixing formulas and applications: IEE Electromagnetic Waves Series, **47**, London, UK, 284 pp.

Sillitoe, R. H., 1973, The tops and bottoms of porphyry copper deposits: Economic Geology, **68**, 799–815.

Stefanescu, S., Schlumberger, C., and Schlumberger, M., 1930, Sur la distribution electrique potentielle autour d'une prise de terrre ponctuelle dans un terrain a couches horizontales homogenes et isotropes: Journ. de Phys. et du Radium, VII, 132–140.

Stroud, D., 1975, Generalized effective medium approach to the conductivity of an inhomogeneous material: Physical Review B, **12**, 3368–3373.

Sumner, J. S., 1976, Principles of Induced Polarization for Geophysical Exploration: Elsevier, Amsterdam, 277 pp.

Sunde, E. D., 1949, Earth conduction effects in transmission systems: D. Van Nostrand Co., New York, 371 pp.

Tagg, G. F., 1964, Earth resistances: George Newnes Ltd., New York, 258 pp.

Titley, S. R., Ed., 1982, Advances in geology of the porphyry copper, Southwestern North America: University of Arizona Press, Tucson, AZ, 560 pp.

Wait, J. R., 1959, The variable-frequency method, *in* Wait, J.R., Ed., Overvoltage research and geophysical applications: Pergamon, Oxford.

Wait, J. R., 1982, Geo-electromagnetism: Academic Press, New York, 268 pp.

Vinegar, H.J., and M. H. Waxman, 1988, In-situ induced polarization method for determining formation permeability: US Patent 4,743,854.

Wong, J., 1979, An electrochemical model of the induced-polarization phenomenon in disseminated sulfide ores: Geophysics, **44**, 1245–1265.

Wong, J., and D. W. Strangway, 1981, Induced polarization in disseminated rocks containing elongated mineralization sulfide ores: Geophysics, **46**, 1258–1268.

Yoshioka, K., and M. S. Zhdanov, 2005, Three-dimensional nonlinear regularized inversion of the induced polarization data based on the Cole-Cole model: Physics of the Earth and Planetary Interiors, **150**, 29–43.

Yuval, and D. W. Oldenburg, 1997, Computation of Cole-Cole parameters from IP data: Geophysics, **62**, 436–448.

Zohdy, A. A. R., 1965, The auxiliary point method of electrical sounding interpretation and its relationship of the dar Zarrouk parameters: Geophysics, **30** (4), 644–660.

Zohdy, A. A. R., 1968, A rapid graphical method for the interpretation of A- and H-type electrical soundings: Geophysics, **33** (5), 822–833.

Zohdy, A. A. R., 1969, The use of Schlumberger and equatorial soundings in ground water investigations near El Paso, Texas: Geophysics, **34** (5), 713–728.

Zohdy, A. A. R., 1978, Toral-field resistivity mapping and sounding over horizontally layered media: Geophysics, **43** (4), 748–766.

Zhdanov, M. S., 1988, Integral transforms in geophysics: Springer-Verlag, Berlin, Heidelberg, New York, London, Paris, Tokyo, 367 pp.

Zhdanov, M. S., 2002, Geophysical inverse theory and regularization problems: Elsevier, Amsterdam, London, New York, Tokyo, 628 pp.

Zhdanov, M. S., 2006, Generalized effective-medium theory of induced polarization: 76th Annual International Meeting, SEG, Expanded Abstracts, 805–809.

Zhdanov, M. S., 2008a, Generalized effective-medium theory of induced polarization: Geophysics, **73** (5), F197–F211.

Zhdanov, M. S., 2008b, Geophysical technique for mineral exploration and discrimination based on electromagnetic methods and associated systems: US Patent 7,324,899 B2.

Zhdanov, M. S. and S. Fang, 1996, 3-D quasi-linear electromagnetic inversion: Radio Science, **31** (4), 741–754.

Zhdanov, M. S., and S. Fang, 1999, 3-D quasi-linear electromagnetic modeling and inversion: Three Dimensional Electromagnetics, SEG Monograph, Tulsa, OK, 233–255.

Zonge, K., 1972, Electrical properties of rocks as applied to geophysical prospecting: Ph. D. thesis, University of Arizona, 156 pp.

Zonge, K., and J. C. Wynn, 1975, Recent advances and applications in complex resistivity measurements: Geophysics, **40**, 851–864.

Zonge, K. L., 1983, Case histories of an electromagnetic method for petroleum exploration: Proprietary Data Sale, Zonge Engineering and Research Organization, Inc.

Zonge, K., J. Wynn, and S. Urquhart, 2005, Resistivity, induced polarization and complex resistivity: in Butler, D. K., Ed., Near-Surface Geophysics, 265–300.

MAGNETOTELLURIC AND MAGNETOVARIATIONAL METHODS

CONTENTS

495

A group of methods for determining the electrical structure of the earth using naturally existing electromagnetic fields rather than fields generated by a controlled source came into use about 1960, based on theoretical concepts originally proposed by Tikhonov in the USSR and by Cagniard in France. Two principal forms of such methods are in wide use, these being the MagnetoTelluric Sounding (MTS) method and the MagnetoVariational (MV) method.

Basic to the operation of these methods is the fact that the ambient electromagnetic field of the earth (the noise field) depends not only on the strengths and other characteristics of the various sources for such fields, but also on the geoelectric structure of the earth. Two forms of electromagnetic excitation from external field sources take place in the earth. One is related to induction from ionospheric and magnetospheric currents, not accompanied by any direct transfer of charge (current) from the ionosphere into the earth. The other is the galvanic transfer of charge from the ionosphere to the earth (in other words, by current flow from the ionosphere vertically into the earth).

The electrical conductivity of the lower atmosphere is 10^{-12} to 10^{-13} S/m, or some ten orders of magnitude less than the conductivity of the solid earth. Therefore, indirect induction of current flow in the earth must be much more important than galvanic flow from the ionosphere (Vanyan and Butkovskaya, 1980). This supposition has been confirmed by experimental efforts to separate the excited fields into inductive and galvanic parts (Berdichevsky and Zhdanov, 1981). As a consequence, we normally can ignore the galvanic contribution, and for electrical exploration, we need consider only the inductive excitation.

13.1 EARTH EM FIELD OF EXTERNAL ORIGIN

The long-term observations show that the magnitude and direction of the Earth's magnetic field continuously change with time. These alterations of the Earth's magnetic field are called *geomagnetic variations*. There are two types of geomagnetic variations – variations caused by internal sources, and those of external origin (Campbell, 2003).

The internal geomagnetic variations are associated with the Earth's main magnetic field and with the complex processes occurring in the Earth's core. These *secular variations* have periods ranging from several decades up to many centuries. They are generated by a *geodynamo* mechanism within the

Earth's interior that continually generates the geomagnetic field. This mechanism is generally assumed to be a convective dynamo operating in the Earth's fluid outer core, which surrounds its solid inner core, both being mainly composed of iron. However, the rigorous mathematical theory of the geomagnetic dynamo is still under development now. Nevertheless, geophysicists successfully use the secular variations to study the deep earth interior.

The geomagnetic variations associated with external sources have periods ranging from the parts of a second up to eleven years. The external variations are caused by the physical processes occurring in the space and in the Sun.

According to the electromagnetic induction laws, geomagnetic variations induce a transient electromagnetic field in the conductive Earth, and, the corresponding electric current. The higher the rate of the geomagnetic variations, the stronger the current induced in the earth. The secular variations have such long periods (centuries!), that they induce practically no current in the Earth. At the same time, the external geomagnetic variations change vary rapidly and can induce a strong current, which is easy to measure. This current is called *telluric* current (from the Latin word *telluris* – Earth's). As a result the entire field of geomagnetic variations and telluric currents is called the *magnetotelluric field*.

The magnetotelluric field at frequencies below 1 hertz is of particular importance, primarily because it can be used as an energy source to probe the earth to great depths. At these low frequencies, the magnetotelluric field originates almost entirely from complex interactions between the Earth's permanent magnetic field and the flow of plasma from the sun.

Along with the electromagnetic energy radiated from the sun, about 1 percent of the energy given off by the sun is in the form of particulate matter. This flow of particulate matter outward from the sun is in effect a *solar wind*. The solar wind is a fully ionized, electrically neutral plasma. It consists of protons, doubly charged helium ions, a small number of other positively charged particles, and enough electrons so that the plasma is electrically neutral.

An important characteristic of a plasma is the close coupling of mechanical and electrical force fields. Each particle in a plasma has a mass and a charge. The solar plasma we are dealing with has distinctly different charge-to-mass ratios for the positive charges, which are protons and helium atoms, and the negative charges, which are electrons. Each particle responds to Newtonian and Coulomb forces according to this ratio. We require that both forces be balanced when the plasma is in equilibrium. This leads to a coupling between mass flow and charge flow, so that any motion of the plasma causes an electric current, and any charge flow causes mass pressure and a resulting motion. It is important to recognize in the ensuing discussion that mass movement of the plasma around the earth requires a related electrical current.

The solar wind is highly variable in time and space. It travels slowly in comparison with the speed of the electromagnetic radiation from the sun; its speed lies between 300 and 700 kilometers per second 95% of the time. Because of this slow speed, the earth penetrates the solar wind at an angle depending on its velocity, as shown by Fig. 13.1. The solar wind has aged by many hours to several days by the time the earth penetrates it.

The solar wind exhibits some characteristic behaviors, so it is not totally unpredictable in behavior. Both the speed and density of the solar wind vary with time, but changes tend to correlate with the period of rotation of the Sun (27 to 32 days, depending on the latitude on the Sun). *Plasma streams* of higher than normal speed are one of the most significant organized features of the solar wind. A particular stream can persist for many months, or longer than a year. They are responsible for periodically recurring magnetic storms in the earth's magnetic field.
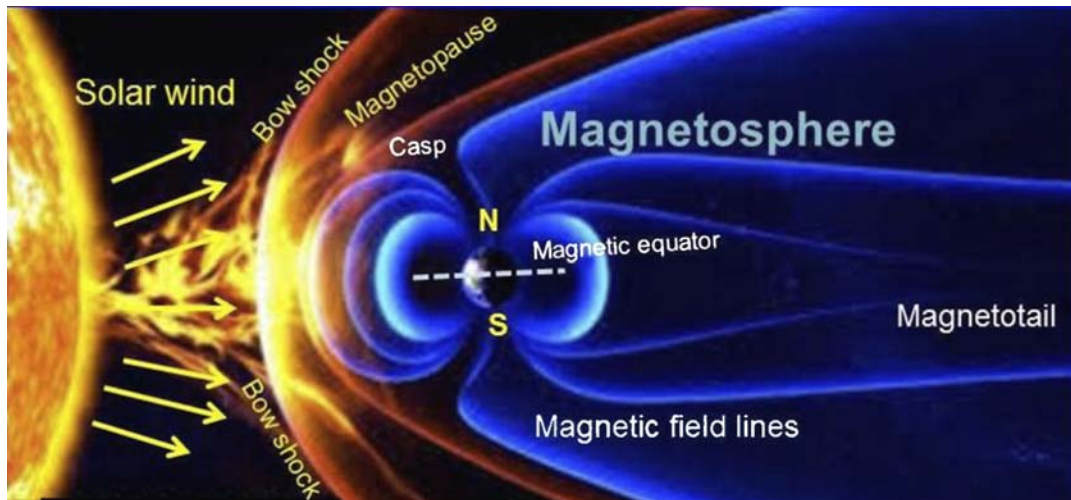
FIGURE 13.1

Magnetosphere of the Earth.

Another significant structure in the solar wind is a *solar flare disturbance*. Flares on the surface of the Sun eject high-speed plasma into the wind. Such a patch of rapidly moving plasma compresses the more slowly traveling normal solar wind in its path, forming a bow wave. This bow wave arrives at the Earth's orbit about 5 to 10 hours before the main body of gas comprising the solar flare disturbance. Because the velocities of the patch of gas forming the solar flare disturbance and its bow wave are so high, it interacts strongly with the Earth's magnetic field when the two meet. *Magnetic storms* occur. In a magnetic storm, the initial phase is caused by the bow wave entering the Earth's magnetic field. The higher than normal density of plasma in the bow wave adds to the normal magnetic field of the Earth. As the main body of disturbed plasma interacts with the Earth's magnetic field, more complicated changes in magnetic field take place, forming the main phase of the magnetic storm.

As the Earth travels into the solar wind, either during quiet periods or during disturbed periods, its magnetic field will interact with the plasma. As the solar wind flows around the earth, the plasma interacts with the Earth's magnetic field in such a way that a cavity is formed into which the solar wind cannot penetrate. Because the speed of travel of the solar wind is almost always supersonic, a shock wave, called the *bow shock,* forms in front of the *magnetospheric cavity*. The usual distance between the center of the earth and the point of closest occurrence of the *magnetopause*, or surface through which the solar wind cannot penetrate, is about 10 earth radii ($10R_E$). The thickness of the shock wave at this same location, where it will be thinnest, is about 3 R_E. The region between the outer shock surface and the magnetopause is called the *magnetosheath*.
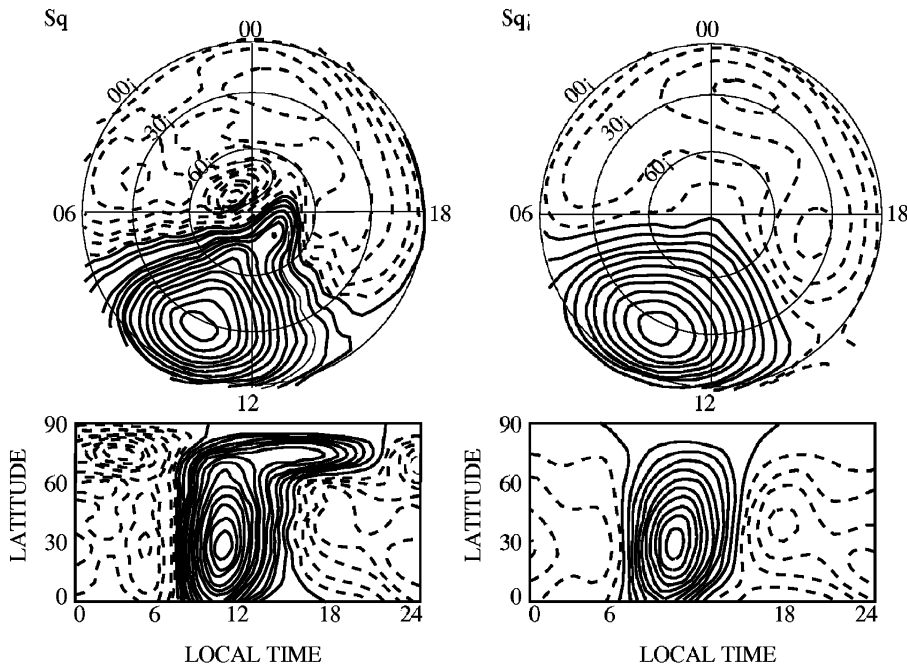
FIGURE 13.2

Ionospheric current pattern used to explain the observed changes in magnetic field on a quiet day. The right-hand panels include only tide-produced currents, while the panels on the left include convecting polar currents as well. The current between adjacent paths is 10,000 amperes in a counterclockwise direction for solid lines, and 10,000 amperes in a clockwise direction for dashed lines.

13.1.1 QUIET-TIME MAGNETIC FIELD VARIATIONS

Even during undisturbed times, the magnetic field effects of the interaction of the solar wind with the earth's magnetic field show predictable behavior caused by the rotation of the earth, and hence, by the movement of an observation point on the earth's surface through a magnetic field structure which is not symmetric about the center of the earth. On undisturbed days, the diurnal in the magnetic field result principally from currents flowing in the E layer of the ionosphere. This quiet-day variation in magnetic field components is called the S_q *field*. In large part, the fields forming S_q appear to be caused by high speed tidal winds produced by solar heating of the atmosphere, causing a part, S_q^O, of the diurnal variation, S_q. However, it is clear that a significant part of the S_q variation, particularly at high latitudes, is caused by induction from magnetic fields in the magnetosphere and magnetosheath. This contribution to S_q is designated as S_q^P. Fig. 13.2 shows global current flow lines (each representing a flow of 10,000 amperes) at E-layer altitudes above the earth.

A very similar pattern correlated with the daily lunar cycle, and caused by lunar tides in the atmosphere and ionosphere, is observed. The lunar-driven currents are less strong by a factor of 20 than are the solar-driven currents.

One notable feature of these planet-wide patterns of current is their behavior in equatorial regions. The *dip equator* is the locus on earth where the earth's constant magnetic field is precisely parallel to the earth's surface. Above the dip equator, the solar and lunar driven quiet day ionospheric currents form a narrow band in which the current is strongly concentrated. This feature is known as the *equatorial electrojet*.

The electrojet is only a few hundred kilometers wide, consisting of a belt in the ionosphere over the dip equator with greatly enhanced conductivity, and hence, a greatly increased capability to carry current when an electric field is present. A Hall current, as described in Chapter 10, flows in the third orthogonal direction to crossed magnetic and electric fields. At the dip equator, this third orthogonal direction is vertical. However, the thickness of the ionosphere is quite limited so that current cannot flow in the vertical direction; instead, the upper and lower boundaries of the ionosphere are charged by the inhibited Hall effect. It has been shown both theoretically and experimentally that as a result, the effective conductivity in the direction of the electric field is enhanced; the additional current flowing in the electric field direction is called a *Cowling current*. If there is even a slight dip to the magnetic vector, the conductivity along the tilted field lines is sufficient to allow the polarization to leak off, and the Cowling conductivity is much less.

13.1.2 MICROPULSATIONS

So far, we have discussed magnetic fields of external origin which are global in scale and which have periods of a day or more. More rapid variations in the magnetic field are caused by smaller scale disturbances in the external magnetic field; these are grouped together as *magnetic micropulsations*. Micropulsations are temporal variations in the Earth's magnetic field that are quasi-periodic with principal frequencies in the range from millihertz (mHz) to a few hertz. The amplitudes of these micropulsations are quite small, usually less than a nanotesla. In comparison, the earth's steady field has an amplitude of 35,000 to 55,000 nanoteslas, depending on where on the earth's surface it is measured.

Geomagnetic micropulsations are temporal variations in the Earth's magnetic field that have a quasi-periodic structure with frequencies in the range from a few millihertz to several hertz. The name "micropulsation" was first applied in the mid 1800s because of the short period and low amplitude of the magnetic variations, which tended to make the magnetograms recorded at magnetic observatories at that time fuzzy in appearance. As more sensitive, wider band magnetographs came into use, these small-scale features were found to be rich in character. For example, the 24-hour magnetogram shown in Fig. 13.3 for a flat response over the micropulsation band but with longer periods rejected has features which are common on such recordings.

A major problem in the early study of micropulsations was the wide variety of signatures such magnetic variations showed, as well as the radically different temporal increases in amplitude that various signatures exhibited. In an attempt to organize our knowledge of the causes of micropulsations, a universal classification for geomagnetic micropulsations was adopted by the 13th General Assembly of the International Union of Geophysics and Geodesy (IUGG) in 1963 in Berkeley, California. Subsequent studies indicated that this first classification was inadequate in detail, and so it was amended at the Second Scientific Assembly of the International Association of Geomagnetism and Aeronomy (IAGA) in 1973 at Kyoto, Japan. Salient features of this classification are listed in Table 13.1.

A typical spectrum of the microvariational magnetic field and a comparable spectrum for the associated electric field in the earth are shown in Fig. 13.4. Electric field power density spectrums vary greatly
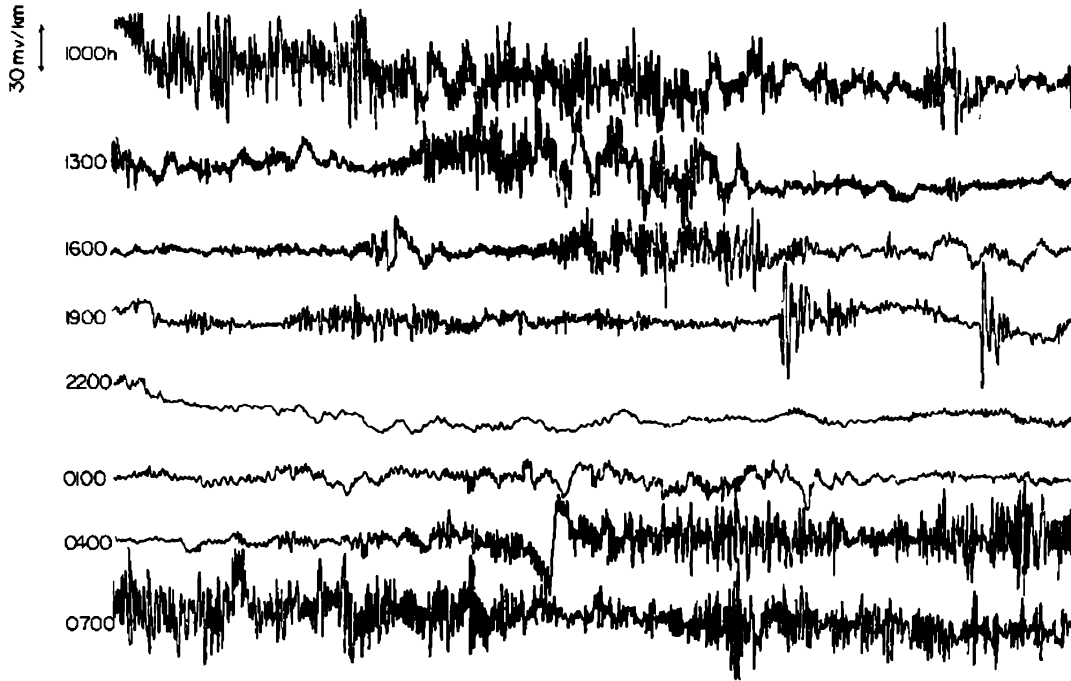
FIGURE 13.3

Twenty-four hour record of electric field variations (north-south component) in the period band from 1 to 200 seconds recorded at the Cecil Green Observatory at Bergen Park, Colorado. Each raster represents one three-hour interval.

in amplitude from location to location because they are proportional to the square root of the resistivity of the earth in which they are measured. Both types of spectrum show an approximate power-law dependence of the power density ($PD\{\}$) of the magnetic and electric fields on frequency. An observed magnetic field power density function normally varies with frequency, ω, roughly as

$$PD\{H\} \approx a\omega^{-3/2}. \tag{13.1}$$

In the following sections of this chapter, we will find that, over a uniform earth, the magnetic and electric power densities are related as

$$PD\{E\}/\omega PD\{H\} \approx \rho_{MT}, \tag{13.2}$$

where ρ_{MT} is the earth resistivity. Substituting Eq. (13.2) into Eq. (13.1), we obtain the corresponding expression for the rough correlation of electric field power density with frequency:

$$PD\{E\} \approx a\rho_{MT}\omega^{-1/2}, \tag{13.3}$$

Table 13.1 Characteristics of Geomagnetic Pulsations (after Jacobs, 1970)

Class	Period (sec.)	Size (nTesla)	Time of occurrence	Characteristics
Pc1	0.2–0.5	0.05–0.1	Daytime in Auroral zone, Night and early morning at mid latitudes	Narrow frequency band. Increased activity a few hours before and a few days after a magnetic storm
Pc2 Pc2 Pc3	5.0–10 10–45 45–150	0.1–1	Daytime	Relatively regular pulsations with distinct mean period. Period shortens with increasing activity.
Pc5	150–160	1–10	Morning and evening hours	Regular pulsations. Occur in local areas. Typical for periods of moderate magnetic activity.
Pi1	1–40	0.01–0.1	Night and early morning hours	Wideband bursts. Maximum in Auroral zones. Close correlation with aurora.
IPDP	1–40	0.01–0.1	Evening hours	Wideband emissions. Maximum in subauroral zones. Occur during main phase of magnetic storms.
Pi2	40-150	1–5	Evening and night hours	Trains of oscillations generally on the night hemisphere. Occur with the initial phase of substorms.
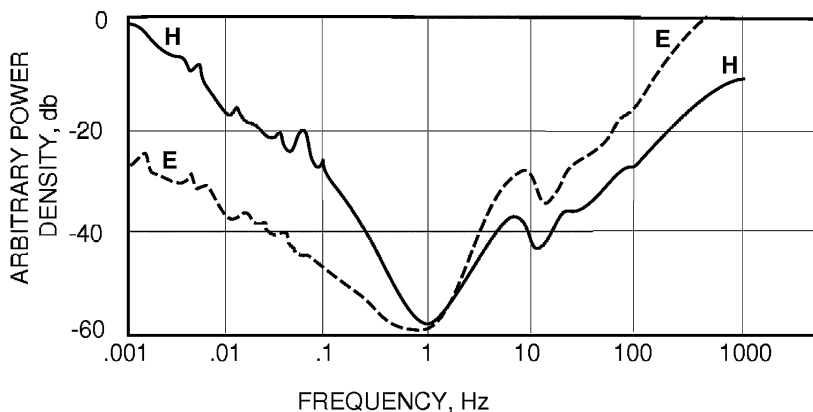
FIGURE 13.4

Typical power density spectrums for the time varying electric and magnetic fields of the Earth. The strength and the detailed structure will vary with time and place.

where the correlation factor has the approximate value $a = 1 \times 10^{-4}$ nanoteslas^2/hertz. These correlation coefficients are useful only in order of magnitude computations, because they vary with location on the earth and the status of the external contributions to the magnetic field.

13.1.3 MAGNETIC STORMS

The variable part of the magnetic field shows changes of character over time. A *disturbed* magnetic field is a term used to describe intervals when the magnetic field departs markedly from its normal, or *quiet-period* behavior. During a disturbed period, magnetic variations can range up to thousands of nanoteslas, and the duration of a disturbed period can range up to several days. The fluctuations often present a picture of chaotic and apparently unpredictable variations in the magnetic field. Disturbances are observed over a limited area, or over the whole Earth. In the latter case, the disturbance is called a *magnetic storm*.

Magnetic storms are associated with solar flares. Flares often cause an increase in ionization, and hence, the electrical conductivity, of the lower levels of the ionosphere over the sunlit hemisphere. During magnetic storms, the quiet-day current systems is augmented with additional currents flowing lower in the ionosphere. The beginning of a storm is most clearly evident in the horizontal component of the magnetic field, which will increase by tens of nanoteslas in a storm with a *sudden commencement* (SC). In a storm with a gradual onset, it is difficult to identify the exact moment of commencement.

Storms have been classified as being *weak*, *moderate*, or *great*. Obviously, the basis for this classification is the size of the magnetic disturbance, though there is no general agreement about the differences between these classes. Weak storms have maximum changes in the vertical field of up to 150 nanoteslas, great storms have changes in the vertical magnetic component of more than 500 nanoteslas, and moderate storms show changes in vertical magnetic field strength someplace in between.

The frequency spectrums of magnetic storms exhibit certain consistent patterns. Storms occur more frequently during periods of high solar activity. Both phenomena, solar activity and frequency of occurrence of storms, show a strong tendency to occur in 11-year cycles (Fig. 13.5). During quiet periods, there may be 6 to 12 storms per year, while during active periods, the number increases to 25 to 40. Also, there is a tendency for storms to be of greater intensity during periods of greater solar activity.

Chapman (1962) proposed a general classification scheme for the components of a magnetic storm based on the physical mechanisms involved. In this scheme, the elements of a storm are named DCF, DR, DP1, and DPC. The DPC element is the disturbance related to the solar wind which forms the ring current in the magnetosphere, DR is the magnetic effect of the development of a ring current beneath the magnetosphere, DP1 is the disturbance in auroral zones, and DPC is the magnetic disturbance over the polar regions. This classification distinguishes between disturbances originating at the surface of the magnetosphere (DCF) and those that originate in the magnetosphere (DR) from those that are partly or completely ionospheric in character (DP1 and DR). The DCF and DR currents flow far above the earth's surface, and therefore, they give rise to more or less homogeneous magnetic disturbances over the entire earth. The DP1 currents flow at lower altitudes (about 100 km above the earth's surface) and give rise to polar magnetic disturbances which are local in character.

13.1.4 SUBSTORMS

The notation DP1 is also used to indicate a class of magnetic disturbances with a maximum intensity in the auroral latitudes ($\phi = 67.5°$). A characteristic feature of these *magnetic substorms* is the variation in field character over short distances on the surface of the earth. Over distances of a few hundred kilometers, the phase of a variation can change by 180° and the amplitude can vary by orders of magnitude. The currents giving rise to substorms flow in the lower ionosphere at an altitude of about 100 kilometers.
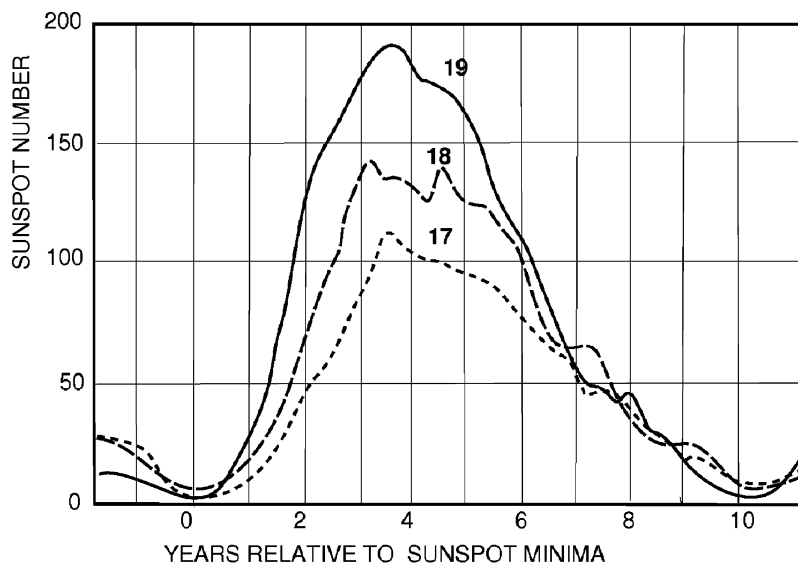
FIGURE 13.5

Sunspot numbers that occurred during sunspot cycle 17 (1933–1944), cycle 18 (1944–1954), and cycle 19 (1954–1964).

In polar regions, other disturbances which differ from substorms in their times of occurrence and geographic location are common. These disturbances are grouped together in the classification as DPC disturbances, though a more detailed subclassification is also used in which different varieties of these disturbances are called DP2, DP3, and DP4 disturbances, each with its own diagnostic features. DP2 disturbances can occur synchronously from the poles to the equator, with a duration of about 1 hour. The DP2 substorms are thought to be generated by a current system consisting of two vortices lying overhead at latitudes less than 30°.

DP3 disturbances commonly are located over one of the polar caps. They last for only a few hours. The current system for a DP3 disturbance has the form of 2 vortices of overhead currents at latitudes of 80 to 83°, and occur during daylight hours.

The DP4 disturbance occurs in the polar cap, and apparently is caused by a single current vortex.

13.2 THE TIKHONOV-CAGNIARD MODEL OF THE MT FIELD

13.2.1 TIKHONOV-CAGNIARD MODEL

It has been shown by mathematical analysis that the magnetotelluric field induced by magnetospheric or ionospheric currents behaves as a plane wave in a uniform or horizontally stratified earth. Because of this, we can make use of a physical model in which the magnetotelluric field has the form of a vertically travelling plane wave to develop a basis for determining the electrical conductivity profile

of the earth. In this assumption, we must remember that the electromagnetic waves have wavelengths in the atmosphere of a hundred or a thousand times the diameter of the earth. In spite of this, in our analysis we will describe the electromagnetic field as being a plane wave. The concepts of *waves* and *wave lengths* as applied to the propagation of magnetotelluric field in the earth are somewhat arbitrary, but the concepts are both useful and traditional in the field of electrical prospecting.

The simplest case worth examining might well be that of a uniform, horizontally stratified earth, in which the conductivity varies only with depth. The solution of Maxwell's equations which makes the behavior of the electromagnetic field for this structure geophysically meaningful was conceived in the 1950s by A. N. Tikhonov in the Soviet Union (Tikhonov, 1950), and by L. Cagniard in France (Cagniard, 1953), working independently. The power in their approach is that it is simple and provides geophysically useful results. The further development of the principles of magnetotelluric theory was accomplished in the works of M. Berdichevsky, V. Dmitriev, U. Schmucker, L. Vanyan, K. Vozoff, J. Weaver, and P. Weidelt, whose efforts transformed the method into the practical tool of deep electromagnetic study of the Earth (e.g., Berdichevsky, 1965; Berdichevsky and Dmitriev, 1976a, 1976b, 2002, 2008; Berdichevsky and Zhdanov, 1981, 1984; Schmucker, 1970; Vanyan and Butkovskaya, 1980; Vozoff, 1972; Weaver, 1994; Weidelt, 1975a).

We have presented in Chapter 5 the basic mathematical theory of a plane EM wave propagation in a layered medium. In the present chapter, we will apply this theory to develop the basic principles of magnetotelluric sounding methods.

13.2.2 CONCEPTS OF APPARENT RESISTIVITY AND SOUNDING

In the magnetotelluric (MT) method the earth's natural electromagnetic field is used as a source field. The receivers record the horizontal and mutually orthogonal components of electric and magnetic fields on the surface of the Earth. The variations in amplitude and phase of the received signals can be interpreted in terms of the resistivity structure of the subsurface using the magnetotelluric impedance, Z, introduced in Chapter 5. As was the case with the various DC methods, it is common practice to define an apparent resistivity in terms of measurements made over an ideally uniform earth. And, as in the case of DC methods, it is common practice to speak of a sounding, or determination of apparent resistivity as a function of depth in the earth. In contrast to the DC methods, where the spacing between electrodes was used as the depth-related measurement, in the magnetotelluric method, the frequency, or more exactly the period, of oscillations comprising the natural electromagnetic field is used as the depth-related measurement. Because of this difference in concept, soundings made with the MT method are termed *parametric*, while DC soundings are termed *geometric*.

If the earth is uniform in electrical character, the expression for impedance in Eq. (5.22) is

$$Z = \omega\mu_0/k_1, \tag{13.4}$$

because in the case of a uniform earth, the layered earth correction factor, R_1, is exactly unity.

This last equation can be solved directly for the electrical resistivity (or its inverse, the electrical conductivity) by using the definition for k_1:

$$k_1 = (i\omega\mu_0/\rho_1)^{1/2}. \tag{13.5}$$

The result is

$$\rho_1 = \frac{1}{\omega\mu_0}|Z|^2. \tag{13.6}$$

This is the Tikhonov-Cagniard formula for apparent resistivity computed from impedance measurements at the surface of the earth. If the earth were perfectly uniform, the formula would give the correct value for the resistivity. If instead, the earth is not uniform, the calculation of apparent resistivity is still possible, but defines only an apparent resistivity loosely related to the actual resistivity distribution in the earth. This relationship can be a meaningful one, as in the case of a simply structured earth consisting of horizontal layers. Or the relationship can be obscure, as in the case of a complicated resistivity distribution.

Solution of Maxwell's equations has shown that the strength of an electromagnetic field penetrating into the earth decreases with depth as electromagnetic energy is converted to heat. This conversion is more rapid at higher frequencies.

The effective depth to which an electromagnetic field penetrates is often said to be a skin depth, or the depth at which the field strength has been reduced by the factor $e^{-1} = 0.3678794411$ (this amount of attenuation is a *neper*, a unit which is dimensionless).

The dependence of attenuation on frequency permits us to use frequency as a means for controlling the depth to which resistivity is measured. The skin depth is a very useful way to express the effect of attenuation because, if a second layer lies at depths greater than one skin depth, the effect of that lower layer on the observed electromagnetic field is almost negligible. On the other hand, if the second layer lies at a depth shallower than the skin depth, it does have an appreciable effect on the observed electromagnetic field strengths. Of course, the transition from the one case to the other is gradual; there is no sharply defined depth at which the second layer becomes nondetectable.

In practice, the results of magnetotelluric soundings are typically presented as a plot of apparent resistivity either as a function of skin depth, or in terms of the square root of wave period, which differs from skin depth only by the multiplying constant $(2\pi\mu_0\sigma)^{-1/2}$. These sounding curves thus reflect progressively the influence of rocks at greater depths as one goes to greater skin depths (or periods).

13.2.3 RELATIONSHIPS BETWEEN THE MT SOUNDING CURVE AND THE ACTUAL 1-D RESISTIVITY MODEL

The magnetotelluric sounding curve can be constructed for any geoelectric structure, but has its principal utility in cases in which the earth is at least approximately layered. For a one-dimensional earth, the relationship between the sounding curve and the actual profile of resistivity with depth in the earth can be obtained using Eq. (5.7) and a similar equation for the vertical derivative of the magnetic field:

$$dE_x(z)/dz = i\omega\mu_0 H_y(z), \tag{13.7}$$

$$\rho_n(z)dH_y(z)/dz = -E_x(z), \tag{13.8}$$

where $\rho_n(z) = 1/\sigma_n$ is the one-dimensional resistivity profile.

Multiplying the left-hand side of Eq. (13.7) by the right-hand side of Eq. (13.8) and the right-hand side of Eq. (13.7) by the left-hand side of Eq. (13.8), we have:

$$E_x(z)\frac{dE_x(z)}{dz} = -i\omega\mu_0\rho_n(z)H_y(z)\frac{dH_y(z)}{dz}.$$

Moving the fields $E_x(z)$ and $H_y(z)$ under the differentiation sign, we obtain:

$$\frac{1}{2}\frac{dE_x^2(z)}{dz} = -i\omega\mu_0\rho_n(z)\frac{1}{2}\frac{dH_y^2(z)}{dz}.$$

Dividing by the multiplier $1/2$ and integrating over z from 0 to infinity (recognizing that $E_x \to 0$ for $z \to \infty$), we can write:

$$E_x^2(0) = i\omega\mu_0 \int_0^\infty \rho_n(z)\frac{dH_y^2(z)}{dz}dz. \tag{13.9}$$

Substituting (13.9) into (5.28) and then, into (13.6), we find the following expression for apparent resistivity, ρ_a:

$$\rho_a = \left| \frac{1}{H_0^2} \int_0^\infty \rho_n(z)\frac{d}{dz}H_y^2(z)dz \right|, \tag{13.10}$$

where $H_0 = H_y(0)$.

We often model a stratified earth as a set of layers within each of which the resistivity is constant; hence, the resistivity-depth profile is a *piecewise constant function*. For such a profile, the integral in Eq. (13.10) can be easily evaluated over each segment in the piecewise continuous profile, resulting in the expression

$$\rho_a = \left| \frac{1}{H_0^2} \sum_{j=1}^N \rho_j \int_{z_{j-1}}^{z_j} \frac{d}{dz}H_y^2(z)dz \right| = \left| \sum_{j=1}^N \rho_j q_j \right|, \tag{13.11}$$

where

$$q_j = (1/H_0^2)[H_y^2(z_j) - H_y^2(z_{j-1})], \tag{13.12}$$

and

$$\left| \sum_{j=1}^N q_j \right| = 1, \ z_N = \infty.$$

We recognize that apparent resistivity is merely a weighted average of the true resistivities in the layered sequence. The greater the amount of attenuation of the magnetic field in a given layer at depth, the greater the weighting factor, q_j, which determines the contribution of that layer to the apparent resistivity. The greatest weight is given to the layers that lie within a skin depth of the surface. A highly
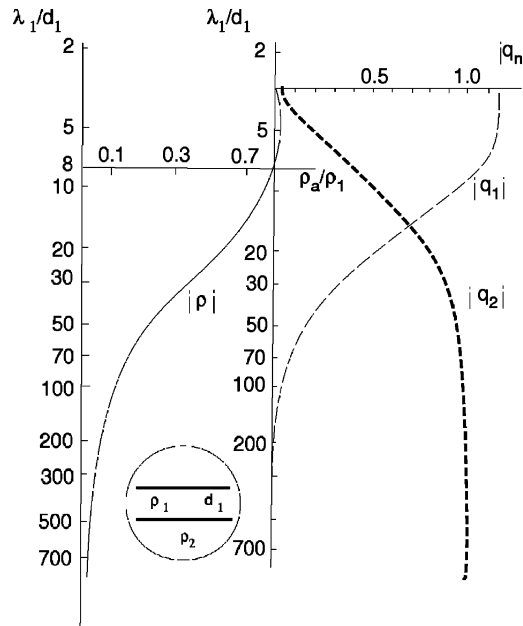
FIGURE 13.6

Construction of an MT curve for two layers, the lower one having 1/9 the resistivity of the upper one, by summation of the contribution from each of the two layers.

conducting layer has a much more favorable weighting factor than does a poorly conducting layer. With lower frequencies, the skin effect diminishes in the upper layers, and so their weighting factors decrease, while the weighting factors for deeper layers increase (Berdichevsky and Dmitriev, 1976a, 1976b).

In Fig. 13.6, the independent variable plotted on the abscissa is λ_1/d_1 and the dependent variable plotted on the ordinate is ρ_a/ρ_1. The curve is plotted to bilogarithmic coordinates, a practice which is valuable in plotting scaled information. Consider that you might wish to use this curve for a specific set of resistivities and a specific thickness for the overburden. You accomplish this by desalting the variables; that is, by multiplying the abscissa by d_1 and the ordinate by k_1. When the data are presented on a bilogarithmic coordinate system, this multiplication is achieved by shifting the points on the curve by a single distance horizontally and vertically. The curve shape is not changed, but only the coordinates of the plot have been shifted by the distances log ρ_1 and log d_1.

The right-hand part of Fig. 13.6 displays the magnitudes of the weighting factors q_1 and q_2. With decreasing frequency, the modulus of q_1 decreases from the value in the overburden, while the modulus of q_2 increases. At the same time, the apparent resistivity ρ_a changes gradually from ρ_1 to ρ_2.

Figs. 13.7 through 13.10 show MT sounding curves computed for a two-layer model, consisting of a single uniform overburden resting on a lower half-space for various contrasts in resistivity between the overburden and the half-space. It should be noted here that we need not specify the actual resistivity of

NORMALIZED RESISTIVITY
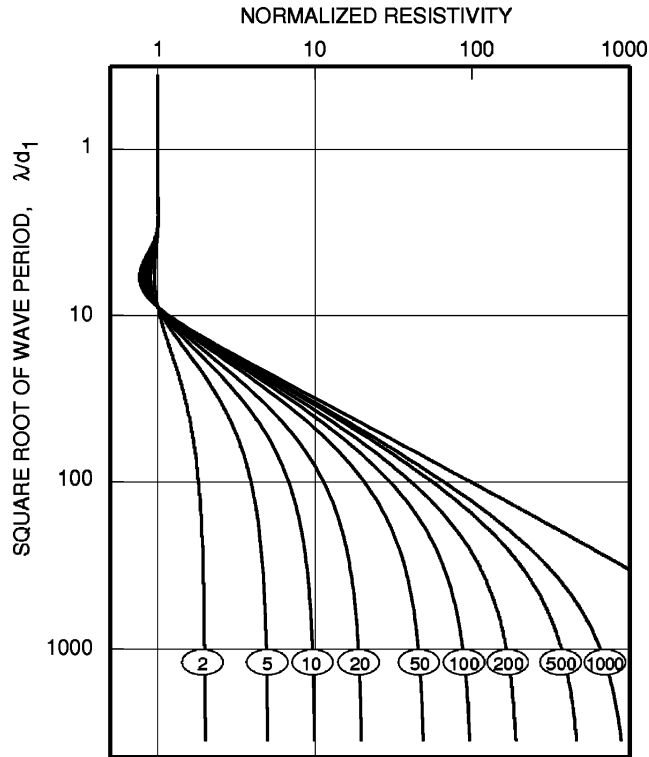
FIGURE 13.7

Magnetotelluric sounding curves for a two-layer sequence in which the second layer is more resistive than the first. The contrast in resistivity between the second layer and the first is specified by the label on each curve. The normalized wave period is λ_1/d_1. The normalized resistivity is ρ_2/ρ_1.

the two layers, but only the ratio. Similarly, it is not necessary to specify the thickness of the layer, but only the ratio of the thickness to the wavelength (or skin depth). These convenient factors arise because the equation for the layered earth correction factor is linearly scalable, that is, each resistivity in the equation can be divided by some reference resistivity (often the resistivity of the surface layer) and each length, either a layer thickness or a wavelength, can be divided by some reference length (often the wavelength in the surface layer, or the thickness of the first layer). When this scaling of variables in the expression for the layered earth correction factor is carried out, R is seen to be a function of only a set of dimensionless scaled variables.

Apparent resistivity computed using the Tikhonov-Cagniard equation is a complex quantity, normally represented by magnitude and phase. The magnitude of the apparent resistivity curves is shown in Figs. 13.7 and 13.9, and the corresponding phase curves are shown in Figs. 13.8 and 13.10.

These apparent resistivity curves have the character desired for an electrical sounding curve: at short wave periods (high frequencies), the apparent resistivity approaches closely the actual resistivity
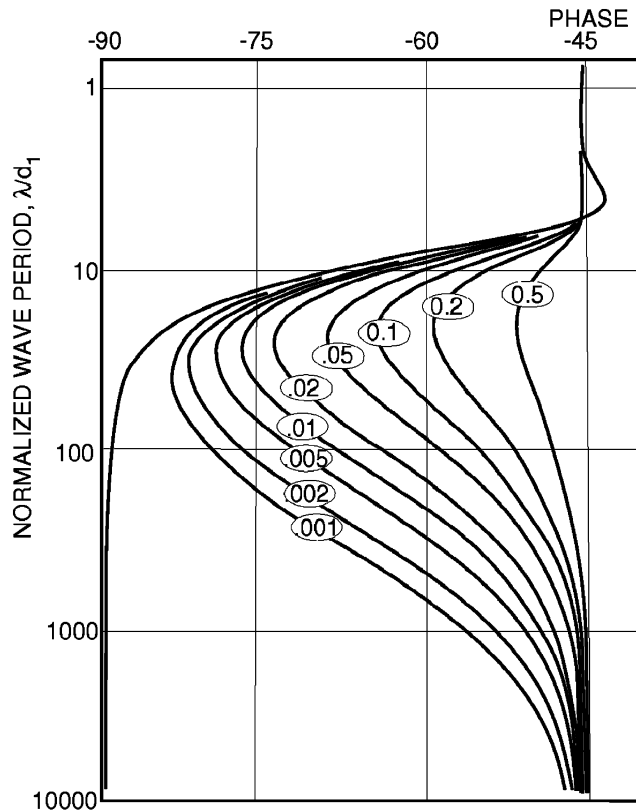
FIGURE 13.8

Phase of the magnetotelluric apparent resistivity curves. The contrast in conductivity between the second layer and the first is specified by the label on each curve.

of the surface layer, and at long periods (low frequencies) the apparent resistivity gradually approaches the actual resistivity for the lower half-space.

The curves for phase show a different behavior; they approach a phase shift of $-45°$ both at short periods and at long periods. The phase deviates from $-45°$ at periods over which the apparent resistivity is changing from one extremal value to another. If the lower half-space is relatively conductive, the phase becomes greater, approaching zero for a perfectly conductive lower half-space. On the other hand, if the lower half-space is relatively resistive, the phase shift becomes more negative, reaching $-90°$ if the lower half-space is a perfect insulator.

The apparent resistivity curves do not change from the resistivity of the surface layer to the resistivity of the lower half-space monotonically as the wave period increases; rather, the apparent resistivity oscillates weakly around the resistivity for the surface layer at short periods (Fig. 13.11). These oscillations are caused by constructive or destructive interference as electromagnetic fields return to the
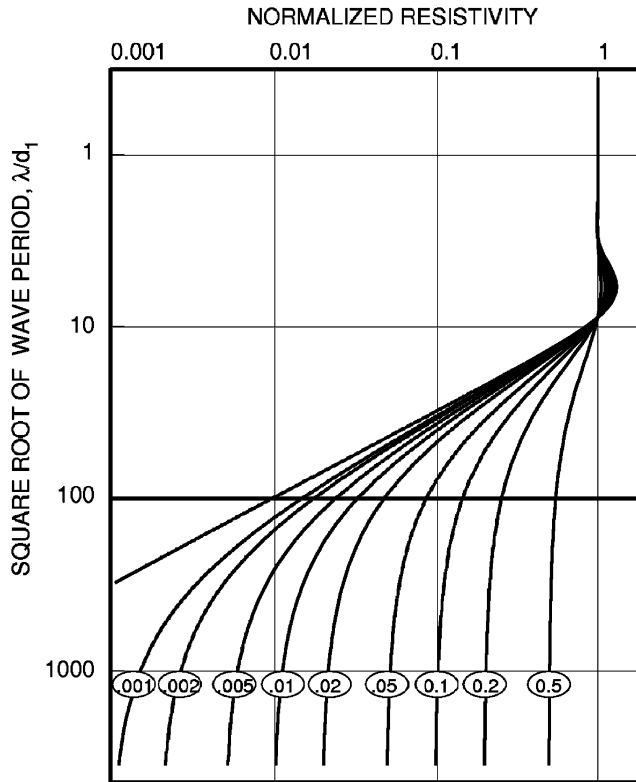
FIGURE 13.9

Magnetotelluric sounding curves for a two-layer sequence in which the second layer is more conductive than the first. The contrast between the resistivity of the second layer and the resistivity of the first is indicated by the label on each curve.

surface after having been shifted in phase on travel through the earth. These fields are also strongly attenuated by travel through the earth, so the interference is weak, and becomes rapidly weaker at higher frequencies (shorter wave periods).

An important feature of the apparent resistivity and phase curves in Figs. 13.7 through 13.10 is that the curve sets are mirror images of one another. The curves in Figs. 13.9 and 13.10 could have been obtained simply by imaging the curves in Figs. 13.7 and 13.8 about the vertical axis.

Figs. 13.12 through 13.15 display two sets of three-layer magnetotelluric sounding curves. It can be seen that the sounding curve does give a qualitative indication of the variation of true resistivity with depth. The variation of ρ_a with inverse frequency follows the change in ρ_t with depth, though in a much smoother manner.

A fundamental question which arises in the interpretation of an MT field curve, whether it be done by curve matching, as above, or rigorous inversion methods, described in Chapters 7 and 8, is the
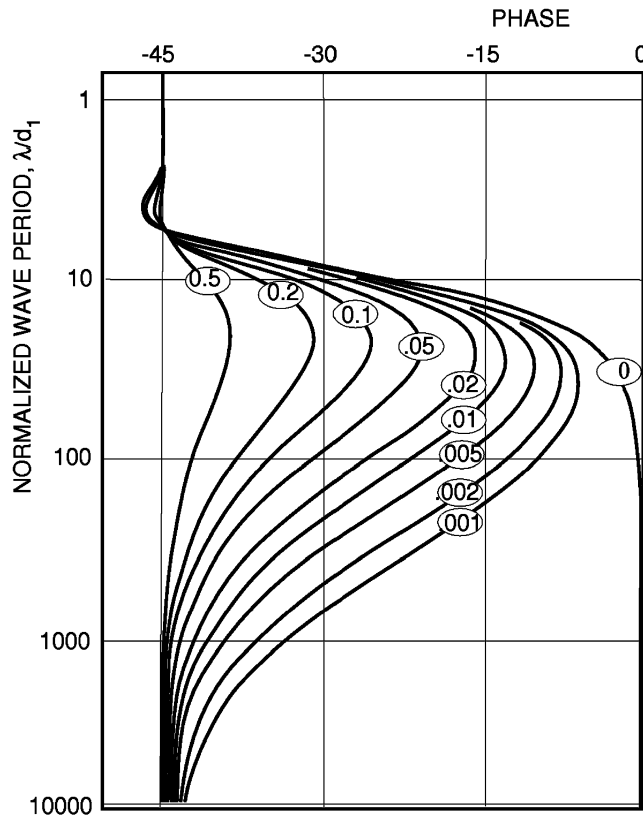
FIGURE 13.10

Phase of the magnetotelluric apparent resistivity curves. The contrast in resistivity between the second layer and the first is specified by the label on each curve.

question of *uniqueness*. Is there only one earth structure which will give rise to a specific sounding curve, or are there several earth structures which can give rise to the same observed impedances? If the latter is the case, unique determination is not possible. The question is difficult to answer in general, but in 1965, Tikhonov demonstrated uniqueness of inversion of the MT sounding curve for a horizontally layered earth.

While the inversion of the MT sounding curve for a laterally uniform earth is unique, the possibility of ambiguity is not totally eliminated. The question remains as to uniqueness if the earth is permitted to have a more complicated structure. Also, uniqueness does not guarantee that two earth models which differ from one another can be distinguished even if the curves are unique, because in the real world, field curves are determined only within some experimental error and the differences between two unique curves can be lost. This aspect of ambiguity was examined in more detail in Chapter 7.
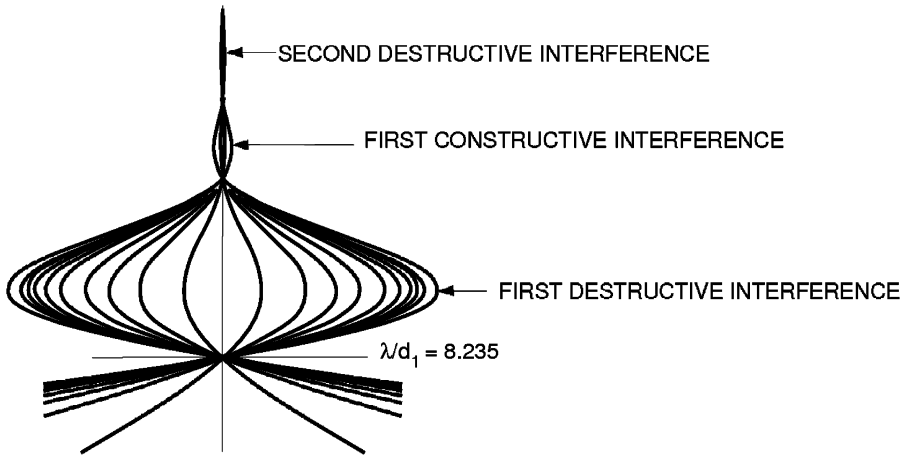
FIGURE 13.11

Detail of the magnetotelluric sounding curves in the neighborhood of the first crossing of the unit axis.

13.3 THEORY OF THE MT AND MV TRANSFER FUNCTIONS

The expression for impedance, developed in Chapter 5, is misleadingly simple:

$$Z = E_x/H_y = -E_y/H_x.$$

We have assumed linearity of the relationships between mutually orthogonal electric and magnetic components of the field which are used in determining the Tikhonov-Cagniard impedance:

$$E_x = ZH_y,$$
$$E_y = -ZH_x. \tag{13.13}$$

It is most important to consider the question of the validity of this assumption of linearity when we are dealing with a real, inhomogeneous earth. The answer to this question rests on a detailed analysis of the linearity between the various components of the magnetotelluric field. We will do this analysis using some elementary concepts of linear algebra.

13.3.1 MAGNETOTELLURIC OPERATORS: IMPEDANCE AND ADMITTANCE, TELLURIC AND MAGNETIC

In a general case, a monochromatic field satisfies the equations,

$$curl\ \mathbf{H} = \sigma \mathbf{E} + \mathbf{j}^Q,$$
$$curl\ \mathbf{E} = i\omega\mu_0\mathbf{H}, \tag{13.14}$$
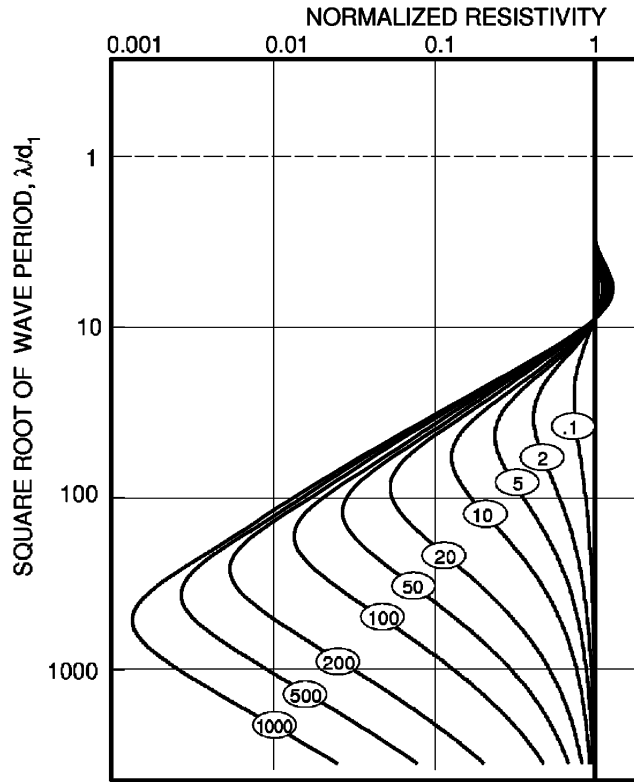
FIGURE 13.12

Magnetotelluric sounding curves for a three-layer sequence. The middle layer is more conductive than the first and last layers, which both have the same resistivity. The resistivity of the middle layer is indicated by the label on each curve.

where $\mathbf{j}^Q$ is the volume density of the external ionospheric and magnetospheric currents which give rise to the magnetotelluric field. On the strength of Maxwell's equations being linear, it is possible to write the electric and magnetic fields as linear transformations of the current density vector, $\mathbf{j}^Q$ (see integral equation method in Chapter 6):

$$\mathbf{E}(\mathbf{r}) = \iiint_Q \hat{G}^E(\mathbf{r}|\mathbf{r}', \omega, \sigma)\mathbf{j}^Q(\mathbf{r}')dv',$$

$$\mathbf{H}(\mathbf{r}) = \iiint_Q \hat{G}^H(\mathbf{r}|\mathbf{r}', \omega, \sigma)\mathbf{j}^Q(\mathbf{r}')dv', \qquad (13.15)$$

where Q is the region within which the currents $\mathbf{j}^Q$ are present, and $\hat{G}^E$ and $\hat{G}^H$ are linear operators related to the radius vector $\mathbf{r}$ defining the location at which the field is observed and the radius vectors $\mathbf{r}'$
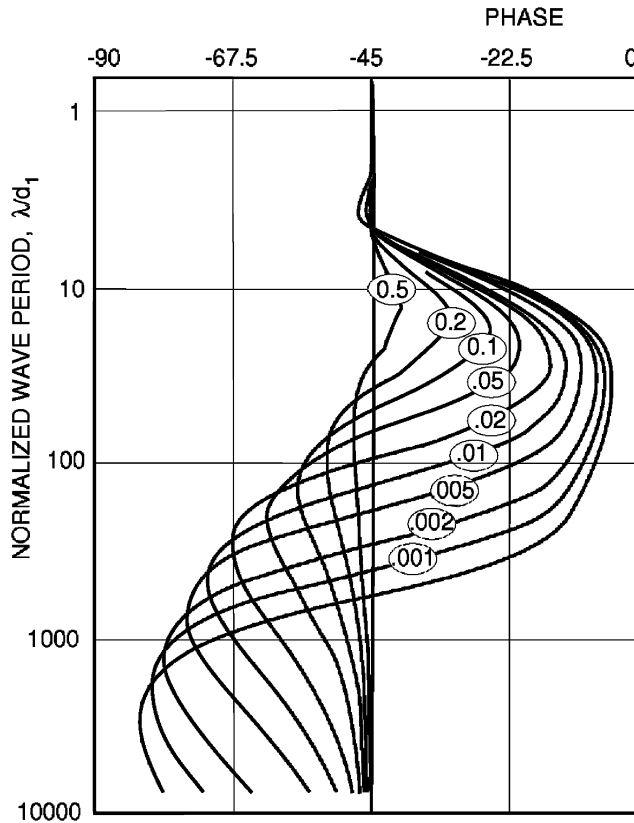
FIGURE 13.13

Phase for the magnetotelluric apparent resistivity curves shown in previous Figure.

defining the points at which the source currents $\mathbf{j}^Q(\mathbf{r}')$ are flowing. These operators are functions only of the field frequency ω and the distribution of electrical conductivity in the medium, σ. A prime, $'$, indicates that differentiation has been carried out with respect to $\mathbf{r}'$.

In the theory of linear relationships between the components of the magnetotelluric fields (Berdichevsky and Zhdanov, 1981, 1984), it has been shown that for most types of geomagnetic variations (pulsations, microstorms, quiet-day diurnal variations and worldwide storms), $\mathbf{j}^Q$ can be represented as a linear transformation of some independent vector $\mathbf{A}$ (either real or complex) realized using a linear operator $\hat{a}$ (see Appendix E for some definitions and properties of the linear operators and their matrices):

$$\mathbf{j}^Q(\mathbf{r}) = \hat{a}(\mathbf{r})\mathbf{A}. \tag{13.16}$$

NORMALIZED RESISTIVITY
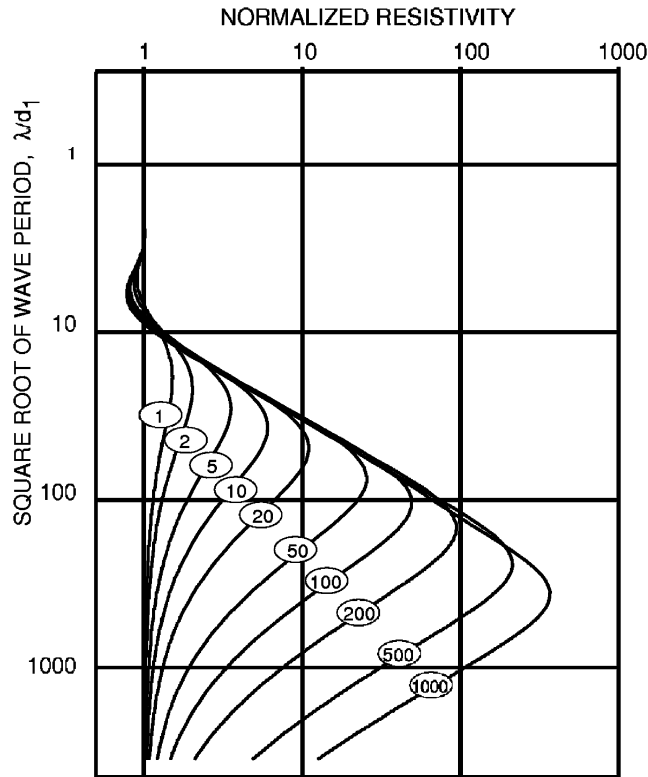
FIGURE 13.14

Magnetotelluric sounding curves for a three-layer sequence. The middle layer is a virtual insulator, while the first and last layers have a common resistivity. The ratio of the thickness of the second layer to that of the first is indicated by the label on each curve.

The vector $\mathbf{A}$ is independent of the coordinate system. It characterizes the polarization and strength of the currents flowing in the ionosphere and magnetosphere, and is called the *vector field characteristic*.

The operator $\hat{a}$ in a general case depends on the spatial coordinates and characterizes the geometry of the external currents, that is, the excitation of the magnetotelluric field. It is called the *excitation operator*. The excitation operator does not change for one specific type of variation (micropulsations, microstorms, S_q variations, worldwide storms), but may change from one type of variation to another.

We substitute Eq. (13.16) into (13.15). Then

$$\mathbf{E}(\mathbf{r}, \omega) = \hat{e}(\mathbf{r}, \omega, \sigma)\mathbf{A}, \tag{13.17}$$

$$\mathbf{H}(\mathbf{r}, \omega) = \hat{h}(\mathbf{r}, \omega, \sigma)\mathbf{A}, \tag{13.18}$$
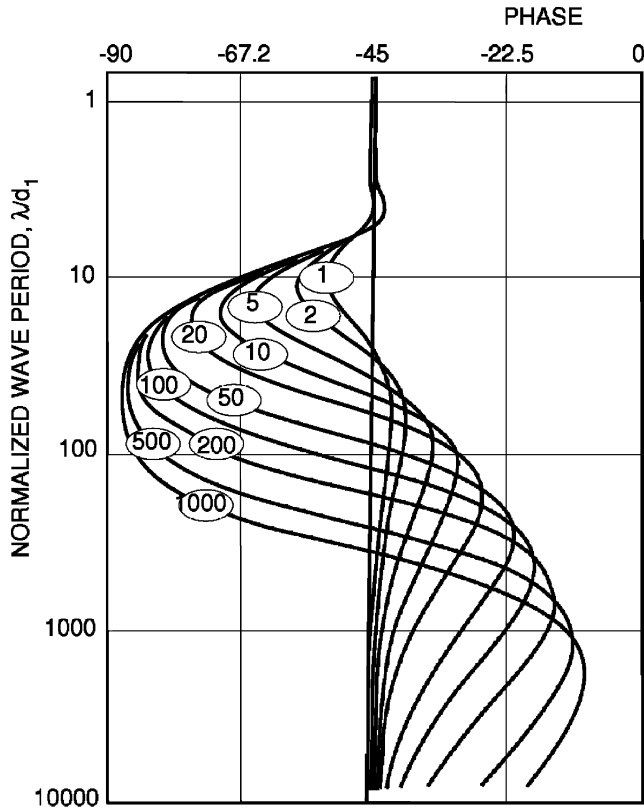
FIGURE 13.15

Phase of the magnetotelluric apparent resistivity curves of the previous Figure.

where

$$\hat{e}(\mathbf{r}, \omega, \sigma) = \iiint_Q \hat{G}^E(\mathbf{r}|\mathbf{r}', \omega, \sigma)\hat{a}(\mathbf{r}')dv',$$

$$\hat{h}(\mathbf{r}, \omega, \sigma) = \iiint_Q \hat{G}^H(\mathbf{r}|\mathbf{r}', \omega, \sigma)\hat{a}(\mathbf{r}')dv'.$$

We see that the operators $\hat{e}$ and $\hat{h}$ depend on the coordinates of the observation point, $\mathbf{r}$, the frequency, ω, and the distribution of electrical conductivity in the medium, σ. These are called the electrical and magnetic characteristic field operators. It must be stressed that while these operators, as well as the excitation operator, $\hat{a}$, are constant with respect to a given type of excitation, they can change as one type of variation is replaced by another (as, for example, the transition from observations of storm-time variations to quiet-time variations).

Let us now assume that both characteristic operators, $\hat{e}$ and $\hat{h}$, are invertible (that is, inverse operators $\hat{e}^{-1}$ and $\hat{h}^{-1}$ exist). Then, in accord with Eqs. (13.17) and (13.18),

$$\mathbf{A} = \left\{ \begin{array}{c} \hat{e}^{-1}(\mathbf{r}, \omega, \sigma)\mathbf{E}(\mathbf{r}, \omega) \\ \hat{h}^{-1}(\mathbf{r}, \omega, \sigma)\mathbf{H}(\mathbf{r}, \omega) \end{array} \right\}. \tag{13.19}$$

Substituting the bottom expression from Eq. (13.19) into (13.17) and the top expression from Eq. (13.19) into (13.18), we obtain

$$\begin{aligned} \mathbf{E}(\mathbf{r}, \omega) &= \hat{e}(\mathbf{r}, \omega, \sigma)\hat{h}^{-1}(\mathbf{r}, \omega, \sigma)\mathbf{H}(\mathbf{r}, \omega) \\ &= \hat{Z}(\mathbf{r}, \omega, \sigma)\mathbf{H}(\mathbf{r}, \omega), \end{aligned} \tag{13.20}$$

$$\begin{aligned} \mathbf{H}(\mathbf{r}, \omega) &= \hat{h}(\mathbf{r}, \omega, \sigma)\hat{e}^{-1}(\mathbf{r}, \omega, \sigma)\mathbf{E}(\mathbf{r}, \omega) \\ &= \hat{Y}(\mathbf{r}, \omega, \sigma)\mathbf{E}(\mathbf{r}, \omega)). \end{aligned} \tag{13.21}$$

Here, $\hat{Z}$ and $\hat{Y}$ are operators representing impedance and admittance, respectively

$$\hat{Z}(\mathbf{r}, \omega, \sigma) = \hat{e}(\mathbf{r}, \omega, \sigma)\hat{h}^{-1}(\mathbf{r}, \omega, \sigma), \tag{13.22}$$

$$\hat{Y}(\mathbf{r}, \omega, \sigma) = \hat{h}(\mathbf{r}, \omega, \sigma)\hat{e}^{-1}(\mathbf{r}, \omega, \sigma). \tag{13.23}$$

If we should measure $\mathbf{E}$ and $\mathbf{H}$ at several points on the earth's surface (with radius vectors $\mathbf{r}$ and $\mathbf{r}_0$), then, using Eqs. (13.17), (13.18), and (13.19), we can write

$$\begin{aligned} \mathbf{E}(\mathbf{r}, \omega) &= \hat{e}(\mathbf{r}, \omega, \sigma)\hat{e}^{-1}(\mathbf{r}_0, \omega, \sigma)\mathbf{E}(\mathbf{r}_0, \omega) \\ &= \hat{t}(\mathbf{r}|\mathbf{r}_0, \omega, \sigma)\mathbf{E}(\mathbf{r}_0), \end{aligned} \tag{13.24}$$

$$\begin{aligned} \mathbf{H}(\mathbf{r}, \omega) &= \hat{h}(\mathbf{r}, \omega, \sigma)\hat{h}^{-1}(\mathbf{r}_0, \omega, \sigma)\mathbf{H}(\mathbf{r}_0, \omega) \\ &= \hat{m}(\mathbf{r}|\mathbf{r}_0, \omega, \sigma)\mathbf{H}(\mathbf{r}_0). \end{aligned} \tag{13.25}$$

Here, $\hat{t}$ and $\hat{m}$ are telluric and magnetic operators;

$$\hat{t}(\mathbf{r}|\mathbf{r}_0, \omega, \sigma) = \hat{e}(\mathbf{r}, \omega, \sigma)\hat{e}^{-1}(\mathbf{r}_0, \omega, \sigma),$$

$$\hat{m}(\mathbf{r}|\mathbf{r}_0, \omega, \sigma) = \hat{h}(\mathbf{r}, \omega, \sigma)\hat{h}^{-1}(\mathbf{r}_0, \omega, \sigma). \tag{13.26}$$

The operators $\hat{Z}$, $\hat{Y}$, $\hat{t}$, and $\hat{m}$, are called the *magnetotelluric operators*. The four operators evoke the transformation of the electric and magnetic fields one to the other. Each type of magnetotelluric variation is characterized by its own set of operators, $\hat{Z}$, $\hat{Y}$, $\hat{t}$, and $\hat{m}$, which depend only on frequency, the location of the observation point, the strength and orientation of the ionospheric and magnetospheric currents, and the distribution of electrical conductivity in the medium, σ.

The magnetotelluric operators on a given set of basis functions have corresponding matrices which are called the *magnetotelluric matrices*. Differences in these matrices reflect differences in the type of variation being observed. For micropulsations and storm-time excitation observed at low to mid latitudes (that is, for the variations which are most commonly used in geophysical exploration because of the frequency window), the dimensionality of the magnetotelluric matrix is twofold (Berdichevsky

and Zhdanov, 1984). For such fields, if the horizontal components of the electric and magnetic fields are recorded, the matrix operators $\hat{Z}$, $\hat{Y}$, $\hat{t}$ and $\hat{m}$, in accord with the rules of linear algebra, take the form:

$$[Z_{\alpha\beta}] = \begin{bmatrix} Z_{xx} & Z_{xy} \\ Z_{yx} & Z_{yy} \end{bmatrix}, \tag{13.27}$$

$$[Y_{\alpha\beta}] = \begin{bmatrix} Y_{xx} & Y_{xy} \\ Y_{yx} & Y_{yy} \end{bmatrix}, \tag{13.28}$$

$$[t_{\alpha\beta}] = \begin{bmatrix} t_{xx} & t_{xy} \\ t_{yx} & t_{yy} \end{bmatrix}, \tag{13.29}$$

$$[m_{\alpha\beta}] = \begin{bmatrix} m_{xx} & m_{xy} \\ m_{yx} & m_{yy} \end{bmatrix}. \tag{13.30}$$

Consequently, in cases of operator relationships, Eqs. (13.20), (13.21), (13.24), and (13.25), we can write (Berdichevsky and Zhdanov, 1981, 1984):

$$\begin{aligned} E_x &= Z_{xx} H_x + Z_{xy} H_y, \\ E_y &= Z_{yx} H_x + Z_{yy} H_y, \end{aligned} \tag{13.31}$$

$$\begin{aligned} H_x &= Y_{xx} E_x + Y_{xy} E_y, \\ H_y &= Y_{yx} E_x + Y_{yy} E_y, \end{aligned} \tag{13.32}$$

$$\begin{aligned} E_x &= t_{xx} E_x(\mathbf{r}_0) + t_{xy} E_y(\mathbf{r}_0), \\ E_y &= t_{yx} E_x(\mathbf{r}_0) + t_{yy} E_y(\mathbf{r}_0), \end{aligned} \tag{13.33}$$

$$\begin{aligned} H_x &= m_{xx} H_x(\mathbf{r}_0) + m_{xy} H_y(\mathbf{r}_0), \\ H_y &= m_{yx} H_x(\mathbf{r}_0) + m_{yy} H_y(\mathbf{r}_0). \end{aligned} \tag{13.34}$$

13.3.2 INDUCTION VECTORS AND MAGNETIC AND ELECTRIC TIPPERS

When surveys are carried out in regions with a horizontally inhomogeneous geoelectric structure, the magnetic field **H** will have a significant vertical component (of course, the earth's steady magnetic field has a significant vertical component H_z almost everywhere, but it does not contribute to electromagnetic induction). In the case of a sea-bottom magnetoteluric survey over an area with a horizontally inhomogeneous geoelectric structure, the electric field **E** will have a significant vertical component E_z. In the theory of linear relationships, it can be shown that in cases of linear correlations of the type given in Eq. (13.31) through Eq. (13.34), supplementary formulas can be used:

$$\begin{aligned} H_z &= W_{zx} H_x + W_{zy} H_y, \end{aligned} \tag{13.35}$$
$$\begin{aligned} E_z &= V_{zx} E_x + V_{zy} E_y. \end{aligned} \tag{13.36}$$

Relationship (13.35) bears the name *Wiese-Parkinson relationship*. Formula (13.36) is an electric analog of the Wiese-Parkinson relationship. These relationships reflect the fact that the vertical components of the magnetic field H_z or electric field E_z at every point are linearly related to the horizontal components of the same field. As was the case with the various linear relationships described earlier, the Wiese-Parkinson relationship and its electric analog depend only on the coordinates of the observation point, $\mathbf{r}$, the frequency, ω, and the distribution of electrical conductivity in the medium. The values W_{zx} and W_{zy}, V_{zx}, and V_{zy} form complex vectors:

$$\mathbf{W} = W_{zx}\mathbf{d}_x + W_{zy}\mathbf{d}_y, \tag{13.37}$$
$$\mathbf{V} = V_{zx}\mathbf{d}_x + V_{zy}\mathbf{d}_y, \tag{13.38}$$

in which the real and imaginary parts are:

$$Re(\mathbf{W}) = Re\ W_{zx}\mathbf{d}_x + Re\ W_{zy}\mathbf{d}_y,\ Im(\mathbf{W}) = Im\ W_{zx}\mathbf{d}_x + Im\ W_{zy}\mathbf{d}_y, \tag{13.39}$$
$$Re(\mathbf{V}) = Re\ V_{zx}\mathbf{d}_x + Re\ V_{zy}\mathbf{d}_y,\ Im(\mathbf{V}) = Im\ V_{zx}\mathbf{d}_x + Im\ V_{zy}\mathbf{d}_y \tag{13.40}$$

Vector $\mathbf{W}$ is named the *Wiese-Parkinson vector*, or the *induction vector*. Vector $\mathbf{W}$ is often called a (magnetic) *tipper*.

By analogy, we will call vector $\mathbf{V}$ an *electric tipper*. Note that on land the vertical component of an electric field is negligibly small, $E_z = 0$, which results in a linear relationship between the horizontal components of the electric field:

$$V_{zx}E_x + V_{zy}E_y = 0. \tag{13.41}$$

However, in the case of measurements conducted on the sea bottom, $E_z \neq 0$, and the electric tipper reflects the horizontal inhomogeneities of the sea-bottom formations.

In summary, it has been shown that for an arbitrary distribution of electrical conductivity in the earth, a linear functional relationship of the type in Eqs. (13.31) through (13.38) exists between the components of the magnetotelluric field. The coefficients in these linear relationships (that is, the elements of the magnetotelluric matrix) are *transfer functions*. The elements of the magnetotelluric matrix are invariant on rotation: they reflect the distribution of electrical conductivity in the earth, but are independent of changes in the sources of the field – the magnetospheric and ionospheric currents. The transfer functions are also called *electrical conductivity functions*. The electrical conductivity functions, in contrast to measured electric and magnetic fields, carry information only about the internal geoelectric structure of the earth. Determining the electrical conductivity function is the basic step in application of the magnetotelluric method.

Determination of the conductivity function can be accomplished through use of statistical analysis methods including cross- and auto-correlation of field components and calculation of the coefficients of multiple linear regression. We will review in detail the techniques currently in use for determining the magnetotelluric matrix in the following sections.

We note in conclusion that linear operators can be considered as examples of rather more esoteric objects in linear algebra – tensors. Frequently, the magnetotelluric operators are called magnetotelluric tensors, and we speak of *tensor impedance*, *tensor admittance*, and *telluric* and *magnetic tensors*. In this text, in order to retain some simplicity in mathematical presentation, we will accept the linear operator approach and only mention the use of the tensor terminology.
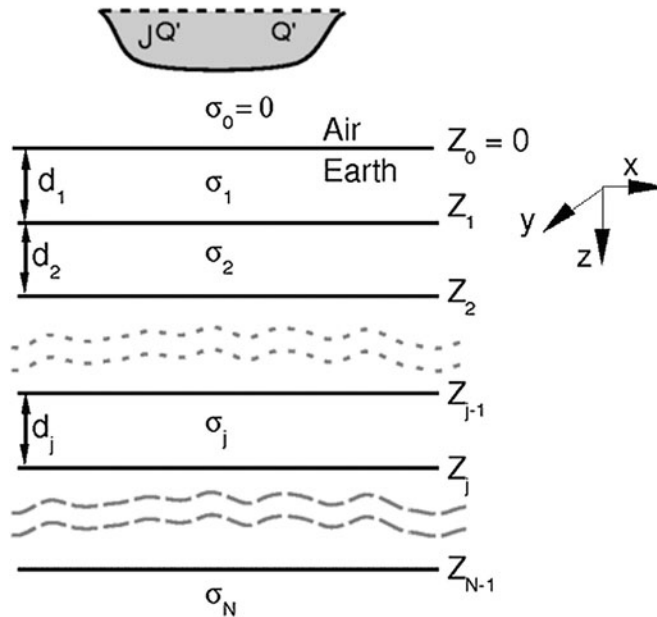
Model used in discussion of a magnetotelluric sounding of a layered earth. The source of the field is assumed to be a current system circulating at high attitude. The downward traveling electromagnetic field excites current flow in conductive layers in the earth. The electric field induced in the earth and the secondary magnetic field accompanying currents in the earth are the quantities to be measured in carrying out a magnetotelluric sounding.

13.3.3 SPECTRAL MAGNETOTELLURIC IMPEDANCES

In the Tikhonov-Cagniard model, which is fundamental to the theory underlying the magnetotelluric method, the external field is taken to be a plane wave vertically incident on the earth's surface. This model, as we have already noted, permits the easy development of a theory for magnetotelluric sounding in a horizontally homogeneous geoelectric medium. However, it is also important to solve the problem of excitation by an arbitrary system of magnetospheric currents (Fig. 13.16). This problem is of fundamental importance to electromagnetic sounding with controlled sources also.

We have demonstrated in Chapter 5 that, in this case we can use the spatial frequency domain (SFD) representation of the electromagnetic field, which allows us to determine the spectral magnetotelluric impedances.

In field practice, determination of the impedance ratios $h_z/h_z'\,|_{z=+0}$, $e_x/e_x'\,|_{z=+0}$ and $e_y/e_y'\,|_{z=+0}$ is difficult, inasmuch as they are the vertical derivatives of spatial spectrums. It is necessary to transform these ratios to use them. From the results of transformation we proceed to the ideas of magnetotelluric and magnetovariational impedances as introduced by M. N. Berdichevsky, L. L. Vanyan, and Ye. B. Fainberg in 1969.

- Definition 1. The ratio of the spatial spectrums from mutually orthogonal components of the electric and magnetic fields is called the *magnetotelluric spectral impedance*:

$$Z_{xy}^* = \frac{e_x}{h_y} |_{z=0} , \tag{13.42}$$

$$Z_{yx}^* = -\frac{e_y}{h_x} |_{z=0} . \tag{13.43}$$

- Definition 2. The ratio of the spatial spectrums of the vertical component to one of the horizontal components of the magnetic field is called the *magnetovariational transfer functions*:

$$Z_{h_x}^* = \frac{\omega\mu_0 k_x}{n_0^2} \frac{h_z}{h_x} |_{z=0} , \tag{13.44}$$

$$Z_{h_y}^* = \frac{\omega\mu_0 k_y}{n_0^2} \frac{h_z}{h_y} |_{z=0} , \tag{13.45}$$

where $n_0^2 = k_x^2 + k_y^2$.

We note, however, that the spectral impedance can be evaluated either on the surface of a horizontally homogeneous layered earth or on the surface of an inhomogeneous earth. In either case, without regard to the distribution of electrical conductivity, the magnetovariational impedances are always equal:

$$Z_{h_x}^* = Z_{h_y}^* = Z_h^*. \tag{13.46}$$

To demonstrate this, consider the first Maxwellian equation in the insulating upper half-space:

$$curl\mathbf{H} = 0 \text{ for } z \leq -0.$$

Hence, in particular

$$\partial H_y/\partial x - \partial H_x/\partial y = 0 \text{ for } z \leq -0.$$

Transforming this expression to spatial spectrums, we obtain:

$$-ik_x h_y - (-ik_y h_x) = 0,$$

or $h_y/k_y = h_x/k_x$ for negative z.

Recognizing the requirement for continuity of the spectrums of the horizontal components of the field at the earth-air interface, we write:

$$\frac{h_y}{k_y}\bigg|_{z=0} = \frac{h_x}{k_x}\bigg|_{z=0} . \tag{13.47}$$

This last formula indicates that the spectrums for the horizontal components of the magnetic field on the surface of the earth are always linearly polarized (independent of the distribution of either the ionospheric currents or the conductivity of the earth). This means that the spectrum for one of the

components of the field can always be determined from the spectrum of the other. Substitution of Eq. (13.47) into (13.44) also leads to Eq. (13.46).

The expression for the magnetovariational impedance spectrum can be written in the form

$$Z_h^* = \left.\frac{\omega\mu_0 h_z}{k_x h_x + k_y h_y}\right|_{z=0}. \tag{13.48}$$

On the basis of Maxwell's condition on the divergence of the magnetic field vector:

$$div\mathbf{H} = \partial H_x/\partial x + \partial H_y/\partial y + \partial H_z/\partial z,$$

and writing it in the frequency domain

$$-ik_x h_x - ik_y h_y + h_z' = 0,$$

and hence

$$h_z' = i(k_x h_x + k_y h_y). \tag{13.49}$$

Substituting Eq. (13.49) into Eq. (13.48), we finally write

$$Z_h^* = \left.i\omega\mu_0\frac{h_z}{h_z'}\right|_{z=0}. \tag{13.50}$$

In summary, we have two magnetotelluric impedance spectrums, Z_{xy}^* and Z_{yx}^* and one magnetovariational impedance, Z_h^*, specified by Eq. (13.46), (13.48), or (13.50). In general, the presence of two-dimensional or three-dimensional conductivity distributions is indicated by these three impedances not all being equal. All three impedances will be equal when measured on the surface of a horizontally uniform layered earth.

Furthermore, with a horizontally stratified section, we can use formula (5.19) to write

$$h_x = -\frac{1}{i\omega\mu_0}e_y', \tag{13.51}$$

$$h_y = \frac{1}{i\omega\mu_0}e_x'. \tag{13.52}$$

Substituting Eq. (13.52) into (13.42) and (13.51) into (13.43), we obtain

$$Z_{xy}^* = \left.i\omega\mu_0\frac{e_x}{e_x'}\right|_{z=+0},$$

$$Z_{yx}^* = \left.i\omega\mu_0\frac{e_y}{e_y'}\right|_{z=+0}. \tag{13.53}$$

Considering Eqs. (5.184) and (5.203), Eqs. (13.50) and (13.53) can be combined into one:

$$Z_h^* = Z_{xy}^* = Z_{yx}^* = (-i\omega\mu_0/n_1)R_N^*, \tag{13.54}$$

where

$$n_1 = (k_x^2 + k_y^2 - k_1^2)^{1/2} = (k_x^2 + k_y^2 - i\omega\mu_0\sigma_1)^{1/2}, \ Re(n_1) > 0.$$

Thus, both the magnetotelluric and magnetovariational impedances are expressed in terms of the reduced impedance spectrum R_N^*, and so, each of these impedances in a one-dimensional geoelectric model can be designated as Z^* and called the *spectral impedance of a horizontally layered earth*:

$$Z^* = -(i\omega\mu_0/n_1)R_N^*. \tag{13.55}$$

At this point we can review some simple properties of the spectral impedance Z^*. First of all, we note that, for a homogeneous half-space, the spectral impedance is

$$Z^* = -i\omega\mu_0/n_1, \tag{13.56}$$

inasmuch as

$$R_1(d_1 \to \infty) = coth(n_1 d_1) = 1$$

for this case.

Next, we will consider the high- and low-frequency (with respect to the temporal variable ω) asymptotes to Eqs. (13.44) and (13.45).

- 1. Let $\omega \to 0$ (the low-frequency asymptote). Then

$$Z^*(\omega \to 0) \sim -i\omega\mu_0/n_0, \tag{13.57}$$

where the sign $\sim$ indicates an asymptotic equality.

We see that the right-hand side of Eq. (13.57) is independent of conductivity; that is, the earth is transparent to the passage of electromagnetic fields at low frequencies.

- 2. Let ω become infinite (the high frequency asymptote). Then it can readily be shown that

$$n_1(\omega \to \infty) \sim -ik_1. \tag{13.58}$$

The minus sign in this last equation indicates that $Im(k_1) > 0$. Consequently, Eq. (13.58) corresponds to Eq. (13.48) with Re $(n_1) > 0$.

Substituting Eq. (13.58) into Eq. (13.56), we have

$$Z^*_{\omega \to \infty} \sim \omega\mu_0/k_1. \tag{13.59}$$

That is, the spectral impedance at high temporal frequency asymptotically approaches the Tikhonov-Cagniard impedance for a homogeneous half-space with the wave number of the near-surface rocks (Eq. (13.48)).

This behavior can be extended in general to an N-layer sequence:

$$Z^*_{\omega \to 0} \sim Z = \frac{\omega\mu_0}{k_1}R_N, \tag{13.60}$$

where Z is the usual Tikhonov-Cagniard impedance and R_N is given by Eq. (5.183).
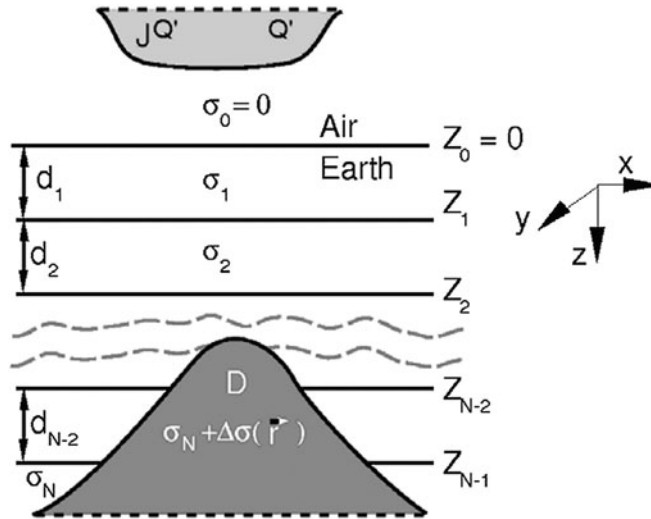
Model used in developing the concepts of internal, external, normal, and anomalous parts of an electromagnetic field. In contrast to the model in Fig. 13.16, this model includes a region, D, with a resistivity distribution that differs from a one-dimensional resistivity profile.

13.4 MAGNETOTELLURIC FIELDS IN HORIZONTALLY INHOMOGENEOUS MEDIA

Up to this point, we have organized our analysis only for a simple geoelectric model, that of a horizontally stratified medium. But, the real earth is inhomogeneous both horizontally and vertically. To construct a complete model for the magnetotelluric methods, we must consider the basic features of the propagation of the MT field in inhomogeneous conducting media (that is, for two-dimensional and three-dimensional models, as well as one-dimensional models).

13.4.1 CONCEPTS OF EXTERNAL AND INTERNAL, NORMAL AND ANOMALOUS PARTS OF AN ELECTROMAGNETIC FIELD

We will examine a model in which a conducting earth is bounded at $z = 0$ by a uniform insulating half-space (Fig. 13.17). The distribution of electrical conductivity in the earth will be represented in the form:

$$\sigma(\mathbf{r}) = \sigma_n(z) + \Delta\sigma(\mathbf{r}), \tag{13.61}$$

where $\sigma_n(z)$ is the normal distribution of electrical conductivity, characteristic of an N-layered horizontally stratified earth, $\Delta\sigma$ is the anomalous (disturbing) electrical conductivity, defined as the deviation

of resistivity in an inhomogeneous region D from that of the normal section,

$$\Delta\sigma(\mathbf{r}) = \sigma(\mathbf{r}) - \sigma_n(z), \ \mathbf{r} \in D. \tag{13.62}$$

The field in this model is excited by the flow of currents with a density $\mathbf{j}^Q$ in a region Q in the upper half-space (Fig. 13.17).

The distinction between internal and external fields is of great importance in the theory of electromagnetic induction in the earth.

Definition 1. The field excited by the magnetospheric-ionospheric currents $\mathbf{j}^Q$ in the absence of a conducting earth is called the *external field*. It is designated with the symbols $\mathbf{H}^e$ and $\mathbf{E}^e$.

Definition 2. The part of the total field excited by telluric currents induced in a conducting earth is called the *internal field*, and is designated by the symbols $\mathbf{H}^i$ and $\mathbf{E}^i$.

With these definitions, the total electromagnetic field in the model will be the sum of the internal and external fields:

$$\mathbf{H} = \mathbf{H}^e + \mathbf{H}^i,$$
$$\mathbf{E} = \mathbf{E}^e + \mathbf{E}^i. \tag{13.63}$$

In these equations, the external fields take the form

$$curl\ \mathbf{H}^e = \mathbf{j}^Q,$$
$$curl\ \mathbf{E}^e = i\omega\mu_0\mathbf{H}. \tag{13.64}$$

To describe the electromagnetic field in the model we are considering, in addition to the terms in Eq. (13.63), we can also represent the total fields as the sum of normal $\mathbf{H}^n$ and $\mathbf{E}^n$ and anomalous $\mathbf{H}^a$ and $\mathbf{E}^a$ fields:

$$\mathbf{H} = \mathbf{H}^n + \mathbf{H}^a,$$
$$\mathbf{E} = \mathbf{E}^n + \mathbf{E}^a. \tag{13.65}$$

Definition 3. The field excited by the magnetospheric-ionospheric currents $\mathbf{j}^Q$ in normal, horizontally stratified earth, $\sigma_n(z)$, is called the *normal field*.

Definition 4. The part of the total field contributed by the distortion of current flow, $\mathbf{j}^D = \Delta\sigma\mathbf{E}$, in the inhomogeneous region D is called the *anomalous field*.

The normal field satisfies the equations:

$$curl\ \mathbf{H}^n = \begin{pmatrix} \mathbf{j}^Q, z \leq 0 \\ \sigma_n\mathbf{E}, z \geq 0 \end{pmatrix},$$
$$curl\ \mathbf{E}^n = i\omega\mu_0^n\mathbf{H}. \tag{13.66}$$

13.4.2 ANOMALOUS ELECTROMAGNETIC FIELDS AND THEIR CLASSIFICATION

Anomalous electromagnetic fields, or electromagnetic anomalies, reflect the effect of horizontal geo-electric inhomogeneities. Depending on the depth to the geoelectric inhomogeneity, electromagnetic anomalies can be divided into two classes:

* a) *near-surface anomalies*, indicating inhomogeneities in the shallow layers forming the sedimentary complex and ocean basins; and
* b) *deep-seated anomalies*, related to inhomogeneities in earth's crystalline crust and upper mantle.

If near-surface and deep-seated anomalies are coincident in location, the distinction between the two is difficult. Anomalous fields from shallow-seated structures affect current flow in deep-seated regions, while anomalous fields from the deep-seated regions excite effects in the near surface. The two forms of anomaly can interact in such a way that the combined effect is not merely the sum of a deep anomaly and a shallow anomaly. Such anomalies can often be distinguished on the basis of the distribution of deviant currents.

Broad anomalies which extend for hundreds or even thousands of kilometers over the surface of the earth, are called *regional anomalies*. Regional anomalies are found over major geological structures, such as depressions in the crystalline basement surface filled with conductive sedimentary rocks, or zones of enhanced conductivity in the upper mantle. Anomalies associated with coastal effects and the ocean basins are also regional in character.

Against a background of regional anomalies, one finds local anomalies which have dimensions of tens of kilometers. These local anomalies are often associated with lateral changes in the character of sedimentary rocks, deep faults and displacements, hydrothermal action, and many other factors which will affect the conductivity of rocks locally. The form of an electromagnetic anomaly will depend on the geometry of the geoelectric inhomogeneity. In electrical prospecting, we talk of two-dimensional and three-dimensional inhomogeneities. Two-dimensional inhomogeneities might be considered to be mathematical abstractions, existing only in theory. However, if the real inhomogeneity has a length which is considerably greater than its width, there is considerable merit in treating it as two-dimensional, that is, independent of one coordinate. We might call such anomalies *quasi two-dimensional*. Structures which cannot be called two dimensional by any stretch of the imagination are considered to be *three-dimensional*.

13.4.3 FIELDS IN TWO-DIMENSIONALLY INHOMOGENEOUS MEDIA AND THE CONCEPTS OF E AND H POLARIZATION

In order to simplify or discussion of two-dimensional structures, we will always use coordinate systems in which the long extent of the two-dimensional structure lies along the y axis (Fig. 13.17). We will also assume that the current density in the magnetosphere and ionosphere will not vary along the y direction. Therefore, the electromagnetic field in a given model will also be two-dimensional; that is, it will not vary along the y axis.

For such two-dimensional models, we can simplify Maxwell's equations,

$$curl\mathbf{H} = \sigma\mathbf{E} + \mathbf{j}^Q,$$
$$curl\,\mathbf{E} = i\omega\mu_0\mathbf{H},$$

as follows. Considering that all derivatives with respect to y are zero, the scalar expressions for Maxwell's equations can be written as

$$-\partial H_y/\partial z = \sigma E_x + j_x^Q. \tag{13.67}$$

$$\partial H_x/\partial z - \partial H_z/\partial x = \sigma E_y + j_y^Q, \tag{13.68}$$

$$\partial H_y/\partial x = \sigma E_z + j_z^Q, \tag{13.69}$$

$$-\partial E_y/\partial z = i\omega\mu_0 H_x, \tag{13.70}$$

$$\partial E_x/\partial z - \partial E_z/\partial x = i\omega\mu_0 H_y, \tag{13.71}$$

$$\partial E_y/\partial x = i\omega\mu_0 H_z, \tag{13.72}$$

where $\sigma = \sigma(x, z)$ is the conductivity as a function of location in the xz plane.

We find that only the field components E_x, H_y, and E_z are present in Eqs. (13.67), (13.69), and (13.71), while only the components H_x, E_y, and H_z are present in Eqs. (13.68), (13.70), and (13.72). The advantage of using two-dimensional models lies largely in the fact that Maxwell's equations separate naturally into two independent systems:

$$-\partial H_y/\partial z = \sigma E_x + j_x^Q, \tag{13.73}$$

$$\partial E_x/\partial z - \partial E_z/\partial x = i\omega\mu_0 H_y, \tag{13.74}$$

$$\partial H_y/\partial x = \sigma E_z + j_z^Q, \tag{13.75}$$

and

$$-\partial E_y/\partial z = i\omega\mu_0 H_x, \tag{13.76}$$

$$\partial H_x/\partial z - \partial H_z/\partial x = \sigma E_y + j_y^Q, \tag{13.77}$$

$$\partial E_y/\partial x = i\omega\mu_0 H_z. \tag{13.78}$$

At this point, we introduce a standard notation:

$$\mathbf{E}^H = (E_x, 0, E_z),$$
$$\mathbf{H}^H = (0, H_y, 0), \tag{13.79}$$
$$\mathbf{E}^E = (0, E_y, 0),$$
$$\mathbf{H}^E = (H_x, 0, H_z). \tag{13.80}$$

The field $\mathbf{E}^H$, $\mathbf{H}^H$ is called an *H-polarized field* because the magnetic field has only a single component, H_y, which is nonzero (that is, the magnetic field is polarized to lie always on the long axis of the structure). Likewise, the field $\mathbf{E}^E$, $\mathbf{H}^E$ is called an *E-polarized field* because only the single component E_y of the electric field is nonzero (the electric field is polarized to lie always on the long axis of the structure). Eqs. (13.73) to (13.75) characterize the behavior of the H-polarized field, and Eqs. (13.76) to (13.78) characterize the behavior of the E-polarized field. Because these two sets of equations are independent of one another, we conclude that when the earth is structured in only two dimensions, the

total electromagnetic field reduces to the sum of H- and E-polarized fields which propagate in the earth independently of one another:

$$\mathbf{E} = \mathbf{E}^H + \mathbf{E}^E,$$
$$\mathbf{H} = \mathbf{H}^H + \mathbf{H}^E.$$

The problem of studying the interaction of an electromagnetic field with a two-dimensionally structured earth reduces to the solution of two far simpler problems, the solution of problems for E-polarized and H-polarized fields separately. The simplicity lies in the fact that when E-polarized or H-polarized fields are considered, Maxwell's vector equations reduce to scalar differential equations.

Initially, let us examine a case with E polarization (Eqs. (13.68), (13.70), and (13.72)). Substituting Eqs. (13.70) and (13.72) into (13.68), we obtain

$$\tilde{\nabla}^2 E_y + k^2 E_y = -i\omega\mu_0 j_y^Q, \tag{13.81}$$

where $\tilde{\nabla}^2$ is a two-dimensional Laplace operator, $\partial^2/\partial x^2 + \partial^2/\partial z^2$, and $k^2 = k^2(x, z) = i\omega\mu_0\sigma(x, z)$.

Thus, the y component of the electric field for E polarization satisfies a two-dimensional Helmholtz equation with the variable wave number, $k(x, z)$. The magnetic components of the field in this case are found simply by differentiating E_y according to Eqs. (13.70) and (13.72).

In the case of H polarization, by substituting Eqs. (13.73) and (13.75) into Eq. (13.74), we find

$$\frac{\partial}{\partial x}\left(\frac{1}{k^2}\frac{\partial H_y}{\partial x}\right) + \frac{\partial}{\partial z}\left(\frac{1}{k^2}\frac{\partial H_y}{\partial z}\right) + H_y = 0. \tag{13.82}$$

In summary, two-dimensional models permit a great reduction in the amount of computation necessary for the solution of forward or inverse geoelectric problems. Because of this, such models are widely used in most forms of electrical exploration.

13.5 MAGNETOTELLURIC AND MAGNETOVARIATIONAL SURVEYS

Over the years, many effective and practical systems for observing the magnetotelluric field have been developed. A number of basically different field survey approaches have been introduced: magnetotelluric sounding (MTS), magnetotelluric profiling (MTP), telluric current mapping (TCM), magnetovariation sounding (MVS), magnetovariational profiling (MVP), geomagnetic deep sounding (GDS), and comprehensive geoelectric deep sounding. We will now characterize each of these methods briefly.

13.5.1 THE MTS, MTP, AND TCM METHODS

The standardized magnetotelluric sounding method on land consists of recording the five components of the magnetotelluric field, E_x, E_y, H_x, H_y, and H_z (E_z is considered to be nonexistent on the earth's surface), simultaneously at one or several locations. The standard field sensing system makes use of two mutually perpendicular E-field sensing electrode pairs, M_1N_1 and M_2N_2, laid out to detect two orthogonal E-field components, and three mutually perpendicular magnetic field sensors to detect three
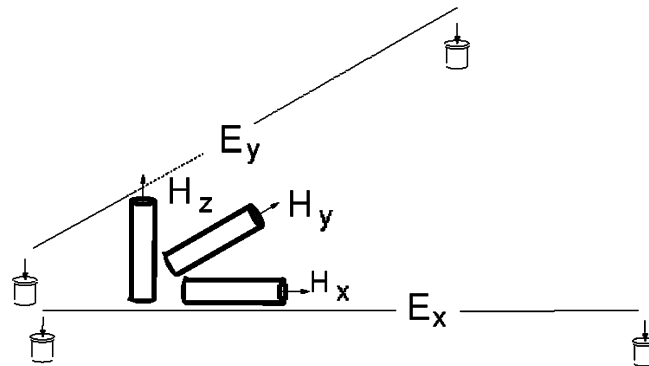
FIGURE 13.18

Layout of sensors for a single magnetotelluric sounding. Three components of the magnetic field are measured, using sensitive vector magnetometers, often induction coils. Two components of the electric field are detected by measuring the voltage between pairs of electrodes, usually separated by a distance of a few hundred meters.

magnetic field components, H_x, H_y, and H_z (Fig. 13.18). The usual convention is to measure the electric field in millivolts per kilometer. This strange unit was suggested by Cagniard as being appropriate for geophysicists, because the electrode separations normally used are of the order of a kilometer, and the voltages normally detected are of the order of a millivolt. A unit more commonly used for expressing electric fields by electrical engineers is the microvolt per meter, which is numerically the same as the millivolt per kilometer.

The magnetic field components are measured in nanoteslas, a nanotesla being one part in a billion of the tesla, the MKS unit for magnetic field strength. Cagniard had taken the "gamma," an antiquated geophysical unit for the magnetic field, as his convention for defining apparent resistivity derived from magnetotelluric data. Fortunately for geophysicists, when the MKS system is used rather than the older cgs system of units, the geophysical unit, the *gamma*, is numerically the same as the new unit, the *nanotesla*.

In computations, it is useful to remember that the MKS unit, the nanotesla, is convertible to the earlier used unit, the ampere per meter, as follows:

$$1 \, nT = .01/4\pi \ A/m$$

or

$$1 \, A/m = 1 \, nT/1256.$$

The separation between electrode contacts used in measuring the electric field commonly ranges from 200 to 500 meters, though for special purposes, separations of as little as a few meters and as large as many kilometers can be used. It is normal field practice to have the two pairs of electrodes separated along lines in orthogonal directions; this leads to a slight simplification in determining normal components of the field, but is not necessary. The best orientations for the two pairs of electrodes

is determined by practical considerations, such as ease of access, and by technical considerations. The primary technical consideration is the *strike* of the geology. If the geology is two-dimensional in character, as often is the case, experience has shown that, from a practical point of view, better results are often obtained if the sensors are oriented parallel and transverse to the strike of the geological formation.

The range of periods normally recorded will lie in the so-called magnetotelluric window; that is, in the range of periods from one millisecond to one kilosecond. For very deep soundings, periods of one hour (3.6 kiloseconds) or one day (86.4 kiloseconds) may be needed.

Data processing includes conversion of the time series actually measured in recording the five field components to power density spectrums in the frequency domain and determination of the impedance tensor, Z, and the admittance tensor, Y. The elements of these tensors are, as was shown earlier, functions of conductivity; that is, they depend only on the location of the field station, the temporal frequency and the distribution of electrical conductivity in the earth. These functions are used in further interpretation to construct apparent resistivity curves and in inversion to obtain a geoelectric model. Data processing and inversion are discussed in detail in other sections of this book.

A modification of the MTS method which is simpler in concept is the magnetotelluric profiling method. The same general type of observation equipment is used, but measurements are made over a relatively narrow band of periods. Often the periods used cover the Pc-2 to Pc-3 bands, in the range of 10 to 100 seconds. This band is easily observable at most times, and for many regions, the impedance which is determined lies on a rising branch of the MT sounding curve, so that even though the curve is not defined over a broad enough period range to allow inversion to obtain a layered model, values for the cumulative conductance can be derived. In this respect, the MTP method has proved to be most effective in regions where measurements are made over a sedimentary sequence of a few kilometers thickness resting on a high resistivity basement. In such areas, the value for S can be used to map areal changes in the thickness and character of the sedimentary rocks. Maps of changing conductance can often be used to infer the structure on the basement surface. However, such information must be supplemented by independent information on the conductivity of the sedimentary sequence, possibly available from electrical well logs run in control wells.

In the telluric current mapping (TCM) method, two components of the horizontal electric field, E_x and E_y, are recorded simultaneously at two sites, one used as a fixed base station, and the other serving as a roving station. The base station remains at its single location, while the roving station is moved from site to site to complete a survey.

Reduction of TCM observations can be done either by visual identification of quasi-stationary variations (manual data reduction), or by temporal power density analysis of the varying telluric electric field with subsequent determination of the telluric transfer function $t(r/r_0)$. Here, r is the radius vector from some arbitrarily chosen origin for a coordinate system on the earth's surface to the location of the roving station, and r_0 is the radius vector to the base station. Experience suggests that the distance between the base station and the roving station should not exceed 80 to 100 kilometers, or the telluric transfer function may prove not to be invariant (that is, the two electric fields may not be exactly linearly correlative over large distances). If a large area is to be surveyed, several base stations may be required, with the network of observations from one base station being "tied" to the network of observations using the next base station.

The results of the data reduction process are used to construct maps showing the areal distribution of various elements in the telluric-electric transfer function, or various parameters derived from those

elements. These parameters are functions of the electrical conductivity structure. In particular, the most useful of these maps is the map showing the distribution of cumulative conductance, S.

In the case of marine MT method, which has become widely used recently, all six components of magnetotelluric field, E_x, E_y, E_z, H_x, H_y, and H_z, are measured on the sea bottom.

13.5.2 MVS AND MVP SURVEY METHODS

The magnetovariation profiling method consists of recording the three time-varying components of the magnetic field, H_x, H_y, and H_z, simultaneously. Observations can be carried out using only a single observation location which moves progressively along a profile, or by using two stations, one a base station and the other a roving station (similar to the field procedure used in the TCM method). Depending on the nature of the geologic problem being studied, the period band may range from windows covering periods of a few seconds to windows covering periods of a few hours or even a few days. Reduction of field data is accomplished either using visual identification of events (manual processing) or by temporal power density analysis with the subsequent determination of a magnetic transfer function, $\hat{m}(\mathbf{r}, \mathbf{r}_0)$ or magnetic induction vector. The scalar components of the transfer function or the induction vector depend only on the location of the observation site, the temporal frequency, and the geoelectric section. Qualitative and quantitative analysis of maps showing the areal distribution of these measurement-derived quantities often lead to meaningful conclusions of geological importance, such as the construction of contour maps of S, the conductance of some part of the crust.

A modification of the MVP method which has not yet been widely used is the method of *magnetovariational sounding* (MVS). In the field, the same measurement technique as is used in magneto-variational profiling is used for magnetovariational sounding. Only the objective is changed; we wish to determine the variation of conductivity with depth, rather than along a horizontal profile. The MVS method can be considered to be the equivalent of the MTS method, but with gradients of the magnetic field components being used in place of the electric field observations required in the MTS method. Using data recorded simultaneously with an array of at least three field sites which lie at relatively short distances from one another, one can determine the horizontal gradients of the magnetic fields approximately, using the differences between pairs of stations. One can then compute a transfer function, T, from the following formula, assuming the magnetic field components and their spatial derivatives are linearly related:

$$T = -i\omega\mu_0 \frac{H_z}{\partial H_x/\partial x + \partial H_y/\partial y}. \tag{13.83}$$

This transfer function, T, is numerically equal to the Tikhonov-Cagniard impedance, Z, in a laterally uniform (stratified) medium. Using this transfer function, one can derive an apparent resistivity for the medium and construct a sounding curve.

If the medium is laterally inhomogeneous, the MVS and MTS methods will give different representations of the medium. The use of the two methods together gives the potential for a more definitive description of the geoelectric section than does the use of either method separately. The MVS method offers the possibility of resolving the problem of "static shift," which is described in another section. Static shift is the most serious practical limitation that we encounter to the applicability of the MTS method.

13.5.3 CGDS SURVEY METHOD

It has come to be recognized that perhaps the most effective way to probe the earth with natural electromagnetic fields is through the combined use of magnetotelluric and magnetovariational methods in what can well be called "comprehensive geoelectric deep sounding." Such a method would require the simultaneous observation of all five components of the field at two locations, one a base station and the other a roving station, over a wide range of periods.

Analysis of such data sets would first consist of a temporal power density analyses for each recorded field component, followed by a determination of each appropriate transfer function, including the impedances, Z, the admittances, Y, the telluric and magnetic transfer functions, t and m, and the induction vector. The redundancy provided by the determination of all these quantities related to the geoelectric structure of the earth should permit modeling of the geoelectric structure with a much higher degree of confidence than is possible when only one or two of these functions is used in interpretation.

13.6 PROCESSING AND ANALYSIS OF MT AND MV DATA

Processing of the data observed in magnetotelluric and magnetovariational surveys involves determination of the magnetotelluric transfer functions Z, Y, t, and m and the components of the magnetic and electric tippers, W and V. Along with the elements of the transfer function matrices, several other matrix invariants are also determined, including the effective impedance, $Z_{ef} = (Det[Z])^{1/2}$ the effective admittance, $Y_{ef} = (Det[Y])^{1/2}$, the telluric parameter, $K = (Det[t])^{1/2}$, and the magnetic parameter, $L = (Det[m])^{1/2}$.

It should be noted that in practice, the linear correlation between the components of the magnetotelluric field expressed by the functional relationships of the forms in Eqs. (13.31)–(13.34) is only approximate, not exact. In the linear systems describing the conductivity of the earth, there exists some noise, apparently arising from 1) departure of the actual field from the simplified form assumed in deriving the linear relationships (for example, departure from plane-wave behavior), and 2) measurement noise arising from instrumentally generated error signals, or proximity to errant currents of industrial or electrochemical origin, or other sources.

Because of this, it is necessary to introduce an additive term characterizing errors in the linear relationship into Eqs. (13.31)–(13.34). For example, the impedance equation, Eq. (13.31), might be written as:

$$E_x = Z_{xx} H_x + Z_{xy} H_y + r_x,$$
$$E_y = Z_{yx} H_x + Z_{yy} H_y + r_y, \tag{13.84}$$

while the corresponding magnetic and electric tipper equations might be written as:

$$H_z = W_{zx} H_x + W_{zy} H_y + r_z, \tag{13.85}$$
$$E_z = V_{zx} E_x + V_{zy} E_y + r_z^E, \tag{13.86}$$

where r_x, r_y, r_z, and r_z^E, are the corresponding error functions (residual noise). Similar terms describing errors in linearity arise in the practical reduction of experimental data in all of the Eqs. (13.32)–(13.34).

In summary, the problem of reducing magnetotelluric observational data is essentially a statistical problem of establishing a linear correlation between various experimental parameters in the presence of significant noise. In this section, we will examine the most widely used methods of data reduction, starting with the traditional method of least squares, and progressing to the newer techniques of remote referencing and robust estimation of spectrums.

13.6.1 THE LEAST-SQUARES METHOD

Perhaps the most commonly used method of determining the parameters defining the linear relationships between experimental data is the method of least squares. We assume that in a series of measurements, we have obtained N independent values of each component of the electric and magnetic fields at a given temporal frequency, ω:

$$E_i^x, E_i^y, E_i^z, H_i^z, H_i^x, H_i^y, i = 1, 2, ..., N.$$

In practice, these values have been obtained by Fourier transformation of various segments of experimentally observed time series. In accord with Eqs. (13.84) through (13.86), we write

$$E_{x_i} = Z_{xx} H_{x_i} + Z_{xy} H_{y_i} + r_{x_i}, \tag{13.87}$$

$$E_{y_i} = Z_{yx} H_{x_i} + Z_{yy} H_{y_i} + r_{y_i}, \tag{13.88}$$

$$H_{z_i} = W_{zx} H_{x_i} + W_{zy} H_{y_i} + r_{z_i}, \tag{13.89}$$

$$E_{z_i} = V_{zx} E_{x_i} + V_{zy} E_{y_i} + r_{z_i}^E. \tag{13.90}$$

We note that the linear relationships are complex vector functions including the error terms, $r_{x_i}, r_{y_i}, r_{z_i}$, and $r_{z_i}^E$.

The least-squares method permits us to find some transfer function (that is, the elements of a magnetotelluric or magnetovariational matrix) which minimizes the sum of the squares of the moduli of the errors in the linear relationship:

$$\phi_x(Z_{xx}, Z_{xy}) = \sum_{i=1}^{N} |r_{x_i}|^2 = \sum_{i=1}^{N} |E_{x_i} - Z_{xx} H_{x_i} - Z_{xy} H_{y_i}|^2 = \min, \tag{13.91}$$

$$\phi_y(Z_{yx}, Z_{yy}) = \sum_{i=1}^{N} |r_{y_i}|^2 = \sum_{i=1}^{N} |E_{y_i} - Z_{yx} H_{x_i} - Z_{yy} H_{y_i}|^2 = \min, \tag{13.92}$$

$$\phi_z(W_{zx}, W_{zy}) = \sum_{i=1}^{N} |r_{z_i}|^2 = \sum_{i=1}^{N} |H_{z_i} - W_{zx} H_{x_i} - W_{zy} H_{y_i}|^2 = \min, \tag{13.93}$$

$$\phi_z^E(V_{zx}, V_{zy}) = \sum_{i=1}^{N} |r_{z_i}^E|^2 = \sum_{i=1}^{N} |E_{z_i} - V_{zx} E_{x_i} - V_{zy} E_{y_i}|^2 = \min. \tag{13.94}$$

In particular, the condition for minimizing the function $\phi_z(W_{zx}, W_{zy})$ permitting us to find the Wiese-Parkinson vector, is the following relationship:

$$\frac{\partial \phi_z}{\partial W_{zx}} = \frac{\partial \phi_z}{\partial W_{zy}} = 0. \tag{13.95}$$

We note that

$$|r_{z_i}|^2 = r_{z_i} r_{z_i}^*$$
$$= (H_{z_i} - W_{zx} H_{x_i} - W_{zy} H_{y_i})(H_{z_i} - W_{zx} H_{z_i} - W_{zy} H_{y_i})^*,$$

where the symbol (*) denotes a complex conjugate value.

Considering this last relationship and carrying out some simple algebraic operations on Eq. (13.95), we obtain:

$$\sum_{i=1}^N (H_{z_i} - W_{zx} H_{x_i} - W_{zy} H_{y_i}) H_{x_i}^* = 0,$$

$$\sum_{i=1}^N (H_{z_i} - W_{zx} H_{x_i} - W_{zy} H_{y_i}) H_{y_i}^* = 0. \tag{13.96}$$

Finally, solving Eq. (13.96) for W_{zx} and W_{zy}, we can write

$$\mathbf{W} = \mathbf{S}_{H_z H} \cdot \hat{S}_{HH}^{-1}, \tag{13.97}$$

where $\mathbf{W}$, $\mathbf{S}_{H_z H}$... are columnar matrices (vectors):

$$\mathbf{W} = [W_{zx}, W_{zy}],$$

$$\mathbf{S}_{H_z H} = \left[\sum_{i=1}^N H_{z_j} H_{x_i}^*, \sum_{i=1}^N H_{z_i} H_{y_i}^* \right], \tag{13.98}$$

and $\hat{S}_{HH}$ is a square matrix:

$$\hat{S}_{HH} = \begin{bmatrix} \sum_{i=1}^N H_{x_i} H_{x_i}^* & \sum_{i=1}^N H_{x_i} H_{y_i}^* \\ \sum_{i=1}^N H_{y_i} H_{x_i}^* & \sum_{i=1}^N H_{y_i} H_{y_i}^* \end{bmatrix}. \tag{13.99}$$

Using a similar approach, we find the following conditions for minimizing the functions $\phi_x(Z_{xx}, Z_{xy})$ and $\phi_y(Z_{yx}, Z_{yy})$:

$$\frac{\partial \phi_x}{\partial Z_{xx}} = \frac{\partial \phi_x}{\partial Z_{xy}} = 0, \tag{13.100}$$

$$\frac{\partial \phi_y}{\partial Z_{yy}} = \frac{\partial \phi_y}{\partial Z_{yx}} = 0. \tag{13.101}$$

We determine the impedance matrix as:

$$\hat{Z} = \hat{S}_{EH} \cdot \hat{S}_{HH}^{-1}, \tag{13.102}$$

where

$$\hat{Z} = \begin{bmatrix} Z_{xx} & Z_{xy} \\ Z_{yx} & Z_{yy} \end{bmatrix}, \tag{13.103}$$

$$\hat{S}_{EH} = \begin{bmatrix} \sum_{i=1}^{N} E_{x_i} H_{x_i}^* & \sum_{i=1}^{N} E_{x_i} H_{y_i}^* \\ \sum_{i=1}^{N} E_{y_i} H_{x_i}^* & \sum_{i=1}^{N} E_{y_i} H_{y_i}^* \end{bmatrix}. \tag{13.104}$$

We point out that the elements of matrices (13.99) and (13.104) are summations of N realizations of temporal power density or related spectral weights for components of the electric and magnetic fields. The spectral densities can be calculated using the auto-correlation and cross-correlation functions K_{EH} evaluated for an i-th interval ΔT_i, recorded as a time series of experimental data. For example,

$$E_{x_i} H_{y_i}^* = E_{x_i}(\omega) H_{y_i}^*(\omega) = \int_{\Delta T_i} K_{E_x H_y}(\tau) e^{i\omega\tau} d\tau, \tag{13.105}$$

where

$$K_{E_x H_y}(\tau) = \frac{1}{\Delta T_i} \int_{\Delta T_i} E_x(t) H_y(t + \tau) dt, \tag{13.106}$$

and similarly, for other components of the magnetotelluric field.

First, the time series of experimental data are filtered using a frequency filter or by applying a time-domain filter with the purpose of decreasing the influence of noise on the results. Narrow-band digital filters developed by Bezruk et al. (1978) and by Berdichevsky and Bezruk (1980) are widely used in practice. Here we will describe one such method taken from the work of Berdichevsky and Zhdanov (1984).

Using a data set $U(t)$ extending across a complex time window W_{ω_c} of width $2T_F$, there exists a frequency characteristic which is triangular narrow-band filter, $f_{\omega_c}(\omega)$, constructed on a center frequency, ω_c (Fig. 13.19):

$$U_{\omega_c}(t) = \int_{t-T_F}^{t+T_F} U(\tau) W_{\omega_c}(t - \tau) d\tau, \tag{13.107}$$

where

$$W_{\omega_c}(t) = Re W_{\omega_c}(t) + i Im W_{\omega_c}(t) = \frac{1}{\pi} \int_0^{\infty} f_{\omega_c}(\omega) e^{-i\omega t} d\omega. \tag{13.108}$$

It is clear that a narrow-band filter transforms the recorded time series of magnetotelluric data into a quasi-monochromatic variation with a center frequency ω_c equal to the characteristic frequency of the digital filter. Consequently, linear relationships of the type in Eqs. (13.87) through (13.90) can be used for multiple values (for different moments in time, t_i) of filtered quasi-chromatic fields $E_{x_{\omega_c}}(t_i)$, $E_{y_{\omega_c}}(t_i)$, $H_{x_{\omega_c}}(t_i)$, $H_{y_{\omega_c}}(t_i)$, and $H_{z_{\omega_c}}(t_i)$:

$$E_{x_{\omega_c}}(t_i) = Z_{xx}(\omega_c) H_{x_{\omega_c}}(t_i) + Z_{xy}(\omega_c) H_{y_{\omega_c}}(t_i) + r_{x_{\omega_c}}(t_i),$$
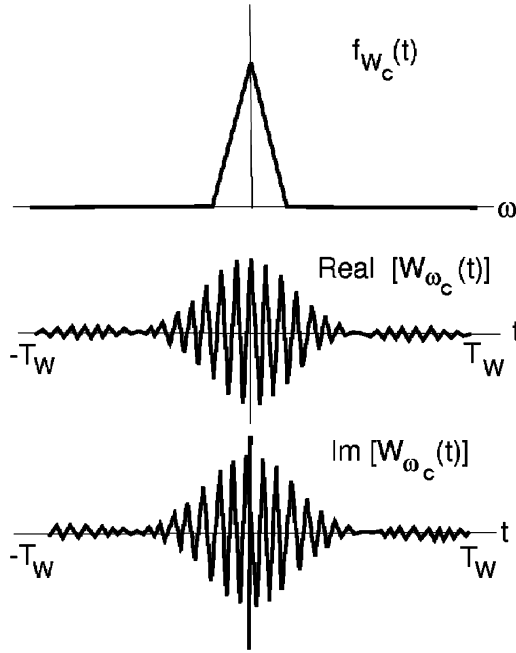
FIGURE 13.19

Frequency and time domain characterization of a filter response used in processing of magnetotelluric data.

$$E_{y_{\omega_c}}(t_i) = Z_{yx}(\omega_c)H_{x_{\omega_c}}(t_i) + Z_{yy}(\omega_c)H_{y_{\omega_c}}(t_i) + r_{y_{\omega_c}}(t_i), \tag{13.109}$$

$$H_{z_{\omega_c}}(t_i) = W_{zx}(\omega_c)H_{x_{\omega_c}}(t_i) + W_{zy}(\omega_c)H_{y_{\omega_c}}(t_i) + r_{z_{\omega_c}}(t_i), \tag{13.110}$$

$$E_{z_{\omega_c}}(t_i) = V_{zx}(\omega_c)E_{x_{\omega_c}}(t_i) + V_{zy}(\omega_c)E_{y_{\omega_c}}(t_i) + r^E_{z_{\omega_c}}(t_i), \tag{13.111}$$

with $i = 1, 2, ..., N$ and where $r_{x_{\omega_c}}$, $r_{y_{\omega_c}}$, $r_{z_{\omega_c}}$, and $r^E_{z_{\omega_c}}$, are noise terms rejected with some filter f_{ω_c}.

Solving the system of Eqs. (13.109), (13.110), and (13.111) using the least squares method, we can, as earlier, determine, for example, the impedance matrix and the Wiese-Parkinson vector for the frequencies ω_c:

$$\hat{Z} = \hat{F}_{EH}\hat{F}^{-1}_{HH}, \tag{13.112}$$

$$\mathbf{W} = \mathbf{F}_{H_z H}\hat{F}^{-1}_{HH}. \tag{13.113}$$

Here,

$$\hat{F}_{EH} = \begin{bmatrix} \sum_{i=1}^{N} E_{x_{\omega_c}}(t_i)H^*_{x_{\omega_c}}(t_i) & \sum_{i=1}^{N} E_{x_{\omega_c}}(t_i)H^*_{y_{\omega_c}}(t_i) \\ \sum_{i=1}^{N} E_{y_{\omega_c}}(t_i)H^*_{x_{\omega_c}}(t_i) & \sum_{i=1}^{N} E_{y_{\omega_c}}(t_i)H^*_{y_{\omega_c}}(t_i) \end{bmatrix},$$

$$\hat{F}_{HH} = \begin{bmatrix} \sum_{i=1}^{N} H_{x_{\omega_c}}(t_i) H_{x_{\omega_c}}^*(t_i) & \sum_{i=1}^{N} H_{x_{\omega_c}}(t_i) H_{y_{\omega_c}}^*(t_i) \\ \sum_{i=1}^{N} H_{y_{\omega_c}}(t_i) H_{x_{\omega_c}}^*(t_i) & \sum_{i=1}^{N} H_{y_{\omega_c}}(t_i) H_{y_{\omega_c}}^*(t_i) \end{bmatrix},$$

$$\mathbf{F}_{H_z H} = \left[\sum_{i=1}^{N} H_{z_{\omega_c}}(t_i) H_{x_{\omega_c}}^*(t_i), \sum_{i=1}^{N} H_{z_{\omega_c}}(t_i) H_{y_{\omega_c}}^*(t_i) \right]. \tag{13.114}$$

Similar equations can be written for the electric tipper, $\mathbf{V}$, as well.

The summations in Eq. (13.114) are done with the various instantaneous values for the complex amplitudes of the filtered fields, $E_{x_{\omega_c}}(t_i)$, $E_{y_{\omega_c}}(t_i)$, $H_{x_{\omega_c}}(t_i)$, $H_{y_{\omega_c}}(t_i)$, and $H_{z_{\omega_c}}(t_i)$. The asterisk indicates a complex conjugate value. In order to have some control of the accuracy with which the magnetotelluric and magnetovariational matrices are determined, *error predictors* are calculated for E_x, E_y, and H_z with respect to H_x and H_y. The term *predictor* is used to describe a computation in which one component of the field is computed from the others using the determined matrices $\hat{Z}$ and $\mathbf{W}$. The results of processing a data set are taken to be acceptable if the error does not exceed a few percent.

We must stress that the least-squares method, which is the basis for the approach to data reduction that has been described above, gives the best statistically based estimates for the magnetotelluric and induction matrices only when the residual noise components r_{x_i}, r_{y_i}, r_{z_i}, $r_{z_i}^E$ in Eqs. (13.87)–(13.90) satisfy the following three conditions. First, the noise components must be noncorrelated. Second, they must be normally distributed (that is, they must follow a Gaussian distribution). Third, the errors must be characterized by the same dispersion, σ^2.

In practice, any or all of the three conditions may be violated to some extent, and this can result in an unacceptable impact on the reliability of the magnetotelluric matrices determined using the least-squares method. For example, correlated noise is common in field measurements, resulting in significant confusion in the computed magnetotelluric matrix. More rarely, one encounters error predictors computed using the least-squares approach in cases where the errors in the observed data differ markedly from normally distributed (Gaussian) errors. Finally, uniform dispersion is not always present inasmuch as the observed dispersion of errors is linearly dependent on the amplitudes of the magnetotelluric micropulsations, particularly at long periods. All of these factors cause the magnetotelluric processes to be nonstationary in practice.

In more recent years, a number of improvements to the procedures for reducing magnetotelluric data have been advanced which will permit us to overcome the problems with the least-squares method which are listed above. Contemporary methods for processing magnetotelluric data will be described in the next several sections.

The weighted least-squares method

Let us consider the situation in which the noise terms r_{x_i}, r_{y_i}, and r_{z_i}, in the linear relationships of (13.87)–(13.90) are uncorrelated, normally distributed, and the dispersions differ one from another. This case has been examined by Egbert and Booker (1986); their approach is the basis for the following development. We first scale each term in Eqs. (13.87)–(13.90) in terms of the corresponding standard variations σ_{x_i}, σ_{y_i}, σ_{z_i}, $\sigma_{z_i}^E$:

$$E_{x_i}/\sigma_{x_i} = Z_{yy} H_{x_i}/\sigma_{x_i} + Z_{xy} H_{y_i}/\sigma_{x_i} + r_{x_i}/\sigma_{x_i}, \tag{13.115}$$

$$E_{y_i}/\sigma_{y_i} = Z_{yx} H_{x_i}/\sigma_{y_i} + Z_{yy} H_{y_i}/\sigma_{y_i} + r_{y_i}/\sigma_{y_i}, \tag{13.116}$$

$$H_{z_i}/\sigma_{z_i} = W_{zx}H_{x_i}/\sigma_{z_i} + W_{zy}H_{y_i}/\sigma_{z_i} + r_{z_i}/\sigma_{z_i}, \tag{13.117}$$

$$E_{z_i}/\sigma_{z_i}^E = V_{zx}E_{x_i}/\sigma_{z_i}^E + V_{zy}E_{y_i}/\sigma_{z_i}^E + r_{z_i}^E/\sigma_{z_i}^E. \tag{13.118}$$

Now, all of the errors in Eqs. (13.115)–(13.118) have unit dispersion. Thus, the standard method of least-squares can be used to find, for example, the magnetotelluric matrix $\hat{Z}$ and induction vector $\mathbf{W}$:

$$\sum_{i=1}^N \frac{r_{\alpha_i}}{\sigma_{\alpha_i}} \cdot \frac{r_{\alpha_i}^*}{\sigma_{\alpha_i}} = \min. \tag{13.119}$$

We define a set of weights, g_{α_i}, which are inversely proportional to the dispersions of the errors:

$$g_{\alpha_i} = 1/\sigma_{\alpha_i}^2 \tag{13.120}$$

so that Eq. (13.119) can be written as:

$$\sum_{i=1}^N g_{\alpha_i} r_{\alpha_i} r_{\alpha_i}^* = \min. \tag{13.121}$$

Expressing the errors r_{α_i} $(\alpha = x, y, z)$ in terms of the components of the electromagnetic field and the magnetotelluric and induction matrices through Eqs. (13.87)–(13.90), and accepting the standard scheme for computations by the least squares method, we find the desired expression for the elements of the magnetotelluric and induction matrices.

We will show next the technique for such calculations for determining the Wiese-Parkinson vector (magnetic tipper).

First, we designate

$$\phi_z^g(W_{zx}, W_{zy}) = \sum_{i=1}^N g_{z_i} r_{z_i} r_{z_i}^*.$$

Then, the conditions for minimizing the function ϕ_z^g to determine relationships are written in the form:

$$\sum_{i=1}^N g_{z_i}(H_{z_i} - W_{zx}H_{x_i} - W_{zy}H_{y_i})H_{x_i}^* = 0,$$

$$\sum_{i=1}^N g_{z_i}(H_{z_i} - W_{zx}H_{x_i} - W_{zy}H_{y_i})H_{y_i}^* = 0. \tag{13.122}$$

Solving this set of equations for W_{zx} and W_{zy}, we find:

$$\mathbf{W} = \mathbf{S}_{H_z g_z H} \cdot \hat{S}_{H g_z H}^{-1}, \tag{13.123}$$

where

$$\mathbf{S}_{H_z g_z H} = \left[\sum_{i=1}^N g_{z_i} H_{z_i} H_{x_i}^*, \sum_{i=1}^N g_{z_i} H_{z_i} H_{y_i}^* \right], \tag{13.124}$$

$$\hat{S}_{Hg_z H}^{-1} = \begin{bmatrix} \sum_{i=1}^{N} g_{z_i} H_{x_i} H_{x_i}^* & \sum_{i=1}^{N} g_{z_i} H_{x_i} H_{y_i}^* \\ \sum_{i=1}^{N} g_{z_i} H_{y_i} H_{x_i}^* & \sum_{i=1}^{N} g_{z_i} H_{y_i} H_{y_i}^* \end{bmatrix}. \tag{13.125}$$

The elements of the magnetotelluric matrix can be found in a similar way. Now let us designate the first and second columns of the impedance matrix as $\mathbf{Z}_x$ and $\mathbf{Z}_y$:

$$\mathbf{Z}_x = [Z_{xx}, Z_{xy}]$$
$$\mathbf{Z}_y = [Z_{yx}, Z_{yy}]. \tag{13.126}$$

Then

$$\mathbf{Z}_x = \mathbf{S}_{E_x g_x H} \hat{S}_{Hg_x H}^{-1}, \tag{13.127}$$

$$\mathbf{Z}_y = \mathbf{S}_{E_y g_y H} \hat{S}_{Hg_y H}^{-1}, \tag{13.128}$$

where

$$\mathbf{S}_{E_x g_x H} = \left[\sum_{i=1}^{N} g_{x_i} E_{x_i} H_{x_i}^*, \ \sum_{i=1}^{N} g_{x_i} E_{x_i} H_{y_i}^* \right],$$

$$\mathbf{S}_{E_y g_y H} = \left[\sum_{i=1}^{N} g_{y_i} E_{y_i} H_{x_i}^*, \ \sum_{i=1}^{N} g_{y_i} E_{y_i} H_{y_i}^* \right], \tag{13.129}$$

and the square matrices $\hat{S}_{Hg_x H}^{-1}$, $\hat{S}_{Hg_y H}^{-1}$ that are obtained from Eq. (13.125) carry the multiplier g_{z_i} to g_{x_i} and g_{y_i}, respectively.

It can be seen that all of the elements in the matrices present in the right-hand parts of Eqs. (13.123), (13.127), and (13.128) are (within the accuracy of the multiplier $1/(N-1)$) averaged values of spectral density and cross-spectral density for the various components of the magnetotelluric field.

In summary, the least-squares method with weights allows us to exclude or reduce the effect of systematic errors with unequal dispersions on the results obtained in reducing magnetotelluric data. We note that such a situation is readily identified on graphical presentations of the noise densities $r_{\alpha_i} r_{\alpha_i}^*$ ($\alpha = x, y, z$) plotted as a function of the magnetic field densities $H_{x_i} H_{x_i}^*$ or $H_{y_i} H_{y_i}^*$ (see, for example, Egbert and Booker, 1986). However, this method cannot provide acceptable results for those data volumes for which the noise is not normally distributed. In such cases, it is necessary to use a *robust* method for evaluating errors. A robust method is one in which some data are discarded on the basis of some arbitrary decision.

13.6.2 REMOTE REFERENCE METHOD

It has already been mentioned that in practice, there are situations in which correlated noise is present. The basic source of such noise is of industrial origin, which when present has a profound impact on data reduction. The effect of cross-correlated noise on the results of data reduction is abundantly clear from Eqs. (13.97) and (13.102), which contain matrices obtained by cross correlation of various components of the magnetotelluric field. If the noise present in the several recording channels is cross correlated,

the matrix elements in Eqs. (13.97) and (13.102) will be distorted, which in turn leads to distortion in the determination of the magnetotelluric and induction matrices. To avoid this problem, Gamble et al. (1979) proposed that magnetotelluric or magnetovariational observations be made simultaneously at two locations; one, M, an observation point, and the other, M_R, a reference point, which are separated one from the other by a distance L.

The distance, L, is chosen such that on the one hand, the noise is not cross correlated between the two stations, and on the other, that the geoelectrical structure is reasonably similar at the two sites. The usual distance between a station and its remote reference is a few kilometers. In the remote reference method, the impedance and Wiese-Parkinson matrices at the observation site M are found using Eqs. (13.97) and (13.102), with all elements of the matrices being computed using the cross correlation of field components at the site M and at the reference site M_R:

$$\widehat{Z} = \widehat{S}_{EH_R} \cdot \widehat{S}_{HH_R}^{-1}, \tag{13.130}$$

$$\mathbf{W} = \mathbf{S}_{H_z H_R} \cdot \widehat{S}_{HH_R}^{-1}. \tag{13.131}$$

We can see that, so long as there is uncorrelated noise at points M and M_R, remote referencing can reduce its impact on the magnetotelluric matrix to a low value. The remote reference method provides much better results than single-station data sets in areas in which there is a strong industrial noise component. If there is no correlated noise problem, remote referencing provides no improvement in results.

If narrow-band digital filtering is used along with remote referencing, Eqs. (13.112) and (13.113) for determining the impedance and Wiese-Parkinson impedances can be written as

$$\hat{Z} = \hat{F}_{EH_R} \cdot \hat{F}_{HH_R}^{-1}, \tag{13.132}$$

$$\mathbf{W} = \mathbf{F}_{H_z H_R} \cdot \hat{F}_{HH_R}^{-1}. \tag{13.133}$$

Similarly, it is possible to use the weighted least-squares method with remote referencing. In so doing, the basic equations for this approach, (13.123), (13.127), and (13.128), take the form

$$\mathbf{W} = \mathbf{S}_{H_z g_{z,R} H_R} \cdot \hat{S}_{H g_{z,R} H_R}^{-1}, \tag{13.134}$$

$$\mathbf{Z}_x = \mathbf{S}_{E_x g_{x,R} H_R} \cdot \hat{S}_{H g_{x,R} H_R}^{-1}, \tag{13.135}$$

$$\mathbf{Z}_y = \mathbf{S}_{E_y g_{y,R} H_R} \cdot \hat{S}_{H g_{y,R} H_R}^{-1}, \tag{13.136}$$

where $g_{x,R}$, $g_{y,R}$, and $g_{z,R}$ are weights inversely proportional to the dispersion of errors at a given location.

13.6.3 ROBUST ESTIMATION OF MAGNETOTELLURIC AND INDUCTION MATRICES

The basis for the least-squares and weighted least-squares methods is the minimization of errors in the linear relationship; that is, the error measured between a value predicted for one field component on the basis of the other observed components, and the observed values. However, within these methods, one can identify "bad" data on the basis that the error for a given point may lie at a distance of many standard deviations from a predicted value. Such bad points strongly affect the ultimate determination

of the electrical conductivity function. In times past, this difficulty was avoided by arbitrary deletion of some data after a visual inspection of the field data. Egbert and Booker (1986) have suggested an approach to deletion of bad data on a statistical basis rather than by empirical selection. Having a well defined basis for deleting data facilitates the implementation on a computer of an editing process which will delete a small number of observed points.

The logical flow of such a method developed by Egbert and Booker (1986) is as follows. We examine the question of minimizing the sum of least-squares Eqs. (13.67), (13.68), and (13.69), or weighted least-squares, Eq. (13.121), or in terms of the minimization of some more general function L_α, $\alpha = x, y, z$ (these general functions are termed *loss functions*),

$$
\begin{aligned}
L_x(Z_{xx}, Z_{xy}) &= \min, \\
L_y(Z_{yx}, Z_{yy}) &= \min, \\
L_z(W_{zx}, W_{zy}) &= \min, \\
L_z^E(V_{zx}, V_{zy}) &= \min,
\end{aligned}
\tag{13.137}
$$

where

$$
L_\alpha = \sum_{i=1}^{N} \rho(r_{\alpha_i}/\sigma_\alpha), \alpha = x, y, z; \ L_z^E = \sum_{i=1}^{N} \rho(r_{z_i}^E/\sigma_z^E).
\tag{13.138}
$$

Here: 1) $\rho(\chi)$ is some auxiliary function chosen as a function of the norm used in minimizing the error in the linear relationships (norm L_2 indicates a least squares minimization; norm L_1 indicates a minimax minimization), and 2) we have assumed that each of the error terms r_{x_i}, r_{y_i}, r_{z_i}, and $r_{z_i}^E$ is characterized by the standard variations σ_x, σ_y, σ_z, and σ_z^E respectively.

In the standard approach, the least-squares function $\rho(r)$, in accord with Eqs. (13.91) through (13.93), has the form

$$
\rho(r) = r \cdot r^*.
\tag{13.139}
$$

That is, we use the L_2 norm.

The primary value in the choice of a loss function, as pointed out above, is in the way in which it "selects out" the bad points, or statistical outliers. Experience in other fields indicates that best results are obtained by using the L_1 or minimax norm:

$$
\rho(r) = |r|.
\tag{13.140}
$$

In the theory of mathematical statistics, it has been established that this choice of loss function leads to optimal evaluation of the statistical measures in situations in which the noise follows a Laplace distribution. In magnetotelluric studies, noise appears to be best described as Gaussian after deletion of a small number of bad points. Such behavior is observed with many physical problems. Therefore, the most satisfactory basis for eliminating data, according to Huber (1981) is a hybrid norm: the L_2 norm for small errors in the linear relationships, and the L_1 norm for large errors:

$$
\rho(r) = \begin{cases} rr^*, & |r| < a \\ 2a|r| - a^2, & |r| \geq a \end{cases},
\tag{13.141}
$$

where the choice of $a = 1.5$ is recommended.

The problem of minimizing the loss function in Eq. (13.138) with the auxiliary function $\rho(\chi)$ as defined in Eq. (13.131) can be solved using routine methods.

As an example, we will examine the problem in finding the Wiese-Parkinson matrix for the vector **W**. The corresponding loss function takes the form

$$L_z(W_{zx}, W_{zy}) = \sum_{i=1}^{N} \rho(r_{z_i}/\sigma_z) = \min, \tag{13.142}$$

where

$$r_{z_i} = H_{z_i} - W_{zx} H_{x_i} - W_{zy} H_{y_i}. \tag{13.143}$$

The conditions for minimizing the function in Eq. (13.142), obviously, are:

$$\frac{\partial L_z}{\partial W_{zx}} = -\frac{1}{\sigma_z} \sum_{i=1}^{N} \rho'(r_{z_i}/\sigma_z) H_{x_i} = 0,$$

$$\frac{\partial L_z}{\partial W_{zy}} = -\frac{1}{\sigma_z} \sum_{i=1}^{N} \rho'(r_{z_i}/\sigma_z) H_{y_i} = 0, \tag{13.144}$$

where "prime" denotes a derivative of the function $\rho(r)$.

In accord with Eq. (13.141), we have:

$$\rho'(r_z/\sigma_z) = \left(\begin{array}{ll} r_z^*/\sigma_z, & |r_z/\sigma_z| < a \\ \frac{a}{\sigma_z}(r_z^*/r_z)^{1/2}, & |r_z/\sigma_z| \geq a \end{array}\right. \tag{13.145}$$

We introduce the terminology

$$g(r) = \rho'(r)/r^*. \tag{13.146}$$

In view of Eq. (13.145),

$$g(r_z/\sigma_z) = \left(\begin{array}{ll} 1, & |r_z/\sigma_z| < a \\ a/|r_z|, & |r_z/\sigma_z| \geq a \end{array}\right. \tag{13.147}$$

Consequently, after substituting Eq. (13.146) into (13.144), we can write

$$\sum_{i=1}^{N} g(r_{z_i}/\sigma_z) r_{z_i}^* H_{x_i} = 0,$$

$$\sum_{i=1}^{N} g(r_{z_i}/\sigma_z) r_{z_i}^* H_{y_i} = 0. \tag{13.148}$$

Finally, expressing Eq. (13.148) in complex amplitudes and taking Eq. (13.143) into account, we write

$$\sum_{i=1}^{N} g(r_{z_i}/\sigma_z)(H_{x_i} - W_{zx}H_{x_i} - W_{zy}H_{y_i})H_{x_i}^* = 0,$$

$$\sum_{i=1}^{N} g(r_{z_i}/\sigma_z)(H_{z_i} - W_{zx}H_{x_i} - W_{zy}H_{y_i})H_{y_i}^* = 0. \tag{13.149}$$

Comparing Eq. (13.149) with (13.122), we see that these formulas are identical when $g_{z_i} = g(r_{z_i}/\sigma_z)$. Thus, the robust method just described is conceptually equivalent to the weighted least-squares method, but the weights are determined directly from the observed data. Data which exhibit small errors in the linear relationship obtained in accord with Eq. (13.146) are assigned unit weight, while bad data have lower weights the further out they fall on the error distribution. Normalizing the dispersion with respect to σ_z in Eq. (13.146) permits us to determine specifically which errors are large and which errors are small.

Egbert and Booker (1986) following the work of Huber (1981) propose the use of the following iterative algorithm in the solution of Eq. (13.149).

Designating the elements of the Wiese-Parkinson matrices obtained using the conventional least-squares method as W_{zx}^0 and W_{zy}^0, we will calculate the error in the predicted vertical component of the magnetic field H_z in these matrices:

$$r_{z_i}^0 = H_{z_i} - \tilde{H}_{z_i}^0, \tag{13.150}$$

where

$$\tilde{H}_{z_i}^0 = W_{zx}^0 H_{x_i} + W_{zy}^0 H_{y_i}, \tag{13.151}$$

and evaluate the dispersion of the error σ_{z0}:

$$\sigma_{z0} = \left[\frac{1}{N-1} \sum_{i=1}^{N} r_{z_i}^0 (r_{z_i}^0)^* \right]. \tag{13.152}$$

We will introduce the term "modified" vertical component of the field, $H_z^{(1)}$:

$$H_{z_i}^{(1)} = \tilde{H}_{z_i} + g(r_{z_i}^0/\sigma_{z0})r_{z_i}^0, \tag{13.153}$$

where g is determined from Eq. (13.147).

Clearly, the modified data will coincide with the desired data for small errors ($g = 1$ for $r_{z_i}^0 < a\sigma_{z0}$) while for large errors, the modified values of the field will approximately match the predicted values (that is, $g < 1$ for $r_{z_i}^0 \geq a\sigma_{z0}$).

We will replace the observed data H_{z_0} with the modified data $H_{z_i}^{(1)}$ and again apply the standard least-squares method, Eq. (13.97):

$$\mathbf{W}^{(1)} = \mathbf{S}_{H_z^{(1)}} \hat{S}_{HH}^{-1}. \tag{13.154}$$

For these matrices, we will compute the error of prediction $r_{z_i}^{(1)}$ and its dispersion $\sigma_z^{(1)}$:

$$r_{z_i}^{(1)} = H_{z_i}^{(1)} - \tilde{H}_{z_i}^{(1)}, \tag{13.155}$$

where $\tilde{H}_{z_i}^{(1)}$ is the "estimated" value for the vertical component:

$$\tilde{H}_{z_i}^{(1)} = W_{zx}^{(1)} H_{x_i} + W_{zy}^{(1)} H_{y_i}. \tag{13.156}$$

Now, we will repeat the modification of the data,

$$H_{z_i}^{(2)} = \tilde{H}_{z_i}^{(1)} + g(r_{z_i}^{(1)}/\sigma_z^{(1)})r_{z_i}, \tag{13.157}$$

and repeat all the computations. This iterative procedure is repeated until the result $\mathbf{W}^{(n)}$ does not improve the solution of Eq. (13.149).

A similar approach is used to construct an algorithm for minimizing the loss functions $L_x(Z_{xx}, Z_{xy})$ and $L_y(Z_{yx}, Z_{yy})$, permitting us to obtain a robust evaluation for the impedance matrices. In accord with Eq. (13.130), the corresponding iterative procedures have the form:

$$\hat{Z}^{(n+1)} = \hat{S}_{E^{(n+1)}H} \hat{S}_{HH}^{-1}, \tag{13.158}$$

where

$$E_{\alpha_i}^{(n+1)} = \tilde{E}_{\alpha_i} + g(r_{\alpha_i}^{(n)}/\sigma_\alpha^{(n)})r_{\alpha_i}^{(n)}, \ \alpha = x, y, \tag{13.159}$$

and $\tilde{E}_{\alpha_i} \ (\alpha = x, y)$ is the value for the horizontal components of the electric field predicted at the n-th stage of iteration:

$$\begin{aligned} E_{x_i}^{(n)} &= Z_{xx}^{(n)} H_{x_i} + Z_{xy}^{(n)} H_{y_i}, \\ E_{y_i}^{(n)} &= Z_{yx}^{(n)} H_{x_i} + Z_{yy}^{(n)} H_{y_i}. \end{aligned} \tag{13.160}$$

The method of robust processing can be used as well in analysis of data obtained with a remote reference (Chave et al., 1987). In this case, we should use the cross-correlation of field components at the points M and M_R to determine the appropriate terms in the matrices in Eqs. (13.154) and (13.158):

$$\mathbf{W}^{(n+1)} = \mathbf{S}_{H_z^{(n+1)}H^R} \hat{S}_{HH^R}^{-1}, \tag{13.161}$$

$$\hat{Z}^{(n+1)} = \hat{S}_{E^{(n+1)}H^R} S_{HH^R}^{-1}. \tag{13.162}$$

In conclusion, these schemes for reducing magnetotelluric and magnetovariational data are used at the present time in computer routines which are widely used in the practice of magnetotelluric surveys.

13.6.4 GRAPHICAL PRESENTATION OF MAGNETOTELLURIC AND INDUCTION MATRICES

It is necessary to carry out a qualitative analysis of magnetotelluric data before a quantitative interpretation can be undertaken. Such quantitative procedures include the identification of normal and

anomalous responses, classification of anomalies with respect to their geometric and frequency characteristics, diagnosis of near-surface effects, localization of distorting bodies, and the choice of a class of models which can be used in obtaining an inverse solution. The procedures used in this first stage of interpretation mostly are graphic in nature, based on various representations of the interaction of the electromagnetic field with the earth. Interpretation usually begins with the compilation of phase and amplitude maps for various components of the field. In studying the relationship of anomalies to frequency and polarization of the field, the number of maps that can be generated is so large that one wonders if there is so much information content in such maps as to prohibit their use. In more advanced analyses, it is useful to make *dynamic presentations* through the use of video sequences or some form of virtual reality.

In an effort to have a compact and useful approach, we turn to representations of the magnetotelluric and induction matrices. There are many ways in which such information can be compiled graphically. For example, Wiese and Schmucker have proposed the idea of vector-based presentations. Polar diagrams have been suggested by Berdichevsky (1965) and by Lilley and Sloane (1976). In this book, we will limit ourselves to consideration of vector and polar presentations.

We will take a model of an inhomogeneous earth, energized by a vertically-incident plane wave. The Wiese-Parkinson vector $\mathbf{W}$ describes the relationship between the vertical magnetic component, H_z, and the horizontal magnetic components, H_x and H_y. We represent $\mathbf{W}$ in terms of a pair of vectors which are real and imaginary.

The vectors Re $\mathbf{W}$ and Im $\mathbf{W}$ are plotted on maps as induction arrows (real and imaginary). Maps are compiled for a sequence of frequencies. The directions of the induction vectors coincides with an axis of polarization of the horizontal magnetic field, indicating the maximum sizes of the real and imaginary parts of H_z. The length of an arrow is scaled to be proportional to the magnitude of these quantities. In a two-dimensional model uniform in the y direction, the real and imaginary induction arrows are perpendicular to the axis of homogeneity. A useful characteristic of the real induction vector is the fact that it points towards zones of increased conductivity. The behavior of the imaginary induction arrows depends on the nature of the anomaly. If the direction reverses as the frequency decreases, the behavior indicates a near-surface effect.

The components of the Wiese-Parkinson vectors are determined from a frequency analysis of magnetotelluric micropulsations. In order to obtain information more quickly, a preliminary evaluation is based on an examination of instantaneous values of the field.

The relationship between the elements of the magnetotelluric and induction matrices and the directions of the coordinate axes x and y are best characterized through the use of *polar diagrams*. A polar diagram is the trace of the tip of a vector as the direction of that vector moves through 360°. The vector quantity plotted can be the modulus, phase, or real or imaginary part of any element of the magnetotelluric or induction matrices. Comparison of the polar diagrams is based on formulas for the transformation of the vector or tensor component as it rotates about the z axis. The most informative diagram is that based on the modulus of a vector. In such diagrams

$$|a_{xx}(\theta)| = |a_{yy}(\theta + \frac{\pi}{2})|$$
$$= |a_{xx}'' \cos^2\theta + (a_{xy}'' + a_{yx}'') \sin\theta \cos\theta + a_{yy}'' \sin^2\theta|$$
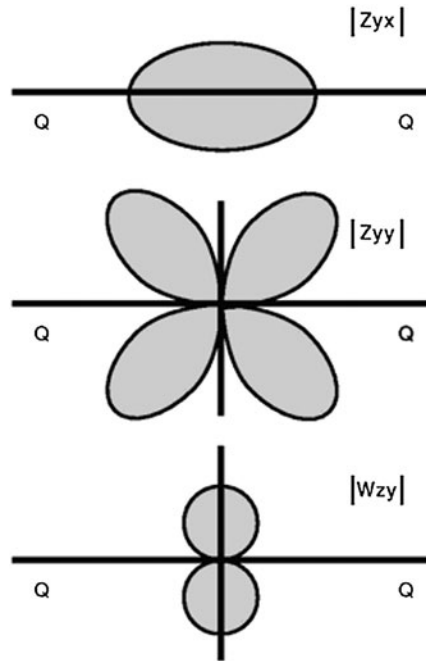
FIGURE 13.20

Typical forms of polar diagrams for MT soundings over a two-dimensional geoelectric.

$$|a_{yx}(\theta)| = |a_{xy}(\theta + \frac{\pi}{2})|$$
$$= |a''_{yx} \cos^2\theta + (a''_{xx} - a''_{yy}) \sin\theta \sin\theta - a''_{xy}\sin^2\theta|$$
$$|a_{zx}(\theta)| = |a_{zy}(\theta + \frac{\pi}{2})|$$
$$= |a'_{zx}\cos\theta - a'_{zy}\sin\theta|, \tag{13.163}$$

where $a''_{xx}, a''_{xy}, a''_{yx}, a''_{yy}$ are elements of the matrix a determined with respect to the basis $\{\mathbf{d}'_x, \mathbf{d}'_y, \mathbf{d}'_z\}$, and θ is the angle between $\mathbf{d}'_x$ and $\mathbf{d}_x$ measured counterclockwise.

Fig. 13.20 shows typical polar diagrams for $|Z_{xy}|$, $|Z_{yy}|$, and $|W_{zy}|$ which might be observed for a two-dimensional medium. In the case of three-dimensional inhomogeneities, the form of the polar diagram changes from that characteristic of a two-dimensional geoelectric structure, the change being greater for greater departures from two-dimensionality. Polarization diagrams can be used to make judgments about the geometry of an inhomogeneity.

13.7 ONE-DIMENSIONAL INTERPRETATION OF MT DATA

The information obtained from a reduction of MTS data is contained in the elements of an impedance matrix:

$$[\hat{Z}] = \begin{bmatrix} Z_{xx} & Z_{xy} \\ Z_{yx} & Z_{yy} \end{bmatrix}. \tag{13.164}$$

For a horizontally homogeneous medium, this matrix has a simpler form

$$\begin{bmatrix} 0 & Z \\ Z & 0 \end{bmatrix}. \tag{13.165}$$

For a horizontally uniform geoelectric model, the following relationships hold

$$Z_{xx} = Z_{yy} = 0,$$
$$Z_{xy} = -Z_{yx} = Z. \tag{13.166}$$

The elements Z_{xy} and Z_{yx} are called the *principal impedances*, while the elements Z_{xx} and Z_{yy} are called the *auxiliary impedances*. In general, Z_{xx} and Z_{yy} are nonzero, and Z_{xy} and Z_{yx} are unequal. The sizes of the principal and auxiliary impedances depend on the bearings of the coordinate system (usually, the coordinate system coincides with the bearings of orthogonal electric and magnetic sensors). On rotating the coordinate axes through a rotation angle θ, we obtain the impedance polar diagrams described in the last section. An invariant of the magnetotelluric tensor (that is, a parameter which does not change on rotation of axes) is its determinant, which defines the *effective impedance*:

$$Z_{ef} = (Z_{xx}Z_{yy} - Z_{xy}Z_{yx})^{1/2}. \tag{13.167}$$

We can see that, if Eq. (13.166) is substituted into Eq. (13.167), the effective impedance is identical with the true impedance for a horizontally homogeneous medium.

The standard form of presentation for MTS data is the apparent resistivity curve. Such curves are constructed using the definition of apparent resistivity for the magnetotelluric method, Eq. (13.6). In practice, two different forms of apparent resistivity curves are usually used:

- 1) Maximum/minimum MT sounding curves, based on the principal impedance values

$$\rho_{xy} = \frac{1}{\omega\mu_0} \left| Z_{xy} \right|^2,$$
$$\rho_{yx} = \frac{1}{\omega\mu_0} \left| Z_{yx} \right|^2, \tag{13.168}$$

where the resistivity ρ_{xy} is assigned the direction of the x axis, while the resistivity ρ_{yx} is assigned the direction of the y axis.

- 2) Effective MT sounding curves, based on the effective impedance:

$$\rho_{ef} = \frac{1}{\omega\mu_0} \left| Z_{ef} \right|^2. \tag{13.169}$$

In the one-dimensional Tikhonov-Cagniard model, the three curves are identical, but in a real earth, they are not.

"Geoelectric" interpretation of magnetotelluric data consists of the construction of a model of the geoelectric structure of the earth which is most compatible with the observed magnetotelluric information. The simplest models which are used are those based on a one-dimensional (horizontally homogeneous) earth model. Unfortunately, in a real earth, there is always some departure from ideal one-dimensionality, or horizontal inhomogeneity. As a consequence, there will always be some departure of an observed MT sounding curve from an ideal (normal) curve computed theoretically for some specific layered-earth model at a given sounding site. Such departures are called distortions to an MTS curve, and the observed curves in such cases are called distorted curves. Formal interpretation of MT sounding curves in terms of a one-dimensional structure, ignoring such distortions, leads to the construction of a preliminary (rough) geoelectric structure. Such preliminary sections are sometimes called *stitched* sections, because individual one-dimensional interpretations are sewn together like a quilt, with no attention being paid to the way in which each sounding is affected by the change in section indicated by the adjacent sounding.

Consideration of distortions caused by lateral change in the geoelectric section is the most vital step in interpretation. In summary, interpretation of magnetotelluric data in one dimension consists of two stages:

- 1) A qualitative step in interpretation consisting of an analysis of distortions to the MTS curves, outlining of regions within the survey area characterized by similar forms of distortion, and specification of a qualitative geoelectric model.
- 2) Quantitative interpretation, consisting of one-dimensional interpretations of the least distorted curves to obtain a regional characterization of the quasi one-dimensional structure of the region.

We will describe the most effective methods for each stage in the next section.

13.7.1 ANALYSIS OF DISTORTED MTS CURVES

Distorted MTS curves exhibit both galvanic and inductive effects. Galvanic effects occur when the currents causing a distortion flow across boundaries in electrical conductivity; induction effects occur when the currents causing a distortion flow entirely within a region with constant conductivity.

In regions characterized by linear geologic structures, the axes of the measurement system are aligned with the y axis lying along the strike of the structure, and the x axis being in the dip direction. The corresponding MTS curves are called the *longitudinal* curve and the *transversal* curve, respectively. They reflect longitudinal and transversal directions of current flow, which correspond to the cases of E and H polarization in two-dimensional structures.

Transverse curves (H polarized) are distorted by galvanic effects for the following reasons.

- 1) The term *S-effect* or *static shift* is used to describe the distortion of the MTS curves by a shift of the right-hand part of the sounding curve up or down along the apparent resistivity scale. It is caused by a change in the cumulative conductance of a shallow or intermediate conductive horizon encased in more resistant rocks.
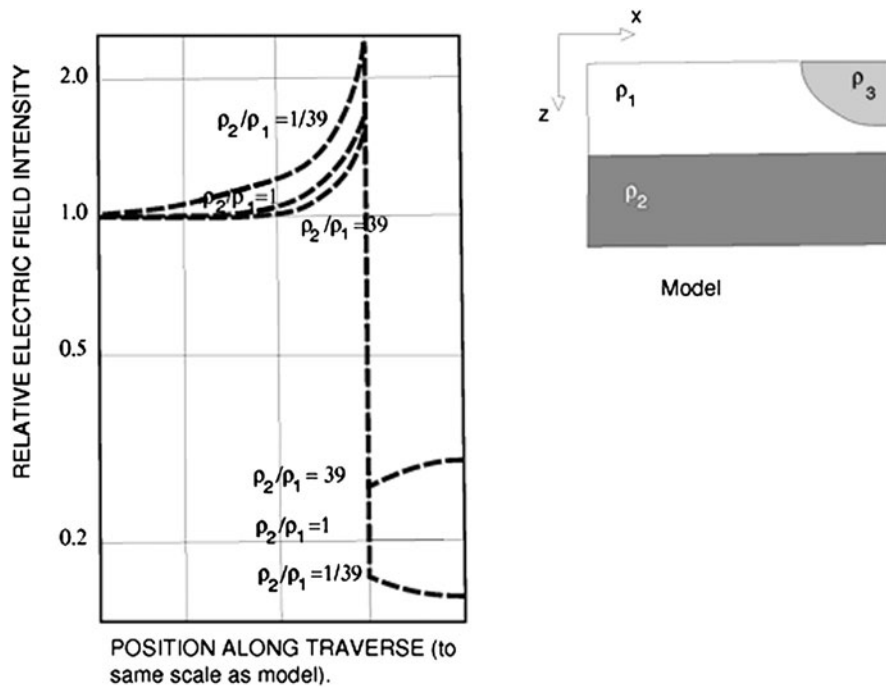
FIGURE 13.21

Behavior of a static electric field for a two-layer model with a hemispheroidal conductive pod in the surface layer. The pod has a resistivity 1/9 of that of the rest of the surface layer.

An example of static shift of a magnetotelluric sounding is shown in Fig. 13.21. The model is that of a two-layer earth, but with the inclusion of a conductive hemispheroidal mass in the surface layer. The electric field observed within the conductive mass is significantly lower than the electric field observed outside the mass. The magnetic field, which is contributed by currents over a very large area when observations are made at low frequencies, is changed by an insignificant amount by the presence of the conductive mass. As a consequence, the magnetotelluric sounding curve is shifted towards lower apparent resistivities as shown in Fig. 13.22.

In areas where conductive masses are common, they can well cause incorrect interpretations of the geoelectric structure if one-dimensional interpretation procedures are used. An example of this is shown in Fig. 13.23, characterizing the results of a magnetotelluric survey made in central Utah (USA) in the search for geothermal energy. The area of the survey is an intermontane valley, in the center of which there was a dry lake bed. One-dimensional interpretations of the MT soundings yielded an apparent locally conductive surface zone coincident with the dry lake bed. Also, these interpretations indicated a shallowing of the conductive region of the lower crust and upper mantle to depths of less than 10 kilometers beneath the dry lake. The depth to the same zone is many tens of kilometers outside the lake area. Clear evidence that the structure is caused by static shift of the
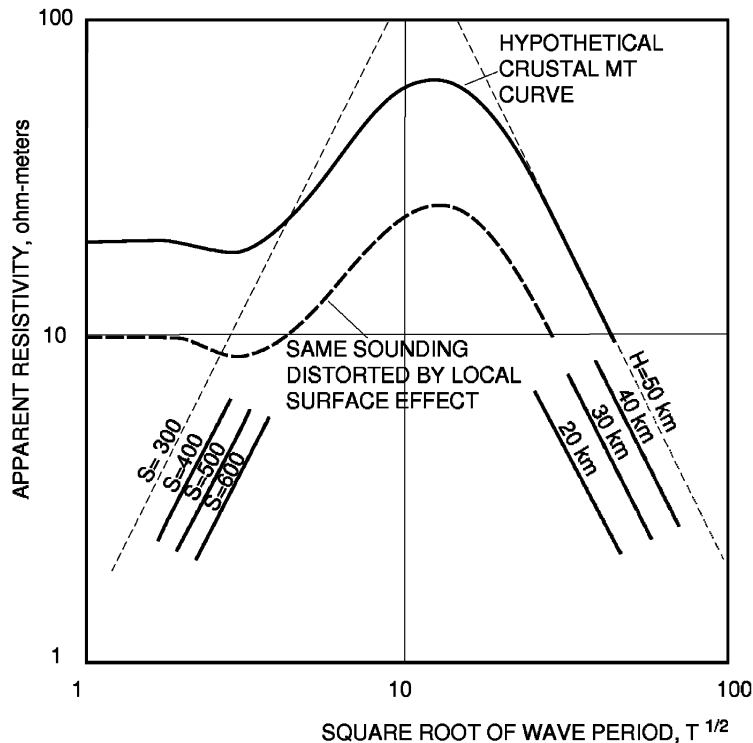
FIGURE 13.22

Static shift of a magnetotelluric curve occurs when the electric field measurement is distorted proportionately more than the magnetic field by a small-scale inhomogeneity in the conductivity of the rock in which the electrodes to measure the electric field are sited. Static shift usually causes an overestimate of the conductance of the surface layer and an underestimate of the depth to the conductive part of the crust.

MT curves recorded over the dry lake is given by the close inverse correlation between the interpreted conductance of the surface layer and the interpreted depth to a crustal conductor, as shown in Fig. 13.23.

Interpretation of a curve distorted by a static shift using the conventional one-dimensional approach leads to the appearance of false geoelectric structures in the lower part of the section.

Static shift is a major impediment to the use of magnetotelluric sounding in areas where the resistivity of the surface layer is not uniform laterally. There are some direct ways to minimize the distortions caused by static shift. If the electric field is detected with very large separations between electrode contacts (distances comparable to the maximum depth of investigation), the effects of local inhomogeneities in electrical resistivity of the surface layer will tend to average out. Another approach is to measure the electric field with a short separation between electrode contacts, but at a great number of locations over an area having a radius comparable to the maximum depth of inves-
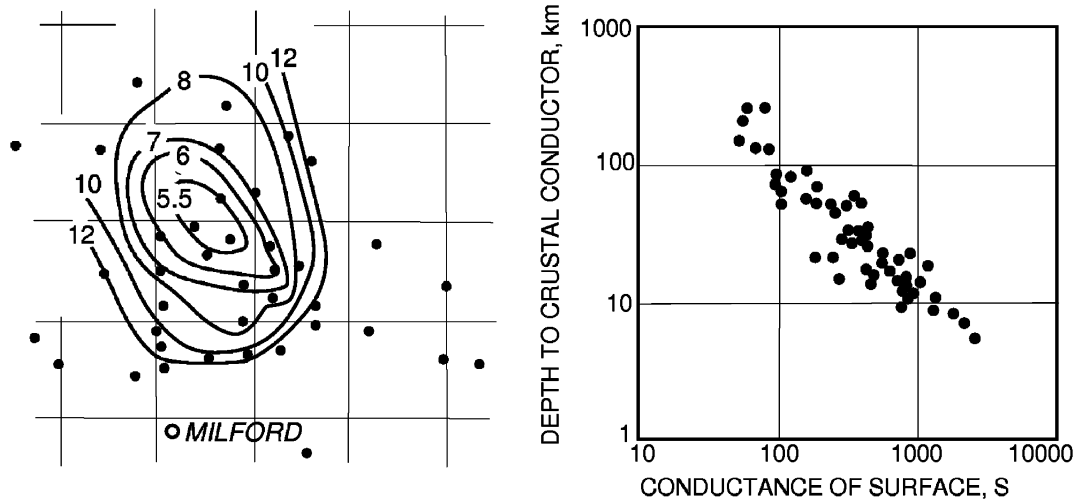
FIGURE 13.23

Example of the generation of a false crustal structure by static shift. An MT survey was carried out in central Utah near the town of Milford as shown on the map at the left. Depth to a postulated crustal conductor was estimated from the descending asymptote of the observed magnetotelluric sounding curves, with the depths shown as contoured. The plot on the right shows the correlation between the conductance of the near-surface layer, as estimated by the rising asymptote of the MT curves, and the estimated depth to the crustal conductor. The close inverse correlation between these two quantities is strong evidence for the feature being generated by static shift of the MT curves. (The grid on the map at the left has a ten kilometer grid superimposed.)

tigation. When this is done, an estimate of a representative value of the electric field is obtained by averaging the electric field observations or by constructing a model of the electrical inhomogeneities in the surface layer. This model is used in the interpretation of geoelectric structures lying at greater depths.

Both of these approaches to reducing the effect of static shift are strongly labor intensive and the cost is often difficult to justify. Still another approach to combatting static shift is the use of phase data to compute a curve resembling the magnetotelluric sounding curve. This is possible because in most cases the phase of an MT curve is not independent of the magnitude of the apparent resistivity. One curve can be computed from the other using the Hilbert transform. The Hilbert transform can be used to find the phase curve from the magnetotelluric resistivity magnitude curve or the shape of the magnitude curve from the phase curve.

The phase to magnitude transformation yields a curve for which the magnitude scale is unscaled; that is, the magnitude at short periods tends to unity. To obtain a scaled apparent resistivity curve, it is necessary to assign a resistivity for the first layer in the sequence. Because all transformed curves start at the same value, the effect of static shift is not present and does not mislead the interpreter in his initial evaluation of a profile of MT sounding curves.
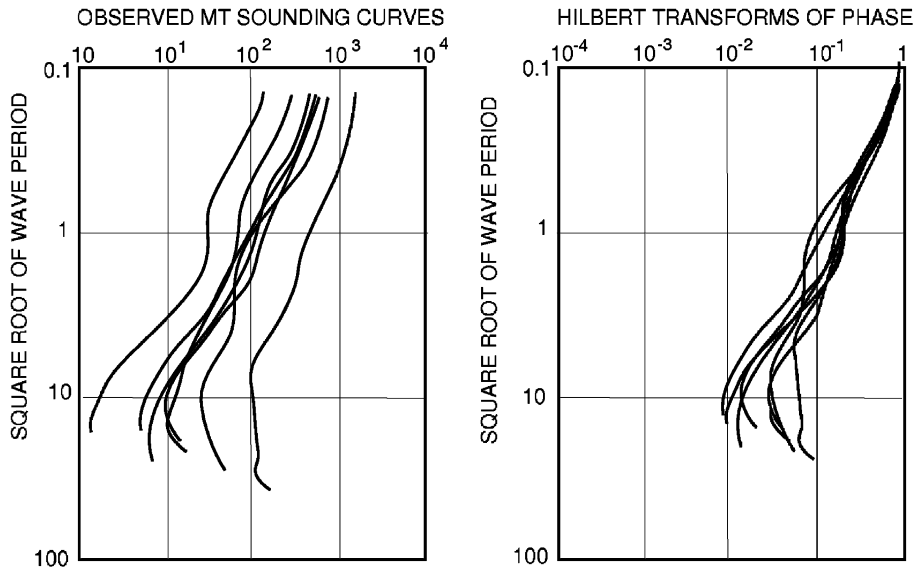
FIGURE 13.24

Example of the suppression of static shift by using the Hilbert transform of the phase curves to obtain unscaled apparent resistivity curves. On the left, a series of MT sounding curves recorded along a profile in southern British Columbia is shown. The differences between curves is due largely to static shift. Unscaled Hilbert transforms of the corresponding phase curves are shown on the right.

An example of the use of the Hilbert transform is shown in Fig. 13.24. The example is taken from an extensive magnetotelluric survey carried out in southern British Columbia (Canada) in an effort to map a Mesozoic section (conductive) covered by a Precambrian thrust sheet (resistive). The MT soundings were located along seismic reflection profiles to identify the probable lithology associated with mappable reflections. MT sounding curves recorded at intervals of a few kilometers along a profile are shown in Fig. 13.24 (the left panel). It is important to note that while the curves appear to all have roughly the same shape, the resistivities vary by as much as an order of magnitude from curve to curve. The similarity in shape despite the differences in apparent resistivity is a strong indication of static shift between curves.

Apparent resistivity curves (unscaled) obtained by Hilbert transformation of the corresponding phase curves are shown in Fig. 13.24 (the right panel). The curves lie nearly on top of one another.

The Hilbert-transformed curves can be converted to scaled curves suitable for interpretation by assigning an appropriate resistivity for the surface layer. This assignation can be done in several ways. One way which has been used on occasion is to carry out a regional survey of the resistivity of the surface layer using either an electromagnetic sounding method (described in Chapter 14) or a DC vertical electrical sounding method (described in Chapter 12).

- 2) Screening effects caused by the presence of high resistivity zones at intermediate depths. When MTS curves are interpreted formally with a one-dimensional model, the relief on deep-seated geoelectric boundaries is exaggerated.

  This effect can be recognized by comparing structural relief maps compiled for both the longitudinal and transverse MTS curves. A diagnostic behavior is the absence or near absence of a structure on the transverse map in combination with an exaggerated structure on the longitudinal map.

- 3) Edge effects – the *channeling* of current along an elongate synclinal structure or adjacent to a steeply dipping edge of a high-resistivity horst leads to distortions. Such edge effects cause a pronounced weakening of the component of the electric field in the dip direction (normal to the strike of the edge). As a consequence, the long-period part of the curve $\rho_\perp$ is shifted downward along the apparent resistivity axis and is deformed. This deformation is related to hypothetical "charges" which one might visualize at surfaces where current flows across boundaries in resistivity, giving rise to a distortion that can be viewed as galvanic in origin. These arise at any frequency of the electromagnetic field.

  The edge effect gives rise to an effective polarization of low frequency telluric currents along the axes of syncline-like structures, inasmuch as the component of the telluric field flowing along the structure exhibits practically no change from normal. Thus, $\rho_\parallel$ is unchanged and induction effects do appear: $\rho_\perp$ decreases near positive structural elements (anticlines) and increases near negative structure elements (synclines).

  In summary, for E polarization, $\rho_\perp$ curves are distorted by an induction effect which causes false inflections and minimums to appear. Because the amount of electromagnetic induction increases with increasing frequency, distortion caused by induction effects will decrease at low frequencies.

  Fig. 13.25 shows longitudinal and transversal MTS curves which would be observed over a two-dimensional horst-like geoelectrical structure. The transverse curve, $\rho_\perp$, is distorted by the S effect, which shifts the left-hand part of the curve upward. Routine one-dimensional interpretation of these curves leads to an exaggerated depth to the conducting basement ($\rho_3 = 0$).

  A longitudinal curve located over the center of the horst shows the effects of distortion by induction: it has a false minimum caused by channeling effects of the conductive zones adjacent to the horst. At lower frequencies, the induction effects are diminished, and the downward trending part of the sounding curve permits determination of the correct depth to the conducting basement.

  It should be noted that in regions of complex geology which are described as three-dimensional geoelectrical models, the same effects are observed as in the two-dimensional models, though to a lesser degree. However, these effects are commonly complicated by the presence of specific three-dimensional distorting effects of polarization and depolarization (focusing and defocusing) of currents in the neighborhood of quasi-spherical bodies.

  The causes for various distortions to MTS curves are studied using numerical modeling of geologic settings peculiar to each individual surveyed region.
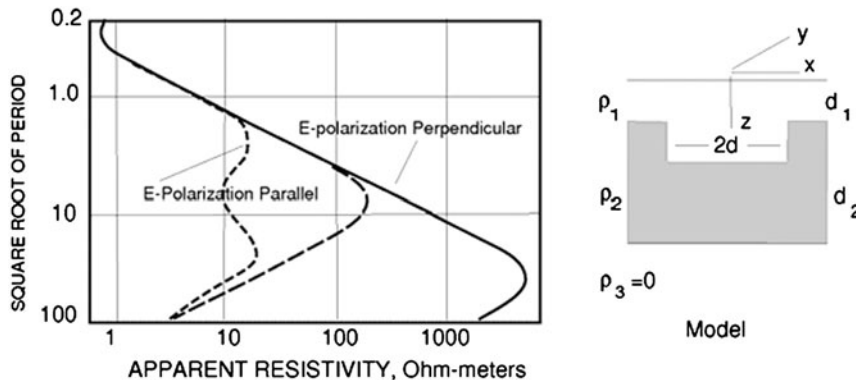
FIGURE 13.25

Distortion caused to magnetotelluric sounding curves by lateral changes in the geoelectric structure. The model is that of a graben extending in the y-direction. The solid curve and the short-dashed curve were computed for electric-field polarizations as indicated. The long-dashed curve is the curve corresponding to a one-dimensional model in which the surface layer has the thickness corresponding to the depth of the graben.

13.7.2 QUICK AND DIRTY MTS ANALYSIS

After analysis and identification of distortions, one may proceed with a formal one-dimensional interpretation of the least distorted curves, using a one-dimensional inversion scheme. As is the case with inversion of other types of geoelectric data, the inversion of magnetotelluric data is an ill-posed problem in the mathematical sense; that is, large changes in the forward model can cause only negligible changes in the observed field, and conversely. Consequently, regularization of the problem is required; that is, the inversion must be done in terms of some equivalent well-posed problem. The choice of an equivalent well posed model depends on the use of any supplementary information which may be available, along with various hypotheses about which structures are geologically reasonable in the area of the survey.

The principal stumbling block met in interpretation by inversion is that the process is nonlinear. As a consequence, inversion must proceed as a trial and error process; that is, the error between a postulated model and a set of field data is progressively reduced in an iterative process. If the initial choice of a model is made poorly, the number of iterations needed to improve the model may be quite large. This leads to the need for a procedure to make a reasonable choice for the initial model used in inversion. The procedure to arrive at an approximate model with a minimum of effort has been called *quick and dirty* interpretation, or interpretation by *rules of thumb*.

First of all, we will describe the use of asymptotic formulas to obtain generalized parameters for the section. We will consider two alternative models: model 1, in which a sequence of layers with a cumulative longitudinal conductance, S, lies on an insulating substratum, and model 2, in which a sequence of layers with a total thickness, D, lies on a perfectly conducting substratum. In accord with the expressions for the low frequency asymptote of the Tikhonov-Cagniard impedance we have:

Model 1:

$$\text{as } \omega \to 0, Z \sim 1/S,$$
$$\text{and } \rho_a \approx 1/\omega\mu_0 S^2. \tag{13.170}$$

Model 2:

$$\text{as } \omega \to 0, Z \sim -i\omega\mu_0 D,$$
$$\text{and } \rho_a \approx \omega\mu_0 D^2. \tag{13.171}$$

The low-frequency portions of MT apparent resistivity curves plotted to bilogarithmic coordinates (the Napierian transform) will approach straight lines, $x = a + by$, asymptotically:

Model 1:

$$\log \rho_a = 2 \log T^{1/2} - \log 2\pi\mu_0 S^2.$$

Model 2:

$$\log \rho_a = -2 \log T^{1/2} + \log 2\pi\mu_0 D^2,$$

with loci that depend directly on S and D. The asymptotes are called *S-* and *D*-lines (Fig. 13.22). D and S are found easily from these loci:

$$S^2 = T_S/(2\pi\mu_0),$$
$$D^2 = T_D/(2\pi\mu_0), \tag{13.172}$$

where T_S and T_D are the abscissas at which the S and D lines intersect the horizontal line $\rho_a = 1$.

A very rapid approach to rough interpretation of a magnetotelluric sounding curve is the fitting of rising and falling asymptotes which characterize the conductance of conductive layers and the thickness of resistive layers. A set of such asymptotic curves is given in Fig. 13.26. To use these curves, an MT field curve to be interpreted is plotted to the same dimensioned coordinates as used in Fig. 13.26. The sheet with the field curve is superimposed exactly over the plot of Fig. 13.26. Rising and falling asymptotes are then picked which yield the conductances and thicknesses of the corresponding layers.

Approaches which lead to definition of a quick and dirty model with higher resolution are provided by various algebraic and differential transformations of the ρ_a curve. Many such transformations have been proposed, but the most popular at present seems to be the *Niblett* or *Bostick* transform which can be developed as follows. Inasmuch as ρ_a is a weighted average resistivity, it might be represented approximately as

$$\rho_a \approx z/\int_0^z \sigma(z)dz,$$

where the running variable z is an *effective depth of penetration*, defined from Eqs. (13.170) and (13.171) as

$$z^2 = D^2 = \frac{\rho_a}{\omega\mu_0} = \frac{\rho_a T}{2\pi\mu_0}. \tag{13.173}$$
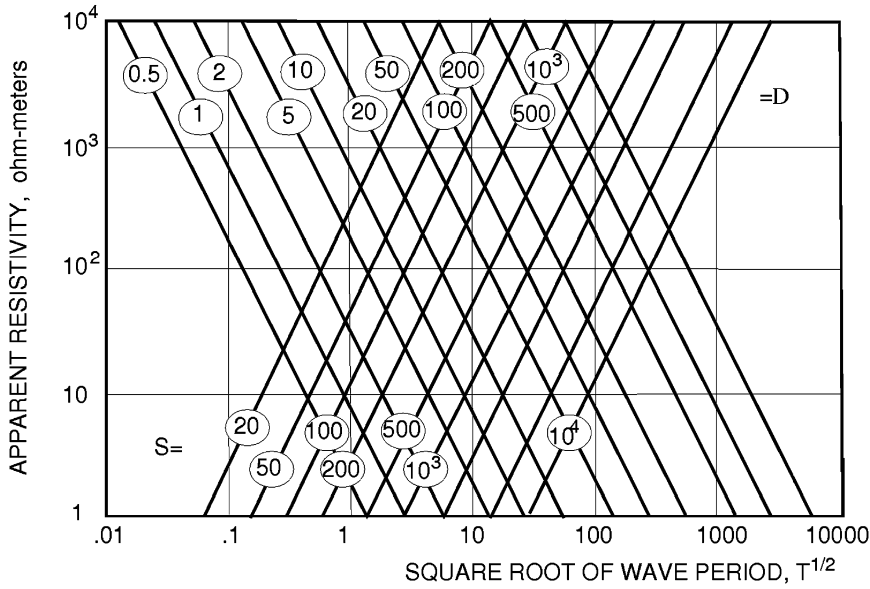
FIGURE 13.26

Dimensioned asymptotes to magnetotelluric sounding curves for two-layer cases with a perfect insulator at depth (*S*-curves) or a perfect insulator at depth (*D*-curves).

Then

$$z/\rho_a \approx \int_0^z \sigma(z)dz. \tag{13.174}$$

Differentiating both sides of this last equation with respect to z, we have

$$\rho(z) = \left[\frac{d}{dz}\left(\frac{z}{\rho_a}\right) \right]^{-1}, \tag{13.175}$$

where

$$\frac{d}{dz}\frac{z}{\rho_a} = \frac{1}{\rho_a} - \frac{z}{\rho_a^2}\frac{d\rho_a}{dz} = \frac{1}{\rho_a} - \frac{d\rho_a}{\rho_a}/\frac{dz}{z}. \tag{13.176}$$

On the strength of Eq. (13.173),

$$dz = \frac{1}{\sqrt{2\pi\mu_0}}(\sqrt{\rho_a}d\sqrt{T} + \sqrt{T}d\sqrt{\rho_a}),$$
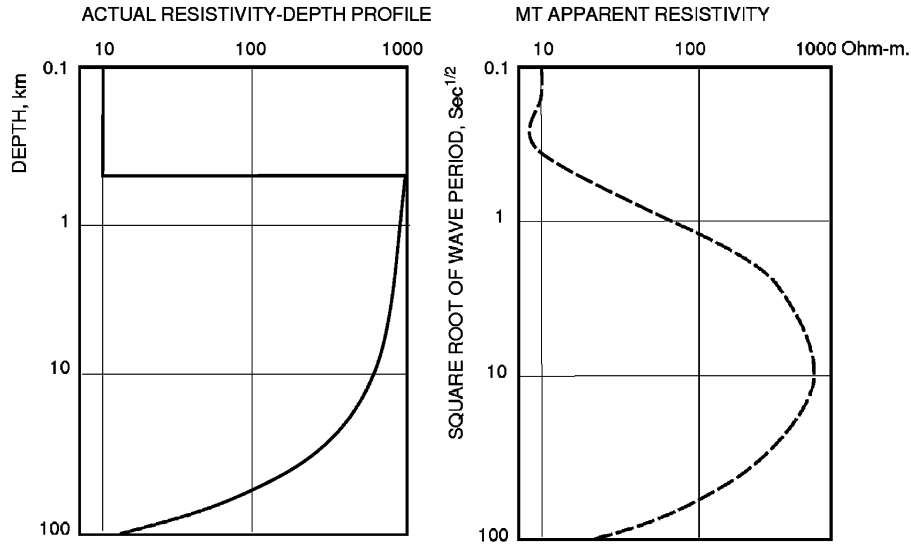
FIGURE 13.27

Example of the use of the Niblett-Bostick transform to obtain an approximate inversion of an MT sounding curve. The actual resistivity-depth profile is shown on the left. The curve on the right is the Niblett transform of the magnetotelluric curve for the model on the left.

and so

$$\frac{dz}{z} = \left(\frac{d\sqrt{T}}{\sqrt{T}} + \frac{d\sqrt{\rho_a}}{\sqrt{\rho_a}} \right) = \left(\frac{d\sqrt{T}}{\sqrt{T}} + \frac{1}{2}\frac{d\rho_a}{\rho_a} \right). \tag{13.177}$$

Substituting Eq. (13.177) into (13.176), and then into (13.175), we have

$$\rho(z) = \rho_a \left(\frac{2d\sqrt{T}/\sqrt{T} + d\rho_a/\rho_a}{2d\sqrt{T}/\sqrt{T} - d\rho_a/\rho_a} \right).$$

Introducing the notation

$$\frac{d\rho_a}{\rho_a} / \frac{d\sqrt{T}}{\sqrt{T}} = d \, \log \, \rho_a / d \, \log \sqrt{T} = m, \tag{13.178}$$

finally we can write

$$\rho(z) = \rho_a (2 + m)/(2 - m). \tag{13.179}$$

Fig. 13.27 shows a theoretical MTS curve for a two-layer model with a uniform upper layer and a lower region in which the conductivity increases exponentially with depth. Transformation of the MTS curve using Eqs. (13.174) and (13.177) leads to a sharpening of the resultant curve at the base of

the surface layer, and the resistivity at greater depths is closer to the actual resistivity. Such a *pseudo-inversion* is reasonably correct and easy to carry out, and even though the procedure is quick and dirty, the curve computed from the pseudo-inverted model is very similar to a correctly inverted resistivity profile.

13.7.3 QUANTITATIVE INTERPRETATION OF MTS CURVES WITH ONE-DIMENSIONAL MODELS

In the middle of the last century, at the beginning of the development of the MTS method, sophisticated manual techniques for matching an observed MTS curve to a precalculated set of theoretical curves were developed. The modern interpretation methods are based on the principle of the regularized inversion discussed in Chapter 7. Such methods are reliable and have the advantage that interpretations can be made uniformly.

The standard methods of interpreting MTS data are based on the automatic determination of a "best" model compatible with the data. In the inversion algorithms, one of the quick and dirty interpretation methods described in the last section can be used to formulate an "initial estimate" (sometimes disparagingly called a "first guess") of a resistivity-depth profile.

13.8 INTERPRETATION OF MVP AND GDS DATA

Magnetovariational and magnetotelluric surveys carried out over the last several decades in many different geological regions have in many cases led to the recognition of examples of anomalous behavior of the natural electromagnetic field of the earth. These anomalies represent inhomogeneities in the geoelectric structure of the earth's crust and mantle related to relief on the surface of the crystalline basement, tectonic faults, the presence of oil and gas reservoirs, hydrothermal phenomena, and simply tectonic pressure effects. Such studies are of great value because they provide important information on the petrophysical character, thermodynamics, and phase composition of rocks at great depth in the earth, information which cannot be obtained with any other method. All of this information is useful in regional predictions of the prospective mineral and energy resources. The study of these deep-seated anomalies is carried out with magnetovariational profiling (MVP) and with geomagnetic deep sounding (GDS), an approach which, when applied to its fullest extent, involves a combination of magnetotelluric and magnetovariational measurements.

The existence of a linear relationship between the components of the earth's natural electromagnetic field makes it unnecessary that all observations be done simultaneously over a network of stations, as often has been done in the past. The spatial behavior of the field can be determined using simultaneous observations at only two sites, one of which serves as a base station, M_o, and the other being a roving station, M. If the telluric, $\hat{t}$, and magnetic, $\hat{m}$, transfer functions are determined for the pairs of stations, for each roving location,

$$\mathbf{E}(\mathbf{r}) = \hat{t}(\mathbf{r}|\mathbf{r}_o)\hat{Z}^0\mathbf{H}^0,$$
$$\mathbf{H}(\mathbf{r}) = \hat{m}(\mathbf{r}|\mathbf{r}_0)\mathbf{H}^0, \tag{13.180}$$

where $\hat{Z}^0 = \hat{Z}(\mathbf{r}_0)$ and $\mathbf{H}^0 = \mathbf{H}(\mathbf{r}_0)$ are impedance and magnetic field observed at the base station, and $\mathbf{H}^0$ is an arbitrarily specified vector.

Knowing $\hat{t}$, $\hat{m}$, and $\hat{Z}^0$, it is possible to find the distribution of $\mathbf{E}$ and $\mathbf{H}$ for any polarization of the normalizing magnetic field.

For magnetic micropulsations and storms, Eq. (13.180) takes the following scalar form:

$$E_{\tilde{\alpha}}(\mathbf{r}) = \sum_{\tilde{\gamma}=x,y} t_{\tilde{\alpha}\tilde{\gamma}}(\mathbf{r}|\mathbf{r}_0) \sum_{\tilde{\beta}=x,y} Z^0_{\tilde{\gamma}\tilde{\beta}} H^0_{\tilde{\beta}}, \tilde{\alpha} = x, y;$$

$$H_{\tilde{\alpha}}(\mathbf{r}) = \sum_{\tilde{\beta}=x,y} m_{\tilde{\alpha}\tilde{\beta}}(\mathbf{r}|\mathbf{r}_0) H^0_{\tilde{\beta}}, \tag{13.181}$$

that is, the distribution of $\mathbf{E}$ and $\mathbf{H}$ is fully described by the horizontal vector $\mathbf{H}^o_\tau$.

Another approach to finding the distribution of $\mathbf{E}$ and $\mathbf{H}$ is based on the arbitrarily specified electric field, $\mathbf{E}^0 = \mathbf{E}(\mathbf{r}_0)$ at the base station:

$$E_{\tilde{\alpha}}(\mathbf{r}) = \sum_{\tilde{\beta}=x,y} t_{\tilde{\alpha}\tilde{\beta}}(\mathbf{r}|\mathbf{r}_0) E^0_{\tilde{\beta}} \tag{13.182}$$

$$H_\alpha(\mathbf{r}) = \sum_{\tilde{\gamma}=x,y} m_{\tilde{\alpha}\tilde{\gamma}}(\mathbf{r}|\mathbf{r}_0) \sum_{\tilde{\beta}=x,y} Y^0_{\tilde{\gamma}\tilde{\beta}} E^0_{\tilde{\beta}}, \tag{13.183}$$

where $\hat{Y}^0 = \hat{Y}(\mathbf{r}_0)$ is the admittance at the base station. And so, we can find the distribution of $\mathbf{E}$ and $\mathbf{H}$ for any polarization of the electric field at the base station.

The reference fields, both electric and magnetic, must be chosen so that the anomalous field is maximally expressed. In quasi-two-dimensional situations, this can be achieved by using the transverse magnetic field and the longitudinal electric field. For a three-dimensional case, the reference E field can be taken to be that field directly related to the flow of current in the earth. Best results are obtained when the base station is in a region of normal behavior.

And so, after reducing the MVP or GDS data, we obtain maps of the spatial distribution of variations of the magnetic and telluric fields over some region, or along some profile, for a wide range of frequencies. Interpretation of these data consists of the construction of a two-dimensional or even a three-dimensional geoelectric model for the surveyed region. At present, this is done in two steps.

- Step 1. Analysis of the electromagnetic field. This step consists of separating the observed electromagnetic field into internal and external parts, normal and anomalous parts, and shallow and deep anomalies.
- Step 2. Solution of the inverse geoelectric problem.

We will now consider the most effective methods for use in each stage.

13.8.1 SEPARATION OF FIELDS INTO INTERNAL AND EXTERNAL PARTS

One of the first problems to be solved by analysis of the geomagnetic field is the matter of separation into internal and external parts by Gauss in the mid-19th century. The external part of the field is that

part which has its origin in ionospheric and magnetospheric currents when the earth is nonconductive while the internal part is that due to the flow of currents induced within the earth. The importance of separating the internal and external fields is that, by so doing, we can recognize whether an anomalous magnetic field observed at the surface of the earth is associated with an inhomogeneous distribution of current in the ionosphere or an inhomogeneous geoelectric structure in the earth. The internal field, which is separated from the total field, is then further analyzed to determine the earth structure.

Let us consider a planar model in which the upper half-space is the insulating atmosphere and the lower half-space is the conducting earth. The current flow j^Q is localized in a region Q in the upper half-space. The fields in this model satisfy the equations:

$$curl\ \mathbf{H} = \mathbf{j}^Q,$$
$$curl\ \mathbf{E} = i\omega\mu_0\mathbf{H}, \tag{13.184}$$

for $z \leq -0$ and

$$curl\ \mathbf{H} = \sigma\mathbf{E},$$
$$curl\ \mathbf{E} = i\omega\mu_0\mathbf{H}, \tag{13.185}$$

for $z \geq +0$, where σ is the electrical conductivity of the lower half-space.

Introducing the definition $\mathbf{j}^E = \sigma\mathbf{E}$ for the currents induced in the earth, we can write Eq. (13.185) in the form

$$curl\ \mathbf{H} = \mathbf{j}^E,$$
$$curl\ \mathbf{E} = i\omega\mu_0\mathbf{H}. \tag{13.186}$$

Consequently, the total field, written as the sum of internal and external parts, is

$$\mathbf{H} = \mathbf{H}^e + \mathbf{H}^i,$$
$$\mathbf{E} = \mathbf{E}^e + \mathbf{E}^i,$$

where the external fields are related to the currents $\mathbf{j}^Q$ and the internal fields to the current $\mathbf{j}^E$ by the following equations:

$$curl\ \mathbf{H}^e = \mathbf{j}^Q,$$
$$curl\ \mathbf{E}^e = i\omega\mu_0^e\mathbf{H}, \tag{13.187}$$

$$curl\ \mathbf{H}^i = \mathbf{j}^E,$$
$$curl\ \mathbf{E}^i = i\omega\mu_0^i\mathbf{H}. \tag{13.188}$$

Let us divide the total geomagnetic field into external and internal parts. The first step is to express the magnetic field in the upper half-space in terms of a scalar potential:

$$\mathbf{H} = -grad\ U = -\frac{\partial U}{\partial x}\mathbf{d}_x - \frac{\partial U}{\partial y}\mathbf{d}_y - \frac{\partial U}{\partial z}\mathbf{d}_z, \tag{13.189}$$

where

$$\nabla^2 U = 0 \text{ for } z \leq -0, \tag{13.190}$$

and also

$$U = U^e + U^i. \tag{13.191}$$

We will represent U and $\mathbf{H}$ as Fourier transform integrals:

$$U = \frac{1}{4\pi^2} \iint_{-\infty}^{\infty} u e^{-i(k_x x + k_y y)} dk_x dk_y, \tag{13.192}$$

$$\mathbf{H}|_{z=0} = \frac{1}{4\pi^2} \iint_{-\infty}^{\infty} \mathbf{h}|_{z=0} e^{-i(k_x x + k_y y)} dk_x dk_y, \tag{13.193}$$

where k_x and k_y are spatial wave numbers in the axial directions x and y, d_Q is the height of the region Q above the earth's surface, and $u = u(k_x, k_y, z)$ and $\mathbf{h} = \mathbf{h}(k_x, k_y, z)$ are the spectral densities related to U and $\vec{H}$ through the inverse Fourier transform. In accord with Eq. (13.189),

$$h_x|_{z=0} = i k_x u|_{z=0},$$
$$h_y|_{z=0} = i k_y u|_{z=0},$$
$$h_z|_{z=0} = -u'|_{z=0}, \tag{13.194}$$

where the primes designate differentiation with respect to z. In addition to Eq. (13.190), u satisfies the one-dimensional Helmholtz equation

$$u'' = n_0^2 u, \tag{13.195}$$

where

$$n_0^2 = k_x^2 + k_y^2.$$

The general solution to Eq. (13.195) has the form

$$u = u^+ e^{n_0 z} + u^- e^{-n_0 z}, \tag{13.196}$$

where u^- and u^+ are arbitrary constants.

When we represent the potentials for the external and internal fields as Fourier integrals:

$$U^e = \frac{1}{4\pi^2} \iint_{-\infty}^{\infty} u^e e^{-i(k_x x + k_y y)} dk_x dk_y,$$

$$U^i = \frac{1}{4\pi^2} \iint u^i e^{-i(k_x x + k_y y)} dk_x dk_y, \tag{13.197}$$

it is obvious that

$$u^e = u^- e^{-n_0 z},$$
$$u^i = u^+ e^{n_0 z}, \tag{13.198}$$

because the external field decays as z becomes $-\infty$, and the internal field as z approaches $+\infty$.

In summary, the problem of determining the external and internal parts of the geomagnetic field for a given earth model reduces to evaluating the constants u^+ and u^-. We will now solve this problem. To do so, we substitute Eq. (13.196) into (13.194):

$$h_x|_{z=0} = ik_x(u^+ + u^-),$$
$$h_y|_{z=0} = ik_y(u^+ + u^-),$$
$$h_z|_{z=0} = -n_0(u^+ - u^-), \tag{13.199}$$

and hence

$$u^+ = \frac{1}{2}\left(\frac{h_x}{ik_x}\bigg|_{z=0} - \frac{1}{n_0}h_z\bigg|_{z=0}\right),$$
$$u^- = \frac{1}{2}\left(\frac{h_x}{ik_x}\bigg|_{z=0} + \frac{1}{n_0}h_z\bigg|_{z=0}\right). \tag{13.200}$$

It is a simple matter to determine the spectral densities for the potentials of the external and internal parts of the field; we merely substitute Eq. (13.200) into (13.198). Inasmuch as each component of the external and internal fields is related to a corresponding formula for potential like Eq. (13.194), by considering Eqs. (13.198) and (13.200) we can write:

$$h_x^e|_{z=0} = \frac{1}{2}\left(h_x\bigg|_{z=0} + \frac{ik_x}{n_0}h_z\bigg|_{z=0}\right),$$
$$h_y^e|_{z=0} = \frac{1}{2}\left(h_y\bigg|_{z=0} + \frac{ik_y}{n_0}h_z\bigg|_{z=0}\right),$$
$$h_z^e|_{z=0} = \frac{1}{2}\left(h_z\bigg|_{z=0} + \frac{n_0}{ik_x}h_x\bigg|_{z=0}\right) = \frac{1}{2}\left(h_z|_{z=0} + \frac{n_0}{ik_y}h_y|_{z=0}\right),$$
$$h_x^i|_{z=0} = \frac{1}{2}\left(h_x\bigg|_{z=0} - \frac{ik_x}{n_0}h_z\bigg|_{z=0}\right),$$
$$h_y^i|_{z=0} = \frac{1}{2}\left(h_y\bigg|_{z=0} - \frac{ik_y}{n_0}h_z\bigg|_{z=0}\right),$$
$$h_z^i|_{z=0} = \frac{1}{2}\left(h_z\bigg|_{z=0} - \frac{n_0}{ik_x}h_x\bigg|_{z=0}\right) = \frac{1}{2}\left(h_z\bigg|_{z=0} - \frac{n_0}{ik_y}h_y\bigg|_{z=0}\right), \tag{13.201}$$

where it has been taken into account that, because

$$curl_z\mathbf{H}|_{z=0} = 0,$$

the spectral densities for the horizontal components of the magnetic field are proportional to one another:

$$k_xh_y|_{z=0} = k_yh_x|_{z=0}. \tag{13.202}$$

Synthesizing Eq. (13.201), we have

$$\mathbf{H}^{e,i}|_{z=0} = \frac{1}{4\pi^2} \iint_{-\infty}^{\infty} \mathbf{h}^{e,i}\Big|_{z=0} e^{-i(k_x x + k_y y)} dk_x dk_y \ . \tag{13.203}$$

And so, the problem of separating a field into its external and internal parts has been solved.

We take note that knowledge of the ratio of the spectral densities for the potentials characterizing the external and internal parts of the field permits us to determine the spectrum of the magnetic impedance. Furthermore, we have

$$Z_h^* = \frac{i\omega\mu_0}{n_0} \cdot \frac{u^i - u^e}{u^i + u^e}\Big|_{z=0} = \frac{i\omega\mu_0}{n_0} \cdot \frac{1 - u^e/u^i}{1 + u^e/u^i} /u^i\Big|_{z=0} \ . \tag{13.204}$$

On the other hand, $u^e/u^i |_{z=0}$ can be expressed in terms of impedance:

$$\frac{u^e}{u^i}\Big|_{z=0} = \frac{u^-}{u^+} = \frac{i\omega\mu_0/n_0 - Z_h^*}{i\omega\mu_0/n_0 + Z_h^*} \ , \tag{13.205}$$

and moreover

$$h_x^e/h_x^i = h_y^e/h_y^i = u^-/u^+ = u^e/e^i \ . \tag{13.206}$$

In summary, the ratio of the spectral densities for the external and internal parts of the magnetic potential at the surface of an earth with an arbitrary distribution of electrical conductivity is controlled only by the magnetic spectral impedance of the earth.

We should note in the conclusion of this section, that in a similar way one can separate the field into the upgoing and downgoing parts. This problem arises in the case of the marine electromagnetic surveys, which will be discussed in Chapter 15.

13.8.2 SEPARATION OF FIELDS INTO NORMAL AND ANOMALOUS PARTS

Simple methods for separating a geomagnetic field into normal and anomalous parts are based on differences in the spatial structures of the normal and anomalous fields (assuming that short wavelength anomalies in the anomalous field are superimposed on longer wavelength variations in the normal field). Based on this, smoothing and extrapolation are our tools. Such an approach should also be effective for recognizing local anomalies, but it may also show very deep phenomena if a strong regional component is present. The problem at hand can be formulated as follows: the distribution of an electromagnetic field $\mathbf{E}$, $\mathbf{H}$ is given over the surface of the earth; it is required that we separate the field into normal and anomalous parts using whatever information is available about the normal geoelectric section. The problem is logically related to Gauss's problem of dividing the field into external and internal parts. In this respect, we select the external field and compute a spectral impedance for a normal earth. From this, we predict the normal internal field and then by simple decomposition we find the normal and anomalous parts of the whole field.

From another point of view, the anomalous field found on the surface of the earth, as noted earlier, can be separated into two major groups:

- 1) surficial anomalies caused by inhomogeneities in the uppermost layers of the crust, and
- 2) deep-seated anomalies associated with supposed conductive and insulating zones in the crust and upper mantle.

The methods used in interpreting the two types of anomaly differ one from the other. However, both types of anomaly occur together; that is, an anomalous field can be the combined effect from two causative regions in the earth, electromagnetically interlinked.

Therefore, it is important in interpretation to distinguish between surficial anomalies and deep-seated anomalies. The problem can be stated as follows: the distribution of an electromagnetic field **E**, **H** on the surface of the earth has been established; it is necessary to separate the anomalies in this field contributed by surficial features and deep-seated features, using whatever information is available about the normal geoelectric section and about inhomogeneities in the uppermost layers (Berdichevsky and Zhdanov, 1984).

13.9 3-D MAGNETOTELLURIC INVERSION

As we have demonstrated above, in magnetotelluric (MT) method the observed data are not usually recorded as pure electric or magnetic field components. In particular, the results of magnetotelluric measurements are the *apparent resistivity* and *phase* calculated from the mutually orthogonal electric and magnetic field components. Let us denote an arbitrary horizontal electric field component by E, and define H as the magnetic field component perpendicular to the direction of E at a particular receiver site. Note that both E and H are complex numbers. The *magnetotelluric impedance* is defined as the ratio of E and H:

$$Z = \frac{E}{H}. \tag{13.207}$$

Since the impedance does not depend on the actual strength of the source, it is a very practical parameter for natural electromagnetic field observations. The magnetotelluric apparent resistivity is calculated from Z, using

$$\rho = \frac{1}{\omega\mu_0}|Z|^2. \tag{13.208}$$

If the incident field is a plane wave and the model is a homogeneous half-space, ρ is equal to the true resistivity, making it indicative of the resistivity structure of the subsurface.

Another commonly measured parameter is the phase angle of the impedance:

$$\phi = \tan^{-1}\frac{\mathrm{Im}Z}{\mathrm{Re}Z}. \tag{13.209}$$

This quantity is less sensitive to the effect of shallow subsurface anomalies, so it is particularly useful for the detection of deep structures.

To obtain a simple relationship between the anomalous field components and the MT parameters, let us express the logarithm of Z by writing $E = E^b + E^a$ and $H = H^b + H^a$:

$$\ln Z = \ln \frac{E^b + E^a}{H^b + H^a} = \ln \left(\frac{E^b + E^a}{E^b} \cdot \frac{H^b}{H^b + H^a} \cdot \frac{E^b}{H^b} \right). \tag{13.210}$$

Thus,

$$\ln Z = \ln \left(1 + E^a/E^b \right) - \ln \left(1 + H^a/H^b \right) + \ln Z^b, \tag{13.211}$$

where $Z^b = E^b/H^b$ is the *background impedance*.

From Eq. (13.208) we obtain

$$\ln |Z| = \ln \left[(\omega\mu_0\rho)^{1/2} \right] = \frac{1}{2} \ln(\omega\mu_0) + \frac{1}{2} \ln \rho. \tag{13.212}$$

The same relationship holds for the background impedance as well. Considering the identities $\ln Z = \ln |Z| + i\phi$ and $\ln Z^b = \ln |Z^b| + i\phi_b$ we find

$$\frac{1}{2} \ln \rho_a + i\phi_a = \ln \left(1 + E^a/E^b \right) - \ln \left(1 + H^a/H^b \right), \tag{13.213}$$

where $\ln \rho_a = \ln \rho - \ln \rho_b$ is the *log-anomalous apparent resistivity*, and $\phi_a = \phi - \phi_b$ is the *anomalous phase*. Knowing the background cross-section, we can easily obtain these quantities from the measured total apparent resistivities and phases. The apparent resistivities and phases can be used as the input data for magnetotelluric inversion (e.g., Zhdanov, 2009).

In a general case, however, interpretation of magnetotelluric data is based on the calculation of all components of impedance tensor, which serve as the transfer functions between the horizontal components of the electric and magnetic field (Berdichevsky and Dmitriev, 2002, 2008):

$$Z = \begin{bmatrix} Z_{xx} & Z_{xy} \\ Z_{yx} & Z_{yy} \end{bmatrix}. \tag{13.214}$$

The technique of determining the components of the impedance tensor was outlined above, and it can be summarized as follows. The linear relationships between the EM field components are characterized by the following equation:

$$E_x = Z_{xx} H_x + Z_{xy} H_y, \tag{13.215}$$
$$E_y = Z_{yx} H_x + Z_{yy} H_y. \tag{13.216}$$

The expressions for the Z_{xx} and Z_{xy} components of the full impedance tensor are:

$$Z_{xy} = \frac{E_x^{(1)} H_x^{(2)} - E_x^{(2)} H_x^{(1)}}{H_y^{(1)} H_x^{(2)} - H_y^{(2)} H_x^{(1)}}, \quad Z_{xx} = \frac{E_x^{(1)} H_y^{(2)} - E_x^{(2)} H_y^{(1)}}{H_x^{(1)} H_y^{(2)} - H_x^{(2)} H_y^{(1)}}. \tag{13.217}$$

Similarly, using Eq. (13.216), the components of the full impedance tensor Z_{yx} and Z_{yy} are expressed:

$$Z_{yy} = \frac{E_y^{(1)} H_x^{(2)} - E_y^{(2)} H_x^{(1)}}{H_y^{(1)} H_x^{(2)} - H_y^{(2)} H_x^{(1)}}, \; Z_{yx} = \frac{E_y^{(1)} H_y^{(2)} - E_y^{(2)} H_y^{(1)}}{H_x^{(1)} H_y^{(2)} - H_x^{(2)} H_y^{(1)}}. \tag{13.218}$$

13.9.1 TIKHONOV REGULARIZATION IN THE FULL MT IMPEDANCE TENSOR INVERSION

We can describe the rigorous MT inverse problem as a solution of an operator equation:

$$\mathbf{d} = \mathbf{A}(\mathbf{m}), \tag{13.219}$$

where $\mathbf{d}$ stands for a *data vector* formed by all four components of the full MT impedance tensor, $\mathbf{m} = \Delta\boldsymbol{\sigma}$ is model parameters vector describing the conductivity distribution, and $\mathbf{A}$ is the nonlinear forward operator symbolizing the governing equations of the MT modeling problem. We call Eq. (13.219) an *impedance equation*. The impedance equation is ill posed, i.e., the solution can be nonunique and unstable. The conventional way of solving ill-posed inverse problems, according to regularization theory (Chapter 7), is based on minimization of the Tikhonov parametric functional:

$$P(\mathbf{m}) = \phi(\mathbf{m}) + \alpha S(\mathbf{m}) = min, \tag{13.220}$$

where $\phi(\mathbf{m}) = ||\mathbf{A}(\mathbf{m}) - \mathbf{d}||_2^2$ is the misfit functional between the predicted data $A(\mathbf{m})$ and the observed data $\mathbf{d}$, $s(\mathbf{m})$ is a stabilizing functional, and α is a regularization parameter. The optimal value of α_{opt} is determined from the misfit condition,

$$\varphi\left(\mathbf{m}_{\alpha_{opt}}\right) = \delta_d, \tag{13.221}$$

where δ_d is the noise level of the data.

We discussed in Chapter 7, that the traditional way to implement regularization in the solution of the inverse problem is based on a consideration of the class of inverse models with a smooth distribution of the model parameters. Within the framework of classical Tikhonov regularization, one can select a smooth solution by introducing the corresponding minimum norm, or "smoothing" stabilizing functionals. This approach is widely used in geophysics and has proven to be a powerful tool for stable inversion of geophysical data.

The traditional inversion algorithms providing smooth solutions for geoelectrical structures have difficulties, however, in describing the sharp geoelectrical boundaries between different geological formations. This problem arises, for example, in inversion for the local conductive target with sharp boundaries between the conductor and the resistive host rocks, which is a typical model in mining exploration. In these situations, it can be useful to search for the stable solution within the class of inverse models with sharp geoelectrical boundaries.

The mathematical technique for solving this problem is described in Chapter 7. It is based on introducing a special type of stabilizing functional, the so-called minimum support or minimum gradient support functionals. These stabilizers select the inverse models from a class of models with the minimum volume of the domain with the anomalous parameter distribution (MS stabilizer) or with

a minimum volume of area where the gradient of the model parameters is nonzero (MGS stabilizer). These classes of models describe compact objects (minimum support) or objects with sharp boundaries (minimum gradient support), which are typical targets in geophysical mineral exploration, for example. We call this technique a focusing regularized inversion to distinguish it from the traditional smooth regularized inversion.

We can use the regularized conjugate gradient (RCG) method to solve a nonlinear inverse problem (13.219). The basic principles of the RCG method are outlined in Chapter 8. This method can incorporate both a smooth regularized inversion, which generates a smooth image of the inverted conductivity, and a focusing regularized inversion, producing a sharp, focused image of the geoelectrical target. In particular, a re-weighted method of the regularized inversion can be used for implementation of the focusing stabilizers (Zhdanov, 2002).

13.9.2 PRINCIPLES OF THE RE-WEIGHTED REGULARIZED INVERSION

In this section, as an example, we present a short summary of the basic principles of the re-weighted regularized inversion with a minimum support stabilizer. Let us consider a general discrete geophysical inverse problem, described by the operator equation:

$$\mathbf{d} = \mathbf{A}(\mathbf{m}), \tag{13.222}$$

where, in general, $\mathbf{A}$ is a nonlinear vector operator, $\mathbf{m}$ represents the model parameters, and $\mathbf{d}$ are observed geophysical data. We assume that N_d measurements are performed in some geophysical experiment. Then we can treat these values as the components of the N_d-dimensional vector $\mathbf{d}$ (note that components of vector $\mathbf{d}$ can be complex numbers). Similarly, some model parameters can be represented as the components of a vector $\mathbf{m}$ of the order N_m:

$$\mathbf{d} = [d_1, d_2, d_3, ..., d_{N_d}]^T,$$
$$\mathbf{m} = [m_1, m_2, m_3, ..., m_{N_m}]^T,$$

where the superscript T denotes the transpose of the two vectors.

We solve this ill-posed inverse problem (13.222), using minimization of the Tikhonov parametric functional:

$$P^\alpha(\mathbf{m}) = \varphi(\mathbf{m}) + \alpha s(\mathbf{m}) \rightarrow \min, \tag{13.223}$$

where $\varphi(\mathbf{m})$ is a misfit functional between the theoretical values $\mathbf{A}(\mathbf{m})$ and the observed data $\mathbf{d}$, $s(\mathbf{m})$ is a stabilizing functional, and α is a regularization parameter.

The misfit functional $\varphi(\mathbf{m})$ is usually selected in the complex Euclidean metric of data space as a weighted norm square of the difference between the observed and predicted data (errors):

$$\varphi(\mathbf{m}) = \|\widehat{\mathbf{W}}_d(\mathbf{A}(\mathbf{m}) - \mathbf{d})\|^2 = (\mathbf{A}(\mathbf{m}) - \mathbf{d})^*\widehat{\mathbf{W}}_d^2(\mathbf{A}(\mathbf{m}) - \mathbf{d}), \tag{13.224}$$

where asterisk "*" denotes a transposed complex conjugate matrix, $\mathbf{W}_d$ is the data weighting matrix which allows us to set the variance for each datum to its appropriate level.

The optimal value of α is determined from the misfit condition,

$$\varphi(\mathbf{m}) = \delta_d, \tag{13.225}$$

where δ_d is the noise level of the data.

The stabilizing functional $s(\mathbf{m})$ can be selected, for example, as a norm square of the difference between the current and a priori model:

$$s_{MN}(\mathbf{m}) = \left\| \mathbf{m} - \mathbf{m}_{apr} \right\|^2 = \left(\mathbf{m} - \mathbf{m}_{apr} \right)^T \left(\mathbf{m} - \mathbf{m}_{apr} \right), \tag{13.226}$$

where superscript "T" denotes a transposed matrix. This is a so-called minimum norm stabilizer which provides, usually, a relatively smooth image of the inverse model. Substituting (13.224) and (13.226) into (13.223), we arrive at the conventional Tikhonov parametric functional:

$$P^\alpha(\mathbf{m}) = (\mathbf{A}(\mathbf{m}) - \mathbf{d})^* \mathbf{W}_d^2 (\mathbf{A}(\mathbf{m}) - \mathbf{d}) + \alpha \left(\mathbf{m} - \mathbf{m}_{apr} \right)^T \left(\mathbf{m} - \mathbf{m}_{apr} \right) \to \min. \tag{13.227}$$

In order to generate a compact image of a geophysical model with sharp boundaries, we can apply a minimum support stabilizer, which is a nonquadratic functional of the form (see Chapter 7):

$$s_{MS}(\mathbf{m}) = (\mathbf{m} - \mathbf{m}_{apr})^T \left[\left(\widehat{\mathbf{m}} - \widehat{\mathbf{m}}_{apr} \right)^2 + e^2 \widehat{\mathbf{I}} \right]^{-1} (\mathbf{m} - \mathbf{m}_{apr}), \tag{13.228}$$

where $\widehat{\mathbf{m}}$ and $\widehat{\mathbf{m}}_{apr}$ are the $N_m \times N_m$ diagonal matrices of inverse model parameters (current and a priori, respectively):

$$\widehat{\mathbf{m}} = \mathbf{diag}\left(m_1, m_2, ..., m_{N_m} \right), \ \ \widehat{\mathbf{m}}_{apr} = \mathbf{diag}\left(m_{1apr}, m_{2apr}, ..., m_{N_m apr} \right),$$

e is focusing parameter, and $\widehat{\mathbf{I}}$ is $N_m \times N_m$ identity matrix. It was shown by Portniaguine and Zhdanov (1999a) that this functional minimizes an area of nonzero parameters distribution (minimizes the support of the inverse model), if e tends to zero: $e \to 0$.

Following Zhdanov (2002), we note that this stabilizing functional can be expressed as a pseudo-quadratic functional of the model parameters:

$$s_{MS}(\mathbf{m}) = \left[\widehat{\mathbf{W}}_e (\mathbf{m} - \mathbf{m}_{apr}) \right]^T \widehat{\mathbf{W}}_e (\mathbf{m} - \mathbf{m}_{apr}), \tag{13.229}$$

where $\widehat{\mathbf{W}}_e$ is a diagonal matrix:

$$\widehat{\mathbf{W}}_e = \left[\left(\widehat{\mathbf{m}} - \widehat{\mathbf{m}}_{apr} \right)^2 + e^2 \widehat{\mathbf{I}} \right]^{-1/2}. \tag{13.230}$$

This matrix depends on $\mathbf{m}$, which is why we call (13.229) a "pseudo-quadratic" functional. We can introduce a linear transformation of the original model parameters into the space of the weighted model parameters:

$$\mathbf{m}^w = \widehat{\mathbf{W}}_e \mathbf{m}. \tag{13.231}$$

As a result of this transformation, we arrive at the traditional quadratic minimum norm functional, $s_{MN}(\mathbf{m}^w)$, for the weighted parameters $\mathbf{m}^w$:

$$s_{MS}(\mathbf{m}) = s_{MN}(\mathbf{m}^w) = (\mathbf{m}^w - \mathbf{m}_{apr}^w)^T (\mathbf{m}^w - \mathbf{m}_{apr}^w) = \left\| \mathbf{m}^w - \mathbf{m}_{apr}^w \right\|^2. \tag{13.232}$$

We also introduce the weighted data $\mathbf{d}^w$ as

$$\mathbf{d}^w = \widehat{\mathbf{W}}_d \mathbf{d}.$$

Using these notations, we can rewrite the parametric functional (13.223) as follows:

$$
\begin{aligned}
P^\alpha(\mathbf{m}^w) &= \left\| \mathbf{A}^w(\mathbf{m}^w) - \mathbf{d}^w \right\|^2 + \alpha \left\| \mathbf{m}^w - \mathbf{m}^w_{apr} \right\|^2 \\
&= \left(\mathbf{A}^w(\mathbf{m}^w) - \mathbf{d}^w \right)^* \left(\mathbf{A}^w(\mathbf{m}^w) - \mathbf{d}^w \right) + \alpha \left(\mathbf{m}^w - \mathbf{m}^w_{apr} \right)^T \left(\mathbf{m}^w - \mathbf{m}^w_{apr} \right) \to \min,
\end{aligned}
$$

(13.233)

where $\mathbf{A}^w(\mathbf{m}^w) = \widehat{\mathbf{W}}_d \mathbf{A}(\widehat{\mathbf{W}}_e^{-1} \mathbf{m}^w)$.

Note that the unknown parameters now are weighted model parameters, $\mathbf{m}^w$. In order to obtain the original model parameters, we have to apply inverse weighting to the result of minimization of the parametric functional (13.233):

$$\mathbf{m} = \widehat{\mathbf{W}}_e^{-1} \mathbf{m}^w.$$

(13.234)

Therefore, the problem of minimizing the parametric functional, given by Eq. (13.223), can be treated in a similar way to the minimization of the conventional Tikhonov functional (13.227). The only difference is that now we introduce some variable weighting matrix $\mathbf{W}_e$ for the model parameters. The minimization problem (13.233) can be solved using any gradient type technique, say, by the conjugate gradient (CG) method (Chapter 7).

Portniaguine and Zhdanov (1999a) have developed a simplified approach to minimizing the parametric functional (13.233), using the so-called re-weighted regularized conjugate gradient (RRCG) method. In the framework of this approach, the variable weighting matrix $\mathbf{W}_e$ is precomputed on each iteration, $\mathbf{W}_e = \mathbf{W}_{en} = \mathbf{W}_e(\mathbf{m}_n)$, based on the values $\mathbf{m}_n$, obtained on the previous iteration. This linear transformation is updated after a fixed number of intermediate iterations, which is equivalent to the re-weighting of the model parameters. The advantage of this approach is in its simplicity. The disadvantage is related to the fact that due to re-weighting, the misfit and stabilizing functionals can change, and even increase from iteration to iteration (Zhdanov, 2002). In the next section we consider a different method of the minimum support nonlinear inversion, which does not have the problems mentioned above, and at the same time does not require minimization of a nonconvex functional. This technique is based on a nonlinear parameterization, outlined below.

13.9.3 MINIMUM SUPPORT NONLINEAR PARAMETERIZATION

Zhdanov and Tolstaya (2004) suggested using a nonlinear transformation of the nonquadratic minimum support stabilizing functional into a quadratic one by using a specially selected nonlinear transformation of the model parameters, described by the formula

$$\widetilde{m}_i = \frac{m_i - m_{apr_i}}{\sqrt{\left(m_i - m_{apr_i} \right)^2 + e^2}},$$

(13.235)

where $\mathbf{m} = \{m_i\}$, $i = 1..N_m$, is the original vector of the model parameters, and $\widetilde{\mathbf{m}} = \{\widetilde{m}_i\}$, $i = 1..N_m$ is a new vector of the nonlinear parameters. The following inverse transform holds:

$$m_i - m_{apr_i} = \frac{\widetilde{m}_i e}{\sqrt{1 - \widetilde{m}_i^2}}. \tag{13.236}$$

A transformation pair, (13.235) and (13.236), can be written in matrix notation as

$$\widetilde{\mathbf{m}} = \widehat{\mathbf{W}}_e \left(\mathbf{m} - \mathbf{m}_{apr}\right) = \left[\left(\widehat{\mathbf{m}} - \widehat{\mathbf{m}}_{apr}\right)^2 + e^2\widehat{\mathbf{I}}\right]^{-1/2} \left(\mathbf{m} - \mathbf{m}_{apr}\right), \tag{13.237}$$

and

$$\mathbf{m} - \mathbf{m}_{apr} = e \left[\widehat{\mathbf{I}} - \widehat{\widetilde{\mathbf{m}}}^2\right]^{-1/2} \widetilde{\mathbf{m}}, \tag{13.238}$$

where $\widehat{\widetilde{\mathbf{m}}}$ is the diagonal matrix $N_m \times N_m$ with the diagonal formed by nonlinear model parameters, $\widehat{\widetilde{\mathbf{m}}} = \mathbf{diag}\left(\widetilde{m}_1, \widetilde{m}_2, ..., \widetilde{m}_{N_m}\right)$.

Substituting (13.238) into the Tikhonov parametric functional (13.223), we arrive at the conventional parametric functional with a minimum norm stabilizer:

$$P[\widetilde{\mathbf{m}}] = ||\mathbf{A}^w \left(\mathbf{m}_{apr} + e \left[\widehat{\mathbf{I}} - \widehat{\widetilde{\mathbf{m}}}^2\right]^{-1/2} \widetilde{\mathbf{m}}\right) - \mathbf{d}^w||^2 + \alpha ||\widetilde{\mathbf{m}} - \widetilde{\mathbf{m}}_{apr}||^2. \tag{13.239}$$

We call the transformation, described by formulae (13.237) and (13.238), *a minimum support nonlinear parameterization*, because it automatically ensures that the solution belongs to the class of models with a minimum support.

Note that, in implementing the CG method, we have to calculate on every iteration n the Fréchet derivative matrix, $\widehat{\widetilde{\mathbf{F}}}_{(n)}$, with respect to a new model parameter vector, $\widetilde{\mathbf{m}}_n$, which is equal to

$$\widehat{\widetilde{\mathbf{F}}}_{(n)} = e\widehat{\mathbf{F}}_{(n)} \left[\widehat{\mathbf{I}} - \widehat{\widetilde{\mathbf{m}}}_n^2\right]^{-3/2}, \tag{13.240}$$

where $\widehat{\mathbf{F}}_{(n)}$ is a Fréchet derivative of our original operator $\mathbf{A}^w$ at a point $\mathbf{m}_n$.

Finally, we can write the following regularized conjugate gradient (RCG) algorithm (Zhdanov, 2002, p. 149) for the minimization of the parametric functional (13.239):

$$\mathbf{r}_n = \mathbf{A}^w \left(\mathbf{m}_n\right) - \mathbf{d}^w, \tag{13.241}$$

$$\mathbf{l}_n = Re\left[\widehat{\widetilde{\mathbf{F}}}_{(n)}^* \mathbf{r}_n\right] + \alpha \left(\widetilde{\mathbf{m}}_n - \widetilde{\mathbf{m}}_{apr}\right), \tag{13.242}$$

$$\widetilde{\mathbf{l}}_n = \mathbf{l}_n + \widetilde{\mathbf{l}}_n \frac{||\mathbf{l}_n||}{||\mathbf{l}_{n-1}||}, \ \widetilde{\mathbf{l}}_0 = \mathbf{l}_0, \tag{13.243}$$

$$k_n = \widetilde{\mathbf{l}}_n^* \mathbf{l}_n \left[\left\|\widehat{\widetilde{\mathbf{F}}}_n \widetilde{\mathbf{l}}_n\right\|^2 + \alpha \left\|\widetilde{\mathbf{l}}_n\right\|^2\right]^{-1}, \tag{13.244}$$

$$\widetilde{\mathbf{m}}_{n+1} = \widetilde{\mathbf{m}}_n - k_n \widetilde{\mathbf{l}}_n, \tag{13.245}$$

$$\mathbf{m}_{n+1} = e \left[\widehat{\mathbf{I}} - \widehat{\widetilde{\mathbf{m}}}_{n+1}^2\right]^{-1/2} \widetilde{\mathbf{m}}_{n+1} + \mathbf{m}_{apr}. \tag{13.246}$$

We should notice, however, that in the case of a minimum support nonlinear parameterization, we must consider a constrained optimization, with absolute value of $\widetilde{\mathbf{m}}$ being less than 1. In order to keep the true model parameter $\mathbf{m}$ within the known bounds, we also should impose additional constraints on $\widetilde{\mathbf{m}}$ and require that

$$\widetilde{m}_i^- < \widetilde{m}_i < \widetilde{m}_i^+, \tag{13.247}$$

where

$$\widetilde{m}_i^- = \frac{m_i^-}{\sqrt{m_i^{-2} + e^2}}, \text{ and } \widetilde{m}_i^+ = \frac{m_i^+}{\sqrt{m_i^{+2} + e^2}}, \text{ for } i = 1..N_m, \tag{13.248}$$

where $\mathbf{m}^+ = \{m_i^+\}$, and $\mathbf{m}^- = \{m_i^-\}$ are the known upper and lower boundaries for material property.

Therefore, we will use the gradient projection method (Bertsekas, 1999), and take the projection of the parameters $\widetilde{\mathbf{m}}$ onto the compact set, bounded by (13.247). We will perform minimization in a space of new parameters, $\mathbf{m}^p \in (-\infty; \infty)$, and then take the projection onto this set, using the following function for the projection:

$$\widetilde{m}_i = \widetilde{m}_i^- + \frac{\widetilde{m}_i^+ + \widetilde{m}_i^-}{2} \left[\frac{2}{\pi} \tan^{-1}\left(\widetilde{m}_i^p - \frac{\widetilde{m}_i^+ + \widetilde{m}_i^-}{2} \right) + 1 \right].$$

This is a one-to-one transformation, which insures (13.247) and has the inverse transformation:

$$\widetilde{m}_i^p = \frac{\widetilde{m}_i^+ + \widetilde{m}_i^-}{2} + \tan \frac{(\widetilde{m}_i - \widetilde{m}_i^-)\pi}{(\widetilde{m}_i^+ - \widetilde{m}_i) - \pi/2}.$$

The expression for the Fréchet derivative $\widehat{\widetilde{\mathbf{F}}}_{p(n)}$ with respect to a new model parameter vector $\mathbf{m}_n^p$ at the n-th iteration of the CG method will take the form

$$\widehat{\widetilde{\mathbf{F}}}_{p(n)} = e\widehat{\mathbf{F}}_{(n)} \left[\mathbf{I} - \widehat{\widetilde{\mathbf{m}}}_n^2 \right]^{-3/2} \mathbf{diag}\left[\frac{\widetilde{m}_{ni}^+ - \widetilde{m}_{ni}^-}{\pi} \left(1 + (\widetilde{m}_{ni}^p)^2 \right)^{-1}, i = 1..N_m \right].$$

The following formulae summarize the RCG method with two parameterizations:

$$\mathbf{r}_n = \mathbf{A}^w (\mathbf{m}_n) - \mathbf{d}^w, \tag{13.249}$$

$$\mathbf{l}_n = Re\left[\widehat{\widetilde{\mathbf{F}}}_{p(n)}^* \mathbf{r}_n \right] + \alpha \widetilde{\mathbf{m}}_n^p, \tag{13.250}$$

$$\widetilde{\mathbf{l}}_n = \mathbf{l}_n + \widetilde{\mathbf{l}}_n \frac{||\mathbf{l}_n||}{||\mathbf{l}_{n-1}||}, \ \widetilde{\mathbf{l}}_0 = \mathbf{l}_0 \tag{13.251}$$

$$k_n = \widetilde{\mathbf{l}}_n^* \mathbf{l}_n \left[\left\| \widehat{\widetilde{\mathbf{F}}}_{p(n)} \widetilde{\mathbf{l}}_n \right\|^2 + \alpha \left\| \widetilde{\mathbf{l}}_n \right\|^2 \right]^{-1}, \tag{13.252}$$

$$\widetilde{\mathbf{m}}_{n+1}^p = \widetilde{\mathbf{m}}_n^p - k_n \widetilde{\mathbf{l}}_n, \tag{13.253}$$

$$\widetilde{\mathbf{m}}_{n+1} = \widetilde{\mathbf{m}}^- + \frac{1}{2}(\widetilde{\mathbf{m}}^+ - \widetilde{\mathbf{m}}^-) \left(\frac{2}{\pi} \tan^{-1}(\widetilde{\mathbf{m}}_{n+1}^p) + 1 \right), \tag{13.254}$$

$$\mathbf{m}_{n+1} = e \left[\widehat{\mathbf{I}} - \widehat{\widehat{\mathbf{m}}}_{n+1}^2 \right]^{-1/2} \widetilde{\mathbf{m}}_{n+1} + \mathbf{m}_{apr}. \tag{13.255}$$

The difficulty with nonlinear parameters is that, in the case of a zero initial approximation ($\widetilde{\mathbf{m}} = 0$) in the conjugate gradient algorithm, we will get almost zeros for the Fréchet derivative, because $\mathbf{m}^p$ would be too big, and we will not step away from the zero starting point. To overcome this difficulty, we use as a starting point for minimum support inversion a solution, $\mathbf{m}_0$, obtained with the minimum norm stabilizer.

After introducing a trigonometric parameterization, we can proceed with the minimum support nonlinear parameterization and find the minimum of the Tikhonov parametric functional using the regularized conjugate gradient (RCG) algorithm (13.249)–(13.255). This completes the formulation of the inversion scheme based on the minimum support nonlinear parameterization.

13.9.4 FRÉCHET OPERATOR AND ITS ADJOINT FOR TWO-COMPONENT IMPEDANCE INVERSION

The regularized conjugate gradient methods, outlined above, require the corresponding Fréchet matrices calculation. Once the forward operator with the corresponding Fréchet matrices and the minimization scheme are implemented, an inversion can be successfully performed. We will discuss the effective technique of the Fréchet matrix calculation in the next section.

This section is provided for comparison of the inversion of two principal components with the inversion of full, four component MT impedance. Usually only one or both principal components of the impedance are used for the inversion. For the TM mode it is Z_{xy}, for the TE mode it is Z_{yx}, and for joint inversion of TE and TM modes both components are taken into account simultaneously.

Let us consider the Fréchet derivative of the impedances with respect to anomalous conductivity, $\delta \Delta \sigma$. First, notations for the x-, y-, or z-component of the Fréchet operator $F_{E,H_\alpha}[\delta \Delta \sigma]$, will be introduced, correspondingly, where α is equal to x, y, or z. The Fréchet derivative operator for the principal components of the impedance tensor (13.214) will be

$$\delta Z_{\alpha\beta}[\delta \Delta \sigma] = \frac{1}{H_\beta} F_{E_\alpha}[\delta \Delta \sigma] - \frac{E_\alpha}{H_\beta^2} F_{H_\beta}[\delta \Delta \sigma], \tag{13.256}$$

where α and β mean x or y components of the electric or magnetic fields, and $F_{E_\alpha}[\delta \Delta \sigma]$ and $F_{H_\beta}[\delta \Delta \sigma]$ are Fréchet derivatives.

Now, let us write the expression for the operator adjoint to (13.256). A definition of an adjoint operator is as follows: the *adjoint* operator L^* to the linear operator $L \in \mathcal{L}(M \to D)$ is an operator acting from D to M, which always satisfies the following rule:

$$(L\mathbf{m}, L\mathbf{d}) = (\mathbf{m}, L^*\mathbf{d}), \text{ where } \mathbf{m} \in M, \text{ and } \mathbf{d} \in D. \tag{13.257}$$

According to the definition of the adjoint operator (Zhdanov, 2002), we have:

$$\left(\delta Z_{\alpha\beta}, \frac{1}{H_\beta} F_{E_\alpha}[\delta \Delta \sigma] - \frac{E_\alpha}{H_\beta^2} F_{E_\alpha}[\delta \Delta \sigma] \right) = \left(F_{E_\alpha}^* \left[\frac{\delta Z}{H_\beta^*} \right] - F_{H_\beta}^* \left[\delta Z \frac{E_\alpha^*}{H_\beta^{2*}} \right], \delta \Delta \sigma \right). \tag{13.258}$$

The adjoint Fréchet operator will be the following:

$$\delta \Delta \sigma = F_{E_\alpha}^* \left[\frac{\delta Z_{\alpha\beta}}{H_\beta^*} \right] - F_{H_\beta}^* \left[\delta Z_{\alpha\beta} \frac{E_\alpha^*}{H_\beta^{2*}} \right], \tag{13.259}$$

where α and β mean x or y components of the electrical or magnetic fields, and $F_{E_\alpha}^*[\delta \Delta \sigma]$ and $F_{E_\alpha}^*[\delta \Delta \sigma]$ are computed according to expressions (8.94). For joint inversion of both modes the adjoint operator would be

$$\delta \Delta \sigma = F_{E_x}^* \left[\frac{\delta Z_{xy}}{H_y^{(1)*}} \right] - F_{H_y}^* \left[\delta Z_{xy} \frac{E_x^{(1)*}}{H_y^{(1)2*}} \right] + F_{E_y}^* \left[\frac{\delta Z_{yx}}{H_x^{(2)*}} \right] - F_{H_x}^* \left[\delta Z_{yx} \frac{E_y^{(2)*}}{H_x^{(2)2*}} \right], \tag{13.260}$$

where superscript 1 means TM mode, and subscript 2 means TE mode.

13.9.5 FRÉCHET OPERATOR FOR THE FULL MAGNETOTELLURIC IMPEDANCE TENSOR INVERSION

In this section the formulas for computing Fréchet derivatives for all four components of the tensor (13.214) will be derived.

$$\delta Z_{xy} = \sum_{i=1,2} \left(\frac{\partial Z_{xy}}{\partial E_x^{(i)}} F_{E_x^{(i)}}[\delta \Delta \sigma] + \sum_{\alpha=x,y} \frac{\partial Z_{xy}}{\partial H_\alpha^{(i)}} F_{H_\alpha^{(i)}}[\delta \Delta \sigma] \right). \tag{13.261}$$

Here i means the mode, $i = 1$ for the TM mode, and $i = 2$ for TE mode. Now the expressions for the partial derivatives of the impedance with respect to the field components, necessary for the computation of (13.261), take the following form:

$$\frac{\partial Z_{xy}}{\partial E_x^{(1)}} = \frac{H_x^{(2)}}{H_y^{(1)} H_x^{(2)} - H_y^{(2)} H_x^{(1)}} \tag{13.262}$$

$$\frac{\partial Z_{xy}}{\partial H_x^{(2)}} = \frac{H_x^{(1)} \left[E_x^{(2)} H_y^{(1)} - E_x^{(1)} H_y^{(2)} \right]}{\left[H_y^{(1)} H_x^{(2)} - H_y^{(2)} H_x^{(1)} \right]^2} \tag{13.263}$$

$$\frac{\partial Z_{xy}}{\partial H_x^{(1)}} = \frac{H_x^{(2)} \left[E_x^{(1)} H_y^{(2)} - E_x^{(2)} H_y^{(1)} \right]}{\left[H_y^{(1)} H_x^{(2)} - H_y^{(2)} H_x^{(1)} \right]^2} \tag{13.264}$$

$$\frac{\partial Z_{xy}}{\partial H_y^{(1)}} = \frac{H_x^{(2)} \left[E_x^{(2)} H_x^{(1)} - E_x^{(1)} H_x^{(2)} \right]}{\left[H_y^{(1)} H_x^{(2)} - H_y^{(2)} H_x^{(1)} \right]^2} \tag{13.265}$$

$$\frac{\partial Z_{xy}}{\partial H_y^{(2)}} = \frac{H_x^{(1)} \left[E_x^{(1)} H_x^{(2)} - E_x^{(2)} H_x^{(1)} \right]}{\left[H_y^{(1)} H_x^{(2)} - H_y^{(2)} H_x^{(1)} \right]^2} \tag{13.266}$$

$$\frac{\partial Z_{xy}}{\partial E_x^{(2)}} = -\frac{H_x^{(1)}}{H_y^{(1)} H_x^{(2)} - H_y^{(2)} H_x^{(1)}}. \tag{13.267}$$

The final expression for the Fréchet derivative of impedance tensor component Z_{xy} may be obtained by combining expressions (13.261)–(13.267) and taking into account the mode of the background field.

Now let us find the derivative of Z_{yx} with respect to $\Delta \sigma$.

$$\delta Z_{yx} = \sum_{i=1,2} \left(\frac{\partial Z_{yx}}{\partial E_y^{(i)}} F_{E_y}^{(i)} [\delta \Delta \sigma] + \sum_{\alpha=x,y} \frac{\partial Z_{yx}}{\partial H_\alpha^{(i)}} F_{H_\alpha}^{(i)} [\delta \Delta \sigma] \right). \tag{13.268}$$

The following expressions describe the partial derivatives of the impedance with respect to the field components:

$$\frac{\partial Z_{yx}}{\partial E_y^{(1)}} = \frac{H_y^{(2)}}{H_x^{(1)} H_y^{(2)} - H_x^{(2)} H_y^{(1)}} \tag{13.269}$$

$$\frac{\partial Z_{yx}}{\partial H_y^{(2)}} = \frac{H_y^{(1)} \left[E_y^{(2)} H_x^{(1)} - E_y^{(1)} H_x^{(2)} \right]}{\left[H_x^{(1)} H_y^{(2)} - H_x^{(2)} H_y^{(1)} \right]^2} \tag{13.270}$$

$$\frac{\partial Z_{yx}}{\partial H_y^{(1)}} = \frac{H_y^{(2)} \left[E_y^{(1)} H_x^{(2)} - E_y^{(2)} H_x^{(1)} \right]}{\left[H_x^{(1)} H_y^{(2)} - H_x^{(2)} H_y^{(1)} \right]^2} \tag{13.271}$$

$$\frac{\partial Z_{yx}}{\partial H_x^{(1)}} = \frac{H_y^{(2)} \left[E_y^{(2)} H_y^{(1)} - E_y^{(1)} H_y^{(2)} \right]}{\left[H_x^{(1)} H_y^{(2)} - H_x^{(2)} H_y^{(1)} \right]^2} \tag{13.272}$$

$$\frac{\partial Z_{yx}}{\partial H_x^{(2)}} = \frac{H_y^{(1)} \left[E_y^{(1)} H_y^{(2)} - E_y^{(2)} H_y^{(1)} \right]}{\left[H_x^{(1)} H_y^{(2)} - H_x^{(2)} H_y^{(1)} \right]^2} \tag{13.273}$$

$$\frac{\partial Z_{yx}}{\partial E_y^{(2)}} = -\frac{H_y^{(1)}}{H_x^{(1)} H_y^{(2)} - H_x^{(2)} H_y^{(1)}}. \tag{13.274}$$

The final expression for the Fréchet derivative of Z_{yx} impedance tensor component may be obtained by combining expressions (13.268)–(13.274) and taking into account the mode of the background field.

The expressions for derivatives of the diagonal impedance components Z_{xx} and Z_{yy} are the following:

$$\delta Z_{xx} = \sum_{i=1,2} \left(\frac{\partial Z_{xx}}{\partial E_x^{(i)}} F_{E_x}^{(i)} [\delta \Delta \sigma] + \sum_{\alpha=x,y} \frac{\partial Z_{xx}}{\partial H_\alpha^{(i)}} F_{H_\alpha}^{(i)} [\delta \Delta \sigma] \right). \tag{13.275}$$

The partial derivatives can be computed according to the following formulas:

$$\frac{\partial Z_{xx}}{\partial E_x^{(1)}} = \frac{H_y^{(2)}}{H_x^{(1)} H_y^{(2)} - H_x^{(2)} H_y^{(1)}} \tag{13.276}$$

$$\frac{\partial Z_{xx}}{\partial H_y^{(2)}} = \frac{H_y^{(1)} \left[E_x^{(2)} H_x^{(1)} - E_x^{(1)} H_x^{(2)} \right]}{\left[H_x^{(1)} H_y^{(2)} - H_x^{(2)} H_y^{(1)} \right]^2} \tag{13.277}$$

$$\frac{\partial Z_{xx}}{\partial H_y^{(1)}} = \frac{H_y^{(2)} \left[E_x^{(1)} H_x^{(2)} - E_x^{(2)} H_x^{(1)} \right]}{\left[H_x^{(1)} H_y^{(2)} - H_x^{(2)} H_y^{(1)} \right]^2} \tag{13.278}$$

$$\frac{\partial Z_{xx}}{\partial H_x^{(1)}} = \frac{H_y^{(2)} \left[E_x^{(2)} H_y^{(1)} - E_x^{(1)} H_y^{(2)} \right]}{\left[H_x^{(1)} H_y^{(2)} - H_x^{(2)} H_y^{(1)} \right]^2} \tag{13.279}$$

$$\frac{\partial Z_{xx}}{\partial H_x^{(2)}} = \frac{H_y^{(1)} \left[E_x^{(1)} H_y^{(2)} - E_x^{(2)} H_y^{(1)} \right]}{\left[H_x^{(1)} H_y^{(2)} - H_x^{(2)} H_y^{(1)} \right]^2} \tag{13.280}$$

$$\frac{\partial Z_{xx}}{\partial E_x^{(2)}} = - \frac{H_y^{(1)}}{H_x^{(1)} H_y^{(2)} - H_x^{(2)} H_y^{(1)}}. \tag{13.281}$$

The last component, Z_{yy}, is

$$\delta Z_{yy} = \sum_{i=1,2} \left(\frac{\partial Z_{yy}}{\partial E_y^{(i)}} F_{E_y}^{(i)} [\delta \Delta \sigma] + \sum_{\alpha=x,y} \frac{\partial Z_{yy}}{\partial H_\alpha^{(i)}} F_{H_\alpha}^{(i)} [\delta \Delta \sigma] \right). \tag{13.282}$$

The expressions for partial derivatives of the impedance with respect to the field components take the form:

$$\frac{\partial Z_{yy}}{\partial E_y^{(1)}} = \frac{H_x^{(2)}}{H_y^{(1)} H_x^{(2)} - H_y^{(2)} H_x^{(1)}} \tag{13.283}$$

$$\frac{\partial Z_{yy}}{\partial H_x^{(2)}} = \frac{H_x^{(1)} \left[E_y^{(2)} H_y^{(1)} - E_y^{(1)} H_y^{(2)} \right]}{\left[H_y^{(1)} H_x^{(2)} - H_y^{(2)} H_x^{(1)} \right]^2} \tag{13.284}$$

$$\frac{\partial Z_{yy}}{\partial H_x^{(1)}} = \frac{H_x^{(2)} \left[E_y^{(1)} H_y^{(2)} - E_y^{(2)} H_y^{(1)} \right]}{\left[H_y^{(1)} H_x^{(2)} - H_y^{(2)} H_x^{(1)} \right]^2} \tag{13.285}$$

$$\frac{\partial Z_{yy}}{\partial H_y^{(1)}} = \frac{H_x^{(2)} \left[E_y^{(2)} H_x^{(1)} - E_y^{(1)} H_x^{(2)} \right]}{\left[H_y^{(1)} H_x^{(2)} - H_y^{(2)} H_x^{(1)} \right]^2} \tag{13.286}$$

$$\frac{\partial Z_{yy}}{\partial H_y^{(2)}} = \frac{H_x^{(1)} \left[E_y^{(1)} H_x^{(2)} - E_y^{(2)} H_x^{(1)} \right]}{\left[H_y^{(1)} H_x^{(2)} - H_y^{(2)} H_x^{(1)} \right]^2} \tag{13.287}$$

$$\frac{\partial Z_{yy}}{\partial E_y^{(2)}} = -\frac{H_x^{(1)}}{H_y^{(1)} H_x^{(2)} - H_y^{(2)} H_x^{(1)}}. \tag{13.288}$$

The final expression for the Fréchet derivative of the Z_{xx} and Z_{yy} impedance tensor components may be obtained by combining expressions (13.275)–(13.288) with regard to the mode of the background field.

13.9.6 FRÉCHET DERIVATIVE CALCULATION USING QUASI-ANALYTICAL APPROXIMATION FOR A VARIABLE BACKGROUND (QAVB)

Expressions (13.275) through (13.282) require calculation of the Fréchet derivatives of the EM field components. We can use a formula for these Fréchet derivatives based on quasi-analytical approximation for a variable background (QAVB) (Gribenko and Zhdanov, 2007):

$$\left. \frac{\partial \mathbf{E}(\mathbf{r}_j)}{\partial \Delta \sigma_a(\mathbf{r})} \right|_{\Delta \sigma_a} = \mathbf{F}_E(\mathbf{r}_j \mid \mathbf{r}), \quad \left. \frac{\partial \mathbf{H}(\mathbf{r}_j)}{\partial \Delta \sigma_a(\mathbf{r})} \right|_{\Delta \sigma_a} = \mathbf{F}_H(\mathbf{r}_j \mid \mathbf{r}), \tag{13.289}$$

where the vector functions $\mathbf{F}_E$ and $\mathbf{F}_H$ are the kernels of the integral Fréchet derivative operators:

$$\mathbf{F}_{E,H}(\mathbf{r}_j \mid \mathbf{r}) = \left[\frac{1}{1 - g^Q(\mathbf{r})} \widehat{\mathbf{G}}_{E,H}(\mathbf{r}_j \mid \mathbf{r}) + \widehat{\mathbf{K}}(\mathbf{r}_j \mid \mathbf{r}) \right] \mathbf{E}^b(\mathbf{r}), \tag{13.290}$$

and

$$\widehat{\mathbf{K}}(\mathbf{r}_j \mid \mathbf{r}) = \iiint_D \frac{\Delta \sigma_a(\mathbf{r}')}{\left(1 - g^Q(\mathbf{r}')\right)^2} \widehat{\mathbf{G}}_E(\mathbf{r}_j \mid \mathbf{r}') \cdot \mathbf{E}^b(\mathbf{r}') \left[\frac{\mathbf{E}^{b*}(\mathbf{r}')}{\mathbf{E}^b(\mathbf{r}') \cdot \mathbf{E}^{b*}(\mathbf{r}')} \cdot \widehat{\mathbf{G}}_E(\mathbf{r}' \mid \mathbf{r}) \right] dv'. \tag{13.291}$$

Function g^Q is determined by the expression:

$$g^Q(\mathbf{r}) = \frac{\mathbf{E}^Q(\mathbf{r}) \cdot \mathbf{E}^{b*}(\mathbf{r})}{\mathbf{E}^b(\mathbf{r}) \cdot \mathbf{E}^{b*}(\mathbf{r})}, \tag{13.292}$$

and $\mathbf{E}^Q$ is the quasi-Born approximation of the anomalous electric field:

$$\mathbf{E}^Q = \mathbf{G}_E \left[\Delta \sigma_a \mathbf{E}^b \right].$$

We can use expressions (13.289)–(13.291) for computing the Fréchet derivatives required by the RCG algorithm. Indeed, we can treat the electric field $\mathbf{E}^{(n)}$ found on iteration number n as a background field $\mathbf{E}^b$ for a subsequent iteration $(n + 1)$, $\mathbf{E}^b = \mathbf{E}^{(n)}$. In this case, the Fréchet derivative at iteration number n can be found by direct integration from expressions (13.289)–(13.291) involving the electric field $\mathbf{E}^{(n)}$ computed on the current iteration:

$$\mathbf{F}_{E,H}\left(\mathbf{r}_j \mid \mathbf{r}\right) = \left[\frac{1}{1 - g^Q\left(\mathbf{r}\right)}\widehat{\mathbf{G}}_{E,H}\left(\mathbf{r}_j \mid \mathbf{r}\right) + \widehat{\mathbf{K}}\left(\mathbf{r}_j \mid \mathbf{r}\right)\right]\mathbf{E}^{(n)}\left(\mathbf{r}\right), \qquad (13.293)$$

and

$$\widehat{\mathbf{K}}\left(\mathbf{r}_j \mid \mathbf{r}\right) = \iiint_D \frac{\Delta\sigma_n\left(\mathbf{r}'\right)}{\left(1 - g^Q\left(\mathbf{r}'\right)\right)^2}\widehat{\mathbf{G}}_E\left(\mathbf{r}_j \mid \mathbf{r}'\right) \cdot \mathbf{E}^{(n)}\left(\mathbf{r}'\right)\left[\frac{\mathbf{E}^{(n)*}\left(\mathbf{r}'\right)}{\mathbf{E}^{(n)}\left(\mathbf{r}'\right) \cdot \mathbf{E}^{(n)*}\left(\mathbf{r}'\right)} \cdot \widehat{\mathbf{G}}_E\left(\mathbf{r}' \mid \mathbf{r}\right)\right]dv'.$$
$$(13.294)$$

Note that, the electric field $\mathbf{E}^{(n)}$ is computed, as a rule, using the rigorous IE forward modeling method. However, to speed up the computations, different numerical techniques can be used, as was discussed above. We use systematically the QAVB approximation for computing the Fréchet derivatives, based on formulas (13.293) and (13.294). As we can see, in the inversion algorithm, the background field required by the QAVB approximation is equal to the predicted electric field found on the previous iteration. Therefore, no extra computation is required to find the background field for the Fréchet derivative calculation. The corresponding numerical method of the Fréchet derivative computations is based on the discrete form of the explicit integral expressions (13.293) and (13.294), which simplifies all calculations dramatically. However, as with conventional inversion techniques, we do not need to keep the entire Fréchet derivative matrix in the computer memory. We save the results of the application of the adjoint Fréchet matrix to the weighted residual field, $\mathbf{F}_n^\star\mathbf{W}_d^\star\mathbf{W}_d\mathbf{r}_\mathbf{n}$, only.

The major difference between the conventional approach and QAVB approach is that in the first case one has to solve the full 3-D EM forward problem on every iteration of the inversion in order to find the term $\mathbf{F}_n^\star\mathbf{W}_d^\star\mathbf{W}_d\mathbf{r}_\mathbf{n}$. In QAVB method we do not need to solve any forward problem to find the Fréchet derivative, because we compute this term by direct algebraic expression arising from our new integral representation of the Fréchet matrix. The same algebraic expression is used to find the optimal length of the iteration step according to expression (13.244). As a result, our new inversion technique, based on the IE method, requires just one forward modeling on every iteration step without any extra memory usage, while the conventional inversion schemes require, as a rule, at least three forward modeling solutions per inversion iteration (one to compute the predicted data, another one to compute the gradient direction, and the last one for optimal calculation of the iteration step). This approach results in a very efficient inversion method.

13.10 3D INVERSION OF MAGNETOTELLURIC PHASE TENSOR

We have already learned in the previous sections of this chapter that, the galvanic distortions represent a very serious problem in magnetotelluric (MT) data interpretation. The distortions of the electric field are caused by the accumulation of excess charges, formed at high frequency in the near-surface

conductivity heterogeneities (Berdichevsky and Dmitriev, 1976a, 1976b, 2002; Berdichevsky and Zhdanov, 1984; Jiracek, 1990). However, these charges affect the MT data in the low-frequency range, distorting the information from the deep geoelectrical structures. That is why the galvanic effects manifest themselves as vertical shift of the right-hand part of the MT sounding curve up or down along the apparent resistivity scale, while the shape of shifted curves and the corresponding sections of phase curves remain unaffected (Berdichevsky and Dmitriev, 1976a, 1976b; Zhdanov and Keller, 1994; Zhdanov, 2009).

Static shift is a major impediment to the use of MT sounding in areas where the resistivity of the surface layer is not uniform laterally. There are some direct ways to minimize the distortions caused by static shift. If the electric field is detected with very large separations between electrode contacts (distances comparable to the maximum depth of investigation), the effects of local inhomogeneities in electrical resistivity of the surface layer will tend to average out. Another approach is to measure the electric field with a short separation between electrode contacts, but at a great number of locations over an area having a radius comparable to the maximum depth of investigation. When this is done, an estimate of a representative value of the electric field is obtained by averaging the electric field observations or by constructing a model of the electrical inhomogeneities in the surface layer. This model is used in the interpretation of geoelectrical structures lying at greater depths.

Recent developments in 3D electromagnetic (EM) modeling and inversion offer a number of methods for the static shift correction. These methods reduce to statistical averaging, filtering and 3D numerical modeling of the effect of near surface inhomogeneities (Berdichevsky and Dmitriev, 2002). One possible approach in dealing with static shift is to finely discretize the near-surface region to allow an inversion algorithm to recover small near-surface inhomogeneities. However, low frequency data may not have enough sensitivity to accurately recover conductivities of the small cells. Also, this approach may result in prohibitive number of inversion parameters. Another approach is to include static shift as an inversion parameter (Sasaki, 2004).

As we noted above, the amplitude of the observed electric field may be drastically distorted by a near-surface heterogeneity, resulting in a shift in the MT apparent resistivity, while the phase relationship between the electric and (horizontal) magnetic field vectors can be virtually unaffected (Zhdanov and Keller, 1994). Based on this assumption, Caldwell et al. (2004) introduced an MT phase tensor, and demonstrated that the regional phase information can be recovered directly from the observed impedance tensor. According to Caldwell et al. (2004) the phase tensor is derived directly from the conventional MT impedances, and it does not require extra measurements.

In this section, we consider a method of 3D inversion of the phase tensor data following the paper by Gribenko and Zhdanov (2011). We derive the relationships between Fréchet derivatives of the phase tensor and those of the MT impedance components. Once the sensitivities are known, the method closely follows 3D MT inversion algorithm discussed above. The inversion is based on the integral (IE) formulation of the EM field equations.

13.10.1 MT PHASE TENSOR

As we discussed above, the interpretation of magnetotelluric data is usually based on the calculation of the transfer functions between the horizontal components of the electric and magnetic field, using the

magnetotelluric impedance:

$$Z = \begin{bmatrix} Z_{xx} & Z_{xy} \\ Z_{yx} & Z_{yy} \end{bmatrix}. \tag{13.295}$$

Note that, the components of the impedance tensor are complex functions. Separating the real and imaginary parts, we can write:

$$Z = \begin{bmatrix} X_{xx} & X_{xy} \\ X_{yx} & X_{yy} \end{bmatrix} + i \begin{bmatrix} Y_{xx} & Y_{xy} \\ Y_{yx} & Y_{yy} \end{bmatrix} = X + iY, \tag{13.296}$$

where

$$X = \begin{bmatrix} X_{xx} & X_{xy} \\ X_{yx} & X_{yy} \end{bmatrix}, \text{ and } Y = \begin{bmatrix} Y_{xx} & Y_{xy} \\ Y_{yx} & Y_{yy} \end{bmatrix}, \tag{13.297}$$

are the real and imaginary impedance tensors.

Following Caldwell et al. (2004), we introduce the MT phase tensor Φ according to the following formula:

$$\Phi = X^{-1}Y, \tag{13.298}$$

where X^{-1} is the inverse of X, and the components of tensor Φ are real functions.

In a given Cartesian coordinate system (x, y), the matrix of the phase tensor can be found from the following expression:

$$\begin{bmatrix} \Phi_{xx} & \Phi_{xy} \\ \Phi_{yx} & \Phi_{yy} \end{bmatrix} = \frac{1}{\det(X)} \begin{bmatrix} X_{yy}Y_{xx} - X_{xy}Y_{yx} & X_{yy}Y_{xy} - X_{xy}Y_{yy} \\ X_{xx}Y_{yx} - X_{yx}Y_{xx} & X_{xx}Y_{yy} - X_{yx}Y_{xy} \end{bmatrix} \tag{13.299}$$

where $\det(X)$ is determinant of matrix X. Note that, the diagonal components of the phase tensor are principal, i.e. they are not equal to zero in the case of 1D conductivity distribution.

13.10.2 FRÉCHET DERIVATIVE OF THE PHASE TENSOR

Let us consider the Fréchet differential of the phase tensor:

$$\begin{aligned} \delta\Phi = \delta\left(X^{-1}Y\right) &= \delta\left(X^{-1}\right)Y + X^{-1}\delta(Y) \\ &= -X^{-1}\delta(X)X^{-1}Y + X^{-1}\delta(Y), \end{aligned} \tag{13.300}$$

where

$$\delta(X) = \text{Re }\delta Z, \ \ \delta(Y) = \text{Im }\delta Z. \tag{13.301}$$

Thus, the Fréchet derivative can be computed as:

$$\begin{aligned} F_\Phi = \frac{\delta\Phi}{\delta\sigma} &= -X^{-1}\text{Re}\frac{\delta Z}{\delta\sigma}X^{-1}Y + X^{-1}\text{Im}\frac{\delta Z}{\delta\sigma} \\ &= -X^{-1}\text{Re}(F_Z)X^{-1}Y + X^{-1}\text{Im}(F_Z), \end{aligned} \tag{13.302}$$

where F_Z is a Fréchet derivative of the conventional MT impedance tensor:

$$F_Z = \begin{bmatrix} F_{Z_{xx}} & F_{Z_{xy}} \\ F_{Z_{yx}} & F_{Z_{yy}} \end{bmatrix}. \tag{13.303}$$

The corresponding expressions for a Fréchet derivative of the MT impedance tensor were given above in section 13.10.

Once the expressions for the Fréchet derivatives are determined, we can use a standard re-weighted regularized conjugate gradient method RRCG of the inversion outlined above in section 13.9. Note that, by using QAVB method we do not need to solve any forward problem to find the Fréchet derivative, because we compute this term by direct algebraic expression arising from our new integral representation of the Fréchet matrix. The same algebraic expression is used to find the optimal length of the iteration step according to RRCG algorithm. As a result, the phase tensor inversion technique, based on the IE method, requires just one forward modeling on every iteration step without any extra memory usage, while the conventional inversion schemes would require, as a rule, at least three forward modeling solutions per inversion iteration (one to compute the predicted data, another one to compute the gradient direction, and the last one for optimal calculation of the iteration step).

REFERENCES AND RECOMMENDED READING TO CHAPTER 13

Backus, G., R., Parker, and C. Constable, 2005, Foundations of geomagnetism: Cambridge University Press, 383 pp.

Balch, S. J., 2000, Geophysics in mineral exploration: Fundamentals and case histories. Ni-Cu sulphide deposits with examples from Voisey's Bay: *in* Practical Geophysics III, Northwest Mining Association.

Banks, R. J., 1973, Data processing and interpretation in geomagnetic deep sounding data: Physics of the Earth and Planetary Interiors, **7**, 339–348.

Berdichevsky, M. N., 1965, Electrical prospecting with the telluric current method: Colorado School of Mines, **60** (1), 1–216.

Berdichevsky, M. N., and I. A. Bezruk, 1980, Magnetotelluric methods in electric prospecting: *in* A. G. Tarkhov, Ed., Reference book for geophysicists: Nedra, Moscow, 246–273.

Berdichevsky, M. N., and V. I. Dmitriev, 1976a, Basic principles of interpretation of magnetotelluric sounding curves: *in* A. Adam, Ed., Geoelectric and Geothermal Studies: Akademai Kaido, Budapest, 165–221.

Berdichevsky, M. N., and V. I. Dmitriev, 1976b, Distortions of magnetic and electrical fields by near-surface lateral inhomogeneities: Acta Geodaet., Geophys. et Monatanist., Akad. Sci. Hung., **34** (11), 447–483.

Berdichevsky, M. N., and V. I. Dmitriev, 2002, Magnetotellurics in the context of theory of ill-posed problems: Society of Exploration Geophysicists, Tulsa, OK, 215 pp.

Berdichevsky, M. N., and V. I. Dmitriev, 2008, Models and methods of magnetotellurics: Springer-Verlag, Berlin, Heidelberg, 563 pp.

Berdichevsky, M. N., L. L. Vanyan, and Ye. B. Fainberg, 1969, Frequency sounding of the Earth using the results of spherical analysis of electromagnetic variations: Geomagnetism and Aeronomy, **9**, 372–374.

Berdichevsky, M. N., and M. S. Zhdanov, 1981, Interpretation of anomalous variations of the electromagnetic field of the Earth: Nedra, Moscow, 327 pp.

Berdichevsky, M. N., and M. S. Zhdanov, 1984, Advanced theory of deep geomagnetic sounding: Elsevier, Amsterdam, London, New York, Tokyo, 410 pp.

Berdichevsky, M. N., E. B. Fainberg, N. M. Rotanova, J. B. Smirnova, and L. L. Vanyan, 1976, Deep electromagnetic investigations: Annals of Geophysics, **32**, 143–155.

Bertsekas, D., P., 1999, Nonlinear programming, 2nd ed.: Athena Scientific, Belmont, Massachusetts, 791 pp.

Bezruk, I. A., G. A. Chernyavskiy, and O. M. Chenareva, 1978, Processing of magnetotelluric variations in the period interval from 10 to 1000 s.: Prikladnaya Geofizika, **91**, 87–94.

Bracewell, R., 1965, The Fourier transform and its applications: McGraw-Hill Book Company, New York, 381 pp.

Cagniard, L., 1953, Basic theory of the magnetotelluric method of geophysical prospecting: Geophysics, **18**, 605–635.

Caldwell, T. G., H. M. Bibby, and C. Brown, 2004, The magnetotelluric phase tensor: Geophysical Journal International, **158**, 457–469.

Campbell, W. H., 2003, Introduction to geomagnetic fields: 2nd ed.: Cambridge University Press, 337 pp.

Chapman, S., and J. Bartels, 1940, Geomagnetism: Oxford University Press, London, 1049 pp.

Chapman, S., 1962, Geomagnetism: Clarendon Press, 504 pp.

Chave, A. D., 1983, On the theory of electromagnetic induction in the earth by ocean currents: Journal of Geophysical Research, **88**, 3531–3542.

Chave, A. D., D. J. Thomson, and M. E. Ander, 1987, On the robust estimation of power spectra, coherences and transfer functions: Journal of Geophysical Research, **92**, 633–648.

Dmitriev, V. I., and M. N. Berdichevsky, 1979, The fundamental problem of magnetotelluric sounding: Proceedings IEEE, **67**, 1034–1044.

Egbert, G. D., and J. R. Booker, 1986, Robust estimation of geomagnetic transfer functions: Geophysical Journal of the Royal Astronomical Society, **87**, 173–194.

Egbert, G. D., 1997, Robust multiple-station magnetotelluric data processing: Geophysical Journal International, **130**, 475–496.

Eggers, D. E., 1982, An eigenstate formulation of the magnetotelluric impedance tensor: Geophysics, **47** (8), 1204–1214.

Fainberg, E. B., 1981, On the inverse problem of deep electromagnetic sounding of the earth: Geomagnetism and Aeronomy, **21**, 715–719.

Filloux, J. H., 1979, Magnetotelluric and related electromagnetic investigations in geophysics: Reviews of Geophysics and Space Physics, **17** (2), 282–294.

Frazer, M. C., 1974, Geomagnetic deep sounding with arrays of magnetometers: Reviews of Geophysics and Space Physics, **12** (3), 401–420.

Gamble, T., W. M. Goubau, and J. Clarke, 1979, Magnetotellurics with a remote magnetic reference: Geophysics, **44** (1), 53–68.

Gough, D. I., 1973, The interpretation of magnetometer array studies: Geophysical Journal of the Royal Astronomical Society, **35**, 83–98.

Gough, D. I., and M. R. Ingham, 1983, Interpretation methods for magnetometer arrays: Reviews of Geophysics and Space Physics, **21** (4), 805–827.

Goubau, W. M., T. D. Gamble, and J. Clarke, 1978, Magnetotelluric data analysis: removal of bias: Geophysics, **43**, 1157–1166.

Green, V. R., and J. T. Weaver, 1978, Two-dimensional induction in a thin sheet of variable integrated conductivity at the surface of a uniformly conducting earth: Geophysical Journal of the Royal Astronomical Society, **55**, 721–736.

Gribenko, A. and M. S. Zhdanov, 2007, Rigorous 3D inversion of marine CSEM data based on integral equation method: Geophysics, **72** (2), WA73–WA84.

Gribenko, A., and M. S. Zhdanov, 2011, 3D modeling and inversion of the magnetotelluric phase tensor: Proceedings of Annual Meeting of Consortium for Electromagnetic Modeling and Inversion, 249–264.

Habashy, T. M., R. W. Groom, and B. R. Spies, 1993, Beyond the Born and Rytov approximations: a nonlinear approach to electromagnetic scattering: Journal of Geophysical Research, **98**, (B2), 1759–1775.

Huber, P. J., 1981, Robust statistics: Wiley, New York.

Jacobs, J. A., 1970, Geomagnetic micropulsations: Springer-Verlag, New York, 179 pp.

Jacobs, J. A., 1989, Geomagnetism: Academic Press, London, **3**, Trija Publishing, 533 pp.

Jiracek, G. R., 1990, Near-surface and topographic distortions in electromagnetic induction: Surveys in Geophysics, **11**, 163–203.

Jones, A. G., 1988, Static shift of magnetotelluric data and its removal in a sedimentary basin environment: Geophysics, **53** (7), 967–978.

Jursa, A. S., Ed., 1985, Handbook of geophysics and the space environment: U. S. National Technical Information Service, Springfield, Virginia.

Kaufman, A. A., and G. V. Keller, 1981, The magnetotelluric sounding method: Elsevier, Amsterdam, 595 pp.

Lilley, F. E. M., and M. N. Sloane, 1976, On estimating electrical conductivity using gradient data from magnetometer arrays: Journal of Geomagnetism and Geoelectricity, **28**, 321–328.

Naldrett, A. J., H. Keats, K. Sparkes, and S. Moore, 1996, Geology of the Voisey's Bay Ni-Cu-Co Deposit, Labrador, Canada: Exploration Mining Geology, **5**, 169–179.

Reddy, I. K., D. Rankin, and R. J. Phillips, 1977, Three-dimensional modeling in magnetotelluric and magnetic variational sounding: Geophysical Journal of the Royal Astronomical Society, **51**, 313–325.

Portniaguine, O., and M. S. Zhdanov, 1999a, Focusing geophysical inversion images: Geophysics, **64** (3), 874–887.

Portniaguine, O., and M. S. Zhdanov, 1999b, Parameter estimation for 3D geoelectromagnetic inverse problems: Three Dimensional Electromagnetics, SEG Monograph, Tulsa, OK, 222–232.

Price, A. T., 1949, The induction of electric currents in non-uniform thin sheets and shells: Quarterly Journal of Mechanics and Applied Mathematics, **2**, 283–310.

Sasaki, Y., 2004, Three-dimensional inversion of static-shifted magnetotelluric data: Earth Planets Space, **56**, 239–248.

Schmucker, U., 1970, Anomalies of geomagnetic variations in the southwestern United States: University of California Press, 165 pp.

Simpson, F., and K. Bahr, 2005, Practical magnetotellurics: Cambridge University Press, 270 pp.

Svetov, B. S., and M. I. Shemelevich, 1988, Magnetotelluric variation processing: Surveys in Geophysics, **9**, 259–285.

Tikhonov, A. N., 1950, On the determination of electrical characteristics of deep layers of the Earth's crust (*in Russian*): Dokladi Akademii Nauk SSSR, **73**, 295–297.

Vanyan, L. L., and A. I. Butkovskaya, 1980, Magnetotelluric sounding of layered media (*in Russian*): Nedra, Moscow.

Varentsov, Iv. M., and EMTESZ-PomeraniaWorking Group, 2006, Method of horizontal magnetovariational sounding: Techniques and applications in the EMTESZ-Pomerania project, *in* O. Ritter and H. Brasse, Eds., Protokoll 21. Kolloquium Elektromagnetische Tiefenforschung, Haus Wohldenberg, Holle, 111–123.

Vozoff, K., 1972, The magnetotelluric method in the exploration of sedimentary basins: Geophysics, **37** (1), 98–141.

Wannamaker, P. E., G. W. Hohmann, and S. H. Ward, 1984, Magnetotelluric responses of three-dimensional bodies in layered earths: Geophysics, **49** (9), 1517–1533.

Wannamaker, P. E., J. A. Stodt, L. Pellerin, S. L. Olsen, and D. B. Hall, 2004, Structure and thermal regime beneath South Pole region, East Antarctica, from magnetotelluric measurements: Geophysical Journal International, **157**, 36–54.

Weaver, J. T., 1994, Mathematical methods for geoelectromagnetic induction: RSP, Willey, 330 pp.

Weaver, J. T., and C. R. Brewitt-Taylor, 1978, Improved boundary conditions for the numerical solution of E-polarization problems in geomagnetic induction: Geophysical Journal of the Royal Astronomical Society, **54**, 309–317.

Weidelt, P., 1975a, Electromagnetic induction in three-dimensional structures: Jour. Geophysics, **41** (1), 85–109.

Zhdanov, M. S., 1988, Integral transforms in geophysics: Springer-Verlag, Heidelberg, 367 pp.

Zhdanov, M. S., 2002, Geophysical inverse theory and regularization problems: Elsevier, Amsterdam, London, New York, Tokyo, 628 pp.

Zhdanov, M. S., 2009, Geophysical electromagnetic theory and methods: Elsevier, 848 pp.

Zhdanov, M. S., V. I. Dmitriev, S. Fang, and G. Hursán, 2000, Quasi-analytical approximations and series in electromagnetic modeling: Geophysics, **65**, 1746–1757.

Zhdanov, M. S., and N. G. Golubev, 2003, Three-dimensional inversion of magnetotelluric data in complex geological structures: in J. Macnae, and G. Liu, Eds., Three-dimensional electromagnetics III, Australian Society of Exploration Geophysicists, 39 pp.

Zhdanov, M. S., and G. Hursán, 2000, 3-D electromagnetic inversion based on quasi-analytical approximation: Inverse Problems, **16**, 1297–1322.

Zhdanov, M. S., and G. W. Keller, 1994, The geoelectrical methods in geophysical exploration: Elsevier, 873 pp.

Zhdanov, M. S., and E. Tolstaya, 2004, Minimum support nonlinear parameterization in the solution of 3-D magnetotelluric inverse problem: Inverse Problems, **20**, 937–952.

ELECTROMAGNETIC METHODS IN THE FREQUENCY AND TIME DOMAINS

CONTENTS

A major category of geoelectrical methods we will consider in detail comprises the *controlled-source electromagnetic* (*CSEM*) *methods*. These differ from the DC methods described in Chapter 12 in that we will consider a transient electromagnetic field; they differ from the natural-field methods described in Chapter 13 in that the parameters of the source of the electromagnetic field will be specified (in other words, we will use a *controlled-source)*. These two differences make the discussion of the behavior of the fields more difficult, but we will find that controlled-source methods are powerful, and are an important group of weapons in our arsenal. Controlled-source electromagnetic sounding is the third approach to sounding of the earth that we will have covered. The combination of the three approaches – DC methods, magnetotelluric methods, and controlled-source electromagnetic methods – comprises a powerful *troika* or *triad* of methods to explore an earth structure. The three approaches have competing and complementary capabilities, but together, they present the most powerful set of tools for exploring the subsurface that is available in geophysics.

    Originally, CSEM methods were used mainly for vertical sounding of an earth structure which was considered to be approximately one-dimensional (horizontally layered). Profiling with CSEM methods was used just for approximate characterization of bodies with a finite size.

Modern achievements in the numerical methods of electromagnetic modeling and inversion have changed everything. Today CSEM methods can be used for exploration, studying, and characterization of the complex three-dimensional geoelectrical structures typical for ore deposits and hydrocarbon reservoirs.

The one-dimensional (horizontally layered) model, however, still represents a fundamental geoelectrical model for the CSEM method. This model helps us to understand the basic physical properties of the electromagnetic field used in the controlled-source methods. That is why one of the first problems of the theory of the CSEM methods is the problem of the propagation in the layered earth of the electromagnetic field generated by a given controlled-source. The simplest model of the source is electric and/or magnetic dipole generating a time-harmonic or transient electromagnetic signal. The propagation of the controlled-source field in the fundamental horizontally layered model was studied in Chapter 5. The more advanced problems of modeling and inversion of CSEM data in 3D inhomogeneous geoelectrical structures were considered in Chapter 6. In the current chapter we will discuss the basic principles of the controlled-source EM methods.

14.1 ELECTROMAGNETIC SOUNDING IN THE FREQUENCY AND TIME DOMAINS

Eqs. (5.235) and (5.236), which describe the electromagnetic field generated by a current dipole source over a layered earth, and Eqs. (5.260) through (5.264), which describe the electromagnetic field generated by a vertical axis magnetic dipole for the same case, comprise the set of theory on which numerous techniques for controlled-source electromagnetic soundings are based. These techniques differ one from another in two respects:

- 1) Either separation between transmitter and receiver or the frequency content of the transmitted signal can be used to control the depth of investigation,
- 2) The geometric form of the electromagnetic field transmitted can be that of a current dipole, a magnetic dipole, or other special form as desired.

As with the two sounding methods which were discussed in Chapters 12 and 13, (VES and MTS), in controlled-source electromagnetic sounding, we make measurements as a function of some parameter reflecting the depth to which the electromagnetic field is significantly affected by the geoelectrical structure. In sounding, our overriding assumption is that of a one-dimensional earth, in which resistivity varies only in the z direction.

With controlled-source electromagnetic sounding, as with direct-current and magnetotelluric sounding methods, all the theoretical results are scalable; that is, each theoretically derived expression for the field can be written with all the parameters describing the earth expressed in dimensionless form. Resistivity values can be normalized to one reference resistivity, usually that of the surface layer. Dimensions, either of the geoelectrical model or of the electrical array being used can also be normalized to a reference length, usually the thickness of the surface layer for one-dimensional earth structures. And in the electromagnetic methods, the frequency used can be expressed as an electrical

distance:

$$\delta = (2/\omega\mu_0\sigma)^{1/2} = 1/Re\ k,\tag{14.1}$$

where δ has the dimensions of length. The electrical distance, δ, can be normalized to the thickness of the first layer as h_1 or to an array dimension, such as the distance from transmitter to receiver, R.

In direct current methods, the frequency is fixed at zero, and so, only the array dimensions can be used to change the depth to which the earth affects a measurement. Hence, in VES, the array spacing, a, is used to characterize the depth being investigated. In the magnetotelluric sounding method, there is no physical dimension assigned to the measurement system, and so only the frequency expressed as an electrical distance, δ, can be varied to determine the depth of investigation. The electrical distance can be normalized to a layer thickness in scaling MT sounding curves. This distinction between the DC and MT methods in the way in which the depth of penetration is defined is profound. For DC soundings, the control of depth of investigation by varying the geometric dimensions of the array is recognized by terming such methods *geometric sounding methods*. In the case of MT sounding, where the depth of investigation is determined by the frequency factor in the expression for electrical distance, the term *parametric sounding* is applied.

With controlled-source methods, the depth to which the field is significantly affected by the earth is a function of the normalized electrical distance, δ/R. There are two controllable parameters in the ratio, δ/R; the frequency, and the transmitter-receiver separation. If the transmitter-receiver separation is varied to obtain a sounding curve, such a sounding is called a geometric sounding. If the frequency is varied, the sounding is a parametric sounding. If both are changed, the sounding is a hybrid geometric-parametric sounding. It is no wonder that so many variants to controlled-source electromagnetic sounding have been developed. To characterize a controlled-source electromagnetic sounding system, we must first describe the source and the geometry of the field it broadcasts, and then the components of the field detected at a receiver site. In frequency domain electromagnetic sounding, two types of source are used much more commonly than any others, these being a current dipole or a magnetic dipole.

A transmitter is considered to be a *current dipole transmitter* if it consists of a grounded length of wire, with a length much smaller than any other length involved in the measurement; that is, the length of the source wire must be much less than the distance to the receiver. Recall in Chapter 5 that it was demonstrated that the current flowing in the wire causes only a vertical magnetic field component over the surface of the earth, and that the return current flow in the earth generates no magnetic field, if the earth is laterally uniform. The same is true for diffusing electromagnetic fields at higher frequencies.

A magnetic dipole is constructed by driving current through an endless length of wire, either wound on a rigid frame which determines its shape, or laid as a free-form loop on the ground. If the axis of the magnetic dipole is vertical, it will generate a very simple toroidal electric field in the earth. The electric field vector lies on circles concentric with the axis of the dipole. In a layered earth, none of the electric field lines intersect the boundaries between layers, and so, no secondary poloidal currents develop in the medium.

A horizontal axis magnetic dipole can be used in sounding, but suffers from significant disadvantages compared to a vertical axis magnetic dipole. First, it is difficult to construct a horizontal axis magnetic dipole with a large moment. Secondly, the electric field caused by the source intersects the boundaries of the layers, creating secondary poloidal currents, and generally confusing the interaction between the field and the earth.

Current dipole sources are sometimes called *galvanic* sources, while magnetic dipole sources are sometimes called *inductive* sources. An important advantage of inductive sources is that no electrical contact need be made with the earth; it is quite possible to do a sounding with the system out of direct contact with the earth, as in an airborne system.

At the receiver, any one of the six components of the electromagnetic field might be measured, or any combination of 2 or more components. The nature of sources and sensors was described in more detail in Chapter 11.

A simple classification of the more commonly used transmitter – receiver combinations is as follows (Fig. 14.1):

- 1. *Dipole — Dipole array* (Fig. 14.1A). A current-carrying wire grounded at electrodes *A* and *B* is used to excite the electromagnetic field. Components of the electric field are detected and measured using closely-spaced pairs of electrode contacts, *M* and *N*, *O* and *P*. The placement of the receiving electrodes can be specified as being in line with the source dipole, parallel to the source dipole, radial to the center of the source dipole, or randomly placed. Usually in the latter case, two receiving dipoles are used so that the horizontal electric field vector can be determined. These arrays are equivalent to similar dipole arrays described in Chapter 12.
- 2. *Grounded wire — coil array* (Fig. 14.1B). In this array, a current-carrying grounded wire is used to excite the field. Normally, only the vertical component of the time-rate of change of magnetic induction is detected and measured. A simple device for measuring the time rate of change of magnetic induction is a toroidal coil of wire wrapped on a frame, or laid on the ground in a free form.
- 3. *Loop — grounded wire* (Fig. 14.1C). In this array, current flowing through a closed loop of wire is used to excite the field. The electric field is measured with two closely spaced electrode pairs, oriented approximately at right angles to one another. In contrast with the dipole array, any receiver location will be radially displaced from the source.
- 4. *Loop — loop* or *coil — coil arrays* (Fig. 14.1D). The field is caused by current flowing in one loop or coil of wire, and the vertical component of the time-rate of change of magnetic induction is detected and measured with a second loop or coil displaced radially from the first.
- 5. *Central loop induction* or *loop–in-loop method* (Fig. 14.1E). In this array, the field is caused by current flowing in a large loop, with its axis vertical. The vertical component of the time-rate of change in magnetic induction is detected and measured at the center of the small loop located exactly at the center of the large loop (in nonsounding applications, the small loop is often used to map the field in detail in and around the source loop). This array is, surprisingly, exactly mathematically equivalent to the loop – grounded wire method (Fig. 14.1C). This can be seen if one imagines the transmitting loop to be made up of a number of short grounded wires.

The concept of using a monochromatic transmitted field to construct a sounding curve with either frequency or transmitter-receiver separation being varied developed early in the history of electrical geophysics. The method is described in detail by various authors, including Vanyan (1967), Frischknecht (1967), Keller (1968) and Kaufman and Keller (1983). We refer you to these references if you wish to read further on frequency-domain electromagnetic sounding.
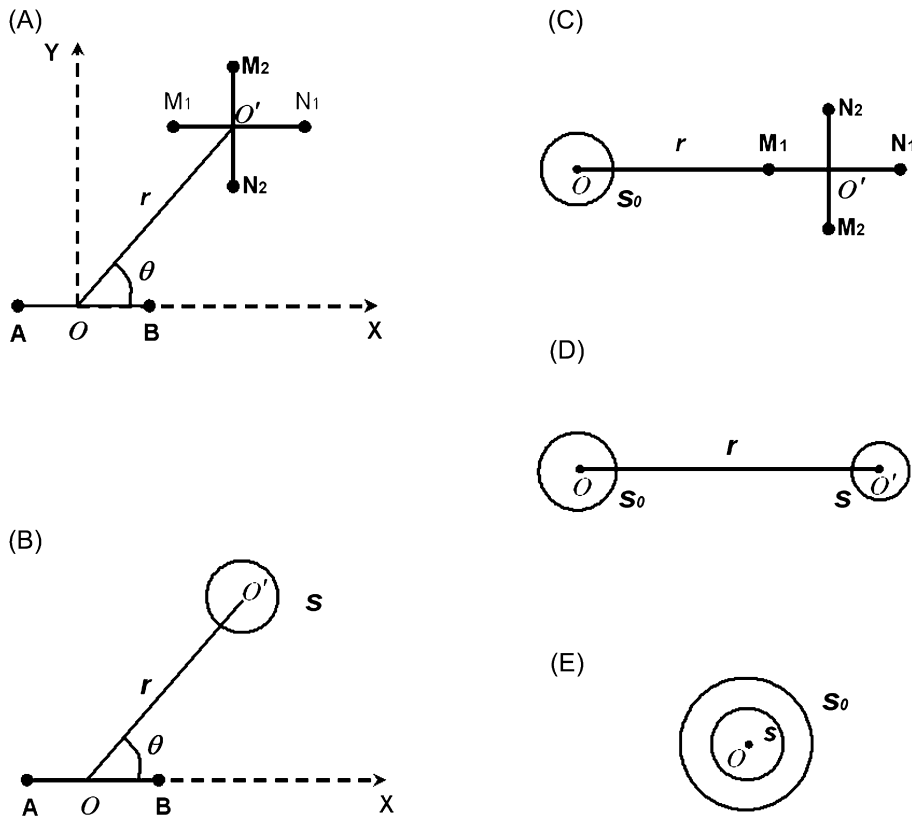
FIGURE 14.1

Plan view of commonly used transmitter-receiver pairs. When small loops are used as magnetic dipoles, either transmitting or receiving, their orientation is best described in terms of the direction of their moment, which is normal to the plane of the coil.

14.1.1 MUTUAL COUPLING

The definition of "apparent resistivity" is not straightforward for controlled-source electromagnetic sounding methods because, in general, there is no expression for electromagnetic fields over a uniform half-space that can be solved for that value. Therefore, the presentation of sounding data with a controlled-source electromagnetic method is not well standardized. Instead, a quantity know as *mutual impedance*,

$$Z = E_R/I_T, \tag{14.2}$$

is most often used, where E_R is the signal produced by the instrument used to sense either the electric field or the time rate of change of the magnetic field, and I_T is the current used to drive the transmitter.

The voltage and the current need not and usually are not in phase; the impedance is a complex number, in general.

Mutual impedance requires two numbers for specification, either a real and imaginary part:

$$Z = Re(E_R/I_T) + i Im(E_R/I_T), \tag{14.3}$$

or an amplitude and phase:

$$Z = |Z| e^{-i\omega(t-\phi)}, \tag{14.4}$$

where ϕ is the phase of the mutual impedance.

Let us consider two of these controlled-source electromagnetic sounding systems, the loop-loop system and the wire-loop system. We will consider that the loop is used as a detector of the time rate of change of the vertical component of magnetic field in both cases. The output of an ideal receiver loop, E_r is:

$$E_r = -\mu_0 A_r n_r \frac{\partial H_z}{\partial t} = i\mu_0 \omega A_r n_r H_z \tag{14.5}$$

where ω is the angular frequency of the monochromatic field, A_r is the physical area of the receiver loop, and n_r is the number of turns in the receiver loop. Substituting Eq. (5.269), the magnetic field caused by a magnetic dipole sources at a distance R from the receiver loop when both lie on the surface of a uniform earth characterized by a wave number $k^2 = i\omega\mu_0\sigma_1$, we have:

$$E_r = \frac{n_r n_t A_r A_t I_T}{2\pi\sigma} \frac{1}{R^5} [9 - e^{ikR}(9 - 9ikR - 4k^2R^2 + ik^3R^3)] \tag{14.6}$$

where A_t is the physical area of the transmitter loop, and n_t is the number of turns in the transmitter loop.

Let us define a reference mutual coupling between the two loops as being the mutual coupling in free space. This is equivalent to setting $k = 0$ in the last equation. Expanding the exponential factor as a series and retaining only the largest term in the resulting expression, we will have for the expression in square brackets:

$$\left[9 - e^{ikR}(9 - 9ikR - 4k^2R^2 + ik^3R^3) \right]$$
$$= \left[9 - \left(1 + ikR - \frac{(kR)^2}{2} - i\frac{(kR)^3}{3!} + o(k^3R^3) \right) (9 - 9ikR - 4k^2R^2 + ik^3R^3) \right]$$
$$= -\frac{k^2R^2}{2} + o(k^3R^3). \tag{14.7}$$

Substituting Eq. (14.7) into (14.6), we obtain an expression for the output of an ideal receiver loop, E_r:

$$E_r \approx -\frac{k^2 n_r n_t A_r A_t I_T}{4\pi\sigma R^3} = -\frac{i\omega\mu_0 n_r n_t A_r A_t I_T}{4\pi R^3}. \tag{14.8}$$

Real Component
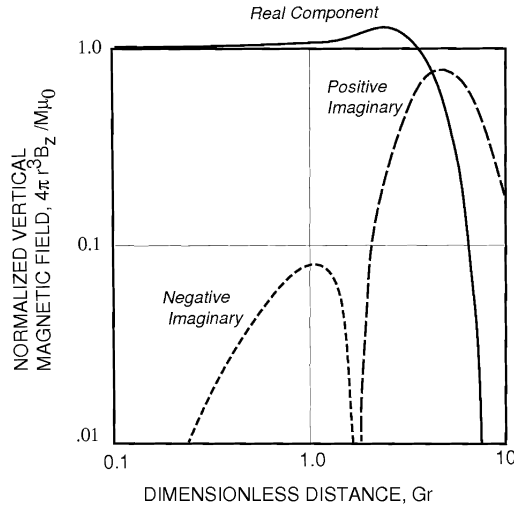
FIGURE 14.2

Normalized mutual impedance for two vertical-axis loops lying on the surface of a uniform half-space as a function of the normalized separation between the loops. The plots show the absolute values of the real and imaginary parts of the normalized mutual impedance in logarithmic scale.

Finally, from Eqs. (14.2) and (14.8) we have for a *mutual impedance*

$$Z_0 = E_0/I = -\frac{i\omega\mu_0 n_r n_t A_r A_t}{4\pi R^3}. \tag{14.9}$$

Using the free-space mutual impedance, Z_0, we can normalize the observed mutual impedance, Z, to remove its dependence on the parameters defining the measurement system and on the separation between transmitter and receiver:

$$Z/Z_0 = -\frac{2}{k^2 R^2}\left[9 - e^{ikR}(9 - 9ikR - 4k^2 R^2 + ik^3 R^3)\right]. \tag{14.10}$$

Fig. 14.2 shows graphically the dependence of the normalized mutual impedance between two loops lying on the surface of a uniform earth as a function of the normalized separation between the loops, $R|k|$. We note that for scaled separations of less than unity, $Re\,(Z/Z_0)$ is almost independent of the scaled separation, and therefore, not of use in determining the resistivity profile in a layered earth. At short, scaled distances, only $Im(Z/Z_0)$, which is very weak compared to $Re(Z/Z_0)$, can be used to study the resistivity profile. At scaled distances greater than unity, corresponding to higher frequencies if the loop separation is fixed, both the real and imaginary parts of the normalized mutual coupling can be used in sounding.

We can follow the same procedure in determining the free-space mutual coupling between a loop and a grounded wire. Eq. (5.248) gives the vertical component of the magnetic field when that field is caused by a grounded dipole at a distance R, when both lie on a uniform half-space with the wave

number k. Let us substitute the quantity IL for the current dipole moment, p, with L being the length of the current dipole source and I being the current flowing in it (Eq. (14.5)):

$$Z = -\frac{n_r A_r L}{2\pi\sigma} \frac{1}{R^4}[3 - e^{ikR}(3 - 3ikR - k^2R^2)]\sin\theta, \tag{14.11}$$

where θ is the angle between the equatorial axis of the current dipole source and the radius vector from the source to the receiver.

Let us define the free-space mutual coupling, Z/Z_0, by taking a limit as $k \to 0$, expanding the exponential term as a series, and retaining only the largest term in the result, according to Eq. (5.274):

$$\begin{aligned}
Z_0 &= -\frac{n_r A_r L}{2\pi\sigma} \frac{1}{R^4}\left[-\frac{1}{2}k^2R^2 + o(k^2R^2)\right]\sin\theta \\
&= \frac{i\omega\mu_0 n_r A_r L \sin\theta}{4\pi R^2}
\end{aligned} \tag{14.12}$$

The normalized mutual impedance, (Z/Z_0), between a wire and a loop on the surface of a uniform half-space is:

$$Z/Z_0 = \frac{-2}{k^2R^2}\left[3 - e^{ikR}(3 - 3ikR - k^2R^2)\right]. \tag{14.13}$$

The coupling between a loop and a grounded wire on the surface of a uniform earth is shown graphically in Fig. 14.3. Here, as with the mutual coupling between two loops lying on the earth, Re (Z/Z_0) is insensitive to the earth for scaled separations less than unity.

Referencing the observed signal to the strength of the field generated by the source is not the only way in which to normalize the observed fields in a controlled-source electromagnetic sounding system. Actually, there are three quite distinct approaches to normalization of the observed fields: *source referencing*, *self-referencing*, and *cross-field referencing*.

In source referencing, which is the mutual impedance method described in the preceding paragraphs, one assumes that all the geometric characteristics of the survey system can be measured accurately and conveniently and that lateral structures between the transmitter and receiver do not distort the field at the receiver.

Self-referencing is based on the fact that at low frequencies, the electromagnetic coupling between transmitter and receiver becomes independent of induction in the earth. By referencing the voltages detected in the course of making a sounding to the voltage observed at a very low frequency, the sounding curve is normalized in much the same way as though the free-space coupling were calculated and used as a normalizing factor:

$$Z/Z_0 = V_r(\omega)I(\omega \to 0)/V_r(\omega \to 0)I(\omega), \tag{14.14}$$

where V_r is the output of the magnetic field detector, assuming that there is no change in the sensitivity of the detector as a function of frequency. If there should be a nonuniform system response for the field detector, it is necessary to compensate for such response with both the source referenced and self-referenced methods of normalization.

Note that in Eq. (14.14), the only measured quantities needed are the voltage as a function of frequency at the receiver, and the current as a function of frequency at the source. If the geometric
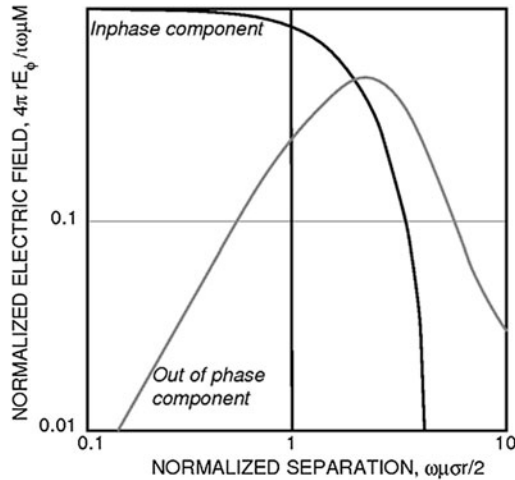
FIGURE 14.3

Tangential electric field on the surface of a uniform earth generated by a vertical-axis magnetic dipole source. The plots show the absolute values of the real and imaginary parts of the normalized mutual impedance in logarithmic scale. Note that according to the principle of reciprocity, these same curves apply to the case of a current dipole source and detection of the vertical component of magnetic induction.

parameters are measured separately, both normalizations can be carried out. The similarity or differences between the two sounding curves carries information in itself. If some mistake has been made in recording any of the geometric parameters for the array, this mistake will become obvious in the form of a shift between the two mutual impedance curves when they are presented as Napierian transforms (Fig. 14.4).

14.1.2 THEORETICAL CURVES FOR EM SOUNDING IN THE FREQUENCY DOMAIN

Let us consider a frequency sounding system based on the use of a grounded wire source and a vertical-axis loop receiver. The receiver detects the time-rate of change of the vertical component of the magnetic field, B_z. Considering equation for the far zone limit for this array, a geometric factor, K_{B_z} can be defined:

$$\rho_a = \rho_{a,\omega} = K_{B_z} \frac{V_{B_z}}{I}, \tag{14.15}$$

where V_{B_z} is the voltage produced by the receiving coil and I is the current driven through the source wire, $\rho_a = \rho_{a,\omega}$ is frequency domain apparent resistivity. The voltage produced by an ideal vertical axis coil with a harmonic monochromatic field B_z is:

$$V_{B_z} = -nA_r \frac{\partial B_z}{\partial t} = i\omega\mu_0 n A_r H_z, \tag{14.16}$$
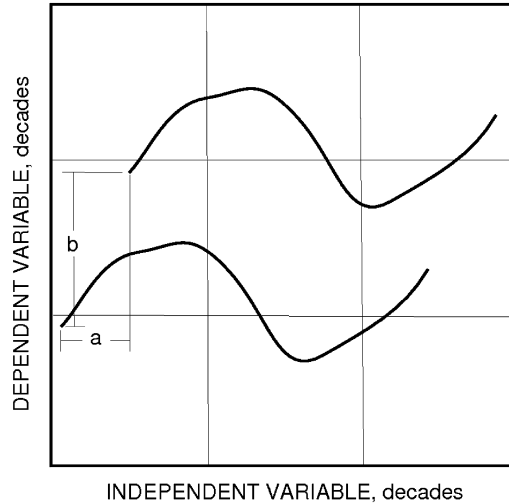
FIGURE 14.4

Property of shape preservation in the Napierian domain. Consider the lower plotted curve. If the independent variable is multiplied by a and the dependent variable by b, the curve is shifted without change in shape by distances of $log_{10}a$ in the horizontal direction and $log_{10}b$ in the vertical direction.

where ω is the frequency of the field, A_r is the cross-sectional area of the loop, and n is the number of turns in the coil. Substituting this into Eq. (14.15), we have

$$\rho_{a,\omega} = -i\frac{2\pi r^4 \omega \mu_0}{3IL\sin\theta} H_z,$$

(14.17)

where r is the separation between the centers of the transmitting wire and the receiving loop and L is the length of the source wire.

Substituting Eq. (5.227) and (5.236) into this last equation, we have

$$\rho_{a,\omega} = -\frac{2\pi r^4 \omega \mu_0}{3IL\sin\theta}\frac{1}{4\pi^2}\iint_{-\infty}^{\infty}\frac{k_y Z^*}{(i\omega\mu_0 - n_0 Z^*)}e^{-i(k_x x + k_y y)}dk_x dk_y.$$

(14.18)

This expression is a basic formula for calculating theoretical curves for frequency-domain electromagnetic sounding using the grounded-wire source/vertical-axis loop receiver sounding system. Corresponding curves in the time domain are obtained by Fourier transformation of the frequency domain theoretical curves. The integral in Eq. (14.18) in general is not tabulated and must be evaluated numerically.

However, if we consider only the far zone, Eq. (14.18) can be considerably simplified. In the following analysis consider that the earth consists of a set of layers with properties such that

$$|k_j r| \gg 1, j = 1, 2, \cdots, N$$

(14.19)

for the range of frequencies used. In a physical sense, this condition requires that the distance of the receiver from the source be sufficiently great that we can assume the only significant part of the electromagnetic field propagates over the surface of the earth from source to receiver, propagating vertically into the earth as a quasi plane wave in the vicinity of the receiver. This condition is commonly called the *wave-zone condition*, and the theoretical curves computed for this condition are called *frequency-domain wave zone curves*.

If we examine only cases in which the separation, r, from transmitter to receiver is effectively infinite, we make use of the Fourier limit theorem, discussed earlier in Chapter 5. Considering that

$$f(n_0) \sim \lim_{n_0 \to 0} \tilde{f}(n_0), \tag{14.20}$$

then

$$\iint_{-\infty}^{\infty} f(n_0) e^{-i(k_x x + k_y y)} dk_x dk_y \sim \lim_{r \to \infty} \iint_{-\infty}^{\infty} \tilde{f}(n_0) e^{-i(k_x x + k_y y)} dk_x dk_y. \tag{14.21}$$

We see from Eq. (14.19) that:

$$\frac{k_y Z^*}{i\omega\mu_0 - n_0 Z^*} \sim \lim_{n_0 \to 0} \frac{k_y Z}{i\omega\mu_0 - n_0 Z}$$

$$= \frac{1}{i\omega\mu_0} \frac{k_y Z}{(1 - n_0 Z / i\omega\mu_0)} \approx \frac{1}{i\omega\mu_0} k_y Z \left(1 + \frac{n_0 Z}{i\omega\mu_0}\right), \tag{14.22}$$

where Z is the simple Tikhonov-Cagniard impedance.

In accord with Eqs. (14.21) and (14.22), Eq. (14.17) for $\rho_{a,\omega}$ can be approximated as:

$$\rho_{a,\omega} \approx i \frac{2\pi r^4}{3 \sin \theta} Z \left\{ A_1 + \frac{Z}{i\omega\mu_0} A_2 \right\}, \tag{14.23}$$

where

$$A_1 = \frac{1}{4\pi^2} \iint_{-\infty}^{\infty} k_y e^{-i(k_x x + k_y y)} dk_x dk_y$$

$$= i \frac{\partial}{\partial y} \frac{1}{4\pi^2} \iint_{-\infty}^{\infty} e^{-i(k_x x + k_y y)} dk_x dk_y; \tag{14.24}$$

$$A_2 = \frac{1}{4\pi^2} \iint_{-\infty}^{\infty} k_y n_0 e^{-i(k_x x + k_y y)} dk_x dk_y$$

$$= i \frac{\partial}{\partial y} \frac{1}{4\pi^2} \iint_{-\infty}^{\infty} n_0 e^{-i(k_x x + k_y y)} dk_x dk_y. \tag{14.25}$$

But, in accord with Eq. (5.65),

$$\frac{1}{4\pi^2} \iint_{-\infty}^{-\infty} e^{-i(k_x x + k_y y)} dk_x dk_y = -\frac{\partial}{\partial z} \left\{ \frac{1}{4\pi^2} \iint \frac{e^{-n_0 z}}{n_0} e^{-i(k_x x + k_y y)} dk_x dk_y \right\} |_{z=0}$$

$$= -\frac{1}{2\pi} \frac{\partial}{\partial z} \left(\frac{1}{\tilde{r}}\right) |_{z=0} = 0. \tag{14.26}$$

Similarly, we can show

$$\frac{1}{4\pi^2} \iint_{-\infty}^{\infty} n_0 e^{-i(k_x x + k_y y)} dk_x dk_y = \frac{1}{2\pi} \frac{\partial^2}{\partial z^2} \left(\frac{1}{\tilde{r}}\right)|_{z=0} = -\frac{1}{2\pi r^3}, \tag{14.27}$$

where $\tilde{r} = \sqrt{x^2 + y^2 + z^2}$ and $r = \sqrt{x^2 + y^2}$.

Substituting from Eqs. (14.26) and (14.27) into Eqs. (14.24) and (14.25), we can write

$$A_1 = 0$$

$$A_2 = -\frac{i}{2\pi} \frac{\partial}{\partial y} \frac{1}{r^3} = -\frac{i}{2\pi} \frac{(-3)}{r^4} \frac{y}{r} = \frac{3i}{2\pi r^4} \sin\theta. \tag{14.28}$$

Consequently, from Eq. (14.22), we have the expression for apparent resistivity,

$$\rho_{a,\omega} \approx -\frac{2\pi r^4}{3i \sin\theta} \frac{Z^2}{i\omega\mu_0} \frac{3i \sin\theta}{2\pi r^4} = -\frac{1}{i\omega\mu_0} Z^2, \tag{14.29}$$

where Z is the simple Tikhonov-Cagniard impedance:

$$Z = \left(\frac{\omega\mu_0}{k_1}\right) R_N, \tag{14.30}$$

and R_N is the layered earth correction factor defined earlier in Eq. (5.24).

Substituting this last result into the equation immediately preceding, we have

$$\rho_{a,\omega}/\rho_1 \approx R_N^2. \tag{14.31}$$

Let us next consider a case in which the sequence of layers assumed above rests on a lowermost insulating half-space (the electrical basement). The condition of Eq. (14.19) obviously cannot be met in an insulating layer. The field which penetrates through the conducting layers above will propagate laterally with no loss, and on reaching a position beneath the receiver, it will contribute an upward traveling component which is detected in addition to the component which traveled over the surface from the source. The expression for the two components can be written as:

$$\rho_{a,\omega}/\rho_1 \approx R_N^2 + \Pi_N^2, \tag{14.32}$$

where Π_N^2 is a complementary term representing the energy which has traveled in the lower insulating layer.

As an example, consider a two-layer case in which the second layer is an insulating half-space:

$$\Pi_2^2 = \coth^2 k_1 d_1 - 1, \tag{14.33}$$

where d_1 is the depth to the top of the insulating half-space. At the same time

$$R_2^2 = \coth^2 k_1 d_1.$$

Substituting this last expression into Eq. (14.32), we can write the final result

$$\rho_{a,\omega}/\rho_1 = 2\coth^2 k_1 d_1 - 1. \tag{14.34}$$

14.1.3 TIME-DOMAIN ELECTROMAGNETIC SOUNDING

Beginning in the 1960s, interest developed in the use of controlled-source electromagnetic sounding to explore to depths of importance in exploration for oil and gas and for geothermal systems. This required penetration of the electromagnetic field through several, or even many kilometers of rock with a relatively low resistivity. Considering that the depth of investigation scales by the inverse wave number, $1/k = 1/(i\omega\mu_0\sigma)^{1/2}$, the frequency content transmitted by the controlled-source decreases by the square of the depth to be investigated. Moreover, the frequency must also be lowered in proportion to the square of the conductivity, inasmuch as the typical oil and gas or geothermal exploration problems involve earth resistivities that are lower by factors of 10 or more than the average resistivity of the earth. Instead of using frequencies ranging from a few Hz to a few kHz, in these new problems, it is often necessary to consider frequencies in the range from a few mHz to a few Hz.

Moving to a frequency window some three decades lower, a number of practical problems arise; for example, even the generation of an alternating current of large amplitude is not an easy task at frequencies of mHz. Moreover, the sequential observation of field components at various frequencies in the mHz range can require an extraordinary amount of time. An obvious solution to both practical problems is the use of a repeated square wave to power the source. Square waves are simple to generate at low repetition rates, and contain a wide spectrum of frequencies at as each cycle is transmitted.

Another important advantage of the time-domain electromagnetic sounding over a frequency-domain method is an ability to sound to depth when the source and receiver are close together.

TDEM sounding can be carried out with a variety of sources and receivers, but by far the greatest amount of use has been based on the coupling between a short grounded wire and a sensor that detects the time rate of change of the vertical component of the magnetic field from the square-wave energized source, or the coupling between two concentric ungrounded loops. These are analytically identical systems, but do differ to some extent in operating characteristics. The two arrays are shown in Fig. 14.5.

As with all sounding methods, the conversion of observed data to values of apparent resistivity is to be desired, but with controlled-source electromagnetic methods, the definition of apparent resistivity is neither standard nor obvious. The concepts of early and late apparent resistivity for the TDEM method were first proposed by Keller (1969) and by Kaufman and Morozova (1970) for the most commonly used system for time-domain electromagnetic sounding, one in which an electromagnetic field is generated using a current dipole source and the vertical component of the magnetic field is observed. If the system is deployed on the surface of a uniform half-space, the vertical component of the magnetic field is:

$$\frac{\partial H_z}{\partial t} = \frac{3Id\ell\sin\theta}{2\pi\mu_0\sigma R^4}\left[\Phi(u_t) - \left(\frac{2}{\pi}\right)^{1/2} e^{-u_t^2/2}u_t\left(1 + \frac{u_t^2}{3}\right)\right], \tag{14.35}$$

where $u_t = 2\pi R/\tau_t$ and $\tau_t = 2\pi\sqrt{2t\rho/\mu_0}$. Also, R is the separation between the source and receiver, I is the amplitude of the current step supplied to the source dipole, $d\ell$ is the length of the source dipole ($Id\ell = M$ is the "moment" of the source), t is the time following initiation of the Heaviside step, ρ_t is
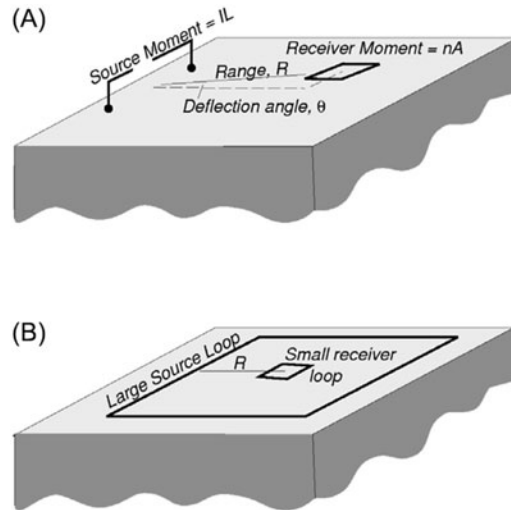
FIGURE 14.5

Two typical layouts for doing time-domain electromagnetic soundings. **A**. Grounded wire source method for carrying out time-domain electromagnetic soundings. The grounded source is energized with a square-wave current. The receiver is a sensitive magnetometer, shown here as a vertical-axis induction loop. **B.** Central loop induction method for carrying out time-domain electromagnetic soundings. The large loop is energized with a square-wave current. The receiver, a sensitive magnetometer, is placed at the center of the source loop.

the resistivity of the half-space, and ϕ is the angle as defined in Fig. 14.5. The function $\Phi()$ is the error function (Abramowitz and Stegun, 1965).

Apparent resistivity is a useful concept. It permits the conversion of field observations to numerical estimates of earth resistivity which can then be used as a guide to the meaning of the measurements made in the field. With controlled-source electromagnetic methods, a more limited form of apparent resistivity can be used for the same purpose by taking only limiting values for the field at very short and very long times. For example, if one takes a limit for the expression in Eq. (14.35) for very short times, and then takes a time derivative of the limit, we have:

$$\frac{\partial B_z}{\partial t} = \frac{3\rho_t I d\ell \sin\phi}{2\pi R^4}, \tag{14.36}$$

where $B_z = \mu_0 H_z$. This expression for the early-time limit is algebraically simple and can easily be inverted to find ρ_t:

$$\rho_{a,early} = \frac{2\pi R^4}{3 A_r n_r I d\ell \sin\phi} V_{coil}, \tag{14.37}$$

where it has been assumed that the field is detected using a vertical-axis coil with an area A_r with n_r turns producing a voltage output, $V_{coil}(t)$.

EARLY TIME APPARENT RESISTIVITY
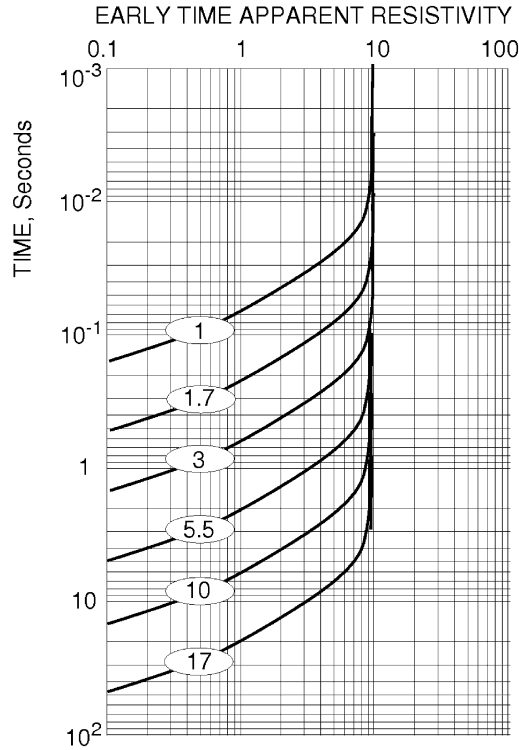
FIGURE 14.6

Time-domain electromagnetic sounding curves for a uniform earth with a resistivity of 10 ohm-meters. The source-receiver separation (in kilometers) is indicated by the label on each curve.

This expression is used widely in the application of TDEM soundings, but it must be observed that it is meaningful only for the very early portions of a recorded transient. Transient curves transformed to apparent resistivity curves using this formula are shown in Figs. 14.6 and 14.8. The set of curves noted as "early-time" curves in Fig. 14.6 show the effect of varying the separation between source and receiver on the location of the curves, while the corresponding curves in Fig. 14.8 show the effect of the resistivity of the medium for a fixed source-receiver separation.

A limit can be taken for the expression in Eq. (14.35) for the condition $t \to \infty$ as well:

$$\frac{\partial B_z}{\partial t} = \frac{\mu_0^{5/2} M R \sin \phi}{40 \pi^{3/2} t^{5/2} \rho^{3/2}}. \tag{14.38}$$

LATE TIME APPARENT RESISTIVITY
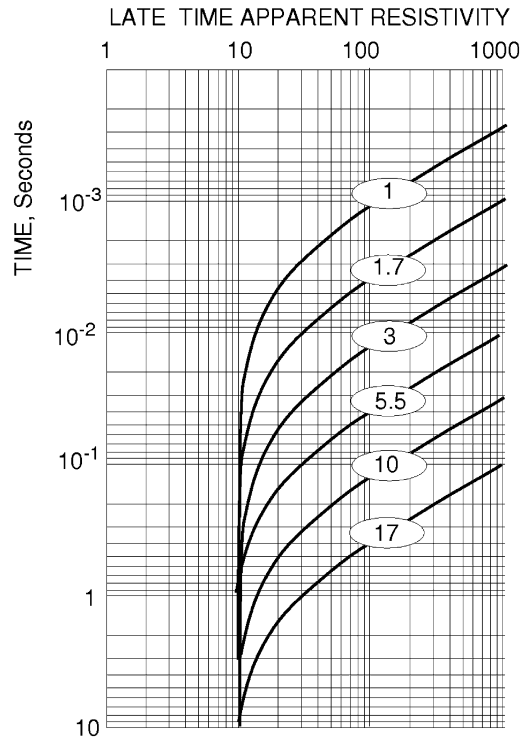
FIGURE 14.7

Time-domain electromagnetic sounding curves for a uniform earth with a resistivity of 10 ohm-meters. The source-receiver separation (in kilometers) is indicated by the label on each curve.

This, too, can easily be solved for a definition of apparent resistivity:

$$\rho_{a,late} = \left(\frac{\mu_0^{5/2} A_r n_r M R \sin\phi}{40\pi^{3/2} t^{5/2} V_{coil}} \right)^{2/3}. \tag{14.39}$$

Transient curves transformed to apparent resistivity curves using this formula are shown with the notation "late-time" curves in Figs. 14.7 and 14.9, again for the case of a uniform half-space. Both the resistivity of the half-space and transmitter-receiver separation determine the earliest time at which this "late-time" definition of apparent resistivity is reasonably valid.

On examining these two definitions of apparent resistivity, one valid for early time (or long separation) and the other for late time (or short separation), we see a surprising thing: in early time, the voltage observed from the receiving loop grows with the resistivity of the earth, while in late time, the same voltage decreases as the resistivity in the earth grows. One can conclude that at some intermediate range in time, the voltage from the receiving coil is relatively independent of the resistivity in the earth.
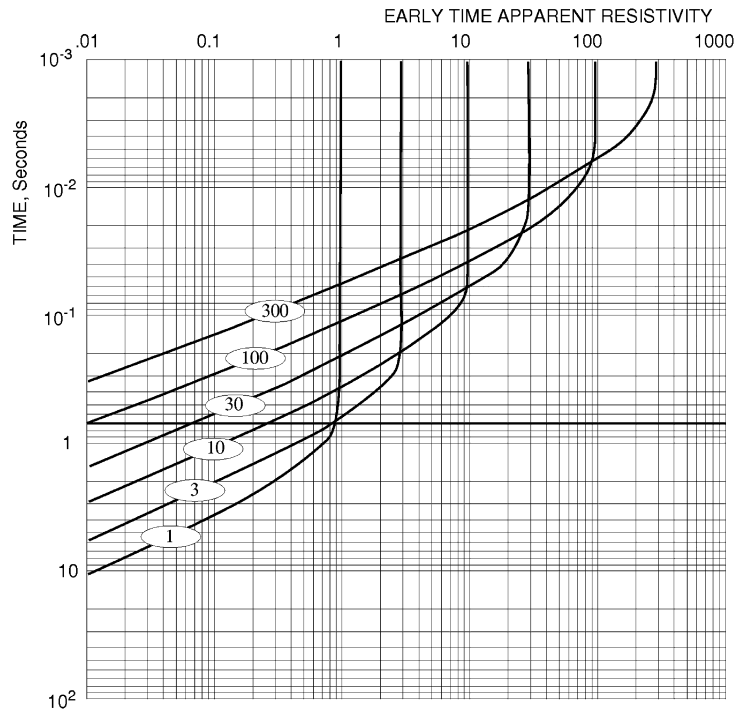
FIGURE 14.8

Apparent resistivity curves computed with the early-time asymptotic expression for a uniform earth. The separation from transmitter to receiver is 1000 meters. The resistivity of the earth is shown by the label on each curve.

The definitions of apparent resistivity in Eqs. (14.37) and (14.39) are source referenced; that is, the received signal is assumed to be directly proportional to the moment of the source, $M = I\ell$. This is a meaningful way to define apparent resistivity only if the earth is laterally uniform. In such a case, current flow in the earth is sufficiently symmetric that it makes no contribution to the vertical magnetic field component at the receiver. The vertical magnetic component is contributed only by the current flowing along the wire forming the source dipole.

If the earth is not laterally uniform, asymmetric current flow in the earth can give rise to an additional vertical magnetic field component at the receiver which will "distort" the received signal. Most often, this distortion consists of a reduction of the signal level at the receiver, causing the early and late part of the signal to give contradictory values of apparent resistivity. The effect is analogous to the static shift which causes serious problems in MT sounding.

Distortion of TDEM signals caused by asymmetry in current flow near the source can be largely eliminated by referring the signal observed at the receiver location to the static level of the vertical magnetic field at that point instead of to the moment of the source. The static magnetic field at the
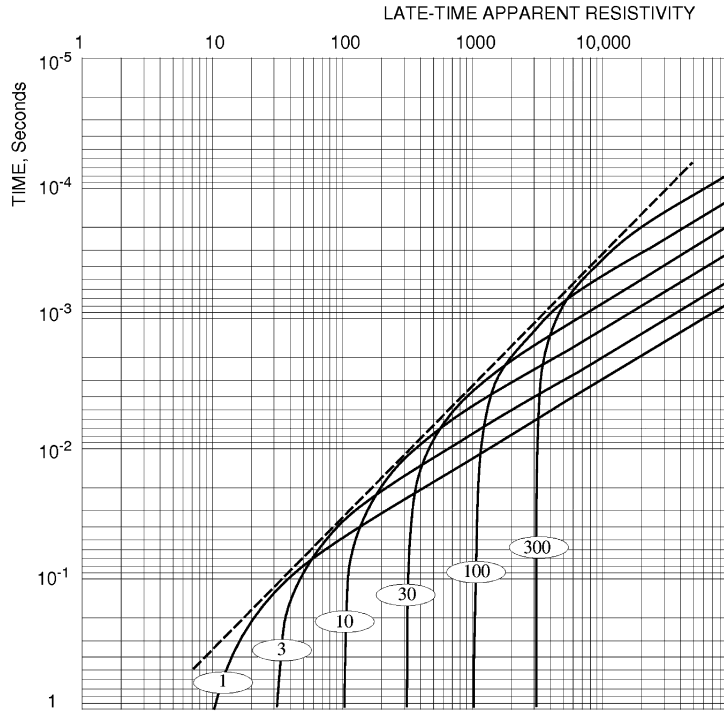
FIGURE 14.9

Apparent resistivity curves computed using the late-time asymptotic expression for a uniform earth. The separation from transmitter to receiver is 1000 meters. The resistivity of the earth is shown on the label on each curve.

receiver location can be found simply by integrating the observed transient signal:

$$Q = \int_0^\infty V_{coil} dt = -\mu_0 n_r A_r \int_0^\infty \frac{\partial H_z}{\partial t} dt$$
$$= \mu_0 n_r A_r H_{0,z}, \tag{14.40}$$

where Q is the area beneath the observed TDEM signal curve and $H_{0,z}$ is the vertical component of the static (zero-frequency) magnetic field.

We now can use Gauss's law to determine the source moment which would produce the observed static magnetic field:

$$M_{ef} = 4\pi R^2 Q / \mu_0 n_r A_r. \tag{14.41}$$

The effective moment, M_{ef}, can now be used in place of the real moment, M, in Eqs. (14.37) and (14.39):

$$\rho_{a,early} = \frac{\mu_0 R^2}{6Q} V_{coil},$$ (14.42)

$$\rho_{a,late} = \left(\frac{\mu_0^{3/2} R^3 Q}{10\sqrt{\pi t} t^2 V_{coil}} \right)^{2/3}.$$ (14.43)

Most commonly in TDEM soundings, only the vertical component of the magnetic field is observed at a receiving site. On occasion, the other two magnetic field components, H_x and H_y, are also measured. Apparent resistivity formulas can be developed for these components but are valid only in the early and late time limits (Kaufman and Keller, 1985). Formulas for source-referenced apparent resistivities are:

$$\rho_{a,early}^{H_x} = \frac{16\pi^3 t R^6}{9\mu_0 A^2 M^2 \sin^2 2\phi} V_x^2,$$ (14.44)

$$\rho_{a,early}^{H_y} = \frac{16\pi^3 t R^6}{\mu_0 A^2 M^2 (3\cos 2\phi - 1)^2} V_y^2,$$ (14.45)

$$\rho_{a,late}^{H_x} = \left(\frac{-\mu_0^3 A M \sin 2\phi R^2}{512\pi t^3 V_x} \right)^{1/2},$$ (14.46)

$$\rho_{a,late}^{H_y} = \frac{\mu_0^2 M A}{64\pi t^2 V_y}.$$ (14.47)

In these expressions, the superscript on ρ_a indicates the field component used in calculating apparent resistivity. Each of these four definitions makes use of source-moment referencing and is based on an assumption of symmetry of current flow in the earth. Referencing to a static magnetic field requires that we examine the static field from the currents flowing in the earth, because the current flowing along the wire causes only a vertical component of static magnetic field on the surface of the earth. The static field from the return current flow in a radially uniform earth causes only a horizontal magnetic field on the surface, which can be derived from expressions given by Kaufman and Keller (1983, p. 239):

$$H_{0,x} = -\frac{M}{2\pi R^2} \sin 2\phi,$$ (14.48)

$$H_{0,y} = \frac{M}{4\pi R^2} \cos 2\phi,$$ (14.49)

where $H_{0,x}$ and $H_{0,y}$ are the x and y directed components of the static magnetic field.

The effective source moments, $M_{x,ef}$ and $M_{y,ef}$, can be defined by integrating the corresponding curves for the transient magnetic field components, as was done for the vertical magnetic components:

$$M_{x,ef} = 2\pi R^2 Q_x / \mu_0 A_r \sin 2\phi,$$ (14.50)

$$M_{y,ef} = 4\pi R^2 Q_y / \mu_0 A_r \cos 2\phi,$$ (14.51)

where Q_x and Q_y are the integrals, respectively, of the transient magnetic field components in the x and y directions at the receiver location.

The expressions for apparent resistivity based on horizontal components of the magnetic field given above in Eqs. (14.44) through (14.47) can be rewritten in a self-referenced form as follows:

$$\rho_{a,early}^{H_x} = \frac{R^2 \pi \mu_0^4 t}{9 Q_x^2} V_x^2, \tag{14.52}$$

$$\rho_{a,early}^{H_y} = \frac{\pi \mu_0 t R^2 \cos^2 2\phi}{Q_y^2 (3\cos 2\phi - 1)^2} V_y^2, \tag{14.53}$$

$$\rho_{a,late}^{H_x} = \frac{\mu_0 R^2}{16} \left(\frac{Q_x}{t^3 V_x} \right)^{1/2}, \tag{14.54}$$

$$\rho_{a,late}^{H_y} = \frac{-\mu_0 R^2 Q_y}{16 t^2 \cos 2\phi V_y}. \tag{14.55}$$

Still another way to arrive at expressions for apparent resistivity is through the use of the "tilt" of the magnetic field vector at a receiving site. We can easily define the tilts as follows:

$$X = H_z / H_x, \quad Y = H_z / H_y.$$

Magnetic field tilts can be computed easily only if we use early and late time asymptotic values for the field components. When we do, we arrive at the following four expressions for magnetic field tilt:

$$X_{early} = -\frac{1}{R} \left(\frac{\pi \rho t}{\mu_0 \cos^2 \phi} \right)^{1/2}, \tag{14.56}$$

$$Y_{early} = \frac{6\sqrt{\rho \pi t} \sin \phi}{\sqrt{\mu_0} R (3\cos 2\phi - 1)}, \tag{14.57}$$

$$X_{late} = -\frac{32}{5 R \cos \phi} \left(\frac{\rho t}{\pi \mu_0} \right)^{1/2}, \tag{14.58}$$

$$Y_{late} = \frac{8 \sin \phi}{5} \left(\frac{\mu_0}{\pi \rho t} \right)^{1/2}. \tag{14.59}$$

Each of these magnetic tilt expressions can be solved for a definition of apparent resistivity, which is effectively the cross referencing of a pair of measurements without regard to source strength or static field strength:

$$\rho_{a,early}^X = \frac{\mu_0 R^2 X_{early}^2}{\pi t} \cos^2 \phi, \tag{14.60}$$

$$\rho_{a,early}^Y = \frac{\mu_0 R^2 Y_{early}^2 (3\cos 2\phi - 1)^2}{36 \pi t \sin^2 \phi}, \tag{14.61}$$

$$\rho_{a,late}^X = \frac{25 \pi \mu_0 R^2 X_{late}^2 \cos^2 \phi}{1024 t}, \tag{14.62}$$

$$\rho_{a,late}^{Y} = \frac{64\mu_0 R^2 \sin^2\phi}{25\pi t Y_{late}^2}.$$

(14.63)

All of these varied definitions for apparent resistivity have a common form:

$$\rho_a \sim c F_c^b,$$

where F is the component or ratio of components used to compute apparent resistivity. The apparent resistivity is proportional to one (or two) of the field components raised to a power, b. The parameter b has important implications with respect to the way in which a TDEM survey should be carried out in order to obtain the most reliable information on the resistivity in the earth. Consider that any physical measurement of a field component is accompanied by some error, which we expect to be small:

$$F_{c,measured} = F_{c,correct}(1 + \epsilon),$$

(14.64)

where ϵ is the fractional error in measurement. When the field component is raised to a power, b, in computing apparent resistivity, this expression becomes:

$$F_{c,measured}^b = F_{c,correct}^b(1 + b\epsilon + ...).$$

(14.65)

For small errors, the higher-order terms can be neglected. The parameter, b, serves as a multiplier to the error expected in computed resistivity caused by the error in observation. Reviewing the various definitions of apparent resistivity, we see 4 classes of measurements:

- 1) Those in which the measured field component is raised to the power $1/2$ or $2/3$, as is the case with late-time observations. The error in apparent resistivity is less than the error in observation.
- 2) Those in which the apparent resistivity is directly proportional to the measured field component. The error in apparent resistivity is the same as the error of observation.
- 3) Those in which the measured field quantity is squared, as is the case with early-time observations of the horizontal magnetic field components. The error in apparent resistivity is twice as large as the error of observation.
- 4) Those in which a ratio of measured field quantities is used to compute apparent resistivity. If the error in measurement of both field quantities is the same, the error made in computing apparent resistivity will be four times as large.

14.1.4 PROPERTIES OF TDEM SOUNDING CURVES

Let us consider the implications of the fundamental property of electromagnetic transient signals plotted in the Napierian domain — wave-form preservation. Electromagnetic transient signals depend only on scaled variables, dimensionless time and dimensionless signal strength. In view of this, we can represent any earth model as a set of compartments where the conductivity in each compartment is normalized to some reference conductivity, and the dimensions of each compartment are normalized to some reference length. This presents us with a classical philosophical question in exploration geophysics: if knowledge of a given structure of the earth permits us to determine precisely the shape of an electromagnetic transient signal (the so-called forward problem), then does not knowledge of only the

shape of the Napierian plot of the electromagnetic transient signal permit us to determine the structure of the earth (the inverse problem)? Surely it does, at least within the limitations usually accompanying an ill-posed inverse problem.

This is a surprisingly powerful result — the tight relationship between the shape of the transient electromagnetic signal and the geoelectrical structure of the earth. Conventional wisdom in electrical prospecting tells us that in order to determine the electrical structure, we must make measurements of two quantities, one being related to the strength of the source, and the other being related to the strength of the electromagnetic field at an observation point. For example, in the DC resistivity method, apparent resistivity values are computed from the ratio of the voltage measured between the receiving electrodes and the current driven through the source electrodes. Even in the case of magnetotelluric sounding where no information about the source strength is required, the observed electric field must be normalized to the observed magnetic field in order to determine the geoelectric structure.

With two-quantity field observations, an exact relationship between the two measured quantities assumed in theory is never holds precisely. Uncertainty arises when different parts of the earth have a differing effect on each of the two required measurements. For example, in DC resistivity sounding, a local inhomogeneity in the electrical structure of the earth near the receiving electrodes will affect the current in the source and the voltage at the receiver quite differently. The result is that as the spacing between electrodes is changed to perform a depth sounding, the depth sounding curve exhibits scatter limiting the accuracy with which it can be fit with a model in interpretation. A scatter of 5% to DC apparent resistivity curves is considered to represent high quality. This scatter has been called "geological noise" by many electrical geophysicists, and so, like many other aspects of geology, beyond our ken and control.

The problem is even more frustrating with the magnetotelluric sounding method in which non-random distortions are caused by local structures near an observation site. The biasing effect in magnetotelluric data collection has become well recognized (Kaufman, 1989; others). A local geo-electric inhomogeneity at the observation site can cause a shift in the electric field measurement that would otherwise be appropriate for the magnetic field measurement, causing a shift in the resulting magnetotelluric sounding curve. Magnetotelluric data often show stochastic error, but static shift of magnetotelluric sounding curves often leads to gross misinterpretation about which no warning is provided. Because of this, the MT method is virtually useless in areas where strong surface inho-mogeneities are present.

The normalizing factors that are the basis for obtaining the Napierian domain electromagnetic waveforms appear to require information both on the strength of the source and the signal strength at the receiver. Thus, we appear to need two measurements, even for the TDEM method. Fortunately, the moment of the source can be computed from the static magnetic field at the receiver site, which can be determined by integration over time of the transient magnetic field. This involves no approximation; integration of the time derivative of the magnetic field yields the static level of that field.

The ratio of the strength of a transient magnetic field to its time integral does not depend on a number of system parameters, including source moment and receiver calibration. If the Napierian shape of the transient magnetic field alone is determined, it contains all the available information about the geoelectric structure in the vicinity of the receiver.

Can we measure the shape of the transient magnetic field accurately? Accurate detection of the shape of a time-domain pulse requires the use of measurement systems with a very large, virtually infinite bandwidth of response. Use of such bandwidths is often not practical even with digital systems,

because a very great dynamic range would also be necessary. The natural electromagnetic field has both a whitish component and virtual delta function components. The whitish component contributes a noise level proportional to bandwidth, so that in practice, one must compromise with the desire for an infinite bandwidth of response. The δ-function components pose a lesser problem, but their rejection even by digital filters imposes some limitation on our ability to record an undistorted pulse shape.

In practice, one chooses a recording system which has limited bandwidth as well as some filtering to reject discrete frequencies. The effect of these limitations on fidelity of recording a pulse shape are then compensated in subsequent data processing by deconvolution. The ultimate capability of the TDEM method is limited only by the accuracy with which the infinite bandwidth response function can be reconstructed.

Deconvolution of electromagnetic pulses differs from deconvolution of seismic pulses in fundamental ways. The amplitude of an electromagnetic signal arising from excitation of a source current dipole with a Heaviside step changes from zero to some finite value instantaneously at zero time on any time scale we are likely to use in exploration geophysics. As a consequence, the full Fourier transform cannot be evaluated at the beginning of the pulse because of Gibb's phenomenon.

Consider a continuous TDEM signal as produced by an analog detection system with some impulse response in the time domain given by $r(t)$:

$$o(t) = s(t) * r(t), \tag{14.66}$$

where $o(t)$ is the analog output of the detection system, and $s(t)$ is the undistorted signal needed for processing and interpretation. A direct approach to removal of the system response consists of inversion of Eq. (14.66):

$$s(t) = o(t) * r(t)^{-1}. \tag{14.67}$$

Eq. (14.67) can be converted to numerical form for evaluation. The method is widely used, but suffers from significant problems because of the computational time required and the instability involved in the evaluation of the inverse, $r(t)^{-1}$.

A second approach which is also commonly used consists of transformation of Eq. (14.67) to the frequency domain for evaluation. Let us first convert the analog signal, $s(t)$, to digital form by multiplying it by a Dirac comb consisting of equally spaced delta functions located symmetrically on the time axis from $-N\Delta t$ to $+N\Delta t$:

$$s(n\Delta t) = \sum_{n=-N}^{n=+N} s_n \delta(t - n\Delta t). \tag{14.68}$$

We now have a set of $2N + 1$ values for s_n, a time series representing the ideal signal as it appears at the input terminals of our recording system.

The Fourier transform approach is based on transformation of Eq. (14.66) to the frequency domain:

$$S(\omega) = \frac{O(\omega)}{R(\omega)}, \tag{14.69}$$

where $S(\omega)$, $O(\omega)$, and $R(\omega)$ are the spectrums of the time functions, $s(t)$, $o(t)$, and $r(t)$. The desired compensated time domain signal, $s(t)$, is obtained by inverse Fourier transformation of the signal spectrum, $S(\omega)$.

In a third approach to deconvolution, convolution is defined by the Duhamel integral. The integral is written in finite-difference form and backward solved to obtain an undistorted transient waveform. To develop the Duhamel integral, we view each of the samples as a voltage impulse that excites the impulse response, r, of the recording system. We can specify the output signal, $o_n(n\Delta t)$, as the sum of appropriately delayed values from a sequence of impulse responses. At time $t = 0$, corresponding to the instant at which the Heaviside function switches on at the source, the output of the recording system is zero, despite the fact that a finite voltage has appeared at the input of the recording system:

$$o_0 = 0. \tag{14.70}$$

A short time later, at time $t = 1\Delta t$, the voltage at the input consists of the voltage described at a time $1\Delta t$ for the impulse at the input at time $t = 0$, plus the zero voltage arising from the second impulse:

$$o_1(1\Delta t) = r(1\Delta t)s(0\Delta t). \tag{14.71}$$

As we write the output voltages at progressively later times, it will consist of more terms, representing delayed impulses appearing at the terminals of the recording system:

$$o_2(2\Delta t) = r(2\Delta t)s(0\Delta t) + r(1\Delta t)s(1\Delta t), \tag{14.72}$$

$$o_3(3\Delta t) = r(3\Delta t)s(0\Delta t) + r(2\Delta t)s(1\Delta t) + r(1\Delta t)s(2\Delta t), \tag{14.73}$$

$$o_4(4\Delta t) = r(4\Delta t)s(0\Delta t) + r(3\Delta t)s(1\Delta t) + r(2\Delta t)s(2\Delta t) + r(1\Delta t)s(3\Delta t), \tag{14.74}$$

and so on for the number of points in the time series.

This set of equations can be solved, at least formally, for the sampled original waveform:

$$s(0\Delta t) = \frac{o(1\Delta t)}{r(1\Delta t)},$$

$$s(1\Delta t) = \frac{o(2\Delta t) - r(2\Delta t)s(0\Delta t)}{r(1\Delta t)},$$

$$s(2\Delta t) = \frac{o(3\Delta t) - r(3\Delta t)s(0\Delta t) - r(2\Delta t)s(1\Delta t)}{r(1\Delta t)},$$

$$s(3\Delta t) = \frac{o(3\Delta t) - r(4\Delta t)s(0\Delta t) - r(3\Delta t)s(1\Delta t) - r(2\Delta t)s(2\Delta t)}{r(1\Delta t)}. \tag{14.75}$$

Deconvolution using this approach works perfectly only for noise-free data. Even with the small round-off error involved in digital computing, errors build catastrophically as one works into the signal. The principal reason for the instability of the formal solution as given in Eq. (14.67) is that the deconvolution problem is an ill-posed problem. For the moment, let us merely see if we can re-express the deconvolution problem in a form which provides for a more stable solution. Let us go back to the continuous form of Duhamel's integral:

$$o(t) = \int_0^t s(t - \tau)r(\tau)d\tau. \tag{14.76}$$

This is an integral equation of the Fredholm type of the first kind, equations which are well known to be ill-posed in general. Svetov and others (in Velikhov, 1989) have devised a method to obtain a more stable solution of Eq. (14.76) as follows. Let us represent the undistorted signal, $s(t)$, as an integral transform with the exponential function, $e^{-\lambda t}$ as a weighting function:

$$s(t) = \int_0^\infty S(\lambda)e^{-\lambda t}d\lambda, \tag{14.77}$$

where $s(t)$ and $S(\lambda)$ now form a transform pair in the t and λ domains. Svetov and others (in Velikhov, 1989) have shown that such a transform exists for any transient electromagnetic waveform. We call the λ-domain characterization of the signal, $S(\lambda)$, the *exponential spectrum* of the signal, $s(t)$.

We can use an approximating function in the form of a sequence of polygons, $B_n(\lambda)$ (for example, by a cubic spline):

$$S(\lambda) = \sum_{n=1}^N c_n B_n(\lambda), \tag{14.78}$$

where the c_n are the unknown coefficients for the spline. Substituting Eq. (14.78) into Eq. (14.77), we have

$$s(t) = \sum_{n=1}^N c_n b_n(t), \tag{14.79}$$

where

$$b_n(t) = \int_0^\infty B_n(\lambda)e^{-\lambda t}d\lambda. \tag{14.80}$$

Substituting Eq. (14.78) into Eq. (14.76), we obtain

$$o(t) = \sum_{n=1}^N c_n \int_0^T b_n(t-\tau)r(\tau)d\tau. \tag{14.81}$$

Implementing Eq. (14.81) for a sequence of times, $t = t_1, t_2, \cdots, t_N$, we obtain a system of linear equations involving the unknown coefficients $c_n (n = 1, 2, \cdots, N)$:

$$o(t_i) = \sum_{n=1}^N c_n p_{n_i}, \tag{14.82}$$

where $i = 1, 2, \cdots, M$ and

$$p_{n_i} = \int_0^T b_n(t_i - \tau)r(\tau)d\tau. \tag{14.83}$$

The system of Eqs. (14.82) provides a stable solution of the integral equation (Eq. (14.76)).

14.2 INTERPRETATION OF CONTROLLED-SOURCE TIME DOMAIN EM DATA USING THE THIN-SHEET APPROACH

The notion of apparent resistivity is used in EM sounding methods, if we substitute a homogeneous conductive half-space model for a given inhomogeneous geoelectrical structure. It is possible, however, to use another simple model for interpretation of time domain electromagnetic (TDEM) data. This model can be represented by a thin conductive sheet, submerged in a nonconductive full space. The conductance of this thin sheet plays a similar role in the analysis of the TDEM data to the apparent resistivity considered above. In the present section we will discuss in details an effective method of TDEM data interpretation based on the thin-sheet approach.

14.2.1 THE PRICE-SHEINMAN AND TIKHONOV-DMITRIEV THIN-FILM MODELS WITH LATERALLY VARYING CONDUCTANCE

The theory for electromagnetic induction in thin conducting layers was first developed by A. Price and S. M. Sheinman; their model has become known as the *thin film* model. The theory for such models was extended by A. N. Tikhonov and V. I. Dmitriev to cases in which layers with nonzero thickness, d, could be included.

We will consider a thin layer of constant thickness but continuously variable conductivity over the layer, $\sigma(x, y)$. The upper surface of this layer, S^-, is the plane $z = 0$, and the lower surface, S^+, is the plane $z = d$. We assume that within the layer, the conductivity does not vary with depth. This requires that the point at which we are observing the field is far from the field sources in comparison with the thickness of the layer. Moreover, the thickness of the layer must be much less than the wavelength of the electromagnetic field in that layer.

Because the field does not change with depth in the layer, we can expand the expression for the field as a Taylor's series, retaining only the first two terms of the expansion. Considering Maxwell's equations, we can write

$$E_x^+ = E_x^- + d \cdot \partial E_x^+ / \partial z = E_x^- + d \cdot \{i\omega\mu_0 H_y^- + \partial E_x^- / \partial x)$$
$$= E_x^- + i\omega\mu_0 d H_y^- + d \frac{\partial}{\partial x}\left(\frac{1}{\sigma}\left(\frac{\partial H_y^-}{\partial x} - \frac{\partial H_x^-}{\partial y}\right)\right), \tag{14.84}$$

where the indices $-$ and $+$ indicate the upper and lower boundaries of the thin layer, respectively.

Similarly,

$$E_y^+ = E_y^- - i\omega\mu_0 d H_x^- + d \frac{\partial}{\partial y}\left[\frac{1}{\sigma}\left(\frac{\partial H_y^-}{\partial x} - \frac{\partial H_x^-}{\partial y}\right)\right]. \tag{14.85}$$

Now, consider the magnetic field:

$$H_x^+ = H_x^- + d \frac{\partial H_x^-}{\partial z} = H_x^- + d\left[\sigma E_y^- + \frac{\partial H_z^-}{\partial x}\right]$$
$$= H_x^- + \sigma d E_y^- + \frac{d}{i\omega\mu_0}\frac{\partial}{\partial x}\left[\frac{\partial E_y^-}{\partial x} - \frac{\partial E_x^-}{\partial y}\right], \tag{14.86}$$

and similarly

$$H_y^+ = H_y^- - \sigma d E_x^- + \frac{d}{i\omega\mu_o} \frac{\partial}{\partial y} \left[\frac{\partial E_y^-}{\partial x} - \frac{\partial E_x^-}{\partial y} \right]. \tag{14.87}$$

These modified boundary conditions, called the *Tikhonov-Dmitriev Boundary Conditions,* represent the tangential components of the electromagnetic field at the surfaces of a thin film. The statement of a more general set of boundary conditions based on the use of almost all the terms of a Taylor's series can be found in Berdichevsky and Zhdanov (1984).

We define the longitudinal conductance of the thin film as

$$S(x, y) = \sigma(x, y)d.$$

In Eqs. (14.84) through (14.87), we take a limit as the thickness, $d \to 0$, and the conductivity, $\sigma \to \infty$, with the conductance remaining constant:

$$\lim_{d \to 0} \sigma(x, y)d = S(x, y). \tag{14.88}$$

With this limiting process, the thin conducting layer becomes a vanishingly thin sheet or film characterized only by its surface conductance, S, and Eqs. (14.84) through (14.87) become:

$$E_x^- - E_x^+ = [E_x]_{z=0} = 0,$$
$$E_y^- - E_y^+ = [E_y]_{z=0} = 0, \tag{14.89}$$

$$H_x^- - H_x^+ = [H_x]_{z=0} = -S(x, y)E_y^- = -I_y^S,$$
$$H_y^- - H_y^+ = [H_y]_{z=0} = S(x, y)E_x^- = I_x^S, \tag{14.90}$$

where $I_{x(y)}$ is the surface current density in the film,

$$I_x^S = E_x^- S(x, y),$$
$$I_y^S = E_y^- S(x, y), \tag{14.91}$$

and where the square brackets indicate a step in the value of the field components through the sheet.

In view of Maxwell's second equation

$$i\omega\mu_0 H_z = \frac{\partial E_y}{\partial x} - \frac{\partial E_x}{\partial y}, \tag{14.92}$$

and on the basis of Eq. (14.89)

$$H_z^- - H_z^+ = [H_z]_{z=0} = 0. \tag{14.93}$$

Eqs. (14.89), (14.90), and (14.93) are called the *Price-Sheinman boundary conditions for a thin film.*

We will examine a particularly important case, that of a thin conducting sheet in an otherwise insulating full space, in detail. In this model, the behavior of the magnetic field outside of the sheet is magnetostatic, and the magnetic field can be expressed in terms of only a scalar potential:

$$\mathbf{H} = -grad\, U,$$

from which

$$\mathbf{H}^+ - \mathbf{H}^- = -grad(U^+ - U^-), \tag{14.94}$$

where $U^+ = U|_{S^+}$ and $U^- = U|_{S^-}$.

We now introduce a flux function ψ using the formula

$$-\psi = U^+ - U^-. \tag{14.95}$$

Substituting Eqs. (14.94) and (14.95) into Eq. (14.90), we have

$$I_x^S = -\partial\psi/\partial y,$$
$$I_y^S = \partial\psi/\partial x. \tag{14.96}$$

Expressing E_x, E_y in terms of I_x^S, I_y^S and substituting them in Eq. (14.92), we write an expression for the flux function ψ:

$$\frac{\partial}{\partial x}\left(\frac{1}{S}\frac{\partial\psi}{\partial x}\right) + \frac{\partial}{\partial y}\left(\frac{1}{S}\frac{\partial\psi}{\partial y}\right) = i\omega\mu_0 H_z|_{z=0}. \tag{14.97}$$

This equation bears the name *Price's equation*. It can be written as follows in a compact form;

$$div\left(\frac{1}{S}grad\psi\right) = i\omega\mu_0 H_z|_{z=0}. \tag{14.98}$$

This formula is quite important in investigating various aspects of electromagnetic induction in thin inhomogeneous layers present in a relatively nonconducting region of the earth.

Through use of the Price-Sheinman and Tikhonov-Dmitriev model of a thin conducting sheet, it is possible to consider almost any form of three-dimensional anomaly in near surface structures. A number of computer codes have been developed based on this model.

14.2.2 TRANSIENT FIELD OF A MAGNETIC DIPOLE ABOVE A CONDUCTING THIN SHEET

Particularly important in the application of transient electromagnetic fields to sounding (particularly for short distances between transmitter and receiver) is the behavior of a step-induced transient magnetic field excited by a vertical-axis magnetic loop source (a magnetic dipole source) for a medium which consists of a single conducting sheet in an otherwise insulating full space. Let us assume that an electromagnetic field is caused by current flowing in a loop of wire lying in the horizontal plane forming a vertical-axis magnetic dipole with a moment $\mathbf{I}^M$ at a height d_0 above a sheet with a uniform integral conductance, S. The waveform of the current flowing in the coil, I, is that of a Heaviside function

(instantaneous change in level), $I = I_0 \mathcal{H}(t)$. We wish to find the field from this source at some height, d_0, above the sheet, this height being the surface of the earth where the source is situated and where the field is observed. This solution is obtained from a formula developed earlier using a Cartesian coordinate system with its origin located on the thin sheet (not the earth's surface) directly beneath the transmitting coil.

In accord with Eqs. (5.287) and (5.293), the magnetic field at the surface of the earth ($z = -d_0$) caused by a source excited with a Heaviside wave form is

$$H_z^{\mathcal{H}}(t) \mid_{z=-d_0} = \frac{1}{2\pi} \int_{-\infty}^{\infty} \frac{1}{4\pi^2} \iint_{-\infty}^{\infty} h_z \mid_{z=-d_0} e^{-i(k_x x + k_y y)} dk_x dk_y \left\{ \pi \delta(\omega) - \frac{1}{i\omega} \right\} e^{-i\omega t} d\omega,$$

(14.99)

where $h_z \mid_{z=-d_0}$ is the spatial spectrum of the vertical component of the magnetic field from the dipole source driven at a single harmonic frequency (the response for the actual Heaviside excitation will be obtained by Fourier summation of frequencies). Values for $h_z \mid_{z=-d_0}$ can be found by analytic continuation of the dipole field from the surface of the sheet ($z = 0$) to the surface of the earth ($z = -d_0$). We also can find the spatial spectrum of the field, $h_z \mid_{z=-d_0}$, on the surface of the earth from a previously developed equation (Eq. (5.264)):

$$h_z \mid_{z=-d_0} = -I^M n_0^2 \frac{e^{-n_0 d_0} Z^*}{i\omega\mu_0 - n_0 Z^*},$$

(14.100)

where Z^* is the spectral impedance for the sequence lying beneath the plane $z = 0$. In our particular problem, we will obtain the spectral impedance function by the method described in the preceding section by taking a limit for a two-layer sequence in which the conductivity of the sheet, σ_1, becomes large without limit at the same time that its thickness, h_1, becomes vanishingly small:

$$\lim_{\sigma_1 \to \infty, h_1 \to 0} \sigma_1 d_1 = S.$$

(14.101)

In accord with Eqs. (5.204) and (13.55) and using the asymptotic condition that $\lim_{x \to 0} \coth x = 1/x$, we have for two layers,

$$Z^* = -\frac{i\omega\mu_0}{n_1} \coth \left[n_1 d_1 + \coth^{-1} \frac{n_1}{n_0} \right] = -\frac{i\omega\mu_0}{n_1} \frac{1 + \coth n_1 d_1 \frac{n_1}{n_0}}{\coth n_1 d_1 + \frac{n_1}{n_0}}$$

$$\sim_{d_1 \to 0} -\frac{i\omega\mu_0}{n_1} \frac{1 + \left(\frac{1}{n_1 d_1} \right) \left(\frac{n_1}{n_0} \right)}{\frac{1}{n_1 d_1} + \frac{n_1}{n_0}} = -i\omega\mu_0 \frac{d_1 n_0 + 1}{n_0 + n_1^2 d_1}.$$

Now, passing to the limits for $d_1 \to 0$ and $\sigma_1 \to \infty$ and with consideration of Eq. (14.101), we obtain:

$$Z^* \approx \frac{-i\omega\mu_0}{n_0 - i\omega\mu_0 S}.$$

(14.102)

Substituting Eq. (14.102) into Eq. (14.100), we can write

$$h_z \mid_{z=0} = I^M n_0^2 \frac{e^{-n_0 d_0}}{n_0 - i\omega\mu_0 S}. \tag{14.103}$$

And so, we have calculated the spectrum of the magnetic field, h_z, on the surface of a sheet with conductance S. In order to calculate this field at the earth's surface (at $z = -d_0$), we represent the spectrum of the field at depth as the sum of internal and external parts of the magnetic field in a manner analogous to that used in Chapter 13:

$$h_z \mid_{z=0} = h_z^e \mid_{z=0} + h_z^i \mid_{z=0},$$

where h_z^e is the spectrum of the vertical component of the external field in the absence of the conducting sheet, obtained from Eq. (14.103) with $S = 0$:

$$h_z^e \mid_{z=0} = \frac{1}{2} n_0 I^M e^{-n_0 d_0}. \tag{14.104}$$

Therefore, the spectrum of the internal field is

$$
\begin{aligned}
h_z^i \mid_{z=0} = h_z \mid_{z=0} - h_z^e \mid_{z=0} &= I^M n_0^2 \frac{e^{-n_0 d_0}}{2n_0 - i\omega\mu_0 S} - \frac{1}{2} n_0 I^M e^{-n_0 d_0} \\
&= \frac{1}{2} I^M n_0 e^{-n_0 d_0} \frac{i\omega\mu_0 S}{2n_0 - i\omega\mu_0 S}.
\end{aligned} \tag{14.105}
$$

In accord with Eqs. (13.196) and (13.198), at any level in the upper half-space

$$h_z \mid_z = h_z^i \mid_{z=0} e^{n_0 z} + h_z^e \mid_{z=0} e^{-n_0 z}.$$

In particular, at the earth's surface, $z = -d_0$:

$$h_z \mid_{z=-d_0} = h_z^i \mid_{z=0} e^{-n_0 d_0} + h_z^e \mid_{z=0} e^{n_0 d_0}. \tag{14.106}$$

Substituting from Eqs. (14.104) and (14.105) into Eq. (14.106), we write:

$$h_z \mid_{z=-d_0} = \frac{1}{2} I^M n_0 e^{-2n_0 d_0} \frac{i\omega\mu_0 S}{2n_0 - i\omega\mu_0 S} + \frac{1}{2} n_0 I^M. \tag{14.107}$$

It remains only to substitute Eq. (14.107) into Eq. (14.99) in order to calculate the magnetic field from a Heaviside source at the earth's surface:

$$
\begin{aligned}
&H_z^{\mathcal{H}}(t) \mid_{z=-d_0} \\
&= \frac{1}{2\pi} \int_{-\infty}^{\infty} \frac{I^M}{8\pi^2} \iint_{-\infty}^{\infty} n_0 \left\{ 1 + \frac{i\omega\mu_0 S e^{-2n_0 d_0}}{2n_0 - i\omega\mu_0 S} \right\} e^{-i(k_x x + k_y y)} dk_x dk_y \left\{ \pi\delta(\omega) - \frac{1}{i\omega} \right\} e^{-i\omega t} d\omega.
\end{aligned} \tag{14.108}
$$

Interchanging the order of integration, we can write

$$H_z^{\mathcal{H}}(t) \mid_{z=-d_0} = \frac{I^M}{8\pi^2} \iint_{-\infty}^{\infty} n_0[A_1(t) + A_2(t, n_0)]e^{-i(k_x x + k_y y)} dk_x dk_y, \tag{14.109}$$

where

$$A_1(t) = \frac{1}{2\pi} \int_{-\infty}^{\infty} \left\{ \pi \delta(\omega) - \frac{1}{i\omega} \right\} e^{-i\omega t} d\omega = \mathcal{H}(t), \tag{14.110}$$

and

$$A_2(t, n_0) = -\frac{\mu_0 S e^{-2n_0 d_0}}{2\pi} \int_{-\infty}^{\infty} \frac{e^{-i\omega t}}{2n_0 - i\omega \mu_0 S} d\omega. \tag{14.111}$$

This last integral can be evaluated using the tabulated form:

$$\frac{1}{2\pi} \int_{-\infty}^{\infty} \frac{g(\omega)}{f(\omega)} d\omega = -i \frac{g(\omega_0)}{\pi \frac{\partial f}{\partial \omega}\Big|_{\omega_0}}, \tag{14.112}$$

where $g(\omega) = e^{-i\omega t}$, $f(\omega) = 2n_0 - i\omega\mu_0 S$, and ω_0 is the kernel of the equation $f(\omega) = 0$. It should be obvious that

$$\omega_0 = 2n_0/i\mu_0 S. \tag{14.113}$$

Substituting Eq. (14.113) into Eq. (14.112) and the results into Eq. (14.111), we write:

$$A_2(t, n_0) = -\mu_0 S e^{-2n_0 d_0} \frac{-i e^{-2n_0 t/\mu_0 S}}{-i\mu_0 S}$$
$$= -e^{-2n_0(d_0 + t/\mu_0 S)}. \tag{14.114}$$

Considering Eqs. (14.114) and (14.110), Eq. (14.109) can be written as

$$H_z^{\mathcal{H}}(t) \mid_{z=-d_0} = \frac{I^M \mathcal{H}(t)}{8\pi^2} \iint_{-\infty}^{\infty} n_0 e^{-i(k_x x + k_y y)} dk_x dk_y$$
$$- \frac{I^M}{8\pi^2} \iint_{-\infty}^{\infty} n_0 e^{-2n_0(d_0 + t/\mu_0 S)} e^{-i(k_x x + k_y y)} dk_x dk_y$$
$$= \frac{I^M \mathcal{H}(t)}{8\pi^2} I_2 - \frac{I^M}{8\pi^2} F_1(t), \tag{14.115}$$

where $\mathcal{H}(t)$ is the Heaviside step function. In accord with Eqs. (5.246) and (5.247),

$$I_2 = -2\pi/r^3, \tag{14.116}$$

and the value of $F_1(t)$ is evaluated with the aid of Eq. (5.65):

$$F_1(t) = \iint_{-\infty}^{\infty} n_0 e^{-2n_0(d_0 + t/\mu_0 S)} e^{-i(k_x x + k_y y)} dk_x dk_y$$

$$= \frac{(\mu_0 S)^2}{4} \frac{\partial^2}{\partial t^2} \iint_{-\infty}^{\infty} \frac{e^{-2n_0(d_0 + t/\mu_0 S)}}{n_0} e^{-i(k_x x + k_y y)} dk_x dk_y$$

$$= \frac{(\mu_0 S)^2}{4} \frac{\partial^2}{\partial t^2} \left[\frac{2\pi}{\sqrt{r^2 + 4(d_0 + t/\mu_0 S)^2}} \right], \tag{14.117}$$

where $r = \sqrt{x^2 + y^2}$ is the distance from transmitter to receiver. Carrying out the indicated differentiation in the last equation, we have:

$$F_1(t) = -2\pi \frac{[r^2 - 8(d_0 + t/\mu_0 S)^2]}{[r^2 + 4(d_0 + t/\mu_0 S)^2]^{5/2}}. \tag{14.118}$$

Substituting Eqs. (14.118) and (14.116) into Eq. (14.115), we finally have

$$H_z^{\mathcal{H}}(t) \mid_{z=-d_0} = -\frac{I^M \mathcal{H}(t)}{4\pi} \frac{1}{r^3} + \frac{I^M}{4\pi} \frac{[r^2 - 8(d_0 + t/\mu_0 S)^2]}{[r^2 + 4(d_0 + t/\mu_0 S)^2]^{5/2}}, \tag{14.119}$$

where the first term represents the external field and the second term, the internal field.

We should also write the expression for the time-rate of change of the magnetic field because this is the physical quantity measured with an induction coil receiver. Differentiating Eq. (14.119) with respect to time, we have

$$\frac{\partial H_z^{\mathcal{H}}(t)}{\partial t} \bigg|_{z=-d_0} = -\frac{I^M \delta(t)}{4\pi} \frac{1}{r^3} + \frac{I^M}{\pi \mu_0 S} \frac{(d_0 + t/\mu_0 S)[-9r^2 + 24(d_0 + t/\mu_0 S)^2]}{[r^2 + 4(d_0 + t/\mu_0 S)^2]^{7/2}}. \tag{14.120}$$

We can see from these last two equations that the spreading of the internal part of the magnetic field into the medium at the very first instants of time is markedly nonuniform. This nonuniformity is present both in the horizontal direction [which is apparent from Eqs. (14.119) and (14.120)], and with depth [which can be seen from the analytic continuation of Eqs. (14.119) and (14.120) in the upper and lower half-spaces].

But, as time progresses the internal field becomes more uniform in its spreading into the medium. In this respect, at sufficiently late times and sufficiently near the source such that $r^2 \ll (d_0 + t/\mu_0 S)^2$, Eqs. (14.119) and (14.120) simplify to

$$H_z^{\mathcal{H}}(t) \mid_{z=-d_0} \approx -\frac{I^M}{4\pi} \frac{1}{r^3} - \frac{I^M}{16\pi} \frac{1}{(d_0 + t/\mu_0 S)^3}, \tag{14.121}$$

$$\frac{\partial H^{\mathcal{H}}(t)}{\partial t} \bigg|_{z=-d_0} \approx \frac{3 I^M}{16\pi \mu_0 S} \frac{1}{(d_0 + t/\mu_0 S)^4}. \tag{14.122}$$

Finally, at intermediate times, the internal field propagates in a reasonably uniform manner so that the depth to the conducting plane can be neglected:

$$H_z^{\mathcal{H}}(t)\,|_{z=-d_0} \approx -\frac{I^M}{4\pi}\frac{1}{r^3} - \frac{I^M(\mu_0 S)^3}{16\pi t^3}, \tag{14.123}$$

$$\left.\frac{\partial H_z^{\mathcal{H}}(t)}{\partial t}\right|_{z=-d_0} \approx \frac{3 I^M \mu_0^3 S^3}{16\pi t^4},\ t \gg \mu_0 S d_0. \tag{14.124}$$

These expressions can be used for approximate calculations of the late stage of a transient electromagnetic field for a horizontally uniform sequence of conductive layers resting on an insulating basement. To do this, a single thin sheet is assigned a conductance equal to the integral conductance for all of the layers making up the conductive sequence, and the depth to the equivalent thin sheet is taken to be the conductivity-weighted depth to the center of conductance of the sequence of conductive layers:

$$d_0 = \frac{\sum_{i=1}^{N-1} h_i S_i}{\sum_{i=1}^{N-1} S_i}, \tag{14.125}$$

where h_i are the depths to the center of each conductive layer and S_i are the conductances of the individual layers.

It should be noted that this last equation permits solution of the inverse problem – that of determining the depth, d_0, and the conductance, S, for a thin sheet equivalent to a conductive sequence of layers.

14.2.3 S-INVERSION METHOD

S-inversion is a fast-imaging technique for TDEM data interpretation based on the thin sheet model approach (Tartaras et al., 2000). The foundations of the thin sheet model approach for conductivity-depth imaging lie in the theory of EM induction in thin conducting layers outlined above.

S-inversion method was originally developed in Russia by Sidorov and Tickshaev (1969) and later was introduced independently by Liu and Asten (1993) for conductance-depth imaging of transient EM data. It is based on the calculation for every time moment of the conductance, S, and depth, d, of the equivalent thin sheet, which can be used to determine vertical conductivity profiles of the geoelectrical cross section. This technique was originally applied only to central-loop TDEM data or cases with small transmitter-receiver separations. However, it was extended later for variable transmitter-receiver separations (Tartaras et al., 2000; Zhdanov and Pavlov, 2001).

Theoretical formulation of S-inversion

The time rate of change of the transient magnetic field induced by a vertical magnetic dipole on the surface of a medium which consists of a single conducting sheet in an otherwise insulating full space is described by Eq. (14.120).

This expression can be used for calculations of the transient EM field for a horizontally uniform sequence of conductive layers resting on an insulating basement. To do this, a single thin sheet is assigned a conductance equal to the integral conductance of all the layers making up the conductive

sequence, and the depth to the equivalent thin sheet is taken to be the conductivity-weighted depth to the center of the sequence of conductive layers according to Eq. (14.125). This last equation permits solution of the inverse problem – that of determining the depth, d_o, and the conductance, S, for a thin sheet equivalent to a conductive sequence of layers. In this way, based on the observed time derivatives of the vertical component of the magnetic field, we can obtain the conductance-depth curve. Conductance, however, is a function of conductivity with depth:

$$S(z) = \int_0^z \sigma(z')dz'. \tag{14.126}$$

Therefore, by differentiating the conductance-depth curve with respect to depth, we can finally obtain the conductivity change with depth:

$$\sigma(z) = \frac{\partial S(z)}{\partial z}. \tag{14.127}$$

A detail description of the inversion technique to solve an inverse problem with respect to the depth, d_o, and the conductance, S, for an equivalent thin sheet can be found in the paper by Tartaras et al. (2000). In the following section we will discuss the basic principles of this technique.

Regularized S-inversion

Using Eq. (14.120) for the calculation of field response, we fit the data measured at adjacent time channels in order to obtain the depth and conductance of a thin sheet. Since we invert for two parameters, S and d, we can use data from just two adjacent time channels for each inversion. However, to make the solution more stable to the noise, we select several adjacent time channels (usually 4 or 5) that form a sliding time window $(t - \Delta t/2, t + \Delta t/2)$, where Δt is the width of the window. Every fixed position of the sliding window center t corresponds to the specific depth z of the EM field penetration in the earth. We solve numerically the inverse problem and find the parameters of the thin sheet, $S(z)$ and $d(z)$, which is equivalent to the conducting thickness of the earth above the depth of penetration z. These values, $S(z)$ and $d(z)$, when plotted together, form the conductance-depth curve.

We use the adaptive regularized Newton method for the solution of the inverse problem (Chapter 7). The use of regularization is important in order to stabilize the inversion, especially when we are dealing with noisy data.

In the adaptive regularized Newton method we minimize the parametric functional, P^α:

$$P^\alpha(m) = \phi(m) + \alpha S(m), \tag{14.128}$$

where $\phi(m)$ is the misfit functional,

$$\phi(m) = \|R(m)\|^2, \tag{14.129}$$

α is the regularization parameter, and $S(m)$ is the stabilizing functional,

$$S(m) = ||m - m_{apr}||^2, \tag{14.130}$$

which is used in order to ensure the stability of the inversion algorithm. In the above equations $R(m)$ denotes the residual:

$$R(m) = A(m) - A_o, \tag{14.131}$$

A is the forward operator, A_o is the data we are trying to fit, m_{apr} is the *a priori* model, and $\|...\|$ denotes the L_2 norm.

In the framework of the Newton method the model m_{n+1} in the $(n+1)th$ iteration is given by:

$$m_{n+1} = m_n + \Delta m_n, \tag{14.132}$$

where m_n is the model in the nth iteration and Δm_n is the iteration step:

$$\Delta m_n = -(\widehat{H}_{m_n} + \alpha\widehat{I})^{-1}(\widehat{F}^T R + \alpha(m_n - m_{apr})). \tag{14.133}$$

In the last equation $\widehat{H}$ is the Hessian matrix given by $\widehat{H} = \widehat{F}^*\widehat{F}$, where $\widehat{F}$ is the Fréchet derivative matrix.

The iteration process is automatically terminated when the normalized misfit reaches the desired value. Eq. (14.120) is used as the forward solution.

After we have determined the depth and conductance values of the thin sheet for every time window, we differentiate the conductance curve with respect to depth, as described in the previous subsection, to obtain the conductivity-depth curve.

Note in conclusion of this section, that recently the S-inversion method was extended in two different directions. First, S-inversion technique was generalized for models containing thin sheets with anomalous conductivity and anomalous magnetic permeability (Zhdanov and Pavlov, 2001). This method is called Sμ-inversion. It provides useful information about both subsurface conductivity and magnetic permeability distributions.

Another generalization of the S-inversion is localized S-inversion (Zhdanov et al., 2002), which extends the S-inversion technique, approximating the conductivity cross section by adding a local inhomogeneous disk with an excess conductance ΔS to the horizontal conductive thin sheet used in S-inversion. Localized S-inversion determines the distribution of this excess conductance as a function of a depth and a horizontal coordinate. This method takes into account the limited horizontal extent of the inhomogeneities, making inversion local. The numerical modeling results and inversion of practical TDEM data demonstrate that the method resolves local geological targets better than traditional 1-D inversion and original S-inversion (Zhdanov et al., 2002). The method can be applied to interpretation of both ground and airborne TDEM data sets.

14.3 ELECTROMAGNETIC PROFILE AND ARRAY SURVEYS

So far in this Chapter we have dealt with controlled-source electromagnetic sounding, for which the geoelectric model is a plane-layered earth. The exploration problems which can be attacked using such an approach include exploration for oil and gas, ground-water exploration, crustal studies of an academic nature, and any other application in which the earth can be considered to be even roughly plane layered. However, it must be recognized that the most successful application of controlled-source electromagnetic methods has been in exploration for highly conductive metal-bearing ore bodies, or for highly resistive hydrocarbon reservoirs. These three-dimensional (3-D) targets cannot be represented by a layered model, and they cannot be found by a single-point EM sounding. Exploration for a 3-D target requires measurement along the profile or over the area of observation in order to apply 3-D

inversion/imaging methods discussed in the previous chapters of the book. In this section we will present some of these methods.

14.3.1 PROFILING WITH TWO LOOPS

The *slingram* method makes use of two small loops separated by a fixed distance. One of the loops serves as a transmitter, the other a receiver. Most commonly, the two loops are oriented to be horizontal and coplanar. For this reason, the slingram method is sometimes referred to as the horizontal loop method. However, other orientations for the loops, such as vertical coaxial or vertical coplanar configurations may also be used. The broadside technique can be used with small loop separations in at areas where trees and brush pose no problem. For most reconnaissance work, an interval between stations of one-half the loop spacing is satisfactory.

14.3.2 PROFILING WITH LARGE FIXED SOURCES

The depth that can be explored is sometimes inadequate when moving-source moving-receiver profiling is carried out. When this is the case, a large fixed source can be used, with the field being observed along profiles. One such method is the *turam* method in which the ratio of field strengths at two successive points along a profile is measured.

In a typical turam survey, a cable several hundred meters or even kilometers long is used for a source. The cable is laid out parallel to the probable strike of the ore deposits or conductive zones being sought, and grounded at both ends. Measurements are made with receiver coils placed in line along traverses perpendicular to the cable. When there is no conductive material present, accurate measurements can be made at distances up to one kilometer from a long cable carrying one ampere of current. Ordinarily, the spacing between the coils is fixed at a distance of approximately 25 *m*; however, when near-surface conducting zones are to be studied in detail, the spacing can be made smaller, or in some cases, the separation between the coils may be varied from 5 to 25 *m* by leaving the lagging coil in one position while the leading coil is moved away from it. When this is done, the lagging coil is moved up to the farthermost position occupied by the leading coil in advancing the coil pair, to make the computation of the field easy.

14.3.3 TRANSIENT ELECTROMAGNETIC TECHNIQUES: UTEM, LOTEM, AND MTEM METHODS

Over decades, many different transient electromagnetic surveys have been introduced for geophysical exploration. As an example of the most promising techniques, which were developed during the past years, we can mention the UTEM system, the LOTEM system, and the MTEM method.

The **UTEM** (the University of Toronto EM) system uses a large fixed horizontal transmitter loop as a source. An array of receivers located both inside and outside of the transmitter loop measures all three components of the magnetic field (H_x, H_y, and H_z) and the horizontal components of the electric field (E_x and E_y). The UTEM transmitter sends a low-frequency current of precise triangular waveform through the transmitter loop. The magnetic field sensed at the receiver coil is the time derivative of the transmitted magnetic field, so that in "free space" a precise square wave voltage would be induced in the receiver. In the presence of subsurface conductors the received waveform is substantially distorted

from a square wave. This distortion is used to determine the conductivity distribution in underground formations. The UTEM system has a relatively limited depth range. It is primarily applied in mineral exploration.

The long-offset transient electromagnetic (**LOTEM**) technique was designed for deep penetration in the ground. The LOTEM system consists of a grounded wire transmitter and an induction loop and electric field receivers. A typical distance between transmitter and receiver is approximately equal to or greater than the exploration depth. A detailed description of the LOTEM method can be found in Strack (1999). The data acquisition and processing is similar to that of a seismic system. After prestack processing the data are stacked and finally converted into apparent resistivities after further poststack processing. The apparent resistivities are then either inverted or directly transformed into subsurface resistivity images.

Recently, demands on EM methods have been growing in the exploration for hydrocarbons (oil and gas) both on land and in marine environments. Due to the difference in resistivities between water-bearing layers (low resistivity) and hydrocarbon-bearing layers (high resistivity), EM methods are considerably useful tools to reduce the risk of drilling dry wells. However, compared to seismic methods, which are the primary methods of choice, the resolution of conventional EM methods was not satisfactory enough to be used practically in exploration for hydrocarbons. After several years of research and improvement of the instruments of EM methods, a new modification to TDEM methods was introduced by Wright et al. (2002) and Hobbs et al. (2005); the technique was called the multitransient electromagnetic (MTEM) method.

The survey configurations of the **MTEM** method are very similar to those of seismic surveys with multiple receivers and multiple transmitters. The transmitter is a current bipole source and the receivers are also a line of bipoles with two electrodes. The key characteristic of the MTEM survey is the use of multiple transmitter-receiver separations, which results in the combination of the parametric sounding and profiling. The current in bipole transmitters has a waveform of a finite-length signal formed by a pseudo-random binary sequence (PRBS) of the step functions. The current in the transmitter and the time-varying voltage response between each pair of receiver electrodes are measured simultaneously. Data are recorded with a fine sampling rate (about 0.05 ms), to improve the resolution of the MTEM survey. The equivalent impulse response (electric field) of the subsurface of the earth is recovered from these two measurements by deconvolution (Wright et al., 2002).

The rapid interpretation of the MTEM data is based on the apparent resistivity calculation and 1-D inversion of the data obtained for every transmitter-receiver pairs. The more efficient interpretation of impulse response obtained by the MTEM method can be performed by time domain electromagnetic migration, considered in Chapter 9, to create images of geoelectrical structure in the earth's subsurface, which can be used for detecting the location of mineral deposits. Finally, a comprehensive interpretation of the MTEM data can be achieved by the rigorous 3-D inversion discussed in Chapter 8 of the text.

REFERENCES AND RECOMMENDED READING TO CHAPTER 14

Abramowitz, M., and I. A. Stegun, 1965, Handbook of mathematical functions with formulas, graphs, and mathematical tables: National Bureau of Standards, Applied Mathematics Series 55, U. S. Gov. Printing Office, Washington, DC, 1046 pp.

Berdichevsky, M. N., and M. S. Zhdanov, 1981, Interpretation of anomalous variations of the electromagnetic field of the Earth: Nedra, Moscow, 327 pp.

Berdichevsky, M. N., and M. S. Zhdanov, 1984, Advanced theory of deep geomagnetic sounding: Elsevier, Amsterdam, London, New York, Tokyo, 410 pp.

Frischknecht, F. C., 1967, Fields about an oscillating magnetic dipole over a two-layer earth, and application to ground and airborne electromagnetic surveys: Colorado School of Mines Quarterly, **62** (1), 1–326.

Hobbs, B., G. Li, C. Clarke, and J. Linfoot, 2005, Inversion of multi-transient electromagnetic data: 68th EAGE Conference & Exhibition, Expanded Abstracts, A015.

Hordt, A., V. L. Druskin, L. Knizhnerman, and K.-M. Strack, 1992, Interpretation of 3-D effects in long-offset transient electromagnetic (LOTEM) soundings in the Munsterland area, Germany: Geophysics, **57** (9), 1127–1137.

Kaufman, A. A., 1979, Harmonic and transient fields on the surface of a two-layer medium: Geophysics, **44** (7), 1208–1217.

Kaufman, A. A., 1989, A paradox in geoelectromagnetism, demonstrating the equivalence of frequency and transient domain methods: Geoexploration, **25**, 287–317.

Kaufman, A. A., and G. M. Morozova, 1970, Theoretical basis for the transient sounding method in the near-zone: Nauka, Novosibirsk, 122 pp.

Kaufman, A. A., and G. V. Keller, 1983, Frequency and transient soundings: Elsevier, Amsterdam, 685 pp.

Kaufman, A. A., and G. V. Keller, 1985, Inductive mining prospecting, Part I: Theory: Elsevier, Amsterdam, 620 pp.

Keller, G. V., 1968, Electrical prospecting for oil: Quarterly of the Colorado School of Mines, **63** (2), 1–268.

Keller, G. V., 1969, Electromagnetic surveys in the Central Volcanic Region, Preliminary Report: Dept. of Scientific and Industrial Research, New Zealand, Report 55, 65 pp.

Keller, G. V., and F. C. Frischknecht, 1966, Electrical methods in geophysical prospecting: Pergamon Press, Oxford, 517 pp.

Liu, G., and M. Asten, 1993, Conductance-depth imaging of airborne TEM data: Exploration Geophysics, **24** (4), 655–662.

Macnae, J., and Y. Lamontagne, 1987, Imaging quasi-layered conductive structures by simple processing of electromagnetic data: Geophysics, **52** (4), 545–554.

March, H. W., 1953, The field of a magnetic dipole in the presence of a conducting sphere: Geophysics, **18** (3), 671–684.

Nabighian, M. N., and J. C. Macnae, 1991, Time domain electromagnetic prospecting methods: *in* Nabighian, M. N., and J. D. Corbett, Eds., Electromagnetic methods in applied geophysics, Volume 2, Applications: Society of Exploration Geophysicists, Tulsa, Oklahoma, 427–520.

Sidorov, V. A., and V. V. Tickshaev, 1969, Electrical prospecting with transient field in near zone: Saratov University, U.S.S.R.

Spies, B. R., 1989, Depth of investigation of electromagnetic sounding methods: Geophysics, **54** (7), 872–888.

Spies, B. R., and F. C. Frischknecht, 1991, Electromagnetic Sounding: *in* Nabighian, M. N., and J. D. Corbett, Eds., Electromagnetic methods in applied geophysics, Volume 2, Applications: Society of Exploration Geophysicists, Tulsa, Oklahoma, 285–425.

Strack, K. M., 1999, Exploration with deep transient electromagnetics: Elsevier, Amsterdam, 374 pp.

Tartaras, E., M. S. Zhdanov, K. Wada, A. Saito, and T., Hara, 2000, Fast imaging of TDEM data based on S-inversion: Journal of Applied Geophysics, **43**, 15–32.

Vanyan, L. L., 1967, Electromagnetic depth soundings: Consultants Bureau, New York, 312 pp.

Vanyan, L. L., 1997, Electromagnetic soundings (in *Russian*): Moscow, Scientific Word, 219 pp.

Vanyan, L. L., and A. I. Butkovskaya, 1980, Magnetotelluric sounding of layered media (in *Russian*): Nedra, Moscow.

Velikhov, Ye. P., Ed., 1989, Geoelectric investigations with strong current sources on the Baltic Shield: Moscow, Nauka, 272 pp.

Wait, J. R., 1954, Mutual coupling of loops lying on the ground: Geophysics, **19** (2), 290–296.

Wait, J. R., 1955, Mutual electromagnetic coupling of loops over a homogeneous ground: Geophysics, **20**, 630–637.

Wait, J. R., 1960, Some solutions for electromagnetic induction problems involving spheroidal, spherical, and cylindrical bodies: Jour. Res. Natl. Bur. Standards, B64, 15–32.

Wait, J. R., 1960, On the electromagnetic response of a conducting sphere to a dipole field: Geophysics, **25** (3), 649–658.

Wait, J. R., 1982, Geo-electromagnetism: Academic Press, New York, 268 pp.

Ward, S. H., and G. W. Hohmann, 1988, Electromagnetic theory for geophysical applications, *in* Nabighian, M. N., and J. D. Corbett, Eds., Electromagnetic methods in applied geophysics – Theory, Volume 1, Society of Exploration Geophysicists, Tulsa Oklahoma, 131–314.

Weidelt, P., 1983, The harmonic and transient electromagnetic response of a thin dipping dike: Geophysics, **48**, 934–952.

Wright, D., A. Ziolkowski, and B. Hobbs, 2002, Hydrocarbon detection and monitoring with a multicomponent transient electromagnetic (MTEM) survey, The Leading Edge, **21**, 852–864.

Zhdanov, M. S., 1986, Electrical prospecting (in Russian): Moscow, Nedra, 316 pp.

Zhdanov, M. S., and D. A. Pavlov, 2001, Analysis and interpretation of anomalous conductivity and magnetic permeability effects in time domain electromagnetic data. Part II: Sμ-inversion: Journal of Applied Geophysics, **46**, 235–248.

Zhdanov, M. S., D. A. Pavlov, and R. Ellis, 2002, Localized S-inversion of time domain electromagnetic data: Geophysics, **67**, 1115–1125.

Zhdanov, M. S., and G. W. Keller, 1994, The geoelectrical methods in geophysical exploration: Elsevier, Amsterdam, London, New York, Tokyo, 873 pp.

MARINE ELECTROMAGNETIC METHODS

Geophysical electromagnetic methods were originally introduced for land observations only. It was originally thought that seawater was so conductive that useful amounts of an electromagnetic field would not penetrate, and so, electrical exploration methods were not feasible in the oceans. To the contrary, it was discovered in the mid-twentieth century that various electromagnetic methods can be used quite effectively on and in the World Ocean.

The first experiments with marine electromagnetic field measuring were conducted by Russian geophysicists in the Arctic Ocean (e.g., Novysh and Fonarev, 1966; Trophimov and Fonarev, 1972). The first results of deep magnetotelluric sounding of the sea bottom were obtained in the Caspian Sea (Dubrovskiy and Kondratieva, 1976). In the late 1970s Scripps Institution of Oceanography conducted several deep-water marine EM experiments in the Pacific Ocean (Filloux, 1979; Spiess et al., 1980; Young and Cox, 1981; Cox, 1981). There have been several EM methods for mapping and imaging sub-sea-bottom geoelectrical structures (e.g., Sinha et al., 1990; Chave et al., 1991), especially for application to the study of the oceanic lithosphere and actively spreading midocean ridges (Shneyer et al., 1991; Evans et al., 1994; Constable and Cox, 1996; MacGregor and Sinha, 2000; MacGregor et al., 2001). Marine geoelectrical investigations have been extensively developed in the former Soviet Union. A review of this research can be found in Berdichevsky et al. (1989).

Since then, the number of marine electromagnetic investigations has increased dramatically. Marine EM methods are used both in academic applications to study the deep structure of the earth crust and upper mantle, and in exploration for mineral resources. A large number of academic research projects

are focused on studying the tectonically active zones and mid-ocean ridges. The main electromagnetic methods used in these studies are magnetotelluric and magnetovariational soundings.

Marine electromagnetic exploration for sea-bottom hydrocarbon reservoirs was carried out routinely in Russia (former USSR) since 1970s. In the West, this method was not widely used by industry until late 1990s, when several major oil corporations, including ExxonMobil, Statoil, Shell and many others began using marine controlled-source electromagnetic (MCSEM) surveys for offshore hydrocarbon exploration (Srnka et al., 2006).

The modern-days success of the application of EM methods to the offshore hydrocarbon exploration is based on the fundamental fact that oil and gas containing structures are characterized by very high resistivity, while the surrounding sea-bottom formations filled with salt water are very conductive. EM enables geologists to distinguish between a hydrocarbon-filled reservoir, which has high resistivity, and one filled with water or shale, which has lower resistivity. Therefore, a petroleum reservoir represents a clear target for EM methods.

The majority of existing EM technologies for marine geophysical exploration are based either on using magnetotelluric (MT) methods or applying marine version of controlled-source electromagnetic (CSEM) methods. At the same time, there are two major types of marine CSEM methods. One widely used technique employees an electric bipole transmitter towed by a vessel and a set of electric and magnetic receivers deployed on the seafloor. This system was originally developed by Charles Cox of Scripps Institution of Oceanography in the late 1970s (Cox, 1981). Another widely used method is based on the data acquisition system consisting of an electric bipole transmitter and an array of electric field receivers towed by a vessel. The moving platform geometry of a towed EM system enables EM data to be acquired over very large areas relatively fast compared to conventional MCSEM methods with the fixed sea-floor receivers. We shall discuss below these three methods in detail.

15.1 MARINE MAGNETOTELLURIC METHOD

The methodics of the marine magnetotelluric (MT) method are similar to those used on the land. The geoelectrical study of the sea bottom, however, is not the same as geoelectrical studies conducted on land. There are significant differences between the physical conditions for electromagnetic field generation and observation on the sea bottom and the physical conditions on land. These differences result in different techniques for measuring the EM field in the seawater and in different behaviors of the observed electromagnetic fields in comparison with land observations.

15.1.1 MAIN CHARACTERISTIC OF SEAFLOOR EM EQUIPMENT

In the case of a deep electromagnetic sounding of the earth's crust and upper mantle, marine MT observations are usually conducted at periods of 10^2 to 10^5 s, while for relatively shallow targets typical in hydrocarbon exploration the corresponding period range is within 1 Hz to 100 Hz. The magnetic and electric field measurements within this range are accomplished using induction coils for the magnetic field and specially designed electrometers and amplifiers for the electric field. The principles of induction-coil measurement were discussed in detail in Chapter 11. In the current chapter we will focus on the principal design of marine electrometers.

The measurement of electric fields in a conductive medium – seawater – is an extremely difficult task. The problem is that the electric field is very small in a conductive medium, which requires the use of electric field sensors with very high sensitivity. Also it is necessary to note that there is no physical sensor measuring the electric field vector, $\mathbf{E}$, directly. As we discussed in Chapters 2 and 3, the electric voltage, or the work of the electric field along some path, can be used for a meaningful representation of the electric field. This value is determined by measuring the difference between the electric potential at two points:

$$\int_{L_{AB}} \mathbf{E} \cdot d\,\boldsymbol{\ell} = -\int_{L_{AB}} dU = U_A - U_B, \tag{15.1}$$

where U_A and U_B are electric potentials at the points A and B, respectively. For example, if the integration line, L_{AB}, goes along the X axis, and the points A and B are separated by a distance Δx, the x component of the electric field, E_x, can be approximately determined as

$$E_x \approx \frac{U_A - U_B}{\Delta x}. \tag{15.2}$$

As for determining the difference between electric potentials, the simplest way to do is with the help of a couple of electrodes placed in direct contact with the medium at points A and B, respectively. Unfortunately, together with ensuring of E_x sensing, the direct contact with the medium (which is salt water in the case of marine measurements) gives rise to the side offset contact potential difference between the electrode and the medium or to the electrodes' own potentials, U_A^n and U_B^n, which represents the noise in the data. Taking these additional potentials into account, on the basis of Eq. (15.2), we get for a measured field, E_x^m,

$$E_x^m \approx \left(\frac{U_A - U_B}{\Delta x}\right) + \left(\frac{U_A^n - U_B^n}{\Delta x}\right). \tag{15.3}$$

In the last equation the first term in brackets is the useful signal, E_x, and the second one is the noise, E_x^n. The separation of these values in order to obtain a high signal/noise ratio is an extremely difficult problem when extremely low-frequency fluctuations of the electric field are investigated. That is because the E_x^n spectrum is mainly centered in the same frequency band, and its power is much higher than that of E_x (Iyengard, 1999). So, all the skill of the designer of the device for the E_x measurement in conductive media is concentrated upon the methodology of E_x^n reduction. For each medium these methods are different, having but one common purpose – to try to decrease as much as possible the E_x^n value or at least, according to the second bracket in Eq. (15.2), to make them as equal as possible for the two electrodes composing the pair.

It was found by extensive research and testing that Ag–AgCl electrodes and Pb–PbCl$_2$ electrodes produce the least noise and have relatively long-term stability. The standard design of the marine electrometer is shown in Fig. 15.1. The two electrodes, El_1 and El_2, are electrically insulated one from another. Each of these electrodes is connected with the seawater through long insulating pipes, which are called the *salt bridges*. The open end of the pipe connected to the electrode El_1, is located at point A, while another insulating pipe, filled with the seawater, connects electrode El_2 with point B. Taking into account the relatively low resistivity of the seawater (about 0.3 ohm-m), we can approximately assume that electrode El_1 measures the electric potential U_A at point A, and electrode El_2

$$\Delta U_p = \left(U_A + U_1^n\right) - \left(U_B + U_2^n\right)$$
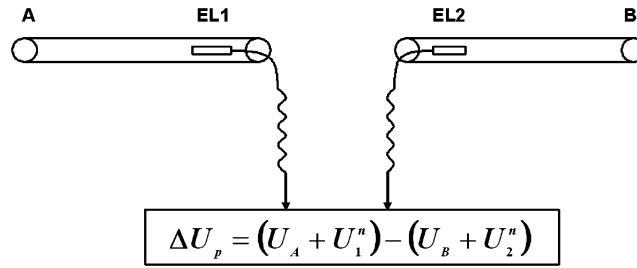
FIGURE 15.1

A standard design of the marine electrometer.

$$\Delta U_{p1} = \left(U_A + U_1^n\right) - \left(U_B + U_2^n\right)$$
$$\Delta U_{p2} = \left(U_B + U_1^n\right) - \left(U_A + U_2^n\right)$$
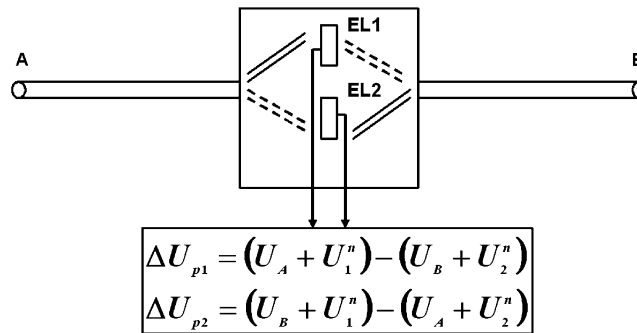
FIGURE 15.2

Design of a simple water-chopper mechanism used in marine electrometers.

measures the potential U_B at point B, respectively. Note that, because the parameters of the salt bridge are known, one can always make the necessary corrections for the salt bridge effect on the measured potentials, taking into account that the water channel in the pipes has a resistance of the order of a kilo-Ohm. However, what is not known is the self-potential of the electrodes (their noise), U_1^n and U_2^n.

It was proposed in the pioneering work of Filloux (1973), that the unknown signal bias due to electrode self-potentials can be removed by means of electrode reversal, which is similar to the chopping technique used in drift removal for DC amplifiers. This approach acquired the name "water chopper." Fig. 15.2 illustrates the design of a simple water-chopper mechanism used in marine electrometers. The water chopper acts like an electrical switch connecting the electrodes to points A and B, respectively, by the moving seawater channels and salt bridges. In the first position of the channels of the water chopper (shown by the solid lines in Fig. 15.2), the measured potential difference between two electrodes is:

$$\Delta U_{p1} = \left(U_A + U_1^n\right) - \left(U_B + U_2^n\right). \tag{15.4}$$
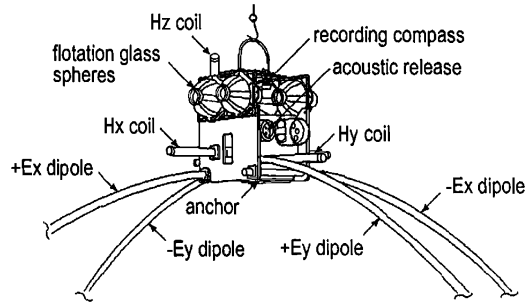
FIGURE 15.3

Typical design of a sea-bottom MT instrument. (Modified from Constable et al., 1998.)

In the second position of the channels of the water chopper (shown by the dashed lines in Fig. 15.2), the electrodes measure the following difference of the potentials:

$$\Delta U_{p2} = \left(U_B + U_1^n\right) - \left(U_A + U_2^n\right). \tag{15.5}$$

Subtracting Eq. (15.5) from Eq. (15.4), we arrive at the basic formula of the chopping technique:

$$U_A - U_B = \left(\Delta U_{p1} - \Delta U_{p2}\right)/2. \tag{15.6}$$

The last formula illustrates the noise correction capabilities of the water-chopping system.

As we mentioned above, for measuring the magnetic field at the sea bottom one can use practically the same magnetic field sensors as on the land, which may include flux-gate and induction coil magnetometers, discussed in Chapter 11. A typical design of a sea-bottom MT instrument is shown in Fig. 15.3. The electric field components, E_x and E_y are measured by the silver-silver chloride electrodes connected to the seawater through a water chopper mechanism and two insulating plastic pipes of 5 cm diameter and 5 m length. Three magnetic field components, H_x, H_y, and H_z, are measured by the induction-coil sensors. The instrument is dropped from the survey vessel in free fall in the water and sinks to the seafloor anchored to 60 kg of concrete, connected to the instrument by a mechanical device with an acoustic release system. The compass is used for evaluation of the general orientation of the instrument at the seafloor. After the completion of data acquisition, the concrete anchor is released by the acoustic system upon receipt of a command from the survey vessel. The instrument rises to sea level with the help of the glass flotation sphere, and is retrieved by the vessel.

This device can be used both in marine MT surveys and in the marine CSEM method.

15.1.2 COMPARISON BETWEEN LAND AND SEA-BOTTOM ELECTROMAGNETIC ANOMALIES

There are significant differences in the physical conditions for electromagnetic field generation and behavior on the sea bottom and on land. The most comprehensive study of this phenomenon has been conducted in the monograph by Berdichevsky et al. (1989). In the cited monograph the authors

present the results of a comparative study of sea-bottom and land electromagnetic anomalies. It has been demonstrated that there exists electric- and magnetic-fields "swap effect."

This effect has been established by direct comparison between land and sea-bottom electromagnetic anomalies for a typical geoelectric model. Let us assume that the geoelectrical cross sections on land and on the sea bottom are exactly the same. The main difference is that in the case of marine MT the model contains a conductive layer of seawater, and the observation points are located at the sea-bottom. However, this difference changes completely the physics of the observed EM field anomalies on the sea bottom.

Indeed, in the case of surface observations on land, the vertical component of the electric field, E_z, is always negligibly small, because the resistivity of air is very high in comparison with ground resistivity. That is why land EM surveys usually measure only five components of the EM field: E_x, E_y, H_x, H_y, H_z. Also, in the presence of horizontal geoelectrical inhomogeneities, on land, we typically have the strongest anomalies of the horizontal electric field components, E_x and E_y, and of the vertical magnetic field component, H_z.

In the case of sea-bottom observations, the situation is completely different. First of all, all six components of the EM field can be measured at the sea bottom. In the presence of horizontal geoelectrical inhomogeneities, in the sea-bottom sediments, the strongest anomalies are observed for the horizontal magnetic field components and the vertical electric field component. This phenomenon is called the *electric- and magnetic-fields "swap effect."*

The physics of this effect is related to the different physical properties of the upper half-space in the case of the land and marine observations: on the land the conductive earth contacts with the resistive air, while in the seawater the conductive sea-bottom sediments contact a very conductive sea-water layer. This difference is reflected in the behavior of MT sounding curves as well.

It is important to remember that the "swap effect" has to be taken into account in interpretation of the results of sea-bottom electromagnetic surveys.

15.2 MARINE CONTROLLED-SOURCE ELECTROMAGNETIC METHODS

In discussing the use of electromagnetic methods at sea, we will examine two kinds of seas:

- 1) Shallow-water seas and continental shelves. The maximum water depth is 200 m, providing a conductance of up to 750 Siemens. Many measurements can be made from the surface of the sea.
- 2) Deep oceans. Water depths average 6 km, providing several tens of thousands of Siemens conductance. Source energy for carrying out electrical surveys must be generated at the seafloor, and observations of the field must be made there too.

The resources to be sought are quite different in these two environments. Shallow seas and continental shelves are part of the continents, and resource occurrences will be like those we see on dry land. The world's young sedimentary basins in which much oil and gas occur lie largely on the continental shelves. In other localities, continental shelves are expressed as drowned extensions of continental basement, and one might well expect to see mineral deposits similar to the ones found on the continents.

There is growing interest in deep-water exploration for energy and mineral resources as well. Significant amounts of hydrocarbons are thought to be associated with deep ocean, but the means for

discovering and developing such an energy resource are still in the very early stage. The recent advances in the offshore exploration using electromagnetic methods have proved that these methods provide a valuable information about the sub-sea-bottom structure of deep oceans.

15.2.1 ELECTRICAL EXPLORATION IN SHALLOW WATER

We will consider shallow water to be any depth of water in which electrical surveys can be carried out without the water layer interfering with our ability to see the target of exploration beneath the body of water. When a water layer is much more conductive than the rock beneath the water, the presence of the water reduces our ability to recognize geoelectrical structure within some zone immediately below the bottom of the water layer. This screening effect is most severe if the water is highly saline, as in the World's oceans and shallow seas.

We should note that extensive marine electrical surveys have been carried out as early as during the 1940s and 1950s, with large areas of the Atlantic and Gulf coasts of the United States having been surveyed, as well as large areas of the Caspian and Black Seas. Surveys have been carried out using the DC methods with electrode arrays towed behind one or two ships. For the surveys off the coasts of the United States, Schlumberger and Wenner towed arrays were used, while in the Caspian and Black Seas, dipole arrays were used. Plouff et al. (1961) describe the use of dipole vertical electric soundings with an array established on drifting ice in the Arctic Ocean northwest of Canada. More recently, Velikhov (1989) has described the use of a shore-based source, with measurements being made of the fields generated by that source at distances up to 100 kilometers off shore in the Barents Sea, north of Russia. Our primary consideration is to define the meaning of "shallow" as it applies to electrical survey operations at sea. One way of approaching the problem is through the use of a resolution analysis based on Fréchet derivatives, as was explained in Chapters 6 and 7.

Let us consider a model as shown in Fig. 15.4 in which a layer characterized by a conductance S_{sea} formed by an ocean with a depth d_{sea} and a conductivity σ_{sea} covers a lower half-space with a conductivity σ_{bottom}. We then embed a thin layer at a depth z_i in the lower half-space with a conductance $\Delta S = c S_I(z_i)$, where $S_I(z)$ is the integral conductance as a function of depth, z, beneath the seafloor,

$$S_I(z) = \int_0^{z_i} \sigma(z) z \, dz,$$

and c is some small number, such as .01. The maximum difference between an electrical sounding curve for a perturbed case and that for an unperturbed case is then used as a measure of the resolvability of the embedded thin layer.

We expect resolvability to be a function of both the conductance in the overlying sea and the depth at which the seafloor is perturbed. Fig. 15.5 shows a series of curves for the maximum change in apparent resistivity caused by the presence of the perturbing thin layer at various depths beneath the seafloor for the Schlumberger array deployed at the surface of a sea with various depths (conductances). Each curve reflects a different resistivity assumed for the seafloor.

The maximum resolvability, $\Delta \rho_a^{(max)} / \Delta S$, is observed when no sea layer is present. This resolvability is reduced by introducing the sea layer on top of the lower half-space, and is reduced most for perturbing layers at shallow depths beneath the seafloor and for large resistivity contrasts between the sea and the rock beneath the sea.
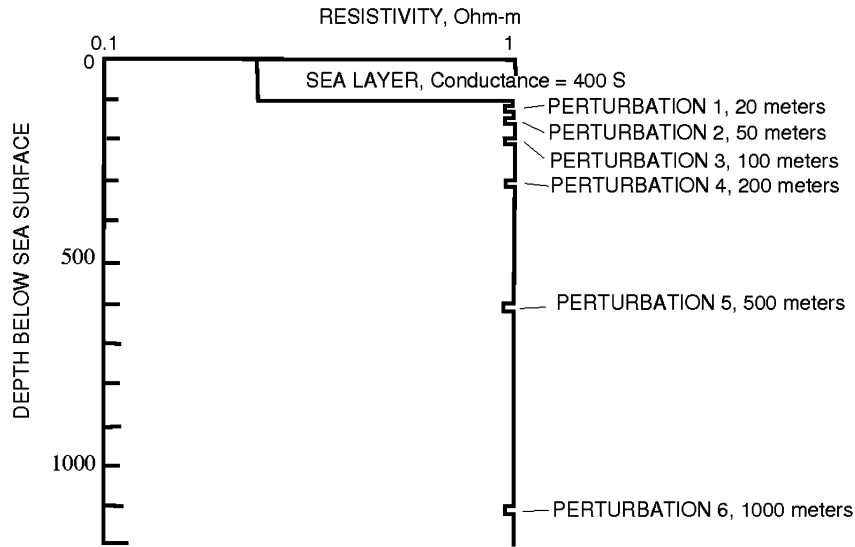
FIGURE 15.4

Model illustrating a resolution analysis for a shallow-water electrical survey.

We expect that the screening effect will be different for an electromagnetic induction method than for a DC method. Let us assume that we attempt to make magnetotelluric soundings from the surface of the sea, though this is operationally difficult. Carrying out the same computations as outlined in the preceding paragraph, we arrive at the set of resolvability curves as shown in Fig. 15.6. The behavior of these curves is similar to that of the curves for DC sounding, but differs in detail.

How do we decide on the difference between shallow seas and deep seas? We do so by arbitrarily specifying what degree of screening we are prepared to accept before it is worth the effort to instrument for sea-floor measurements. Measurements made with ocean-surface-based systems have certain advantages over even dry-land-based measurements. The uniformity of the sea layer reduces the scatter to measurements caused by geologic noise on dry land. Easier mobility at sea makes it possible to obtain high data density along traverse. These factors lead to a lower requirement for resolvability when measurements are made at sea.

Ultimately, as the sea becomes deeper and/or the contrast in resistivity between the seafloor and the sea becomes greater, screening forces one to consider sea-floor-based measurements.

15.2.2 ELECTRICAL EXPLORATION BENEATH DEEP OCEANS

If screening by seawater makes use of seafloor-based instrumentation necessary, a host of operational problems as well as the requirement for more detailed consideration of the theory for interaction of electromagnetic fields with the earth must be faced. The problems of instrumentation for and operating at great depths in the ocean have been discussed above.
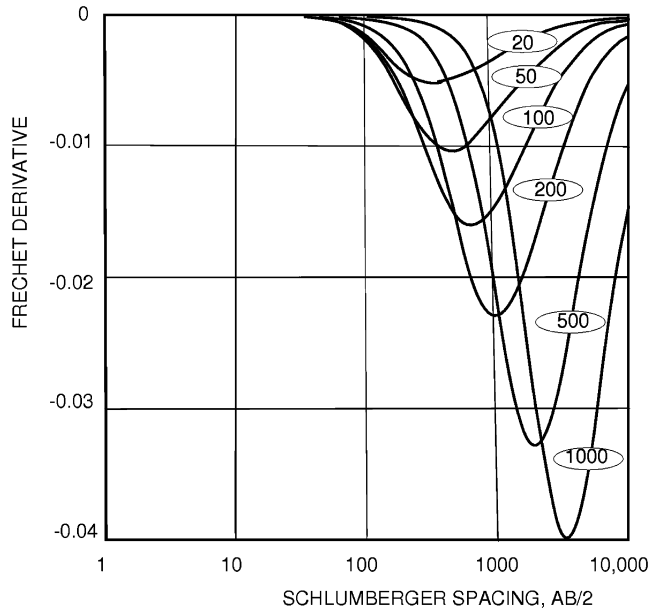
FIGURE 15.5

A set of curves for the maximum change in apparent resistivity caused by the presence of the perturbing thin layer at various depths beneath the seafloor for the Schlumberger array deployed at the surface of a sea with various depths (conductances).

Despite these difficulties, electrical methods are being employed on the seafloor on an increasing scale. Deployment of gear to record magnetotelluric soundings on the seafloor has advanced to the point of being routine. The development of systems for marine controlled-source electromagnetic surveying on the seafloor has become widely used for offshore geophysical exploration as well. We will concentrate our attention here on the theory for EM measurements on the seafloor to better understand how such measurements should be made.

The conductivity in the saline waters filling the deep oceans is about 4 S/m. Much of the deep ocean has a depth of 6 to 7 kilometers. The frequency of an electromagnetic wave for which this is a single skin depth is, correspondingly, 1/36 to 1/49 of a Hz. Except for a thin veneer of bottom sediments with a conductivity of the order of 1 S/m, rocks comprising the seafloor will have conductivities lower by a factor of 100 to 10,000. If frequencies in the range 1/36 to 1/49 Hz are used to probe the deep oceans, the skin depths in the crust beneath the deep oceans will be measured in hundreds of kilometers. It is impractical to use such low frequencies to study the seafloors in any detail. It appears that a useful system for doing seafloor electrical surveying must be based on the seafloor or very close to it.

Let us examine the behavior of an electromagnetic field originating from a source on the seafloor. Of course, within homogeneous layers that electromagnetic field must obey the diffusion equation form
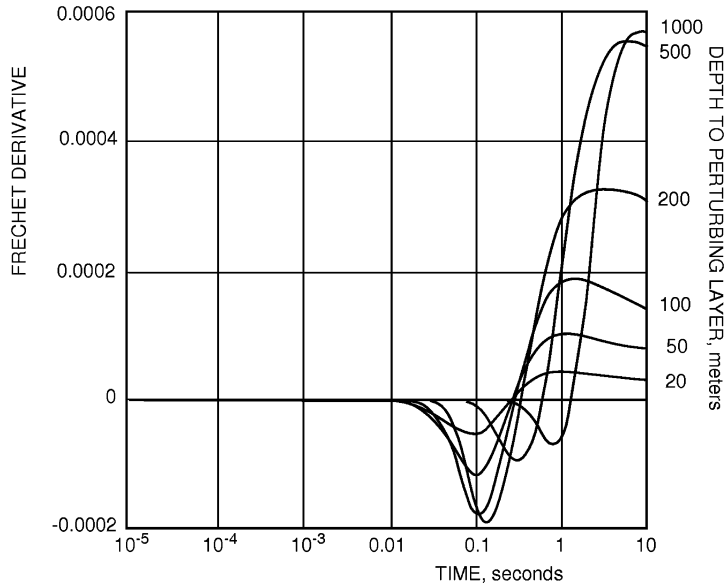
FIGURE 15.6

Fréchet derivative curves for a continental shelf sedimentary model. The ocean was assigned a depth of 100 meters and a resistivity of 0.25 ohm-meters. The sea floor was assigned a uniform resistivity of 1 ohm-meter. A perturbing layer with a resistivity of 0.9 ohm meters and a thickness of 10% of the depth was inserted at various depths beneath the sea floor as indicated on each curve. The system modeled is a wire-loop TDEM sounding system with a source receiver separation of 1000 meters.

of Maxwell's equations written as

$$(\nabla^2 + k^2)\mathbf{E} = 0$$

and

$$(\nabla^2 + k^2)\mathbf{H} = 0,$$

just as in all previous chapters of this book. Using the spatial spectrum transformation technique developed in Chapter 5, a solution can be obtained for a small vertical-axis magnetic dipole source located on the plane separating two half-spaces (Fig. 15.7):

$$E_\varphi = \frac{-3i\omega\mu_0 M}{2\pi(k_1^2 - k_0^2)r^4}\left[e^{ik_0 r}(1 - ik_0 r - \frac{1}{3}k_0^2 r^2) - e^{ik_1 r}(1 - ik_1 r - \frac{1}{3}k_1^2 r^2)\right],$$
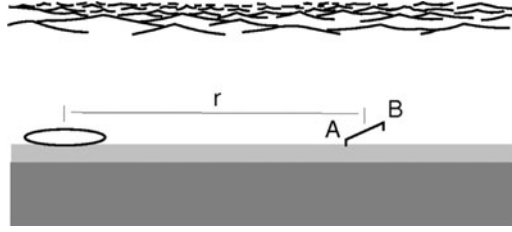
FIGURE 15.7

Simple sea-bottom survey design: measurement of the electric field originating from a horizontal loop source on the seafloor.

$$H_z = \frac{9M}{2\pi(k_1^2 - k_0^2)r^5} \times$$
$$\times \left[e^{ik_0 r}\left(1 - ik_0 r - \frac{4}{9}k_0^2 r^2 + \frac{1}{9}ik_0^3 r^3\right) - e^{ik_1 r}\left(1 - ik_1 r - \frac{4}{9}k_1^2 r^2 + \frac{1}{9}ik_1^3 r^3\right) \right], \tag{15.7}$$

where E_φ, and H_z, are the components of the electromagnetic field that will be observed on the seafloor at a distance, r, from the source. The quantity, M, is the moment of the source, $k_0^2 = i\omega\mu\sigma_{water}$ is the wave number for the upper half-space filled with seawater, and $k_1^2 = i\omega\mu_0\sigma_{bottom}$ is the wave number for the lower half-space beneath the sea floor.

Earlier, in discussing these fields for the case in which the upper half-space is the atmosphere in which the wave number $k_0^2 = i\omega\mu_0\epsilon \approx 0$, these equations were somewhat simplified.

Let us now examine the behavior of the electromagnetic fields described by Eq. (15.7). Specifically, consider the tangential electric field, E_φ. Assume that the separation and the frequency are appropriate for small induction numbers, such that $|k_0 r| < 1$ and $|k_1 r| < 1$. We can write the expression for the electric field as a series by expanding the exponents:

$$E_\varphi = \frac{-i\omega\mu_0 M}{2\pi(k_1^2 - k_0^2)r^4} \sum_{n=2}^{\infty} i^n \frac{(n-1)(n-3)}{n!}(k_0^n - k_1^n)r^n. \tag{15.8}$$

Discarding all but the first three terms,

$$E_\varphi = \frac{i\omega\mu_0 M}{4\pi r^2}\left[1 + \frac{1}{4}(k_0^2 + k_1^2)r^2 + \frac{2}{15}i\frac{k_0^5 - k_1^5}{k_0^2 - k_1^2}r^3 + \cdots\right]. \tag{15.9}$$

Here, the first term represents the primary field contributed by only the time variation of the primary magnetic field. The second term describes the in-phase component of E_φ at low frequencies when coupling between current filaments is negligible. The third term contains information about the quadrature component of the secondary field.

Let us write Eq. (15.9) as

$$E_\varphi = \frac{i\omega\mu_0 M}{4\pi r^2}\left[1 + \left(1 + \frac{\sigma_{bottom}}{\sigma_{sea}}\right)\frac{k_0^2 r^2}{4} + \frac{1 - \left(\frac{\sigma_{bottom}}{\sigma_{sea}}\right)^{5/2}}{1 - \frac{\sigma_{bottom}}{\sigma_{sea}}}\frac{2}{15}ik_1^3 r^3 + \cdots\right]. \tag{15.10}$$

We see that at low frequencies, the field is defined mainly by currents flowing in the sea.

Next, let us consider cases in which $r/\delta > 1$, with $\delta^2 = 2/i\omega\mu_0\sigma_{sea}$. The tangential electric field can be expressed as

$$E_\varphi \approx -\frac{3M\rho_{sea}}{2\pi r^4}e^{ik_1 r}\left(1 - ik_1 r - \frac{1}{3}k_1^2 r^2\right), \tag{15.11}$$

when $r/\lambda_1 \geq 1$ and $\sigma_{bottom}/\sigma_{sea} \ll 1$.

In the range of separations which satisfy the stated condition, the existence of the sea above the system manifests itself simply in terms of a multiplying constant, $1/\sigma_{sea}$. In principle at least, it is possible to obtain information about σ_{bottom} even though σ_{bottom} may be much smaller than σ_{sea}.

If the parameter r/δ_1 can also be taken as being small, Eq. (15.11) can be expanded in a series;

$$E_\varphi = -\frac{3M}{2\pi\sigma_{sea}r^4}\left[1 - \frac{1}{3}\sum_{n=2}^{\infty}\frac{(3-n)(n-1)}{n!}(ik_1 r)^n\right]. \tag{15.12}$$

Keeping only the first three terms of the expansion, we obtain:

$$E_\varphi \approx -\frac{3M}{2\pi\sigma_{sea}r^4}[1 + \frac{1}{6}k_1^2 r^2 + \frac{1}{24}k_1^4 r^4 + \frac{1}{45}ik_2^5 r^5 - \cdots]. \tag{15.13}$$

The real and imaginary parts of the electric field as approximated in Eq. (15.13) are equal to

$$1 + \frac{1}{6}k_1^2 r^2 + \frac{1}{24}k_1^4 r^4 = 1 + \frac{1}{6}i\omega\mu_0\sigma_{bottom}r^2 - \frac{1}{24}(\omega\mu_0\sigma_{bottom})^2 r^4$$

$$\mathrm{Re}\, E_\varphi \approx -\frac{3M}{2\pi\sigma_{sea}r^4}\left[1 - \frac{(\omega\mu_0\sigma_{bottom})^2}{24}r^4\right], \tag{15.14}$$

and

$$\mathrm{Im}\, E_\varphi \approx -\frac{M}{4\pi\sigma_{sea}r^2}\omega\mu_0\sigma_{bottom}. \tag{15.15}$$

Note that both the imaginary part of E_φ and the second term in the real part are proportional to the conductivity of the bottom. This suggests that the conductivity of the seafloor can readily be determined from the difference in the real part of the electric field measured at two frequencies, ω_1 and ω_2:

$$\Delta(\mathrm{Re}\, E_\varphi) = M(\omega_2^2 - \omega_1^2)\frac{(\mu_0\sigma_{bottom})^2}{16\pi\sigma_{sea}}. \tag{15.16}$$

It is also an easy matter to determine the electromagnetic field behavior when the magnetic dipole source is excited with a Heaviside function by carrying out the appropriate Fourier transform on the expression for the tangential electric field, Eq. (15.7):

$$
E_\varphi(t) = \frac{3M}{\left(1 - \frac{\sigma_{bottom}}{\sigma_{sea}}\right) 2\pi \sigma_{sea} r^4} \times
$$
$$
\times \left\{ \left[\Phi(u_0) - \sqrt{\frac{2}{\pi}} e^{-u_0^2/2} u_0 (1 + \frac{1}{3} u_0^2) \right] - \left[\Phi(u_1) - \sqrt{\frac{2}{\pi}} e^{-u_1^2/2} u_1 (1 + \frac{1}{3} u_1^2) \right] \right\}, \quad (15.17)
$$

where $u_0^2 = 8\pi^3 r^4 \mu_0 \sigma_{sea}/t$ and $u_1^2 = 8\pi^3 r^4 \mu_0 \sigma_{bottom}/t$, and $\Phi(u)$ is the probability integral function.

In order to see how the conductivity of the sea bottom might be determined by measuring this field, let us consider the asymptotic behavior at early and late times. During the early stage, as both parameters u_1 and u_2 increase in value, the field given by Eq. (15.17) approaches zero because $\Phi(u) \to 1$ as $u \to \infty$.

Except for a relatively thin veneer of seafloor sediment, we expect the seafloor to have a much higher resistivity than the seawater above. Let us examine Eq. (15.17) for the conditions $\sigma_{bottom}/\sigma_{sea} \ll 1$ and $u_1 \gg 1$:

$$
E_\varphi = -\frac{3M}{2\pi \sigma_{sea} r^4} \left\{ 1 - \left[\Phi(u_2) - \sqrt{\frac{2}{\pi}} e^{-u_2^2/2} u_2 (1 + \frac{1}{3} u_2^2) \right] \right\}. \quad (15.18)
$$

We see that the tangential electric field caused by a vertical-axis magnetic dipole source on a high resistivity seafloor consists of the sum of two terms. The first term is

$$
E_\varphi^{(1)} = \frac{3M\rho_{sea}}{2\pi r^4}. \quad (15.19)
$$

This is exactly the same expression as one gets for the electric field for the same source on the surface of the sea, with the upper half-space being an insulator. We should not be surprised by this result, inasmuch as to a first approximation, we have also assumed the seafloor to be an insulator. However, the second term in Eq. (15.18) does reflect the effect of finite resistivity on the sea bottom:

$$
E_\varphi^{(2)} = -\frac{3M\rho_{sea}}{2\pi r^4} \left[\Phi(u_2) - \sqrt{\frac{2}{\pi}} e^{-u_2^2/2} u_2 (1 + \frac{1}{3} u_2^2) \right]. \quad (15.20)
$$

This term is time dependent and contains information about σ_{bottom}. For late time, the probability integral can be expanded as a power series:

$$
\Phi(u) \approx \sqrt{\frac{2}{\pi}} \left(u - \frac{u^3}{6} + \frac{u^5}{40} + \cdots \right). \quad (15.21)
$$

Substituting this into Eq. (15.20), we have

$$
E_\varphi^{(2)} \approx \frac{3M\rho_{sea}}{2\pi r^4} \left(1 - \frac{1}{15} \sqrt{\frac{2}{\pi}} u_2^5 \right). \quad (15.22)
$$

Measurement of the slope to the late-stage transient coupling for Heaviside excitation provides a direct means for determining seafloor conductivity for the conditions $8\pi^2 t/\mu_0\sigma_{sea}r^2 < 1$ and $8\pi^2 t/\mu_0\sigma_{bottom}r^2 > 1$:

$$
\begin{aligned}
\Delta E_\varphi^{(2)} &= \frac{M\rho_{sea}}{10\pi r^4}\sqrt{\frac{2}{\pi}}\Delta u_2^5 \\
&= -\frac{2^8 M\pi\sigma_{bottom}^{5/2}r^6}{10\sigma_{sea}}\left(\frac{1}{t_1^{5/2}}-\frac{1}{t_2^{5/2}}\right),
\end{aligned}
\tag{15.23}
$$

where t_1 and t_2 are the two times at which the transient electric field is sampled.

In both the frequency and time domains, with the right choice of frequency or time and separation between transmitter and receiver, it should be possible to determine the conductivity of the seafloor without concern about the effect of the overlying highly conductive seawater. While the analysis carried out above pertains only to a vertical axis magnetic dipole source, the development for a horizontal current-carrying wire on the seafloor is very similar. In fact, using reciprocity, the results developed above can be argued to apply also for a grounded wire source on the seafloor with the vertical component of the magnetic field being measured.

Thus, this analysis is laying a foundation for the marine controlled-sourced electromagnetic (MCSEM) methods.

15.3 MCSEM METHOD WITH ARRAYS OF FIXED OCEAN BOTTOM RECEIVERS AND TOWED TRANSMITTERS

15.3.1 GENERAL SURVEY CONFIGURATION OF THE MCSEM METHOD

Conventional marine CSEM surveys are characterized by arrays of fixed ocean bottom receivers and towed transmitters (Eidesmo et al., 2002; Ellingsrud et al., 2002). During recent years, these surveys have become extensively used for offshore petroleum exploration (e.g., Tompkins, 2004; Srnka et al., 2006; Carazzone et al., 2005; Hesthammer and Boulaenko, 2005). The success of the EM method's application for the search for oil and gas reservoirs is based on the fundamental fact that oil- and gas-containing structures are characterized by very high resistivity, while the surrounding sea-bottom formations filled with salt water are very conductive. Therefore, a petroleum reservoir represents a clear target for EM methods.

At the same time, it is difficult to detect the resistive layers associated with the hydrocarbon (HC) reservoirs using the MT method. The MT field, because of its regional nature, is practically uniform in the horizontal direction and generates a relatively weak vertical currents. As a result, the MT field has very limited sensitivity and resolution with respect to the thin horizontal resistive targets typical for the sea-bottom HC reservoirs. In addition, the downward-propagating MT field attenuates rapidly within the conductive layer of the seawater, which limits the practical application of the MT method in deep-water surveys.

MCSEM methods employ the electric bipole transmitter which generates an EM field with strong vertical electric and magnetic field components. A thin horizontal resistive layer possesses a significant
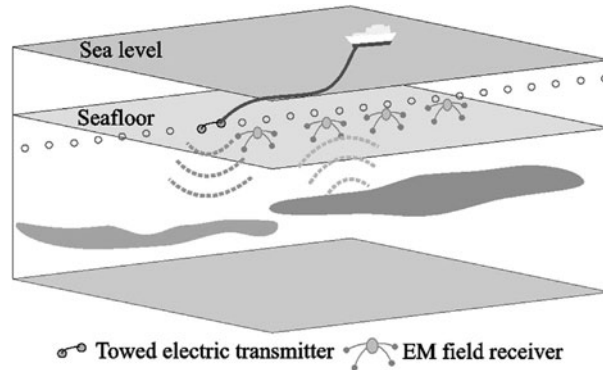
FIGURE 15.8

General survey configuration of the MCSEM method. An electric bipole transmitter towed by the survey vessel generates an EM signal, while the fixed multicomponent EM field receivers located on the seafloor measure the EM response from the geoelectrical structure beneath the seafloor.

resistance to the vertical current, which results in a measurable anomaly of the observed electromagnetic field.

Fig. 15.8 demonstrates the general survey configuration of the MCSEM method. A set of multicomponent electromagnetic receivers (typically 10 to 50) is deployed at the seafloor along the survey profile line(s). Usually these receivers are dropped off from the survey vessel and fall down to the seafloor freely. The transmitting horizontal electric bipole typically has a length of several hundred meters and is towed by the survey vessel via an umbilical cable. This transmitter generates a low-frequency (typically from 0.1 to 10 Hz) EM field, which propagates both upwards in the sea-water and downwards within the sea bottom. The receivers measure the amplitude and the phase of the electric and/or magnetic fields, generated by the transmitter. The recorded signal is formed both by the primary field from the transmitter and by the EM response from the geoelectrical structure beneath the seafloor. After the data acquisition is completed, the receivers float up to the surface by jettisoning away their weight, which previously held them to the seafloor, and are then retrieved by the survey vessel.

In order to understand better the basic properties of the MCSEM survey, we consider a simple basic survey design consisting of just one receiver and an electric dipole transmitter moving above this receiver in the x direction along a 16 km line at an elevation of 50 m above the sea bottom (Fig. 15.9). The receiver is located at the seafloor and measures the E_x component of the electric field and the H_y component of the magnetic field. The transmitter generates a frequency domain EM field with a frequency of 0.25 Hz from points every 100 m along the transmitter line. The maximum and minimum transmitter-receiver offsets are 7 km and 600 m, respectively. The background geoelectric model consists of a sea-water layer with a thickness of 300 m and a resistivity of 0.25 ohm-m and a layer of conductive sea-bottom sediments with a resistivity of 1 ohm-m. A typical sea-bottom HC reservoir of resistivity 50 ohm-m with the fixed length of 5 km and width of 1.5 km is submerged in the conductive sea-bottom sediments. The thickness of the reservoir varies from 50 m to 300 m, and the depth of the top of the reservoir varies from 350 m to 1850 m.
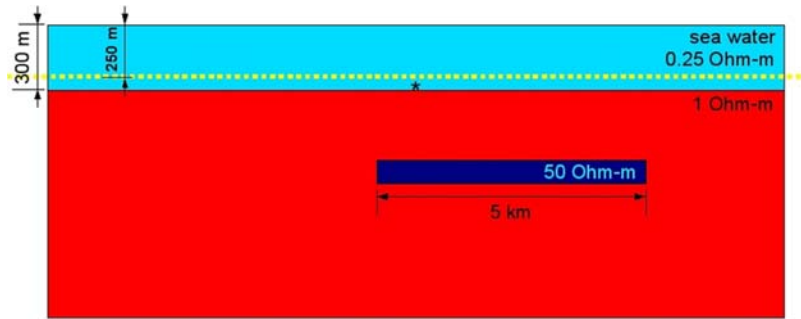
FIGURE 15.9

Model of a resistive rectangular target (petroleum reservoir) located within a conductive sea-bottom formation.
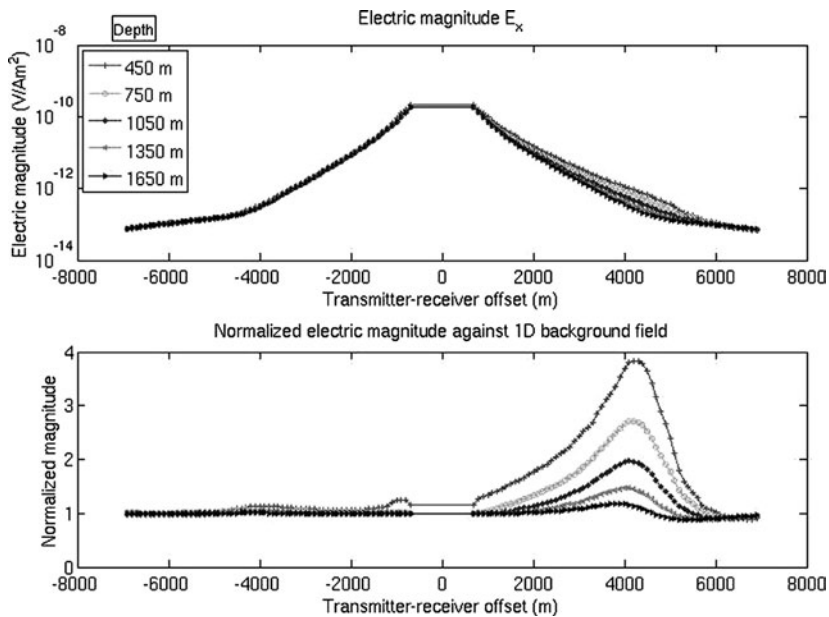
FIGURE 15.10

Plots of the electric field magnitude versus offset for a model with the resistive reservoir located at different depths.

Figs. 15.10 and 15.11 present the plots of the electric field magnitude and phase versus the offset. These data were computer simulated using integral equation based forward modeling code. The top panels in these figures show the synthetic electric field data, observed in the receivers. We should note that these plots look very similar for different depths of the reservoir, because the attenuation
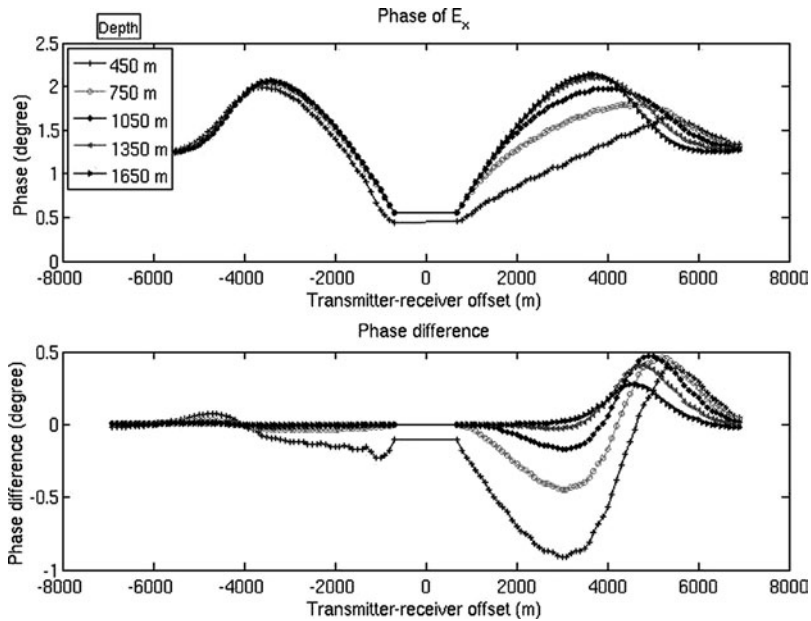
FIGURE 15.11

Plots of the electric field phase versus offset for a model with the resistive reservoir located at different depths.

of the primary field with the transmitter-receiver offset is the major factor determining the shape of all plots. In order to highlight the electric field anomaly associated with the presence of the resistive HC reservoir, we normalize the magnitude of the observed in-line (E_x) component of electric field by the magnitude of the corresponding background electric field (E_x^b) generated by the same transmitters in the model with the 1-D background conductivity. In other words, the 1-D background field is the field produced in the absence of the reservoir. The bottom panel in Fig. 15.10 shows the plots of these normalized electric fields. One can see significant anomalies in this figure which decrease with the depth of the reservoir. In a similar way, we calculate the phase differences between the observed and background electric field, shown in the bottom panel of Fig. 15.11. Again, the anomalies in the phase differences clearly indicate the presence of the resistive target. Thus, the anomalous behavior of the curves around 4000 m on the plots of the magnitude and phase of E_x fields versus offsets corresponds to the effect of the resistive reservoir.

One can compute the integrated sensitivity for this model using the method discussed in Chapter 6. For example, the integrated sensitivity for different thicknesses and depths of the resistive body is shown in Fig. 15.12: the closer the body to the seafloor, the higher the sensitivity. The dependence of the sensitivity on the thickness of the reservoir is significantly weaker. However, the larger thickness corresponds to the higher sensitivity. Thus, the plots in Fig. 15.12 illustrate how well the depth and the thickness of the reservoir can be resolved based on the MCSEM data.
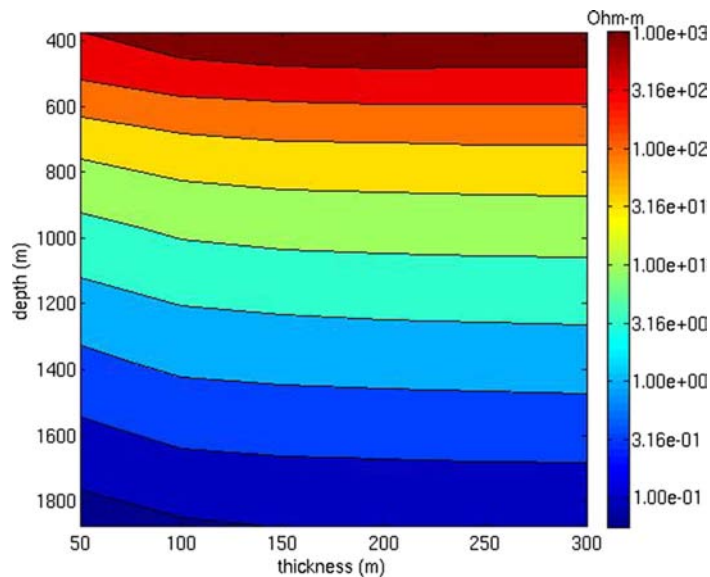
FIGURE 15.12

The integrated sensitivity for different thicknesses and depths of the resistive body.

15.3.2 INTERPRETATION OF MCSEM DATA

Interpretation of MCSEM data is still a very challenging problem, especially if one would like to take into account a real three-dimensional (3-D) structure of a sea-bottom geological formation. The inversion of MCSEM data is complicated by the fact that the EM response of a petroleum reservoir is very weak in comparison with a background EM field generated by an electric dipole transmitter in layered geoelectrical structures formed by a conductive sea-water layer and bottom sediments.

There were several publications recently reporting a significant progress in 3-D inversion of MC-SEM data based on the finite-difference (FD) method (Newman and Boggs, 2004; Hoversten et al., 2005, 2006). We will discuss here the application of the IE method to the MCSEM data inversion, following the paper by Gribenko and Zhdanov (2007).

A typical MCSEM survey consists of a set of sea-bottom electrical and magnetic receivers and a horizontal electric dipole transmitter towing at some elevation above the sea bottom. The transmitter generates a frequency-domain EM field. The main goal of MCSEM data interpretation is to determine the anomalous conductivity distribution, $\Delta\sigma$, within sea-bottom geological formations, where $\Delta\sigma$ is the difference between the total conductivity, σ, and some known background conductivity, σ_b:

$$\Delta\sigma = \sigma - \sigma_b.$$

In the hydrocarbon (HC) exploration the background conductivity is associated with the conductivity of the sea-bottom sediments, while the HC reservoir has a very low conductivity. In this situation the anomalous conductivity is always negative.

Mathematically, we can represent the corresponding EM inverse problem in the form of operator equation:

$$d = A (\Delta\sigma), \tag{15.24}$$

where A is a forward modeling operator, d stands for the observed EM data in the sea-bottom receivers, and $\Delta\sigma$ is the anomalous conductivity within the targeted domain.

Eq. (15.24) describes an ill-posed inverse problem. The regularized solution of this problem can be obtained by minimization of the corresponding Tikhonov parametric functional, $P^{\alpha}(\Delta\sigma)$ (see Chapter 7):

$$P^{\alpha}(\Delta\sigma) = \|W_d (A(\Delta\sigma) - d)\|^2_{L_2} + \alpha s (\Delta\sigma) = \min, \tag{15.25}$$

where W_d is the data weighting operator, α is a regularization parameter, and $s(\Delta\sigma)$ is a stabilizing functional.

It has been discussed in Chapter 7 that, the major role of stabilizing functionals is selecting the appropriate solution of the inverse problem from the class of models with assigned properties. There are several possible choices for the stabilizer (Zhdanov, 2002). For example, the following stabilizers can be used:

1. The minimum norm stabilizer (s_{MN}), which is equal to the square L_2 norm of the difference between the current model $\Delta\sigma$ and an appropriate a priori model $\Delta\sigma_{apr}$:

$$s_{MN}(\Delta\sigma) = \left\| W_m (\Delta\sigma - \Delta\sigma_{apr}) \right\|^2_{L_2}, \tag{15.26}$$

where W_m is the weighting operator of the model parameters.

2. The minimum support stabilizer (s_{MS}), which is proportional to the volume (support) of the nonzero values of the difference between the current model $\Delta\sigma$ and the a priori model $\Delta\sigma_{apr}$:

$$s_{MS}(\Delta\sigma) = \iiint_D \frac{(\Delta\sigma - \Delta\sigma_{apr})^2}{(\Delta\sigma - \Delta\sigma_{apr})^2 + e^2} dv, \tag{15.27}$$

where e is the focusing parameter.

3. The minimum gradient support stabilizer (s_{MGS}), which is proportional to the volume (support) of the nonzero values of the gradient of the model parameter, $\Delta\sigma$:

$$s_{MGS}(\Delta\sigma) = \iiint_D \frac{|\nabla\Delta\sigma(\mathbf{r})|^2}{|\nabla\Delta\sigma(\mathbf{r})|^2 + e^2} dv. \tag{15.28}$$

4. The minimum vertical support stabilizer, $s_{MVS}(\Delta\sigma)$, which is proportional to the vertical size of nonzero values of the difference between the current model $\Delta\sigma$ and an appropriate a priori model $\Delta\sigma_{apr}$ in a horizontal section S:

$$s_{MVS}(\Delta\sigma) = \iiint_D \frac{(\Delta\sigma - \Delta\sigma_{apr})^2}{\iiint_S (\Delta\sigma - \Delta\sigma_{apr})^2 ds + e^2} dv. \tag{15.29}$$
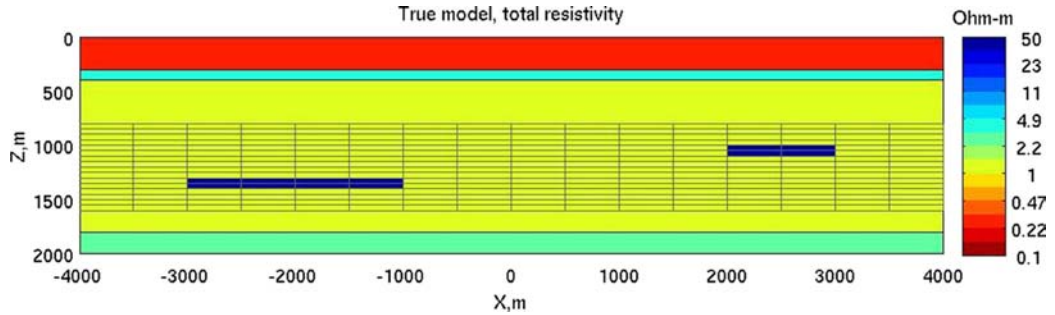
FIGURE 15.13

Model 1 formed by two resistive reservoirs located at different depths. The area shown with grids defines the extent of the anomalous domain in the inversions.

5. The minimum vertical gradient support stabilizer, $s_{MVGS}(\mathbf{m})$, which is proportional to the vertical size of nonzero values of the gradient of the model parameter:

$$s_{MVGS}(\Delta\sigma) = \iiint_D \frac{|\nabla\Delta\sigma(\mathbf{r})|^2}{\iiint_S |\nabla\Delta\sigma(\mathbf{r})|^2 \, ds + e^2} dv. \tag{15.30}$$

The minimum norm stabilizer selects the inverse model from the class of models with the least square norm. The minimum support stabilizer insures that the solution belongs to the class of models with the smallest domain of anomalous conductivity. This stabilizer works well if we have a local target with an anomalous conductivity, e.g. an HC reservoir. The minimum vertical support, $s_{MVS}(\mathbf{m})$, and the minimum vertical gradient support, $s_{MVGS}(\mathbf{m})$, stabilizers are specially designed to invert for a thin, sub-horizontal structures typical for an HC reservoirs.

We will investigate two simplified models of marine CSEM surveys. First, we analyze a 2-D CSEM survey, which is currently the most widely used in offshore exploration. Second, we consider an example of a 3-D survey.

Model 1

A typical 2-D survey consists of a set of receivers located along a line at the sea bottom and of an electric bipole transmitter towed parallel to and above the receivers. In our numerical experiment we assume that a synthetic CSEM survey is conducted in relatively shallow water with a sea depth of 300 m (Fig. 15.13). The survey consists of nine sea-bottom receivers and an electric dipole transmitter moving along a line passing directly above the receivers at an elevation of 50 m above the sea bottom. The separation between the receivers is 1000 m. The transmitter generates a frequency domain EM field with two frequencies of 0.25 and 0.75 Hz from points every 200 m along the transmitter line. The maximum transmitter-receiver offset is 10 km. The background geoelectric model consists of a sea-water layer with a thickness of 300 m and a resistivity of 0.25 ohm-m, a sea-bottom gas-hydrate layer with a thickness of 100 m and a resistivity of 5 ohm-m, conductive sea-bottom sediments with a thickness of 1400 m and a resistivity of 1 ohm-m, and a more resistive basement with a resistivity of
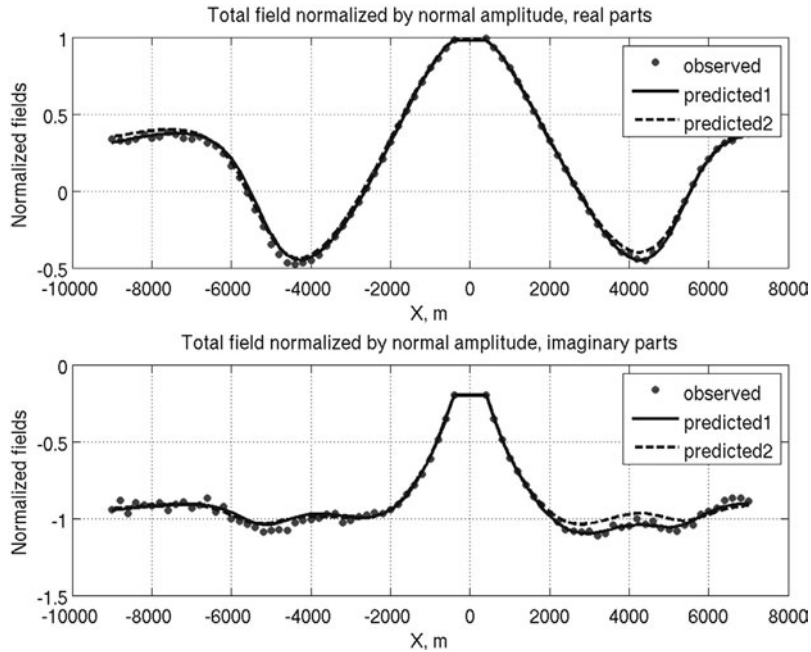
FIGURE 15.14

Model 1. Plots of the real (top panel) and imaginary (bottom panel) parts of the normalized observed and predicted in-line electric fields E_x at a frequency of 0.25 Hz for receiver #3 ($x = -6000$ m, $y = 0$ m). The dots show the noisy observed data, while the predicted data for a model obtained by the inversion are plotted by lines. The solid line corresponds to the predicted data ("predicted 1") obtained by inversion with the true 1-D background model, while the dashed line shows the predicted data ("predicted 2") computed for 3-D inversion result obtained with the background model found by 1-D inversion.

3.33 ohm-m (Fig. 15.13). We assume that we have two petroleum reservoirs with the same thickness of 100 m and a resistivity of 50 ohm-m, but located at depths of 1300 m and 1000 m respectively below sea level (Fig. 15.13). The horizontal dimensions of the reservoirs are 2 km and 1 km in the x direction and 1.8 km in the y direction, respectively.

The synthetic CSEM data were computed for this model using the rigorous IE method. These data were contaminated with random Gaussian noise. The noise level increases linearly from 1% at zero offset up to 7% at 10,000 m offset to simulate the typical noise behavior in the field data. The typical in-line electric field data recorded in receiver #3 for two frequencies are shown in Figs. 15.14 and 15.15. We plot here the real and imaginary parts of the total electric field E_x normalized by the absolute values of the normal electric field, E_x^{norm}, generated in the horizontally-layered background model formed by the seawater, the sea-bottom gas hydrate layer, the conductive sea-bottom sediments, and a relatively resistive basement. One can see rather complex anomalous behavior of the observed field.

We have applied our inversion algorithm to these noisy data. We should note that we use 3-D forward modeling and inversion to process the data observed by this 2-D synthetic survey. The area
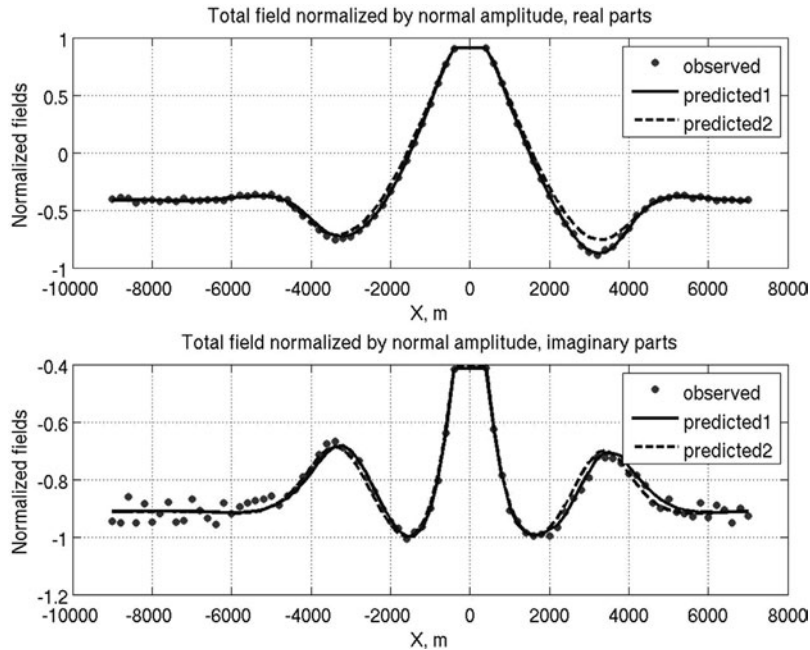
FIGURE 15.15

Model 1. Plots of the real (top panel) and imaginary (bottom panel) parts of the normalized observed and predicted in-line electric fields E_x at a frequency of 0.75 Hz for receiver #3 ($x = -6000$ m, $y = 0$ m). The dots show the noisy observed data, while the predicted data for a model obtained by the inversion are plotted by the lines. The solid line corresponds to the predicted data ("predicted 1") obtained by inversion with the true 1-D background model, while the dashed line shows the predicted data ("predicted 2") computed for 3-D inversion result obtained with the background model found by 1-D inversion.

of inversion is extended from -4000 m to 4000 m in the x direction, from -900 m to 900 in the y direction, and from 800 m to 1600 m at a depth with cell sizes equal to 500 m, 600 m, and 50 m in the x, y, and z directions, respectively.

Note that the first iteration of the RRCG method is computed with the regularization parameter $\alpha = 0$. After about 50 iterations of the rigorous inversion, the normalized residual reaches 3%. Fig. 15.16 shows a vertical section of the inversion result. As one can see, the depth and the horizontal extent of both reservoirs are recovered well in the inverse image. This example illustrates the stability of the method with respect to the noise in the data and "modeling noise" related to the different forward modeling solvers used for synthetic observed data calculation and in the inversion algorithm.

In the previous examples we have assumed that the true 1-D background conductivity model was known. We now investigate a more realistic situation where this background model is unknown. In this case, we can apply the 1-D inversion to the data recorded by receivers #1 and #9, located outside of the area with two resistivity reservoirs. As a result of 1-D inversion, we have found the following parameters of the new 1-D background model:
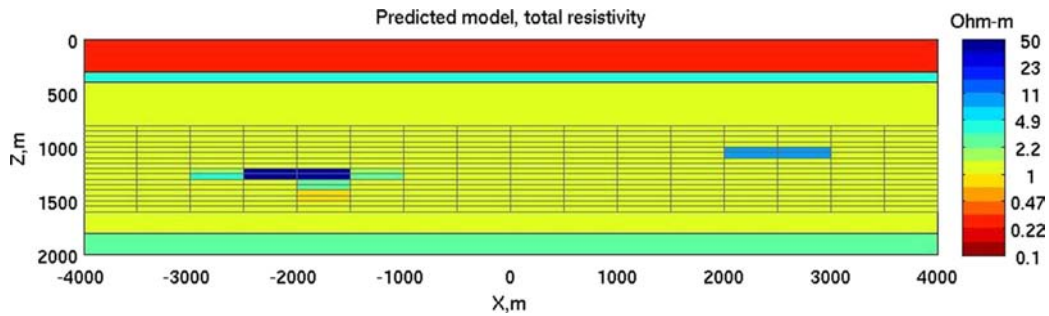
FIGURE 15.16

Model 1. The vertical section of the result of the inversion of the data contaminated by random noise. The noise level increases linearly from 1% at zero offset up to 7% at 10,000 m offset. The true layered-earth background conductivity model is used in the inversion. The area shown with grids defines the extent of the anomalous domain in the inversions.
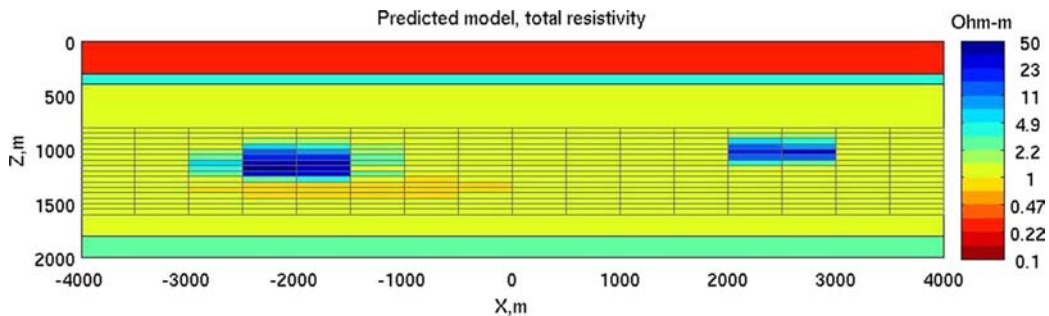
FIGURE 15.17

Model 1. The vertical section of the result of the inversion of the data contaminated by random noise. The noise level increases linearly from 1% at zero offset up to 7% at 10,000 m offset. The 3D inversion result is obtained with the background model found by 1D inversion. The area shown with grids defines the extent of the anomalous domain in the inversions.

a) thicknesses of the layers – 300, 100, and 1400 m.

b) resistivities of the layers – 0.25, 5.44, 0.97, and 4.29 ohm-m.

We have applied the IE-based inversion algorithm to the same noisy data, as in the previous case. However, we use a new 1-D background model found by 1-D inversion. We run practically the same number of RRCG iterations for this case, as for the examples, considered above. Fig. 15.17 presents the vertical section of the resulting inverse model. The dashed blue lines in Figs. 15.14 and 15.15 show the predicted data computed for the 3-D inversion result obtained with the background model found by 1-D inversion. One can see in these figures that the predicted data still fit the observed noisy data within the level of the noise, and the inverse model shown in Fig. 15.17 represents a reasonable image of the targets.
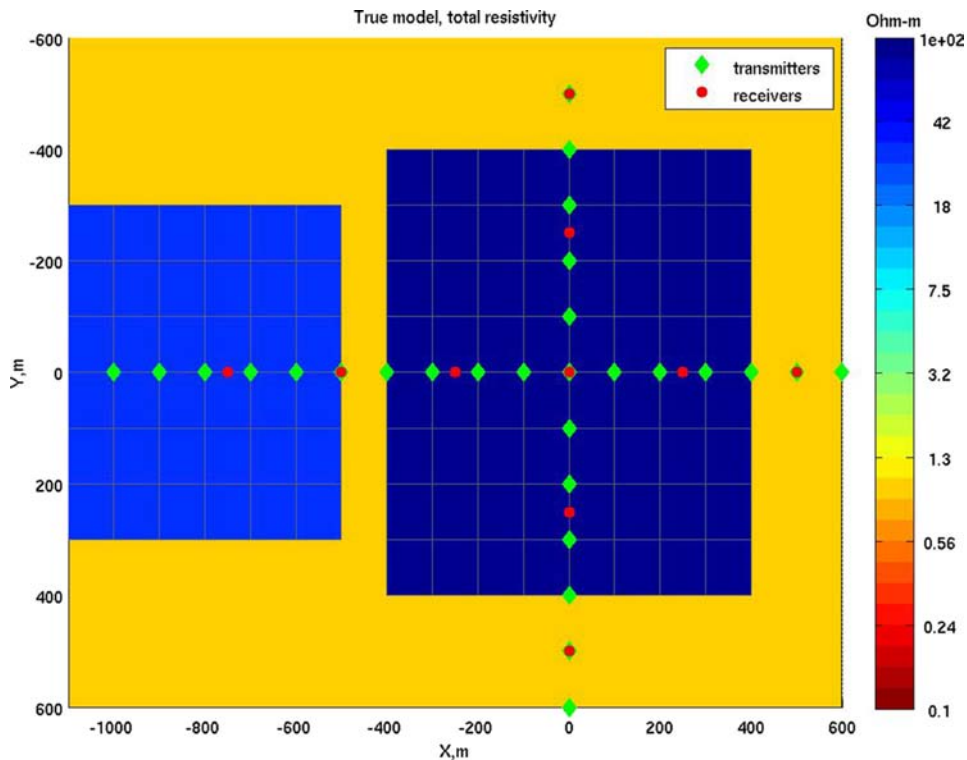
FIGURE 15.18

Model 2. A petroleum reservoir in the presence of a salt dome structure (plan view). The positions of the receivers are shown by the dots, while the diamonds show the transmitters locations.

This example shows that the interpretation of the practical MCSEM data should consist of two stages. In the first stage we find the horizontally-layered background geoelectric model by 1-D inversion of the observed data. In the second stage we run full 3-D inversion using the corresponding 1-D inverse model as a background.

Model 2

In the next numerical experiment we consider a 3-D CSEM survey over a truly 3-D target: a petroleum reservoir in the presence of a salt dome structure. Figs. 15.18 and 15.19 show a plan view and a vertical cross section of the model. The sea-bottom reservoir is approximated by a thin resistive body located at a depth of 900 m below sea level, with a thickness of 100 m, and a horizontal size of 800 m × 800 m. The resistivity of the reservoir is 50 ohm-m. There is located, also, an irregular-shaped salt dome structure close to the reservoir at a depth of 700 m below the sea bottom. The resistivity of the salt dome is 30 ohm-m. The depth of the sea bottom is 500 m from the surface, and the seawater resistivity is assumed to be equal to 0.25 ohm-m. The salt dome and the reservoir are submerged into
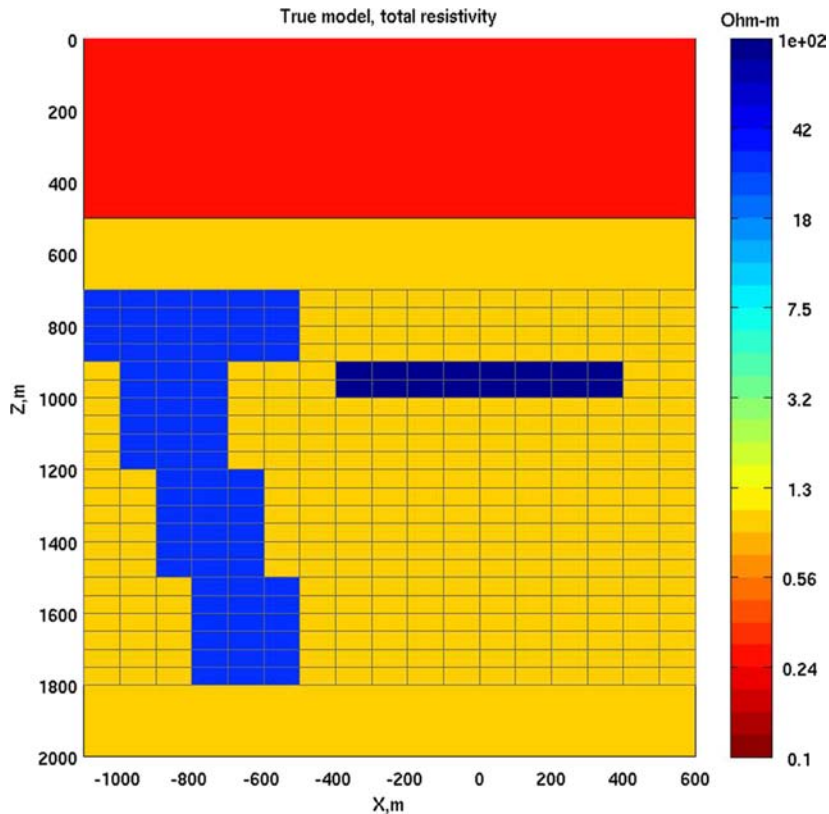
FIGURE 15.19

Model 2. A petroleum reservoir in the presence of a salt dome structure (vertical section). The area shown with grids defines the extent of the anomalous domain in the inversions.

the conductive thickness of the sea-bottom sediments with a resistivity of 1 ohm-m. A 3-D image of the true model is shown in Fig. 15.20.

A synthetic CSEM survey consists of fourteen sea-bottom receivers and an electric dipole transmitter moving along two mutually orthogonal lines at an elevation of 50 m above the sea bottom. The positions of the receivers are shown by the dots in Fig. 15.18. The separation between the receivers is 250 m. The locations of the transmitters are shown by diamonds in the same figure. The transmitter sends a frequency domain EM signal with two frequencies of 0.25 Hz and 0.75 Hz from points located every 100 meters along the transmitter's line. The receivers measure the in-line components of the electric field only. The observed data are computed with the rigorous IE forward modeling code and are contaminated by random Gaussian noise, with the noise level increasing linearly from 5% at zero offset up to 10% at 3000 m offset to simulate the typical noise behavior in the field data. The area of inversion is extended from -600 m to 600 m in the x direction, from -600 m to 600 m in the y
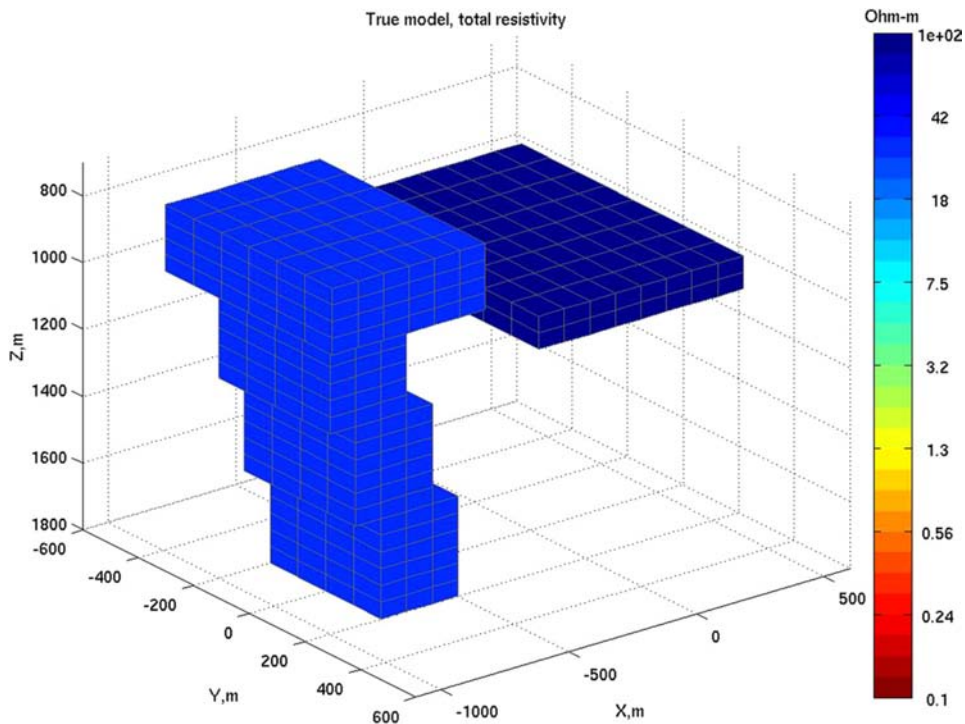
FIGURE 15.20

A 3D image of true Model 2 of a petroleum reservoir in the presence of a salt dome structure.

direction, and from 700 m to 1200 m depth. We discretize the inversion domain into 1320 prismatic cells with the cell sizes equal to 100 m, 100 m, and 50 m in the x, y, and z directions, respectively.

In this numerical experiment, we have used an approach based on inhomogeneous background conductivity (see Chapter 6). We have assumed that the position of the salt dome is known, and we have included a salt dome in the inhomogeneous background. This approach seems to be quite realistic. There are practical cases of offshore geophysical exploration where the salt dome structure is known from seismic data, but the location of the petroleum reservoir is unknown. Our inversion method makes it possible to include this known information in the background geoelectric model. We ran the rigorous IE-based inversion and after 45 iterations we obtained a normalized weighted residual between the observed noisy data and predicted data equal to 5%. The corresponding inverse model is shown in Figs. 15.21 and 15.22. One can see that, the depth and the horizontal extent of the reservoir and its resistivity are recovered well in the inverse image. However, we can see some artificial resistive structures in the corners of the 3-D inversion domain. The presence of these "noisy" elements in the inverse image is easily explained by the effect of the noise in the data, and by the fact that these corners of the inversion domain are located far away from the observational lines.
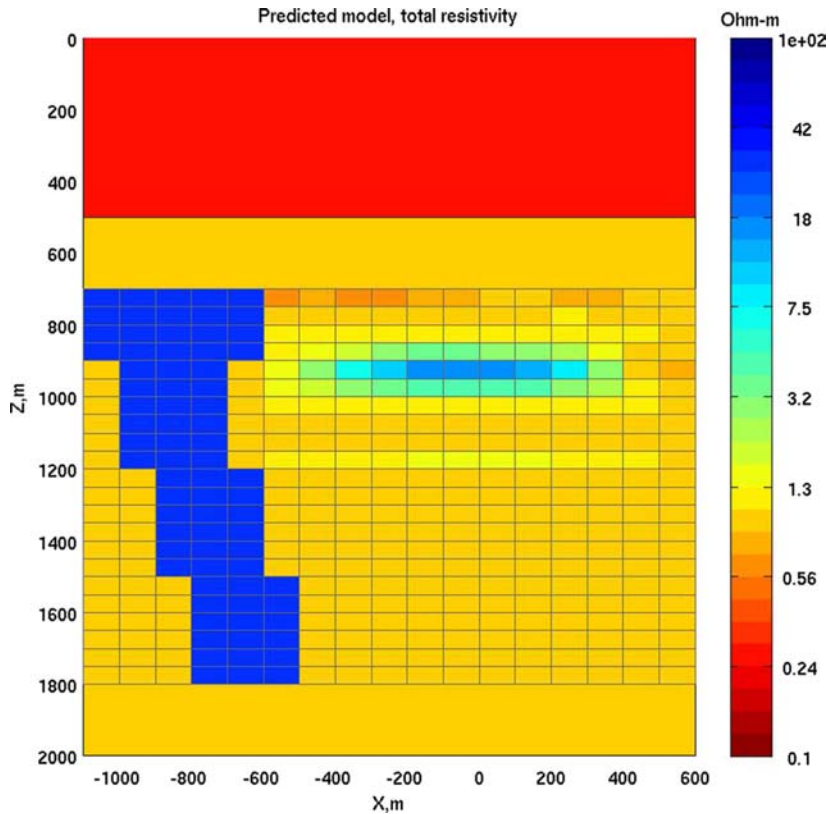
FIGURE 15.21

Model 2. The vertical section of the result of the inversion of the data contaminated by random noise. The noise level increases linearly from 5% at zero offset up to 10% at 3000 m offset. The true salt dome background conductivity model is used in the inversion. The area shown with grids defines the extent of the anomalous domain in the inversions.

The examples presented above show that the MCSEM data have a good potential to discover and locate a resistive HC reservoir in the conductive sea-bottom formations. This method is now widely used in industry, and it has proven to be an important tool in offshore petroleum exploration.

15.4 TOWED STREAMER ELECTROMAGNETIC METHOD
15.4.1 GENERAL PRINCIPLES OF THE TOWED STREAMER EM METHOD

Another widely used marine EM method is based on the data acquisition system consisting of an electric bipole transmitter and an array of electric field receivers towed by a vessel (Fig. 15.23). In a
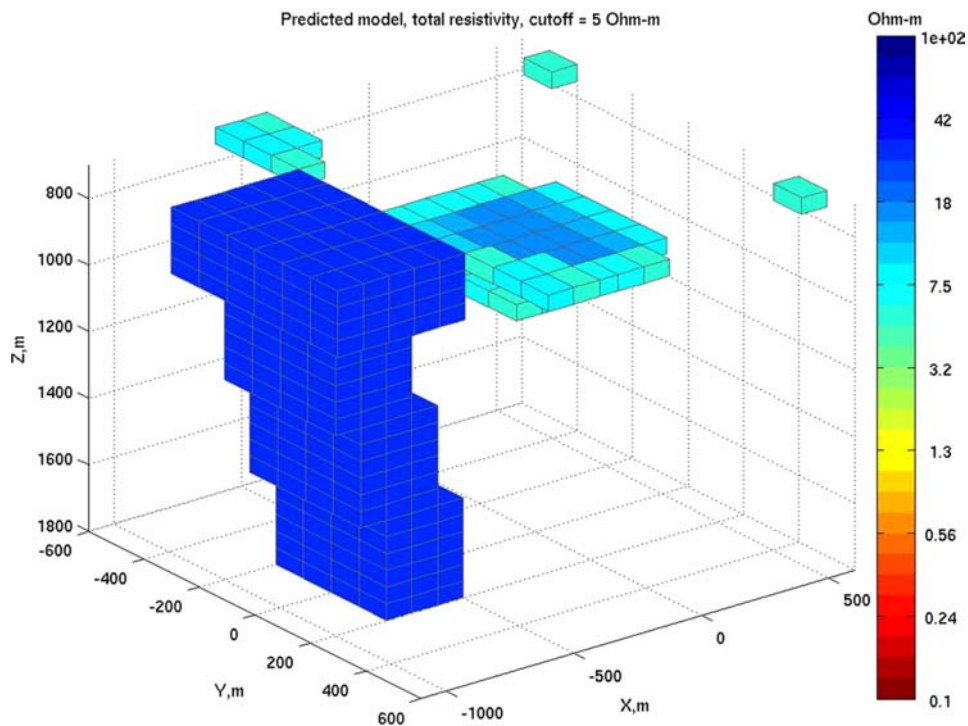
FIGURE 15.22

Model 2. 3-D image of the result of the inversion of the data contaminated by random noise. The true salt dome background conductivity model is used in the inversion.
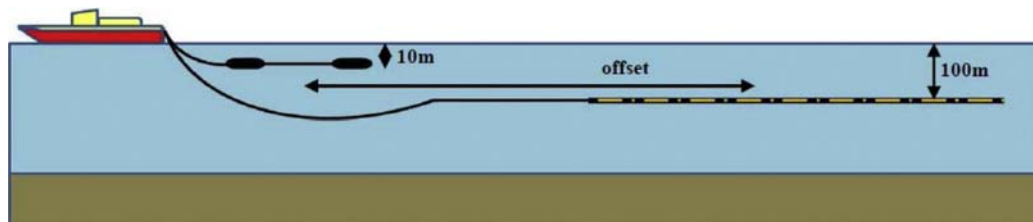
FIGURE 15.23

General survey configuration of the towed streamer EM method, consisting of an electric bipole transmitter and an array of electric field receivers towed by a vessel.

typical towed streamer EM survey configuration (Anderson and Mattsson, 2010; Mattsson et al., 2012; Zhdanov et. al., 2015), an 800 m long bipole electric current source at 1500 A is towed at a depth

of 10 m towed 10 m below the sea surface. The electric dipole source generates a frequency domain electric field at a discrete set of frequencies ranging typically from 0.2 Hz to 1.2 Hz. The receivers measure the in-line electric field components along the streamer cable, towed 100 m below the sea surface (see Fig. 15.23), as electric potential differences in distributed electrode pairs with offsets from 500 to up to 10,000 m. We should note that, it is possible to use a short-offset towed EM system. For example, this system was developed for gas hydrate mapping in the Gulf of Mexico by Weitemeyer and Constable (2010).

This moving platform geometry enables EM data to be acquired over very large areas with a high production rate and relatively low costs compared to conventional marine CSEM method, introduced above. As a result of the towed streamer EM survey, geophysicists may collect several thousands line kms of the data, which cover several thousands of square kms of the survey area. The typical target of these surveys are the resistive HC reservoirs located within the conductive sea-bottom sediments. These exploration targets are characterized by a very weak response in comparison to the measured total fields. Therefore, the quantitative interpretation of EM data is inherently difficult and should rely on 3D earth models generated by a rigorous 3D inversion. Moreover, 3D inversion of towed streamer EM data poses a significant challenge because of the size of the surveys, the requirement for high resolution models, and a huge number of transmitter-receiver pairs relative to conventional MCSEM surveys. Indeed, large-scale conventional CSEM surveys may have in the order of hundreds of fixed receivers, and in the order of thousands of transmitter positions. Reciprocity is routinely exploited in 3D conventional CSEM modeling and inversion to minimize the number of source terms that need to be solved (e.g., Zhdanov et al., 2011a). Towed streamer EM surveys may have millions of transmitter and receiver positions. Reciprocity cannot be exploited for any computational efficiency. To overcome this fundamental problem, Zhdanov et al. (2014a, 2014b) introduced a concept of moving sensitivity domain (MSD). We will discuss this concept in more details below.

15.4.2 INTERPRETATION OF TOWED STREAMER EM DATA

Inversion methodology for interpretation of the towed streamer EM data is similar to that for conventional MCSEM method, described above. One have to apply a method of regularized solution of ill-posed inverse problem, which is based on minimization of the Tikhonov parametric functional $P^\alpha(\Delta\sigma)$ (see Chapter 7 and Eq. (15.25)).

As was shown in Chapter 8, the problem of minimization of Tikhonov parametric functional can be solved by regularized conjugate-gradient (RCG) method with adaptive regularization. This method is based on iterative updates of the conductivity model $\Delta\sigma_n(\mathbf{r}) = \mathbf{m}_n$ as shown in the following formulas:

$$
\begin{aligned}
\mathbf{r}_n = A(\mathbf{m}_n) - \mathbf{d}, \quad \mathbf{l}_n = \mathbf{l}(\mathbf{m_n}) = \mathrm{Re}\, \mathbf{F}_n^\star \mathbf{W}_d^\star \mathbf{W}_d \mathbf{r_n} + \alpha \mathbf{W}_m^\star \mathbf{W}_m (\mathbf{m}_n - \mathbf{m}_{apr}), \quad &(a) \\
\beta_n = \|\mathbf{l}_n\|^2 / \|\mathbf{l}_{n-1}\|^2, \quad \tilde{\mathbf{l}}_n = \mathbf{l}_n + \beta_n \tilde{\mathbf{l}}_{n-1}, \quad \tilde{\mathbf{l}}_0 = \mathbf{l}_0, \quad &(b) \\
k_n = \left(\tilde{\mathbf{l}}_n, \, \mathbf{l}_n\right) / \left\{ \left\| \mathbf{W}_d \mathbf{F}_n \tilde{\mathbf{l}}_n \right\|^2 + \alpha \, \left\| \mathbf{W}_m \tilde{\mathbf{l}}_n \right\|^2 \right\}, \quad &(c) \\
\mathbf{m}_{n+1} = \mathbf{m}_n - k_n \, \tilde{\mathbf{l}}_n, \quad &(d)
\end{aligned}
\tag{15.31}
$$

where k_n is a length of the iteration step; $\mathbf{W}_m$ is the model weighting matrix; $\mathbf{l}_n$ is the gradient direction, computed using the adjoint Fréchet derivative matrix, $\mathbf{F}_n^\star$; and star denotes the adjoint operator (matrix).

The appropriate selection of the data and model weighting matrices is extremely important for the success of the inversion. The methods of solving this problem were discussed in details in Chapter 8 as well.

In order to apply the minimum support or minimum gradient support stabilizers, we use the re-weighted regularized conjugate gradient (RRCG) method introduced in Zhdanov (2002, pp. 161–166). In the framework of this algorithm, we conduct the inversion in the space of the weighted model parameters $\mathbf{m}_n^w$, which are determined by the following formula:

$$\mathbf{m}_n^w = \mathbf{W}_m \tilde{\mathbf{W}}_{en} \tilde{\mathbf{m}}_n. \tag{15.32}$$

In the framework of this approach, the variable weighting matrix $\tilde{\mathbf{W}}_{en}$ is precomputed on each iteration, based on the values $\mathbf{m}_n$, obtained on the previous iteration. This linear transformation is updated every several iterations, which is equivalent to the re-weighting of the model parameters. In other words, a set of linear transformations with the repeatedly updated weighting matrices is applied to transform the nonquadratic functional into the quadratic stabilizer similar to a minimum norm stabilizer (15.26). We refer the interested readers to the book on inversion theory by Zhdanov (2002, 2015) for in-depth explanation of the RRCG technique, which is widely used now in different geophysical applications.

In expression (15.32) we use the logarithmic model parameters, vector $\tilde{\mathbf{m}}$, with the scalar components $\tilde{m}_i$ given by the formula:

$$\tilde{m}_i = \ln \left(\frac{\Delta \sigma_i - \Delta \sigma_i^-}{\Delta \sigma_i^+ - \Delta \sigma_i} \right). \tag{15.33}$$

This parameterization forces the scalar components of the original conductivity vector $\Delta \boldsymbol{\sigma}$ to remain within the interval $(\Delta \sigma_i^-, \Delta \sigma_i^+)$:

$$\Delta \sigma_i^- \le \Delta \sigma_i \le \Delta \sigma_i^+, \ i = 1, 2, ...L. \tag{15.34}$$

Following Zhdanov (2002), we apply the *adaptive* regularization method. The regularization parameter α is updated in the process of the iterative inversion as follows:

$$\alpha_n = \alpha_1 q^{n-1}; \ \ n = 1, 2, 3.....; \ 0 < q < 1. \tag{15.35}$$

We begin an iteration from a value of α_1, which is a ratio of the misfit functional and the stabilizer for an initial model, then reduce α_n according to formula (15.35) on each subsequent iteration until the misfit condition is reached:

$$r_{n0}^w = \left\| \mathbf{W}_d \left(\mathbf{A} \left(\mathbf{m}_{\alpha_{n0}} \right) - \mathbf{d} \right) \right\|_{L_2} / \left\| \mathbf{W}_d \mathbf{d} \right\|_{L_2} = \delta, \tag{15.36}$$

where r_{n0}^w is the normalized L_2 norm of the weighted residual, and δ is the relative level of noise in the weighted observed data. Note that L_2 norms are determined as the square roots of the sum of the squares of the weighted residuals and of the weighted data.

Parameter q controls the rate of decrease of the regularization parameter in the process of inversion. If parameter q is too small (e.g., $q < 0.5$), the regularization parameter, determined by formula (15.35), decreases too fast, which results in diminishing the effect of the stabilizing functional on the inversion.

If parameter q is close to unit (e.g., $0.9 < q < 1$), the convergence of the RRCG method may become too slow. Our practical experience shows that this parameter should usually be selected within an interval $[0.5; 0.9]$.

In practical applications of the regularized iterative inversion, we begin the inverse process with the minimum norm (smooth) inversion to produce an initial image of the target. After a few minimum norm iterations we switch the iterative process to the minimum vertical support inversion by introducing the reweighting matrix $\tilde{\mathbf{W}}_{en}$, according to Eq. (15.32), and continue with the focusing inversion until the misfit functional reaches the required misfit level. We should note, however, that there are some limitations of the use of the focusing stabilizers related to the fact that the inverse images can be "overfocused" with unrealistically strong conductivity contrasts. This problem can be avoided by limiting the number of re-weightings in the RRCG algorithm and imposing some constraints on the boundaries of the conductivity variations and gradient values.

15.4.3 MOVING SENSITIVITY DOMAIN APPROACH

The sensitivity (Fréchet derivative) calculation is the most expensive item in the inversion not only in terms of the computation time, but also in the computer memory required for its storage. The number of entries in the Fréchet derivative matrix is equal to the number of data points times the number of cells in the inversion domain. With large amounts of data and vast inversion regions typical for the towed streamer EM survey, the computer memory requirements may become prohibitive. To reduce the storage requirements, one can use a moving sensitivity domain (MSD) approach in the towed streamer EM inversion (Zhdanov and Cox, 2012; Zhdanov et al., 2014a, 2014b).

In the framework of the MSD approach, we select a subset of the towed streamer EM survey formed by a selected set of transmitter and receiver positions. The integrated sensitivity of the data, $\mathbf{d}_s$, measured by this subset, to model parameter, δm_k, is determined as the ratio of the norm of perturbation of the observed data, $\delta \mathbf{d}_s$, to the corresponding perturbation of the parameters of the examined medium (Zhdanov, 2002):

$$S_k = \frac{\|\delta \mathbf{d}_s\|}{\delta \sigma_k} = \sqrt{\sum_i \left(F_{ik} F_{ik}^* \right)}, \tag{15.37}$$

where F_{ik} are the scalar components of the Fréchet derivative matrix, $\mathbf{F}_n$. The diagonal matrix with diagonal elements equal to $S_k = \|\delta \mathbf{d}_s\| / \delta m_k$ is an integrated sensitivity matrix of a subset of the towed streamer EM survey:

$$\mathbf{S} = \mathbf{diag} \left(\sqrt{\sum_i \left(F_{ik} F_{ik}^* \right)} \right) = \mathbf{diag} \left(\mathbf{F}^* \mathbf{F} \right)^{1/2}. \tag{15.38}$$

Matrix $\mathbf{S}$ is formed by the norms of the columns of the Fréchet derivative matrix, $\mathbf{F}$. The integrated sensitivity subdomains for selected subsets of the towed streamer EM survey are determined as the volumes where the integrated sensitivity of the subset is greater than a predetermined threshold. The total integrated sensitivity of the towed streamer EM survey is determined as the superposition of the sensitivities from all of the integrated sensitivity subdomains. The 3D inversion/imaging of the fields
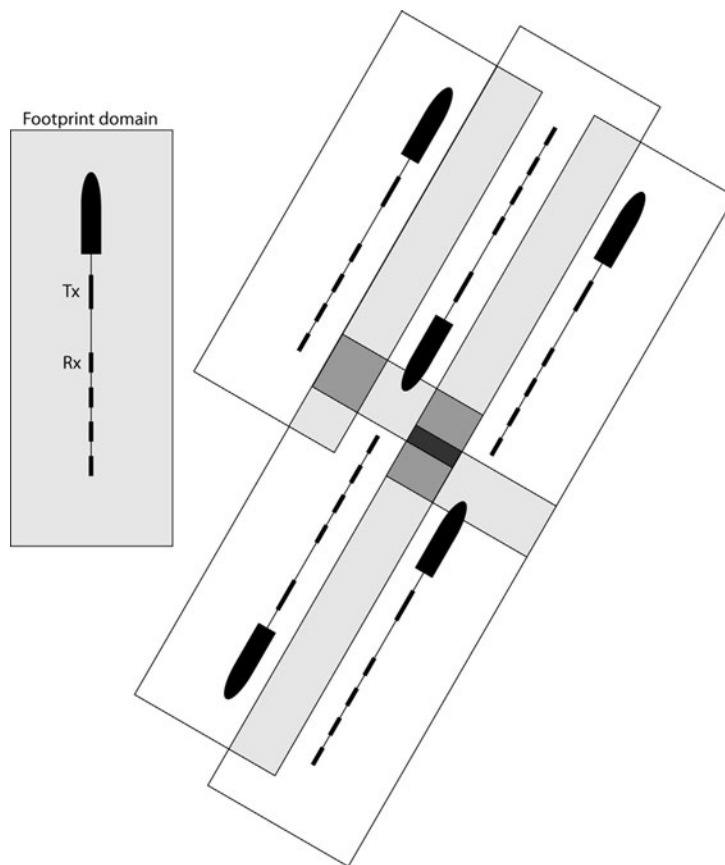
FIGURE 15.24

Plan view of multiple towed streamer EM sensitivity domains superimposed over the same 3D earth model. Darker shading indicates a higher fold of different sensitivity domains.

measured for each combination of transmitters and receivers for the entire towed streamer EM survey is based on the total sensitivity calculated as the superposition of the sensitivities from all of the integrated sensitivity subdomains (Zhdanov and Cox, 2012).

To illustrate this concept, Fig. 15.24 shows a plan view of multiple towed streamer EM sensitivity domains superimposed over the same 3D earth model. Darker shading indicates a higher fold of different sensitivity domains. As an example of the size of the sensitivity domain, we can calculate the integrated sensitivities for a towed streamer EM system consisting of a 300 m long electric bipole transmitter towed 10 m below the sea surface, and inline electric field receivers towed 100 m below the sea surface at offsets between 1325 m and 2545 m at 0.10 and 1.00 Hz. While the actual system may have intermediate offsets and other frequencies, these are representative of both the highest frequency – shortest offset, and the lowest frequency – longest offset configurations. The earth model consisted of

(A)

(B)

log_{10} (Normalized S)

(C)

(D)
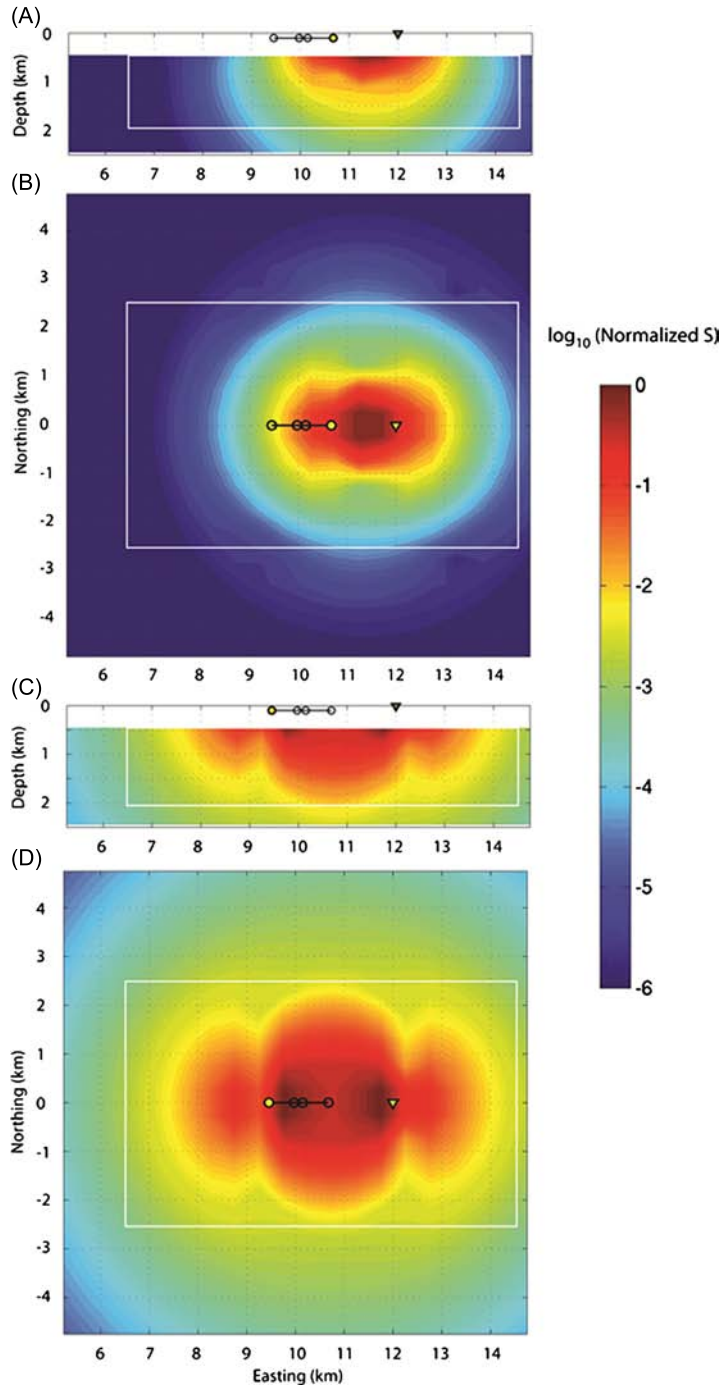
FIGURE 15.25

Example of the vertical (panels A and C) and horizontal (panels B and D) sections of a sensitivity domain used in the Peon model study. This figure presents the integrated sensitivities for a towed streamer EM system consisting of a 300 m long electric bipole transmitter towed 10 m below the sea surface, and inline electric field receivers towed 100 m below the sea surface at offsets between 1325 m for 1.00 Hz (panels A and B) and 2545 m for 0.10 Hz (panels C and D). The earth model consisted of a 384 m thick 0.3 ohm-m water column overlying an otherwise homogeneous, isotropic half-space of 3.0 ohm-m. A sensitivity domain of dimension 8 km × 5 km × 1.5 km (white box) captures over 95% of the integrated sensitivity for the towed streamer EM system for all frequencies and offsets.

a 384 m thick 0.3 ohm-m water column overlying an otherwise homogeneous, isotropic half-space of 3.0 ohm-m. Since the isosurfaces of the integrated sensitivities are the functions of transmitter-receiver geometry, frequency, and earth model, it is convenient to encapsulate them in a rectangular domain. For example, as can be seen in Fig. 15.25, a sensitivity domain of dimension 8 km × 5 km × 1.5 km captures over 95% of the integrated sensitivity for the towed streamer EM system for all frequencies and offsets. Note that this sensitivity domain is significantly smaller than the size of the actual Peon earth model presented later in this paper. Moreover, we note that the sensitivity domain dimensions don't need to be constant, and can vary as a function of offset and frequency.

Thus, we compute and store the Fréchet derivative inside the inversion cells within a predetermined sensitivity subdomains only. Therefore, Fréchet derivatives for towed streamer EM data can be computed and stored only for regions much smaller than the entire inversion domain, resulting in dramatic reduction of the computer memory requirements. The sensitivity domain size is determined based on the rate of integrated sensitivity attenuation of towed streamer EM data, which provides the optimal memory and computation use while retaining maximum accuracy.

A case study of practical application of the towed streamer EM survey is presented in Chapter 17.

REFERENCES AND RECOMMENDED READING TO CHAPTER 15

Anderson, C., and J. Mattsson, 2010, An integrated approach to marine electromagnetic surveying using a Towed Streamer and source: First Break, **28** (5), 71–75.

Berdichevsky, M. N., O. N. Zhdanova, and M. S. Zhdanov, 1989, Marine deep geoelectrics: Nauka, Moscow, 80 pp.

Carazzone, J. J., O. M. Burtz, K. E. Green, and D. A. Pavlov, 2005, Three dimensional imaging of marine CSEM data: 75th Annual International Meeting, SEG, Expanded Abstracts, 575–578.

Chen, J., G. M. Hoversten, D. W. Vasco, Y. Rubin, and Z. Hou, 2004, Joint inversion of seismic AVO and EM data for gas saturation estimation using a sampling-based stochastic mode: 74th Annual International Meeting, SEG, Expanded Abstracts.

Chave, A. D., S. C. Constable, and R. N. Edwards, 1991, Electrical exploration methods for the seafloor, *in* Nabighian, M. N., and J. D. Corbett, Eds., Electromagnetic methods in applied geophysics, Volume 2, Applications: Society of Exploration Geophysicists, Tulsa, Oklahoma, 931–966.

Constable, S., and C. Cox, 1996, Marine controlled-source electromagnetic sounding – II: The PEGASUS experiment: Journal of Geophysical Research, **97**, 5519–5530.

Constable, S. C., A. Orange, G. M. Hoversten, and H. F. Morrison, 1998, Marine magnetotellurics for petroleum exploration, Part I: A sea-floor equipment system: Geophysics, **63**, 816–825.

Constable, S. C., R. L. Parker, and C. G. Constable, 1987, Occam's inversion: A practical algorithm for generating smooth models from electromagnetic sounding data: Geophysics, **52** (3), 289–300.

Constable S. 2010. Ten years of marine CSEM for hydrocarbon exploration. Geophysics, **75** (5), 75A67–75A81.

Cox, C. S., 1981, On the electrical conductivity of the oceanic lithosphere: Physics of the Earth and Planetary Interiors, **25** (3), 196–201.

de Groot Hedlin, C., and S. Constable, 1990, Occam's inversion to generate smooth two dimensional models from magnetotelluric data: Geophysics, **55** (12), 1613–1624.

Dubrovskiy, V. G., and N. V. Kondratieva, 1976, basic results of the magnetotelluric soundings in the Turkmen sector of the Caspian Sea: Izvestia AN SSSR, Physics of the Earth, (3), 67–76.

Eidesmo, T., S. Ellingsrud, L. M. MacGregor, S. Constable, M. C. Sinha, S. Johansen, F. N. Kong, and H. Westerdahl, 2002, Sea Bed Logging (SBL), a new method for remote and direct identification of hydrocarbon filled layers in deepwater areas: First Break, **20**, 144–152.

Ellingsrud, S., T. Eidesmo, and S. Johansen, 2002, Remote sensing of hydrocarbon layers by seabed logging (SBL): Results from a cruise offshore Angola: The Leading Edge, **21**, 972–982.

Evans, R. L., M. C. Sinha, S. Constable, and M. J. Unsworth, 1994, On the electrical nature of the axial melt zone at 13° N on the East Pacific Rise: Journal of Geophysical Research, **99** (B1), 577–588.

Filloux, J. H., 1973, Techniques and instrumentation for study of natural electromagnetic induction at sea: Physics of the Earth and Planetary Interiors, **7**, 323–338.

Filloux, J. H., 1979, Magnetotelluric and related electromagnetic investigations in geophysics: Reviews of Geophysics and Space Physics, **17** (2), 282–294.

Filloux, J. H., 1981, Magnetotelluric exploration of the North Pacific: Progress report and preliminary soundings near a spreading ridge: Physics of the Earth and Planetary Interiors, **25**, 187–195.

Filloux, J. H., 1982, Magnetotelluric experiment over the ROSE area: Journal of Geophysical Research, **87**, 8364–8378.

Filloux, J. H., 1987, Instrumentation and experimental methods for oceanic studies, *in* Jacobs, A. J., Ed., Geomagnetism, Volume 1: Academic Press, London, 143–246.

Golubev, N., and M. S. Zhdanov, 2005, Accelerated integral equation inversion of 3-D magnetotelluric data in models with inhomogeneous background: 75th Annual International Meeting, SEG, Expanded Abstracts, 530–533.

Gribenko, A. and M. S. Zhdanov, 2007, Rigorous 3-D inversion of marine CSEM data based on the integral equation method: Geophysics, **72** (2), WA73–WA84.

Hesthammer, J., and M. Boulaenko, 2005, The offshore EM challenge: First break, **23**, 59–66.

Hoversten, G. M., F. Cassassuce, and G. A. Newman, 2004, Direct reservoir parameter estimation using joint inversion of seismic AVO and marine CSEM data: 74th Annual International Meeting, SEG, Expanded Abstracts, 1507–1510.

Hoversten, G. M., J. Chen, E. Gasperikova, and G. A. Newman, 2005, Integration of marine CSEM and seismic AVA data for reservoir parameter estimation: 75th Annual International Meeting, SEG, Expanded Abstracts, 579–582.

Hoversten, G. M., F. Cassassuce, E. Gasperikova, G. A. Newman, J. Chen, Y. Rubin, Z. Hou, and D. Vasco, 2006, Direct reservoir parameter estimation using joint inversion of marine seismic AVO and CSEM data: Geophysics, **71**, C1–C13.

Iyengard, R. V., 1999, On the design of ocean bottom electrometer: Deep Electromagnetic Exploration, Springer-Verlag, Narosa Publishing House, 248–259.

Johansen, S. E., H. E. F. Amundsen, T. Rosten, S. Ellingsrud, T. Eidesmo, and A. H. Bhuyian, 2005, Subsurface hydrocarbons detected by electromagnetic sounding: First Break, **23**, 31–36.

Key, K. W., 2003, Application of broadband marine magnetotelluric exploration to a 3-D salt structure and a fast spreading ridge: Ph.D. Thesis, University of California, San Diego.

Key, K. W., S. C. Constable, and C. J. Weiss, 2006, Mapping 3-D salt using the 2-D marine magnetotelluric method: Case study from Gemini Prospect, Gulf of Mexico: Geophysics, **71**, B17.

MacGregor, L. M., and M. C. Sinha, 2000, Use of marine controlled-source electromagnetic sounding for sub-basalt exploration: Geophysical Prospecting, **48** (6), 1091–1106.

MacGregor, L. M., M. C. Sinha, and S. Constable, 2001, Electrical resistivity structure of the Valu Fa Ridge, Lau basin, from marine controlled-source electromagnetic sounding: Geophysical Journal International, **146** (1), 217–236.

Mattsson, J., P. Lindqvist, R. Juhasz, and E. Bjőrnemo, 2012, Noise reduction and error analysis for a towed EM System: 82nd Annual International Meeting, SEG, Houston, Texas.

Newman, G. A., and P. T. Boggs, 2004, Solution accelerators for large-scale three-dimensional electromagnetic inverse problems, Inverse Problems, **20**, S151–S170.

Novysh, V. V., and G. A. Fonarev, 1966, The results of the electromagnetic study in the Arctic Ocean: Geomagnetism and Aeronomy, **6**, 406–409.

Ogilvie, J. S., and G. W. Purnell, 1996, Effects of salt related mode conversions on subsalt prospecting: Geophysics, **61** (2), 331–348.

Plouff, D., G. V. Keller, F. C. Frischknecht, and R. R. Wahl. 1961, Geophysical studies on IGY drifting station Bravo, T-3, 1958 to 1959: Geology of the Arctic **1** (1961): 709–716.

Portniaguine, O., and M. S. Zhdanov, 1999a, Focusing geophysical inversion images: Geophysics, **64** (3), 874–887.

Shneyer, V. S., I. L. Trofimov, Yu. M. Abramov, M. S. Zhdanov, V. A. Machinin, and S. V. Shabelyansky, 1991, Some results of gradient electromagnetic sounding in Doldrums Mid-Atlantic Ridge fracture: Physics of The Earth and Planetary Interiors, **66** (3–4), 259–264.

Smith, W. H. F., and D. T. Sandwell, 1997, Global seafloor topography from satellite altimetry and ship depth soundings: Science, **277**, 1956–1962.

Spiess, F. N., K. C. Macdonald, T. Atwater, R. Ballard, A. Carranza, D. Cordoba, C. Cox, V. M. Diaz Garcia, J. Francheteau, J. Guerrero, J. Hawkings, R. Haymon, R. Hessler, T. Juteau, M. Kastner, R. Larson, B. Luyendyk, J. D. Macdougall, S. Miller, W. Normark, J. Orcutt, and C. Rangin, 1980, East Pacific Rise: Hot springs and geophysical experiments: Science, **207**, 1421–1433.

Sinha, M. C., P. D. Patel, M. J. Unsworth, T. R. E. Owen, and M. G. R. MacCormack, 1990, An active source electromagnetic sounding system for marine use: Marine Geophysical Researches, **12**, (1–2), 59–68.

Srnka, L. J., J. J. Carazzone, M. S. Ephron, and E. A. Eriksen, 2006, Remote reservoir resistivity mapping: The Leading Edge, **25**, 972–975.

Tikhonov, A. N., and V. Y. Arsenin, 1977, Solution of ill-posed problems: V. H. Winston and Sons, 258 pp.

Tompkins, M. J., 2004, Marine controlled-source electromagnetic imaging for hydrocarbon exploration: Interpreting subsurface electrical properties: First Break, **22**, 45–51.

Trofimov, I. L., and G. A. Fonarev, 1972, Some results of the magnetotelluric profiling in the Arctic ocean: Izvestia AN SSSR, Physics of the Earth, (2), 81–92.

Ueda, T., and M. S. Zhdanov, 2006, Fast numerical modeling of multitransmitter electromagnetic data using multigrid quasi-linear approximation: IEEE Transactions on Geoscience and Remote Sensing, **44** (4), 1428–1434

Velikhov, Ye. P., Ed., 1989, Geoelectric investigations with strong current sources on the Baltic Shield: Moscow, Nauka, 272 pp.

Wan, L., and M. S. Zhdanov, 2004, New development in 3-D marine MT modeling and inversion for petroleum exploration: Proceedings of Annual Meeting of Consortium for Electromagnetic Modeling and Inversion, 311–332.

Weitemeyer K. and Constable S. 2010, Mapping shallow geology and gas hydrate with marine CSEM surveys: First Break, **28**, 97–102.

Young, P. D., and C. S. Cox, 1981, Electromagnetic active source sounding near the East Pacific Rise: Geophysical Research Letters, **8**, 1043–1046.

Zhdanov M. S., V. I. Dmitriev, S. Fang, and G. Hursán, 2000, Quasi-analytical approximations and series in electromagnetic modeling: Geophysics, **65**, 1746–1757.

Zhdanov, M. S., and G. Hursán, 2000, 3-D electromagnetic inversion based on quasi-analytical approximation: Inverse Problems, **16**, 1297–1322.

Zhdanov, M. S., 2002, Geophysical inverse theory and regularization problems: Elsevier, Amsterdam, London, New York, Tokyo, 628 pp.

Zhdanov, M. S., and G. A. Wilson, 2004, 3-D Quasi-analytical inversion of electromagnetic fields in the models with inhomogeneous background: 74th Annual International Meeting, SEG, Expanded Abstracts, 692–695.

Zhdanov, M. S., and E. Tolstaya, 2004, Minimum support nonlinear parameterization in the solution of 3-D magnetotelluric inverse problem: Inverse Problems, **20**, 937–952.

Zhdanov, M. S., L. Cox, A. Gribenko, and G. A. Wilson, 2006, Controlled-source electromagnetic inversion using quasi-analytical approximation with variable background: Proceedings of Annual Meeting of Consortium for Electromagnetic Modeling and Inversion, 83–102.

Zhdanov, M. S., S. K. Lee, and K. Yoshioka, 2006, Integral equation method for 3-D modeling of electromagnetic fields in complex structures with inhomogeneous background conductivity: Geophysics, **71** (6), G333–G345.

Zhdanov, M. S., M. Cuma, and T. Ueda, 2008, Three-dimensional electromagnetic holographic imaging in offshore petroleum exploration: 78th Annual International Meeting, SEG, Expanded Abstracts.

Zhdanov, M. S., 2010, Electromagnetic geophysics: Notes from the past and the road ahead: Geophysics, **75** (5), 75A49–75A66.

Zhdanov, M. S., M. Čuma, G.A. Wilson, E. P. Velikhov, N. Black, and A. Gribenko, 2011a, Iterative electromagnetic migration for 3D inversion of marine CSEM data: Geophysical Prospecting, **59** (6), 101–1113.

Zhdanov, M. S., M. Endo, L. H. Cox, M. Cuma, J. Linfoot, C. Anderson, N. Black, and A. V. Gribenko, 2014a, Three-dimensional inversion of towed streamer electromagnetic data: Geophysical Prospecting, **62** (3), 552–572.

Zhdanov, M. S., M. Endo, D. Yoon, M. Čuma, J. Mattsson, and J. Midgley, 2014b, Anisotropic 3D inversion of towed-streamer electromagnetic data: Case study from the Troll West Oil Province. Interpretation, **2** (3), SH97–SH113.

AIRBORNE ELECTROMAGNETIC METHODS

CONTENTS

Up to this point, we have developed the basis for using electrical methods presuming that exploration will be carried out either on the Earth's dry surface or in the ocean in a straightforward approach to measure either the electrical conductivity structure of the subsurface or the induced polarization responses. While the majority of exploration efforts employing electrical methods are of this ilk, other applications are also of considerable value. In particular, the other platforms which must be recognized are aircraft as a means for carrying part or all of the electrical surveying equipment rapidly over an area to be explored. The first practical application of the airborne electromagnetic (AEM) method was made as early as in 1951 (Becker, 1979; Fountain, 1998). Since then, AEM can be credited with directly aiding in the discovery of hundreds mineral deposits (e.g., Witherly, 2000). Many different frequency- and time-domain AEM systems have been developed over the last 75 years (e.g., Best, 1985; Fitterman, 1990; Palacky and West, 1991). The theoretical foundation of these methods is the same as has already been discussed for surface-based applications. So, we will discuss AEM methods mainly in terms of the operational features peculiar to the use of aircraft.

In spite of all technological achievements and advances in airborne EM systems, however, until recently, the interpretation of AEM data was still based on simple 1-D layered earth models. Despite their widespread use, it was repeatedly demonstrated that the 1-D methods were often invalid for recovering even simple 2-D and 3-D targets (e.g., Ellis, 1998), let alone anything resembling geological complexity (e.g., Raiche et al., 2001). Though 3-D parameterized inversion methods such as thin sheets embedded in conductive hosts were successful for certain types of targets (e.g., Keating and Crossley, 1990; Wolfgram and Golden, 2001), the routine use of more generalized 3-D modeling and inversion methods has not been yet realized.

The problem with 3-D modeling of AEM data is that it is necessary to solve as many large linear systems of equations as there are transmitter positions in the survey. Considering that the modern airborne surveys cover thousands of line kms, a rigorous 3-D inversion seems to be impractical even with the use of modern supercomputers. Various 3-D modeling approximations have been introduced over the last decade which simplify the nonlinear physics of AEM to a series of linear problems (e.g.,

Zhdanov and Tartaras, 2002; Zhdanov and Chernyavskiy, 2004). Avoiding such approximations, various 3-D inversion softwares were introduced recently (e.g., Yang et al., 2014; McMillan et al., 2015; Fournier et al., 2017). While more complete in their modeling of the physics of AEM, they too cannot be used for a large-scale airborne survey

In order to overcome these difficulties, Cox and Zhdanov (2007, 2008) and Cox et al. (2010, 2012) applied the moving sensitivity domain (MSD) approach to 3-D inversion of airborne electromagnetic data, similar to one discussed above in Chapter 15 for the marine towed streamer EM surveys. The use of a moving sensitivity domain allows for the inversion only of those parts of the model within the sensitivity domain of a particular transmitter-receiver pair. As the sensitivity domains of all the transmitter-receiver pairs superimpose themselves on the same 3-D model, the sensitivity matrix is constructed. This approach finally makes 3-D inversion of AEM data a practical consideration. The MSD approach is outlined in this chapter as well.

16.1 FREQUENCY DOMAIN AIRBORNE SURVEYS

The concept of airborne electromagnetic surveying is straightforward. The objective is to carry out electromagnetic profiling rapidly, especially in areas where access on the ground is difficult. This can be accomplished by mounting part or all of one of the standard electromagnetic profiling systems on an airborne platform.

Construction of a practical airborne electromagnetic system presents more difficult technical problems than are met with a counterpart surface based system for several reasons:

- 1) *Sensitivity:* When an electromagnetic coupling system is mounted on an aircraft, it is further removed from the conductive targets which are the objects of exploration than in the case of surface-based surveys. In such circumstances, the signals scattered from conductors in the earth will be quite weak compared to the field that arrives directly at the receiver from the source. It is necessary to detect the electromagnetic field with great precision, because the ratio of the scattered field to the primary field is on the order of a few tens of parts per million.
- 2) *Noise:* In addition to the ambient electromagnetic noise which always limits the capabilities of a field system, in airborne operations, there are additional noise sources. Noise is generated by the erratic movement of the induction receiver through the earth's magnetic field. Noise is also generated by induction from the source in the metal parts of the aircraft, particularly those which move, particularly the control surfaces. Noise is generated by relative motions between the transmitter and the receiver, and it is generated by the electrical systems on board the aircraft. All of these are largely random noise sources, but the approach of stacking repeated transmissions in order to improve the signal-to-noise ratio, as is done in many surface-based measurements, is far more difficult to accomplish in an airborne system, because by the time normal stacking would be completed, the platform has moved a significant distance.
- 3) *Navigation:* The location of the aircraft must be known precisely. For one reason, when an anomalous response from the earth is detected, often its position must be known within a few meters in order that a ground crew can go back to identify the target on the surface of the earth. For another reason, if an aircraft wanders from its intended straight-line course or if it changes altitude along a profile by even minor amounts, the spatial character of the coupling is distorted. Fortunately, the

FIGURE 16.1

Helicopter carrying frequency domain airborne electromagnetic system. Image courtesy of CGG Multi-Physics.

modern global positioning system (GPS) makes it possible to provide a very accurate position of the aircraft.

A typical frequency-domain airborne EM survey is based on the same principles as a ground EM survey. Several transmitter and receiver coils are housed in a "bird" towed behind a platform such as a helicopter (e.g., Fig. 16.1) or an airplane. The platform flies over the survey area towing this bird and continuously transmits an electromagnetic field with specific frequencies excited by transmitter coils. The EM field propagates into the ground and reaches some geoelectrical target such as an ore body. The electric currents induced in the ground and within the anomalous body generate a secondary electromagnetic field. The receiver coils measure the total EM field (a superposition of the primary field generated by the transmitter and the secondary EM field) at the bird's location. The goal of the survey is to find the location and electrical parameters of the underground geoelectrical formations. Note that the typical airborne EM system has several transmitter-receiver pairs. For example, typical AEM systems have transmitter-receiver pairs forming coplanar arrays, where both the transmitter and receiver coils of which can transmit/measure the vertical components of the EM field only, and coaxial arrays, with the transmitter and receiver coils transmitting/measuring the horizontal components of the EM field only. For example, the DIGHEM (Digital Helicopter EM) system (Fig. 16.2) has five transmitter-receiver pairs, three of which form a coplanar array with the transmitter and receiver coils transmitting/measuring only the vertical components of the EM field, and two coils forming a coaxial array with the transmitter and receiver coils transmitting/measuring only the horizontal components of the field. It is often said that coplanar array is sensitive to the horizontally layered structure and useful for resistivity mapping, while the coaxial array is sensitive to vertical structures such as dikes or intrusions.

In the frequency domain EM method, the observed magnetic field is described by a complex number. The real part of the EM field is often called the "in-phase" component, which means the phase of the measured EM field is the same as the phase of the primary EM field that is sent out by the
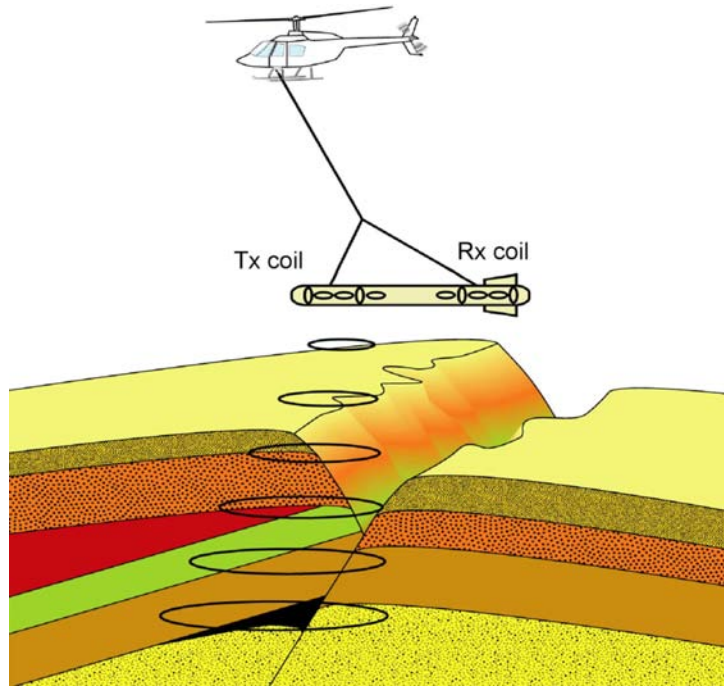
A typical airborne EM system has several transmitter-receiver pairs. For example, the DIGHEM system has five transmitter-receiver pairs, three of which form a coplanar array with the transmitter and receiver coils transmitting/measuring only the vertical components of the EM field, and two coils forming a co-axial array with the transmitter and receiver coils transmitting/measuring only the horizontal components of the field.

source. The imaginary part of the EM field is called the "quadrature" component, which means the phase of the measured field is 90 degrees ahead/behind the phase of the transmitted field. Usually these EM fields are normalized by the free-space EM field value and represented in ppm (parts per million) units (10^{-6}). The free-space EM field value is measured at the end of each survey line by flying high enough to avoid the effect of the ground. During the survey, the location of the sensors (or platform) can be determined by a video camera installed in the platform or global positioning system (GPS). This GPS technology dramatically improves the accuracy of the position and increases the application of the airborne EM method. This is another reason why the application of airborne geophysical surveys has increased recently.

16.2 TIME DOMAIN AIRBORNE SURVEYS

The problem in achieving adequate sensitivity in an AEM system is that of detecting very small secondary fields from the earth in the presence of a larger primary field. This problem can be largely

avoided by using a pulsed primary field and by measuring the transient secondary field from the earth while the primary field is zero.

While our most serious problem in making airborne measurements is eliminated by using transient response measurements, other problems become more severe and new problems arise. In most cases, only a small part of the energy in the secondary field remains after the end of the energizing pulse. As a consequence, an intense primary field must be used in order to obtain a measurable signal. Also, because the receiving system must be wide band rather than tuned to a single frequency, all forms of noise become more difficult to deal with.

A typical ATEM system uses an alternating polarity half-sine or square-wave pulses to energize the source. A large, vertical-axis transmitter loop is stretched wing tips to tail around the aircraft (Fig. 16.3). A horizontal-axis coil with its axis aligned with the flight direction is towed in a bird at the end of a long cable, 100 m behind and 65 m below the aircraft. The purpose in using such a long cable to tow the bird is to remove the receiving coil as far as possible from noise sources in the aircraft, and to permit the aircraft to fly at safer heights.

The primary field is blocked from reaching the receiver amplifiers during the time the transmitter is being energized (Fig. 16.4). The secondary field present at the receiver during the transmitter-off cycle is sampled at six (or more) times following the turnoff of transmitter power. Each sample is the average of the transient voltage over some short time interval, or *window*. The length of the excitation pulse is typically a few milliseconds, with the off cycle persisting for a slightly longer time. The times of the windows are selected so that the earliest will be somewhat responsive to poor conductors, including conductive overburden. Other channels are centered on a geometric progression of times, so that the late channels will sense only conductors having a large value for the response parameter.

Because the coil configurations are much the same, the shapes of the anomaly curves obtained with the ATEM systems are similar to the shapes of the anomaly curves obtained with the dual-frequency
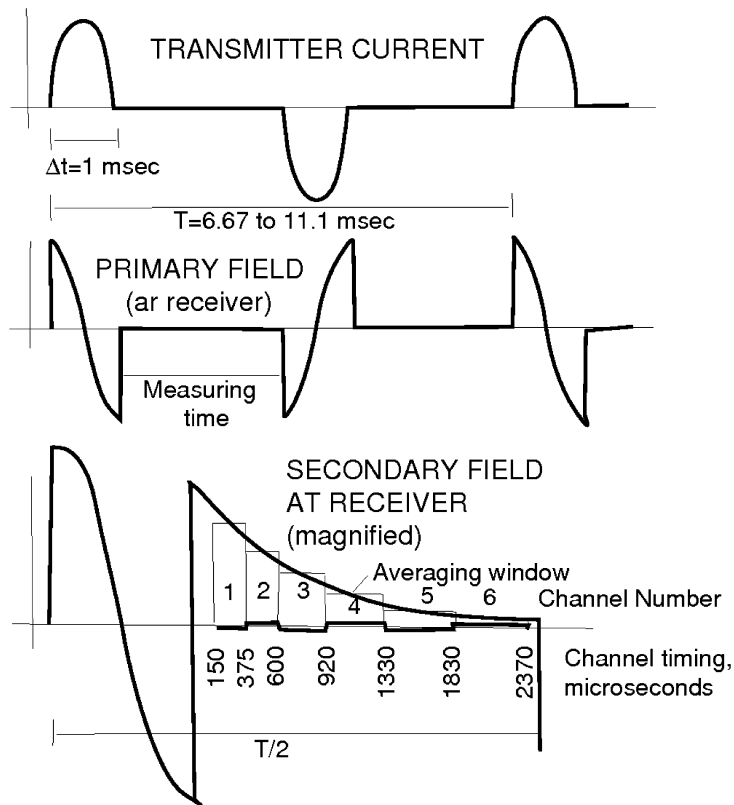
FIGURE 16.4

Description of the operation of the ATEM airborne electromagnetic system. A transmitter coil is energized with separated half-sinusoidal current pulses. These generate a primary field in the form of half-cosinusoids at a receiver coil towed behind the aircraft. The secondary signal caused by induction in the earth is a transient waveform which appears during the transmitter-off period. This secondary signal is sampled over six boxcars, as indicated.

phase-shift system. Precise predictions of shape and amplitude of ATEM anomalies can be determined from model studies in which airborne circuitry is simulated or by calculation from frequency-domain responses.

Mostly, ATEM surveys are used in exploration for massively conductive ore bodies, particularly when they are present in a shield terrain having very low host conductivity. Other applications can also be made if there is a significant contrast in conductivities between the host and target. An interesting application is reported by Zollinger et al. (1987) in measuring ocean depth in shallow water. Any of the ATEM systems described above should be capable of producing information from which ocean depths can be estimated up to some tens of meters.

16.3 3-D MODELING AND INVERSION OF AIRBORNE EM DATA

The airborne platform represents a very powerful tool for surveying large areas rapidly and relatively inexpensively. Surveys may cover thousands of line kilometers with multicomponent and multifrequency soundings every few meters. This enables collecting a huge amount of data about the electrical properties of the earth. However, interpreting the massive amounts of data gathered poses a significant challenge. Any 3-D inversion must discretize the earth into thousands of cells representing the conductivity distribution. Computationally, this problem is exacerbated by the fact that, for each sounding point and channel, a new electric field is introduced into the earth. This requires solving a large number of equations simultaneously for a full rigorous inversion.

Due to these fundamental difficulties with 3-D modeling and inversion, the practical interpretation of the AEM data was based on a simple one-dimensional (1-D) model of a layered earth (e.g., Chen and Raiche, 1998; Farquharson et al., 2003) or on simple conductivity-depth transforms (e.g., Macnae et al., 1998) similar to S-inversion discussed in Chapter 14. However, the one-dimensional models do not take into account the true three dimensional nature of the subsurface. As shown by Ellis (1998), even when the predicted 1-D model response is within a few percent of the observed data, the resulting conductivity model may be a poor approximation of the true model.

To overcome these difficulties, Cox and Zhdanov (2006, 2007, 2008), Cox et al. (2010), and Zhdanov and Cox (2012) introduced the concept of 3-D AEM inversion with a moving sensitivity domain (MSD). According to this concept, one needs only to calculate the AEM responses and sensitivities for that part of the 3-D earth model that is within the AEM system's sensitivity domain for a particular transmitter receiver pair. These sensitivities are then superimposed for all transmitter-receiver pairs into a single, sparse sensitivity matrix for the entire 3-D earth model. This approach has resulted in a paradigm change for AEM data interpretation. It makes it possible on high-end workstations, to invert entire AEM surveys with no approximations into high resolution 3-D earth geoelectrical models.

As an illustration, Fig. 16.5 shows percent of total response as a function of distance and a homogeneous half-space resistivity. The frequency-domain system resolution is limited to a few hundred meters even in a resistive background. The resolution of the time-domain system is usually considerably larger.

The percent of total response (as calculated from integrated sensitivities) is a function of a sensitivity domain (footprint) size for different background (e.g., homogeneous half space) resistivities.

These sensitivity plots can be useful for estimating the maximum line spacing; i.e., for 3-D inversion, there should be overlap in the sensitivities from different lines. These sensitivity sizes also demonstrate how small the sensitivity domain of a single sounding is.

With a moving sensitivity domain, the Fréchet matrix can be constructed as a sparse matrix with memory and computational requirements reduced by several orders of magnitude. The number of nonzero elements in each row of the sensitivity matrix is just the number of elements within each sensitivity domain (in an order of hundreds or thousands) rather than the total number of elements in the domain (hundreds of thousands to millions).

Due to potentially large variations in the conductivities over the AEM survey areas, it is advantageous to allow data points and their MSDs to have different background conductivity structure.

Modeling of AEM data can be accomplished by any of the numerical methods discussed in Chapter 6. The AEM data in time domain can be obtained by either direct time-domain solutions or by Fourier transformation of frequency-domain solutions. The latter offers three distinct advantages. First,
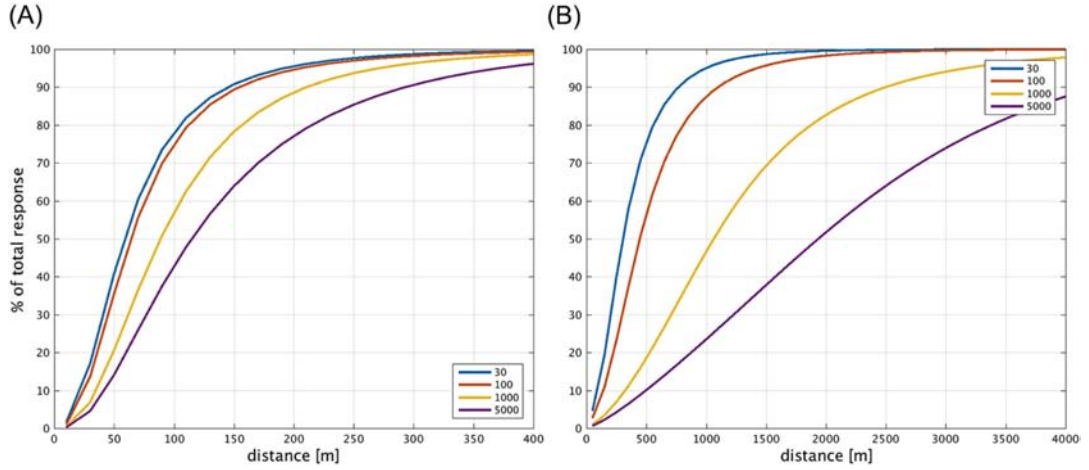
FIGURE 16.5

Percent of total response (as calculated from integrated sensitivities) as a function of footprint size for the different half-space resistivities for the (A) frequency-domain, and (B) time-domain systems. Note the 10× larger distance scale in the plot for the time-domain system.

the effects of frequency-dependent conductivity, such as induced polarization, can be modeled. Second, artificial dispersion effects that arise in direct time-domain solutions are avoided. Third, the matrix equations for multiple right-hand side source terms can be rapidly solved with iterative solutions. Thus, in the framework of this approach, one calculates the forward modeling response in the frequency domain, and in the case of time domain data, this response is then transformed to the time domain.

For example, in the forward modeling, one can use the integral equation (IE) method, with the EM field represented as a sum of the background, $\{\mathbf{E}^b, \mathbf{H}^b\}$, and anomalous, $\{\mathbf{E}^a, \mathbf{H}^a\}$, fields:

$$\mathbf{E} = \mathbf{E}^b + \mathbf{E}^a, \quad \mathbf{H} = \mathbf{H}^b + \mathbf{H}^a, \tag{16.1}$$

where the background field is a field generated by the given sources in the model with a background distribution of conductivity σ_b, and the anomalous field is produced by the anomalous conductivity distribution $\Delta\sigma(\mathbf{r}), \mathbf{r} \in D_a \subset R^3$.

Then, the electric and magnetic fields can be obtained by the following integral equations:

$$\mathbf{E}(\mathbf{r}') - \mathbf{E}^b(\mathbf{r}') = $$
$$\iiint_{D_a} \mathbf{G}_E(\mathbf{r}', \mathbf{r}) \Delta\sigma \mathbf{E}(\mathbf{r}) \, d\mathbf{v} = \mathbf{G}_E^{D_a}(\Delta\sigma \mathbf{E}), \tag{16.2}$$

$$\mathbf{H}(\mathbf{r}') - \mathbf{H}^b(\mathbf{r}') = $$
$$\iiint_{D_a} \mathbf{G}_H(\mathbf{r}', \mathbf{r}) \Delta\sigma \mathbf{E}(\mathbf{r}) \, d\mathbf{v} = \mathbf{G}_H^{D_a}(\Delta\sigma \mathbf{E}), \tag{16.3}$$

where $\mathbf{G}_E$ and $\mathbf{G}_H$ are the electric and magnetic Green's tensors for a layered model with conductivity σ_n.

In Eqs. (16.2) and (16.3), the symbols $\boldsymbol{G}_E^{D_a}$ and $\boldsymbol{G}_H^{D_a}$ denote the electric and magnetic Green's operators with a volume integration of D_a, respectively.

The process of solving the forward electromagnetic problem according to Eqs. (16.2) and (16.3) consists of two parts. First, it is necessary to find the electric fields inside domain D_a (where $\Delta\sigma_a \neq 0$), which requires the solution of an integral equation (*domain equation*) (16.2) for $\boldsymbol{r}' \in D_a$. Second, using the *data equations*, (16.2) and (16.3), with $\boldsymbol{r}' \in P$, we calculate the magnetic field in the receiver's domain P (see Chapter 6, Section 6.1).

The inversion of the AEM data is an ill-posed problem; i.e., solutions are nonunique and unstable. It was demonstrated in Chapter 7 that, the regularization must be introduced so as to obtain a unique and stable solution, by minimization of the Tikhonov parametric functional, $P^\alpha(\boldsymbol{\sigma})$:

$$P^\alpha(\boldsymbol{\sigma}) = \phi(\boldsymbol{\sigma})^2 + \alpha\|\boldsymbol{\sigma} - \boldsymbol{\sigma}_{apr}\|^2 \to \ \min , \tag{16.4}$$

where A is the nonlinear forward operator, $\boldsymbol{\sigma}$ is the N_m length vector of conductivities, $\mathbf{d}$ is the N_d length vector of observed data, $\boldsymbol{\sigma}_{apr}$ is the N_m length vector of the a priori conductivities, and $\| \ldots \|$ denotes the respective Euclidean norm. Data and model weights can be introduced to Eq. (16.4) through data and model weighting matrices, $\mathbf{W}_d$ and $\mathbf{W}_m$, respectively. The first term of Eq. (16.4) describes the misfit functional (or residual errors) between the predicted and observed AEM data.

$$\phi(\boldsymbol{\sigma}) = ||\mathbf{W}_d(\mathbf{d}_{pred} - \mathbf{d}_{obs})||^2. \tag{16.5}$$

The general principles of selecting the data weights were discussed in Chapter 7. In a case of the airborne survey, one can select data weighting matrix, $\mathbf{W}_d$, as a diagonal matrix with the diagonal elements equal to:

$$w_d = \frac{1}{\epsilon}, \tag{16.6}$$

where ϵ is a vector of the estimated errors in each data point. The error in each data point is estimated as

$$\epsilon = |d_{obs}\frac{\epsilon_{per}}{100}| + \epsilon_{abs} \tag{16.7}$$

where ϵ_{per} is the estimated error in each data point in percent, and ϵ_{abs} is the estimated absolute error in data units. This method normalizes the importance of all data channels with respect to their uncertainty. Hence, data points of large magnitude are not made overly important, yet small magnitude noisy data are not fitted to tight tolerances.

The second term of Eq. (16.4) describes the stabilizing functional. The choice of a stabilizer determines the class of the solutions from which a model is sought, and needs not be restricted to the so-called "smooth" stabilizers only; the regularization parameter, α, provides a balance (or bias) between the misfit and stabilizing functionals (see Chapter 7).

The parametric functional is usually minimized iteratively, with either the steepest descent or conjugate gradient method, using a two-level minimization approach. After each forward modeling update (higher level iteration), one can perform a number of conductivity model updates using the same Fréchet derivative, until a threshold of difference between the current conductivity and the conductivity used in the previous modeling step is reached. This may triggers another forward modeling update.

16.4 GROUND-BASED TRANSMITTER AND NATURAL EM FIELD AIRBORNE SURVEYS

All of the AEM methods discussed above make use of mobile transmitters mounted on board an aircraft. An AEM system can be simplified to some extent if a ground-based transmitter or natural fields are used. One of these systems (far field AEM method) is based on detection of signals transmitted from radio stations that operate at a low enough frequency to be of interest in exploration. Another recently introduced airborne system is based on measuring the vertical component of the natural magnetic field over the entire survey area from the airborne platform, while the variations of horizontal fields are recorded at a ground-based reference station (z-axis tipper electromagnetic method or ZTEM; Legault et al., 2012). We will discuss these two systems below.

16.4.1 FAR FIELD AEM METHODS

A number of systems are in use based on detection of signals transmitted from radio stations that operate at a low enough frequency to be of interest in exploration.

Most radio stations operate at broadcast band radio frequencies, between 640 and 1400 kHz. At these frequencies, penetration of the field into the earth is usually so limited as to give no information beyond the properties of the soil and weathered layer. Fields from power distribution systems which operate at 50 and 60 Hz, along with some odd harmonics, would be capable of providing information from considerable depths. Unfortunately, power line systems are so highly reticulated that the field seen from them appears to come from a vast number of sources, each characterized by its own distance. Hence, such ambient sources can be used in practice only when measurements can be made close to a single line. For larger-scale surveys, the use of power line energy is difficult. Fortunately, one class of radio station, the long-range stations, operate in a frequency range which is of use in geophysical applications and for which a small number of stations, each identifiable by its operating frequency.

The propagation of long wave length radio waves has been of great importance in long-range communication since the early days of the 20th century. At short distances from a transmitting antenna, the received signal is chiefly energy which travels along the earth's surface. At very low frequencies (VLF) in the range from 0 to 30 kHz, the strength of the radiated field is almost inversely proportional to distance. At greater distances, the intensity falls at a faster rate because of losses of energy by induction in the ground and because of the curvature of the earth. These losses increase with frequency. Fig. 16.6 shows field strength as a function of distance from a short vertical antenna radiating 1 kilowatt of power over a spherical earth with a conductivity of .005 S/m and a dielectric relative permittivity of 15. Fig. 16.7 shows similar curves for propagation of a ground wave over the oceans, with a conductivity of 5 S/m and a relative permittivity of 80. At distances beyond 3000 kilometers, ground-wave propagation provides the most effective means for radio communication.

The curves shown in these last two illustrations were computed for the fundamental mode of a wave guide formed between the earth and the ionosphere. Watt (1967) gives an approximate expression for computing electric field strength in the far field when only the normal mode of propagation need be considered:

$$E_z = 44.3 + 10 \log P - 10 \log f - 20 \log h_i - 10 \log \left[a \sin \frac{r}{a} \right] - \alpha r - 0.5, \qquad (16.8)$$
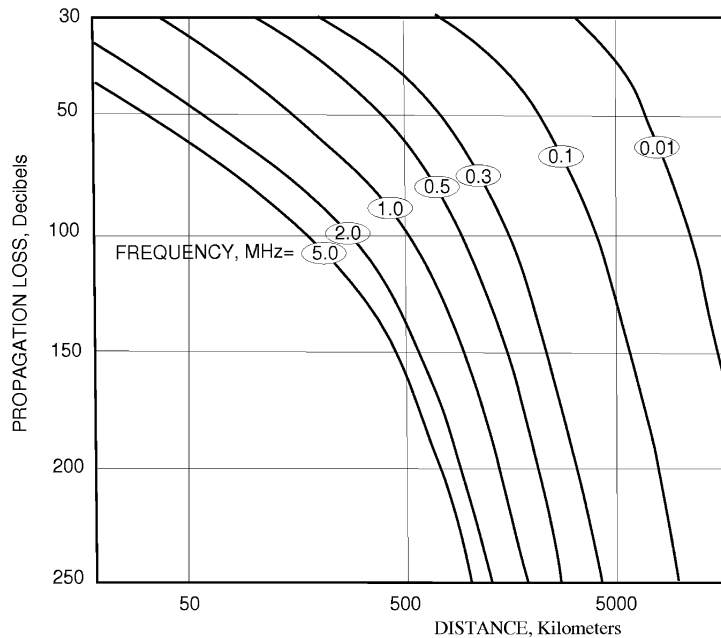
FIGURE 16.6

Propagation loss for electromagnetic surface waves traveling over a smooth spherical earth. Assumed conductivity of 0.005 S/m and relative dielectric constant of 15. Energy is radiated from a short vertical antenna. Power radiated is 1 kilowatt which produces a field strength of 300 millivolts per meter at 1 kilometer from the antenna.

where E_z is the vertical electric field in db below 1 mV/m, P is the radiated power in kw, f is frequency in kHz, h_i is the effective height of the ionosphere in km, a is the radius of the earth in Mm, r is the distance from the transmitter, in Mm, and α is the power lost to the earth and the ionosphere. Fig. 16.8 (McNeill and Labson, 1991) shows ground-wave decay curves for travel paths over the ocean in the VLF frequency range of interest to geophysicists.

$$H_\phi = E_z - 51.5. \tag{16.9}$$

Fig. 16.9 shows the locations of 11 major VLF transmitters. These stations make use of horizontal, or *Beverage*, antennas of great length, center fed, to achieve a high radiated power. As such, they can be treated in the same way as a grounded-wire antenna used for TDEM surveys, described in Chapter 14.

Instrumentation to make use of the fields caused by VLF radio stations is relatively simple. The field is detected with a magnetic sensor, consisting of a solenoid wrapped on a ferrite core. Because the strength of the signal can vary with time for many reasons, including variations in transmitter power and changes in the height to the ionosphere along the propagation path there is a need for self referencing the field strength at the receiver. One way in which this is done is to use two receiving
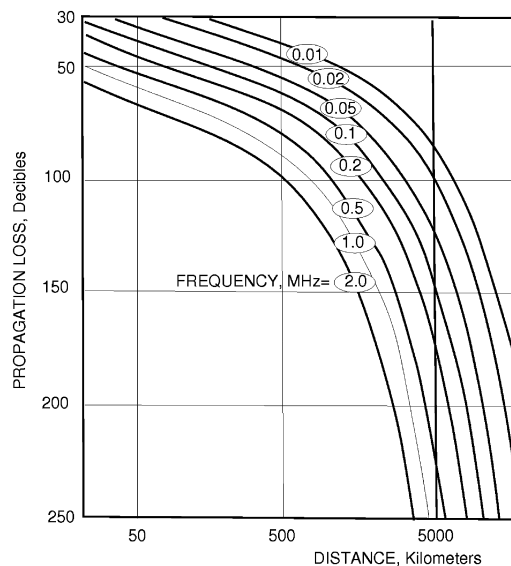
FIGURE 16.7

Propagation loss for electromagnetic surface waves traveling over a smooth spherical surface. Conductivity is assumed to be 5 S/m and the relative dielectric constant is 80. The source is short vertical antenna. Power radiated is 1 kilowatt, causing an electric field of 300 millivolts per meter at a distance of 1 kilometer.
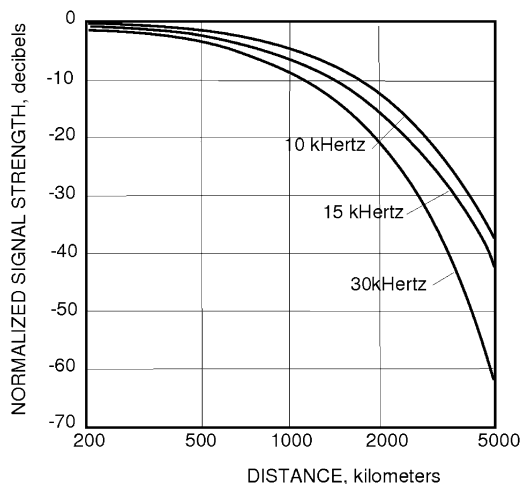
FIGURE 16.8

Decay of the ground wave for VLF (very low frequency) transmitters operating in the range from 10 to 30 kilohertz (McNeill and Labson, 1991).
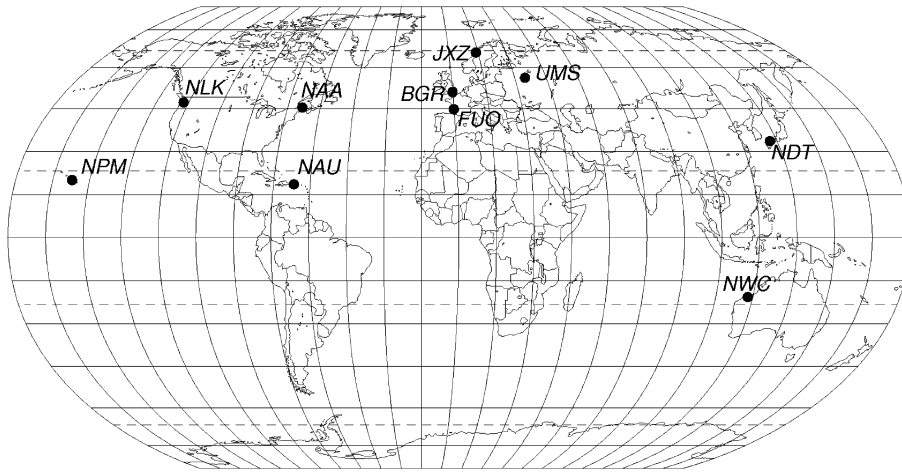
FIGURE 16.9

Locations of major VLF transmitters.

antennas, one oriented vertically and the other either in line with the transmitting antenna or tangential to this direction. The ratio of these two components of the magnetic field provides one measure of the spatially varying response from the earth, and the phase difference between the two gives another measure.

Numerous charts showing the response of the field to various geoelectrical structures have been published by McNeill and Labson (1991).

16.4.2 ZTEM METHOD

It has long been recognized that magnetovariational (MV) data, being the ratio of the localized vertical magnetic field to the orthogonal horizontal magnetic fields, can provide information about the 3D (three-dimensional) conductivity distribution in the earth (e.g., Berdichevsky and Zhdanov, 1984). The basic reasoning is that the vertical magnetic field is zero for plane waves vertically propagating into a 1D (one-dimensional) earth. Nonzero vertical magnetic fields are thus directly related to 2D or 3D structures. This reasoning served as the basis for the original development of the audio-frequency magnetic (AFMAG) method (Ward, 1959) whereby two orthogonal coils were towed behind an airborne platform to determine the tilt angle of the plane of polarization of natural magnetic fields. The natural magnetic fields of interest originate from atmospheric thunderstorm activity and propagate over large distances with little attenuation in the earth-ionosphere waveguide. These fields propagate vertically into the earth as per magnetotelluric (MT) fields. The tilt angle is zero over a 1D earth, and hence the AFMAG method was effective when crossing conductors. However, the direction and amplitude of the natural magnetic fields randomly vary with time, meaning AFMAG data were not repeatable (Ward, 1959). By using MT processing techniques for ground-based orthogonal horizontal magnetic
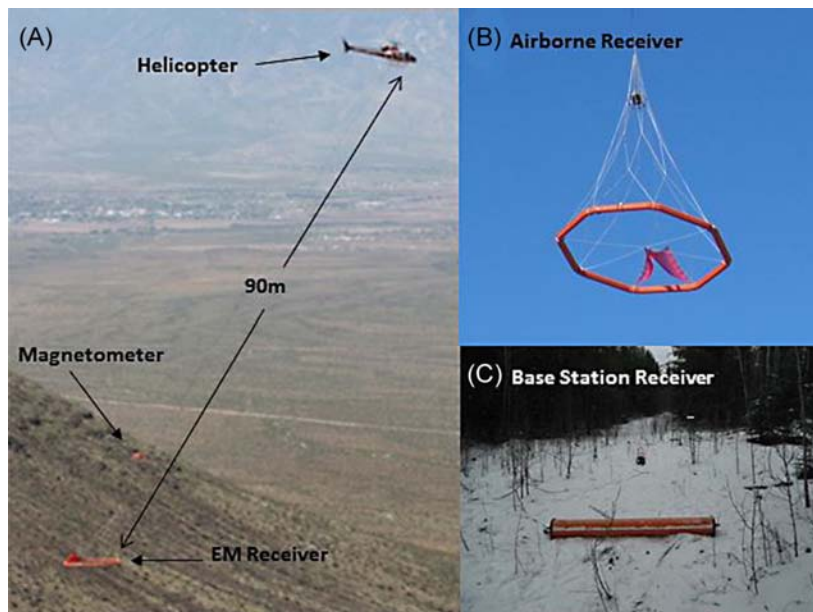
FIGURE 16.10

The z-axis tipper electromagnetic (ZTEM) system measures the fields of natural audio-frequency sources using an airborne vertical magnetic field receiver and a pair of horizontal, magnetic field ground receivers at a base station.

field measurement, Labson et al. (1985) demonstrated that repeatable tipper data could be recovered from measured magnetic fields.

The AFMAG method remained largely undeveloped until the commercialization of the Z-axis Tipper Electromagnetic (ZTEM) airborne system by Geotech (Legault et al., 2012). The z-axis tipper electromagnetic (ZTEM) system measures the fields of natural audio-frequency sources using an airborne vertical magnetic field receiver and a pair of horizontal, magnetic field ground receivers at a base station (Fig. 16.10). In the framework of the ZTEM method, the receiver is flown via helicopter, meaning data can be rapidly acquired over large survey areas for relatively low cost compared to equivalent ground surveys. The time series of the magnetic fields are recorded at fixed sampling rates, and the data are binned and processed to generate in-phase and quadrature transfer functions (i.e., tippers) in the frequency domain as per Labson et al. (1985). The lowest frequency of the tipper depends on the speed of the helicopter, and the highest frequency depends on the sampling rate. Tippers are typically obtained at five frequencies from 30 Hz to 360 Hz, giving skin depths ranging between 600 m and 2000 m for terrain conductivities typically encountered in ZTEM surveys.

Theoretical principles of ZTEM method are very similar to magnetovariational (MV) method (see Chapter 13). The following relationship between magnetic field components holds true (Berdichevsky

and Zhdanov, 1984):

$$H_z = W_{zx} H_x + W_{zy} H_y. \tag{16.10}$$

This relationship is called the *Weiss-Parkinson relationship*. It reflects the fact that the vertical component of the magnetic field H_z at every point is linearly related to the horizontal components of the same field. It was demonstrated by Berdichevsky and Zhdanov (1984) that the coefficients of the Weiss-Parkinson relationship depend on the coordinates of the observation point, the frequency, and the distribution of electrical conductivity in the medium only. The values W_{zx} and W_{zy} form a complex vector, named the *Weiss-Parkinson Vector*, or *induction vector*, or the *tipper*. In what follows, we use the commonly used term *tipper*.

The tipper, in contrast to the measured magnetic field, contains information about the internal geoelectrical structure of the earth independent of the magnetic field's source. The tipper components can be determined from the following system of equations:

$$H_z^{(1)} = W_{zx} H_x^{(1)} + W_{zy} H_y^{(1)}, \tag{16.11}$$
$$H_z^{(2)} = W_{zx} H_x^{(2)} + W_{zy} H_y^{(2)},$$

where upper indices (1) and (2) correspond to different polarizations of the plane wave external field.

Solving this system, we find:

$$W_{zx} = \frac{H_z^{(1)} H_y^{(2)} - H_z^{(2)} H_y^{(1)}}{H_x^{(1)} H_y^{(2)} - H_x^{(2)} H_y^{(1)}}, \quad W_{zy} = \frac{H_x^{(1)} H_z^{(2)} - H_x^{(2)} H_z^{(1)}}{H_x^{(1)} H_y^{(2)} - H_x^{(2)} H_y^{(1)}}. \tag{16.12}$$

The geophysical technique based on measuring the tipper and subsequently determining the conductivity distribution is called the *magnetovariational (MV) method*.

The vertical component of the magnetic field, H_z, can be measured from the air. Airborne surveys can cover large areas and collect data in an efficient manner. To be able to apply the MV method, one needs to know the values of the horizontal magnetic field components, H_x and H_y, at the same locations as the vertical component, H_z. Unfortunately, accurate airborne measurement of the horizontal components is technically challenging. However, it was shown by Berdichevsky and Zhdanov (1984), that magnetovariational transfer functions, similar to a conventional tipper, can be calculated using the measurements of the horizontal field components, H_{x0} and H_{y0}, at a fixed reference station only. Then

$$H_z = W_{zx}^{ZTEM} H_{x0} + W_{zy}^{ZTEM} H_{y0}. \tag{16.13}$$

Provided two measurements of the fields in two different polarizations, ZTEM tippers take the following form:

$$W_{zx}^{ZTEM} = \frac{H_z^{(1)} H_{y0}^{(2)} - H_z^{(2)} H_{y0}^{(1)}}{H_{x0}^{(1)} H_{y0}^{(2)} - H_{x0}^{(2)} H_{y0}^{(1)}}, \quad W_{zy}^{ZTEM} = \frac{H_{x0}^{(1)} H_z^{(2)} - H_{x0}^{(2)} H_z^{(1)}}{H_{x0}^{(1)} H_{y0}^{(2)} - H_{x0}^{(2)} H_{y0}^{(1)}}. \tag{16.14}$$

We can describe the ZTEM forward modeling problem by the operator equation:

$$\mathbf{d}^{ZTEM} = \mathbf{A}^{ZTEM}(\Delta\sigma), \tag{16.15}$$

where $\mathbf{d}^{ZTEM}$ stands for the data vector formed by the components of the ZTEM tipper, and $\mathbf{A}^{ZTEM}$ is the nonlinear forward operator encapsulating the governing equations of the ZTEM forward modeling problem. One can solve the 3-D forward modeling problem, using one of the numerical modeling method, discussed in Chapter 6.

The inverse problem described by Eq. (16.15) is ill posed, i.e., the solution is nonunique and unstable. As per MT and MV methods, we use Tikhonov regularization to solve this problem, based on minimization of the Tikhonov parametric functional:

$$P^{ZTEM}(\boldsymbol{\Delta\sigma}) = \phi^{ZTEM}(\boldsymbol{\Delta\sigma}) + \alpha S(\boldsymbol{\Delta\sigma}) = min, \quad (16.16)$$

where $\phi^{ZTEM}(\boldsymbol{\Delta\sigma}) = ||\mathbf{A}^{ZTEM}(\boldsymbol{\Delta\sigma}) - \mathbf{d}^{ZTEM}||_2^2$ is the misfit functional between the predicted data $A^{ZTEM}(\boldsymbol{\Delta\sigma})$ and the observed data $\mathbf{d}^{ZTEM}$, $s(\boldsymbol{\Delta\sigma})$ is a stabilizing functional, and α is the regularization parameter.

The common approach to minimization of the parametric functional (16.16) is based on gradient methods. For example, one can use the regularized conjugate-gradient (RCG) method with adaptive regularization (see Chapter 8). In order to restrict the variation of the anomalous conductivity within some reasonable bounds, it is convenient to use logarithmic model parameters, which contain the anomalous conductivities $\boldsymbol{\Delta\sigma}$ within the lower and upper bounds, $\boldsymbol{\Delta\sigma_i^-}$ and $\boldsymbol{\Delta\sigma_i^+}$, respectively. As we discussed in Chapter 7, the inversion allows for different stabilizers, requiring the solution to posses certain a priori physical properties. The most common choice is the minimum norm (MN) stabilizer, which favors the solutions with minimum changes from the a priori model, resulting in a smooth image of the conductivity distribution. In order to obtain a stable solution with sharp conductivity boundaries, we can apply a variety of focusing stabilizing functionals, including minimum-support (MS), minimum gradient-support (MGS), and minimum vertical-support (MVS) stabilizers (Zhdanov, 2002, 2015).

In order to use the RCG method for the minimization of the parametric functional (16.16), it is necessary to calculate the derivative of the data parameters with respect to the model parameters; i.e., the Fréchet derivatives, or sensitivities matrix of the ZTEM forward modeling operator, $\mathbf{A}^{ZTEM}(\boldsymbol{\Delta\sigma})$. To calculate the Fréchet derivative of the ZTEM tippers with respect to the anomalous conductivity, $\Delta\sigma$, we apply a variational operator to Eq. (16.14). For the W_{zx}^{ZTEM} component, we obtain:

$$\delta W_{zx}^{ZTEM} = \sum_{i=1,2} \left(\frac{\partial W_{zx}^{ZTEM}}{\partial H_z^{(i)}} F_{H_z^{(i)}}[\delta\Delta\sigma] + \sum_{\alpha=x,y} \frac{\partial W_{zx}^{ZTEM}}{\partial H_\alpha^{(i)}} F_{H_\alpha^{(i)}}[\delta\Delta\sigma] \right). \quad (16.17)$$

Here $i = 1, 2$ corresponds to different polarizations of the plane wave external field. The expressions for the partial derivatives of the tippers with respect to the field components, necessary for the computation of Eq. (16.17), take the following form:

$$\frac{\partial W_{zx}}{\partial H_x^{(1)}} = -\frac{H_y^{(2)} \left[H_z^{(1)} H_y^{(2)} - H_z^{(2)} H_y^{(1)} \right]}{\left[H_x^{(1)} H_y^{(2)} - H_x^{(2)} H_y^{(1)} \right]^2},$$

$$\frac{\partial W_{zx}}{\partial H_x^{(2)}} = \frac{H_y^{(1)} \left[H_z^{(1)} H_y^{(2)} - H_z^{(2)} H_y^{(1)} \right]}{\left[H_x^{(1)} H_y^{(2)} - H_x^{(2)} H_y^{(1)} \right]^2},$$

$$\frac{\partial W_{zx}}{\partial H_y^{(1)}} = \frac{H_y^{(2)}\left[H_x^{(2)}H_z^{(1)} - H_x^{(1)}H_z^{(2)}\right]}{\left[H_x^{(1)}H_y^{(2)} - H_x^{(2)}H_y^{(1)}\right]^2},$$

$$\frac{\partial W_{zx}}{\partial H_y^{(2)}} = \frac{H_y^{(1)}\left[H_x^{(1)}H_z^{(2)} - H_z^{(1)}H_x^{(2)}\right]}{\left[H_x^{(1)}H_y^{(2)} - H_x^{(2)}H_y^{(1)}\right]^2},$$

$$\frac{\partial W_{zx}}{\partial H_z^{(1)}} = \frac{H_y^{(2)}}{H_x^{(1)}H_y^{(2)} - H_x^{(2)}H_y^{(1)}},$$

$$\frac{\partial W_{zx}}{\partial H_z^{(2)}} = \frac{-H_y^{(1)}}{H_x^{(1)}H_y^{(2)} - H_x^{(2)}H_y^{(1)}}.$$

Eq. (16.17) contains the Fréchet derivatives $F_H^{(i)}$ of the field components themselves, which can be calculated in a similar manner, as was done in Chapter 13 for the case of inversion of MT impedances.

In summary, ZTEM presents a practical airborne electromagnetic method for mapping regional scale conductivity contrasts to depths in excess of 1 km. Interpretation of ZTEM data is analogous to magnetovariational (MV) data, and, in principle, similar to magnetotelluric (MT) data. As an airborne extension of the magnetovariational method, the ZTEM transfer functions contain information about the 3-D conductivity distribution within the earth.

REFERENCES AND RECOMMENDED READING TO CHAPTER 16

Becker, A., 1979, Airborne electromagnetic methods: *in* Hood, P. J., Ed., Geophysics and Geochemistry in the Search for Metallic Ores: Geol. Surv. of Canada Econ. Geol. Report, **31**, 33–43.

Berdichevsky, M. N., and M. S. Zhdanov, 1984, Advanced theory of deep geomagnetic sounding: Elsevier, Amsterdam.

Best, M. E., 1985, A systematic approach for evaluating electromagnetic systems: Geophysical Prospecting, **33**(4), 577–599.

Chen, J., and A. Raiche, 1998, Inverting AEM data using a damped eigenparameter method: Exploration Geophysics, **29** (2), 128–132.

Cook, J. C., 1975, Radar transparencies of mine and tunnel rocks: Geophysics, **40** (5), 865–877.

Corwin, R. F., and D. B. Hoover, 1979, The self-potential method in geothermal exploration: Geophysics, **44** (2), 226–235.

Cox, L. H., and M. S. Zhdanov, 2006, Rapid and rigorous 3-D inversion of airborne electromagnetic data: Proceedings of Annual Meeting of Consortium for Electromagnetic Modeling and Inversion, 103–120.

Cox, L. H., and M. S. Zhdanov, 2007, Large-scale 3-D inversion of HEM data using a moving footprint. 77th SEG Annual Meeting, San Antonio, Texas.

Cox, L. H., and M. S. Zhdanov, 2008, Advanced computational methods of rapid and rigorous 3-D inversion of airborne electromagnetic data: Communications in Computational Physics, **3** (1), 160–179.

Cox, L. H., G. A. Wilson, and M. S. Zhdanov, 2010, 3-D inversion of airborne electromagnetic data using a moving footprint. Exploration Geophysics, **41**, 250–259.

Cox, L. H., G. A. Wilson, and M. S. Zhdanov, 2012, 3D inversion of airborne electromagnetic data: Geophysics, **77** (4), WB59–WB69.

Daniels, J. J., 1983, Hole-to-surface resistivity measurements: Geophysics, **48** (1), 87–97.

DeMoully, G., and A. Becker, 1983, Automated interpretation of airborne electromagnetic data: Geophysics, **49** (8), 1301–1312.

Dyck, A. V., 1991, Drill-hole electromagnetic methods: *in* Nabighian, M. N., and J. D. Corbett, Eds., Electromagnetic methods in applied geophysics, Volume 2, Applications: Society of Exploration Geophysicists, Tulsa, Oklahoma, 881–930.

Edwards, R. N., 1988, Two-dimensional modeling of a towed in-line electric dipole-dipole sea-floor electromagnetic system: The optimum time delay or frequency for target resolution: Geophysics, **53**, (6), 846–853.

Edwards, R. N., and A. D. Chave, 1986, A transient electric dipole-dipole method for mapping the conductivity of the sea floor: Geophysics, **51** (4), 984–987.

Ellis, R. G., 1998. Inversion of airborne electromagnetic data: SEG Technical Program Expanded Abstracts, **17** (1), 2016–2019.

Farquharson, C. G., D. W. Oldenburg, and P. S. Routh, 2003, Simultaneous 1-D inversion of loop-loop electromagnetic data for magnetic susceptibility and electrical conductivity: Geophysics, **68** (6), 1857–1869.

Fitterman, D. V., 1990, Ed., Developments and Applications of Modern Airborne Electromagnetic Surveys: U. S. Geol. Survey Bulletin 1925, 216 pp.

Fisher, E., G. A. McMecham, A. P. Annan, and S. W. Cosway, 1992, Examples of reverse-time migration of single-channel, ground-penetrating radar profiles: Geophysics, **57** (4), 577–586.

Fountain, D., 1998, Airborne electromagnetic systems—50 years of development: Exploration Geophysics, **29**, 1–11.

Fournier, D., S. Kang, M. S. McMillan, and D. W. Oldenburg, 2017, Inversion of airborne geophysics over the DO-27/DO-18 kimberlites, Part II: Electromagnetics: Interpretation, 5.

Keating, P. B., and D. J. Crossley, 1990, The inversion of time-domain airborne electromagnetic data using the plate model: Geophysics, **55** (6), 705–711.

Labson, V. F., A. Becker, H. F. Morrison, and U. Conti, 1985, Geophysical exploration with audiofrequency natural magnetic fields: Geophysics, **50**, 656–664.

Legault, J., G. A. Wilson, A. V. Gribenko, M. S. Zhdanov, S. Zhao, and K. Fisk, 2012, An overview of the ZTEM and AirMt airborne electromagnetic systems: a case study from the Nebo–Babel Ni–Cu–PGE deposit, West Musgrave, Western Australia: Preview, 158, 26–32.

McMillan, M. S., C. Schwarzbach, E. Haber, and D. W. Oldenburg, 2015, 3D parametric hybrid inversion of time-domain airborne electromagnetic data: Geophysics, **80** (6), K25–K36.

Macnae, J., A. King, N. Stolz, A. Osmakoff, and A. Blaha, 1998, Fast AEM data processing and inversion: Exploration Geophysics, **29**, 163–169.

McNeill, J. D., and V. Labson, 1991, Geological mapping using VLF radio fields: *in* Nabighian, M. N., and J. D. Corbett, Eds., Electromagnetic methods in applied geophysics, Volume 2, Applications: Society of Exploration Geophysicists, Tulsa, Oklahoma, 521–640.

Palacky, G. F., and G. F. West, 1991, Airborne electromagnetic methods: *in* Nabighian, M. N., and J. D. Corbett, Eds., Electromagnetic methods in applied geophysics, Volume 2, Applications: Society of Exploration Geophysicists, Tulsa, Oklahoma, 811–880.

Raiche, A., D. Annetts, and F. Sugeng, 2001, EM target response in complex hosts: presented at ASEG 15th Geophysical Conference and Exhibition, Brisbane.

Sengpiel, K. P., and B. Siemon, 2000, Advanced inversion methods for airborne electromagnetic exploration: Geophysics **65** (6), 1983–1992.

Telford, W. M., L. P. Geldardt, and R. E. Sheriff, 1990. Applied Geophysics, 2nd ed.: Cambridge University Press, New York, 770 pp.

Watt, A. D., 1967, VLF Radio engineering: Pergamon Press, Oxford.

Ward, S. H., 1959, AFMAG-airborne and ground: Geophysics, **24** (4), 761–787.

Ward, S. H., 1980, Electrical, electromagnetic and magnetotelluric methods: Geophysics, **45** (11), 1659–1666.

Wolfgram, P. and H. Golden, 2001, Airborne EM applied to sulphide nickel – examples and analysis: Exploration Geophysics, **32**, 136–140.

Witherly, K., 2000, The quest for the Holy Grail in mining geophysics: A review of the development and application of airborne EM systems over the last 50 years: The Leading Edge, **19**, 270–274.

Yang, D., D. W. Oldenburg, and E. Haber, 2014, 3-D inversion of airborne electromagnetic data parallelized and accelerated by local mesh and adaptive soundings: Geophysical Journal International, **196**, 1492–1507.

Zollinger, R., H. F. Morrison, P. G. Lazenby, and A. Becker, 1987, Airborne electromagnetic bathymetry: Geophysics, **52** (8), 1127–1137.

Zhdanov, M. S., and A. Chernyavskiy, 2004, Rapid three-dimensional inversion of multi-transmitter electromagnetic data using the spectral Lanczos decomposition method: Inverse Problems, **20**, S233–S256.

Zhdanov, M. S., and L. H. Cox, 2012, Method of real time subsurface imaging using electromagnetic data acquired from moving platform: Patent No. US 9322910.

Zhdanov, M. S., 2002, Geophysical inverse theory and regularization problems: Elsevier, Amsterdam, London, New York, Tokyo, 628 pp.

Zhdanov, M. S., and Chernyavskiy, A., 2004, Rapid three-dimensional inversion of multi-transmitter electromagnetic data using the spectral Lanczos decomposition method: Inverse Problems, **20**, S233–S256.

Zhdanov, M. S., and G. W. Keller, 1994, The geoelectrical methods in geophysical exploration: Elsevier, Amsterdam, London, New York, Tokyo, 873 pp.

Zhdanov, M. S., and E. Tartaras, 2002, Inversion of multi-transmitter 3-D electromagnetic data based on the localized quasi-linear approximation: Geophysical Journal International, **148**, (3), 506–519.

CASE HISTORIES

CONTENTS

In the final chapter of the book, we present several case histories representing different applications of electromagnetic methods, from a regional scale to deposit scale. The first case history is related to a large-scale application of the magnetotelluric method in the framework of the EarthScope project. The second case history presents a crustal study based on the use of a powerful source of electromagnetic energy – a pulsed magneto-hydrodynamic (MHD) generator. The third and forth case histories illustrate the application of both land and airborne electromagnetic surveys for studying mineral deposits. The fifth case study provides an example of off-shore hydrocarbon exploration using a marine towed streamer EM system. Finally, we consider an example of a marine MT survey conducted in the Gulf of Mexico for mapping the salt structures.

17.1 TECTONIC STUDIES – EARTHSCOPE MT SURVEY IN THE NORTHWESTERN UNITED STATES

The deep geological structure of the northwestern United States and southwestern Canada has been extensively studied by seismologists during recent years with the deployment of the National Science Foundation (NSF) EarthScope project's USArray program, managed by the Incorporated Research Institutions for Seismology (IRIS), and regional seismic networks (e.g., Xue and Allen, 2007; Roth et al., 2008; Obrebski et al., 2010, 2011). One of the objectives of these studies was imaging the extent of the subducted Juan de Fuca plate in the mantle east of the Cascades beneath Oregon, and understanding the character of its interaction with the Yellowstone hotspot plume. It was shown in these publications that the subducting Juan de Fuca slab is expressed in the seismological models as a high-velocity anomaly which dips at approximately 46° to the east and extends down to a depth of about 400 km. For example, Obrebski et al. (2010, 2011) demonstrated that the subducting Juan de Fuca slab is clearly imaged by their P- and S-wave tomographic models, which also show a low-velocity anomaly associated with the Yellowstone hot spot. Xue and Allen (2007) suggested that the

absence of the slab below 400 km today is due to the arrival of the Yellowstone plume head about 17 Ma, which destroyed the Juan de Fuca slab at depths greater than the thickness of the continental lithosphere.

An important part of the EarthScope program is the EMScope project, which is the magnetotelluric (MT) component of the USArray program, managed by Oregon State University on behalf of IRIS. By the end of 2011, long-period MT data had been collected at 330 stations located in the following states: Oregon, Washington, Idaho, Wyoming, Montana, California, Nevada, Utah, and Colorado. Several research papers dedicated to interpretation of the EarthScope MT data collected over Washington, Oregon, Montana, and Idaho were published over several recent years (e.g., Patro and Egbert, 2008; Zhdanov et al., 2011b, 2012; Bedrosian and Feucht, 2013; Meqbel et al., 2013). Zhdanov et al. (2011b) and Čuma et al. (2017) presented one of the first 3D geoelectrical models of the upper mantle beneath Yellowstone based on the 3D inversion of EarthScope MT data from Montana, Idaho, and Wyoming. These images showed a highly conductive body associated with the tomographically imaged mantle plume-like layer of hot material emerging from the upper mantle toward the Yellowstone volcano. The conductive body identified in those images was west-dipping in a similar way to a P-wave low-velocity body (Smith et al., 2009). In the present chapter, as an example of a large-scale MT inversion, I present the results of the large-scale 3D MT inversion to EarthScope MT data collected over Oregon, Washington, Idaho, Wyoming, Montana, California, Nevada, Utah, and Colorado up to 2011.

Considering the extremely large scale of the inversion of the entire EarthScope MT data collected in nine states of the northwestern United States, one has to use a moving sensitivity domain (MSD) approach outlined in Chapter 16 as applied to airborne EM data. In the framework of the MSD approach, for a given MT station one computes and stores the sensitivity matrix (Fréchet derivative) inside the inversion cells within a predetermined horizontal distance from this station only, i.e., within a sensitivity domain. Thus, Fréchet derivatives for an MT station can be computed and stored only for regions much smaller than the entire inversion domain, resulting in dramatic reduction of the computer memory requirements. The sensitivity domain size is determined based on the rate of sensitivity attenuation of the MT data. As the sensitivity attenuates faster for higher frequencies, one can vary the sensitivity domain size with frequency, which provides optimal memory and computation use while retaining maximum accuracy. Note that, the MSD approach is applied for the Fréchet derivative calculation only and not for the computations of the predicted field. By using all of the cells in the forward modeling computations, one can ensure an accurate result for the calculations of the predicted MT field components and impedances in the receivers.

3D inversion was applied to the EarthScope MT data collected at 260 stations shown by black stars in the physiographic map of the northwestern United States (Fig. 17.1). The station coverage extends from ~123°W to ~105°W and from ~38°N to ~49°N. The inversion was applied to all four components of the impedance tensor for 16 periods logarithmically spaced between 10 s and 10,000 s. The considered range of periods corresponds to a depth of investigation down to ~500 km in a 100 Ohm-m host medium. The inversion domain was spanned in the X (geographic E-W), Y (geographic N-S), and Z (vertical downward) directions extending 1650 km, 1350 km, and 500 km, respectively. The sensitivity domain size for each station was determined as 450 km based on the rate of sensitivity attenuation of the MT data in a model of a 100 Ohm-m half space. The inversion domain contained 2,138,400 cells, and had an initial model of a 100 Ohm-m half space. The inversion was run until the L2 norm of the residuals between the observed and theoretically predicted MT data,
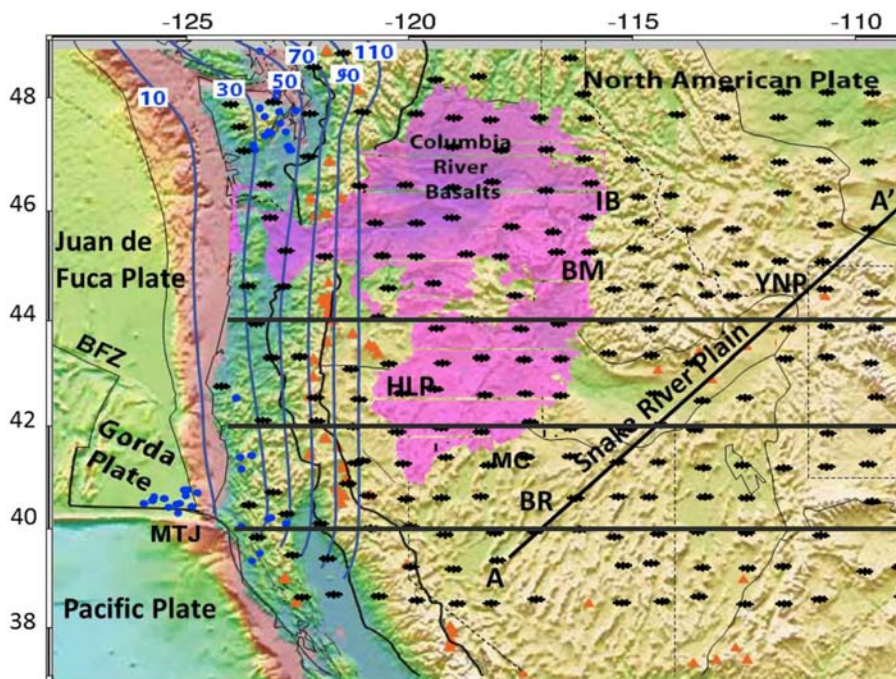
FIGURE 17.1

Physiographic map of the northwestern United States indicating primary geologic-tectonic features [modified from Obrebski et al., 2011]. BM = Blue Mountains; BFZ = Blanco Fracture Zone; BR = Basin and Range; CR = Coast Range; IB = Idaho Batholith; HLP = High Lava Plains; MTJ = Mendocino Triple Junction; YNP = Yellowstone National Park. The locations of 260 MT stations used in the inversion are shown by black stars.

normalized by the L2 norm of the observed data, had decreased to about 10%. For the model presented in this chapter, the discretization cells had a horizontal size of 10 km by 10 km, and a vertical size starting from 1 km at the surface and logarithmically increasing with depth.

The conductivity distribution as recovered by a 3D inversion of the EarthScope MT data reflects the regional lithological features of the northwestern United States. The inverse geoelectrical model correlates well with the seismic P- and S-velocity models obtained from inversion of body-wave travel times and surface-wave phase velocities (Obrebski et al., 2011). Fig. 17.1 shows major geologic-tectonic features of northwestern North America overlaid on topography and bathymetry (modified from Obrebski et al., 2010). They encompass the Cascadia subduction zone, including the descending Juan de Fuca and Gorda plates, which are the remnants of the convergent plate margin spanned over coastal western North America. According to modern geological and geophysical data, the Juan de Fuca plate is subducting beneath the North American plate. The estimated depth of the top of the subducting slab is shown with blue contours (labeled in km) in Fig. 17.1. The locations of all M > 4 earthquakes with depths >35 km since 1970 are shown as blue dots. Volcanoes are shown as orange triangles. The Snake River Plain traces the path of the North American plate over the Yellowstone hotspot, now centered
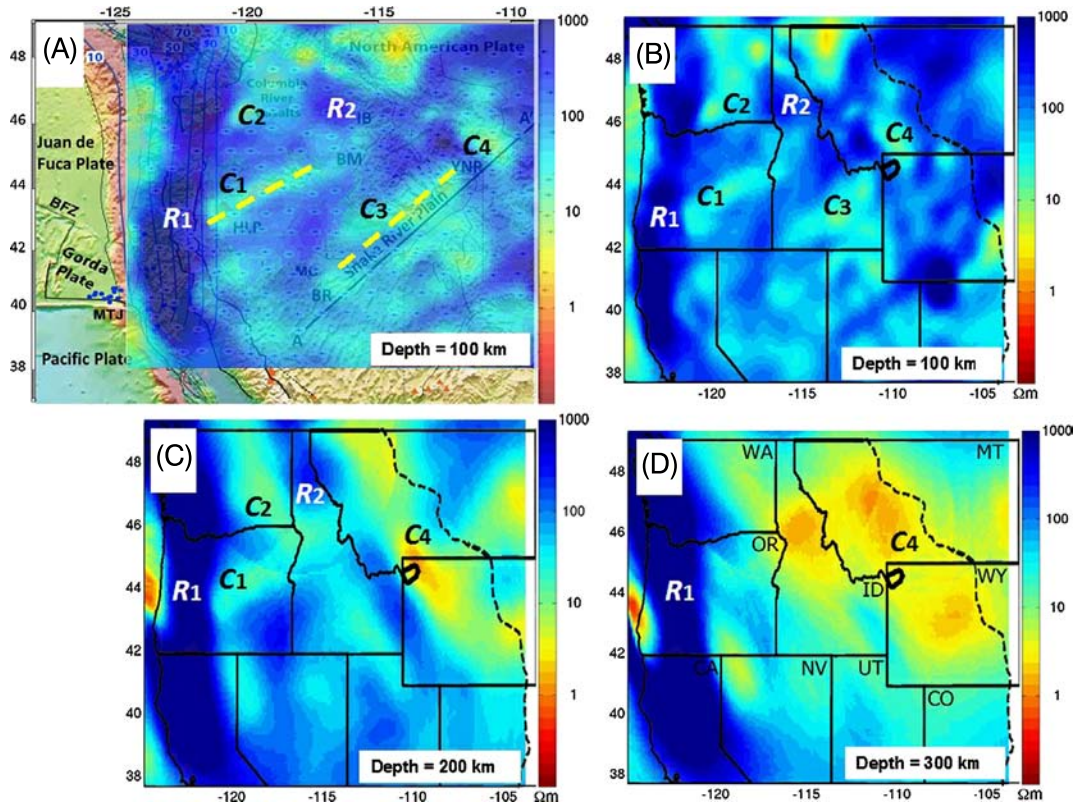
FIGURE 17.2

Panel A: horizontal section of the geoelectrical model at a depth of 100 km, overlapped with a map of the major tectonic features of the northwestern United States. Panels B, C, and D: horizontal sections of the geoelectrical model at depths of 100 km, 200 km, and 300 km, respectively.

in Yellowstone National Park (YNP). The Columbia River Flood Basalt Province represents a massive outpouring of basalt from ~16.6 to ~15.0 Ma and is shown in pink (Camp and Ross, 2004).

Fig. 17.2 presents horizontal sections of a geoelectrical model at depths of 100 km, 200 km, and 300 km (panels B, C, and D), respectively. Panel A of Fig. 17.2 shows a horizontal section at a depth of 100 km overlapped with a map of the major geologic-tectonic features of the Pacific Northwest of the United States, shown in Fig. 17.1. The subducting Juan de Fuca slab is clearly imaged in these horizontal sections. It is characterized by the zone of very high resistivity (≥1000 Ohm-m) shown by the dark blue vertical strip R1 in panels A, B, C, and D, which corresponds well to the known fact that the subducting oceanic lithosphere is very resistive (e.g., Wannamaker et al., 1989). We observe several conductive lineaments in the resistivity maps at 100 km depth. For example, conductive lineament C1 extends under the High Lava Plains to the NW toward the Blue Mountains (panels A and B). It can be associated with the northwestward propagating High Lava Plains volcanic lineament, and it
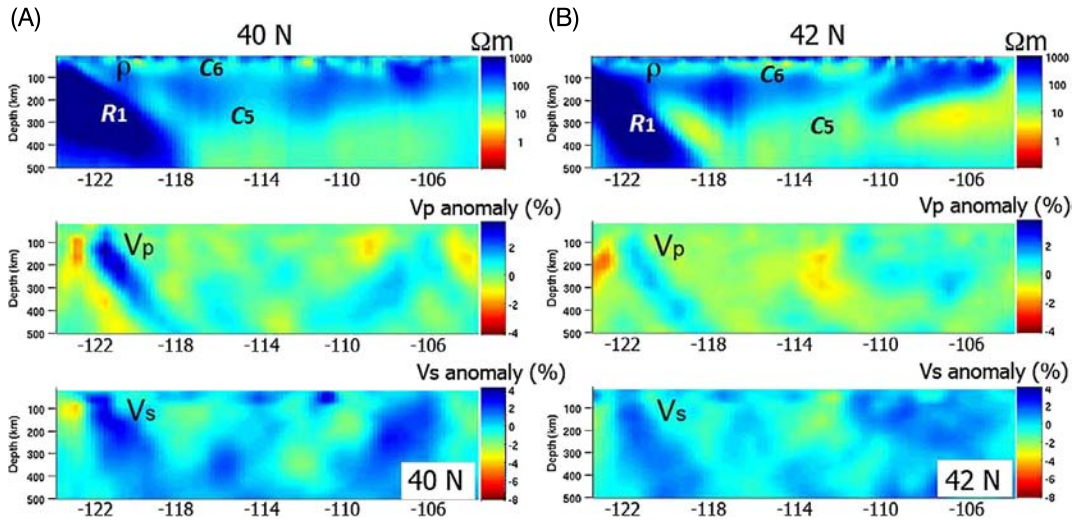
FIGURE 17.3

Comparisons of the MT inversion result with the DNA09 seismic tomography model of Obrebski et al. (2011). The MT inversion result is presented as the vertical resistivity sections. Vp and Vs seismic velocities are shown as deviations from the mean value in percent. We present the vertical sections of the geoelectrical model and the P-wave and S-wave velocity models for the profiles, proceeding along the lines at latitude 40°N (panel A) and 42°N (panel B), respectively.

corresponds to the reduced velocity zone (RVZ) beneath the Newberry region, identified by Roth et al. (2008) from high-resolution, 3D P-wave tomography. Roth et al. (2008) explained the low-velocity anomaly beneath Newberry and the High Lava Plains by the presence of partially melted material due to the release of fluids from the downgoing slab. This partially melted material may also result in the decreased resistivity (∼5 Ohm-m), which is observed beneath the western side of the Blue Mountains. This hypothesis is supported by the geochemical characteristics of the Newberry basalts, which, according to Carlson et al. (2008) are strongly influenced by subducted slab-derived fluids. Another conductivity anomaly extends beneath the Columbia River basalts in south-central Washington (C2). This anomaly (∼5 Ohm-m) corresponds well to the reduced velocity zone identified by Roth et al. (2008) beneath the thick sections of the Columbia River basalts as related to the geothermal processes in the surrounding areas.

An important feature of the inverse geoelectrical model is conductive lineament C3 extending beneath Yellowstone – Snake River Plain (YSRP) (Fig. 17.3, panels A and B). This conductive structure corresponds well to the reduced velocity anomaly within the Precambrian lithosphere identified by both Roth et al. (2008) and Obrebski et al. (2010, 2011), and is characterized by high temperatures and low density. We observe also conductivity anomaly C4 rising from the mantle at a depth of ∼100–200 km beneath Yellowstone, associated with the Yellowstone conductive plume-like layer identified by Zhdanov et al. (2011b) using a subset of the EarthScope MT survey of 28 MT stations located over the area surrounding Yellowstone National Park. The highly conductive body is associated with
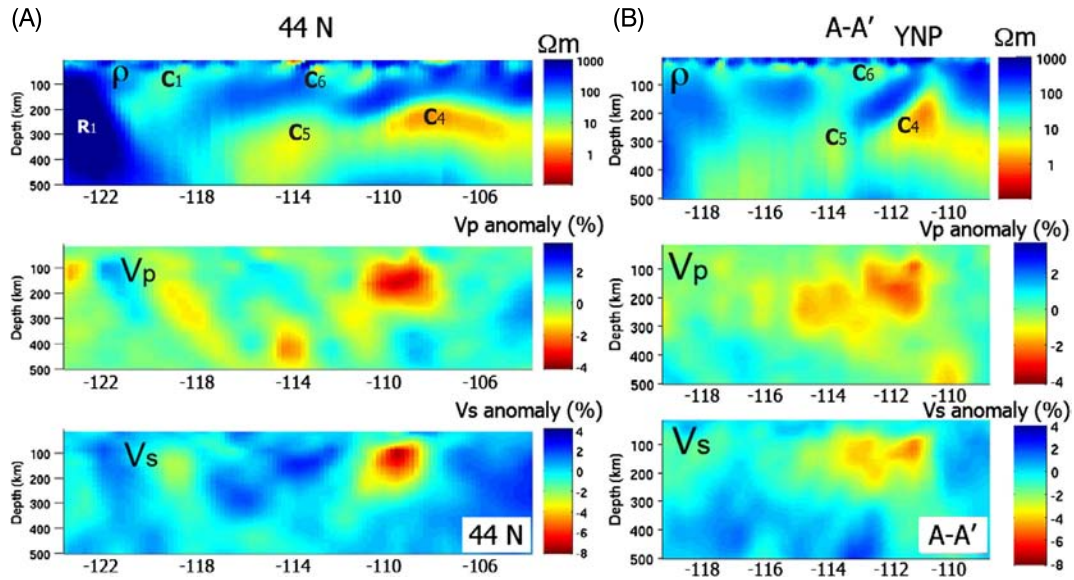
FIGURE 17.4

Comparisons of the MT inversion result with the DNA09 seismic tomography model of Obrebski et al. (2011) for the profile proceeding along the line at latitude 44°N (panel A), and for profile AA′ along the Snake River Plain (panel B).

the tomographically imaged mantle plume-like layer emerging from the upper mantle toward the Yellowstone volcano (e.g., Schutt and Dueker, 2008; Schutt et al., 2008; Schmandt and Humphreys, 2010; Yuan and Dueker, 2005; Waite et al., 2005; Smith et al., 2009).

Figs. 17.3 and 17.4 show comparisons of the MT inversion result with the DNA09 seismic tomography model of Obrebski et al. (2011). The MT inversion result is presented as the vertical resistivity sections along the lines at altitude 400 N, and 420 N, respectively. Vp and Vs seismic velocities are shown as deviations from the mean value in percent. The subducting Juan de Fuca slab is clearly imaged by the geoelectrical model as a high-resistivity anomaly (R1) dipping east under 450. It is manifested in the P- and S-wave tomographic models of Obrebski et al. (2010, 2011) as the high-velocity anomaly which dips east under a similar ~46°. We also can see the conductive zone of partially melted material directly above the subducting slab, which can be explained by the release of fluids from the down-going slab. Vertical resistivity sections of the geoelectrical model of the northwestern United States show large zones of moderate-to-high conductivity (~5–10 Ohm-m) below 100–200 km in the upper mantle, which represent the electrical properties of the conductive electrical asthenosphere (C5).

Fig. 17.4, panel B, presents vertical sections of the geoelectrical model and P-wave and S-wave velocity models for the profile AA′, proceeding along the Snake River Plain (see Fig. 17.1) over the traces of the path of the North American plate over the Yellowstone hotspot. The Yellowstone hot conductive layer is clearly imaged in the geoelectrical model as a low-resistivity (~1–5 Ohm-m) anomaly

(C4). It is also manifested in the P- and S-wave tomographic models of Obrebski et al. (2010, 2011) as the low velocity zone. The conductivity of the plume-like layer is higher in the relatively shallow part (~150 km) and decreases with the depth, diffusing below 300 km. This observation correlates well with the seismic models of Obrebski et al. (2010, 2011), which are characterized by the lower velocity anomaly at the shallow, elongated part of the plume-like layer extending to depths of about ~300 km. Both of these observations are consistent with the presence of partial melt, which decreases the seismic velocity and increases the electric conductivity. As was discussed in Zhdanov et al. (2011b), the low resistivity of the conductive structure (on an order of 1 to 5 Ohm-m) is comparable to the resistivity of silicate melts determined from laboratory experiments (Pommier et al., 2008), and it is explained by a combination of high temperature partial melt, and the presence of highly saline fluids present in magmatic processes. The low velocities and high conductivity layer initially dip slightly toward the northwest in the upper mantle, consistent with the northwest dip of the mantle plume-like layer seen in published images beneath Yellowstone (e.g., Smith et al., 2009; Zhdanov et al., 2011b).

17.2 CRUSTAL STUDIES – THE KHIBINI EXPERIMENT

In the development of modern EM methods capable of exploring the Earth to depths of many kilometers, the limit to the depths that can be reached is always imposed by the signal strength. For example, to double the depth that can be reached, one has to increase the strength of the source by about an order of magnitude. The source strength for an EM field is measured in terms of the source moment. Therefore an increase in source moment by an order of magnitude requires an increase in source power by two orders of magnitude. This can be achieved in several ways. The most direct approach is through the use of a transmitter of greater power. Another approach to increasing the strength of a signal is by repetitious transmissions of low power, with synchronous stacking of the signals at a single receiver site. With long-term robust stacking, the ratio of signal level to noise grows roughly as the square root of the number of transmissions. The energy expended in stacking increases in direct proportion to the number of transmissions.

Both of these approaches to increasing effective source moment have very real practical limits. Increasing the power available to energize a source requires the use of a primary energy source whose mass grows more or less directly with power capability, if only conventional generators are considered. So the maximum practical generator size and the longest stacking time that can be afforded should be taken into account when designing EM surveys. To achieve significantly greater depth of sounding requires a departure from the use of conventional EM sources.

An idea for the application of pulsed magneto-hydrodynamic (MHD) generators in EM surveying was originally introduced in the 1970s by Russian physicist Evgeny Pavlovich Velikhov (Velikhov et al., 1975). An MHD generator extracts energy from a stream of heated, ionized gas as it flows through a magnetic field. The primary energy source is a charge of solid fuel, not unlike rocket fuel, but with chemical additives, such as a potassium salt, to make the temperature of the burning plume of fuel hot enough to ionize to a significant degree. The ionized gas, or plasma, is directed through an electromagnet, which causes the cations and anions in the plasma to deflect in opposite directions. These ions then flow into a channel, where they are collected on plates connected to an external ground circuit. Initially, when the generator is first fired, the magnetic field is powered with batteries which

cause current to flow in an excitation loop. Once current flow is established in the external circuit, a portion of the produced current is diverted to excite the magnetic field.

One of the first practical applications of an MHD generator for EM soundings was performed in the framework of the Khibini experiment, conducted in the 1980s in the USSR. The Khibini experiment was designed to test the concept of using single, immensely strong impulses of an MHD generator (Velikhov, 1989). This powerful MHD generator was used to energize a single conductor, 11 km in length, connecting grounding structures in the Barents Sea on either side of the Sredniy and Ryabachiy Peninsulas. The maximum current provided to the cable was 22,000 A, in pulses with a duration of 5 to 10 seconds. The site for the Khibini source was selected so that the current from the two grounding structures would travel around the Sredniy and Ryabachiy peninsulas, forming an equivalent loop in the horizontal plane. Observations belong to two groups, one comprising the stations to the south on the Precambrian Shield of the Kola Peninsula (Fig. 17.5, bottom panel), and the other comprising stations to the north, off the shore of the Kola Peninsula, over the Barents Basin (Fig. 17.5, top panel). The geological formations beneath the Barents Sea are formed by young sedimentary rocks with significant potential for oil or gas production. For example, the massive Shtokman gas field is located within this area. Evaluation of the deep potential of the Pechenga deposit was another important problem that was solved using EM surveying with MHD-generated pulses (Velikhov et al., 1987).

The data obtained as part of the Khibini experiment were used for a variety of purposes: to study the electrical conductivity profile in the earth to depths of several hundred kilometers, to study the electrical structure of major ore deposits in the Kola Peninsula, and to determine the character of the sedimentary basin beneath the Barents Sea. A profile of MHD soundings was established across the Pechenga mineral deposit located on the Kola Peninsula, and a major source of nickel ore. The Proterozoic Pechenga complex consists of a laminar sequence of alternating metasedimentary and metavolcanic rock (Kozlovskiy, 1987). The total thickness of this sequence may be as great as 8–9 kilometers. The ore body lies in a simple graben-like structure on the surface of the Archean basement. The underlying Archean complex is composed principally of gneisses which have been repeatedly metamorphosed and which have undergone regional granitization of varying degree.

The extent of the ore in the Pechenga deposit is not yet fully known. Levels which have been developed to date extend to depths of 1500 to 2000 meters, but it is believed that substantial reserves remain undiscovered at depths between 3 and 5 kilometers. Evaluation of the deep potential of the Pechenga deposit was considered to be an important problem that might be solved using MHD-generated pulses.

Inversion of the data collected in the framework of the Khibini experiment has indicated that in northern Finland, there is a very rapid decrease in resistivity from values of the order of 500 Ohm-meters to values of the order of 10 Ohm-meters at depths ranging from 140 to 170 kilometers. On the other hand, the inversions of sounding curves from the Kola Peninsula and Karelia indicated a gradational decrease in resistivity starting at a depth of about 150 kilometers. In these cases, the resistivity does not decrease to a resistivity of a few tens of Ohm-meters until depths of 300 kilometers or more are reached. The results of the Khibini experiment can be summarized as follows (Velikhov and Panchenko, 2010):

– ten large geoelectrical blocks and zones in the upper section of the earth's crust up to depth of 10–15 km with dimensions about 50 km × 50 km have been detected;

– the resistivity of the blocks varies from ∼10 Ohm-m to ∼100 Ohm-m;
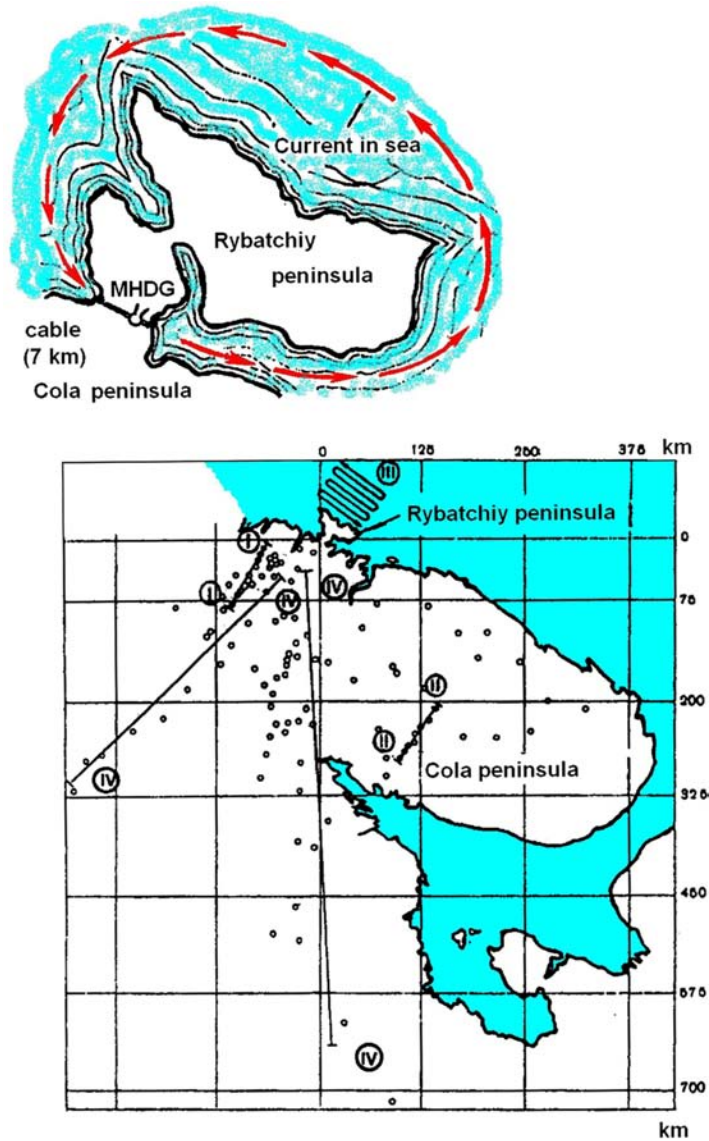
FIGURE 17.5

Survey configuration of the Khibini experiment. The red line in the top panel schematically shows the current flow off the shore of the Kola Peninsula, over the Barents Sea. The bottom panel presents the locations of the observation stations in the Kola Peninsula shown by circles. The black lines show the profiles of detailed EM soundings: (I–I) – Pechenga ore-bearing structure, (II–II) – Imandra-Varzug ore-bearing area, (III) – Barents Sea shelf, (IV–IV) – profile of the deep sounding of the Baltic Shield.

– the blocks with high resistivity usually correspond to the outcrops of the most ancient granitoid rocks;

– the blocks with low resistivity, as a rule, are connected to the outcrops of the younger rocks, and they are considered to be prospective zones for exploration for ore deposits and other mineral resources.

The Khibini experiment was one of the first large-scale experiments of deep EM sounding using high-power pulses. It provided geophysicists with a unique opportunity to test new technologies for studying a deep earth interior using a controlled-source EM field. However, the further development of an EM surveying system with a very powerful MHD generator was limited by the high cost of this exploration tool. With the progress in MHD technology and the simplification and cheapening of the operation, this method could become a power tool in regional and crustal tectonic study associated with the exploration of the Earth's resources.

17.3 MINERALS EXPLORATION – IP SURVEY IN MONGOLIA

The induced polarization (IP) geophysical method has been widely used for mineral exploration. This method makes it possible to estimate not only the resistivity distribution but also the chargeability distribution of the underground remotely using the surface electromagnetic (EM) data. However, the

Mineral Name	Volume fraction, %
Quartz	48.11
Feldspar	45.83
Pyrite	2.64
Chlorite	2.98
Dolomite	0.78
Ti (mx)	0.35
Sulphates	0.33
Background	0.33
Calcite	0.22
Chalcopyrite	0.15
Apatite	0.07
Zircon	0.05
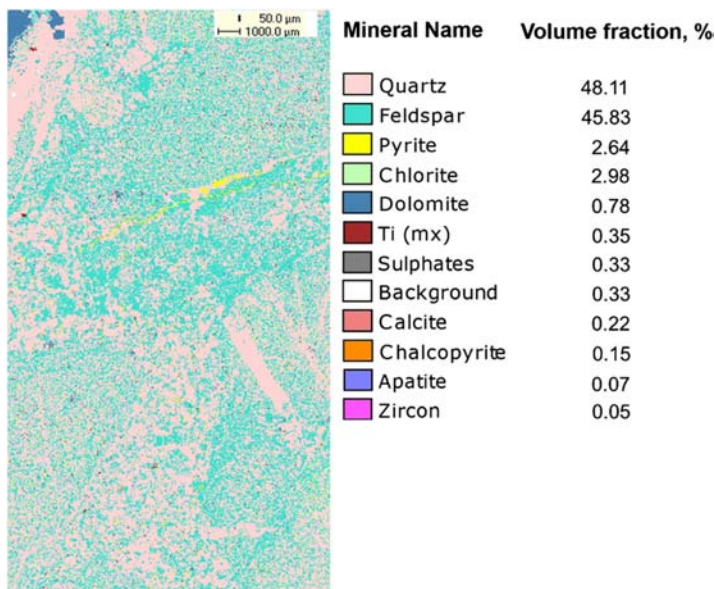
FIGURE 17.6

A QEMSCan image of rock sample A from the Au-Cu deposit, with a phase analysis shown on the right. The feldspar and quartz are designated by the dark green and light pink colors, respectively, while the dolomite is shown by blue, the chalcopyrite by orange, and the pyrite by yellow in this image.
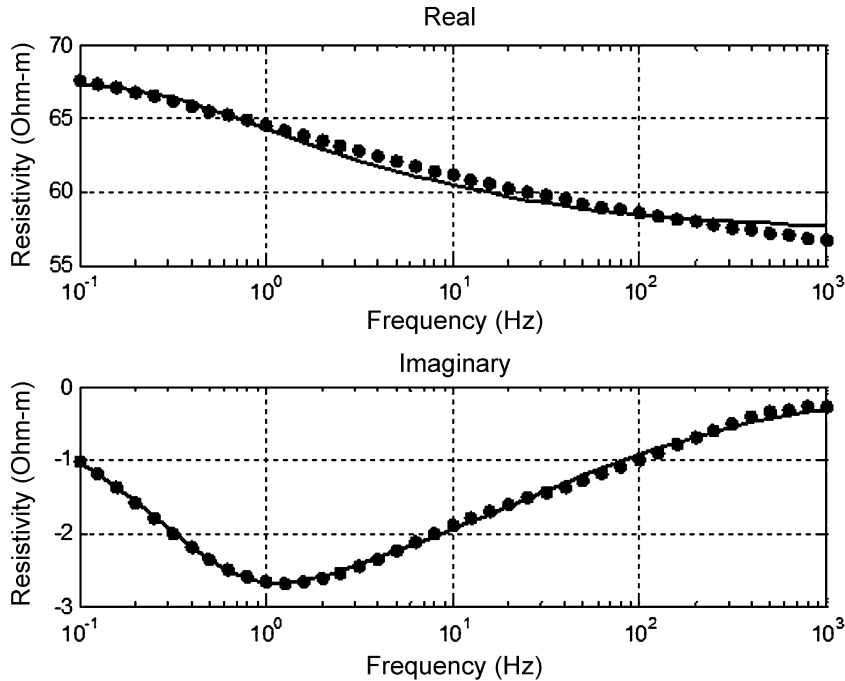
FIGURE 17.7

Real (top panel) and imaginary (bottom panel) parts of the observed complex resistivity spectrum (black dots) and the data predicted based on the GEMTIP model (black lines) for the rock sample A. The predicted data were obtained using three-phase GEMTIP model.

IP effect depends not only on the resistivity and chargeability. Several other geoelectrical parameters affect the IP data as well. A comprehensive analysis of IP phenomena is usually based on models with frequency dependent complex conductivity distribution. One of the most popular models is the Cole-Cole relaxation model (Cole and Cole, 1941). This model was introduced for studying the IP effect in the pioneering papers of Pelton (1977) and Pelton et al. (1978). It was demonstrated in Chapter 12 that the generalized effective-medium theory of induced polarization (GEMTIP), based on a rigorous physical-mathematical description of heterogeneous conductive media, provides a more accurate representation of the IP phenomenon than the Cole-Cole model. The GEMTIP model of multiphase conductive media provides a quantitative tool for evaluation of the type of mineralization, and the volume content of different minerals using electrical and/or electromagnetic data.

The time-domain IP geophysical survey with pole-dipole and gradient electrode arrays, were carried out over the Cu-Au deposit in Mongolia in an area located about 1800 km west from Ulan Bator, and about 150 km from the Bayan-Ulugii province center. The copper-gold ore is hosted in the hydrothermal alteration zone. The mineralization is a low-sulfide type. The distribution of the mineralization is uneven and it was determined that the mineralization is generally distributed in or in the vicinity of the quartz-carbonate gangue located inside of the hydrothermal alteration zone. Mineralization is
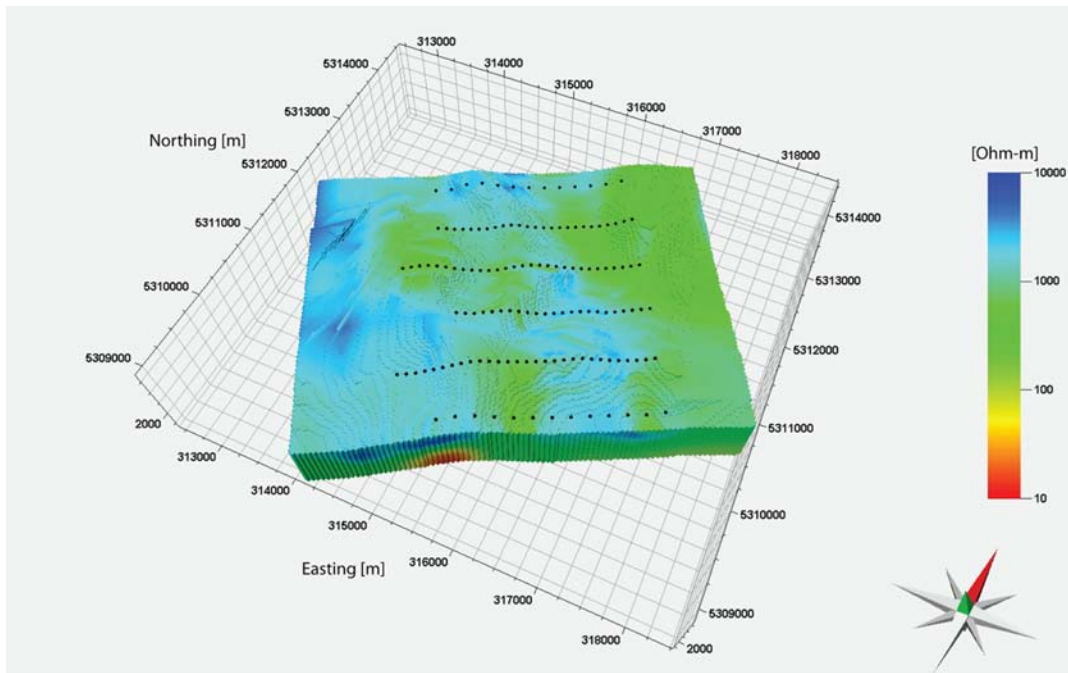
FIGURE 17.8

A 3D view of the 3D resistivity model recovered from 3D inversion of pole-dipole IP data.

associated with chalcopyrite related to early quartz veins. The main exploration problem in this case is the ability to differentiate between normally barren pyrite-bearing alteration phases and mineralized chalcopyrite phases. These geological systems generally always have pyrite but not all are mineralized with Cu bearing sulfides. Discrimination between pyrite and chalcopyrite could be considered as an important application of the IP survey.

The main objective of this survey was to determine the alteration and mineralization zones of the known copper deposit. The mineralogical analyses of mineral and host rock samples from the survey area were performed using the quantitative evaluation of minerals by the scanning electron microscopy (QEMSCan) system, developed from the research pioneered by the CSIRO in Australia. QEMSCan combines features found in other analytical instruments such as a scanning electron microscope (SEM) or electron probe micro analyzer (EPMA) into a next generation solution designed for automated analysis of minerals, rocks and materials. QEMSCan uses electron beam technology combined with high resolution BSE (back scattered electron) and SE (secondary electron) imaging, and state-of-the-art energy dispersive spectrometers (EDS) to analyze minerals.

QEMSCan provides detailed particle mineralogical analysis including quantification of mineral proportions, average grain size for selected minerals, average grain density, estimated minerals frac-
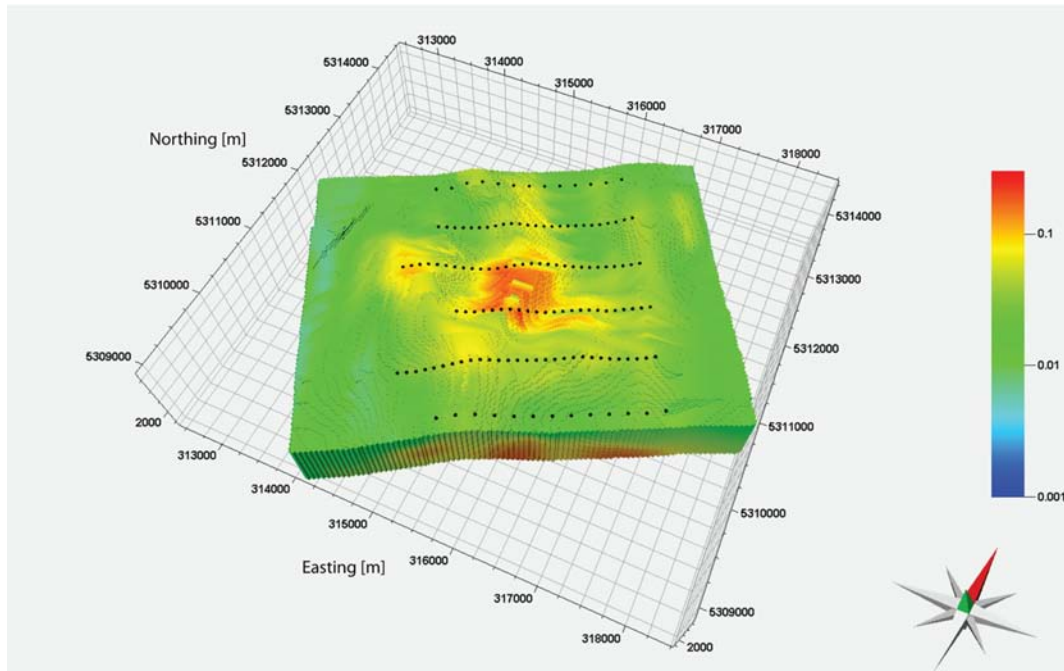
FIGURE 17.9

A 3D view of the 3D chargeability model recovered from 3D inversion of pole-dipole IP data.

tion volumes, etc. The final QEMSCan images were used for determination of the fraction volume of different minerals.

As an example, Fig. 17.6 presents the results of the QEMSCan analysis for a rock sample A.

A QEMSCan image of rock sample A (Fig. 17.6) contains quartz (light pink, veins) and feldspar (light green, matrix) with 2.64% of pyrite (yellow) and 0.15% of chalcopyrite (orange). The sulfides are located inside of quartz veins in this sample.

The electrical properties of the same samples from the Cu-Au deposit in Mongolia were determined using the laboratory complex resistivity (CR) measurements.

Fig. 17.7 shows the real and imaginary parts of the complex resistivity spectra measured for the same sample A analyzed above. We can see that the maximum IP response in the imaginary part of the complex resistivity curves (the minimum of imaginary part) corresponds to a frequency of around 1 Hz in this case. The observed CR data were inverted into the IP parameters using a three-phase GEMTIP model with elliptical inclusions (see section 12.3.6). In this case, it was assumed, based on the results of the QEMSCan analysis, that one phase was represented by pyrite, another phase by chalcopyrite, and the third phase was formed by other nonpolarizable minerals. The predicted data obtained using the three-phase GEMTIP model are shown by the black lines in Fig. 17.7.
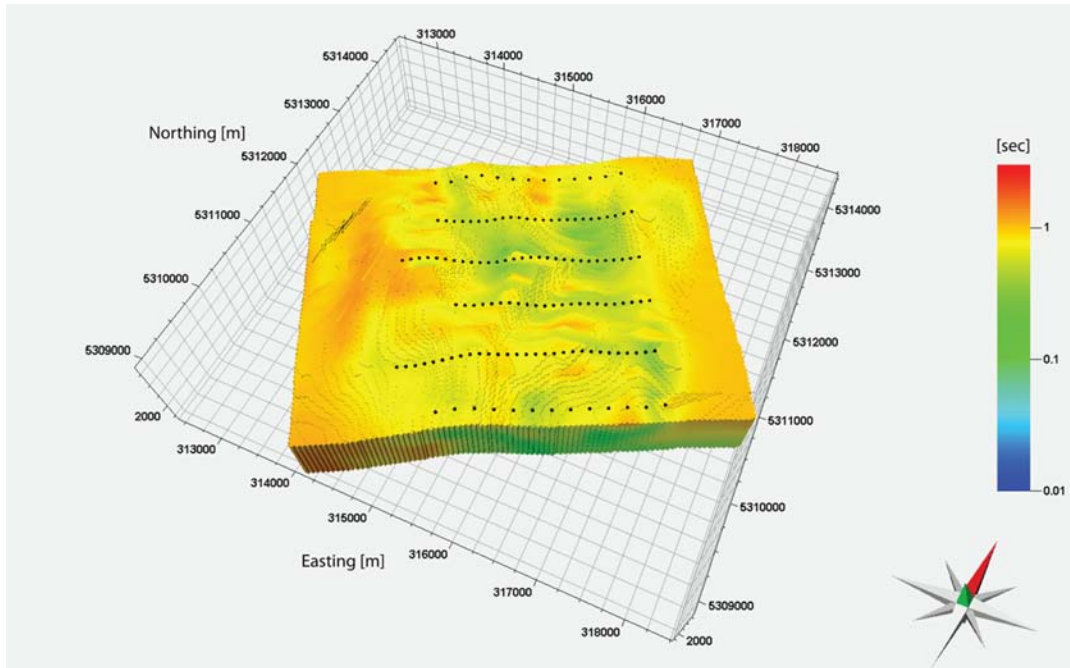
FIGURE 17.10

A 3D view of the 3D time constant model recovered from 3D inversion of pole-dipole IP data.

As a result, one can establish relationships between the mineral composition of the rocks, determined using QEMSCan analysis, and the parameters of the GEMTIP model defined from lab measurements of the electrical properties of the rocks. These relationships open the possibility for remote estimation of types of mineralization and for mineral discrimination using spectral IP data.

The time-domain IP data, collected by the IP survey, were inverted for the GEMTIP model parameters, DC resistivity, chargeability, time constant, and relaxation parameter, using the inversion method discussed in section 12.4.

Figs. 17.8 through 17.11 show the 3D distributions of resistivity, chargeability, time constant, and relaxation parameter, recovered from 3D inversion of pole-dipole IP data.

It was possible to locate the target mineralization zones by using geoelectrical models recovered from 3D inversion of the IP data, petrophysical and mineralogical analyses of the rock samples, and assay data analysis of the drill cores. The result of this comprehensive interpretation is shown in Fig. 17.12, which presents a 3D view of the interpreted target mineralized zones. In that figures, the color of the body corresponds to the chargeability value recovered from the 3D inversion of the IP data (hot color – high chargeability; cold color – low chargeability). The drilling results confirmed a good correlation between the interpreted bodies and known mineralization. This opens a possibility to
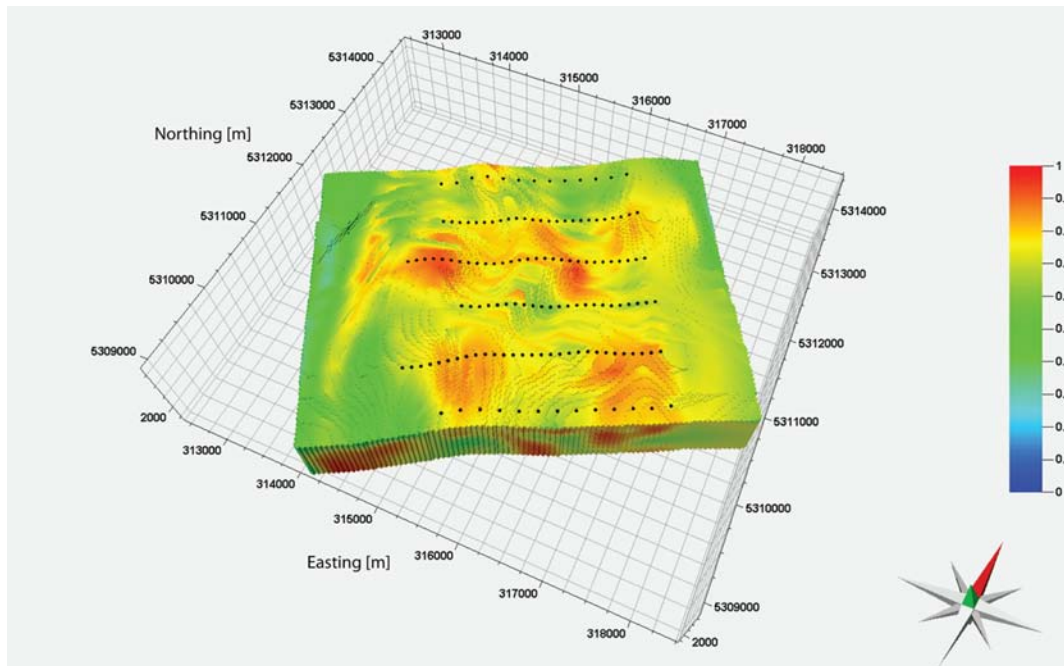
FIGURE 17.11

A 3D view of the 3D relaxation parameter model recovered from 3D inversion of pole-dipole IP data.

estimate the target mineralized zones by using a rigorous 3D inversion of the IP data interpreted with petrophysical and mineralogical analyses of rock samples, and assay data analysis.

17.4 MINERALS EXPLORATION – AIRBORNE SURVEY IN REID-MAHAFFY SITE, CANADA

The Reid-Mahaffy site is located in the Abitibi Subprovince, immediately east of the Mattagami River Fault. The area is underlain by Archean (about 2.7 b.a.) mafic to intermediate metavolcanic rocks in the south, and felsic to intermediate metavolcanic rocks in the north, with a roughly EW-striking stratigraphy (Fig. 17.13). Narrow horizons of chemical metasedimentary rocks and felsic metavolcanic rocks have been mapped, as well as a mafic-to-ultramafic intrusive suite to the southeast. NNW-striking Proterozoic diabase dikes are evident from the aeromagnetic data. Copper and lead-zinc vein/replacement and stratabound volcanogenic massive sulfide (VMS) mineralization occur in the immediate vicinity. The world-class Kidd Creek VMS deposit occurs to the southeast of the test site. Drill holes within the
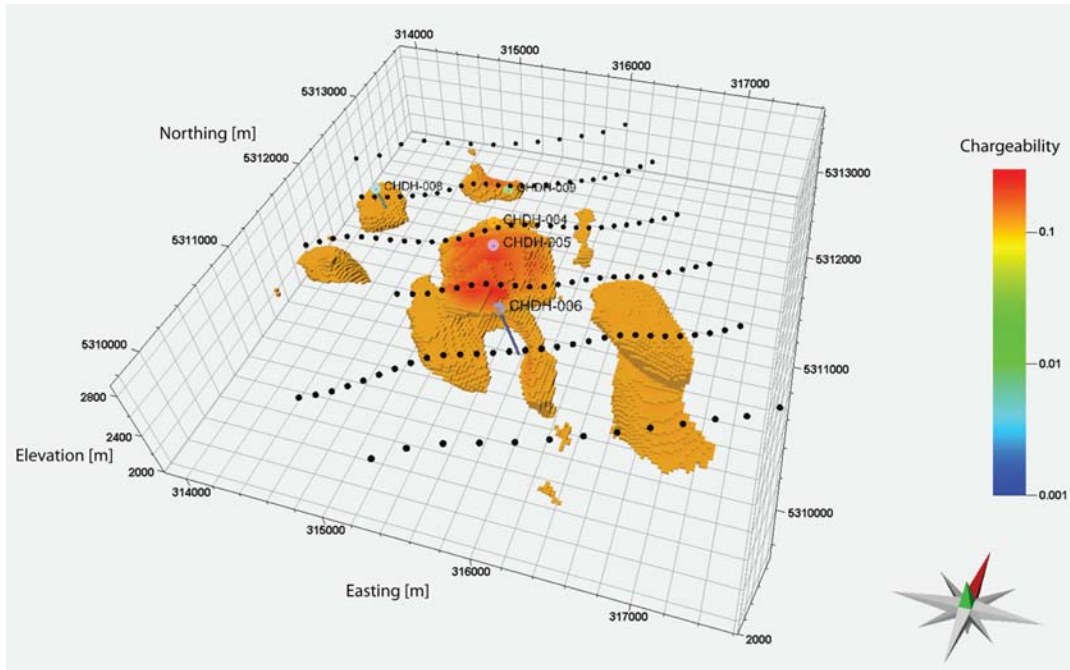
FIGURE 17.12

A 3D view of the interpreted target mineralized zones.

test site were targeting conductive targets, and encountered massive sulfides and graphite with minor copper and zinc mineralization.

Many different airborne systems have been tested in this area, including the DIGHEM frequency domain system, which is the focus of this paper. The DIGHEM system was configured with five operating frequencies: 868, 7025, and 56,374 Hz horizontal coplanar, and 1068 and 4820 Hz vertical coaxial. The transmitter-receiver separation was 6.3 m for the highest frequency and 8.0 m for the remainder. The survey was flown with a nominal bird height of approximately 32 m.

The AEM data from the Reid-Mahaffy test site have previously been interpreted using a variety of 1D AEM methods (e.g., Sattel, 2005; Vallée and Smith, 2007, 2009), as well as 3-D inversion from Cox et al. (2010, 2012). I present hear the inversion result for a 3-D conductivity model with elements that were 20 m in the in-line direction and 25 m in the cross-line direction, and varied from 5 m to 20 m in the vertical direction. The model had a total depth of 160 m. The sensitivity domain of the DIGHEM system was set at 280 m. The 3-D inversion for the DIGHEM data converged to a final misfit of 5% from an initial misfit of 70%.

Fig. 17.14 is an example of the conductivity model recovered from the 3-D inversion. It clearly shows conductive overburden between 20 Ohm-m and 50 Ohm-m, and three vertical conductors in the correct location as determined by drill holes.
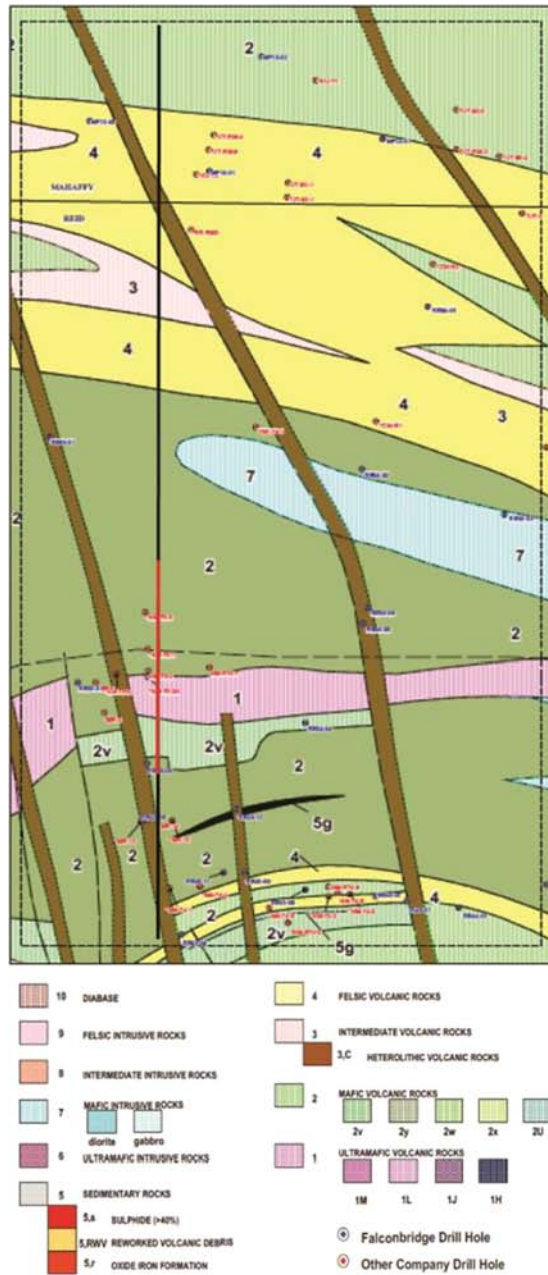
FIGURE 17.13

Geologic map of the Reid-Mahaffy survey area.
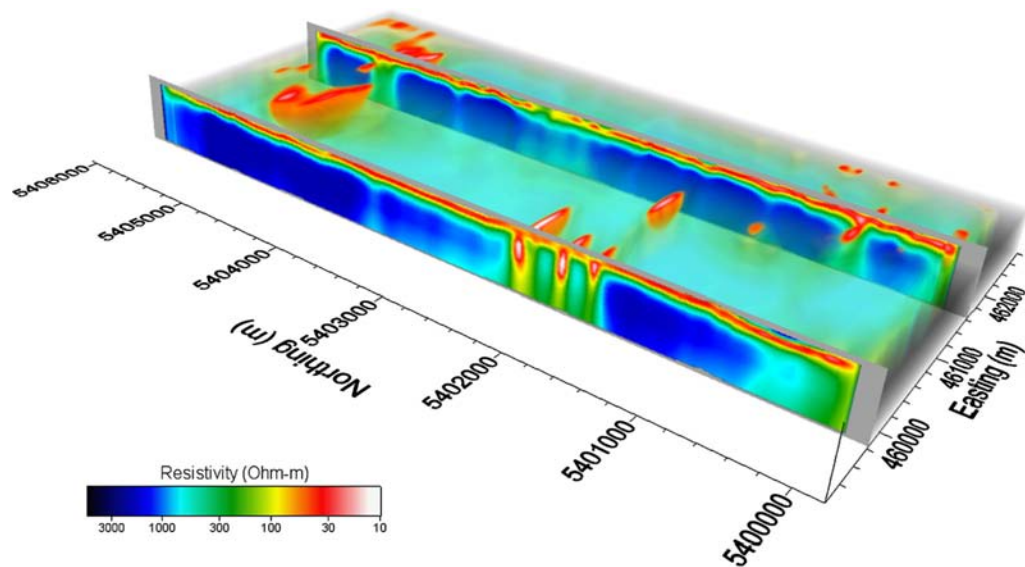
FIGURE 17.14

Perspective view of the resistivity model recovered from 3-D FE-IE-based inversion of the Reid-Mahaffy test site, Ontario. For clarity, the conductive overburden has been removed from the volume rendering in this image, but is clearly seen in the opaque slices.
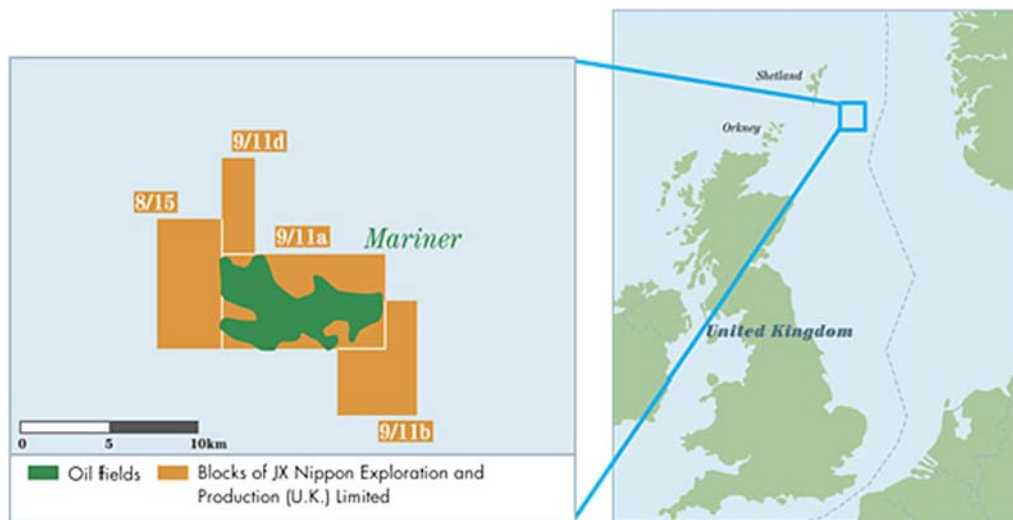
FIGURE 17.15

The location of the Mariner field in the North Sea.
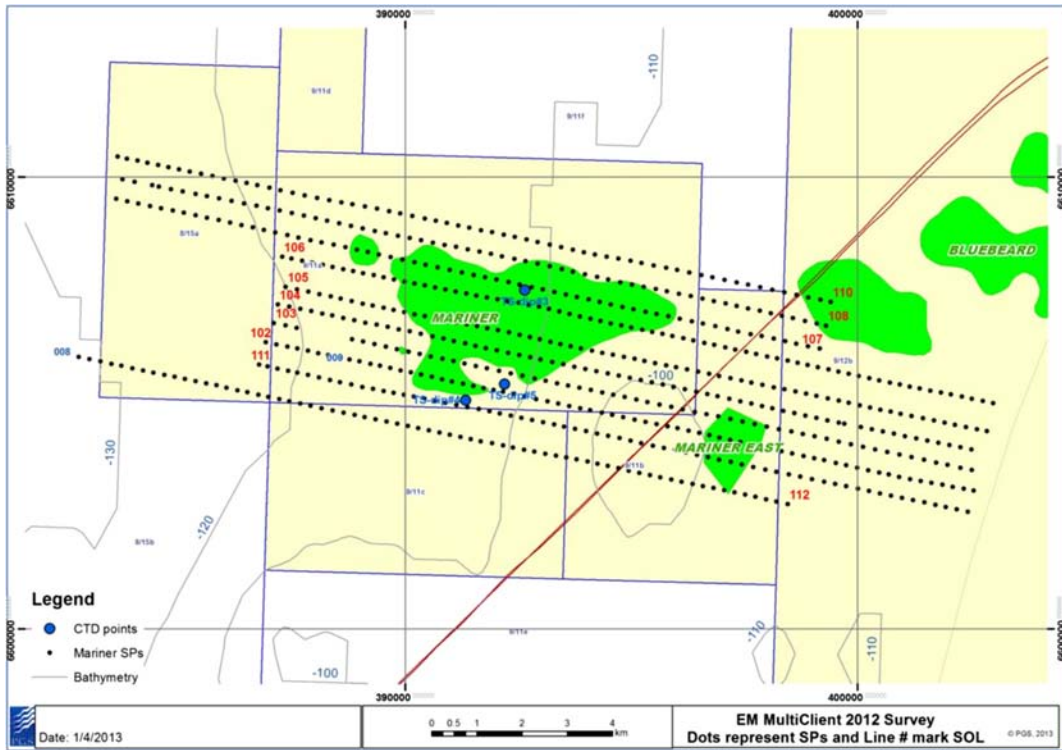
A map of the Mariner area showing the acquired lines and shot points.

17.5 HYDROCARBON EXPLORATION – OFF-SHORE EM SURVEY IN NORTH SEA

As an example of application of the EM methods for off-shore hydrocarbon exploration, let us consider a case study of analysis of the towed streamer EM data acquired over the Mariner heavy oil field located in the UK North Sea (Zhdanov et al., 2015). The Mariner field is located on the East Shetland Platform of the UK North Sea approximately 150 km east of the Shetland Isles (Fig. 17.15). The Mariner oil field development entails investments of more than USD 7 billion and is the largest new offshore development in the UK in more than a decade. It is expected to start production in 2017. The field is estimated to produce for 30 years, with average production of around 55,000 barrels of oil per day over the plateau period from 2017 to 2020. The Mariner field consists of two shallow reservoirs, the Maureen Formation and the Heimdal Sandstones of the Lista Formation, with nearly 2 billion barrels of oil in place and expected reserves of more than 250 million barrels of oil. Both formations yield heavy oil of around 12 to 14 API. Due to the low well flow rates and early water break-through there is a need for many wells and a process designed to handle large liquid rates and oil-water emulsions.
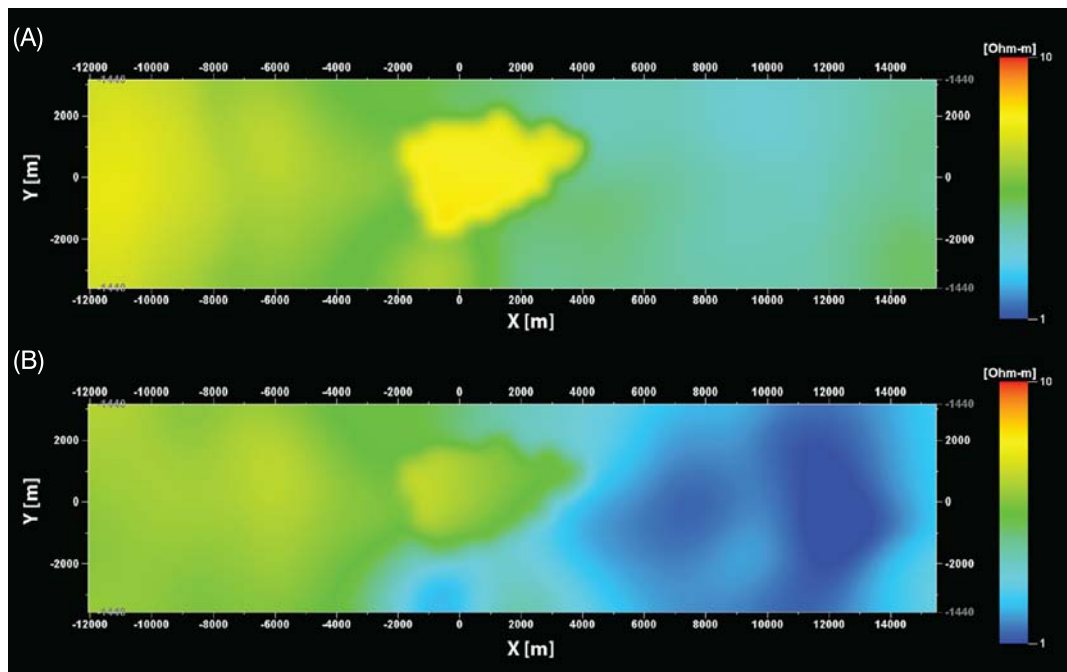
FIGURE 17.17

Horizontal sections of the 3D resistivity distributions at a depth of 1425 m: (A) vertical resistivity, (B) horizontal resistivity, recovered from anisotropic 3D inversion.

All production wells will have stand-alone sand screens and electric submersible pumps (ESPs) for lifting.

17.5.1 THE ACQUISITION CONFIGURATION AND SURVEY LAYOUT

The main features of the towed streamer EM configuration for the Mariner survey (Mattsson et al., 2012; Zhdanov et al., 2015) are shown in Fig. 15.23. The bipole electric current source is 800 m long with a towing depth of 10 m. The source runs at 1500 A, and the frequencies range from 0.2 to 1.2 Hz with a step of 0.2 Hz. The survey consisted of 10 lines separated by 500 m, as shown in Fig. 17.16. The length of each line was about 15 km. Each line recorded 60 shots of 120 s lengths.

In order to construct an appropriate 3D geoelectrical model which is used as the starting model in the anisotropic 3D inversion, one can apply anisotropic 1D inversion for each survey line. For all 1D inversions, the bathymetry in the survey area was taken into account, and the response data at five frequencies from 0.2 to 1.0 Hz with 18 offsets ranging approximately from 1750 to 7450 m were used. The final starting model was constructed using a 3D model from the results of 1D inversions, geometrically constrained by seismic and well-log information (Zhdanov et al., 2015).
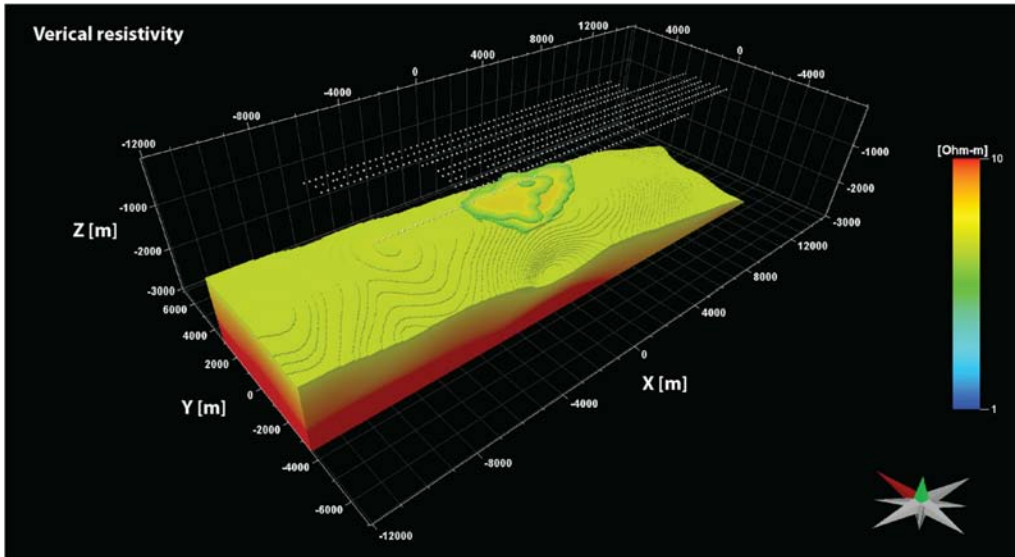
FIGURE 17.18

A 3D view of the 3D vertical resistivity distribution recovered from anisotropic 3D inversion.
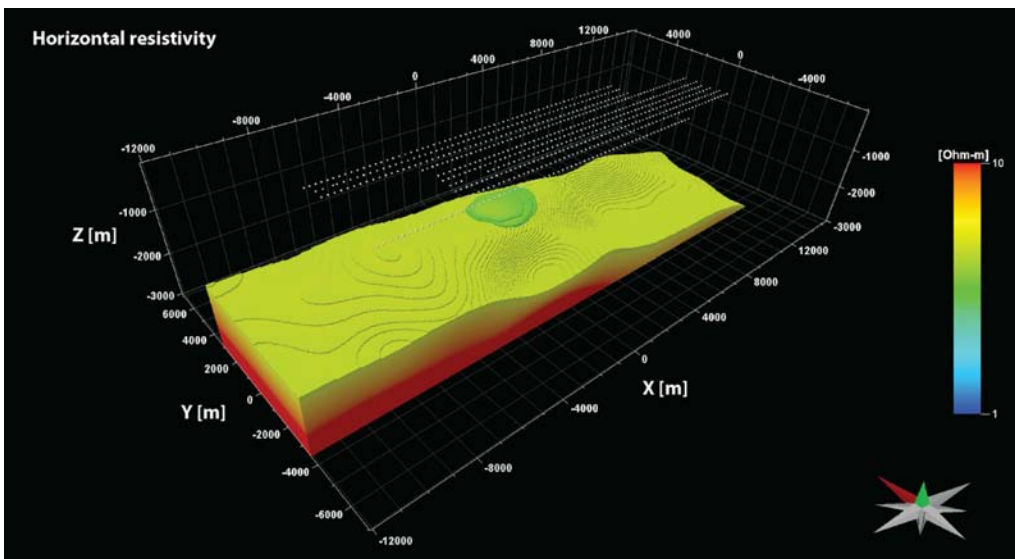
FIGURE 17.19

A 3D view of the 3D horizontal resistivity distribution recovered from anisotropic 3D inversion.
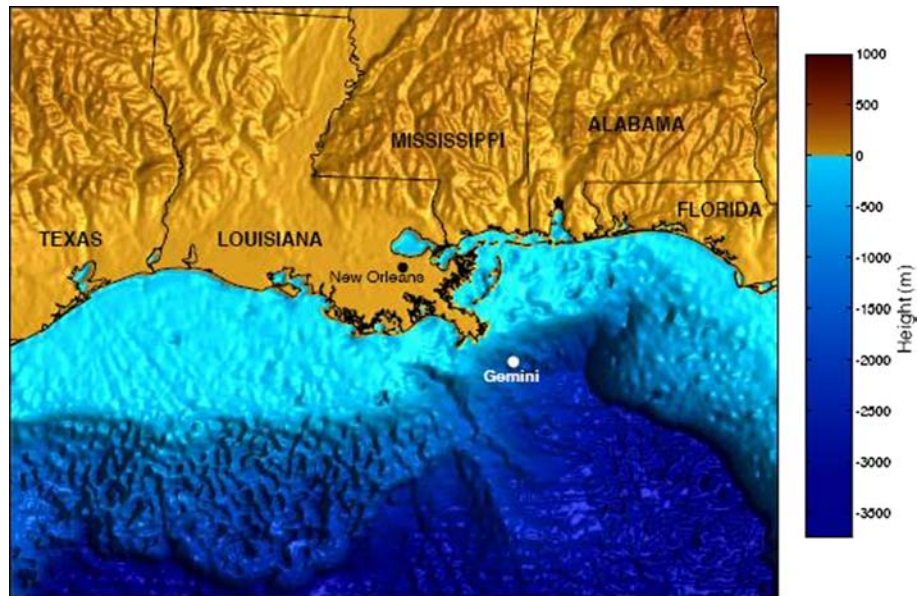
FIGURE 17.20

Location of Gemini Prospect in the northern Gulf of Mexico.

17.5.2 3D ANISOTROPIC INVERSIONS OF THE TOWED STREAMER EM DATA

In the anisotropic 3D inversion of the data collected from all the survey lines, the inversion domain was selected to cover all sensitive parts of the subsurface. The dimensions of the inversion domain were selected as follows: from $-12,000$ m to 16,000 m in the x direction; from -3600 m to 3600 m in the y direction; from 90 m to 3000 m in the z direction (positive downward). This rectangular region was discretized into cells of 50 m $\times$ 50 m $\times$ 25 m. The selected data for the inversion consisted of 323 shots with 18 offsets (approximately from 1750 m to 7450 m) and five frequencies (0.2, 0.4, 0.6, 0.8, and 1.0 Hz).

The RCG algorithm of inversion was terminated when a resulting misfit of 5.4% was reached. Fig. 17.17 presents examples of the horizontal sections of the 3D resistivity models at a depth of 1425 m recovered from the anisotropic 3D inversion.

Figs. 17.18 and 17.19 show 3D perspective views of the 3D resistivity models recovered from the anisotropic 3D inversion of the towed streamer EM data for vertical and horizontal resistivities, respectively. It can be seen that a resistive and anisotropic anomaly is showing up on top of a resistive chalk/basement underburden. This anomaly coincides well with the horizontal extent of the Heimdal and Maureen reservoirs even though this information was not exactly utilized in the anisotropic 3D inversion. Also, the recovered anisotropic feature in the reservoir volume agrees well with the known geoelectrical characteristics of the Maureen and Heimdal reservoirs.
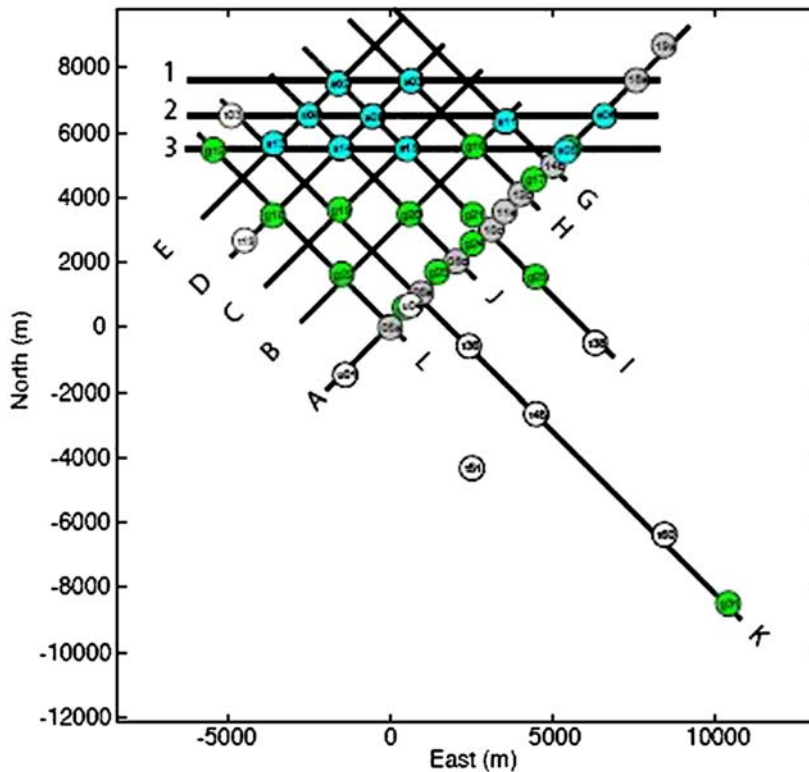
FIGURE 17.21

Location of the MT profiles with the observation sites in Gemini Prospect. (After Key, 2003.)

17.6 MARINE MAGNETOTELLURICS IN THE GULF OF MEXICO

There were several marine MT surveys conducted during the last decade in different areas of the World Ocean. We will discuss here, as an example, an application of the marine MT method for mapping the salt structures in the Gulf of Mexico. Salt bodies are usually characterized by a higher seismic wave velocity and higher resistivity than the surrounding sea-bottom sediments. They represent a very difficult target for marine seismic exploration, but can be clearly identified by marine EM methods.

In this section we discuss the results for the marine MT surveys in the Gemini Prospect, which lies about 200 km southeast of New Orleans in about 1 km deep water in the northern Gulf of Mexico, which is shown in Fig. 17.20.

The reflection imaging technique, widely available and ever popular in exploration, can provide detailed images of the top and base of a salt surface, sedimentary layer, and basement formations. However, seismic imaging may not always provide sufficient details to interpret salt and nearby sedimentary structures. Common problems associated with salt include multiple reflection and mode conversion, the
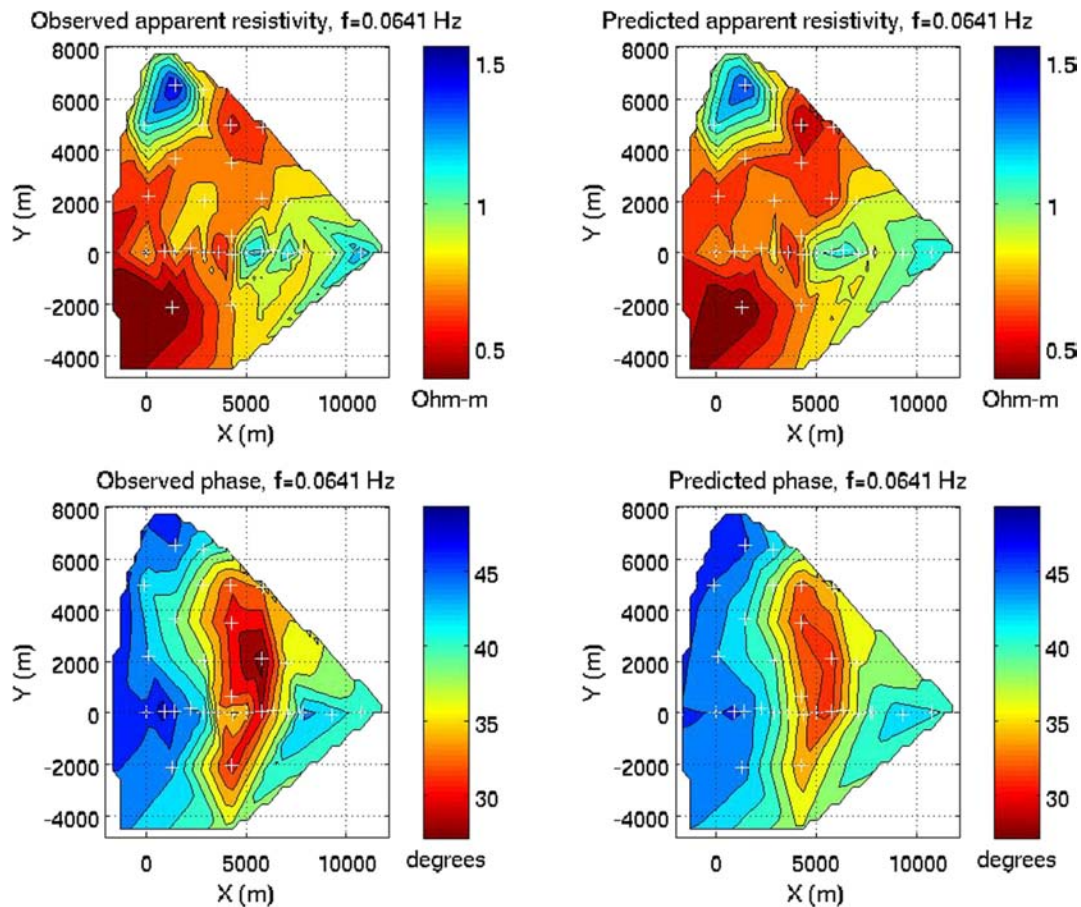
FIGURE 17.22

Plots of the observed (left-hand panels) and predicted (right-hand panels) apparent resistivity and phase for the MT data collected at the MT sites in the Gemini Prospect area.

loss of reflected energy from steeply dipping salt surfaces, and lack of coherent features beneath salt structures. The salt in the Gulf of Mexico has a high acoustic contrast with surrounding sediments, which makes seismic sections difficult to interpret.

It is generally well known that rocks with high seismic velocity and impedance contrast are also higher in electrical resistance than surrounding sediments. The high contrast in electrical conductivity between the salt and the surrounding sediments makes Gemini Prospect an attractive target for MMT method.

The sea-bottom MT surveys were conducted by the Scripps Institution of Oceanography in 1997, 1998, 2001, and 2003, at a total of 42 MT sites.
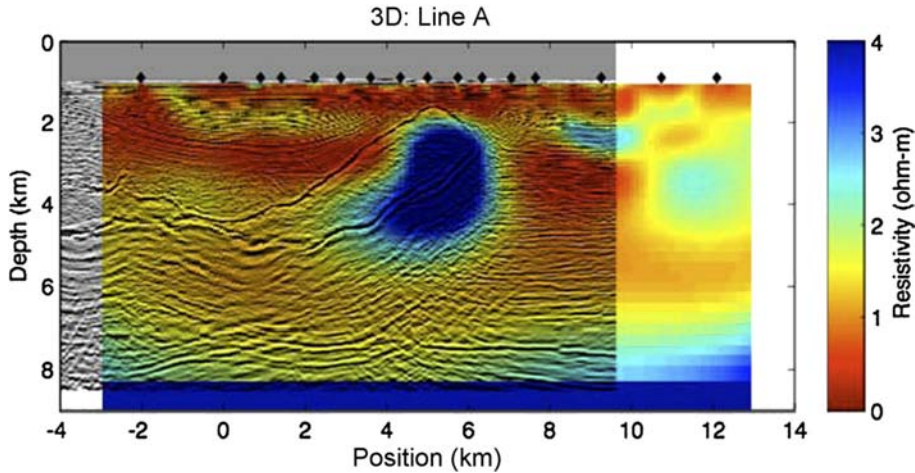
FIGURE 17.23

A vertical cross section of 3-D focusing inversion results provided over line A. The observational profile is oriented from southwest (left) to northeast (right). The MT site locations are shown as black diamonds. The resistivity distribution in the inverse model is shown on a linear scale. The inverse geoelectrical model is overlapped with the depth-migrated seismic reflections from a 3-D seismic survey.

The Gemini salt body lies 1.5 km beneath the seafloor in 1 km deep water and has a high electrical resistivity compared with the surrounding sediments, making it a suitable target for electrical methods. The subsalt gas deposit at Gemini is located at a depth of about 4 km on the southeastern edge of the Gemini structure. Fig. 17.21 shows the location of the MT sites.

Constable and Key (Key, 2003) conducted a detailed analysis of the Gemini MT data, using 2-D Occam's inversion code (Constable et al., 1987; de Groot Hedlin and Constable, 1990). The results obtained by 2-D inversion of the MT data were in a good agreement with the seismic data (Key, 2003; Key et al., 2006).

We consider here the results of a rigorous 3-D MT inversion of the same data using a fine discretization grid following the paper by Zhdanov et al. (2011c). We analyzed the MT data from all 42 sites simultaneously. Inversion is conducted by the re-weighted regularized conjugate gradient method, RRCG (Chapter 8). The discretization is $128 \times 120 \times 64 = 983,040$ cells. The iterative process is terminated when the relative norm of the difference between the observed and predicted data, computed over all MT sites, reaches the noise level of 7%.

Fig. 17.22 presents plots of the observed and predicted apparent resistivity and phase for the MT data collected in the observational sites shown in Fig. 17.21. We observe a good fit between the observed and predicted data in this figure.

Fig. 17.23 presents, as an example, the vertical cross section of a 3-D resistivity model obtained by focusing inversion along the observational line A, shown in Fig. 17.21.

The depth-migrated seismic reflections from a 3-D seismic survey are shown by the black line, for comparison. We can see the top part of the salt dome very clearly in these figures as a thick resistive
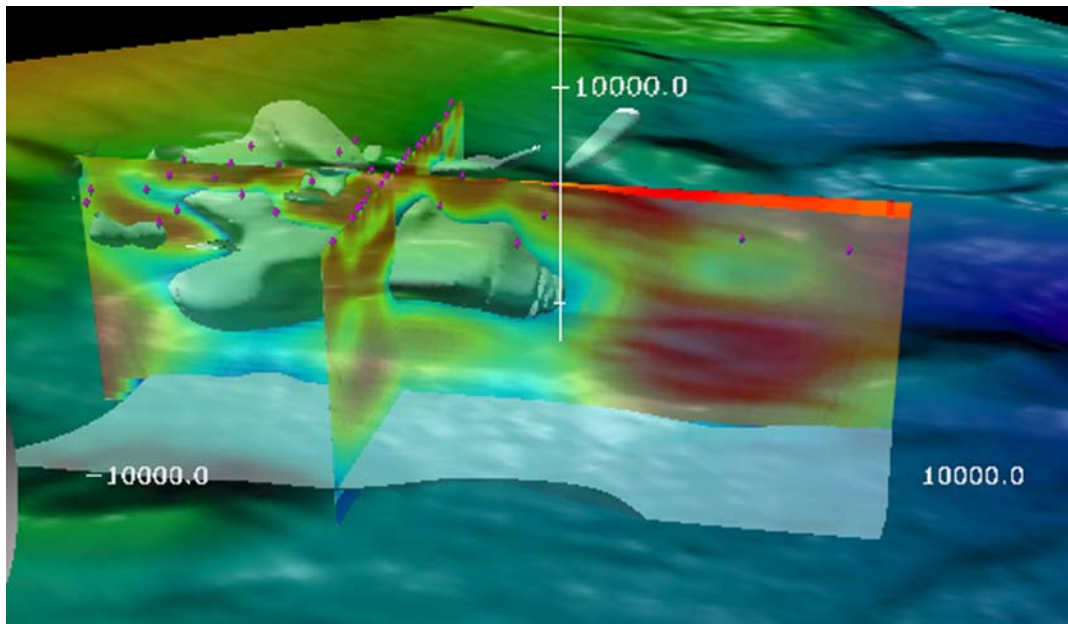
FIGURE 17.24

3D image of the inversion result for the Gemini Prospect MT data in the presence of the sea-bottom bathymetry.

body. Fig. 17.24 presents a 3D view of the geoelectrical inverse model and the bathymetry in the area of the survey. The inversion results reveal a resistive salt structure which is confirmed by a comparison with the seismic data. These inversion results demonstrate that we can map resistive geoelectrical structures like salt domes with reasonable accuracy using 3D inversion of marine MT data.

REFERENCES AND RECOMMENDED READING TO CHAPTER 17

Bedrosian, P. A., and D. W. Feucht, 2013, Structure and tectonics of the northwestern United States from EarthScope USArray magnetotelluric data: Earth and Planetary Science Letters, **402**, 275–289.

Berdichevsky, M. N., and V. I. Dmitriev, 1976, Distortions of magnetic and electrical fields by near-surface lateral inhomogeneities: Acta Geodaetica, Geophysica et Monatanista Akademy of Science Hungary, **34** (11), 447–483.

Camp, V. E., and M. E. Ross, 2004, Mantle dynamics and genesis of mafic magmatism in the intermountain Pacific Northwest: Journal of Geophysical Research, **109**, B08204.

Carlson, R. W., T. L. Grove, and J. M. Donnelly-Nolan, 2008, Concentrating the slab-fluid input to Newberry volcano: Geochim. Cosmochim. Acta, **72** (12), A136.

Cole, K. S., and Cole, R. H., 1941, Dispersion and absorption in dielectrics, Journal of Chemical Physics, **9**, 343–351.

Constable, S. C., R. L. Parker, and C. G. Constable, 1987, Occam's inversion: A practical algorithm for generating smooth models from electromagnetic sounding data: Geophysics, **52** (3), 289–300.

Cox, L. H., G. A. Wilson, and M. S. Zhdanov, 2010, 3D inversion of airborne electromagnetic data using a moving footprint: Exploration Geophysics, **41**, 250–259.

Cox, L. H., G. A. Wilson, and M. S. Zhdanov, 2012, 3D inversion of airborne electromagnetic data: Geophysics, **77** (4), WB59–WB69.

Čuma, M, A. Gribenko, and M. S. Zhdanov, 2017, Inversion of magnetotelluric data using integral equation approach with variable sensitivity domain: application to EarthScope MT data: Physics of the Earth and Planetary Interiors, **270**, 113–127.

de Groot Hedlin, C., and S. Constable, 1990, Occam's inversion to generate smooth two dimensional models from magnetotelluric data: Geophysics, **55** (12), 1613–1624.

Key, K. W., 2003, Application of broadband marine magnetotelluric exploration to a 3-D salt structure and a fast spreading ridge: Ph.D. Thesis, University of California, San Diego.

Key, K. W., S. C. Constable, and C. J. Weiss, 2006, Mapping 3-D salt using the 2-D marine magnetotelluric method: Case study from Gemini Prospect, Gulf of Mexico: Geophysics, **71**, B17.

Kozlovskiy, Ye. A., Ed., 1987, The superdeep well of the Kola Peninsula: Springer Verlag, Berlin, 558 pp.

Mattsson, J., P. Lindqvist, R. Juhasz, and E. Bjőrnemo, 2012, Noise reduction and error analysis for a towed EM system: 82nd Annual International Meeting, SEG, Houston, Texas.

Meqbel, N. M., G. D. Egbert, P. E.,Wannamaker, A. Kelbert, and A. Schultz, 2013, Deep electrical resistivity structure of the northwestern u.s. derived from 3-d inversion of USArray magnetotelluric data: Earth and Planetary Science Letters, **402**, 290–304.

Obrebski, M., R. M. Allen, M. Xue, and S. H. Hung, 2010, Slab-plume interaction beneath the Pacific Northwest: Geophysical Research Letters, **37**, L14305.

Obrebski, M., R. M. Allen, F. Pollitz, and S. Hung (2011), Lithosphere-asthenosphere interaction beneath the western United States from the joint inversion of body-wave travel times and surface-wave phase velocities: Geophysical Journal International, **185**, 1003–1021.

Patro, P. K., and G. D. Egbert, 2008, Regional conductivity structure of Cascadia: Preliminary results from 3D inversion of USArray transportable array magnetotelluric data: Geophysical Research Letters, **35**, L20311.

Pelton, W. H., B. D. Smith, and W. R. Sill, 1975, Inversion of complex resistivity and dielectric data: Geophysics, **40**, 153.

Pelton, W. H., 1977, Interpretation of induced polarization and resistivity data, Ph.D. thesis, University of Utah.

Pelton, W.H., L. Rijo, and C.M. Swift, Jr., 1978, Inversion of two-dimensional resistivity and induced-Polarization data: Geophysics, **43**, 788–803.

Pommier, A., F. Gaillard, M. Pichavant, and B. Scaillet, 2008, Laboratory measurements of electrical conductivities of hydrous and dry Mt. Vesuvius melts under pressure: Journal of Geophysical Research, **113**, B05205.

Roth, J. B., M. J. Fouch, D. E. James, and R. W. Carlson, 2008, Three-dimensional seismic velocity structure of the northwestern United States: Geophysical Research Letters, **35**, L15304.

Sattel, D, 2005, Inverting airborne electromagnetic data with Zohdy's method: Geophysics, **70**, G77–G85.

Schmandt, B., and E. Humphreys, 2010, Complex subduction and small-scale convection revealed by body-wave tomography of the western United States upper mantle: Earth and Planetary Science Letters, **297** (3–4), 435–445.

Schutt, D. L., and K. Dueker, 2008, Temperature of the plume layer beneath the Yellowstone hotspot: Geology, **36**, 623–626.

Schutt, D. L., K. Dueker, and H. Yuan, 2008, Crust and upper mantle velocity structure of the Yellowstone hotspot and surroundings: Journal of Geophysical Research, **113**, B03310.

Smith, R. B., M. Jordan, B. Steinberger, C. M. Puskas, J. Farrell, G. P. Waite, S. Husen, W. Chang, and R. O'Connell, 2009, Geodynamics of the Yellowstone hotspot and mantle plume: Seismic and GPS imaging, kinematics, and mantle flow: J. Volcanol. Geotherm. Res., **188**, 26–56.

Tikhonov, A. N., and V. Y. Arsenin, 1977, Solution of ill-posed problems: Winston and Sons, New York.

Vallée, M. A., and R. S. Smith, 2007, Comparison of fixed-wing airborne electromagnetic 1D inversion methods: In Proceedings of Exploration 07: Fifth Decennial International Conference on Mineral Exploration, Prospectors and Developers Association of Canada, 1067–1072.

Vallée, M. A. and R. S. Smith, 2009. Application of Occam's inversion to airborne time-domain electromagnetics: The leading edge, **28** (3), 284–287.

Velikhov, E. P., Yu. M. Volkov, and B. P. D'yakonov, 1975, Application of pulsed MHD generators for geophysical studies and earthquake prediction: Proceedings of VI International Conference on MHD Power Conversion, Washington D.C., **5**, 211–228.

Velikhov, Ye. P., Ed., 1989, Geoelectric investigations with strong current sources on the Baltic Shield: Moscow, Nauka.

Velikhov, Ye. P., M.S. Zhdanov, and M.A. Frenkel, 1987, Interpretation of MHD-sounding data from the Kola Peninsula by the electromagnetic migration method: Physics of the Earth and Planetary Interior, **45**, 300–317.

Velikhov, E. P., and V. P. Panchenko, 2010, Large-scale geophysical surveys of the earth's crust using high-power electromagnetic pulses: in Active Geophysical Monitoring, Eds. J. Kasahara, V. Korneev, and M.S. Zhdanov, Elsevier, 29–54.

Waite, G. P., D. L. Schutt, and R. B. Smith, 2005, Models of lithosphere and asthenosphere anisotropic structure of the Yellowstone hotspot from shear wave splitting: Journal of Geophysical Research, **110**, B113-04.

Wannamaker, P. E., J. R. Booker, A. G. Jones, A. D. Chave, J. H. Filloux, H. S. Waff, and L. K. Law, 1989, Resistivity cross section through the Juan de Fuca ridge subduction system and its tectonic implications: Journal of Geophysical Research, X, 14127–14144.

Xue, M., and R. M. Allen, 2007, The fate of the Juan de Fuca plate: Implications for a Yellowstone plume head: Earth and Planetary Science Letters, **264**, 266–276.

Yuan, H., and K. Dueker, 2005, Teleseismic P-wave tomogram of the Yellowstone plume: Geophysical Research Letters, **32**, L07304.

Zhdanov, M. S., 2002, Geophysical inverse theory and regularization problems: Elsevier, Amsterdam.

Zhdanov, M. S., 2009, Geophysical electromagnetic theory and methods: Elsevier, Amsterdam.

Zhdanov, M. S., R. B. Smith, A. Gribenko, M. Čuma, and M. Green, 2011b, Three-dimensional inversion of large-scale EarthScope magnetotelluric data based on the integral equation method: Geoelectrical imaging of the Yellowstone conductive mantle plume: Geophysical Research Letters, **38**, L08307, 1–7.

Zhdanov, M. S., L. Wan, A. Gribenko, M. Cuma, K. Key, and S. Constable, 2011c, Large-scale 3D inversion of marine magnetotelluric data: Case study from the Gemini Prospect, Gulf of Mexico: Geophysics, **76** (1), F77–F87.

Zhdanov, M. S., A. Gribenko, M. Čuma, and M. Green, 2012, Geoelectrical structure of the lithosphere and asthenosphere beneath the northwestern United States: Journal of Geology and Geosciences, 1, 1–6.

Zhdanov, M. S., M. Endo, D. Sunwall, and J. Mattsson, 2015, Advanced 3D imaging of complex geoelectrical structures using towed streamer EM data over the Mariner field in the North Sea: First Break, **33** (11), 59–63.

ALGEBRA OF DIFFERENTIAL FORMS

A

CONTENTS

The theory of differential forms provides the necessary mathematical foundation for an extension of vector field calculus into multidimensional spaces. In appendices A and B we will discuss the mathematical tools necessary for understanding this theory. They are based on the methods of linear algebra and differential geometry. In general, we can introduce the differential forms as expressions on which integration operates. There exist differential forms of different degrees depending on the dimensions of the domain of integration. In particular, a differential form of degree p, or a p-form, is an integrand of an integral over a domain of dimension p. We shall start our discussion by introducing the basic concept of the differential forms in three-dimensional Euclidean space where the degree of forms p varies from 0 to 3. A 0-form is a scalar function which is "integrated" over a region of zero dimension. In three-dimensional space the differential forms are closely related to the vector fields, and the algebraic and differential operations on the forms can be defined by conventional vector algebra and calculus, which makes it easier to understand for the reader familiar with conventional vector field theory.

A.1 DIFFERENTIAL FORMS IN THREE-DIMENSIONAL SPACE
A.1.1 1-, 2-, AND 3-FORMS

The differential forms in three-dimensional space were introduced in Chapter 1 as elementary work, dW, an elementary scalar flux, $dF_{\mathbf{B}}^{ds}$, and an elementary source, dQ, of a vector field $\mathbf{B}$.

In particular, an elementary voltage, dV, of the vector field $\mathbf{B}$ along an infinitesimally small element of curve $d\mathbf{l}$, represents a *differential 1-form φ* :

$$\varphi = \mathbf{B} \cdot d\mathbf{l} = dW. \tag{A.1}$$

An elementary scalar flux, $dF_{\mathbf{B}}^{ds}$, of the vector field $\mathbf{B}$ through an infinitesimally small oriented element of surface $d\mathbf{s}$ represents a *differential 2-form* $\underset{(2)}{\psi}$:

$$\underset{(2)}{\psi} = \mathbf{B} \cdot d\mathbf{s} = dF_{\mathbf{B}}^{ds}. \tag{A.2}$$

An elementary source, dQ, of the vector field $\mathbf{B}$ within an infinitesimally small element of volume dv is a *differential 3-form* $\underset{(3)}{\theta}$:

$$\underset{(3)}{\theta} = div\mathbf{B}dv = dQ. \tag{A.3}$$

Assuming that a small vector element of surface $d\mathbf{s}$ can be formed by two vectors, $d\mathbf{a}$ and $d\mathbf{b}$, and that a small element of volume dv is a parallelepiped formed by three vectors, $d\mathbf{a}$, $d\mathbf{b}$, and $d\mathbf{c}$, we can write the 2-form $\underset{(2)}{\psi}$ and the 3-form $\underset{(3)}{\theta}$ as

$$\underset{(2)}{\psi} = \underset{(2)}{\psi}(d\mathbf{a}, d\mathbf{b}) = \mathbf{B} \cdot [d\mathbf{a} \times d\mathbf{b}],$$
$$\underset{(3)}{\theta} = \underset{(3)}{\theta}(d\mathbf{a}, d\mathbf{b}, d\mathbf{c}) = div\mathbf{B}(d\mathbf{a}, d\mathbf{b}, d\mathbf{c}). \tag{A.4}$$

We have established also in Chapter 1 that all three forms are antisymmetric linear functions of their arguments (vectors):

$$\underset{(2)}{\psi}(d\mathbf{a}, d\mathbf{b}) = - \underset{(2)}{\psi}(d\mathbf{b}, d\mathbf{a}),$$
$$\underset{(3)}{\theta}(d\mathbf{a}, d\mathbf{b}, d\mathbf{c}) = - \underset{(3)}{\theta}(d\mathbf{b}, d\mathbf{a}, d\mathbf{c}), \quad \underset{(3)}{\theta}(d\mathbf{a}, d\mathbf{b}, d\mathbf{c}) = - \underset{(3)}{\theta}(d\mathbf{a}, d\mathbf{c}, d\mathbf{b}), \text{ etc.} \tag{A.5}$$

The simplest operation on the differential forms is addition. It is obvious that the addition of two antisymmetric linear forms is determined as a conventional summation of two functions. This operation satisfies the traditional commutative and associative laws, and the distributive laws with respect to multiplication by a scalar, which we will formulate below.

The multiplication of the differential forms requires introducing a special algebraic operation, called an *exterior product*, which will be discussed in detail in the next subsection.

A.1.2 EXTERIOR PRODUCT OF THE DIFFERENTIAL FORMS

The exterior product of the differential forms is introduced as a new linear form, which is obtained by two subsequent operations (see Chapter 1): 1) conventional multiplication of the original forms, and 2) antisymmetrization of this product.

For example, the exterior product of two 1-forms, $\varphi(d\mathbf{a})$ and $\chi(d\mathbf{b})$, is given by the formula:

$$\Phi(d\mathbf{a}, d\mathbf{b}) = \varphi(d\mathbf{a}) \wedge \chi(d\mathbf{b}) = \left[\varphi(d\mathbf{a}) \chi(d\mathbf{b}) - \varphi(d\mathbf{b}) \chi(d\mathbf{a}) \right]. \tag{A.6}$$

We use the symbol "wedge" ($\wedge$) to denote the exterior product operation. That is why it is often called a *wedge product*. It is easy to check that the new linear function, $\Phi(d\mathbf{a}, d\mathbf{b})$, is indeed an antisymmetric function.

Note that addition and exterior multiplication operations of 1-forms satisfy the following laws:
1) Commutative and associative laws of addition:

$$\varphi + \chi = \chi + \varphi \text{ and } \varphi + (\chi + \eta) = (\varphi + \chi) + \eta. \tag{A.7}$$

2) Anticommutative law of exterior multiplication of two 1-forms:

$$\varphi \wedge \chi = -\chi \wedge \varphi. \tag{A.8}$$

3) Distributive law of multiplication over addition:

$$\varphi \wedge (\chi + \eta) = \varphi \wedge \chi + \varphi \wedge \eta \text{ and } (\varphi + \chi) \wedge \eta = \varphi \wedge \eta + \chi \wedge \eta. \tag{A.9}$$

It comes immediately from the anticommutative law (A.8), that

$$\varphi \wedge \varphi = 0. \tag{A.10}$$

The exterior product of 1-form $\varphi = \varphi\,(d\mathbf{l})$ and 2-form $\psi\,(d\mathbf{a}, d\mathbf{b})$ is equal to:

$$\begin{aligned}\Omega = \varphi \wedge \psi = \{&\varphi\,(d\mathbf{l})\,\psi\,(d\mathbf{a}, d\mathbf{b}) + \varphi\,(d\mathbf{a})\,\psi\,(d\mathbf{b}, d\mathbf{l}) + \varphi\,(d\mathbf{b})\,\psi\,(d\mathbf{l}, d\mathbf{a}) \\ -\,&\varphi\,(d\mathbf{l})\,\psi\,(d\mathbf{b}, d\mathbf{a}) - \varphi\,(d\mathbf{a})\,\psi\,(d\mathbf{l}, d\mathbf{b}) - \varphi\,(d\mathbf{b})\,\psi\,(d\mathbf{a}, d\mathbf{l})\}.\end{aligned} \tag{A.11}$$

In a similar way we can calculate the exterior product of the 1-forms:

$$\begin{aligned}\Theta = \varphi \wedge \chi \wedge \eta \\ = \{&\varphi\,(d\mathbf{l})\,\chi\,(d\mathbf{a})\,\eta\,(d\mathbf{b}) + \varphi\,(d\mathbf{a})\,\chi\,(d\mathbf{b})\,\eta\,(d\mathbf{l}) + \varphi\,(d\mathbf{b})\,\chi\,(d\mathbf{l})\,\eta\,(d\mathbf{a}) \\ -\,&\varphi\,(d\mathbf{l})\,\chi\,(d\mathbf{b})\,\eta\,(d\mathbf{a}) - \varphi\,(d\mathbf{a})\,\chi\,(d\mathbf{l})\,\eta\,(d\mathbf{b}) - \varphi\,(d\mathbf{b})\,\chi\,(d\mathbf{a})\,\eta\,(d\mathbf{l})\}.\end{aligned} \tag{A.12}$$

We can see now that the exterior product of two 1-forms generates a 2-form, while the exterior product of three 1-forms produces a 3-form. The important fact is that any 2-form and any 3-form can be expressed as the exterior products of two 1-forms and three 1-forms respectively. We will prove this statement in the following sections.

A.1.3 BASIS OF DIFFERENTIAL FORMS

Let us apply the operation of the exterior product to the differential forms (A.1)–(A.4). Note first that, we can represent each of the vectors $d\mathbf{l}$, $d\mathbf{a}$, $d\mathbf{b}$, and $d\mathbf{c}$, in some Cartesian system of coordinates with the basis $(\mathbf{d}_x, \mathbf{d}_y, \mathbf{d}_z)$ as

$$\begin{aligned}d\mathbf{l} &= l_x dx \mathbf{d}_x + l_y dy \mathbf{d}_y + l_z dz \mathbf{d}_z, \\ d\mathbf{a} &= a_x dx \mathbf{d}_x + a_y dy \mathbf{d}_y + a_z dz \mathbf{d}_z, \\ d\mathbf{b} &= b_x dx \mathbf{d}_x + b_y dy \mathbf{d}_y + b_z dz \mathbf{d}_z,\end{aligned}$$

and

$$d\mathbf{c} = c_x dx \mathbf{d}_x + c_y dy \mathbf{d}_y + c_z dz \mathbf{d}_z. \tag{A.13}$$

Using these representations, we can express the differential forms as a linear combination of the differentials of the Cartesian coordinates, dx, dy, dz, where we can think of dx, dy, dz, as infinitesimal increments in the variables x, y, z.

Basis of differential 1-forms

Let us consider first the 1-form $\underset{(1)}{\varphi}$. According to Eqs. (A.1) and (A.13), we can calculate this 1-form as:

$$\underset{(1)}{\varphi} = \underset{(1)}{\varphi}(d\mathbf{l}) = \mathbf{B} \cdot d\mathbf{l} = \varphi_x dx + \varphi_y dy + \varphi_z dz, \tag{A.14}$$

where vector $\mathbf{B}$ has components (B_x, B_y, B_z), and $\varphi_\alpha = B_\alpha l_\alpha$, $\alpha = x, y, z$.

Representation (A.14) shows that the differentials, dx, dy, and dz, can be treated as the basis functions for 1-forms. Any 1-form can be expressed as a linear combination of the differentials with the coefficients, φ_x, φ_y, and φ_z, which are called the differential form *components*. In this sense, we have a complete analogy between the vectors and 1-forms. Both of these mathematical objects can be expressed as a linear combination of the basic objects (vector basis for the vectors, or a basis, formed by the basic forms for the differential forms).

The conventional geometric interpretation of a vector is a directed line segment. We can give a similar geometrical interpretation of the 1-form as a directed line segment determined by the components of the form, φ_x, φ_y, and φ_z. In particular, one can express a 1-form in a short way, using components, as

$$\underset{(1)}{\varphi} = \boldsymbol{\varphi} \cdot d\mathbf{r}, \tag{A.15}$$

where vector $\boldsymbol{\varphi}$ is formed by the components of the 1-form, and the components of vector $d\mathbf{r}$ are the differentials:

$$\boldsymbol{\varphi} = (\varphi_x, \varphi_y, \varphi_z), \ d\mathbf{r} = (dx, dy, dz).$$

Thus, conventional vectors and 1-forms have the same geometrical image. That is why a 1-form is often called a *co-vector*.

There may be some confusion about the notations used for the basis forms, dx, dy, and dz, introduced above. Indeed, the conventional meaning of the expressions dx, dy, and dz, is just a differential of the corresponding variables x, y, and z, respectively. However, expression (A.14) clearly demonstrates that these differentials can be treated as 1-forms. In order to emphasize this new meaning of the differential we may use, temporary, the following notations:

$$\underset{(1)}{\varphi}^{(x)} = dx, \ \underset{(1)}{\chi}^{(y)} = dy, \ \underset{(1)}{\eta}^{(z)} = dz. \tag{A.16}$$

The geometrical meaning of the basis 1-forms is simple and corresponds to their notations well: 1-form dx can be treated as a conventional vector $dx\mathbf{d}_x$, directed along the axis x, 1-form dy corresponds to a conventional vector $dy\mathbf{d}_y$, directed along the axis y, and 1-form dz can be described as a conventional vector $dz\mathbf{d}_z$, directed along the axis z.

Basis of differential 2-forms

According to the definition of the exterior product (A.6) and to the rules of exterior multiplication of 1-forms, (A.8), (A.9), we have two identities:

$$\left(a_y dy + a_z dz\right) \wedge \left(b_y dy + b_z dz\right) = 2a_{[y}b_{z]}dydz, \tag{A.17}$$

and

$$\left(a_y dy + a_z dz\right) \wedge \left(b_y dy + b_z dz\right) = 2a_{[y}b_{z]}dy \wedge dz. \tag{A.18}$$

From Eqs. (A.17) and (A.18), we can conclude that:

$$dy \wedge dz = dydz = ds_x. \tag{A.19}$$

A similar identity can be written for the products of other pairs of differentials:

$$dz \wedge dx = dzdx = ds_y, \ dx \wedge dy = dxdy = ds_z.$$

Therefore, the 2-form can be calculated as:

$$
\begin{aligned}
\underset{(2)}{\psi} = \underset{(2)}{\psi} \left(d\mathbf{a}, d\mathbf{b}\right) = \mathbf{B} \cdot [d\mathbf{a} \times d\mathbf{b}] &= \begin{vmatrix} B_x & B_y & B_z \\ a_x dx & a_y dy & a_z dz \\ b_x dx & b_y dy & b_z dz \end{vmatrix} \\
&= \psi_{yz} dydz + \psi_{zx} dzdx + \psi_{xy} dxdy \\
&= \psi_{yz} dy \wedge dz + \psi_{zx} dz \wedge dx + \psi_{xy} dx \wedge dy,
\end{aligned} \tag{A.20}
$$

where

$$\psi_{yz} = 2B_x a_{[y}b_{z]}, \ \psi_{zx} = 2B_y a_{[z}b_{x]}, \ \psi_{xy} = 2B_z a_{[x}b_{y]},$$

and square brackets around indices denote antisymmetrization defined by

$$a_{[y}b_{z]} = \frac{1}{2}\left[a_y b_z - a_z b_y\right], \ a_{[z}b_{x]} = \frac{1}{2}\left[a_z b_x - a_x b_z\right], \ a_{[x}b_{y]} = \frac{1}{2}\left[a_x b_y - a_y b_x\right].$$

The coefficients $\psi_{\alpha\beta}$ are called the differential 2-form *components*. They can be displayed in the matrix form as

$$\psi_{\alpha\beta} = \begin{bmatrix} 0 & \psi_{xy} & \psi_{xz} \\ -\psi_{xy} & 0 & \psi_{yz} \\ -\psi_{xz} & -\psi_{yz} & 0 \end{bmatrix},$$

which reflects the antisymmetric property of the 2-forms:

$$\psi_{\alpha\beta} = -\psi_{\beta\alpha}. \tag{A.21}$$

Eq. (A.20) shows that any 2-form can be presented as a linear combination of the exterior product of two 1-forms:

$$\underset{(2)}{\psi} = \underset{(2)}{\psi}\,(d\mathbf{a}, d\mathbf{b}) = \psi_{yz}ds_x + \psi_{zx}ds_y + \psi_{xy}ds_z$$

$$= \psi_{yz}dy \wedge dz + \psi_{zx}dz \wedge dx + \psi_{xy}dx \wedge dy. \tag{A.22}$$

Based on Eq. (A.22), we conclude that, the combination of the exterior products of differentials, $ds_x = dy \wedge dz$, $ds_y = dz \wedge dx$, and $ds_z = dx \wedge dy$, forms the basis of 2-forms. As in the case of 1-forms, we can express any 2-form $\underset{(2)}{\psi}$ as a linear combination of the basis 2-forms, with the coefficients, ψ_{yz}, ψ_{zx}, and ψ_{xy}. Every basis 2-form can be geometrically treated as an oriented parallelogram formed by the vectors $dy\mathbf{d}_y$ and $dz\mathbf{d}_z$, or by the vectors $dz\mathbf{d}_z$ and $dx\mathbf{d}_x$, or by the vectors $dx\mathbf{d}_x$ and $dy\mathbf{d}_y$, respectively (see Fig. 1.5). The linear combination of these parallelepipeds forms an oriented parallelogram $d\Sigma$ according to the rules of vector algebra:

$$d\Sigma = ds_x\mathbf{d}_x + ds_y\mathbf{d}_y + ds_z\mathbf{d}_z.$$

We can present Eq. (A.22) using the vector notations. Indeed, let us introduce a vector $\boldsymbol{\psi}$ with the scalar components equal to the components of the 2-form:

$$\boldsymbol{\psi} = \psi_{yz}\mathbf{d}_x + \psi_{zx}\mathbf{d}_y + \psi_{xy}\mathbf{d}_z.$$

Thus, we have from Eq. (A.22):

$$\underset{(2)}{\psi} = \boldsymbol{\psi} \cdot d\Sigma. \tag{A.23}$$

Basis of differential 3-forms

Repeating calculations similar to the above, for a 3-form we have:

$$\underset{(3)}{\theta}\,(d\mathbf{a}, d\mathbf{b}, d\mathbf{c}) = q(d\mathbf{a}, d\mathbf{b}, d\mathbf{c})$$

$$= q\begin{vmatrix} a_x dx & a_y dy & a_z dz \\ b_x dx & b_y dy & b_z dz \\ c_x dx & c_y dy & c_z dz \end{vmatrix} = 3!qa_{[x}b_yc_{z]}dxdydz, \tag{A.24}$$

where square brackets around indices denote antisymmetrization defined by

$$a_{[x}b_yc_{z]} = \frac{1}{3!}\left(a_xb_yc_z + a_yb_zc_x + a_zb_xc_y - a_xb_zc_y - a_yb_xc_z - a_zb_yc_x\right).$$

Note that the right-hand side of Eq. (A.24) can be expressed as a triple exterior product of 1-forms. Indeed, according to a definition of the exterior product (A.11),

$$\left(a_x dx + a_y dy + a_z dz\right) \wedge \left(b_x dx + b_y dy + b_z dz\right) \wedge \left(c_x dx + c_y dy + c_z dz\right)$$

$$= 3!a_{[x}b_yc_{z]}dx \wedge dy \wedge dz = 3!a_{[x}b_yc_{z]}dxdydz. \tag{A.25}$$

From formula (A.25) we can see that the combination

$$dx \wedge dy \wedge dz = dxdydz = dv, \tag{A.26}$$

is a 3-form itself. It has a simple geometrical representation as an oriented parallelepiped spanned over three vectors, $dx\mathbf{d}_x$, $dy\mathbf{d}_y$ and $dz\mathbf{d}_z$. The 3-form $dx \wedge dy \wedge dz$ is often called a *volume element*.

Substituting expression (A.26) back into formulas (A.24), we have

$$\underset{(3)}{\theta} (d\mathbf{a}, d\mathbf{b}, d\mathbf{c}) = \theta dx \wedge dy \wedge dz, \tag{A.27}$$

where $\theta = 3!qa_{[x}b_yc_{z]}$.

Thus, all differential forms in three-dimensional Euclidean space E_3 can be expressed as the linear combinations of the basis forms, dx, dy, and dz, or their exterior products. These representations are called the *canonical representations* for the differential forms. This result is summarized in the following table:

$$\text{0-forms} \quad : \quad \underset{(0)}{\varphi} = f, \tag{A.28}$$

$$\text{1-forms} \quad : \quad \underset{(1)}{\varphi} = \varphi_x dx + \varphi_y dy + \varphi_z dz = \boldsymbol{\varphi} \cdot d\mathbf{r}, \tag{A.29}$$

$$\text{2-forms} \quad : \quad \underset{(2)}{\psi} = \psi_{yz} dy \wedge dz + \psi_{zx} dz \wedge dx + \psi_{xy} dx \wedge dy = \boldsymbol{\psi} \cdot d\boldsymbol{\Sigma}, \tag{A.30}$$

$$\text{3-forms} \quad : \quad \underset{(3)}{\theta} = \theta dx \wedge dy \wedge dz = \theta dv. \tag{A.31}$$

Finally, we conclude that for any vector field $\mathbf{B}$ we can assign two differential forms: a 1-form, describing the work of the vector field, $\mathbf{B} \cdot d\mathbf{r}$, and a 2-form, describing the flux of the vector field, $\mathbf{B} \cdot d\boldsymbol{\Sigma}$. We have seen in Chapter 3 that these two forms, work and flux, represent the most important characteristics of the EM field.

A.2 DIFFERENTIAL FORMS IN MULTIDIMENSIONAL SPACES
A.2.1 EUCLIDEAN SPACE

Conventional physical space has three dimensions. Any point in this space can be represented by three Cartesian coordinates (x_1, x_2, x_3). The natural generalization of three dimensional (3-D) physical space is the n dimensional Euclidean space E_n (or R_n), which can be described as the set of all possible vectors of the order n:

$$\mathbf{a} = (a_1, a_2, a_3, ...a_n),$$

where the scalars $a_1, a_2, a_3, ...a_n$ are usually real numbers.

By analogy with the length of the vector in 3-D physical space, we can introduce a *norm of the vector* $\|\mathbf{a}\|$ as

$$\|\mathbf{a}\| = \sqrt{a_1^2 + a_2^2 + a_3^2 + ... + a_n^2}. \tag{A.32}$$

It is easy to check that the norm introduced above satisfies the conditions

$$\|\mathbf{a}\| > 0 \text{ if } \mathbf{a} \neq 0, \ \|\mathbf{a}\| = 0 \text{ if } \mathbf{a} = 0, \tag{A.33}$$

$$\|\lambda \mathbf{a}\| = |\lambda| \, \|\mathbf{a}\|, \tag{A.34}$$

$$\|\mathbf{a} + \mathbf{b}\| \leq \|\mathbf{a}\| + \|\mathbf{b}\|. \tag{A.35}$$

The last inequality is called a *triangle inequality*. In a general case of n dimensional Euclidean space, the triangular inequality comes from the Cauchy inequality, which we will discuss below.

We can introduce also an operation on two vectors, called the *inner (dot) product*, as follows:

$$\mathbf{a} \cdot \mathbf{b} = \sum_{i=1}^{n} a_i b_i. \tag{A.36}$$

Obviously, a norm can be determined as a square root of the dot product of the vector with itself:

$$\|\mathbf{a}\| = \sqrt{\mathbf{a} \cdot \mathbf{a}}. \tag{A.37}$$

By analogy with conventional 3-D physical space, we can say that the two vectors $\mathbf{a}$ and $\mathbf{b}$ are orthogonal if

$$\mathbf{a} \cdot \mathbf{b} = 0.$$

The following vectors play a similar role in the space E_n as the vectors of the Cartesian basis in 3-D space:

$$\mathbf{e}_1 = (1, 0, 0, \dots 0), \ \mathbf{e}_2 = (0, 1, 0, \dots 0), \ \mathbf{e}_3 = (0, 0, 1, \dots 0), \dots$$
$$\mathbf{e}_n = (0, 0, 0, \dots 1).$$

We will call these vectors $\mathbf{e}_1, \mathbf{e}_2, \dots \mathbf{e}_n$, *a basis* of Euclidean space. Any vector $\mathbf{a} \in E_n$ can be represented as a linear combination of the basis vectors

$$\mathbf{a} = a_1 \mathbf{e}_1 + a_2 \mathbf{e}_2 + \dots + a_n \mathbf{e}_n = \sum_{i=1}^{n} a_i \mathbf{e}_i, \tag{A.38}$$

where numbers $a_1, a_2, a_3, \dots a_n$ are the scalar components of the vector $\mathbf{a}$. Evidently

$$\mathbf{e}_i \cdot \mathbf{e}_k = 0; \ \text{if} \ i \neq k, \ \mathbf{e}_k \cdot \mathbf{e}_k = 1, \tag{A.39}$$
$$\mathbf{a} \cdot \mathbf{e}_i = a_i.$$

Using the dot product operation, we can prove the *Cauchy inequality:*

$$\mathbf{a} \cdot \mathbf{b} \leq \|\mathbf{a}\| \|\mathbf{b}\|, \tag{A.40}$$

which in scalar form can be written as

$$\left(\sum_{i=1}^{n} a_i b_i \right)^2 \leq \left(\sum_{i=1}^{n} a_i^2 \right) \left(\sum_{i=1}^{n} b_i^2 \right). \tag{A.41}$$

Proof. Let us introduce a nonnegative function $\varphi(x)$:

$$\varphi(x) = \sum_{i=1}^{n} (a_i x + b_i)^2 \geq 0.$$

Opening the brackets in the last equation, we obtain

$$\left(\sum_{i=1}^{n} a_i^2\right) x^2 + 2 \left(\sum_{i=1}^{n} a_i b_i\right) x + \sum_{i=1}^{n} b_i^2 \geq 0. \tag{A.42}$$

Inequality (A.42) means that the equation

$$\left(\sum_{i=1}^{n} a_i^2\right) x^2 + 2 \left(\sum_{i=1}^{n} a_i b_i\right) x + \sum_{i=1}^{n} b_i^2 = 0 \tag{A.43}$$

has only one real root, or no real roots at all, which is possible only if its discriminant is nonpositive:

$$\left(\sum_{i=1}^{n} a_i b_i\right)^2 - \left(\sum_{i=1}^{n} a_i^2\right)\left(\sum_{i=1}^{n} b_i^2\right) \leq 0. \qquad \square$$

Thus, one can introduce Cartesian coordinates in the space E_n formed by the basis vectors $\mathbf{e}_1, \mathbf{e}_2, \ldots\ldots\mathbf{e}_n$. Any point in the n-dimensional Euclidean space can be represented by n Cartesian co-ordinates $(x_1, x_2, x_3, \ldots..x_n)$.

A.2.2 DIFFERENTIAL FORMS IN EUCLIDEAN SPACE E_n

The concept of the differential forms, discussed in Chapter 1, can be extended to the multidimensional Euclidean space of multidimensional vectors, E_n. Let us introduce in the E_n an orthogonal system of coordinates, $x_1, x_2, \ldots..x_n$. In a general case, a differential form of degree p, or p-form, is a linear combination of the exterior products of the differentials:

$$\underset{(p)}{\Omega} = \sum_{i_1, \ldots i_p = 1}^{n} \varphi_{i_1, \ldots i_p} dx_{i_1} \wedge \ldots \wedge dx_{i_p}, \tag{A.44}$$

where $\varphi_{i_1, \ldots i_p}$ are the differentiable functions called the *components* of $\underset{(p)}{\Omega}$.

For example, a 0-form on E_n is simply a differentiable function of coordinates $f(x_1, x_2, \ldots..x_n)$. The 1-form can be expressed as

$$\underset{(1)}{\Omega} = \sum_{i_1=1}^{n} \varphi_{i_1} dx_{i_1} = \varphi_1 dx_1 + \varphi_2 dx_2 + \ldots + \varphi_n dx_n.$$

A 2-form is equal to:

$$\underset{(2)}{\Omega} = \sum_{i_1 i_2 = 1}^{n} \psi_{i_1 i_2} dx_{i_1} \wedge dx_{i_2}.$$

A general $(n-1)$-form can be written as

$$\underset{(n-1)}{\Omega} = \sum_{i=1}^{n} \chi_i dx_1 \wedge .. \wedge \widehat{dx_i} \wedge .. \wedge dx_n = \chi_1 dx_2 \wedge dx_3 \wedge .... \wedge dx_n +$$

$$+ \chi_2 dx_1 \wedge dx_3 \wedge .... \wedge dx_n + ... + \chi_n dx_1 \wedge dx_2 \wedge .... \wedge dx_{n-1}, \tag{A.45}$$

where a symbol "hat" above dx_i means that this term should be excluded from the product.

Finally, an n-form in the n-dimensional Euclidean space consists of just one term:

$$\underset{(n)}{\Omega} = \theta dx_1 \wedge dx_2 \wedge .... \wedge dx_n. \tag{A.46}$$

We have demonstrated above that in three-dimensional space the form $\underset{(3)}{\Omega}$ is proportional to the volume of the parallelepiped built on the corresponding vector arguments of this form. By analogy, an n-form in the n-dimensional Euclidean space is called a *volume form*.

We should note in the conclusion of this section that the exterior product of differential p-forms satisfies the *graded commutativity law*:

$$\underset{(k)}{\Omega} \wedge \underset{(l)}{\Psi} = (-1)^{kl} \underset{(l)}{\Psi} \wedge \underset{(k)}{\Omega}, \tag{A.47}$$

for all k-forms and all l-forms.

The proof of this statement can be obtained by using the canonical representations of the corresponding forms and by successively applying the alternating property of exterior multiplication (A.8) of two basic 1-forms, dx_i and dx_j.

A.2.3 DIFFERENTIAL FORMS IN MINKOWSKIAN SPACE M_4

An important example of multidimensional space is four-dimensional Minkowskian space M_4 with three conventional spatial coordinates, $x_1 = x$, $x_2 = y$, and $x_3 = z$, and a fourth coordinate, x_4, proportional to time: $x_4 = \tau = ct$, where c is a speed of light equal to

$$c = 1/\sqrt{\mu_0 \varepsilon_0},$$

and ε_0 and μ_0 are the dielectric constant and magnetic permeability of the free space, respectively. The Minkowskian space is a suitable mathematical model of our physical space-time world.

We can introduce the following forms in the Minkowskian space M_4.

A 0-form is a differentiable function of the spatial and time coordinates:

$$\underset{(0)}{\Omega} = f(x_1, x_2, x_3, \tau).$$

A 1-form is written as

$$\underset{(1)}{\Omega} = \varphi_1 dx_1 + \varphi_2 dx_2 + \varphi_3 dx_3 + \varphi_\tau d\tau. \tag{A.48}$$

This form is characterized by 4 coefficients which are the differentiable functions of the spatial coordinates and time:

$$\varphi_i = \varphi_i (x_1, x_2, x_3, \tau), \; i = 1, 2, 3; \; \varphi_\tau = \varphi_\tau (x_1, x_2, x_3, \tau).$$

A 2-form has six coefficients:

$$\underset{(2)}{\Omega} = \sum_{i<j}^{6} \psi_{ij} dx_i \wedge dx_j = \psi_{12} dx_1 \wedge dx_2 +$$

$$+ \psi_{23} dx_2 \wedge dx_3 + \psi_{31} dx_3 \wedge dx_1 + \psi_{14} dx_1 \wedge d\tau + \psi_{24} dx_2 \wedge d\tau + \psi_{34} dx_3 \wedge d\tau. \tag{A.49}$$

A 3-form in the space M_4, according to definition (A.49), has four coefficients again:

$$\underset{(3)}{\Omega} = \chi_1 dx_2 \wedge dx_3 \wedge d\tau + \chi_2 dx_1 \wedge dx_3 \wedge d\tau + \chi_3 dx_1 \wedge dx_2 \wedge d\tau + \chi_\tau dx_1 \wedge dx_2 \wedge dx_3. \tag{A.50}$$

Finally, a 4-form in M_4 is a volume form equal to

$$\underset{(4)}{\Omega} = \theta dx_1 \wedge dx_2 \wedge dx_3 \wedge d\tau. \tag{A.51}$$

Simple analysis of Eqs. (A.48)–(A.51) shows that a form in the Minkowskian space M_4 can be split into its spatial and temporal components.

For example, 1-form $\underset{(1)}{\Omega}$ can be split in spatial 1-form $\underset{(1)}{\varphi}$ and a temporal 1-form $\underset{(1)}{\Theta} = f d\tau$:

$$\underset{(1)}{\Omega} = \underset{(1)}{\varphi} + \underset{(1)}{\Theta} = \boldsymbol{\varphi} \cdot d\mathbf{r} + f d\tau, \tag{A.52}$$

where

$$\underset{(1)}{\varphi} = \varphi_1 dx_1 + \varphi_2 dx_2 + \varphi_3 dx_3 = \boldsymbol{\varphi} \cdot d\mathbf{r}, \; f = \varphi_\tau (x_1, x_2, x_3, \tau).$$

A 2-form can be represented as

$$\underset{(2)}{\Omega} = \underset{(2)}{\psi} + \underset{(1)}{\eta} \wedge d\tau = \boldsymbol{\psi} \cdot d\boldsymbol{\Sigma} + (\boldsymbol{\eta} \cdot d\mathbf{r}) \wedge d\tau, \tag{A.53}$$

where

$$\underset{(2)}{\psi} = \psi_{12} dx_1 \wedge dx_2 + \psi_{23} dx_2 \wedge dx_3 + \psi_{31} dx_3 \wedge dx_1 = \boldsymbol{\psi} \cdot d\boldsymbol{\Sigma},$$

and

$$\underset{(1)}{\eta} = \psi_{14} dx_1 + \psi_{24} dx_2 + \psi_{34} dx_3 = \boldsymbol{\eta} \cdot d\mathbf{r}$$

A 3-form $\underset{(3)}{\Omega}$ can be split as well:

$$\underset{(3)}{\Omega} = \chi_\tau dx_1 \wedge dx_2 \wedge dx_3 + (\chi_1 dx_2 \wedge dx_3 + \chi_2 dx_1 \wedge dx_3 + \chi_3 dx_1 \wedge dx_2) \wedge d\tau$$

$$= h dv + (\boldsymbol{\chi} \cdot d\boldsymbol{\Sigma}) \wedge d\tau, \tag{A.54}$$

where

$$\boldsymbol{\chi} \cdot d\boldsymbol{\Sigma} = \underset{(2)}{\chi} = \chi_1 dx_2 \wedge dx_3 + \chi_2 dx_1 \wedge dx_3 + \chi_3 dx_1 \wedge dx_2,$$
$$h = \chi_\varphi (x_1, x_2, x_3, \tau), \ dv = dx_1 \wedge dx_2 \wedge dx.$$

Finally, a 4-form can be written as

$$\underset{(4)}{\Omega} = \theta dx_1 \wedge dx_2 \wedge dx_3 \wedge d\tau = \theta dv \wedge d\tau. \tag{A.55}$$

In summary, we can write the p-forms in the four-dimensional Minkowskian space M_4, using the three-dimensional vector notations:

$$
\begin{array}{lll}
\text{0-forms} & : & \underset{(0)}{\Omega} = f, \\[2mm]
\text{1-forms} & : & \underset{(1)}{\Omega} = \boldsymbol{\varphi} \cdot d\mathbf{r} + f d\tau, \\[2mm]
\text{2-forms} & : & \underset{(2)}{\Omega} = \boldsymbol{\psi} \cdot d\boldsymbol{\Sigma} + (\boldsymbol{\eta} \cdot d\mathbf{r}) \wedge d\tau, \\[2mm]
\text{3-forms} & : & \underset{(3)}{\Omega} = h dv + (\boldsymbol{\chi} \cdot d\boldsymbol{\Sigma}) \wedge d\tau, \\[2mm]
\text{4-forms} & : & \underset{(4)}{\Omega} = \theta dv \wedge d\tau.
\end{array}
\tag{A.56}
$$

The last formulas clearly show that 0-forms and 4-forms in the space M_4 are defined by one scalar function, f and θ, respectively. The 0-form is nothing else but a scalar function of the spatial and time coordinates, while the 4-form can be treated as a volume density of the source distribution in the space-time M_4.

The 1-forms and the 3-forms are determined by one scalar and one vector functions, $(f, \boldsymbol{\varphi})$ and $(h, \boldsymbol{\chi})$, respectively. The 1-form can be treated as an elementary work, $dW = \boldsymbol{\varphi} \cdot d\mathbf{r}$, of the vector field $\boldsymbol{\varphi}$ along an infinitesimally small element of spatial curve $d\mathbf{r}$ plus a time differential of a scalar field, $f d\tau$.

The 3-form is a combination of an elementary source, $h dv$, within an infinitesimally small element of volume dv and a time differential of the elementary scalar flux, $dF_\chi^{d\Sigma} = \boldsymbol{\chi} \cdot d\boldsymbol{\Sigma}$, of the vector field $\boldsymbol{\chi}$ through an infinitesimally small vector element of surface $d\boldsymbol{\Sigma}$.

The 2-form in the four-dimensional space is defined by two vector functions, $\boldsymbol{\psi}$ and $\boldsymbol{\eta}$. It is a super-position of an elementary scalar flux, $dF_\psi^{d\Sigma} = \boldsymbol{\psi} \cdot d\boldsymbol{\Sigma}$, of the vector field $\boldsymbol{\psi}$ through an infinitesimally small vector element of surface $d\boldsymbol{\Sigma}$, and a time differential of the elementary work, $dW = \boldsymbol{\eta} \cdot d\mathbf{r}$, of the vector field $\boldsymbol{\eta}$ along an infinitesimally small element of spatial curve $d\mathbf{r}$.

Thus, the 1-, 2-, and 3-forms in the four-dimensional Minkowskian space M_4 can be expressed as a linear combination of the scalar flux and work and/or their time differentials. Notably, it is shown in

Chapter 3 that the scalar flux and work represent the key characteristics of the electromagnetic field, which is the main subject of this text.

Finally, the 0-form is a function, and the 4-form is the volume and time differential of a scalar function.

CALCULUS OF DIFFERENTIAL FORMS

CONTENTS

B.1 EXTERIOR DIFFERENTIATION OF THE FORMS

In the beginning of Chapter 1 we introduced a physical field as any physical value which is a function of the observation point. We have also noticed that physical fields can be characterized by different mathematical objects. For example, we can consider a field formed by a spatial distribution of the p-forms.

Definition 44. We say that we have *a p-form field* $\Omega\,(\mathbf{r})$ in the Euclidean space E_n, if, for any point $\mathbf{r} = (x_1,\ x_2, ...x_n)$ from E_n, one specific p-form $\Omega\,(\mathbf{r})$ is determined by the following expression:

$$\Omega\,(\mathbf{r}) = \underset{(p)}{\Omega}\,(\mathbf{r}) = \sum_{i_1,...i_p=1}^{n} a_{i_1,...i_p}\,(\mathbf{r})\ dx_{i_1} \wedge .... \wedge dx_{i_p}, \tag{B.1}$$

where all components $a_{i_1,...i_p}$ are the differentiable functions of the coordinates:

$$a_{i_1,...i_p}\,(\mathbf{r}) = a_{i_1,...i_p}\,(x_1,\ x_2, ...x_n)\,.$$

In the case of the vector field theory, we have introduced the rules of the vector differential operations on these fields. However, those rules were strictly defined for three-dimensional space only. The advantage of the differential form theory is that we can introduce the differential operations for a p-form field defined in a multidimensional space. The remarkable property of this operation is that, in the case of three-dimensional space, it reduces to the conventional vector differential operations.

B.1.1 EXTERIOR DIFFERENTIAL OPERATOR IN MULTIDIMENSIONAL SPACE E_n

Let us consider a 0-form $\underset{(0)}{\Omega} = f(\mathbf{r})$. The differential operator d operating on a scalar function $f(\mathbf{r})$ is defined as the following 1-form:

$$df = \sum_{i=1}^{n} \frac{\partial f}{\partial x_i} dx_i. \tag{B.2}$$

Thus, operator d is similar to the conventional differential operator applied to the function of many variables.

However, we treat the result of this operator application as a 1-form, $\underset{(0)}{\Omega} = df$, with the components given by the partial derivatives, $\partial f / \partial x_i$. Obviously, this operation satisfies the Leibniz rule (or chain rule), if we apply it to the product of two functions:

$$d(fg) = fdg + gdf.$$

We can now determine the differential operation for a p-form according to the formula:

$$\underset{(p)}{d\,\Omega} = \sum_{i_1,\dots i_p = 1}^{n} da_{i_1,\dots i_p} \wedge dx_{i_1} \wedge \dots \wedge dx_{i_p}, \tag{B.3}$$

where the differential of the scalar components $a_{i_1,\dots i_p}$ of the p-form is calculated according to the rule (B.2).

The operation described by Eq. (B.3) is called *exterior differentiation*.

The exterior differential has the following properties.

(i) Differential operator d is a linear operator:

$$d\left(c_1 \underset{(p)}{\Omega} + c_2 \underset{(p)}{\Psi}\right) = c_1 d\underset{(p)}{\Omega} + c_2 d\underset{(p)}{\Psi}, \tag{B.4}$$

where c_1 and c_2 are some scalar coefficients.

(ii) Differential operator d satisfies a generalized Leibniz rule:

$$d\left(\underset{(p)}{\Omega} \wedge \underset{(q)}{\Theta}\right) = d\underset{(p)}{\Omega} \wedge \underset{(q)}{\Theta} + (-1)^p \underset{(p)}{\Omega} \wedge d\underset{(q)}{\Theta}. \tag{B.5}$$

(iii) Double differential operator d is always equal to zero for any p-form:

$$d\left(d\underset{(p)}{\Omega}\right) = 0. \tag{B.6}$$

The proof of properties (i) and (ii) is straightforward, and we leave this to the reader. The property (iii) of the exterior differentiation operator seems to be very unusual from the first look. However, it can be easily proved as well.

Proof of property (iii). According to definition (B.3), we have

$$d\left(d\underset{(p)}{\Omega}\right) = d\left(\sum_{i_1,\ldots i_p=1}^{n} da_{i_1,\ldots i_p} \wedge dx_{i_1} \wedge \ldots \wedge dx_{i_p}\right),\tag{B.7}$$

where the differential $da_{i_1,\ldots i_p}$ is determined by expression (B.2):

$$da_{i_1,\ldots i_p} = \sum_{i=1}^{n} \frac{\partial a_{i_1,\ldots i_p}}{\partial x_i} dx_i.\tag{B.8}$$

Substituting (B.8) back into (B.7), and applying the rule (B.2) again, we find:

$$d\left(d\underset{(p)}{\Omega}\right) = \sum_{i_1,\ldots i_p=1}^{n} \left[\sum_{i=1}^{n}\sum_{j=1}^{n} \frac{\partial^2 a_{i_1,\ldots i_p}}{\partial x_i \partial x_j} dx_j \wedge dx_i\right] \wedge dx_{i_1} \wedge \ldots \wedge dx_{i_p}.\tag{B.9}$$

Note that the term in the square brackets is equal to zero,

$$\sum_{i=1}^{n}\sum_{j=1}^{n} \frac{\partial^2 a_{i_1,\ldots i_p}}{\partial x_i \partial x_j} dx_j \wedge dx_i = 0,$$

because for the differentiable functions the second order partial derivatives are equal,

$$\frac{\partial^2 a_{i_1,\ldots i_p}}{\partial x_i \partial x_j} = \frac{\partial^2 a_{i_1,\ldots i_p}}{\partial x_j \partial x_i},$$

while the exterior product of two differentials is anticommutative,

$$dx_j \wedge dx_i = -dx_i \wedge dx_j.$$

Hence,

$$d\left(d\underset{(p)}{\Omega}\right) = 0. \qquad\qquad \square$$

We will give the following definitions.

Definition 45. We say that the differential p-form $\Omega(\mathbf{r})$ is closed if $d\Omega(\mathbf{r}) = 0$.

Definition 46. A differential p-form $\Psi(\mathbf{r})$ is exact if there exists a $(p-1)$-form $\Phi(\mathbf{r})$ such that $\Psi(\mathbf{r}) = d\Phi(\mathbf{r})$.

Note that, from property (iii) of the exterior differential operator, it follows immediately that every exact form is closed. This simple fact is called *Poincare's lemma*.

The inverse statement of Poincare's lemma is given by the following theorem.

Theorem 47 (de Rham's theorem). *If $\underset{(p)}{\Omega}$ is a p-form $(1 \leq p < n)$ in multidimensional space E_n and $d\underset{(p)}{\Omega} = 0$, there exist $(p-1)$-form $\underset{(p-1)}{\Omega}$ with the property that $\underset{(p)}{\Omega} = d\underset{(p-1)}{\Omega}$.*

B.1.2 EXTERIOR DIFFERENTIAL OPERATOR IN FOUR-DIMENSIONAL SPACE M_4

In four-dimensional Minkowskian space the exterior differential operator $d = d_{M_4}$ can be formally written as a 1-form:

$$d_{M_4} = dx\frac{\partial}{\partial x} + dy\frac{\partial}{\partial y} + dz\frac{\partial}{\partial z} + d\tau\frac{\partial}{\partial \tau} = d_{E_3} + d\tau\frac{\partial}{\partial \tau}. \tag{B.10}$$

Applying this operator to the 0-form field, $f(\mathbf{r}, t)$, which is a scalar field in the space M_4, we have:

$$df = d_{M_4}f = d_{E_3}f + d\tau\frac{\partial}{\partial \tau}f$$

$$= grad\, f \cdot d\mathbf{r} + d\tau\frac{\partial}{\partial \tau}f. \tag{B.11}$$

The exterior differentiation of a 1-form field, $\underset{(1)}{\Omega} = \boldsymbol{\varphi} \cdot d\mathbf{r} + f\, d\tau$, is calculated as:

$$d\underset{(1)}{\Omega} = d_{M_4} \wedge \underset{(1)}{\Omega} = \left(d_{E_3} + d\tau\frac{\partial}{\partial \tau}\right) \wedge (\boldsymbol{\varphi} \cdot d\mathbf{r} + f\, d\tau)$$

$$= d_{E_3} \wedge (\boldsymbol{\varphi} \cdot d\mathbf{r}) + d\tau \wedge \left(\frac{\partial \boldsymbol{\varphi}}{\partial t} \cdot d\mathbf{r}\right) + d_{E_3}f \wedge d\tau, \tag{B.12}$$

where we use the linear property (i) of the d operator.

Note that, according to Eq. (1.81) we have:

$$d_{E_3} \wedge (\boldsymbol{\varphi} \cdot d\mathbf{r}) = curl\,\boldsymbol{\varphi} \cdot d\boldsymbol{\Sigma}$$

and

$$d\underset{(1)}{\Omega} = curl\,\boldsymbol{\varphi} \cdot d\boldsymbol{\Sigma} + d\tau \wedge \left(\frac{\partial \boldsymbol{\varphi}}{\partial t} \cdot d\mathbf{r}\right) + (grad\, f \cdot d\mathbf{r}) \wedge d\tau$$

$$= curl\,\boldsymbol{\varphi} \cdot d\boldsymbol{\Sigma} + d\tau \wedge \left(\frac{\partial \boldsymbol{\varphi}}{\partial t} - grad\, f\right) \cdot d\mathbf{r}, \tag{B.13}$$

where we took into account the anticommutative law (A.8), according to which

$$(grad\, f \cdot d\mathbf{r}) \wedge d\tau = -d\tau \wedge (grad\, f \cdot d\mathbf{r}),$$

because $(grad\, f \cdot d\mathbf{r})$ and $d\tau$ are 1-forms.

In a similar way we can calculate the exterior derivative of the 2-form field:

$$d\underset{(2)}{\Omega} = d_{M_4} \wedge \underset{(2)}{\Omega} = \left(d_{E_3} + d\tau\frac{\partial}{\partial \tau}\right) \wedge \left[\boldsymbol{\psi} \cdot d\boldsymbol{\Sigma} + (\boldsymbol{\eta} \cdot d\mathbf{r}) \wedge d\tau\right]$$

$$= d_{E_3} \wedge \left[\boldsymbol{\psi} \cdot d\boldsymbol{\Sigma} + (\boldsymbol{\eta} \cdot d\mathbf{r}) \wedge d\tau\right] + d\tau\frac{\partial}{\partial \tau} \wedge \left[\boldsymbol{\psi} \cdot d\boldsymbol{\Sigma} + (\boldsymbol{\eta} \cdot d\mathbf{r}) \wedge d\tau\right]$$

$$= d_{E_3} \wedge \boldsymbol{\psi} \cdot d\boldsymbol{\Sigma} + \left[d_{E_3} \wedge (\boldsymbol{\eta} \cdot d\mathbf{r})\right] \wedge d\tau + d\tau\frac{\partial}{\partial \tau} \wedge (\boldsymbol{\psi} \cdot d\boldsymbol{\Sigma}).$$

According to Eqs. (1.81) and (1.82),

$$d_{E_3} \wedge \boldsymbol{\psi} \cdot d\boldsymbol{\Sigma} = (div\boldsymbol{\psi}) \, dv \text{ and } d_{E_3} \wedge (\boldsymbol{\eta} \cdot d\mathbf{r}) = curl\boldsymbol{\eta} \cdot d\boldsymbol{\Sigma}.$$

Therefore, we finally have

$$d \underset{(2)}{\Omega} = d_{M_4} \wedge \underset{(2)}{\Omega} =$$

$$= (div\boldsymbol{\psi}) \, dv + (curl\boldsymbol{\eta} \cdot d\boldsymbol{\Sigma}) \wedge d\tau + d\tau \wedge \left(\frac{\partial}{\partial \tau} \boldsymbol{\psi} \cdot d\boldsymbol{\Sigma} \right)$$

$$= (div\boldsymbol{\psi}) \, dv + d\tau \wedge \left(\frac{\partial}{\partial \tau} \boldsymbol{\psi} + curl\boldsymbol{\eta} \right) \cdot d\boldsymbol{\Sigma}, \tag{B.14}$$

where we took into account the graded commutativity law (A.47), according to which

$$(curl\boldsymbol{\eta} \cdot d\boldsymbol{\Sigma}) \wedge d\tau = (-1)^{2 \times 1} d\tau \wedge (curl\boldsymbol{\eta} \cdot d\boldsymbol{\Sigma}) = d\tau \wedge (curl\boldsymbol{\eta} \cdot d\boldsymbol{\Sigma}),$$

because $(curl\boldsymbol{\eta} \cdot d\boldsymbol{\Sigma})$ is a 2-form, and $d\tau$ is a 1-form.

For an exterior differential of the 3-form in the Minkowskian space, taking into account Eq. (1.82), we find:

$$d \underset{(3)}{\Omega} = d_{M_4} \wedge \underset{(3)}{\Omega} = \left(d_{E_3} + d\tau \frac{\partial}{\partial \tau} \right) \wedge \left[hdv + (\boldsymbol{\chi} \cdot d\boldsymbol{\Sigma}) \wedge d\tau \right]$$

$$= d_{E_3} \wedge (\boldsymbol{\chi} \cdot d\boldsymbol{\Sigma}) \wedge d\tau + d\tau \frac{\partial}{\partial \tau} \wedge hdv$$

$$= (div\boldsymbol{\psi}) \, dv \wedge d\tau + d\tau \wedge \frac{\partial}{\partial \tau} hdv = d\tau \wedge \left[\frac{\partial}{\partial \tau} h - div\boldsymbol{\psi} \right] dv. \tag{B.15}$$

In the last formula we took into account the graded commutativity law (A.47), according to which

$$(div\boldsymbol{\psi}) \, dv \wedge d\tau = (-1)^{3 \times 1} d\tau \wedge (div\boldsymbol{\psi}) \, dv = -d\tau \wedge (div\boldsymbol{\psi}) \, dv,$$

because $(div\boldsymbol{\psi}) \, dv$ is a 3-form, and $d\tau$ is a 1-form.

Finally, it is evident based on the definition that the exterior derivative of the 4-form in a four-dimensional space is just zero:

$$d \underset{(4)}{\Omega} = d_{M_4} \wedge \underset{(4)}{\Omega} = \left(d_{E_3} + d\tau \frac{\partial}{\partial \tau} \right) \wedge (\theta dv \wedge d\tau) = 0.$$

For convenience, we summarize these results in the following table:

$$\text{0-forms} \quad : \quad d_{M_4} \underset{(0)}{\Omega} = grad f \cdot d\mathbf{r} + d\tau \frac{\partial}{\partial \tau} f \tag{B.16}$$

$$\text{1-forms} \quad : \quad d_{M_4} \underset{(1)}{\Omega} = curl\boldsymbol{\varphi} \cdot d\boldsymbol{\Sigma} + d\tau \wedge \left(\frac{\partial \boldsymbol{\varphi}}{\partial t} - grad f \right) \cdot d\mathbf{r}, \tag{B.17}$$

$$\text{2-forms} \quad : \quad d_{M_4} \underset{(2)}{\Omega} = (div\boldsymbol{\psi}) \, dv + d\tau \wedge \left(\frac{\partial}{\partial \tau} \boldsymbol{\psi} + curl\boldsymbol{\eta} \right) \cdot d\boldsymbol{\Sigma}, \tag{B.18}$$

$$\text{3-forms} \quad : \quad d_{M_4} \underset{(3)}{\Omega} = d\tau \wedge \left[\frac{\partial}{\partial \tau} h - div\boldsymbol{\psi} \right] dv, \tag{B.19}$$

$$\text{4-forms} \quad : \quad d_{M_4} \underset{(4)}{\Omega} = 0. \tag{B.20}$$

Finally, we will present the same equations, (B.16) through (B.20), in a way, which is more convenient for application of these formulas in field theory. We introduce the arbitrary differentiable scalar functions $U(\mathbf{r}, \tau)$ and $q(\mathbf{r}, \tau)$ and the vector functions $\mathbf{A}(\mathbf{r}, \tau)$, $\mathbf{H}(\mathbf{r}, \tau)$, $\mathbf{D}(\mathbf{r}, \tau)$, and $\mathbf{j}(\mathbf{r}, \tau)$, in the Minkowskian space, M_4. Using these functions, we can define differential forms of five different orders in the four-dimensional space M_4. According to Eq. (A.56), these forms can be expressed using the three-dimensional vector notations as:

$$\text{0-forms} \quad : \quad \underset{(0)}{\Omega} = U, \tag{B.21}$$

$$\text{1-forms} \quad : \quad \underset{(1)}{\Omega} = \mathbf{A} \cdot d\mathbf{r} - U d\tau, \tag{B.22}$$

$$\text{2-forms} \quad : \quad \underset{(2)}{\Omega} = \mathbf{D} \cdot d\boldsymbol{\Sigma} - (\mathbf{H} \cdot d\mathbf{r}) \wedge d\tau, \tag{B.23}$$

$$\text{3-forms} \quad : \quad \underset{(3)}{\Omega} = q dv - (\mathbf{j} \cdot d\boldsymbol{\Sigma}) \wedge d\tau, \tag{B.24}$$

$$\text{4-forms} \quad : \quad \underset{(4)}{\Omega} = q dv \wedge d\tau. \tag{B.25}$$

Note that we use the negative sign in the second term of Eqs. (B.23) and (B.24) in order to have a structure of the differential form equations similar to the Maxwell's equations (see Chapters 2 and 3).

Using these notations, we can rewrite expressions (B.16) through (B.20) for the exterior derivatives of these forms as

$$\text{0-forms} \quad : \quad d_{M_4} \underset{(0)}{\Omega} = \underset{(1)}{\Phi} = gradU \cdot d\mathbf{r} + \frac{\partial}{\partial t} U d\tau, \tag{B.26}$$

$$\text{1-forms} \quad : \quad d_{M_4} \underset{(1)}{\Omega} = \underset{(2)}{\Phi} = curl\mathbf{A} \cdot d\boldsymbol{\Sigma} - \left(gradU + \frac{\partial \mathbf{A}}{\partial t} \right) \cdot d\mathbf{r} \wedge d\tau, \tag{B.27}$$

$$\text{2-forms} \quad : \quad d_{M_4} \underset{(2)}{\Omega} = \underset{(3)}{\Phi} = (div\mathbf{D}) \, dv + \left(\frac{\partial}{\partial t} \mathbf{D} - curl\mathbf{H} \right) \cdot d\boldsymbol{\Sigma} \wedge d\tau, \tag{B.28}$$

$$\text{3-forms} \quad : \quad d_{M_4} \underset{(3)}{\Omega} = \underset{(4)}{\Phi} = - \left[div\mathbf{j} + \frac{\partial}{\partial \tau} q \right] dv \wedge d\tau \tag{B.29}$$

$$\text{4-forms} \quad : \quad d_{M_4} \underset{(4)}{\Omega} = 0. \tag{B.30}$$

Eqs. (B.26) through (B.30) constitute the fundamental system of differential form equations in the Minkowskian space, M_4.

B.2 INTEGRATION OF THE FORMS
B.2.1 THREE-DIMENSIONAL SPACE E_3

We begin our analysis of the basic rules of integration with the differential forms in three-dimensional Euclidean space, E_3. We can recall that 1-, 2-, and 3-forms were introduced as differential expressions, which were integrated over a curve L, surface S, or volume D, respectively.

Therefore, according to Eqs. (1.69), (1.70), and (1.71), we can introduce a linear integral of a 1-form, a surface integral of a 2-form, and a volume integral of a 3-form as:

$$\int_{L\ (1)} \varphi = \int_L \left(\varphi_x dx + \varphi_y dy + \varphi_z dz \right) = \int_L \boldsymbol{\varphi} \cdot d\mathbf{r}, \tag{B.31}$$

$$\iint_{S\ (2)} \psi = \iint_S \left(\psi_{yz} dy \wedge dz + \psi_{zx} dz \wedge dx + \psi_{xy} dx \wedge dy \right) = \iint_S \boldsymbol{\psi} \cdot d\boldsymbol{\Sigma}, \tag{B.32}$$

$$\iiint_{D\ (3)} \theta = \iiint_D \theta dx \wedge dy \wedge dz = \iiint_D \theta dv. \tag{B.33}$$

Let us assume that we are given an exact 1-form,

$$\underset{(1)}{\Omega} = d_{E_3} f, \tag{B.34}$$

where $f = f(\mathbf{r})$ is a scalar field. Substituting Eq. (1.80) into (B.34) and integrating over a curve L, we have:

$$\int_{L\ (1)} \Omega = \int_L d_{E_3} f = \int_L grad f(\mathbf{r}) \cdot d\mathbf{r} = f(\mathbf{r}_B) - f(\mathbf{r}_A), \tag{B.35}$$

where $\mathbf{r}_A$ and $\mathbf{r}_B$ are two end points of the curve L.

We assume also that the exact 2-form is equal to

$$\underset{(2)}{\Omega} = d_{E_3} \wedge \underset{(1)}{\varphi} = d_{E_3} \wedge (\boldsymbol{\varphi} \cdot d\mathbf{r}).$$

Integrating this exact 2-form over the surface S according to formula (B.32), we find

$$\iint_{S\ (2)} \Omega = \iint_S d_{E_3} \wedge \underset{(1)}{\varphi} = \iint_S curl\boldsymbol{\varphi} \cdot d\boldsymbol{\Sigma}. \tag{B.36}$$

According to Stoke's theorem of vector calculus (1.44), the scalar flux of the curl of the vector field $\boldsymbol{\varphi}$ through an open surface S is equal to the circulation of this field along the close boundary L of the surface, where the orientations of the curve L and surface S are selected based on the standard convention illustrated in Fig. 1.4:

$$\iint_S curl\boldsymbol{\varphi} \cdot d\boldsymbol{\Sigma} = \int_L \boldsymbol{\varphi} \cdot d\mathbf{r} = \int_{L\ (1)} \varphi . \tag{B.37}$$

Substituting Eq. (B.37) into (B.36), we have:

$$\iint_S d_{E_3} \wedge \underset{(1)}{\varphi} = \int_L \underset{(1)}{\varphi} \,. \tag{B.38}$$

Let us consider now the exact 3-form equal to:

$$\underset{(3)}{\Omega} = d_{E_3} \wedge \underset{(2)}{\psi} = d_{E_3} \wedge (\boldsymbol{\psi} \cdot d\boldsymbol{\Sigma}) \,. \tag{B.39}$$

The volume integral of this 3-form can be calculated, using the Gauss's theorem (1.38), as follows:

$$\iiint_D \underset{(3)}{\Omega} = \iiint_D d_{E_3} \wedge \underset{(2)}{\psi} = \iiint_D d_{E_3} \wedge (\boldsymbol{\psi} \cdot d\boldsymbol{\Sigma})$$

$$= \iiint_D (div\boldsymbol{\psi}) \, dv = \iint_S \boldsymbol{\psi} \cdot d\boldsymbol{\Sigma} = \iint_{S\,(2)} \psi \,, \tag{B.40}$$

where volume D is enclosed by the surface S, and the positive normal to S according to a standard rule is oriented outside the volume.

We can write all three equations, (B.35), (B.38), and (B.40), in a unified symbolic notations, using the language of the differential forms:

$$\int_{C_k} d_{E_3} \wedge \underset{(k)}{\Omega} = \int_{\partial C_k} \underset{(k-1)}{\Omega} \,, \ k = 1, 2, 3; \tag{B.41}$$

where C_3 denotes volume D, C_2 denotes Surface S, and C_1 denotes curve L, while $\int_{C_k}$ stands for the volume integral ($k = 3$), surface integral ($k = 2$), or linear integral ($k = 1$), respectively. We use a standard notation of multidimensional calculus, ∂C_k, for a boundary of the geometrical element C_k. For example, ∂C_3 denotes an oriented (according to the standard rule discussed above) surface, S, of the volume, D. The element ∂C_2 denotes an oriented (according to the standard rule discussed above) boundary line, L, of the surface, S. The element ∂C_1 is formed by two end points, $\mathbf{r}_A$ and $\mathbf{r}_B$, of the curve L.

Thus, formula (B.41) combines in one equation all three fundamental theorems of vector field integration: the work Theorem 1.1, and the Stokes's and Gauss's theorems, Eqs. (1.44) and (1.38). In other words, Eq. (B.41) combines together the properties of the vector field work, and scalar and vector fluxes. This formula is often referred to as a Stokes's theorem for the differential forms. The most important fact is that Stokes's theorem (B.41) can be naturally extended to multidimensional spaces, thus allowing us to develop a multidimensional analogue of the fundamental integral theorems of vector calculus.

B.2.2 BEYOND THREE-DIMENSIONAL SPACE

Consider now the Euclidean space E_n. A general differential $(p-1)$-form in space E_n is defined by Eq. (B.1):

$$\Omega\left(\mathbf{r}\right) = \underset{(p-1)}{\Omega}\left(\mathbf{r}\right) = \sum_{i_1,\dots i_{p-1}=1}^{n} a_{i_1,\dots i_p} dx_{i_1} \wedge \dots \wedge dx_{i_{p-1}}.$$

Let us introduce the exact p-form equal to:

$$\underset{(p)}{\Omega}\left(\mathbf{r}\right) = d\underset{(p-1)}{\Omega} = \sum_{i_1,\dots i_{p-1}=1}^{n} da_{i_1,\dots i_{p-1}} \wedge dx_{i_1} \wedge \dots \wedge dx_{i_{p-1}}. \tag{B.42}$$

The general Stokes's theorem states that

$$\int_{C_p} \underset{(p)}{\Omega} = \int_{C_p} d\underset{(p-1)}{\Omega} = \int_{\partial C_p} \underset{(p-1)}{\Omega}, \quad p = 1, 2, \dots n; \tag{B.43}$$

where ∂C_p stands for the boundary of the geometrical element C_p from the space E_n.

Note that geometrical element C_p can be treated as a p-dimensional domain in a multidimensional space. The interested reader can find a rigorous definition of multidimensional domains and the proof of the general Stokes's theorem in textbooks on the mathematical theory of differential forms.

In the present text we restrict our discussion to the intuitive explanation of this important mathematical theory. For example, the following formal derivation should give some idea of how we can arrive at the Stokes's theorem. Indeed, we can substitute representation (B.42) into the left-hand part of Eq. (B.43), and, after some algebra, we obtain the right-hand part of this formula:

$$\int_{C_p} \underset{(p)}{\Omega} = \int_{C_p} d\underset{(p-1)}{\Omega} = \underbrace{\int\int\dots\int}_{p\text{ times}} \sum_{i_1,\dots i_{p-1}=1}^{n} da_{i_1,\dots i_{p-1}} \wedge dx_{i_1} \wedge \dots \wedge dx_{i_{p-1}}$$

$$= \underbrace{\int\int\dots\int}_{p-1\text{ times}} \sum_{i_1,\dots i_{p-1}=1}^{n} \int da_{i_1,\dots i_{p-1}} \wedge dx_{i_1} \wedge \dots \wedge dx_{i_{p-1}}$$

$$= \underbrace{\int\int\dots\int}_{p-1\text{ times}} \sum_{i_1,\dots i_{p-1}=1}^{n} a_{i_1,\dots i_{p-1}} \wedge dx_{i_1} \wedge \dots \wedge dx_{i_{p-1}} = \int_{\partial C_p} \underset{(p-1)}{\Omega}.$$

In conclusion, we note that the three-dimensional form of the Stokes's theorem (1.44) comes as a special case of the general formula (B.43).

LINEAR OPERATORS AND THEIR MATRICES

C

The fundamental objects used in linear algebra are vectors, defined in some three dimensional space with basis functions $\{\mathbf{d}_x, \mathbf{d}_y, \mathbf{d}_z\}$.

Definition 48. A linear transformation of a vector is evoked by a rule f which assigns the vector $\mathbf{B}$ on the basis of an arbitrary vector, $\mathbf{A}$: $\mathbf{B} = f(\mathbf{A})$, and this rule possesses the property of linearity if the following identity applies:

$$f\left(\lambda_1^{(1)}\mathbf{A} + \lambda_2^{(2)}\mathbf{A}\right) = \lambda_1 f\left(\mathbf{A}^{(1)}\right) + \lambda_2 f\left(\mathbf{A}^{(2)}\right),$$

where $\mathbf{A}^{(1)}$, $\mathbf{A}^{(2)}$ are arbitrary vectors and λ_1, λ_2 are arbitrary scalars.

The rule evoking a linear transformation of a vector is often simply called a linear operator, f. All linear operators evoke the linear transformation of a vector.

Decomposing the vectors $\mathbf{A}$ and $\mathbf{B}$ onto the basis vectors $\{\mathbf{d}_x, \mathbf{d}_y, \mathbf{d}_z\}$, we have:

$$\mathbf{A} = A_x\mathbf{d}_x + A_y\mathbf{d}_y + A_z\mathbf{d}_z = \sum_{\beta=x,y,z} A_\beta\mathbf{d}_\beta,$$

$$\mathbf{B} = B_x\mathbf{d}_x + B_y\mathbf{d}_y + B_z\mathbf{d}_z = \sum_{\alpha=x,y,z} B_\alpha\mathbf{d}_\alpha.$$

Making use of the property of linearity for the operator $\widehat{f}$, we obtain

$$\sum_{\alpha=x,y,z} B_\alpha\mathbf{d}_\alpha = f\left(\sum_{\beta=x,y,z} A_\beta\mathbf{d}_\beta\right) = \sum_{\beta=x,y,z} A_\beta f\left(\mathbf{d}_\beta\right).$$

Furthermore, applying the operator f to the orthogonal basis vectors $\mathbf{d}_x$, $\mathbf{d}_y$, $\mathbf{d}_z$, we obtain some vector $\mathbf{f}_\beta$ which can be decomposed with respect to the basis vectors:

$$\mathbf{f}_\beta = f\left(\mathbf{d}_\beta\right) = f_{x\beta}\mathbf{d}_x + f_{y\beta}\mathbf{d}_y + f_{z\beta}\mathbf{d}_z$$
$$= \sum_{\alpha=x,y,z} f_{\alpha\beta}\mathbf{d}_\alpha,$$

where $\beta = x, y, z$.

We can now write

$$\sum_{\alpha=x,y,z} B_\alpha\mathbf{d}_\alpha = \sum_{\alpha=x,y,z}\left(\sum_{\beta=x,y,z} f_{\alpha\beta}A_\beta\right)\mathbf{d}_\alpha.$$

Equating the coefficients of the unit orthogonal vectors done by one, we have

$$B_\alpha = \sum_{\beta=x,y,z} f_{\alpha\beta} A_\beta.$$

Clearly, the coefficients $f_{\alpha\beta}$ $(\alpha = x, y, z; \beta = x, y, z)$ form a 3 by 3 matrix:

$$\left[f_{\alpha\beta} \right] = \begin{bmatrix} f_{xx} & f_{xy} & f_{xz} \\ f_{yx} & f_{yy} & f_{yz} \\ f_{zx} & f_{zy} & f_{zz} \end{bmatrix},$$

which is called the linear operator matrix, $\widehat{f}$, on the given basis function. Therefore, in the language of matrices, this last equation can be written as:

$$\begin{bmatrix} B_x \\ B_y \\ B_z \end{bmatrix} = \begin{bmatrix} f_{xx} & f_{xy} & f_{xz} \\ f_{yx} & f_{yy} & f_{yz} \\ f_{zx} & f_{zy} & f_{zz} \end{bmatrix} \cdot \begin{bmatrix} A_x \\ A_y \\ A_z \end{bmatrix}$$

and the components are

$$B_x = f_{xx} A_x + f_{xy} A_y + f_{xz} A_z,$$
$$B_y = f_{yx} A_x + f_{yy} A_y + f_{yz} A_z,$$
$$B_z = f_{zx} A_x + f_{zy} A_y + f_{zz} A_z.$$

Note that, if the vectors **A** and **B** that we are considering lie only in the horizontal plane XOY, the matrix form of writing the linear operator f is as follows:

$$\begin{bmatrix} B_x \\ B_y \end{bmatrix} = \begin{bmatrix} f_{xx} & f_{xy} \\ f_{yx} & f_{yy} \end{bmatrix} \cdot \begin{bmatrix} A_x \\ A_y \end{bmatrix}$$

and accordingly

$$B_x = f_{xx} A_x + f_{xy} A_y,$$
$$B_y = f_{yx} A_x + f_{yy} A_y.$$

We need still another concept from linear algebra.

Definition 49. The linear transformation evoked by the operator f is called *non-degenerate* if the determinant of the linear transformation matrix is not zero:

$$Det \left[f_{\alpha\beta} \right] \neq 0$$

Definition 50. If this is not true, the linear transformation is called *degenerate*.

Non-degenerate transformation evokes a reversible transformation of the vector **A** to the vector **B**. This means that an inverse linear operator, f^{-1}, exists which permits the inversion of the vector **B** to the vector **A**:

$$f^{-1} (\mathbf{B}) = f^{-1} f (\mathbf{A}).$$

An operator f which causes a non-degenerate transformation is called an *invertible operator*. Operators which result in degenerate transformations are called *non-invertible*; that is, no inverse operators exist in such cases.

MATHEMATICAL NOTATIONS

Vectors are indicated with bold symbols, as in **E** for the electric field. Scalar components of vectors are indicated by an appropriate subscript for the coordinate axis onto which the vector has been projected, as in E_x, E_y, E_z. Matrices are indicated by hats, as in $\widehat{\mathbf{A}}$. In complex numbers, we use the symbol i for $\sqrt{-1}$. The real or imaginary part of a complex number is indicated by the operators **Re** or **Im**, respectively.

Definitions of variables:

x, y, z : Cartesian coordinate system.

r, z, θ : Polar coordinate system.

R, θ, φ : Spherical coordinate system (note that $r^2 + z^2 = R^2$).

ω : Angular frequency, radians per second.

μ_0 : Magnetic permeability.

ϵ : Dielectric permittivity.

ρ_j, σ_j : Resistivity, conductivity of unit j.

m : Separation variable, inverse distance.

$k_j = \sqrt{i\omega\mu_0\sigma_j + \omega^2\mu_0\epsilon} \approx \sqrt{i\omega\mu_0\sigma_j} = G + iG, G = \sqrt{i\omega\mu_0\sigma_j/2}$: Wave number.

$n_j = \sqrt{n_0^2 + k_j^2}$: Spatial frequency-domain wave number for medium i.

$n_0 = \sqrt{k_x^2 + k_y^2}$.

k_x and k_y : Spatial frequencies.

$J_0(n_0 r), J_1(n_0 r)$: Bessel's functions of the first kind of the orders 1 and 2 for the argument $(n_0 r)$.

I^M : Source moment of a dipole.

$\tau = \sqrt{2\pi t/\sigma_j} \times 10^{3.5}$: Electrical distance in the time domain.

$\Phi(x)$: Error function of the argument x.

$I_0\left(k_j r\right), I_1\left(k_j r\right), K_0\left(k_j r\right), K_1\left(k_j r\right)$: Bessel's functions of the second kind of orders 0 and 1 for the argument $(k_j r)$.

E : Electric field, either vector or scalar component, as indicated by a bold letter or subscript.

e : The spatial spectrums of the electric field, either vector or scalar component as indicated by a bold letter or subscript.

D : Electric displacement field, either vector or scalar component, as indicated by a bold letter or subscript.

B : Magnetic induction, either vector or scalar component, as indicated by a bold letter or subscript.

H : Magnetic field, either vector or scalar component, as indicated by a bold letter or subscript.

h : The spatial spectrums of the magnetic field, either vector or scalar component, as indicated by a bold letter or subscript.

j : Current density, either vector or scalar component, as indicated by a bold letter or subscript.

Q, q : Charge, charge density.

$\widehat{\mathbf{G}}_H \left(\mathbf{r} \mid \mathbf{r}' \right)$: Magnetic Green's tensor.

$\widehat{\mathbf{G}}_E \left(\mathbf{r} \mid \mathbf{r}' \right)$: Electric Green's tensor.

Z_{ij} : Impedance, ohms, specifically in the equation $E_i = Z_{ij} H_i$.

T_{ij} : Transfer function, defined by a linear correlation between two vector quantities which are expressed by the same units: $H_i^{(1)} = T_{ij} H_j^{(2)}$, where the magnetic excitation at locations (1) and (2) are linearly correlated.

U : Electric potential, volts.

u : The spatial spectrums of the electric potential.

V : Voltage, or difference in electric potential between two points.

W : Work of a vector field along the curve.

$\varphi_{(1)}$: Differential 1-form.

$\psi_{(2)}$: Differential 2-form.

$\theta_{(3)}$: Differential 3-form.

EMF : Electromotive force, or voltage appearing at the output of an induction coil.

R : Layered earth correction factor developed from the boundary condition requiring continuity of the vertical component of current density in a horizontally stratified geoelectric structure.

R^* : Layered earth correction factor developed from the boundary condition requiring continuity of the horizontal component of magnetic excitation in a horizontally stratified geoelectric structure.

$R_N^0 = \lim_{\omega \to 0} R$: Layered earth correction factor for DC behavior for N layers.

$R_N^* = \lim_{r \to 0} R^*$: Layered earth correction factor for a vertically traveling plane electromagnetic wave (the magnetotelluric assumption) for N layers.

$\mathbf{p}$: Moment of a current dipole source, measured as the product of length, L, and current, I.

$\widehat{Y}$: Admittance, or the inverse impedance, $H_i = Y_{ij} E_j$.

A, B : Current injection points.

M, N : Points at which potential is measured.

O, P : Midpoints of AB or MN electrode pairs, respectively.

$\varphi(\mathbf{m})$: Misfit functional of some model $\mathbf{m}$.

$s(\mathbf{m})$: Stabilizing functional of some model $\mathbf{m}$.

$P^\alpha(\mathbf{m}, \mathbf{d})$: Tikhonov parametric functional of some model $\mathbf{m}$ and data vector $\mathbf{d}$.

α : Regularization parameter.

DEFINITION OF FIELDS AND UNITS

E

We use the definitions of fields and units as set forth by Sommerfeld (1952). We describe the physical universe with four fundamental units; the meter (M), kilogram (K), second (S), and coulomb (Q).

Maxwell's equations comprise a unified description of electromagnetic field phenomena in terms of current density, electric flux density, and magnetic flux density. We follow Sommerfeld's nomenclature in naming various simplified versions of Maxwell's equations; *static*, *stationary*, *quasi-stationary*, and *rapidly varying (nonstationary)* fields.

For static behavior, we take $\partial \mathbf{B}/\partial t$, $\partial \mathbf{D}/\partial t$, $\partial q/\partial t$, $\mathbf{j} \equiv 0$. The electric and magnetic fields are uncoupled. *Electrostatic* and *magnetostatic* fields are uncoupled and must be treated separately.

In stationary behavior, we still consider the three time derivatives to be zero but current can flow in regions with non-zero conductivity. There can be no charge resident within the conductive regions. The electric field must satisfy the equation $curl\,\mathbf{E} = 0$, but $curl\,\mathbf{H} = 0$ only outside the regions in which current flows.

In the quasi-stationary regime, fields are determined as in the stationary regime but we take into account their time dependence in a first approximation. In this approximation, solutions to Maxwell's equation resemble diffusion processes.

For convenience, Table E.1 shows the dimensions of the different physical quantities in m.k.s. units, while Table E.2 gives the numerical relationships of Gaussian units to m.k.s. units.

Table E.1 Dimensions of the different physical quantities in m.k.s. units

Quantity	Symbol	Dimensions	m.k.s. unit
Force	F	MLT^{-2}	Newton (N)
Energy	Σ	ML^2T^{-2}	Joule (J)
Power	P	ML^2T^{-3}	Watt (W)
Charge	Q	Q	Coulomb (C)
Current	I	$T^{-1}Q$	Ampere (A)
Charge density	q	$L^{-3}Q$	Coulomb/cubic meter
Current density	j	$L^{-2}T^{-1}Q$	Ampere/square meter
Resistance	R	$ML^2T^{-1}Q^{-2}$	Ohm (Ω)
Conductivity	σ	$M^{-1}L^{-3}TQ^2$	Siemens/meter
Electric potential	U	$ML^2T^{-2}Q^{-1}$	Volt (V)
Electric field	E	$MLT^{-2}Q^{-1}$	Volt/meter
Capacitance	C	$M^{-1}L^{-2}T^2Q^2$	Farad (F)
Electric displacement	D	$L^{-2}Q$	Coulomb/square meter
Inductive capacity	c	$M^{-1}L^{-3}T^2Q^2$	Farad/meter
Electric dipole moment	p	LQ	Coulomb-meter
Magnetic flux	Φ	$ML^2T^{-1}Q^{-1}$	Weber (Wb)
Magnetic induction	B	$MT^{-1}Q^{-1}$	Tesla (T) = Weber/square meter
Magnetomotive force	m.m.f.	$T^{-1}Q$	Ampere-turn
Magnetic field	H	$L^{-1}T^{-1}Q$	Ampere/meter
Inductance	L	ML^2Q^{-2}	Henry (H)
Permeability	μ	MLQ^{-2}	Henry/meter
Magnetic dipole moment	M	$L^2T^{-1}Q$	Ampere-square meter

Table E.2 Numerical relationships of Gaussian units to m.k.s. units

Quantity	Symbol	Gaussian unit[*]	m.k.s. unit
Capacitance	C	9×10^{11} cm (esu/statvolt)	= 1 F
Charge	Q	3×10^9 esu	= 1 C
Conductivity	σ	3×10^9 s^{-1}	= 1 (Ω·m)$^{-1}$
Current	I	3×10^9 esu/s (= 10^{-1} abamp)	= 1 A
Electric displacement	D	$12\pi \times 10^5$ dyne/esu	= 1 C/m^2
Electric field	E	$1/3 \times 10^{-4}$ dyne/esu	= 1 V/m
Energy	Σ	10^7 erg	= 1 J
Force	F	10^5 dyne	= 1 N
Inductance	L	$1/9 \times 10^{-11}$ s^2/cm	= 1 H
Magnetic flux	Φ	10^8 maxwell	= 1 Wb
Magnetic induction	B	10^4 gauss	= 1 T
Magnetic field	H	$4\pi \times 10^3$ oersted (gauss)	= 1 A/m
Potential	U	1/300 erg/esu	= 1 V
Resistance	R	$1/9 \times 10^{-11}$ s^2/cm (statvolt·s/esu)	= 1 Ω

[*] *The factor 3 ($9 = 3^2$) in the conversions comes from the velocity of light, c $\cong 3 \times 10^8$ m/s. For greater accuracy, use 2.9979 instead of 3.*

BIBLIOGRAPHY

Abramowitz, M., Stegun, I.A., 1965. Handbook of Mathematical Functions with Formulas, Graphs, and Mathematical Tables. National Bureau of Standards, Applied Mathematics Series, vol. 55. U.S. Gov. Printing Office, Washington, DC. 1046 pp.

Abubakar, A., van der Berg, P.M., 2004. Iterative forward and inverse algorithms based on domain integral equations for three-dimensional electric and magnetic objects. J. Comput. Phys. 195, 236–262.

Airy, G.B., 1868. Comparison of magnetic disturbances recorded by the self-registering magnetometers at the Royal Observatory, Greenwich, with magnetic disturbances deduced from the corresponding terrestrial galvanic currents recorded by the self-registering galvanometers of the Royal Observatory. Philos. Trans. R. Soc. Lond. 158, 465–472.

Alfano, L., 1984. A computation method for D. C. geoelectric fields. In: Rapolla, A., Keller, G.V. (Eds.), Geophysics of Geothermal Areas: State of the Art and Future Development. Colorado School of Mines Press, Golden, Colorado, pp. 127–152.

Alfvén, H., Fälthammer, C.G., 1963. Cosmical Electrodynamics. The Clarendon Press, Oxford. 228 pp.

Alpin, L.M., 1966. Theory of the Field. Nedra, Moscow. 384 pp.

Alpin, L.M., Berdichevsky, M.N., Vedrintsev, G.A., Zagarmistr, A.M., 1966. Dipole Methods for Measuring Earth Conductivity. Consultants Bureau, New York. 302 pp.

Alumbaugh, D.L., Newman, G.A., 1997. Three-dimensional massively parallel inversion – II. Analysis of a cross-well electromagnetic experiment. Geophys. J. Int. 128, 355–363.

Anderson, C., Mattsson, J., 2010. An integrated approach to marine electromagnetic surveying using a Towed Streamer and source. First Break 28 (5), 71–75.

Arfken, G., Weber, H.J., 1995. Mathematical Methods for Physicists, 4th ed. Academic Press, San Diego, New York, Boston, London, Tokyo, Toronto. 1029 pp.

Asch, T., Morrison, H.F., 1989. Mapping and monitoring electrical resistivity with surface and subsurface electrode arrays. Geophysics 54 (2), 235–244.

Avdeev, D.B., 2005. Three-dimensional electromagnetic modelling and inversion from theory to application. Surv. Geophys. 26, 767–799.

Avdeev, D.B., Kuvshinov, A.V., Pankratov, O.V., Newman, G.A., 2002. Three-dimensional induction logging problems, part I: an integral equation solution and model comparisons. Geophysics 67, 413–426.

Backus, G., Parker, R., Constable, C., 2006. Foundations of Geomagnetism. Cambridge University Press. 369 pp.

Balch, S.J., 2000. Geophysics in mineral exploration: fundamentals and case histories. Ni–Cu sulphide deposits with examples from Voisey's Bay. In: Practical Geophysics III. Northwest Mining Association.

Banks, R.J., 1973. Data processing and interpretation in geomagnetic deep sounding data. Phys. Earth Planet. Inter. 7, 339–348.

Bates, R.L., Jackson, J.L., 1980. Glossary of Geology. American Geological Institute, Falls Church, Va. 749 pp.

Becker, A., 1979. Airborne electromagnetic methods. In: Hood, P.J. (Ed.), Geophysics and Geochemistry in the Search for Metallic Ores. In: Econ. Geol. Report, vol. 31. Geological Survey of Canada, pp. 33–43.

Bedrosian, P.A., Feucht, D.W., 2013. Structure and tectonics of the northwestern United States from EarthScope USArray magnetotelluric data. Earth Planet. Sci. Lett. 402, 275–289.

Beltzer, A.I., 1990. Variational and Finite Element Methods, a Symbolic Computational Approach. Springer-Verlag, Berlin, Heidelberg, New York, London, Paris, Tokyo. 254 pp.

Berdichevsky, M.N., 1965. Electrical prospecting with the telluric current method. Colo. Sch. Mines Q. 60 (1), 1–216.

Berdichevsky, M.N., Bezruk, I.A., 1980. Magnetotelluric methods in electric prospecting. In: Tarkhov, A.G. (Ed.), Reference Book for Geophysicists. Nedra, Moscow, pp. 246–273.

Berdichevsky, M.N., Dmitriev, V.I., 1976a. Basic principles of interpretation of magnetotelluric sounding curves. In: Adam, A. (Ed.), Geoelectric and Geothermal Studies. Akademai Kaido, Budapest, pp. 165–221.

Berdichevsky, M.N., Dmitriev, V.I., 1976b. Distortions of magnetic and electrical fields by near-surface lateral inhomogeneities. Acta Geod. Geophys. Montan. Acad. Sci. Hung. 34 (11), 447–483.

Berdichevsky, M.N., Dmitriev, V.I., 2002. Magnetotellurics in the Context of Theory of Ill-Posed Problems. Society of Exploration Geophysicists, Tulsa, OK. 215 pp.

Berdichevsky, M.N., Dmitriev, V.I., 2008. Models and Methods of Magnetotellurics. Springer-Verlag, Berlin, Heidelberg. 563 pp.

Berdichevsky, M.N., Fainberg, E.B., Rotanova, N.M., Smirnova, J.B., Vanyan, L.L., 1976. Deep electromagnetic investigations. Ann. Geophys. 32, 143–155.

Berdichevsky, M.N., Vanyan, L.L., Fainberg, Ye.B., 1969. Frequency sounding of the Earth using the results of spherical analysis of electromagnetic variations. Geomagn. Aeron. 9, 372–374.

Berdichevsky, M.N., Zhdanova, O.N., Zhdanov, M.S., 1989. Marine Deep Geoelectrics. Nauka, Moscow. 80 pp.

Berdichevsky, M.N., Zhdanov, M.S., 1981. Interpretation of Anomalous Variations of the Electromagnetic Field of the Earth. Nedra, Moscow. 327 pp.

Berdichevsky, M.N., Zhdanov, M.S., 1984. Advanced Theory of Deep Geomagnetic Sounding. Elsevier, Amsterdam, London, New York, Tokyo. 410 pp.

Berenger, J., 1993. A perfectly matched layer for the absorption of electromagnetic waves. J. Comput. Phys. 114, 185–200.

Berkhout, A.J., 1980. Seismic Migration – Imaging of Acoustic Energy by Wave Field Extrapolation. Elsevier, Amsterdam, Oxford, New York. 339 pp.

Bernabini, M., Cardarelli, E., 1991. Geoelectrical surveys of dipping structures. Geophys. Prospect. 39 (7), 953–966.

Berryman, J.G., 2006. Effective medium theories for multicomponent poroelastic composites. J. Eng. Mech. 132, 519–531.

Bertin, J., Loeb, J., 1976. Experimental and Theoretical Aspects of Induced Polarization, Vol. 1, Presentation and Application of the IP Method Case Histories. Gebruder Borntraeger, Berlin. 250 pp.

Bertsekas, D.P., 1999. Nonlinear Programming, 2nd ed. Athena Scientific, Belmont, Massachusetts. 780 pp.

Best, M.E., 1985. A systematic approach for evaluating electromagnetic systems. Geophys. Prospect. 33 (4), 577–599.

Bezruk, I.A., Chernyavskiy, G.A., Chenareva, O.M., 1978. Processing of magnetotelluric variations in the period interval from 10 to 1000 s. Prikl. Geofiz. 91, 87–94.

Biro, O., Preis, K., 1990. Finite element analysis of 3-D eddy currents. IEEE Trans. Magn. 26 (2), 418–423.

Black, K., 1998. Spectral element approximations and infinite domains. J. Math. Syst. Estim. Control 8 (2), 1–20.

Blackman, R.B., 1965. Linear Data Smoothing and Prediction in Theory and Practice. Addison-Wesley Publishing, Reading, Massachusetts. 182 pp.

Bleistein, N., 1984. Mathematical Methods for Wave Phenomena. Academic Press Inc. (Harcourt Brace Jovanovich Publishers), New York. 341 pp.

Bleistein, N., Gray, S.H., 1985. An extension of the Born inversion method to a depth dependent reference profile. Geophys. Prospect. 33 (7), 999–1022.

Blok, H., Oristaglio, M., 1995. Wavefield Imaging and Inversion in Electromagnetics and Acoustics. Delft University of Technology. Report number: Et/EM 1995-21, 132 pp.

Bloom, A.L., 1960. Optical pumping. Sci. Am. 203, 72–97.

Bockrig, J., Reddy, A.K.N., 1973. Modern Electrochemistry: Vols. 1 and 2. Plenum Press.

Born, M., 1933. Optik. Springer, Berlin. 591 pp.

Born, M., Wolf, E., 1980. Principles of Optics, 2nd ed. Pergamon Press, New York. 808 pp.

Bracewell, R., 1965. The Fourier Transform and Its Applications. McGraw-Hill Book Company, New York. 381 pp.

Bruggeman, D.A., 1935. Effective medium model for the optical properties of composite material. Ann. Phys. (Leipz.) 5 (24), 636–664.

Cagniard, L., 1953. Basic theory of the magnetotelluric method of geophysical prospecting. Geophysics 18, 605–635.

Cai, H., Xiong, B., Han, M., Zhdanov, M.S., 2014. 3D controlled-source electromagnetic modeling in anisotropic medium using edge-based finite element method. Comput. Geosci. 73, 164–176.

Caldwell, T.G., Bibby, H.M., Brown, C., 2004. The magnetotelluric phase tensor. Geophys. J. Int. 158, 457–469.

Camp, V.E., Ross, M.E., 2004. Mantle dynamics and genesis of mafic magmatism in the intermontane Pacific northwest. J. Geophys. Res. 109, B08204.

Campbell, W.H., 2003. Introduction to Geomagnetic Fields, 2nd ed. Cambridge University Press. 350 pp.

Carazzone, J.J., Burtz, O.M., Green, K.E., Pavlov, D.A., Xia, C., 2005. Three-dimensional imaging of marine CSEM data. In: 75th Annual International Meeting, SEG, Expanded Abstracts, pp. 575–578.

Carlson, R.W., Grove, T.L., Donnelly-Nolan, J.M., 2008. Concentrating the slab-fluid input to Newberry volcano. Geochim. Cosmochim. Acta 72 (12), A136.

Carmichael, R.S., 1989. Practical Handbook of Physical Properties of Rocks and Minerals. CRC Press, Boca Raton, Florida. 741 pp.

Chapman, S., 1962. Geomagnetism. Clarendon Press. 504 pp.

Chapman, S., Bartels, J., 1940. Geomagnetism. Oxford University Press, London. 1049 pp.

Chastenet de Gery, J., Kunetz, G., 1956. Potential and apparent resistivity over dipping beds. Geophysics 21 (3), 780–793.

Chave, A.D., 1983. On the theory of electromagnetic induction in the Earth by ocean currents. J. Geophys. Res. 88, 3531–3542.

Chave, A.D., Constable, S.C., Edwards, R.N., 1991. Electrical exploration methods for the seafloor. In: Nabighian, M.N., Corbett, J.D. (Eds.), Electromagnetic Methods in Applied Geophysics, Vol. 2, Applications. Society of Exploration Geophysicists, Tulsa, Oklahoma, pp. 931–966.

Chave, A.D., Thomson, D.J., Ander, M.E., 1987. On the robust estimation of power spectra, coherences and transfer functions. J. Geophys. Res. 92, 633–648.

Chen, J., Hoversten, G.M., Vasco, D.W., Rubin, Y., Hou, Z., 2004. Joint inversion of seismic AVO and EM data for gas saturation estimation using a sampling-based stochastic mode. In: 74th Annual International Meeting, SEG, Expanded Abstracts.

Chen, J., Raiche, A., 1998. Inverting AEM data using a damped eigenparameter method. Explor. Geophys. 29 (2), 128–132.

Chew, W.C., 1990. Waves and Fields in Inhomogeneous Media. Van Nostrand Reinhold, New York. 608 pp.

Chew, W.C., Weedon, W.H., 1994. A 3-D perfectly matched medium from modified Maxwell's equations with stretched coordinates. Microw. Opt. Technol. Lett. 7, 599–604.

Choy, T.C., 1999. Effective Medium Theory, Principles and Applications. Oxford Science Publications. 182 pp.

Claerbout, J.F., 1985. Imaging the Earth's Interior. Blackwell Scientific Publications, Oxford, London, Edinburgh. 399 pp.

Coggon, J.Z., 1971. Electromagnetic and electrical modeling by the finite-element method. Geophysics 36, 132–155.

Cole, K.S., Cole, R.H., 1941. Dispersion and absorption in dielectrics. J. Chem. Phys. 9, 343–351.

Constable, S., Cox, C., 1996. Marine controlled-source electromagnetic sounding – II: the PEGASUS experiment. J. Geophys. Res. 97, 5519–5530.

Constable, S.C., Orange, A., Hoversten, G.M., Morrison, H.F., 1998. Marine magnetotellurics for petroleum exploration, part I: a sea-floor equipment system. Geophysics 63, 816–825.

Constable, S.C., Parker, R.L., Constable, C.G., 1987. Occam's inversion: a practical algorithm for generating smooth models from electromagnetic sounding data. Geophysics 52 (3), 289–300.

Constable, S., 2010. Ten years of marine CSEM for hydrocarbon exploration. Geophysics 75 (5), 75A67–75A81.

Cook, J.C., 1975. Radar transparencies of mine and tunnel rocks. Geophysics 40 (5), 865–877.

Corwin, R.F., Hoover, D.B., 1979. The self-potential method in geothermal exploration. Geophysics 44 (2), 226–235.

Cox, C.S., 1981. On the electrical conductivity of the oceanic lithosphere. Phys. Earth Planet. Inter. 25 (3), 196–201.

Cox, C.S., Kroll, N., Pistek, P., Watson, K., 1978. Electromagnetic fluctuations induced by wind waves on the deep sea floor. J. Geophys. Res. 83, 431–442.

Cox, L.H., Zhdanov, M.S., 2006. Rapid and rigorous 3-D inversion of airborne electromagnetic data. In: Proceedings of Annual Meeting of Consortium for Electromagnetic Modeling and Inversion, pp. 103–120.

Cox, L.H., Zhdanov, M.S., 2007. Large-scale 3D inversion of HEM data using a moving footprint. In: 77th SEG Annual Meeting. San Antonio, Texas.

Cox, L.H., Zhdanov, M.S., 2008. Advanced computational methods of rapid and rigorous 3-D inversion of airborne electromagnetic data. Commun. Comput. Phys. 3 (1), 160–179.

Cox, L.H., Wilson, G.A., Zhdanov, M.S., 2010. 3D inversion of airborne electromagnetic data using a moving footprint. Explor. Geophys. 41, 250–259.

Cox, L.H., Wilson, G.A., Zhdanov, M.S., 2012. 3D inversion of airborne electromagnetic data. Geophysics 77 (4), WB59–WB69.

Čuma, M., Gribenko, A., Zhdanov, M.S., 2017. Inversion of magnetotelluric data using integral equation approach with variable sensitivity domain: application to EarthScope MT data. Phys. Earth Planet. Inter. 270, 113–127.

Daniels, J.J., 1983. Hole-to-surface resistivity measurements. Geophysics 48 (1), 87–97.

da Silva, N.V., Morgan, J.V., MacGregor, L., Warner, M., 2012. A finite element multifrontal method for 3D CSEM modeling in the frequency domain. Geophysics 77 (2), E101–E115.

Davis, H.F., Snider, A.D., 1979. Introduction to Vector Analysis. Allyn & Bacon, Boston.

Davydycheva, S., Rykhlinsky, N., Legeido, P., 2004. An electrical prospecting method for oil search using induced polarization effect. In: 74th Annual International Meeting, SEG, Expanded Abstracts, Electronic Volume.

de Groot Hedlin, C., Constable, S., 1990. Occam's inversion to generate smooth two dimensional models from magnetotelluric data. Geophysics 55 (12), 1613–1624.

de Lugao, P., Portniaguine, O., Zhdanov, M.S., 1997. Fast and stable two-dimensional inversion of magnetotelluric data. J. Geomagn. Geoelectr. 49, 1469–1497.

de Lugao, P., Wannamaker, P.E., 1996. Calculating the two-dimensional magnetotelluric Jacobian in finite elements using reciprocity. Geophys. J. Int. 127, 806–810.

Deaver, B.S., Fairbank, W.M., 1961. Experimental evidence for quantized flux in superconducting cylinders. Phys. Rev. Lett. 7, 43–46.

DeMoully, G., Becker, A., 1983. Automated interpretation of airborne electromagnetic data. Geophysics 49 (8), 1301–1312.

Deschamps, G.A., 1981. Electromagnetics and differential forms. Proc. IEEE 69 (6), 676–696.

Dieter, K., Paterson, N.R., Grant, F.S., 1969. I.P. and resistivity type curves for three dimensional bodies. Geophysics 34 (4), 615–632.

Dmitriev, V.I., 1969. Electromagnetic Fields in Inhomogeneous Media: Proceeding of Computational Center. Moscow State University (in Russian).

Dmitriev, V.I., Berdichevsky, M.N., 1979. The fundamental problem of magnetotelluric sounding. Proc. IEEE 67, 1034–1044.

Dmitriev, V.I., Berdichevsky, M.N., Bulychov, A.A., 2004. Lectures on the Theory of the Geophysical Fields. Geophysical Department of Moscow State University, Moscow.

Dmitriev, V.I., Nesmeyanova, N.I., 1992. Integral equation method in three-dimensional problems of low-frequency electrodynamics. Comput. Math. Model. 3, 313–317.

Dmitriev, V.I., Pozdniakova, E., Zhdanov, M.S., Fang, S., 1999. Quasi-analytical solutions for EM field in inhomogeneous structures based on unified iterative quasi-linear method. In: 68th Annual International Meeting, SEG, Expanded Abstracts, pp. 444–447.

Doll, R., Nabauer, M., 1961. Experimental proof of magnetic flux quantization in a superconducting ring. Phys. Rev. Lett. 7, 51–52.

Dorn, O., Bertete-Aguire, H., Berryman, J.G., Papanicolau, G.C., 1999. A nonlinear inversion for 3-D electromagnetic imaging using adjoint fields. Inverse Probl. 15, 1523–1558.

Dortman, N.B. (Ed.), 1992a. Handbook of Petrophysics, Vol. I., Rocks and Ores. Nedra, Moscow (in Russian), 392 pp.

Dortman, N.B. (Ed.), 1992b. Handbook of Petrophysics, Vol. II, Techniques and Methods of Investigation. Nedra, Moscow (in Russian), 256 pp.

Dortman, N.B. (Ed.), 1992c. Handbook of Petrophysics, Vol. III, the Earth's Crust and Mantle. Nedra, Moscow (in Russian), 286 pp.

Druskin, V., Knizhnerman, L., 1994. Spectral approach to solving three-dimensional Maxwell's diffusion equations in the time and frequency domains. Radio Sci. 29, 937–953.

Druskin, V., Knizhnerman, L., Lee, P., 1999. New spectral Lanczos decomposition method for induction modeling in arbitrary 3-D geometry. Geophysics 64 (3), 701–706.

Dubrovskiy, V.G., Kondratieva, N.V., 1976. Basic results of the magnetotelluric soundings in the Turkmen sector of the Caspian Sea. Izv. Akad. Nauk SSSR, Phys. Earth 3, 67–76.

Dukhin, S.S., 1971. Dielectric Properties of Disperse Systems. Surface and Colloid Science, vol. 3. Wiley Interscience.

Dyck, A.V., 1991. Drill-hole electromagnetic methods. In: Nabighian, M.N., Corbett, J.D. (Eds.), Electromagnetic Methods in Applied Geophysics, Vol. 2, Applications. Society of Exploration Geophysicists, Tulsa, Oklahoma, pp. 881–930.

Eaton, P.A., 1989. 3-D electromagnetic inversion using integral equations. Geophys. Prospect. 37 (4), 407–426.

Edwards, R.N., 1988a. A downhole magnetometric resistivity technique for electrical sounding beneath a conductive surface layer. Geophysics 53 (4), 528–536.

Edwards, R.N., 1988b. Two-dimensional modeling of a towed in-line electric dipole–dipole sea-floor electromagnetic system: the optimum time delay or frequency for target resolution. Geophysics 53 (6), 846–853.

Edwards, R.N., Chave, A.D., 1986. A transient electric dipole–dipole method for mapping the conductivity of the sea floor. Geophysics 51 (4), 984–987.

Edwards, R.N., Howell, E.C., 1976. A field test of the magnetometric resistivity (MMR) method. Geophysics 41 (6), 1170–1183.

Edwards, R.N., Nabighian, M.N., 1990. The magnetometric resistivity method. In: Nabighian, M.N., Corbett, J.D. (Eds.), Electromagnetic Methods in Applied Geophysics, Vol. 2, Applications. Society of Exploration Geophysicists, Tulsa, Oklahoma, pp. 47–104.

Egbert, G.D., 1997. Robust multiple-station magnetotelluric data processing. Geophys. J. Int. 130, 475–496.

Egbert, G.D., Booker, J.R., 1986. Robust estimation of geomagnetic transfer functions. Geophys. J. R. Astron. Soc. 87, 173–194.

Eggers, D.E., 1982. An eigenstate formulation of the magnetotelluric impedance tensor. Geophysics 47 (8), 1204–1214.

Eidesmo, T., Ellingsrud, S., MacGregor, L.M., Constable, S., Sinha, M.C., Johansen, S., Kong, F.N., Westerdahl, H., 2002. Sea Bed Logging (SBL), a new method for remote and direct identification of hydrocarbon filled layers in deepwater areas. First Break 20, 144–152.

Ellingsrud, S., Eidesmo, T., Johansen, S., 2002. Remote sensing of hydrocarbon layers by seabed logging (SBL): results from a cruise offshore Angola. Lead. Edge 21, 972–982.

Ellis, R.G., 1998. Inversion of airborne electromagnetic data. SEG Tech. Program Expand. Abstr. 17 (1), 2016–2019.

Emond, A.M., 2007. Electromagnetic Modeling of Porphyry Systems from the Grain-Scale to the Deposit-Scale Using the Generalized Effective Medium Theory of Induced Polarization. M.S. thesis. University of Utah.

Emond, A., Zhdanov, M.S., Petersen, E.U., 2006. Electromagnetic modeling based on the rock physics description of the true complexity of rocks: applications to porphyry copper deposits. In: 76th Annual International Meeting, SEG, Expanded Abstracts, Electronic Volume.

Evans, R.L., Sinha, M.C., Constable, S., Unsworth, M.J., 1994. On the electrical nature of the axial melt zone at 13° N on the East Pacific Rise. J. Geophys. Res. 99 (B1), 577–588.

Everett, M.E., 1999. Finite element formulation of electromagnetic induction with coupled potentials. In: Three-Dimensional Electromagnetics. In: Geophysical Development Series. Society of Exploration Geophysics, Tulsa, OK, pp. 444–450.

Everett, M.E., Schultz, A., 1996. Geomagnetic induction in a heterogeneous sphere: azimuthally symmetric test computations and the response of an undulating 660-km discontinuity. J. Geophys. Res. 101, 2765–2783.

Fainberg, E.B., 1981. On the inverse problem of deep electromagnetic sounding of the Earth. Geomagn. Aeron. 21, 715–719.

Falco, C.M., Schuller, I.K., 1980. SQUIDs and their sensitivity for geophysical applications. In: Weinstock, H., Overton, W.C. (Eds.), SQUID Applications to Geophysics. Society of Exploration Geophysicists, Tulsa, pp. 13–18.

Farquharson, C.G., Oldenburg, D.W., Routh, P.S., 2003. Simultaneous 1-D inversion of loop-loop electromagnetic data for magnetic susceptibility and electrical conductivity. Geophysics 68 (6), 1857–1869.

Fecko, M., 2006. Differential Geometry and Lie Groups for Physicists. Cambridge University Press. 697 pp.

Felsen, L., Marcuvitz, N., 1994. Radiation and Scattering of Waves. IEEE Press, New York. 888 pp.

Filloux, J.H., 1973. Techniques and instrumentation for study of natural electromagnetic induction at sea. Phys. Earth Planet. Inter. 7, 323–338.

Filloux, J.H., 1979. Magnetotelluric and related electromagnetic investigations in geophysics. Rev. Geophys. Space Phys. 17 (2), 282–294.

Filloux, J.H., 1981. Magnetotelluric exploration of the North Pacific: progress report and preliminary soundings near a spreading ridge. Phys. Earth Planet. Inter. 25, 187–195.

Filloux, J.H., 1982. Magnetotelluric experiment over the ROSE area. J. Geophys. Res. 87, 8364–8378.

Filloux, J.H., 1987. Instrumentation and experimental methods for oceanic studies. In: Jacobs, A.J. (Ed.), Geomagnetism, Vol. 1. Academic Press, London, pp. 143–246.

Fisher, E., McMechan, G.A., Annan, A.P., Cosway, S.W., 1992. Examples of reverse-time migration of single-channel, ground-penetrating radar profiles. Geophysics 57 (4), 577–586.

Fitterman, D.V. (Ed.), 1990. Developments and Applications of Modern Airborne Electromagnetic Surveys. U.S. Geological Survey Bulletin, vol. 1925. 216 pp.

Fletcher, R., 1995. Practical Methods of Optimization. John Wiley & Sons, Chichester, New York. 436 pp.

Fountain, D., 1998. Airborne electromagnetic systems—50 years of development. Explor. Geophys. 29, 1–11.

Fournier, D., Kang, S., McMillan, M.S., Oldenburg, D.W., 2017. Inversion of airborne geophysics over the DO-27/DO-18 kimberlites, part II: electromagnetics. Interpret. 5.

Fox, R.W., 1820. On the electromagnetic properties of metalliferous veins in the mines of Cornwall. Philos. Trans. R. Soc. Lond. 120, 399–414.

Frazer, M.C., 1974. Geomagnetic deep sounding with arrays of magnetometers. Rev. Geophys. Space Phys. 12 (3), 401–420.

Frischknecht, F.C., 1967. Fields about an oscillating magnetic dipole over a two-layer Earth, and application to ground and airborne electromagnetic surveys. Colo. Sch. Mines Q. 62 (1), 1–326.

Furness, P., 1992. An integral equation for the geoelectric response of thin resistive bodies. Geophys. Prospect. 40 (7), 701–720.

Gamble, T., Goubau, W.M., Clarke, J., 1979. Magnetotellurics with a remote magnetic reference. Geophysics 44 (1), 53–68.

Gazdag, J., 1978. Wave equation migration with the phase-shift method. Geophysics 43 (7), 1342–1351.

Gish, O.H., Rooney, W.J., 1925. Measurement of resistivity of large masses of undisturbed Earth. Terr. Magn. Atmos. Electr. 30, 161–188.

Golub, G.H., Van Loan, C.F., 1996. Matrix computations, 3rd ed. Johns Hopkins University Press, Baltimore. 694 pp.

Grayver, A.V., Bürg, M., 2014. Robust and scalable 3-D geo-electromagnetic modelling approach using the finite element method. Geophys. J. Int. 198 (1), 110–125.

Grayver, A.V., Streich, R., Ritter, O., 2013. Three-dimensional parallel distributed inversion of CSEM data using a direct forward solver. Geophys. J. Int. 193 (3), 1432–1446.

Gribenko, A., Zhdanov, M.S., 2007. Rigorous 3D inversion of marine CSEM data based on integral equation method. Geophysics 72 (2), WA73–WA84.

Gribenko, A., Zhdanov, M.S., 2011. 3D modeling and inversion of the magnetotelluric phase tensor. In: Proceedings of Annual Meeting of Consortium for Electromagnetic Modeling and Inversion, pp. 249–264.

Godunov, S.K., 1959. Difference method of numerical calculating the break solutions of hydrodynamic equations. Mat. Sb. 47 (3), 271–306 (in Russian).

Golubev, N., Zhdanov, M.S., 2005. Accelerated integral equation inversion of 3-D magnetotelluric data in models with inhomogeneous background. In: 75th Annual International Meeting, SEG, Expanded Abstracts, pp. 530–533.

Goubau, W.M., Gamble, T.D., Clarke, J., 1978. Magnetotelluric data analysis: removal of bias. Geophysics 43, 1157–1166.

Gough, D.I., 1973. The interpretation of magnetometer array studies. Geophys. J. R. Astron. Soc. 35, 83–98.

Gough, D.I., Ingham, M.R., 1983. Interpretation methods for magnetometer arrays. Rev. Geophys. Space Phys. 21 (4), 805–827.

Green, V.R., Weaver, J.T., 1978. Two-dimensional induction in a thin sheet of variable integrated conductivity at the surface of a uniformly conducting Earth. Geophys. J. R. Astron. Soc. 55, 721–736.

Guozhong, G., Torres-Verdin, C., Fang, S., 2004. Fast 3D modeling of borehole induction measurements in dipping and anisotropic formations using a novel approximation technique. Petrophysics 45, 335–349.

Habashy, T.M., Groom, R.W., Spies, B.R., 1993. Beyond the Born and Rytov approximations: a nonlinear approach to electromagnetic scattering. J. Geophys. Res. 98 (B2), 1759–1775.

Habberjam, G.M., 1979. Apparent Resistivity Observations and the Use of Square Array Techniques. Gebruder Borntraeger, Berlin. 152 pp.

Haber, E., Ascher, U.M., Aruliah, D.A., Oldenburg, D.W., 2000. Fast simulation of 3-D electromagnetic problems using potentials. J. Comput. Phys. 163 (1), 150–171.

Hahlbohm, H.D., Lubbig, H. (Eds.), 1977. SQUID: Superconducting Quantum Interference Devices and Their Applications. Walter de Gruyter, Berlin. 606 pp.

Hamming, R.W., 1977. Digital Filters. Prentice-Hall, Englewood Cliffs, New Jersey. 226 pp.

Hansen, C., 1998. Rank-Deficient and Discrete Ill-Posed Problems. Numerical Aspects of Linear Inversion. Department of Mathematical Modeling, Technical University of Denmark, Lyngby. 247 pp.

Harrington, R.F., 1961. Time Harmonic Electromagnetic Fields. McGraw-Hill Book Co., New York. 480 pp.

Harrington, R.F., 1993. Field Computation by Moment Methods. Wiley-IEEE Press. 240 pp.

Harthill, N., 1978. A quadripole resistivity survey of the Imperial Valley, California. Geophysics 43 (7), 1485–1500.

Heiland, C.A., 1926. Instruments and methods for the discovery of useful mineral deposits. Eng. Min. J. 121 (9), 47–49.

Hendrix, C.E., 1975. Radio-frequency holography. US Patent # 3,887,923.

Hesthammer, J., Boulaenko, M., 2005. The offshore EM challenge. First Break 23, 59–66.

Hobbs, B., Li, G., Clarke, C., Linfoot, J., 2005. Inversion of multi-transient electromagnetic data. In: 68TH EAGE Conference & Exhibition, Expanded Abstracts. A015.

Hodges, G., 2001. Technical notes – helicopter electromagnetics. http://www.fugroairborne.com.au.

Hohmann, G.W., 1975. Three-dimensional induced polarization and electromagnetic modeling. Geophysics 40 (2), 309–324.

Hohmann, G.W., 1988. Numerical modeling for electromagnetic methods in geophysics. In: Nabighian, M.N., Corbett, J.D. (Eds.), Electromagnetic Methods in Applied Geophysics – Theory, Vol. 1. Society of Exploration Geophysicists, Tulsa, Oklahoma, pp. 313–364.

Hokstad, K., Røsten, T., 2007. On the relationships between depth migration of controlled-source electromagnetic and seismic data. Lead. Edge 26 (3), 342–347.

Hordt, A., Druskin, V.L., Knizhnerman, L., Strack, K.M., 1992. Interpretation of 3-D effects in long-offset transient electromagnetic (LOTEM) soundings in the Munsterland area, Germany. Geophysics 57 (9), 1127–1137.

Hoversten, G.M., Chen, J., Gasperikova, E., Newman, G.A., 2005. Integration of marine CSEM and seismic AVO data for reservoir parameter estimation. In: 75th Annual International Meeting, SEG, Expanded Abstracts, pp. 579–582.

Hoversten, G.M., Cassassuce, F., Gasperikova, E., Newman, G.A., Chen, J., Rubin, Y., Hou, Z., Vasco, D., 2006. Direct reservoir parameter estimation using joint inversion of marine seismic AVO and CSEM data. Geophysics 71, C1–C13.

Huber, P.J., 1981. Robust Statistics. Wiley, New York. 308 pp.

Hummel, J.N., 1932. Foundations of geoelectrical methods of prospecting (in German). In: Beitrage zur angewandten Geophysik, vol. 5, pp. 32–132.

Hursán, G., Zhdanov, M.S., 2002. Contraction integral equation method in three-dimensional electromagnetic modeling. Radio Sci. 37 (6), 1089. http://dx.doi.org/10.1029/2001RS002513.

Iyengard, R.V., 1999. On the Design of Ocean Bottom Electrometer: Deep Electromagnetic Exploration. Springer-Verlag, Narosa Publishing House, pp. 248–259.

Jacobs, J.A., 1970. Geomagnetic Micropulsations. Springer-Verlag, New York. 179 pp.

Jacobs, J.A., 1989. Geomagnetism, Vol. 3. Academic Press, London. Trija Publishing, 533 pp.

Jakosky, J.J., 1940. Exploration Geophysics. Times-Mirror Press, Los Angeles.

Jaysaval, P., Shantsev, D., de la Kethulle de Ryhove, S., 2014. Fast multimodel finite difference controlled source electromagnetic simulations based on a Schur complement approach. Geophysics 79 (6), E315–E327.

Jin, J.M., 2002. The finite element method. In: Theory and Computation of Electromagnetic Fields, pp. 342–398.

Jiracek, G.R., 1990. Near-surface and topographic distortions in electromagnetic induction. Surv. Geophys. 11, 163–203.

Johansen, S.E., Amundsen, H.E.F., Rosten, T., Ellingsrud, S., Eidesmo, T., Bhuyian, A.H., 2005. Subsurface hydrocarbons detected by electromagnetic sounding. First Break 23, 31–36.

Jones, A.G., 1988. Static shift of magnetotelluric data and its removal in a sedimentary basin environment. Geophysics 53 (7), 967–978.

Josephson, B.D., 1962. Possible new effect in super-conductive tunneling. Phys. Lett. 1, 251–253.

Jursa, A.S. (Ed.), 1985. Handbook of Geophysics and the Space Environment. U.S. National Technical Information Service, Springfield, Virginia.

Kamenetsky, F.M., 1997. Transient Geo-Electromagnetics. GEOS, Moscow. 162 pp.

Kaufman, A.A., 1979. Harmonic and transient fields on the surface of a two-layer medium. Geophysics 44 (7), 1208–1217.

Kaufman, A.A., 1989. A paradox in geoelectromagnetism, demonstrating the equivalence of frequency and transient domain methods. Geoexploration 25, 287–317.

Kaufman, A.A., 1992. Geophysical Field Theory and Method, Part A, Gravitational, Electric and Magnetic Fields. Academic Press, New York. 581 pp.

Kaufman, A.A., 1994a. Geophysical Field Theory and Method, Part B, Electromagnetic Fields I. Academic Press, New York. 217 pp.

Kaufman, A.A., 1994b. Geophysical Field Theory and Method, Part C, Electromagnetic Fields II. Academic Press, New York. 335 pp.

Kaufman, A.A., Morozova, G.M., 1970. Theoretical Basis for the Transient Sounding Method in the Near-Zone. Nauka, Novosibirsk. 122 pp.

Kaufman, A.A., Keller, G.V., 1981. The Magnetotelluric Sounding Method. Elsevier, Amsterdam. 595 pp.

Kaufman, A.A., Keller, G.V., 1983. Frequency and Transient Soundings. Elsevier, Amsterdam. 685 pp.

Kaufman, A.A., Keller, G.V., 1985. Inductive Mining Prospecting, Part I: Theory. Elsevier, Amsterdam. 620 pp.

Kaufman, A.A., Eaton, P.A., 2001. The Theory of Inductive Prospecting. Elsevier, Amsterdam. 702 pp.

Kaufman, A.A., Hoekstra, P., 2001. Electromagnetic Soundings. Elsevier, Amsterdam. 548 pp.

Kazatchenko, E., Markov, M., Mousatov, A., 2004. Joint inversion of acoustic and resistivity data for carbonate microstructure valuation. Petrophysics 45, 130–140.

Keating, P.B., Crossley, D.J., 1990. The inversion of time-domain airborne electromagnetic data using the plate model. Geophysics 55 (6), 705–711.

Keller, G.V., 1959. Directional resistivity measurements in exploration for uranium deposits on the Colorado Plateau. U.S. Geol. Surv. Bull. 1083, 37–72.

Keller, G.V., 1966. Dipole method for deep resistivity studies. Geophysics 31 (6), 1088–1104.

Keller, G.V., 1968. Electrical prospecting for oil. Colo. Sch. Mines Q. 63 (2), 1–268.

Keller, G.V., 1969. Electromagnetic Surveys in the Central Volcanic Region. Preliminary Report. Department of Scientific and Industrial Research, New Zealand. Report 55, 65 pp.

Keller, G.V., Frischknecht, F.C., 1966. Electrical Methods in Geophysical Prospecting. Pergamon Press, Oxford. 517 pp.

Keller, G.V., Furgerson, R., Lee, C.Y., Harthill, N., Jacobson, J.J., 1975. The dipole mapping method. Geophysics 40 (3), 451–472.

Ketola, M., 1972. Some points of view concerning mise-a-la-masse measurements. Geoexploration 10 (1), 1–22.

Key, K.W., 2003. Application of Broadband Marine Magnetotelluric Exploration to a 3-D Salt Structure and a Fast Spreading Ridge. Ph.D. thesis. University of California, San Diego.

Key, K.W., Constable, S.C., Weiss, C.J., 2006. Mapping 3-D salt using the 2-D marine magnetotelluric method: Case study from Gemini Prospect, Gulf of Mexico. Geophysics 71, B17.

Kharkevich, A.A., 1960. Spectra and Analysis. Consultants Bureau, New York. 222 pp.

Klein, J.D., Biegler, T., Horne, M.D., 1984. Mineral interfacial processes in the method of induced polarization. Geophysics 49 (7), 1105–1114.

Koefoed, O., 1968. The Application of the Kernel Function in Interpreting Geoelectrical Resistivity Measurements. Gebruder Borntraeger, Berlin. 111 pp.

Kolundzija, B.M., Djordjevic, A.R., 2002. Electromagnetic Modeling of Composite Metallic and Dielectric Structures. Artech House.

Komarov, V.A., 1980. Electrical Prospecting by Induced Polarization Method. Nedra, Leningrad.

Kong, J.A., 1975. Theory of Electromagnetic Waves. John Wiley & Sons, New York. 348 pp.

Kong, J.A., 2000. Electromagnetic Wave Theory. EMW Publishing, Cambridge, Massachusetts, USA. 1007 pp.

Kozlovskiy, Ye.A. (Ed.), 1987. The Superdeep Well of the Kola Peninsula. Springer Verlag, Berlin. 558 pp.

Kuc, R., 1988. Introduction to Digital Signal Processing. McGraw-Hill, New York. 414 pp.

Kunetz, G., 1966. Principles of Direct Current Resistivity Prospecting. Gebruder Borntraeger, Berlin. 103 pp.

Kunetz, G., Chastenet de Gery, J., 1956. La representation conforme et divers problems de potentiel dans les milieux de « permeabilite » differente. Revue de Inst. Tech. Francais Pet., pp. 1179–1192.

Labson, V.F., Becker, A., Morrison, H.F., Conti, U., 1985. Geophysical exploration with audiofrequency natural magnetic fields. Geophysics 50, 656–664.

Lamont, J.V., 1862. Der Erdstrom und der Zusammen desselben mit dem Erdmagnetismus. Leopold-Voss-Verlag.

Landau, L.D., Pitaevsky, L.P., Lifshitz, E.M., 1984. Electrodynamics of Continuous Medium, 2nd ed. Elsevier, Butterworth-Heinemann.

Landauer, R., 1978. Electrical conductivity in inhomogeneous media. In: AIP Conference Proceedings, vol. 40, pp. 2–45.

Lee, S., McMechan, G.A., Aiken, S.L.V., 1987. Phase-field imaging: the electromagnetic equivalent of seismic migration. Geophysics 52 (5), 678–693.

Legault, J., Wilson, G.A., Gribenko, A.V., Zhdanov, M.S., Zhao, S., Fisk, K., 2012. An overview of the ZTEM and AirMt airborne electromagnetic systems: a case study from the Nebo–Babel Ni–Cu–PGE deposit, West Musgrave, Western Australia. Preview 158, 26–32.

Levenberg, K., 1944. A method for the solution of certain nonlinear problems in least squares. Q. Appl. Math. 2, 164–168.

Li, Y., Oldenburg, D.W., 2000. 3-D inversion of induced polarization data. Geophysics 65 (6), 1931–1945.

Li, Y., Oldenburg, D.W., 1991. Aspects of charge accumulation in DC resistivity experiments. Geophys. Prospect. 39 (6), 803–826.

Lilley, F.E.M., Sloane, M.N., 1976. On estimating electrical conductivity using gradient data from magnetometer arrays. J. Geomagn. Geoelectr. 28, 321–328.

Lindell, I.V., 2004. Differential Forms in Electromagnetics. IEEE Press, John Wiley & Sons. 253 pp.

Lipskaya, N.V., 1953. Some relationships between harmonics of variations of the Earth electromagnetic field. Izv. Akad. Nauk SSSR, Ser. Geofiz. 1, 17–29.

Liu, G., Becker, A., 1990. Two-dimensional mapping of sea ice keels with airborne electromagnetics. Geophysics 55 (2), 239–248.

Liu, G., Asten, M., 1993. Conductance-depth imaging of airborne TEM data. Explor. Geophys. 24 (4), 655–662.

London, F., 1950. Superfluids, Vol. 1. Wiley, New York. 161 pp.

London, F., 1954. Superfluids, Vol. 2. Wiley, New York. 217 pp.

Lundberg, H., 1922. Practical Experience in Electrical Prospecting. Geological Survey of Sweden.

Luo, Y., Zang, G., 1998. Theory and Application of Spectral Induced Polarization. Society of Exploration Geophysicists, Tulsa, OK. 171 pp.

MacGregor, L.M., Sinha, M.C., 2000. Use of marine controlled-source electromagnetic sounding for sub-basalt exploration. Geophys. Prospect. 48 (6), 1091–1106.

MacGregor, L.M., Sinha, M.C., Constable, S., 2001. Electrical resistivity structure of the Valu Fa Ridge, Lau basin, from marine controlled-source electromagnetic sounding. Geophys. J. Int. 146 (1), 217–236.

MacInnes, S., 2007. Complex resistivity modeling: presented at the IP symposium. In: 77th Annual International Meeting, SEG.

Mackie, R.L., Madden, T.R., Wannamaker, P.E., 1993. Three-dimensional magnetotelluric modeling using difference equations – theory and comparisons to integral equation solutions. Geophysics 58 (2), 215–226.

Mackie, R.L., Smith, J.T., Madden, T.R., 1994. Three-dimensional electromagnetic modeling using finite difference equations: the magnetotelluric example. Radio Sci. 29, 923–935.

Mackie, R.L., Watts, M.D., 2004. The use of 3D magnetotelluric inversion for exploration in complex geologic environments; potential pitfalls and real world examples. Eos Trans. AGU 85, GP14A-01.

Macnae, J., King, A., Stolz, N., Osmakoff, A., Blaha, A., 1998. Fast AEM data processing and inversion. Explor. Geophys. 29, 163–169.

Macnae, J., Lamontagne, Y., 1987. Imaging quasi-layered conductive structures by simple processing of electromagnetic data. Geophysics 52 (4), 545–554.

Madden, T.R., Mackie, R.L., 1989. 3-D magnetotelluric modelling and inversion. Proc. IEEE 77, 318–332.

Maillet, R., 1947. The fundamental equations of electrical prospecting. Geophysics 12 (4), 529–556.

Maillet, R., Doll, H.G., 1932. Sur un theorem relatif aux milieux electgriquement anisotropes et ses applications a la prospection electrique en courant continu. Ergänz.heft Angew. Geophys. 3, 109–124.

Mantell, C.L., 1970. Batteries and Energy Systems. McGraw-Hill, New York. 221 pp.

March, H.W., 1953. The field of a magnetic dipole in the presence of a conducting sphere. Geophysics 18 (3), 671–684.

Marquardt, D.W., 1963. An algorithm for least squares estimation of nonlinear parameters. J. Soc. Ind. Appl. Math. 11, 431–441.

Marshall, D.J., Madden, T.R., 1959. Induced polarization, a study of its causes. Geophysics 24 (4), 790–816.

Mattsson, J., Lindqvist, P., Juhasz, R., Björnemo, E., 2012. Noise reduction and error analysis for a towed EM system. In: 82nd Annual International Meeting. SEG, Houston, Texas.

Maxwell, J.C., 1954. A Treatise on Electricity and Magnetism. Dover Publications, New York (unabridged and unaltered republication of the third edition of 1891), 506 pp.

McGillivray, P.R., Oldenburg, D.W., 1990. Methods for calculating Fréchet derivatives and sensitivities for the nonlinear inverse problem: a comparative study. Geophys. Prospect. 38 (5), 499–524.

McGillivray, P.R., Oldenburg, D.W., Ellis, R.G., Habashy, T.M., 1994. Calculation of sensitivities for the frequency-domain electromagnetic problem. Geophys. J. Int. 116, 1–4.

McMillan, M.S., Schwarzbach, C., Haber, E., Oldenburg, D.W., 2015. 3D parametric hybrid inversion of time-domain airborne electromagnetic data. Geophysics 80 (6), K25–K36.

McNeill, J.D., Labson, V., 1991. Geological mapping using VLF radio fields. In: Nabighian, M.N., Corbett, J.D. (Eds.), Electromagnetic Methods in Applied Geophysics, Vol. 2, Applications. Society of Exploration Geophysicists, Tulsa, Oklahoma, pp. 521–640.

Meqbel, N.M., Egbert, G.D., Wannamaker, P.E., Kelbert, A., Schultz, A., 2013. Deep electrical resistivity structure of the northwestern U.S. derived from 3-D inversion of USArray magnetotelluric data. Earth Planet. Sci. Lett. 402, 290–304.

Mehanee, S., Zhdanov, M.S., 2001. 3-D finite-difference forward modeling based on the balance method. In: 71st Annual International Meeting, SEG, Expanded Abstracts, pp. 1443–1446.

Mehanee, S., Zhdanov, M.S., 2002. Magnetotelluric inversion of blocky geoelectrical structures using the minimum support method. J. Geophys. Res., Solid Earth 107 (B4). http://dx.doi.org/10.1029/2001JB000191.

Mendelson, K.S., Cohen, M.H., 1982. The effect of grain anisotropy on the electrical properties of sedimentary rocks. Geophysics 47 (2), 257–263.

Meyer, S.L., 1975. Data Analysis for Scientists and Engineers. John Wiley & Sons. 513 pp.

Misner, C.W., Thorne, K.S., Wheeler, J.A., 1973. Gravitation. Freeman, San Francisco. 1279 pp.

Mittet, R., Maaø, F., Aakervik, O.M., Ellingsrud, S., 2005. A two-step approach to depth migration of low-frequency electromagnetic data. In: 75th Annual International Meeting, SEG, Expanded Abstracts, Electronic Volume.

Molano, C.E., Salamanca, M., van Overmeeren, R.A., 1990. Numerical modeling of standard and continuous vertical electrical soundings. Geophys. Prospect. 38 (7), 705–718.

Mooney, H.M., Wetzel, W.W., 1956. The Potentials About a Point Electrode and Apparent Resistivity Curves for a Two-, Three-, and Four-Layer Earth. The University of Minnesota Press, Minneapolis. 146 pp.

Moran, J.H., Gianzero, S.C., 1979. Effects of formation anisotropy on resistivity logging measurements. Geophysics 44, 1266–1286.

Morse, P.M., Feshbach, H., 1953. Methods of Theoretical Physics. McGraw Hill Book Co., New York. 1978 pp.

Mukherjee, S., Everett, M.E., 2011. 3D controlled-source electromagnetic edge-based finite element modeling of conductive and permeable heterogeneities. Geophysics 76, F215–F226.

Nabighian, M.N., Macnae, J.C., 1991. Time domain electromagnetic prospecting methods. In: Nabighian, M.N., Corbett, J.D. (Eds.), Electromagnetic Methods in Applied Geophysics, Vol. 2, Applications. Society of Exploration Geophysicists, Tulsa, Oklahoma, pp. 427–520.

Naldrett, A.J., Keats, H., Sparkes, K., Moore, S., 1996. Geology of the Voisey's Bay Ni–Cu–Co deposit, Labrador, Canada. Explor. Min. Geol. 5, 169–179.

Nedelec, J.C., 1980. Mixed finite elements in R^3. Numer. Math. 35, 315–341.

Nelson, P.H., 1997. Induced polarization research at Kennecott, 1965–1977. Lead. Edge 16 (1), 29–33.

Newman, G.A., Alumbaugh, D.L., 1997. Three-dimensional massively parallel inversion – I. Theory. Geophys. J. Int. 128, 345–354.

Newman, G.A., Alumbaugh, D.L., 2000. Three-dimensional magnetotelluric inversion using non-linear conjugate gradients. Geophys. J. Int. 140, 410–424.

Newman, G.A., Boggs, P.T., 2004. Solution accelerators for large-scale three-dimensional electromagnetic inverse problems. Inverse Probl. 20, S151–S170.

Niwas, S., Israel, M., 1989. Matrix method for the transformation of resistivity sounding data of one electrode configuration to that of another configuration. Geophys. Prospect. 37 (2), 209–221.

Norris, A.N., Sheng, P., Callegari, A.J., 1985. Effective medium theories for two-phase dielectric media. Appl. Phys. Lett. 57, 1990–1996.

Novozhilov, U.V., Yappa, U.A., 1981. Electrodynamics. Mir Publishers, Moscow. 352 pp.

Novysh, V.V., Fonarev, G.A., 1966. The results of the electromagnetic study in the Arctic Ocean. Geomagn. Aeron. 6, 406–409.

Obrebski, M., Allen, R.M., Xue, M., Hung, S.H., 2010. Slab-plume interaction beneath the Pacific Northwest. Geophys. Res. Lett. 37, L14305.

Obrebski, M., Allen, R.M., Pollitz, F., Hung, S., 2011. Lithosphere–asthenosphere interaction beneath the western United States from the joint inversion of body-wave travel times and surface-wave phase velocities. Geophys. J. Int. 185, 1003–1021.

Obukhov, G.G., 1968. About some properties of the nonstationary electromagnetic fields in the Earth and their applications in electrical prospecting. Izv. Akad. Nauk SSSR, Phys. Earth 9, 62–71.

Ogilvie, J.S., Purnell, G.W., 1996. Effects of salt related mode conversions on subsalt prospecting. Geophysics 61 (2), 331–348.

Oldenburg, D.W., 1990. Inversion of electromagnetic data: an overview of new techniques. Surv. Geophys. 11, 231–270.

Oldenburg, D., Li, Y., 1994. Inversion of induced polarization data. Geophysics 59 (9), 1327–1341.

Olhoeft, G.R., 1980. Electrical properties in rocks. In: Thoulaikian, Y.S., Judd, W.R., Roy, R.F. (Eds.), Physical Properties of Rocks and Minerals. McGraw-Hill, New York, pp. 257–330.

Oristaglio, M.L., 1989. An inverse scattering formula that uses all the data. Inverse Probl. 5, 1097–1105.

Oristaglio, M., Dorozynski, A., 2009. A Sixth Sense: The Life and Science of Henry-Georges Doll, Oilfield Pioneer and Inventor. Overlook Duckworth.

Palacky, G.F., West, G.F., 1991. Airborne electromagnetic methods. In: Nabighian, M.N., Corbett, J.D. (Eds.), Electromagnetic Methods in Applied Geophysics, Vol. 2, Applications. Society of Exploration Geophysicists, Tulsa, Oklahoma, pp. 811–880.

Pankratov, O.V., Avdeev, D.B., Kuvshinov, A.V., 1995. Electromagnetic field scattering in heterogeneous Earth: a solution to the forward problem. Phys. Solid Earth (Engl. Ed.) 31, 201–209.

Pankratov, O.V., Kuvshinov, A.V., Avdeev, D.B., 1997. High-performance three-dimensional electromagnetic modeling using modified Neumann series. Anisotropic Earth. J. Geomagn. Geoelectr. 49, 1541–1547.

Papoulis, A., 1962. The Fourier Integral and Its Applications. McGraw-Hill Book Company Inc., New York. 318 pp.

Parks, T.W., Burrus, C.S., 1987. Digital Filter Design. John Wiley & Sons, New York. 330 pp.

Patro, P.K., Egbert, G.D., 2008. Regional conductivity structure of Cascadia: preliminary results from 3D inversion of USArray transportable array magnetotelluric data. Geophys. Res. Lett. 35, L20311.

Pavlov, D., Zhdanov, M.S., 2001. Analysis and interpretation of anomalous conductivity and magnetic permeability effects in time domain electromagnetic data. Part I: numerical modeling. Appl. Geophys. 46 (4), 217–233.

Pekeris, C.L., 1940. Direct method of interpretation in resistivity prospecting. Geophysics 5 (1), 31–42.

Pellerin, L., Johnston, J.M., Hohmann, G.W., 1993. Three-dimensional inversion of electromagnetic data: expanded abstracts. In: 63rd Annual International Meeting, SEG, Expanded Abstracts, pp. 360–363.

Pelton, W.H., 1977. Interpretation of Induced Polarization and Resistivity Data. Ph.D. thesis. University of Utah.

Pelton, W.H., Ward, S.H., Hallof, P.G., Sill, W.R., Nelson, P.H., 1978. Mineral discrimination and removal of inductive coupling with multifrequency IP. Geophysics 43 (3), 588–609.

Pierce, F.W., Bolm, J.G. (Eds.), 1995. Porphyry Copper Deposits of the American Cordillera. Arizona Geological Society Digest, vol. 20.

Plouff, D., 1966. Magnetotelluric soundings in the southwestern United States. Geophysics 31 (6), 1145–1152.

Plouff, D., Keller, G.V., Frischknecht, F.C., Wahl, R.R., 1961. Geophysical studies on IGY drifting station Bravo, T-3, 1958 to 1959. In: Geology of the Arctic, vol. 1, pp. 709–716.

Pommier, A., Gaillard, F., Pichavant, M., Scaillet, B., 2008. Laboratory measurements of electrical conductivities of hydrous and dry Mt. Vesuvius melts under pressure. J. Geophys. Res. 113, B05205.

Portniaguine, O., Zhdanov, M.S., 1999a. Focusing geophysical inversion images. Geophysics 64 (3), 874–887.

Portniaguine, O., Zhdanov, M.S., 1999b. Parameter estimation for 3D geoelectromagnetic inverse problems: three dimensional electromagnetics. In: Three Dimensional Electromagnetics. In: SEG Monograph. Society of Exploration Geophysicists, Tulsa, OK, pp. 222–232.

Portniaguine, O., Zhdanov, M.S., 2002. 3-D focusing inversion of electromagnetic data. In: Zhdanov, M.S., Wannamaker, P.E. (Eds.), Three Dimensional Electromagnetics. Elsevier, pp. 173–192.

Press, W.H., Flannery, B.P., Teukolsky, S.A., Vettering, W.T., 1987. Numerical Recipes, the Art of Scientific Computing, Vols. I and II. Cambridge University Press, Cambridge. 1447 pp.

Price, A.T., 1949. The induction of electric currents in non-uniform thin sheets and shells. Q. J. Mech. Appl. Math. 2, 283–310.

Puahengsup, P., Wan, L., Zhdanov, M.S., 2008. Digital filters for electromagnetic migration of marine electromagnetic data. In: Proceedings of Annual Meeting of Consortium for Electromagnetic Modeling and Inversion, pp. 227–272.

Raiche, A.P., 1974. An integral equation approach to three-dimensional modelling. Geophys. J. R. Astron. Soc. 36, 363–376.

Raiche, A., Annetts, D., Sugeng, F., 2001. EM target response in complex hosts: presented at ASEG 15th Geophysical Conference and Exhibition, Brisbane.

Rapolla, A., 1974. Natural electric field survey in three southern Italy geothermal areas. Geothermics 3 (3), 118–121.

Ratcliffe, J.A., 1959. The Magneto-Ionic Theory and Its Applications to the Ionosphere. Cambridge University Press, Cambridge. 206 pp.

Reddy, I.K., Rankin, D., Phillips, R.J., 1977. Three-dimensional modeling in magnetotelluric and magnetic variational sounding. Geophys. J. R. Astron. Soc. 51, 313–325.

Richtmyer, R.D., Morton, K.W., 1967. Difference Methods for Initial Value Problems. John Wiley and Sons, New York. 401 pp.

Rikitake, T., 1950. Electromagnetic induction within the earth and its relation to the electrical state of the earth's interior. 2. Bull. Earthq. Res. Inst. Univ. Tokyo 28, 263–283.

Rodi, W.L., 1976. A technique for improving the accuracy of finite element solutions for magnetotelluric data. Geophys. J. R. Astron. Soc. 44, 483–506.

Roth, J.B., Fouch, M.J., James, D.E., Carlson, R.W., 2008. Three-dimensional seismic velocity structure of the northwestern United States. Geophys. Res. Lett. 35, L15304.

Røsten, T., Hokstad, K., Arntsen, B., 2006. 3D depth migration operators for marine controlled-source electromagnetic data. In: 75th Annual International Meeting, SEG, Expanded Abstracts, pp. 770–774.

Rudin, L.I., Osher, S., Fatemi, E., 1992. Nonlinear total variation based noise removal algorithms. Physica D 60, 259–268.

Saad, Y., 2003. Iterative Methods for Sparse Linear Systems, 2nd ed. Society for Industrial and Applied Mathematics, Philadelphia, PA, USA.

Samarsky, A.A., 1984. Theory of the Difference Schemes. Nauka Publishing House, Moscow (in Russian), 656 pp.

Sasaki, Y., 2001. Full 3D inversion of electromagnetic data on PC. J. Appl. Geophys. 46, 45–54.

Sasaki, Y., 2004. Three-dimensional inversion of static-shifted magnetotelluric data. Earth Planets Space 56, 239–248.

Sattel, D., 2005. Inverting airborne electromagnetic data with Zohdy's method. Geophysics 70, G77–G85.

Schey, H.M., 1973. Div, Grad, Curl, and All That: An Informal Text on Vector Calculus. W.W. Norton & Co., New York. 163 pp.

Schlumberger, C., 1920. Etude sur la prospection electrique du sours-sol. Gauthier-Villars et Cie, Paris.

Schmandt, B., Humphreys, E., 2010. Complex subduction and small-scale convection revealed by body-wave tomography of the western United States upper mantle. Earth Planet. Sci. Lett. 297 (3–4), 435–445.

Schmucker, U., 1970. Anomalies of Geomagnetic Variations in the Southwestern United States. University of California Press. 165 pp.

Schneider, W.A., 1978. Integral formulation for migration in two and three dimensions. Geophysics 43 (1), 49–76.

Schutt, D.L., Dueker, K., 2008. Temperature of the plume layer beneath the Yellowstone hotspot. Geology 36, 623–626.

Schutt, D.L., Dueker, K., Yuan, H., 2008. Crust and upper mantle velocity structure of the Yellowstone hotspot and surroundings. J. Geophys. Res. 113, B03310.

Seigel, H.O., 1959a. A theory for induced polarization effects (for step-function excitation). In: Wait, J.R. (Ed.), Overvoltage Research and Geophysical Applications. Pergamon Press, New York, pp. 4–21.

Seigel, H.O., 1959b. Mathematical formulation and type curves for induced polarization. Geophysics 24 (3), 547–565.

Seigel, H.O., Howland-Rose, A.W., 1990. Magnetic induced polarization method. In: Ward, S.H. (Ed.), Induced Polarization, Applications and Case Histories. Society of Exploration Geophysicists, Tulsa, Oklahoma, pp. 23–56.

Seigel, H.O., Nabighian, M., Parasnis, D., Vozoff, K., 2007. The early history of the induced polarization method. Lead. Edge 26 (3), 312–321.

Sen, P., Scala, C., Cohen, M.H., 1981. A self-similar model for sedimentary rocks with application to the dielectric constant of fused glass beads. Geophysics 46 (5), 781–796.

Sengpiel, K.P., Siemon, B., 2000. Advanced inversion methods for airborne electromagnetic exploration. Geophysics 65 (6), 1983–1992.

Sheinman, S.M., 1969. Contemporary Physical Foundations of the Electrical Prospecting Theory. Nedra, Moscow.

Sheng, P., 1991. Consistent modeling of the electrical and elastic properties of sedimentary rocks. Geophysics 56 (8), 1236–1243.

Shneyer, V.S., Trofimov, I.L., Abramov, Yu.M., Zhdanov, M.S., Machinin, V.A., Shabelyansky, S.V., 1991. Some results of gradient electromagnetic sounding in doldrums mid-Atlantic ridge fracture. Phys. Earth Planet. Inter. 66 (3–4), 259–264.

Shuey, R.T., Johnson, M., 1973. On the phenomenology of electrical relaxation in rocks. Geophysics 38 (1), 37–48.

Shuey, R.T., 1975. Semiconducting Ore Minerals. Elsevier, Amsterdam. 415 pp.

Shwartz, L.M., 1994. Effective medium theory of electrical condition in two-component anisotropic composites. Physica A 207, 131–136.

Sidorov, V.A., Tickshaev, V.V., 1969. Electrical Prospecting with Transient Field in Near Zone. Saratov University, U.S.S.R.

Sihvola, A., 1999. Electromagnetic Mixing Formulas and Applications. IEE Electromagnetic Waves Series, vol. 47. Springer, London, UK. 284 pp.

Sillitoe, R.H., 1973. The tops and bottoms of porphyry copper deposits. Econ. Geol. 68, 799–815.

Silva, N.V., Morgan, J.V., MacGregor, L., Warner, M., 2012. A finite element multifrontal method for 3D CSEM modeling in the frequency domain. Geophysics 77, E101–E115.

Simpson, F., Bahr, K., 2005. Practical Magnetotellurics. Cambridge University Press. 270 pp.

Singer, B.Sh., 1995. Method for solution of Maxwell's equation in non-uniform media. Geophys. J. Int. 120, 590–598.

Singer, B.Sh., Fainberg, E.B., 1997. Fast and stable method for 3-D modeling of electromagnetic field. Explor. Geophys. 28 (2), 130–135.

Singer, B.Sh., Mezzatesta, A., Wang, T., 2003. Integral equation approach based on contraction operators and Krylov subspace optimisation. In: Macnae, J., Liu, G. (Eds.), Three-Dimensional Electromagnetics III. Australian Society of Exploration Geophysicists.

Sinha, M.C., Patel, P.D., Unsworth, M.J., Owen, T.R.E., MacCormack, M.G.R., 1990. An active source electromagnetic sounding system for marine use. Mar. Geophys. Res. 12 (1–2), 59–68.

Siripunvaraporn, W., Uyeshima, M., Egbert, G., 2004. Three-dimensional inversion for network-magnetotelluric data. Earth Planets Space 56, 893–902.

Siripunvaraporn, W., Egbert, G., Lenbury, Y., Uyeshima, M., 2005. Three-dimensional magnetotelluric inversion; data-space method. Phys. Earth Planet. Inter. 150, 3–14.

Slater, J.C., Frank, N.H., 1947. Electromagnetism. McGraw-Hill, New York. 240 pp.

Smith, J.T., 1996. Conservative modeling of 3-D electromagnetic fields; part II: bi-conjugate gradient solution and an accelerator. Geophysics 61 (5), 1319–1324.

Smith, J.T., Booker, J.R., 1991. Rapid inversion of two- and three-dimensional magnetotelluric data. J. Geophys. Res. 96, 3905–3922.

Smith, R.B., Jordan, M., Steinberger, B., Puskas, C.M., Farrell, J., Waite, G.P., Husen, S., Chang, W., O'Connell, R., 2009. Geodynamics of the Yellowstone hotspot and mantle plume: seismic and GPS imaging, kinematics, and mantle flow. J. Volcanol. Geotherm. Res. 188, 26–56.

Smith, W.H.F., Sandwell, D.T., 1997. Global seafloor topography from satellite altimetry and ship depth soundings. Science 277, 1956–1962.

Sommerfeld, A., 1912. Die Greensche Function der Schwingungsgleichung. Jahresber. Dtsch. Math.-Ver. 21. 309 pp.

Sommerfeld, A., 1952. Electrodynamics, Lectures on Theoretical Physics, Vol. III. Academic Press, New York. 371 pp.

Spies, B.R., 1989. Depth of investigation of electromagnetic sounding methods. Geophysics 54 (7), 872–888.

Spies, B.R., Frischknecht, F.C., 1991. Electromagnetic sounding. In: Nabighian, M.N., Corbett, J.D. (Eds.), Electromagnetic Methods in Applied Geophysics, Vol. 2, Applications. Society of Exploration Geophysicists, Tulsa, Oklahoma, pp. 285–425.

Spiess, F.N., Macdonald, K.C., Atwater, T., Ballard, R., Carranza, A., Cordoba, D., Cox, C., Diaz Garcia, V.M., Francheteau, J., Guerrero, J., Hawkings, J., Haymon, R., Hessler, R., Juteau, T., Kastner, M., Larson, R., Luyendyk, B., Macdougall, J.D., Miller, S., Normark, W., Orcutt, J., Rangin, C., 1980. East Pacific rise: hot springs and geophysical experiments. Science 207, 1421–1433.

Srnka, L.J., Carazzone, J.J., Ephron, M.S., Eriksen, E.A., 2006. Remote reservoir resistivity mapping. Lead. Edge 25, 972–976.

Stearns, S.D., David, R.A., 1988. Signal Processing Algorithms. Prentice-Hall, Englewood Cliffs, New Jersey. 349 pp.

Stefanescu, S., Schlumberger, C., Schlumberger, M., 1930. Sur la distribution electrique potentielle autour d'une prise de terrre ponctuelle dans un terrain a couches horizontales homogenes et isotropes. J. Phys. Radium VII, 132–140.

Stolt, R.M., 1978. Migration by Fourier transform. Geophysics 43 (1), 23–49.

Strack, K.M., 1999. Exploration with Deep Transient Electromagnetics. Elsevier, Amsterdam. 374 pp.

Strakhov, V.N., 1968. Numerical solution of incorrect problems representable by integral equations of convolution type. DAN SSSR 178 (2), 299 (in Russian).

Strakhov, V.N., 1969a. Theory of approximate solution of the linear ill-posed problems in a Hilbert space and its application in applied geophysics, part I. Izv. Akad. Nauk SSSR, Phys. Earth 8, 30–53 (in Russian).

Strakhov, V.N., 1969b. Theory of approximate solution of the linear ill-posed problems in a Hilbert space and its application in applied geophysics, part II. Izv. Akad. Nauk SSSR, Phys. Earth 9, 64–96 (in Russian).

Stratton, J.A., 1941. Electromagnetic Theory. McGraw-Hill Book Company, New York and London. 615 pp.

Streich, R., 2009. 3D finite-difference frequency-domain modeling of controlled-source electromagnetic data: direct solution and optimization for high accuracy. Geophysics 74 (5), F95–F105.

Stroud, D., 1975. Generalized effective medium approach to the conductivity of an inhomogeneous material. Phys. Rev. B 12, 3368–3373.

Sumner, J.S., 1976. Principles of Induced Polarization for Geophysical Exploration. Elsevier, Amsterdam. 277 pp.

Sunde, E.D., 1949. Earth Conduction Effects in Transmission Systems. D. Van Nostrand Co., New York. 371 pp.

Svetov, B.S., Shemelevich, M.I., 1986. Magnetotelluric variation processing. Surv. Geophys. 9, 259–285.

Tabarovsky, L.A., 1975. Application of Integral Equation Method to Geoelectrical Problems. Nauka, Novosibirsk (in Russian).

Tagg, G.F., 1964. Earth Resistances. George Newnes Ltd., New York. 258 pp.

Tamm, I.E., 1979. Fundamentals of the Theory of Electricity. Mir Publishers, Moscow. 684 pp.

Tarantola, A., 1984. Inversion of seismic reflection data in the acoustic approximation. Geophysics 49, 1259–1266.

Tarantola, A., 1987. Inverse Problem Theory. Elsevier, Amsterdam, Oxford, New York, Tokyo. 613 pp.

Tartaras, E., Zhdanov, M.S., Wada, K., Saito, A., Hara, T., 2000. Fast imaging of TDEM data based on S-inversion. J. Appl. Geophys. 43, 15–32.

Telford, W.M., Geldardt, L.P., Sheriff, R.E., 1990. Applied Geophysics, 2nd ed. Cambridge University Press, New York. 770 pp.

Terada, T., 1917. On rapid periodic variations of terrestrial magnetism. J. Coll. Sci., Imp. Univ. Tokyo 37, 56–84.

Tikhonov, A.N., 1950. On the determination of electrical characteristics of deep layers of the Earth's crust. Dokl. Akad. Nauk SSSR 73, 295–297 (in Russian).

Tikhonov, A.N., 1963a. Solution of ill-posed problems and the regularization method. Sov. Math. Dokl. 4, 1035–1038 (in Russian).

Tikhonov, A.N., 1963b. Regularization of ill-posed problems. Sov. Math. Dokl. 4, 1624–1627 (in Russian).

Tikhonov, A.N., 1999. Mathematical Geophysics. Moscow State University (in Russian), 476 pp.

Tikhonov, A.N., Arsenin, V.Y., 1977. Solution of Ill-Posed Problems. V.H. Winston and Sons. 258 pp.

Titley, S.R. (Ed.), 1982. Advances in Geology of the Porphyry Copper, Southwestern North America. University of Arizona Press, Tucson, AZ. 560 pp.

Tompkins, M.J., 2004. Marine controlled-source electromagnetic imaging for hydrocarbon exploration: interpreting subsurface electrical properties. First Break 22, 27–33.

Tong, P., Rossettos, J.N., 1977. Finite Element Method. MIT Press, Cambridge. 332 pp.

Torres-Verdin, C., Habashy, T.M., 1994. Rapid 2.5-dimensional forward modeling and inversion via a new scattering approximation. Radio Sci. 29 (4), 1051–1079.

Tozer, D.C., 1981. The mechanical and electrical properties of the Earth's asthenosphere. Phys. Earth Planet. Inter. 25, 280–296.

Tralli, N., 1963. Classical Electromagnetic Theory. McGraw-Hill, New York. 308 pp.

Trofimov, I.L., Fonarev, G.A., 1972. Some results of the magnetotelluric profiling in the Arctic ocean. Izv. Akad. Nauk SSSR, Phys. Earth 2, 81–92.

Ueda, T., Zhdanov, M.S., 2006. Fast numerical modeling of multitransmitter electromagnetic data using multigrid quasi-linear approximation. IEEE Trans. Geosci. Remote Sens. 44 (4), 1428–1434.

Ueda, T., Zhdanov, M.S., 2008. Fast numerical methods for marine controlled-source electromagnetic (EM) survey data based on multigrid quasi-linear approximation and iterative EM migration. Explor. Geophys. 39 (1), 60–67.

Vallèe, M.A., Smith, R.S., 2007. Comparison of fixed-wing airborne electromagnetic 1D inversion methods. In: Proceedings of Exploration 07: Fifth Decennial International Conference on Mineral Exploration. Prospectors and Developers Association of Canada, pp. 1067–1072.

Vallèe, M.A., Smith, R.S., 2009. Application of Occam's inversion to airborne time-domain electromagnetics. Lead. Edge 28 (3), 284–287.

Vanyan, L.L., 1959. Some questions of theory of frequency soundings. Prikl. Geofiz., Nedra 23, 3–45.

Vanyan, L.L., 1967. Electromagnetic Depth Soundings. Consultants Bureau, New York. 312 pp.

Vanyan, L.L., 1997. Electromagnetic Soundings. Scientific Word, Moscow (in Russian), 219 pp.

Vanyan, L.L., Butkovskaya, A.I., 1980. Magnetotelluric Sounding of Layered Media. Nedra, Moscow (in Russian).

Varentsov, Iv.M., EMTESZ-Pomerania Working Group, 2006. Method of horizontal magnetovariational sounding: techniques and applications in the EMTESZ-Pomerania project. In: Ritter, O., Brasse, H. (Eds.), Protokoll 21. Kolloquium Elektromagnetische Tiefenforschung. Haus Wohldenberg, Holle, pp. 111–123.

Velikhov, E.P., Volkov, Yu.M., D'yakonov, B.P., 1975. Application of pulsed MHD generators for geophysical studies and earthquake prediction. In: Proceedings of VI International Conference on MHD Power Conversion, Vol. 5. Washington D.C., pp. 211–228.

Velikhov, Ye.P. (Ed.), 1989. Geoelectric Investigations with Strong Current Sources on the Baltic Shield. Nauka, Moscow. 272 pp.

Velikhov, Ye.P., Zhdanov, M.S., Frenkel, M.A., 1987. Interpretation of MHD-sounding data from the Kola Peninsula by the electromagnetic migration method. Phys. Earth Planet. Inter. 45 (2), 149–160.

Velikhov, E.P., Panchenko, V.P., 2010. Large-scale geophysical surveys of the Earth's crust using high-power electromagnetic pulses. In: Kasahara, J., Korneev, V., Zhdanov, M.S. (Eds.), Active Geophysical Monitoring. Elsevier, pp. 29–54.

Vinegar, H.J., Waxman, M.H., 1988. In-situ induced polarization method for determining formation permeability. US Patent 4,743,854.

Vogel, C.R., Oman, M.E., 1998. Fast total variation based reconstruction of noisy, blurred images. IEEE Trans. Image Process. 7 (6), 813–824.

von Hippel, A.R., 1954. Dielectrics and Waves. John Wiley & Sons, New York. 284 pp.

von Hippel, A.R., 1958. Dielectrics. In: Condon, E.U., Odishaw, H. (Eds.), Handbook of Physics. McGraw-Hill, New York, pp. 103–125.

Vozoff, K., 1972. The magnetotelluric method in the exploration of sedimentary basins. Geophysics 37 (1), 98–141.

Wait, J.R., 1954. Mutual coupling of loops lying on the ground. Geophysics 19 (2), 290–296.

Wait, J.R., 1955. Mutual electromagnetic coupling of loops over a homogeneous ground. Geophysics 20, 630–637.

Wait, J.R., 1959. The variable-frequency method. In: Wait, J.R. (Ed.), Overvoltage Research and Geophysical Applications. Pergamon, Oxford.

Wait, J.R., 1960a. On the electromagnetic response of a conducting sphere to a dipole field. Geophysics 25 (3), 649–658.

Wait, J.R., 1960b. Some solutions for electromagnetic induction problems involving spheroidal, spherical, and cylindrical bodies. J. Res. Natl. Bur. Stand. B 64, 15–32.

Wait, J.R., 1962. Electromagnetic Waves in Stratified Media. Pergamon Press, Oxford.

Wait, J.R., 1982. Geo-Electromagnetism. Academic Press, New York. 268 pp.

Waite, G.P., Schutt, D.L., Smith, R.B., 2005. Models of lithosphere and asthenosphere anisotropic structure of the Yellowstone hotspot from shear wave splitting. J. Geophys. Res. 110, B113-04.

Wan, L., Zhdanov, M.S., 2004. New development in 3-D marine MT modeling and inversion for petroleum exploration. In: Proceedings of Annual Meeting of Consortium for Electromagnetic Modeling and Inversion, pp. 311–332.

Wang, T., Hohmann, G.W., 1993. A finite difference time-domain solution for three dimensional electromagnetic modeling. Geophysics 58 (6), 797–809.

Wang, T., Oristaglio, M., Tripp, A., Hohmann, G.W., 1994. Inversion of diffusive transient electromagnetic data by a conjugate-gradient method. Radio Sci. 29 (4), 1143–1156.

Wannamaker, P.E., 1991. Advances in three-dimensional magnetotelluric modeling using integral equations. Geophysics 56, 1716–1728.

Wannamaker, P.E., Booker, J.R., Jones, A.G., Chave, A.D., Filloux, J.H., Waff, H.S., Law, L.K., 1989. Resistivity cross section through the Juan de Fuca ridge subduction system and its tectonic implications. J. Geophys. Res. X, 14127–14144.

Wannamaker, P.E., Hohmann, G.W., Ward, S.H., 1984. Magnetotelluric responses of three-dimensional bodies in layered earths. Geophysics 49 (9), 1517–1533.

Wannamaker, P.E., Stodt, J.A., Pellerin, L., Olsen, S.L., Hall, D.B., 2004. Structure and thermal regime beneath South Pole region, East Antarctica, from magnetotelluric measurements. Geophys. J. Int. 157, 36–54.

Wannamaker, P.E., Stodt, J.A., Rijo, L., 1987. A stable finite element solution for two-dimensional magnetotelluric modeling. Geophys. J. R. Astron. Soc. 88, 277–296.

Wapenaar, K., 2007. General representations for wavefield modeling and inversion in geophysics. Geophysics 72 (5), SM5–SM17.

Ward, S.H., 1959. AFMAG-airborne and ground. Geophysics 24 (4), 761–787.

Ward, S.H., 1980. Electrical, electromagnetic and magnetotelluric methods. Geophysics 45 (11), 1659–1666.

Ward, S.H., Hohmann, G.W., 1988. Electromagnetic theory for geophysical applications. In: Nabighian, M.N., Corbett, J.D. (Eds.), Electromagnetic Methods in Applied Geophysics – Theory, Vol. 1. Society of Exploration Geophysicists, Tulsa, Oklahoma, pp. 131–314.

Watt, A.D., 1967. VLF Radio Engineering. Pergamon Press, Oxford.

Weaver, J.T., 1994. Mathematical Methods for Geoelectromagnetic Induction. RSP, Willey. 330 pp.

Weaver, J.T., Brewitt-Taylor, C.R., 1978. Improved boundary conditions for the numerical solution of E-polarization problems in geomagnetic induction. Geophys. J. R. Astron. Soc. 54, 309–317.

Weidelt, P., 1975a. Electromagnetic induction in three-dimensional structures. J. Geophys. 41 (1), 85–109.

Weidelt, P., 1975b. Inversion of two-dimensional conductivity structures. Phys. Earth Planet. Inter. 10, 282–291.

Weidelt, P., 1983. The harmonic and transient electromagnetic response of a thin dipping dike. Geophysics 48, 934–952.

Weitkunat, R. (Ed.), 1990. Digital Biosignal Processing. Elsevier, Amsterdam.

Weitemeyer, K., Constable, S., 2010. Mapping shallow geology and gas hydrate with marine CSEM surveys. First Break 28, 97–102.

Wenner, F., 1928. A Method of Measuring Earth Resistivity. U.S. Bureau of Standards Bulletin, p. 258.

Whittaker, E., 1960a. A History of the Theories of Aether and Electricity: Vol. I: The Classical Theories. Harper and Brothers, New York. 434 pp.

Whittaker, E., 1960b. A History of the Theories of Aether and Electricity: Vol. II: The Modern Theories. Harper and Brothers, New York. 319 pp.

Wiener, N., 1964. Generalized Harmonic Analysis and Tauberian Theorems. The MIT Press, Cambridge, Massachusetts. 242 pp.

Witherly, K., 2000. The quest for the Holy Grail in mining geophysics: a review of the development and application of airborne EM systems over the last 50 years. Lead. Edge 19, 270–274.

Wolfgram, P., Golden, H., 2001. Airborne EM applied to sulphide nickel – examples and analysis. Explor. Geophys. 32, 136–140.

Wong, J., 1979. An electrochemical model of the induced-polarization phenomenon in disseminated sulfide ores. Geophysics 44, 1245–1265.

Wong, J., Strangway, D.W., 1981. Induced polarization in disseminated rocks containing elongated mineralization sulfide ores. Geophysics 46, 1258–1268.

Wright, D., Ziolkowski, A., Hobbs, B., 2002. Hydrocarbon detection and monitoring with a multicomponent transient electromagnetic (MTEM) survey. Lead. Edge 21, 852–864.

Wyllie, G., 1960. Theory of polarization and absorption in dielectrics, an introductory survey. In: Progress in Dielectrics. John Wiley and Sons, Inc., New York, pp. 1–28.

Xiong, Z., 1992. Electromagnetic modeling of 3-D structures by the method of system iteration using integral equations. Geophysics 57, 1556–1561.

Xiong, Z., Kirsch, A., 1992. Three-dimensional Earth conductivity inversion. J. Comput. Appl. Math. 42, 109–121.

Xue, M., Allen, R.M., 2007. The fate of the Juan de Fuca plate: implications for a Yellowstone plume head. Earth Planet. Sci. Lett. 264, 266–276.

Yang, D., Oldenburg, D.W., Haber, E., 2014. 3-D inversion of airborne electromagnetic data parallelized and accelerated by local mesh and adaptive soundings. Geophys. J. Int. 196, 1492–1507.

Yavich, N., Zhdanov, M.S., 2016. Contraction pre-conditioner in finite-difference electromagnetic modeling. Geophys. J. Int. 206 (3), 1718–1729.

Yee, K.S., 1966. Numerical solution of initial boundary problems involving Maxwell's equations in isotropic media. IEEE Trans. Antennas Propag. 14 (3), 302–307.

Yoshioka, K., Zhdanov, M.S., 2005. Three-dimensional nonlinear regularized inversion of the induced polarization data based on the Cole–Cole model. Phys. Earth Planet. Inter. 150, 29–43.

Young, P.D., Cox, C.S., 1981. Electromagnetic active source sounding near the East Pacific Rise. Geophys. Res. Lett. 8, 1043–1046.

Yuan, H., Dueker, K., 2005. Teleseismic P-wave tomogram of the Yellowstone plume. Geophys. Res. Lett. 32, L07304.

Yuval, Oldenburg, D.W., 1997. Computation of Cole–Cole parameters from IP data. Geophysics 62, 436–448.

Zaslavsky, M., Druskin, V., Davydycheva, S., Knizhnerman, L., Abubakar, A., Habashy, T., 2011. Hybrid finite-difference integral equation solver for 3D frequency domain anisotropic electromagnetic problems. Geophysics 76 (2), F123–F137.

Zemanian, A.H., 1987. Generalized Integral Transforms. Dover, New York. 300 pp.

Zhdanov, M.S., 1973a. On analytic continuation of three-dimensional electromagnetic fields. Izv. Akad. Nauk SSSR, Phys. Earth 4, 66–78.

Zhdanov, M.S., 1973b. On analytic continuation of two-dimensional electromagnetic fields. Izv. Akad. Nauk SSSR, Phys. Earth 6, 61–69.

Zhdanov, M.S., 1973c. Separation of transient electromagnetic fields of the Earth. Izv. Akad. Nauk SSSR, Phys. Earth 6, 43–54.

Zhdanov, M.S., 1975. Theory of interpretation of deep electromagnetic anomalies using the analytical continuation methods. Izv. Akad. Nauk SSSR, Phys. Earth 9, 59–73.

Zhdanov, M.S., 1980a. Cauchy integral analogs for the separation and continuation of electromagnetic fields within conducting matter. Geophys. Surv. 4, 115–136.

Zhdanov, M.S., 1980b. Consideration of the effect of the World Ocean on the transient geomagnetic field by means of a finite-thickness spherical shell. Geomagn. Aeron. 20, 523–529.

Zhdanov, M.S., 1981. Continuation of non stationary electromagnetic fields in geoelectrical problems. Izv. Akad. Nauk SSSR, Phys. Earth 12, 60–69.

Zhdanov, M.S., 1984. Analogs of Cauchy Type Integrals in the Theory of Geophysical Fields. Nauka, Moscow (in Russian), 326 pp.

Zhdanov, M.S., 1986. Electrical Prospecting. Nedra, Moscow (in Russian), 316 pp.

Zhdanov, M.S., 1988. Integral Transforms in Geophysics. Springer-Verlag, Berlin, Heidelberg, New York, London, Paris, Tokyo. 367 pp.

Zhdanov, M.S., 1993. Tutorial: Regularization in Inversion Theory: CWP-136. Colorado School of Mines. 47 pp.

Zhdanov, M.S., 1999. Electromagnetic migration. In: Deep Electromagnetic Exploration. Springer-Verlag, Narosa Publishing House, New Delhi, pp. 283–298.

Zhdanov, M.S., 2001. Method of broad band electromagnetic holographic imaging. US Patent 6,253,100 B1.

Zhdanov, M.S., 2002. Geophysical Inverse Theory and Regularization Problems. Elsevier, Amsterdam, London, New York, Tokyo. 628 pp.

Zhdanov, M.S., 2006. Generalized effective-medium theory of induced polarization. In: 76th Annual International Meeting, SEG, Expanded Abstracts, pp. 805–809.

Zhdanov, M.S., 2007. The Theory of Inverse Problems in Geophysics. Nauchny Mir, Moscow (in Russian), 710 pp.

Zhdanov, M.S., 2008a. Generalized effective-medium theory of induced polarization. Geophysics 73 (5), F197–F211.

Zhdanov, M.S., 2008b. Geophysical technique for mineral exploration and discrimination based on electromagnetic methods and associated systems. US Patent 7,324,899 B2.

Zhdanov, M.S., 2009. Geophysical Electromagnetic Theory and Methods. Elsevier. 848 pp.

Zhdanov, M.S., 2010. Electromagnetic geophysics: notes from the past and the road ahead. Geophysics 75 (5), 75A49–75A66.

Zhdanov, M.S., 2015. Inverse Theory and Applications in Geophysics. Elsevier. 730 pp.

Zhdanov, M.S., Chernyavskiy, A., 2004. Rapid three-dimensional inversion of multi-transmitter electromagnetic data using the spectral Lanczos decomposition method. Inverse Probl. 20, S233–S256.

Zhdanov, M.S., Cox, L.H., 2012. Method of real time subsurface imaging using electromagnetic data acquired from moving platform. Patent No. US 9322910.

Zhdanov, M.S., Cox, L., Gribenko, A., Wilson, G.A., 2006a. Controlled-source electromagnetic inversion using quasi-analytical approximation with variable background. In: Proceedings of Annual Meeting of Consortium for Electromagnetic Modeling and Inversion, pp. 83–102.

Zhdanov, M.S., Cuma, M., Ueda, T., 2008. Three-dimensional electromagnetic holographic imaging in offshore petroleum exploration. In: 78th Annual International Meeting, SEG, Expanded Abstracts.

Zhdanov, M.S., Čuma, M., Wilson, G.A., Velikhov, E.P., Black, N., Gribenko, A., 2011a. Iterative electromagnetic migration for 3D inversion of marine CSEM data. Geophys. Prospect. 59 (6), 101–1113.

Zhdanov, M.S., Dmitriev, V.I., Fang, S., Hursán, G., 2000a. Quasi-analytical approximations and series in electromagnetic modeling. Geophysics 65, 1746–1757.

Zhdanov, M.S., Dmitriev, V.I., Gribenko, A., 2007a. Integral electric current method in 3-D electromagnetic modeling for large conductivity contrast. IEEE Trans. Geosci. Remote Sens. 45 (5).

Zhdanov, M.S., Endo, M., Cox, L.H., Cuma, M., Linfoot, J., Anderson, C., Black, N., Gribenko, A.V., 2014a. Three-dimensional inversion of towed streamer electromagnetic data. Geophys. Prospect. 62 (3), 552–572.

Zhdanov, M.S., Endo, M., Yoon, D., Čuma, M., Mattsson, J., Midgley, J., 2014b. Anisotropic 3D inversion of towed-streamer electromagnetic data: case study from the Troll West Oil Province. Interpret. 2 (3), SH97–SH113.

Zhdanov, M.S., Fang, S., 1996a. Quasi-linear approximation in 3-D EM modeling. Geophysics 61, 646–665.

Zhdanov, M.S., Fang, S., 1996b. 3-D quasi-linear electromagnetic inversion. Radio Sci. 31 (4), 741–754.

Zhdanov, M.S., Fang, S., 1997. Quasi linear series in 3-D EM modeling. Radio Sci. 32 (6), 2167–2188.

Zhdanov, M.S., Fang, S., 1999. 3-D quasi-linear electromagnetic modeling and inversion. In: Three Dimensional Electromagnetics. In: SEG Monograph. Society of Exploration Geophysicists, Tulsa, OK, pp. 233–255.

Zhdanov, M.S., Fang, S., Hursán, G., 2000b. Electromagnetic inversion using quasi-linear approximation. Geophysics 65 (5), 1501–1513.

Zhdanov, M.S., Frenkel, M.A., 1983a. The solution of the inverse problems on the basis of the analytical continuation of the transient electromagnetic field in reverse time. J. Geomagn. Geoelectr. 35, 747–765.

Zhdanov, M.S., Frenkel, M.A., 1983b. Electromagnetic migration. In: Hjelt, S.E. (Ed.), The Development of the Deep Geoelectric Model of the Baltic Shield, Part 2. Univ. of Oulu, Oulu, pp. 37–58.

Zhdanov, M.S., Golubev, N.G., 2003. Three-dimensional inversion of magnetotelluric data in complex geological structures. In: Macnae, J., Liu, G. (Eds.), Three-Dimensional Electromagnetics III. Australian Society of Exploration Geophysicists. 39 pp.

Zhdanov, M.S., Golubev, N.G., Spichak, V.V., Varentsov, I.M., 1982. The construction of effective methods for electromagnetic modeling. Geophys. J. R. Astron. Soc. 68, 589–607.

Zhdanov, M.S., Gribenko, A.V., Čuma, M., 2007b. Regularized focusing inversion of marine CSEM data using minimum vertical support stabilizer. In: 77th Annual International Meeting, SEG, Expanded Abstracts, pp. 579–583.

Zhdanov, M.S., Gribenko, A., Čuma, M., Green, M., 2012. Geoelectrical structure of the lithosphere and asthenosphere beneath the northwestern United States. J. Geol. Geosci. 1, 1–6.

Zhdanov, M.S., Hursán, G., 2000. 3-D electromagnetic inversion based on quasi-analytical approximation. Inverse Probl. 16, 1297–1322.

Zhdanov, M.S., Keller, G.W., 1994. The Geoelectrical Methods in Geophysical Exploration. Elsevier, Amsterdam, London, New York, Tokyo. 873 pp.

Zhdanov, M.S., Kennedy, W.D., Peksen, E., 2001. Foundations of tensor induction well-logging. Petrophysics 42, 588–610.

Zhdanov, M.S., Lee, S.K., Yoshioka, K., 2006b. Integral equation method for 3-D modeling of electromagnetic fields in complex structures with inhomogeneous background conductivity. Geophysics 71 (6), G333–G345.

Zhdanov, M.S., Matusevich, V.U., Frenkel, M.A., 1988. Seismic and Electromagnetic Migration. Nauka, Moscow. 376 pp.

Zhdanov, M.S., Pavlov, D.A., 2001. Analysis and interpretation of anomalous conductivity and magnetic permeability effects in time domain electromagnetic data. Part II: $S\mu$-inversion. J. Appl. Geophys. 46, 235–248.

Zhdanov, M.S., Pavlov, D.A., Ellis, R., 2002. Localized S-inversion of time domain electromagnetic data. Geophysics 67, 1115–1125.

Zhdanov, M.S., Portniaguine, O., 1997. Time domain electromagnetic migration in the solution of the inverse problems. Geophys. J. Int. 131, 293–309.

Zhdanov, M.S., Smith, R.B., Gribenko, A., Čuma, M., Green, M., 2011b. Three-dimensional inversion of large-scale EarthScope magnetotelluric data based on the integral equation method: geoelectrical imaging of the Yellowstone conductive mantle plume. Geophys. Res. Lett. 38, 1–7. L08307.

Zhdanov, M.S., Spichak, V.V., 1989a. Mathematical modeling of three-dimensional quasi-stationary electromagnetic fields in geoelectrics. DAN SSSR 309 (1), 57–60 (in Russian).

Zhdanov, M.S., Spichak, V.V., 1989b. The calculation of local and regional three-dimensional conductivity models using the balance technique. Ann. Geophys., Spec. Issue, 84–93.

Zhdanov, M.S., Spichak, V.V., 1992. Mathematical Modeling of Electromagnetic Fields in Three-Dimensional Inhomogeneous Media. Nauka, Moscow (in Russian), 188 pp.

Zhdanov, M.S., Tartaras, E., 2002. Inversion of multi-transmitter 3-D electromagnetic data based on the localized quasi-linear approximation. Geophys. J. Int. 148 (3), 506–519.

Zhdanov, M.S., Tolstaya, E., 2004. Minimum support nonlinear parameterization in the solution of 3-D magnetotelluric inverse problem. Inverse Probl. 20, 937–952.

Zhdanov, M.S., Tolstaya, E., 2006. A novel approach to the model appraisal and resolution analysis of regularized geophysical inversion. Geophysics 71, R79–R90.

Zhdanov, M.S., Traynin, P., Portniaguine, O., 1995. Resistivity imaging by time domain electromagnetic migration (TDEMM). Explor. Geophys. 26 (3), 186–194.

Zhdanov, M.S., Traynin, P., Booker, J., 1996. Underground imaging by frequency domain electromagnetic migration. Geophysics 61, 666–682.

Zhdanov, M.S., Traynin, P., 1997. Migration versus inversion in electromagnetic imaging technique. J. Geomagn. Geoelectr. 49, 1415–1437.

Zhdanov, M.S., Varentsov, I.M., Golubev, N.G., Krylov, V.A., 1990. Methods of Modeling Electromagnetic Fields. Nauka, Moscow (in Russian), 199 pp.

Zhdanov, M.S., Varentsov, I.M., Weaver, J.T., Golubev, N.G., Krylov, V.A., 1997. Methods for modeling electromagnetic fields. Results from COMMEMI – the international project on the comparison of modeling methods for electromagnetic induction. J. Appl. Geophys. 37, 1–273.

Zhdanov, M.S., Wan, L., Gribenko, A., Cuma, M., Key, K., Constable, S., 2011c. Large-scale 3D inversion of marine magnetotelluric data: case study from the Gemini Prospect, Gulf of Mexico. Geophysics 76 (1), F77–F87.

Zhdanov, M.S., Wannamaker, P.E. (Eds.), 2002. Three-Dimensional Electromagnetics. Elsevier, Amsterdam, New York, Tokyo. 290 pp.

Zhdanov, M.S., Wilson, G.A., 2004. 3-D quasi-analytical inversion of electromagnetic fields in the models with inhomogeneous background. In: 74th Annual International Meeting, SEG, Expanded Abstracts, pp. 692–695.

Zhdanov, M.S., Yoshioka, K., 2003. Cross-well electromagnetic imaging in three dimensions. Explor. Geophys. 34 (1–2), 34–40.

Zhdanov, O.N., Zhdanov, M.S., 1999. Methods for the analysis and interpretation of the sea floor electromagnetic fields. In: Deep Electromagnetic Exploration. Springer-Verlag, Narosa Publishing House, pp. 248–259.

Zhdanov, M.S., Endo, M., Sunwall, D., Mattsson, J., 2015. Advanced 3D imaging of complex geoelectrical structures using towed streamer EM data over the Mariner field in the North Sea. First Break 33 (11), 59–63.

Zienkiewicz, O.C., Taylor, R.L., 1989. The Finite Element Method, 4th ed. McGraw-Hill, New York.

Zohdy, A.A.R., 1965. The auxiliary point method of electrical sounding interpretation and its relationship of the Dar Zarrouk parameters. Geophysics 30 (4), 644–660.

Zohdy, A.A.R., 1968. A rapid graphical method for the interpretation of A- and H-type electrical soundings. Geophysics 33 (5), 822–833.

Zohdy, A.A.R., 1969. The use of Schlumberger and equatorial soundings in ground water investigations near El Paso, Texas. Geophysics 34 (5), 713–728.

Zohdy, A.A.R., 1978. Toral-field resistivity mapping and sounding over horizontally layered media. Geophysics 43 (4), 748–766.

Zollinger, R., Morrison, H.F., Lazenby, P.G., Becker, A., 1987. Airborne electromagnetic bathymetry. Geophysics 52 (8), 1127–1137.

Zonge, K.L., 1983. Case Histories of an Electromagnetic Method for Petroleum Exploration: Proprietary Data Sale. Zonge Engineering and Research Organization, Inc.

Zonge, K., 1972. Electrical Properties of Rocks as Applied to Geophysical Prospecting. Ph.D. thesis. University of Arizona. 156 pp.

Zonge, K., Wynn, J.C., 1975. Recent advances and applications in complex resistivity measurements. Geophysics 40, 851–864.

Zonge, K., Wynn, J., Urquhart, S., 2005. Resistivity, induced polarization and complex resistivity. In: Butler, D.K. (Ed.), Near-Surface Geophysics, pp. 265–300.

INDEX

Foundations of
Geophysical Electromagnetic
Theory and Methods

Michael S. Zhdanov

A fully revised guide to both theoretical and practical aspects of electromagnetic geophysics

KEY FEATURES

- Presents theoretical and methodological foundations of geophysical field theory
- Brings together fundamental theory and the most recent achievements of electromagnetic (EM) geophysical methods in the framework of a unified systematic exposition
- Discusses practical aspects of EM exploration for mineral and energy resources
- Is unique in its breadth and completeness in providing a general picture of the current state-of-the-art in EM geophysical technology

Foundations of Geophysical Electromagnetic Theory and Methods, **Second Edition**, builds on the strength of the first edition to offer a systematic exposition of geophysical electromagnetic theory and methods. The book begins with the presentation of the foundational theory of electromagnetic fields and of the methods of solution to electromagnetic forward and inverse problems. It then describes the physical-mathematical principles of the major geophysical electromagnetic methods, including direct current (DC), natural field (magnetotelluric), and controlled source electromagnetic methods in the frequency and time domain.

Written by one of the world's foremost experts, this new edition of *Foundations of Geophysical Electromagnetic Theory and Methods* highlights recent discoveries in the field, with a special focus on advances in marine and airborne electromagnetic methods. It illustrates these topics with recent case histories on practical applications in tectonic studies, mineral exploration, and off-shore hydrocarbon exploration. This is a valuable reference for geoscientists working in all areas of geophysics, including exploration geophysics, and applied physics, as well as graduate students and researchers working in the field of electromagnetic theory and methods.

Michael S. Zhdanov is a Distinguished Professor of Geophysics in the Department of Geology and Geophysics at the University of Utah in Salt Lake City and the Director of the University of Utah's Consortium for Electromagnetic Modeling and Inversion (CEMI). He is also a Full Member of the Russian Academy of Natural Sciences, Honorary Member of the Society of Exploration Geophysicists, and Fellow of the Electromagnetics Academy, USA.

ELSEVIER   elsevier.com/books-and-journals

Geophysics